PACIFIC DEEP-SEA DISCOVERIES: GEOLOGICAL AND BIOLOGICAL EXPLORATION, PATTERNS, AND PROCESSES

EDITED BY: Randi D. Rotjan, Diva Amon, William W. Chadwick and Stephen Hammond

PUBLISHED IN: Frontiers in Marine Science

frontiers Research Topics

Frontiers eBook Copyright Statement

The copyright in the text of individual articles in this eBook is the property of their respective authors or their respective institutions or funders. The copyright in graphics and images within each article may be subject to copyright of other parties. In both cases this is subject to a license granted to Frontiers.

The compilation of articles constituting this eBook is the property of Frontiers.

Each article within this eBook, and the eBook itself, are published under the most recent version of the Creative Commons CC-BY licence. The version current at the date of publication of this eBook is CC-BY 4.0. If the CC-BY licence is updated, the licence granted by Frontiers is automatically updated to the new version.

When exercising any right under the CC-BY licence, Frontiers must be attributed as the original publisher of the article or eBook, as applicable.

Authors have the responsibility of ensuring that any graphics or other materials which are the property of others may be included in the CC-BY licence, but this should be checked before relying on the CC-BY licence to reproduce those materials. Any copyright notices relating to those materials must be complied with.

Copyright and source acknowledgement notices may not be removed and must be displayed in any copy, derivative work or partial copy which includes the elements in question.

All copyright, and all rights therein, are protected by national and international copyright laws. The above represents a summary only. For further information please read Frontiers' Conditions for Website Use and Copyright Statement, and the applicable CC-BY licence.

ISSN 1664-8714
ISBN 978-2-88966-682-9
DOI 10.3389/978-2-88966-682-9

About Frontiers

Frontiers is more than just an open-access publisher of scholarly articles: it is a pioneering approach to the world of academia, radically improving the way scholarly research is managed. The grand vision of Frontiers is a world where all people have an equal opportunity to seek, share and generate knowledge. Frontiers provides immediate and permanent online open access to all its publications, but this alone is not enough to realize our grand goals.

Frontiers Journal Series

The Frontiers Journal Series is a multi-tier and interdisciplinary set of open-access, online journals, promising a paradigm shift from the current review, selection and dissemination processes in academic publishing. All Frontiers journals are driven by researchers for researchers; therefore, they constitute a service to the scholarly community. At the same time, the Frontiers Journal Series operates on a revolutionary invention, the tiered publishing system, initially addressing specific communities of scholars, and gradually climbing up to broader public understanding, thus serving the interests of the lay society, too.

Dedication to Quality

Each Frontiers article is a landmark of the highest quality, thanks to genuinely collaborative interactions between authors and review editors, who include some of the world's best academicians. Research must be certified by peers before entering a stream of knowledge that may eventually reach the public - and shape society; therefore, Frontiers only applies the most rigorous and unbiased reviews.
Frontiers revolutionizes research publishing by freely delivering the most outstanding research, evaluated with no bias from both the academic and social point of view. By applying the most advanced information technologies, Frontiers is catapulting scholarly publishing into a new generation.

What are Frontiers Research Topics?

Frontiers Research Topics are very popular trademarks of the Frontiers Journals Series: they are collections of at least ten articles, all centered on a particular subject. With their unique mix of varied contributions from Original Research to Review Articles, Frontiers Research Topics unify the most influential researchers, the latest key findings and historical advances in a hot research area! Find out more on how to host your own Frontiers Research Topic or contribute to one as an author by contacting the Frontiers Editorial Office: frontiersin.org/about/contact

PACIFIC DEEP-SEA DISCOVERIES: GEOLOGICAL AND BIOLOGICAL EXPLORATION, PATTERNS, AND PROCESSES

Topic Editors:
Randi D. Rotjan, Boston University, United States
Diva Amon, Natural History Museum (United Kingdom), United Kingdom
William W. Chadwick, Oregon State University, United States
Stephen Hammond, Office of Oceanic and Atmospheric Research (NOAA), United States

Citation: Rotjan, R. D., Amon, D., Chadwick, W. W., Hammond, S., eds. (2021). Pacific Deep-Sea Discoveries: Geological and Biological Exploration, Patterns, and Processes. Lausanne: Frontiers Media SA. doi: 10.3389/978-2-88966-682-9

Table of Contents

06 ***Discovery of an Extensive Deep-Sea Fossil Serpulid Reef Associated With a Cold Seep, Santa Monica Basin, California***
Magdalena N. Georgieva, Charles K. Paull, Crispin T. S. Little, Mary McGann, Diana Sahy, Daniel Condon, Lonny Lundsten, Jack Pewsey, David W. Caress and Robert C. Vrijenhoek

24 ***The Contribution of Fine Sieve Fractions (63–150 μm) to Foraminiferal Abundance and Diversity in an Area of the Eastern Pacific Ocean Licensed for Polymetallic Nodule Exploration***
Andrew J. Gooday and Aurélie Goineau

41 ***Patterns in Bathyal Demersal Biodiversity and Community Composition Around Archipelagos in the Tropical Eastern Pacific***
Jonatha Giddens, Whitney Goodell, Alan Friedlander, Pelayo Salinas-de-León, Charles Shepard, Brad Henning, Eric Berkenpas, Enric Sala and Alan Turchik

56 ***The NE Lau Basin: Widespread and Abundant Hydrothermal Venting in the Back-Arc Region Behind a Superfast Subduction Zone***
Edward T. Baker, Sharon L. Walker, Gary J. Massoth and Joseph A. Resing

71 ***Deep-Sea Carnivorous Sponges From the Mariana Islands***
Jon Thomassen Hestetun, Hans Tore Rapp and Shirley Pomponi

93 ***ROV Observations on Reproduction by Deep-Sea Cephalopods in the Central Pacific Ocean***
Michael Vecchione

97 ***The Extent of Fault-Associated Modern Authigenic Barite Deposits Offshore Northern Baja California Revealed by High-Resolution Mapping***
Roberto H. Gwiazda, Charles K. Paull, David W. Caress, Christina Marie Preston, Shannon B. Johnson, Eve M. Lundsten and Krystle Anderson

110 ***The Unknown and the Unexplored: Insights Into the Pacific Deep-Sea Following NOAA CAPSTONE Expeditions***
Brian R. C. Kennedy, Kasey Cantwell, Mashkoor Malik, Christopher Kelley, Jeremy Potter, Kelley Elliott, Elizabeth Lobecker, Lindsay McKenna Gray, Derek Sowers, Michael P. White, Scott C. France, Steven Auscavitch, Christopher Mah, Virginia Moriwake, Sarah R. D. Bingo, Meagan Putts and Randi D. Rotjan

131 ***Corrigendum: The Unknown and the Unexplored: Insights Into the Pacific Deep-Sea Following NOAA CAPSTONE Expeditions***
Brian R. C. Kennedy, Kasey Cantwell, Mashkoor Malik, Christopher Kelley, Jeremy Potter, Kelley Elliott, Elizabeth Lobecker, Lindsay McKenna Gray, Derek Sowers, Michael P. White, Scott C. France, Steven Auscavitch, Christopher Mah, Virginia Moriwake, Sarah R. D. Bingo, Meagan Putts and Randi D. Rotjan

133 ***Recent Eruptions Between 2012 and 2018 Discovered at West Mata Submarine Volcano (NE Lau Basin, SW Pacific) and Characterized by New Ship, AUV, and ROV Data***
William W. Chadwick Jr., Kenneth H. Rubin, Susan G. Merle, Andra M. Bobbitt, Tom Kwasnitschka and Robert W. Embley

158 ***Patterns of Fine Ash Dispersal Related to Volcanic Activity at West Mata Volcano, NE Lau Basin***
Sharon L. Walker, Edward T. Baker, John E. Lupton and Joseph A. Resing

173 ***Preliminary Observations of the Abyssal Megafauna of Kiribati***
Erik Simon-Lledó, Samuel Thompson, Andrew Yool, Adrian Flynn, Christina Pomee, John Parianos and Daniel O. B. Jones

186 ***Distributions of the Pelagic Holothurian* Pelagothuria *in the Central Pacific Ocean as Observed by Remotely-Operated Vehicle Surveys***
Gina M. Selig, Amanda N. Netburn and Mashkoor Malik

204 ***Fine Scale Assemblage Structure of Benthic Invertebrate Megafauna on the North Pacific Seamount Mokumanamana***
Nicole B. Morgan, Savannah Goode, E. Brendan Roark and Amy R. Baco

225 ***"Little Red Jellies" in Monterey Bay, California (Cnidaria: Hydrozoa: Trachymedusae: Rhopalonematidae)***
George I. Matsumoto, Bastian Bentlage, Rob Sherlock, Kristine Walz and Bruce H. Robison

239 ***Animal Community Dynamics at Senescent and Active Vents at the 9°N East Pacific Rise After a Volcanic Eruption***
Sabine Gollner, Breea Govenar, Pedro Martinez Arbizu, Lauren S. Mullineaux, Susan Mills, Nadine Le Bris, Markus Weinbauer, Timothy M. Shank and Monika Bright

257 ***Oceanographic Drivers of Deep-Sea Coral Species Distribution and Community Assembly on Seamounts, Islands, Atolls, and Reefs Within the Phoenix Islands Protected Area***
Steven R. Auscavitch, Mary C. Deere, Abigail G. Keller, Randi D. Rotjan, Timothy M. Shank and Erik E. Cordes

272 ***Discovery and Mapping of the* Triton Seep *Site,* Redondo Knoll*: Fluid Flow and Microbial Colonization Within an Oxygen Minimum Zone***
Jamie K. S. Wagner, Clara Smart and Christopher R. German

282 ***Hydrothermal Activity and Seismicity at Teahitia Seamount: Reactivation of the Society Islands Hotspot?***
Christopher R. German, Joseph A. Resing, Guangyu Xu, Isobel A. Yeo, Sharon L. Walker, Colin W. Devey, James W. Moffett, Gregory A. Cutter, Olivier Hyvernaud and Dominique Reymond

293 ***Lava Flows Erupted in 1996 on North Gorda Ridge Segment and the Geology of the Nearby Sea Cliff Hydrothermal Vent Field From 1-M Resolution AUV Mapping***
David A. Clague, Jennifer B. Paduan, David W. Caress, James McClain and Robert A. Zierenberg

318 ***Dissolved Gas and Metal Composition of Hydrothermal Plumes From a 2008 Submarine Eruption on the Northeast Lau Spreading Center***
Tamara Baumberger, Marvin D. Lilley, John E. Lupton, Edward T. Baker, Joseph A. Resing, Nathaniel J. Buck, Sharon L. Walker and Gretchen L. Früh-Green

333 ***ROV's Video Recordings as a Tool to Estimate Variation in Megabenthic Epifauna Diversity and Community Composition in the Guaymas Basin***
Pedro H. López-Garrido, James P. Barry, Juan Ignacio González-Gordillo and Elva Escobar-Briones

349 ***Control of Deep Currents on Sediment and Cold-Water Coral Distribution on the Northern Manihiki Plateau***
Sara Bashah, Kimberly C. Galvez, Gregor P. Eberli and Kasey Cantwell

358 ***Deep-Sea Debris in the Central and Western Pacific Ocean***
Diva J. Amon, Brian R. C. Kennedy, Kasey Cantwell, Kelley Suhre, Deborah Glickson, Timothy M. Shank and Randi D. Rotjan

frontiers in Marine Science

ORIGINAL RESEARCH
published: 19 March 2019
doi: 10.3389/fmars.2019.00115

Discovery of an Extensive Deep-Sea Fossil Serpulid Reef Associated With a Cold Seep, Santa Monica Basin, California

Magdalena N. Georgieva[1], Charles K. Paull[2], Crispin T. S. Little[3], Mary McGann[4], Diana Sahy[5], Daniel Condon[5], Lonny Lundsten[2], Jack Pewsey[3], David W. Caress[2] and Robert C. Vrijenhoek[2]*

[1] Department of Life Sciences, Natural History Museum, London, United Kingdom, [2] Monterey Bay Aquarium Research Institute, Moss Landing, CA, United States, [3] School of Earth and Environment, University of Leeds, Leeds, United Kingdom, [4] United States Geological Survey, Menlo Park, CA, United States, [5] NERC Isotope Geosciences Laboratory, British Geological Survey, Keyworth, United Kingdom

Multibeam bathymetric mapping of the Santa Monica Basin in the eastern Pacific has revealed the existence of a number of elevated bathymetric features, or mounds, harboring cold seep communities. During 2013–2014, mounds at ∼600 m water depth were observed for the first time and sampled by Monterey Bay Aquarium Research Institute's ROV *Doc Ricketts*. Active cold seeps were found, but surprisingly one of these mounds was characterized by massive deposits composed of fossil serpulid worm tubes (Annelida: Serpulidae) exhibiting various states of mineralization by authigenic carbonate. No living serpulids with equivalent tube morphologies were found at the site; hence the mound was termed "Fossil Hill." In the present study, the identity of the fossil serpulids and associated fossil community, the ages of fossils and authigenic carbonates, the formation of the fossil serpulid aggregation, and the geological structure of the mound are explored. Results indicate that the tubes were most likely made by a deep-sea serpulid lineage, with radiocarbon dating suggesting that they have a very recent origin during the Late Pleistocene, specifically to the Last Glacial Maximum ∼20,000 years ago. Additional U-Th analyses of authigenic carbonates mostly corroborate the radiocarbon dates, and also indicate that seepage was occurring while the tubes were being formed. We also document similar, older deposits along the approximate trajectory of the San Pedro Basin Fault. We suggest that the serpulid tube facies formed *in situ*, and that the vast aggregation of these tubes at Fossil Hill is likely due to a combination of optimal physical environmental conditions and chemosynthetic production, which may have been particularly intense as a result of sea-level lowstand during the Last Glacial Maximum.

Keywords: tubeworm, last glacial maximum, gas hydrate, vesicomyidae, Annelida, paleobiology, eastern Pacific, methane seep

OPEN ACCESS

Edited by:
Randi D. Rotjan,
Boston University, United States

Reviewed by:
Lorenzo Angeletti,
Istituto di Scienze Marine (ISMAR), Italy
Americo Montiel,
University of Magallanes, Chile

****Correspondence:***
Magdalena N. Georgieva
m.georgieva@nhm.ac.uk;
magdalena.n.georgieva@gmail.com

Specialty section:
This article was submitted to Deep-Sea Environments and Ecology, a section of the journal Frontiers in Marine Science

Received: *01 November 2018*
Accepted: *25 February 2019*
Published: *19 March 2019*

Citation:
Georgieva MN, Paull CK, Little CTS, McGann M, Sahy D, Condon D, Lundsten L, Pewsey J, Caress DW and Vrijenhoek RC (2019) Discovery of an Extensive Deep-Sea Fossil Serpulid Reef Associated With a Cold Seep, Santa Monica Basin, California. Front. Mar. Sci. 6:115. doi: 10.3389/fmars.2019.00115

INTRODUCTION

Cold seeps are remarkable marine environments characterized by the effluence of near ambient-temperature reduced fluids, usually rich in methane or hydrogen sulfide, from the seafloor. In recent years, information from autonomous underwater vehicle (AUV) surveys has greatly aided the discovery of cold seeps in the deep sea, which are recognized by the presence of patches of irregular

bathymetry in areas of otherwise undifferentiated sediment (Hovland and Judd, 1988; MacDonald et al., 2003; Wagner et al., 2013; Paull et al., 2015). Cold seeps often manifest as topographic mounds, pockmarks and outcrops of authigenic carbonates (Wagner et al., 2013), and are renowned for the often vast chemosynthesis-supported biological productivity that occurs at these sites compared to the otherwise generally food-limited deep sea. Cold seeps are also known to have been important habitats for deep-sea fauna throughout Earth's history since at least the Paleozoic (Peckmann et al., 1999b; Barbieri et al., 2004), and today, siboglinid tubeworms (Annelida), bathymodiolin mussels and vesicomyid clams (Bivalvia) thrive at seeps (Kiel, 2010), because they host chemoautotrophic endosymbionts that obtain nutrients from seeping fluids (Dubilier et al., 2008). The elevated productivity of cold seeps also provides habitats for a wealth of additional organisms that have not yet been found to possess such symbionts, such as fish, brachyuran crabs, polynoids, and serpulid tubeworms. The latter (Annelida: Serpulidae) are remarkable for their ability to form vast reef-like aggregations in shallow marine and brackish waters. While serpulids can occur in large numbers at deep-sea seeps (Olu et al., 1996a,b; Levin et al., 2012; Amon et al., 2017), they rarely construct sizeable reef structures below the photic zone. Here, we report on the discovery of, and investigations into, an unusually large accumulation of fossil serpulids within deep-sea waters that occurs in association with an active cold seep.

Serpulid worms are common in all marine environments, occurring from the intertidal down to hadal depths (Ippolitov et al., 2014), and possess an anterior end that terminates in a fan-like structure (crown) used for suspension-feeding (Kupriyanova et al., 2006). These annelids are easily recognized by their dwelling tubes, which are comprised of calcium carbonate and typically secured to a hard substrate. Members of this family are also notable for their gregarious behavior, amassing to form vast reefs by using the tubes of conspecifics as settlement substrate (ten Hove and van den Hurk, 1993). These worms can hence function as important ecosystem engineers, altering local hydrodynamics, and providing habitat structure utilized by other marine organisms (Schwindt et al., 2001), but can also accumulate to foul marine structures and modify ecosystems within which they are invasive. Large serpulid aggregations or reefs are commonly found in enclosed embayments of normal salinity or in brackish estuaries or lagoons (Bianchi et al., 1995). Conditions such as reduced competition for food and space, reduced predation, larval retention and possibly also high primary production are considered to promote reef formation behavior by serpulids, under which they can form reefs reaching tens of square meters in extent and over one meter in thickness (ten Hove and van den Hurk, 1993; Bianchi et al., 1995; Hoeksema and ten Hove, 2011). Although rare, there are also reports of serpulid reefs from deeper waters, such as serpulid-coral aggregations that were observed at depths of 450–650 m in the Adriatic Sea (Sanfilippo et al., 2013). In 1999, the discovery of an extensive reef comprised almost exclusively of the species *Serpula narconensis* at 91–105 m depth off the South Georgia continental shelf was reported, from where a single trawl collected over 1.5 tons of tubes made by this species (Ramos and San Martín, 1999). Serpulids have also been found to occur in high abundance within deep-sea cold seep environments (Vinn et al., 2013, 2014). Species of *Laminatubus* sp. are present in large numbers at the hydrothermal seeps of Jaco Scar on the Costa Rica convergent margin (Levin et al., 2012), and other serpulid species at cold seeps off northern Peru (Olu et al., 1996a), at the Barbados Accretionary Prism (Olu et al., 1996b) where they gather at high densities on concretions around mussel beds, and at seeps off Trinidad and Tobago (Amon et al., 2017). Within cold seeps, large serpulid populations are likely sustained by filter-feeding on the greater concentrations of organic matter in the water column at these sites, and have not yet been reported to possess microbial epi- or endo-symbionts.

Serpulid build-ups are also known from the fossil record, dating back to the Late Triassic (ten Hove and van den Hurk, 1993). One of the most extensive fossil serpulid reefs occurs at the Triassic-Lias boundary in southern Spain, in which a unit comprised mainly of tubes of the species *Filograna socialis* outcrops for 75 m and reaches 25 m in thickness. This reef is reported to have formed in deep water, but still within the photic zone (Braga and Lopez-Lopez, 1989). Large aggregations of tubes preserved in several fossil cold seep deposits have also been ascribed to the serpulids, such as the tube fossils of the Cretaceous Sada limestone (Nobuhara et al., 2008) and the Miocene Ca' Fornace and Marmorito carbonates of northern Italy (C.T.S. Little pers. obs.; Peckmann et al., 1999a; Kiel et al., 2018). In the Sada limestone deposit, the maximum observed thickness of the serpulid facies is greater than 6 m (Nobuhara et al., 2016). The identification of the serpulid species comprising fossil reefs can be problematic as the systematics of extant serpulids is based mainly on characteristics associated with the animals (Ippolitov et al., 2014). Nevertheless, a number of tube characteristics can be helpful such as tube aggregation, coiling/curving, attachment to substrate and external sculpture (see Ippolitov et al., 2014). Increasingly the ultrastructure of tubes is also used in relating fossil to recent taxa, in cases where the tube walls of fossil serpulids have not been significantly diagenetically altered (Vinn, 2005, 2008; Taylor and Vinn, 2006; Vinn et al., 2008a).

Multibeam bathymetric mapping of the Santa Monica Basin, southern California, has helped to reveal the existence of a number of elevated bathymetric features, or mounds, harboring cold seep communities (Normark et al., 2003; Hein et al., 2006). Exploration of these mounds using AUV-based 1-m resolution mapping and subbottom profiling, followed by ROV exploration and sampling, has revealed the presence of sub-surface gas hydrates. Paull et al. (2008) have hypothesized hydrate formation as a mechanism for mound uplift, while the proximity of some of the mounds to the trajectory of the San Pedro Basin fault system (Ryan et al., 2012) suggests that their formation may be associated with fault activity (Fisher et al., 2003; Gardner et al., 2003). During 2013–2014 Monterey Bay Aquarium Research Institute (MBARI) expeditions, an additional mound that had not previously been explored by remotely operated vehicle (ROV) was observed to be comprised predominantly of a large number of fossil serpulid tubes exhibiting various states of mineralization by authigenic carbonate. The mound was hence termed "Fossil Hill." In this study, results of extensive exploration of this

enigmatic mound are presented with the aim to characterize the physical and biological features of this anomalous structure, as well as to ascertain its mode of formation, and whether this is associated with fluid seepage.

MATERIALS AND METHODS

Seafloor Mapping and Sample Collection

High-resolution mapping and sub-bottom profiling surveys of selected topographic features within the Santa Monica Basin region were conducted in March 2013 using an AUV equipped with 400 kHz Reson 7125 multibeam sonar, 110 kHz chirp sidescan sonar, and a 1–6 kHz sweep chirp subbottom profiler (see Caress et al. (2008) for further methodological details). An objective was to explore along the inferred trace of the San Pedro Basin fault looking for the morphologies indicative of seafloor seepage sites (Paull et al., 2015), and evidence of recent movements along the fault (Ryan et al., 2012). AUV dives 20133006m1 and 20130311m1 revealed areas of anomalously rough seafloor both south or north of Santa Monica Canyon respectively, Fossil Hill being one of these (**Figure 1**). These areas were further explored during two ROV diving cruises of the R/V *Western Flyer* in May 2013 and June 2014. The AUV survey of the Fossil Hill site was repeated in April 2018 (AUV dive 201807m1) following improvement in processing software.

Samples were obtained from the Fossil Hill mound, as well as nearby seafloor exhibiting similar topography along the approximate axis of the San Pedro Basin Fault (**Figure 1**). Sample collection from these sites took place during seven dives of the ROV *Doc Ricketts*; DR476 and DR626-631 (**Supplementary Table S1**). The manipulator arms of the ROV were used to collect more heavily mineralized rock samples, while loose tube and bivalve shell rubble, as well as living bivalves, were collected using an ROV operated scoop and through push-coring (up to 22 cm long). A vibracorer mounted to the ROV was used to collect up to 165 cm long cores in areas of soft sediment. Push cores were extruded on board the ship, and all rock and fossil samples were subsequently rinsed in fresh water and dried, while live bivalves were preserved in 80% ethanol. Vibracores were logged, split, photographed and preserved at the United States Geological Survey, Menlo Park, CA, United States. **Supplementary Figure S1** shows locations of rock, vibracore, and push-core sampling at Fossil Hill. Video footage from a systematic ROV flight during DR627 was used to construct a video mosaic of a sub-region of the Fossil Hill mound (**Figure 1**). During this dive, the ROV was maintained ∼1 m above the seabed in order to collect multiple, overlapping parallel sweeps of video footage over the region of interest. Still images were later extracted from the video footage, and loaded into PhotoScan Pro (v. 1.1.6, Agisoft LLC) to build the mosaic.

Fossil Identification

Fossil serpulid tubes were photographed and imaged in greater detail using an Olympus SZH10 stereomicroscope. Five fragments of tubes from a range of diameters were also imaged using a Hitachi S-3400N-II variable pressure scanning electron microscope (SEM) at Moss Landing Marine Laboratories, CA, United States. Transverse and longitudinal broken surfaces of the tubes were mounted onto SEM stubs, gold coated, and observed using both secondary and backscatter electrons. The composition of four tube fragments was analyzed using fourier transform infrared spectroscopy (FTIR) to determine the form of calcium carbonate present in the tubes. Tubes were ground to a powder to incorporate material from all layers, and analyzed at Imperial College London, United Kingdom, in attenuated total reflectance mode. Additional fossil taxa associated with the fossil serpulid tubes were examined using a combination of light and scanning electron microscopy, using an FEI Quanta 650 FEG-ESEM at the University of Leeds, Leeds, United Kingdom. Identifications of associated taxa to the lowest possible taxonomic level were used to create a presence-absence matrix based on their occurrence within non-vibracore samples. Several non-parametric species richness estimators such as the incidence-based coverage estimator (ICE; Lee and Chao, 1994), and the iChao2 richness estimator; Chiu et al., 2014) were calculated using R (R Core Team, 2014; Chao et al., 2015). Authigenic carbonates from a subset of rock specimens were also prepared as thin sections to observe carbonate petrography.

Dating of Fossil Fauna and Authigenic Carbonates

Eight tube and bivalve fragments not cemented by methane-derived authigenic carbonates (MDAC, Paull et al., 1992) were selected for radiocarbon analysis. These were cleaned to ensure removal of attached debris and mineralization using the following technique: cleaning using paintbrush and fresh water, placement in an ultrasonic bath for 5 min, suspension in weak hydrochloric acid (0.25 N HCl) for 2 min, placement in distilled water in an ultrasonic bath for 5 min, drying in an oven at 50°C for ∼1 h. Radiocarbon measurements were obtained by accelerator mass spectrometry (AMS) at the National Ocean Sciences Accelerator Mass Spectrometry (NOSAMS) facility, Woods Hole Oceanographic Institution, MA, United States. The radiocarbon ages were obtained by a $^{14}C/^{12}C$ ratio using a ^{14}C half-life of 5,568 years (Stuiver and Polach, 1977). The raw radiocarbon ages were then converted to calibrated calendar ages (cal yr B.P.) using the CALIB 7.1 program (Stuiver et al., 2018). The calibrated ages are reported as the peak probability ages and the 2 sigma ranges are also included (**Table 1**). A reservoir age of 1750 year was applied to the worm tubes and mollusks following Mix et al. (1999) because they occupied the same substrate as bottom-dwelling (benthic) foraminifera.

The above cleaning steps were performed to minimize any effect of old carbon from seepage fluids on radiocarbon dates (Paull et al., 1989; Pohlman et al., 2011), while for samples affected by obvious MDAC mineralization, U-Th dating was used in order to eliminate any age bias from old carbon. MDAC cements present on the outer walls of serpulid tubes and bivalve shells, as well as infilling serpulid tubes, were dated using this technique at facilities at the NERC Geochronology and Tracers Facility, British Geological Survey, United Kingdom, following the analytical protocol outlined by

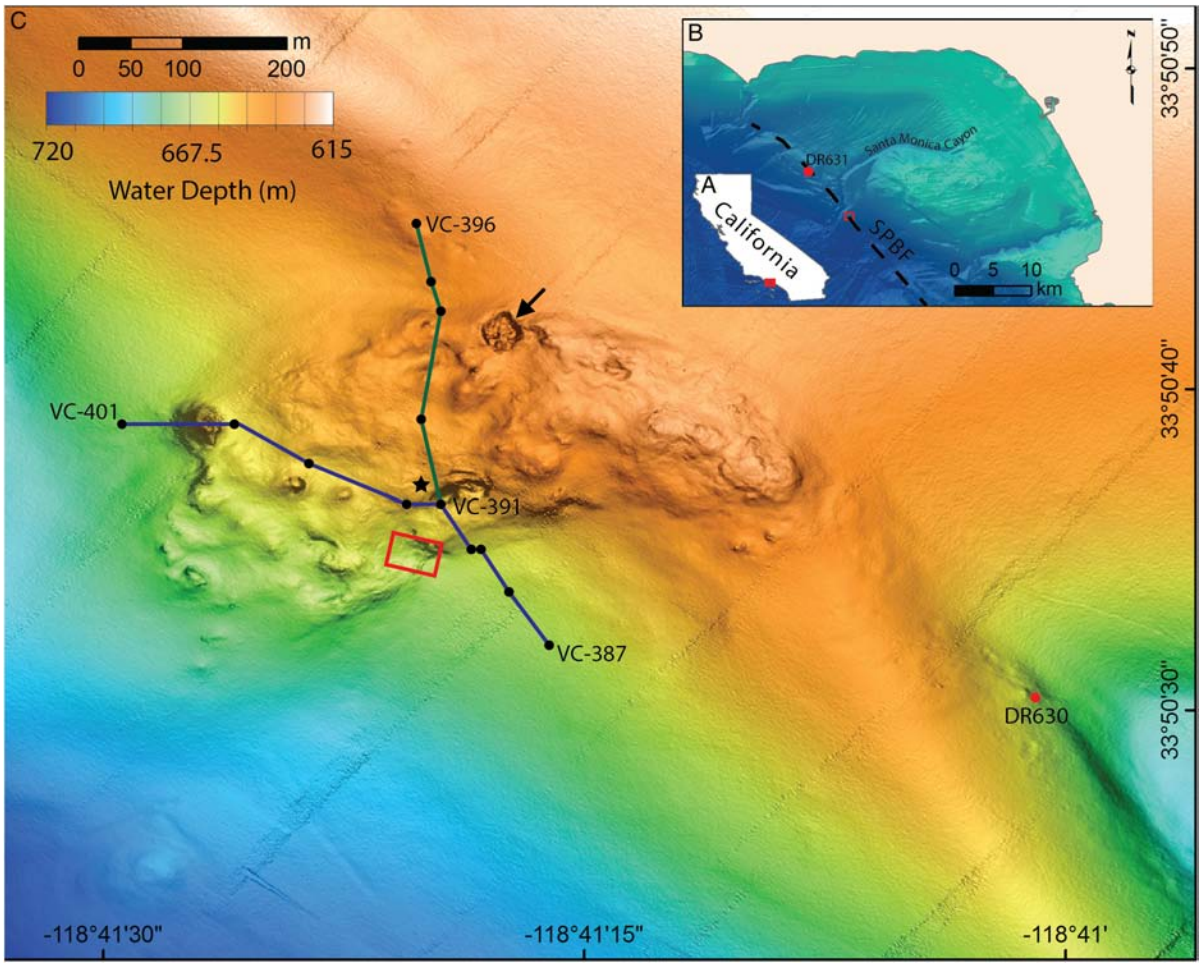

FIGURE 1 | Location and bathymetry of Fossil Hill. **(A)** Map of California showing the location of the Santa Monica Bay area, red box shows area pictured in **B**. **(B)** Santa Monica Bay showing the location of Fossil Hill (red box, pictured in detail in **C**) in relation to the Santa Monica canyon and the approximate position of the San Pedro Basin fault (SPBF, dashed black line; Ryan et al., 2012). The location of the sampling site northeast of Fossil Hill (DR631) is also shown. **(C)** Detailed bathymetry of the Fossil Hill mound. Blue and green lines show the tracks of the elevation profiles in **Figure 6**. The black dots within these tracks represent individual vibracore locations, with start, and end vibracore numbers labeled. Red box shows area in which video-mosaic (**Figure 3**) was performed. Black star denotes the location of an extensive live clam and bacterial mat bed, and a large pockmark (27 m wide, 4 m deep) on the northern margin is indicated with an arrow. The sampling site southeast of Fossil Hill (DR630) is labeled.

Crémière et al. (2016). Additional carbon ($\partial^{13}C$) and oxygen ($\partial^{18}O$) isotope measurements conducted at the above facility were also used to confirm whether Fossil Hill carbonates are methane-derived **(Supplementary Table S2)**.

Age interpretation of U-Th isotope data from MDAC requires a correction for the amount of initial ^{230}Th incorporated into the carbonate either via the inclusion of detrital material or through adsorption of Th from the decay of dissolved U in the water column onto particle surfaces. In order to determine a site-specific correction for Fossil Hill, the U-Th composition of five sediment samples from four vibracores collected during dive DR630 was analyzed. Unfortunately, the sediment samples proved unsuitable for the purpose of determining an initial ^{230}Th correction, as their measured ($^{234}U/^{238}U$) activity ratios were greater than 1, indicating the presence of young $CaCO_3$ of either biogenic or authigenic origin. Instead, the initial ^{230}Th correction used for the Fossil Hill MDAC was interpolated for a water depth of 650 m based on U-Th measurements of carbonate-free sediment samples from Baltimore Canyon (ca. 400 m depth) and Norfolk Canyon (ca. 1600 m depth) on the US Atlantic margin (Prouty et al., 2016). All U-Th data are listed in (**Supplementary Table S3**), with a selection of dates considered accurate presented in **Table 2**.

RESULTS

Characteristics of Fossil Hill and Associated Carbonate Deposits

The AUV surveys reveal that Fossil Hill has a lobate shape which is approximately 500 m long and 270 m at its widest extent (**Figure 1C**). Fossil Hill is positioned on seafloor which gently

TABLE 1 | Radiocarbon (^{14}C) dates of Fossil Hill bivalve shells and serpulid tubes.

NOSAMS accession number	Sample reference	Sample description	Radiocarbon age (^{14}C yrs BP)	Error	$\delta^{13}C_{VPDB}$ (‰)	Minimum calibrated age (cal yrs BP) 2 sigma	Maximum calibrated age (cal yrs BP) 2 sigma	Mean calibrated age (cal yrs BP) 2 sigma
OS-121607	DR476 A-1	*E. elongata* bivalve shell	1,260	20	−1.4	Recent	Recent	Recent
OS-121608	DR627 BIO-2	*P. soyoae* bivalve shell	21,100	60	1.06	23,037	23,540	23,294
OS-121623	DR476 A-1	Serpulid tube	22,300	65	−18.06	24,437	25,047	24,729
OS-121624	DR626 PSC-66	Serpulid tube	21,500	60	−11.11	23,550	24,006	23,778
OS-121626	DR626 R-4	Serpulid tube	21,500	55	−12.26	23,556	24,001	23,778
OS-121625	DR627 PSC-53	Serpulid tube	21,800	60	−14.88	23,898	24,321	24,108
OS-121742	DR629 VC-400 (159–163 cm depth)	Serpulid tube	21,800	120	−12.87	23,799	24,420	24,110
OS-121743	DR629 VC-400 (159–163 cm depth)	Serpulid tube	22,400	130	−12.98	24,456	25,264	24,863
OS-113658	DR629 VC-400 (160–162 cm depth)	Serpulid tube	22,300	80	−13.01	24,419	25,077	24,733

All samples were analyzed using hydrolysis and all radiocarbon results were corrected for isotopic fractionation using unreported $\delta^{13}C$ values measured on the accelerator. $\delta^{13}C$ values are reported relative to the VPDB standard.

TABLE 2 | U-Th composition and age interpretation of Fossil Hill methane-derived authigenic carbonate (MDAC) samples and shells and tubes.

Sample reference	Sample description	^{238}U (ppm)	^{232}Th (ppm)	$^{230}Th/^{232}Th$	$^{234}U/^{238}U$	U-Th age (corr. ka BP)
DR626 R-1 A	MDAC infill of serpulid tube	12.2	1.697	7.2	1.1471 ± 0.021	31.7 ± 2.9
DR626 R-2 C	MDAC infill of serpulid tube	13.4	1.908	8.8	1.1513 ± 0.022	43.4 ± 2. 9
DR626 R-4 A	MDAC infill of serpulid tube	10.1	3.228	3.6	1.1396 ± 0.051	30.9 ± 7.1
DR626 R-4 B	MDAC surrounding tube	6.4	1.168	3.8	1.1320 ± 0.028	17.4 ± 3.8
DR626 R-4 C	MDAC infill of serpulid tube	4.3	0.947	3.7	1.1371 ± 0.034	20.6 ± 4.6
DR627 R-4 tube 1	Serpulid tube	58.0	0.287	118.8	1.1416 ± 0.002	20.1 ± 0.1
DR627 R-4 tube 2	Serpulid tube	38.2	0.616	37.7	1.1470 ± 0.003	20.3 ± 0.3
DR627 shell 1 B	*P. soyoae* bivalve shell	1.0	0.049	10.7	1.1495 ± 0.007	16.1 ± 0.8
DR627 shell 2 A	*P. soyoae* bivalve shell	2.8	0.175	8.8	1.1465 ± 0.008	17.0 ± 1.1
DR627 shell 2 B	*P. soyoae* bivalve shell	2.6	0.102	13.7	1.1471 ± 0.005	17.2 ± 0.7
DR628 R-5 A	MDAC cementing bivalve shells	3.1	0.055	13.7	1.1470 ± 0.003	7.1 ± 0.4
DR628 R-5 B	MDAC cementing bivalve shells	3.7	0.044	19.5	1.1485 ± 0.002	7.1 ± 0.2
DR629 R-3 1/2 A	MDAC surrounding tube	2.0	0.047	27.2	1.1499 ± 0.004	21.3 ± 0.5
DR629 R-3 2/2 A	MDAC surrounding tube	2.5	0.034	43.1	1.1478 ± 0.004	19.0 ± 0.3
DR629 R-3 1/2 B	MDAC infill of serpulid tube	2.9	0.067	22.2	1.1454 ± 0.003	16.5 ± 0.5
DR629 R-3 2/2 B	MDAC surrounding tube	2.7	0.065	24.4	1.2326 ± 0.016	17.6 ± 0.5
DR630 R-3 B	MDAC cementing bivalve shells	3.4	0.101	21.2	1.1459 ± 0.005	20.8 ± 0.6
DR630 R-4 A	Late-stage cement, MDAC with serpulid tubes	1.3	0.125	17.2	1.1342 ± 0.009	31.7 ± 1.1

Uncertainties are ±2s (abs).

slopes to the south-west with the highest elevation reaching 622 m depth, and extending down slope to 672 m depth. The surface of Fossil Hill is 5–15 m higher than the surrounding seafloor with an overall uneven appearance, punctuated by discrete circular depressions and topographic highs. The roughly circular depressions range from a few meters to 27 m in diameter, the latter being a ∼4 m deep sinkhole or pockmark which occurs on the northern margin of Fossil Hill (**Figure 1C**, arrowed). The circular topographic highs are less than 50 m in diameter and up to 6 m high. The seafloor lineation that is interpreted as the approximate trace of the San Pedro Basin fault (Ryan et al., 2012) runs very close (∼50 m) to the eastern edge of Fossil Hill (**Figure 1B**). Sub-bottom chirp profiles across both Fossil Hill and the site 290 m to the southeast show a strong seafloor reflection where the carbonate rocks are exposed on the seafloor. Fossil Hill is positioned on top of a ridge-like tectonic feature (**Figure 2**), and appears to have formed on the eroded crest of this ridge where accumulating sediment was thin or absent. A thin drape of sediment seems to have covered the northern and southern ends of Fossil Hill, while reflectors passing under the deposit indicate that it is less than 5 m thick (**Figures 2A–A',D–D'**). On the flanks of Fossil Hill, the strong reflector dives into the subsurface and is onlapped by a package of finely layered reflectors that are up to 45 m thick (**Figures 2C–C'**). This geometry reveals that the Fossil Hill deposit and the southeastern outcrop continue into the subsurface.

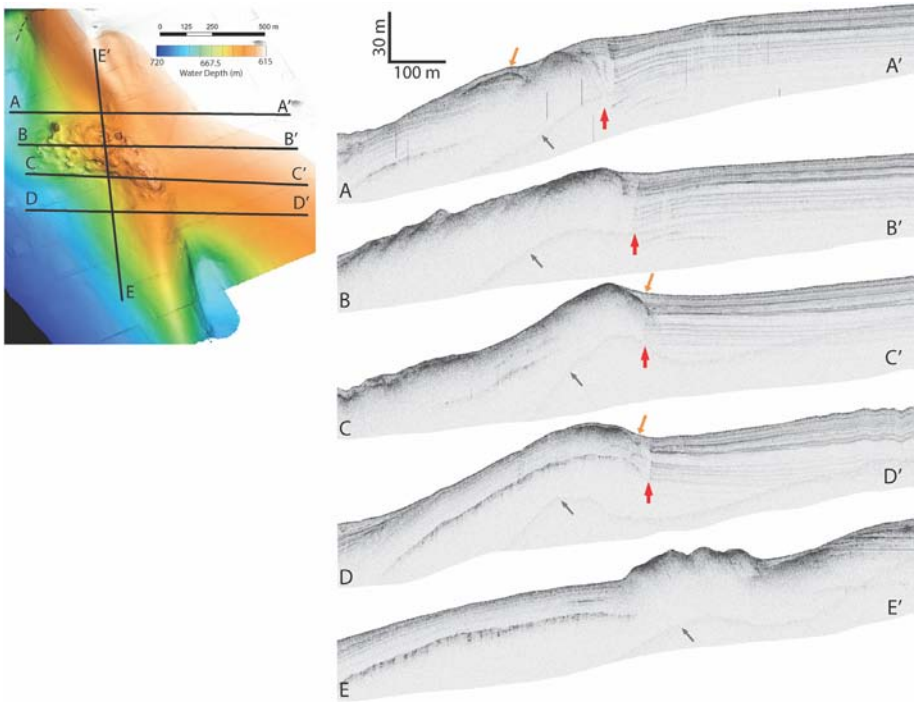

FIGURE 2 | Chirp profiles taken across the Fossil Hill main mound structure. Colored insert shows the locations of the paths of profiles **A–A'**, **B–B'**, **C–C'**, **D–D'**, **E–E'**. The locations of recent fault offsets (red arrows), sediment drape covering or lapping onto the mound (orange arrows), and artifacts associated with a multiple reflection off the sea surface (gray arrows) are shown.

The ROV surveys show that large slabs or blocks of carbonate rock are exposed between areas of sediment drape on the surface of Fossil Hill (**Figure 3**). The carbonate rocks are separated by cracks and gullies, and holes at the bases of these reveal >10 cm high open cavities underneath the slabs (**Figure 3**). The large pockmark to the north of Fossil Hill (**Figure 1C**) is rimmed by large flattened carbonate slabs that at multiple locations are sloping into the crater (**Figure 4A**), and the crater floor is littered with boulders that appear to be a former carapace that has fallen into the depression.

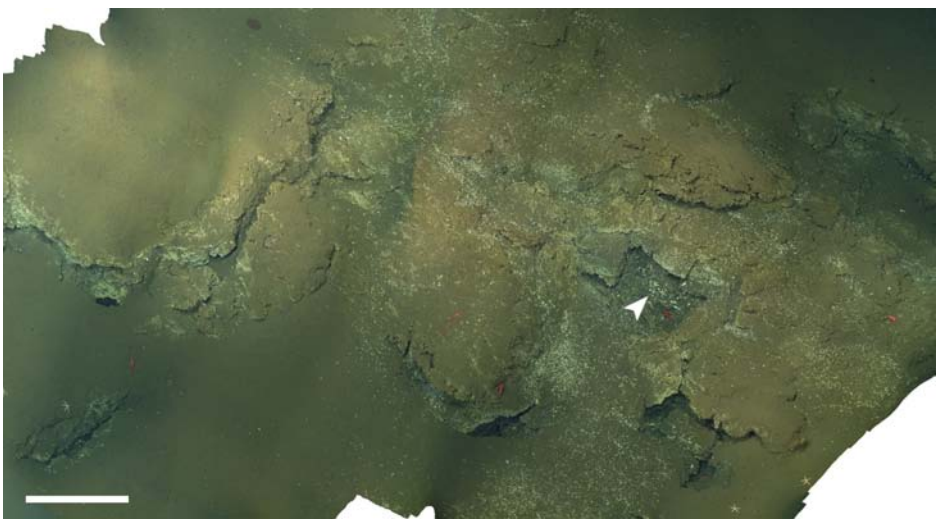

FIGURE 3 | Video-mosaic of a section of Fossil Hill (area shown in **Figure 1C**). White arrow head shows locations of the depression with overhang figured in more detail in **Figure 4E**, scale bar is approximately 2 m.

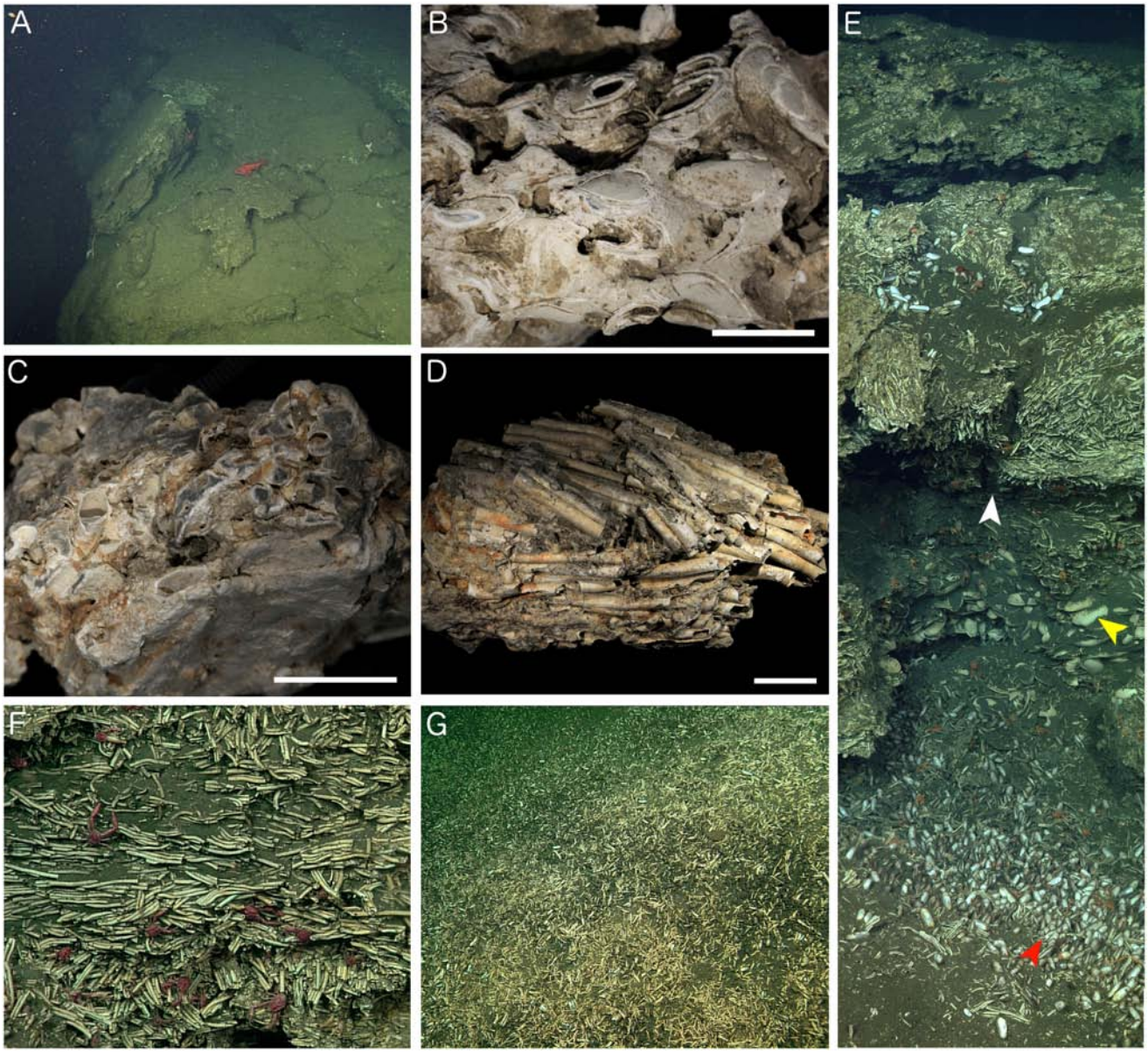

FIGURE 4 | Characteristics of Fossil Hill. **(A)** Large carbonate slabs on the edge of large pockmark structure (**Figure 1C**) which appear to be sliding into the hole (hole is to the left in the image). **(B)** Carbonate rock recovered south of the main Fossil Hill mound containing many preserved bivalves, sample DR630 R-3, and scale bar is 20 mm. **(C)** Fossil Hill carbonate with embedded worm tubes, sample DR629 R-2, and scale bar is 20 mm. **(D)** Densely packed and aligned tube fragments that are only weakly cemented by carbonate, DR626 R-4, and scale bar is 20 mm. **(E)** Mosaic of the wall of a small depression pictured in **Figure 3**, showing interlayered fossil worm tubes and bivalve shells. Perspective of **F** (white arrow), large bivalve shells (yellow arrow), and smaller living bivalves (red arrow) are highlighted. **(F)** Detail of the fossil worm tubes from the depression in **E** (white arrow), showing that they are only weakly cemented together and are aligned in parallel. Red munidopsid squat lobsters were common. **(G)** Slope on the southern side of Fossil Hill littered with tube and bivalve hash.

Neither gas bubbles or gas hydrates were observed during the ROV explorations.

The majority of samples of authigenic carbonate rock from Fossil Hill contained fossil serpulid worm tubes as well as bivalve and gastropod shells (**Figures 4B–D** and **Supplementary Table S1**), held together with variable amounts of carbonate cement comprised of isopachous fibrous aragonite (**Figure 5**). Most rock samples primarily contained worm tubes. The worm tube-dominated samples exhibited variable degrees of cementation, ranging between rock exhibiting many tubes filled with carbonate cement and strongly cemented together (**Figure 4C**) to weakly cemented tubes (**Figure 4D**). Tubes within rock samples also exhibited altering orientations, at times being mostly aligned in parallel (**Figures 4D,F**). Bivalve and gastropod shells rarely dominated carbonate rock faunal content (**Figure 4B**). The authigenic carbonate cements comprised a

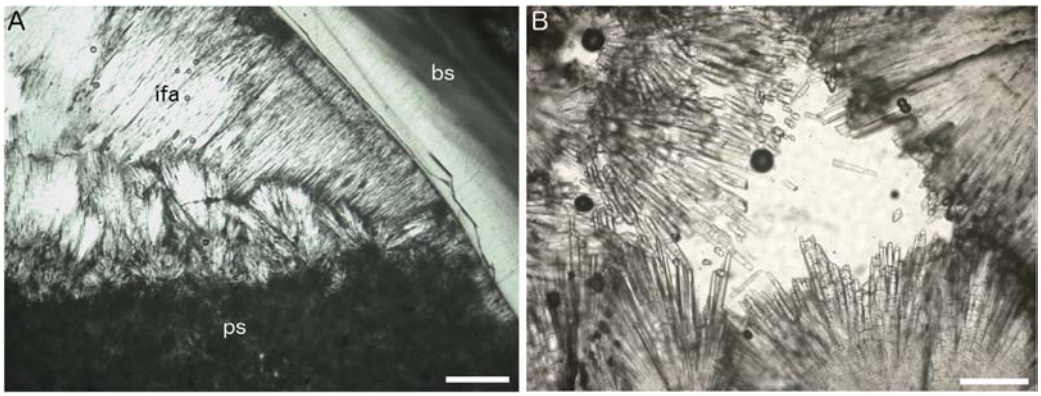

FIGURE 5 | Petrographic thin section images of Fossil Hill seep carbonates. **(A)** Isopachous fibrous aragonite cement (ifa) and peloidal micritic sediment (ps) forming geopetal fill within shelter cavity formed by articulated vesicomyid bivalve shell (bs), plain polarized light, sample DR630 R-3, and scale bar is 200 μm. **(B)** Detail of isopachous fibrous aragonite crystals, plain polarized light, sample DR629 R-5, and scale bar is 80 μm.

variable proportion of dark micrite, sometimes with distinct peloids (**Figure 5A**), and isopachous fibrous aragonite, often growing into open spaces within serpulid tubes and articulated bivalve shells (**Figures 5A,B**). In these cases the micritic cements obviously formed before the aragonite cements. In some serpulid worm tube-rich samples, they occurred as geopetal structures, indicating the tubes were horizontal to the palaeo-seafloor while they were being mineralized and after the death of the worms forming them. This was evident in the orientation of some the tubes in **Figure 4F**. Many of the carbonate rock samples were heavily corroded (e.g., **Figures 4B,C**) and had a chalky texture. Further, some had iron and manganese-rich crusts on the surfaces exposed to seawater, indicating they had been present on the seafloor for a considerable period of time. In addition, encrusting organisms were present on some of the samples, including bryozoans (*Schizoporella* species), small serpulids and sponges.

A worm tube-rich deposit was especially evident within one of the depressions encountered with the ROV (**Figures 3**, **4E**), in which a large proportion of the walls were exclusively built up of loose worm tubes aligned in parallel to each other (**Figure 4F**). These tubes were positioned on top of a layer of large bivalve shells with a shell length of up to 100 mm, while the base of the depression contained smaller, living bivalves with a shell length of up to 48 mm (**Figure 4E**, see section "Taxa Associated With the Fossil Serpulids"). Worm tube and bivalve shell rubble was also found to be eroding from these loosely consolidated deposits, and to be flowing down slopes (**Figure 4G**) as well as collecting within depressions. Vibracores collected in areas of soft sediment on Fossil Hill revealed that in some areas, depths of over 1 m of tube rubble had accumulated (**Figure 6** and (**Supplementary Table S1**) which were generally overlain by bivalve shell rubble, however tubes and bivalves were mixed together in a number of the cores. While the tubes were very abundant throughout Fossil Hill, no live animals were found within the tubes and no live bivalves with a shell length of up to 100 mm and pictured in **Figure 4E** were observed. Living bivalves (shell length of up to 48 mm) were abundant at Fossil Hill, occurring in depressions between carbonate slabs (**Figure 4E**), and colonizing an extensive patch at high densities at which they were also overgrown by bacterial mats (location shown in **Figure 1**). Subsequent morphological and molecular investigations showed that the living bivalves are predominantly the vesicomyid species *Ectenagena elongata*. Indications of the local reworking of the Fossil Hill deposit, and the presence of living bivalves in depressions (e.g., **Figure 4E**), appear to disrupt stratigraphic order at the site, and hence make it difficult to derive age relationships from stratigraphy.

Two other regions identified as elevated areas of rough topography in the 1-m bathymetric grids lying along the axis of the San Pedro Basin Fault were also visited during ROV dives DR630 and DR631 (**Figure 1**). They were found to have similar deposits consisting of fossilized serpulid tubes, bivalves and gastropods entombed within authigenic carbonates. The first (visited on ROV dive DR630) is a ∼5 m outcrop with >1 m of relief in 660 m water depth, located 290 m to the southeast of Fossil Hill on the flanks of the ridge (**Figure 1C**). The other (DR631) is within a ∼1.6 km long and >350 m wide area located 7.9 km northwest of Fossil Hill on the north side of Santa Monica Canyon in 509–530 m water depths, and lying on the extension of the same ridge (**Figure 1B**). The carbonate rock samples from these two sites generally contained fewer serpulid tubes and much less authigenic aragonite cement than the Fossil Hill samples, with these cements forming thin veins within often siliciclastic-rich micrites. The exposed surfaces of many of the DR630 and DR631 samples were heavily corroded and bored by *Polydora* sp. annelid worms. They were often also encrusted by bryozoans (including *Haywardipora* cf. *orbicula* and *Schizoporella* species), small serpulids, hydroids and sponges. These are all indications of long seafloor exposure.

Fossil Hill Paleo-Community

Fossil Serpulid Tubes

No complete worm tubes were found, however, the lack of diagenetic alteration of many of the Fossil Hill tube fragments enabled their morphology to be assessed in detail. The tubes either occurred singly, or more commonly as two or more

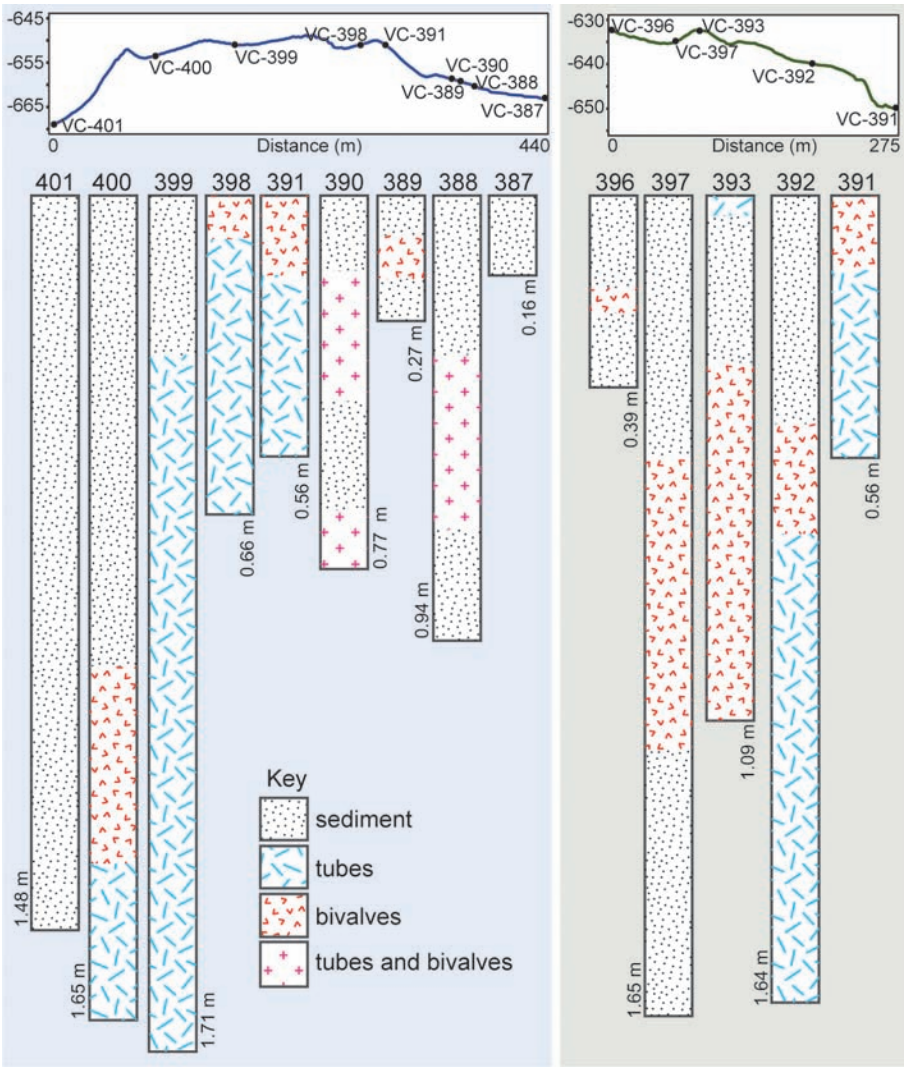

FIGURE 6 | Elevation profiles through parts of Fossil Hill along which vibracores were collected, and contents of cores (78 mm diameter) collected along the above profiles. Annotations on cores show core depths in meters, and sediment refers to fine-grained hemipelagic sediment. Tracks along which elevation profiles were created are illustrated in **Figure 1C**.

attached to each other along a longitudinal edge (**Figures 7A,B**). The majority of fragments were straight with only occasional strongly sinuous tubes observed (**Figures 7A,B**) and were generally circular or near-circular in cross-section. The tubes ranged from 1 to 7 mm in diameter (mean = 3.5 mm, n = 219; (**Supplementary Table S1**), very small tubes up to 1 mm in diameter were occasionally observed, and several were found attached to larger tubes (**Figure 7C**). The outer tube walls exhibited a texture of closely spaced, fine transverse wrinkles or growth-lines, that were more obvious in a subset of the tubes, and also appeared to be present in the tube layer below the outermost (**Figure 7D**). Many of the tubes also contained a single distinct undulating keel on their outer surfaces (**Figures 7A,E**), as well as peristomes, or occasional thickenings of short transverse sections of the tube wall (**Figure 7F**). Intricate ribbed calcareous tabulae were also found inside a subset of the tubes (**Figure 7G**). The above morphological characteristics were generally shared across the majority of tube fragments observed from Fossil Hill.

Analysis of the ultrastructure of the tubes (**Figure 8**) revealed them to be comprised of two distinct layers – a fine-grained inner layer and a coarser-grained outer layer (**Figure 8A**). The innermost tube layer was composed of acicular crystallites approximately 5 μm in length, arranged in multiple orientations and known in serpulid tubes as an irregularly oriented prismatic (IOP) tube ultrastructure (**Figure 8B**). This texture continued further into the tube wall, where it was partially mixed with homogeneous carbonate cement (**Figure 8C**), or was in patches replaced by a grainy texture that is either primarily comprised of homogeneous cement, or is a recrystallized version of

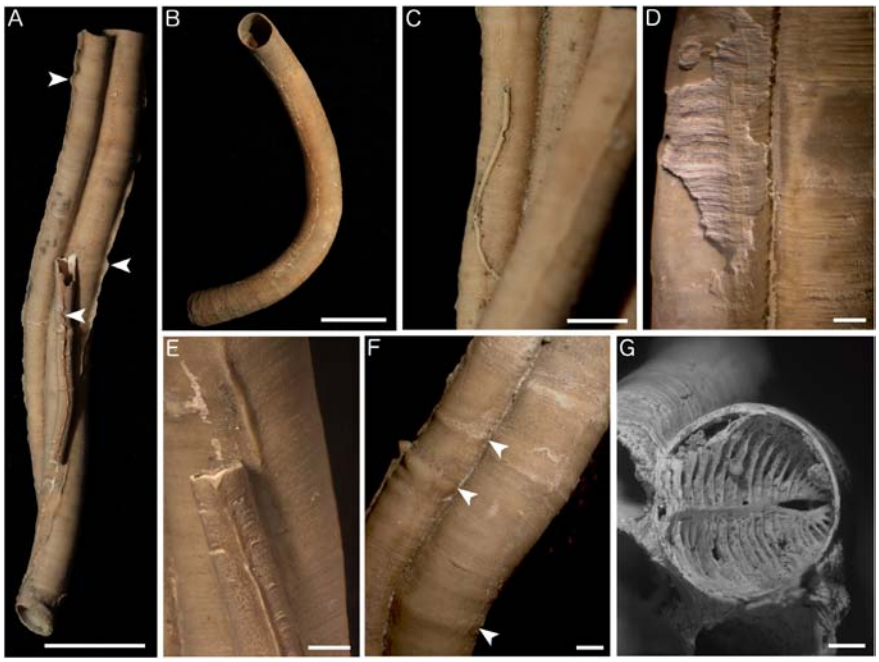

FIGURE 7 | Morphology of Fossil Hill serpulid tubes. **(A)** Several attached tube fragments with keels (white arrows) showing gregarious growth, sample DR476 A-1, and scale bar is 10 mm. **(B)** Curved nature of some of the fragments, sample DR629 PSC-52, and scale bar is 10 mm. **(C)** Small tube attached to larger tube, sample DR626 PSC-66, and scale bar is 2 mm. **(D)** Detail of transverse wrinkles apparent on some outer tube surfaces which are also present in the tube layer beneath the outermost, sample DR476 A-1, and scale bar is 1 mm. **(E)** Detail of tube keels, sample DR476 A-1, and scale bar is 1 mm. **(F)** Detail of peristomes occasionally present on the tubes (white arrows), sample DR476 A-1, and scale bar is 1 mm. **(G)** Detail of a tabula inside one of the tubes, sample DR476 A-1, and scale bar is 1 mm.

the irregularly oriented prismatic texture in **Figures 8B,C**. Longitudinal sections of tubes also revealed that the irregularly oriented prismatic texture was more intact toward the inside of the tube wall, and becomes increasingly homogeneous in nature toward the outer tube wall (**Figure 8E**). The crystals of the outer tube wall are approximately 25–30 μm in length and represent a spherulitic prismatic structure (SPHP) (**Figure 8F**). Comparison to established FTIR spectra for calcite and aragonite as well as mixtures of the two forms (Loftus et al., 2015) revealed that the Fossil Hill serpulid tubes to be predominantly comprised of calcite (based on the absence of a double peak at the 711 and 700 cm^{-1} wavelength positions; see **Supplementary Figure S2**).

We interpret all of the tubes as belonging to the same species, as significant differences between them were not observed (smaller differences could be due to intraspecific variation and the observed presence of a range of ontogenic stages), and as dense serpulid settlement is often dominated by a single taxon. The long, straight sections of the Fossil Hill serpulid tube fragments are typical of dense settlement of these annelids, which often results in tubes growing in an upright position away from their settlement substrate and leads to parallel erect tube morphologies (ten Hove, 1979). Gregarious behavior and reef formation is commonly observed in serpulid genera such as *Hydroides*, *Ficopomatus*, and *Serpula*, all of which are known from the eastern Pacific (Bastida-Zavala, 2008), however, generally not from deep waters. The size of the Fossil Hill tubes is consistent with those made by *Serpula* and *Protula*, however *Serpula* tubes commonly have funnel-shaped peristomes (Ippolitov et al., 2014; **Figures 2F,G**) which were not observed on any of the Fossil Hill tubes, and *Protula* tubes from the region do not have peristomes (Reish and Mason, 2003). The species *Serpula columbiana* is described from the west coast of North America and thus locally to Fossil Hill, but *S. columbiana* tubes also notably lack the longitudinal keels observed on the Fossil Hill tubes (Kupriyanova, 1999). In addition, the ultrastructure of the tubes of three *Serpula* species examined by Vinn et al. (2008b) does not match that of the Fossil Hill tubes.

Deep-sea serpulid genera include *Bathyvermilia*, *Neovermilia* and *Laminatubus*, and the occurrence of the Fossil Hill tubes in deep water, their presence in great numbers, as well as and the undulating keel observed on the larger tube fragments from Fossil Hill, are features more consistent with genera such as *Neovermilia* and *Laminatubus* which can also have similar keels and can occur in vast numbers at deep-sea sites of organic enrichment (E. Kupriyanova *pers. comm.*). The tube ultrastructure presented by the Fossil Hill tubes of an inner IOP layer and an outer SPHP layer, as well as their calcite composition, is also observed in *Laminatubus alvini* tubes (ten Hove and Zibrowius, 1986). The latter species is described from eastern Pacific hydrothermal vents and can have substantial unattached tube portions with a circular cross-section, however, comparison of these sections with those of Fossil Hill tubes revealed differences in the smoothness of the outer tube wall, as well as degree of undulation of the keels. *Neovermilia* has

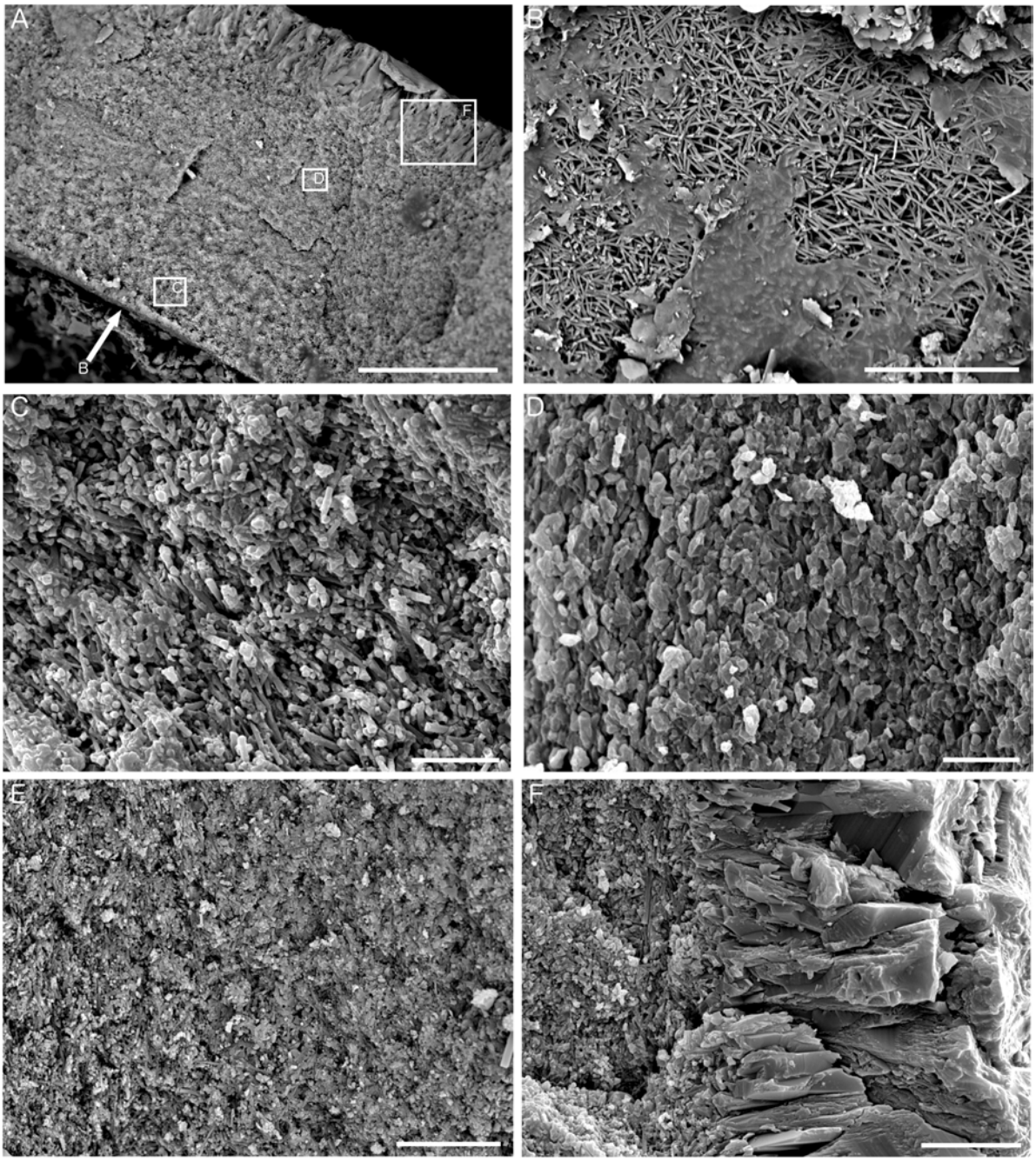

FIGURE 8 | Ultrastructure of Fossil Hill tubes. **(A)** Transverse section of a tube showing fine-grained inner layer and coarse-grained outer layer, sample DR476 A-1, and scale bar is 50 μm. Arrow shows perspective of **B**, and boxes show representative locations for the textures pictured in **C**, **D**, and **F**. **(B)** View looking down onto the inner tube surface showing irregularly oriented prismatic (IOP) ultrastructure comprised of crystallites approximately 5 μm in length, sample DR626 R-4, and scale bar is 20 μm. **(C)** Detail of inner tube layer in transverse section showing IOP ultrastructure with homogeneous cement, sample DR626 R-4, and scale bar is 10 μm. **(D)** Detail of outer part of fine-grained tube layer showing a grainy appearance, sample DR626 R-4, and scale bar is 5 μm. **(E)** Fine-grained inner tube layer in transverse section showing a transition from a prismatic structure to a grainy/platy structure from left to right, sample DR629 BB, and scale bar is 15 μm. **(F)** Detail of outer coarse-grained tube layer showing spherulitic prismatic (SPHP) ultrastructure, sample DR626 R-4, and scale bar is 10 μm.

not yet been documented from the above region, although there is some similarity in tube ultrastructure (Vinn et al., 2008b). There is also very little information on the occurrence of tabulae in the tubes of modern serpulid species from the genera mentioned above. These "floors" inside serpulid tubes form in response to damage of the posterior tube ending, and are likely produced through the pygidium of the serpulid worm acting as a mold for carbonate precipitation (Hedley, 1958).

Tabulae could thus potentially be formed by a variety of serpulids, and their morphology can be somewhat variable even within a species, thus diminishing their utility taxonomically. Based on the above considerations, the morphology and ultrastructure of the Fossil Hill serpulid tubes is most consistent with the deep-sea genus *Laminatubus*, and we therefore give them the tentative identification of ?*Laminatubus*. The tubes may indeed belong to a now extinct species despite their recent age, or the conditions which led to such a large proliferation of these serpulids may have produced particular tube morphotypes that have not yet been observed in extant species.

Taxa Associated With the Fossil Serpulids

Many of the Fossil Hill samples contained dead benthic mollusk shells in addition to the serpulid tubes (**Supplementary Table S4**). *E. elongata* was the most common of these associated mollusks, and many specimens in the vibracores (**Figure 6**) and also as rubble on slopes (**Figure 4G**) appeared relatively fresh, with remaining periostracum and a lack of overgrowing authigenic carbonate cement, indicating they were relatively young amongst the rest of the samples (see section "Ages of Fossil Hill Faunas and Authigenic Carbonates"). Other specimens of *E. elongata* in the rock samples were worn and chalky, indicating a greater age. Other bivalve taxa in the Fossil Hill samples included species that are known or strongly suspected to host sulfide-oxidizing chemosymbionts in live specimens. These were the solemyid *Acharax johnsoni* (**Figure 9I**), the vesicomyids *Archivesica packardana* (**Figures 3B**, **9C**), *Phreagena soyoae* (=*P. kilmeri* jr. syn.) (**Figures 4E**, **9A**) and *Pliocardia stearnsii*, the lucinid *Lucinoma aequizonata* (**Figure 9D**), and the thyasirids *Thyasira flexuosa* (**Figure 9E**) and *Axinopsida serricata* (**Figure 9F**). The vesicomyid taxa are all known from methane seep sites further north in Monterey Bay (e.g., Goffredi and Barry, 2002; Johnson et al., 2016). The other bivalve taxa are typical of deep-sea fauna in the East Pacific: the pectinid *Delectopecten vancouverensis* (**Figure 9H**) and the nuculid *Nucula carlottensis* (**Figure 9G**; Coan et al., 2000).

The benthic gastropods in the Fossil Hill samples (**Supplementary Table S4**) are a mixture of taxa occurring at other methane seep sites to the north and south, including the peltospirid *Depressigyra* sp. (**Figure 9J**), the leptodrilid *Lepetodrilus* sp. (**Figure 9U**), the neolepetopsid *Paralepetopsis* sp. (**Figures 9P,Q**), the provannids *Provanna laevis* (**Figure 9K**), *Provanna lomana* (**Figure 9L**) and the pyropeltid *Pyropelta corymba* (**Figure 9T**; Warén and Bouchet, 1993; Levin et al., 2015), and Eastern Pacific deep-sea taxa: the raphitomid *Pleurotomella* sp. and fissurellid *Puncturella rothi* (**Figures 9N,O**; McLean, 1984). The curved shape of the apertures of many of the *Paralepetopsis* sp. and *Pyropelta* spp. specimens (**Figure 9R**), as well as their intimate association with the serpulid tubes in the lightly to heavily mineralized samples strongly indicates they lived on the tubes during life, probably scraping microbial mats from the tube surfaces. This tight association between worm tubes and grazing limpets has been commonly noted from modern and fossil cold seep sites (e.g., Okutani et al., 1992; Jenkins et al., 2007; Saether et al., 2012), although in these cases the tubes are those of siboglinids and not serpulids.

The mollusk taxa associated with the DR630 and DR631 samples are of lower diversity than those in the Fossil Hill samples, and are a sub-set of them (**Supplementary Table S4**). One exception is sample DR631 R-3, which contains specimens of the pteropod *Cavolinia uncinata*, which were derived from the water column and then incorporated into the authigenic carbonates as they formed within the sediments. While 24 taxa were recorded, species richness estimation based on data within **Supplementary Table S4** predicted a minimum of 30–53 fossil species (ICE: 29.5; iChao2: 53.3) from Fossil Hill and associated sites.

Ages of Fossil Hill Faunas and Authigenic Carbonates

Radiocarbon measurements made on the carbonate in the walls of serpulid tubes from several locations around Fossil Hill resulted in a narrow range of calculated ages ranging between 23 and 25 cal ka BP (1000 years before present; **Table 1**). The $\delta^{13}C_{VPDB}$ values of the same samples ranged from −18.06 to −11.01‰. Thus, these Late Pleistocene radiocarbon ages should be treated as a maximum due to potential addition of old carbon effects outlined earlier. Radiocarbon dating of bivalve specimens produced an age similar to that of serpulid tubes for a specimen of *P. soyoae* (23 cal ka BP; **Table 1**), while a shell of the bivalve *E. elongata* was shown to be recent using this technique.

Cements occurring on fossil taxa showed very depleted $\delta^{13}C$ signatures (**Supplementary Table S2**). U-Th dating of cements and fossils was largely consistent with radiocarbon dates, however, U-Th age interpretation was complicated by the fact that most ROV samples yielded a wide range of ages, spanning several tens of ka. Given the size of the samples, such age variation most likely results from some degree of open system behavior through U loss. As a result, the youngest date from each sample was assumed to be representative for the respective locality, provided that its initial ($^{234}U/^{238}U$) activity ratio was within uncertainty of the mean seawater value of 1.1468 (Andersen et al., 2010). Based on this approach we estimate the age of tube-associated authigenic carbonates recovered during dives DR626-630 to be around 17–30 ka (**Table 2**). The older end of this age range is underpinned by statistically equivalent data from three different samples, with only one date from DR626 indicative of a potential older age of around 43 ka. Samples recovered during dive DR631 were analyzed, but returned results consistent with open system behavior, which precluded age interpretation. U-Th dating of cements on bivalve shells from specimens collected on the northern end of Fossil Hill produced ages of approximately 7.1 ka, while carbonate cement on fossil bivalve specimens from the DR630 dive site yielded an age of 20.8 ka (**Table 2**).

DISCUSSION

As serpulid tubes were observed along much of Fossil Hill's extent of over 500 m by 250 m, this mound appears to host one of the largest known accumulations of fossil serpulids, greatly exceeding the dimensions of the Triassic-early Jurassic fossil serpulid reefs

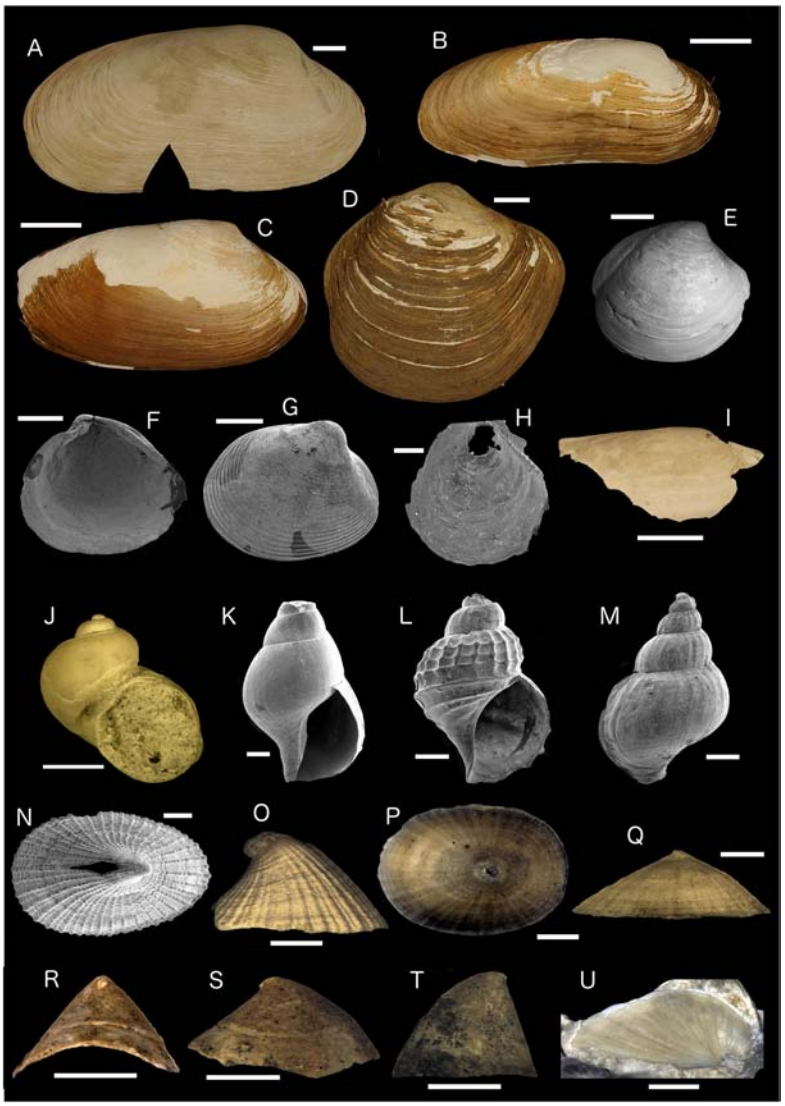

FIGURE 9 | Images of representative bivalves and gastropods from Fossil Hill samples. **(A)** *Phreagena soyoae*, right valve external view, DR627 Bio-2 clam scoop, and scale bar is 10 mm. **(B)** *Ectenagena elongata*, right valve external view, DR626 A-1, and scale bar is 10 mm. **(C)** *Archivesica packardana*, right valve external view, DR626 A-1, and scale bar is 10 mm. **(D)** *Lucinoma aequizonata*, right valve external view, DR629 PSC-61, and scale bar is 10 mm. **(E)** *Thyasira flexuosa*, right valve external view, DR627 (BB), and scale bar is 5 mm. **(F)** *Axinopsida serricata*, right valve internal view, DR627 R-2, SEM, and scale bar is 1 mm. **(G)** *Nucula carlottensis*, left valve external view, DR627 R-2, SEM, and scale bar is 1 mm. **(H)** *Delectopecten vancouverensis*, right valve external view, DR627 BB, SEM, and scale bar is 0.5 mm. **(I)** *Acharax johnsoni*, partial left valve external view, DR627 BIO-2, and scale bar is 10 mm. **(J)** *Depressigyra* sp. apertural view, DR476 A-1, and scale bar is 1 mm. **(K)** *Provanna laevis*, apertural view, DR476 A-1, SEM, and scale bar is 1 mm. **(L)** *Provanna lomana*, apertural view, DR476 A-1, SEM, and scale bar is 1 mm. **(M)** *Provanna* sp., adapertural view, DR476 A-1, SEM, and scale bar is 1 mm. **(N)** *Puncturella rothi*, apical view, DR627 R-2, SEM, and scale bar is 1 mm. **(O)** *Puncturella rothi*, lateral view, DR628 R-3, and scale bar is 2 mm. **(P,Q)** *Paralepetopsis* sp., apical **(P)** and lateral **(Q)** views, DR627 R-2, and scale bars are 1 mm. **(R,S)** *Pyropelta* "low-spired," anterior **(R)** and lateral **(S)** views, DR627 R-2, and scale bars are 1 mm. **(T)** *Pyropelta corymba*, lateral view, DR627 R-2, and scale bar is 1 mm. **(U)** *Lepetodrilus* sp., lateral view, DR629 R-2, and scale bar is 2 mm.

from southern Spain (Braga and Lopez-Lopez, 1989). The Fossil Hill serpulid accumulation is also unusual in being found in deep-sea waters, in association with fossil cold seep faunas, and at a site that still supports an active chemosynthetic biological community with a different assemblage of species. While many mounds characterized by active seepage have been discovered off the coast of California in deep waters (e.g., Orange et al., 2002; Paull et al., 2008, 2015), Fossil Hill and the associated exposures documented in this study are the only examples so far dominated by fossil serpulid tube facies. All of the Fossil Hill serpulid tubes analyzed through radiocarbon dating have maximum ages of 23–24 cal ka BP (**Table 1**) while U-Th dating suggests some tubes are over 16–30 ka old (**Table 2**), demonstrating that this accumulation is remarkably recent in origin and that the species responsible for the accumulation may still be extant.

The current topography of Fossil Hill (**Figure 1C**) appears to be largely a result of differential erosion which has exposed authigenic carbonates and vast quantities of serpulid tube fossils, and this process is likely also responsible for exposing similar facies ∼8 km to the northwest, and ∼300 m to the southeast along the same fault zone as Fossil Hill. Our data are consistent with the formation of the serpulid tube accumulation within deep-sea waters at the Fossil Hill site. This is strongly suggested by the concentrated, well-sorted and oriented nature of the Fossil Hill serpulid tube facies (**Figure 4E**). As only the anterior ends of the tubes were found, there appears to have been some reworking of the deposit. However, based on the considerations above, reworking has likely been spatially constrained to mostly within the Fossil Hill mound area. While Fossil Hill is located in close proximity to the base of the Santa Monica Canyon (**Figure 1**), the mound is situated over 500 m from the main channel in a part of the seabed unlikely to be influenced by canyon transport processes. It therefore appears unlikely that the tubes could have been transported to their current location from shallower, photic zone waters. The morphology of the Fossil Hill tubes is also more consistent with a deep-sea serpulid genus, further suggesting that they likely formed in deep water at the Fossil Hill site.

Is Formation of the Fossil Hill Serpulid Reef Linked to Seepage?

As cold seeps are renowned for supporting greater productivity in comparison to many other deep-sea environments, an apparent explanation for the occurrence of such a large colony of serpulids within a deep-sea cold seep is that its formation is related to productivity from seepage. There are clear indications that active fluid seepage existed at Fossil Hill at the time of tube formation, and may therefore have contributed to the proliferation of these annelids and thus the size of the resulting reef deposit. U-Th dating of MDAC cements on tube surfaces (**Table 2**), and both radiocarbon and U-Th dating of tubes (**Table 1**), indicate that tube formation and fluid seepage were contemporaneous at Fossil Hill during the period 20–25 cal ka BP, while dating of shells additionally suggests that the larger chemosynthetic bivalve species, *Phreagena soyoae*, was also living at the site during this time (**Table 1**). Large vesicomyid bivalves have sulfur-oxidizing bacterial symbionts and require sulfide-rich reducing environments (Krylova and Sahling, 2010), therefore it is likely that the Fossil Hill *P. soyoae* specimens (**Figure 9A**), as well as many of the other fossil fauna (section "Taxa Associated With the Fossil Serpulids"; **Figures 9B–U**) associated with the *?Laminatubus* sp. tubes, would have relied on seeping fluids at the site for their nutrition. In addition, $\delta^{13}C$ values for the fossil serpulid tubes (**Table 1**) also indicate the involvement and importance of methane within the environment at the time the serpulid tubes were forming. The $\delta^{13}C$ values of serpulid tubes are considered to closely resemble those of the waters within which they grew. However vital effects have been reported for this group, whereby tube $\delta^{13}C$ values are shifted to more negative values by 4–7‰ (Videtich, 1986; Lojen et al., 2014). The mechanisms leading to the above effects are however unclear, and a metabolic influence on the low $\delta^{13}C$ values of the Fossil Hill serpulid tubes therefore cannot be ruled out.

While some U-Th measurements suggest slightly older ages for Fossil Hill *?Laminatubus* sp. of 30–43 ka, most U-Th dates, as well as radiocarbon measurements on the above tubes and *P. soyoae* cluster at 16–25 cal ka BP (**Tables 1**, **2**). This may indicate that a discrete event could have occurred during this time period, leading firstly to a vast proliferation of, and subsequently the local extinction of serpulids at the Fossil Hill site. The radiocarbon ages of the tubes approximately coincide with the last glacial maximum (LGM; 20 cal ka BP), during which sea-levels are estimated to have been 110–130 m lower than at present (Lambeck and Chappell, 2001; Bintanja et al., 2005). Intensity of fluid seepage is believed to vary with climatic conditions, in part because ocean warming or a lowering of pressure associated with sea-level changes can lead to dissociation of gas hydrate sequestered near the gas hydrate stability boundary (Kvenvolden, 1988; MacDonald et al., 2003; Buffett and Archer, 2004). For example, the intensity of methane seepage at cold seeps off the coast of mainland Norway and western Svalbard has been linked to isostatic rebound and pulses of sedimentation associated with glaciation during the Late Pleistocene, which altered the stability of gas hydrates (Karstens et al., 2018; Wallmann et al., 2018). Fossil Hill is now at 600 m water depth, near the top of the present methane hydrate stability zone in the Santa Monica Basin (Paull et al., 2008). However, the over 100 m sea-level drop during the LGM likely caused the methane hydrate stability conditions to shift enough for methane hydrate in near-seafloor sediments to decompose, and for methane to be released from sediments. The occurrence of pockmarks, cracks, gullies and caverns on the Fossil Hill mound could indicate the historical presence of gas hydrates that have dissociated, leaving void spaces in the strata and morphologies that suggest seafloor collapse. Methane released from the dissociation of gas hydrate inventoried within near-seafloor sediments, and linked to the LGM sea-level lowstand could have promoted heightened productivity and hence the proliferation of a serpulids as well as chemosynthetic fauna at the Fossil Hill site.

An intriguing question presented by the above scenario is why serpulids, rather than symbiont-bearing chemosynthetic fauna, would have dominated Fossil Hill during a possible period of intense methane seepage during the LGM. It is possible that the Fossil Hill *?Laminatubus* sp. could have possessed chemosynthetic symbionts. While serpulids with such symbiotic associations have not yet been formally described, *Laminatubus* sp. from the Jaco Scar seeps have been found to possess microbial communities on their crowns, and research into the nature of their association with the worms is currently in progress (S. Goffredi, *pers. comm.*). The reason for the extinction of Fossil Hill *?Laminatubus* sp. are however unclear. While there appears to have been active seepage at the Fossil Hill mound during 20–16 ka and 7 ka from MDAC cements (**Table 2**), we cannot at present determine if it was continuous, therefore the possibility exists that the serpulids may have become locally extinct at Fossil Hill during substantial periods of seepage quiescence. Indeed, the bivalve *P. soyoae* appears to also be locally extinct at the Fossil Hill site

despite the occurrence of living populations of these species in nearby seeps (Goffredi and Barry, 2002).

Serpulid Reef Formation and Other Factors

Aspects of the physical environment such as an advantageous position along a fault scarp that provides optimal access to nutrients entrained in water currents, or an unusual composition of the seeping fluid, may also account for why a taxon not deemed to be chemosynthetic was so abundant and co-occurred with seepage at Fossil Hill. Faults can provide conduits for the migration of fluids and are known to be associated with cold seep communities (Zitter et al., 2008), and could additionally have provided serpulids with hard substrate in the form of MDAC for attachment. While other mounds off the Californian coast were generally not found to harbor large abundances of fossil serpulids, serpulid tubes similar to those of Fossil Hill were recovered at the two additional authigenic carbonate outcrops along the approximate trajectory of the San Pedro Basin Fault sampled during dives DR630 and DR631 (**Figure 1**). Therefore, the proximity of fossil serpulid tube facies to the San Pedro Basin Fault may indicate an association between this facies and fault activity. The subset of Fossil Hill U-Th dates that also predate the LGM could suggest that factors other than nutritional benefits from seepage productivity may have been responsible for serpulid reef growth. However, data on historical fault and water current movements are very limited, and it thus remains difficult to account for why serpulids are extinct at the Fossil Hill site today.

It is likely that the formation of the fossil serpulid reef at Fossil Hill is due to a combination of favorable environmental conditions as well as heightened productivity from seepage, particularly ∼20 ka. Serpulid populations in general are known to boom for discrete time periods under which distinct environmental conditions prevail (ten Hove and van den Hurk, 1993), which the Triassic-early Jurassic fossil serpulid reefs from southern Spain (Braga and Lopez-Lopez, 1989) as well as those found near South Georgia (Ramos and San Martín, 1999) demonstrate can occur away from coastal settings in more open, near-deep to deep-sea waters. The large extent of the Fossil Hill deposit, and the known role of serpulids as ecosystem engineers in virtue of reef construction, means that Fossil Hill likely constituted a significant deep-sea habitat for other marine fauna, with the mollusk fauna associated with Fossil Hill serpulids (and the estimated fossil species richness) attesting to this. During the time of active serpulid reef growth during the Late Pleistocene, Fossil Hill could therefore potentially be classed as an "animal forest" (Rossi, 2013; Reyes-Bonilla and Jordán-Dahlgren, 2017) in virtue of providing three-dimensional habitat complexity that can alter physical and biological characteristics of the site.

CONCLUSION

Detailed AUV surveys in combination with extensive ROV sampling have revealed the existence of a massive serpulid paleo-colony dominated by ∼20 cal ka BP tubeworms off southern California. The deposit also contains fossil cold seep faunas and methane-derived carbonates. Similar massive-sized deposits dominated by serpulids have not previously been documented in the deep sea. However, the proportion of the seafloor that has been explored with tools and techniques that allow features like this to be identified is still very small. Further exploration has the potential to shed insight into whether living populations of the Fossil Hill ?*Laminatubus* serpulids may yet still exist within the southern California region, to elucidate the relationship between these tubeworms and fluid seepage, and thus provide answers to the intriguing question as to whether these serpulids may have had chemosymbionts.

DATA AVAILABILITY

All datasets generated for this study are included in the manuscript and/or the **Supplementary Files**.

AUTHOR CONTRIBUTIONS

Samples were collected by CP and RV, with assistance from MG. MM performed radiocarbon dating. DS and DC performed U-Th dating. DWC processed AUV data. LL provided seafloor video mosaic data. MG, CL, and JP analyzed the data and the manuscript was drafted by MG with input from CP, RV, and CL. All authors read and approved the final manuscript.

FUNDING

This study was provided by the David and Lucile Packard Foundation via the Monterey Bay Aquarium Research Institute. MG gratefully acknowledges funding from NERC grants NE/K500847/1 and NE/R000670/1.

ACKNOWLEDGMENTS

We thank the crew of R/V *Western Flyer*, as well as the AUV and ROV *Doc Ricketts* pilots. We are grateful to Ivano Aiello for assistance with SEM at Moss Landing Marine Laboratories, to Hilary Sloane for assistance with stable isotope analyses, to Harry ten Hove, Elena Kupriyanova, Greg Rouse, and Olev Vinn for their advice on the identification of serpulid tubes, and Alexei Ippolitov for advice on SEM examination of serpulid tubes. We also thank Roberto Gwiazda, Esther Sumner, and Shannon Johnson for their assistance with sample collection, as well as Krystle Anderson and Eve Lundsten for their assistance with mapping data and figures. We are also grateful to Jonathan Watson and Mark Sephton for their access to and help with FTIR, to Elena Krylova, Shana Goffredi, Paul Valentich-Scott, Daniel Geiger, Anders Warén, John Taylor, Arie Janssen, and Henry Chaney for their assistance with the identification of mollusk and other taxa, and to

Shannon Johnson for verification of the *E. elongata* identification using DNA sequences from Johnson et al. (2016), as well as additional mollusk identifications. We also thank two reviewers and Harry ten Hove for their valuable comments on the manuscript draft.

SUPPLEMENTARY MATERIAL

The Supplementary Material for this article can be found online at: https://www.frontiersin.org/articles/10.3389/fmars.2019.00115/full#supplementary-material

REFERENCES

Amon, D. J., Gobin, J., Van Dover, C. L., Levin, L. A., Marsh, L., and Raineault, N. A. (2017). Characterization of methane-seep communities in a deep-sea area designated for oil and natural gas exploitation off Trinidad and Tobago. *Front. Mar. Sci.* 4:342. doi: 10.3389/fmars.2017.00342

Andersen, M. B., Stirling, C. H., Zimmermann, B., and Halliday, A. N. (2010). Precise determination of the open ocean 234 U/ 238 U composition. *Geochem. Geophys. Geosyst.* 11:Q12003. doi: 10.1029/2010GC003318

Barbieri, R., Ori, G. G., and Cavalazzi, B. (2004). A silurian cold-seep ecosystem from the middle atlas. *Morocco. Palaios* 19, 527–542. doi: 10.1669/0883-1351(2004)019<0527:ASCEFT>2.0.CO;2

Bastida-Zavala, R. (2008). Serpulids (Annelida: Polychaeta) from the Eastern Pacific, including a brief mention of Hawaiian serpulids. *Zootaxa* 1722, 1–61.

Bianchi, C. N., Aliani, S., and Morri, C. (1995). Present-day serpulid reefs, with reference to an on-going research project on *Ficopomatus enigmaticus*. *Pubblications du Serv. Géologique du Luxemb.* 29, 61–65.

Bintanja, R., van de Wal, R. S. W., and Oerlemans, J. (2005). Modelled atmospheric temperatures and global sea levels over the past million years. *Nature* 437, 125–128. doi: 10.1038/nature03975

Braga, J. C., and Lopez-Lopez, I. R. (1989). Serpulid bioconstructions at the triassic-liassic boundary in southern Spain. *Facies* 21, 1–10. doi: 10.1007/BF02536829

Buffett, B., and Archer, D. (2004). Global inventory of methane clathrate: sensitivity to changes in the deep ocean. *Earth Planet. Sci. Lett.* 227, 185–199. doi: 10.1016/j.epsl.2004.09.005

Caress, D., Thomas, H., Kirkwood, W., McEwen, R., Henthorn, R., Clague, D., et al. (2008). "High-Resolution Multibeam, Sidescan, and Subbottom Surveys Using the MBARI AUV D. Allan B," in *Marine Habitat Mapping Technology for Alaska*, eds J. R. Reynolds and H. G. Greene (Fairbanks: Alaska Sea Grant, University of Alaska Fairbanks), 47–70. doi: 10.4027/mhmta.2008.04

Chao, A., Ma, K. H., Hsieh, T. C., and Chiu, C. H. (2015). *Online Program SpadeR (Species-richness Prediction And Diversity Estimation in R). Program and User's Guide*. Available at: http://chao.stat.nthu.edu.tw/wordpress/software_download/

Chiu, C. H., Wang, Y. T., Walther, B. A., and Chao, A. (2014). An improved nonparametric lower bound of species richness via a modified good–turing frequency formula. *Biometrics* 70, 671–682. doi: 10.1111/biom.12200

Coan, E. V., Valentich Scott, P., and Bernard, F. R. (2000). Bivalve seashells of western North America: marine bivalve mollusks from Arctic Alaska to Baja California. *St. Barbar. Museum Nat. Hist. Monogr.* 2:764.

Crémière, A., Lepland, A., Chand, S., Sahy, D., Condon, D. J., Noble, S. R., et al. (2016). Timescales of methane seepage on the Norwegian margin following collapse of the Scandinavian Ice Sheet. *Nat. Commun.* 7:11509. doi: 10.1038/ncomms11509

Dubilier, N., Bergin, C., and Lott, C. (2008). Symbiotic diversity in marine animals: the art of harnessing chemosynthesis. *Nat. Rev. Microbiol.* 6, 725–740. doi: 10.1038/nrmicro1992

Fisher, M. A., Normark, W. R., Bohannon, R. G., Sliter, R. W., and Calvert, A. J. (2003). Geology of the continental margin beneath Santa Monica Bay, Southern California, from seismic-reflection data. *Bull. Seismol. Soc. Am.* 93, 1955–1983. doi: 10.1785/0120020019

Gardner, J. V., Dartnell, P., Mayer, L. A., and Hughes Clarke, J. E. (2003). Geomorphology, acoustic backscatter, and processes in Santa Monica Bay from multibeam mapping. *Mar. Environ. Res.* 56, 15–46. doi: 10.1016/S0141-1136(02)00323-9

Goffredi, S., and Barry, J. (2002). Species-specific variation in sulfide physiology between closely related vesicomyid clams. *Mar. Ecol. Prog. Ser.* 225, 227–238. doi: 10.3354/meps225227

Hedley, R. H. (1958). Tube formation by *Pomatoceros triqueter* (Polychaeta). *J. Mar. Biol. Assoc.* 37, 315–322. doi: 10.1017/S0025315400023717

Hein, J. R., Normark, W. R., McIntyre, B. R., Lorenson, T. D., and Powell, C. L. II. (2006). Methanogenic calcite, 13C-depleted bivalve shells, and gas hydrate from a mud volcano offshore southern California. *Geology* 34, 108–112. doi: 10.1130/G22098.1

Hoeksema, B. W., and ten Hove, H. A. (2011). Aggregation of the reef-building tube worm *Filogranella elatensis* at Semporna, eastern Sabah, Malaysia. *Coral Reefs* 30:839. doi: 10.1007/s00338-011-0785-8

Hovland, M., and Judd, A. G. (1988). *Seabed Pockmarks and Seepages: Impact on Geology, Biology and the Marine Environment*. London: Graham and Trotman.

Ippolitov, A., Vinn, O., Kupriyanova, E., and Jäger, M. (2014). Written in stone: history of serpulid polychaetes through time. *Mem. Mus. Vic.* 71, 123–159. doi: 10.24199/j.mmv.2014.71.12

Jenkins, R. G., Kaim, A., and Hikida, Y. (2007). Antiquity of the substrate choice among acmaeid limpets from late cretaceous chemosynthesis-based communities. *Acta Palaeontol. Pol.* 52, 369–373.

Johnson, S. B., Krylova, E. M., Audzijonyte, A., Sahling, H., and Vrijenhoek, R. C. (2016). Phylogeny and origins of chemosynthetic vesicomyid clams. *Syst. Biodivers.* 15, 346–360. doi: 10.1080/14772000.2016.1252438

Karstens, J., Haflidason, H., Becker, L. W. M., Berndt, C., Rüpke, L., Planke, S., et al. (2018). Glacigenic sedimentation pulses triggered post-glacial gas hydrate dissociation. *Nat. Commun.* 9:635. doi: 10.1038/s41467-018-03043-z

Kiel, S. (ed.). (2010). *The Vent, and Seep Biota: Aspects from Microbes to Ecosystems*, Vol. 33. Dordrecht: Springer. doi: 10.1007/978-90-481-9572-5

Kiel, S., Sami, M., and Taviani, M. (2018). A serpulid-*Anodontia*-dominated methane-seep deposit from the miocene of northern italy. *Acta Palaeontol. Pol.* 63, 569–577. doi: 10.4202/app.00472.2018

Krylova, E. M., and Sahling, H. (2010). Vesicomyidae (Bivalvia): current taxonomy and distribution. *PLoS One* 5:e9957. doi: 10.1371/journal.pone.0009957

Kupriyanova, E. K. (1999). The taxonomic status of *Serpula* cf. columbiana Johnson, 1901 from the American and Asian coasts of the North Pacific ocean. *Ophelia* 50, 21–34. doi: 10.1080/00785326.1999.10409386

Kupriyanova, E. K., Macdonald, T. A., and Rouse, G. W. (2006). Phylogenetic relationships within Serpulidae (Sabellida, Annelida) inferred from molecular and morphological data. *Zool. Scr.* 35, 421–439. doi: 10.1186/1471-2148-9-189

Kvenvolden, K. A. (1988). Methane hydrates and global climate. *Global Biogeochem. Cycles* 2, 221–229. doi: 10.1029/GB002i003p00221

Lambeck, K., and Chappell, J. (2001). Sea level change through the last glacial cycle. *Science* 292, 679–686. doi: 10.1126/science.1059549

Lee, S.-M., and Chao, A. (1994). Estimating population size via sample coverage for closed capture-recapture models. *Biometrics* 50, 88–97. doi: 10.2307/2533199

Levin, L. A., Mendoza, G. F., Grupe, B. M., Gonzalez, J. P., Jellison, B., Rouse, G., et al. (2015). Biodiversity on the rocks: macrofauna inhabiting authigenic carbonate at costa rica methane seeps. *PLoS One* 10:e0131080. doi: 10.1371/journal.pone.0131080

Levin, L. A., Orphan, V. J., Rouse, G. W., Rathburn, A. E., Ussler, W., Cook, G. S., et al. (2012). A hydrothermal seep on the Costa Rica margin: middle ground in a continuum of reducing ecosystems. *Proc. R. Soc. B Biol. Sci.* 279, 2580–2588. doi: 10.1098/rspb.2012.0205

Loftus, E., Rogers, K., and Lee-Thorp, J. (2015). A simple method to establish calcite:aragonite ratios in archaeological mollusc shells. *J. Quat. Sci.* 30, 731–735. doi: 10.1002/jqs.2819

Lojen, S., Cukrov, M., and Cukrov, N. (2014). Variability of stable isotope fingerprints of the serpulid *Ficopomatus enigmaticus* within a permanently stratified estuary: implications for (palaeo)environmental interpretations. *Estuaries Coast.* 37, 436–448. doi: 10.1007/s12237-013-9685-1

MacDonald, I. R., Sager, W. W., and Peccini, M. B. (2003). Gas hydrate and chemosynthetic biota in mounded bathymetry at mid-slope hydrocarbon

seeps: northern Gulf of Mexico. *Mar. Geol.* 198, 133–158. doi: 10.1016/S0025-3227(03)00098-7

McLean, J. H. (1984). New species of northeast pacific archaeogastropods. *Veliger* 26, 233–239.

Mix, A. C., Lund, D. C., Pisias, N. G., Bodén, P., Bornmalm, L., Lyle, M., et al. (1999). "Rapid climate oscillations in the Northeast Pacific during the last deglaciation reflect Northern and Southern Hemisphere sources," in *Mechanisms for Global Climate Change at Millennial Time Ccales*, eds P. Clark, R. S. Webb, and L. D. Keigwin (Washington, D. C: American Geophysical Union), 127–148. doi: 10.1029/GM112p0127

Nobuhara, T., Onda, D., Kikuchi, N., Kondo, Y., Matsubara, K., Amano, K., et al. (2008). Lithofacies and fossil assemblages of the upper cretaceous sada limestone, Shimanto City, Kochi Prefecture, Shikoku, Japan. *Fossils* 84, 47–60.

Nobuhara, T., Onda, D., Sato, T., Aosawa, H., Ishimura, T., Ijiri, A., et al. (2016). Mass occurrence of the enigmatic gastropod *Elmira* in the late cretaceous sada limestone seep deposit in southwestern Shikoku, Japan. *PalZ* 90, 701–722. doi: 10.1007/s12542-016-0326-4

Normark, W. R., Hein, J. R., Powell, C. L. I. I., Lorenson, T. D., Lee, H. J., and Edwards, B. D. (2003). Methane hydrate recovered from a mud volcano in santa monica basin, offshore southern California. *EOS Trans. Am. Geophys. Union* 84, 51B–0855B.

Okutani, T., Tsuchida, E., and Fujikura, K. (1992). Five bathyal gastropods living within or near the *Calyptogena*-community of the Hatsushima Islet, Sagami Bay. *Venus* 51, 137–148.

Olu, K., Duperret, A., Sibuet, M., Foucher, J., and Fiala-Medoni, A. (1996a). Structure and distribution of cold seep communities along the Peruvian active margin: relationship to geological and fluid patterns. *Mar. Ecol. Prog. Ser.* 132, 109–125. doi: 10.3354/meps132109

Olu, K., Sibuet, M., Harmegnies, F., Foucher, J., and Fiala-Medoni, A. (1996b). Spatial distribution of diverse cold seep communities living on various diapiric structures of the southern Barbados prism. *Prog. Oceanogr.* 38, 347–376. doi: 10.1016/S0079-6611(97)00006-2

Orange, D. L., Yun, J., Maher, N., Barry, J., and Greene, G. (2002). Tracking California seafloor seeps with bathymetry, backscatter and ROVs. *Cont. Shelf Res.* 22, 2273–2290. doi: 10.1016/S0278-4343(02)00054-7

Paull, C. K., Caress, D. W., Thomas, H., Lundsten, E., Anderson, K., Gwiazda, R., et al. (2015). Seafloor geomorphic manifestations of gas venting and shallow subbottom gas hydrate occurrences. *Geosphere* 11, 491–513. doi: 10.1130/GES01012.1

Paull, C. K., Chanton, J., Neumann, A. C., Coston, J. A., Martens, C. S., and Showers, W. (1992). Indicators of methane-derived carbonates and chemosynthetic organic carbon deposits: examples from the Florida Escarpment. *Palaios* 7, 361–375. doi: 10.2307/3514822

Paull, C. K., Martens, C. S., Chanton, J. P., Neumann, A. C., Coston, J., Jull, A. J. T., et al. (1989). Old carbon in living organisms and young CaCO3 cements from abyssal brine seeps. *Nature* 342, 166–168. doi: 10.1038/342166a0

Paull, C. K., Normark, W. R., Ussler, W., Caress, D. W., and Keaten, R. (2008). Association among active seafloor deformation, mound formation, and gas hydrate growth and accumulation within the seafloor of the Santa Monica Basin, offshore California. *Mar. Geol.* 250, 258–275. doi: 10.1016/j.margeo.2008.01.011

Peckmann, J., Thiel, V., Michaelis, W., Clari, P., Gaillard, C., Martire, L., et al. (1999a). Cold seep deposits of Beauvoisin (Oxfordian, southeastern France) and Marmorito (Miocene, northern Italy): microbially induced authigenic carbonates. *Int. J. Earth Sci.* 88, 60–75. doi: 10.1007/s005310050246

Peckmann, J., Walliser, O. H., Riegel, W., and Reitner, J. (1999b). Signatures of hydrocarbon venting in a middle devonian carbonate mound (Hollard Mound) at the Hamar Laghdad (Antiatlas Morocco). *Facies* 40, 281–296. doi: 10.1007/BF02537477

Pohlman, J. W., Bauer, J. E., Waite, W. F., Osburn, C. L., and Chapman, N. R. (2011). Methane hydrate-bearing seeps as a source of aged dissolved organic carbon to the oceans. *Nat. Geosci.* 4, 37–41. doi: 10.1038/ngeo1016

Prouty, N. G., Sahy, D., Ruppel, C. D., Roark, E. B., Condon, D., Brooke, S., et al. (2016). Insights into methane dynamics from analysis of authigenic carbonates and chemosynthetic mussels at newly-discovered Atlantic Margin seeps. *Earth Planet. Sci. Lett.* 449, 332–344. doi: 10.1016/j.epsl.2016.05.023

R Core Team (2014). *R: A Language and Environment for Statistical Computing*. Vienna: R Foundation for Statistical Computing.

Ramos, A., and San Martín, G. (1999). On the finding of a mass occurrence of *Serpula narconensis* Baird, 1885 (Polychaeta, Serpulidae) in South Georgia (Antarctica). *Polar Biol.* 22, 379–383. doi: 10.1007/s003000050432

Reish, D. J., and Mason, A. Z. (2003). Radiocarbon dating and metal analyses of fossil and living tubes of *Protula* (Annelida: Polychaeta). *Hydrobiologia* 496, 371–383. doi: 10.1023/A:1026186024182

Reyes-Bonilla, H., and Jordán-Dahlgren, E. (2017). "Caribbean Coral Reefs: Past, Present, and Insights into the Future," in *Marine Animal Forests*, eds S. Rossi, L. Bramanti, A. Gori, and C. Orejas (Cham: Springer), doi: 10.1007/978-3-319-17001-5_2-1

Rossi, S. (2013). The destruction of the 'animal forests' in the oceans: towards an over-simplification of the benthic ecosystems. *Ocean Coast. Manag.* 84, 77–85. doi: 10.1016/j.ocecoaman.2013.07.004

Ryan, H. F., Conrad, J. E., Paull, C. K., and McGann, M. (2012). Slip rate on the San Diego trough fault zone, inner California Borderland, and the 1986 Oceanside earthquake swarm revisited. *Bull. Seismol. Soc. Am.* 102, 2300–2312. doi: 10.1785/0120110317

Saether, K. P., Little, C. T. S., Marshall, B. A., and Campbell, K. A. (2012). Systematics and palaeoecology of a new fossil limpet (Patellogastropoda: Pectinodontidae) from Miocene hydrocarbon seep deposits, East Coast Basin, North Island, New Zealand with an overview of known fossil seep pectinodontids. *Molluscan Res.* 32, 1–15.

Sanfilippo, R., Vertino, A., Rosso, A., Beuck, L., Freiwald, A., and Taviani, M. (2013). *Serpula* aggregates and their role in deep-sea coral communities in the southern Adriatic Sea. *Facies* 59, 663–677. doi: 10.1007/s10347-012-0356-7

Schwindt, E., Bortolus, A., and Iribarne, O. O. (2001). Invasion of a reef-builder polychaete: direct and indirect impacts on the native benthic community structure. *Biol. Invasions* 3, 137–149. doi: 10.1023/A:1014571916818

Stuiver, M., and Polach, H. A. (1977). Discussion: reporting of 14C data. *Radiocarbon* 19, 355–363. doi: 10.1017/S0033822200003672

Stuiver, M., Reimer, P. J., and Reimer, R. W. (2018). *CALIB 7.1 [WWW program]*. Available at: http://calib.org, accessed 2018-9-26

Taylor, P. D., and Vinn, O. (2006). Convergent morphology in small spiral worm tubes ('*Spirorbis*') and its palaeoenvironmental implications. *J. Geol. Soc. London.* 163, 225–228. doi: 10.1144/0016-764905-145

ten Hove, H. (1979). "Different causes of mass occurrence in serpulids," in *Biology and Systematics of Colonial Organisms*, eds G. Larwood and B. R. Rosen (London: Academic Press), 281–298.

ten Hove, H., and van den Hurk, P. (1993). A review of Recent and fossil serpulid 'reefs'; actuopalaeontology and 'Upper Malm' serpulid limestones in NW Germany. *Geol. en Mijnb* 72, 23–67.

ten Hove, H., and Zibrowius, H. (1986). Laminatubus alvini gen. et sp. n. and Protis hydrothermica sp. n. (Polychaeta, Serpulidae) from the bathyal hydrothermal vent communities in the eastern Pacific. *Zool. Scr.* 15, 21–31. doi: 10.1111/j.1463-6409.1986.tb00205.x

Videtich, P. E. (1986). Stable-isotope compositions of serpulids give insights to calcification processes in marine organisms. *Palaios* 1, 189–193. doi: 10.2307/3514514

Vinn, O. (2005). The tube ultrastructure of serpulids (Annelida, Polychaeta) Pentaditrupa subtorquata, Cretaceous, and Nogrobs cf. vertebralis, Jurassic, from Germany. *Proc. Estonian Acad. Sci. Geol.* 54, 260–265.

Vinn, O. (2008). Tube ultrastructure of the fossil genus *Rotularia* DeFrance, 1827 (Polychaeta, Serpulidae). *J. Paleontol.* 82, 206–212. doi: 10.1666/06-125.1

Vinn, O., Hryniewicz, K., Little, C. T. S., and Nakrem, H. A. (2014). A Boreal serpulid fauna from Volgian-Ryazanian (latest Jurassic-earliest Cretaceous) shelf sediments and hydrocarbon seeps from Svalbard. *Geodiversitas* 36, 527–540. doi: 10.5252/g2014n4a2

Vinn, O., Jäger, M., and Kirsimäe, K. (2008a). Microscopic evidence of serpulid affinities of the problematic fossil tube *Serpula etalensis* from the Lower Jurassic of Germany. *Lethaia* 41, 417–421. doi: 10.1111/j.1502-3931.2008.00093.x

Vinn, O., ten Hove, H., Mutvei, H., and Kirsimae, K. (2008b). Ultrastructure and mineral composition of serpulid tubes (Polychaeta, Annelida). *Zool. J. Linn. Soc.* 154, 633–650. doi: 10.1111/j.1096-3642.2008.00421.x

Vinn, O., Kupriyanova, E. K., and Kiel, S. (2013). Serpulids (Annelida, Polychaeta) at Cretaceous to modern hydrocarbon seeps: ecological and evolutionary patterns. *Palaeogeogr. Palaeoclimatol. Palaeoecol.* 390, 35–41. doi: 10.1016/j.palaeo.2012.08.003

Wagner, J. K., McEntee, M. H., Brothers, L. L., German, C. R., Kaiser, C. L., Yoerger, D. R., et al. (2013). Cold-seep habitat mapping: high-resolution spatial characterization of the blake ridge diapir seep field. *Deep Sea Res. II* 92, 183–188. doi: 10.1016/j.dsr2.2013.02.008

Wallmann, K., Riedel, M., Hong, W. L., Patton, H., Hubbard, A., Pape, T., et al. (2018). Gas hydrate dissociation off Svalbard induced by isostatic rebound rather than global warming. *Nat. Commun.* 9:83. doi: 10.1038/s41467-017-02550-9

Warén, A., and Bouchet, P. (1993). New records, species, genera, and a new family of gastropods from hydrothermal vents and hydrocarbon seeps. *Zool. Scr.* 22, 1–90. doi: 10.1111/j.1463-6409.1993.tb00342.x

Zitter, T. A. C., Henry, P., Aloisi, G., Delaygue, G., Çagatay, M. N., Mercier de Lepinay, B., et al. (2008). Cold seeps along the main marmara fault in the sea of marmara (Turkey). *Deep Sea Res. Part I Oceanogr. Res. Pap.* 55, 552–570. doi: 10.1016/j.dsr.2008.01.002

Conflict of Interest Statement: The authors declare that the research was conducted in the absence of any commercial or financial relationships that could be construed as a potential conflict of interest.

Copyright © 2019 Georgieva, Paull, Little, McGann, Sahy, Condon, Lundsten, Pewsey, Caress and Vrijenhoek. This is an open-access article distributed under the terms of the Creative Commons Attribution License (CC BY). The use, distribution or reproduction in other forums is permitted, provided the original author(s) and the copyright owner(s) are credited and that the original publication in this journal is cited, in accordance with accepted academic practice. No use, distribution or reproduction is permitted which does not comply with these terms.

frontiers in Marine Science

ORIGINAL RESEARCH
published: 02 April 2019
doi: 10.3389/fmars.2019.00114

The Contribution of Fine Sieve Fractions (63–150 μm) to Foraminiferal Abundance and Diversity in an Area of the Eastern Pacific Ocean Licensed for Polymetallic Nodule Exploration

Andrew J. Gooday and Aurélie Goineau*

National Oceanography Centre, University of Southampton, Waterfront Campus, Southampton, United Kingdom

OPEN ACCESS

Edited by:
Randi D. Rotjan,
Boston University, United States

Reviewed by:
Ellen Pape,
Ghent University, Belgium
Akkur Vasudevan Raman,
Andhra University, India

***Correspondence:**
Andrew J. Gooday
ang@noc.ac.uk

Specialty section:
This article was submitted to Deep-Sea Environments and Ecology, a section of the journal Frontiers in Marine Science

Received: *05 October 2018*
Accepted: *25 February 2019*
Published: *02 April 2019*

Citation:
Gooday AJ and Goineau A (2019) The Contribution of Fine Sieve Fractions (63–150 μm) to Foraminiferal Abundance and Diversity in an Area of the Eastern Pacific Ocean Licensed for Polymetallic Nodule Exploration. Front. Mar. Sci. 6:114. doi: 10.3389/fmars.2019.00114

The sieve mesh sizes used in benthic foraminiferal studies exert a strong influence on faunal densities and composition. We examined the consequences of including finer (63–150 μm) size classes in a study of Rose Bengal stained ('live') and dead foraminifera in 5 Megacorer samples (0–1 cm layer) from abyssal sites in the eastern Clarion-Clipperton Zone (CCZ; equatorial Pacific), a region with commercially significant deposits of polymetallic nodules. More than 60% of intact specimens originated from the finer (<150 μm) fractions, with over half being picked from 63 to 125 μm residues. Test fragments, mainly agglutinated tubes, were also abundant but were more evenly distributed between coarser and finer residues. The two fractions yielded the same main groups (a mixture of formal taxa and informal groupings) and were dominated by single-chambered forms ('monothalamids'), the majority undescribed. Some were disproportionately abundant in finer fractions: rotaliids in the stained ('live'), textulariids in the dead, and trochamminids, *Lagenammina* spp., *Nodellum*-like forms, saccamminids and spheres in both assemblages. However, the most striking difference was the much greater abundance of tiny, largely undescribed spherical agglutinated morphotypes in the <150-μm fractions. Our 5 samples yielded 462 morphospecies, of which 313 occurred in <150-μm fraction and 170 were confined to this fraction. Twelve of the 31 top-ranked species in the stained assemblage were more or less limited (>90%) to the finer fractions; the corresponding number for the stained + dead assemblage was 12 out of 35. Of the 46 most abundant species in the stained + dead assemblage, 35 were monothalamids (mainly spheres, *Lagenammina* spp., *Nodellum*-like forms, and saccamminids), the remainder being rotaliids (3), hormosinids (3), trochamminids (3) and textulariids (2). By far the most abundant species overall, a tiny agglutinated sphere, was almost entirely confined to the finer fractions. Although small foraminifera that pass through a 150-μm screen are time-consuming to analyze, they constitute an important

part of abyssal Pacific assemblages and may include opportunistic species that respond to episodic food pulses as well as pioneer recolonizers of defaunated substrates. It is therefore important to consider them in studies of possible mining impacts on abyssal benthic communities.

Keywords: polymetallic nodules, Clarion-Clipperton Zone, baseline survey, abyssal benthic foraminifera, sieve mesh size, biodiversity, recolonization

INTRODUCTION

The use of different sized meshes to sieve sediment samples is an important issue in meiofaunal research, the mesh acting as a filter that strongly influences important assemblage metrics, notably faunal densities, biomass, diversity and taxonomic composition of taxa such as nematodes (Leduc et al., 2010). A mesh size of 32 μm is now the widely accepted lower limit for the metazoan meiofauna. In the case of foraminifera, however, different studies have used a variety of different sized meshes (Sen Gupta et al., 1987). The most common are 150, 125, and 63 μm, although larger (250 or 300 μm; e.g., Bernstein et al., 1978; Lutze and Coulbourne, 1984; Gooday et al., 2001) or smaller (45 or 32 μm; e.g., Gooday, 1986; Pawlowski and Lapierre, 1988; Pawlowski, 1991; Gooday et al., 1995; Nozawa et al., 2006; Szarek et al., 2007) sizes have been adopted occasionally. The need to analyze finer sieve fractions (63–125 μm or 63–150 μm) becomes more pressing in deep-sea settings, where benthic organisms are generally small in size compared to shallower waters (Thiel, 1975, 1983; Shirayama and Horikoshi, 1989). Although this involves a larger investment of time compared to the analysis of larger-sized fractions, Schröder et al. (1987) argue that the extra effort is worthwhile because valuable faunal information, including a large proportion of specimens belonging to environmentally important 'indicator' species, is lost by ignoring sieve residues <150 μm. For example, at bathyal depths in the North Atlantic, small-sized species include several that respond opportunistically to seasonally pulsed food inputs (Gooday and Hughes, 2002; Duchemin et al., 2007; Phipps et al., 2012).

Relatively few studies based on fine sieve fractions have been undertaken in the Pacific Ocean. Snider et al. (1984) analyzed the 45–150 and 150–300 μm fractions for meiofaunal organisms, mainly foraminifera, many of them single-chambered forms (monothalamids). More recently, Nozawa et al. (2006) used a 32 μm mesh in a study of foraminifera, again dominated by monothalamids, from the 'Kaplan East' site in the eastern Clarion-Clipperton Zone (CCZ, abyssal equatorial Pacific), a region where large tracts of seafloor are covered with commercially significant deposits of polymetallic nodules. Radziejewska et al. (2006) presented some preliminary observations of monothalamids and other foraminifera based on the >32-μm fractions of samples from the same general area. Ohkawara et al. (2009) described a tiny new spherical monothalamid that was abundant in samples from the Kaplan Central site in the deeper and more central part of the CCZ. The present contribution is part of the AYSSLINE (ABYSSal baseLINE) project, a baseline survey of foraminifera in two areas, also in the eastern CCZ, licensed by the International Seabed Authority for seabed exploration to the UK Seabed Resources Ltd. (UK-1 area), and Ocean Mineral Singapore Pte Ltd. (OMS area). The UK-1 area was sampled in 2013 and both areas were sampled in 2015 during ABYSSLINE research cruises. Previous studies on meiofaunal foraminifera within the framework of this project have described novel species that use radiolarian shells as microhabitats (Goineau and Gooday, 2015) and foraminiferal composition and diversity in >150 μm size fractions (Goineau and Gooday, 2017). Here, we extend this earlier research by describing assemblages of stained and dead benthic foraminifera retained on 63 and 125 μm mesh sieves and comparing them with assemblages in residues >150 μm. We address two main questions. (1) How much information on foraminiferal abundance and diversity is added by analyzing these finer fractions? (2) What are the differences in foraminiferal assemblage composition between the larger and smaller size fractions?

MATERIALS AND METHODS

General information about the ABYSSLINE project is given by Glover et al. (2015). For environmental information about the study area see Amon et al. (2016) and Goineau and Gooday (2017). Pape et al. (2017) provide further environmental data (sediment granulometry, porosity and sorting, total organic carbon and total nitrogen content) for the GSR license area, located to the west of the UK-1 and OMS areas and in somewhat deeper water (∼4500 m). In general terms, our shipboard and laboratory methods followed those described by Goineau and Gooday (2017). We use the term 'stained' to refer to specimens that were inferred to be alive when stained.

Sampling

Samples were collected during two ABYSSLINE cruises at 5 sites (**Supplementary Table S1**) in three 30 × 30 km study areas ('strata') located within the UK-1 and OMS exploration contract areas (**Figure 1**). Two were obtained in Stratum A of the UK-1 license area, centered around 13°49′ N, 116°36′ W, during the first cruise (AB01, R/V *Melville,* cruise MV1313, 3–27 October 2013), two in UK-1 Stratum B, centered around 12° 28.9′ N, 116° 36.3′ W, and one in the OMS Stratum, centered around 12° 8.2′ N, 117° 17.7′ W during the second cruise (AB02: R/V *Thomas G Thompson* cruise TN319; 12 February to 25 March, 2015). In each case the samples were recovered using a hydraulically dampened Megacorer (BCMEGA OSIL Bowers & Connelly type), equipped with 12 polycarbonate coring tubes. As soon as possible

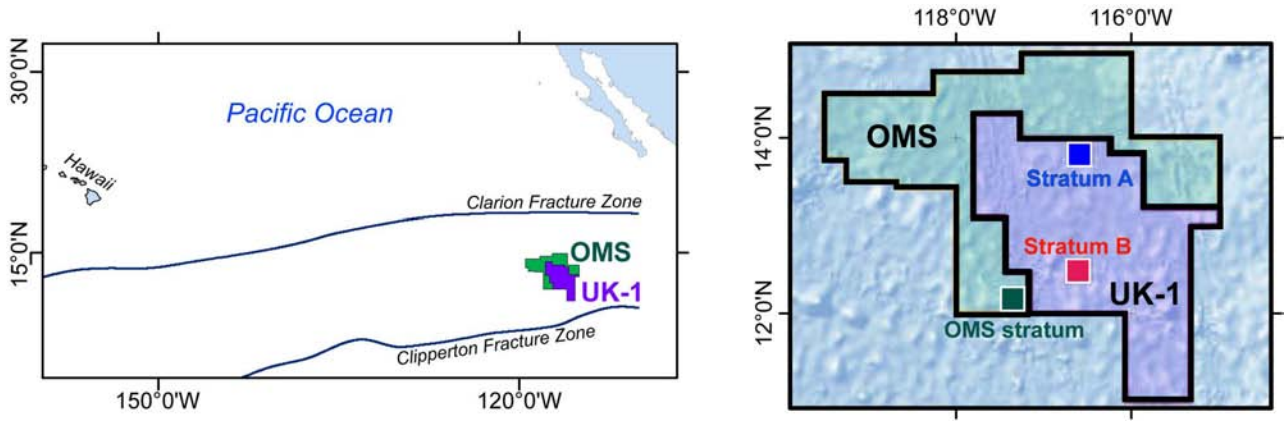

FIGURE 1 | (Left) Location of the Ocean Mineral Singapore (OMS) and UK-1 exploration contract areas in the eastern Clarion-Clipperton Zone, equatorial Pacific. **(Right)** Location of UK-1 Strata A and B and the OMS stratum within the two contract areas.

after collection, the cores were sliced, using a metal plate, into 0.5-cm thick layers to 2 cm depth and 1-cm thick layers from 2 to 10 cm depth and each layer preserved separately in a 500 ml plastic bottle with 10% formalin buffered with borax. Any nodules present in the core were carefully removed in order to facilitate slicing and sediment adhering to them washed into the appropriate sample bottle.

Laboratory Processes

The 0–0.5 and 0.5–1.0 cm sediment layers were used for this study. In the laboratory, the volume of each slice was measured by settling the sediment in a graduated cylinder for 2 days (after which the volume stabilized) followed by splitting into 8 parts using a wet splitter (Jensen, 1982). One split was selected for analysis and its volume measured in the same way. It was then sieved on a series of meshes (300, 150, 125, 63 μm) and each residue stained overnight on the sieve in Rose Bengal solution (1 g in 1 l of tapwater). The stained residues were transferred in water to a Petrie dish and examined under a stereo-microscope. All foraminifera (stained and unstained) and metazoan meiofaunal animals were removed using a glass pipette. In most cases they were stored on cavity slides in a small volume of glycerol, the cavities being left uncovered in order to allow easy access to the specimens. Some delicate organic-walled foraminifera that shrank in glycerol were placed in 1.25 ml Nalgene® cryovials, while calcareous foraminifera, which were rare, were placed on dry slides in order to avoid dissolution in the glycerol. Foraminifera with stained cytoplasm and (if present) fresh stercomata were considered to have been alive when sampled (see **Supplementary Material** for discussion of criteria for distinguishing stained from dead tests).

All foraminiferal specimens were examined under an Olympus BH-2 compound microscope and photographed using an SLR digital camera (Canon EOS 350D) attached to the microscope. Calcareous and delicate organic-walled foraminifera were placed in a cavity slide with water for this purpose, but the majority of specimens were photographed in glycerol. Specimens were grouped into working morphospecies based mainly on observations of test morphology and wall structure, and assigned to genera or species where possible. Those that could not be placed in known taxa were given a descriptive working name.

Some of the methodological challenges involved in analyzing benthic foraminifera in sediment residues from the abyssal CCZ are outlined in the **Supplementary Material**.

Statistical Methods

T-tests to compare the relative abundances of major groups in the >150 and <150 μm fractions were computed using Excel. Based on complete specimens only (stained and stained plus dead combined), we used the open source software EstimateS (Version 9) (Colwell et al., 2012) to calculate the Fisher alpha (α) and Shannon (H', using natural logarithm) diversity indices, and rarefied species richness values [$E(S_{100})$] – the expected number of species represented by 100 individuals) using the open source software EstimateS (Version 9) (Colwell et al., 2012).

RESULTS

Abundance

We picked a total of 2341 complete stained ('live') foraminiferal tests, 1093 complete dead tests, and 1381 fragments (stained and dead combined) from the >300, 150–300, 125–150, and 63–125 μm fractions combined of the five 1/8th sample splits. Individual splits yielded 269–777 (=274–791.10 cm^{-2}) stained tests, 125–329 (=127–335.10 cm^{-2}) dead tests and 115–497 (=117–506.10 cm^{-2}) test fragments.

A majority (62.2%) of complete stained foraminiferal tests originated from the two finer sieve fractions (<150 μm; i.e., 63–125 and 125–150 μm combined), with more than half (52.7% overall) being found in the 63–125 μm fraction alone (**Table 1**). The dead assemblage showed a similar proportion; 64.8% overall in the two finer fractions with 53.7% in the 63–125 μm fraction. Fragmented tests (live + dead combined, mainly tube fragments) were more evenly distributed between the two fractions, with 47.5%

TABLE 1 | Numbers and percentages of complete foraminiferal tests (stained + dead) in the 5 sample splits of which the >150 μm and 63–150 μm fractions were analyzed.

	N range	%range	Mean N	Mean%	
Stained					
300 μm	8–56	2.48–7.99	29.8	6.15	37.8% >150 μm
150–300 μm	43–284	13.3–35.3	153	31.6	
125–150 μm	26–72	4.97–13.6	46.0	9.49	62.2% <150 μm
63–125 μm	137–330	44.5–70.6	121	52.7	
Dead					
300 μm	7–17	3.35–8.08	11.6	5.73	35.2% >150 μm
150–300 μm	39–71	14.5–46.2	55.8	29.5	
125–150 μm	13–46	7.92–15.2	22.6	11.1	64.8% <150 μm
63–125 μm	42–190	35.3–70.6	121	53.7	

originating from the >150 μm and 52.5% from the <150 μm fraction (**Table 2**).

Main Groups

Species were divided into a series of main categories, a mixture of formal taxa (e.g., rotaliids, hormosinids, trochamminids) and informal morphology-based groupings (e.g., spheres, tubes, and 'other monothalamids'). The latter encompasses monothalamids that are difficult to catorgorise morphologically; some examples are illustrated in **Supplementary Figures S1A–C,E–G, S2A,B**. The same main taxa and morphological groupings are represented in both the >150 μm and <150 μm fractions (**Tables 3**, **4**). Among groups represented by complete tests (stained and dead), most tend to be more abundant in absolute terms in the finer fractions. This difference is particularly clear in the case of rotaliids and trochamminids (**Figures 2A,D–H** and **Supplementary Figures S3C–E**, **S4A–D**), *Lagenammina* spp. (**Supplementary Figures S5A–F**), *Nodellum*-like forms (**Supplementary Figure S6**), saccamminids (**Supplementary Figure S7**), spheres (**Figure 4**; **Supplementary Figure S8**), and organic-walled forms (**Supplementary Figures S9A–E**) in the live assemblage, and textualariids (**Figures 2B,C** and **Supplementary Figures S4E,F**), trochamminids, *Lagenammina* spp., *Nodellum*-like forms, saccamminids, and spheres in the dead assemblage. On the other hand, complete tubes and spindles, chains, 'other monothalamids' and Komokiacea ('komoki'; families Baculellidae and Komokiidae, putative monothalamids; **Figure 3K** and **Supplementary Figure S1D**) are more abundant in the coarser fractions, particularly in the case of stained specimens. The only groups that are significantly more abundant in the finer fractions, however, are the saccamminids and spheres (**Tables 3**, **4**). The difference is particularly striking in the case of the stained spheres, which, on average, are some 5 times more abundant in the 63–150 μm than in the >150 μm fraction. This difference is highly significant ($p < 0.001$) for stained specimens (**Table 3**) and significant ($p < 0.05$) for the dead specimens (**Table 4**). These tiny spheres form a substantial proportion of the stained assemblage. They are largely undescribed and in most cases regarded as indeterminate since it was not possible to consistently distinguish morphologically distinct types amongst them. Some examples of the more common forms are shown in **Figure 4** and **Supplementary Figure S8**.

Test fragments (stained and dead combined) are dominated by tubes and spindle-shaped morphotypes (grouped together), with lesser contributions from komokiaceans (Baculellidae and Komokiidae) (**Figure 3**). However, the only clear differences between fractions are the greater average absolute and relative abundance of baculellid fragments in the coarser fractions and, to a lesser extent, of komokiids in the finer fractions (**Supplementary Table S2**). The differences were not significant ($p > 0.05$), however. In the case of the komokiids, it reflected the large number of small fragments of a *Reticulum* species (**Figure 3K**) in the 63–125 and 125–150 μm fractions of the MC13 sample.

Table 5 presents data for the calcareous and agglutinated taxa that have more robust tests and therefore the potential to survive in the fossil record. We include here all of the multichambered foraminifera (Globothalamea and Tubulothalamea) (**Figure 2** and **Supplementary Figures S3A–E**, **S4**), together with species of *Lagenammina* (**Supplementary Figures S5A–F**), which,

TABLE 2 | Numbers and percentages of fragmentary foraminiferal tests (stained + dead) in the 5 sample splits of which the >150 μm and 63–150 μm fractions were analyzed.

	N range	%range	Mean N	Mean%	
300 μm	15–46	6.38–34.3	34.6	13.0	
150–300 μm	20–308	14.9–52.7	160	34.5	47.5% >150 μm
125–150 μm	27–95	8.87–20.1	53.6	15.2	
63–125 μm	41–246	24.5–62.1	140	37.3	52.5% <150 μm
Total per 10 cm^2	17–84				

TABLE 3 | Mean and percentage abundances (±standard deviations) of major groups based on complete stained specimens in the two size fractions and both fractions combined of 5 samples.

	All fractions		>150 μm		63–150 μm	
	N	%	N	%	N	%
Foraminiferal group						
Rotaliids	12.8 ± 8.47	3.01 ± 2.61	3.80 ± 2.86	3.92 ± 6.83	9.20 ± 5.81	3.12 ± 1.94
Miliolids	1.60 ± 1.34	0.35 ± 0.35	0.40 ± 0.55	0.15 ± 0.23	1.40 ± 1.14	0.44 ± 0.39
Lagenids	0.60 ± 0.89	0.15 ± 0.25	0	0	0.60 ± 0.89	0.20 ± 0.30
Ammodiscids	0.20 ± 0.45	0.04 ± 0.08	0.20 ± 0.45	0.10 ± 0.25	0.20 ± 0.45	0.06 ± 0.13
Textulariids	3.20 ± 1.00	0.65 ± 0.18	1.20 ± 0.45	1.00 ± 0.80	2.40 ± 1.67	0.79 ± 0.45
Trochamminids	5.00 ± 4.36	1.04 ± 1.04	0.40 ± 0.55	0.19 ± 0.28	4.40 ± 4.28	1.32 ± 1.34
Hormosinids	14.8 ± 6.38	3.04 ± 1.16	6.20 ± 5.45	3.28 ± 2.23	6.60 ± 5.37	2.65 ± 1.90
Nodellum-like	14.4 ± 12.1	2.74 ± 2.01	2.4 ± 2.07	1.21 ± 1.17	11.6 ± 10.0	3.64 ± 2.70
Lagenammina	21.0 ± 8.94	4.44 ± 2.19	2.40 ± 1.67	2.56 ± 3.77	18.6 ± 8.17	5.80 ± 1.90
Flasks	16.4 ± 12.7	3.41 ± 2.64	8.40 ± 5.55	5.03 ± 5.10	8.00 ± 9.30	2.32 ± 2.65
Chambers 2 tubes	5.60 ± 3.21	1.15 ± 0.57	1.60 ± 1.82	1.04 ± 1.60	4.00 ± 2.83	1.19 ± 0.67
Saccamminids	17.6 ± 6.58	4.05 ± 1.96	2.20 ± 2.59	0.90 ± 1.18	15.4 ± 8.02	5.39 ± 2.77
Spheres	171 ± 36.8	37.6 ± 8.11	**27.8 ± 18.3**	14.94 ± 5.86	**143 ± 22.1**	49.4 ± 13.3
Organic-walled	14.0 ± 7.87	2.88 ± 1.31	3.80 ± 3.90	1.58 ± 0.92	10.2 ± 5.63	3.56 ± 2.13
Hyperammina	0.60 ± 1.34	0.08 ± 0.19	0.20 ± 0.45	0.06	0.40 ± 0.89	0.102 ± 0.22
Tubes/spindles	56.2 ± 38.2	11.1 ± 4.43	38.4 ± 22.4	21.4 ± 5.85	20.2 ± 17.3	6.12 ± 3.82
Other monothalamids	59.8 ± 65.1	10.5 ± 8.40	36.2 ± 38.0	18.2 ± 8.48	23.6 ± 27.4	6.47 ± 6.76
Chains	4.00 ± 3.87	0.69 ± 0.64	2.80 ± 3.83	1.18 ± 2.00	1.20 ± 1.30	0.34 ± 0.34
Komoki-like	14.4 ± 11.5	2.54 ± 1.59	6.25 ± 5.54	3.12 ± 2.51	8.40 ± 8.53	2.37 ± 1.98
Komoki: baculellids	10.4 ± 8.41	1.91 ± 1.05	9.60 ± 8.02	4.52 ± 1.89	0.80 ± 0.83	0.24 ± 0.25
Komoki: komokiids	4.60 ± 1.81	0.97 ± 0.24	4.40 ± 1.95	2.96 ± 1.71	0.20 ± 0.45	0.07 ± 0.15
Radiolarian Inhabitants	22.4 ± 12.4	5.44 ± 2.80	17.6 ± 14.0	10.9 ± 7.10	5.00 ± 6.40	1.69 ± 2.17
Total numbers	2386		929		1457	
Gromiids (n = 21)	4.80 ± 4.44	1.08 ± 1.22	0.40 ± 0.89	0.125	4.40 ± 4.16	1.41 ± 1.38

Values that are significantly different between the two fractions are underlined ($p < 0.05$) or bold and underlined ($p < 0.001$).

although monothalamous, have more or less rigid test walls and are known as fossils. Hormosinids (23.2% of stained and 25.1% of dead specimens) and *Lagenammina* species (40.8% of stained and 25.0% of dead specimens) are abundant constituents of the both stained and dead assemblages when the coarser and finer fractions are combined, and are joined in the dead assemblage by the textulariids (21.5%). Rotaliids are relatively more common in the stained (19.6%) than in the dead (8.38%) assemblage. The overall composition of the >150 μm and <150 μm assemblages is similar. However, hormosinids are relatively less abundant in the finer fractions (stained 19.1% vs. 33.7%; dead 23.2% vs. 30.2%), a pattern reversed in the case of *Lagenammina* spp. (stained 42.7% vs. 36.0%; dead 30.2% vs. 11.3%).

Common Species

Supplementary Tables S3–S6 detail the 30 or so most abundant species in the stained + dead and stained only assemblages; in each case, data for all fractions combined, and the <150 μm fraction only, are shown separately. All 44 species listed in these tables are illustrated in **Figures 2–4** and the **Supplementary Figures** and brief descriptions are given the taxonomic notes included in the **Supplementary Material**. More than three-quarters (34) are monothalamids, among which spheres, *Lagenammina* species, and 'other monothalamids' make up the majority. Most of the multichambered species are textulariids, including several *Reophax* species. By far the most abundant species, both overall and in particular categories, is a small agglutinated sphere (Psammosphaerid sp. 20) that is almost entirely confined (99.4%) to the finer residues. Seven other species (*Spiroplectammina subcylindrica,* 'lobed spheres,' *Lagenammina* yellowish with long neck, *Lagenammina* sp. 9, Saccamminid sp. A, Saccamminid sp. 5) are found exclusively in the <150 μm fractions (stained + dead assemblage). The 30 most common species (stained + dead) in the <150-μm fraction include 23 that are also in the top 32 for the combined residues (>150 + <150 μm). In the case of the stained-only assemblage in the <150-μm fraction, the top 30 species include 22 that are also among the top-ranked species in the two residues combined; these include all of the 17 most abundant species.

Diversity

The five samples combined yielded a total of 462 provisional morphospecies of testate protists (stained and dead, complete and fragmentary tests) that were regarded as foraminifera. Of these, 54 were represented only by fragmented specimens, 279 occurred in the >150 μm fraction, 313 occurred in

TABLE 4 | Mean and percentage abundances (± standard deviations) of major groups based on complete dead specimens in the two size fractions and both fractions combined of 5 samples.

	All fractions		>150 μm		63–150 μm	
	N	%	N	%	N	%
Foraminiferal group						
Rotaliids	12.6 ± 19.3	4.83 ± 6.34	5.80 ± 8.58	7.38 ± 10.0	6.80 ± 10.8	3.62 ± 4.58
Miliolids	0.60 ± 0.55	0.28 ± 0.28	0.50 ± 0.55	0.80 ± 0.74	0	0
Lagenids	0.80 ± 1.30	0.31 ± 0.48	0.20 ± 0.45	0.26 ± 0.58	1.00 ± 1.41	0.69 ± 0.98
Ammodiscids	5.80 ± 4.09	2.64 ± 1.47	2.60 ± 2.70	4.03 ± 4.57	4.20 ± 4.44	2.98 ± 2.27
Textulariids	24.6 ± 15.9	11.2 ± 5.95	8.00 ± 2.83	11.8 ± 5.11	17.0 ± 14.4	12.03 ± 8.37
Trochamminids	13.8 ± 11.5	6.22 ± 3.94	4.20 ± 3.56	6.01 ± 5.00	9.60 ± 8.73	6.64 ± 4.01
Hormosinids	30.2 ± 18.3	13.2 ± 4.94	9.80 ± 4.44	14.7 ± 8.32	20.4 ± 15.0	12.6 ± 3.79
Nodellum-like	12.0 ± 7.84	5.87 ± 3.46	0.60 ± 0.89	0.82 ± 1.19	11.4 ± 7.60	8.88 ± 4.58
Lagenammina	29.6 ± 17.8	12.7 ± 3.68	4.80 ± 3.56	6.69 ± 4.42	24.8 ± 12.0	15.1 ± 4.92
Flasks	6.80 ± 3.83	3.52 ± 2.16	2.60 ± 2.07	3.70 ± 2.96	3.60 ± 2.69	2.64 ± 2.72
Chambers 2 tubes	7.00 ± 2.82	3.51 ± 1.48	2.80 ± 2.77	4.16 ± 4.25	4.20 ± 2.81	2.58 ± 1.16
Saccamminids	8.25 ± 3.77	3.85 ± 0.85	1.60 ± 1.67	2.40 ± 2.54	6.80 ± 3.03	4.96 ± 1.43
Spheres	28.8 ± 13.7	13.7 ± 3.57	5.60 ± 2.97	7.76 ± 3.58	23.2 ± 14.3	16.78 ± 7.87
Organic-walled	0.40 ± 0.55	0.16 ± 0.16	0	0	0.40 ± 0.55	0.22 ± 0.32
Hyperammina	1.20 ± 0.84	0.57 ± 0.38	0.60 ± 0.89	0.98 ± 1.48	0.60 ± 0.89	0.36 ± 0.58
Tubes/spindles	11.0 ± 4.85	5.59 ± 2.27	5.40 ± 2.07	7.96 ± 3.22	6.60 ± 5.94	4.85 ± 3.89
Other monothalamids	10.0 ± 2.55	4.91 ± 1.44	6.00 ± 3.39	8.84 ± 5.20	4.00 ± 2.92	2.52 ± 0.95
Chains	1.80 ± 3.49	1.00 ± 2.28	0.80 ± 1.79	1.04 ± 2.32	1.00 ± 1.73	0.92 ± 1.82
Komoki-like	1.80 ± 2.39	0.93 ± 1.64	1.40 ± 2.61	1.80 ± 3.39	0.40 ± 0.55	0.23 ± 0.32
Komoki: baculellids	3.20 ± 3.11	1.55 ± 1.93	2.80 ± 2.68	3.72 ± 3.56	0.40 ± 0.55	0.34 ± 0.49
Komoki: komokiids	2.20 ± 1.79	1.07 ± 0.76	2.00 ± 1.87	2.64 ± 2.20	0.20 ± 0.45	0.13 ± 0.30
Radiolarian inhabitants	2.20 ± 1.79	1.07 ± 0.71	2.20 ± 1.79	3.05 ± 2.47	0	0
Total numbers	1140		413		727	
Gromiids	0	0	0	0	0	0

Values that are significantly different are underlined ($p < 0.05$).

the <150-μm fractions and 170 were confined to these fine fractions (**Table 6**). The most diverse groups were the tubes with 77 species, 20 of them confined to fractions <150 μm, and the spheres, with 61 species, 25 confined to the fine fractions. Among multichambered groups, textulariids (32 species, 18 only in <150 μm fractions) and hormosinids (30 species, 6 only in <150 μm fractions) were the most specious. If the >150 μm dataset is expanded to include six additional sample splits for which the fine fractions were not analyzed (Goineau and Gooday, unpublished), then the number of morphospecies found only in the >63 μm fraction is halved from 170 to 84.

Detailed diversity metrics based on complete individuals are summarized in **Table 7** (stained plus dead specimens combined) and **Table 8** (stained specimens only). Species numbers and diversity indices [H′, Fisher α, $E(S_{100})$] are generally higher in samples that include the 63–125-μm plus 125–150-μm fractions compared to those based on only the 150–300-μm plus >300 μm fractions. Except for sample MC21, where stained specimens were 3.5 times more abundant in the finer than the coarser residues, Rank 1 Dominance (R1D) is higher in the case of the <150-μm assemblages. However, inclusion of the finer fractions has an inconsistent influence on R1D values when the two fractions are combined.

Gromiids, Unknown Testate Structures, and Metazoan Meiofauna

The <150-μm residues yielded 21 specimens with transparent organic tests that were regarded as gromiids based on the presence of an oral capsule (Hedley, 1960; Rothe et al., 2010). Most had more or less elongate, droplet-like tests that tapered toward the oral capsule (**Supplementary Figures S9G,I**), but a few were sausage-shaped (**Supplementary Figure S9F**) or spherical (**Supplementary Figure S9H**). They are tentatively assigned to 8 morphospecies, all confined to the fine fractions, although variability in test morphology made it difficult to discriminate between some of these forms.

The fine fractions (mainly the 63–125 μm fraction) of some samples also yielded a variety of more or less spherical, organic-walled structures that gave rise to relatively short blind-ending processes (**Figure 5**). They were concentrated in the MC11 and MC13 samples and included three main types. Type A varies in shape from spherical to oval or somewhat irregular and is characterized by a variable number (2–10) of short tubular

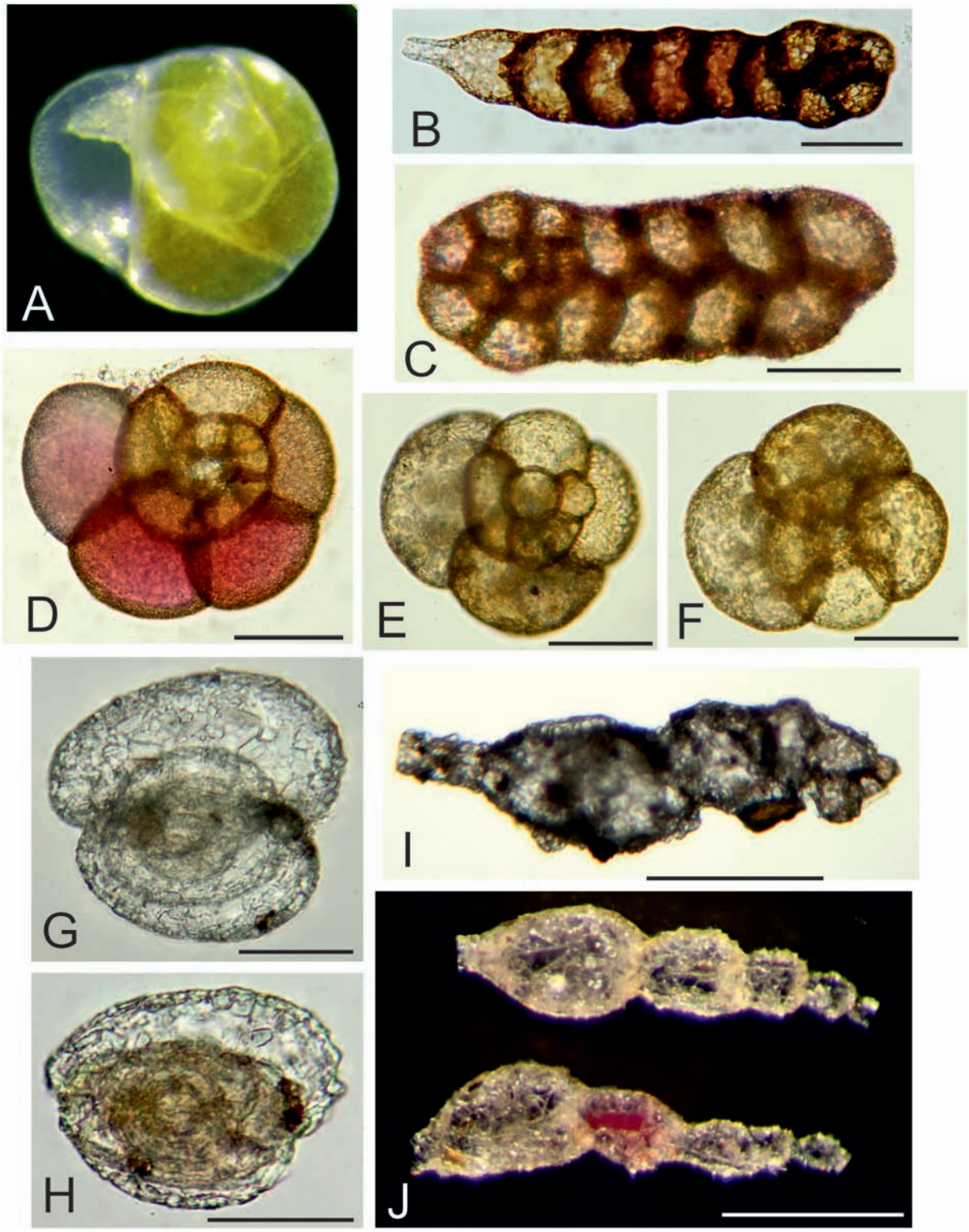

FIGURE 2 | Multichambered foraminifera. **(A)** *Epistominella exigua* Brady; 'live' specimen with green cytoplasm, picked from >150 μm residue at sea. **(B)** *Ammobaculites filiformis* Earland; MC09, 0–0.5 cm, 63–125 μm fraction. **(C)** *Spiroplectammina subcylindrica* Earland; MC21 G 0–0.5 cm, 63–125 μm. **(D)** Trochamminacean sp. 1; MC21, 0.5–1.0 cm, 63–125 μm fraction. **(E,F)** Trochamminacean sp. 2; MC21, 0.5–1.0 cm, 63–125 μm fraction. **(G,H)** *Adercotryma* sp.; MC21, 0.5–1.0 cm, 63–125 μm fraction. **(G)** Rounded specimen. **(H)** More elongate specimen. **(I)** *Reophax scorpiurus* Montfort, MC11, 0.5–1.0 cm, 150–300 μm fraction. **(J)** *Reophax* sp. 1, MC05, 0–0.5 cm, >300 μm fraction. Scale bars = 50 μm **(A–H)**, 250 μm **(I)**, 500 μm **(J)**.

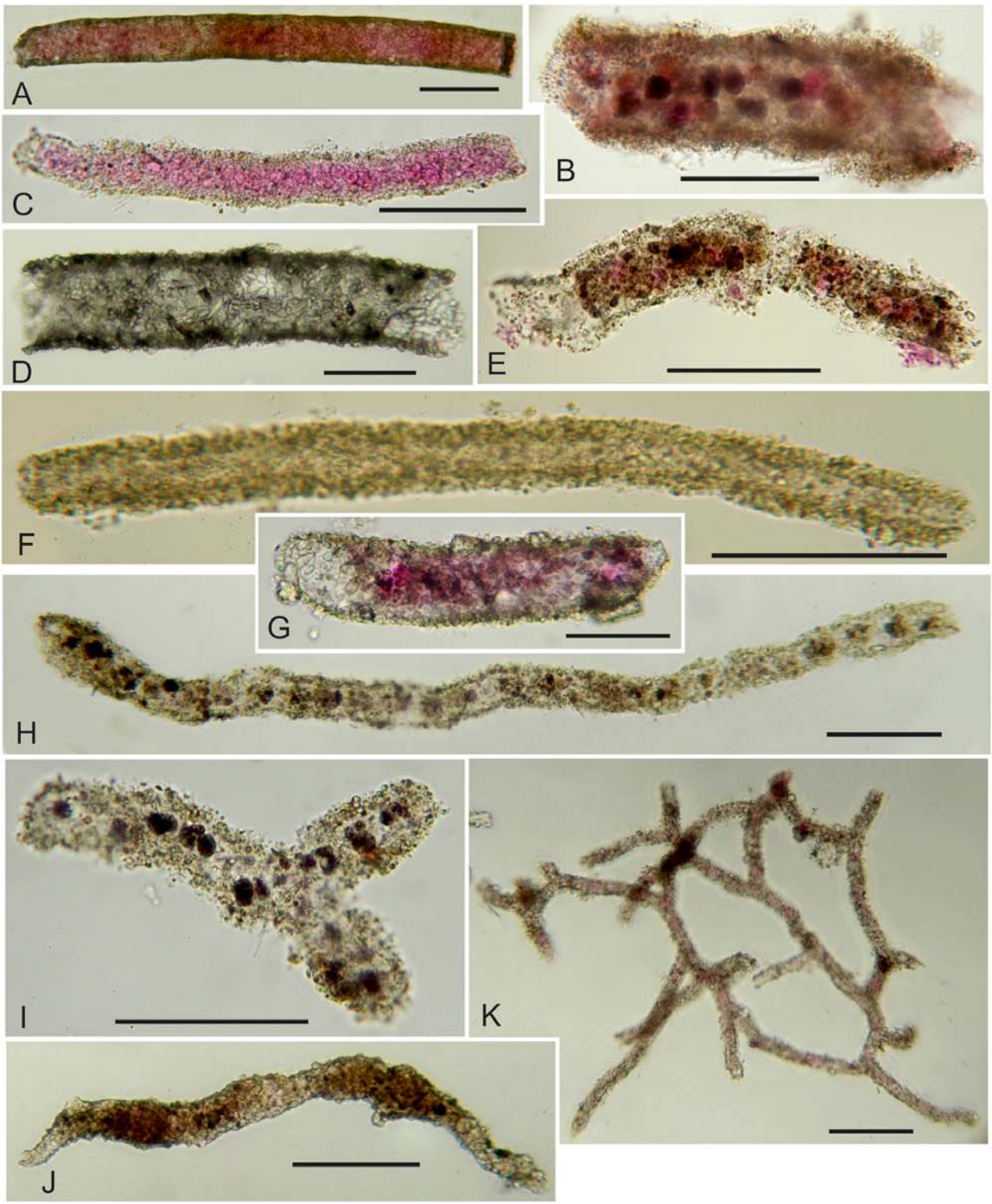

FIGURE 3 | (A–F) Undescribed tubular foraminifera (fragments unless stated otherwise). **(A)** Stained; MC21, 0.5–1.0 cm, 63–125 μm fraction. **(B)** Stained with stercomata; MC13, 0–0.5 cm, 125–150 μm fraction. **(C)** Stained; MC11, 0–0.5 cm, 63–125 μm fraction. **(D)** Dead; MC13, 0–0.5 cm, 125–150 μm fraction. **(E)** Stained; MC09, 0–0.5 cm, 63–125 μm fraction. **(F)** Dead; MC21, 0.5–1.0 cm, 63–125 μm fraction. **(G)** Stained, complete test; MC05, 0.5–1.0 cm, 63–125 μm fraction. **(H)** Dead tubular fragment with stercomata; MC11, 0–0.5 cm, 63–125 μm fraction. **(I) C**omplete tubular specimen; MC11, G, 0–0.5 cm, 63–125 μm fraction. **(J)** *Marsipella* sp.; MC11, 0–0.5 cm, 63–125 μm fraction. **(K)** Stained fragment of *Reticulum* (komokiacean); MC13, 0–0.5 cm, 125–150 μm fraction. Scale bars = 100 μm.

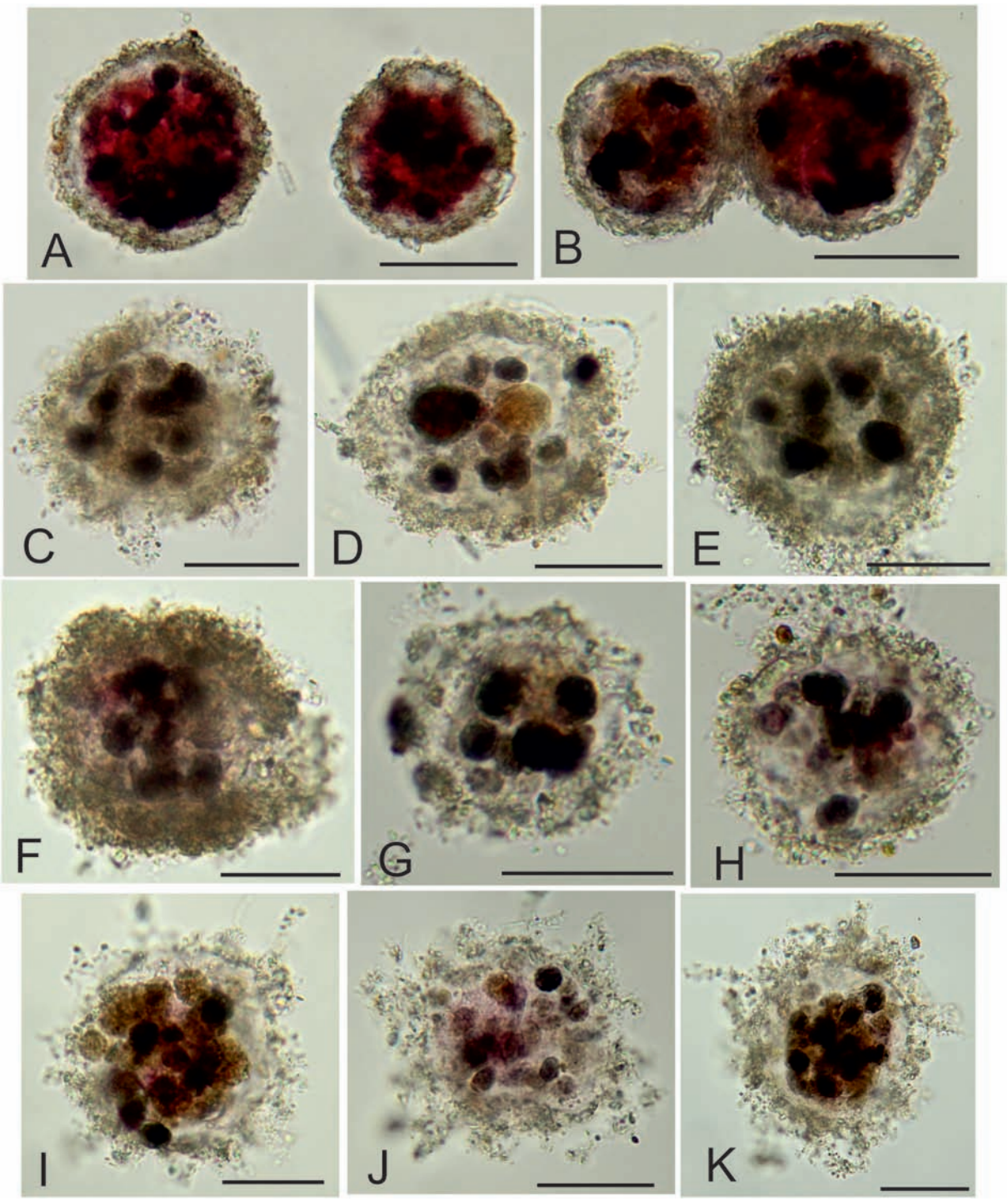

FIGURE 4 | Undescribed spherical foraminifera from 63 to 125 μm fractions. **(A,B)** Psammosphaerid sp. 20, the most abundant morphospecies species in the stained assemblage; MC13, 0.5–1.0 cm. **(C–H)** Morphotype with delicate, fine-grained wall enclosing stercomata and sparse cytoplasm; all are from sample MC05. **(I–K)** Similar morphotype in which the wall includes an organic layer with finely agglutinated particles and gives rise to short filament-like structures; all are from sample MC05. Scale bars = 50 μm.

extensions with longitudinal striations and ending in a thin-walled bulb. This was by far the commonest form, particularly in the MC13 sample where it was represented by 174 specimens. Type B has relatively longer, narrower, and often somewhat tapered tubular processes, sometimes ending in a small bulb. Three specimens were found inside other structures in the MC11

TABLE 5 | Absolute and relative abundance of complete foraminifera belonging to more robust (fossilizable) taxa, mainly multichambered.

	>150 μm				<150 μm				Combined			
	'Live'		Dead		'Live'		Dead		'Live'		Dead	
	N	%	N	%	N	%	N	%	N	%	N	%
Rotaliids	19	22.1	24	15.1	41	18.6	24	5.80	60	19.6	48	8.38
Miliolids	0	0	3	1.89	6	2.73	0	0	6	1.96	3	0.52
Ammodiscids	0	0	9	5.66	2	0.91	25	6.04	2	0.65	34	5.93
Lageniids	0	0	1	0.63	6	2.73	8	1.93	6	1.96	9	1.57
Textulariids	4	4.65	36	22.6	9	4.09	87	21.0	13	4.24	123	21.5
Trochamminids	3	3.49	20	12.6	20	9.09	49	11.8	23	7.52	69	12.0
Hormosinids	29	33.7	48	30.2	42	19.1	96	23.2	71	23.2	144	25.1
Lagenammina	31	36.0	18	11.3	94	42.7	125	30.2	125	40.8	143	25.0
Total	86		159		220		414		306		573	

The numbers are totals from all 5 samples. L = 'Live' (stained); D = Dead.

TABLE 6 | Number of morphospecies assigned to different foraminiferal groups, and to gromiids.

Foraminiferal group	All species	>150 μm	<150 μm	<150 only
Rotaliids	19	11	14	8
Miliolids	4	1	3	3
Ammodiscids	6	1	6	5
Lageniids	5	3	5	2
Textulariids	32	13	24	18
Trochaminiids	18	10	16	8
Hormosiniids	30	23	20	6
Lagenammina	15	4	13	11
Nodellum-like	17	8	15	8
Flasks	4	3	4	1
Droplet chambers	2	0	2	2
Chambers 2 tubes	2	0	2	0
Saccamminids	28	8	22	19
Spheres	61	35	36	25
Organic-walled (allogromiids)	19	6	15	13
Hyperammina	6	3	3	3
Tubes/spindles	77	54	57	20
Other monothalamids	56	43	25	12
Chains	10	9	6	0
Komoki-like	15	13	9	2
Komoki: baculellids	19	19	9	0
Komoki: komokiids	17	12	7	4
Total number of species	462	279	313	170
Gromiids	8	0	8	8

The numbers are totals from all 5 samples.

sample. Type C is spherical and was represented by 2 specimens from the MC13 sample with several (3 and 5) rounded bumps on the surface of the organic wall.

A total of 167 metazoan meiofaunal organisms (not counting 7 polychaete fragments without heads), all of which were well stained and assumed to have been alive when collected, were picked from the 5 sample residues (i.e., 1/8th splits of the top 1-cm layer of five 10-cm diameter sediment cores). This number corresponds to an overall density of 34.0 individuals per 10 cm^2. Nematodes were the most common metazoans (62.3%), followed by harpacticoid copepods (19.7%), nauplii (15.6%), 2 ostracods, 1 bivalve and 1 kinorhynch.

DISCUSSION

Stained complete foraminiferal tests were more than an order of magnitude more abundant in our five sample splits from the eastern CCZ than metazoan meiofaunal animals (i.e., 2341 stained tests compared with 167 metazoans, corresponding to overall densities of 496 and 34 individuals per 10 cm^2, respectively). The metazoan densities are generally lower than those typical for the CCZ (11–394 individuals per 10 cm^2 in nine studies; summarized in Radziejewska, 2014, Table 3.4 therein) and the mean values (88 ± 55 to 151 ± 54 individuals per 10 cm^2) recently reported by Pape et al. (2017) from the GSR license area in the northeastern CCZ. Moreover, the proportion (62.3%) of nematodes is relatively low and the proportion of nauplii relatively high (15.6%), compared to previous studies. For example, nematodes represented 85–93% and nauplii 1.1–7.1% of the metazoan meiofauna in the study of Pape et al. (2017). These discrepancies probably reflect methodological differences. In particular, while the 63 μm lower limit used in the present study is normal for foraminifera (Murray, 2014), it is not appropriate for analyzing metazoan meiofauna, for which 32 μm is now the generally accepted lower limit (Leduc et al., 2010). Nevertheless, although metazoans were not adequately sampled, our results do suggest that stained foraminifera outnumber metazoan meiofaunal animals in CCZ sediments.

The nature of the organic-walled structures with blind-ending processes remains unresolved. They are almost certainly not dinoflagellate cysts (Dr. Ian Harding, University of Southampton, personal communication). The most likely identification, at least for the common forms from sample MC13 (**Figures 5A–D**), are that they are metazoan eggs, possibly those of a crustacean (Dr. Manuel Bringué; Geological Survey of Canada – Calgary).

TABLE 7 | Diversity metrics for the stained + dead assemblage in different samples.

	MC09			MC11			MC05			MC13			MC21		
	UK-1 Stratum A			UK-1 Stratum A			UK-1 Stratum B			UK-1 Stratum B			OMS Stratum		
	>150	<150	Total	>150	<150	Total	>150	<150	Total	>150	<150	Total	>150	<150	Total
N	208	340	547	345	426	771	208	233	442	144	161	305	99	350	448
S	95	100	164	99	113	177	82	89	150	57	57	100	50	120	150
H'(log_e)	4.27	4.03	4.59	3.96	4.07	4.55	3.95	4.02	4.52	3.57	3.22	3.96	3.53	4.19	4.38
Fisher α	67.6	47.7	85.0	47.2	50.2	74.0	49.9	52.6	83.1	37.3	32.1	56.9	40.3	64.5	79.1
E(S_{100})	63.6	52.0	63.3	50.4	52.2	60.2	52.4	54.9	62.1	46.7	44.0	53.0	50.0	56.0	59.0
R1D	7.21	9.71	6.63	10.14	12.7	7.03	6.44	12.4	6.58	24.1	44.7	26.1	15.1	10.0	7.81

TABLE 8 | Diversity metrics for the stained assemblage in different samples.

	MC09			MC11			MC05			MC13			MC21		
	UK-1 Stratum A			UK-1 Stratum A			UK-1 Stratum B			UK-1 Stratum B			OMS Stratum		
	>150	<150	Total	>150	<150	Total	>150	<150	Total	>150	<150	Total	>150	<150	Total
N	152	171	323	292	307	597	123	167	290	85	114	199	42	170	212
S	74	72	129	80	87	144	61	61	115	30	36	57	26	70	83
H'(log_e)	4.03	3.844	4.438	3.69	3.756	4.260	3.69	3.635	4.293	2.883	2.492	3.209	3.072	3.820	3.851
Fisher α	58.7	46.29	84.92	36.3	40.93	60.27	36.35	35.19	69.52	16.20	18.77	27.40	29.11	44.25	51.89
E(S_{100})	58.8	52.3	65.1	44.2	47.6	54.2	44.2	47.0	59.8	30.0	34.2	39.60	26.0	51.7	52.75
R1D	7.89	11.6	10.9	12.0	17.3	8.88	8.12	16.5	9.18	24.1	46.8	27.1	9.52	11.7	17.1

The majority of complete stained (61.1%) as well as dead (63.8%) foraminiferal tests originated from the 63–150 μm fractions. These results are consistent with previous studies of deep-sea meiofauna, including foraminifera (e.g., Gooday, 1986; Schewe, 2001), as well as with the general tendency for small-sized organisms to become increasingly important with increasing water depth (Thiel, 1975, 1983). Duchemin et al. (2007) report that the 63–150 μm fraction of the top 1-cm of a core from 1000 m in the Bay of Biscay yielded the vast majority (97.5%) of stained foraminifera. In one of the most comprehensive studies, Phipps et al. (2012) found that stained foraminiferal densities in the 63–150 μm fraction of samples taken along a down-slope transect (262 – 4987 m water depth) on the Portuguese margin were consistently more than twice those in the >150 μm fraction. Interestingly, the proportion increased with depth, reaching a peak at 3908 m, where 88% of stained foraminifera were picked from the fine sieve residues.

Comparison With Modern Abyssal Assemblages

Fractions <150-μm were dominated by monothalamids, many of them more or less spherical forms. These tiny spheres represented an average of 37.6 ± 8.1% of complete stained foraminifera in all fractions combined and 49.4 ± 13.3% in the 63–150 μm fraction, with a significantly lower numbers in the 150–300 μm compared to the 63–150 μm fraction (**Table 1**). Many have delicate, fine-grained test walls and contain stercomata (**Figures 4C–K**). Numerous agglutinated spheres are also reported in previous studies of abyssal Pacific samples. According to Snider et al. (1984), spherical ('sac-shaped') morphotypes made up almost third (31.3%) of meiofaunal foraminifera in the central North Pacific (5800 m depth). Nozawa et al. (2006), found an even greater predominance (33.5 – 94.5%) of tiny, undescribed 'psammosphaerids' in small samples from the Kaplan East site, located immediately to the west of the UK-1/OMS area and at a similar water depth. The higher proportion probably reflects the fact that Nozawa et al. (2006) examined even finer fractions (>32 μm) fractions than those analyzed for the present study. Later, Ohkawara et al. (2009) established a new species, *Saccammina minimus,* based on numerous tiny agglutinated spheres from the deeper (∼5000 m) Kaplan Central site, located in the central part of the CCZ (∼14°N, 130°W). The majority of spheres in our samples are undescribed, but some are probably the same as *S. minimus,* while other somewhat larger forms resemble *Thurammina albicans*. Small agglutinated spheres also occur in the abyssal North Atlantic. They represented 7.2 – 12.4% of assemblages >63 μm at the Porcupine Abyssal Plain and an even higher proportion (17.8%, 21.0%) in two samples from the Cape Verde Abyssal Plain (Gooday, 1996). Very small agglutinated tests were reported by Gooday et al. (1995) in North Atlantic sediments sieved on 32 and 20 μm meshes. However, the spheres with a soft 'fluffy' wall and containing stercomata (**Figures 4C–K**), which are common in our samples, have not been observed in the Atlantic material.

The finer residues yielded many tubular and spindle-shaped morphotypes (**Figure 3**). Stained specimens judged to be complete were again more common in the >150-μm

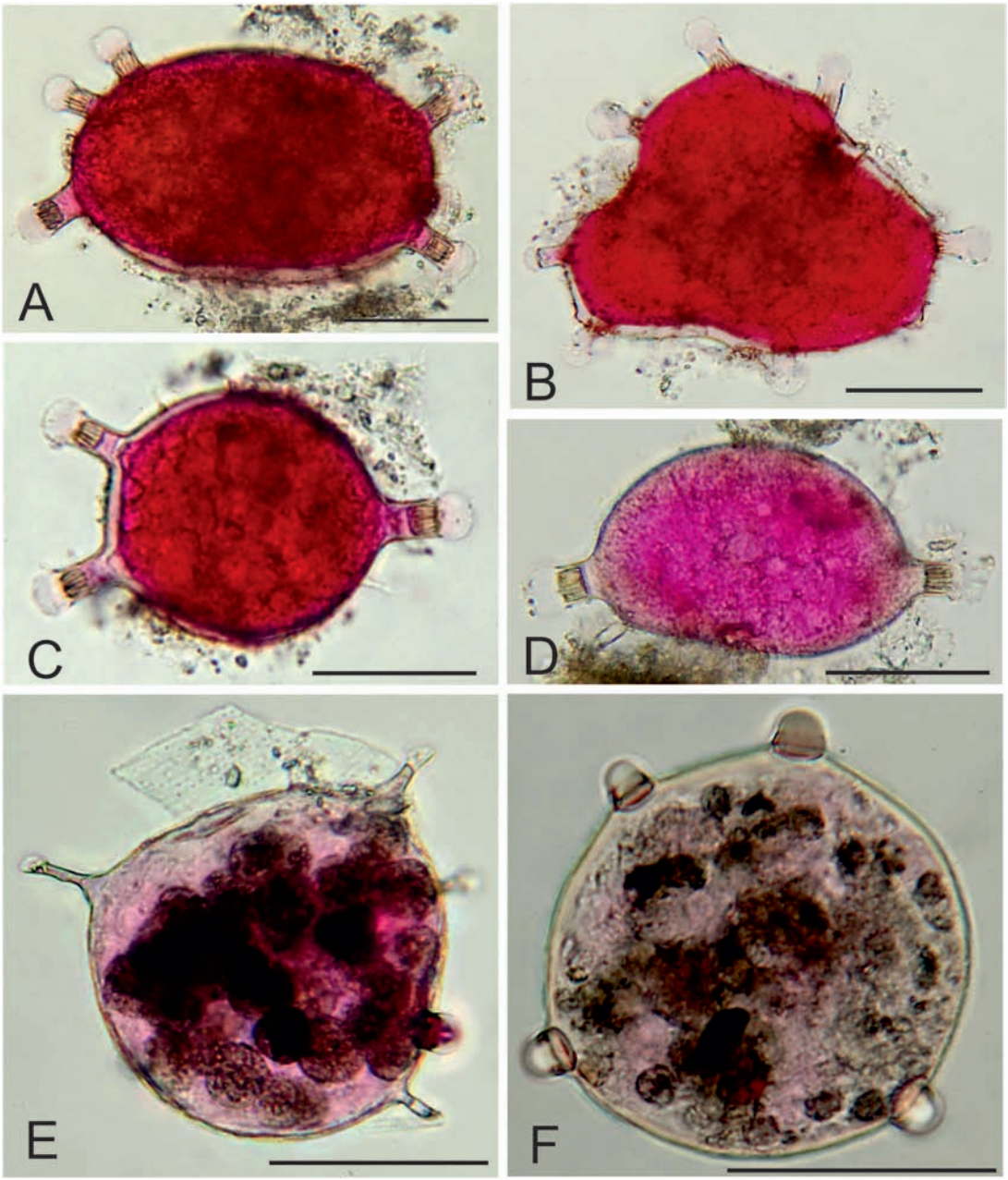

FIGURE 5 | Unidentified organic-walled structures (?metazoan eggs) from 63–125 μm fractions. **(A–C)** Type A with short striated tubes ending in thin-walled bulbs; MC11, 0–0.5 cm layer. **(D,E)** Type B with relatively long slender tubes, sometimes ending in a small thin-walled bulb; MC11, 0–0.5 cm. **(F)** Type C with rounded bumps; MC13, 0.5–1.0 cm layer. Scale bars = 50 μm.

(mean 21.4%) than the <150-μm (mean 6.12%) fraction (**Table 3**). Tubular fragments (stained as well as stained and dead combined) were also very numerous, representing >60% in both size fractions (**Supplementary Table S2**). Similar fragments are often common in abyssal samples. Bernstein et al. (1978) recorded 30,938 fragments compared to 5,079 complete foraminiferal tests in 5 unstained box-corer residues (>297 μm fraction) from the central North Pacific. Snider et al. (1984) likewise found numerous fragments in their North Pacific samples (42–1000-μm fraction). Based on the conservative assumption that all fragments of a similar type within a sediment layer and adjacent layers were derived from one individual, they calculated that 24% of monothalamids were tubular forms.

Our samples also yielded small, multichambered foraminifera that are similar to those reported in previous studies of modern abyssal benthic foraminifera. They include agglutinated species (e.g., *Cribrostomoides subglobosum, Cyclammina trullisata, Cystammina galatea, Cystammina pauciloculata, Deuterammina*

grahami, Glomospira spp., *Hormosinella ovicula, Hyperammina cylindrica, Lagenammina difflugiformis, Paratrochammina scotiaensis, Reophax scorpiurus, Spiroplectammina subcylindrica*, *Hormosinella distans, Veleroninoides wiesneri*), and calcareous species [*Epistominella exigua, Nuttallides umbonatus, Cibicidoides mundulus* (as *C. cf mundulus), Fissurina staphyllearia* and *Melonis pompiliodes*] previously reported from abyssal depths in the North and equatorial Pacific by authors such as Smith (1973), Burministrova et al. (2007), and Enge et al. (2012). Many of these are well-known morphospecies that are widely distributed in modern ocean basins (Gooday and Jorissen, 2012; Holbourn et al., 2013).

Comparison With Fossil Assemblages

There are some similarities between the agglutinated foraminifera in our samples and certain assemblages of multichambered taxa of Late Cretaceous and Paleogene age recovered in Deep-Sea Drilling Project (DSDP) and Ocean Drilling Project (ODP) cores. Krasheninnikov described Upper Cretaceous faunas devoid of calcareous foraminifera in red-brown clays from the Pacific (1973) and Indian (1974) Oceans. He interpreted these as having been deposited in oceanic sediments below the CCD. They consisted mainly of small species, often with smooth, fine-grained test walls, assigned to genera such as *Haplophragmoides, Labrospira, Trochammina,* and *Recurvoides.* Similar abyssal faunas are known from the North Atlantic Plantagenet Formation, where they also include 'rhizamminids' and 'fossil forms which resemble modern Komokiaceans' (Kuhnt et al., 1989). However, our multichambered assemblages also contain some calcareous taxa (mainly rotaliids), reflecting their location close to, rather than well below, the CCD. In this respect, they have more in common with the mixed calcareous and agglutinated assemblages described by Hemleben and Troester (1984) from DSDP Hole 543A in the central Atlantic.

Species of *Reophax* and other hormosinids, which consistently constitute the most common multichambered foraminifera in our samples, are often not well represented in the Late Cretaceous assemblages, possibly a result of the low fossilization potential of their fairly delicate tests (Schröder, 1986). Some more robust species, however, are preserved as fossils in deep-sea sediments (e.g., Kuhnt and Moullade, 1991).

Possible Ecological Significance

Responses to Food Inputs

One rationale for including finer sieve fractions (63–150 μm) in ecological studies of bathyal and abyssal foraminifera is that small species often display opportunistic responses to seasonally pulsed food ('phytodetritus') inputs to the seafloor (e.g., Gooday, 1988, 2003; Gooday and Lambshead, 1989; Corliss and Silva, 1993; Silva et al., 1996; Ohga and Kitazato, 1997; Gooday and Rathburn, 1999; Gooday and Hughes, 2002; Kitazato et al., 2003; Heinz and Hemleben, 2006; Duchemin et al., 2007). This suggests that they play an active role in the processing fresh organic carbon on the ocean floor, an inference supported by *in situ* experimental studies using ^{13}C-labeled algae (Moodley et al., 2002), some of which reveal different species-level responses to food inputs (Nomaki et al., 2005, 2006).

The deposition of phytodetritus on the deep-sea floor is well documented at temperate latitudes in the NE Atlantic. In the Pacific the phenomenon is reported from various sites along the North American continental margin (Beaulieu, 2002), notably at the intensively studied abyssal (4100 m depth) Station M on the Californian margin (Beaulieu and Smith, 1998). Here, as in the NE Atlantic, the presence of these deposits on the seafloor has a distinct seasonal component (Lauerman and Kaufmann, 1998). There is also evidence for seafloor phytodetritus in the abyssal equatorial Pacific. Deposition in this open ocean setting, however, is not seasonal (Beaulieu, 2002) and is linked to upwelling created by easterly trade winds (Smith and Demopoulos, 2003). Gardner et al. (1984) observed 'dark globs of material' that were '1–4 cm across and appear fluffy and organic in nature. . .' in seafloor photographs taken at a site to the south of the central CCZ (4°N, 136°W; 4469 m depth). Smith et al. (1996) recovered phytodetritus in multicore samples collected along the 140°W line from 5°N to 5°S. Further east, and within the CCZ, Radziejewska (2002) observed a 'very thin layer of a fluffy material, greenish-brown in color' (i.e., phytodetritus) on the surfaces of some cores collected in 1997 in part of the IOM contract area (centered at 11° 04′N, 119° 40′W; 4380–4430 m depth) that had been subject 2 years earlier to an experimental disturbance designed to simulate the effects of nodule mining (see also Radziejewska, 2014). Samples of this material, which was very patchily distributed, contained chloropigments and intact diatoms. Phytodetritus was not present on the surfaces of cores recovered in 1995 or 2000. Its presence in 1997 was believed to be largely responsible for the greatly increased abundance of the nematode genera *Desmoscolex* and *Pareudesmoscolex* compared to 1995 (Radziejewska et al., 2001). Increases in metazoan megafauna in nodule-bearing parts of the IOM area was likewise attributed to the increased food supply originating from phytodetrital inputs (Radziejewska and Stoyanova, 2000).

Small lumps of phytodetritus-like material were occasionally found in our sieve residues, but these deposits were not observed on the surfaces of any megacores collected during the present study. However, our residues yielded small numbers of species, notably *Alabaminella weddellensis* and *Epistominella exigua,* which are known to exploit phytodetritual inputs in the abyssal NE Atlantic (e.g., Gooday, 1988, 1993). *Epistominella exigua,* in particular, contained bright green cytoplasm indicating ingestion of fresh chlorophyll-bearing particles (**Figure 2A**). Darker green cytoplasm is typical of *Nuttallides umbonifera,* the most common rotaliid in our samples (**Supplementary Figure S3D**). If inputs of phytodetritus do occur from time to time in the UK and OMS claim areas, as they appear to do in the nearby IOM area, then these and perhaps other species are likely to respond to this fresh food source with rapid reproduction and population growth. All but 2 of the 25 specimens (stained and dead) of *A. weddellensis* and *E. exigua* were extracted from residues <150 μm, demonstrating the importance of examining finer sediment fractions in order to recover small, opportunistic foraminiferal species that may be

important players in the processing of fresh organic matter on the ocean floor.

Possible Importance in Recolonization

Alve (1999) reviewed how sediments that have been defaunated by natural or anthropogenic processes can be repopulated by benthic foraminifera. In relatively tranquil settings, initial recolonization may proceed in a series of stages, starting with quick-growing, opportunists that are succeeded by slower-growing, more specialized species. Relatively few studies of foraminiferal recolonization have been conducted in deep-water settings. Probably the best direct evidence comes from samples collected during 5 cruises (spring 1994, summer and winter 1996, summer 1998, spring 1999) in an area of the South China Sea (∼2500 m depth) blanketed by a layer of volcanic ash from the 1991 Mt Pinatubo eruption (Hess and Kuhnt, 1996; Hess et al., 2001; Kuhnt et al., 2005). Although the material involved was different, the ash fall to some extent mimicked the deposition of resuspended sediment expected to result from seabed mining. In samples sieved on a 63-μm mesh, the initial recolonizers of the 2- to 6-cm-thick ash layer appeared to be a small species of *Textularia,* followed by *Reophax dentaliniformis* and later by *R. bilocularis* and *R. scorpiurus,* the rotaliid *Bolivina difformis* and the miliolid *Quinqueloculina seminula* (Hess et al., 2001). A second wave of recolonizers included *Trochammina* spp., *Adercotryma glomerata,* and *Subreophax guttifera.*

Analysis of sediments deposited by turbidity currents in submarine canyons has provided insights into the recolonization by foraminifera of physically disturbed areas of seafloor. According to Duros et al. (2017), the initial recolonizers in the >150 μm fraction of a turbidite deposit at upper bathyal depths (983 m, 1454 m) in the Capbreton Canyon (Bay of Biscay) were *Fursenkoina bradyi, R. dentaliniformis* and *Technitella melo.* However, the 63–150 μm fraction from the 983-m site, as well as two shallower sites (251 m, 301 m), were dominated by juveniles of *Bolivina subaenariensis,* which was interpreted as representing a second stage of recolonization. The same species dominated low diversity assemblages (63–150-μm fraction) of two cores collected in the same canyon at a 600 m site that had been impacted by a turbidity current 1.5 years earlier (Hess et al., 2005; Hess and Jorissen, 2009). Here, *B. subaenariensis* may have been responding to organic matter associated with the turbidite, as well as participating in the recolonization process.

These studies suggest that azoic substrates, originating either from deposited material (ash) or physical disturbance of the seafloor (turbidite), are colonized by a succession of foraminiferal species. In both cases, the colonizing species were considered to have been infaunal. Some of these species are larger (e.g., *Reophax* spp., which are fairly common in our samples) and more likely to be retained in the >150-μm fraction, but smaller species or juveniles are also involved. Our finer fractions yielded small agglutinated species belonging to genera such as *Ammobaculites*, *Spiroplectammina*, and *Textularia* that are rare in the stained assemblages. It is possible that such species may be important during initial phases of recolonization following mining-related disturbances.

CONCLUSION

Is the considerable additional effort required to analyze foraminifera in 63–150 μm fractions of samples from areas that could be disturbed by seabed mining worthwhile? In the present study, the fine-fraction assemblages contained >60% of stained and dead test as well as 170 species that were not present in the coarser fractions. They also yielded greater absolute abundances than >150-μm fractions of several monothalamid groups, notably *Lagenammina* spp., *Nodellum*-like forms, saccamminids, and particularly spherical forms, as well as some multichambered taxa, namely rotaliids (stained only), hormosinids (dead only), textulariids (dead only), and trochamminids. An important part of the foraminiferal assemblage was therefore confined to these fine fractions. As argued elsewhere (e.g., Gooday et al., 2008; Goineau and Gooday, 2017), multichambered taxa, particularly the calcareous rotaliids, may be metabolically more active than stercomata-bearing monothalamids in deep-sea settings, and therefore more important in terms of ecosystem functioning. Although rotaliids are relatively uncommon in our samples, their greater absolute (but not relative) abundance in the <150-μm fractions provides one incentive for analyzing fine sieve residues. Another justification is the potentially important role that small multichambered opportunistic species could play in the recolonization of sediments disturbed by mining. Nevertheless, the fact remains that this work is very time-consuming and difficult to undertake routinely.

A number of studies have used foraminiferal faunal data and diversity metrics as bio-indicators of human impacts in marine environments (e.g., Jorissen et al., 2009 and references therein). This has led to the formulation of a series of recommendations, the FOMIBO initiative, aimed at standardizing methodologies applied in such studies (Schönfeld et al., 2012). One of the 'mandatory' recommendations is that, although samples should be sieved on a 63-μm mesh, detailed analysis should be based on the >125-μm fraction. However, they also add the 'advisory' recommendation that in some eutrophic settings, where small opportunistic species are abundant, it may also be necessary to analyze the finer 63–125-μm as well as the >125 μm fraction. A similar conclusion was reached by Sen Gupta et al. (1987). A sensible compromise in the case of baseline studies of foraminifera in Pacific nodule fields would therefore be to concentrate efforts on analyzing coarser residues from all samples but to examine finer fractions (63–150 μm), either quantitatively or qualitatively, in a subset of samples or sample splits. Similar approaches have been adopted by a number of authors working in the NE Atlantic deep-sea samples (e.g., Phipps et al., 2012; Duros et al., 2017). It may be particularly important to do this during monitoring exercises, i.e., where deep-sea sediments have been defaunated by seabed mining and are in the early stages of recolonization by meiofaunal organisms. To conclude, foraminifera and particularly monothalamids are a major constituent of benthic faunas in the CCZ nodule fields. Despite the methodological challenges that they pose, we would encourage other researchers to consider including them in studies of areas where seabed mining may occur in the future.

DATA AVAILABILITY

All datasets generated for this study are included in the manuscript and/or the **Supplementary Files**.

AUTHOR CONTRIBUTIONS

AJG conceived the project, analyzed the <150 μm fractions, and prepared the figures and tables. AG analyzed the >150 μm fractions. Both authors integrated and analyzed the <150 μm and >150 μm fraction data. The manuscript was largely written by AG with contributions from AJG.

FUNDING

The ABYSSLINE project was funded through a commercial arrangement with UK Seabed Resources Ltd.

ACKNOWLEDGMENTS

We are grateful to Craig Smith for his leadership of the overall ABYSSLINE project and particularly the AB01 and AB02 cruises, as well as Ivan Voltski (AB01) and Alexandra Weber (AB02) for their help with core collection and processing at sea. We would like to thank Dr. Ian Harding and Dr. Manuel Bringué for their advice regarding the identity of the unidentified organic-walled structures and two reviewers for their comments, which helped to improve the manuscript.

SUPPLEMENTARY MATERIAL

The Supplementary Material for this article can be found online at: https://www.frontiersin.org/articles/10.3389/fmars.2019.00114/full#supplementary-material

REFERENCES

Alve, E. (1999). Colonization of new habitats by benthic foraminifera: a review. *Earth Sci. Rev.* 46, 167–185. doi: 10.1016/S0012-8252(99)00016-1

Amon, D. J., Ziegler, A. F., Dahlgren, T. G., Glover, A. G., Goineau, A., Gooday, A. J., et al. (2016). Insights into the abundance and diversity of abyssal megafauna in a polymetallic-nodule. *Sci. Rep.* 6:30492. doi: 10.1038/srep30492

Beaulieu, S. E. (2002). Accumulation and fate of phytodetritus on the sea floor. *Oceanogr. Mar. Biol. Ann. Rev.* 40, 171–232. doi: 10.1201/9780203180594.ch4

Beaulieu, S. E., and Smith, K. L. (1998). Phytodetritus entering the benthic boundary layer and aggregated on the sea floor in the abyssal NE Pacific: macro- and microscopic composition. *Deep Sea Res. II* 45, 781–815. doi: 10.1016/S0967-0645(98)00003-4

Bernstein, B. B., Hessler, R. R., Smith, R., and Jumars, P. A. (1978). Spatial dispersion of benthic Foraminifera in the abyssal central North Pacific. *Limnol. Oceanogr.* 23, 401–416. doi: 10.4319/lo.1978.23.3.0401

Burministrova, I. I., Khusid, T. A., Belyaeva, N. V., and Chekhovskaya, M. P. (2007). Agglutinated abyssal foraminifers of the equatorial Pacific. *Oceanology* 47, 824–832. doi: 10.1134/S0001437007060070

Colwell, R. K., Chao, A., Gotelli, N. J., Lin, S. Y., Mao, C. X., Chazdon, R. L., et al. (2012). Models and estimators linking individual-based and sample-based rarefaction, extrapolation and comparison of assemblages. *J. Plant Ecol.* 5, 3–21. doi: 10.1093/jpe/rtr044

Corliss, B., and Silva, K. A. (1993). Rapid growth of deep-sea benthic foraminifera. *Geology* 21, 991–994. doi: 10.1130/0091-7613(1993)021<0991:RGODSB>2.3.CO;2

Duchemin, G., Fontanier, F. C., Jorissen, F. J., Barras, C., and Griveaud, C. (2007). Living small-sized (63–150 μm) foraminifera from mid-shelf to mid-slope environments in the Bay of Biscay. *J. Foramin. Res.* 37, 12–32. doi: 10.2113/gsjfr.37.1.12

Duros, P., Silva Jacinto, R., Dennielous, B., Schmidt, S., Martinez Lamas, R., Gautier, E., et al. (2017). Benthic foraminiferal response to sedimentary disturbance in the Capbreton canyon (Bay of Biscay, NE Atlantic). *Deep Sea Res. I* 120, 61–75. doi: 10.1016/j.dsr.2016.11.012

Enge, A. J., Kucera, M., and Heinz, P. (2012). Diversity and microhabitats of living benthic foraminifera in the abyssal Northeast Pacific. *Mar. Micropal.* 9, 84–104. doi: 10.1016/j.marmicro.2012.08.004

Gardner, W. D., Sullivan, L. G., and Thorndike, E. M. (1984). Long-term photographic, current, and nephelometer observations of manganese nodule environments in the Pacific. *Earth Planet. Sci. Lett.* 70, 95–109. doi: 10.1016/0012-821X(84)90212-7

Glover, A. G., Dahlgren, T. G., Wiklund, H., Mohrbeck, I., and Smith, C. R. (2015). An end-to-end DNA taxonomy methodology for benthic biodiversity survey in the Clarion-Clipperton Zone, central Pacific abyss. *J. Mar. Sci. Eng.* 4:2. doi: 10.3390/jmse4010002

Gooday, A. J., and Jorissen, F. J. (2012). Benthic foraminiferal biogeography: controls on global distribution patterns in deep-water settings. *Ann. Rev. Mar. Sci.* 4, 237–262. doi: 10.1146/annurev-marine-120709-142737

Gooday, A. J., and Lambshead, P. J. D. (1989). Influence of seasonally deposited phytodetritus on benthic foraminiferal populations in the bathyal northeast Atlantic: the species response. *Mar. Ecol. Prog. Ser.* 58, 53–67.

Gooday, A. J., Nomaki, H., and Kitazato, H. (2008). "Modern deep-sea benthic foraminifera: a brief review of their biodiversity and trophic diversity," in *Biogeochemical Controls on Palaeoceanographic Environmental Proxies*, Vol. 303, eds W. E. N. Austin and R. H. James, (London: Geological Society, Special Publications), 97–119.

Goineau, A., and Gooday, A. J. (2015). Radiolarian tests as microhabitats for novel benthic foraminifera: observations from the abyssal eastern equatorial Pacific (Clarion–Clipperton Fracture Zone). *Deep Sea Res. I* 103, 73–85. doi: 10.1016/j.dsr.2015.04.011

Goineau, A., and Gooday, A. J. (2017). Novel benthic foraminifera are abundant and diverse in an area of the abyssal equatorial Pacific licensed for polymetallic nodule exploration. *Sci. Rep.* 7:45288. doi: 10.1038/srep45288

Gooday, A. J. (1986). Meiofaunal foraminiferans from the bathyal Porcupine Seabight (northeast Atlantic): size structure, standing stock, taxonomic composition, species diversity and vertical distribution in the sediment. *Deep Sea Res.* 33, 1345–1373. doi: 10.1016/0198-0149(86)90040-3

Gooday, A. J. (1988). A response by benthic foraminifera to phytodetritus deposition in the deep sea. *Nature* 332, 70–73. doi: 10.1038/332070a0

Gooday, A. J. (1993). Deep-sea benthic foraminiferal species which exploit phytodetritus: characteristic features and controls on distribution. *Mar. Micropaleontol.* 22, 187–205. doi: 10.1016/0377-8398(93)90043-W

Gooday, A. J. (1996). Epifaunal and shallow infaunal foraminiferal communities at three abyssal NE Atlantic sites subject to differing phytodetritus regimes. *Deep Sea Res.* 43, 1395–1431. doi: 10.1016/S0967-0637(96)00072-6

Gooday, A. J. (2003). Benthic foraminifera (Protista) as tools in deep-water palaeoceanography: a review of environmental influences on faunal characteristics. *Adv. Mar. Biol.* 46, 1–90. doi: 10.1016/S0065-2881(03)46002-1

Gooday, A. J., Carstens, M., and Thiel, H. (1995). Micro- and nanoforaminifera from abyssal northeast Atlantic sediments: a preliminary report. *Int. Rev. Ges. Hydrobiol.* 80, 361–383. doi: 10.1002/iroh.19950800223

Gooday, A. J., and Hughes, J. A. (2002). Foraminifera associated with phytodetritus deposits at a bathyal site in the northern Rockall Trough (NE Atlantic):

seasonal contrasts and a comparison of stained and dead assemblages. *Mar. Micropaleontol.* 46, 83–110. doi: 10.1016/S0377-8398(02)00050-6

Gooday, A. J., Hughes, J. A., and Levin, L. A. (2001). The foraminiferan macrofauna from three North Carolina (U.S.A.) slope sites with contrasting carbon flux: a comparison with the metazoan macrofauna. *Deep Sea Res. I* 48, 1709–1739. doi: 10.1016/S0967-0637(00)00098-4

Gooday, A. J., and Rathburn, A. E. (1999). Temporal variability in living deep-sea benthic foraminifera: a review. *Earth Sci. Rev.* 46, 187–212. doi: 10.1016/S0012-8252(99)00010-0

Hedley, R. H. (1960). The iron-containing shell of *Gromia oviformis* (Rhizopoda). *Q. J. Microsc. Sci.* 101, 279–293.

Heinz, P., and Hemleben, Ch (2006). Foraminiferal response to the Northeast Monsoon in the western and southern Arabian Sea. *Mar. Micropaleontol.* 58, 103–113. doi: 10.1016/j.marmicro.2005.10.001

Hemleben, C., and Troester, J. (1984). Campanian-Maestrichian deep-water foraminifers from Hole 543A, deep-sea drilling project. *Initial Rep.* DSDP 78, 509–532.

Hess, S., and Jorissen, F. J. (2009). Distribution patterns of living benthic foraminifera from Cap Breton canyon, Bay of Biscay: faunal response to sediment instability. *Deep Sea Res. I* 56, 1555–1578. doi: 10.1016/j.dsr.2009.04.003

Hess, S., Jorissen, F. J., Venet, V., and Abu-Zied, R. (2005). Benthic foraminiferal recovery after recent turbidite deposition in Cap Breton canyon, Bay of Biscay. *J. Foramin. Res.* 35, 114–129. doi: 10.2113/35.2.114

Hess, S., and Kuhnt, W. (1996). Deep-sea benthic foraminiferal recolonization of the 1991 Mt. Pinatubo ash layer in the South China Sea. *Mar. Micropaleontol.* 28, 171–197. doi: 10.1016/0377-8398(95)00080-1

Hess, S., Kuhnt, W., Hill, S., Kaminski, M. A., Holbourn, A., and de Leon, M. (2001). Monitoring the recolonization of the Mt. Pinatubo 1991 ash layer by benthic foraminifera. *Mar. Micropaleontol.* 43, 119–142. doi: 10.1016/S0377-8398(01)00025-1

Holbourn, A., Henderson, A., and McLeod, N. (2013). *Atlas of Benthic Foraminifera*. Hoboken, NJ: Willey-Blackwell. doi: 10.1002/9781118452493

Jensen, P. (1982). A new meiofaunal splitter. *Ann. Zool. Fennici* 19, 233–236.

Jorissen, F. J., Bicchi, E., Duchemin, G., Durrieu, J., Galgani, F., Cazes, L., et al. (2009). Impact of oil-based drill mud disposal on benthic foraminiferal assemblages on the continental margin off Angola. *Deep Sea Res. II* 56, 2270–2291. doi: 10.1016/j.dsr2.2009.04.009

Kitazato, H., Nakatsuka, T., Shimanaga, M., Kanda, J., Soh, W., Kato, Y., et al. (2003). Long-term monitoring of the sedimentary processes in the central part of Sagami Bay, Japan: rationale, logistics and overview of results. *Prog. Oceanogr.* 57, 3–16. doi: 10.1016/S0079-6611(03)00047-8

Kuhnt, W., Hess, S., Holbourn, A., Paulsen, H., and Salomon, B. (2005). The impact of the 1991 Mt. Pinatubo eruption on deep-sea foraminiferal communities: a model for the Cretaceous–Tertiary (K/T) boundary? *Palaeogeogr. Palaeocl. Palaeoecol.* 224, 83–107. doi: 10.1016/j.palaeo.2005.03.042

Kuhnt, W., Kaminski, M. A., and Moullade, M. (1989). Late Cretaceous deep-water agglutinated foraminiferal assemblages from the North Atlantic and its marginal seas. *Geol. Rundsch.* 78, 1121–1140. doi: 10.1007/BF01829336

Kuhnt, W., and Moullade, M. (1991). Quantitative analysis of Upper Cretaceous abyssal agglutinated foraminiferal distribution in the North Atlantic – paleoceanographic implications. *Rev. Micropaleontol.* 34, 313–349.

Lauerman, L. M. L., and Kaufmann, R. S. (1998). Deep-sea epibenthic echinoderms and a temporally varying food supply: results from a one year time series in the N.E. *Pacific. Deep Sea Res. II* 45, 817–842. doi: 10.1016/S0967-0645(98)00004-6

Leduc, D., Probert, P. K., and Nodder, S. D. (2010). Influence of mesh size and core penetration on estimates of deep-sea nematode abundance, biomass and diversity. *Deep Sea Res. I* 57, 1354–1362. doi: 10.1016/j.dsr.2010.06.005

Lutze, G. F., and Coulbourne, W. T. (1984). Recent benthic foraminifera from the continental margin of northwest Africa: community structure and distribution. *Mar. Micropaleontol.* 8, 361–401. doi: 10.1016/0377-8398(84)90002-1

Moodley, L., Middelburg, J. J., Boschker, H. T. S., Duineveld, G. C. A., Pel, R., Herman, P. M. J., et al. (2002). Bacteria and Foraminifera: key players in a short-term deep-sea benthic response to phytodetritus. *Mar. Ecol. Prog. Ser.* 236, 23–29. doi: 10.3354/meps236023

Murray, J. W. (2014). Some trends in sampling modern living (stained) benthic foraminifera in fjord, shelf and deep sea: Atlantic Ocean and adjacent seas. *J. Micropalaeontol.* 34, 101–104. doi: 10.1144/jmpaleo2014-004

Nomaki, H., Heinz, P., Nakatsuka, T., Shimanaga, M., and Kitazato, H. (2005). Species-specific ingestion of organic carbon by deep-sea benthic foraminifera and meiobenthos: in situ tracer experiments. *Limnol. Oceanogr.* 50, 134–146. doi: 10.4319/lo.2005.50.1.0134

Nomaki, H., Heinz, P., Nakatsuka, T., Shimanaga, M., Ohkouchi, N., Ogawa, N. O., et al. (2006). Different ingestion patterns of 13C-labeled bacteria and algae by deep-sea benthic foraminifera. *Mar. Ecol. Prog. Ser.* 310, 95–108. doi: 10.3354/meps310095

Nozawa, F., Kitazato, H., Tsuchiya, M., and Gooday, A. J. (2006). 'Live' benthic foraminifera at an abyssal site in the equatorial Pacific nodule province: abundance, diversity and taxonomic composition. *Deep Sea Res. I* 51, 1406–1422. doi: 10.1016/j.dsr.2006.06.001

Ohga, T., and Kitazato, H. (1997). Seasonal changes in bathyal foraminiferal populations in response to the flux of organic matter (Sagami Bay, Japan). *Terra Nova* 9, 33–37. doi: 10.1046/j.1365-3121.1997.d01-6.x

Ohkawara, N., Kitazato, H., Uematsu, K., and Gooday, A. J. (2009). A minute new species of *Saccammina* (monothalamous Foraminifera; Protista) from the abyssal Pacific. *J. Micropalaeontol.* 28, 143–151. doi: 10.1144/jm.28.2.143

Pape, E., Bezerra, T. N., Hauquier, F., and Vanreusel, A. (2017). Limited spatial and temporal variability in meiofauna and nematode communities at distant but environmentally similar sites in an area of interest for deep-sea mining. *Front. Mar. Sci.* 4:205. doi: 10.3389/fmars.2017.00205

Pawlowski, J. (1991). Distribution and taxonomy of some benthic tiny foraminifers from the Bermuda Rise. *Micropaleontology* 37, 163–172. doi: 10.2307/1485556

Pawlowski, J., and Lapierre, L. (1988). Foraminifères benthiques actuels de l'Atlantique Nord-Est. *Rev. Paléontol.* 2, 873–878.

Phipps, M., Jorissen, F., Pusceddu, A., Bianchelli, S., and De Stigter, H. (2012). Live benthic foraminiferal faunas along a bathymetrical transect (282–4987 m) on the Portuguese margin (NE Atlantic). *J. Foramin. Res.* 42, 66–81. doi: 10.2113/gsjfr.42.1.66

Radziejewska, T. (2002). Responses of deep-sea meiobenthic communities to sediment disturbance simulating effects of polymetallic nodule mining. *Internat. Rev. Ges. Hydrobiol.* 87, 457–477. doi: 10.1002/1522-2632(200207)87:4<457::AID-IROH457>3.0.CO;2-3

Radziejewska, T. (2014). *Meiobenthos in the Sub-Equatorial Pacific Abyss: a Proxy in Anthropogenic Impact Evaluation*. Heidelberg: Springer. doi: 10.1007/978-3-642-41458-9

Radziejewska, T., Drzycimski, I., Galtsova, V. V., Kulangieva, L. V., and Stoyanova, V. (2001). "Changes in genus-level diversity of meiobenthic free-living nematodes (Nematoda) and harpacticoids (Copepoda Harpacticoida) at an abyssal site following experimental sediment disturbance," in *Proceedings 4th Ocean Mining Symposium, Szczecin, Poland*, eds J. S. Chung and V. Stoyanova (Cupertino, CA: ISOPE), 38–43.

Radziejewska, T., Gooday, A. J., Koltan, M., and Szyrweil, E. (2006). Deep-sea non-calcareous Foraminifera: some examples from the Pacific's abyssal nodule field. *Meiofauna Mar.* 15, 3–10.

Radziejewska, T., and Stoyanova, V. (2000). Abyssal epibenthic megafauna of the Clarion-Clipperton area (NE Pacific): changes in time and space versus anthropogenic environmental disturbance. *Oceanol. Stud.* 29, 83–101.

Rothe, N., Gooday, A. J., Cedhagen, T., and Hughes, J. A. (2010). Biodiversity and distribution of the genus *Gromia* (Protista, Rhizaria) in the deep Weddell Sea (Southern Ocean). *Polar Biol.* 43, 69–81. doi: 10.1007/s00300-010-0859-z

Schewe, I. (2001). Small-sized benthic organisms of the alpha ridge, Central Arctic Ocean. *Internat. Rev. Hydrobiol.* 86, 317–335. doi: 10.1002/1522-2632(200106)86:3<317::AID-IROH317>3.0.CO;2-V

Schönfeld, J., Alve, E., Geslin, E., Jorissen, F. J., Korsun, S., Spezzaferri, S., et al. (2012). The FOBIMO (FOraminiferal BIo-MOnitoring) initiative—Towards a standardised protocol for soft-bottom benthic foraminiferal monitoring studies. *Mar. Micropaleontol.* 94–95, 1–13. doi: 10.1016/j.marmicro.2012.06.001

Schröder, C. J. (1986). Deep-water arenaceous foraminifera in the northwest Atlantic Ocean. *Can. Tech. Rep. Hydrogr. Ocean Sci.* 71, 1–191.

Schröder, C. J., Scott, D. B., and Medioli, F. S. (1987). Can smaller benthic foraminifera be ignored in paleoenvironmental analyses? *J. Foramin. Res.* 17, 101–105. doi: 10.2113/gsjfr.17.2.101

Sen Gupta, B. K., Shin, I. C., and Wendler, S. T. (1987). Relevance of specimen size in distribution studies of deep-sea benthic foraminifera. *Palaios* 2, 332–338. doi: 10.2307/3514758

Shirayama, Y., and Horikoshi, M. (1989). Comparison of the benthic size structure between sublittoral, upper slope and deep-sea areas of the Western Pacific. *Int. Rev. Ges. Hydrobiol.* 74, 1–13. doi: 10.1002/iroh.19890740102

Silva, K. A., Corliss, B. C., Rathburn, A. E., and Thunnell, R. C. (1996). Seasonality of living benthic foraminifera from the San Pedro Basin, California Borderland. *J. Foramin. Res.* 26, 71–93. doi: 10.2113/gsjfr.26.1.71

Smith, C. R., and Demopoulos, A. W. J. (2003). "The deep Pacific Ocean floor," in *Ecosystems of the Deep Oceans Ecosystems of the World 28*, ed. P. Tyler (Amsterdam: Elsevier), 179–218.

Smith, C. R., Hoover, D. J., Doan, S. E., Pope, R. H., DeMaster, D. J., Dobbs, F. C., et al. (1996). Phytodetritus at the abyssal seafloor across 10° of latitude in the central equatorial Pacific. *Deep Sea Res. II* 43, 1309–1338. doi: 10.1016/0967-0645(96)00015-X

Smith, P. B. (1973). Foraminifera of the North Pacific Ocean, United States geological survey professional publication. 766, 1–17. doi: 10.3133/pp766

Snider, L. J., Burnett, B. R., and Hessler, R. R. (1984). The composition and distribution of meiofauna and nanobiota in a central North Pacific deep-sea area. *Deep Sea Res.* 31, 1225–1249. doi: 10.1016/0198-0149(84)90059-1

Szarek, R., Nomaki, H., and Kitazato, H. (2007). Living deep-sea benthic foraminifera from the warm and oxygen-depleted environment of the Sulu Sea. *Deep Sea Res I* 54, 145–176. doi: 10.1016/j.dsr2.2006.02.017

Thiel, H. (1975). The size structure of the deep-sea benthos. *Internat. Rev. Ges. Hydrobiol.* 60, 575–606. doi: 10.1111/gcb.12480

Thiel, H. (1983). "Meiobenthos and nanobenthos of the deep sea," in *The Sea*, Vol. 8, ed. G. T. Rowe (New York, NY: Wiley Interscience), 167–230.

Conflict of Interest Statement: The authors declare that the research was conducted in the absence of any commercial or financial relationships that could be construed as a potential conflict of interest.

Copyright © 2019 Gooday and Goineau. This is an open-access article distributed under the terms of the Creative Commons Attribution License (CC BY). The use, distribution or reproduction in other forums is permitted, provided the original author(s) and the copyright owner(s) are credited and that the original publication in this journal is cited, in accordance with accepted academic practice. No use, distribution or reproduction is permitted which does not comply with these terms.

frontiers in Marine Science

ORIGINAL RESEARCH
published: 09 July 2019
doi: 10.3389/fmars.2019.00388

Patterns in Bathyal Demersal Biodiversity and Community Composition Around Archipelagos in the Tropical Eastern Pacific

Jonatha Giddens[1,2], Whitney Goodell[1,2,3], Alan Friedlander[2,3], Pelayo Salinas-de-León[3,4], Charles Shepard[1], Brad Henning[1], Eric Berkenpas[1], Enric Sala[3] and Alan Turchik[1]*

[1] Exploration Technology Lab, National Geographic Society, Washington, DC, United States, [2] Fisheries Ecology Research Laboratory, Hawaii Institute of Marine Biology, Kaneohe, HI, United States, [3] Pristine Seas, National Geographic Society, Washington, DC, United States, [4] Charles Darwin Research Station, Puerto Ayora, Ecuador

OPEN ACCESS

Edited by:
William W. Chadwick,
Pacific Marine Environmental Laboratory (NOAA), United States

Reviewed by:
Ellen Pape,
Ghent University, Belgium
Mustafa Yucel,
Middle East Technical University, Turkey

***Correspondence:**
Jonatha Giddens
Jonatha@hawaii.edu

Specialty section:
This article was submitted to Deep-Sea Environments and Ecology, a section of the journal Frontiers in Marine Science

Received: 12 March 2019
Accepted: 20 June 2019
Published: 09 July 2019

Citation:
Giddens J, Goodell W, Friedlander A, Salinas-de-León P, Shepard C, Henning B, Berkenpas E, Sala E and Turchik A (2019) Patterns in Bathyal Demersal Biodiversity and Community Composition Around Archipelagos in the Tropical Eastern Pacific. Front. Mar. Sci. 6:388. doi: 10.3389/fmars.2019.00388

Deep-sea fauna of the Tropical Eastern Pacific (TEP) have remained largely undescribed because exploration has historically been a challenge in these remote locations. Consequently, little is currently known about deep-ocean biodiversity in the TEP. An enriched understanding of biogeographic patterns and the factors that influence them is crucial to the success of efforts to conserve deep-sea communities. The objectives of this research were to provide the first assessment of biodiversity and community composition of bathyal demersal (200 – 3,000 m) fauna across multiple ocean/island archipelagos in the TEP. To better understand biodiversity and its drivers in the region, we tested the hypotheses that biodiversity and faunal assemblage composition vary with location and environmental drivers (e.g., bathymetry, oxygen concentration). Using Deep-Ocean Dropcams, we collected video footage from Clipperton, Galápagos, Revillagigedo, and Malpelo oceanic islands, in depths ranging from 200 to 3,000 m. Taxa richness, Shannon diversity, and Simpson diversity were calculated for each location. In general, biodiversity values were high closer to the equator and closer to the continent, and low in the locations farther north and farther west. Fish family biodiversity was highest in the Galápagos, followed by Malpelo. In contrast, Clipperton had significantly lower fish family richness compared to all other locations. For invertebrate orders, Revillagigedo was significantly lower in biodiversity compared to the Galápagos and Malpelo. Broad-scale Bathymetric Position Index (BPI) and dissolved oxygen had a positive effect on fish diversity metrics. Both fish and invertebrate assemblages were significantly different among locations. Around each of the island groups are vastly different current patterns, which likely accounts for some of the variation we observed in biodiversity and community composition. Due to the longitudinal East Pacific Rise, which limits population connectivity by creating a spatial barrier to gene flow and dispersal among marine organisms, the TEP is largely isolated from the wider Pacific. The islands

and archipelagos likely represent important stepping-stones and corridors for species connectivity across the TEP and the wider Pacific. Therefore, the preservation of these intact ecosystems is crucial for maintaining biodiversity both within the TEP as well as across the wider Pacific region.

Keywords: deep-sea community ecology, deep-sea biogeography, bathyal demersal fauna, biodiversity, Galápagos, Clipperton Atoll, Malpelo Island, Revillagigedo

INTRODUCTION

The deep-sea is a severely under-sampled ecosystem and much remains to be understood about deep-sea biogeography (reviewed in Wilson and Kaufmann, 1987; Rogers, 1994). An enriched understanding of biogeographic patterns and the factors that influence them is crucial to the success of efforts to conserve deep-sea communities, especially in remote islands and archipelagos in the Tropical Eastern Pacific (TEP).

The TEP is separated from the central and western Pacific by the East Pacific Rise, a divergent tectonic plate boundary on the Pacific floor running north to south that coincides with the boundaries of a unique biogeographic province with a high proportion of endemic species (Ekman, 1953; Allen, 2008; **Figure 1**). The TEP can be divided into three biogeographic provinces based on shore fish (0 – 100 m) assemblage similarities (Robertson and Cramer, 2009). The continental coast contains two provinces: the Cortez (Gulf of California and lower Pacific Baja) and the Panamic (southward province). These two distinct areas are identified by a peak in abundance of local endemics and overall species richness. The third province within the TEP consists of five isolated ocean islands and archipelagos: the Galápagos, Revillagigedo, Clipperton, Cocos, and Malpelo; collectively termed the "Ocean Island Province" (Hubbs and Briggs, 1974; Robertson and Cramer, 2009).

Small ocean islands, such as those in the TEP, typically support faunal assemblages of lower species richness compared to adjacent continental areas. The fauna of these oceanic islands also have different functional-group composition, including both more broad-ranging species and more localized endemics. Thus, this area forms a hotspot for both the origin and maintenance of biodiversity in the sea (Robertson and Cramer, 2009).

The smaller size of island assemblages compared with neighboring mainland areas makes them more sensitive to extinctions (Dulvy et al., 2003; Hobbs et al., 2011). Due to the longitudinal East Pacific Rise, which limits population connectivity by creating a spatial barrier to gene flow and dispersal among marine organisms, the TEP is largely isolated from the wider Pacific (Lessios and Robertson, 2006). The islands and archipelagos likely represent important stepping-stones and corridors for species connectivity across the TEP and the wider Pacific (Glynn et al., 1996).

Previous research has assessed marine biodiversity at these islands, but has focused largely on the shallow-water ecosystems (Allen and Robertson, 1994; Glynn et al., 1996; Jost and Andréfouët, 2006; Alzate et al., 2014; Fourriére et al., 2014). Overall, the TEP is noted for its high level of endemism (72%) and relatively diverse shore-fish assemblages (Zapata and Ross Robertson, 2007). Additionally, the eutrophic mesopelagic zone (200 m – 1000 m), hosts a large proportion of endemic deep-water fish species adapted to the low oxygen in these waters (Priede, 2017).

However, the bathyal demersal (200 m – 3000 m) fauna of the TEP have remained largely undescribed because exploration has historically been a challenge in these remote locations (but see Auster et al., 2016; Lubetkin et al., 2018; Sánchez-Jiménez et al., 2018). Slopes and seamounts around Isla del Coco (Costa Rica) have been surveyed to depths of 450 m using manned submersibles (Cortés and Blum, 2008), recent explorations at the Galápagos used Remotely Operated Vehicles and manned submersibles to depths of 4000 m (Carey et al., 2016). Besides these localized studies, little is currently known about biodiversity in deep waters across multiple oceanic islands in the TEP.

The objectives of this research were to characterize biodiversity and community composition of bathyal (200 m – 3000 m) demersal fauna at four ocean/island archipelagos to better understand deep-ocean biogeography and its drivers in the TEP. We tested the hypotheses that biodiversity and faunal assemblage composition vary with location and environmental variables such as bathymetry and oxygen concentration. Our study represents the first characterization of deep-sea biodiversity across multiple islands and archipelagos in the region.

MATERIALS AND METHODS

Study Region

The TEP is characterized oceanographically by extensive stratification with a sharp permanent pycnocline that prevents local ventilation of subsurface waters, a shallow thermocline (<80 m), and very low oxygen (<50 $\mu mol \cdot kg^{-1}$ in the largest extent of the oxygen minimum zone at ∼ 10 degrees north) (Karstensen et al., 2008; Robertson and Cramer, 2009; Fiedler and Lavín, 2017; Priede, 2017). The boundaries of this biogeographic region are located northward to Magdalena Bay, Baja California (∼25°N) and southward to the Gulf of Guayaquil's southern shore (∼4°S). These northern and southern boundaries are defined not by hard physical barriers, but by sharp water temperature gradients between tropical and temperate conditions (**Figure 1**).

The TEP is a region of complex oceanographic patterns. These waters lie between the two large subtropical gyres of the North and South Pacific, and at the convergence of two eastern boundary currents, coming from the north (California Current) and the south (Peru, or Humboldt, Current) (Kessler, 2006). Revillagigedo sits in the North Equatorial Current (NEC) and at

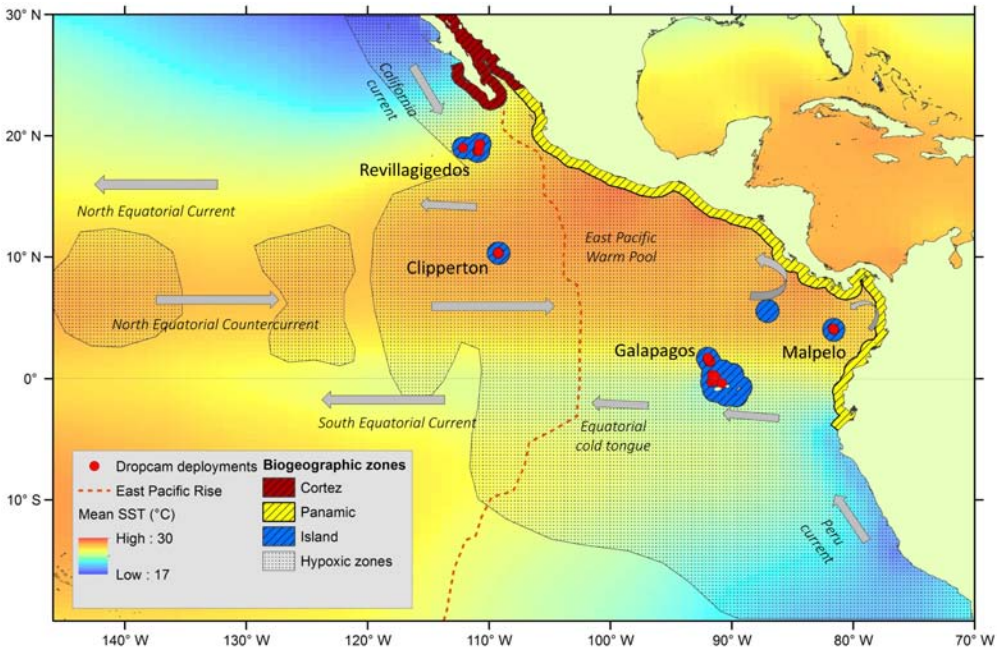

FIGURE 1 | Four study locations in the Tropical Eastern Pacific (TEP), and the associated currents influencing each site, with mean sea surface temperature (World Ocean Atlas) (adapted from Fiedler and Talley, 2006; Kessler, 2006), areas of severe hypoxia (<0.2 ml l^{-1}; adapted from Diaz and Rosenberg, 1995), axis of the East Pacific Rise, and biogeographic provinces (adapted from Robertson and Cramer, 2009).

the terminus of the colder waters of the California Current along the eastern boundary from the north (**Figure 1**). Clipperton, located ∼1,000 km to the south of Revillagigedo, sits in the East Pacific Warm Pool, a region of warm surface waters between the NEC and the North Equatorial Countercurrent (NECC) (Wang and Enfield, 2001). Moving south and eastward, the Galápagos Islands straddle the equator, and are influenced by the cold tongue of the South Equatorial Current, and the Peru (or Humboldt) Current, which brings cold waters along the eastern boundary from the south. Malpelo Island, furthest to the east and five degrees north of the equator, sits in the eastern curve of the northern gyre (NEC and NECC).

Data Collection

National Geographic's Exploration Technology Lab developed Deep-Ocean Dropcams to observe deep-sea life *in situ* by capturing high quality imagery of the sea floor (Turchik et al., 2015). Deep-Ocean Dropcams are autonomous (free-falling) lander instruments, with high definition cameras (Sony Handycam HDR-XR520V 12 megapixel) encased in a 43-cm diameter borosilicate glass sphere that are rated to 10,000 m depth. We also deployed a Dropcam Mini, encased in a 33-cm diameter borosilicate glass sphere and rated to 7,000 m. This Dropcam Mini housed a Sony Handycam FDR-AX33 4K Ultra-High Definition video with a 20.6 megapixel still image capability. Viewing area per frame for both cameras was between 2 and 6 m^2, depending on the steepness of the slope where the Dropcam landed. Cameras were baited with ∼1 kg of previously frozen fish (bonito, mackerel, and tuna) and deployed for 6 to 9 h. Over the deployment period, cameras were programmed to record in 30–60 min intervals.

Biological Data

Using the Dropcams, we collected video footage from four ocean island/archipelago sites in the TEP: Clipperton, Galápagos, Revillagigedo, and Malpelo, in depths ranging from 200 m to ∼3000 m (n = 9–34 drops per site). From the video footage, fauna were classified to the lowest possible taxonomic level. Invertebrates were typically identified to taxonomic levels of order or class, whereas fish were identified to family level in most cases. The relative abundance of each identifiable taxon was calculated as the maximum number of individuals per frame (MaxN). For presence/absence analyses, these observations were converted to incidence per deployment.

Geospatial Data

Environmental predictor data were derived from publicly available geospatial databases. Variables examined included environmental/oceanographic data [e.g., Particulate Organic Carbon (POC) flux, and dissolved oxygen], geographic data (e.g., distance to geomorphic features), and bathymetric/habitat feature data [e.g., slope-of-slope (second derivative of slope), bathymetric position index (BPI)] (**Supplementary Table S1**). Data were extracted for each Dropcam deployment, based on the deployment's lat/long position. For some predictor variable datasets, data were extracted directly from the source data pixel underlying the deployment point. For others, data were derived from source data via geoprocessing steps, such as calculating a maximum value of a variable within a given radius of the

deployment point. All geoprocessing was executed in ArcMap 10.2 (ESRI, 2011). Here, we describe only the variables included in the final model, but see **Supplementary Table S1** for more details on all geospatial variables examined.

Oxygen availability is a limiting factor for deep-sea faunal distributions (Levin, 2003; Stramma et al., 2010). Data for dissolved oxygen (annual mean) for defined depth bins were derived from the National Oceanographic Data Center (NODC) World Ocean Atlas (WOA05) and resampled by Watling et al. (2013) to 1 km × 1 km grids for defined depth bins. Dissolved oxygen values were extracted from the corresponding depth layer from Watling et al. (2013) associated with each deployment's depth (**Supplementary Table S1**).

BPI, an index which highlights areas of topographic anomalies (Jones and Brewer, 2012), is a continuous metric of the elevation of a pixel relative to other pixels in a landscape (Lundblad et al., 2006), used to identify benthic features (e.g., ridges and valleys). Positive BPI values indicate features that are higher than the surrounding area, such as peaks and ridges, while negative cell values indicate features such as troughs. BPI values at and near zero are either flat areas or areas of constant slope, while sharp peaks or pits are represented by higher absolute values (Lundblad et al., 2006; Wright et al., 2012). BPI was calculated in ArcMap 10.2 using the Benthic Terrain Modeler extension (Wright et al., 2012). BPI can be calculated at broad or fine scales, with the scale of detected features dependent on the scale of BPI. Both broad- and fine-scale BPI have been shown to be associated with variations in marine faunal communities (Dolan et al., 2008; Jones and Brewer, 2012; Robert et al., 2015), including those of the deep-ocean (Leitner et al., 2017). Chosen BPI scales reflected the resolution of the available bathymetric and geomorphic data (100 m and ∼1 km, respectively) and the scale of the geomorphic features assessed (**Supplementary Table S1**). Fine scale BPI used an inner radius of 1 cell (100 m) and an outer radius of 10 cells (1000 m). Broad-scale BPI used an inner radius of 25 cells (2500 m) and an outer radius of 50 cells (5000 m).

Substrate type for each deployment was classified into either hard or soft bottom habitat. Hard bottom habitats were generally rocky outcrops or pavement and consisted of <20% sand, whereas soft-bottom habitats were areas with greater than ≥80% sand (**Table 1**).

Statistical Methods

Biodiversity Indices

Hill numbers (or the effective number of species) have been increasingly used to quantify the species/taxonomic diversity of an assemblage. The sample-size- and coverage-based integrations of rarefaction (interpolation) and extrapolation (prediction) of Hill numbers represent a unified standardization method for quantifying and comparing species diversity across multiple assemblages. To assess biodiversity, taxon observations were converted to incidence matrices. Three Hill numbers were calculated for each site: species richness, Shannon diversity, and Simpson diversity (Hill, 1973; Chao et al., 2014). We extrapolated biodiversity and assessed sample completeness for each location in the R package iNEXT Version 2.0.19 (Hsieh et al., 2016). Differences in biodiversity among locations, habitats (hard vs. soft), and depth zones (**Table 1**) were tested using linear analysis of variance (ANOVA) with a Tukey HSD *post hoc* test in the R programing environment, Version 1.0.136 (R Core Team, 2016).

Generalized Linear Mixed Effects Models

We used Generalized Linear Mixed Effects Models (GLMMs) to investigate environmental drivers of biodiversity among locations, as well as faunal assemblage composition among sites (islands/archipelagos) and sea-floor types (hard vs. soft bottom habitat).

To test for environmental drivers of biodiversity, the response variables (richness, Shannon diversity, Simpson diversity) were modeled as a Poisson distribution. For all hierarchical mixed models, location (island/archipelago) was included as a random effect to account for the nested sampling structure of the dataset. Model parameter significance was assessed using a Likelihood Ratio Test (LRT) with the statistical package LmerTest (Bates et al., 2014). All data analyses were performed in the R programing environment, Version 1.0.136 (R Core Team, 2016).

For community composition models, biological data were subset for taxa that occurred in more than three samples (drops). The probability of taxa occurrence was assessed using a GLMM with random slopes and intercepts for each taxon, allowing the taxon-specific relationship to vary by location or sea-floor type (hard vs. soft bottom), and modeled as a binomial distribution in the statistical package lme4 (Bates et al., 2014). The mixed model allowed individual taxon to respond differentially to location or sea-floor type, and the change in community composition was quantified in terms of how much the slopes of the response differ across taxa.

Multivariate Analysis

To describe the patterns of variation in community structure (patterns of distribution of abundance of fish families and invertebrate taxa) and their relationship with environmental data (**Supplementary Table S1**) we used indirect gradient analysis. Non-linear models were most appropriate for our data because a preliminary detrended correspondence analysis showed long gradient lengths (>2 SD) (ter Braak and Šmilauer, 2002). We performed Canonical Correspondence Analysis (CCA) on square root-transformed numerical abundance of fish families and invertebrate taxa using the ordination program CANOCO for Windows version 5.0 (ter Braak, 1994). Fish families and invertebrate taxa that occurred in <5% of the samples were excluded from the analyses. Environmental data were centered and standardized for analyses.

RESULTS

Fish and Invertebrate Assemblages of the Bathyal Zone

From a total of 70 deployments of the Deep-Ocean Dropcams, 43 different fish families and 42 different invertebrate orders were identified across four survey locations in the TEP Ocean

TABLE 1 | Number of drops per site, including number per benthic habitat type (hard vs. soft), and number per depth zone (Mesobenthic vs. Bathybenthic).

Location	Number of drops per Habitat		Number of drops per Depth Zone		Total number of drops
	Hard	Soft	Mesobenthic (200 m–1500 m)	Bathybenthic (<1500 m–3000 m)	
Clipperton	8	6	9	4	13
Galápagos	11	15	15	11	26
Malpelo	11	14	9	10	19
Revillagigedos	8	7	5	7	12

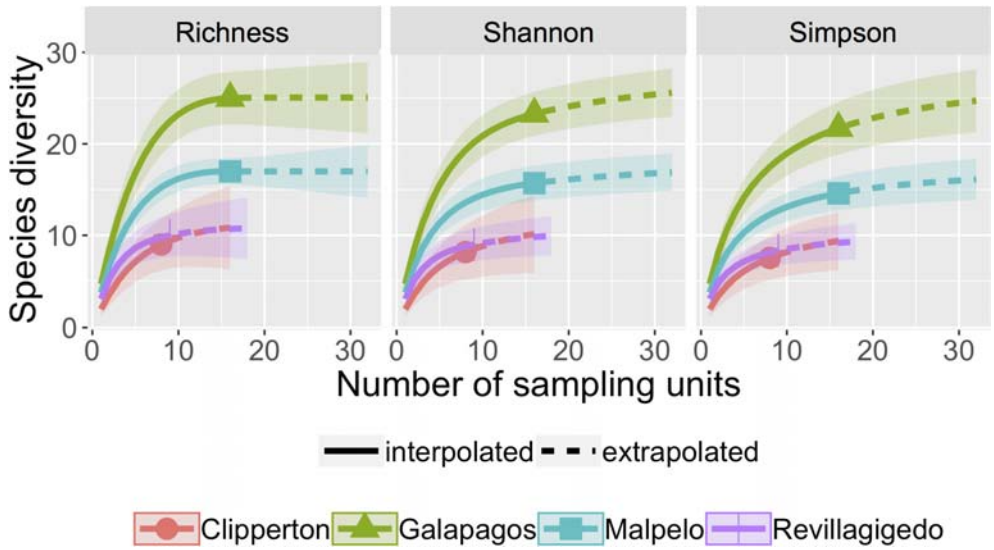

FIGURE 2 | Rarefaction/extrapolation curves for asymptotic fish family diversity indices: Richness, Shannon, and Simpson calculated by incidence frequency matrices. Sample-size-based rarefaction (solid line segment) and extrapolation (dotted line segments) sampling curves with 95% confidence intervals (shaded areas) for four locations in the TEP, separately by diversity family. The solid dots/triangles represent the reference samples.

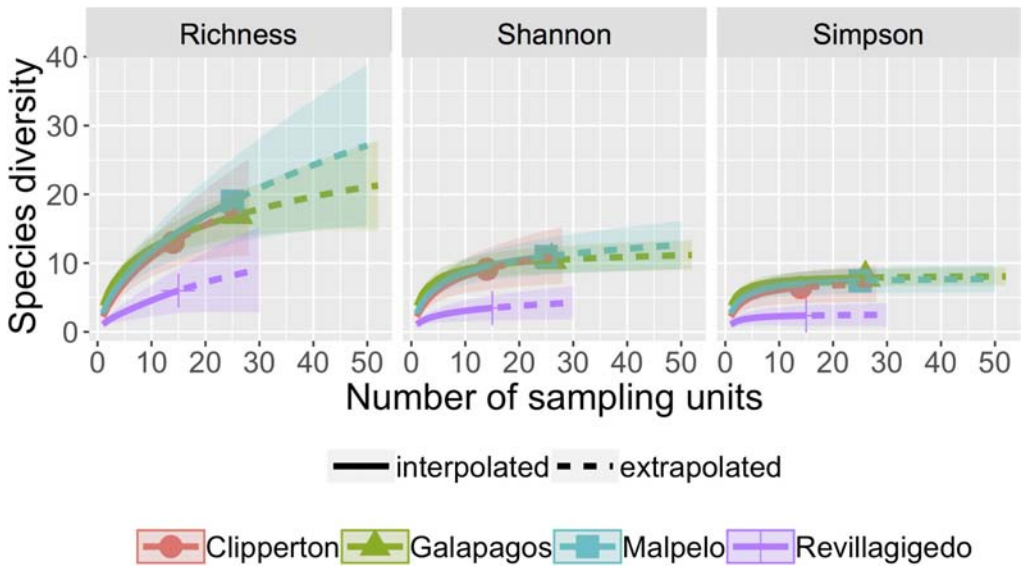

FIGURE 3 | Rarefaction/extrapolation curves for asymptotic invertebrate order diversity indices: Richness, Shannon, and Simpson calculated by incidence frequency matrix. Sample-size-based rarefaction (solid line segment) and extrapolation (dotted line segments) sampling curves with 95% confidence intervals (shaded areas) for four locations in the TEP, separately by diversity order. The solid dots/triangles represent the reference samples.

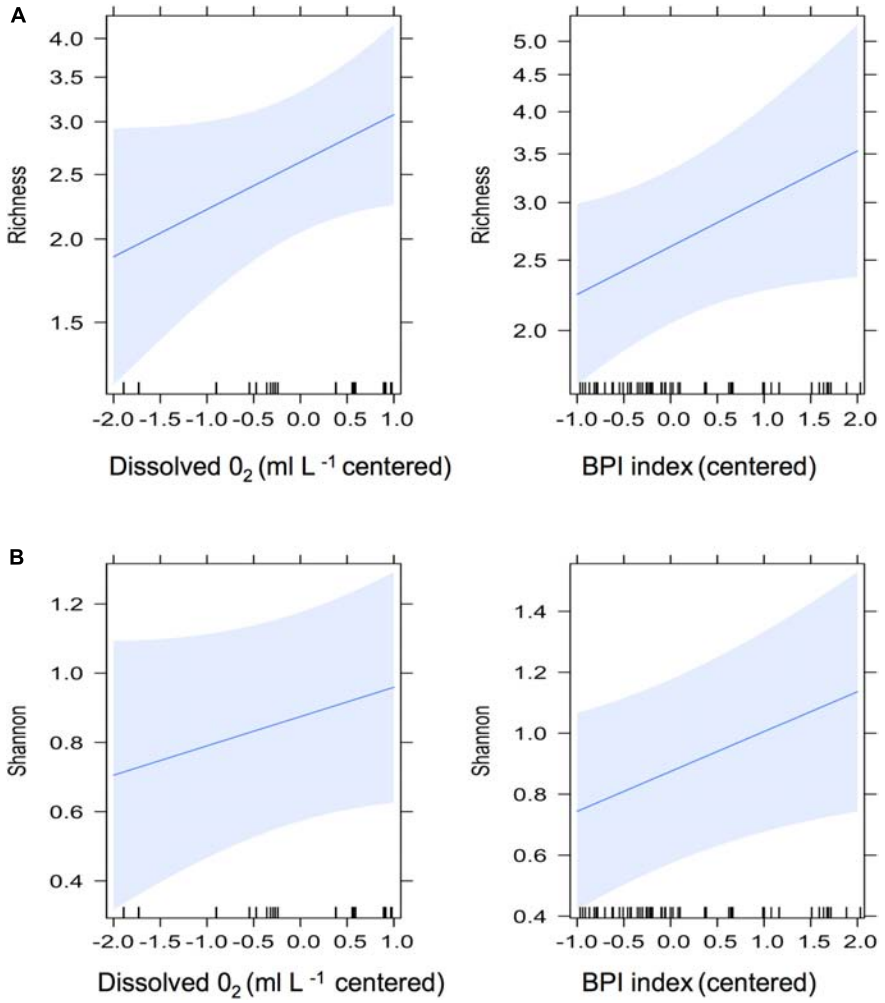

FIGURE 4 | GLMM fixed effects from fish family Richness **(A)** and Shannon diversity **(B)**, for scaled and centered dissolved oxygen (left panels) and Bathymetric Position Index (BPI) (right panels). Blue bands are 95% confidence intervals.

Island Province. Hard and soft habitats were surveyed roughly evenly among the four locations (**Table 1**). Within the bathyal zone (200 m–3,000 m), mesobenthic (200 m–1,500 m), and bathybenthic (<1,500 m–3,000 m) were also sampled roughly evenly (**Table 1**).

For fishes, comparisons between habitat types (hard vs. soft bottom) showed no difference in richness ($F_{1,78} = 0.11$, $P = 0.74$), Shannon ($F_{1,68} = 0.01$, $P = 0.93$), or Simpson ($F_{1,68} = 0.01$, $P = 0.94$) diversity, therefore samples were pooled among habitats for further analyses. For invertebrates, soft bottom habitats had significantly lower diversity than hard bottom habitats for all three diversity indices: ($F_{5,64} = 9.66$, $P = 0.001$), Shannon ($F_{5,64} = 12.42$, $P = 0.002$), and Simpson ($F_{5,64} = 11.86$, $P = 0.024$).

Biodiversity Among Locations

Fishes

For all sites, three diversity indices were in agreement, showing consistent trends across sites (**Figure 2**). Asymptotic diversities indicated that the Galápagos were highest in richness [index value 25 (SE 0.27)], followed by Malpelo [index value 17 (SE 0.72)]. The Revillagigedo [index value 10 (SE 1.69)], and Clipperton [index value 11 (SE 3.09)] had similarly, low diversities and overlapping 95% confidence intervals on the rarefaction/extrapolation curve (**Figure 2**). Assessment of sample completeness for locations were: Clipperton (84.3%), Galápagos (99.1%), Malpelo (100%), and Revillagigedo (94.9%).

Richness ($F_{3,76} = 6.91$, $P < 0.001$), Shannon ($F_{3,66} = 8.81$, $P < 0.001$), and Simpson ($F_{3,66} = 10.68$, $P < 0.001$) diversity were statistically different among locations based on linear analysis of variance. Clipperton had significantly lower fish family richness compared to all other locations ($P < 0.05$). Shannon and Simpson diversity were significantly lower at Clipperton compared to Galápagos and Malpelo ($P < 0.001$). Although not significant, differences in Simpson diversity between Clipperton and Revillagigedo were suggestive ($P = 0.06$). Galápagos, Malpelo, and Revillagigedo overlapped in 95% confidence intervals around mean richness and diversity estimates. Geographically,

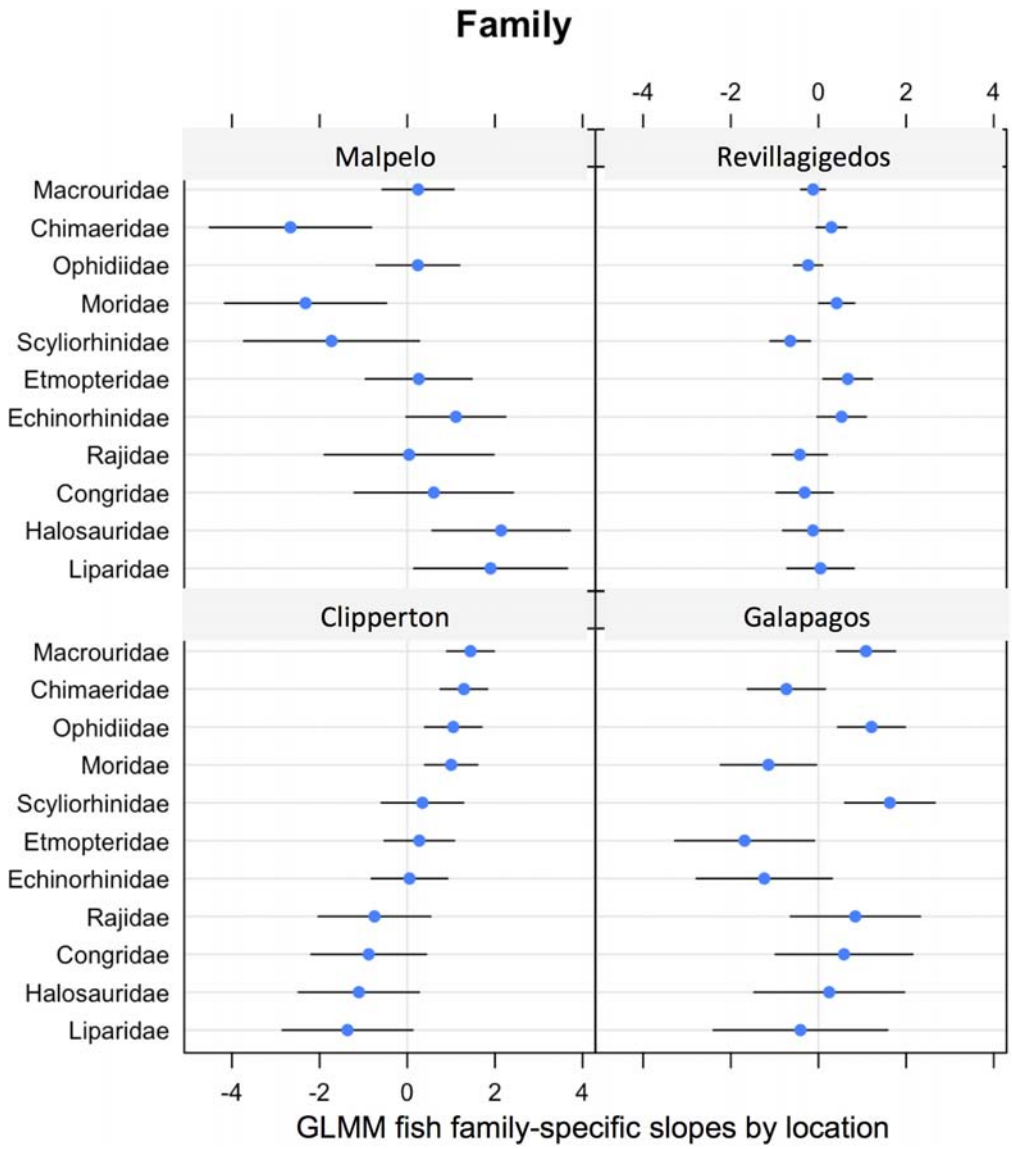

FIGURE 5 | GLMM random effects (modeled slopes) for fish family specific probability of occurrence by location.

locations closer to the equator and closer to the continent had higher richness and diversity, while assemblages in locations farther north and farther west were lower in species richness and diversity.

Invertebrates

Similar to fish biodiversity methods, rarefaction/extrapolation curves were constructed for invertebrate diversity indices (**Figure 3**). For all of these sites, the three diversity indices were in agreement, showing consistent trends across sites. Asymptotic diversities indicated that the Revillagigedo [index value 13.5 (SE 10.9)] had lower richness than the other three sites, with Clipperton having 24.3 (SE 12.2), Galápagos 25.6 (SE 9.8), and Malpelo 43.0 (SE 23.3) for richness asymptotic estimates. Assessment of sample completeness for locations were: Clipperton (84.6%), Galápagos (95.1%), Malpelo (89.1%), and Revillagigedo (87.3%).

For invertebrates, richness ($F_{3,66} = 10.68$, $P < 0.001$), Shannon ($F_{3,66} = 15.6$, $P < 0.001$), and Simpson ($F_{5,64} = 11.86$, $P = 0.02$) diversities were statistically different among locations based on linear analysis of variance. The Revillagigedos were significantly lower compared to the Galápagos and Malpelo for richness ($F_{3,66} = 10.68$, $P < 0.001$), Shannon ($F_{3,66} = 10.68$, $P < 0.001$), and Simpson diversity ($F_{5,64} = 11.86$, $P < 0.001$).

Environmental Drivers of Biodiversity

Fishes

Twelve environmental variables were included in the global GLMM model (**Supplementary Table S1**). The reduced model, selected by AICc, included broad scale BPI and dissolved

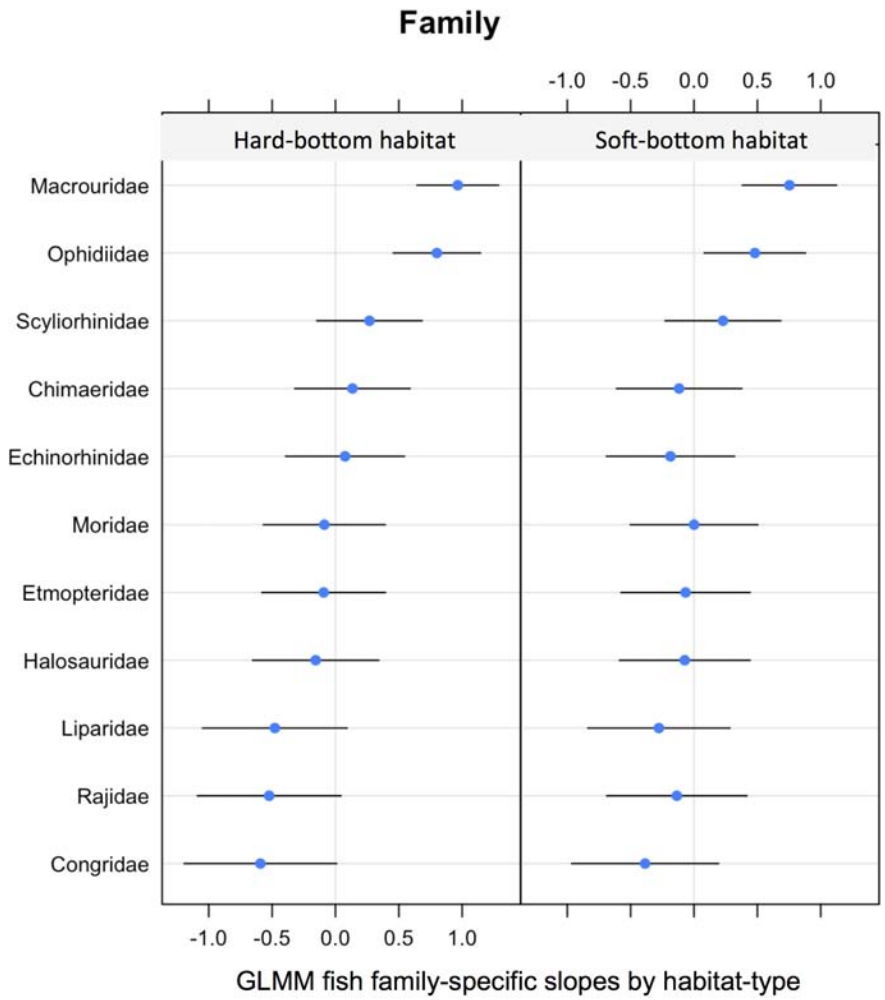

FIGURE 6 | GLMM random effects (modeled slopes) for fish family specific probability of occurrence by habitat (hard vs. soft bottom).

oxygen. In all fish models, both BPI and dissolved oxygen had a positive effect on fish diversity metrics. The pattern was stronger with Richness and Shannon diversity, showing significant positive effects. Richness ($\beta = 0.151$, se = 0.08, $P = 0.05$) and Shannon diversity ($\beta = 0.12$, se = 0.06, $P = 0.05$) were both marginally significant [richness: LRT: $\chi^2(2) = 3.56$, $P = 0.05$; Shannon: LRT: $\chi^2(2) = 3.78$, $P = 0.05$], but only explained a small portion of the variability in these data (Richness $R^2 = 0.17$; Shannon $R^2 = 0.30$) (**Figures 4A,B**, respectively). Simpson diversity had a positive effect of BPI, though not statistically significant ($\beta = 0.04$, se = 0.03, $P = 0.13$) [LRT: $\chi^2(2) = 2.31$, $P = 0.12$]. Dissolved oxygen positively effected diversity metrics, though not significant for all three metrics tested; (richness: $\beta = 0.16$, se = 0.09, $P = 0.08$; Shannon: $\beta = 0.07$, se = 0.06, $P = 0.25$; and Simpson: $\beta = 0.03$, se = 0.08, $P = 0.27$).

Invertebrates

Invertebrate biodiversity models showed no significant effect of BPI and dissolved oxygen concentration. Hierarchical models with location as a random effect significantly explained variation in the invertebrate taxa data for Shanon and Simpson diversity, but not for richness [Shannon diversity LRT: $\chi^2(5) = 6.17$, $P = 0.01$; Simpson diversity LRT: $\chi^2(5) = 8.69$, $P < 0.01$; richness LRT: $\chi^2(4) = 1.21$, $P = 0.27$].

Assemblage Composition Among Locations

Fishes

Models showed significantly different assemblages [LRT: $\chi^2(14) = 56.2$, $P < 0.001$] among locations. The change in community composition was quantified in terms of how much the slopes of the response differ across families. The magnitude of variation was 5.35 (se = 0.71) on a logit scale, indicating that the change in community composition was substantial in terms of which fish families were present, depending on location. The variation in the location effect across families was large as standard deviation ranged from 0.5 to 1.8 (on the logit scale) depending on location (**Figure 5**).

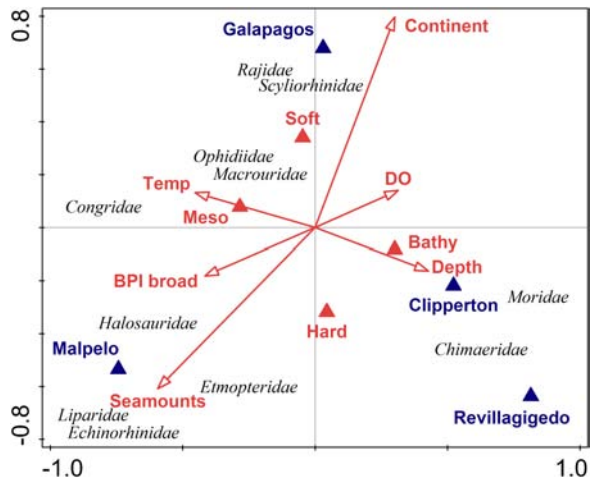

FIGURE 7 | Canonical Correspondence Analysis (CCA) of fish family numerical abundance. Vectors indicate direction and strength (length) of relationships between taxa and explanatory geospatial variables defined in **Supplementary Table S1** [e.g., location; distance to seamounts; continent; or slope; depth; bathybenthic strata (bathybenthic vs. mesobenthic); and habitat type (hard vs. soft); particulate organic carbon (POC); dissolved oxygen (DO); and temperature].

TABLE 2 | Results of Canonical Correspondence Analysis (CCA) on square root-transformed fish abundance data.

Statistic	Axis 1	Axis 2	Axis 3	Axis 4
Eigenvalues	0.40	0.33	0.11	0.09
Explained variation (cumulative)	14.47	26.62	30.66	34.03
Pseudo-canonical correlation	0.83	0.80	0.63	0.58
Explained fitted variation (cumulative)	34.56	63.58	73.23	81.27
Name	**% explained**	**pseudo-F**	**P**	
Location: Malpelo	11.3	8.0	0.002	
Seamounts	10.1	7.1	0.002	
Location: Galápagos	9.7	6.8	0.002	
Continent	9.6	6.7	0.002	
Location: Revillagigedo	7.2	4.9	0.002	
Depth	5.5	3.7	0.002	
Hard	4.9	3.2	0.008	
Soft	4.9	3.2	0.002	
Temp	4.8	3.2	0.006	
Bathybenthic	4.4	2.9	0.004	
Mesobenthic	4.4	2.9	0.008	
BPI broad	4.0	2.6	0.014	
Dissolved oxygen	3.8	2.5	0.008	

Many fish family occurrences were highly variable. Their modeled slopes overlapped with zero in all but four - six families per location (**Figure 5**). Grenadiers (Macrouridae) were common at three locations (with less at the Revillagigedos), with the highest association at Clipperton. Chimaeras (Chimaeridae) were common at Clipperton and the Revillagigedos, but were not frequently encountered at the Galápagos or Malpelo. Catsharks (Scyliorhinidae) were the most common family encountered at the Galápagos, but less common at Malpelo. Morids (Moridae) were less common at Galápagos and Malpelo (**Figure 5**).

Similar binomial GLMMs were used to test for family specific effects of habitat (hard vs. soft). While these did show a slight shift in community composition these were not statistically significant [LRT: $\chi^2(5) = 4.90$, $P = 0.08$] (**Figure 6**).

Fish family assemblage structure could be explained by several environmental variables. The first two axes of the CCA plot explained 27% of the explained variation and 66% of the explained fitted variation (**Figure 7** and **Table 2**). The main factors influencing this ordination were location (e.g., Malpelo, Galápagos, and Revillagigedo), distance to seamounts, and distance to the continent. Chimaeridae and Moridae were correlated with depth and bathybenthic strata. Liparidae, Echinorhinidae, and Etmopteridae were most closely correlated with seamounts. Rajiidae and Scyliorhinidae were correlated with soft bottoms and closer to the continent.

Invertebrates

Models showed significantly different assemblages [LRT: $\chi^2(9) = 69.9$, $P < 0.001$] among locations. The change in community composition was quantified in terms of how much the slopes of the response differ across orders. The magnitude of variation was 5.35 (se = 2.35) on a logit scale, indicating that the change in community composition was substantial in terms of which invertebrate orders were present, depending on location. The variation in the location effect across orders was large. The standard deviation ranged from 1.3 to 3.6 (on the logit scale) depending on location (**Figure 8**).

Each site was unique in terms of invertebrate order probability of occurrence (**Figure 8**). The Revillagigedos showed the least variability in estimates, but no strong affinities, whereas Malpelo showed a large variability, with sea stars (Paxillosida) strongly negatively associated with the site, and amphipods (Amphipoda), and krill (Euphausiacea) strongly positively associated with the site.

Similar binomial GLMMs were used to test for invertebrate order-specific effects of habitat (hard vs. soft). These did not show a shift in community composition [LRT: $\chi^2(2) = 1.36$, $P = 0.50$] (**Figure 9**). The signal and variation were greater in hard bottom habitats (standard deviation 0.79 on the logit scale) compared to soft bottom habitat (standard deviation 0.24 on the logit scale).

Invertebrate community structure was correlated with a number of environmental variables. The first two axes of the CCA plot explained 26% of the explained variation and 65% of the explained fitted variation (**Figure 10** and **Table 3**). The main factors influencing this ordination were location (e.g., Clipperton, Malpelo, Galápagos, and Revillagigedo), distance to seamounts and distance to the continent. POC and slope also explained modest amounts of variation in invertebrate community structure. Echinodermata, Asteroidea, and Sceptrulophora were correlated with seamounts. Alcyonacea was most closed correlated with proximity

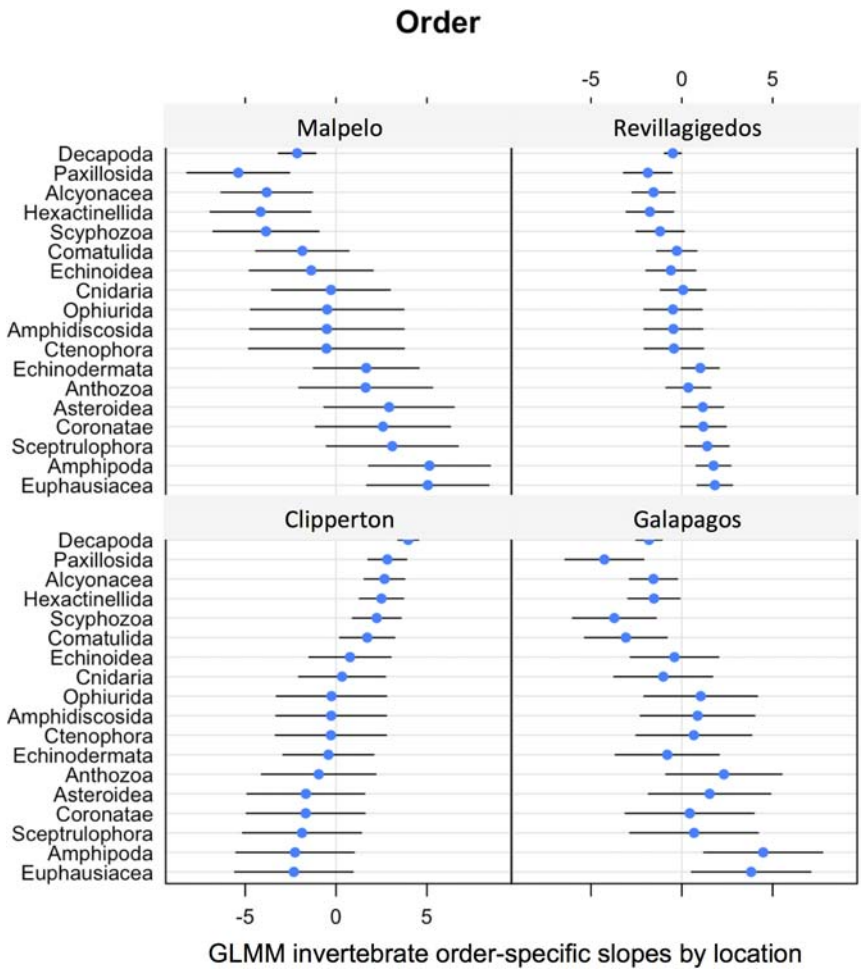

FIGURE 8 | GLMM random effects (modeled slopes) for invertebrate order-specific probability of occurrence by location.

to the continent, while Ophiurida and Amphipoda were correlated with POC.

DISCUSSION

Patterns in Biodiversity Across Islands/Archipelagos

The overall geographic pattern of biodiversity revealed higher values closer to the equator and closer to the continent, and lower values in the locations farther north and farther west. This finding is consistent with the biodiversity pattern predicted based on marine species ranges across latitudinal gradients (Costello and Chaudhary, 2017). Fish family biodiversity was highest in the Galápagos, followed by Malpelo. In contrast, Clipperton had significantly lower fish family richness compared to all other locations. For invertebrate orders, the Revillagigedos were significantly lower in biodiversity compared to the Galápagos and Malpelo.

The strong location effect could be explained, in part, by the vastly different current regimes around each island group, and the unique hydrographic and environmental characteristics of the associated water masses (**Figure 1**). Gradients in environmental parameters, such as temperature, salinity, nutrients, and oxygen, vary drastically across this region and co-occur within larger oceanographic processes, such as current regimes [see review by Fiedler and Talley (2006)]. These interrelated variables affect patterns in biodiversity through influencing the physiology, biology, and interactions of marine organisms (Levin et al., 2001). Similarly, co-varying environmental parameters have been implicated in causing depth zonation in the deep-sea (Rex, 1976; Carney, 2005; Yeh and Drazen, 2009) and latitudinal gradients in biodiversity (Fortes and Absalão, 2010; Costello and Chaudhary, 2017). While depth zonation has been well documented, current regimes will require further assessment as large-scale drivers of biodiversity within the region (Levin et al., 2001).

Benthic habitat types (hard vs. soft bottom) had little influence on fish diversity in our study. This finding is not surprising given that highly mobile bathyal demersal fishes are expected to have large ranges, irrespective of habitat type (Ekman, 1953; Pineda, 1993; Stevens, 1996; Smith and Brown, 2002). Of

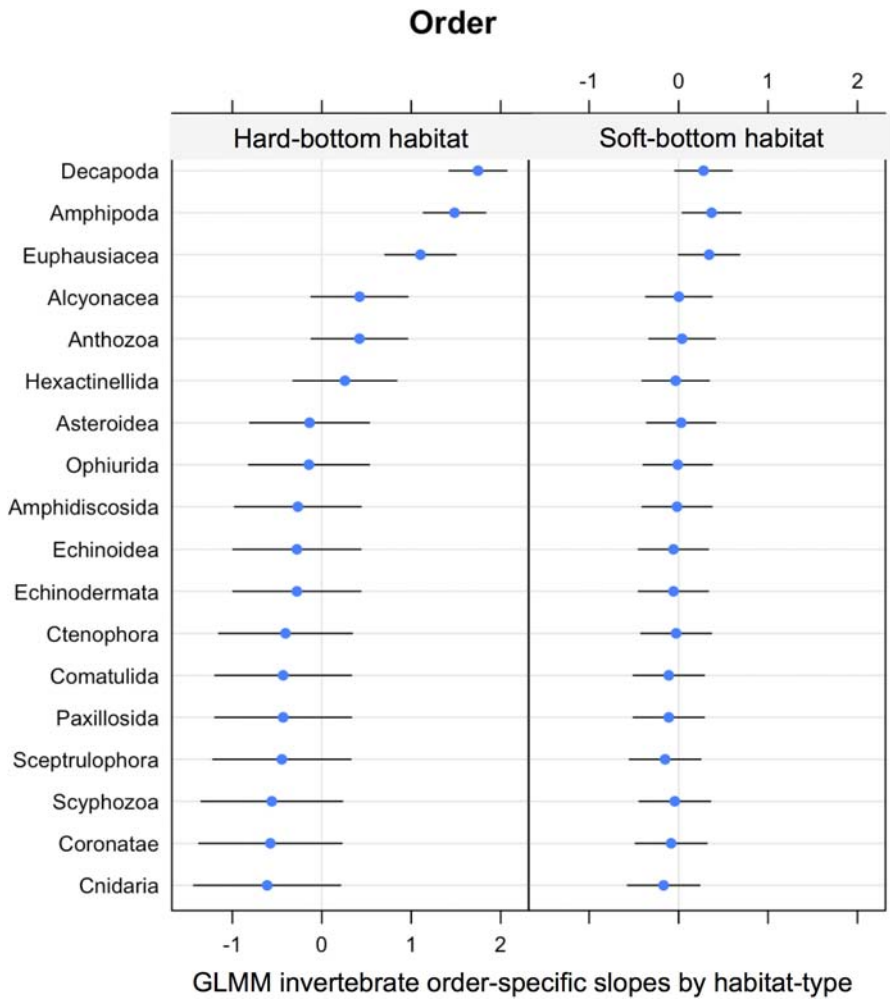

FIGURE 9 | GLMM random effects (modeled slopes) for invertebrate order-specific probability of occurrence by habitat (hard vs. soft bottom).

the 284 described fish species with circumglobal distributions, more than 80% of these species are represented by deep-sea fishes (Gaither et al., 2016). In contrast, for the low-mobility macro invertebrates assessed in this study, soft bottom habitats harbored significantly lower diversity compared to hard bottom habitats for all three diversity indices. This finding is consistent with the well-documented positive association of low-mobility benthic fauna diversity and measures of habitat heterogeneity (Etter and Grassle, 1992; Leduc et al., 2012).

Faunal Assemblage Composition Across Islands/Archipelagos

Our results show significant differences in community composition among locations for fish and invertebrate assemblages. Variations in the spatial distribution in fish families were mostly explained by location, distance to seamounts, distance to the continent, and depth. Temperature, and broad-scale complexity (BPI) were also important in explaining the distribution of fish family abundance within the region. Similarly, invertebrate community structure was explained by location, distances to seamounts and to the continent, as well as POC and bathymetric slope.

Habitat effects (hard vs. soft) on fish family composition were suggestive, though not statistically significant in our GLMMs, a finding that is similar to comparisons of abyssal scavenging community composition in the Pacific (Leitner et al., 2017). In contrast, studies of bathyal fish-habitat associations on seamounts in the Atlantic found significant differences in community composition between substrate types (Porteiro et al., 2013). The loose habitat association detected here could be expected given that the assemblage of scavengers/predators observed are highly mobile. In contrast, for invertebrates, the shifts in composition with habitat were significant. The order-specific signal and variation in habitat effects were greater in hard compared to soft bottom habitats, likely due to increased habitat heterogeneity (Etter and Grassle, 1992). The positive associations could be related to a greater abundance and diversity of potential epibenthic prey items for less-mobile invertebrate taxa (McClain and Barry, 2010).

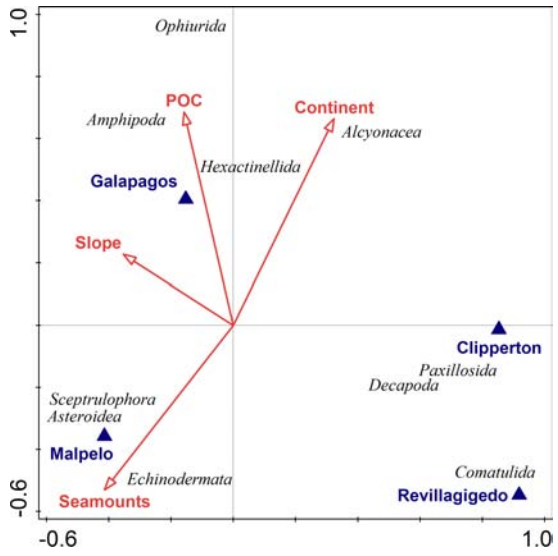

FIGURE 10 | Canonical Correspondence Analysis (CCA) of invertebrate taxa numerical abundance. Vectors indicate direction and strength (length) of relationships between taxa and explanatory geospatial variables defined in **Supplementary Table S1** (e.g., location; distance to seamounts; and continent; and POC).

TABLE 3 | Results of Canonical Correspondence Analysis (CCA) on square root-transformed invertebrate abundance data.

Statistic	Axis 1	Axis 2	Axis 3	Axis 4
Eigenvalues	0.58	0.27	0.11	0.10
Explained variation (cumulative)	17.95	26.31	29.84	32.92
Pseudo-canonical correlation	0.95	0.78	0.69	0.63
Explained fitted variation (cumulative)	44.40	65.09	73.82	81.45
Name	**% explained**	**pseudo-F**	**P**	
Location: Clipperton	10.7	7.7	0.002	
Location: Malpelo	9.3	6.6	0.002	
Seamounts	6.6	4.5	0.002	
Continent	6.3	4.3	0.002	
Location: Revillagigedo	5.9	4	0.002	
Location: Galápagos	5.7	3.9	0.002	
POC	5.4	3.7	0.028	
Slope	3.3	2.2	0.024	

Overall, measures of seascape configuration (e.g., distance to seamounts, distance to the continent) were stronger explanatory variables structuring community composition in our study, compared to gradients in environmental parameters (e.g., temperature, salinity) (**Supplementary Table S1**). These co-varying environmental parameters respond to large-scale oceanographic processes, such as currents, and are affected by seascape configuration (Levin et al., 2001; McClain and Barry, 2010).

Environmental Predictors of Deep-Sea Biodiversity

We measured a significant relationship between bathyal fish biodiversity and bathymetric predictors, namely broad-scale (2,500 m) BPI. As a topographic variable, BPI is used to identify benthic features (e.g., ridges and valleys), with positive values indicating peaks in topography while negative values indicate troughs. Fish diversity increased with BPI, indicating a positive association with ridges and peaks as opposed to valleys on the seafloor. Our findings are consistent with previous studies in the Pacific (Leitner et al., 2017), which also detected changes in diversity along topographic gradients. Broad-scale BPI provides a metric for bathymetric characteristics at a spatial scale appropriate for highly mobile species, such as those that dominate the fish communities assessed in this study. Lower-mobility invertebrate communities did not show a significant relationship with either fine- or broad-scale BPI. Likely these communities are influenced by topographic metrics at a scale finer than the BPI scale (minimum inner radius 100 m) afforded by the resolution of our bathymetric data (Dolan et al., 2008; Guinan et al., 2009; Turner et al., 2018).

Dissolved oxygen concentration emerged as a positive significant predictor of fish diversity. Annual mean dissolved oxygen values derived from depth bins associated with deployment sites indicate that many of the biological communities sampled would have been under severely hypoxic conditions (<0.2 ml l^{-1}) (**Figure 1**). More specifically, deployments at intermediate depths were located in oxygen minima. In the TEP, oxygen minima lie below the surface layer where high productivity peaks oxygen consumption, and above depths replenished by advection of oxygenated waters subducted at higher latitudes (Fiedler and Talley, 2006). These oxygen minimum zones (OMZs) typically exhibit low macrofaunal and megafaunal species richness, with communities highly dominated by only a few taxa (Levin et al., 2001). This pattern was apparent for fish communities in our study, and has been observed elsewhere in the eastern Pacific (Levin et al., 1991). This pattern of increased community diversity with dissolved oxygen concentration has also been observed for invertebrate macrofauna (Diaz and Rosenberg, 1995) and megafauna (Levin, 2003), though was not detected in our study. As large taxa are more sensitive than small taxa to hypoxia (Levin et al., 2001), we expect that with more extensive sampling, and finer resolution taxonomic classification, patterns of association between dissolved oxygen concentration and invertebrate diversity may be revealed. These may not be linear, but rather unimodal, with peaks in diversity at intermediate levels of oxygen concentration (Levin et al., 2001).

We did not see positive influence of POC flux (a proxy for food availability) on biodiversity, a surprise given that primary productivity is implicated in generating latitudinal diversity gradients (Rex et al., 1993). However, the relationship between biodiversity, horizontal variation in vertical POC flux, and the many interrelated factors across water masses and current regimes that co-occur with latitude, requires additional sampling (Lampitt and Antia, 1997; Lutz et al., 2007;

McClain and Hardy, 2010). For example, food availability to the seafloor declines exponentially with depth (Lutz et al., 2007; Smith et al., 2008) therefore POC effects could be dampened by the strong influence of bathymetry on surrounding environments. In abyssal depths of the eastern Pacific, peaks and ridges, rather than the overlying surface productivity were implicated in influencing abyssal scavenging community composition and diversity at local scales, owing to either decreased food availability in bathymetric lows, or to enhanced flow and food flux to suspension feeders in bathymetric highs (Leitner et al., 2017).

Limitations and Data Gaps

Many environmental predictor datasets in our study remain at a coarse scale, potentially shrouding relationships between predictors and biodiversity. For example, the oxygen data applied in our analysis were for coarse vertical zones (i.e., 800–3500 m; Watling et al., 2013), therefore the insignificant relationship with invertebrate orders could be an artifact of data resolution. More extensive sampling, and ideally *in situ* environmental measurements, would greatly enhance our ability to determine the individual effects of environmental parameters on patterns in biodiversity. Nevertheless, this study represents the first assessment of bathyal demersal biodiversity across multiple Ocean Island Province sites in the TEP, and while sampling coverage limits our ability to detect the individual influence of co-occurring hydrographic and environmental variables, significant differences among locations in fish and invertebrate diversity were apparent. These may be attributed, within the limitations of the study, to the different current regimes around each island/archipelago.

CONCLUSION

Biodiversity and community composition of bathyal demersal fauna differ across the TEP associated with large-scale oceanographic processes. We have provided insight into differences in biological communities among four island groups, and identified several environmental drivers of these variations, including dissolved oxygen concentration and habitat type for some fauna. This expands the previously limited knowledge of biodiversity patterns and its drivers in the TEP. Because the TEP is largely isolated from the wider Pacific (Lessios and Robertson, 2006), the islands and archipelagos of the Ocean Island Province likely represent important stepping-stones and corridors for species connectivity across the TEP and the wider Pacific (Glynn et al., 1996). Therefore, the preservation of these intact ecosystems is important for maintaining biodiversity both within the TEP as well as across the wider Pacific region.

DATA AVAILABILITY

The raw data supporting the conclusions of this manuscript will be made available by the authors, without undue reservation, to any qualified researcher.

AUTHOR CONTRIBUTIONS

JG, WG, and AF wrote the manuscript, performed the statistical analyses, processed the imagery, and identified the species. PS identified the species. BH, CS, and AT built the Dropcams and collected the data on expeditions. EB, AT, and ES organized the research program. All authors assisted in manuscript editing.

FUNDING

Funding for this study was provided by the National Geographic Society, Washington, DC, United States.

ACKNOWLEDGMENTS

We thank the Pristine Seas team and boat crews who assisted in data collection. Jessica Elfadl of the Exploration Technology Lab assisted tremendously with expedition logistics and equipment. We thank the experts who assisted with species identification, including Chris Kelley, Ross Robertson, Bruce Mundy, Beatriz Mejía-Mercado, and Dave Ebert. Graham Wilhelm was instrumental in setting up the initial mechanical design of the Dropcams. We thank Graham and all members of the National Geographic Exploration Technology Lab. The Galápagos Islands research was authorized by the Galápagos National Park Directorate under the permit PC-26-15. This publication is contribution number 2275 of the Charles Darwin Foundation for the Galápagos Islands. The insightful comments of the two reviewers and the editor greatly improved the quality of this manuscript.

SUPPLEMENTARY MATERIAL

The Supplementary Material for this article can be found online at: https://www.frontiersin.org/articles/10.3389/fmars.2019.00388/full#supplementary-material

REFERENCES

Allen, G. R. (2008). Conservation hotspots of biodiversity and endemism for Indo-Pacific coral reef fishes. *Aquat. Conserv.* 18, 541–556. doi: 10.1002/aqc.880

Allen, G. R., and Robertson, D. R. (1994). *Fishes of the Tropical Eastern Pacific*. Honolulu, HI: University of Hawaii Press.

Alzate, A., Zapata, F. A., and Giraldo, A. (2014). A comparison of visual and collection-based methods for assessing community structure of coral reef fishes in the Tropical Eastern Pacific. *Rev. Biol. Trop.* 62, 359–371.

Auster, P. J., Sánchez-Jiménez, A., Rodríguez-Arrieta, J. A., Quesada, A. J., Cinthya, P., and Naranjo-Elizondo, B. (2016). Facilitative behavioral interactions between deepwater piscivores at Isla del Coco National Park and Las Gemelas Seamount. *Costa Rica. Rev. Biol. Trop.* 64, 187–196.

Bates, D., Mächler, M., Bolker, B., and Walker, S. (2014). Fitting linear mixed-effects models using lme4. *arXiv* 14065823.

Carey, S., Fisher, C. R., de Leon, P. S., Roman, C., Nicole, A. R., and Jennifer, S. (2016). Exploring the undersea world of the Galápagos Islands. *Ocean Mag.* 29, 32–34.

Carney, R. S. (2005). "Zonation of deep biota on continental margins," in *Oceanography and Marine Biology*, eds R. N. Gibson, R. J. A. Atkinson, and J. D. M. Gordon (Boca Raton, FL: CRC Press), 221–288.

Chao, A., Chiu, C.-H., and Jost, L. (2014). Unifying species diversity, phylogenetic diversity, functional diversity, and related similarity and differentiation measures through Hill numbers. *Annu. Rev. Ecol. Evol. Syst.* 45, 297–324. doi: 10.1146/annurev-ecolsys-120213-091540

Cortés, J., and Blum, S. (2008). Life to 450 m depth at Isla del Coco, Costa Rica. *Rev. Biol. Trop.* 56(Suppl. 2), 189–206.

Costello, M. J., and Chaudhary, C. (2017). Marine biodiversity, biogeography, deep-sea gradients, and conservation. *Curr. Biol.* 27, R511–R527.

Diaz, R. J., and Rosenberg, R. (1995). Marine benthic hypoxia: a review of its ecological effects and the behavioural responses of benthic macrofauna. *Oceanogr. Mar. Biol. Annu. Rev.* 33, 245–303.

Dolan, M. F., Grehan, A. J., Guinan, J. C., and Brown, C. (2008). Modelling the local distribution of cold-water corals in relation to bathymetric variables: adding spatial context to deep-sea video data. *Deep Sea Res. Part I Oceanogr. Res. Pap.* 55, 1564–1579. doi: 10.1016/j.dsr.2008.06.010

Dulvy, N. K., Sadovy, Y., and Reynolds, J. D. (2003). Extinction vulnerability in marine populations. *Fish Fish.* 4, 25–64. doi: 10.1046/j.1467-2979.2003.00105.x

Ekman, S. (1953). *Zoogeography of the Sea*, Vol. 9. London: Sidgwick and Jackson.

ESRI (2011). *ArcGIS Desktop: Release 10*. Redlands, CA: Environmental Systems Research Institute.

Etter, R. J., and Grassle, J. F. (1992). Patterns of species diversity in the deep sea as a function of sediment particle size diversity. *Nature* 360:576. doi: 10.1038/360576a0

Fiedler, P. C., and Lavín, M. F. (2017). "Oceanographic conditions of the Eastern Tropical Pacific," in *Coral Reefs of the Eastern Tropical Pacific*, eds P. Glynn, D. Manzello, and I. Enochs (Dordrecht: Springer), 59–83. doi: 10.1007/978-94-017-7499-4_3

Fiedler, P. C., and Talley, L. D. (2006). Hydrography of the eastern tropical Pacific: a review. *Prog. Oceanogr.* 69, 143–180. doi: 10.1016/j.pocean.2006.03.008

Fortes, R., and Absalão, R. (2010). The latitudinal and bathymetric ranges of marine fishes: a global analysis to test the application of Rapoport's Rule. *Mar. Ecol.* 31, 483–493.

Fourriére, M., Reyes-Bonilla, H., Rodríguez-Zaragoza, F. A., and Crane, N. (2014). Fishes of Clipperton Atoll, Eastern Pacific: checklist, endemism, and analysis of completeness of the inventory. *Pac. Sci.* 68, 375–395. doi: 10.2984/68.3.7

Gaither, M. R., Bowen, B. W., Rocha, L. A., and Briggs, J. C. (2016). Fishes that rule the world: circumtropical distributions revisited. *Fish Fish.* 17, 664–679. doi: 10.1111/faf.12136

Glynn, P. W., Veron, J., and Wellington, G. M. (1996). Clipperton Atoll (eastern Pacific): oceanography, geomorphology, reef-building coral ecology and biogeography. *Coral Reefs* 15, 71–99. doi: 10.1007/s003380050029

Guinan, J., Grehan, A. J., Dolan, M. F., and Brown, C. (2009). Quantifying relationships between video observations of cold-water coral cover and seafloor features in Rockall Trough, west of Ireland. *Mar. Ecol. Prog. Ser.* 375, 125–138. doi: 10.3354/meps07739

Hill, M. O. (1973). Diversity and evenness: a unifying notation and its consequences. *Ecology* 54, 427–432. doi: 10.2307/1934352

Hobbs, J. P., Jones, G., and Munday, P. (2011). Extinction risk in endemic marine fishes. *Conserv. Biol.* 25, 1053–1055. doi: 10.1111/j.1523-1739.2011.01698.x

Hsieh, T., Ma, K., and Chao, A. (2016). iNEXT: an R package for rarefaction and extrapolation of species diversity (Hill numbers). *Methods Ecol. Evol.* 7, 1451–1456. doi: 10.1111/2041-210x.12613

Hubbs, C. L., and Briggs, J. C. (1974). *Marine Zoogeography*. New York, NY: McGraw-Hill.

Jones, D. O., and Brewer, M. E. (2012). Response of megabenthic assemblages to different scales of habitat heterogeneity on the Mauritanian slope. *Deep Sea Res. Part I Oceanogr. Res. Pap.* 67, 98–110. doi: 10.1016/j.dsr.2012.05.006

Jost, C. H., and Andréfouët, S. (2006). Long-term natural and human perturbations and current status of Clipperton Atoll, a remote island of the Eastern Pacific. *Pac. Conserv. Biol.* 12, 207–217.

Karstensen, J., Stramma, L., and Visbeck, M. (2008). Oxygen minimum zones in the eastern tropical Atlantic and Pacific oceans. *Prog. Oceanogr.* 77, 331–350. doi: 10.1016/j.pocean.2007.05.009

Kessler, W. S. (2006). The circulation of the eastern tropical Pacific: a review. *Prog. Oceanogr.* 69, 181–217. doi: 10.1016/j.pocean.2006.03.009

Lampitt, R. S., and Antia, A. N. (1997). Particle flux in deep seas: regional characteristics and temporal variability. *Deep Sea Res. Part 1 Oceanogr. Res. Pap.* 44, 1377–1403. doi: 10.1016/S0967-0637(97)00020-4

Leduc, D., Rowden, A. A., Probert, P. K., Pilditch, C. A., Nodder, S. D., Vanreusel, A., et al. (2012). Further evidence for the effect of particle-size diversity on deep-sea benthic biodiversity. *Deep Sea Res. Part I Oceanogr. Res. Pap.* 63, 164–169. doi: 10.1016/j.dsr.2011.10.009

Leitner, A. B., Neuheimer, A. B., Donlon, E., Smith, C. R., and Drazen, J. C. (2017). Environmental and bathymetric influences on abyssal bait-attending communities of the Clarion Clipperton Zone. *Deep Sea Res. Part I Oceanogr. Res. Pap.* 125, 65–80. doi: 10.1016/j.dsr.2017.04.017

Lessios, H. A., and Robertson, D. R. (2006). Crossing the impassable: genetic connections in 20 reef fishes across the eastern Pacific barrier. *Proc. R. Soc. Lond. B Biol. Sci.* 273, 2201–2208. doi: 10.1098/rspb.2006.3543

Levin, L. A. (2003). Oxygen minimum zone benthos: adaptation and community response to hypoxia. *Oceanogr. Mar. Biol. Annu. Rev.* 41, 1–45.

Levin, L. A., Etter, R. J., Rex, M. A., Gooday, A. J., Smith, C. R., and Jesus, P. (2001). Environmental influences on regional deep-sea species diversity. *Annu. Rev. Ecol. Syst.* 32, 51–93. doi: 10.1146/annurev.ecolsys.32.081501.114002

Levin, L. A., Huggett, C. L., and Wishner, K. F. (1991). Control of deep-sea benthic community structure by oxygen and organic-matter gradients in the eastern Pacific Ocean. *J. Mar. Res.* 49, 763–800. doi: 10.1357/002224091784995756

Lubetkin, M., Carey, S., Kelley, K. A., Robert, G., Cornell, W., and Nicole, R. (2018). Nontronite-bearing tubular hydrothermal deposits from a Galapagos seamount. *Deep Sea Res. Part II Top. Stud. Oceanogr.* 150, 181–194. doi: 10.1016/j.dsr2.2017.09.017

Lundblad, E. R., Wright, D. J., Miller, J., Larkin, E. M., Ronald, R., and David, F. N. (2006). A benthic terrain classification scheme for American Samoa. *Mar. Geodesy* 29, 89–111. doi: 10.1080/01490410600738021

Lutz, M. J., Caldeira, K., Dunbar, R. B., and Behrenfeld, M. J. (2007). Seasonal rhythms of net primary production and particulate organic carbon flux to depth describe the efficiency of biological pump in the global ocean. *J. Geophys. Res. Oceans* 112. doi: 10.1029/2006JC003706

McClain, C. R., and Barry, J. P. (2010). Habitat heterogeneity, disturbance, and productivity work in concert to regulate biodiversity in deep submarine canyons. *Ecology* 91, 964–976. doi: 10.1890/09-0087.1

McClain, C. R., and Hardy, S. M. (2010). The dynamics of biogeographic ranges in the deep sea. *Proc. R. Soc. B Biol. Sci.* 277, 3533–3546. doi: 10.1098/rspb.2010.1057

Pineda, J. (1993). Boundary effects on the vertical ranges of deep-sea benthic species. *Deep Sea Res.* 40, 2179–2192. doi: 10.1016/0967-0637(93)90097-m

Porteiro, F. M., Gomes-Pereira, J. N., Pham, C. K., Tempera, F., and Santos, R. S. (2013). Distribution and habitat association of benthic fish on the Condor seamount (NE Atlantic, Azores) from in situ observations. *Deep Sea Res. Part II Top. Stud. Oceanogr.* 98, 114–128. doi: 10.1016/j.dsr2.2013.09.015

Priede, I. G. (2017). *Deep-Sea Fishes: Biology, Diversity, Ecology and Fisheries*. Cambridge: Cambridge University Press.

R Core Team (2016). *R: A Language and Environment for Statistical Computing*. Vienna: R Foundation for Statistical Computing.

Rex, M. A. (1976). Biological accomodation in the deep-sea benthos: comparative evidence on the importance of predation and productivity. *Deep Sea Res. Oceanogr. Abstr.* 23, 975–987. doi: 10.1016/0011-7471(76)90827-5

Rex, M. A., Stuart, C. T., Hessler, R. R., Allen, J. A., Sanders, H. L., and Wilson, G. D. F. (1993). Global-scale latitudinal patterns of species diversity in the deep-sea benthos. *Nature* 365, 636–639. doi: 10.1038/365636a0

Robert, K., Jones, D. O., Tyler, P. A., Van Rooij, D., and Huvenne, V. A. (2015). Finding the hotspots within a biodiversity hotspot: fine-scale biological predictions within a submarine canyon using high-resolution acoustic mapping techniques. *Mar. Ecol.* 36, 1256–1276. doi: 10.1111/maec.12228

Robertson, D. R., and Cramer, K. L. (2009). Shore fishes and biogeographic subdivisions of the Tropical Eastern Pacific. *Mar. Ecol. Prog. Ser.* 380, 1–17. doi: 10.3354/meps07925

Rogers, A. (1994). The biology of seamounts. *Adv. Mar. Biol.* 30, 305–350. doi: 10.1016/s0065-2881(08)60065-6

Sánchez-Jiménez, A., Naranjo-Elizondo, B., Rodríguez-Arrieta, A., Quesada, A. J., Blum, S., and Auster, P. (2018). Updated catalogue of bony fishes observed in deep waters at Isla del Coco National Park and Las Gemelas Seamount, Costa Rica (Eastern Tropical Pacific). *Rev. Biol. Trop.* 66, S1–S113.

Smith, C. R., De Leo, F. C., Bernardino, A. F., Sweetman, A. K., and Arbizu, P. M. (2008). Abyssal food limitation, ecosystem structure and climate change. *Trends Ecol. Evol.* 23, 518–528. doi: 10.1016/j.tree.2008.05.002

Smith, K. F., and Brown, J. H. (2002). Patterns of diversity, depth range and body size among pelagic fishes along a gradient of depth. *Glob. Ecol. Biogeogr.* 11, 313–322. doi: 10.1046/j.1466-822x.2002.00286.x

Stevens, G. C. (1996). Extending rapoport's rule to Pacific marine fishes. *J. Biogeogr.* 23, 149–154. doi: 10.1046/j.1365-2699.1996.00977.x

Stramma, L., Schmidtko, S., Levin, L. A., and Johnson, G. C. (2010). Ocean oxygen minima expansions and their biological impacts. *Deep Sea Res. Part I Oceanogr. Res. Pap.* 57, 587–595. doi: 10.1016/j.dsr.2010.01.005

ter Braak, C. J. (1994). Canonical community ordination. Part I: basic theory and linear methods. *Ecoscience* 1, 127–140. doi: 10.1080/11956860.1994.11682237

ter Braak, C. J., and Šmilauer, P. (2002). *CANOCO Reference Manual and CanoDraw for Windows User's Guide: Software for Canonical Community Ordination (version 4.5)*.

Turchik, A. J., Berkenpas, E. J., Henning, B. S., and Shepard, C. M. (2015). "The Deep Ocean Dropcam: a highly deployable benthic survey tool," in *Proceedings of the OCEANS'15 MTS/IEEE Washington*, (Washington, DC: IEEE), 1–8.

Turner, J. A., Babcock, R. C., Hovey, R., and Kendrick, G. A. (2018). AUV-based classification of benthic communities of the Ningaloo shelf and mesophotic areas. *Coral Reefs* 37, 763–778. doi: 10.1007/s00338-018-1700-3

Wang, C., and Enfield, D. B. (2001). The tropical Western Hemisphere warm pool. *Geophys. Res. Lett.* 28, 1635–1638. doi: 10.1029/2000gl011763

Watling, L., Guinotte, J., Clark, M. R., and Smith, C. R. (2013). A proposed biogeography of the deep ocean floor. *Prog. Oceanogr.* 111, 91–112. doi: 10.1016/j.pocean.2012.11.003

Wilson, R. R. Jr., and Kaufmann, R. S. (1987). "Seamount biota and biogeography," in *Seamounts, Islands, and Atolls*, Vol. 43, eds B. H. Keating, P. Fryer, R. Batiza, and G. W. Boehlert (Washington, D.C: American Geophysical Union), 355–377. doi: 10.1029/gm043p0355

Wright, D., Pendleton, M., Boulware, J., Walbridge, S., Gerlt, B., et al. (2012). *ArcGIS Benthic Terrain Modeler (BTM), v. 3.0*. Redlands: CA: Environmental Systems Research Institute.

Yeh, J., and Drazen, J. C. (2009). Depth zonation and bathymetric trends of deep-sea megafaunal scavengers of the Hawaiian Islands. *Deep Sea Res. Part I Oceanogr. Res. Pap.* 56, 251–266. doi: 10.1016/j.dsr.2008.08.005

Zapata, F. A., and Ross Robertson, D. (2007). How many species of shore fishes are there in the Tropical Eastern Pacific? *J. Biogeogr.* 34, 38–51. doi: 10.1111/j.1365-2699.2006.01586.x

Conflict of Interest Statement: The authors declare that the research was conducted in the absence of any commercial or financial relationships that could be construed as a potential conflict of interest.

Copyright © 2019 Giddens, Goodell, Friedlander, Salinas-de-León, Shepard, Henning, Berkenpas, Sala and Turchik. This is an open-access article distributed under the terms of the Creative Commons Attribution License (CC BY). The use, distribution or reproduction in other forums is permitted, provided the original author(s) and the copyright owner(s) are credited and that the original publication in this journal is cited, in accordance with accepted academic practice. No use, distribution or reproduction is permitted which does not comply with these terms.

frontiers in Marine Science

ORIGINAL RESEARCH
published: 09 July 2019
doi: 10.3389/fmars.2019.00382

The NE Lau Basin: Widespread and Abundant Hydrothermal Venting in the Back-Arc Region Behind a Superfast Subduction Zone

Edward T. Baker[1,2], Sharon L. Walker[2], Gary J. Massoth[3] and Joseph A. Resing[1,2]*

[1] Joint Institute for the Study of the Atmosphere and Ocean, University of Washington, Seattle, WA, United States, [2] National Oceanic and Atmospheric Administration/Pacific Marine Environmental Laboratory, Seattle, WA, United States, [3] Mass-Ex3 Consulting, LLC, Renton, WA, United States

OPEN ACCESS

Edited by:
Diva Amon,
Natural History Museum,
United Kingdom

Reviewed by:
Jeffrey Seewald,
Woods Hole Oceanographic
Institution, United States
Charles Geoffrey Wheat,
University of Alaska Fairbanks,
United States

***Correspondence:**
Edward T. Baker
Edward.baker@noaa.gov

Specialty section:
This article was submitted to
Deep-Sea Environments and Ecology,
a section of the journal
Frontiers in Marine Science

Received: 21 March 2019
Accepted: 19 June 2019
Published: 09 July 2019

Citation:
Baker ET, Walker SL, Massoth GJ
and Resing JA (2019) The NE Lau
Basin: Widespread and Abundant
Hydrothermal Venting in the Back-Arc
Region Behind a Superfast
Subduction Zone.
Front. Mar. Sci. 6:382.
doi: 10.3389/fmars.2019.00382

The distribution of hydrothermal venting reveals important clues about the presence of magma in submarine settings. The NE Lau Basin in the southwest Pacific Ocean is a complex back-arc region of widespread hydrothermal activity. It includes spreading ridges, arc volcanoes, and intra-plate volcanoes that provide a perhaps unique laboratory for studying interactions between hydrothermal activity and magma sources. Since 2004, multiple cruises have explored the water column of the NE Lau Basin. Here, we use these data to identify and characterize 43 active hydrothermal sites by means of optical, temperature, and chemical tracers in plumes discharged by each site. Seventeen of 20 prominent volcanic edifices dispersed among the Tofua arc, spreading ridges, and plate interiors host active hydrothermal sites. Fourteen apparently discharge high-temperature fluids, including a multi-year submarine eruption at the intra-plate volcano W Mata. The 430 km of spreading ridges host 31 active sites, one an eruption event in 2008. Our data show that the relationship between site spatial density (sites/100 km of ridge crest) and ridge spreading rate (8–42 mm/year) in the NE Lau Basin follows the same linear trend as previously established for the faster-spreading (40–90 mm/year) ridges in the central Lau Basin. The lower site density in the NE Lau Basin compared to the southern Lau is consistent with recent plate reconstructions that more than halved earlier estimates of ∼50–100 mm/year spreading rates in the NE Lau Basin. Combined data from the spreading ridges throughout the entire Lau back-arc basin demonstrates that hydrothermal sites, normalized to spreading rate, are ∼10× more common than expected based on existing mid-ocean ridge data. This increase documents the ability of meticulous exploration, using both turbidity and chemical sensors, to more fully describe the true hydrothermal population of a spreading ridge, compared to conventional techniques. It further reveals that the Lau back-arc basin, benefiting from both ridge and arc magma sources, supports an exceptionally high population of ridge and intra-plate hydrothermal sites.

Keywords: hydrothermal plumes, NE Lau Basin, spreading ridge, submarine volcanoes, subduction zone

INTRODUCTION

The distribution of hydrothermal venting sites depends on the interplay between heat supply by magmatism and crustal permeability caused by tectonism (e.g., Baker et al., 1995). Few oceanic areas combine the abundance of hydrothermal sites and the diversity of geological settings necessary for evaluating the relative importance of each process. One example is the NE Lau Basin, a back-arc basin where complex plate processes have created one of the most densely populated and geologically diverse group of active vents yet studied. We here define the NE Lau Basin as that portion of the larger Lau Basin that is bounded on the east by the Tofua arc, on the north by a subducting plate tear created by the westward bending of the Tonga-Pacific plate boundary, on the west by a series of back-arc ridges along the Niuafo'ou-Tonga plate (and likely an undefined microplate(s) to their north) boundary, and on the south by the near intersection of the Niuafo'ou plate and the Tofua arc (**Figure 1**; Conder and Wiens, 2011; Sleeper and Martinez, 2016).

Volcanism in the NE Lau Basin occurs on and between these boundaries. The active Niua volcano marks the northern end of the Tofua arc. The Northeast Lau Spreading Center (NELSC), the Mangatolou Triple Junction (MTJ) segments, and the Fonualei Rift and Spreading Center (FRSC) define the western edge of the northern Tonga plate, and that of the undefined plate(s) to the north. Multiple active cone and caldera volcanoes populate its intra-plate portion. The Zellmer and Taylor (2001) three-plate kinematic model derived spreading rates increasing from 50 mm/year (full rate here and throughout the text) at the south end of the FRSC to 100 mm/year along the MTJ. Bird (2003) extended these predictions to the NELSC, deriving speeds as high as 126 mm/year. By analogy with world-wide mid-ocean ridges (e.g., Beaulieu et al., 2015), the hydrothermal site density, F_s (sites/100 km of ridge), along this boundary should be among the highest in the entire Lau Basin. A revised plate model (Sleeper and Martinez, 2016), however, predicts spreading rates of only 8–∼40 mm/year along these ridges. This reduction leads to an expectation of significantly fewer hydrothermal sites.

This paper uses water-column survey data collected since 2004 to describe the distribution of hydrothermal activity within the various volcanic/tectonic domains of the NE Lau Basin. Such surveys began with sparse coverage by Arculus (2004),German et al. (2006), and Kim et al. (2009). In 2008, the NOAA Vents (now Earth–Ocean Interaction) program, together with various collaborating institutions and organizations, began a series of cruises (2008, 2009, 2010, 2012, and 2017) to investigate hydrothermal activity in the NE Lau Basin. This work has produced a list of 25 hydrothermal sites in the authoritative InterRidge database[1], but that list is not comprehensive, contains no specific water column information about individual sites, and is based almost exclusively on meeting abstracts and cruise reports. To describe NE Lau Basin sites more fully, we first present optical, temperature, and oxidation-reduction potential (ORP) hydrothermal plume data that identify 43 sites that were active when discovered, including 11 sites where time series data spanning 4–12 years are available. These data allow us to infer discharge as either high- (discrete) or low- (diffuse) temperature. We then describe how the distribution of active sites on volcanic edifices and spreading ridges is related to the apparent sources of magma at the local convergent and divergent plate boundaries. Finally, we compare F_s at different ridge spreading rates in the NE Lau Basin to that of faster-spreading ridges in the southern Lau Basin, and to a global set of mid-ocean ridges available from the InterRidge database.

[1]http://vents-data.interridge.org/

GEOLOGIC SETTING

Spreading Ridges

Sleeper and Martinez (2016) derive southern MTJ and FRSC spreading rates decreasing from 30 mm/year at 15.67°S to ultraslow rates (8–14 mm/year) south of ∼17.17°S. Their analysis further implies that rates on MTJ and NELSC increase steadily northward from 32 mm/year at 15.7°S to 42 mm/year at 15.2°S (J. D. Sleeper, University of Hawaii, personal communication). Morphological changes follow this spreading rate trend (Sleeper et al., 2016). Near 15.2°S, the NELSC is a high-standing ridge ∼6 km wide with an elevation approaching 600 m (**Figure 2**). On the southern segment, the axial profile narrows and elevation increases to ∼1000 m at the bathymetric high (15.385°S), which is bookended by prominent volcanic cones (Maka and Tafu). An ongoing eruption at the bathymetric high was serendipitously discovered in November 2008 (Baker et al., 2011; Baumberger et al., in review). The morphology of the NELSC is similar to that of the southern Eastern Lau Spreading Center (ELSC; a section of the ELSC also known as the Valu Fa Ridge (VFR)] and the southern Mariana back-arc spreading center, both slow-spreading ridges that are close (<70 km) to an active arc and have enhanced hydrothermal activity relative to their spreading rates (30–50 mm/year) (Martinez et al., 2006; Baker et al., 2017).

The MTJ lies only 30 km west of the NELSC but contrasts sharply in morphology. It includes three spreading centers in a ridge-ridge-ridge triple junction (**Figure 3**; Hawkins, 1995). The northern limb is considerably wider (∼15–18 km) than the NELSC, with a broad (∼12 km) axial high split by a narrow axial cleft in the north and a narrow (∼3 km) axial high in the south. The southern limb includes two off-set segments with deep, flat, ∼5 km-wide floors bounded by faults (Sleeper et al., 2016). The western limb is similar but narrower.

The FRSC overlaps the MTJ, beginning as a ∼10 km-wide axial valley with discontinuous axial ridges (**Figure 3**). As the spreading rate decreases to <∼14 mm/year near 17.1°S, the axial valley widens (∼15–20 km) and large volcanic peaks replace axial ridges (Sleeper et al., 2016). The extremely rugged bathymetry of the FRSC complicates the inference of source locations from plume observations. Large volcanic cones are prominent on the FRSC south of ∼16.6°S, notably at 16.67°S, 17.11°S, 17.54°S, and 17.78°S (**Figure 3**). These volcanoes have reliefs of 1200–2000 m.

Non-ridge Volcanoes

Niua (aka Volcano "P") is the northern-most volcano of the Tofua arc and the only submarine arc volcano bordering the NE

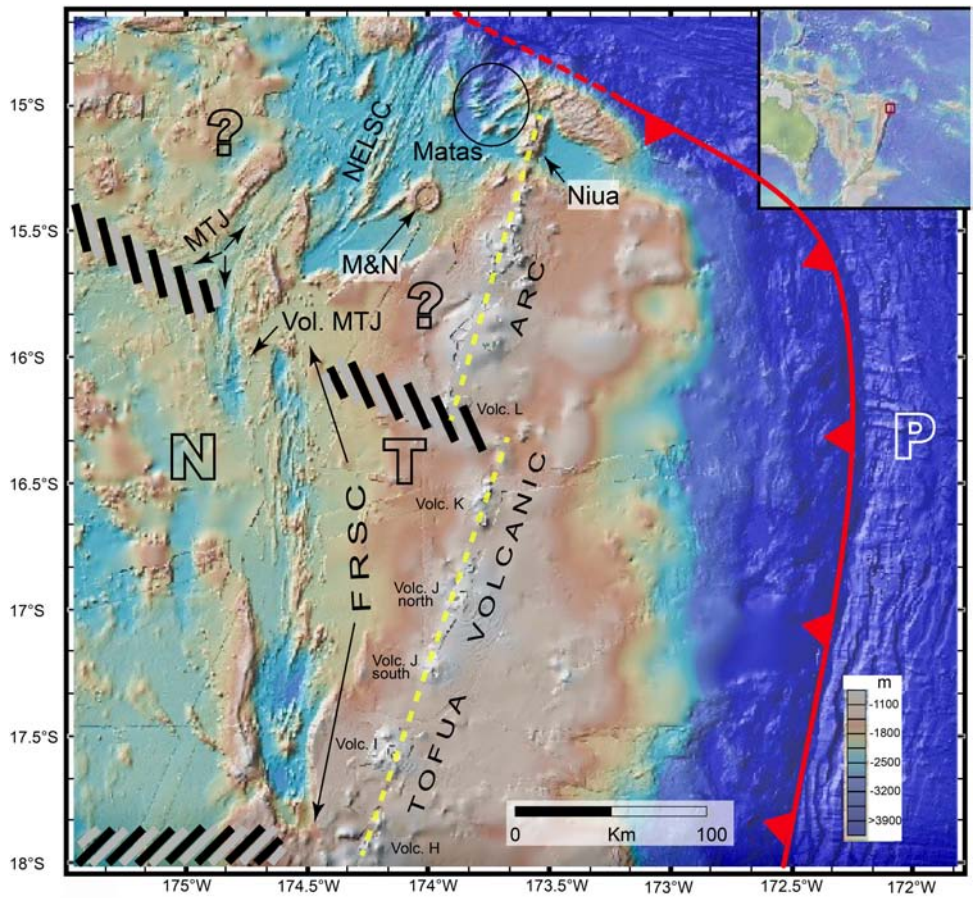

FIGURE 1 | Hydrothermally active areas of the NE Lau Basin. Spreading centers along the Mangatolou Triple Junction (MTJ) and the Fonualei Rift and Spreading Center (FRSC), separate the Tonga (T) and Niuafo'ou (N) plates. The southern N-T boundary is a diffuse boundary or a deformation zone, (right-tilting gray and black bars) (Sleeper and Martinez, 2016). The NE Lau Spreading Center (NELSC) is within an area where plate boundaries (north of the left-tilting gray and black bars) between N&T and more northerly plates (?) are undetermined (Conder and Wiens, 2011). Niua volcano is on the Tofua arc, whereas the nine Mata volcanoes, Motutahi (M), Niuatahi (N) and MTJ are intra-plate volcanoes. Other known but apparently inactive submarine Tofua arc volcanoes (H–L) are also labeled. The NE Lau Basin is constrained on the north by the subduction boundary between the T and Pacific (P) plates (solid red line) that becomes a subducting plate tear (dashed red line) after turning westward. Figure made with GeoMapApp (www.geomapapp.org).

Lau Basin confirmed hydrothermally active (Arculus, 2004). The Niua edifice is elongated N-S with shallow (700 m) and deep (1200 m) cones (**Figure 4**).

Niuatahi (aka "Volcano O") is a 15-km-diameter caldera just east of the NELSC (**Figure 2**; Kim et al., 2009). Ongoing E-W extension of the caldera is indicated by short gaps in the wall north and south of the cone, and by ridges that extend outward from those gaps. The central cone, Motutahi, reaches a depth of ∼1300 m, and a deeper volcanic edifice to the southeast summits at ∼1500 m.

The nine Mata volcanoes form an *en echelon* crescent path lying 12–30 km west of the Tofua arc (**Figure 4**; Resing et al., 2011b; Rubin and Embley, 2012). The northern seven are smaller (900–1300 m elevation) and deeper (summit depths of 1900–2400 m) than the southern W and E Mata (1400–1700 m relief, summit depths of 1200–1330 m). All nine are elongated in a roughly WSW-ENE orientation, evidently controlled by smaller crustal tears linked to the major crustal tear fault where the N-S Tongan subduction trend changes to E-W strike-slip motion (Govers and Wortel, 2005; Embley et al., 2009). Resing et al. (2011a) confirmed a boninite lava eruption on W Mata lasting at least from 2008 to 2010. They suggested that hydrothermal activity on the Matas may be stimulated by the upwelling of high-temperature mantle (Wiens et al., 2006) and/or the hot Samoan mantle plume passing through a tear in the Pacific plate into the NE Lau Basin (Falloon et al., 2007). Lupton et al. (2015) recently offered a different interpretation, using plots of $C/^3He$ versus $^3He/^4He$ for NE Lau Basin rock and fluid samples that clearly define fields of ridge and arc influence. Those data place all the intra-plate volcanos (including Niuatahi) clearly in the arc field with Niua (Lupton et al., 2015). This interpretation supports a powerful magmatic influence from the superfast [convergence as much as ∼240 mm/year (Bevis et al., 1995)] Tonga subduction zone.

Surprisingly, in 2012 we found another hydrothermally active, apparently intra-plate, volcano just 6 km east of the eastern wall

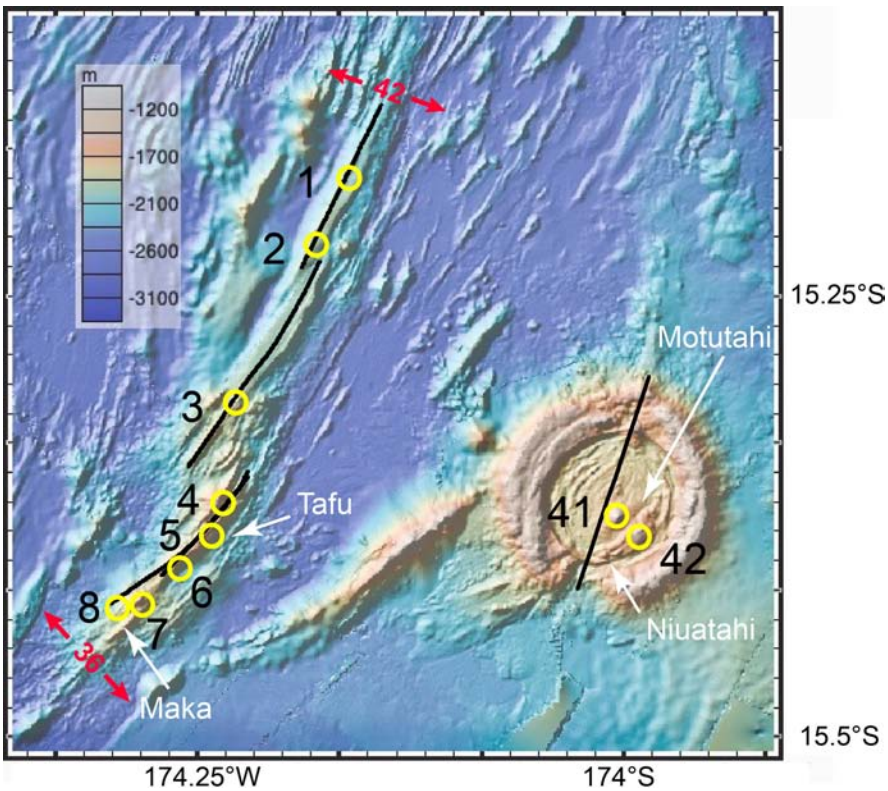

FIGURE 2 | Survey tow lines (black) and active hydrothermal sites (yellow circles) of the NELSC and the Niuatahi volcano (within which is the Motutahi volcanic cone). Numbers correspond to sites in **Tables 1**, **2**. Red arrows indicate full rate spreading values (mm/year). Figure made with GeoMapApp (www.geomapapp.org).

of the southern limb of the MTJ spreading ridge but >100 km distant from any other intra-plate or arc volcano (**Figure 1**). Referred to here as "Volcano MTJ," it features a ∼100-m-deep, ∼500-m-diameter crater at a summit depth of 1200 m. This volcano is a glaring contrast to the apparently low magma budget of the southern MTJ. Its location due east of site 17 in the MTJ may be a coincidence or an indication of a common magma source. A profile over a deeper volcanic structure east of site 16 showed no indication of hydrothermal activity.

MATERIALS AND METHODS

Instrumentation

Most hydrothermal plumes were mapped by means of vertical casts and tow-yos using a *SeaBird 911plus* conductivity-temperature-depth (CTD) package with light back-scattering (*Seapoint* turbidity) and chemical (PMEL ORP) sensors. Eighty percent of the plume data used here (**Tables 1**, **2**) was collected using tow-yos, which create two-dimensional plume images (e.g., Baker et al., 2017). Some data were acquired using only PMEL Miniature Autonomous Plume Recorders, self-contained packages with light back-scattering, ORP (in some cases), and pressure sensors (e.g., German et al., 2006). The light back-scattering and ORP sensors were identical to those used on the CTD.

The light back-scattering sensor [measuring non-dimensional Nephelometric Turbidity Units (NTU; American Public Health Association [APHA], 1985)] detects particle-rich discharge, generally at source temperatures >200°C, containing precipitated metals or sulfur-rich minerals that create plumes extending kilometers from their source. The notation ΔNTU indicates the NTU value (0–5 V range on the sensor) above the local ambient water. Continual plume mixing and particle sedimentation strongly affects instantaneous ΔNTU values of any plume.

We calculate the hydrothermal temperature anomaly ($\Delta\theta$) in a neutrally buoyant plume from the expression $\Delta\theta = \theta - (m_1 + m_2\sigma_\theta + m_3\sigma_\theta^2)$, where θ is potential temperature, σ_θ is potential density, and m_1, m_2, and m_3 are constants in a linear or polynomial regression between θ and σ_θ in hydrothermally unaffected water around the plume (Lupton et al., 1985). We multiply the calculated $\Delta\theta$ values by 3.4 based on the local θ-salinity gradient and assuming the vent fluid salinity is close to the salinity of ambient seawater (McDuff, 1995; Baker et al., 2011). Vent fluid salinities higher than seawater would lower the correction factor by about half, but vent salinities lower than ∼20 PSU would increase the correction by a factor of 10 or more.

The ORP sensor responds within a 1 s sampling interval to the presence of nanomolar concentrations of reduced hydrothermal chemicals (e.g., Fe^{+2}, HS^-, H_2) from vents of any temperature (Walker et al., 2007; Resing et al., 2009; Baker et al., 2016).

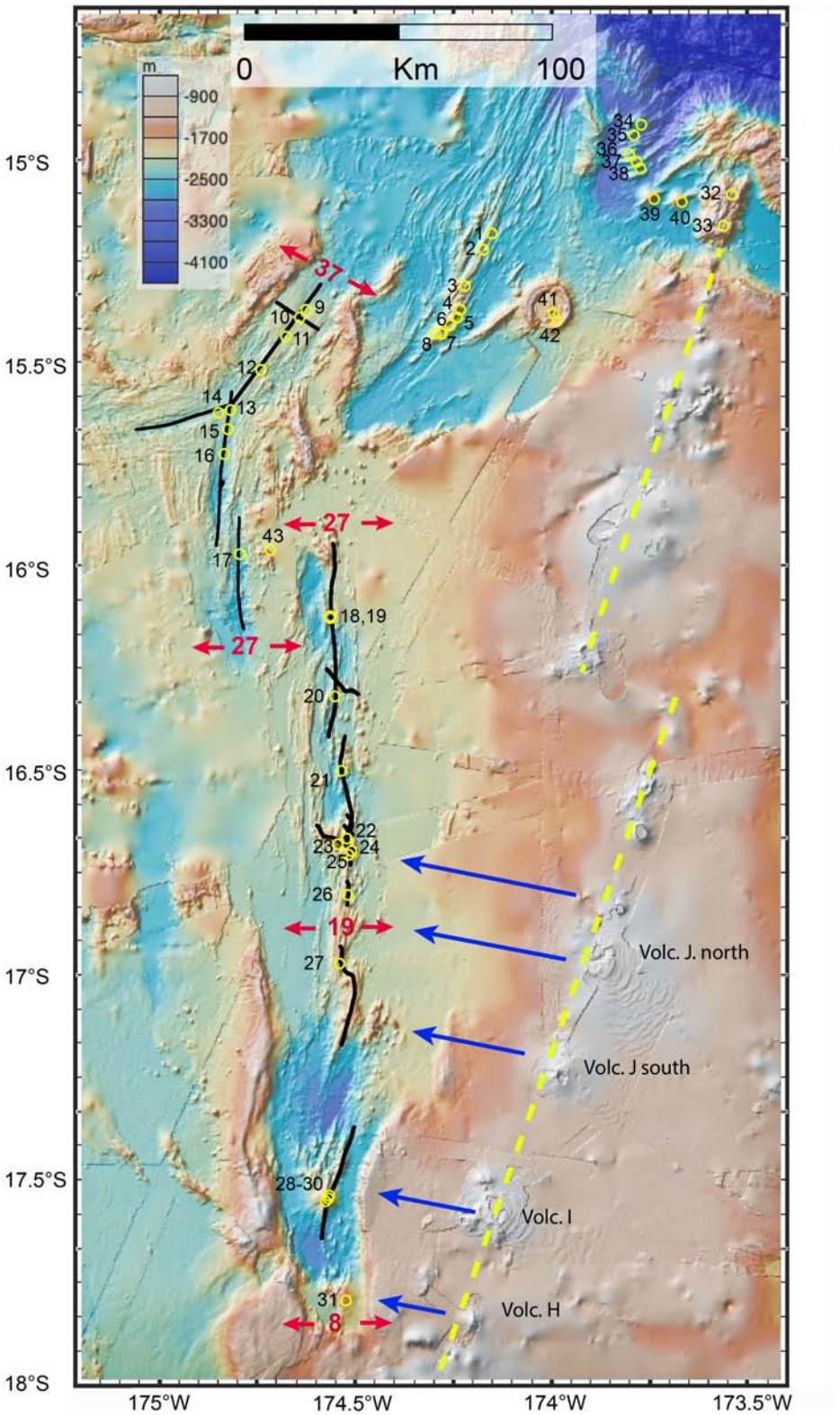

FIGURE 3 | Survey tow lines (black) and active hydrothermal sites (yellow circles) of the MTJ and the FRSC. Numbers correspond to sites in **Table 1**. This figure also includes all the known active sites in the NE Lau Basin (**Tables 1**, **2**). Red arrows indicate full rate spreading values (mm/year). Tofua arc strike follows the dashed yellow line. Blue arrows, aligned in the direction of the Pacific slab flow line, indicate correspondence between arc and FRSC volcanoes within 70 km of the Tofua arc (Sleeper et al., 2016). Figure made with GeoMapApp (www.geomapapp.org).

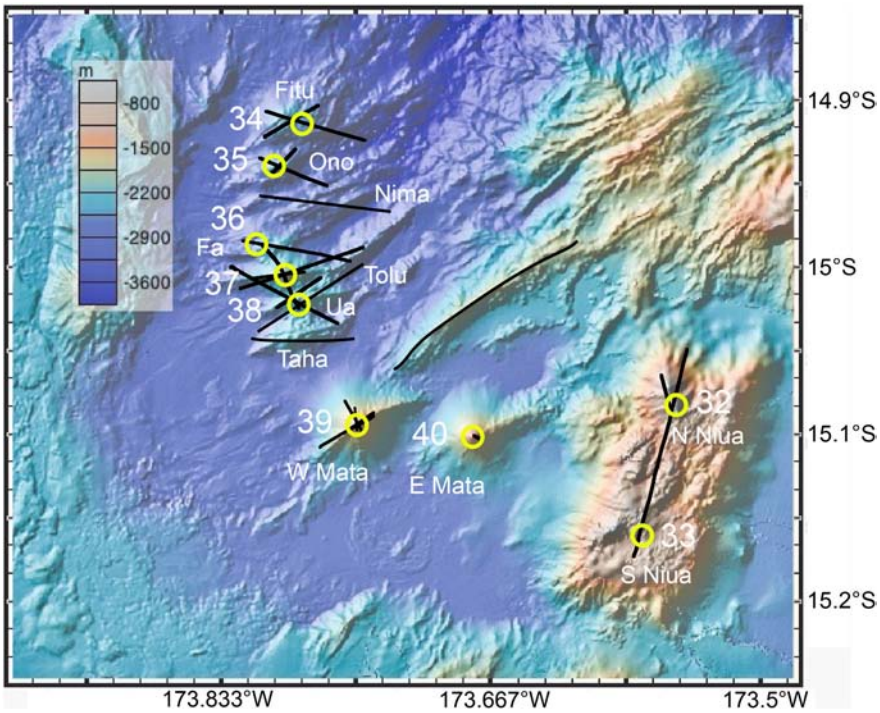

FIGURE 4 | Survey tow lines (black) and active hydrothermal sites (yellow circles) of the Matas and Niua. Numbers correspond to sites in **Table 2**. Figure made with GeoMapApp (www.geomapapp.org).

Because these chemicals rapidly oxidize, biotically or abiotically, close (∼1 km) to their seafloor source (Baker et al., 2016), an ORP response provides a far more precise indication of source location than does ΔNTU or Δθ. The magnitude of an ORP anomaly (ΔE, mV) is calculated as the difference between the value prior to entering a plume and the most negative value reached before the values begin steadily increasing again (a more intense signal has a greater negative value), or by a negative time rate of change in E as the sensor encounters a plume (dE/dt). The absolute value of E varies among individual ORP sensors, but ΔE and dE/dt values are comparable (Walker et al., 2007; Baker et al., 2016). We consider values of $\Delta E > 2$ mV to be diagnostic of a plume (Baker et al., 2017), but even values as low as 1 mV, when correlated with ΔNTU or Δθ, can be reliably hydrothermal.

Inferring Vent Fluid Temperatures

We use plume data to infer whether sites were high-temperature ("black smokers" and associated low-temperature discharge) or low-temperature only (diffuse flow) sites. Of the 43 identified sites, remotely operated vehicles (ROVs) have visited only 13 (11 on discrete volcanoes). All but two dives measured high-temperature (>250°C) fluids or made observations consistent with such discharge (e.g., "black smoke," sulfur particles). Of the remaining 29 sites, we classified some as high-temperature based on a single measurement type, but most required a combination of criteria to assign them as high- or low-temperature. We emphasize that these are inferred classifications that may change as a site ages or when direct observations are eventually made.

To make this decision, we use three criteria, listed here in order of importance: (1) Plume rise: high-temperature discharge typically rises >∼150 m (subject to the local vertical gradient of σ_θ) and creates a roughly vertically symmetrical plume profile with a pronounced maximum in tracer values. Sites with multiple sources or strong current effects (which bend plumes and depress rise height) can display multiple maxima at different depths. Because the precise location and depth of many inferred sources remains uncertain, especially at low spreading rates where axial valleys are wide and bathymetry rugged, plume rise can be difficult to estimate accurately. (2) ΔNTU value: high-temperature discharge produces copious particles and higher ΔNTU (very roughly >∼0.02), but values decrease as the plume dilutes and particles are removed. Conversely, a low ΔNTU coupled with high ΔE is characteristic of low-temperature discharge. (3) Δθ values: The Δθ value of low-temperature sources dilutes rapidly, so measurable values, especially when significantly correlated with ΔNTU, argue for a high-temperature source. Values for these criteria for each site (where data permits) are given in **Tables 1**, **2**.

Data Sources

In addition to the cited papers and abstracts, extensive background information on work in the NE Lau Basin can be found in published cruise reports, which are not specifically referenced in the text. These include the following years: 2008[2],

[2]https://www.pmel.noaa.gov/eoi/laubasin/documents/tn227-nelau-report-final.pdf

TABLE 1 | Characteristics of plumes from NE Lau Basin spreading ridges.

Site	ID[a]	Rate (mm/year)	Long.	Lat.	Max ΔNTU	Max ΔE (mV)	Max Δθ (°C)	Max plume rise (m)	Vent type[b]	Plume depths (m)	Presumed seafloor depth (m)
1	T08C12	42	−174.159	−15.180	0.006	1	0.040	130	1	1970–2000	2100
2	T08C12	39	−174.179	−15.218	0.008	25	0.110	120	1	1880–1920	2000
3	T08C11	38	−174.226	−15.308	0.08	10	0.060	200	1	1770–1900	1980
4	Tafu, 2017	37	−174.238	−15.365					2*		1423
5	T08C18	36	−174.245	−15.384	0.02	72	0.440	30	1	1630–1650	1670
5	T09C01	36	−174.245	−15.384	0.006	1	0.030	ND	2*	1550–1650	1670
6	T08C18	36	−174.263	−15.403	0.064	137	0.120	40	1	1760–1780	1800
6	T08C09	36	−174.263	−15.403	0.07	17	0.140	100	1	1700–1740	1800
7	T08C09	36	−174.300	−15.425	0.13	3	0.020	250	1	1830–1920	
8	Maka, 2008	36	−174.285	−15.423	0.13	200	0.130	250	1*	1300–1500	1580
8	Maka, 2009	36	−174.285	−15.423	0.086	120	ND	200	1*	1370–1560	1580
9	T08C05	37	−174.627	−15.365	0.019	1	ND	150	1	2150	2250
10	T08C05	37	−174.643	−15.385	0.02	48	0.040	130	1	2000–2100	2170
11	T08C05	35	−174.678	−15.431	0.022	5	0.030	300	1	1950–2150	2250
12	T08C05	34	−174.741	−15.513	0.009	2	0.065	200	1	1900–2050	2100
13	T08C04	32	−174.820	−15.610	0.038	0	0.016	200	1	2050–2150	2250
14	T08C04	32	−174.849	−15.619	0.009	0	0.006	70	2	2200–2250	2300
15	T08C03	32	−174.825	−15.657	0.024	0	0.015	200	1	2050–2100	2280
16	T08C03	32	−174.834	−15.719	0.013	0	ND	300	1	2100–2200	2400
17	V08C02	29	−174.796	−15.963	0.008	3	ND	120	2	2300–2400	2400
18	14b, 2008	27	−174.568	−16.115	0.03	12	ND	200	1	2000–2200	2250
19	14b, 2008	27	−174.568	−16.120	0.008	10	ND	ND	2	1800–1840	2250
20	14b, 2008	25	−174.555	−16.311	0.015	40	0.025	350	1	2000–2200	2380
21	MAPR, 2004	23	−174.539	−16.491	0.036	0	ND	ND	1	1650–1820	2300
22	11-CT2, 2008	21	−174.525	−16.657	0.48	60	0.330	250	1	1550–1700	1800
23	11b, 2008	21	−174.548	−16.670		2	ND	ND	2	1080–1100	1800
24	11b, 2008	21	−174.514	−16.689	0.01	3	ND	400	1	1350–1450	1800
25	11a-1, 2008	21	−174.521	−16.697	0.018	6	ND	150	2	1250–1300	1400
26	11a-3, 2008	20	−174.523	−16.795	0.01	0	0.050	250	1	1550–1700	1800–2000
27	11a-2, 2008	18	−174.543	−16.963	0.094	15	0.076	250	1	1450–1650	1750
28	12a, 2008	11	−174.569	−17.530	0.015	7	0.090	80	1*	1480–1540	1620
29	12a, 2008	11	−174.571	−17.537	0.004	12	ND	ND	2	1150–1300	950
30	ROV, 2012	11	−174.577	−17.543					1*		950
31	T12A-01	8	−174.526	−17.785	0.002	18	ND	30	2	480	500

*[a]Operation type: For NELSC and MTJ (sites 1–17), "T08/V08" = year of tow or cast, followed by operation designator "C12." For FRSC (sites 18–31), different nomenclature giving operation name and year (except site 31). [b]Type 1 = high temperature, Type 2 = low temperature. *Visually confirmed. ND = value not determinable, empty cell = no data.*

2009[3], 2010[4], 2012[5], and 2017[6]. Vertical profiles of the plume tracers ΔNTU, Δθ, and Δ*E*, along with plots of ΔNTU/Δθ, at each site location where available, and the corresponding data sets, are available in the **Supplementary Materials**.

[3]https://www.pmel.noaa.gov/eoi/laubasin/documents/tn234-NELRC-CruiseReport-final.pdf and http://mnf.csiro.au/~{}/media/Files/Voyage-plans-and-summaries/Southern-Surveyor/Voyage%20plans-summaries/2009/VOYAGE%20SUMMARY%20SS02-09.ashx

[4]https://www.pmel.noaa.gov/eoi/laubasin/documents/2010-LauBasin-KM1008-cruise-report.pdf

[5]https://www.pmel.noaa.gov/eoi/laubasin/documents/SRoF12-cruisereport-final.pdf

[6]https://www.pmel.noaa.gov/eoi/laubasin/documents/FK171110-CruiseReport-with-logs.pdf

RESULTS

Spreading Ridges

Plumes over the NELSC were first surveyed by German et al. (2006) and Kim et al. (2009), and those data identified sites 4, 5, 7, and 8 (**Figure 2**). Comprehensive CTD tows in 2008 (Baker et al., 2011) surveyed 15°–15.47°S and identified four additional high-temperature sites (1–3, 6). Sites 5 and 6 likely became high-temperature during the eruption that preceded our 2008 survey by only days; by 2009 both sites had degraded to low-temperature. Tafu (site 4) may be episodically active: a 2004 vertical cast detected no plume (German et al., 2006), a 2006 tow mapped a plume at least 3 km long apparently emanating from Tafu (Kim et al., 2009), 2008 surveys found no plume

TABLE 2 | Characteristics of plumes from NE Lau Basin non-ridge volcanoes.

Site	Volcanoes	Cast/Tow[a]	Long.	Lat.	Max ΔNTU	Max ΔE (mV)	Max Δθ (°C)	Max plume rise (m)	Vent type[b]	Plume depths (m)	Presumed seafloor depth (m)
32	N Niua	T08C14	−173.553	−15.083	4.9	151	ND	150	1	600–750	1375
32	N Niua	T12A10	−173.556	−15.083	5	233	ND	100	1*	600–750	1375
33	S Niua	T08C14	−173.574	−15.161	0.32	124	0.18	100	1	1000–1100	1100
33	S Niua	V12A06	−173.565	−15.174	0.013	59	ND	100	1*	1000–1100	1100
34	Fitu	T10B04	−173.782	−14.914	0.31	41	0.15	170	1	2400–2500	2585–2627
34	Fitu	T12A09	−173.786	−14.911	0.052	13	0.035	200	1*	2350–2550	2585–2627
34	Fitu	V17B06	−173.788	−15.017	0.03	120	0.11	220	1*	2400–2560	2750
35	Ono	T10B03	−173.799	−14.939	0.2	22	0.05	300	1	2300–2500	2400–2600
35	Ono	T12A07	−173.795	−14.938	0.065	88	0.05	150	1	2300–2500	2400–2600
36	Fa	T10B05	−173.81	−14.986	0.07	52	0.07	150	1	2400–2500	2400–2600
37	Tolu	T10B02	−173.793	−15.005	0.029	97	0.06	150	1	1750–1850	1840
37	Tolu	T12A02	−173.793	−15.005	0.032	95	0.05	200	1*	1750–1900	1840
37	Tolu	T17B03	−173.793	−15.005	0.016	10	0.025	120	1*	1780–1820	1900
38	Ua	T10B13	−173.784	−15.022	0.3	110	0.11	200	1	2100–2300	2200–2400
38	Ua	T12A05	−173.787	−15.017	0.114	92	0.06	300	1*	2050–2350	2200–2400
38	Ua	T17B03	−173.785	−15.025	0.2	85	0.09	300	1*	2080–2330	2200–2401
39	W Mata	T08C17	−173.748	−15.095	5	300	0.4	150	1	1000–1150	1200
39	W Mata	V09C01	−173.748	−15.095	2	150	0.24	70	1*	1070–1130	1200
39	W Mata	V10B03	−173.748	−15.095	3.5	130	1.5	250	1	900–1180	1200
39	W Mata	T12A03	−173.749	−15.094	0.25	3.2	0.17	65	1*	1190–1210	1200
39	W Mata	T17B01	−173.75	−15.093	0.07	57	0.07	150	1*	1050–1150	1200
40	E Mata	V08C24	−173.678	−15.101	0.002	122	ND	50	2	1240–1280	1350
40	E Mata	V10B05	−173.678	−15.101	0.008	70	ND	30	2	1280–1320	1350
40	E Mata	T12A06	−173.676	−15.102	0.014	28	ND	60	2	1250–1350	1350
40	E Mata	V17B11	−173.678	−15.102	0.1	76	0.05	110	2	1175–1280	1300
41	Motutahi	T08C15	−174.003	−15.376	0.25	180	0.062	100	1	1171	1250
41	Motutahi	V10B11	−174.003	−15.376	5	254	0.33	100	1	1140–1220	1250
41	Motutahi	V12A02	−174.003	−15.376	0.55	132	0.065	80	1*	1200	1250
41	Motutahi	V17B02	−174.003	−15.376	1.4	150	0.13	200	1	1050–1150	1250
42	Niuatahi	T08C15	−174.017	−15.391	0.17	5	0.02	200	1	1450–1700	1875
43	MTJ	V12A04	−174.711	−15.954	0.046	41	0.126	135	1	1200–1330	1330

*[a]Operation type: "T08/V08" = year of tow or cast, followed by operation designator "C14." [b]Type 1 = high temperature, Type 2 = low temperature. *Visually confirmed. ND = value not determinable.*

(Baker et al., 2011), and a 2017 ROV dive found 5°C fluids. Plumes above Maka (site 8) indicated high-temperature discharge in 2004 (German et al., 2006), 2006 (Kim et al., 2009), 2008 (Baker et al., 2011), and 2009. Nautilus Minerals Inc., made the first visual confirmation of high-temperature Maka fluids (∼315°C) in 2008 (Baker et al., 2011). All NELSC sites were located by ΔE anomalies or ROV observations.

Six of the nine MTJ sites are on its northern limb or near the triple junction (**Figure 3**). Sites 9–12 on the northern limb occur along the strike of the narrow axial cleft of a broad axial high; sites 10–12 show multiple plume maxima distributed 100–200 m vertically that imply high-temperature sites at a variety of buoyancy fluxes. Based on low rise heights and weak ΔNTU and Δθ values (**Table 1**), sites 14 and 17 appear to be low-temperature discharge. ΔE values were measurable at sites 9–12, and 17.

Conductivity-temperature-depth tows along the FRSC first occurred in 2009 (Crowhurst et al., 2009). Fifteen sites occupy three morphological regions: near prominent axial ridges (north of 16.67°S), near an axial ridge or off-axis discrete volcano (16.67–17.03°S), or associated with large arc-like volcanoes where an axial ridge is negligible (south of 17.03°S) (**Figure 3**). This morphological trend follows the spreading rate decline from 27 to 8 mm/year (Sleeper et al., 2016). Sites in the slowest-spreading portion of the ridge tend to cluster near volcanoes: four (22–25) around an axial volcano at 16.67°S, three (28–30) around an isolated volcano at 17.54°S, and one (31) on an isolated volcano at 17.78°S. We judge four of these sites as high-temperature discharge, and at each volcano we observed a plume (or seafloor venting) at a depth corresponding to the summit depth. A hydrothermally diagnostic ΔE value was observed at 11 of the 14 sites.

Non-ridge Volcanoes

All the active Mata volcanoes except E Mata create plumes with ΔNTU, Δθ, and ΔE characteristic of high-temperature discharge. ROV dives subsequently confirmed high-temperature discharge

at all sites except Fa and E Mata. Plume values at the north Mata volcanoes, first observed in 2010, have remained relatively stable at those volcanoes where plume mapping occurred again in 2012 and 2017. W and E Mata have a lengthier time series: 2008, 2009 (W only), 2010, 2012, and 2017. E Mata has been conspicuously stable, except for higher ΔNTU and the first detectable Δθ in 2017. Unlike other Mata volcanoes, plume values at W Mata have varied substantially over the 9 year observation period. Intense plumes in 2008 evidenced eruptive activity, which was confirmed by ROV in 2009 (Resing et al., 2011b; Baumberger et al., 2014). A sharp reduction in eruption gasses (^{3}He, H_2; Baumberger et al., 2014) in 2010 and 2012, and in plume ΔNTU, Δθ, and Δ*E*, signaled reduced volcanic activity. Plume tracers reached their lowest values in 2017, although the plume rise height was unusually high (150 m).

Arculus (2004) first reported strong hydrothermal plumes above Motutahi, and recovered possible eruption residue such as sulfide-rich material and native S. In 2006, Kim et al. (2009) also mapped strong particle plumes from Motutahi. Our data from 2008, 2010, 2012, and 2017 (**Table 2**) consistently shows two primary plume levels, with peaks <1200 and >1200 m, attesting to long-lasting differences in source buoyancy fluxes. ΔNTU values have been consistently high, and in 2010 exceeded the sensor range of 5 NTU. Plumes elsewhere that consistently reach 5 ΔNTU have contained exceedingly high concentrations of particulate S (>18,000 nM) (Resing et al., 2011a). Kim et al. (2009) also identified a deeper, active volcanic edifice within Niuatahi, southeast of Motutahi, which we confirmed in 2008. Unpublished results from a recent R.V. Sonne expedition (K. Haase, Chief Scientist) indicate other minor venting areas, typical of a large caldera volcano.

In both 2008 and 2012, ΔNTU plume values at N Niua reached the sensor maximum of 5 V (**Table 2**), again suggestive of a vigorous, S-rich hydrothermal system. The S Niua cone was also active both years, although the single vertical cast in 2012 found ΔNTU values an order of magnitude less than in 2008.

The plume within the crater of MTJ displayed high anomalies in all plume tracers, perhaps because of the constraining geometry of the ∼100-m-deep crater at its summit.

DISCUSSION

Site Distribution and Apparent Magma Sources

The most intense plume anomalies overwhelmingly occurred over the summits or flanks of discrete volcanoes, wherever their location. Volcanoes accounted for 11 of the top 12 ΔNTU values, 9 of the top 11 Δθ values, and the top 10 Δ*E* values (**Tables 1**, **2** and **Figures 5**–**7**). These statistics describe an uncommonly active group of ridge, arc, and intra-plate discrete volcanoes in the NE Lau Basin. Of the 20 prominent volcanoes, only three (the FRSC at 17.11°S and Mata volcanoes Nima and Taha) lacked evidence of hydrothermal activity. High-temperature discharge, confirmed by ROV observation (9 sites) or plume characteristics (5 sites), occurred on all active volcanoes except for E Mata, Tahu, and the southernmost FRSC cone. Even more remarkable, plume data indicated an erupting W Mata in 2008, 2009 (when confirmed by ROV), and 2010, and uncommonly intense venting (ΔNTU > 5) at Motutahi in 2010 and N Niua in 2008/2012. And surprisingly, MTJ is adjacent to an apparently low-magmatic-budget spreading ridge but >100 km distant from any other intra-plate or arc volcano.

Although the Mariana, Kermadec, and Izu–Bonin subduction zones feature cross-arc chains of intra-plate volcanoes (Wright et al., 1996; Stern et al., 2003, 2006, 2013), those of the NE Lau Basin may be unique (Rubin and Embley, 2012). They follow no linear trace, present a diversity ranging from small cones to a sizeable caldera, and display near unanimous hydrothermal activity. Possible magma sources supporting this high overall activity include magma captured from the Tofua arc due to increased melting driven by slab-derived hydration of mantle wedge (Martinez and Taylor, 2002; Lupton et al., 2015), and magma leakage through deep crustal tears of the subducting Pacific plate (Govers and Wortel, 2005; Falloon et al., 2007).

Compared to the discrete volcanoes, plume anomalies are more varied on NE Lau ridges, where the site distribution appears influenced by both ridge and arc magma sources. Globally, lengthy sections of ridge crest spreading at 20–40 mm/year occur almost exclusively along the Mid-Atlantic and Central Indian Ridges, where deep axial valleys dominate. The NELSC and the FRSC (north of ∼17.17°S), however, feature prominent axial ridges, similar to other slow-spreading back-arc ridges close (<∼70 km) to an active arc. Examples include the southern Mariana and VFR, where the capture of arc magma facilitates the creation of axial ridges (Martinez et al., 2006; Stern et al., 2013; Brounce et al., 2016).

Even though the NELSC lies within ∼70 km of the Tofua arc (**Figure 1**), C/^{3}He—^{3}He/^{4}He data indicate that both the ridge and Maka volcano (site 8) are mid-ocean ridge basalt (Lupton et al., 2015). However, trace element data from NELSC basalts also suggest the presence of an enriched mantle source similar to basalts from the Samoan hotspot (Rubin et al., 2009; Lupton et al., 2015), testifying to a multiplicity of magma sources in the rapidly evolving NE Lau Basin.

Axial ridges are also present on the FRSC between 16° and 17.17°S, increasing in sharpness and relief progressing south, indicative of an increasing contribution of slab-derived melts as the axis nears the arc (Sleeper et al., 2016). The effect of magma supply is expressed differently in the southern half of the FRSC, where ultra-slow spreading focuses magma to point sources (Sleeper et al., 2016) and creates hydrothermally active discrete volcanoes. FRSC isotope data [C/^{3}He and ^{3}He/^{4}He (Lupton et al., 2015)] from five rock samples and one vent fluid fall between ridge and arc characteristics, suggesting at least a minor arc influence as interpreted by Sleeper et al. (2016). This influence is also implied by the observation that the FRSC volcanoes lie on the slab flow lines corresponding to prominent Tofua arc volcanoes (**Figure 3**).

The MTJ is a stark contrast to the NELSC and FRSC. Pronounced axial ridges are absent, suggesting a present-day magma budget lower than the NELSC or FRSC, perhaps a consequence of a location more distant (∼100 km) from the supply of Tofua arc magma (Baker et al., 2017). The southern and

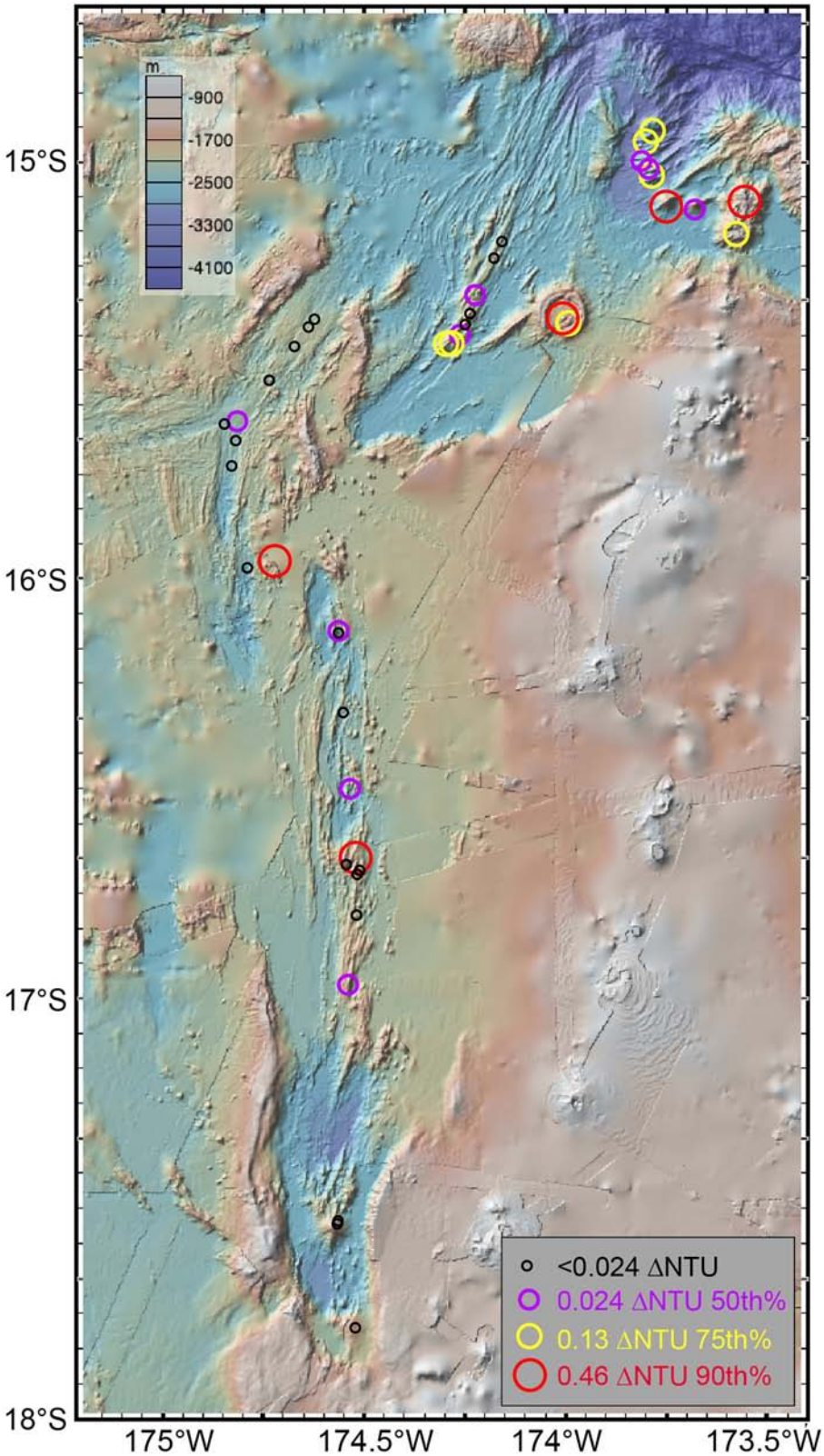

FIGURE 5 | Distribution of maximum ΔNTU at each site: ≥90th percentile (red), ≥70th–90th percentile (yellow), ≥50th–70th percentile (lavender), <50th percentile (black). Values given in **Tables 1**, **2**. Figure made with GeoMapApp (www.geomapapp.org).

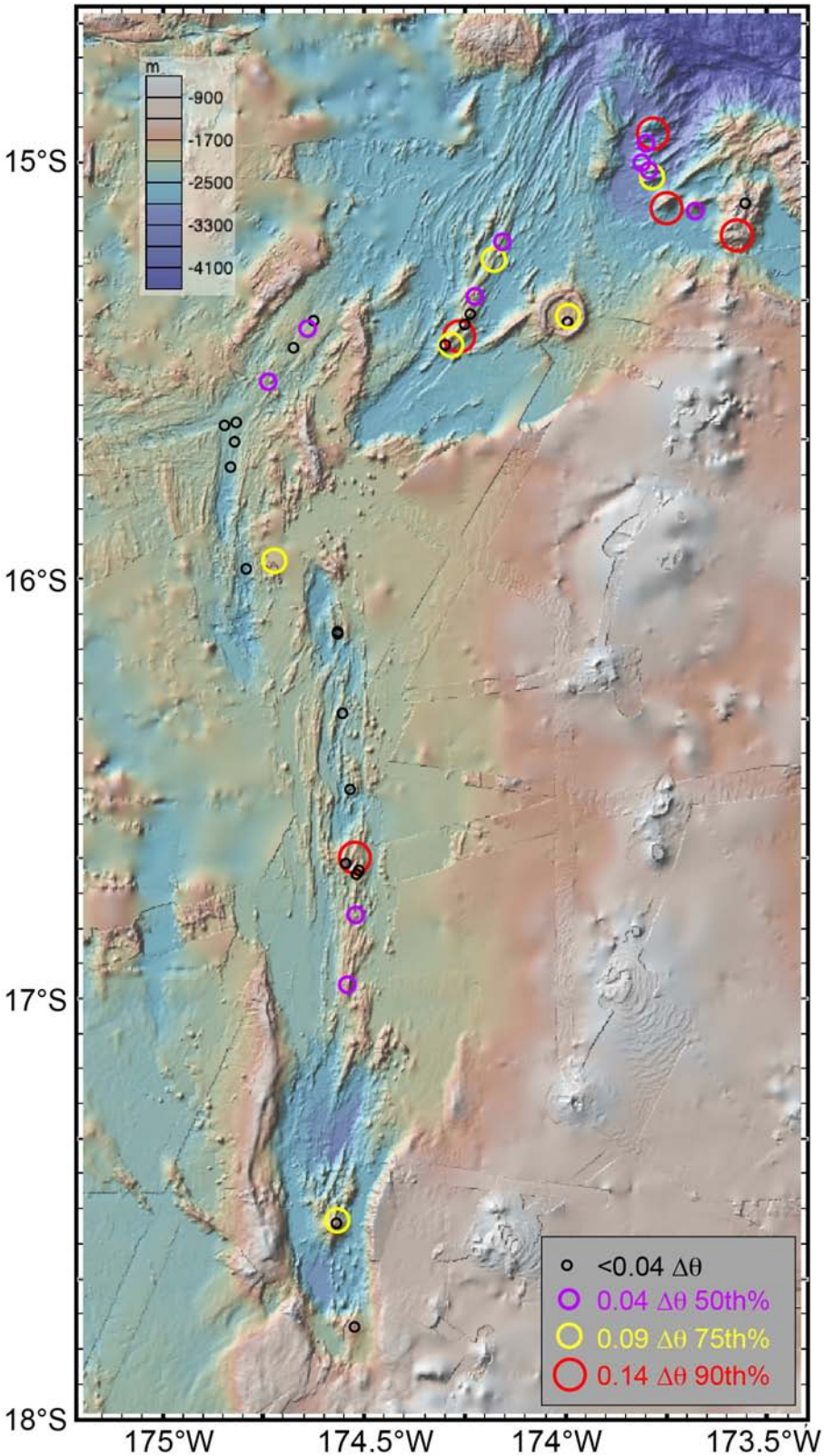

FIGURE 6 | Distribution of maximum Δθ (°C) at each site: ≥90th percentile (red), ≥70th–90th percentile (yellow), ≥50th–70th percentile (lavender), <50th percentile (black). Values given in **Tables 1**, **2**. Figure made with GeoMapApp (www.geomapapp.org).

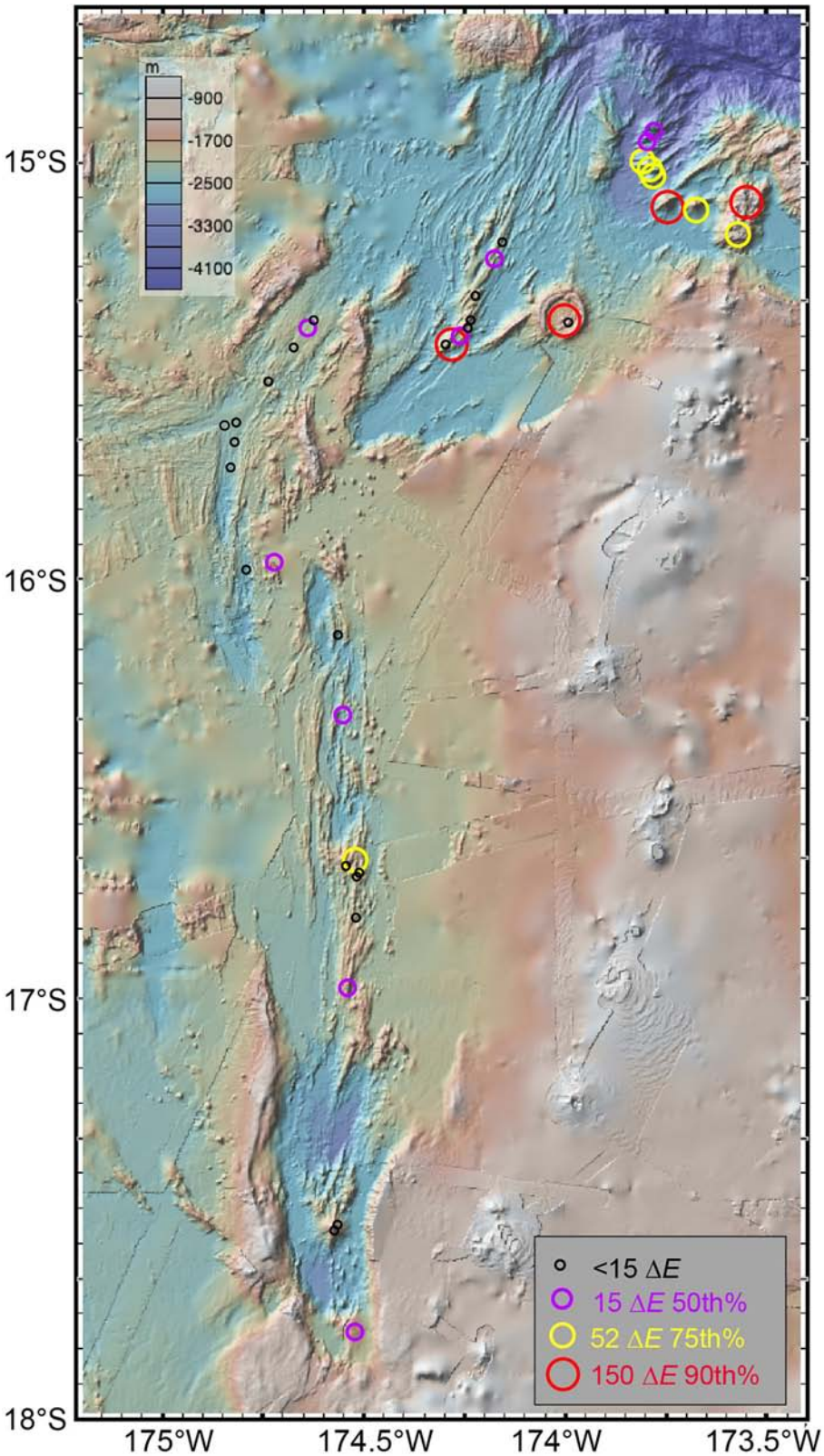

FIGURE 7 | Distribution of maximum Δ*E* (mV)at each site: ≥90th percentile (red), ≥70th–90th percentile (yellow), ≥50th–70th percentile (lavender), <50th percentile (black). Values given in **Tables 1**, **2**. Figure made with GeoMapApp (www.geomapapp.org).

western arms feature deep, flat valleys and no plume anomalies above the 50th percentile. The most robust plumes were found along the cleft of the broad, low-relief axial high of the northern arm. The origin of Volcano MTJ is thus enigmatic.

Site Distribution and Ridge Spreading Rates

The boundaries of the Tonga plate have been explored extensively for hydrothermal activity over the last 20 years. At present counting, the VFR/ELSC ridge segments (19°–24°S) host 95 active sites (Baker et al., 2016) and the Kermadec/Tofua arc (21.1°–36.45°S) adds 33 active volcanic centers containing 44 active sites, totaling ∼20% of the 650 globally known submarine vent sites [http://vents-data.interridge.org/, updated from Beaulieu et al. (2015)]. Our data add 31 ridge and 12 arc/intra-plate volcano sites, 17 of which are not currently in the InterRidge database.

The number of known active sites on any spreading ridge depends not only on the local magmatic budget (proxies include spreading rate on long time scales (∼100 Kyr) and bathymetric characteristics (e.g., axial ridges) on shorter time scales) but also on the effectiveness of exploration techniques. Roughly 80% of global sites have been discovered using water-column profiles, generally spaced at intervals of ∼10 km or wider along axis (Baker, 2017). This approach is cost-effective but inadequate. Most of the remaining sites have been discovered by two-dimensional surveys using towed instruments, primarily employing real-time turbidity and temperature sensors. This approach is far more effective, but can easily overlook low-temperature sites emitting plumes deficient in turbidity and temperature but rich in reduced chemicals (e.g., "Lost City" on the Mid-Atlantic Ridge; Larson et al., 2015). Only a few ridge sections have benefited from towed surveys that include an ORP sensor sensitive to low-temperature emissions. These sections uniformly show higher F_s values than other ridge sections with comparable spreading rates but conventional exploration efforts, including those previously surveyed (Baker et al., 2016; Baker, 2017).

Our detailed exploration methods support two conclusions from Sleeper and Martinez (2016) and Sleeper et al. (2016): spreading rates on the Niuafo'ou/Tonga border are much lower than proposed by Zellmer and Taylor (2001), and magma delivery becomes sharply focused into large axial volcanoes at FRSC spreading rates <14 mm/year. F_s values along ridge segments in the NE Lau Basin steadily increase as the spreading rate increases northward from 8 to 42 mm/year, but remain lower than on the faster-spreading VFR/ELSC (**Figure 8**). The relatively low F_s on the NE Lau Basin ridges is consistent with lower spreading rates calculated by Sleeper and Martinez (2016). And on the slowest-spreading section of the FRSC (south of 17°S), the presumed sites of volcano construction by focusing of arc magma are the only sites where we found hydrothermal activity.

Notably, the F_s trend along NE Lau Basin ridges follows that calculated from the VFR/ELSC ridge (Baker et al., 2017), where spreading rates (u_s) range from 40 to 90 mm/year. The F_s/u_s least-squares regression slope for the entire suite of hydrothermally surveyed Lau ridges (0.29) is ∼10× greater than for a global suite of 26 mid-ocean ridge sections (0.025) from Beaulieu et al. (2015) (**Figure 8**). Much of this difference is a function of improved exploration, as described above, but the entire Lau region appears hydrothermally enhanced even compared to other well-explored ridge sections with similar spreading rates (Baker, 2017). F_s values in the 40–60 mm/year range are more than twice that measured along the Galapagos Ridge using the same exploration techniques. And in the 80–90 mm/year range, Lau F_s values are comparable to those observed on well-explored fast- to superfast-spreading ridges (100–140 mm/year).

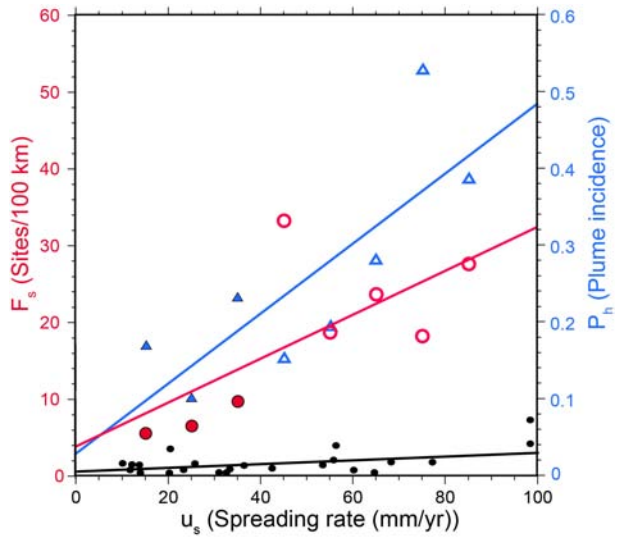

FIGURE 8 | Spreading rate (u_s) versus relative hydrothermal activity (F_s, red circles; p_h, blue triangles) in the Lau Basin (in 10 mm/year u_s bins), and for a selection of 26 mid-ocean ridge sections (black circles) (mean u_s for each section). Back-arc ridges in the NE Lau Basin (this paper) shown as solid red and blue symbols, VFR/ELSC ridge (Martinez et al., 2006) shown as open red and blue symbols. Ridge data (Beaulieu et al., 2015) are F_s only. Corresponding regression equations (solid lines) are: Lau F_s: $F_s = 3.7 + 0.29u_s$, $r = 0.69$; Lau p_h: $p_h = 2.7 + 0.46u_s$, $r = 0.80$; Mid-ocean ridge F_s: $F_s = 0.61 + 0.025u_s$, $r = 0.77$.

Note that the F_s value for Lau Basin trend at u_s = 40–50 mm/year (the southern VFR) is almost double the predicted value (**Figure 8**). We suggest that this anomalous point, which is closer (<50 km) to the Tofua arc than any in the Lau Basin (except for the ultra-slow southern segments of the FRSC, where arc magma supply is differently expressed), is a consequence of heightened magma capture from the arc (Martinez and Taylor, 2002). A similar effect is also apparent on nearest-arc sections of the Mariana and Manus backarcs (Baker et al., 2017).

Interestingly, this anomaly does not appear when using the simpler hydrothermal index of plume incidence (p_h), the fraction of ridge crest overlain by a ΔNTU plume (Baker and Hammond, 1992). This difference arises because p_h is based on ΔNTU alone, and 43% of active sites in the 40–50 mm/year VFR section are ΔE only, with no ΔNTU signature (Baker et al., 2016).

Trends of spreading rate versus hydrothermal activity along Lau Basin ridges are similar whether using F_s or p_h. A strong linear relationship results from either index, although here F_s gives a lower correlation (r = 0.69 versus r = 0.80) because the 40–50 mm/year VFR section is not anomalous in the p_h data. This consistency between F_s and p_h trends, based on ∼850 km of well-explored and spreading-rate-variable ridge crests in the Lau Basin, validates 25 years of using p_h as an approximate predictor of apparent magma budget.

CONCLUSION

The NE Lau Basin, bounded by a series of back-arc spreading ridges and the Tofua arc, is a product of the fastest subducting plate boundary on Earth. A compilation of water-column data from 10 cruises over 16 years describes an area of extraordinary hydrothermal activity. Optical, thermal, and chemical sensors identified discharge plumes from 43 active sites, distributed among back-arc ridges (31), the Tofua arc (2), and intra-plate volcanic edifices (10). At least 32 of the sites appear to be high-temperature (emitting precipitated mineral particles), two of which were sampled during seafloor eruptions. When combined with existing data from ridges farther south (VFR and ELSC), the spatial density of active sites (sites/100 km of ridge crest) along all Lau Basin back-arc spreading ridges was a robust (r = 0.69) linear function of ridge spreading rate, extending across a spreading rate range of 8–90 mm/year. The Lau Basin site density versus spreading rate trend is an order of magnitude higher than currently recognized for mid-ocean ridges generally. This enhancement is likely the result, primarily, of meticulous exploration along Lau Basin ridges, and, secondarily, of a regional magmatic budget augmented by superfast Kermadec-Tonga subduction rates.

DATA AVAILABILITY

All datasets generated for this study are included in the manuscript and/or the **Supplementary Files**.

AUTHOR CONTRIBUTIONS

SW processed and controlled the quality of the data. EB provided the original text, figures, and tables, with contributions and insights from SW, GM, and JR. All authors collected the data at sea.

FUNDING

This work was supported by the NOAA/PMEL Earth-Ocean Interactions Program, the Joint Institute for the Study of the Atmosphere and Ocean (JISAO) under the NOAA Cooperative Agreements NA11OAR4320091 and NA10OAR4320148, the NOAA Office of Exploration and Research, the National Science Foundation (OCE0930025, OCE0934660, and OCE15-38121), the Schmidt Ocean Institute (FK171110), and the Nautilus Minerals Inc. NOAA/PMEL covered salary and publication costs for SW. NOAA/PMEL and JISAO covered salary and publication costs for EB and JR. There are no specific grant numbers associated with the NOAA funds. The NOAA Office of Exploration and Research, the National Science Foundation, and the Schmidt Ocean Institute funded at-sea costs for various cruises that collected data used in this manuscript.

ACKNOWLEDGMENTS

We thank the numerous colleagues who worked with us on the many cruises dedicated to exploring the NE Lau Basin, especially to other Chief Scientists R. Embley, W. Chadwick, J. Lupton, and K. Rubin. We thank Nautilus Minerals Inc., for access to proprietary data. The reviewers CW and JS provided insightful and useful comments. PMEL contribution number 4913.

SUPPLEMENTARY MATERIAL

The Supplementary Material for this article can be found online at: https://www.frontiersin.org/articles/10.3389/fmars.2019.00382/full#supplementary-material

REFERENCES

American Public Health Association [APHA] (1985). *Standard Methods for the Examination of Water and Wastewater*. Washington D.C: A.P.H.A.

Arculus, R. J. (2004). *Voyage Summary SS11/2004*. Canberra: CSIRO.

Baker, E. T. (2017). Exploring the ocean for hydrothermal venting: new techniques, new discoveries, new insights. *Ore. Geol. Rev.* 86, 55–69. doi: 10.1016/j.oregeorev.2017.02.006

Baker, E. T., German, C. R., and Elderfield, H. (1995). "Hydrothermal plumes over spreading-center axes: Global distributions and geological inferences," in *Seafloor Hydrothermal Systems: Physical, Chemical, Biological, and Geological Interactions, Geophys. Monogr. Ser*, Vol. 91, eds S. Humphris, R. Zierenberg, L. S. Mullineaux, and R. Thomson (Washington D.C: AGU).

Baker, E. T., and Hammond, S. R. (1992). Hydrothermal venting and the apparent magmatic budget of the Juan de Fuca Ridge. *J. Geophys. Res.* 97, 3443–3456. doi: 10.1029/91jb02671

Baker, E. T., Lupton, J. E., Resing, J. A., Baumberger, T., Lilley, M., Walker, S. L., et al. (2011). Unique event plumes from a 2008 eruption on the Northeast Lau Spreading Center. *Geochem. Geophys. Geosyst.* 12:Q0AF02. doi: 10.1029/2011GC003725

Baker, E. T., Resing, J. A., Haymon, R. M., Tunnicliffe, V., Lavelle, W., Martinez, F., et al. (2016). How many vent fields? New estimates of vent field populations on ocean ridges from precise mapping of hydrothermal discharge locations. *Earth Planet. Sci. Lett.* 449, 186–196. doi: 10.1016/j.epsl.2016.05.031

Baker, E. T., Walker, S. L., Resing, J. A., Chadwick, W. W., Merle, S. G., Anderson, M. O., et al. (2017). The effect of arc proximity on hydrothermal activity along spreading centers: New evidence from the Mariana back arc (12.78N–18.38N). *Geochem. Geophys. Geosyst.* 18, 4211–4228. doi: 10.1002/2017GC007234

Baumberger, T., Lilley, M. D., Resing, J. A., Lupton, J. E., Baker, E. T., Butterfield, D. A., et al. (2014). Understanding a submarine eruption through time series hydrothermal plume sampling of dissolved and particulate constituents: West Mata, 2008–2012. *Geochem. Geophys. Geosyst.* 15, 4631–4650. doi: 10.1002/2014GC005460

Beaulieu, S. E., Baker, E. T., and German, C. R. (2015). Where are the undiscovered hydrothermal vents on oceanic spreading ridges? *Deep Sea Res. Part II* 121, 202–212. doi: 10.1016/j.dsr2.2015.05.001

Bevis, M., Taylor, F. W., Schutz, B. E., Recy, J., Isacks, B. L., Helu, S., et al. (1995). Geodetic observations of very rapid convergence and back-arc extension at the Tonga arc. *Nature* 374, 249–251. doi: 10.1038/374249a0

Bird, P. (2003). An updated digital model of plate boundaries. *Geochem. Geophys. Geosyst.* 4:1027. doi: 10.1029/2001GC000252

Brounce, M., Kelley, K. A., Stern, R., Martinez, F., and Cottrell, E. (2016). The Fina Nagu volcanic complex: Unusual submarine arc volcanism in the rapidly deforming southern Mariana margin. *Geochem. Geophys. Geosyst.* 17, 4078–4091. doi: 10.1002/2016GC006457

Conder, J. A., and Wiens, D. A. (2011). Shallow seismicity and tectonics of the central and northern Lau Basin. *Earth Planet. Sci. Lett.* 304, 538–546. doi: 10.1016/j.epsl.2011.02.032

Crowhurst, P. V., Arculus, R. J., Massoth, G. J., Baptista, L., Stevenson, I., Angus, R., et al. (2009). "Discovery of New Hydrothermal Venting Sites in the Lau Basin, Tonga Back Arc," in *Proceedings of the American Geophysical Union, Fall Meeting 2009*, Washington, DC.

Embley, R. W., Merle, S. G., Lupton, J. E., Resing, J., Baker, E. T., Lilley, M. D., et al. (2009). "Extensive and Diverse Submarine Volcanism and Hydrothermal Activity in the NE Lau Basin," in *Proceedings of the American Geophysical Union, Fall Meeting 2009*, Washington, DC.

Falloon, T. J., Danyushevsky, L. V., Crawford, T. J., Maas, R., Woodhead, J. D., Eggins, S. M., et al. (2007). Multiple mantle plume components involved in the petrogenesis of subduction-related lavas from the northern termination of the Tonga Arc and northern Lau Basin: evidence from the geochemistry of arc and backarc submarine volcanics. *Geochem. Geophys. Geosyst.* 8:Q09003. doi: 10.1029/2007GC001619

German, C. R., Baker, E. T., Connelly, D. P., Lupton, J. E., Resing, J., Prien, R. D., et al. (2006). Hydrothermal exploration of the Fonualei Rift and Spreading Center and the Northeast Lau Spreading Center. *Geochem. Geophys. Geosyst.* 7:Q11022. doi: 10.1029/2006GC001324

Govers, R., and Wortel, M. J. R. (2005). Lithosphere tearing at STEP faults: response to edges of subduction zones. *Earth Planet. Sci. Lett.* 236, 505–523. doi: 10.1016/j.epsl.2005.03.022

Hawkins, J. W. (1995). "The Geology of the Lau Basin," in *Backarc Basins - Tectonics and Magmatism*, ed. T. Brian (New York, NY: Plenum Press), 63–138. doi: 10.1007/978-1-4615-1843-3_3

Kim, J., Son, S. K., Son, J. W., Kim, K. H., Shim, W. J., Kim, C. H., et al. (2009). Venting sites along the Fonualei and Northeast Lau Spreading Centers and evidence of hydrothermal activity at an off-axis caldera in the northeastern Lau Basin. *Geochem. J.* 43, 1–13. doi: 10.2343/geochemj.0.0164

Larson, B. I., Lang, S. Q., Lilley, M. D., Olson, E. J., Lupton, J. E., Nakamura, K., et al. (2015). Stealth export of hydrogen and methane from a low temperature serpentinization system. *Deep-Sea Res. Part II* 121, 233–245. doi: 10.1016/j.dsr2.2015.05.007

Lupton, J., Rubin, K. H., Arculus, R., Lilley, M., Butterfield, D., Resing, J., et al. (2015). Helium isotope, C/3He, and Ba-Nb-Ti signatures in the northern Lau Basin: distinguishing arc, back-arc, and hotspot affinities. *Geochem. Geophys. Geosyst.* 16, 1133–1155. doi: 10.1002/2014GC005625

Lupton, J. E., Delaney, J. R., Johnson, H. P., and Tivey, M. K. (1985). Entrainment and vertical transport of deep-ocean water by buoyant hydrothermal plumes. *Nature* 316, 621–623. doi: 10.1038/316621a0

Martinez, F., and Taylor, B. (2002). Mantle wedge control on back-arc crustal accretion. *Nature* 416:417. doi: 10.1038/416417a

Martinez, F., Taylor, B., Baker, E. T., Resing, J. A., and Walker, S. L. (2006). Opposing trends in crustal thickness and spreading rate along the back-arc Eastern Lau Spreading Center: implications for controls on ridge morphology, faulting, and hydrothermal activity. *Earth Planet. Sci. Lett.* 245, 655–672. doi: 10.1016/j.epsl.2006.03.049

McDuff, R. E. (1995). "Physical dynamics of deep-sea hydrothermal plumes," in *Seafloor Hydrothermal Systems: Physical, Chemical, Biological, and Geological Interactions, Geophysical Monograph Series*, Vol. 91, eds S. Humphris, et al. (Washington, DC: American Geophysical Union), 357–368. doi: 10.1029/gm091p0357

Resing, J. A., Baker, E. T., Lupton, J. E., Walker, S. L., Butterfield, D. A., Massoth, G. J., et al. (2009). Chemistry of hydrothermal plumes above submarine volcanoes of the Mariana Arc. *Geochem. Geophys. Geosyst.* 10:Q02009. doi: 10.1029/2008GC002141

Resing, J. A., Baker, E. T., Lupton, J. E., Lilley, M. D., Rubin, K. H., and Buck, N. J. (2011a). *The Chemistry of Hydrothermal Venting at a Volcano "O", a Large Submarine Volcano in the NE Lau Basin. Abstract V53D-2652 Presented at 2011 Fall Meeting*. San Francisco, CA: AGU.

Resing, J. A., Rubin, K. H., Embley, R. W., Lupton, J. E., Baker, E. T., Dziak, R. P., et al. (2011b). Active submarine eruption of boninite in the northeastern Lau Basin. *Nat. Geosci.* 4:799. doi: 10.1038/ngeo1275

Rubin, K. H., and Embley, R. W. (2012). Identification and implications of a submarine monogenetic field in the NE Lau Basin. *Abstract V44C-08 Presented at 2012 Fall Meeting*, AGU, San Francisco, CA.

Rubin, K. H., Embley, R. W., Clague, D. A., Resing, J. A., Michael, P. J., Keller, N. S., et al. (2009). Lavas from active boninite and very recent basalt eruptions at two submarine NE Lau Basin sites. *EOS. Trans. Am. Geophys. Un. Fall Meeting Suppl. Abstr.* 90, V431–05.

Sleeper, J. D., and Martinez, F. (2016). Geology and kinematics of the Niuafo'ou microplate in the northern Lau Basin. *J. Geophys. Res. Solid Earth* 121, 4852–4875. doi: 10.1002/2016JB013051

Sleeper, J. D., Martinez, F., and Arculus, R. (2016). The Fonualei Rift and spreading center: effects of ultraslow spreading and arc proximity on axial morphology. *J. Geophys. Res. Solid Earth* 121, 4814–4835. doi: 10.1002/2016JB013050

Stern, R. J., Fouch, M. J., and Klemperer, S. L. (2003). "An over- view of the Izu-Bonin-Mariana subduction factory," in *Inside the Subduction Factory, Geophys. Monogr. Ser*, Vol. 138, ed. J. Eiler (Washington, D. C: AGU), 175–222. doi: 10.1029/138gm10

Stern, R. J., Kohut, E., Bloomer, S. H., Leybourne, M., Fouch, M., and Vervoort, J. (2006). Subduction factory processes beneath the Guguan cross-chain, Mariana Arc: no role for sediments, are serpentinites important? *Cont. Mineral. Petrol.* 151, 202–221. doi: 10.1007/s00410-005-0055-2

Stern, R. J., Tamura, Y., Masuda, H., Fryer, P., Martinez, F., Ishizuka, O., et al. (2013). How the Mariana Volcanic Arc ends in the south. *Island Arc.* 22, 133–148. doi: 10.1111/iar.12008

Walker, S. L., Baker, E. T., Resing, J. A., Nakamura, K., and McLain, P. D. (2007). "A new tool for detecting hydrothermal plumes: An ORP Sensor for the PMEL MAPR," in *Proceedings of the American Geophysical Union, Fall Meeting 2007*, (Washington, DC: AGU).

Wiens, D. A., Kelley, K. A., and Plank, T. (2006). Mantle temperature variations beneath back-arc spreading centers inferred from seismology, petrology, and bathymetry. *Earth Planet. Sci. Lett.* 248, 30–42. doi: 10.1016/j.epsl.2006.04.011

Wright, I. C., Parson, L. M., and Gamble, J. A. (1996). Evolution and interaction of migrating cross-arc volcanism and backarc rifting: An example from the southern Havre Trough (35 20'–37 S). *J. Geophys. Res.* 101, 22071–22086. doi: 10.1029/96jb01761

Zellmer, K. E., and Taylor, B. (2001). A three-plate kinematic model for Lau Basin opening. *Geochem. Geophys. Geosyst.* 2:GC000106.

Conflict of Interest Statement: GM was funded by Nautilus Minerals Inc., for the at-sea collection of data and has no present connection with the company.

The remaining authors declare that the research was conducted in the absence of any commercial or financial relationships that could be construed as a potential conflict of interest.

Copyright © 2019 Baker, Walker, Massoth and Resing. This is an open-access article distributed under the terms of the Creative Commons Attribution License (CC BY). The use, distribution or reproduction in other forums is permitted, provided the original author(s) and the copyright owner(s) are credited and that the original publication in this journal is cited, in accordance with accepted academic practice. No use, distribution or reproduction is permitted which does not comply with these terms.

frontiers in Marine Science

ORIGINAL RESEARCH
published: 10 July 2019
doi: 10.3389/fmars.2019.00371

Deep-Sea Carnivorous Sponges From the Mariana Islands

Jon Thomassen Hestetun[1], Hans Tore Rapp[1,2] and Shirley Pomponi[3]*

[1] NORCE Environment, Norwegian Research Centre (NORCE), Bergen, Norway, [2] Department of Biological Sciences, University of Bergen, Bergen, Norway, [3] Harbor Branch Oceanographic Institute, Florida Atlantic University, Fort Pierce, FL, United States

Carnivorous sponges belonging to family Cladorhizidae (Porifera, Demospongiae, Poecilosclerida) are unique within phylum Porifera due to their ability to capture and envelop small prey. While other sponges use an aquiferous system to filter water, the aquiferous system of the cladorhizids is partially reduced or completely absent. Carnivorous sponges can be found worldwide at all depths, but are more common in the deep sea, where oligotrophic conditions containing less suspended particles may favor a carnivorous feeding strategy. Here, we provide formal descriptions of eight cladorhizid sponge species from 1229 to 5813 m depth collected as part of the NOAA 2016 Deepwater Exploration of the Marianas with the NOAA ship *Okeanos Explorer* (EX1605) during the investigation of the bathyal and abyssal seafloor off the Northern Mariana Islands and Guam: the harp sponge *Chondrocladia* (*Symmetrocladia*) *lyra*, *Chondrocladia* (*Chondrocladia*) *coronata* sp. nov., *Lycopodina subtile* sp. nov., *Abyssocladia fryerae* sp. nov., *Abyssocladia kellyae* sp. nov., *Abyssocladia marianensis* sp. nov., *Abyssocladia stegosaurensis* sp. nov., and *Abyssocladia villosa* sp. nov. We also provide a phylogenetic analysis showing the systematic position of the described species. Our results show that the deep-sea seafloor off the Mariana Islands contains a diverse and previously virtually unknown cladorhizid fauna. The examined species display similarities with species from other parts of the Pacific, and add considerably to the available information for the genus *Abyssocladia*. The high number of new species is consistent with other recent publications from the Pacific and Indian Ocean, and shows that despite recent sampling efforts, the cladorhizid fauna of these areas remains very poorly investigated. Additional sampling effort will in all probability yield both additional species and a better understanding of the biogeographical distribution of already known cladorhizids.

Life Science Identifiers (LSIDs):

Abyssocladia fryerae urn:lsid:zoobank.org:act:BD7C52A3-146E-48CC-917F-57D7081245BD.

Abyssocladia kellyae urn:lsid:zoobank.org:act:7174B51E-5145-4907-AA63-D218C66DF5E7.

Abyssocladia marianensis urn:lsid:zoobank.org:act:9761A542-C7F7-4449-BADD-E1F988454969.

Abyssocladia stegosaurensis urn:lsid:zoobank.org:act:02F01ACE-2AC1-406E-8C50-65A5EC97F8C5.

OPEN ACCESS

Edited by:
Diva Amon, Natural History Museum, United Kingdom

Reviewed by:
Dorte Janussen, Senckenberg Museum, Germany
Tina Molodtsova, P.P. Shirshov Institute of Oceanology (RAS), Russia

***Correspondence:**
Jon Thomassen Hestetun
jhes@norceresearch.no; jon.hestetun@gmail.com

Specialty section:
This article was submitted to Deep-Sea Environments and Ecology, a section of the journal Frontiers in Marine Science

Received: 29 March 2019
Accepted: 14 June 2019
Published: 10 July 2019

Citation:
Hestetun JT, Rapp HT and Pomponi S (2019) Deep-Sea Carnivorous Sponges From the Mariana Islands. Front. Mar. Sci. 6:371. doi: 10.3389/fmars.2019.00371

Abyssocladia villosa urn:lsid:zoobank.org:act:DAAA1ED2-5D36-40A3-9A78-55994CDE9702.
Chondrocladia coronata urn:lsid:zoobank.org:act:ED85F7AD-84F8-47EC-88E6-87753AD931C4.
Lycopodium subtile urn:lsid:zoobank.org:act:5F73AA9E-3182-49DD-8DD5-EDE501C33E51.

Keywords: carnivorous sponges, Cladorhizidae, taxonomy, deep sea, Marianas, West Pacific, abyssal, *Abyssocladia*

INTRODUCTION

Carnivorous sponges represent a novel innovation within phylum Porifera. These sponges lack or have a reduced aquiferous system, and instead feed by passively capturing prey items such as larvae or small crustaceans (Vacelet, 2007). Carnivorous sponges are typically erect, with stalked or branching bodies and a large number of thin filaments. Prey items become entangled in the filaments, and are subsequently gradually enveloped and digested by sponge cells migrating to the area of contact (Vacelet and Duport, 2004). Carnivory is typically assumed to be an adaptation to oligotrophic conditions in the deep sea, where traditional filter feeding is less effective (Vacelet, 2007). While these sponges are reasonably common in shallow waters, they constitute a larger and more conspicuous part of the total sponge fauna at greater depths (Hestetun et al., 2017b).

All currently reported carnivorous sponges belong to Cladorhizidae Dendy, 1922, a large poecilosclerid family with nine genera containing more than 175 currently recognized species (Van Soest et al., 2019). The majority of early species descriptions are from the North Atlantic (e.g., Carter, 1874, 1876; Topsent, 1892; Lambe, 1900; Lundbeck, 1905; Topsent, 1909), though a smaller number of older species descriptions also exist for the Pacific (e.g., Ridley and Dendy, 1886; Lévi, 1964; Koltun, 1970).

Over the last 25 years, a number of studies have contributed to significantly expanding the number of described species and the known morphological variation within the family (e.g., Cristobo et al., 2005; Vacelet, 2007; Vacelet and Kelly, 2008; Vacelet et al., 2009; Kelly and Vacelet, 2011; Lopes et al., 2011; Dressler-Allame et al., 2016; Goodwin et al., 2017; Hestetun et al., 2017b; Lundsten et al., 2017). The high number of new species described in these articles highlights that the number and distribution of carnivorous sponges are still poorly known.

The Mariana Islands are a chain of islands, part of the Izu–Bonin–Mariana arc system, a convergent plate boundary formed by the subduction of the western Pacific plate. Parts of the system include the Mariana Trench, the Mariana Arc, and the Mariana Trough, a complex and geologically active area including seafloor at various depths and substrates, vent systems, and the volcanic islands of the Mariana Islands themselves (Stern et al., 2004).

Here, we describe carnivorous sponges collected during the first and third legs of the 2016 Deepwater Exploration of the Marianas (EX1605), a sampling effort in the area around the U.S. territories of Guam and the Commonwealth of the Northern Mariana Islands with the National Oceanic and Atmospheric Administration (NOAA) ship *Okeanos Explorer*. The present study provides descriptions of eight carnivorous sponges, including seven previously undescribed species, and expands the current knowledge of carnivorous sponges in the West Pacific in general, and the genus *Abyssocladia* Lévi, 1964, in particular.

MATERIALS AND METHODS

Collection

While the sampling effort of the EX1605 cruise was conducted throughout the deep-sea areas on both sides of the Mariana Islands, most of the cladorhizid samples were recovered from the Mariana Trench part of the system on the eastern side of the islands during the third leg of the cruise (**Figure 1**). In all, nine carnivorous sponge specimens were collected at seven collection localities. Except for the western Mariana Trough specimen (1229 m), all species were recovered from depths below 3000 m (**Table 1**). Samples were collected with the ROV *Deep Discoverer*. Dives were continuously recorded, meaning HD video was available for *in situ* observation of specimen morphology in all but one species. Expedition data, including ROV video, are available from the NOAA Ocean Exploration and Research (OER) Digital Atlas Portal (National Oceanic and Atmospheric Administration [NOAA], 2019).

Most specimens were preserved in 96% ethanol only, or as several subsamples with different fixation media. Collected specimens were deposited in the U.S. Smithsonian Institution Museum of Natural History (voucher IDs in **Table 1**). Subsamples of some of the specimens were also sent to the Ocean Genome Legacy Center for possible future sequencing; however, molecular work here is based on the Smithsonian samples.

Morphological Examination

Examination of specimens was done at the biodiversity labs of the Department of Biosciences at the University of Bergen, Norway. Specimens were photographed on arrival in Bergen, and subsamples were taken for morphological and molecular analysis.

Spicule slides and scanning electron microscopy (SEM) preparations were made from sponge subsamples according to the method described in Boury-Esnault and Rützler (1997), either directly or by recovering the spicules during DNA extraction. A minimum of 30 measurements were made of each

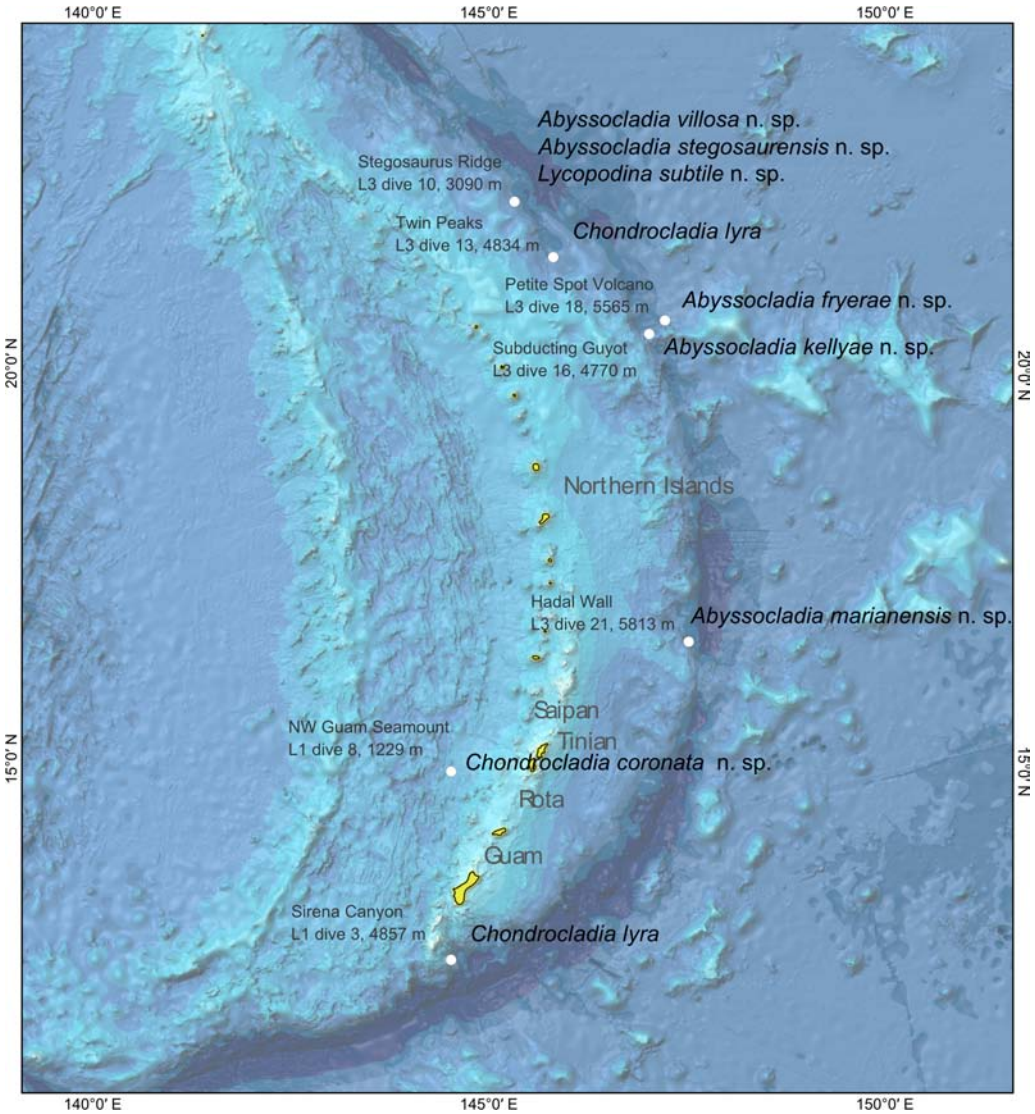

FIGURE 1 | Bathymetric map of the sea floor around the Mariana Islands with collection localities for the species in this study.

TABLE 1 | Collection and voucher information for carnivorous sponge specimens examined in this study.

Species	USNM	Dive	Specimen	Date	Location	N	E	Depth (m)
Abyssocladia								
A. fryerae n. sp.	1424186	L3 dive 18	SPEC03BIO	2016-07-05	Petite Spot Volcano	20.62	147.3	5565
A. kellyae n. sp.	1424180	L3 dive 16	SPEC03GEO_CO1	2016-07-03	Subducting Guyot 1	20.45	147.1	4770
A. marianensis n. sp.	1424192	L3 dive 21	SPEC03BIO	2016-07-08	trench Wall	16.56	147.6	5813
A. stegosaurensis n. sp.	1424164	L3 dive 10	SPEC03BIO_CO2	2016-06-27	Stegosaurus Ridge	22.12	145.4	3090
A. villosa n. sp.	1424162	L3 dive 10	SPEC03BIO	2016-06-27	Stegosaurus Ridge	22.12	145.4	3090
Chondrocladia								
C. (*C.*) *coronata* n. sp.	1424095/1424096	L1 dive 8	SPEC03BIO	2016-04-29	NW Guam Seamount	14.92	144.6	1229
C. (*S.*) *lyra*	1424083	L1 dive 3	SPEC05BIO	2016-04-23	Sirena Canyon	12.54	144.6	4857
C. (*S.*) *lyra*	1424175	L3 dive 13	SPEC01BIO	2016-06-30	Twin Peaks	21.42	145.9	4834
Lycopodina								
L. subtile n. sp.	1424167	L3 dive 10	SPEC03BIO_CO4	2016-06-27	Stegosaurus Ridge	22.12	145.4	3090

spicule type. In the case of diactine megascleres, both length and width (at widest point excluding tyles) were recorded. Measurements in the article are given as minimum and maximum, with average in parenthesis. Spicule terminology follows Boury-Esnault and Rützler (1997), with some additional conventions: fusiform styles are described as mycalostyles *sensu* Hajdu et al. (1994); chelae are described as arcuate or palmate *sensu* Hajdu et al. (1994); the term cleistochela is used for arcuate isochelae with opposite frontal teeth touching or almost touching, while the term abyssochela is used in a more restrictive sense for laterally expanded cleistochelae *sensu* Lopes et al. (2011).

Molecular Methods

Extraction and PCR protocols are identical to Hestetun et al. (2016b): The E.Z.N.A.® Mollusc DNA Kit (Omega Bio-tek) was used, and spicules were removed after initial lysis before adding ethanol. Three partitions were sequenced: partial 28S rRNA, ALG11, and the Folmer and Erpenbeck COI partitions. These partitions were chosen to enable comparison with sequences currently available in GenBank from previous studies, and have been shown to work well for identifying phylogenetic relationships within the Cladorhizidae (e.g., Hestetun et al., 2016b).

The analysis included 102 COI, 75 ALG11, and 91 28S sequences. See **Supplementary Table S1** for accession numbers of all sequences included in the analysis. Accession numbers for new sequences are also listed for each species below. Alignment and concatenated phylogenetic analysis was performed using the same pipeline as in Hestetun et al. (2016b), including Bayesian inference with MrBayes 3.2.2 (GTR+G, 8 chains, $25*10^6$ generations, $5*10^6$ generations burn-in) and maximum likelihood (ML) with RAxML 8.2.10 (GTRGAMMA, 2000 rapid bootstraps).

RESULTS

Taxonomic Index

Phylum Porifera Grant, 1836
Class Demospongiae Sollas, 1885
Subclass Heteroscleromorpha Cárdenas et al., 2012
Order Poecilosclerida Topsent, 1928
Family Cladorhizidae Dendy, 1922
Genus *Abyssocladia* Lévi, 1964
Abyssocladia fryerae n. sp.
Abyssocladia kellyae n. sp.
Abyssocladia marianensis n. sp.
Abyssocladia stegosaurensis n. sp.
Abyssocladia villosa n. sp.
Genus *Chondrocladia* Thomson, 1873
Subgenus *Chondrocladia* Thomson, 1873
Chondrocladia (Chondrocladia) coronata n. sp.
Subgenus *Symmetrocladia* Lee et al., 2012
Chondrocladia (*Symmetrocladia*) *lyra* Lee et al., 2012
Genus *Lycopodina* Lundbeck, 1905
Lycopodina subtile n. sp.

Species Description

Genus *Abyssocladia* Lévi, 1964

Type species

Abyssocladia bruuni Lévi, 1964 (type by monotypy).

Diagnosis

Cladorhizidae most often pedunculate, carrying a disciform or flabelliform body with a radial architecture, in other cases pinnate or branching. Microscleres are a combination of abyssochelae, cleistochelae, arcuate chelae, and/or sigmancistras, but not placochelae (from Hestetun et al., 2016b).

Remarks

The genus *Abyssocladia* contains 26 species in addition to the new species described here (Van Soest et al., 2019). Most species are recorded from the abyssal and deep bathyal Pacific, but some species have also been recorded from shallower areas and from the Indian and Atlantic Oceans.

Abyssocladia fryerae sp. nov.

Type material

R/V *Okeanos Explorer* EX1605L3, ROV *Deep Discoverer*. Holotype: USNM 1424186, dive 18, SPEC03BIO, 2016-07-05, Petite Spot Volcano, 20.62°N, 147.3°E, 5565 m.

Diagnosis

Pedunculate sponge composed of a short stem and a disc-shaped, slightly droplet-formed body with filaments radiating outward in a single plane from the disc margin. Megascleres are subtylostyles 550–1150 μm. Microscleres are arcuate isochelae 75–110 μm and sigmancistras 17–23 μm.

Description

The holotype (**Figures 2A,B**) is a damaged disc-shaped body with a radial skeletal organization, a pair of remaining damaged filaments, and a short piece of the upper stem. ROV images show that the live sponge is stalked and disc-shaped, with filaments radiating from the disc margin at regular intervals, and is connected to the substrate with a short stem. The holotype is 25 mm tall, but the top part of the disc is missing (**Figure 2C**). The stem is 15 mm long and 0.7–0.9 mm wide, and the disc is 12 mm wide. Based on ROV video, intact filaments are approximately 2 cm long. The color of the sponge is white to translucent gray in both live specimen and in ethanol.

Skeleton

The main structural skeleton of the stem is made up of tightly packed subtylostyles and enters the center of the disc-shaped body. The subtylostyles also make up the skeleton of the filaments and the structural skeleton of the soft tissue of the disc.

Spicules

1. Subtylostyles, straight and fusiform, with elongated tyles, 582–1130 (806) μm long and 3.8–23.5 (11.3) μm wide (**Figure 2D**).
2. Arcuate isochelae, with strongly curved shaft and frontal tooth and lateral alae of equal length, around 45% of total length 77.9–110.3 (91.6) μm (**Figure 2E**).
3. Sigmancistras, thick, 17.9–22.9 (20.5) μm (**Figure 2F**).

FIGURE 2 | *Abyssocladia fryerae* n. sp. **(A,B)** *In situ* images from ROV video, **(C)** complete recovered specimen, **(D)** subtylostyle with elongated tyle, **(E)** arcuate isochela, and **(F)** sigmancistra.

GenBank accession numbers

COI, MK922984.

Distribution and habitat

This species is only known from its type locality off the Mariana Islands at the Petite Spot Volcano locality (5565 m) from hard/rocky substrate situated on a small rock.

Etymology

The species is named after Dr. Patricia Fryer, Hawai'i Institute of Geophysics and Planetology, University of Hawai'i at Mānoa, in recognition of >30 years of exploration, discovery, and research on the geology and tectonic evolution of the Mariana forearc. Dr. Fryer was co-science lead on leg 3 of EX1605 and shared in the excitement of discovery and collection of carnivorous sponges from the Mariana Islands.

Remarks

A disc-shaped *Abyssocladia* species closely related to similar Pacific species such as *A. kellyae* n. sp., *A. dominalba* Vacelet, 2006, and *A. lakwollii* Vacelet and Kelly, 2014 (see remarks for *A. kellyae* n. sp., phylogenetic results and **Table 2**). The stem is shorter and the disc larger relative to *A. kellyae* n. sp.

Abyssocladia kellyae sp. nov.

Type material

R/V *Okeanos Explorer* EX1605L3, ROV *Deep Discoverer*. Holotype: USNM 1424180, dive 16, SPEC03GEO_CO1, 2016-07-03, Subducting Guyot 1, 20.45°N, 147.1°E, 4770 m.

Diagnosis

Stalked sponge with a disc-shaped body and filaments radiating in a single plane from the disc margin. Megascleres are mycalostyles 1250–2400 µm, subtylostyles 1000–2000 µm, and tylostyles 270–600 µm. Microscleres are arcuate isochelae 75–135 µm and sigmancistras 21–32 µm.

Description

The holotype (**Figures 3A,B**) is a single stalked sponge with a vertical, flat, disc-shaped body and a solid, flexible stem. The edge of the disc is set with evenly spaced filaments radiating outward in a single plane. The lower stem is widened into a basal

TABLE 2 | Overview of morphological characters and type location for currently known *Abyssocladia* species.

Species	Type locality	Morphology	(Mycalo)styles	Other megascleres	Chelae	Other microscleres
Stalked disc-shaped						
A.carcharias Kelly and Vacelet, 2011	Monowai Seamount, Kermadec Volcanic Arc (25.804°S, 177.175°W, 1071 m)	Stem 7 mm; disc 3.5 mm	510–1070 × 8–19 140–240 × 3–5		CAR: 116–197 CAR: 60–86 CAR: 35–48	CIST: 15–16 CIST: 8–12
A.dominalba Vacelet, 2006	North-Fijian back-arc basin, White Lady (16°59.50′S, 173°55.47′W, 1997 m)		620–2500 × 7–35		ARC: 80–170 AB/CLEI: 40–45 AN: 10–11	CIST: 30–40 CIST: 10–13
A. fryerae sp. nov.	Marianas (20.62°N, 147.3°E, 5565 m)	Total length 25 mm; disc 12 mm	762–1130 × 12–23	SUB: 582–859 × 4–7	ARC: 78–110	CIST: 18–23
A.huitzilopochtli Vacelet, 2006	Middle America Trench (18°17′N, 104°31′W, 3325 m)	Stem 35 mm; disc 7 mm	1050–2500 × 15–30	STR: 560–750 × 21–30	ARC: 67–90 ARC: 40–55 AB: 60–80	CIST: 20–24 CIST: 11–12 ORT: 150–195
A. inflata Vacelet, 2006	East Pacific Rise (24°14.85′S, 115°39.70′W, 3142 m)	Stem 5 mm; disc 3.5 mm	1075–1800 × 21–23	AC.OX: 130–350 × 3–5	ARC: 140–150 AB/CLEI: 80–100	CIST: 15–18
A. kellyae sp. nov.	Marianas (20.45°N, 147.1°E, 4770 m)	Total length 43 mm; disc 7 mm	1262–2321 × 19–32	SUB: 1136–1994 × 20–35 TYL: 275–1200 × 6–15	ARC: 78–132	CIST: 22–32
A. lakwollii Vacelet and Kelly, 2014	Far Eastern Solomon Islands (12°S, 167°E, 1090 m)	Up to 57 mm	750–1800 × 15–31 380–980 × 18–30	STR: 250–1150 × 12–30	ARC: 110–150 ARC: 58–92 ARC/PALM: 27–36 AB/CLEI: 48–70	CIST: 15–21
A. natushimae Ise and Vacelet, 2010	Izu Ogasawara Arc, Southern Japan (32°4.54′N, 139°51.10′E, 862 m)	Oval disc	1350–1940 × 19–27 395–1790 × 10–24	STR: 395–980 × 22–45 STR: 14–250 × 4–10	AB: 38–75	CIST: 20–23 CIST: 9–12
A. polycephalus Hestetun et al., 2016a	Bermuda (33°46′N, 62°36′W, 2829 m)	Several discs on branching stem	720–1040 × 14–22 430–960 × 5–13	STR: 380–780 × 16–22	ARC: 28–50	CIST: 17–31 CIST: 9–11
A. stegosaurensis sp. nov.	Marianas (22.12°N, 145.4°E, 3090 m)	Total length 48 mm; disc 3 mm	846–1741 × 15–53	SUB: 491–1134 × 7–12–17 TYL: 181–573 × 4–7–9	PALM: 20–40	CIST: 6–9
Stalked spherical						
A. claviformis Koltun, 1970	NW Pacific Basin (33°18′N, 149°46′E, 5005–6096 m)	Size 1 mm	600–1600 × 22–50	TYL: 175–850 × 5–11 TYL: 175–650 × 5	ARC: 38–44	CIST: 8–11
A.hemiradiata Hestetun et al., 2017a	Southwest Indian Ridge (37°57.92′S, 050°24.43′E, 1003 m)	Hispid stem	444–1290 × 16–23 508–1166 × 9–17 141–224 × 3–5	TYL: 2000–5000 × 6–12 TYL: 775–1327 × 6–11 TYL: 333–687 × 6–10 TYL: 108–303 × 4–8	ARC: 20–57	SIGM: 11–22 CIST: 5–10
A.oxeata Koltun, 1970	NW Pacific Basin (26°04′N, 153°49′E, 6107–6127 m)	Body diameter 20 mm.	1300–3500 × 16–44	OX: 88–375	ARC/CLEI: 77–105	CIST: 33

(Continued)

TABLE 2 | Continued

Species	Type locality	Morphology	(Mycalo)styles	Other megascleres	Chelae	Other microscleres
A. villosa sp. nov.	Marianas (22.12°N, 145.4°E, 3090 m)	Concave top with filament crown		TYL: 718–1443 × 14–25 TYL: 549–1356 × 7–19 TYL: 154–488 × 4–15	CLEI: 31–90	CIST: 8–12
Stalked umbrella-shaped						
A. bruuni Lévi, 1964	Kermadec Trench (36°07′S, 178°32′W, 5230–5340 m)	Club-like umbrella 13 mm	1300–1650 × 25–28		AB: 70–75	CIST: 29–30
A. marianensis sp. nov.	Marianas (16.56°N, 147.6°E, 5813 m)	Stem 130 mm, body, 14 mm, with crown of long filaments	1824–2458 × 20–39	OX: 289–477 × 4–7	ARC: 68–92	SIGM: 53–59 CIST: 31–46
Branching						
A. diegoramirezensis Lopes et al., 2011	Diego Ramírez islands, South Chile (57°06.70′S, 67°28.73′W, 1753–2056 m)	Opposite filament rows	257–975 × 7–25 287–687 × 3–8	STR: 287–1098 × 13–38	ARC: 50–83 AB: 15–35	CIST: 13–20 SIGM: 10–13
A. koltuni Ereskovsky and Willenz, 2007	Sea of Okhotsk (50°52.3′–50.2′N, 145°07.1′–10.2′E, 500–645 m)	Branches terminate in flattened filament outgrowths	286–398 × 8–10 575–906 × 17–28 474–580 × 11–15		ARC/PALM: 58–83 ARC/PALM: 31–46	SIGM: 35–70 CIST: 11–18
A. leverhulmei Goodwin et al., 2017	Drake Passage (60°36.4′0S, 66°00.29′W, 610–1510 m)	Opposite filament rows	594–846 × 10–28	STR: 78–573 × 11–35	ARC: 47–79 AB: 22–40	SIGM: 8–19
Stem with opposite filament rows						
A. atlantica Lopes and Hajdu, 2014	Campos Basin off Brazil (22°22′S, 39°54′W, 1107–1135 m)		226–903 × 10–33 431–575 × 8–10 226–369 × 10–15	STR: 58–193	CLEI: 23–70	
Abyssocladia corniculiphora Hestetun et al., 2017a	Southwest Indian Ridge (37°56.48′S, 50°26.53′E, 1178–1306 m)	Side branches with terminal swellings	375–722 × 12–22 189–573 × 5–13		CLEI: 23–59 (36)	CIST: 7–12
Abyssocladia faranauti Hestetun et al., 2015	Mid-Atlantic Ridge (15°32′N, 46°33′W, 3578 m)		1020–1640 × 31–55 530–940 × 14–30 280–560 × 8–17 130–270 × 3–8		ARC/PALM: 49–68 PALM/CLEI:22–33	CIST: 6–8
Abyssocladia myojinensis Ise and Vacelet, 2010	Izu Ogasawara Arc, Southern Japan (32°4.54′N, 139°51.06′E, 870 m)	Top portion without filaments	278–1053 × 7–34 605–890 × 11–18		AB: 59–78 AB/CLEI: 28–44	CIST: 5–6
Abyssocladia naudur Vacelet, 2006	E Pacific Rise (17°23.11′S, 113°11.60′W, 2581 m)	40 mm, side branch with terminal swelling	700–1600 × 10–37 330–1000 × 5–15	STR: 30–825 × 8–30	AB/CLEI: 48–72	CIST: 7–10 CIST: 5–8
Abyssocladia tecta Hestetun et al., 2015	Mid-Atlantic Ridge (15°32′N, 46°33′W, 3578 m)		1040–1490 × 20–35 370–860 × 6–17	STR: 45–430 × 8–31	ARC/CLEI: 42–55 AB: 11–14	CIST: 6–8
Abyssocladia umbellata Lopes et al., 2011	Diego Ramírez islands, South Chile (57°04.99′S, 67°31.35′W, 1860–2070 m)		308–564 × 23–45 525–1275 × 5–18	STR: 133–1221 × 20–50	ARC: 75–133 AB: 23–63	CIST: 15–18

(Continued)

TABLE 2 | Continued

Species	Type locality	Morphology	(Mycalo)styles	Other megascleres	Chelae	Other microscleres
Abyssocladia vaceleti Ríos and Cristobo, 2018	Patagonia and Falkland Islands/Malvinas (59.571°S, 46.115°W, 901–1547 m)		212–514 × 6–21	TOR: 601–1385 × 7–19 AC.TYL: 88–99 × 2	ARC: 34–59 AB: 32–44	CIST: 53–59
Stem with radial filaments						
Abyssocladia boletiphora Hestetun et al., 2017a	Southwest Indian Ridge (37°56.48′S, 50°26.53′E, 1178–1306 m)	Side branches with terminal swellings	465–2023 × 18–41 283–400 × 4–10	STR: 164–431 × 11–24	ARC: 65–92 ARC: 21–51 AB: 26–55	CIST: 8–11
Abyssocladia desmophora Hooper and Lévi, 1989	Eastern Australia (17°22.17′S, 147°48.45′E, 1187–1210 m)	Stem 24 × 2 mm, strongly hispid	450–510 × 8–10 320–420 × 6–8	DES: 320–420 × 10–20	ARC/PALM: 60–85	SIGM: 30–40
Abyssocladia flagrum Lehnert et al., 2006	Aleutian Islands (51°18.41′N, 179°31.70′W, 955 m)		980–1320 × 20–28		ARC/PALM: 98–112 ARC/PALM: 28–43	CIST: 37–48 CIST: 17–20
Abyssocladia symmetrica Ridley and Dendy, 1886	Prince Edward Island (46°41′S, 38°10′E, 567 m)		363–1105 × 5–26		ARC: 24–34	CIST: 7–17

The original spicule measurements have been simplified for easier readability. To account for differences in source terminology, mycalostyles and styles are not distinguished in the table. SUB, subtylostyle; TYL, tylostyle; OX, oxea; STR, (sub)strongyle; TOR, tornote; AC, acantho-; DES, desmas; ARC, arcuate; PALM, palmate; CLEI, cleistochela; AB, abyssochela; SIGM, sigma; CIST, sigmancistra; CAR, modified chela in A. carcharias; AN, anisochela; ORT, orthancistra.

plate connected to hard substrate. The holotype is 43 mm tall. The disc is 7 mm in diameter excluding filaments. The stem is 35 mm long and 0.5–0.7 mm wide. The color of the sponge is white to slightly gray in ethanol. No *in situ* video was available for this specimen.

Skeleton

The main structural skeleton is composed of tightly arranged longitudinal mycalostyles. The stem is solid and bare, with no visible surface layer. The mycalostyles of the stem reach into the middle of the sponge body. Radiating filaments are also composed of mycalostyles, while subtylostyles and tylostyles are found within the sponge body itself.

Spicules

4. Mycalostyles, straight, fusiform, in the stem, 1262–2321 (1668) μm long, and 18.7–32.5 (25.7) μm wide (**Figure 3C**).
5. Subtylostyles, straight, fusiform, 1018–1994 (1638) μm long, and 20.0–35.2 (27.2) μm wide (**Figure 3D**).
6. Tylostyles, straight, 275–592 (485) μm long, and 6.3–15.1 (9.3) μm wide.
7. Arcuate isochelae, with frontal tooth and lateral alae of equal length, around 45% of total length, and strongly curved shaft 78.3–132.3 (118.3) μm (**Figures 3E–G**).
8. Sigmancistras, thick, 21.6–31.7 (27.7) μm (**Figure 3H**).

GenBank accession numbers

28S rRNA, MK935688; ALG11, MK922989.

Distribution and habitat

This species is only known from its type locality off the Mariana Islands at the Subducting Guyot 1 locality (4770 m). The specimen was attached by its basal plate to a geological sample.

Etymology

This species is named after Dr. Michelle Kelly at the New Zealand National Institute of Water and Atmospheric Research (NIWA), for her numerous contributions to sponge science, and her work on deep-sea carnivorous and non-carnivorous sponges from the SW Pacific in particular.

Remarks

This species shares similarities with other disc-shaped *Abyssocladia* species. It is a close relative to *A. fryerae* n. sp. and has roughly similar chela and sigmancistra sizes, but has significantly longer subtylostyles and tylostyles are present (lacking in *A. fryerae* n. sp.) (**Table 2**). The phylogenetic results show a close relationship between this species, *A. marianensis* n. sp. and *A. fryerae* n. sp., together with the other Pacific disc-shaped species *A. dominalba* and *A. lakwollii*.

Abyssocladia marianensis sp. nov.

Type material

R/V *Okeanos Explorer* EX1605L3, ROV *Deep Discoverer*. Holotype: USNM 1424192, dive 21, SPEC03BIO, 2016-07-08, trench wall, 16.56°N, 147.6°E, 5813 m.

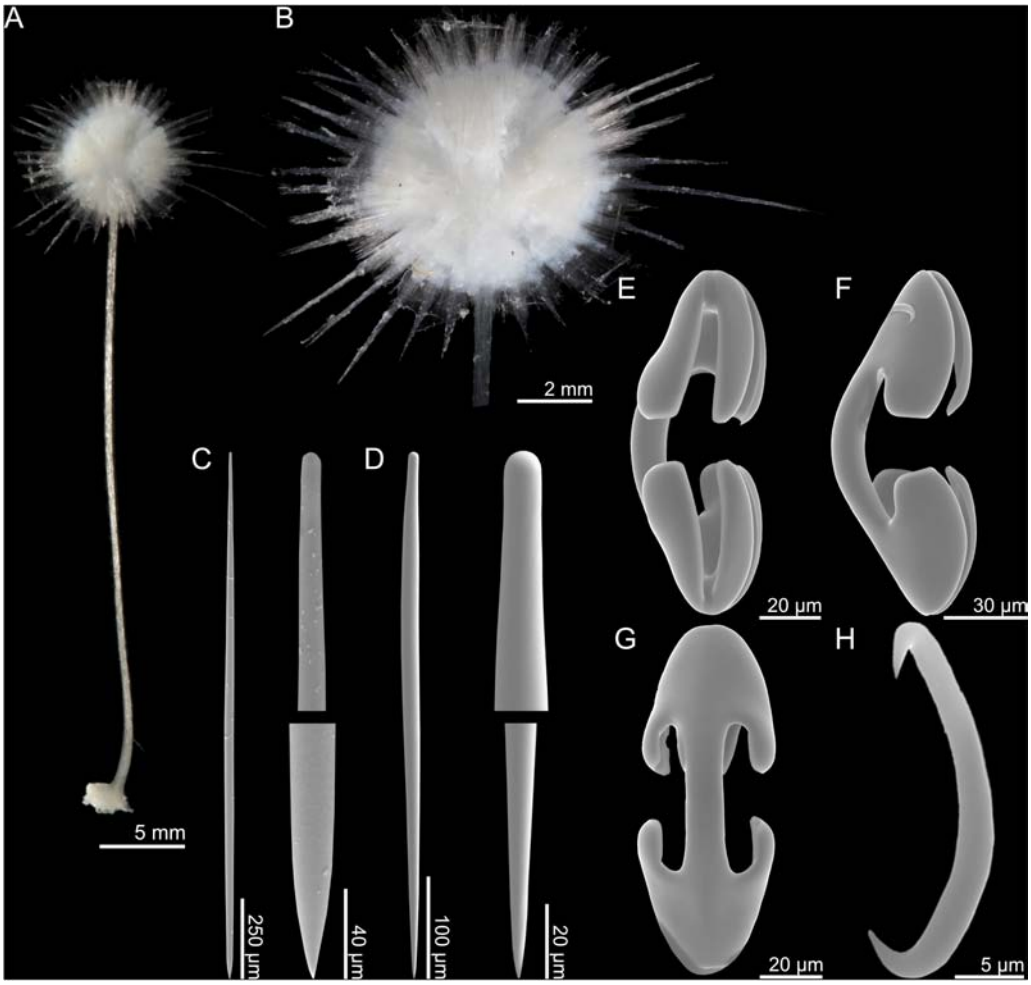

FIGURE 3 | *Abyssocladia kellyae* n. sp. **(A)** whole specimen, **(B)** detail, **(C)** mycalostyle, **(D)** subtylostyle, **(E–G)** arcuate anisochela front, side and back view, and **(H)** sigmancistra.

Diagnosis

Stalked sponge composed of a long stem connected to hard substrate with a small basal plate and ending in an umbrella-shaped body with a pointed apex containing numerous embryos and a horizontally arranged crown of approximately 50 filaments emerging from the sponge margin initially turning slightly downward, then bending slightly upward. Megascleres are mycalostyles, 1800–2500 µm, and oxeas 250–500 µm. Microscleres are arcuate isochelae 65–95 and 24–45 µm, and sigmancistras 50–65 and 30–50 µm.

Description

The holotype (**Figures 4A,C**) consists of a long, rigid, but flexible stem, and an apical, slightly pointed umbrella-shaped body with a single, horizontal filament crown of around 50 filaments emerging from the body margin. Proximal parts of filaments turn slightly downward, and then gently upward at distal end. The sponge is connected to hard substrate with a small basal plate. Numerous embryos are clearly visible through the outer layer of the apical point of the body (**Figure 4D**). Only the proximal parts of the filaments were recovered in the holotype specimen. The holotype is 13 cm tall, and the body 14 mm tall and 20 mm wide excluding filaments. The color of the body is white-to-light beige, while the stem is darker beige in both live specimen and in ethanol.

Skeleton

The skeleton of the stem is composed of tightly packed mycalostyles which are slightly twisted in a counter-clockwise direction. The umbrella is made up of radiating bundles of mycalostyles creating the skeleton of the filaments with soft tissue in between. Oxeas are associated with the fleshy top part containing embryos.

Spicules

9. Mycalostyles, straight, fusiform, very slightly tylote, 1824–2458 (2178) µm long, and 19.7–39.0 (31.3) µm wide (**Figure 4G**).
10. Oxeas, straight, fusiform 289–477 (413) µm long, and 4.1–7.2 (5.7) µm wide (**Figure 4H**).

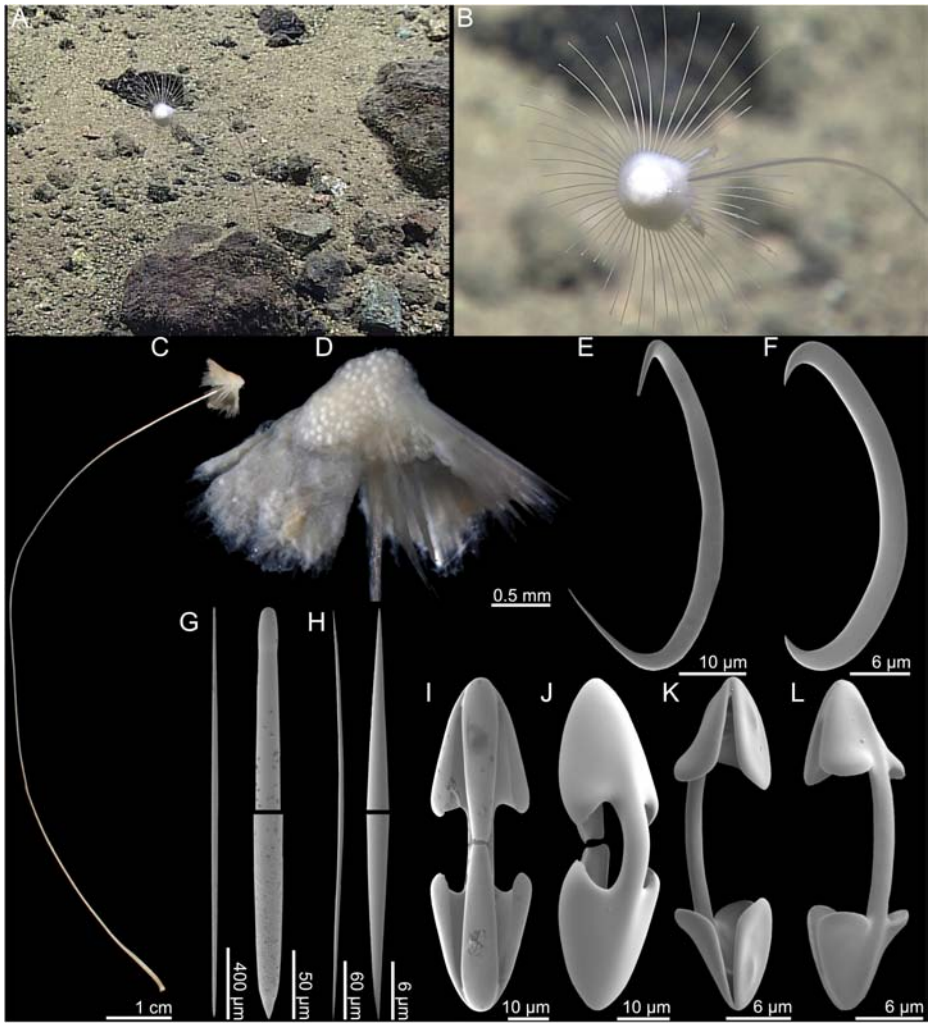

FIGURE 4 | *Abyssocladia marianensis* n. sp. **(A,B)** *In situ* images from ROV feed, **(C)** whole specimen, **(D)** detail of body, **(E)** sigmancistra 1, **(F)** sigmancistra 2, **(G)** mycalostyle with faint tyle, **(H)** oxea, **(I)** cleistochela front view, **(J)** cleistochela back view, **(K)** palmate chela front view, and **(L)** palmate chela back view.

11. Palmate chelae/cleistochelae, palmate forms more common, with frontal tooth and lateral alae of equal length, around 40% of total length, and strongly curved shaft 67.9–91.7 (81.8) µm (**Figures 4I,J**).
12. Palmate chelae/cleistochelae, palmate forms more common, with slightly curved shaft and alae size slightly less than one-third of total chela size, 26.4–42.4 (36.1) µm (**Figures 4K,L**).
13. Sigmancistras 1, 50.5–64.9 (57.3) µm (**Figure 4E**).
14. Sigmancistras 2, 30.7–45.5 (35.8) µm (**Figure 4F**).

GenBank accession numbers

COI, MK922985; 28S rRNA, MK935689; ALG11, MK922990.

Distribution and habitat

This species is only known from its type locality on a trench wall off the Mariana Islands at the (5813 m) on mixed sandy and rocky substrate situated on a small rock.

Etymology

This species is named after its collection locality on a vertical wall of the Mariana Trench off the Mariana Islands.

Remarks

The long stem and umbrella-shaped morphology of this species is unusual for the genus: The only other *Abyssocladia* species described as umbrella-like is *A. bruuni* Lévi, 1964, but the only illustration of this species is in Koltun (1970) which shows a clavate species. Furthermore, Lévi (1964) gives the size of *A. bruuni* as 10 mm, which is much smaller than the present specimen.

Morphologically, it is more reminiscent of a group of deep-sea *Cladorhiza* species such as *C. mirabilis* Ridley and Dendy, 1886 (S Pacific, 4115 m), *C. longipinna* Ridley and Dendy, 1886 (Hawai'i, 5486 m), *C. similis* Ridley and Dendy, 1886 (mid-Pacific, 4362 m), *C. kensmithi* Lundsten et al., 2017, *C. mexicana* Lundsten et al., 2017, and *C. hubbsi* Lundsten et al., 2017. No

molecular data are available for *Cladorhiza* species with stalked rather than branching morphology, which makes it difficult to further investigate evolutionary relationships at this time. Molecular data for the present species show a close relationship with the group of Pacific disc-shaped *Abyssocladia* species also including *A. kellyae* n. sp. and *A. fryerae* n. sp.

Abyssocladia stegosaurensis sp. nov.

Type material

R/V *Okeanos Explorer* EX1605L3, ROV *Deep Discoverer*. Holotype: USNM 1424164, dive 10, SPEC03BIO_CO2, 2016-06-27, Stegosaurus Ridge, 22.12°N, 145.4°E, 3090 m.

Diagnosis

Stalked sponge with a disc-shaped body and filaments radiating in a single plane from the disc margin. Megascleres are mycalostyles 840–1800 μm, subtylostyles 490–1140 μm, and tylostyles 180–580 μm. Microscleres are palmate isochelae, 20–40 μm, and sigmancistras, 5–10 μm.

Description

The holotype (**Figures 5A,B**) is a stalked sponge consisting of a vertical, disc-shaped body on top of a rigid, but flexible stem. Filaments emerge in a radial pattern from the disc edge (**Figure 5C**). The holotype is 48 mm tall. The body excluding filaments is 3 mm in diameter, with filaments up to 6 mm in length. The stem is solid and compact, 45 mm long, and 0.8–1 mm in diameter. The color of the sponge is translucent white to slightly gray in both the live specimen and in ethanol.

Skeleton

The main structural skeleton consists of a core axis made up of longitudinal, tightly arranged mycalostyles. The stem is bare, with little to no soft tissue. Subtylostyles and tylostyles are found in the fleshy parts of the radial sponge body.

Spicules

1. Mycalostyles, very slightly tylote, large, straight, fusiform, 846–1741 (1478) μm long, and 14.8–52.9 (14.8–52.9(28.8)) μm wide (**Figure 5D**).

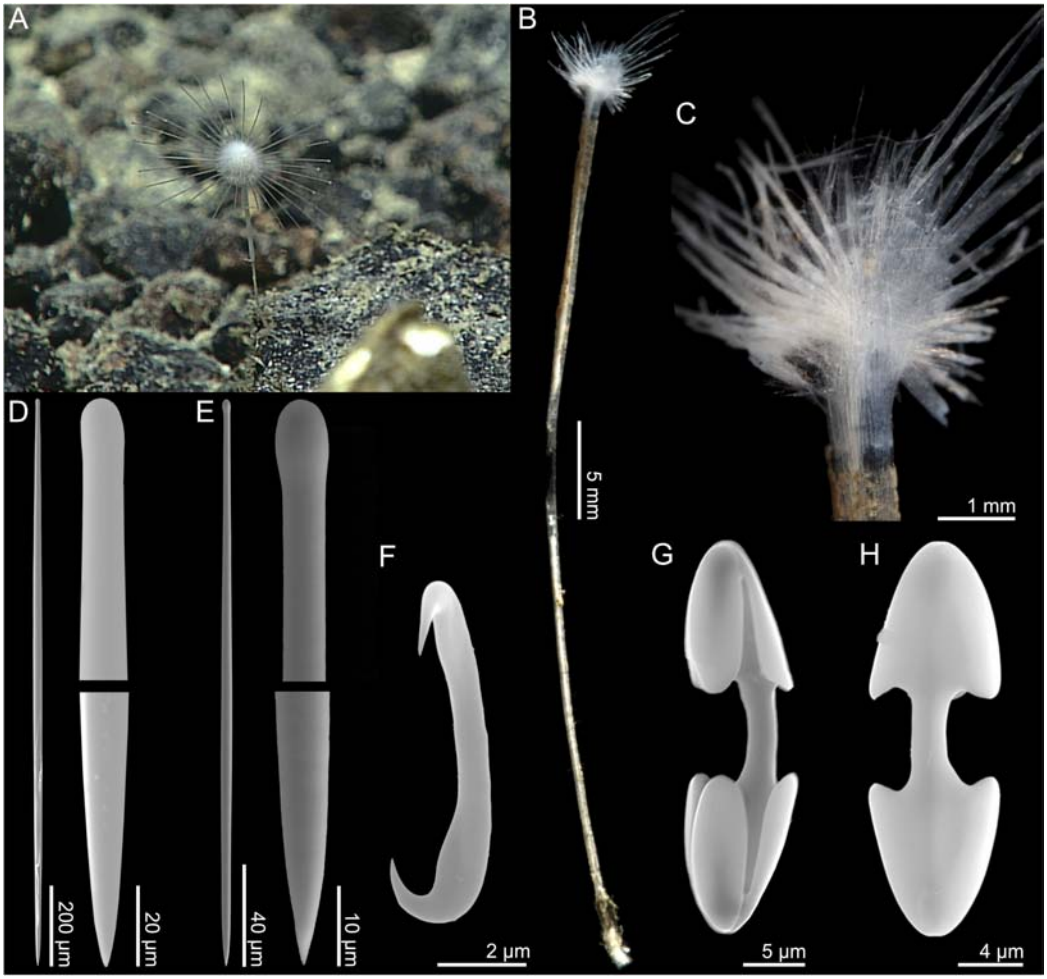

FIGURE 5 | *Abyssocladia stegosaurensis* n. sp. **(A)** *In situ* image from ROV feed, **(B)** whole specimen, **(C)** detail, **(D)** mycalostyle, **(E)** tylostyle, **(F)** sigmancistra, **(G)** palmate chela front view, and **(H)** palmate chela back view.

2. Subtylostyles, straight, fusiform, 491–1134 (736) μm long, and 7.3–16.7 (11.7) μm wide (**Figure 5E**).
3. Tylostyles, straight, not fusiform, 181–573 (423) μm long, and 4.5–9.4 (7.0) μm wide.
4. Palmate isochelae, with frontal tooth and lateral alae of equal length, around 40% of total length, 20.4–39.7 (31.1) μm (**Figures 5H,I**).
5. Sigmancistras, thick, 5.8–9.3 (7.4) μm (**Figure 5G**).

GenBank accession numbers
28S rRNA, MK935690; ALG11, MK922991.

Distribution
While there were several possible observations of the species on the video feed, this species was only collected from the type locality off the Mariana Islands on the Stegosaurus Ridge (3090 m) from hard/rocky substrate situated on a small rock.

Etymology
This sponge is named after the collection locality on the Stegosaurus Ridge off the Northern Mariana Islands.

Remarks
This species shares similarities with other disc-shaped *Abyssocladia* species from the Pacific. Morphologically it is close to *A. kellyae* n. sp. and *A. fryerae* n. sp. in megasclere types and sizes as well as lack of either abyssochelae or cleistochelae. Chelae are small compared to other disc-shaped species in the genus (**Table 2**). The phylogenetic results here imply a more distant relationship, however, placing this species in a basal position relative to other *Abyssocladia* species described in this article.

Abyssocladia villosa sp. nov.

Type material
R/V *Okeanos Explorer* EX1605L3, ROV *Deep Discoverer*. Holotype: USNM 1424162, dive 10, SPEC03BIO, 2016-06-27, Stegosaurus Ridge, 22.12°N, 145.4°E, 3090 m.

Comparative material examined
Abyssocladia hemiradiata Hestetun et al. (2017a), holotype (BMNH 2016.1.13.3).

Diagnosis
Stalked, hispid sponge with a cup-shaped body and horizontal, radial, slightly apically oriented filament crown close to the top margin. Upper stem widens in a conical fashion close to the body. Megascleres are fusiform tylostyles with the broadest part close to the tip, 865–1443 μm, two size categories of straight non-fusiform tylostyles 549–1356 and 154–457 μm long. Microscleres are cleistochelae, 38.2–87.5 μm, and sigmancistras, 7.6–10.0 μm.

Description
The holotype (**Figures 6A,B**) is a single specimen of a stalked sponge consisting of a cup-shaped body with filament crown close to the apical margin, radiating outward and slightly upward, and a hispid stem connected to hard substrate with a small basal plate. The holotype is 5 cm long from the base to the top of the body. The body is 5.5 mm tall and 7.5 mm in diameter. The stem is 45 mm long and 0.5–2 mm in diameter, widening toward the top (**Figures 6C,D**). The color of the body is white to white gray, while the stem is light brown in both live specimen and in ethanol.

Skeleton
The skeleton is composed of a solid core of tightly packed, large longitudinal subtylostyles. The core skeleton of the stem is covered with a thin surface layer of soft tissue, which contains numerous plumose brushes of smaller tylostyles that project outward and give the specimen a hispid surface. The structural skeleton widens toward the top body, which contains a radiating skeleton of the larger tylostyles (**Figures 6D,E**).

Spicules
1. Subtylostyles, straight, fusiform, with the thickest part closest to the tip, and gradually tapering toward the base, 718–1443 (1080) μm long, and 13.8–24.5 (20.8) μm wide (**Figure 6F**).
2. Tylostyles I, straight, not fusiform, 549–1356 (923) μm long, and 7.1–18.7 (12.1) μm wide (**Figure 6G**).
3. Tylostyles II, straight, not fusiform, making up the plumose brushes of the stem, 154–488 (282) μm long, and 4.3–14.8 (7.3) μm wide (**Figure 6H**).
4. Cleistochelae, arcuate isochelae with frontal tooth touching or nearly touching, 30.5–90.3 (58.5) μm (**Figures 6I,J**). This spicule has a large size range, but there is a continuous size distribution, so it is presented as a single category here.
5. Sigmancistras, thick, 7.6–12.4 (9.4) μm (**Figure 6K**).

GenBank accession numbers
COI, MK922986; 28S rRNA, MK935691; ALG11, MK922992.

Distribution and habitat
This species is only known from its type locality off the Mariana Islands on the Stegosaurus Ridge (3090 m) from hard/rocky substrate situated on a large rock.

Etymology
From Latin "*villosa*" meaning shaggy or hairy. The sponge is named after the hispid surface of the stem and apical body.

Remarks
Other *Abyssocladia* species with a spherical pedunculate body include *A. claviformis* Koltun, 1970 and *A. oxeata* Koltun, 1970. These were both collected from the NW Pacific basin, and are possible close relatives to *A. villosa* n. sp.

This species has a hispid surface due to the presence of plumose brushes of the shorter category of tylostyle projecting through the outer layer of the stem. A similar arrangement is found in a small number of other species in the genus, including *A. claviformis* Koltun, 1970, *A. desmophora* (Hooper and Lévi, 1989), and *A. hemiradiata* Hestetun et al., 2017a, and the phylogenetic results confirm a close relationship between this species and *A. hemiradiata*.

Genus *Chondrocladia* Thomson, 1873

Type species
Chondrocladia (*Chondrocladia*) *virgata* Thomson, 1873 (type by monotypy).

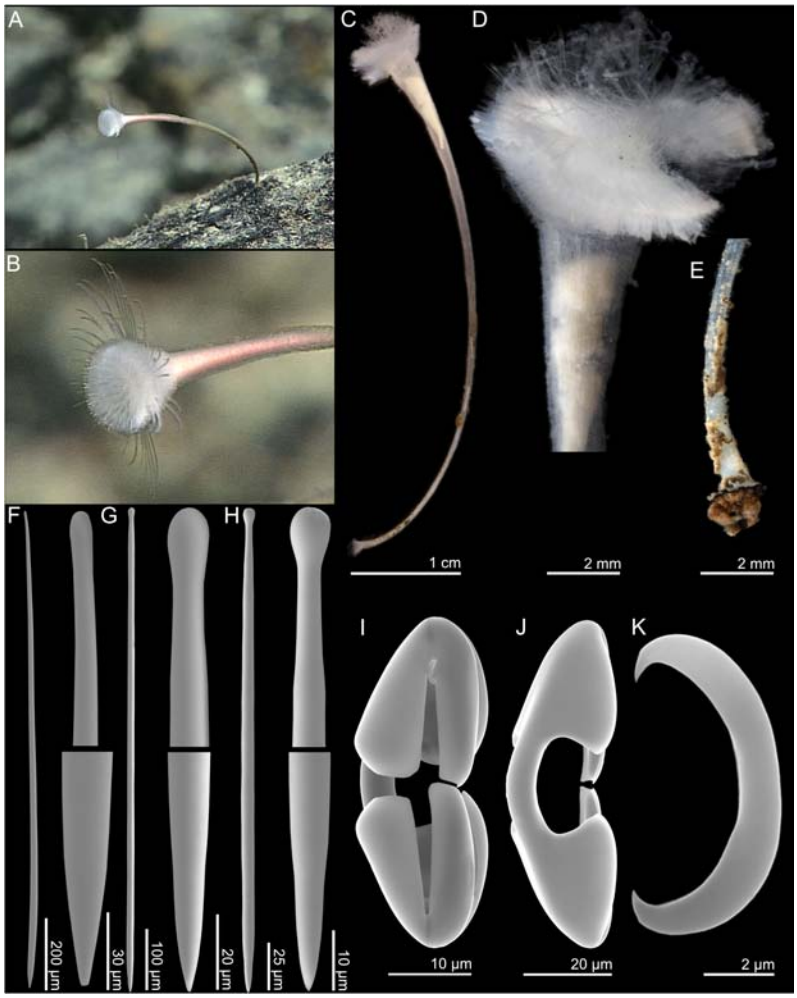

FIGURE 6 | *Abyssocladia villosa* n. sp. **(A,B)** *In situ* images from ROV feed, **(C)** whole specimen, **(D)** detail of body, **(E)** detail of basal plate, **(F)** subtylostyle, **(G)** tylostyle I, **(H)** tylostyle II, **(I)** cleistochela front view, **(J)** cleistochela back view, and **(K)** sigmancistra.

Diagnosis

Cladorhizidae with anchorate isochelae (from Lee et al., 2012).

Remarks

Genus *Chondrocladia* contains 37 species in three subgenera (Van Soest et al., 2019). While species in the genus usually have defined, regional distributions, the genus as a whole is cosmopolitan. Certain species have a shallower distribution of 500–1000 m, while others have been reported from lower bathyal and abyssal depths.

Subgenus *Chondrocladia* Thomson, 1873

Type species

Chondrocladia (*Chondrocladia*) *virgata* Thomson, 1873 (type by monotypy).

Diagnosis

Chondrocladia without a layer of special spicules (subtrochirhabds or trochirhabds), lacking special rostriform (snout-like) subtylostyles in filaments or terminal balls, and without planar vanes formed of evenly spaced upright branches (from Lee et al., 2012).

Remarks

Subgenus *Chondrocladia* contains 30 of the 37 species in genus *Chondrocladia* (Van Soest et al., 2019). It is defined as *Chondrocladia* species lacking any of the diagnostic criteria for the other two subgenera, *Meliiderma* and *Symmetrocladia*.

Chondrocladia (*Chondrocladia*) *coronata* sp. nov.

Type material

R/V *Okeanos Explorer* EX1605L3, ROV *Deep Discoverer*. Holotype: USNM 1424095-1424096, dive 8, SPEC03BIO, 2016-04-29, Northwest Guam Seamount, 14.92°N, 144.6°E, 1229 m (subsample: Ocean Genomic Legacy S24102).

Diagnosis

Erect sponge consisting of a single stem with filaments emerging in a radial pattern along its whole length. Filaments become longer toward the top of the sponge. The top of the main

stem widens into a funnel shape with a ring-like margin and a secondary crown of smaller filaments at a 45° angle pointing apically. Megascleres are straight, fusiform mycalostyles, 1430–2100 μm, and straight, fusiform subtylostyles 475–950 μm. Microscleres are three categories of anchorate isochelae, 40–60, 20–32, and 15–20 μm, and sigmas, 30–50 μm.

Description

The holotype is composed of two fragments of an erect sponge composed of a single stem with numerous side filaments; the larger fragment (USNM 1424096) is a 38 mm piece from the top of the sponge including part of the enlarged apical body (**Figure 7C**), while the smaller fragment (USNM 1424095) is an 8 mm segment of the stem (**Figure 7D**). Both fragments are damaged, and it is only possible to get a complete idea of the morphology of the sponge by examination of the ROV video (**Figures 7A,B**). Based on the video data and recovered fragments, the complete sponge is likely around 10–15 cm tall. The image of the live sponge shows around 150 filaments, emerging in all directions from the stem across its whole length, with filaments getting gradually longer closer to the top of the sponge. The top of the sponge contains

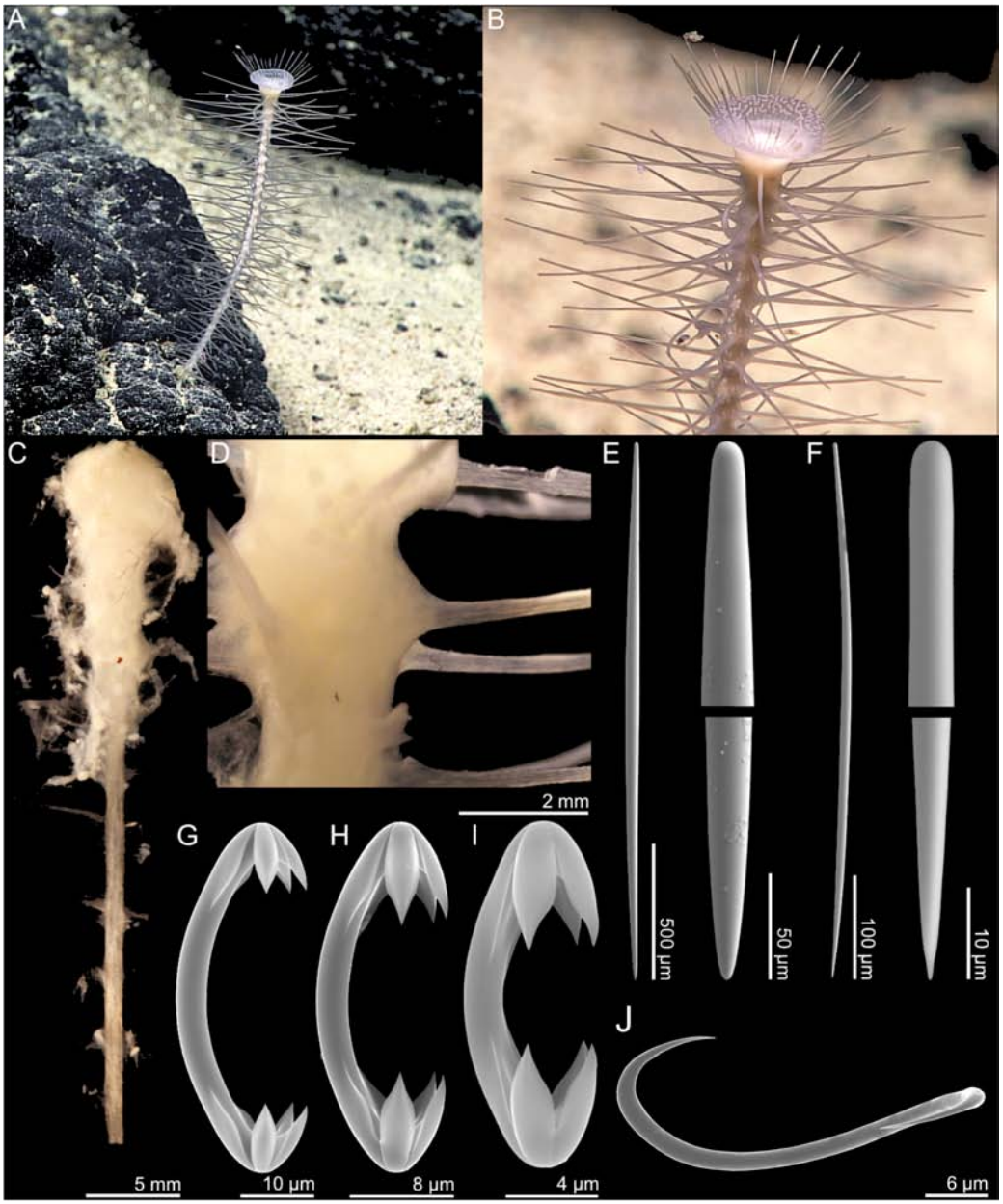

FIGURE 7 | *Chondrocladia coronata* n. sp. **(A,B)** *In situ* images from ROV feed, **(C)** whole specimen, **(D)** stem detail, **(E)** style, **(F)** subtylostyle, **(G)** anchorate chela 1, **(H)** anchorate chela 2, **(I)** anchorate chela 3, and **(J)** sigma.

a funnel-shaped enlargement ending in a fleshy, horizontal ring with a shallow central depression. A secondary, smaller set of around 30 filaments emerge from this ring at a 45° upward angle. Embryos are present in the main stem. The sponge is attached to a rock with a small base, which was not recovered. The color of the live sponge varies from light beige in the main stem, to light gray and white in filaments and top part.

Skeleton

The main structural skeleton of the stem and filaments is made up of a core of longitudinal, tightly packed mycalostyles. Subtylostyles are associated with the fleshy outer surface of the stem and top part, where they are arranged to support the associated tissue. All anchorate chelae size classes are found throughout the sponge. Sigmas are found in the apical crown part of the sponge.

Spicules

1. Mycalostyles, straight, fusiform, 1430–2104 (1734) μm long, and 26.9–52.0 (39.4) μm wide (**Figure 7E**).
2. Subtylostyles, straight, fusiform, 488–948 (642) μm long, and 10.2–27.6 (17.0) μm wide (**Figure 7F**).
3. Anchorate isochelae 1, 40.9–59.8 (52.5) μm, with three teeth of equal length, each around 20% of total length and curved shaft (**Figure 7G**).
4. Anchorate isochelae 2, 21.1–31.5 (26.2) μm, with three teeth of equal length, each around 30% of total length and curved shaft (**Figure 7H**).
5. Anchorate isochelae 3, 14.9–19.6 (17.4) μm, with three teeth of equal length, each around 30% of total length and curved shaft (**Figure 7I**).
6. Sigmas, 33.6–48.7 (39.6) μm (**Figure 7J**)

GenBank accession numbers

COI, MK922987; 28S rRNA, MK935692; ALG11, MK922993.

Distribution and habitat

This species is only known from its type locality off the Mariana Islands at the Guam Seamount (1229 m) from mixed sandy and rocky substrate situated on exposed rock.

Etymology

From Latin, "*coronata*," meaning crowned. Named after the filament crown of the apical body of the sponge.

Remarks

It is difficult to identify close relatives to this species given its unique general morphology within the genus: *Chondrocladia* species are usually either pedunculate with a top body containing filaments, or elongated and club-shaped with fistules emerging from the stem, while this species has a stem with numerous smaller filaments as well as a well-developed top part.

The molecular data suggest a closer affinity to *C.* (*S.*) *lyra* and stalked species such as *C. vaceleti* and *C. fatimae* rather than large, club-shaped species such as *C. grandis* and *C. concrescens*. The current subgenus classification of *Chondrocladia* is likely not monophyletic (Hestetun et al., 2016b). As it is lacking diagnostic characters for the subgenera *Meliiderma* and *Symmetrocladia*, we have placed *C. coronata* n. sp. in subgenus *Chondrocladia*.

Subgenus *Symmetrocladia* Lee et al., 2012

Type species

Chondrocladia (*Symmetrocladia*) *lyra* Lee et al., 2012.

Diagnosis

Chondrocladia with biradial, triradial, tetraradial, or pentaradial symmetry of right triangles (vanes) formed of vertically aligned branches arising unilaterally from basal stolons. Without a stalk. Spicules are styles, rostriform (snout-like) subtylostyles in the filaments and on the terminal balls, and unguiferous anchorate isochelae and sigmas. Trochirhabds and forceps are absent (from Lee et al., 2012).

Chondrocladia (*Symmetrocladia*) *lyra* Lee et al., 2012

Examined material

R/V *Okeanos Explorer*, ROV *Deep Discoverer*. USNM 1424083, EX1605L1, dive 3, SPEC05BIO, 2016-04-23, Sirena Canyon, 12.54°N, 144.6°E, 4857 m (subsample: Ocean Genomic Legacy S24096). USNM 1424175, EX1605L3, dive 13, SPEC01BIO, 2016-06-30, Twin Peaks, 21.42°N, 145.89°E, 4834 m.

Comparative material examined

Chondrocladia (*Symmetrocladia*) *lyra* (subsample from holotype), CASIZ18877, South Escanaba Ridge, CA, 2005-08-30, dive T-891-A2, 40.98°N, 127.49°W, 3318 m.

Diagnosis

Chondrocladia with biradial, triradial, tetraradial, or pentaradial symmetry of right triangles (vanes) formed of vertically aligned branches arising unilaterally from basal stolons. Without a stalk. Spicules are styles, rostriform (snout-like) subtylostyles in the filaments and on the terminal balls, and unguiferous anchorate isochelae and sigmas. Trochirhabds and forceps are absent (from Lee et al., 2012).

Description

Two specimens were recovered, one from Sirena Canyon (4857 m) and one from Twin Peaks (4834 m). Specimen USNM 1424083 (Sirena Canyon) is composed of a short stem and two opposite vanes with 10 and 11 vertical branches (**Figures 8A,B**). The recovered specimen is around 13 cm from end to end, but lacks a couple of branches on each side, meaning the complete animal is larger *in situ*. Branches are around 4–5 cm in length. Both stolon and branches feature a large number of filaments 2–5 mm in length. Stolon or branch swellings are not apparent. ROV footage shows ophiuroids clinging to stolon and branches (**Figure 8B**).

Specimen USNM 1424175 (Twin Peaks) also has two opposite vanes, but the recovered specimen is fragmented. Stolons carry 13 vertical branches each. Branches are longer than in the preceding specimen, and end with terminal swellings (**Figures 8C,D**, **9C**), but no complete branches were recovered, so they could not be measured. The stolons also feature a couple of solid enlargements. Stolon and branches feature a large number of filaments in all directions from the stem.

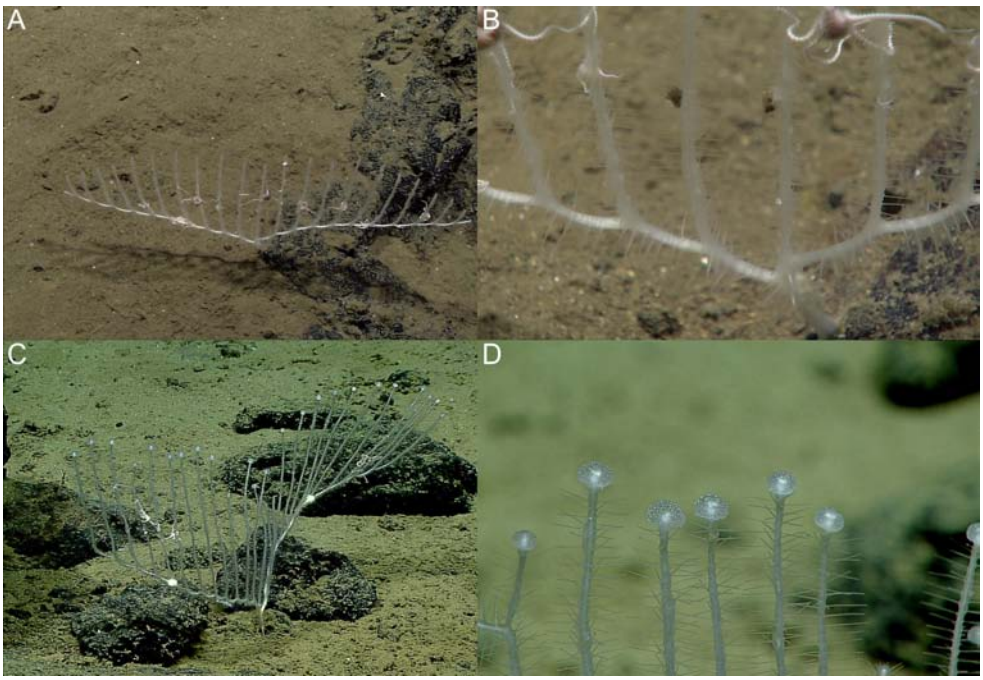

FIGURE 8 | *Chondrocladia* (*Symmetrocladia*) *lyra in situ* images from ROV feed. **(A,B)** Specimen USNM 1424083 and **(C,D)** specimen USNM 1424173.

Both specimens were recovered on mixed sandy and rocky bottom, and are anchored into the sandy sediment with rhizoids.

Skeleton

The mycalostyles make up the main structural skeleton of the stolons and branches, while megascleres found in the filaments and swellings are subtylostyles. Isochelae are found in all parts of the sponge. Large sigmas are common in filaments, while small sigmas are confined to the swellings and were not found in specimen USNM 1424083.

Spicules

1. Mycalostyles, straight, fusiform, stolons and branch stems, 1425–1959 (1726) μm long, and 23.1–41.2 (35.4) μm wide (**Figure 9D**).
2. Subtylostyles, straight, fusiform, filaments, 740–1156 (858) μm long, and 12.6–22.0 (17.2) μm wide (**Figure 9E**).
3. Anchorate isochelae, 41.5–53.1 (47.1) μm, with three teeth of equal length, each around one-sixth of total length, and curved shaft (**Figure 9F**).
4. Sigmas, 78.7–117.7 (98.4) μm (**Figure 9G**). Associated mainly with filaments.
5. Sigmas, 45.9–64.2 (55.5) μm. Associated with terminal swellings.

GenBank accession numbers

USNM 1424083: COI, MK922988; 28S rRNA, MK935693; ALG11, MK922994. USNM 1424175: COI, MK922996.

Distribution and habitat

The type location for *C.* (*S.*) *lyra* is off California at the South Escanaba Ridge with additional reported sightings at the Monterey Canyon and a depth range of 3317–3503 m (Lee et al., 2012). The original source mentions that there are also unpublished records that states that distribution range is probably much larger than specimens specifically described in that article, and gives distribution as NE Pacific (Lee et al., 2012). The distance between the type locality and the Marianas confirms that the species is present on both sides of the Pacific, and most likely has a very wide distribution at bathyal to abyssal depths (∼3000–5000 m).

Remarks

This species is well described in the original article by Lee et al. (2012). Molecular data from the type material are included in the phylogeny of Hestetun et al. (2016b), and the molecular data here confirm that the present material belongs to the same species. Some of the type specimens are larger, with more than two vanes, but the present material is within the variation of the originally published set of specimens.

Because of its unique morphology, Lee et al. (2012) erected a new, monotypic subgenus, *Symmetrocladia*, for *C.* (*S.*) *lyra*. Molecular results in Hestetun et al. (2016b) suggest a basal position to smaller, pedunculate *Chondrocladia* species sometimes informally referred to as "*Crinorhiza*" type in older literature (e.g., Topsent, 1930; Lévi, 1993).

Genus *Lycopodina* Lundbeck, 1905

Type species

Lycopodina lycopodium (Levinsen, 1887) (type by subsequent designation).

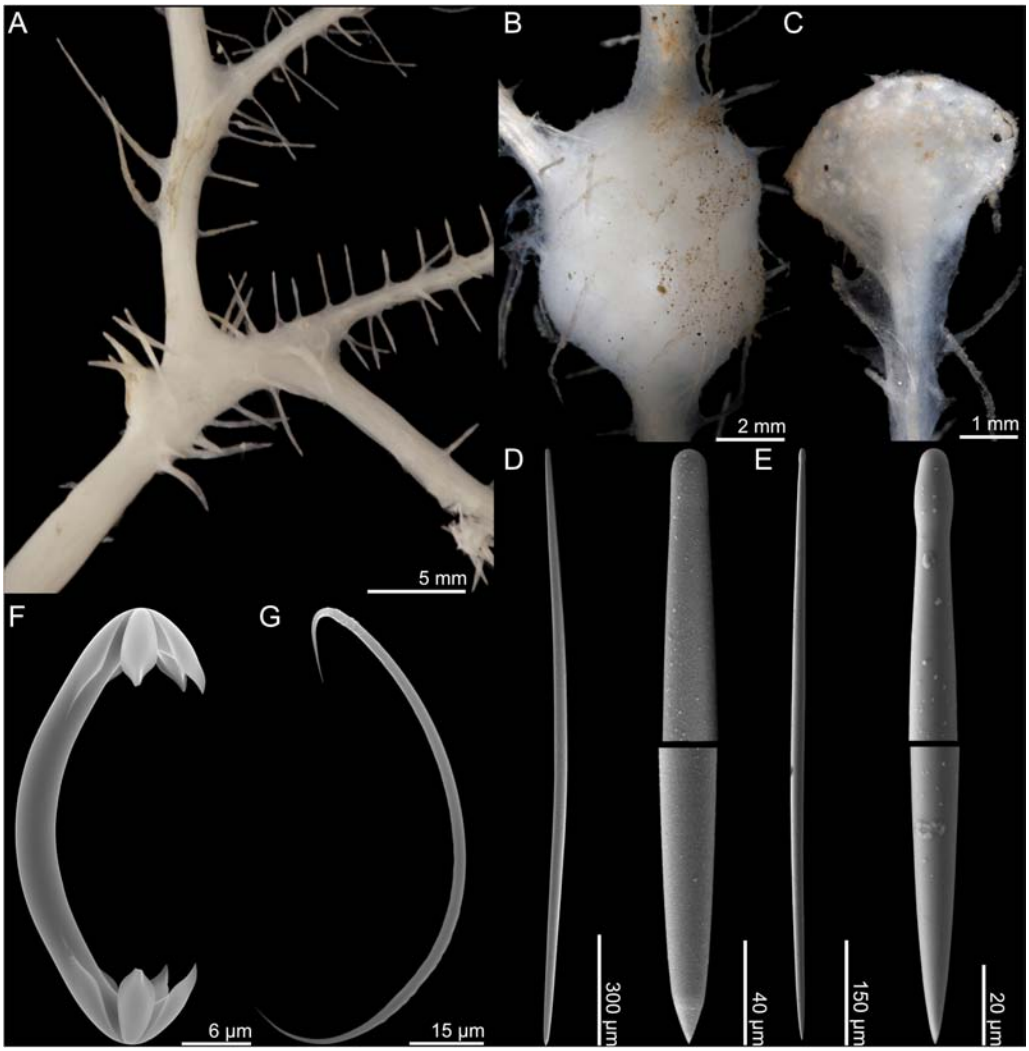

FIGURE 9 | *Chondrocladia* (*Symmetrocladia*) *lyra*. **(A)** Branch detail from USNM 1424083, **(B)** stolon swelling from USNM 1424173, **(C)** terminal swelling from USNM 1424173, **(D)** style, **(E)** subtylostyle, **(F)** anchorate chela, and **(G)** sigma.

Diagnosis

Pedunculate Cladorhizidae with body either in the form of an erect stem or sphere with filaments in all directions, or cup-shaped. Megascleres are mycalostyles and commonly shorter (tylo)styles. Microscleres are one type of arcuate or palmate anisochela where the smaller end is in the shape of a central plate and two rudimentary, flat, lateral teeth, all with serrated edges toward the middle. To this, forceps spicules are often added, but may be rare or absent in particular species or specimens of a single species. Never sigmas or sigmancistras (from Hestetun et al., 2016b).

Remarks

The genus contains 29 species in addition to the species described here (Van Soest et al., 2019). Originally erected as a subgenus by Lundbeck (1905), it was re-erected as a genus based on results from Hestetun et al. (2016b). The genus is cosmopolitan, with species known from all major oceans, and from low tide down to hadal depths.

Lycopodina subtile sp. nov.

Type material

R/V *Okeanos Explorer* EX1605L3, ROV *Deep Discoverer*. Holotype: USNM 1424167, dive 10, SPEC03BIO_CO4, 2016-06-27, Stegosaurus Ridge, 22.12°N, 145.4°E, 3090 m.

Comparative material examined

L. lycopodium (Levinsen, 1887) (ZMBN 103465).

Diagnosis

Sponge composed of a slender stem with a large number of fine filaments emerging in all directions outward from the stem. Spicules are mycalostyles around 400–1500 µm long and palmate anisochelae around 7–11 µm long.

Description

An erect sponge consisting of a thin, vertical stalk with a short basal stem. A large number of filaments are arranged in a radial fashion projecting outward in all directions from the central stalk. The holotype is 34 mm long and 0.5 mm in diameter, with filaments up to 3 mm long. The color of the sponge is translucent white to slightly gray in both live specimen and in ethanol.

Skeleton

The main structural skeleton consists of a core axis made up of longitudinal, tightly arranged mycalostyles. The filaments are composed of mycalostyles perpendicularly inserted into the main stem, radiating at their base. The stem core is covered by a thin surface layer of soft tissue. Palmate anisochelae are found at the surface of the stem and filaments.

Spicules

1. Mycalostyles, very slightly tylote, large, straight, fusiform, 393–1438 (804) μm long, and 6.3–32.1 (18.5) μm wide (**Figures 10D,E**).
2. Palmate anisochelae, with frontal tooth and lateral alae of equal length, around 40% of total length, 7.1–10.7 (9.1) μm (**Figures 10F,H**).

GenBank accession numbers

28S rRNA, MK935694; ALG11, MK922995.

Distribution

This species is only known from its type locality off the Mariana Islands at the Stegosaurus Ridge (3090 m) on a large rock outcropping.

Etymology

From Latin, "*subtile*," meaning fine, slender, or delicate. Named after the small size and slender stem of the sponge.

Remarks

The anisochelae of *L. subtile* n. sp. are small compared to most species of the genus, and are similar in size to the smaller category of chela in *Asbestopluma*. However, the morphology of the spicule and the phylogenetic results show that it is clearly *Lycopodina*.

Species identification within *Lycopodina* can be challenging since spicules like smaller categories of megascleres and forceps spicules seem to be associated with specific parts of the sponge or reproductive structures such as embryos or spermatic cysts (Riesgo et al., 2007). In many cases, larger megascleres and anisochelae are the only spicules that can be reliably found, such as for *L. subtile* n. sp. here.

A stalked morphology with a radial arrangement of filaments is common within the genus, and given intraspecific spicule size variation, exact species boundaries are uncertain for species such as *L. lycopodium*, *L. occidentalis*, *L. lebedi*, and *L. gracilis* (e.g., Koltun, 1962, 1970; Van Soest, 2016; Hestetun et al., 2017b).

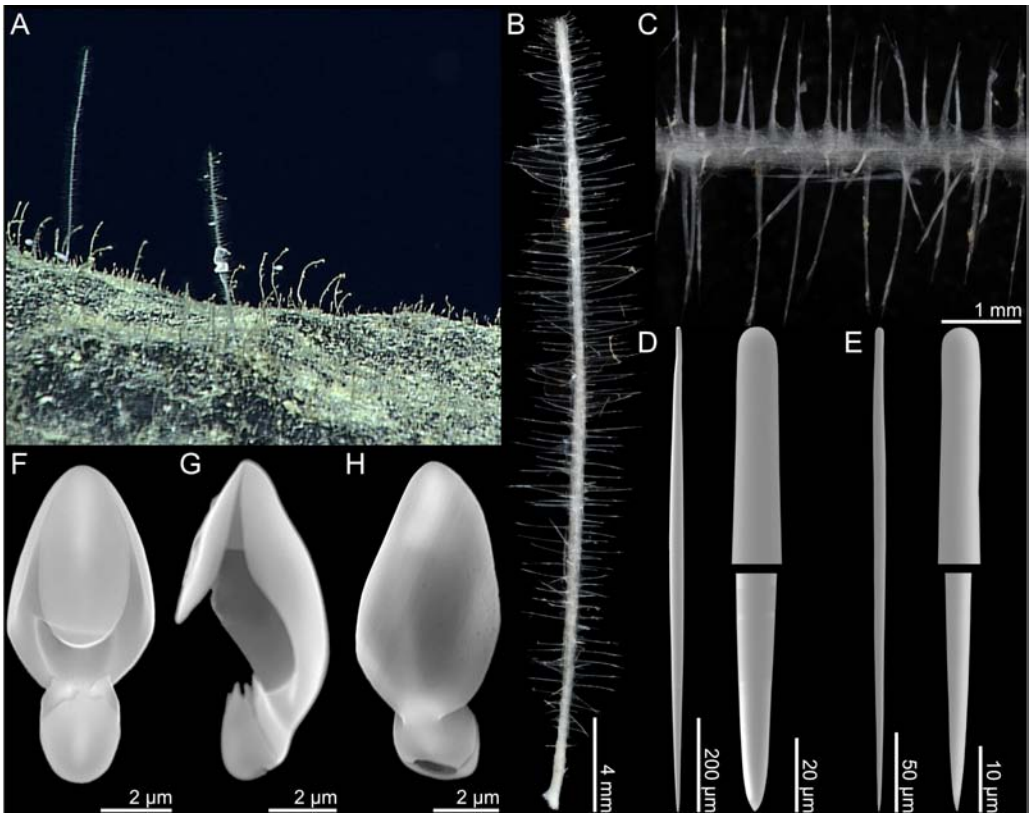

FIGURE 10 | *Lycopodina subtile* n. sp. **(A)** *In situ* image from ROV video, **(B)** holotype USNM 1424167, **(C)** stem detail, **(D)** large style, **(E)** small style, **(F–H)** palmate anisochela front, side and back view.

Only a few stalked *Lycopodina* species have been reported from lower bathyal depths and below: *Lycopodina wolffi* Lévi, 1964 and *Lycopodina hadalis* Lévi, 1964 from the Kermadec and Kuril–Kamchatka Trenches (∼4350–8840) (Lévi, 1964; Koltun, 1970). While Koltun (1970) argued that *L. hadalis* is a synonym of *L. occidentalis*, this is not considered valid here. The phylogenetic results recover L. *subtile* n. sp. with *L. cupressiformis*, though it is likely that it is more closely related to other *Lycopodina* species where molecular data are missing.

Phylogenetic Analysis

The ML best tree from the phylogenetic analysis of the concatenated partial 28S rRNA, COI, and ALG11 dataset is presented here with Bayesian posterior probabilities and ML bootstrap values indicated for nodes recovered in both analyses (**Figure 11**). The analysis includes available cladorhizid sequences on GenBank (see the section "Materials and Methods" for references containing accession numbers) as well as new sequences from the specimens examined in this article (see species descriptions for accession numbers).

In general, genus and species relationships are similar to previous cladorhizid phylogenies in e.g., Hestetun et al. (2016b): *Lycopodina* forms a basal clade followed by *Asbestopluma*, *Eucheliplumа*/*Abyssocladia*, and finally *Cladorhiza* and *Chondrocladia*. The species sequenced for this article are recovered in positions consistent with morphological characters: The new *Chondrocladia* (*S.*) *lyra* specimens are virtually identical to the previously sequenced specimen from the type material. *C. coronata* n. sp. is recovered in a basal position relative to *C.* (*S.*) *lyra* and other *Chondrocladia* species with a *Crinorhiza*-type morphology (cf. discussion of the genus in Hestetun et al., 2016b) (**Figure 11**).

The new *Abyssocladia* species are found in three main positions within the genus: *A. stegosaurensis* n. sp. was recovered basal to other species described here. *A. villosa* n. sp. was recovered as a sister taxon to *A. hemiradiata* Hestetun et al., 2017a. The last three species, *A. kellyae* n. sp., *A. fryerae* n. sp., and *A. marianensis* n. sp., were recovered together with the Pacific disc-shaped species *A. dominalba* Vacelet, 2006 and *A. lakwollii* Vacelet and Kelly, 2014 (**Figure 11**).

DISCUSSION

Abyssocladia Diversity and Distribution

In the 2001 publication of the *Systema Porifera*, the cladorhizid genus *Abyssocladia* Lévi, 1964 was considered a synonym to Phelloderma Ridley and Dendy, 1886 (Van Soest and Hajdu, 2002). Re-erected in 2006 based on a re-examination of chela characters and newly discovered species, *Abyssocladia* at that time contained seven abyssal Pacific species with a short diagnosis that included a pedunculate, disc-shaped body, and abyssochela spicules (Vacelet, 2006). Including the species in the present article, it has over a period of 10 years grown into a genus containing 31 species with considerable morphological and spicule variation, and is now also known from the North and South Atlantic as well as seamounts on the Southwest Indian Ridge (see **Table 2** for references).

Body shapes within the genus now include stalked forms with disc-shaped, spherical- or umbrella-shaped bodies, pinnate forms with opposite rows of filaments or filaments radiating in all directions from the stem, as well as branching forms. Megascleres commonly include mycalostyles, styles, (sub)tylostyles, oxeas, (sub)strongyles, in a couple of cases acantho(tylo)styles or acanthostrongyles, and in one case desmas. Microscleres include arcuate or palmate isochelae, cleistochelae, and abyssochelae, in some cases with specific morphology or modification, and finally sigmas and sigmancistras. As many species only feature arcuate isochelae rather than the previously diagnostic abyssochelae, it is difficult to establish a clear synapomorphy for the genus (**Table 2**).

While the genus can be roughly divided into different body shapes, it is difficult to relate this to the variation in spicule complement and morphology. Sequence data for the genus are limited, and there is yet no clear pattern between morphological characters and phylogenetic position (**Figure 11**). Phylogenetic results indicate that *Eucheliplumа* Topsent, 1909 is a sister group to *Abyssocladia*, but the systematic relationship between *Abyssocladia* and the cladorhizid genera *Cercicladia* Ríos et al., 2011, *Koltunicladia* Hestetun et al., 2016b, and *Lollipocladia* Vacelet, 2008 is unclear (Hestetun et al., 2016b).

Most described *Abyssocladia* species are based on only one specimen or specimens from a single expedition. It is thus likely that the increase in the number of known species will continue, which will provide additional morphological context and fill the gaps between current species of the genus. Cladorhizid specimens are fragile and easily distort or break as a result of preservation. ROV *in situ* video footage, ideally together with high-quality photos during collection prior to preservation, is thus critical to get a complete understanding of the morphology and function of a given cladorhizid species. Increasing the amount of sequence data available for phylogenetic analysis of the carnivorous sponges will allow further exploration of the evolutionary relationships within *Abyssocladia* and its sister taxa. New morphological and molecular data thus both serve to increase the knowledge of the diversity and evolution of the genus and cladorhizids in general.

Pacific Cladorhizid Diversity and the Mariana Islands

Before the present study, no cladorhizid species have been reported for the deep sea around the Mariana Islands. Other records from the West Pacific show that cladorhizids are reasonably common, however, with several recently described species (e.g., Vacelet, 2006; Vacelet et al., 2009; Ise and Vacelet, 2010; Kelly and Vacelet, 2011; Vacelet and Kelly, 2014).

Results from this article demonstrate that the deep-sea seafloor around the Mariana Islands contains a rich and previously unknown cladorhizid fauna. Somewhat surprisingly, only one of the present species, the harp sponge *Chondrocladia* (*Symmetrocladia*) *lyra*, is previously described.

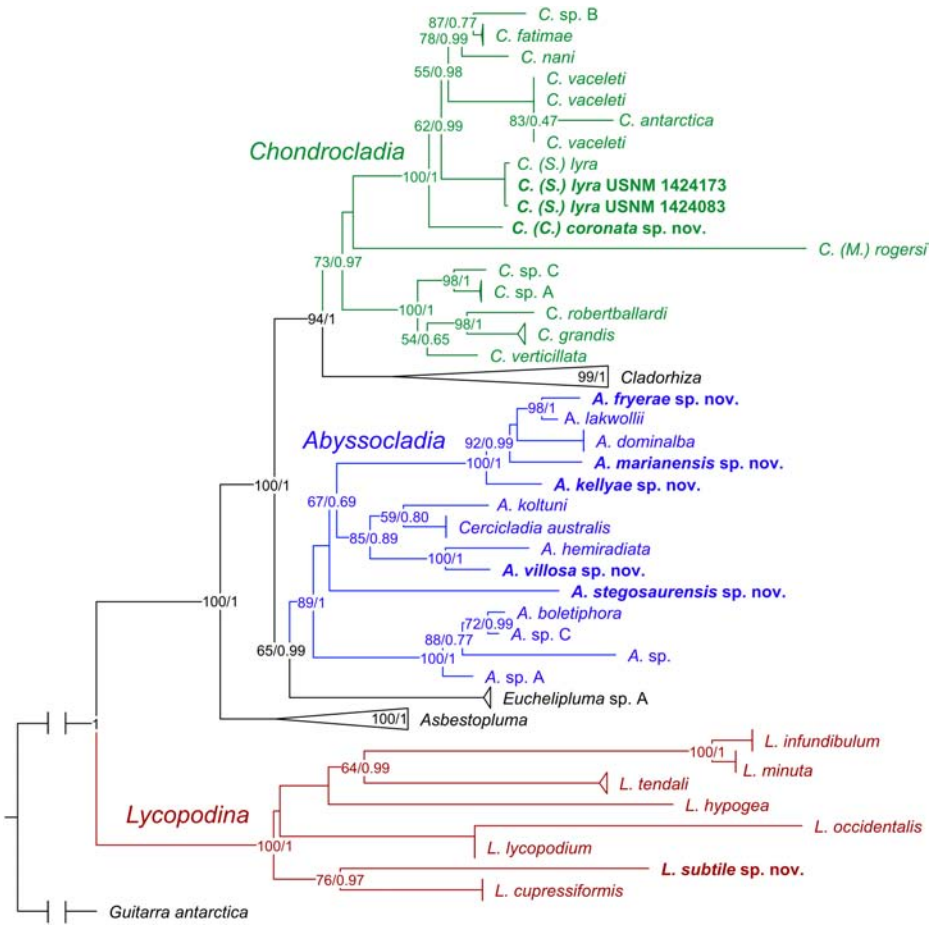

FIGURE 11 | ML consensus tree of a concatenated phylogeny of the Cladorhizidae based on partial 28S rRNA, COI, and ALG11. The analysis includes available cladorhizid sequences from GenBank as well as an outgroup taxon (*Guitarra antarctica*). Sequences for specimens described in this article are indicated in bold. Bayesian posterior probabilities (0–1) and ML bootstrap values (1–100) are indicated for nodes that were recovered in both analyses. Genera including species described in this article are color coded green for *Chondrocladia*, blue for *Abyssocladia*, and red for *Lycopodina*. The genera *Cladorhiza* and *Asbestopluma* and species with sequences from several specimens have been collapsed to aid readability.

While the species here are almost all new to science, they are clearly related to the general cladorhizid fauna of the Pacific, with a high proportion of *Abyssocladia* and extending the known distribution of *C.* (*S.*) *lyra*. The generally poor sampling coverage makes it difficult to assess whether the fauna is unique to the area, or is part of a larger, shared Pacific fauna.

While some cladorhizid species use rhizoid structures to attach to soft bottom substrate, many species are found on hard or mixed bottom types, where they are fastened to rock patches or outcroppings. Their fragile morphology and small size makes it easy to overlook cladorhizids in both video transects and using traditional sampling gear. Still, as demonstrated by the material described in the current study, field personnel with appropriate expertise and a thorough sampling design facilitate preliminary identification and collection of this group.

The results here are also congruent with past studies in previously understudied areas in the Southwest Pacific and elsewhere, in that recovered cladorhizid specimens have a high chance of belonging to undescribed species. It is clear that the deep Pacific is home to a diverse and still very poorly known carnivorous sponge fauna with many unique characters compared to the somewhat better known Atlantic cladorhizids, and that additional sampling is needed to get a better picture of the total diversity of carnivorous sponges in the area.

DATA AVAILABILITY

The datasets generated for this study can be found in GenBank: MK922984, MK922985, MK922986, MK922987, MK922988, MK922989, MK922990, MK922991, MK922992, MK922993, MK922994, MK922995, MK922996, MK935688, MK935689, MK935690, MK935691, MK935692, MK935693, and MK935694.

AUTHOR CONTRIBUTIONS

JTH planned the morphological and molecular analyses, examined the specimens, and wrote the main draft of the article.

HTR facilitated the molecular sequencing and morphological lab work, provided input on specimen data and species descriptions, and worked on the text of the manuscript. SP collected the specimens, provided collection data and footage, and worked on the text of the manuscript.

FUNDING

This work was supported by the NOAA/OER, award number NA14OAR4320260 to the Cooperative Institute for Ocean Exploration, Research, and Technology (to SP) and by the Bergen Research Foundation (BFS) (to HTR).

ACKNOWLEDGMENTS

We are indebted to the U.S. National Oceanic and Atmospheric Administration (NOAA), Office of OER for graciously allowing us to use ROV video footage from the EX1605 expedition for the purposes of documenting the species described in this article. We also thank the captain and crew of the NOAA ship *Okeanos Explorer* and the crew from the Global Foundation for Ocean Exploration, whose expertise in ROV operations enabled the collection of these fragile sponges. We thank the CAPSTONE chief scientist Dr. Christopher Kelley (University of Hawai'i at Mānoa), mission coordinator Kasey Cantwell (NOAA/OER), and leg 3 geology science lead Dr. Patricia Fryer (University of Hawai'i at Mānoa). Furthermore, we would like to thank David John Rees at the Department of Biology at the University of Bergen for sequencing the specimens in this article. Finally, we would like to thank Allen Collins at the National Museum of Natural History for facilitating the loan of the specimens from the USNM.

SUPPLEMENTARY MATERIAL

The Supplementary Material for this article can be found online at: https://www.frontiersin.org/articles/10.3389/fmars.2019.00371/full#supplementary-material

TABLE S1 | List of sequences used for the phylogenetic analysis.

REFERENCES

Boury-Esnault, N., and Rützler, K. (1997). *Thesaurus of Sponge Morphology*. Washington, D.C: Smithsonian Institution Press.

Cárdenas, P., Pérez, T., and Boury-Esnault, N. (2012). Sponge systematics facing new challenges. *Adv. Mar. Biol.* 61, 79–209. doi: 10.1016/B978-0-12-387787-1.00010-6

Carter, H. J. (1874). Descriptions and figures of deep-sea sponges and their spicules from the Atlantic Ocean, dredged up on board H.M.S. *Porcupine*, chiefly in 1869; with figures and descriptions of some remarkable spicules from the Agulhas shoal and Colon, Panama. *Ann. Magaz. Nat. Hist.* 14, 245–257. doi: 10.1080/00222937408680964

Carter, H. J. (1876). Descriptions and figures of deep-sea sponges and their spicules, from the Atlantic Ocean, dredged up on board H.M.S. *Porcupine*, chiefly in 1869 (concluded). *Ann. Magaz. Nat. Hist.* 18, 226–240. doi: 10.1080/00222937608682035

Cristobo, F. J., Urgorri, V., and Ríos, P. (2005). Three new species of carnivorous deep-sea sponges from the DIVA-1 expedition in the Angola Basin (South Atlantic). *Org. Divers. Evol.* 5, 203–213. doi: 10.1016/j.ode.2004.11.004

Dendy, A. (1922). Report on the sigmatotetraxonida collected by H.M.S.'Sealark' in the Indian Ocean. *Trans. Linn. Soc. Lond.* 18, 1–164, pls 1–18.

Dressler-Allame, M., Göcke, C., Kersken, D., Plotkin, A., and Janussen, D. (2016). Carnivorous sponges (Cladorhizidae) of the deep Weddell Sea, with descriptions of two new species. *Deep Sea Res. Part II* 137, 190–206. doi: 10.1016/j.dsr2.2016.08.006

Ereskovsky, A. V., and Willenz, P. (2007). *Esperiopsis koltuni* sp. nov. (Demospongiae: Poecilosclerida: Esperiopsidae), a carnivorous sponge from deep water of the Sea of Okhotsk (North Pacific). *J. Mar. Biol. Assoc. U. K.* 87, 1379–1386. doi: 10.1017/s0025315407058109

Goodwin, C., Berman, J., Downey, R., and Hendry, K. (2017). Carnivorous sponges (Porifera, Demospongiae, Poecilosclerida, Cladorhizidae) from the Drake Passage (Southern Ocean) with a description of eight new species and a review of the family Cladorhizidae in the Southern Ocean. *Invertebr. Syst.* 31, 37–64.

Grant, R. E. (1836). "Animal kingdom," in *The Cyclopaedia of Anatomy and Physiology*, Vol. 1, ed. R. B. Todd (London: Sherwood, Gilbert, and Piper), 1–813.

Hajdu, E., Van Soest, R. W. M., and Hooper, J. N. A. (1994). "Proposal for a phylogenetic subordinal classification of poecilosclerid sponges," in *Sponges in Time and Space*, eds R. W. Van Soest, T. M. Van Kempen, and J.-C. Braekman (Rotterdam: Balkema), 123–139.

Hestetun, J., Fourt, M., Vacelet, J., Boury-Esnault, N., and Rapp, H. (2015). Cladorhizidae (Porifera, Demospongiae, Poecilosclerida) of the deep Atlantic collected during Ifremer cruises, with a biogeographic overview of the Atlantic species. *J. Mar. Biol. Assoc. U. K.* 95, 1311–1342. doi: 10.1017/s0025315413001100

Hestetun, J. T., Pomponi, S., and Rapp, H. T. (2016a). The cladorhizid fauna of the Caribbean and adjacent areas. *Zootaxa* 4175, 521–538. doi: 10.11646/zootaxa.4175.6.2

Hestetun, J. T., Vacelet, J., Boury-Esnault, N., Borchiellini, C., Kelly, M., Ríos, P., et al. (2016b). The systematics of carnivorous sponges. *Mol. Phylogenet. Evol.* 94, 327–345. doi: 10.1016/j.ympev.2015.08.022

Hestetun, J. T., Rapp, H. T., and Xavier, J. (2017a). Carnivorous sponges (Porifera, Cladorhizidae) from the Southwest Indian Ocean Ridge seamounts. *Deep Sea Res. Part II* 137, 166–189. doi: 10.1016/j.dsr2.2016.03.004

Hestetun, J. T., Tompkins-Macdonald, G., and Rapp, H. T. (2017b). A review of carnivorous sponges (Porifera: Cladorhizidae) from the boreal North Atlantic and Arctic. *Zool. J. Linn. Soc.* 181, 1–69. doi: 10.1093/zoolinnean/zlw022

Hooper, J. N. A., and Lévi, C. (1989). *Esperiopsis desmophora* n. sp. (Porifera: Demospongiae): a desma-bearing Poecilosclerida. *Mem. Queensl. Mus.* 27, 437–441.

Ise, Y., and Vacelet, J. (2010). New carnivorous sponges of the genus *Abyssocladia* (Demospongiae, Poecilosclerida, Cladorhizidae) from Myojin Knoll, Izu-Ogasawara Arc, southern Japan. *Zool. Sci.* 27, 888–894. doi: 10.2108/zsj.27.888

Kelly, M., and Vacelet, J. (2011). Three new remarkable carnivorous sponges (Porifera, Cladorhizidae) from deep New Zealand and Australian (Macquarie Island) waters. *Zootaxa* 2976, 55–68.

Koltun, V. M. (1962). Four rayed and siliceous horny sponges from the Pacific shallow waters of Paramushir and Shumshu Islands. *Issledovaniya dal'nevostochnykh morei SSSR* 8, 181–199.

Koltun, V. M. (1970). "Sponge fauna of the northwestern Pacific from the shallows to the hadal depths," in *Fauna of the Kurile-Kamchatka Trench and its environment. Institute of Oceanology of the Academy of Sciences of the U.S.S.R. [English translation, 1972]*, ed. V. Bogorov (Jerusalem: Israel Program for Scientific Translations Ltd.), 1–372, pls I–VIII.

Lambe, L. M. (1900). Sponges from the coasts of northeastern Canada and Greenland. *Trans. R. Soc. Can.* 6, 19–49.

Lee, W. L., Reiswig, H. M., Austin, W. C., and Lundsten, L. (2012). An extraordinary new carnivorous sponge, *Chondrocladia lyra*, in the new subgenus *Symmetrocladia* (Demospongiae, Cladorhizidae), from off of northern California, USA. *Invertebr. Biol.* 131, 259–284. doi: 10.1111/ivb.12001

Lehnert, H., Stone, R., and Heimler, W. (2006). New species of deep-sea demosponges (Porifera) from the Aleutian Islands (Alaska, USA). *Zootaxa* 1250, 1–35.

Lévi, C. (1964). Spongiaires des zones bathyale, abyssale et hadale. *Galath. Rep. Sci. Results Danish Deep Sea Exped. Round World* 7, 63–112, pls II–XI.

Lévi, C. (1993). Porifera demospongiae: spongiaires bathyaux de Nouvelle-Calédonie, récoltés par le «Jean Charcot» Campagne BIOCAL, 1985. *Mém. Mus. Natl. Hist. Nat.* 158, 9–87.

Levinsen, G. M. R. (1887). Kara-havets svampe. *Dijmphna-Togtets zoologisk-botaniske Udbytte* 1, 339–372, pls XXIX–XXXI.

Lopes, D. A., Bravo, A., and Hajdu, E. (2011). New carnivorous sponges (Cladorhizidae: Poecilosclerida: Demospongiae) from off Diego Ramírez Archipelago (south Chile), with comments on taxonomy and biogeography of the family. *Invertebr. Syst.* 25, 407–443.

Lopes, D. A., and Hajdu, E. (2014). Carnivorous sponges from deep-sea coral mounds in the Campos Basin (SW Atlantic), with the description of six new species (Cladorhizidae, Poecilosclerida, Demospongiae). *Mar. Biol. Res.* 10, 329–356. doi: 10.1080/17451000.2013.797587

Lundbeck, W. (1905). Porifera (Part II.) Desmacidonidae. *Dan. Ingolf-Exp.* 6, 1–219.

Lundsten, L., Reiswig, H. M., and Austin, W. C. (2017). Three new species of *Cladorhiza* (Demospongiae, Poecilosclerida, Cladorhizidae) from the Northeast Pacific Ocean. *Zootaxa* 4317, 247–260. doi: 10.11646/zootaxa.3786.2.1

National Oceanic and Atmospheric Administration [NOAA] (2019). *Ocean Exploration and Research (OER) Digital Atlas Portal*. Available at: https://www.ncddc.noaa.gov/website/google_maps/OE/mapsOE.htm (accessed May 30, 2019).

Ridley, S. O., and Dendy, A. (1886). Preliminary report on the monaxonida collected by HMS 'Challenger'. *Ann. Magaz. Nat. Hist.* 5, 470–493. doi: 10.1080/00222938609459998

Riesgo, A., Taylor, C., and Leys, S. P. (2007). Reproduction in a carnivorous sponge: the significance of the absence of an aquiferous system to the sponge body plan. *Evol. Dev.* 9, 618–631. doi: 10.1111/j.1525-142x.2007.00200.x

Ríos, P., and Cristobo, J. (2018). *Abyssocladia vaceleti* (Porifera, Cladorhizidae): a new deep-sea carnivorous sponge from Patagonia. *Zootaxa* 4466, 164–173. doi: 10.11646/zootaxa.4466.1.13

Ríos, P., Kelly, M., and Vacelet, J. (2011). *Cercicladia australis*, a new carnivorous sponge with novel chelae from the tasman basin and the argentine patagonian margin (Porifera, Cladorhizidae). *Zootaxa* 3131, 52–62.

Sollas, W. J. (1885). A classification of the sponges. *Ann. Magaz. Nat. Hist.* 16, 395. doi: 10.1080/00222938509459901

Stern, R. J., Fouch, M. J., and Klemperer, S. L. (2004). An overview of the Izu-Bonin-Mariana subduction factory. *Geophys. Monogr.* 138, 175–222. doi: 10.1029/138gm10

Thomson, C. W. (1873). *The Depths of the Sea*. London: Macmillan and Co., 1–527.

Topsent, E. (1892). Contribution à l'étude des Spongiaires de l'Atlantique Nord (Golfe de Gascogne, Terre-Neuve, Açores). *Résultats des Campagnes Scientifiques Accomplies sur son Yacht Albert 1er Prince Souverain de Monaco* 2, 1–165, pls I–IX.

Topsent, E. (1909). Etude sur quelques *Cladorhiza* et sur *Eucheliplumа pristina* n. g. et n. sp. *Bull. l'Instit. Océanogr. Monaco* 151, 1–23.

Topsent, E. (1928). Spongiaires de l'Atlantique et de la Méditerranée provenant des croisières du Prince Albert ler de Monaco. *Résultats des Campagnes Scientifiques Accomplies par le Prince Albert I. Monaco*, 74, 1–376, pls I–XI. Available at: http://www.marinespecies.org/porifera/porifera.php?p=sourcedetails&id=8393

Topsent, E. (1930). *Chondrocladia yatsui* n. sp., de la Baie de Sagami. *Annot. Zool. Jpn* 1930, 421–432.

Vacelet, J. (2006). New carnivorous sponges (Porifera, Poecilosclerida) collected from manned submersibles in the deep Pacific. *Zool. J. Linn. Soc.* 148, 553–584. doi: 10.1111/j.1096-3642.2006.00234.x

Vacelet, J. (2007). Diversity and evolution of deep-sea carnivorous sponges. *Porifera Res.* 28, 107–115.

Vacelet, J. (2008). A new genus of carnivorous sponges (Porifera: Poecilosclerida, Cladorhizidae) from the deep N-E Pacific, and remarks on the genus *Neocladia*. *Zootaxa* 1752, 57–65. doi: 10.5281/zenodo.181741

Vacelet, J., and Duport, E. (2004). Prey capture and digestion in the carnivorous sponge *Asbestopluma hypogea* (Porifera: Demospongiae). *Zoomorphology* 123, 179–190. doi: 10.1242/jeb.072371

Vacelet, J., and Kelly, M. (2008). New species from the deep Pacific suggest that carnivorous sponges date back to the Early Jurassic. *Nat. Preced.*

Vacelet, J., and Kelly, M. (2014). A new species of *Abyssocladia* (Porifera, Demospongiae, Poecilosclerida, Cladorhizidae) and other carnivorous sponges from the far eastern Solomon Islands. *Zootaxa* 3815, 386–396. doi: 10.11646/zootaxa.3815.3.4

Vacelet, J., Kelly, M., and Schlacher-Hoenlinger, M. (2009). Two new species of *Chondrocladia* (Demospongiae: Cladorhizidae) with a new spicule type from the deep south Pacific, and a discussion of the genus *Meliiderma*. *Zootaxa* 2073, 57–68.

Van Soest, R. W. M. (2016). Sponge-collecting from a drifting ice floe: the Porifera obtained in the Kara Sea by the Dutch Polar Expedition 1882-83. *Contrib. Zool.* 85, 311–336. doi: 10.1163/18759866-08503004

Van Soest, R. W. M., Boury-Esnault, N., Hooper, J. N. A., Rützler, K., De Voogd, N. J., Alvarez, B. D. G., et al. (2019). *World Porifera Database*. Available at: http://www.marinespecies.org/porifera (accessed May 30, 2019).

Van Soest, R. W. M., and Hajdu, E. (2002). "Family Phellodermidae fam. nov," in *Systema Porifera. A Guide to the Classification of Sponges*, eds J. N. Hooper and R. W. Van Soest (New York, NY: Kluwer Academic/Plenum), 621–624. doi: 10.1007/978-1-4615-0747-5_65

Conflict of Interest Statement: The authors declare that the research was conducted in the absence of any commercial or financial relationships that could be construed as a potential conflict of interest.

Copyright © 2019 Hestetun, Rapp and Pomponi. This is an open-access article distributed under the terms of the Creative Commons Attribution License (CC BY). The use, distribution or reproduction in other forums is permitted, provided the original author(s) and the copyright owner(s) are credited and that the original publication in this journal is cited, in accordance with accepted academic practice. No use, distribution or reproduction is permitted which does not comply with these terms.

frontiers in Marine Science

BRIEF RESEARCH REPORT
published: 16 July 2019
doi: 10.3389/fmars.2019.00403

ROV Observations on Reproduction by Deep-Sea Cephalopods in the Central Pacific Ocean

*Michael Vecchione**

NOAA/NMFS National Systematics Laboratory, National Museum of Natural History, Washington, DC, United States

Telepresence-enabled operations by remotely operated vehicles (ROVs) allow many researchers a unique perspective on morphology, behavior, and small-scale distributions of deep-sea animals. I present some examples of cephalopod natural history from recent ROV dives in the central Pacific Ocean. These examples include clues to reproductive behavior of deep-sea squids and cirrate "dumbo" octopods. During March 7–12, 2017, the ROV *Deep Discoverer* (D2) operating from NOAA Ship *Okeanos Explorer* recorded high-definition video of several squid in the genus *Chiroteuthis*. These included a mature male, a mature female, and a moribund squid identifiable as *C. picteti*. The female had obviously mated, with spermatangia implanted in many locations, and was holding in its arms another squid that appeared to be another *Chiroteuthis*. Considered together, these observations may indicate a deep-sea spawning aggregation and, possibly, sexual cannibalism. Another series of observations by D2 revealed eggs of cirrate octopods attached to octocorals. The remarkable thing about these observations was that in two of them (March 18 and May 4) the egg chorion had swollen and burst the external egg capsule. This may explain how the hatching embryo is able to escape from the tough protective coating secreted by the oviducal gland of cirrates but not secreted by the better-known incirrate octopods.

Keywords: Cephalopoda, Cirrata, egg, Chiroteuthidae, mating, aggregation, cannibalism

OPEN ACCESS

Edited by:
Diva Amon,
Natural History Museum,
United Kingdom

Reviewed by:
Rui Rosa,
University of Lisbon, Portugal
José Marian,
University of São Paulo, Brazil
Mark C. Benfield,
Louisiana State University,
United States

***Correspondence:**
Michael Vecchione
vecchiom@si.edu

Specialty section:
This article was submitted to Deep-Sea Environments and Ecology, a section of the journal Frontiers in Marine Science

Received: *01 April 2019*
Accepted: *28 June 2019*
Published: *16 July 2019*

Citation:
Vecchione M (2019) ROV Observations on Reproduction by Deep-Sea Cephalopods in the Central Pacific Ocean. Front. Mar. Sci. 6:403. doi: 10.3389/fmars.2019.00403

INTRODUCTION

The Campaign to Address Pacific Monument Science, Technology, and Ocean Needs (CAPSTONE) was a multi-year study of deep-water United States marine protected areas (Kennedy et al., in press). Observations from the Remotely Operated Vehicle (ROV) *Deep Discoverer* in 2017 included several that were instructive about reproduction by deep-sea cephalopods. I present observations contributing to two separate topics relative to reproduction by deep-sea cephalopods: (1) Cirrate octopod eggs and how they likely hatch, and (2) Mating, possibly in a population aggregation, and possible sexual cannibalism in a chiroteuthid squid species.

Unlike more familiar incirrate octopods, cirrates coat their eggs in a thick layer secreted by the oviducal gland (Vecchione et al., 1998). Vecchione et al. (1998) found that this coating rapidly hardens when exposed to seawater. Also in contrast with incirrates, recent observations of a fully developed cirrate embryo (Shea et al., 2018) found no evidence of a hatching gland. How the hatchling escapes from the thick, hard coating over the chorion has therefore been a mystery.

Observations on mating by deep-sea squids are few, but have indicated diverse patterns (Hoving et al., 2014). Although squids of the genus *Chiroteuthis* have been observed from ROVs and other submersibles several times, especially in the eastern North Pacific (Burford et al., 2015), *in situ* observations of mating behavior or mated individuals are, until now, unknown.

MATERIALS AND METHODS

The general rationale and Methods for CAPSTONE are summarized by Kennedy et al. (in press). Briefly, the CAPSTONE cruises featured "telepresence-enabled" dives by ROVs, in which the live video feed and associated data are transmitted ashore and distributed in "real time" via the internet so that scientists ashore could participate in ROV operations. The ROV operated from

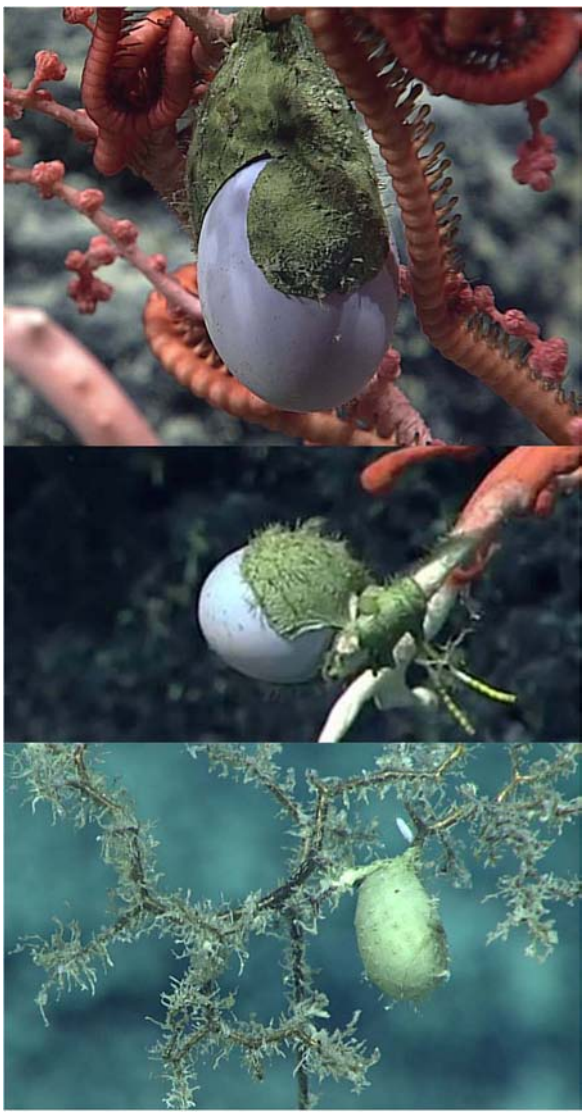

FIGURE 1 | High-definition video frames of cirrate octopod eggs. See **Table 1** for associated environmental data. In top and middle images the outer coating has ruptured and the smooth chorion is visible. The bottom image is intact and differs from the top and middle in both morphology and the cnidarians species to which it is attached.

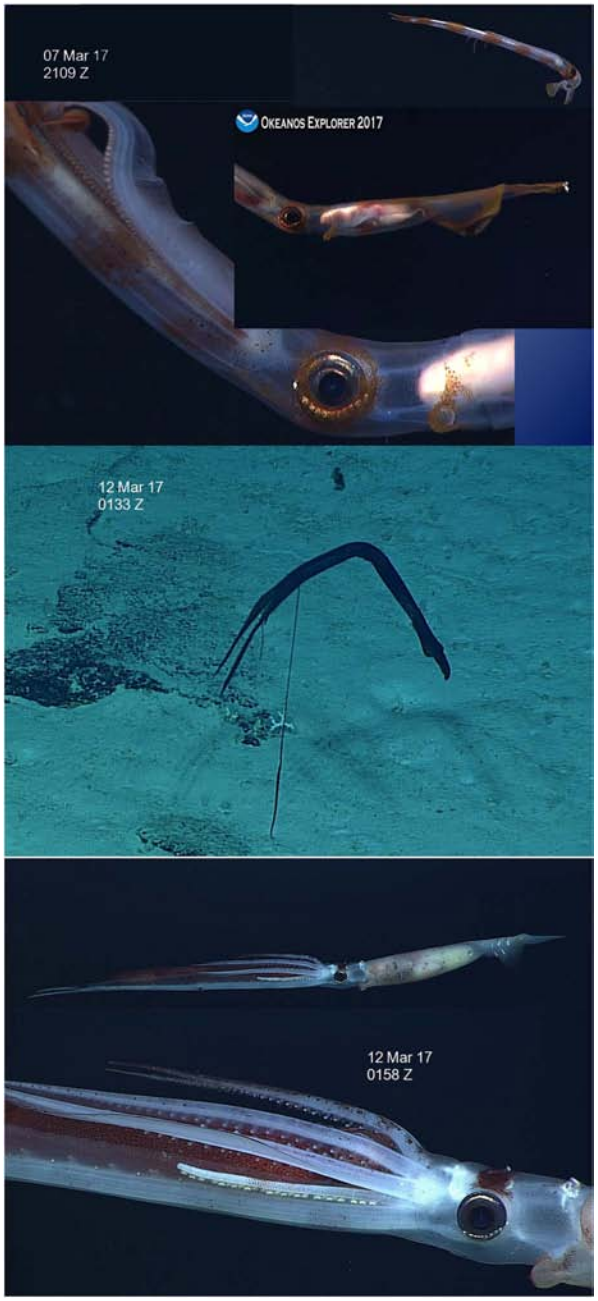

FIGURE 2 | High-definition video frames of squids in the genus *Chiroteuthis*. See **Table 2** for associated environmental data. Top (with insets): a mature male with spermatophores stored in Needham's sac; Middle: modibund, or perhaps dead, individual with tentacle club visible; Bottom (with inset): a mature, mated female with spermatangia (implanted sperm masses) visible on the head, mantle, and fins. This female was holding a long, narrow squid (expanded chormatophores visible) in its arms; this engulfed squid, presumably another *Chiroteuthis*, was motionless and the chromatophores were not contracting.

NOAA Ship *Okeanos Explorer*. Following each cruise, videos and data are archived ashore and available online for further examination and analyses.

During the CAPSTONE cruises, three ROV dives on three separate dates observed cirrate eggs on two different cruise legs (**Table 1**). Two other dives within a few days of each other on a single cruise leg (**Table 2**) included encounters with the squid genus *Chiroteuthis* (see Section "Discussion" for inference of specific identification), all of which included indications consistent with a mating event.

RESULTS

Cirrate Eggs

Three observations (**Table 1** and **Figure 1**) by the ROV Deep Discoverer (D2) revealed eggs of cirrate octopods attached to cnidarian colonies. The remarkable thing about these observations was that in two of them (**Figure 1**, Top and Middle) the egg chorion had swollen and burst the external egg capsule. These two observations were very similar in overall morphology and both eggs were attached to "bubblegum" octocorals. The third observation (**Figure 1**, Bottom) differed in both appearance and attachment from the other two. The external egg capsule was not ruptured and it also differed slightly in surface texture from the other two capsules. It also appeared not quite as dark as the other two, although this could be an artifact of the lighting from the ROV. The substrate to which it was attached was a different octocoral not a "bubblegum".

Chiroteuthis

During March 7–12, 2017, D2 recorded high-definition video of several squid in the genus *Chiroteuthis*. These included a mature male with spermatophores in its Needham's sac (**Figure 2**, Top), a mature female with well-developed nidamental glands as well as large obvious ovary (**Figure 2**, Bottom), and a moribund squid (**Figure 2**, Middle). The female had obviously mated, with spermatangia implanted in many locations, and was holding in its arms another long, thin squid (identifiable as a squid from its chromatophores in the high-definition video) that appeared to be another *Chiroteuthis*. The eye photophores on the male and the female were in multiple series of discrete, circular organs (as opposed to photogenic strips), but whether there were two or three series per eyeball could not be determined for certain. The eye photophoress could not be seen on the moribund individual, but its tentacle club was visible.

DISCUSSION

We have known since the late 1800s that cirrate octopods attach their eggs to deep-sea octocorals. However, unlike incirrate octopods with their well-known maternal egg care, cirrates protect their eggs with a thick, tough coating. It has been unclear how cirrate hatchlings can get through that coating when they hatch. Indeed, Shea et al. (2018) looked for, but did not find, a hatching gland, similar to those used by incirrate octopods to escape the egg, in a cirrate embryo. Cephalopod eggs swell during embryonic development (Boletzky, 1989). These observations from the ROV *Deep Discoverer* show that swelling of the cirrate egg chorion bursts the end of the coating away from the attachment point. This would allow the cirrate embryo to hatch through the chorion as other cephalopods do. This may explain how the hatching embryo is able to escape from the tough protective coating secreted by the oviducal gland of cirrates but not secreted by the better-known incirrate octopods. However, the mechanism used by the cirrate embryo to penetrate the chorion remains a mystery. Identification of these observations is not possible based on our current state of knowledge about cirrate eggs.

Villanueva (1992) illustrated egg capsules of species in the cirrate genus *Opisthoteuthis*. His observations included a smooth distal area in the egg capsule of *O. agassizii* that appears to correspond with the ruptured area in the first two observations here. Also, Villanueva (1992) found a faint line on the egg capsule of *O. vossi* that might correspond with the line of rupture on the present observations.

TABLE 1 | Observations on cirrate octopod eggs.

Cruise	Date	Time (UTC)	Figure	Latitude	Longitude	Depth (m)	Temp °C
EX1703	18 March 2017	211945Z	1 (top)	0.80	−176.7	2215	2.1
EX1705	05 May 2017	010036Z	1 (middle)	−1.51	−159.5	1626	2.7
EX1705	10 May 2017	221527Z	1 (bottom)	5.85	−162.5	2117	2.2

UTC: Universal time coordinated.

TABLE 2 | Observations on chiroteuthid squids.

Cruise	Date	Time (UTC)	Figure	Latitude	Longitude	Depth (m)	Temp °C
EX1703	07 March 2017	210944Z	2 (top, including insets)	−11.05	−171.1	1105	4.1
EX1703	12 March 2017	013355Z	2 (middle)	−4.15	−174.9	1035	4.3
EX1703	12 March 2017	015813Z	2 (bottom, incl. inset)	−4.15	−174.9	1035	4.3

UTC: Universal time coordinated.

Specific identifications are often a problem when dealing with *in situ* imagery for which specimens have not been collected. This series of observations of squid belonging to the genus *Chiroteuthis*, when considered together, indicate reproductive behavior unknown in cephalopods. The series of discrete eye photophores are consistent with species of both the *C. picteti* species group and the *C. joubini* group (Roper et al., 2019). However, tentacle clubs with structure similar to that of the moribund squid are only found in the former. Assuming they are all the same species, the eye photophores of the first and last, together with the tentacle club of the middle squid are diagnostic of *C. picteti*, the dominant species in this species group in the Indo-West Pacific. The first observation was a mature male with spermatophores visible in Needham's sac. The second was floating moribund or dead; reproduction is terminal in many cephalopods. The third was a mature female with nidamental glands visible through the mantle and with spermatangia implanted on the mantle, fins, and head. It was holding in its arms a long narrow squid with motionless chromatophores. The long, narrow morphology is consistent with the genus *Chiroteuthis*, although other rare deep-sea squids have similar morphology. As these are the only CAPSTONE observations of any such squids, it seems likely that the unfortunate squid was another *Chiroteuthis.* This may indicate sexual cannibalism of the male after mating. Conditions expected to be present in sexual cannibalism include (1) terminal reproduction, (2) mature females generally larger than males, and (3) female fecundity increasing with size (Ibánez and Keyl, 2010). Terminal reproduction is typical of deepsea squids, as is increased fecundity with increased size; I assume these to be the situation for Chiroteuthids. Almost nothing is known about mature *Chiroteuthis.* Of the only reported mature specimens of *C. picteti*, the female was much larger than the male (Roper and Young, 2017). Therefore *C. picteti* likely meets the expectations of Ibánez and Keyl (2010) for sexual cannibalism. Furthermore, these three squid, observed close together in time and space, were the only *Chiroteuthis* observed during the CAPSTONE cruises. This co-occurrence may indicate aggregating by this species for mating.

DATA AVAILABILITY

The datasets generated for this study are available on request to the corresponding author.

AUTHOR CONTRIBUTIONS

The author confirms being the sole contributor of this work and has approved it for publication.

ACKNOWLEDGMENTS

I thank NOAA's Ocean Exploration Program and the CAPSTONE participants, both at sea and ashore.

REFERENCES

Boletzky, S. V. (1989). Recent studies on spawning, embryonic development, and hatching in the Cephalopoda. *Adv. Mar. Biol.* 25, 85–115. doi: 10.1016/s0065-2881(08)60188-1

Burford, B. P., Robison, B. H., and Sherlock, R. E. (2015). Behaviour and mimicry in the juvenile and subadult life stages of the mesopelagic squid *Chiroteuthis calyx. J. Mar. Biol. Assoc.* 95, 1221–1235. doi: 10.1017/s0025315414001763

Hoving, H.-J., Perez, J. A. A., Bolstad, K. S. R., Braid, H. E., Evans, A. B., Fuchs, D., et al. (2014). The study of deep-sea cephalopods. *Adv. Mar. Biol.* 67, 235–359.

Ibánez, C. M., and Keyl, F. (2010). Cannibalism in cephalopods. *Rev. Fish Biol. Fish.* 20, 123–136. doi: 10.1007/s11160-009-9129-y

Roper, C. F. E., and Young, R. E. (2017). *Chiroteuthis Picteti Joubin, 1894. Version 10. (Under Construction).* Available at: http://tolweb.org/Chiroteuthis_picteti/19477/2017.10.10 (accessed June 14, 2019).

Roper, C. F. E., Young, R. E., and Vecchione, M. (2019). *Chiroteuthis Orbigny, 1841. Version 26 (Under Construction).* Available at: http://tolweb.org/Chiroteuthis/19462/2019.03.26 (accessed June 14, 2019).

Shea, E. K., Ziegler, A., Faber, C., and Shank, T. M. (2018). Dumbo octopod hatchling provides insight into early cirrate life cycle. *Curr. Biol.* 28, R135–R147. doi: 10.1016/j.cub.2018.01.032

Vecchione, M., Piatkowski, U., and Allcock, A. L. (1998). Biology of the cirrate octopod *Grimpoteuthis glacialis* (Cephalopoda; Opisthoteuthidae) in the South Shetland Islands, Antarctica. *S. Afr. J. Mar. Sci.* 20, 421–428. doi: 10.2989/025776198784126467

Villanueva, R. (1992). Continuous spawning in the cirrate octopods *Opisthoteuthis agassizii* and *O. vossi*: features of sexual maturation defining a reproductive strategy in cephalopods. *Mar. Biol.* 114, 265–275. doi: 10.1007/bf00349529

Conflict of Interest Statement: The author declares that the research was conducted in the absence of any commercial or financial relationships that could be construed as a potential conflict of interest.

Copyright © 2019 Vecchione. This is an open-access article distributed under the terms of the Creative Commons Attribution License (CC BY). The use, distribution or reproduction in other forums is permitted, provided the original author(s) and the copyright owner(s) are credited and that the original publication in this journal is cited, in accordance with accepted academic practice. No use, distribution or reproduction is permitted which does not comply with these terms.

frontiers in Marine Science

ORIGINAL RESEARCH
published: 02 August 2019
doi: 10.3389/fmars.2019.00460

The Extent of Fault-Associated Modern Authigenic Barite Deposits Offshore Northern Baja California Revealed by High-Resolution Mapping

Roberto H. Gwiazda, Charles K. Paull, David W. Caress, Christina Marie Preston, Shannon B. Johnson, Eve M. Lundsten and Krystle Anderson*

Monterey Bay Aquarium Research Institute, Moss Landing, CA, United States

OPEN ACCESS

Edited by:
William W. Chadwick, Pacific Marine Environmental Laboratory (NOAA), United States

Reviewed by:
Samuel Yorks Johnson, Pacific Coastal and Marine Science Center, United States Geological Survey, United States
John William Jamieson, Memorial University of Newfoundland, Canada

***Correspondence:**
Roberto H. Gwiazda
rgwiazda@mbari.org

Specialty section:
This article was submitted to Deep-Sea Environments and Ecology, a section of the journal Frontiers in Marine Science

Received: *26 March 2019*
Accepted: *10 July 2019*
Published: *02 August 2019*

Citation:
Gwiazda RH, Paull CK, Caress DW, Preston CM, Johnson SB, Lundsten EM and Anderson K (2019) The Extent of Fault-Associated Modern Authigenic Barite Deposits Offshore Northern Baja California Revealed by High-Resolution Mapping. Front. Mar. Sci. 6:460. doi: 10.3389/fmars.2019.00460

High-resolution mapping with an autonomous underwater vehicle (AUV) of a section of the San Clemente fault, offshore Southern California, reveals the largest documented cold-seep-associated barite deposits discovered to date. Although barite deposits along this fault, north of the mapped area, have been observed and sampled before in submersible dives, this study reveals massive newly found outcrops. The high-resolution surveys resolve their small-scale morphology, their large geographical extent and the structural controls on their emplacement. Detailed bathymetry (1 m × 1 m × 0.25 m grid resolution) of a ∼12 km^2 area, ranging in water depths between 962 and 1,300 m and intersected by the fault, exhibits quasi-circular mounds of 10–30 m planar dimensions rising up to 11 m above the surrounding seafloor on a 30–45 m high and at least 1,100 m long ridge, and along truncated strata, but not along the main fault strand. Observations from a remotely operated vehicle (ROV) show that the mounds consist of steep sided dark-varnished blocks of barite. Active barite precipitation occurs as white friable spires emerging from the older deposits and as white porous precipitates filling fissures. Upward thinning spires and microbial mat occurrences atop the spires are consistent with aggradational growth due to precipitation from upward flowing solutions. Live *Lamellibrachia* tubeworms are found in association with the fissure-filling barite precipitates. Mapping surveys were also conducted along a short section of the San Clemente fault south of the Navy Fan. In addition, a 9 km^2 area along the San Diego Trough Fault south of the United States-Mexico border was mapped and visited in an ROV dive. In the three mapped regions sub-bottom chirp profiles indicate that often barite precipitation occurs where strata, truncated and uplifted by the fault, has thin or no sediment drape, allowing for Ba-rich solutions, that may have ascended through the main fault zone, to flow along bedding planes and mix with seawater sulfate at the seafloor interface. Despite the massive scale of the barite mounds,

they are not resolvable in surface ship multibeam-generated bathymetry (25 m grid resolution). As only a few areas have been mapped at the high-resolution employed in this study, the full extent of these deposits along the San Clemente Fault and other faults remains unknown.

Keywords: authigenic barite, barite deposits, high-resolution mapping, San Clemente fault, San Diego trough fault, cold seep barite, autonomous underwater vehicle, remotely operated vehicle observations

INTRODUCTION

Seafloor investigations of the California Borderland have occasionally revealed the presence of authigenic barite ($BaSO_4$) deposits. This evidence was collected by exploratory dredges and manned submersible dives (Revelle and Emery, 1951; Lonsdale, 1979; Torres et al., 2000, 2002; Hein et al., 2007). The most comprehensive studies were conducted on a barite outcrop on the San Clemente Fault, first visited by Lonsdale (1979) with the manned submersible *Seacliff*. Later, the same general area was investigated in dives with the manned submersible *Alvin* (Torres et al., 2002). Nevertheless, aside from visual descriptions, photographic images, and samples of barite deposits, the occurrence, geographical extent, structural relationship with faults, and detailed morphology of barite deposits on the California borderland are poorly known.

In addition to the cold-seep barite deposits along the San Clemente Fault, active cold-seep barite deposits in a range of sizes have been documented in several locations around the world. The largest occurrence is in the highly productive Derugin Basin in the Sea of Okhotsk where barite aggregates in column-shaped structures up to 10 m high occur scattered over an area of 22 km^2 in association with authigenic carbonate precipitates and chemosynthetic biological communities (Greinert et al., 2002; Aloisi et al., 2004). An association between exposure of old sediments to bottom waters and the occurrence of cold-seep barite deposits has been noted in several locations. In the Peru Margin, barite deposits were found at sites of fluid seepage along two several-hundred meters tall escarpments and a canyon wall where slope failures exposed older sediment sequences to bottom water (Torres et al., 1996a; Aquilina et al., 1997). Similarly, cold-seep barite precipitates were found in Tubeworm Slump (Naehr et al., 2000), a slide scar on the floor of the highly productive Monterey Bay, offshore California, where old sediment sequences are exposed to bottom seawater. Other known locations with cold-seep barite deposits of a more diffuse character and/or with smaller buildups are the Gulf of Mexico (Feng and Roberts, 2011), Alaska (Suess et al., 1998) and Gulf of California (Canet et al., 2013). Torres et al. (2003), summarized the sequential processes leading to the formation of cold-seep barite deposits: enhanced barium and carbon flux associated with high productivity on overlying waters; remobilization of barium in reduced pore waters devoid of sulfate due to consumption by methane, and precipitation of barite when reduced fluids rich in Ba are exposed to oxic, sulfate-rich bottom waters.

The accumulation of barite at fault-associated cold-seeps is believed to be a modern analog to Paleozoic and older stratiform barite ore deposits, which are the most important source of industrial barite (Clark et al., 2004). This association is based on their similarity in barite crystallography, barite crystal arrangement texture, lack of polymetallic sulfides, lithological character of hosting strata, and association with faults or steep slopes (Torres et al., 2003). Tectonically active basins near continental margins are considered to be suitable environments for the accumulation of these deposits (Torres et al., 2003; Koski and Hein, 2004). In such settings, tectonic motions displace, uplift and expose older organic-rich reduced sediments to bottom seawater. Active flow of Ba-rich fluids to the seafloor creates favorable conditions for the precipitation of authigenic minerals because ascending waters mix with bottom seawater having a different redox and chemical saturation state.

Here we report new discoveries in the California Borderland of barite deposits of a large geographical and vertical extent. During the course of high-resolution mapping with an autonomous underwater vehicle (AUV) to document recent movements along the dextral strike-slip faults that form the transform boundary between the Pacific and North American plates offshore southern California, barite deposits were discovered along segments of the San Clemente Fault and of the San Diego Trough Fault zones (**Figure 1A**). The mapped sections had been selected for higher resolution mapping based on previously collected surface-ship multibeam data that suggested the presence of scarp lineaments indicative of recently faulted strata. In the newly surveyed segment of the San Clemente Fault the high-resolution map reveals kilometer-scale patches of a very rugged morphology. Subsequent inspection with a remotely operated vehicle (ROV) confirmed that the rough bathymetry was composed of massive columnar deposits of authigenic barite. Furthermore, one of these surveys partially covered the site where the earlier observations of barite outcrops had been made. In addition, barite was also found on the San Diego Trough Fault zone. Here we document the morphology and extent of these deposits, as well as their occurrence in relation to the imaged fault segments.

MATERIALS AND METHODS

High-resolution maps and sub-bottom chirp profiles were collected during three AUV surveys, followed by ROV dives at two of the AUV mapped sites (**Figure 1A**). The AUV designed by the Monterey Bay Aquarium Research Institute (MBARI) carried a 200 kHz multibeam sonar and a 1−6 kHz chirp sub-bottom profiler. The vehicle navigated 50 m above the seafloor at a speed of 3 knots for 18 h along predefined lines spaced ∼150 m apart. The overlap between swaths was 60 m. Multibeam data were processed with the software package MB-System (Caress et al.,

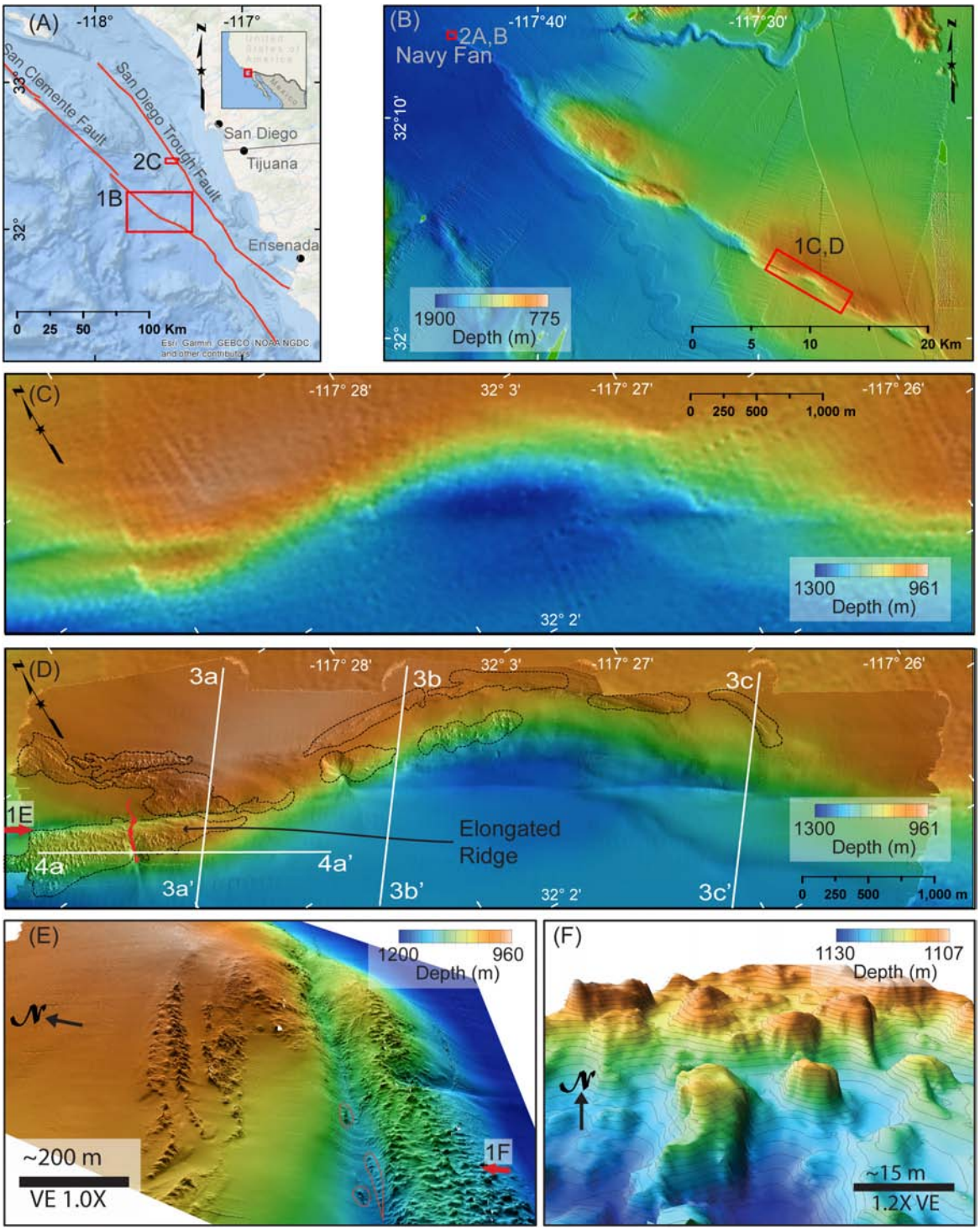

FIGURE 1 | (A) Regional map showing study area offshore California and Mexico's border. **(B)** Surveyed sections of the San Clemente Fault. Red squares identify the locations of **C,D**, **Figures 2A,B**. **(C)** Bathymetry from surface-ship multibeam data of the main area surveyed along the San Clemente Fault. Resolution is 25 × 25 m. **(D)** Bathymetry from AUV data of the same area shown in **C**. Resolution is 1 × 1 × 0.25 m. The red line is the path of ROV dive DR767. White lines are the traces of chirp sub-bottom profiles shown in **Figures 3**, **4**. Black dashed lines encircle areas with rough morphology indicative of barite mounds. Red arrow shows the direction of the perspective view shown in **E**. **(E)** A perspective view showing the rough morphology and central depression where the main strand of the San Clemente fault is presumably located. Abundant barite mounds are found on the elongated ridge south of the main strand of the fault and along strata on the top of the escarpment north of it. Red lines encircle linear arrangements of barite deposits found on the central trough that are parallel to the main strand of the fault. **(F)** A perspective view of barite mounds south of the trough, zoomed in, and vertically exaggerated to show individual mounds. Contours are 2 m.

2008) to generate grids with a resolution of 1 m × 1 m × 0.25 m. The chirp profiles have a vertical resolution of 10 cm and can image up to ∼40 m sub-bottom depths. Video observations and samples were subsequently collected using MBARI's ROV *Doc Ricketts*.

AUV survey-1 was conducted along the San Clemente Fault on a 6 km long × 1.9 km wide section of the seafloor centered at 32.0433°N 117.4632°W over a water depth range of 962 to 1,300 m (**Figure 1D**). ROV dive DR767 was also conducted on this segment of the fault guided by the AUV map (**Figure 1D**). AUV survey-2 was conducted further north along the San Clemente Fault in the Navy Fan (**Figure 1B**). In **Figures 2A,B** we present a map and perspective view of a small 0.25 km^2 area in the Navy Fan that is just slightly north of the site along the San Clemente Fault where the presence of barite deposits in the California Borderland was first described (Lonsdale, 1979; Torres et al., 2000, 2002). The full extent of the Navy Fan AUV map is in Carvajal et al. (2017). AUV survey-3 took place over a 5.7 × 1.6 km section of the San Diego Trough Fault just south of the United States-Mexico border (**Figures 1A**, **2C**). A subsequent ROV dive (DR769) encountered outcrops of barite on the flanks of a ridge abutting the fault trough (**Figure 2C**). No temperature probe was deployed from the ROV in either dive.

Eight rock samples were collected in the ROV dives [San Clemente Fault (n = 6) and San Diego Tough Fault (n = 2)]. Strontium isotopes of the rock samples were measured by Actlabs, Ontario, Canada, via multicollector ICP-MS after hot sodium peroxide fusion, following the procedure described in Holmden et al. (1997). Long term external precision was ± 0.00002 (2σ) for the $^{87}S/^{86}Sr$ ratio based on repeated analyses of SRM 987. Sulfur isotopes of barite and carbon isotopes of carbonate were measured by Isotech laboratories Inc., Illinois, United States. Isotope ratios are expressed in delta notation (per mil deviation from the isotopic ratio of a standard) using the Vienna Canyon Diablo Troilite standard (VCDT) and the Vienna Pee-Dee Belemnite (VPDB) as standards for sulfur and carbon isotope ratios, respectively. Long term reproducibility of isotopic measurements at Isotech laboratories, Inc., is 0.5% (1σ) for $\delta^{34}S$, and 0.3% (1σ) for $\delta^{13}C$. Mineral composition was analyzed by powder X-ray diffraction by Metallurgical Engineering Services Inc., Richardson, Texas. Concentrations of trace elements, chalcophile elements and REE were measured by Actlabs, Ontario, Canada, by ICP-MS after lithium metaborate/tetraborate or hot sodium peroxide fusion, and by neutron activation analyses. Measurements of standard reference materials yielded concentrations inaccuracies of less than 25% in 90% of the of the elements measured (**Supplementary Table S1**).

Microbial mats were peeled off rocks collected by the *ROV* using tweezers, then stored at −80°C until processed. Genomic DNA from several replicates was isolated with a PowerSoil®DNA isolation Kit (MO BIO Laboratories, Carlsbad, CA, United States). Genomic DNA was used for Illumina MiSeq high-throughput amplicon sequencing (Illumina Inc., San Diego, CA, United States) using the 16S rRNA V4 primers 515F (Parada et al., 2016) and 806R (Caporaso et al., 2010, 2011) with Illumina adapters and barcodes per methods of the Earth Microbiome Project (Thompson et al., 2017). Data were analyzed using QIIME 2 (Caporaso et al., 2011).

RESULTS

AUV Mapping

AUV survey-1 mapped a 6 km long area traversed longitudinally by the strike-slip San Clemente Fault. The AUV map and the map obtained from surface ship multibeam data[1] (**Figures 1C,D**) both show the major topographic features in this area: The area is bisected by a linear trough, with the northern side dominated by a 245 m high escarpment (slope ∼22°) and the southern side displaying a central basin and a narrow elongated ridge to the west. However, the AUV-generated map is rich in details not discernible in the surface ship multibeam grid, most notably the large patches of distinctly rough surface morphology.

The high-resolution map shows the rough surface is composed of a field of closely clustered large mounds on the elongated ridge at the western corner of the mapped area (lower left quadrant **Figures 1D,E**). The mound morphology consists of quasi-circular to elongated features, with planar dimensions ranging from 10 to 30 m and heights up to 11 m above the surrounding seafloor (**Figure 1F**). Mounds cover up to 50% of the seafloor area of the 300 to 550 m wide ridge which rises 30 to 45 m above the surrounding seafloor. Some mounds appear to preferentially occur in rows which run parallel to the trough where the main strand of the San Clemente Fault is presumably located (**Figure 1E**). The linear arrangement of the mounds is more evident on the northern side of the fault where they appear to follow the truncated strata exposed along the upper section of the escarpment (**Figures 1E**, **3**). Mounds also occur in several other patches along the face of the escarpment that slopes from the north toward the inferred main fault trace (**Figure 3**). However, this morphology is not present along the main fault trace.

A row of 2−3 m tall cones along the foot of a scarp on the Navy Fan, as well as scattered ∼1 m high lumps on the scarp face, were imaged at the edge of AUV survey-2 (**Figure 2A**). These features are just 500 m further northwest along the trace of the fault from the ≤4 m high mounds found by Lonsdale (1979) and 3 km from the 1 m high mounds observed on *Alvin* dives (Torres et al., 2000, 2002). The size of individual mounds and their geographical extent in this segment of the San Clemente Fault are apparently considerably reduced compared to their size and distribution at the new site discovered in the San Clemente Fault in AUV survey-1, 31 km further to the southwest (**Figure 1D**).

A section of the San Diego Trough Fault just south of the United States-Mexico border was mapped in AUV survey-3 (**Figures 1A**, **2C**). The fault zone manifests on the seafloor as a distinct linear depression bisecting the survey area in a north-northwest to south-southeast direction. The bathymetry is dominated by a set of push-up ridges and pull apart basins created by motion along the fault. Rough seafloor textures like those imaged along the San Clemente Fault were not detected

[1]https://www.ngdc.noaa.gov/mgg/bathymetry/relief.html

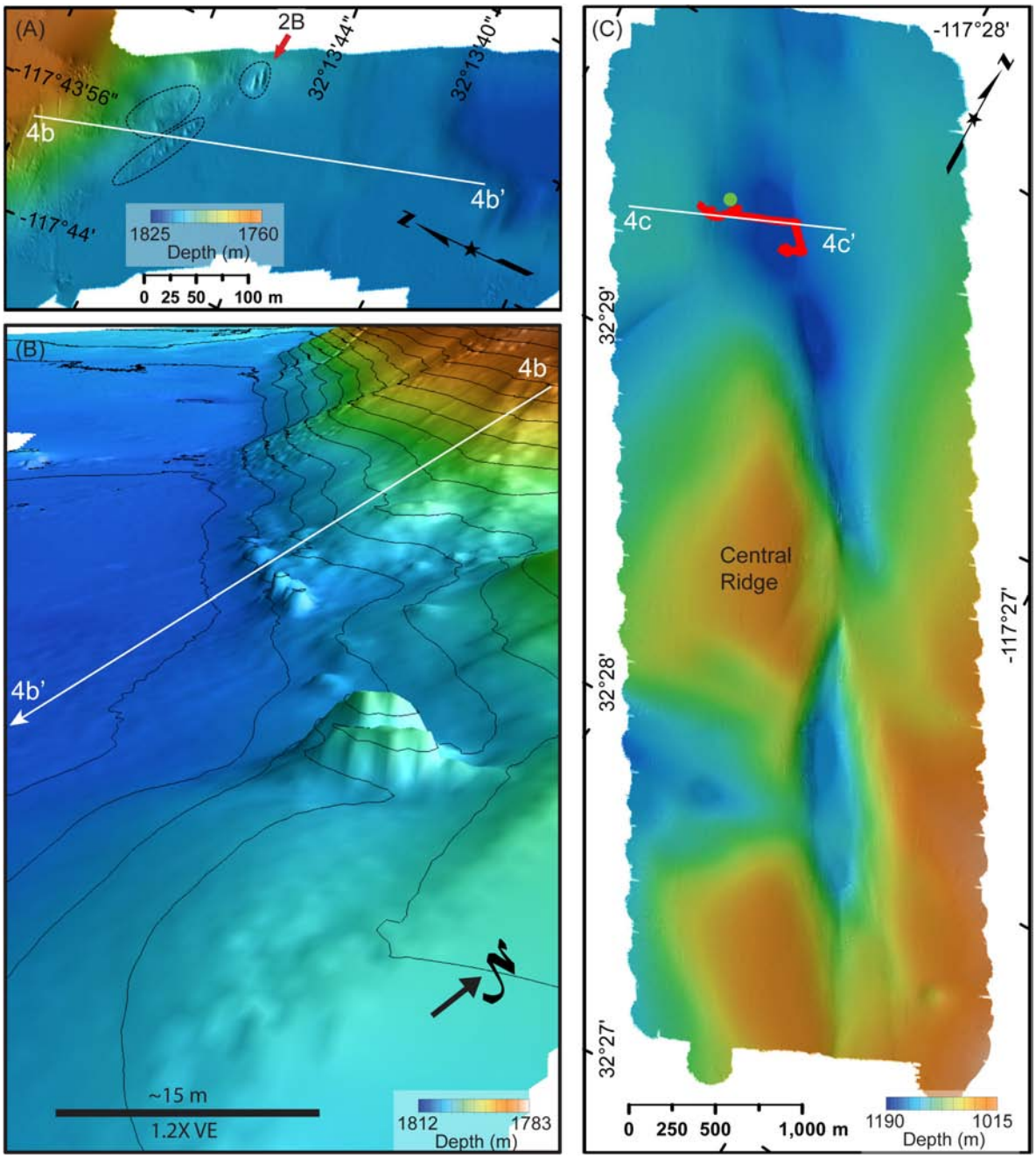

FIGURE 2 | (A) A small section of AUV collected bathymetry on the San Clemente Fault in the Navy Fan area. Black dashed lines encircle areas with rough morphology indicative of barite mounds. Red arrow indicates the direction of the perspective view shown in panel **B**. White line is the location of the chirp sub-bottom profile shown in **Figure 4B**. **(B)** A perspective view of the mounds on the escarpment above the San Clemente Fault. Contours are 2 m. White line is the location of the chirp sub-bottom profile shown in **Figure 4B**. **(C)** AUV collected bathymetry on a section of the San Diego Trough Fault. The red line shows the path of ROV dive DR769. The green dot indicates the location of a barite deposit. White line is the location of the chirp sub-bottom profile shown in **Figure 4C**.

in this survey including the location where barite outcrops were observed in ROV dive DR769 (see below) (**Figure 4C**).

Chirp Profiles

A profile across the San Clemente Fault zone in AUV survey-1 shows that the large mound structures on the elongated ridge appear as a diffuse bumpy fuzz above the seafloor reflection (**Figure 4A**, profile trace 4a−4a′ in **Figure 1D**). Strata uplifted by motion along the fault is documented in the chirp profiles. A profile normal to the fault shows that the dips of the strata on both sides of the fault trough are different and oriented away from the trough (**Figure 3A**, profile trace 3a−3a′ in **Figure 1D**). On the

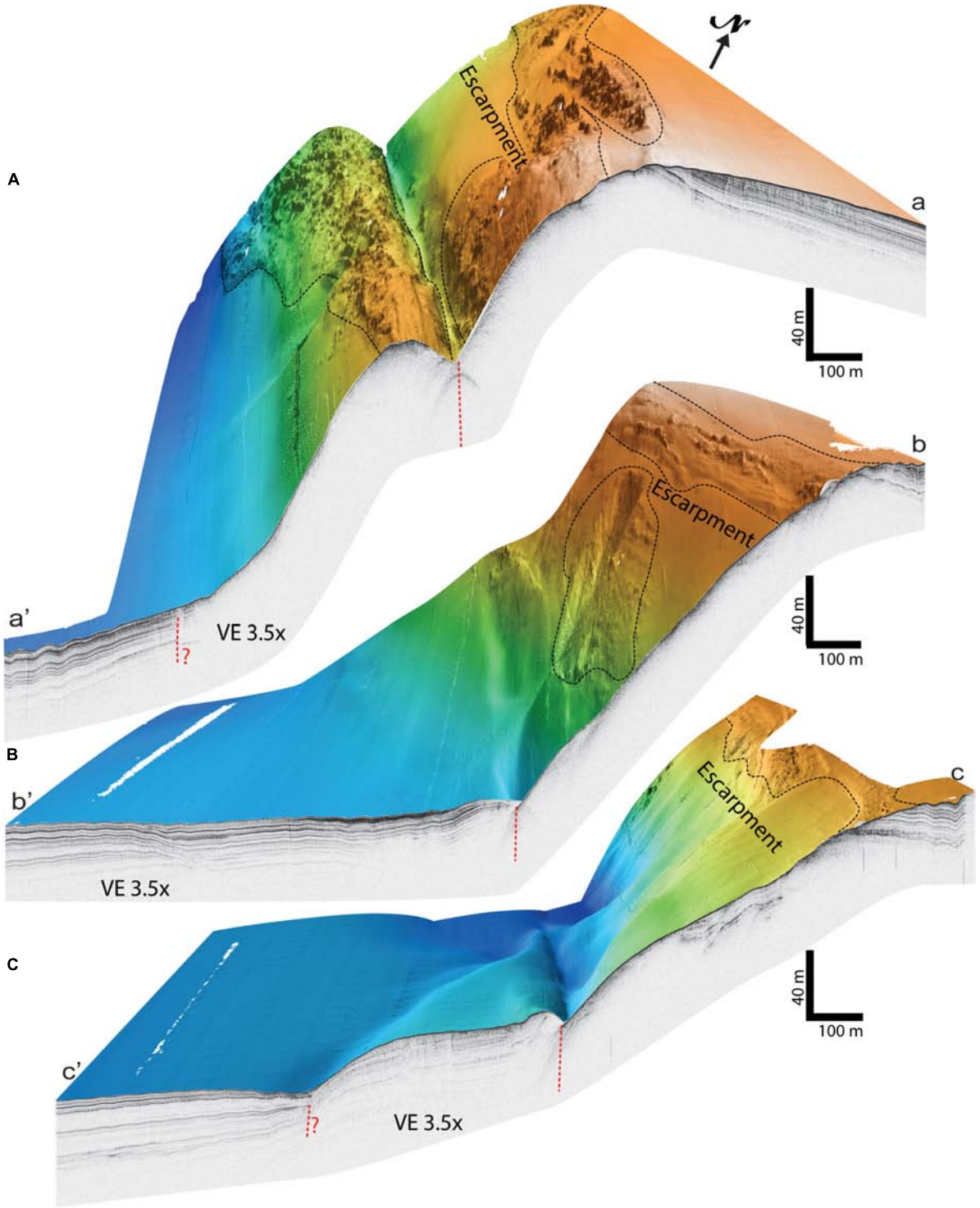

FIGURE 3 | Composite figure showing chirp profiles approximately placed on a perspective view of AUV collected bathymetry at the San Clemente Fault. Location of chirp lines shown in **A–C** are indicated in **Figure 1D**. Faults are shown as dashed red lines. Black dashed lines encircle areas with rough morphology indicative of barite mounds.

northern side of the fault trough, layered sediments are visualized on top of the ridge with an apparent 4° dip to the northeast. Profiles from the nearly flat basin floor on the southern side of the fault zone show up to 40 m of layered sediments which dip 4.5° to the southwest as they approach the main strand of the fault, and either pinch out or lap up on the flank of the ridge before

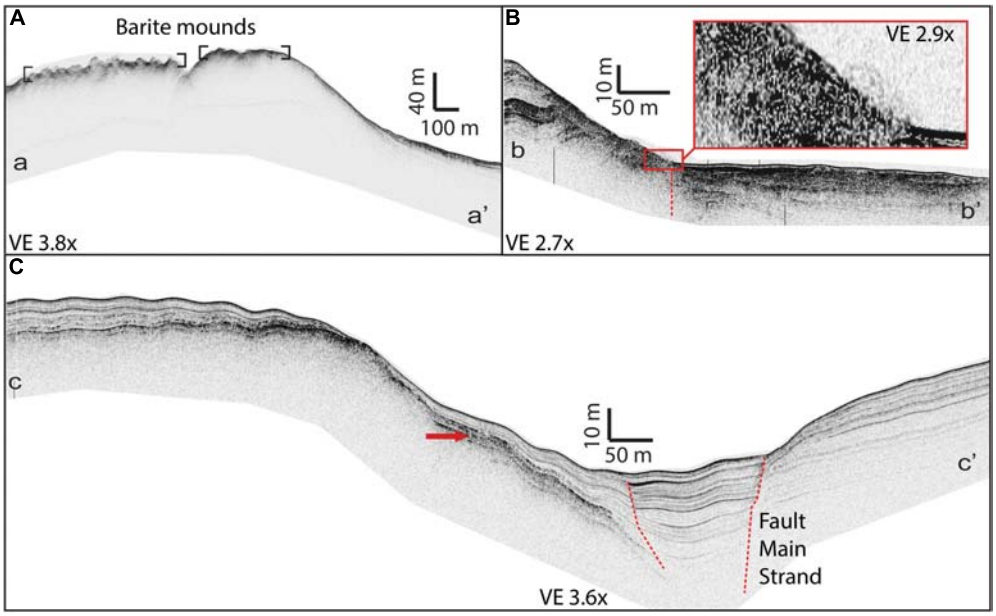

FIGURE 4 | Chirp profiles from study areas on the San Clemente and San Diego Trough Faults. Profile locations are shown in **Figures 1**, **2**. **(A)** Chirp profile parallel to San Clement Fault showing a fuzzy, bumpy appearance indicating the presence of barite mounds. **(B)** Chirp profile that crosses San Clemente Fault near the Navy Fan. Inset in **B** is an enlargement of the fuzzy appearance of barite mounds. **(C)** Chirp profile that crosses the San Diego trough Fault. The arrow in **C** indicates the depth where a barite deposit was found during ROV dive DR769. Faults are shown as dashed red lines.

losing lateral continuity (**Figure 3A**). Interruption of these strata by a fault as they approach the ridge is also possible, however, no significant vertical offset of the layered sediment is observed.

Unequivocally establishing whether the San Clemente Fault is single or multiple stranded where the rough morphology is present is not possible. The narrow depression running along the center of the survey (**Figure 1D**) and delineated by upturned sediment layers in chirp profiles (**Figure 3C**) is obviously the main strand of the fault. However, there is no clear evidence, such as displaced reflectors or offset of piercing points, for the presence of other major fault strands. The appearance of rough topography along the top of the escarpment north of the main fault strand is coincident with truncated strata in all chirp profiles (**Figure 3**).

A chirp line across the San Clemente Fault on the Navy Fan (profile trace 4b−4b′shown in **Figures 2A,B**) shows that the locations of the mounds on the high-resolution map correspond to the section of the escarpment (slope ∼11°) where the sediment drape thickness is minimal (**Figure 4B**). The mounds at the scarp base, which are clearly imaged in the AUV bathymetry (**Figure 2A**), again only appear as a diffuse fuzz above the seafloor reflector (**Figure 4B**, inset).

Sub-bottom profiles from the San Diego Trough Fault (profile trace 4c−4c′ in **Figure 2C**) show thick layered sediment accumulating in all areas except over the steepest slopes (**Figure 4C**) and the top of the central ridge (not shown). The chirp line over which ROV dive DR769 was conducted shows a thick accumulation of layered sediment in the ponded basin, which is disrupted by the main trace of the fault. On the western side of the fault, a barite outcrop was found (see below) where sediment drape thins out upslope on the escarpment.

ROV Dives

Doc Ricketts dive DR767 was conducted on the San Clemente Fault at the southwest corner of the mapped area (left lower quadrant, **Figure 1D**), along a transect that ascended the elongated ridge with the mound morphology, descended to the main fault strand and continued up some of the escarpment on the northern side of the fault (**Figure 1D**). Visual inspection showed that the flanks and tops of the mounds on both sides and top of the southern elongated ridge are composed of aggregates of meter-scale rough-textured clumps (**Figures 5A−C**), hereafter called "heads." The mounds appear to have formed by consolidation of multiple heads along with shed debris. Individual heads are typically dark-varnished, but occasionally are bright white and emerge from either the top or along the sides of the mounds. Chemical analyses of collected samples indicate that the white aggregates are composed of barite. They typically occur as a single mass at the bottom that both widens and branches upward (**Figures 5B,C**). The branches further narrow into upward pointing fingers, which are in places topped by microbial mats (**Figure 5D**). In places, gelatinous microbial mats completely cover the top of the heads with filaments extending into and seen fluttering in the surrounding water (**Figure 5E**). White barite aggregates are also found filling fissures or fractures between the larger dark-varnished blocks of apparently older heads. No shimmering waters were observed that would visually indicate outflow of fluids warmer than bottom waters.

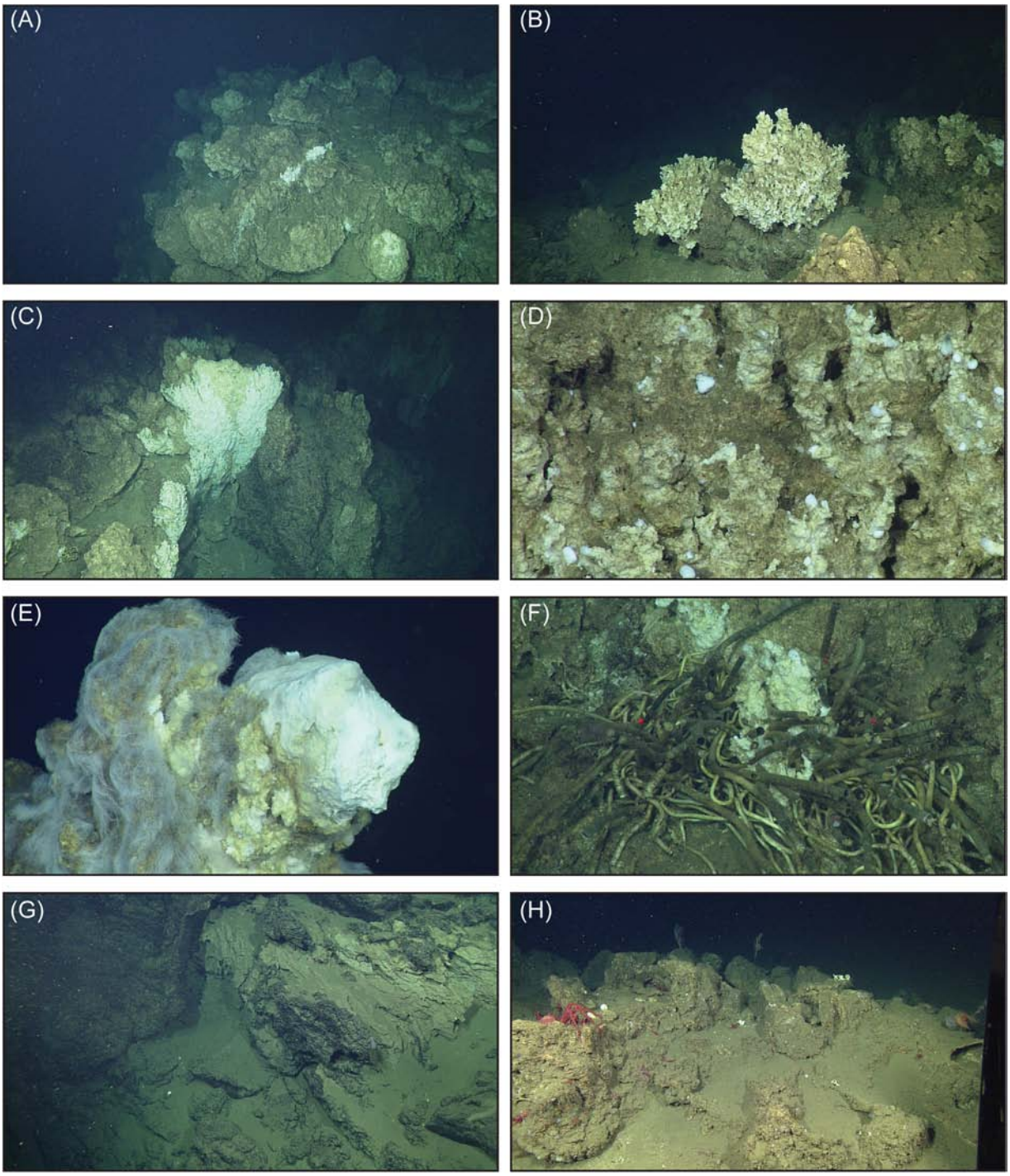

FIGURE 5 | Images collected during ROV dives DR767 and DR769 on the San Clemente Fault and San Diego Trough Fault, respectively. **(A,B)** Barite mounds of presumably different ages as indicated by the accumulation of a muddy drape. **(C)** Barite "heads" with spires ending in "fingers," growing from the sides and top of a barite mound. **(D)** Bacterial mats growing at the ends of barite "fingers." **(E)** Filamentous and gelatinous bacterial mats fully covering a barite "head." **(F)** Barite precipitates engulfing live *Lamellibrachia* tubeworms. Red dots are laser beams separated by 29 cm. **(G)** Sub-horizontal layers of cemented drape intercalated with barite deposits. To the left a barite deposit is draped over the cemented strata. **(H)** Barite deposit found near the San Diego Trough Fault.

Scattered clusters of *Lamellibrachia* tubeworms are present in association with the white precipitates, and in cracks between the darker barite deposits (**Figure 5F**). In some instances, these apparently living tubeworms are engulfed by the mineral precipitates. Sessile megafauna typical of hard-substrate surfaces, such as corals and sponges, is noticeably absent.

In the depressions between mounds there is some rubble derived from the mounds along with shell hash and some hemipelagic sediment drape (**Figure 5G**). However, sediment drape is almost absent on the elevated parts of the mounds. No significant pavements of authigenic carbonate characteristic of methane seeps were observed. Outcrops of sub-horizontal beds of light-colored barite-cemented sediment drape (sample DR767 Rx-4, **Table 1**) are also exposed on both sides of the elongated ridge (**Figure 5G**). Barite heads were found in places draped over exposed outcrops of sub-horizontal bedding (**Figure 5G**).

The mapped area of the San Diego Trough Fault was explored during ROV dive DR769. Two small < 1 m high outcrops were found at a depth of 1172−1175 m (**Figure 5H**), where the sediment drape thins out on the western flank of the trough (**Figure 4C**). Chemical analyses confirmed these heads were composed of friable barite with a yellowish interior, similar to those collected along the San Clemente Fault in dive DR767. Earlier in the dive the ROV navigated along the trace of the fault before climbing the ridge to the west (**Figure 2C**), but did not find other barite deposits along the fault or along the sediment drape covered lower part of the slope.

No ROV dives were conducted on the mounds mapped in the Navy Fan (**Figures 2A,B**).

Geochemistry

Five of the six rock samples collected in the San Clemente Fault ROV dive came from the heads and are composed of very porous and friable aggregates of euhedral to sub-euhedral sub-millimeter weakly cemented crystals. The sixth is a sample of the light-colored sub-horizontal cemented drape found intercalated with the massive blocky deposits on the SW facing slope of the ridge (**Figure 5G**). Based on mineral and elemental analyses, the precipitated white heads are composed of at least 80% by weight barite, with the remainder composed of varying amounts of clays, pyrite and aragonite.

The average $^{87}Sr/^{86}Sr$ ratio of Sr in barites collected in the San Clemente Fault dive is 0.708576 (range 0.70822−0.70898) (**Table 1**). The average $\delta^{34}S$ of the barite samples from the same dive is 23.8% relative to VCTD (range 22.4–24.8%), but the $\delta^{34}S$ of barite in the light-colored sub-horizontal cemented drape is 43.5%. This sample (DR767 Rx-4) is made of non-porous calcium carbonate with barite filling spaces and veins adding up to 10% content by weight. The $\delta^{13}C$ of the carbonate is −24.7% relative to VPDB.

The two San Diego Trough Fault samples had $^{87}Sr/^{86}Sr$ ratios of 0.70848 and 0.70860, within the range of $^{87}Sr/^{86}Sr$ ratios measured in the San Clemente Fault barites, and their $\delta^{34}S$ values of 27.5 and 24.6% are close to the $\delta^{34}S$ of the barite rich samples from the San Clemente Fault.

The concentrations of chalcophile elements are low (**Supplementary Table S1**). The trace element and rare element concentrations are within the concentration ranges of barite samples dredged from the seafloor offshore Southern California and barites recovered on the San Clemente Fault by Alvin, as reported by Hein et al. (2007). No significant differences were found between the chemical composition of samples from the San Clemente Fault and from the San Diego Trough Fault zones.

16S ribosomal RNA gene sequencing of the filamentous and gelatinous mats indicated the presence of both sulfur- and methane- cycling microorganisms, many commonly found in microbial mats and seafloor sediments (Dhillon et al., 2003; Schauer et al., 2011; Salman-Carvalho et al., 2016). Fifty percent of the sequences were similar to epsilonproteobacteria (Helicobacteraceae), gammaproteobacteria (Beggiatoa), and deltaproteobacteria (Desulfobacteraceae). Much rarer (<1%) were sequences affiliated with methane-cycling including Methylococcales, AMNE-1, AMNE-2c, and Methanobacteria.

DISCUSSION

The highly detailed mapping of the distinctive rough topography in AUV surveys on the San Clemente Fault reveals the most extensive authigenic barite deposits discovered to date (**Figure 1D**). These deposits at 962 to 1,300 m water depth are not discernible with currently available surface-ship multibeam mapping technology (**Figure 1C**). However, the enhanced resolution of AUV surveys (**Figure 1D**) allowed for the serendipitous discovery of the large extent, both in geographic and vertical scales, of barite deposits along just one 6 km section of the San Clemente Fault. Furthermore, by chance a small cluster of barite heads were found during an ROV dive in the San Diego Trough Fault in a setting structurally similar to that of the San Clemente Fault. These occurrences further the interpretation that authigenic barite deposits are associated with active fault zones and suggest barite deposits may also occur along other faults of the California Borderland where certain required structural criteria are met.

Structural Controls on Barite Accumulation

The structural elements that control the emplacement of these barite deposits are illustrated in the high-resolution maps, sub-bottom profiles, and ROV observations. The morphology of the spires and the location of bacterial mats are consistent with an upward flow of solutions that promote aggradational growth of barite at the top of the spires, suggesting the outflow of a buoyant fluid.

The massive bodies of barite appear to have formed on the seafloor as a composite of individual heads that are cemented into mounds by new barite precipitate filling gaps between adjacent heads. While no chemical analyses were conducted on the dark surface coating of the mounds, Lonsdale (1979), describes the dark varnish of the barite mounds found in the Navy Fan as a 1 mm-thick Mn-oxide precipitate, and proposed that it occurred after the outflow of barite precipitating fluid has ceased. Thus, the varnish coating on the mounds would attest to their longer exposure to seawater.

The AUV surveys show that barite deposits are typically associated with escarpments having thin or non-existent sediment drape. In the San Clemente Fault section outcropping near the Navy Fan (**Figure 2B**), steep-sided mounds emerge at the foot of the escarpment, and smoother mounds are visible farther up on the slope along the northern side of the fault

TABLE 1 | Isotopic values.

Sample	Location	$^{87}Sr/^{86}Sr$ barite ± 2SE	$\delta^{34}S$ barite, %	$\delta^{13}C$ carbonate, %
DR767 Rx-1	San Clemente Fault	0.70898 ± 0.00002	24.3	
DR767 Rx-2	San Clemente Fault	0.70860 ± 0.00002	24.8	
DR767 Rx-3	San Clemente Fault	0.70822 ± 0.00002	22.4	
DR767 Rx-4	San Clemente Fault	0.70894 ± 0.00002	43.5	−24.7
DR769 Rx-1	San Diego Trough Fault	0.70848 ± 0.00002	27.5	
DR769 Rx-2	San Diego Trough Fault	0.70860 ± 0.00003	24.6	

where sediment cover diminishes, but are absent on the southern side of the fault where sediment cover is thicker. In the main San Clemente Fault survey area, the barite mound morphology along the top of the escarpment on the north side of the fault (**Figure 1E**) clearly follows the horizons of truncated strata where no sediment drape is seen in chirp profiles (**Figure 3**). In the San Diego Trough Fault, the thickest recent sediment accumulations are along the trace of the fault and no barite mounds were detected there, whereas the barite deposit found at this site is on the escarpment with comparatively thin sediment cover (**Figure 4C**). The barite deposits occur where upturned and truncated strata are exposed or have minimal sediment cover.

The arrangement of barite deposits on or along truncated strata suggests the primary conduits for buoyant Ba-rich solutions to reach the seafloor are dipping bedding planes. Lateral variations in heat flow can be sufficient to stimulate weak fluid circulation through sedimentary cover (Langseth et al., 1988). Ba-rich reduced fluids migrating along relatively permeable bedding planes conduits form cold-seep barite deposits when they encounter oxic sulfate-rich bottom waters. A similar mechanism was proposed for barites found in Monterey Bay (Naehr et al., 2000) and the Peru Margin (Torres et al., 1996a), but instead of faulting, in those studies slope failures caused the truncation of bedding planes and their exposure to bottom waters. In the California Borderland, exposure of truncated beds from tectonic displacements along faults is facilitating the formation of barite deposits.

Interestingly, no fluid flow to the seafloor appears to take place along the main strand of the fault in the mapped sections of the San Clemente and the San Diego Trough Faults (**Figure 4C**) because no barite deposits were found along their morphologically obvious main traces. However, while there do not appear to be surface accumulations of barite along the main faults, faults may facilitate the ascent of solutions from depth that later diffuse and reach the seafloor along bedding planes.

Precipitation of barite from Ba-rich solutions when they reach the seafloor is consistent with the aggrading structures documented in the ROV dives and the geochemical signals of samples collected here and elsewhere along the San Clemente Fault (Torres et al., 2003). The $\delta^{34}S$ of the massive barite deposits (range 22.4–24.8%) is close to the seawater value of 21.1%, which indicates that barite precipitated close to the seafloor, and not in oxygen depleted pore waters within the sediment column where $\delta^{34}S$ of sulfate would have been significantly enriched due to the loss of isotopically light sulfur via reduction. Nevertheless, some barite cementation appears to take place in the subsurface. The sample of barite with a $\delta^{34}S$ value much more positive than seawater (DR767 Rx, $\delta^{34}S$ = 43.5%) occurs in association with carbonate partially derived from biogenic methane (carbonate $\delta^{13}C$ = −24.7%) (Paull et al., 1992). The mineral association between barite and methane-derived carbonate and the heavy sulfur isotopic composition are consistent with barite precipitation deeper within the sediment after substantial sulfate reduction.

Cold-Seep Environments With High Rates of Barite-Mineralization

Aloisi et al. (2004), attributed the formation of barite chimneys and the uncharacteristic absence of authigenic carbonate to comparatively high seepage rates of Ba-rich solutions. Rapid formation of the barite mounds can also account for the lack of sediment drape, as newly formed barite deposits incorporate or cover recently accumulated sediment material. Precipitation of barite in the subsurface normally occurs at the depth of the sulfate-methane boundary where ascending solutions rich in barium and methane encounter sulfate-rich porewaters (Torres et al., 1996b; Snyder et al., 2007) leading to barite and authigenic carbonate precipitation. The absence of carbonate precipitation might be due to seepage rates high enough to move the sulfate-methane boundary toward the sediment-water interface where methane could escape, minimizing its rate of conversion to bicarbonate, and ultimately to carbonate precipitation (Aloisi et al., 2004). Barite formation would take place closer to the seafloor and at a rate that surpasses the sedimentation rate, leading to the formation of barite columns raising above the seafloor and thus preventing the accumulation of layered hemipelagic drape.

The absence of fauna typically found on hard bottom substrates (e.g., corals and sponges) as well as chemosynthetic clams is notable. The absence of clams could be due to lack of soft substrates for anchoring. Of all known chemosynthetic vesicomyid clams, only "*Calyptogena magnifica*" is known to inhabit hard substrates (Johnson et al., 2017). The absence of corals and sponges raises the possibility that the barite mound environment is deleterious to these fauna. The existence of fine particle barite suspensions has been hypothesized for the San Clemente basin (Torres et al., 2002), and fine barite particle exposure has been shown, at least in some sponges, to produce adverse effect (Fang et al., 2018).

The rate of growth of surface barite appears to be comparatively rapid. *Lamellibrachia* tubeworms were found

engulfed by fissure-filling barite (**Figure 5G**) indicating that the local rate of growth of authigenic barite on the surface deposits is of the same order as the rate of growth of the tubeworms. *Lamellibrachia* tube worms living in hydrocarbon seeps have been found to grow at variable rates, on the order of a few centimeters per year (Bergquist et al., 2000). Assuming similar order of magnitude rates for the tubeworms found here, the fact that barite precipitates were found in one instance surrounding the upper 3 cm of some living tubeworms indicates that cm/year is a plausible rate of growth of barite surrounding active seep sites. The lack of varnish on the actively growing structures, their weak internal cementation and the lack of sediment drape on the surface deposits all attest to the geologically rapid rate of growth of surface barite deposits. The observation of surface barite deposits that are draped over outcrops of truncated strata devoid of sediment cover (**Figure 5G**) provides further evidence for the geologically fast growth rate of authigenic barite on the seafloor.

Barite Inventory and Barium Sources

Deposits described here are the largest actively forming cold-seep barite deposits documented to date (**Figure 1D**). The mass of barite accumulated on the elongated ridge (∼400 m × 1,000 m) in the SW corner of the mapped area (lower left quadrant **Figure 1D**) amounts to 6.6 million tons of barite, based on 50% coverage of the surface of the ridge by the 11 m tall barite blocks. This is a conservative estimate because the ridge continues to the west farther than the AUV survey reach (**Figure 1B**). The 6.6 million tons of barite found on the <0.5 km^2 ridge area are comparable to the 5 million tons of barite found in chimneys in the Sea of Okhotsk over a 22 km^2 area (Aloisi et al., 2004). The amount of barite in the whole AUV mapped area is even larger because the calculated inventory of 6.6 million tons of barite does not include all other barite mounds present within the survey (**Figures 1D**, **3**).

While the association of the barite mounds and truncated strata is clear, observations in other faults offshore California marking the Pacific Plate-North America Plate boundary, show that faults are often multi-stranded and encompass hundreds of meters wide zones (Johnson and Beeson, 2019). The emergence of barite mounds atop of the ridge could result from the ascent of Ba-rich fluids along a zone of fractures extending the width of the ridge (∼500 m), but too deep to be imaged in the AUV data. Such fluids could be captured by permeable bedding planes. Thus, the association of the mounds and the outcropping bedding planes does not by itself preclude that barium-rich fluids are part of large circulation cells and ultimately migrated from long distance sources along the main fault zone.

A budget calculation is useful to assess whether leaching of San Clemente Basin sediments by fluid circulation is capable of providing sufficient barium to account for the 6.6 million tons of barite found along the ridge. Torres et al., 2002, on the basis of barite $^{87}Sr/^{86}Sr$ ratios and the low concentrations of chalcophile elements, suggested that all Ba found in San Clement Fault barite deposits was sourced from the sediment column. The geochemical profile of barite samples measured here is not significantly different from the geochemical composition of the samples measured by Torres et al. (2002). Thus, in this conservative calculation it is assumed that all Ba in the surface deposits was derived from the sediment column, which dates from the Late Miocene to the present (Teng and Gorsline, 1989), and has a thickness of 400 to 500 m, based on seismic reflection profiles nearby (Normark and Piper, 1972). The sediments that accumulated in the Late Miocene in the California Borderland comprise voluminous diatomaceous sequences (Teng and Gorsline, 1989). Such high-productivity sediments are rich in Ba (Paytan and Griffith, 2007). For example, in the productive Eastern Equatorial Pacific the Ba concentrations in core top sediment are commonly up to 1.5% and sometimes reach 3% (Lyle and Lyle, 2006). Deposition in the California borderland after the Miocene was dominated by clastic inputs (Teng and Gorsline, 1989) with likely lesser Ba content. The thickness of the Late Miocene sequence in the San Clemente Basin is not well known. For simplicity, if it is assumed that the sediment accumulation rate has been constant, Late Miocene (11 to 5 Ma) and younger sediments have 1.5 and 0.2% Ba content, respectively, sediment density is 2,300 kg/m^3, and the area of the sediment pile that is being leached is as large as the surface expression of the surface deposits (400 × 1,000 m), then the amount of Ba potentially available under the elongated ridge is ∼6 million tons of barite, which is equivalent to the amount of barite already accumulated as surface deposits in the mapped area (6.6 million tons). While the deeper pathway of Ba-rich fluids before they reach the seafloor is not known, the current rates of barite growth can be sustained if fluid circulation cells extend wider than the surface expression of the Ba deposits along the fault. This larger inventory of Ba could easily account for the amount of Ba found on the ridge and elsewhere.

CONCLUSION

The world's largest known actively forming cold-seep barite deposit was revealed in a detailed AUV mapping survey along a segment of the San Clemente Fault, where numerous steep sided mounds stand up to 11 m above the surrounding seafloor. These mounds are barite-cemented consolidations of meter-scale rough-textured clumps, which themselves are the remainders of fast accumulating upward branching structures formed by barite aggradation. Despite the large size of the barite blocks and their clustering along a prominent ridge, detection of this morphology at this water depth (962 to 1,300 m) requires a resolution higher than that offered by surface-ship multibeam technology (25 m grid resolution at this depth). Thus, based on the discoveries described here utilizing a high-resolution mapping approach, a plausible hypothesis is that massive barite deposits of the same scale are common along this fault and other faults in the California Borderland where solutions might circulate through organic- and barium-rich sediments. Identification of truncated strata due to fault motion is a useful criterion for the selection of targets where these deposits may occur at other locations offshore Southern California.

DATA AVAILABILITY

The small subunit ribosomal RNA amplicon sequence dataset reported in this study have been deposited in the NCBI Sequence Read Archive (Project No. PRJNA552110).

AUTHOR CONTRIBUTIONS

RG participated in the ROV cruise, did the sample processing and data analyses, and wrote the manuscript. CP conceived and led the project as chief scientist, including the AUV mission planning, ROV cruises participation, data analyses, and manuscript editing. DC led the AUV component including interfacing multibeam and CHIRP instrumentation with the AUV and multibeam and CHIRP data processing. CMP and SJ did 16S DNA analyses and interpretation. EL participated in the ROV cruise, did the AUV data processing and figure drafting and editing. KA participated in the ROV cruise and did the AUV data processing. All authors commented and edited the manuscript.

ACKNOWLEDGMENTS

The Lucille and David Packard Foundation is acknowledged for their continuous and generous support. Juan Carlos Herguera García at the CICESE (Centro de Investigación Científica y de Educación Superior de Ensenada, México) assisted in securing permission to operate in Mexican waters.

SUPPLEMENTARY MATERIAL

The Supplementary Material for this article can be found online at: https://www.frontiersin.org/articles/10.3389/fmars.2019.00460/full#supplementary-material

REFERENCES

Aloisi, G., Wallmann, K., Bollwerk, S. M., Derkachev, A., Bohrmann, G., and Suess, E. (2004). The effect of dissolved barium on biogeochemical processes at cold seeps. *Geochimica et Cosmochimica Acta* 68, 1735–1748. doi: 10.1016/j.gca.2003.10.010

Aquilina, L., Dia, A. N., Boulègue, J., Bourgois, J., and Fouillac, A. M. (1997). Massive barite deposits in the convergent margin off peru: implications for fluid circulation within subduction zones. *Geochimica et Cosmochimica Acta* 61, 1233–1245. doi: 10.1016/S0016-7037(96)00402-4

Bergquist, D. C., Williams, F. M., and Fisher, C. R. (2000). Longevity record for deep-sea invertebrate. *Nature* 403, 499–500. doi: 10.1038/35000647

Canet, C., Anadón, P., Alfonso, P., Prol-Ledesma, R. M., Villanueva-Estrada, R. E., and García-Vallès, M. (2013). Gas-seep related carbonate and barite authigenic mineralization in the northern Gulf of California. *Mar. Pet. Geol.* 43, 147–165. doi: 10.1016/j.marpetgeo.2013.02.011

Caporaso, J. G., Kuczynski, J., Stombaugh, J., Bittinger, K., Bushman, F. D., Costello, E. K., et al. (2010). QIIME allows analysis of high-throughput community sequencing data. *Nat. Methods* 7, 335–336. doi: 10.1038/nmeth.f.303

Caporaso, J. G., Lauber, C. L., Walters, W. A., Berg-Lyons, D., Lozupone, C. A., Turnbaugh, P. J., et al. (2011). Global patterns of 16S rRNA diversity at a depth of millions of sequences per sample. *Proc. Natl. Acad. Sci. U.S.A.* 108(Suppl. 1), 4516–4522. doi: 10.1073/pnas.1000080107

Caress, D. W., THomas, H., Kirkwood, W. J., McEwen, R., Henthorn, R., Clague, D. A., et al. (2008). "High-Resolution multibeam, sidescan, and subbottom surveys using the MBARI AUV D. Allan B," in *Marine Habitat Mapping Technology for Alaska*, eds J. R. Reynolds and H. G. Greene (Fairbanks, AK: University of Alaska Fairbanks).

Carvajal, C., Paull, C. K., Caress, D. W., Fildani, A., Lundsten, E., Anderson, K., et al. (2017). Unraveling the channel–lobe transition zone with high-resolution AUV bathymetry: navy fan, offshore baja california, mexico. *J. Sedimen. Res.* 87, 1049–1059. doi: 10.2110/jsr.2017.58

Clark, S. H. B., Poole, F. G., and Wang, Z. (2004). Comparison of some sediment-hosted, stratiform barite deposits in China, the United States, and India. *Ore Geol. Rev.* 24, 85–101. doi: 10.1016/j.oregeorev.2003.08.009

Dhillon, A., Teske, A., Dillon, J., Stahl, D. A., and Sogin, M. L. (2003). Molecular characterization of sulfate-reducing bacteria in the guaymas basin. *Appl. Environ. Microbiol.* 69, 2765–2772. doi: 10.1128/AEM.69.5.2765-2772.2003

Fang, J. K. H., Rooks, C. A., Krogness, C. M., Kutti, T., Hoffmann, F., and Bannister, R. J. (2018). Impact of particulate sediment, bentonite and barite (oil-drilling waste) on net fluxes of oxygen and nitrogen in arctic-boreal sponges. *Environ. Poll.* 238, 948–958. doi: 10.1016/j.envpol.2017.11.092

Feng, D., and Roberts, H. H. (2011). Geochemical characteristics of the barite deposits at cold seeps from the northern Gulf of Mexico continental slope. *Earth Planet. Sci. Lett.* 309, 89–99. doi: 10.1016/j.epsl.2011.06.017

Greinert, J., Bollwerk, S. M., Derkachev, A., Bohrmann, G., and Suess, E. (2002). Massive barite deposits and carbonate mineralization in the Derugin Basin, Sea of Okhotsk: precipitation processes at cold seep sites. *Earth Planet. Sci. Lett.* 203, 165–180. doi: 10.1016/S0012-821X(02)00830-0

Hein, J. R., Zierenberg, R. A., Maynard, J. B., and Hannington, M. D. (2007). Barite-forming environments along a rifted continental margin, Southern California Borderland. *Deep Sea Res. II: Top. Stud. Oceanogr.* 54, 1327–1349. doi: 10.1016/j.dsr2.2007.04.011

Holmden, C., Creaser, R. A., and Muehlenbachs, K. (1997). Paleosalinities in ancient brackish water systems determined by 87Sr/86Sr ratios in carbonate fossils: a case study from the Western Canada sedimentary basin. *Geochimica et Cosmochimica Acta* 61, 2105–2118. doi: 10.1016/S0016-7037(97)00073-2

Johnson, S. B., Krylova, E. M., Audzijonyte, A., Sahling, H., and Vrijenhoek, R. C. (2017). Phylogeny and origins of chemosynthetic vesicomyid clams. *Systemat. Biodivers.* 15, 346–360. doi: 10.1080/14772000.2016.1252438

Johnson, S. Y., and Beeson, J. W. (2019). Shallow structure and geomorphology along the offshore northern san andreas fault, tomales point to fort ross, californiashallow structure and geomorphology along the offshore northern san andreas fault. *Bull. Seismol. Soc. Am.* 109, 833–854. doi: 10.1785/0120180158

Koski, R. A., and Hein, J. R. (2004). *Stratiform Barite Deposits in the Roberts Mountains Allochthon, Nevada: A Review Of Potential Analogs in Modern Sea-Floor Environments*. Nevada, NV: US Geological Survey.

Langseth, M. E., Mottl, M. A., Hobart, M. A., and Fisher, A. (1988). The distribution of gethermal and geochemical gradients near site 501/504: implications for hydrothermal circulation in the oceanic crust. *Proc. Ocean Drill. Prog.* 111, 23–32. doi: 10.2973/odp.proc.ir.111.1988

Lonsdale, P. (1979). A deep-sea hydrothermal site on a strike-slip fault. *Nature* 281, 531–534. doi: 10.1038/281531a0

Lyle, A. O., and Lyle, M. L. (2006). Organic carbon and barium in eocene sediments: possible controls on nutrient recycling in the eocene equatorial pacific ocean. *Proc. Ocean Drill. Prog. Sci. Res.* 199, 1–33. doi: 10.2973/odp.proc.sr.199.2006

Naehr, T. H., Stakes, D. S., and Moore, W. S. (2000). Mass wasting, ephemeral fluid flow, and barite deposition on the California continental margin. *Geology* 28, 315–318. doi: 10.1130/0091-7613(2000)028<0315:mweffa>2.3.co;2

Normark, W. R., and Piper, D. J. W. (1972). Sediments and growth pattern of navy deep-sea fan, san clemente basin, california borderland. *J. Geol.* 80, 198–223. doi: 10.1086/627725

Parada, A. E., Needham, D. M., and Fuhrman, J. A. (2016). Every base matters: assessing small subunit rRNA primers for marine microbiomes with mock

communities, time series and global field samples. *Environ. Microbiol.* 18, 1403–1414. doi: 10.1111/1462-2920.13023

Paull, C. K., Chanton, J. P., Neumann, A. C., Coston, J. A., Martens, C. S., and Showers, W. (1992). Indicators of methane-derived carbonates and chemosynthetic organic carbon deposits: examples from the florida escarpment. *PALAIOS* 7, 361–375. doi: 10.2307/3514822

Paytan, A., and Griffith, E. M. (2007). Marine barite: recorder of variations in ocean export productivity. *Deep Sea Res. II: Top. Stud. Oceanogr.* 54, 687–705. doi: 10.1016/j.dsr2.2007.01.007

Revelle, R., and Emery, K. O. (1951). Barite concretions from the seafloor. *GSA Bull.* 62, 707–724.

Salman-Carvalho, V., Fadeev, E., Joye, S. B., and Teske, A. (2016). How Clonal is clonal? genome plasticity across multicellular segments of a "*Candidatus* Marithrix sp." filament from sulfidic, briny seafloor sediments in the Gulf of Mexico. *Front. Microbiol.* 7. doi: 10.3389/fmicb.2016.01173

Schauer, R., Røy, H., Augustin, N., Gennerich, H.-H., Peters, M., Wenzhoefer, F., et al. (2011). Bacterial sulfur cycling shapes microbial communities in surface sediments of an ultramafic hydrothermal vent field. *Environ. Microbiol.* 13, 2633–2648. doi: 10.1111/j.1462-2920.2011.02530.x

Snyder, G. T., Dickens, G. R., and Castellini, D. G. (2007). Labile barite contents and dissolved barium concentrations on blake ridge: new perspectives on barium cycling above gas hydrate systems. *J. Geochem. Explor.* 95, 48–65. doi: 10.1016/j.gexplo.2007.06.001

Suess, E., Bohrmann, G., Huene, R., von Linke, P., Wallmann, K., Lammers, S., et al. (1998). Fluid venting in the eastern aleutian subduction zone. *J. Geophys. Res: Solid Earth* 103, 2597–2614. doi: 10.1029/97JB02131

Teng, L. S., and Gorsline, D. S. (1989). Late cenozoic sedimentation in california continental borderland basins as revealed by seismic facies analysis. *GSA Bull.* 101, 27–41. doi: 10.1130/0016-7606(1989)101<0027:lcsicc>2.3.co;2

Thompson, L. R., Sanders, J. G., McDonald, D., Amir, A., Ladau, J., Locey, K. J., et al. (2017). A communal catalogue reveals Earth's multiscale microbial diversity. *Nature* 551, 457–463. doi: 10.1038/nature24621

Torres, M. E., Bohrmann, G., Dubé, T. E., and Poole, F. G. (2003). Formation of modern and paleozoic stratiform barite at cold methane seeps on continental margins. *Geology* 31, 897–900. doi: 10.1130/G19652.1

Torres, M. E., Bohrmann, G., and Suess, E. (1996a). Authigenic barites and fluxes of barium associated with fluid seeps in the peru subduction zone. *Earth Planet. Sci. Lett.* 144, 469–481. doi: 10.1016/S0012-821X(96)00163-X

Torres, M. E., Brumsack, H. J., Bohrmann, G., and Emeis, K. C. (1996b). Barite fronts in continental margin sediments: a new look at barium remobilization in the zone of sulfate reduction and formation of heavy barites in diagenetic fronts. *Chem. Geol.* 127, 125–139. doi: 10.1016/0009-2541(95)00090-9

Torres, M. E., McManus, J., and Goldfinger, C. (2000). *Mapping, Geochemical Sampling and Submersible Observations of Recent Activity on the San Clemente Fault Zone* (No. 180 00-4). Corvallis, OR: College of Oceanic & Atmospheric Sciences.

Torres, M. E., McManus, J., and Huh, C.-A. (2002). Fluid seepage along the san clemente fault scarp: basin-wide impact on barium cycling. *Earth Planet. Sci. Lett.* 203, 181–194. doi: 10.1016/S0012-821X(02)00800-2

Conflict of Interest Statement: The authors declare that the research was conducted in the absence of any commercial or financial relationships that could be construed as a potential conflict of interest.

Copyright © 2019 Gwiazda, Paull, Caress, Preston, Johnson, Lundsten and Anderson. This is an open-access article distributed under the terms of the Creative Commons Attribution License (CC BY). The use, distribution or reproduction in other forums is permitted, provided the original author(s) and the copyright owner(s) are credited and that the original publication in this journal is cited, in accordance with accepted academic practice. No use, distribution or reproduction is permitted which does not comply with these terms.

frontiers in Marine Science

ORIGINAL RESEARCH
published: 06 August 2019
doi: 10.3389/fmars.2019.00480

The Unknown and the Unexplored: Insights Into the Pacific Deep-Sea Following NOAA CAPSTONE Expeditions

Brian R. C. Kennedy[1,2], Kasey Cantwell[2,3], Mashkoor Malik[2], Christopher Kelley[2,4], Jeremy Potter[5], Kelley Elliott[2], Elizabeth Lobecker[2,6], Lindsay McKenna Gray[2,7], Derek Sowers[2,6], Michael P. White[2,6], Scott C. France[8], Steven Auscavitch[9], Christopher Mah[10], Virginia Moriwake[4], Sarah R. D. Bingo[4], Meagan Putts[4] and Randi D. Rotjan[1]**

[1] Department of Biology, Boston University, Boston, MA, United States, [2] NOAA Office of Ocean Exploration and Research, Silver Spring, MD, United States, [3] MAXIMUS, Metro Center, Reston, VA, United States, [4] University of Hawai'i at Manoa Joint Institute of Marine and Atmospheric Research (JIMAR), Honolulu, HI, United States, [5] Bureau of Ocean Energy Management, Camarillo, CA, United States, [6] Cherokee Nation Strategic Programs, Richmond Hwy Suite, Arlington, TX, United States, [7] Athenium Analytics, Dover, DE, United States, [8] Department of Biology, University of Louisiana at Lafayette, Lafayette, LA, United States, [9] Department of Biology, Temple University, Philadelphia, PA, United States, [10] Department of Invertebrate Zoology, National Museum of Natural History, Smithsonian Institution, Washington, DC, United States

OPEN ACCESS

Edited by:
Cinzia Corinaldesi,
Marche Polytechnic University, Italy

Reviewed by:
Franziska Althaus,
Commonwealth Scientific and Industrial Research Organisation (CSIRO), Australia
Pedro A. Ribeiro,
University of Bergen, Norway

***Correspondence:**
Brian R. C. Kennedy
KennedyB@BU.edu
Randi D. Rotjan
RRotjan@BU.edu

Specialty section:
This article was submitted to Deep-Sea Environments and Ecology, a section of the journal Frontiers in Marine Science

Received: 02 April 2019
Accepted: 16 July 2019
Published: 06 August 2019

Citation:
Kennedy BRC, Cantwell K, Malik M, Kelley C, Potter J, Elliott K, Lobecker E, Gray LM, Sowers D, White MP, France SC, Auscavitch S, Mah C, Moriwake V, Bingo SRD, Putts M and Rotjan RD (2019) The Unknown and the Unexplored: Insights Into the Pacific Deep-Sea Following NOAA CAPSTONE Expeditions. Front. Mar. Sci. 6:480. doi: 10.3389/fmars.2019.00480

Over a 3-year period, the National Oceanic and Atmospheric Administration (NOAA) organized and implemented a Pacific-wide field campaign entitled CAPSTONE: Campaign to Address Pacific monument Science, Technology, and Ocean NEeds. Under the auspices of CAPSTONE, NOAA mapped 597,230 km^2 of the Pacific seafloor (with ∼61% of mapped area located within US waters), including 323 seamounts, conducted 187 ROV dives totaling 891.5 h of ROV benthic imaging time, and documented >347,000 individual organisms. This comprehensive effort yielded dramatic insight into differences in biodiversity across depths, regions, and features, at multiple taxonomic scales. For all deep sea taxonomic groups large enough to be visualized with the ROV, we found that fewer than 20% of the species were able to be identified. The most abundant and highest diversity taxa across the dataset were from three phyla (Cnidaria, Porifera, and Echinodermata). We further examined these phyla for taxonomic assemblage patterns by depth, geographic region, and geologic feature. Within each taxa, there were multiple genera with specific distribution and abundance by depth, region, and feature. Additionally, we observed multiple genera with broad abundance and distribution, which may focus future ecological research efforts. Novel taxa, records, and behaviors were observed, suggestive of many new types of species interactions, drivers of community composition, and overall diversity patterns. To date, only 13.8% of the Pacific has been mapped using modern methods. Despite the incredible

amount of new known and unknown information about the Pacific deep-sea, CAPSTONE is far from the culminating experience the name suggests. Rather, it marks the beginning of a new era for exploration that will offer extensive opportunities via mapping, technology, analysis, and insights.

Keywords: ocean exploration, multibeam mapping, biodiversity, seamounts, Okeanos Explorer, Anthozoa, Porifera, Echinodermata

INTRODUCTION

The oceans contain 1,335 million km^3 of water covering 361.9 million km^2 of seafloor across 71% of the planet (Eakins and Sharman, 2010). Abyssal plains cover ∼70% of the seabed, while the oceanic ridge system extends for 80,000 km around the globe, and there are an estimated 100,000 seamounts throughout the world ocean (Wessel et al., 2010). In the past few decades, there has been substantial effort put into mapping and exploring these benthic seafloor habitats (Mayer et al., 2018) fueled by the advent of new technologies that more easily enable deepwater access (Tyler et al., 2016).

Modern day deep-sea exploration has experienced a renaissance in recent years as massive exploratory infrastructure, expeditions, and institutions have entered the landscape (Tyler et al., 2016). Results from these growing efforts have demonstrated that the seafloor possesses a wealth of biodiversity often exceeding that of coastal systems, and rivaling that of coral reefs and tropical rainforests (McClain and Schlacher, 2015). These abundant and diverse ecosystems, and organisms within, play vital roles in carbon sequestration (Zachos et al., 2008), decomposition (Graf, 1989), nutrient cycling (Danovaro et al., 2001), and fisheries (De Leo et al., 2010). Mapping and exploration technology contribute to our understanding of deep-sea ecosystem dynamics, including tectonic spreading centers and subduction zones as well as a variety of seafloor features (Watling and Auster, 2017; Dunn et al., 2018). Benthic storms, down-slope transport, seamount- and canyon-influenced hydrodynamics, turbidity flows, temporal pulses of food, and even tidal dynamics point to an ever-changing deep sea (Levin et al., 2001). From the discovery of deep-sea vents, seamount coral gardens, high-productivity whale falls, and life even in the deepest trenches, we now understand that the deep sea hosts a variety of habitats, each with their own ecology and unique species (Van Dover, 2000; McClain and Schlacher, 2015). Yet, we still have limited knowledge of these ecosystems, which is increasingly problematic as they may be influenced by drivers such as sea level rise, ocean warming, deoxygenation, acidification, commercial fishing, seabed mining, and other dynamic drivers with unknown potential for feedback to the climate system (Sarmiento et al., 2004; Koslow et al., 2011; Ramirez-Llodra et al., 2011; Mengerink et al., 2014).

The Pacific is the worlds' largest ocean, and hosts a large diversity of deep-sea habitat including the deepest troughs on the planet, trenches, ridges, hadal holes, seamounts, abyssal plains, and other benthic features (Jamison, 2015). The Pacific Ocean covers a total area of 161.76 million km^2, and hosts a volume of 660 million km^3 (Eakins and Sharman, 2010). The history of Pacific Ocean exploration dates back to 1521, when Ferdinand Magellan first attempted to measure the depth by deploying a 732 m weighted line but did not reach the bottom (Murray, 1895). The United States' first major foray into the Pacific was the Explorations Expedition (1838–1842); while this expedition mapped many of the Pacific Islands for the first time, it largely ignored the marine fauna and oceanographic conditions (Philbrick, 2004). The first systematic oceanographic exploration of the Pacific (as part of a circumglobal tour) was the Challenger Expedition in the mid-1870s, which discovered 715 new genera and 4,417 new species globally in 4 years, with 37% of the sampling effort focused on the Pacific (Murray, 1895). Despite this Herculean effort, the vast majority of the Pacific still remained (and remains) unexplored.

The United States has approximately 60% of its exclusive economic zone (EEZ) in the Pacific, and characterizing these Pacific benthic habitats is important to (a) fundamentally understand and effectively manage US submerged resources, (b) enable novel insights into Pacific benthic ecosystems, and (c) to establish baselines of these habitats to better understand their vulnerability and resilience to change. To address the growing need for exploration in the Pacific US EEZ, the National Oceanic and Atmospheric Administration (NOAA) launched a 3-year exploration campaign entitled CAPSTONE: Campaign to Address Pacific monument Science, Technology, and Ocean NEeds. Led by NOAA's Office of Ocean Exploration and Research (OER), CAPSTONE was a multiyear initiative to collect deep-water mapping and seafloor characterization data – providing a baseline dataset. These data were primarily acquired via the NOAA Ship *Okeanos Explorer* in and around US EEZ, US marine protected areas (MPAs), and international sister sites in the central and western Pacific (Friedlander et al., 2016). CAPSTONE was initiated in July 2015 and concluded in September of 2017, and engaged nearly 270 scientists, student researchers, and managers, making it one of the largest dedicated ocean exploration efforts ever conducted by the US government (Leonardi et al., 2018).

Deep-water areas documented during CAPSTONE (**Figure 1**; track lines) included nearly every type of marine geological feature, including conical seamounts, guyots, banks, ridges, islands, atolls, vents, and abyssal habitat. Given the consistency in operations over a wide geographic and temporal scale, CAPSTONE may provide one of the largest systematically acquired, basin-wide data sets across the Pacific Ocean with 187 remotely operated vehicle (ROV) dives spanning numerous ecosystem types and 597,230 km^2 of seafloor mapped. These data have created an incredible opportunity to examine broad-scale geographic patterns of benthic deep-sea diversity, and also

present the opportunity for discovery of new taxa and geologic features, as well as the quantification of the unknown.

It is a widely held assumption that most deep-sea biota are yet-to-be-discovered (Mora et al., 2011). As such, the process of exploration in the deep-sea goes hand-in-hand with the task of species collection and description, and pending that, grappling with the unknown. For most of the world's taxa, both extant and extinct, unknowns must be estimated because they cannot be directly measured. For example, with 527 genera of non-avian dinosaurs known from fossil and genetic evidence, there are an estimated ∼1,850 genera total, but the true number may never be known (Wang and Dodson, 2006). Microbial diversity is another area that requires estimation, typically using a combination of genetics and statistics (e.g., Hughes et al., 2001). In the deep-sea, species diversity has also only been estimated to-date. For example in the Mediterranean, species diversity was estimated across taxa and depth with rarefaction curves, and it was found that each unique habitat or ecosystem contributed significantly to biodiversity (Danovaro et al., 2010). Across these (and other) studies, the challenge of adequately estimating species diversity is a major source of attention and debate. However, in the case of CAPSTONE, a unique opportunity is presented in that the unknowns are visually identified as unknown taxa. Each observed organism was assigned the highest confidence taxonomic identification, or characterized as unidentified, creating an inventory of what can (and cannot) be identified by video and images, noting that taxonomic evaluation remains pending for many organisms collected during CAPSTONE.

Benthic exploration science is evolving, looking to answer more sophisticated questions regarding drivers of biodiversity, patterns of reproduction and recruitment, genetic and ecosystem connectivity, oceanographic influences on benthic diversity and abundance, and trophic connectivity (McClain and Rex, 2015; McClain and Schlacher, 2015; Baco et al., 2016). To begin to address these questions, one aim of this paper is to quantitatively assess the contributions of unknown taxa to deep-sea biodiversity. Another objective is to contextualize the known taxa by depth, geologic feature, and geographic region in terms of diversity and abundance patterns. Finally, this paper will describe, with broad strokes, the findings of CAPSTONE in terms of mapping and visual surveys, to become a resource for future investigations of Pacific patterns of diversity and abundance.

In this study, >347,000 individual organisms were recorded across a subset of 168 dives, coupled with over 597,230 km^2 of seafloor mapped, to look for emergent patterns of diversity and abundance by depth, benthic feature, and geographic region. We explored these patterns in more detail for a single class, Anthozoa, and two phyla, Porifera and Echinodermata, which together were the three most characterized biota by both diversity and abundance during CAPSTONE. Because CAPSTONE is the first modern-era exploration expedition of this scope, we describe, in great detail, the technology and methodology employed to obtain data used for analyses. The main goals of this paper are thus to generate a detailed methodological description and a high-level data overview of the CAPSTONE campaign. The specific scientific aims are to (a) describe what we now know about the Pacific deep-ocean, and (b) describe what we still don't know about the Pacific deep-ocean, and how to contextualize these findings and challenges.

MATERIALS AND METHODS

Expeditions

Mapping and exploration took place aboard the NOAA Ship *Okeanos Explorer*, a 68 m vessel equipped with a full suite of mapping sonars capable of telepresence-enabled operations. While CAPSTONE efforts were further augmented by Schmidt Ocean Institute's R/V *Falkor* and other partners, we exclusively worked with *Okeanos Explorer* data in this study. The *Okeanos Explorer* was also equipped with a dedicated two-body ROV system, *Deep Discoverer* (D2) and *Seirios*, with a 6,000 m depth rating. Using telepresence, the ship was able to sail with only two to three scientists onboard while simultaneously interfacing with dozens of scientists onshore to provide real-time, minute-to-minute feedback and scientific expertise (Kennedy et al., 2016). A suite of Internet-based tools connected the remote teams to enable a unique exploration model with global reach, input, and diverse feedback.

This community-driven science agenda was operationalized with a designated science lead or co-science leads, coupled with a NOAA OER expedition coordinator, who together were responsible for building a consensus among the full community of participants and scientists, regardless of their onboard vs. telepresence participation. In this manner, expertise was available organically or "on-call," and interdisciplinary teams of scientists could collaborate on common interests, which were usually focused around organisms, depth range, region, or geological feature. To help guide at-sea operations throughout CAPSTONE, NOAA adopted a set of guiding exploration themes: support priority US Monument and Sanctuary science and management needs; identify and map vulnerable marine habitats – particularly high-density deep-sea coral and sponge communities; characterize seamounts in and around the Prime Crust Zone (PCZ), a region with the highest concentration of commercially valuable deep-sea minerals in the Pacific (Hein et al., 2013); investigate the geologic history of Pacific seamounts; and increase understanding of deep-sea biogeographic patterns across the central and western Pacific (Leonardi et al., 2018). Additional scientific objectives were also solicited in each operating area from local stakeholders, resource managers, and the science community to help address region-specific data gaps and management needs.

Mapping

Acoustic mapping during CAPSTONE was conducted with EM302, EK60, and Knudsen sub-bottom profilers (SBP) (**Supplementary Table 1**). The EM302 is a multibeam sonar with nominal frequency of 30 kHz, capable of providing data to a water depth of ∼7,000 m. The system is capable of producing three different types of data: bathymetry, seafloor backscatter, and water column backscatter. The data were collected using Kongsberg's Seafloor Information System (SIS version: 4.3.2).

The bathymetric data were processed in near real-time and results made available to participating scientists. Acoustic data collected by EM 302, EK60, and Knudsen SBP data, along with preliminary processed products, are publicly available at National Centers for Environment Information (NCEI). To understand the structure of the seafloor, bathymetric data (summarized in **Figure 1**) was examined at a grid resolution of 25–50 m (depth dependent).

Dive Site Selection

All dive sites were chosen through the collaborative process between the ship- and shore-based science participants. Priority targets were submitted pre-cruise, and then refined over a series of dive planning meetings (pre-cruise, pre- and post-each ROV deployment). Throughout the expedition, operational planning meetings streamed data via high-definition video originating on-ship to provide situational awareness for the shore-based team, showing the latest bathymetry and other available data, previous exploration in the region, and current weather conditions. In selecting dive sites, lessons learned were implemented throughout each expedition, and dive targets were refined based on feedback from previous dives. Care was taken to focus dive and mapping effort on sites and depths that were unexplored by previous efforts. For example, in the Hawaiian Islands region, there had been numerous dives by the *Pisces* submersibles (1973–present), and thus CAPSTONE focused efforts below the *Pisces* maximum operating depth of 2,000 m.

ROV Dives

All ROV dives in CAPSTONE were conducted with NOAA's dual body 6,000 m rated ROV system *Deep Discover* (D2) and *Seirios* that were operated by the Global Foundation for Ocean Exploration (GFOE) personnel. ROV dives typically last 8 h, but were occasionally extended to 10+ h based on science objectives, at-sea conditions, and operational limits. Dives were primarily conducted during the day for ease of operations for the crew (described in detail by Quattrini et al., 2015). *Seirios* is negatively buoyant and therefore remains in the water column, directly below the stern of the ship. It is tethered to the *Okeanos Explorer* with a standard oceanographic armored, fiber-optic cable (1.73 cm diameter), and operated 3–10 m above D2, providing additional lighting and allowing for wide landscape views of the seafloor. D2 was linked to *Seirios* with a neutrally buoyant tether, isolating the ROV from surface ship's motion and allowing precise maneuvering in steep bathymetry close to the seafloor (0–4 m). D2 typically traversed the seafloor at a speed of approximately between 0.1 and 0.3 knots (1 knot = 0.514 m s^{-1}) and normally operates between 0 and 1.5 m above the seafloor. Both ROVs were outfitted with a suite of high-definition video cameras, two of which were maneuverable and used principally for scientific observation; these data were recorded for archival and subsequent analysis. All HD video from *Seirios* and D2 were recorded in PRORES 1080i format. In addition, numerous fixed pilot cameras were used in real-time, but data were often not recorded or used for scientific operations. Lighting consisted of numerous LED lamps providing 272,000 lumens of light across both vehicles. D2 has eight LED lamps mounted on four hydraulically positioned booms to allow for precise adjustment to the light field. During every descent, the HD cameras on D2 are color- and white-balanced *in situ* to a known reference card to ensure accurate color on the video. During the dive, expert video engineers made minor color balance adjustments to compensate for changes in water clarity and location of the object of interest within D2 light field (Gregory et al., 2016).

To record physical oceanographic measurements, Sea-bird 911 + conductivity–temperature–depth (CTD) loggers with dissolved oxygen (DO) sensors were attached to both D2 and *Seirios* and recorded for the entire duration of the dive. In 2017, Oxidation and Reduction Potential (ORP) and light scattering sensors (LSSs) were added to the vehicles suite of sensors. In addition to the CTD to log ambient water conditions, D2 was equipped with a high temperature probe to make targeted measurements of vents or brine flows. Paired lasers (10 cm apart) were mounted on the primary high-definition video camera to estimate the size of objects being imaged.

Deep Discover was also equipped with two manipulator arms that were used to collect physical samples. Throughout CAPSTONE, NOAA practiced a limited sampling protocol, only collecting a few voucher samples per dive. During 2015 and 2016, the only biological samples collected were those that were thought to be potential new species, or demonstrate a substantial range extension. In 2017, the sampling protocol was widened to include collection of dominant-morphotype taxa that could not be identified by video. In addition, geological samples were collected on the majority of dives to aid in isotopically dating features and to help characterize the overall geology of the dive site.

Area Imaged

An Ultra Short BaseLine (USBL) navigation system was used on D2. The precision and accuracy of the system is heavily dependent on water depth, and to a lesser degree both sea state and local bathymetry (Wu et al., 2017). The accuracy of this system can range between ∼5 and 50 m depending on these conditions. In addition to this wide range, there were additional operational decisions and technical limitations that made it difficult to quantify the total seafloor area captured on video. These challenges include: (1) distinguishing errors in the USBL navigation versus rapid changes in vehicle position, due to rapid and abrupt movement as D2 searched for new and novel organisms or maneuvered around geological features and (2) the continuous and constant tweaks and adjustments to the camera angle and zoom values that are required to precisely calculate view angle, but were not recorded.

To provide estimates of the seafloor area imaged during CAPSTONE, we quantified the minimum and maximum area of seafloor likely documented during a dive to provide a range of possible area visualized. The average of that range was used to estimate the area of seafloor imaged. To accomplish this, we measured the linear distance traveled by D2 by manually tracing a line of best fit based on the subsampled (1 Hertz) USBL navigation file provided by NOAA as part of the ROV data collection available via the OER Digital Atlas (see the section "Data Management"). When D2 is at an altitude of 1 m, and

the camera angle of the primary HD camera is at a 45-degree angle, the field of view yields 2.7 m of seafloor horizontally across the video frame (assuming a steady ROV heading). Because the pilots were nearly continuously changing the heading of the vehicle while scanning the seafloor, as well as flying the vehicle at variable altitudes as the bathymetry dictated, we estimated a visual swath width of a minimum of 5 m (2.5 m on either side of the vehicle path over the bottom) and a maximum of 50 m (calculated as twice the effective length of the tether connecting D2 and *Seirios*). The minimum range value of 5 m corrects for the changes of altitude and heading changes. The maximum range value of 50 m estimates the effective length of the neutrally buoyant tether between D2 and *Seirios*. While the tether is on average 30 m in length, the effective tether length is more accurately estimated at 25 m given the placement of positively buoyant floats, and the difference in depth between the vehicles. Therefore, the maximum range assumes that D2 can never move >50 m quickly without having to move the ship, which controls the movement and placement of *Seirios*. Any move of >50 m would be slower and would be clear in the USBL navigation, and is easy to distinguish from erroneous readings in navigation files. Based on these assumptions and estimates, we assume that the area surveyed during CAPSTONE dives included the seafloor between 2.5 and 25 m on both sides of the averaged dive track.

Image Annotation

A detailed video analysis was carried out at the University of Hawai'i, supported by NOAA's Deep Sea Coral Research and Technology Program (DSCRTP). The annotation creation process was completed based on benthic video from *Okeanos Explorer* using Video Annotation and Reference System (VARS), created by the Monterey Bay Aquarium Research Institute (Schlining and Stout, 2006) and customized for the University of Hawai'i. VARS was used to generate records of animals from ROV dive video captured while on the seafloor. This system was used to quantify the abundance of deep-sea fishes, corals, sponges, and associated animals observed during CAPSTONE. The records of deep-sea invertebrates and fishes were catalogued and characterized with their *in situ* environmental conditions including habitat, substrate, water chemistry, and geographic location. Animals were identified using a deep water identification guide, with 1,700 reference images prepared with taxonomic assistance from experts around the world[1].

All records were subjected to a custom quality assurance/quality control (QA/QC) protocol, looking for inconsistencies in depth, substrate, and identifications. Any potentially problematic records were re-reviewed in triplicate for QC. In addition, each identification was double-checked against the WoRMs online taxonomic database. The annotations used in this study can be accessed through the DSCRTP web-based data portal[2].

[1]https://oceanexplorer.noaa.gov/okeanos/animal_guide/animal_guide.html
[2]https://www.ncei.noaa.gov/maps/deep-sea-corals/mapSites.htm

In total, there were 89,398 annotations describing the presence of taxa in an area, yielding more than 347,000 individual organisms recorded (abundance) across 168 dives over the 3-year CAPSTONE campaign. While there were 187 ROV dives completed in total during CAPSTONE, we eliminated dives that were focused on marine archeology, midwater exploration, and ROV engineering trials for the purposes of this study, for a total of 168 dives used in this study.

Annotation Limitations

Many annotations made during CAPSTONE expeditions could not be identified to a specific taxon and thus were categorized as "unidentified" or unknown. This category includes several types of unknowns: (a) unclassified species that are new to science, (b) organisms that require microscopy for identification, and (c) bad imagery where the detail required to make an identification is not available. These limitations make it impossible to draw conclusions about the absolute number of unknowns. However, given that all the CAPSTONE annotations were based on video from the same platform, and analyzed by the same team at the University of Hawai'i, data collection and analysis were consistent across the entire 3-year CAPSTONE campaign. Thus, comparisons between unknowns observed across feature, depth, and region are valid as a relative comparison.

Analysis

Sample Selection and Groupings

All dives were characterized by the predominant geological feature on which the dive took place, geographical region, and the depth of the vehicle when the annotation was made.

The *geological feature* categories (**Table 1**) were as follows: (a) Island: emergent land mass at the summit but is not an atoll, (b) Atoll: emergent land mass at the seamount summit with a central lagoon, (c) Bank: a seamount where the summit depth is shallower than 200 m but does not break the surface, (d) Guyot (Tablemount): a flat top seamount that is expected to have a carbonate cap and was thought to have once been emergent, (e) Conical Seamount: an underwater mount rising at least 1,000 m above the surrounding seafloor that has a cone shaped summit, (f) Ridge Seamount: an underwater mount rising at least 1,000 m above the surrounding seafloor that has a ridgeback summit feature that is connected continuously with several other feature to from a subsea ridge, (g) Inactive vent system: any area that was obviously previously hydrothermally altered or has had a recent volcanic activity creating new seafloor, (h) Active vent system: any site that has active warm or hot water venting caused by geological activity, (i) Abyssal: any area between 4,000 and 6,000 m.

The *geographic regions* (**Figure 2** and **Supplementary Figure 1**) were as follows: (1) Hawaiian Islands Region, including the main inhabited Hawaiian Islands, the Northwest Hawaiian Islands, Johnston Atoll, Geologist and Musician Seamounts; (2) Marianas region, including all dives conducted within the US EEZ around Guam and the Commonwealth of the Northern Marianas Islands (CNMI); (3) Western Pacific Region, including the US EEZ surrounding Wake Island and the High Seas between Wake and Guam; (4) South Central Pacific Region, including all

TABLE 1 | Definitions and diversity associated with the nine geological features measured by CAPSTONE.

Geological feature type	Example	Diversity chart	Geological feature type	Example	Diversity chart
Island: Emergent land mass surrounded by water			Ridge seamount: Rising from the seafloor with an elongated summit forming a ridge-like feature	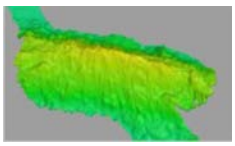	
Atoll: Emergent land and a central lagoon either partially or fully enclosed by land			Inactive vent: recent hydrothermal or volcanic activity that is not currently active		
Bank: A guyot-shaped feature where the shallowest point is <200 m water depth	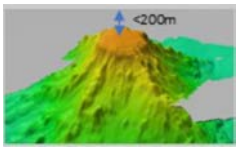	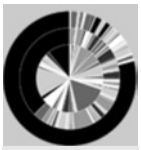	Vent: A dive site with active hydrothermal activity		
Guyot: undersea mountain rising from the seafloor with a flat top deeper than 200 m	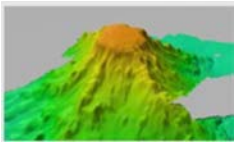		Abyssal: Any dive site between 4,000 and 6,000 m		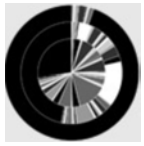
Conical seamount: undersea mountain rising from the seafloor: pointed summit.	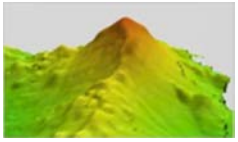				

	Island	Atoll	Bank	Guyot	Conical Seamount	Ridge Seamount	Inactive Vent	Vent	Abyssal
Hawaii	4	4	13	25	15	12	0	0	1
Marianas	3	1	4	4	6	3	4	7	8
Western Pacific	0	2	10	0	0	0	0	0	0
American Samoa	3	3	0	0	6	0	0	1	0
South Centeral Pacific.	6	3	1	9	3	6	0	0	1

Nested pie chart shows overall taxonomic diversity at the family level (inner circle), genus level (middle circle), and species level (outer circle), for all taxa annotated at each feature. Unidentified annotations are represented by the largest black bar originating at 12:00, progressing counter-clockwise. Bottom right-table indicates number of ROV dives per feature (defined in this table) in each geographic region (defined by ***Figure 2****).*

dives conducted in the Phoenix and Line Islands, as well as in the US EEZ around Jarvis Island and along the Manihiki Plateau; and (5) American Samoa, which includes all dives conducted in the US EEZ around American Samoa. The American Samoa region was broken out based on a hypothesized biogeographic break in the area (Watling et al., 2013; Herrera et al., 2018). Of note, the following features were not included in this paper, but do have some limited representation (20 dives) in the CAPSTONE campaign: archeology dives, submerged cultural heritage sites, midwater dives and transects, engineering dives, and special purpose dives for equipment recovery. Archived data associated with these dives can be found via the OER Digital Atlas (see the section "Data Management").

Abundance Calculations

Annotations in the DSCRTP web-based data portal were recorded (1) each time an individual taxa was seen (presence), and (2) the number of individuals seen at the same time (abundance). We used presence data for nested pie-charts and for depth ranges within each taxonomic group. Abundance data were displayed and used for regional comparisons (Shannon–Weiner diversity indices and corresponding heat maps), and for groupings by feature. We chose a conservative cap of a maximum of 100 individuals seen in any one observation period to correct for inaccuracies when organisms were too abundant to count. Thus, our abundance calculations are likely very conservative in total number of organisms.

Diversity Calculations

To visually examine relative taxonomic diversity at the family, genus, and species level within taxa, across region, and across feature, nested pie-charts were generated depicting all known annotated organisms vs. all unknown (represented by the largest black bar originating vertically at the 12 o'clock position, progressing counter-clockwise). In every nested pie-chart, diversity at the family level is represented by the inner circle, the genus level is represented by the middle ring, and species level is shown on the outer ring. Pearson's chi-square statistics was calculated to compare known versus unknown annotations across taxa, or between taxonomic levels. Pearson's chi-square tests were completed using R (version 3.5.1).

To ecologically compare taxonomic diversity between the five geographic regions (American Samoa, Hawaiian Islands, Southern Central Pacific, Western Pacific, and Marianas), video annotations were used to analyze community composition. Annotations were grouped by region and then assessed for abundance, evenness and diversity, using Shannon–Weiner's index (Levin et al., 2009; Rex and Etter, 2010). Overall

diversity, relative abundance (the proportion of focal organisms relative to the total observed), and evenness (a measure of organismal distribution across taxa) were assessed for each region at the family and genus levels. Separately, genus-level diversity, abundance, and evenness were assessed for Anthozoa, Echinodermata, and Porifera, the three taxonomic groups with the largest number of annotations. Annotations that could not be identified to a family or genus (categorized as "unknown") were excluded from family and genus diversity analyses.

Measures of genus-level density were calculated using observation-based rarefaction curves (taxa accumulation curves, in this case, at the genus-level), with 95% confidence intervals. This analytical technique provides a means to standardize taxonomic counts to a given level of sampling-effort, in this case, number of ROV dives conducted. Rarefaction curves were computed using the community ecology Vegan package for R, version 3.5.1 (Oksanen et al., 2018). Results are reported for the number of genera observed for each ROV dive, tabulated separately for Anthozoa, Porifera, and Echinodermata. Rarefaction curves were tabulated by depth, broken down into bins of 0–1,000, 1,000–2,000, 2,000–3,000, 3,000–4,000, and 4,000–6,000 m depth, with the number of ROV dives corresponding to the number of dives per depth.

Non-metric multidimensional scaling (NMDS) plots were created using the 35 most abundant genera for Anthozoa, Porifera, and Echinodermata. Plots were created using Bray–Curtis dissimilarity in the metaNMDS function in the R vegan package (Oksanen et al., 2018). To plot major taxa by geographic region and geologic feature, the most abundant genera were selected; for Anthozoa, any genus represented by >1,500 sightings per km^2 by geologic feature ($N = 37$ genera), for Porifera and Echinodermata, any genus represented by >50 sightings per geologic feature ($N = 33$ and $N = 34$ genera, respectively).

Data Management

In order to facilitate effective collaborative teamwork between ship and shore through telepresence, *Okeanos Explorer* expeditions used real-time data management strategies. Data collected on the ship needed to be moved to shore as quickly as possible to help shore-based participants maintain situational awareness. To facilitate this, OER employed a shore-side repository server where data became immediately accessible through a secure File Transfer Protocol (FTP) site. Once the cruise was complete, data from this intermediate repository server were moved to the NOAA's NCEI long-term archives. This system provided real-time data access during the cruise, and also met the requirements for long-term archival data access and discoverability after the cruise (Mesick et al., 2016). Data were distributed across several different archives within NCEI by data type, and aggregated into a discoverability tool called the OER Digital Atlas[3]. The OER Digital Atlas provides search capability and links the user to the appropriate data archive to access both raw and processed data. All data collected during CAPSTONE were made publicly available through the NCEI data archives (Mesick et al., 2016).

[3]https://service.ncddc.noaa.gov/website/google_maps/OE/mapsOE.htm

Although not analyzed in detail as part of this paper, CAPSTONE expeditions collected biological and geological samples, many of which are thought to be new species, new records, or unusual morphotypes. These specimens were archived for public use and future analysis through the Smithsonian National Museum of Natural History Invertebrate Zoology collection and the Oregon State University Marine and Geology Repository. Additionally, genetic subsamples of most biological specimens are available through the Ocean Genome Legacy Center at Northeastern University (Cantwell et al., 2018a).

RESULTS

Mapping

Campaign to Address Pacific monument Science, Technology, and Ocean NEeds contributed a substantial amount of mapping effort, totaling 597,230 km^2 (**Table 2**), with 323 total seamounts mapped. Specifically, *Okeanos Explorer* mapped 10 atolls, 7 banks, 148 conical seamounts, 114 guyots, 24 islands, and 61 ridge seamounts. Many of these features were located within MPAs, and in many cases, CAPSTONE made major contributions to the overall bathymetry available in these locales (**Figure 1** and **Table 2**). Of the 363,526 km^2 mapped during CAPSTONE, 60.86% was within the US EEZ, amounting to 2.99% of US EEZ total. This effort represents 0.37% of the total Pacific Ocean mapped. While CAPSTONE made a contribution to both domestic and international mapping initiatives, the Pacific Ocean is vast, with only 13.78% currently mapped using modern techniques (**Figure 1** and **Table 2**) – highlighting that there remains a substantial data gap in coverage of the Pacific Ocean.

Analysis of Unknown Diversity

Campaign to Address Pacific monument Science, Technology, and Ocean NEeds logged 891.5 h of ROV bottom time over 168 dives, making 89,398 annotations of biota over an estimated 29.3 km^2 of seafloor imaged (**Table 2**). At the family and genus level, 87.2 and 61.4% of taxa were known and identifiable, respectively. However, at the species level, only 21% of taxa were identifiable, with a corresponding 79% unknown (**Table 1** and **Supplementary Table 2**). This trend is consistent across features, depths, and regions (**Table 1** and **Figures 2**, **3**). Similarly, the highest percentage of identifiable taxa was always at the family level across regions, features, and depth, and within Anthozoa, Porifera, and Echinodermata (**Figures 4–6** inner circle of nested pie-charts; family-level Pearson's chi-square $\chi^2 = 7{,}843.5$, $df = 2$, $p < 0.001$). For echinoderms, there were fewer knowns compared to unknowns at the genus level (**Figures 4–6** middle ring of nested pie-charts; Echinodermata-specific comparison across family, genus, and species Pearson's chi-square $\chi^2 = 8.5642$, $df = 2$, $p < 0.001$). For all taxa at the species level, there were more unknowns than knowns (**Figures 4–6** outer circle of nested pie-charts; species-level Pearson's chi-square $\chi^2 = 2{,}057.3$, $df = 2$, $p < 0.001$). Anthozoa was better categorized at the family and species levels compared to Porifera (**Figures 4**, **5**).

Across geologic features, inactive vents had the least well-characterized biological communities, with the highest

TABLE 2 | CAPSTONE multibeam mapping accomplishments after 3 years of effort by the *Okeanos Explorer*.

Location	Total area (km^2)	Total mapped after CAPSTONE (km^2)	% Area mapped after CAPSTONE	Area mapped by CAPSTONE (km^2)	% Area mapped by CAPSTONE
Pacific Ocean	161,760,000	22,299,018	13.78	597,230	0.37
Papahanaumokuakea MNM	1,508,874	578,008	38.31	94,157	6.24
Johnston Atoll PRIMNM	442,443	122,804	27.76	62,482.4	14.12
Wake Island PRIMNM	406,970	111,580	27.42	53,259	13.09
Marianas Trench MNM	204,543	167,129	81.71	21,611	10.57
Phoenix Islands Protected Area	406,801	68,020	16.72	19,196	4.72
NMS of American Samoa (Muliava Sanctuary Unit/Rose Atoll MNM)	34,934	16,216	46.42	1,1955.4	34.22
Jarvis Island PRIMNM	315,339	58,889	18.67	11,911	3.78
NZ Territory of Tokelau	318,507	79,874	25.08	10,604.2	3.33
Howland Island and Baker Island PRIMNM	51,149	15,041	29.41	6,356.38	12.43
Kingman Reef and Palmyra Atoll PRIMNM	53,175	46,665	87.76	5,379.92	10.12
Marae Moana (proposed)	1,961,280	344,043	17.54	3,776.59	0.19
Swains Island Sanctuary Unit	135	135	99.61	11,2.645	83.22

CAPSTONE expeditions resulted in 597,230 km^2 area mapped for the entire Pacific Ocean (first row) and all marine protected areas depicted in km^2.

unidentifiable taxa at the genus and species levels (**Table 1** and **Supplementary Table 2**). Islands, atolls, banks, guyots, conical seamounts, and ridges, which all share similar vertical relief from the seafloor, were similarly diverse at the genus and species level, with guyots and conical seamounts hosting the highest number of identifications at the family level (**Table 1** and **Supplementary Tables 2–5**). Despite disproportionate dive effort in the Hawaiian Islands Region, all regions showed similar diversity at the species level. However, the South-Central Pacific and Marianas regions are the least well known at the genus level (**Figure 3**).

Of this unknown diversity, CAPSTONE expeditions collected 786 biological and 278 geological samples, many of which are thought to be new species, new records, or unusual morphotypes (**Figure 7**) and are currently available for taxonomic classification.

Diversity of Identifiable "Known" Taxa

Although there were many visual observations unable to be identified, there are data hotspots where more is known than unknown. For example, the best characterized depth is 2,000–2,500 m, where 90% of all taxa were identifiable at the family level (**Figure 3**). Similarly, at the family level, anthozoans are particularly well characterized. Across all regions, features, depths, and most taxa, there were more identifiable annotations at the genus level than the species level. Thus, for all analyses of diversity, we used genus-level taxonomic information unless otherwise noted. The three taxa with the largest number of observations were the class Anthozoa (221,264 individuals), phylum Porifera (46,128 individuals), and phylum Echinodermata (29,934 individuals). Thus, these three taxonomic groups were selected for further analysis by depth, geographic region, and geologic feature (**Figures 4–6**). It is important to note that the focus of the annotations was to document coral and sponge communities, and their associates. As such, not every free living individual invertebrate may have been noted, which may bias the analysis toward corals and sponge symbionts.

The basin-wide scale approach of these data crossed 48 degrees of latitude and 61 degrees of longitude. While postulating biogeographic provinces is outside the scope of this paper, it should be noted that the South-Central Pacific region had highest family (H = 3.23) and genus (H = 3.96) diversity, estimated using the Shannon–Weiner diversity index. The South-Central Pacific region also had the most even distribution (J' = 0.68) of genera among communities observed. Both family and genus diversity were lowest in the American Samoa region (H = 2.10 for family diversity; H = 2.02 for genus diversity). In both assessments, the American Samoa region had the lowest evenness with evidence of dominant taxa. The top three genera in the American Samoa region were all corals: *Enallopsammia*, *Stichopathes*, and *Scleronephthya*, which combined represented 79.5% of genera observed.

Anthozoa

There were 122 anthozoan genera observed during CAPSTONE. To assess whether anthozoan diversity saturates with effort, we conducted rarefaction analyses across depth ranges at the genus level, noting that coral genera can dramatically vary with depth (**Figure 4A**). Most dive efforts were focused at the 1,000–3,000 m depth range, which also showed generic diversity approaching saturation. Genera between 0 and 1,000 m deep accumulated rapidly with increased sampling effort, as did diversity between 3,000 and 4,000 m, with curves not reaching a clear asymptotic value therefore suggesting the need for further sampling effort at those depths (**Figure 4B**). There is a very distinct anthozoan community at shallower depths (**Figure 4A**), but deeper than ∼800 m, coral genera appear more widely distributed across depths (**Figure 4A**).

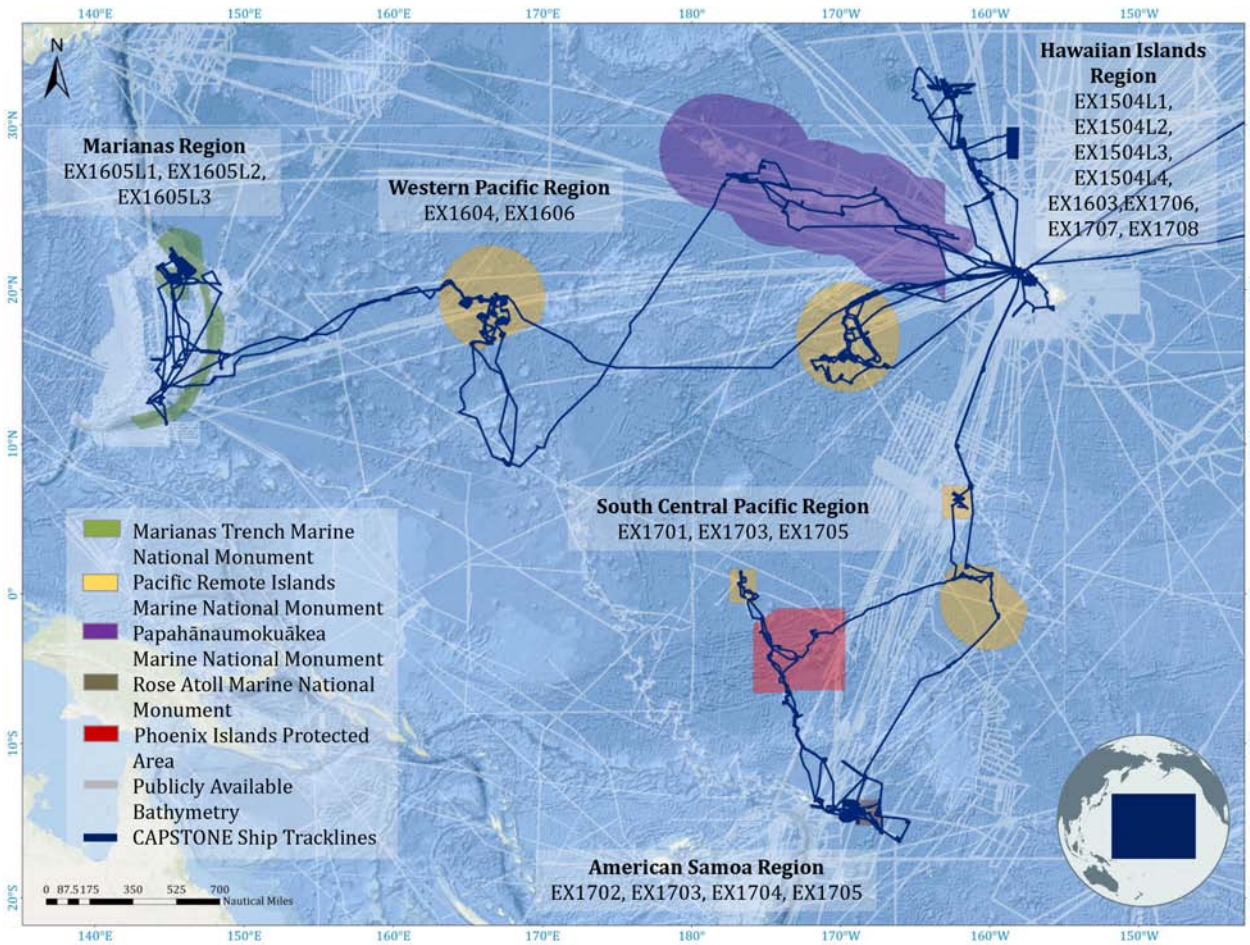

FIGURE 1 | Multibeam EM302 operations conducted by NOAA Ship *Okeanos Explorer* (dark blue ship track lines) during CAPSTONE 2015–2017. Existing bathymetry background layer was obtained from National Centers for Environmental Information (NCEI), made available through a request to NCEI staff to provide multibeam footprint of data held at NCEI.

The South-Central Pacific region had the highest diversity (H = 3.01), using the Shannon–Wiener Diversity Index, and most even distribution (J' = 0.73) among Anthozoa (**Figure 4C**). The American Samoa region had the lowest anthozoan diversity (H = 1.47) and least even distribution (J' = 0.40) of all regions, yet two of the three most abundant genera overall were found there; *Stichopathes* and *Enallopsammia* (**Figure 4C**). Across geologic feature, the most abundant coral genera appear on atolls, with the exception of *Chrysogorgia* and *Narella* (**Figure 4D**). There appears to be higher abundance on atolls compared to islands overall, and higher abundance on banks compared to guyots (**Figure 4D**). There are also some genera that appear to be highly feature-specific. For example, *Anthomastus* spp. are more abundant on ridge seamounts, *Scleronephthya* spp. and *Polymyces* spp. are found almost exclusively on atolls, and there are several genera found almost exclusively on banks, e.g., *Parisis*, *Antipathella*, *Antipathes*, and *Eunicella* spp. (**Figure 4D**). Very few corals are found at vents, but *Pennatula*, *Trissopathes*, *Bathypathes*, and *Enallopsammia* spp. all had representation near vent features.

Overall diversity of the Anthozoa is well characterized at the family level and genus level, though there are more unknowns than knowns at the species level (**Figure 4E**, Pearson's chi-square χ^2 = 55,664, df = 2, p < 0.001). Anthozoans at vent communities were similar to those found on ridge seamounts, guyots, and conical seamounts (**Figure 8**). Islands and atolls shared similar assemblages (**Figure 8**), even though abundances differed dramatically by genus (**Figure 4D**). The top 35 coral genera were not represented in abyssal habitats, even when corrected for effort (**Figures 4D**, **8**). Across regions, the diversity assemblages in the Marianas region were the most distinct (**Figure 8**).

Porifera

There were 55 poriferan genera identified during CAPSTONE (**Figure 5**), which is dramatically lower than the diversity of anthozoans (**Figure 4**). We conducted rarefaction analyses across depth ranges to assess whether poriferan generic diversity saturated with effort, with depth. Genera in Porifera differed

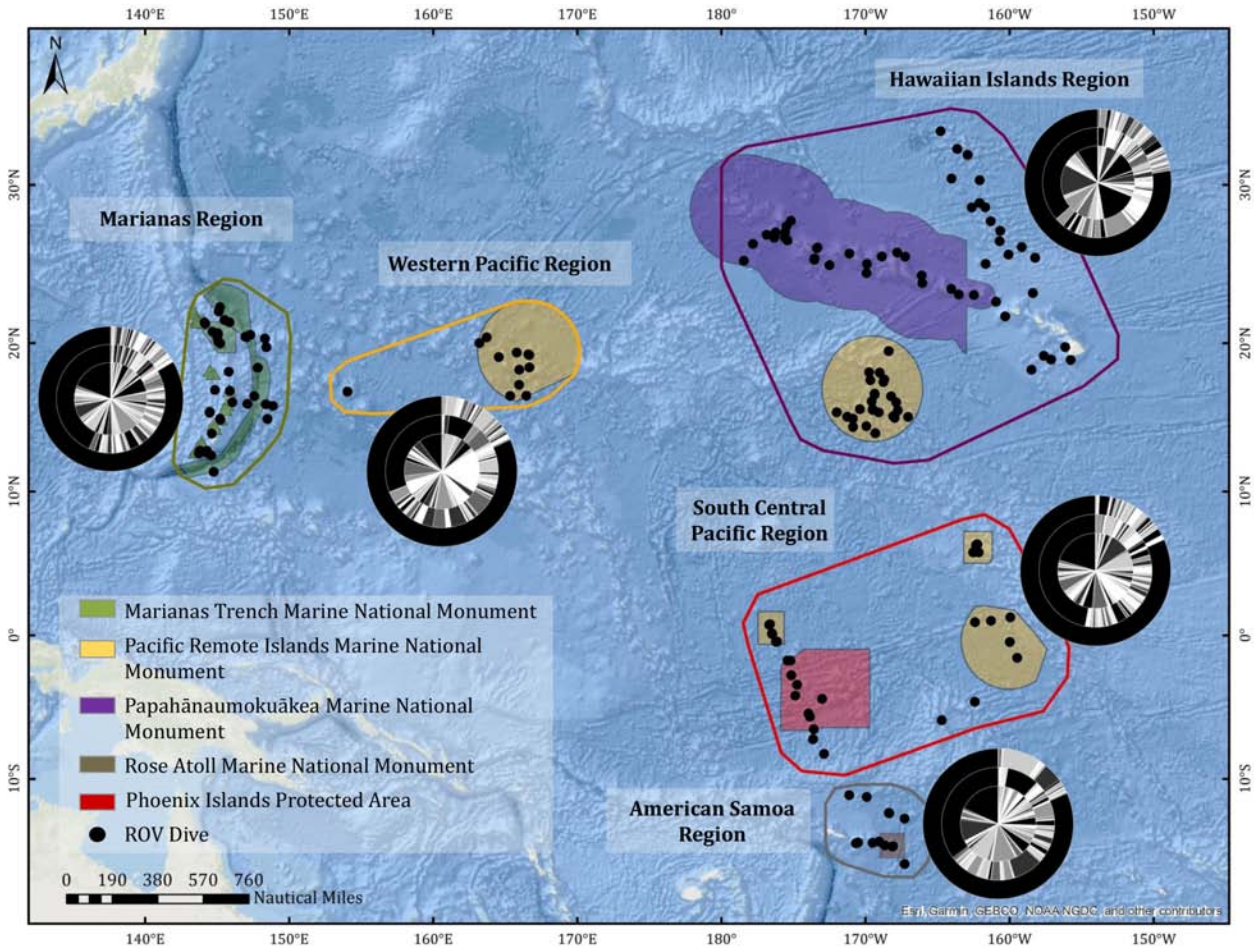

FIGURE 2 | CAPSTONE ROV dive sites (black dots) organized by region (Marianas, Western Pacific, Hawaiian Islands, South-Central Pacific, American Samoa). Marine Protected Areas boundaries are indicated by polygons. Nested pie charts show overall taxonomic diversity at the family level (inner circle), genus level (middle circle), and species level (outer circle), for each region. Unidentified annotations are always represented by the largest black bar originating at 12:00, progressing counter-clockwise.

from Anthozoa, in that the shallowest sponge communities were not the most diverse (**Figure 5B**). Instead, the highest diversity (per effort) was observed 1,000–3,000 m. From 3,000 to 6,000 m, rarefaction curves suggest the potential for greater generic diversity than has previously been documented, given the rapid accumulation with no clear asymptote at those depths (**Figure 5B**). Unlike Anthozoa, poriferan genera appear to be more widely tolerant of depth changes, with few exceptions shallow (e.g., *Leiodermatium* and *Psilocalyx* spp.), and deep (e.g., Cladorhizidae cf. *Chondrocladia*), and some unusually depth-specific taxa in intermediate depths, e.g., cf. *Bolosoma*, *Asceptrulum*, *Bathydorus*, *Polymastia*, and *Corallistes* spp. (**Figure 5A**).

Across regions, the Hawaiian Islands had the highest diversity ($H = 2.69$) using the Shannon–Wiener Diversity Index, and most even distribution ($J' = 0.72$) among 41 genera within Porifera (**Figure 5C**). The Hawaiian Islands also had the highest number of identifiable genera among the regions, with only 18% of annotations excluded due to a lack of taxonomic identification. The lowest diversity among Poriferan genera was observed in the Western Pacific Region (**Figure 5C**; $H = 1.95$); however, 42% of annotations were excluded because they could not be identified reliably to genera. The Marianas Islands had the most unique sponge assemblage at the genus level (**Figure 8**). Across geologic feature, the most abundant sponge genus, *Poecillastra* spp., was most prevalent on islands, but that appears to be the exception among sponges (**Figure 5D**). Broadly across taxa, sponges appeared most abundant on banks, guyots, and ridges, with some taxa appearing almost exclusively on a single feature, e.g., *Asbestopluma* spp. on guyots, *Psilocalyx* and *Semperella* spp. on banks, and *Hertwiga* spp. on ridges (**Figure 5D**). Overall, very few poriferans were identifiable to species (**Figure 5E**). Although the percent identifiable was similar to Anthozoa at the genus level, there are more unknown taxa at the family level (Pearson's chi-square $\chi^2 = 16{,}956$, $df = 2$, $p < 0.001$). Guyots, conical seamounts, and ridge seamounts had relatively similar poriferan communities, whereas banks, island, and atolls had more unique assemblages (**Figure 8**).

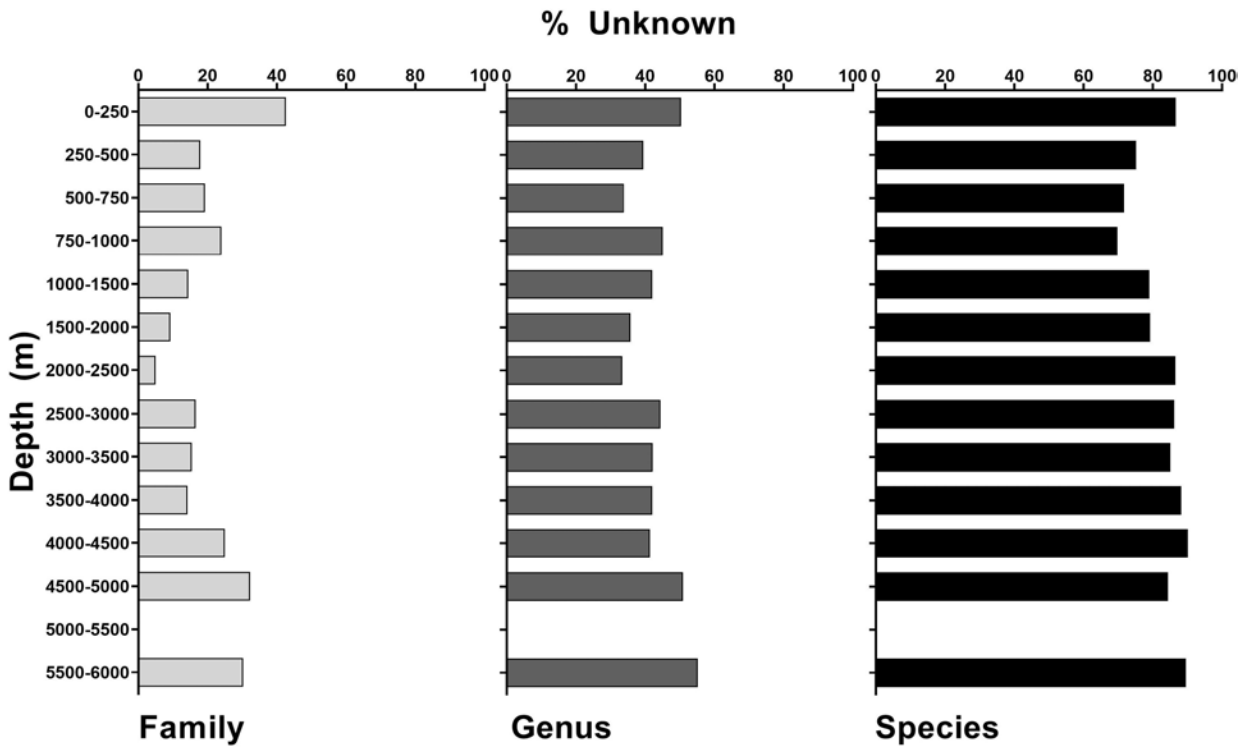

FIGURE 3 | Unidentified annotations (%) across all taxa at the family, genus, and species levels for all of CAPSTONE, demarcated by depth ranges.

Echinodermata

There were 29,934 echinoderm annotations, overall, representing 106 genera (**Figure 6**). Echinoderm genera appear to be highly specific at shallow depths (200–500 m), where each taxon was only observed in a very narrow depth range (**Figure 6A**). In contrast, deepwater genera (3,000–6,000 m) were observed across a much broader depth range, displaying a high degree of flexibility (**Figure 6A**). To examine whether and how diversity saturated with effort, we built rarefaction curves displayed by ROV dive effort, categorized by depth. The highest degree of under sampled diversity was noted in the 3,000–4,000 m depth range (**Figure 8**). Although there was more effort 1,000–2,000 m, shallower depths (0–1,000 m) achieved the same taxonomic saturation (**Figure 8**).

Among Echinodermata, the Western Pacific had the most even distribution ($J' = 0.90$) among observed genera, though all communities were comparatively even with little evidence of a dominant genus (**Figure 8**). One exception was *Ophiocreas* in the Hawaiian Islands, which had 417.32 records (corrected for effort), which was the most abundant of any echinoderm taxon observed (**Figure 8**). Measured using the Shannon–Wiener Diversity Index, the highest diversity among Echinoderm genera was documented in the Southern Central Pacific ($H = 3.19$; **Figure 6C**), though generally all regions had similar diversities (H ranged from 2.65 to 3.11).

When examining the organization of echinoderms on various features, some trends were notable or consistent with their known life mode. For example, many filter-feeding echinoderms were observed on features where they or associated fauna could exploit desirable water currents. The brisingid *Novodinia* and two crinoids, *Glyptometra* spp., and *Thaumatocrinus*, exploit water currents for food, and displayed high abundance on atolls. The feather star *Psathyrometra* as well as two stalked crinoids, *Bathycrinus* and *Proisocrinus*, which are filter-feeders, were observed on guyots and conical seamounts (**Figure 6D**). The deep-sea coral commensal ophiuroid *Ophiocreas* was also observed in high abundance on atolls, likely in association with optimal current habitat of its octocoral host.

The brisingid *Freyastera* was observed on several inactive vents with its arms extended into the water. In contrast, the sea cucumber, cf. *Hansenothuria* spp. was also observed on inactive vent settings but feeding mode was suggested deposit feeding (**Figure 6D**). Other trends included the sea cucumber *Psolus* spp. present only on islands, and brisingid species in the genus *Freyella* were abundant in abyssal habitats (**Figure 6D**). Of all the taxa examined in this study, echinoderms were the least well characterized, showing a higher ratio of knowns to unknowns only at the family level (Pearson's chi-square $\chi^2 = 8{,}564.2$, $df = 2$, $p < 0.001$). In general, community assemblages are similar across ridge and conical seamounts, banks, guyots, atolls, and islands, and surprisingly, vents harbor similar assemblages as well (**Figure 8**). Abyssal and inactive vents have distinct echinoderm communities at the genus level (**Figure 8**). American Samoa displayed the most unique taxonomic assemblage (**Figure 8**).

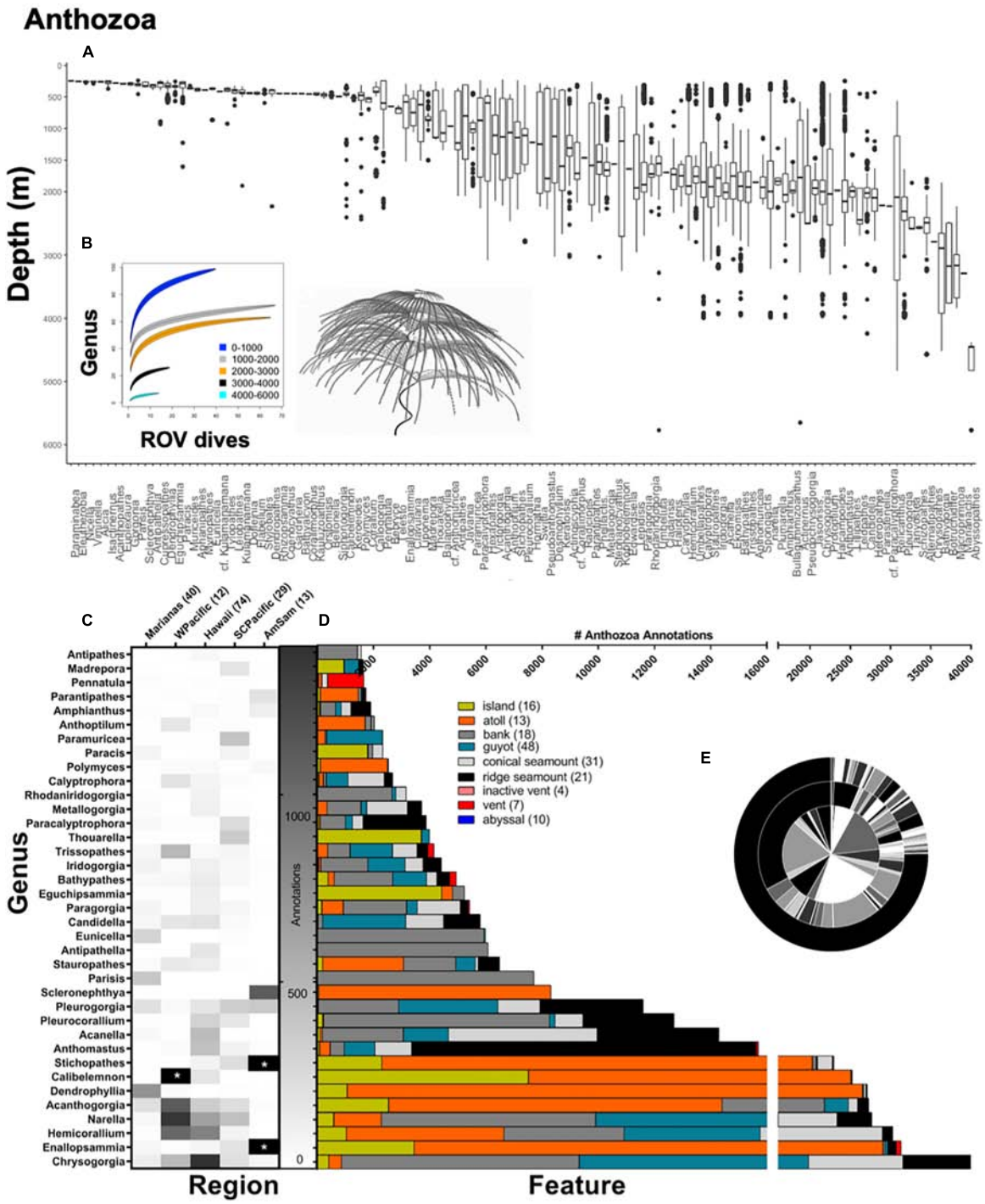

FIGURE 4 | Top panel: **(A)** Anthozoa annotations at the genus-level demarcated by depth (m). A total of 221,264 anthozoan annotations were used to make box-and-whisker plots, organized from shallow to deep along the *x*-axis. A total of 122 anthozoan genera were observed over CAPSTONE. Rarefaction curves **(B)** are shown for all of Anthozoa (122 genera), color coded by depth 0–1,000 m (blue) 1,000–2,000 m (gray), 2,000–3,000 m (orange), 3,000–4,000 m (black), and 4,000–6,000 m (cyan). Lines are drawn with a 95% confidence envelope. Bottom panel: Anthozoa annotations representing at the genus-level demarcated by **(C)** geographic region and **(D)** geologic feature; the number of dives for both are in associated parentheses. A total of 37 anthozoan taxa are shown, representing every genus where 1,500 observations or more were made during CAPSTONE. Starred boxes on heatmap represent abundances outside the range represented, specifically, 33,080.25 *Enallopsammia* spp. corals and 24,342.32 *Stichopathes* spp. were observed (corrected for effort) in American Samoa. Axis breaks by feature do not omit any data; breaks instead allocate annotation effort on different scales. **(E)** Nested pie chart shows overall taxonomic diversity at the family level (inner circle), genus level (middle circle), and species level (outer circle), for all anthozoans annotated. Unidentified annotations are represented by the largest black bar originating at 12:00, progressing counter-clockwise.

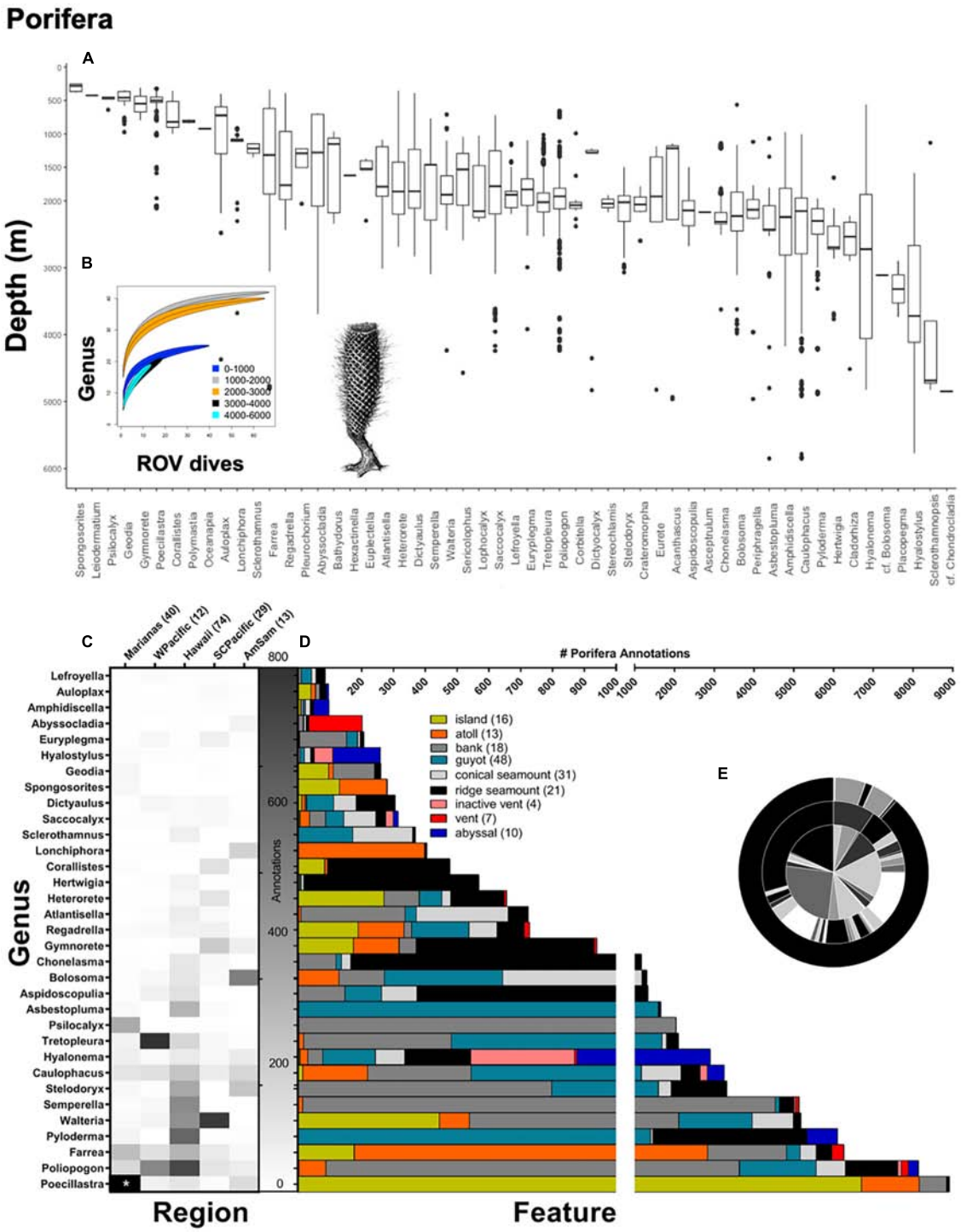

FIGURE 5 | Top panel: **(A)** Poriferan annotations at the genus-level demarcated by depth (m). A total of 46,128 poriferan annotations were used to make box-and-whisker plots, organized from shallow to deep along the *x*-axis. A total of 55 poriferan genera were observed over CAPSTONE. Rarefaction curves **(B)** are shown for all of Porifera (55 genera), color coded by depth 0–1,000 m (blue) 1,000–2,000 m (gray), 2,000–3,000 m (orange), 3,000–4,000 m (black), and 4,000–6,000 m (cyan). Lines are drawn with a 95% confidence envelope. Bottom panel: Porifera annotations representing at the genus-level demarcated by **(C)** geographic region and **(D)** geologic feature; the number of dives for both are in associated parentheses. A total of 33 poriferan taxa are shown, representing every genus where 50 observations or more were made during CAPSTONE. Starred boxes on heatmap represent abundances outside the range represented, specifically, 2,877.59 *Poecillastra* spp. were observed (corrected for effort) in the Marianas Region. Axis breaks by feature do not omit any data; breaks instead allocate annotation effort on different scales. **(E)** Nested pie chart shows overall taxonomic diversity at the family level (inner circle), genus level (middle circle), and species level (outer circle), for all poriferans annotated. Unidentified annotations are represented by the largest black bar originating at 12:00, progressing counter-clockwise.

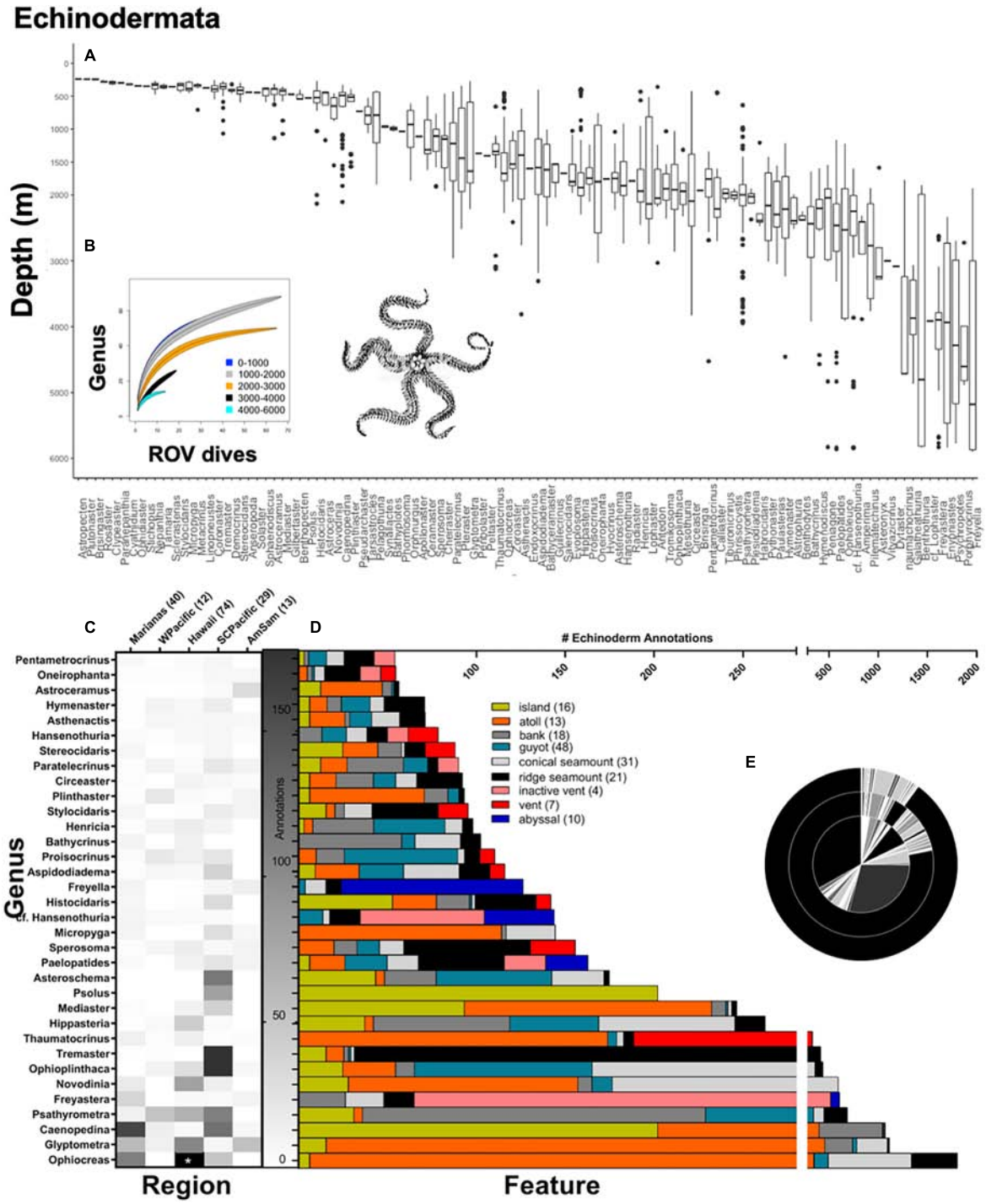

FIGURE 6 | Top panel: Echinoderm annotations at the genus-level demarcated by depth (m). **(A)** A total of 29,934 echinoderm annotations were used to make box-and-whisker plots, organized from shallow to deep along the *x*-axis. A total of 106 echinoderm genera were observed over CAPSTONE. Rarefaction curves **(B)** are shown for all of Echinodermata (106 genera), color coded by depth 0–1,000 m (blue) 1,000–2,000 m (gray), 2,000–3,000 m (orange), 3,000–4,000 m (black), and 4,000–6,000 m (cyan). Lines are drawn with a 95% confidence envelope. Bottom panel: Echinoderm annotations representing at the genus-level demarcated by **(C)** geographic region and **(D)** geologic feature; the number of dives for both are in associated parentheses. A total of 34 echinoderm taxa are shown, representing every genus where 50 observations or more were made during CAPSTONE. Starred boxes on heatmap represent abundances outside the range represented, specifically, 417.32 *Ophiocreas* spp. were observed (corrected for effort) in the Hawaiian Islands Region. Axis breaks by feature do not omit any data; breaks instead allocate annotation effort on different scales. **(E)** Nested pie chart shows overall taxonomic diversity at the family level (inner circle), genus level (middle circle), and species level (outer circle), for all echinoderms annotated. Unidentified annotations are represented by the largest black bar originating at 12:00, progressing counter-clockwise.

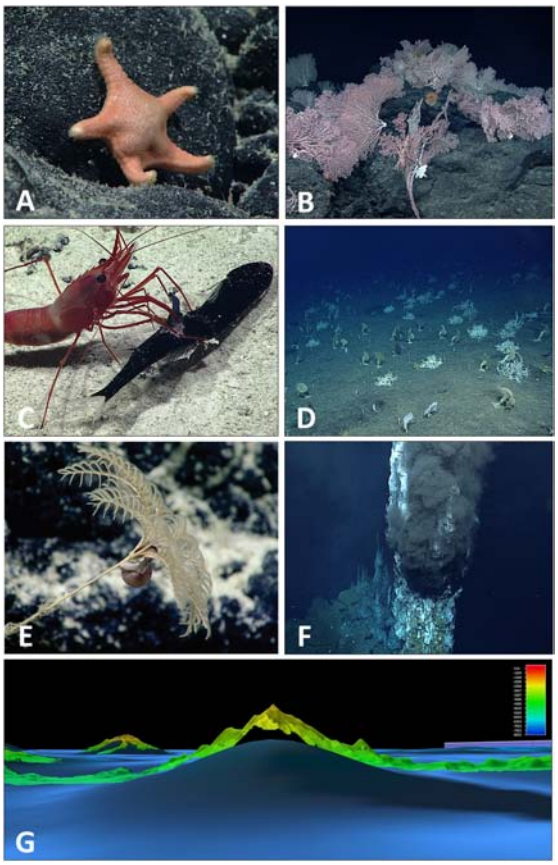

FIGURE 7 | Plate of CAPSTONE curiosities: novel taxa, features, and interactions. Several new genera and new species were observed and collected during CAPSTONE, including **(A)** a previously undescribed genus and species of sea star (family Goniasteridae, class Asteroidea) (C. Mah, personal communication, description in preparation) discovered in the Musicians Seamounts in 2017 (EX1708). In several areas, CAPSTONE expeditions documented deep-sea corals for the first time, including **(B)** in the Musicians Seamounts (EX1708) where coral communities were observed on every dive not focused on water column exploration or archeology characterization. As the number of observations in the deep sea are limited when compared to the size of the biome, every predator–prey interaction observed contributes to our understanding of deep-sea life history. **(C)** A caridean shrimp, *Heterocarpus* sp., was observed capturing and feeding on a mid-water dragonfish, potentially *Astronesthes* sp., at Ufiata Seamount in Tokelau (EX1703), an unusual observation as *Heterocarpus* sp. are typically thought to be scavengers. Of particular interest to CAPSTONE were high density communities. Although most observed during CAPSTONE were composed of corals and sponges (Demopoulos et al., 2018; Smith et al., 2018) **(D)** at Zealandia Bank in the Marianas (EX1603L1) we documented a rarely observed large aggregation of gorgonocephalid basket stars. **(E)** In the deepwater areas around Kingman Reef (EX1705) several gastropods were observed with mouth apparently placed on the anal vent of multiple bathycrinid stalked crinoids, reminiscent of coprophagus snails (Platyceratidae) known from Paleozoic fossils but thought to be extinct. CAPSTONE also included exploration of hydrothermal vents in the Marianas (EX1605L1 and L3) revealing three new site of hydrothermal activity, including **(F)** the first survey of a new black smoker vent field composed of multiple chimneys in the Mariana Back Arc. Multibeam data collected over areas that had previously only been mapped using satellite altimetry, often showed significant differences in depth or form of features. **(G)** In the Jarvis Unit of PRIMNM, multibeam data (EX1701) revealed an approximate 1,700 m height difference when compared to previous satellite altimetry.

Several observations of undescribed echinoderm taxa, including nine new species and two new genera of asteroids, in the families Goniasteridae and Ganeriidae were made during CAPSTONE. Important ecological observations of rarely encountered species, known only from unique or damaged specimens, were also made throughout the campaign. The goniasterid, *Circeaster arandae*, described by Mah (2006), was originally described from two dried specimens collected in the early 20th Century and not seen since. CAPSTONE was the first to observe this species *in situ* and as a significant predator on deep-sea octocorals.

Regional Comparisons

Across anthozoans, poriferans, and echinoderms, the most abundant taxa are concentrated in the Western Pacific, Hawaiian Islands, and South-Central Pacific Regions (**Figures 4–6**). Marianas and American Samoa Regions have unique taxa (heatmaps, **Figures 4–6**). Despite this, all regions show similar patterns of known versus unknown diversity at the family, genus, and species level (**Figure 2**). The Western Pacific Region appears to have the most known diversity at the genus level (**Figure 2**), but note that the majority of dives in this region were on guyots (**Supplementary Figure 1**).

The family Chrysogorgiidae was the only family to be in the top five most abundant for all regions (**Supplementary Table 6**), with abundance ranging from 4.58% (American Samoa region) to 15.50% (Hawaiian region; **Figure 4C**). Isididae was the most abundant family in Hawaiian region, fifth most abundant in Marianas, and was in the top 10 most abundant for all other regions. Primnoidae was the most abundant family in South-Central Pacific (17.59%) and Western Pacific (21.06%) and in the top five most abundant for the Hawaiian region (10%). Primnoidae represented only 3.82% of individuals observed in the Marianas and 0.39% of individuals in the Marianas.

While the family Coralliidae was common in the Hawaiian Region (11.77%), South-Central Pacific (2.76%), and Western Pacific (10.17%), it was completely absent from the American Samoa region and represented only 0.26% of individuals in the Marianas. Conversely, other families were common in the Marianas and absent elsewhere. For example, Stylasteridae only appeared in the top five most abundant families in the Marianas region (14.34%). Although geographically distant, there were some similarities between American Samoa and the Marianas, which generally grouped away from other regions (**Figure 8**). For example, the most abundant family in American Samoa was Dendrophylliidae (39.3%), which was the third most abundant family in the Marianas (10.33%), but not in the top five most abundant for any other region. Antipathidae was only in the top five most abundant families in the American Samoa region (26.08%). There was no overlap between the most abundant genus in each region.

DISCUSSION

The Pacific Ocean, totaling 161,760,000 km^2, has hosted voyaging and discovery since the beginning of human history, and as such

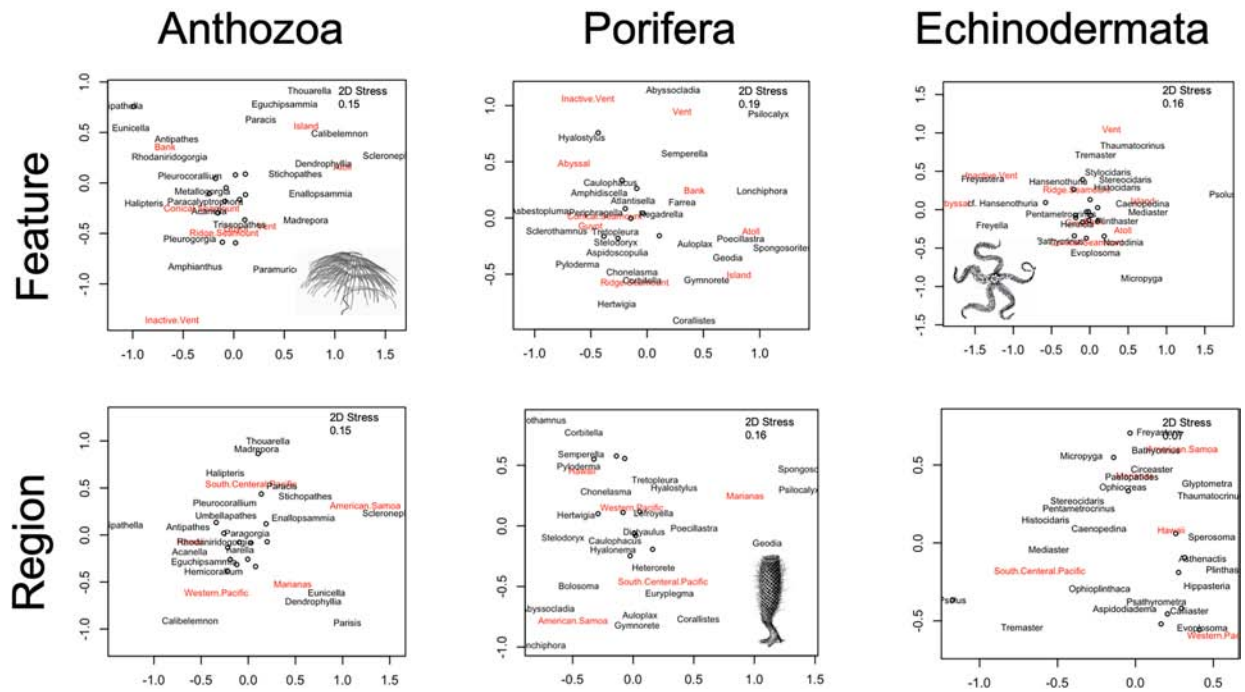

FIGURE 8 | Non-metric multiple dimensional scaling ordination of the Bray–Curtis dissimilarity matrices are displayed, with geologic feature **(top panel)** and geographic region **(bottom panel)** groups noted. Taxonomic assemblages are abundances corrected for effort at the genus-level for the highest frequency genera observed (*N* = 35 for each).

has become an icon of vastness and exploration. CAPSTONE was a systematic exploration effort aimed to increase the mapping and ROV image data available for the Pacific seafloor. In this, CAPSTONE greatly succeeded, and has generated new ideas and hypotheses as well as highlighted challenges and opportunities for future exploration. The main contributions of this paper are therefore (1) providing a high-level overview of the methods, datasets, and key findings of CAPSTONE; (2) conducting a high-level initial analysis of basin-scale patterns of biogeography and biodiversity across the Pacific; (3) generating new hypotheses about distribution of taxa across depth, geographic regions, and geologic features, and (4) highlighting the knowledge gaps in mapping, exploration, and biodiversity in the Pacific deep-ocean.

Prior to CAPSTONE, the best bathymetry available in most of the areas was satellite-derived bathymetry (Amante and Eakins, 2009). The bathymetry acquired during CAPSTONE enabled detailed examination of 323 seamounts and seafloor features, which in turn enabled 168 ROV dives. This overall effort yielded 0.37% bathymetry mapping of the seafloor in the Pacific Ocean. However, because ∼68% of the Pacific is abyssal plain (deeper than 3,000 m), and because CAPSTONE mapping data were disproportionately focused on features of interest (e.g., seamounts, atolls, and vents), the contribution of CAPSTONE to our understanding of Pacific Ocean geology and biology is much >0.37% and 3% of US EEZ. At the same time, these statistics reveal how much is still yet-to-be-explored.

One of the major findings of this paper is the extent of unidentified observations over the 3 years of CAPSTONE. It has long been known that the deep-sea is one of the largest and last earth wildernesses to be explored (Ramirez-Llodra et al., 2011) but the ability to quantify the extent to which we need to explore it has not previously been fully articulated. It is now clear that 86.22% of the Pacific has yet-to-be mapped (**Table 2**), and over 99% of it yet-to-be-imaged (Ramirez-Llodra et al., 2010). For all taxonomic groups examined in the deep sea, we found that fewer than 20% of the species were able to be identified, and this number is limited to the organisms large enough to be visualized in habitats accessible with the ROV. In the Mediterranean deep-sea, biodiversity among different taxa was estimated to the species level across depths, with meiofauna expected to be the most biodiverse (Danovaro et al., 2010). CAPSTONE did not assess any meiofauna, thus even with the incredible diversity measured on this campaign, quantitative unknowns are still likely to underestimate overall diversity. Clearly, more taxonomy and systematics work is needed, in addition to basic mapping and exploration.

Patterns of biodiversity across the Pacific are still unresolved, as there are very few extensive studies that occur over a basin-wide scale. A recent paper proposed biogeographic provinces for the bathyal, abyssal, and hadal faunal communities across the Pacific (Watling et al., 2013), but full tests of the proposed Pacific boundaries have been challenging due to lack of data. The basin-wide scale approach of CAPSTONE crossed 48 degrees of latitude and 61 degrees of longitude. While postulating biogeographic provinces is outside the scope of this paper, the South-Central Pacific region had highest family and genus

diversity, which is consistent with previous evidence showing that the Central Pacific deep sea has relatively high benthic diversity (Lambshead et al., 2002). Although geographically close, American Samoa is very distinct from the South-Central Pacific, likely due to ocean circulation passages in the region that may act as a barrier for larval dispersal, specifically the Samoan Passage (Herrera et al., 2018). In addition, American Samoa lies in close proximity to the intersection of bathyal provinces predicted by Watling et al. (2013), which may also contribute to the difference in community assemblage compared to the South-Central Pacific. In contrast, though geographically distant, American Samoa and Marianas had some unexpected similarities in community assemblages, especially within Anthozoa, that beg further investigation.

More broadly, species biodiversity has been thought to be unimodal with an equatorial peak and a corresponding decline in species richness from the lower to higher latitudes, generally demonstrated in terrestrial (Kaufman, 1995; Gaston, 2000), and shallow-water marine species distributions (Hillebrand, 2004; Fautin et al., 2013). However, Chaudhary et al. (2016) found a dip in shallow marine species richness just below the equator. Although taxonomic assemblages varied widely among regions and features across the Pacific, we found that all regions show similar patterns of known versus unknown diversity at the family, genus, and species level (**Figure 2**), which was relatively surprising. However, the current proposed biogeographic boundaries for bathyal species (Watling et al., 2013) were largely derived from ophiuroid fauna on the Austral plate (O'Hara et al., 2011) and from seamount data largely describing deep-sea sponge and coral communities. We thus similarly restricted our focused taxonomic examinations to the class Anthozoa, and phyla Porifera and Echinodermata, which were the top three most abundant and highest confidence identifications, though CAPSTONE annotation data captured all taxa identifiable by visual surveys on ROV dives.

There are many insights to be gleaned from CAPSTONE data, many of which will require substantial further investigation. For example, we found that Anthozoa, Porifera, and Echinodermata all have some genera that are highly specific to geologic features. This is surprising because, at depth (1,000–4,000 m), no major differences were expected between vertical slopes on islands, atolls, banks, guyots, or conical seamounts. Historically, seamounts have been proposed as deep-sea refugia and stepping stones for dispersal due to similarities among clusters of seamounts (reviewed by Clark et al., 2010; Shank, 2010). Generally, these features are all manganese-encrusted, residing in similar oceanographic conditions (Hein et al., 2000), and often in close geographic proximity. Therefore, we expected that dispersal and recruitment on available structures would be indiscriminate of seamount shape or height. Yet, the apparently preferential distribution and abundance of specific taxa to one feature over another in our data suggests otherwise. Recent work in shallow reef environments has shown that the terrestrial environment has been more important than previously appreciated, mostly mediated by bird guano and nutrient inputs via groundwater and lagoonal flow (McMahon and Santos, 2017; Graham et al., 2018); anthropogenic impacts via wastewater and manure have been shown to affect nutrient coastal fluxes on tropical Pacific islands via groundwater as well (Shuler et al., 2019). Submarine groundwater discharge has been shown to impact marine biota across all kingdoms of life, around the globe (reviewed by Lecher and Mackey, 2018), but the depths to which these impacts reach have thus far remained uninvestigated. Our study tantalizingly suggests that surface or shallow-water dynamics on islands versus atolls versus banks may influence deep-sea benthic communities; this requires further study.

Several new genera and new species were observed and collected during CAPSTONE, including a previously undescribed genus and species of sea star (family Goniasteridae, class Asteroidea) discovered in the Musicians Seamounts in 2017 (**Figure 7**). CAPSTONE data have already been instrumental in the description of 13 new species and two new genera of Primnoid corals (Cairns, 2018), as well as a new species of stylasterid coral, *Crypthelia kelleyi* from the Northwest Hawaiian Islands (Cairns, 2017). One new genus, *Macroprimnoa* spp., possesses some of the largest polyps in the family (Cairns, 2018). A likely novel species of *Neopilina* monoplacophoran was observed in American Samoa, which expands the known diversity of living monoplacophorans (Sigwart et al., 2018), which were previously known from the fossil record but only discovered to be extant in 1952 (Lemche, 1957). New species are still regularly being discovered, to some extent scaling with exploration effort (e.g., Ramirez-Llodra et al., 2010). As such, our rarefaction curves for each taxon, demarcated by depth, should help to focus exploration effort by depth and taxa for the future.

In addition to new taxa, there have been several new records of range, depth, size, or behavior. In the Hawaiian Islands Region, incirrate octopods were discovered deeper than had previously been reported, 4,120–4,197 m (Purser et al., 2016). One of the largest living sponges in existence, a hexactinellid sponge in the subfamily Lanuginellinae, was documented at 2,117 m in the Papahānaumokuākea Marine National Monument in the Hawaiian Islands region (Wagner and Kelley, 2017). The only other living sponges known to be comparable in size are *Monorhaphis chuni* sponges from the East and South China Sea, with spicules reaching up to 2.7 m in length (Jochum et al., 2017). Our study did not examine fish in any detail beyond inclusion in all-taxa diversity pie-charts; however, CAPSTONE has already yielded some teleost discoveries. The first aphyonid-clade brotula fish was observed alive in its natural habitat in the Mariana Archipelago (2,504.2 m); this improbable fish, which is translucent with no swim bladder and diminished eyes, had never been imaged *in situ* prior to CAPSTONE (Mundy et al., 2018). Myriad other new records likely exist in the dataset. For example, in the deepwater areas around Kingman Reef, several gastropods were observed putatively grazing on bathycrinid stalked crinoids, reminiscent of coprophagus snails (Platyceratidae) known from Paleozoic fossils but thought to be extinct (**Figure 7**). These, and other observations have yet to be fully described and require additional analysis.

Whole new features have also been discovered, for example three new sites of hydrothermal activity in the Marianas, including the first survey of a new black smoker vent field composed of multiple chimneys in the Mariana Back Arc

(**Figure 7**). While not covered in this analysis, CAPSTONE also included some of the first-ever midwater ROV exploration dives in many of these areas (Netburn et al., 2018) and collected numerous geological samples that may provide new insights into seafloor history or ferromanganese crust dynamics. Additionally, on the benthos, many more features were discovered with high resolution multibeam mapping over areas that had previously only been mapped using satellite altimetry, often resolving great discrepancies in depth or form of features. For example, in the Jarvis Unit of the Pacific Remote Islands Marine National Monument (PRIMNM), multibeam data revealed an approximate 1,700 m height difference when compared to previous satellite altimetry (**Figure 7G**). Yet, despite these massive leaps forward in mapping, exploration, taxonomic description, and functional insights, the context for our ocean understanding is still derived from a scant 5% of the seafloor explored, with <10% mapped with modern methods (Mayer et al., 2018). Thus, the discovery of new features is expected to increase with additional mapping and exploration effort.

In addition to providing valuable information on the features, habitats, and species in the Pacific, CAPSTONE also contributed publicly accessible baseline data and critical information needed to respond to emerging regional issues such as deep-sea mining, sustainable deep-sea fisheries, and changes in ocean dynamics. During the 3 years of CAPSTONE expeditions, *Okeanos Explorer* visited every US National Marine Monument in the Pacific, including many that previously had no information about their deepwater communities, thus greatly expanding our deep-sea knowledge within these boundaries (Wagner et al., 2017; Cantwell et al., 2018b; Leonardi et al., 2018). These expeditions conducted the deepest surveys in every unit of PRIMNM, Papahānaumokuākea Marine National Monument, and Rose Atoll Marine National Monument/the National Marine Sanctuary of American Samoa. In several areas, CAPSTONE expeditions were the first to explore in deep-water, for example in the Phoenix Islands (in both the United States and Kiribati), Wake Island, Johnston Atoll, and the Musicians Seamounts (Elliott et al., 2016; Bohnenstiehl et al., 2018; Cantwell et al., 2018b; Demopoulos et al., 2018; Smith et al., 2018).

Modern advances are broadening the opportunities for exploration with increased robotics, optics, and telepresence (Kaiser et al., 2012; Gregory et al., 2016; Kennedy et al., 2016; Vogt et al., 2018). While there are still more advances to be made, CAPSTONE represents the largest area of seafloor imaged in a single campaign. While using video data for taxonomic identification has limitations, such as instances of poor image quality and the inability to conduct lab-based analyses, the key advantage is that video annotation affords an efficient and tractable method to study taxa. Given emerging deep-sea technologies and exploits, exploration is a global priority (Cordes and Levin, 2018). Exploration helps to describe species and habitats, understand the drivers of community structure, and generate testable hypotheses about deep-sea ecosystems that will better-serve all users and stakeholders. One major contribution of this paper is intended to be the initial consolidation and presentation of the CAPSTONE data suite, to showcase the opportunities for novel hypothesis-testing and seed novel ideas. Differences between islands vs. atolls, or conical seamounts vs. guyots, for example, were not previously thought to be important in structuring deep-sea communities. Our analyses suggest otherwise, and these observations (and others) in this paper would benefit from future, finer-scale analysis efforts. Additionally, as technology improves, new methods for maximizing the utility of deep-sea video data for biological research will allow the use of emergent technologies such as machine-learning and autonomous data collection platforms to increase the pace of exploration. The current video archive can be re-annotated and mined for new observations and patterns that were not originally intended. Thus, CAPSTONE data offer the opportunity to test how large-scale video analysis and annotation can be creatively used now, and into the future.

Now that data baselines have been set across 168 dive sites in the Pacific, it is important to leverage these visual observations to more thoroughly test mechanisms and drivers of community composition in the deep-sea. Many of the places visited during CAPSTONE are remote and infrequently visited, thus the ability to deploy expendable technology that would continue to record time series data after the ships have departed, without the need to return to for retrieval, will be critical to turn single-visit observations into a much richer dataset. With forward planning, ROV visitation could optimize our ability to understand community distribution, long-term site conditions, and how deep sea fauna interact with their environment and begin to inform connectivity patterns, basin-wide. Especially because most of the Pacific CAPSTONE sites reside within large-scale marine protected areas (LSMPAs), these locales will likely remain free from exploitation, thus serving as valuable benchmarks for deep-sea community response to larger-scale issues and changes in global and Pacific-wide ocean dynamics. Although historically LSMPAs lack sufficient deep-water information for government officials to effectively manage these areas and monitoring these LSMPAs has been shown to be particularly difficult (Friedlander et al., 2016), the baseline provided by CAPSTONE and the potential for future autonomous monitoring will enable managers to better assess LSMPA status.

Coordinated field efforts that result in consistent datasets are absolutely critical in order to reduce "unknowns" in the deep sea. Standardized efforts across large areas offer opportunities to better understand geographic patterning as well as the rare ability to make regional comparisons. CAPSTONE has made major inroads into the necessary data to generate these comparisons, though there are still major gaps in our understanding, due in part to the uneven distribution of effort across feature types and depth ranges that could be remedied with a gap analysis and a future targeted effort to fill exploration gaps by region, and also by depth and feature. Nonetheless, CAPSTONE represented a model of systematic exploration that is critical to understanding one of the earth's largest ecosystems (Ramirez-Llodra et al., 2011). As we look to the future of ocean exploration, coordinated field campaigns should incorporate multiple ships and additional technologies including towed arrays, ship mounted systems, and autonomous systems, in order to maximize data collected.

Projects like Seabed 2030 (Mayer et al., 2018) have set ambitious goals that can only be accomplished through internationally coordinated efforts. If one ship can only map 0.37% of the Pacific in 3 years, additional assets with a diversity of systems will need to work together to map the whole ocean in just over a decade.

Ironically named, CAPSTONE is more of a beginning than a culminating experience. It is the launch of decades of data-mining, visual analyses, hypothesis-generation, and justification for future exploration. The trends highlighted in this paper offer a snapshot of what is known, and what remains unknown, in the Pacific Ocean. What we have learned from 3 years and 891.5 h on the seafloor is that the Pacific is not just a place of historical exploration and voyaging: it is a place that offers extensive opportunities for technology innovations, and insights. In other words, it is a place for future discovery.

DATA AVAILABILITY

The datasets generated by the NOAA Ship *Okeanos Explorer* that were analyzed for this study are archived in the NOAA archives and can be found through the OER Digital Atlas (https://www.ncddc.noaa.gov/website/google_maps/OE/mapsOE.htm). ROV video annotations can be found in the Deep Sea Coral Research and Technologies' Deep Sea Coral Data Portal at https://deepseacoraldata.noaa.gov/.

AUTHOR CONTRIBUTIONS

BK, RR, KC, and MM were primarily responsible for manuscript preparation and data analysis. BK, KC, MM, EL, DS, MW, KE, and LG were responsible for sailing and coordinating all CAPSTONE expeditions. CK, VM, SB, and MP were responsible for creating all the annotations from the ROV video. SA, SF, and CM provided expertise and context on Anthozoa and Echinodermata analysis. JP was responsible for the creation of CAPSTONE and CK was the CAPSTONE science advisor to NOAA. All authors participated in editing and final preparation of the manuscript.

FUNDING

Funding and in-kind contributions for field work were provided by the NOAA's Office of Ocean Exploration and Research, the National Marine National Marine Sanctuaries Program, the Pacific Islands Fisheries Science Center, the Pacific Islands Regional Office, the DSCRTP, and the National Marine Fisheries Service. Funding for the creation of the annotations was provided by the DSCRTP. Funding for data analysis and manuscript preparation was provided by the DSCRTP through a memorandum of understanding with the University Corporation for Atmospheric Research.

ACKNOWLEDGMENTS

We would like to thank the NOAA for their funding and support of CAPSTONE, specifically the Office of Ocean Exploration and Research, the Office of Marine and Aviation Operations, the Pacific Island Fisheries Science Center, the Pacific Islands Regional Office, the DSCRTP, the Office of National Marine Sanctuaries, the National Center for Environmental Information (NCEI), the National Ocean Service, the National Environmental Satellite, Data, and Information Service (NESDIS), the Oceanic and Atmospheric Research (OAR), the National Marine Fisheries Service's (NMFS), and the officers and crew of NOAA Ship *Okeanos Explorer*. Thanks to the Hawai'i Undersea Research Laboratory (HURL), the GFOE, the University of Hawaii, the Smithsonian Natural Museum of Natural History, and the Oregon State University's Marine Geology Repository for their continuous and critical support throughout CAPSTONE. We also acknowledge the Monterey Bay Aquarium Research Institute for its VARS software and support. Additionally, we are grateful to Craig Russell (NOAA OER) and the rest of the expedition science teams from CAPSTONE expeditions for sharing their expertise and guiding operations in real-time as well as all of the regional managers and stakeholders who contributed to expedition planning. We would also like to thank Jesse Varner (NOAA NCEI) who helped process the multibeam footprint for data held at NCEI and Abby Reft (NOAA NMFS) who provided archived sample use information and coordinated Smithsonian participation in this manuscript. Additional funding for analysis was provided by the NOAA DSCRTP through the University Corporation for Atmospheric Research. CAPSTONE was completed in accordance with all regulations regarding environmental compliance and local permitting including the following permits: Kiribati Phoenix Islands Protected Area permit #1/17, Commonwealth of the Northern Mariana Islands Department of Lands and Natural Resources permit #03345, Hawai'i Department of Land and Natural Resources permit #SAP-2016-64, Cook Islands Marae Moana permit #05/17, National Marine Sanctuary of American Samoa permit #NMAS-2017-001, American Samoa Department of Marine and Wildlife Resources permit #2017/001, US Fish and Wildlife Convention on International Trade in Endangered Species (CITES) import permit #17US36207C/9; Papahānaumokuākea Marine National Monument permit #PMN-2015-018; and Marshall Islands Ministry of Foreign Affairs permit #US/98-15. Any use of trade, product, or firm names is for descriptive purposes only and does not imply endorsement by the US Government.

SUPPLEMENTARY MATERIAL

The Supplementary Material for this article can be found online at: https://www.frontiersin.org/articles/10.3389/fmars.2019.00480/full#supplementary-material

REFERENCES

Amante, C., and Eakins, B. W. (2009). *ETOPO1 Arc-Minute Global Relief Model: Procedures, Data Sources and Analysis. NOAA Technical Memorandum NESDIS NGDC-24*. Silver Spring, MD: National Geophysical Data Center, NOAA, doi: 10.7289/V5C8276M

Baco, A. R., Etter, R. J., Ribeiro, P. A., von der Heyden, S., Beerli, P., and Kinlan, B. P. (2016). A synthesis of genetic connectivity in deep-sea fauna and implications for marine reserve design. *Mol. Ecol.* 25, 3276–3298. doi: 10.1111/mec.13689

Bohnenstiehl, D. R., France, S. C., Cantwell, K., and White, M. (2018). Mountains in the deep: exploration of the seamounts of the Central Pacific Basin. *Oceanography* 31, 78–79. doi: 10.5670/oceanog.2018.supplement.01

Cairns, S. D. (2017). New species of stylasterid (Cnidaria: Hydrozoa: Anthoathecata: Stylasteridae) from the Northwestern Hawaiian Islands. *Pacific Sci.* 71, 77–81. doi: 10.2984/71.1.7

Cairns, S. D. (2018). Primnoidae (Cnidaria: Octocorallia: Calcaxonia) of the Okeanos explorer expeditions (CAPSTONE) to the central Pacific. *Zootaxa* 4532, 1–43. doi: 10.11646/zootaxa.4532.1.1

Cantwell, K., Elliott, K., Kelley, C., and Gottfried, S. (2018a). CAPSTONE sampling overview: providing insights in the remote pacific. *Oceanography* 31, 84–85.

Cantwell, K., Elliott, K., and Kennedy, B. R. C. (2018b). Deepwater exploration of the pacific remote islands marine national monument and Central Pacific Basin. *Oceanography* 31, 74–75. doi: 10.5670/oceanog.2018.supplement.01

Chaudhary, C., Saeedi, H., and Costello, M. J. (2016). Bimodality of {Latitudinal} {Gradients} in {Marine} {Species} {Richness}. *Trends Ecol. Evol.* 31, 670–676. doi: 10.1016/j.tree.2016.06.001

Clark, M. R., Rowden, A. A., Schlacher, T., Williams, A., Consalvey, M., Stocks, K. I., et al. (2010). The ecology of seamounts: structure, function, and human impacts. *Ann. Rev. Mar. Sci.* 2, 253–278. doi: 10.1146/annurev-marine-120308-081109

Cordes, E. E., and Levin, L. A. (2018). Exploration before exploitation. *Science* 359:719. doi: 10.1126/science.aat2637

Danovaro, R., Corinaldesi, C., D'Onghia, G., Galil, B., Gambi, C., Gooday, A. J., et al. (2010). Deep-sea biodiversity in the mediterranean sea: the known, the unknown, and the unknowable. *PLoS One* 5:e11832. doi: 10.1371/journal.pone.0011832

Danovaro, R., Dell'Anno, A., Fabiano, M., Pusceddu, A., and Tselepides, A. (2001). Deep-sea ecosystem response to climate changes: the eastern Mediterranean case study. *Trends Ecol. Evol.* 16, 505–510. doi: 10.1016/s0169-5347(01)02215-7

De Leo, F. C., Smith, C. R., Rowden, A. A., Bowden, D. A., and Clark, M. R. (2010). Submarine canyons: hotspots of benthic biomass and productivity in the deep sea. *Proc. R. Soc. B Biol. Sci.* 277, 2783–2792. doi: 10.1098/rspb.2010.0462

Demopoulos, A. W. J., Auscavitch, S., Sowers, D., Pawlenko, N., and Kennedy, B. R. C. (2018). Discovering the deep: exploring remote pacific marine protected areas. *Oceanography* 31, 76–77. doi: 10.5670/oceanog.2018.supplement.01

Dunn, D. C., Van Dover, C. L., Etter, R. J., Smith, C. R., Levin, L. A., Morato, T., et al. (2018). A strategy for the conservation of biodiversity on mid-ocean ridges from deep-sea mining. *Sci. Adv.* 4:eaar4313. doi: 10.1126/sciadv.aar4313

Eakins, B. W., and Sharman, G. F. (2010). *Volumes of the World's Oceans from ETOPO1*. Boulder, CO: NOAA National Geophysical Data Center.

Elliott, K. P., Kennedy, B. R. C., Elizebeth, L., and Potter, J. (2016). Okeanos explorer 2015 field season overview. *Oceanography* 29, 58–61. doi: 10.5670/oceanog.2016.supplement.01

Fautin, D. G., Malarky, L., and Soberón, J. (2013). Latitudinal diversity of sea anemones (cnidaria: Actiniaria). *Biol. Bull.* 224, 89–98. doi: 10.1086/BBLv224n2p89

Friedlander, A. M., Wagner, D., Gaymer, C. F., Wilhelm, T. A., Lewis, N. A., Brooke, S., et al. (2016). Co-operation between large-scale MPAs: successful experiences from the Pacific Ocean. *Aquat. Conserv. Mar. Freshw. Ecosyst.* 26, 126–141. doi: 10.1002/aqc.2645

Gaston, K. J. (2000). Global patterns in biodiversity. *Nature* 405, 220–227.

Graf, G. (1989). Benthic-pelagic coupling in a deep-sea benthic community. *Nature* 341, 437–439. doi: 10.1038/341437a0

Graham, N. A. J., Wilson, S. K., Carr, P., Hoey, A. S., Jennings, S., and Macneil, M. A. (2018). Seabirds enhance coral reef productivity and functioning in the absence of invasive rats. *Nature* 559, 250–253. doi: 10.1038/s41586-018-0202-3

Gregory, T., Lovalvo, D., Mohr, B., McLetchie, K., and Ryan, M. (2016). Advancing undersea technology. *Oceanography* 29, 52–55. doi: 10.5670/oceanog.2016.supplement.01

Hein, J. R., Koschinsky, A., Bau, M., Manheim, F. T., Kang, J.-K., and Roberts, L. (2000). "Cobalt-rich ferromanganese crusts in the Pacific," in *Handbook of Marine Minerals*, ed. D. S. Cronan (Boca Raton, FL: CRC Press), 239–279. doi: 10.1201/9780203752760-9

Hein, J. R., Mizell, K., Koschinsky, A., and Conrad, T. A. (2013). Deep-ocean mineral deposits as a source of critical metals for high- and green-technology applications?: comparison with land-based resources. *Ore Geol. Rev.* 51, 1–14. doi: 10.1016/j.oregeorev.2012.12.001

Herrera, S., Jackson, M. G., Elliott, K., and Lobecker, E. (2018). "Biodiversity of the deep-sea benthic fauna in the American Samoa region," in *Proceedings of the Ocean Sciences Meeting on ME52A-05: Oral Presentation*, (Portland, OR).

Hillebrand, H. (2004). Strength, slope and variability of marine latitudinal gradients. *Mar. Ecol. Prog. Ser.* 273, 251–267. doi: 10.1371/journal.pone.0067596

Hughes, J. B., Hellmann, J. J., Ricketts, T. H., and Bohannan, B. J. M. (2001). Counting the uncountable: statistical approaches to estimating microbial diversity. *Appl. Environ. Microbiol.* 67, 4399–4406. doi: 10.1128/AEM.67.10.4399-4406.2001

Jamison, A. (2015). *The Hadal Zone – Life in the Deepest Ocean*, 1st Edn. Cambridge, MA: Cambridge University Press.

Jochum, K. P., Schuessler, J. A., Wang, X. H., Stoll, B., Weis, U., Müller, W. E. G., et al. (2017). Whole-ocean changes in Silica and Ge/Si ratios during the last deglacial deduced from long-lived giant glass sponges. *Geophys. Res. Lett.* 44, 11,555–11,564. doi: 10.1002/2017GL073897

Kaiser, C. L., Kinsey, J. C., Pinner, W., Yoerger, D. R., German, C. R., and Van Dover, C. L. (2012). "Satellite based remote management and operation of a 6000m AUV," in *Proceeddings of the Ocean 2012 MTS/IEEE Harnessing Power Ocean*, (Hampton Roads, VA), doi: 10.1109/OCEANS.2012.6404900

Kaufman, D. M. (1995). Diversity of New World mammals: universality of the latitudinal gradients of species and bauplans. *J. Mammal.* 76, 322–334. doi: 10.2307/1382344

Kennedy, B. R. C., Elliott, K. P., Cantwell, K., and Mesick, S. (2016). Telepresence-enabled exploration with NOAA ship okeanos explorer. *Oceanography* 29, 50–51. doi: 10.5670/oceanog.2016.supplement.01

Koslow, J. A., Goericke, R., Lara-Lopez, A., and Watson, W. (2011). Impact of declining intermediate-water oxygen on deepwater fishes in the California current. *Mar. Ecol. Prog. Ser.* 436, 207–218. doi: 10.3354/meps09270

Lambshead, P. J. D., Brown, C. J., Ferrero, T. J., Mitchell, N. J., Smith, C. R., Hawkins, L. E., et al. (2002). Latitudinal diversity patterns of deep-sea marine nematodes and organic fluxes: a test from the central equatorial Pacific. *Mar. Ecol. Prog. Ser.* 236, 129–135. doi: 10.3354/meps236129

Lecher, A., and Mackey, K. (2018). Synthesizing the effects of submarine groundwater discharge on marine biota. *Hydrology* 5:60. doi: 10.3390/hydrology5040060

Lemche, H. (1957). A new living deep-sea mollusc of the Cambro-Devonian Class Monoplacophora. *Nature* 179, 413–416. doi: 10.1038/179413a0

Leonardi, A., Armor, J., Montanio, P., and Werner, C. (2018). CAPSTONE: NOAA's campaign to address Pacific monument Science, Technology, and Ocean Needs. *Oceanography* 29, 48–52.

Levin, L. A., Etter, R. J., Rex, M. A., Gooday, A. J., Smith, C. R., Pineda, J., et al. (2001). Environmental influences on regional deep-sea species diversity. *Annu. Rev. Ecol. Syst.* 32, 51–93. doi: 10.1146/annurev.ecolsys.32.081501.114002

Levin, S. A., Godfray, H. C., Kinzing, A. P., Loreau, M., Losos, J., Walker, B., et al. (2009). *The Princeton Guide to Ecology*. Princeton, NJ: Princeton University Press.

Mah, C. L. (2006). Phylogeny and biogeography of the deep-sea goniasterid Circeaster (Echinodermata, Asteroidea, Goniasteridae) including descriptions of six new species. *Zoosystema* 28, 917–954.

Mayer, L., Jakobsson, M., Allen, G., Dorschel, B., Ferrini, V., Snaith, H., et al. (2018). The Nippon foundation—GEBCO seabed 2030 project: the quest to see the world's oceans completely mapped by 2030. *Geosciences* 8:63. doi: 10.3390/geosciences8020063

McClain, C. R., and Rex, M. A. (2015). Toward a conceptual understanding of β-Diversity in the deep-sea benthos. *Annu. Rev. Ecol. Evol. Syst.* 46, 623–642. doi: 10.1146/annurev-ecolsys-120213-091640

McClain, C. R., and Schlacher, T. A. (2015). On some hypotheses of diversity of animal life at great depths on the sea floor. *Mar. Ecol.* 36, 849–872. doi: 10.1111/maec.12288

McMahon, A., and Santos, I. R. (2017). Nitrogen enrichment and speciation in a coral reef lagoon driven by groundwater inputs of bird guano. *J. Geophys. Res. Ocean.* 122, 7218–7236. doi: 10.1002/2013JC009262.Received

Mengerink, K. J., Van Dover, C. L., Ardron, J., Baker, M., Escobar-Briones, E., Gjerde, K., et al. (2014). A call for deep-ocean stewardship. *Science* 344, 696–698. doi: 10.1126/science.1251458

Mesick, S., Gottfried, S., Reser, B., and Woodard, K. (2016). Applied excellence in data management. *Oceanography* 29, 56–57. doi: 10.5670/oceanog.2016.supplement.01

Mora, C., Aburto-Oropeza, O., Ayala-Bocos, A., Ayotte, P. M., Banks, S., Bauman, A. G., et al. (2011). Global human footprint on the linkage between biodiversity and ecosystem functioning in reef fishes. *PLoS Biol.* 9:e1000606. doi: 10.1371/journal.pbio.1000606

Mundy, B. C., Gerringer, M. E., Nielsen, J. G., Fryer, P., and Leitner, A. (2018). First in situ observation of an aphyonid fish (Teleostei, Ophidiiformes, Bythitidae). *Deep. Res. Part II Top. Stud. Oceanogr.* 150, 164–169. doi: 10.1016/j.dsr2.2017.09.009

Murray, J. (1895). *A Summary of the Scientific Results Obtained at the Sounding, Dredging and Trawling Stations of HMS Challenger*, Vol. 1. Richmond: HM Stationery Office.

Netburn, A. N., Ford, M., and Lindsay, D. (2018). 2017 midwater exploration on okeanos explorer. *Oceanography* 31, 61–63. doi: 10.5670/oceanog.2018.supplement.01

O'Hara, T. D., Rowden, A. A., and Bax, N. J. (2011). A Southern Hemisphere bathyal fauna is distributed in latitudinal bands. *Curr. Biol.* 21, 226–230. doi: 10.1016/j.cub.2011.01.002

Oksanen, A. J., Blanchet, F. G., Kindt, R., Legen-, P., Minchin, P. R., Hara, R. B. O., et al. (2018). *Package ' vegan ' version 2.5-2.*

Philbrick, N. (2004). *Sea of Glory: America's Voyage of Discovery, The U.S. Exploring Expedition, 1838-1842*. New York, NY: Penguin Books.

Purser, A., Marcon, Y., Hoving, H. J. T., Vecchione, M., Piatkowski, U., Eason, D., et al. (2016). Association of deep-sea incirrate octopods with manganese crusts and nodule fields in the Pacific Ocean. *Curr. Biol.* 26, R1268–R1269. doi: 10.1016/j.cub.2016.10.052

Quattrini, A. M., Nizinski, M. S., Chaytor, J. D., Amanda, W., Demopoulos, J., Roark, E. B., et al. (2015). Exploration of the canyon-incised continental margin of the northeastern United States reveals dynamic habitats and diverse communities. *PLoS One* 10:e0139904. doi: 10.1371/journal.pone.0139904

Ramirez-Llodra, E., Brandt, A., Danovaro, R., De Mol, B., Escobar, E., German, C. R., et al. (2010). Deep, diverse and definitely different: unique attributes of the world's largest ecosystem. *Biogeosciences* 7, 2851–2899. doi: 10.5194/bg-7-2851-2010

Ramirez-Llodra, E., Tyler, P. A., Baker, M. C., Bergstad, O. A., Clark, M. R., Escobar, E., et al. (2011). Man and the last great wilderness: human impact on the deep sea. *PLoS One* 6:e22588. doi: 10.1371/journal.pone.0022588

Rex, M. A., and Etter, R. J. (2010). *Deep-Sea Biodiversity: Pattern and Scale*. Boston, MA: Harvard University Press.

Sarmiento, J. L., Gruber, N., Brzezinski, M. A., and Dunne, J. P. (2004). High-latitude controls of thermocline nutrients and low latitude biological productivity. *Nature* 427, 56–60. doi: 10.1038/nature02127

Schlining, B. M., and Stout, N. J. (2006). "MBARI ' s video annotation and reference system," in *Proceedings of the Marine Technology Society/Institute of Electrical and Electronics Engineers Oceans Conference*, (Boston, MA), 1–5.

Shank, T. (2010). Seamounts: deep-ocean laboratories of faunal connectivity, evolution, and endemism. *Oceanography* 23, 108–122. doi: 10.5670/oceanog.2010.65

Shuler, C., Amato, D., Veronica Gibson, V., Baker, L., Olguin, A., Dulai, H., et al. (2019). Assessment of terrigenous nutrient loading to coastal ecosystems along a human land-Use gradient, Tutuila, American Samoa. *Hydrology* 6:18. doi: 10.3390/hydrology6010018

Sigwart, J. D., Wicksten, M. K., Jackson, M. G., and Herrera, S. (2018). Deep-sea video technology tracks a monoplacophoran to the end of its trail (Mollusca, Tryblidia). *Mar. Biodivers.* 49, 825–832. doi: 10.1007/s12526-018-0860-2

Smith, J. R., Putts, M. R., Mittelstaedt, E., Cantwell, K., Lobecker, E., and White, M. (2018). Symphony of the deep: exploration of the musicians seamounts. *Oceanography* 31, 82–83.

Tyler, P. A., Baker, M., and Ramirez-Llodra, E. (2016). "Deep-sea benthic habitats," in *Biological Sampling in the Deep Sea*, eds A. A. R. Malcolm, R. Clark, and M. Consalvey (West Sussex: John Wiley and Sons. Ltd), 1–15. doi: 10.1002/9781118332535.ch1

Van Dover, C. L. (2000). *The Ecology of Deep-Sea Hydrothermal Vetns*, 1st Edn. Chichester: Princeton University Press.

Vogt, D. M., Becker, K. P., Phillips, B. T., Graule, M. A., Rotjan, R. D., Shank, T. M., et al. (2018). Shipboard design and fabrication of custom 3D-printed soft robotic manipulators for the investigation of delicate deep-sea organisms. *PLoS One* 13:e0200386. doi: 10.1371/journal.pone.0200386

Wagner, D., and Kelley, C. D. (2017). The largest sponge in the world? *Mar. Biodivers.* 47, 367–368. doi: 10.1007/s12526-016-0508-z

Wagner, D., Tree, J., Kennedy, B. R. C., and Cantwell, K. (2017). 2016 Hohonu Moana: exploring the deep waters off Hawai'i. *Oceanography* 30, 56–57. doi: 10.5670/oceanog.2017.supplement.01

Wang, S. C., and Dodson, P. (2006). Estimating the diversity of dinosaurs. *Proc. Natl. Acad. Sci. U.S.A.* 103, 13601–13605. doi: 10.1073/pnas.0606028103

Watling, L., and Auster, P. J. (2017). Seamounts on the high seas should be managed as vulnerable marine ecosystems. *Front. Mar. Sci.* 4:14. doi: 10.3389/fmars.2017.00014

Watling, L., Guinotte, J., Clark, M. R., and Smith, C. R. (2013). A proposed biogeography of the deep ocean floor. *Prog. Oceanogr.* 111, 91–112. doi: 10.1016/j.pocean.2012.11.003

Wessel, P., Sandwell, D. T., and Kim, S.-S. (2010). The global seamount census. *Oceanography* 23, 24–33. doi: 10.5670/oceanog.2010.60

Wu, Y., Zhu, D., Chu, Z., Zhong, C., and Luo, C. (2017). "Autonomous underwater vehicles navigation method based on ultra short base line and dead reckoning," in *Proceedings of the 2016 IEEE International Conference on Underwater System Technology: Theory and Applications (USYS)*, (Penang), 105–109. doi: 10.1109/USYS.2016.7893934

Zachos, J. C., Dickens, G. R., and Zeebe, R. E. (2008). An early Cenozoic perspective on greenhouse warming and carbon-cycle dynamics. *Nature* 451, 279–283. doi: 10.1038/nature06588

Conflict of Interest Statement: KC is employed by MAXIMUS, LG is employed by Athenium Analytics, and DS, EL, and MW are employed by Cherokee Nation Strategic Programs.

The reviewer FA declared a past co-authorship with one of the authors CM to the handling Editor.

The remaining authors declare that the research was conducted in the absence of any commercial or financial relationships that could be construed as a potential conflict of interest.

Copyright © 2019 Kennedy, Cantwell, Malik, Kelley, Potter, Elliott, Lobecker, Gray, Sowers, White, France, Auscavitch, Mah, Moriwake, Bingo, Putts and Rotjan. This is an open-access article distributed under the terms of the Creative Commons Attribution License (CC BY). The use, distribution or reproduction in other forums is permitted, provided the original author(s) and the copyright owner(s) are credited and that the original publication in this journal is cited, in accordance with accepted academic practice. No use, distribution or reproduction is permitted which does not comply with these terms.

frontiers in Marine Science

CORRECTION
published: 18 February 2020
doi: 10.3389/fmars.2019.00827

Corrigendum: The Unknown and the Unexplored: Insights Into the Pacific Deep-Sea Following NOAA CAPSTONE Expeditions

Brian R. C. Kennedy[1,2], Kasey Cantwell[2,3], Mashkoor Malik[2], Christopher Kelley[2,4], Jeremy Potter[5], Kelley Elliott[2], Elizabeth Lobecker[2,6], Lindsay McKenna Gray[2,7], Derek Sowers[2,6], Michael P. White[2,6], Scott C. France[8], Steven Auscavitch[9], Christopher Mah[10], Virginia Moriwake[4], Sarah R. D. Bingo[4], Meagan Putts[4] and Randi D. Rotjan[1]**

[1] Department of Biology, Boston University, Boston, MA, United States, [2] NOAA Office of Ocean Exploration and Research, Silver Spring, MD, United States, [3] MAXIMUS, Metro Center, Reston, VA, United States, [4] University of Hawai'i at Manoa Joint Institute of Marine and Atmospheric Research (JIMAR), Honolulu, HI, United States, [5] Bureau of Ocean Energy Management, Camarillo, CA, United States, [6] Cherokee Nation Strategic Programs, Richmond Hwy Suite, Arlington, TX, United States, [7] Athenium Analytics, Dover, DE, United States, [8] Department of Biology, University of Louisiana at Lafayette, Lafayette, LA, United States, [9] Department of Biology, Temple University, Philadelphia, PA, United States, [10] Department of Invertebrate Zoology, National Museum of Natural History, Smithsonian Institution, Washington, DC, United States

OPEN ACCESS

Edited by:
Cinzia Corinaldesi,
Marche Polytechnic University, Italy

Reviewed by:
Pedro A. Ribeiro,
University of Bergen, Norway

***Correspondence:**
Brian R. C. Kennedy
kennedyb@bu.edu
Randi D. Rotjan
rrotjan@bu.edu

Specialty section:
This article was submitted to Deep-Sea Environments and Ecology, a section of the journal Frontiers in Marine Science

Received: 18 November 2019
Accepted: 23 December 2019
Published: 18 February 2020

Citation:
Kennedy BRC, Cantwell K, Malik M, Kelley C, Potter J, Elliott K, Lobecker E, Gray LM, Sowers D, White MP, France SC, Auscavitch S, Mah C, Moriwake V, Bingo SRD, Putts M and Rotjan RD (2020) Corrigendum: The Unknown and the Unexplored: Insights Into the Pacific Deep-Sea Following NOAA CAPSTONE Expeditions. Front. Mar. Sci. 6:827. doi: 10.3389/fmars.2019.00827

Keywords: ocean exploration, multibeam mapping, biodiversity, seamounts, Okeanos Explorer, Anthozoa, Porifera, Echinodermata

A Corrigendum on

The Unknown and the Unexplored: Insights Into the Pacific Deep-Sea Following NOAA CAPSTONE Expeditions

by Kennedy, B. R. C., Cantwell, K., Malik, M., Kelley, C., Potter, J., Elliott, K., et al. (2019). Front. Mar. Sci. 6:480. doi: 10.3389/fmars.2019.00480

In the original article, there were three typographical errors. The number of hours of ROV video collected was incorrectly listed as 189 in two places in the article when it should have been 891.5 hours. These two typos were in the text only. All figures, effort correction calculations and conclusions were based on the correct number. There was a third, additional error in **Table 2**: Howland Island and Baker Island were listed as being a PRINMS when in fact it should have read PRIMNM.

A correction has been made to the abstract.

Corrected paragraph: Over a 3-year period, the National Oceanic and Atmospheric Administration (NOAA) organized and implemented a Pacific-wide field campaign entitled CAPSTONE: Campaign to Address Pacific monument Science, Technology, and Ocean NEeds. Under the auspices of CAPSTONE, NOAA mapped 597,230 km^2 of the Pacific seafloor (with ∼61% of mapped area located within US waters), including 323 seamounts, conducted 187 ROV dives totaling 891.5 h of ROV benthic imaging time, and documented >347,000 individual organisms. This comprehensive effort yielded dramatic insight into differences in biodiversity across depths, regions, and features, at multiple taxonomic scales. For all deep sea taxonomic groups large enough to be visualized with the ROV, we found that fewer than 20% of the species were able to be identified. The most abundant and highest diversity taxa across the dataset were from three phyla (Cnidaria, Porifera, and Echinodermata). We further examined these phyla for taxonomic assemblage patterns by depth, geographic region, and geologic feature. Within each taxa, there were multiple genera with specific distribution and abundance by depth, region, and feature. Additionally, we observed

TABLE 2 | CAPSTONE multibeam mapping accomplishments after 3 years of effort by the *Okeanos Explorer*.

Location	Total area (km^2)	Total mapped after CAPSTONE (km^2)	% Area mapped after CAPSTONE	Area mapped by CAPSTONE (km^2)	% Area mapped by CAPSTONE
Pacific Ocean	161,760,000	22,299,018	13.78	597,230	0.37
Papahanaumokuakea MNM	1,508,874	578,008	38.31	94,157	6.24
Johnston Atoll PRIMNM	442,443	122,804	27.76	62,482.4	14.12
Wake Island PRIMNM	406,970	111,580	27.42	53,259	13.09
Marianas Trench MNM	204,543	167,129	81.71	21,611	10.57
Phoenix Islands Protected Area	406,801	68,020	16.72	19,196	4.72
NMS of American Samoa (Muliava Sanctuary Unit/Rose Atoll MNM)	34,934	16,216	46.42	1,1955.4	34.22
Jarvis Island PRIMNM	315,339	58,889	18.67	11,911	3.78
NZ Territory of Tokelau	318,507	79,874	25.08	10,604.2	3.33
Howland Island and Baker Island PRIMNM	51,149	15,041	29.41	6,356.38	12.43
Kingman Reef and Palmyra Atoll PRIMNM	53,175	46,665	87.76	5,379.92	10.12
Marae Moana (proposed)	1,961,280	344,043	17.54	3,776.59	0.19
Swains Island Sanctuary Unit	135	135	99.61	11,2.645	83.22

CAPSTONE expeditions resulted in 597,230 km^2 area mapped for the entire Pacific Ocean (first row) and all marine protected areas depicted in km^2.

multiple genera with broad abundance and distribution, which may focus future ecological research efforts. Novel taxa, records, and behaviors were observed, suggestive of many new types of species interactions, drivers of community composition, and overall diversity patterns. To date, only 13.8% of the Pacific has been mapped using modern methods. Despite the incredible amount of new known and unknown information about the Pacific deep-sea, CAPSTONE is far from the culminating experience the name suggests. Rather, it marks the beginning of a new era for exploration that will offer extensive opportunities via mapping, technology, analysis, and insights.

A correction has been made to the Discussion, Paragraph 14 (last paragraph):

Ironically named, CAPSTONE is more of a beginning than a culminating experience. It is the launch of decades of data-mining, visual analyses, hypothesis-generation, and justification for future exploration. The trends highlighted in this paper offer a snapshot of what is known, and what remains unknown, in the Pacific Ocean. What we have learned from 3 years and 891.5 h on the seafloor is that the Pacific is not just a place of historical exploration and voyaging: it is a place that offers extensive opportunities for technology innovations, and insights. In other words, it is a place for future discovery.

Additionally, there was a mistake in **Table 2**. Row 11 should read Howland Island and Baker Island PRIMNM. The corrected **Table 2** appears above.

The authors apologize for these errors and state that these changes do not alter the scientific conclusions of the article in any way. The original article has been updated.

Copyright © 2020 Kennedy, Cantwell, Malik, Kelley, Potter, Elliott, Lobecker, Gray, Sowers, White, France, Auscavitch, Mah, Moriwake, Bingo, Putts and Rotjan. This is an open-access article distributed under the terms of the Creative Commons Attribution License (CC BY). The use, distribution or reproduction in other forums is permitted, provided the original author(s) and the copyright owner(s) are credited and that the original publication in this journal is cited, in accordance with accepted academic practice. No use, distribution or reproduction is permitted which does not comply with these terms.

frontiers in Marine Science

ORIGINAL RESEARCH
published: 20 August 2019
doi: 10.3389/fmars.2019.00495

Recent Eruptions Between 2012 and 2018 Discovered at West Mata Submarine Volcano (NE Lau Basin, SW Pacific) and Characterized by New Ship, AUV, and ROV Data

William W. Chadwick Jr.[1], Kenneth H. Rubin[2], Susan G. Merle[3], Andra M. Bobbitt[3], Tom Kwasnitschka[4] and Robert W. Embley[3]*

[1] NOAA Pacific Marine Environmental Laboratory, Newport, OR, United States, [2] Department of Earth Sciences, University of Hawai'i at Mānoa, Honolulu, HI, United States, [3] CIMRS, Oregon State University, Newport, OR, United States, [4] GEOMAR, Helmholtz Centre for Ocean Research, Kiel, Germany

OPEN ACCESS

Edited by:
Cristina Gambi,
Marche Polytechnic University, Italy

Reviewed by:
Paraskevi Nomikou,
National and Kapodistrian University of Athens, Greece
Simon James Barker,
Victoria University of Wellington, New Zealand

***Correspondence:**
William W. Chadwick Jr.
william.w.chadwick@noaa.gov

Specialty section:
This article was submitted to Deep-Sea Environments and Ecology, a section of the journal Frontiers in Marine Science

Received: 02 April 2019
Accepted: 22 July 2019
Published: 20 August 2019

Citation:
Chadwick WW Jr, Rubin KH, Merle SG, Bobbitt AM, Kwasnitschka T and Embley RW (2019) Recent Eruptions Between 2012 and 2018 Discovered at West Mata Submarine Volcano (NE Lau Basin, SW Pacific) and Characterized by New Ship, AUV, and ROV Data. Front. Mar. Sci. 6:495. doi: 10.3389/fmars.2019.00495

West Mata is a submarine volcano located in the SW Pacific Ocean between Fiji and Samoa in the NE Lau Basin. West Mata was discovered to be actively erupting at its summit in September 2008 and May 2009. Water-column chemistry and hydrophone data suggest it was probably continuously active until early 2011. Subsequent repeated bathymetric surveys of West Mata have shown that it changed to a style of frequent but intermittent eruptions away from the summit since then. We present new data from ship-based bathymetric surveys, high-resolution bathymetry from an autonomous underwater vehicle, and observations from remotely operated vehicle dives that document four additional eruptions between 2012 and 2018. Three of those eruptions occurred between September 2012 and March 2016; one near the summit on the upper ENE rift, a second on the NE flank away from any rift zone, and a third at the NE base of the volcano. The latter intruded a sill into a basin with thick sediments, uplifted them, and then extruded lava onto the seafloor around them. The most recent of the four eruptions occurred between March 2016 and November 2017 along the middle ENE rift zone and produced pillow lava flows with a shingled morphology and tephra as well as clastic debris that mantled the SE slope. ROV dive observations show that the shallower recent eruptions at West Mata include a substantial pyroclastic component, based on thick (>1 m) tephra deposits near eruptive vents. The deepest eruption sites lack these near-vent tephra deposits, suggesting that pyroclastic activity is minimal below ∼2500 mbsl. The multibeam sonar re-surveys constrain the timing, thickness, area, morphology, and volume of the new eruptions. The cumulative erupted volume since 1996 suggests that eruptions at West Mata are volume-predictable with an average eruption rate of 7.8×10^6 m^3/yr. This relatively low magma supply rate and the high frequency of eruptions (every 1–2 years) suggests that the magma reservoir at West Mata is relatively small. With its frequent activity, West Mata continues to be an ideal natural laboratory for the study of submarine volcanic eruptions.

Keywords: submarine volcanoes, submarine eruptions, seafloor mapping, bathymetry changes, multibeam sonar surveying, lava flow morphology, pyroclastic activity, autonomous and remotely operated underwater vehicle

INTRODUCTION

We learn the most about active volcanic processes by directly observing them, a fact that motivates the establishment of observatories at Earth's most active volcanoes. Eruptions that occur on land have obvious manifestations, making them easy targets for enhanced observation and study, but detecting and observing volcanic eruptions in the deep sea is much more difficult (Rubin et al., 2012), despite the fact that most of Earth's volcanic output occurs in the oceans (Crisp, 1984). Frequently active submarine volcanoes provide a rare and valuable opportunity to learn about the underwater processes associated with individual eruptions as well as how a submarine volcano's activity evolves with time (Staudigel et al., 2006; Watts et al., 2012; Schnur et al., 2017; Allen et al., 2018; Wilcock et al., 2018). West Mata is of special interest because it is an excellent example of such a site.

West Mata is a frequently active submarine volcano with a summit depth at ∼1200 meters below sea level (mbsl) and a base at nearly 3000 mbsl, located in the extensional NE Lau Basin between Fiji and Samoa in the SW Pacific Ocean (**Figure 1**). It is one of only two places on Earth where active submarine eruptions have been directly observed in the deep sea (>500 mbsl depth) (Resing et al., 2011; Rubin et al., 2012). It is also by far the deepest since the other site is NW Rota-1 Seamount in the Mariana arc, which has a summit depth of 517 mbsl (Embley et al., 2006; Chadwick et al., 2008, 2012; Deardorff et al., 2011; Schnur et al., 2017). West Mata is also unique because it is the only known site where lava of boninite composition is being erupted in a modern tectonic setting, a composition often associated with nascent inter-oceanic subduction (Resing et al., 2011; Rubin et al., 2018). West Mata is the largest of nine volcanoes with similar morphology and composition, comprising the "Mata Group," all elongate cones with roughly parallel rift zones that are oriented in a WSW-ENE direction (**Figure 1**), suggesting a regional structural control (Clague et al., 2011; Rubin et al., 2018).

The Mata Group volcanoes lie in a "rear-arc" tectonic setting, between the Tonga volcanic arc to the east, and the NE Lau back-arc spreading center to the west, and in-board of the nearly 90° bend at the northern terminus of the Tonga trench, where it transitions into a plate boundary transform zone (**Figure 1**). The NE Lau Basin hosts the world's highest subduction rates (Bevis et al., 1995) and the fastest opening back-arc basin (Zellmer and Taylor, 2001), which creates an extraordinary concentration and diversity of submarine volcanism in the area (Embley and Rubin, 2018; Rubin et al., 2018) and also hosts an extraordinary number of active hydrothermal vent sites (Baker et al., 2019).

This paper presents new results from West Mata including depth changes between repeated bathymetric surveys from ships, high-resolution mapping from autonomous underwater vehicles (AUVs), and visual observations of the seafloor from remotely operated vehicles (ROVs). The new data reveal and characterize six eruptions at West Mata (**Figure 2**), a collapse pit at the summit, and a landslide scar just east of the summit that all occurred after eruptive activity was first observed at the summit in May 2009 (Resing et al., 2011; Embley et al., 2014). These new observations show that the eruptive style at West Mata changed from continuous to episodic during this time period. The observations also provide information about the character of individual eruptions at different depths, because they span the entire volcano from the summit to abyssal depths (**Figure 2**). We show that the recent eruptions define a linear trend in erupted volume with time, which has implications for the magma supply, the volume of magma storage within the volcano, and the future behavior of the volcano.

PREVIOUS WORK

West Mata first gained attention in November 2008 during a regional hydrographic survey that discovered an intense hydrothermal plume over the summit with high levels of hydrogen and shards of volcanic glass, suggesting it was actively erupting at the time (Resing et al., 2011; Baumberger et al., 2014). This led to a rapid-response expedition 6 months later in May 2009 with ROV *Jason* (Resing et al., 2011) that found two active eruptive vents on the north side of the summit ridge, named Hades and Prometheus. The eruptive activity was continuous at moderate to low effusion rates, and was characterized by explosive bursts that produced both pillow lavas and pyroclasts, especially when large bubbles of magmatic gases up to ∼1 m in diameter (presumably SO_2, CO_2, H_2O) were expelled from the vent (Resing et al., 2011).

During that same expedition in May 2009, the summit and rift zones were mapped at high-resolution (1 m) with the MBARI AUV *D. Allan B.* (Clague et al., 2011; Clague, 2015), revealing the setting of the Hades and Prometheus eruptive vents within embayments of the summit ridge on the upper north slope of the volcano. The high-resolution AUV bathymetry also highlighted the contrast in morphology between the smooth north and south slopes of the volcano, which are covered with volcaniclastic debris shed from vents near the summit, and the hummocky lava flows evident on the ENE and WSW rift zones. The rift zone flows have a distinctive morphology with flat tops and steep sides and are typically arranged in a shingled arrangement along the sloping rift zone axis, locally modified by landslides. Clague et al. (2011) also compared the first ship-based bathymetric survey at West Mata in 1996 to later ones collected in 2008–2010 and found large depth changes at the summit (up to 88 m shallower) and on north flank (up to 96 m shallower), suggesting that eruptive activity from the summit vents had been dominant for more than a decade and had produced thick volcaniclastic deposits on the north flank.

Additional evidence that the eruptive activity directly observed during the brief ROV dives in May 2009 was continuous and prolonged for months to years comes from local and regional hydrophone studies, radiometric dating, and repeated hydrothermal plume measurements in the water column over the volcano. A moored hydrophone deployed ∼48 km SW of West Mata recorded the sounds of continuous but variable eruptive activity at West Mata from January to May 2009 (Resing et al., 2011). During the May 2009 ROV dives, a portable hydrophone characterized from close range the eruptive activity at Hades and Prometheus, which was continuous during the several days of recordings (Dziak et al., 2015). A regional hydrophone array in the Lau Basin ∼650 km to the SSW recorded sustained

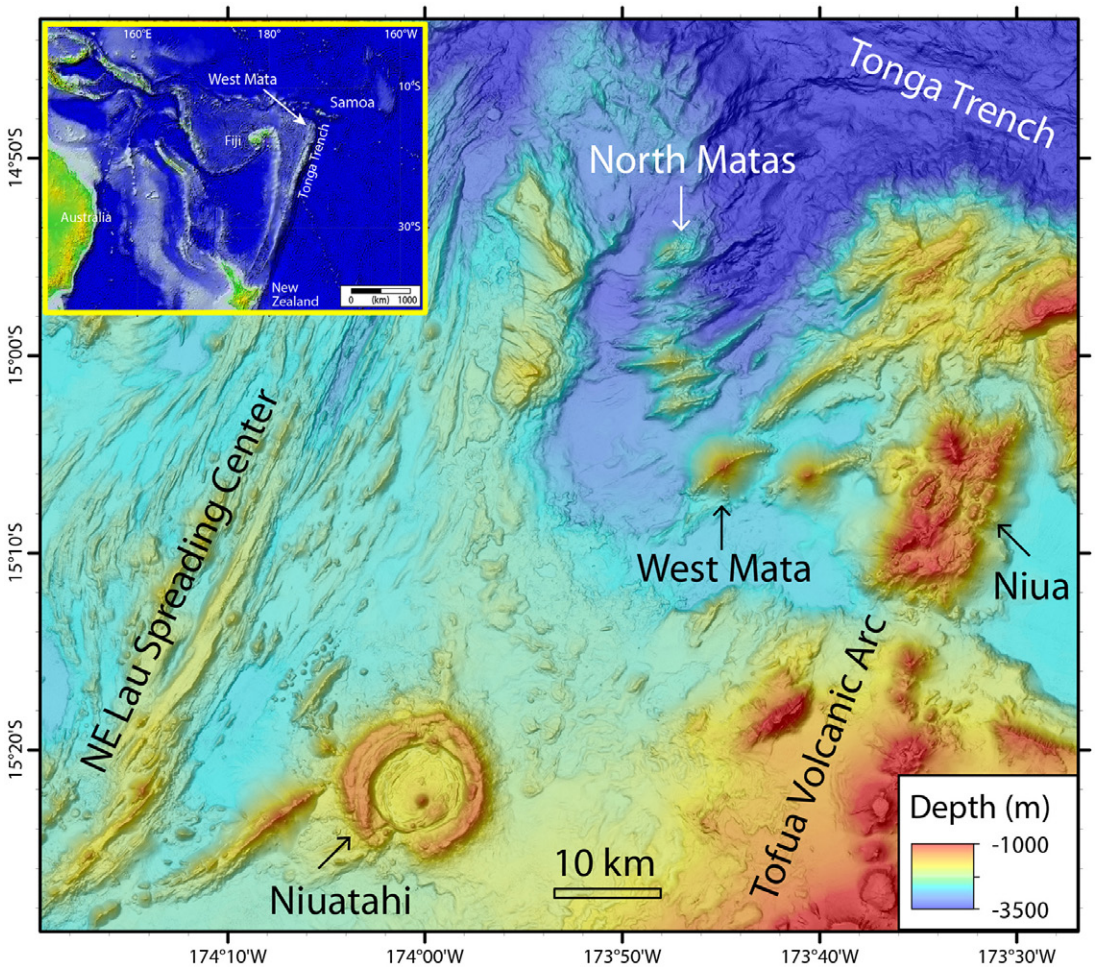

FIGURE 1 | Regional map of the NE Lau Basin, located between Fiji and Samoa (inset), showing West Mata submarine volcano, between the NE Lau back-arc Spreading Center to the west and the Tofua volcanic arc to the east.

low-level activity in the direction of West Mata between January 2009 and April 2010 (Bohnenstiehl et al., 2014). Another local hydrophone array was moored 5–15 km away from the summit from December 2009 to August 2011 and recorded continuous eruptive activity until late 2010, when it began to decline and eventually stopped by February 2011 (Embley et al., 2014; Dziak et al., 2015). Radiometric dating of lavas collected at or near the summit in 2009 and 2012 using short-lived ^{210}Po-^{210}Pb disequilibrium confirmed that effusive volcanism spanned at least April 2007 to December 2010 (Embley et al., 2014).

During the period of continuous eruptive activity, turbidity sensors on one of the hydrophone moorings and on conductivity, temperature, depth (CTD) instruments during infrequent ship-based vertical hydrographic casts showed evidence for occasional mass-wasting events down the flanks of West Mata (Dziak et al., 2015; Walker et al., under review[1]). Similarly, submarine landslides were detected on the north flank of West Mata by the local moored hydrophones between December 2009 and May 2010 (Caplan-Auerbach et al., 2014). Ship-based CTD casts over the summit in November 2008, May 2009, April/May 2010, and September 2012 showed a gradual decrease in the strength of chemical and particle signals in the hydrothermal plume above the summit of West Mata during this time period, consistent with the hydrophone data (Baumberger et al., 2014).

ROV dives in September 2012 confirmed that West Mata was no longer erupting continuously from the summit vents (Embley et al., 2014). Instead, a pit crater ∼200 m wide and ∼100 m deep had formed at the former location of Hades vent. Later analysis of additional repeated ship-based bathymetric surveys from 1996 to 2012 (**Figure 2**) revealed the first evidence for episodic eruptive activity on the rift zones (Embley et al., 2014). Here, we build on those results with the first direct observations of recent eruption sites away from the summit at West Mata from AUV and ROV dives, as well as new evidence for four additional episodic eruption sites on and near the rift zones between 2012 and 2018.

[1] Walker, S. L., Baker, E. T., Lupton, J. E., and Resing, J. A. (under review). Patterns of fine ash dispersal related to volcanic activity at West Mata volcano, NE Lau Basin. *Front. Mar. Sci.*

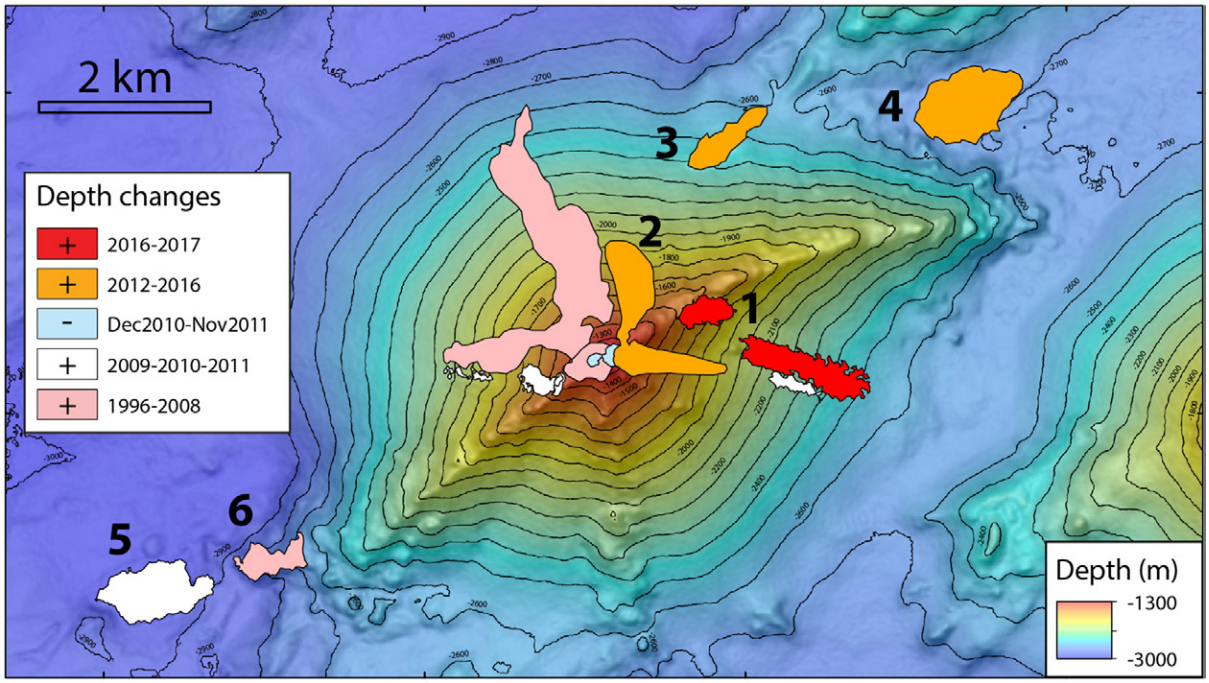

FIGURE 2 | Map of West Mata showing areas where depth changes have been found by repeated bathymetric surveys between 1996 and 2018, documenting recent eruption sites. Those from 1996 to 2012 are from Clague et al. (2011) and Embley et al. (2014); those after 2012 are new (orange and red areas, see legend). The depth changes shown in white are several grouped together within a longer time window (2009–2012) than the time constraints on individual sites (see Embley et al., 2014). The blue areas are negative depth changes from a summit collapse and landslide. Numbers indicate eruption sites discussed in detail in this paper.

MATERIALS AND METHODS

The main method we use for documenting recent eruptions at West Mata is identifying significant depth changes between repeated ship-based multibeam sonar bathymetric surveys. The volcano has been mapped nine times between 1996 and 2018, with eight of those since 2008 (**Table 1** and **Figure 3**). The first survey in 1996 was collected with a lower resolution sonar system and before reliable GPS navigation, so it is notably lower in quality and comparisons with it have higher uncertainty [as discussed by Clague et al. (2011) and Embley et al. (2014)]. Nevertheless, all the surveys since 2008 are of relatively high quality and we generally can use a threshold to identify significant depth changes of ±10 m. Still, not all depth changes above this threshold are real, but false positives can be eliminated by comparing with visual ground truth from submersibles and/or whether they make geologic sense, based on their location and morphology. The timing of the eruptions associated with each confirmed area of depth change is constrained by the dates of the before-and-after bathymetric surveys. All the bathymetric data at West Mata were processed using MB-System software (Caress and Chayes, 2016) and were gridded at a 25-m grid-cell spacing for this analysis.

In this paper, we focus on the depth changes discovered since those documented by Embley et al. (2014) by using the two most recent ship-based bathymetric surveys in March 2016 and in November 2017 (**Table 1**). We use the positive depth changes between bathymetric surveys to calculate the thicknesses, areas, and volumes of erupted material at each site (**Table 2**). We have not re-calculated the volumes reported by Embley et al. (2014) for the depth changes before 2012. For those after 2012, we calculate the areas and volumes of change using ArcMap GIS software by subtracting one bathymetric grid from another within a polygon that was manually drawn to isolate the area of significant depth change. We do not use the AUV bathymetry for the volume calculations because the AUV surveys do not cover all the eruption sites and so the ship data provide a more uniform and consistent way of comparing multiple events.

Most of the new data presented in this paper were collected during a two-leg expedition on *R/V Falkor* to the NE Lau Basin between 10 November and 18 December 2017 (FK171110). The first leg included dives with AUV *Sentry* to collect high-resolution (1 m) bathymetry (at 70 m altitude) and near-bottom photo surveys (at 5 m altitude) of selected areas. Four of six AUV *Sentry* dives were made at West Mata (dives 457, 458, 460, and 463) and the first three collected useful data with its Reson 7125 (200 kHz) multibeam sonar (Merle et al., 2018a); unfortunately the multibeam sonar malfunctioned during the later dive. Where they overlap, the 2017 AUV *Sentry* bathymetry can be compared with the 2009 survey by the MBARI AUV *D. Allan B.* (Clague et al., 2011; Clague, 2015).

TABLE 1 | Multibeam sonar bathymetric surveys at West Mata volcano.

Month-Year	Vessel/vehicle	Cruise ID	Chief Scientist(s)	Sonar system
June-1996	*R/V Melville*	BMRG08MV	S. Bloomer/D. Wright	Seabeam2000
November-2008	*R/V Thompson*	TN227	J. Lupton	EM300
May-2009	*R/V Thompson*	TN234	J. Resing/R. Embley	EM300
May-2009	*AUV D. Allan B.*	TN234	D. Clague/D. Caress	Reson 7125
May-2010	*R/V Kilo Moana*	KM1008	J. Resing	EM122
December-2010	*R/V Kilo Moana*	KM1024	K. Rubin/R. Embley	EM122
November-2011	*R/V Kilo Moana*	KM1129a	F. Martinez	EM122
September-2012	*R/V Revelle*	RR1211	J. Resing/R. Embley	EM122
March-2016	*R/V Falkor*	FK160320	T. Kwasnitschka	EM302
November-2017	*R/V Falkor*	FK171110	K. Rubin/W. Chadwick	EM302
November-2017	*AUV Sentry*	FK171110	K. Rubin/W. Chadwick	Reson 7125

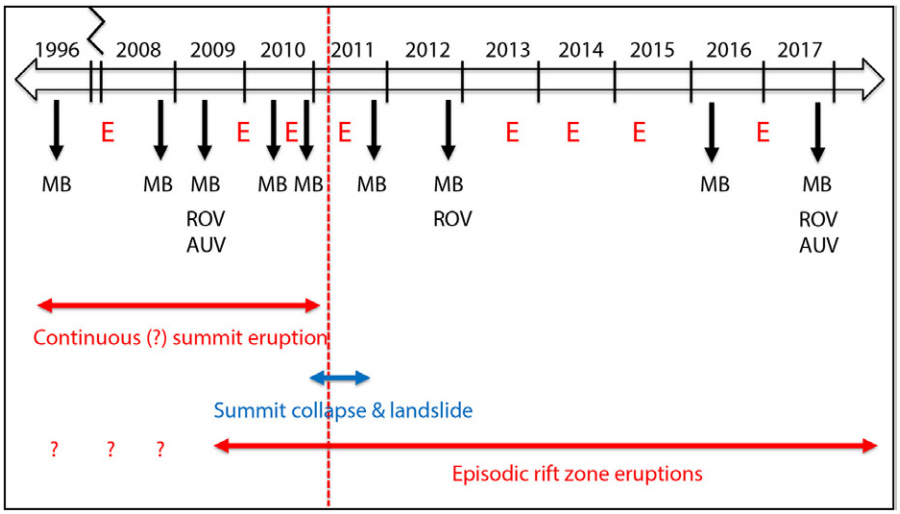

FIGURE 3 | The timeline showing the timing of multibeam sonar bathymetric surveys (MB), AUV and ROV dives in 2009, 2012, and 2017, and the transition in eruptive style from continuous summit activity to episodic rift zone eruptions (represented by red "E's" below the timeline).

TABLE 2 | Estimates of the thicknesses, areas, and volumes of recent eruption sites at West Mata based on depth changes between ship-based bathymetric surveys.

Site name	Bathymetric survey comparison (mo/years)	Geographic area and depth	Mean depth change in meters	Maximum depth change in meters	Area of depth change (x 10^6 m^2)	Volume of depth change (x 10^6 m^3)
Eruption sites newly identified by this study						
Site 1	March 2016 – November 2017	ENE Rift @ 1500 m	26.6	71	0.6	14
Site 2	November 2011 – March 2016	ENE Rift @ 1300 m	38.6	93	0.530	13.8
Site 3	November 2011 – March 2016	NE flank @ 2400 m	27.2	57	0.250	6.7
Site 4	November 2011 – March 2016	NE Base @ 2700 m	29.2	64	0.730	17.1
Areas previously identified by Embley et al. (2014)						
Site 5	May 2010 – November 2011	WSW Rift @ 2900 m	26.2	63	0.61	16
Site 6	May 1996 – November 2008	WSW Rift @ 2700 m	53.5	101	0.22	12

During the second leg of the *R/V Falkor* expedition, dives were made with ROV *SuBastian*, and 7 of 21 dives were made at West Mata (S85–S88, S93, S95, and S103) to make visual observations and collect samples at most of the recent eruption sites documented by bathymetric depth changes. Both cruise legs collected ship-based multibeam bathymetry at West Mata and the surrounding area with the ship's EM302 sonar system (Merle et al., 2018b). Other results from this expedition are described in Rubin et al. (2018), Walker et al., under review[2], and Baker et al. (2019).

[2]Walker, S. L., Baker, E. T., Lupton, J. E., and Resing, J. A. (under review). Patterns of fine ash dispersal related to volcanic activity at West Mata volcano, NE Lau Basin. *Front. Mar. Sci.*

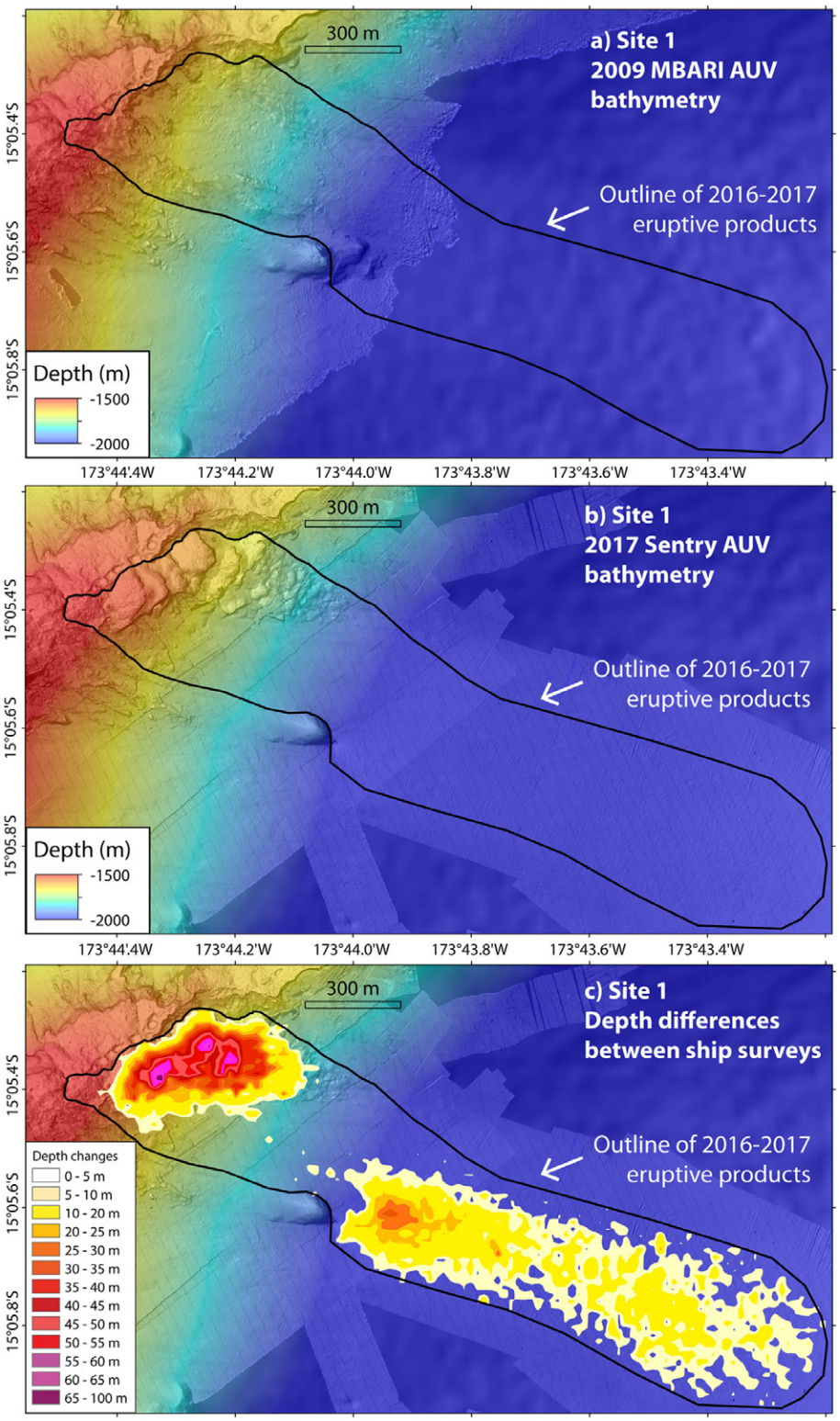

FIGURE 4 | Broad-view maps of eruption site #1, on the middle ENE rift zone of West Mata (see **Figure 2**) showing **(a)** pre-eruption MBARI AUV bathymetry from 2009, **(b)** post-eruption *Sentry* AUV bathymetry from 2017, and **(c)** positive depth differences between ship-based surveys in 2016 and 2017 overlain on 2017 AUV bathymetry (see **Table 2**). Black outlines enclose the site #1 eruption deposits. In this and subsequent figures, the pre-eruption AUV bathymetry was collected in May 2009 by the MBARI AUV *D. Allan B.* (Clague et al., 2011; Clague, 2015), and the post-eruption AUV bathymetry is from surveys in November 2017 with AUV *Sentry* (Merle et al., 2018a).

RESULTS

The summary timeline in **Figure 3** shows the timing of all the ship-based multibeam sonar bathymetric surveys at West Mata between 1996–2018 (black arrows labeled with "MB"), as well as the years with ROV and AUV dives, and how the new data reported here fit into the longer time-series of observations. Remarkably, there is evidence for eruptive activity between almost every bathymetric survey, except between the surveys less than a year apart in 2008 and 2009, and those in 2011 and 2012, which showed no change. The red "E's" in **Figure 3** denote episodic eruptions on the rift zones, whose timing is constrained by the bathymetric surveys. The arrows at the bottom highlight the major transition that occurred in early 2011 when the continuous eruptive activity at the summit ended (Embley et al., 2014). At about the same time, the summit collapsed and a landslide occurred on the SE flank with a headwall just east of the summit (blue arrows in **Figure 3**). Since 2011, all the eruptions at West Mata have been episodic eruptions on the rift zones. Although this was clearly a major change in eruptive behavior, note also that there was some overlap in time between the continuous and episodic activity. The first episodic rift eruption was documented between May 2009 and May 2010 (Embley et al., 2014), and there was an even earlier one sometime between the 1996 and 2008 surveys (although it's possible that event occurred before the continuous activity began).

In this section, we focus on six recent eruption sites: the four discovered on and near the ENE rift zone from the two most recent bathymetric surveys in 2016 and 2017 (sites #1–4 in **Figure 2**), and two previously identified on and near the WSW rift zone by Embley et al. (2014) where we have new data to ground-truth previous interpretations (#5–6 in **Figure 2**). We describe the eruption sites roughly from youngest to oldest, starting with the 2016–2017 site, then the three 2012–2016 eruption sites, and then the older two sites on the WSW rift. However, for the 2012–2016 sites, note that their relative ages are unknown (the positioning of the "E's" in **Figure 3** between 2012 and 2016 is arbitrary), and we therefore proceed from shallowest to deepest among those three sites. Note also that to compute depth differences at the 2012–2016 eruption sites (**Table 2**), we have chosen to compare the 2016 survey to the 2011 survey rather than the one in 2012 because the latter is noisier. So even though we show depth changes between the 2011 and 2016 surveys in the figures and tables, we know that the timing of those depth changes is constrained in time between 2012 and 2016.

Site 1: The 2016–2017 Eruption on the Middle ENE Rift at 1500 mbsl

The most recent known eruption at West Mata occurred between March 2016 and November 2017 and was discovered during the FK171110 expedition on *R/V Falkor*. This eruption was located on the middle part of the ENE rift zone, between 1.0 and 1.5 km east of, and about 300 m below the summit (**Figure 2**). **Figure 4** shows the before-and-after AUV bathymetry at the eruption site. Comparing the AUV bathymetry from 2009 and 2017 shows that the eruptive vents were located along the southern edge of the rift zone, within the headwall of a previous landslide on the SE side of the rift (**Figure 4**). The depth changes between ship-based bathymetric surveys in 2016 and 2017 were greatest near the eruptive vents where lava flows accumulated (up to 71 m thick). Smaller positive depth changes (up to 34 m) extend at least 2.2 km downslope, where the smooth texture in the post-eruption AUV bathymetry and photographs from AUV *Sentry* show that these are volcaniclastic deposits. The area between the thick lava flows and the thinner fragmental deposits downslope had small negative depth changes (up to 5–10 m, not shown in **Figure 4c**), suggesting that some scouring occurred as the volcaniclastic material moved downslope. The total area enclosing the eruptive deposits (black outline in **Figure 4**) is 0.60×10^6 m^2, and their total volume is 14.0×10^6 m^3 (**Table 2**).

A zoomed-in view of the upper part of the eruption site (**Figure 5**) shows that the new lava flows form a series of flat-topped or slightly domed plateaus with steep margins, arranged in an overlapping, shingle-like or stepped pattern, descending to the ENE in the direction parallel to the rift axis. Adjacent to the rift, there are five somewhat equi-dimensional overlapping lava plateaus, each 100–150 m across with downward steps of 20–30 m between them (**Figure 5b**). Below these are a series of lava benches that become progressively smaller and less well-defined with distance downslope, eventually merging into a hummocky lobe of pillow lava that extends 600 m from the rift (**Figure 5b**). The steep downslope margins of the lava benches and plateaus are constructional in some places, but are cut by landslide scarps in others (for example along the scalloped southern edge of the upper-most lava plateaus in **Figure 5b**). Because the lava plateaus are relatively flat-topped but were built outward from the rift on a steeply descending slope, each lava plateau is actually wedge-shaped in cross-section; the bathymetric depth-changes between the AUV surveys show that the lava plateaus are thinnest on their upslope edges and thickest on their downslope edges (**Figure 5c**). This is consistent with their mechanism of formation being similar to that of perched lava ponds on land, as proposed by Clague et al. (2011), in which the relatively flat upper surface of a flow lobe is maintained behind a levee that is constructed from overflows at the edge of the impounded lava flow. In this interpretation, the levee grows upward along with the upper surface of the ponded lava flow. In any case, this "shingled lava plateau" morphology is very common along both rift zones of West Mata.

Visual observations of the 2016–2017 eruptive deposits were made during ROV *SuBastian* dives S86 and S103 in December 2017 (**Figure 5d**). The hummocky lobe of pillow lavas on the lower reaches of the eruption site lies on a moderate slope and has a thin dusting of tephra (**Figure 6a**). Further upslope, the steep margins of the lava plateaus and lava benches are constructional in some places, formed by near-vertical intact pillow tubes (**Figure 6b**), and in other places are vertical cliffs of truncated pillows (**Figure 6c**), where they have been cut by landslides. Below the landslide headwalls are ramps of talus made up of pillow fragments (**Figure 6d**). In contrast, the upper surfaces of the lava plateaus (near the eruptive vents) consist of pillow lavas that are deeply buried by coarse volcanic tephra (**Figure 6e**). The thickness of the tephra appears to be 1–2 m,

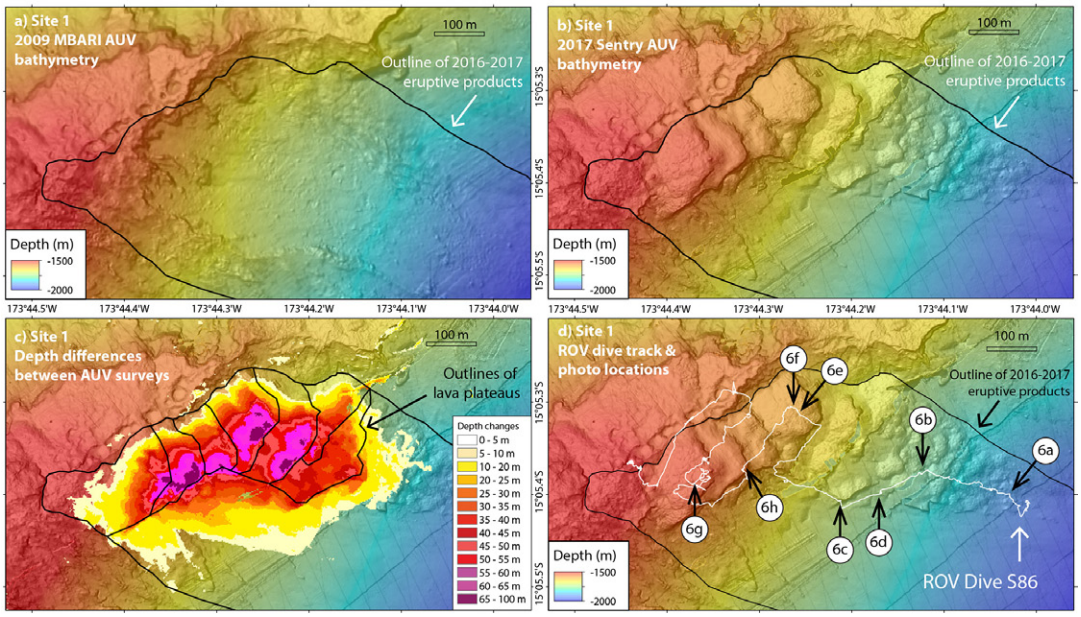

FIGURE 5 | Close-up maps of eruption site #1 showing **(a)** pre-eruption MBARI AUV bathymetry from 2009, **(b)** post-eruption *Sentry* AUV bathymetry from 2017, **(c)** positive depth differences between the AUV surveys (after the 2017 *Sentry* AUV grid was co-registered by shifting it 8 m east and 16 m south), and **(d)** trackline of *SuBastian* ROV dive S86 (white line) on post-eruption *Sentry* AUV bathymetry, with locations of images in **Figure 6** (white numbered circles). Part of *SuBastian* ROV dive S103 also crossed this area, but is not shown in **(d)**. In **(c)** note that shingled lava plateaus thicken downslope away from the rift zone (see text for discussion). Black outlines enclose the site #1 eruption deposits and mark the edges of individual shingled lava plateaus.

based on the fact that most pillows are buried and only the largest poke above the tephra (**Figure 6f**). The tephra layer is pock-marked by numerous bowl-shaped, circular pits, about 0.5–1 m across (**Figures 6e,f**) that apparently formed when tephra "drained" downward into empty cavities among the underlying pillow lavas. Locally, these circular pits have accumulated small yellow flocculent particles of microbial mat (**Figure 6f**), which apparently originally formed on the upper surface of the tephra, but were subsequently dislodged and transported into the pits by bottom currents. Locally, a mosaic of white and yellow microbial mat still blanketed the tephra in some areas (**Figure 6g**). We measured a temperature of 5°C (a few degrees above ambient) in one such area with the ROV's temperature probe as it was pushed downward about 10 cm into the tephra deposit. The steps between the lava plateaus are constructional levees of nearly vertical pillow lava tubes, and were relatively unburied by tephra because of their steepness (**Figure 6h**).

Site 2: The 2012–2016 Eruption East of the Summit at 1300 mbsl

The first of the three eruption sites constrained in time between 2012 and 2016 is located on the uppermost ENE rift zone just east of the summit (**Figure 7**). The shallowest point at the eruptive vent is 1255 mbsl and the deepest extent of the erupted deposits is at least 1950 mbsl on both the SE and N flanks of the rift zone. The area and volume of the 2011–2016 depth differences from this eruption are 0.53 × 10^6 m^2 and 13.8 × 10^6 m^3, respectively (**Table 2**).

Figure 8 shows a smaller area near the summit and eruptive vent in more detail. The 2009–2017 time period between the two AUV surveys captures changes due to several events during that span. A new pit crater formed at the summit between December 2010 and November 2011 when the area that included the Hades and Prometheus vents collapsed (**Figures 8a,b**), perhaps associated with the end of continuous eruptive activity (Embley et al., 2014). The crater has a roughly oval outline, about 200 × 100 m wide and 100 m deep, with the long axis parallel the rift zones (**Figure 8c**). The crater rim on the NW edge displays elongated pillow lava lobes, probably originally fed from Hades vent but now truncated by the collapse (see Figures 10c,d of Embley et al., 2014). The deepest part of the crater (1290 mbls), just 25 m W of the former location of Hades vent, hosted diffuse venting of clear shimmering fluids up to 22°C in 2017. The former location of Hades is now a high-standing pinnacle within the crater, and the former location of Prometheus vent is along the eastern rim of the crater (**Figure 8c**), where it abuts the east-facing headwall of the landslide that also occurred between December 2010 and November 2011 (Embley et al., 2014). The high-standing areas remaining between Hades and Prometheus may have escaped significant collapse (**Figure 8**), perhaps because the former vent areas are underlain by relatively massive intrusive rocks. These are also areas of continuing extensive diffuse hydrothermal venting.

The 2012–2016 eruptive vent is 70 m below and 300 m east of the summit, and was clearly centered within the headwall scar of the 2010–2011 landslide (labeled in **Figure 8c**), where

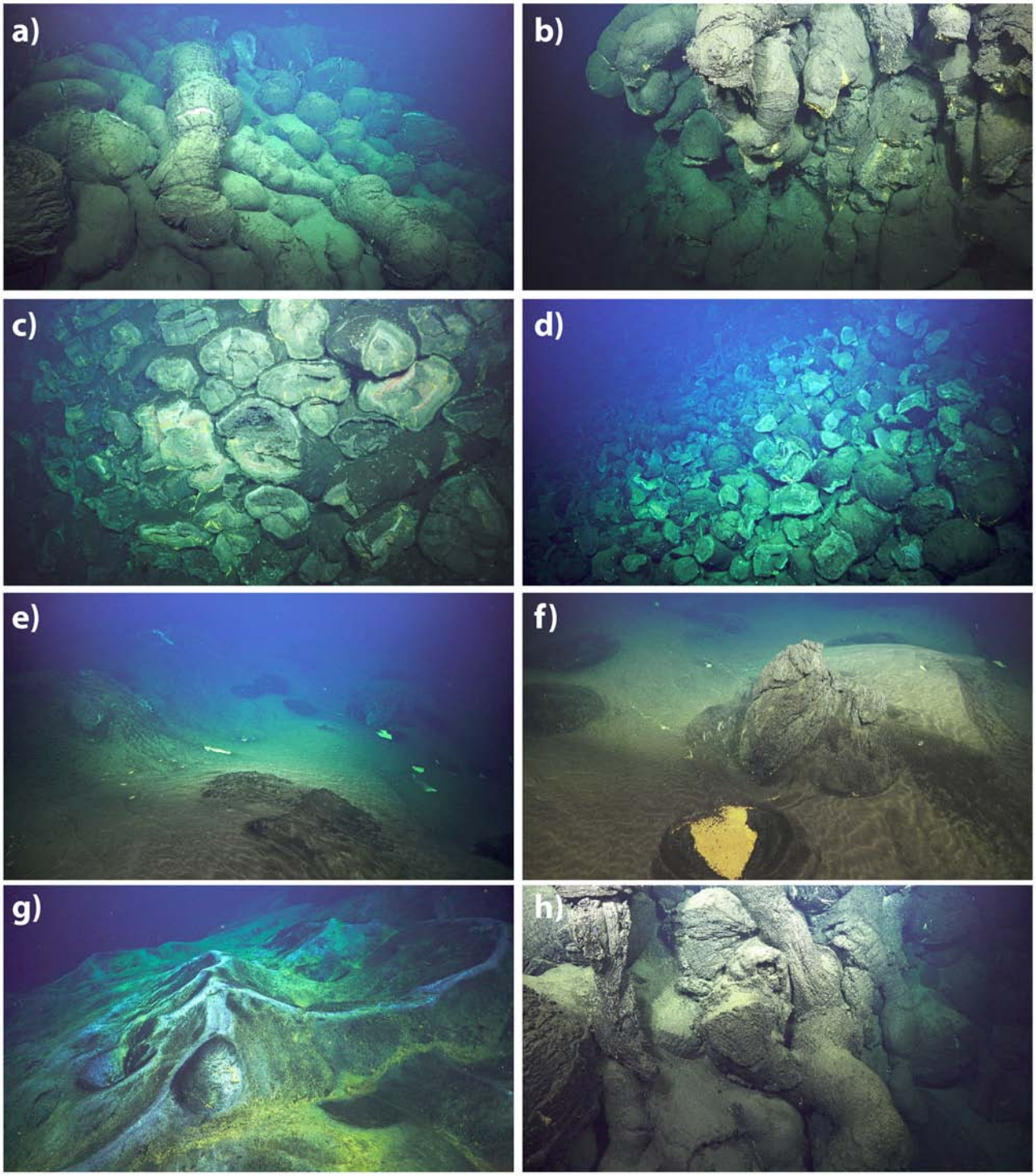

FIGURE 6 | Images of eruption site #1 from ROV *SuBastian* dive S86. All are 2016–2017 eruption products. Numbers in parentheses are time of photo in GMT and horizontal scale. See **Figure 5d** for photo locations. **(a)** Pillow lavas on the slope below the rift zone (19:17:22, 5 m). **(b)** Nearly vertical cliff face of intact pillow lavas (20:09:42, 4 m). **(c)** Nearly vertical cliff of truncated pillows on the headwall of a landslide scarp (20:52:51, 4 m). **(d)** Talus with pillow fragments below a landslide scarp (20:48:50, 10 m). **(e)** Tephra-covered pillow lavas on a shingled lava plateau near the eruptive fissures, with circular pits containing yellow microbial floc in the distance (21:40:18, 10 m). **(f)** Closer view of collapse pit in tephra deposit with yellow microbial floc (bottom) and large partially buried pillow at center (21:47:06, 4 m). **(g)** Colorful microbial mats growing on tephra completely burying pillow lavas on a shingled lava plateau near the eruptive fissures (23:41:48, 6 m). **(h)** Exposed tubular pillow lavas on the steep step between shingled lava plateaus (22:27:47, 3 m).

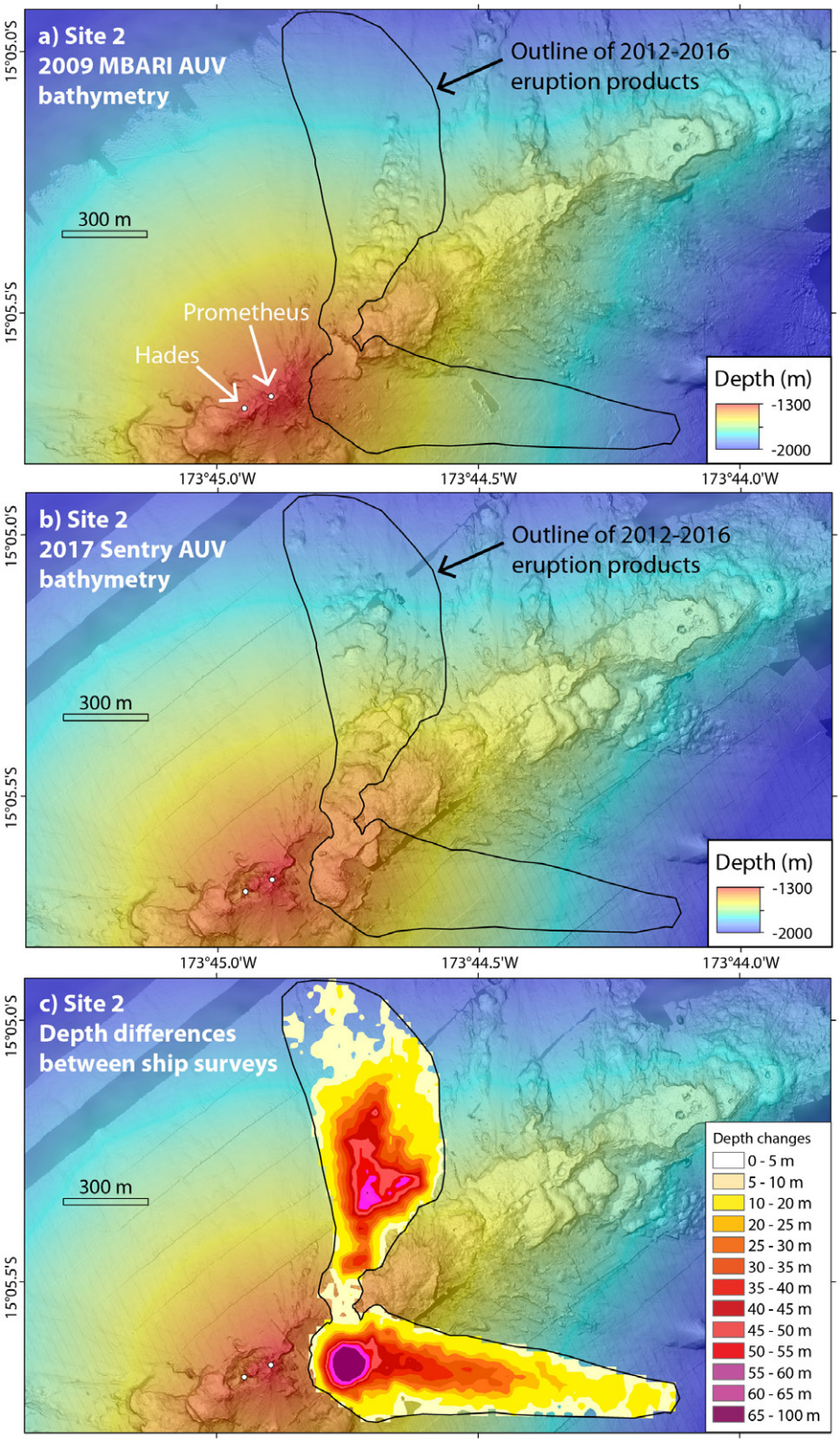

FIGURE 7 | Broad-view maps of eruption site #2, just east of the summit of West Mata (see **Figure 2**) showing **(a)** pre-eruption MBARI AUV bathymetry from 2009, **(b)** post-eruption *Sentry* AUV bathymetry from 2017, and **(c)** positive depth differences between ship-based surveys in 2012 and 2016 (**Table 2**). Black outlines enclose the site #2 eruption deposits. White dots show locations of Hades and Prometheus eruptive vents in May 2009.

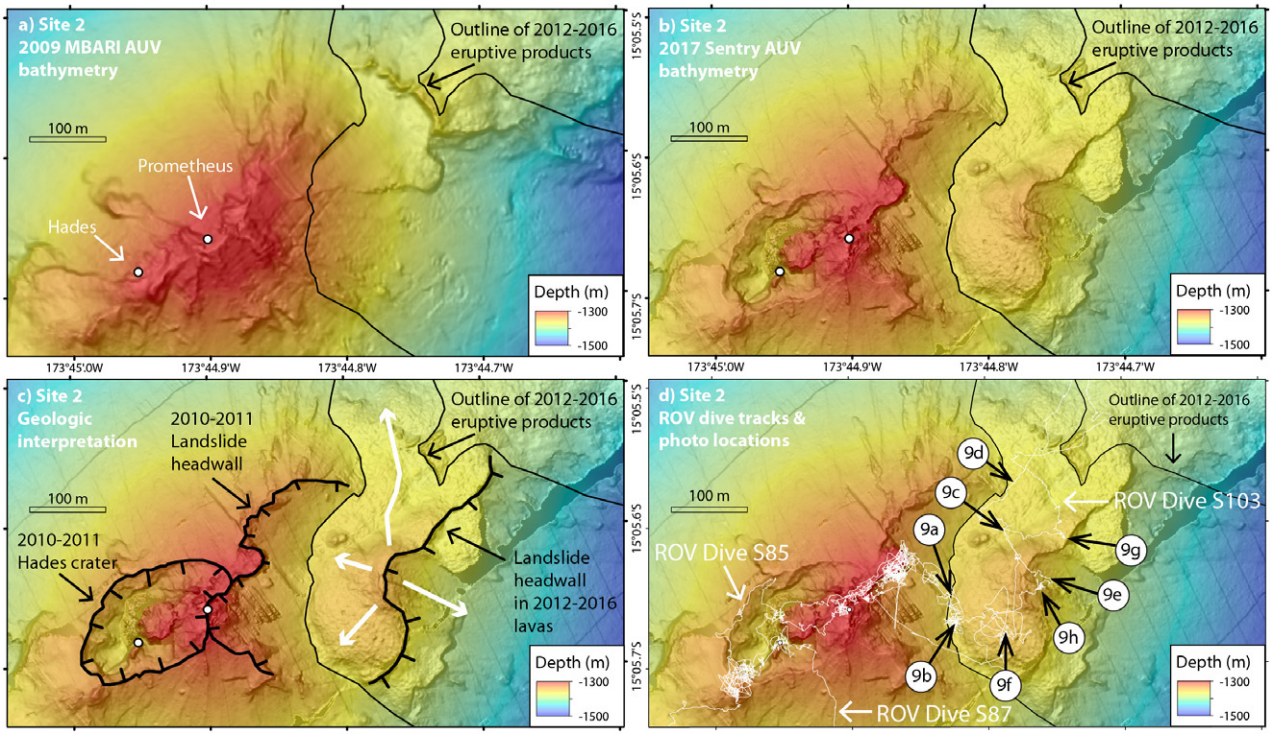

FIGURE 8 | Close-up maps of eruption site #2 showing **(a)** pre-eruption MBARI AUV bathymetry from 2009, **(b)** post-eruption *Sentry* AUV bathymetry from 2017, **(c)** geological interpretation on 2017 AUV bathymetry and **(d)** tracklines of *SuBastian* ROV dives S85, S87, and S103 (white lines) on post-eruption *Sentry* AUV bathymetry, with locations of images in **Figure 9** (white numbered circles). Thick white arrows in **(c)** indicate lava flow directions from eruptive vent; thick black hachured lines are crater rims or landslide headwalls. Thin black outlines enclose the site #2 eruption deposits. White dots show locations of Hades and Prometheus eruptive vents in May 2009.

the new lavas are shallowest and the largest depth differences (up to 93 m) form a circular bullseye pattern (**Figure 7c**). From there, it appears that lava and clastic debris were first deposited downslope to the east >1 km, more or less down the axis of the previous landslide chute, but as the eruption built a constructional mound over the vent, it gained enough elevation to also feed pillow lava flows down the northern flank of the rift zone (**Figure 8c**). The thickest accumulation of lava on the north side of the rift (67 m) is mid-way down the flank (**Figure 7c**). The morphology of the downslope eruptive deposits are notably different on the two sides of the rift zone; on the SE side they are smooth, whereas those on the N side are hummocky (**Figure 7b**). This contrast indicates the early deposits on the SE side are mainly volcaniclastic, suggesting more explosive or higher-effusion rate activity at the beginning of the eruption, whereas those on the north are intact pillow lava flows, suggesting the later phase of the eruption developed a more stable lava distribution system from the vent to the north slope, perhaps at a lower effusion rate. On the axis of the rift zone, the depth differences are relatively thin (4–11 m, **Figure 7c**), but it is clear there is new lava there because of different morphology in the 2017 AUV bathymetry (**Figure 8b**) and our ROV dive observations. Nevertheless, there are some older high-standing features in that area that did not get buried by the new lava flows. The 2017 AUV bathymetry also shows that the 2012–2016 lava flows are themselves cut by east-facing landslide scarps on the south side of the rift zone (**Figure 8c**). These appear to have formed both during and after the eruption since there are some pillow-lava deposits on the slope below the landslide headwall (**Figure 8c**).

ROV *SuBastian* dives S85, S87, and S103 were made in this area (**Figure 8d**) and showed that the near-vent deposits are pillow lavas that form a steep flow front where they abut the 2010–2011 landslide headwall west of the eruptive vent (**Figures 9a,b**). As the eruptive vent was approached, thick deposits of tephra were observed mantling the pillows (**Figure 9c**), and were locally covered by white and yellow microbial mats (**Figure 9d**). Near the eruptive vent spatter-like deposits were observed (**Figure 9e**) providing more evidence for a pyroclastic component to the eruption. Diffuse venting of clear hydrothermal fluids was observed over a large area that was colonized by abundant vent animals including shrimp, squat lobsters, and polychete worms (**Figure 9f**). The edge of the pillow mound that had been cut by a landslide was marked by truncated pillows, some of which were hollow with drained-out interiors (**Figure 9g**). Within the landslide headwall, cross-sections of the pillow mound could be seen in near-vertical outcrops oriented downslope, showing layer upon layer of elongate pillows (**Figure 9h**).

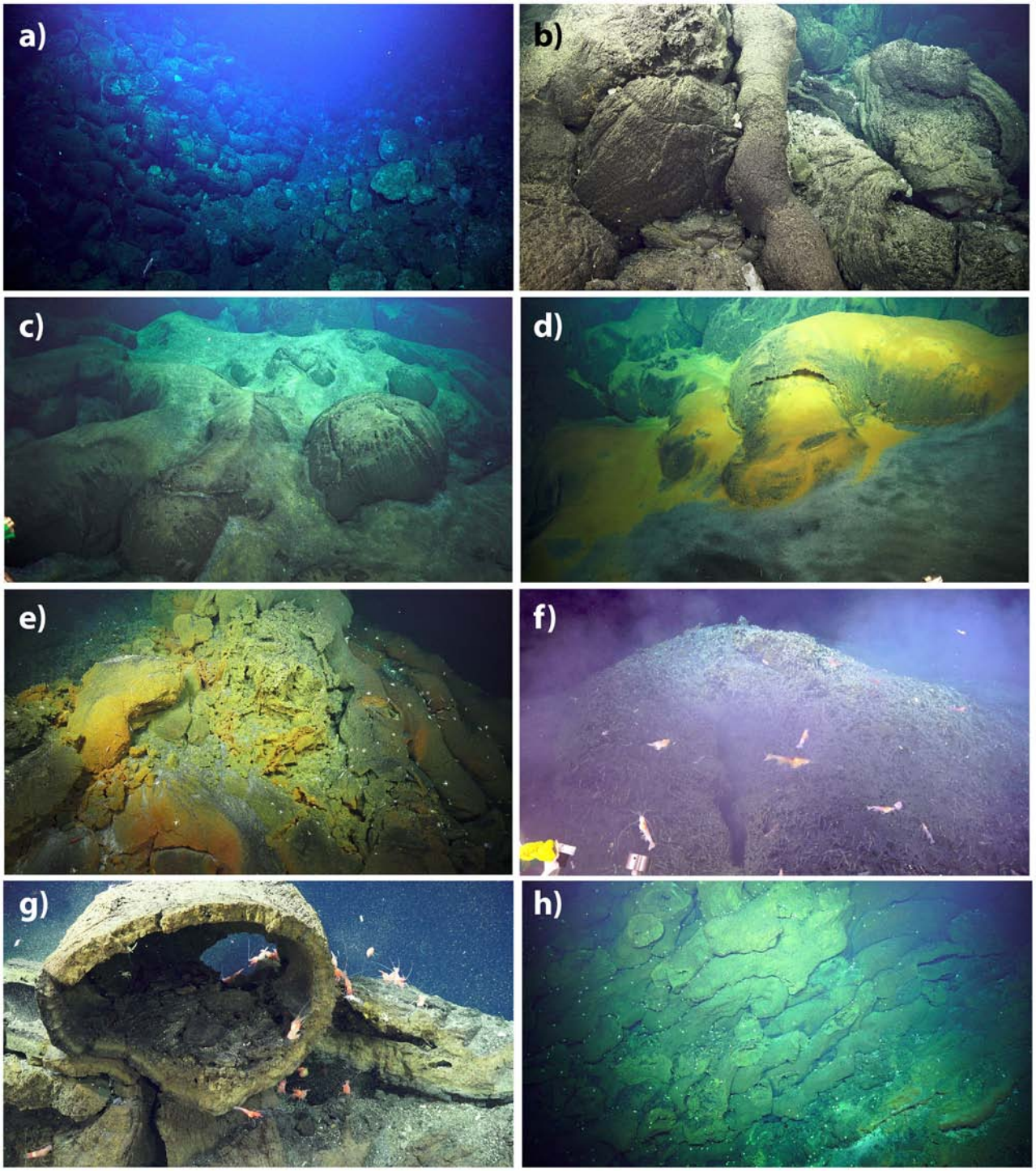

FIGURE 9 | Images of eruption site #2 from ROV *SuBastian* dives S85, S87, and S103. All show 2012–2016 eruption products. Numbers in parentheses are dive number, time of photo in GMT and horizontal scale. See **Figure 8d** for photo locations. **(a)** 2012–2016 flow front at left against the 2010–2011 landslide headwall at right (S85, 01:52:19, 10 m). **(b)** Close up of pillow lavas on flow front (S85, 01:58:13, 3 m). **(c)** Tephra partly burying pillows close to eruptive vent (S85, 02:59:14, 5 m). **(d)** Tephra with white and yellow microbial mats mantling pillows (S85, 03:18:12, 3 m). **(e)** Near-vent spatter deposits with yellow hydrothermal sediment (S85, 02:50:48, 5 m). **(f)** Hydrothermal vent shrimp swarm at active diffuse vent with shimmering cloudy water (S87, 03:19:25, 3 m). **(g)** Hollow drained-out pillow where new lavas are cut by landslide scarp (S103, 02:42:53, 1.5 m). **(h)** Cross-section of stack of elongate pillow lavas cut by landslide scarp, with downslope direction to the left (S85, 02:45:15, 10 m).

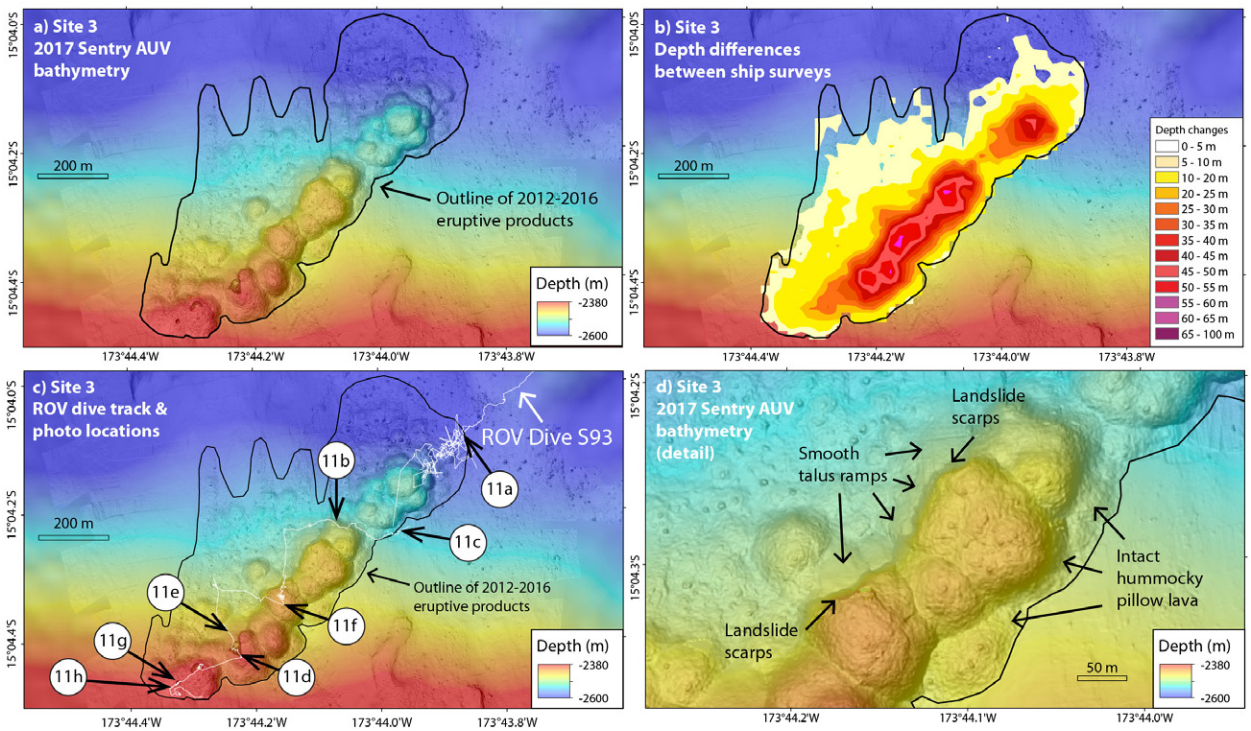

FIGURE 10 | Maps of eruption site #3, the pillow ridge on the NE flank of West Mata (see **Figure 2**) showing **(a)** post-eruption *Sentry* AUV bathymetry from 2017, **(b)** positive depth differences between ship-based surveys in 2012 and 2016 (**Table 2**), **(c)** trackline of *SuBastian* ROV dive S93 (white line) on *Sentry* AUV bathymetry, with locations of images in **Figure 11** (white numbered circles), and **(d)** close-up showing hummocky intact pillow lavas on the gentler upslope side of the ridge contrasting with smooth talus ramps below landslide scarps on the steeper downslope side. Black outlines enclose the site #3 eruption deposits.

Site 3: The 2012–2016 Eruption on the NE Flank at 2400 mbsl

The second recent eruption site constrained in time between 2012 and 2016 is located on the NE flank of West Mata (**Figure 2**). It is unusual because it is well off the ENE rift zone and the smooth morphology of the rest of the NE flank (from volcaniclastic debris produced upslope) makes it clear that eruptions do not occur here often. This site was beyond the coverage of the 2009 AUV survey, so we do not have high-resolution bathymetry before the eruption, but pre-2012 ship-based bathymetry shows a featureless slope. The post-eruption AUV survey in 2017 (**Figure 10a**) shows that the eruption produced a linear ridge of coalesced pillow lava mounds that is rotated ∼26°clockwise to the radial direction from the summit. The orientation of the pillow ridge may have been influenced by basement structure nearby, as it is parallel to an older sedimented and tectonized ridge NE of the volcano (**Figure 2**). Lava was apparently erupted along a fissure ∼1 km long, extending from 2365 to 2635 mbsl on a slope averaging 15–20°. The depth differences between ship-based surveys (**Figure 10b**) show the maximum thickness of the lavas is 57 m, the area of erupted material is 0.25×10^6 m^2, and the volume is 6.7×10^6 m^3 (**Table 2**).

ROV *SuBastian* dive S93 traversed from the NE base of the volcano upslope along the length of the 2012–2016 pillow ridge (**Figure 10c**). The hummocky areas of lesser depth change that extend as fingers downslope from the thick pillow ridge (**Figures 10a,b**) are thinner (<10 m) flows of pillow lava. These were apparently produced in an early phase of the eruption when lava was fed from the fissure at a slightly higher effusion rate before it slowed and became localized at discrete points along the eruptive fissure to produce the thicker pillow mounds. The thinnest margins of the flow field (probably the earliest flows) are covered with rippled deposits of tephra (**Figure 11a**), suggesting downslope transport by turbidity currents during a pyroclastic phase of this eruption. Deposits of tephra are ubiquitous on the thicker pillow lavas, but are less obvious on steeper slopes. On the upslope sides of the pillow mounds, the constructional slopes are nearly vertical (**Figure 11b**) with elongate pillow lava tubes that remained intact all the way to the flow margins (**Figure 11c**). In contrast, on the unbuttressed downslope sides of the pillow mounds, the pillow lavas did not remain intact and formed vertical cliffs of truncated pillows in the upper reaches (**Figure 11d**) and aprons of pillow talus below (**Figure 11e**). This contrast in morphology is evident in the high-resolution AUV bathymetry with intact hummocky flows on the upslope side of the pillow mounds, and cliffs with smooth ramps of pillow talus below on the downslope side (**Figure 10d**). On the flatter tops of the pillow mounds, a thin dusting of yellow sediment (**Figure 11f**) and abundant polychete worms were evidence for

low-level diffuse hydrothermal venting. The tops of the uppermost pillow mounds are marked by small pit craters (**Figure 10a**) with overhanging edges (**Figure 11g**), indicating that some of the mounds had a core of molten lava that drained out and collapsed during the later stages of the eruption. Locally, the tops of the pillow mounds were covered with pyroclastic tephra deposits up to several 10s of cm thick, with occasional collapse pits as seen at site #1 (**Figure 11h**).

Site 4: The 2012–2016 Eruption at the NE Base at 2650 mbsl

The third of the recent eruption sites between 2012 and 2016 is also in an unusual location, at the NE base of the volcano in a basin 1–2 km north of the axis of the deepest part of the ENE rift zone (**Figure 2**). Before the eruption, ship-based bathymetry showed a broad oval basin in the area, 1–1.5 km across and relatively flat at ∼2700 mbsl. The 2009 AUV survey did not extend over this site. After the eruption, ship-based bathymetry shows positive depth changes throughout the basin up to 64 m (**Figure 12b**), covering an area of 0.73×10^6 m^2, and amounting to a volume change of 17.1×10^6 m^3 (**Table 2**).

The AUV bathymetric survey over this site in 2017 was particularly revealing (**Figure 12a**). The high-resolution map showed that much of the eastern half of the basin appeared to be uplifted sediments (**Figure 12c**), smooth seafloor that had been domed upward and cut by numerous longitudinal spreading cracks, like those on a loaf of bread when it comes out of the oven (suggesting a nickname we used for the site: "the muffin"). The uplifted sediments were surrounded by hummocky seafloor that appeared to be young lava flows that flowed around the uplift without a clearly defined eruptive vent (**Figure 12c**).

Observations during ROV *SuBastian* dive S88 confirmed this interpretation (**Figure 12d**). The edges of the young lava flow are marked by thin pillow lobes over the surrounding sediment, with occasional larger higher-standing pillows that have undergone inflation, expansion, and cracking (**Figure 13a**). The new lavas and the surrounding sediments are both covered with volcaniclastic-rich ripple marks that form a zebra-striped polygonal pattern with darker tephra on the ripple crests and lighter-colored pelagic sediment in the troughs (**Figures 13a–d**). The volcaniclastic-rich sediment is about 1–2 cm thick on the young lavas and appears to be evenly distributed throughout the area (on both sediments and lava), with no locally thicker accumulations observed. Because of this, we interpret that the majority of volcaniclastic material is not juvenile (syn-eruptive). Instead, we hypothesize that it was probably deposited by turbidity currents from further upslope after the eruption, such as those documented by Walker et al., under review[3]. This interpretation implies that pyroclastic tephra was not a major component of the eruptive products at this site, the deepest of the four most recent eruption sites (2650–2700 mbsl).

A series of sinuous tumulus structures, up to 125 m long and 5 m high are located between the two areas of uplifted sediment in the AUV bathymetry (**Figure 12c**). Tumuli are formed by internal pressure within inflating lava flows that pushes up the overlying solidified crust in a trap-door fashion on either side of an axial crack (Walker, 1991; Appelgate and Embley, 1992). These tumuli are the shallowest features on the 2012–2016 lava flows (**Figure 13e**), and are in line with the long-axis of the large dome of uplifted sediment, so may overlie the eruptive vents for the lava flows. From there, pillow lavas flowed mostly to the west and then northward, around the uplifted sediment, but also flowed a shorter distance to the east (**Figure 12c**). North of the tumuli, the young lavas lap up onto the uplifted dome of sediment (**Figure 13f**). The longitudinal cracks on the sediment dome that are evident in the AUV bathymetry appear as broad swales, 10–40 m wide and 3–8 m deep, with little or no stratigraphy evident in their walls in the southern half of the dome (**Figure 13g**). However, in the center of the uplifted sediment dome, where the swales are wider and deeper, stratigraphy was exposed in the side walls and yellow microbial mat showed evidence of local diffuse hydrothermal discharge (**Figure 13h**). At that site the ROV's temperature probe measured a temperature of 15°C within the sediments, apparently residual heat from magma intruded below.

Site 5: The 2010–2011 Eruption on the Deep WSW Rift at 2950 mbsl

In December 2017, we also made ROV *SuBastian* dive S95 on two older areas of depth change (sites #5–6, **Figure 2**) documented on the deep WSW rift zone by Embley et al. (2014). These are the first visual observations of these eruption sites and provide ground-truth that these depth changes are indeed associated with young lava flows. They also give additional information on the character of recent eruptions at West Mata, particularly at the deepest depths.

The first of the two eruption sites (site #5) visited on ROV dive S95 (**Figure 14c**) is constrained in time between May 2010 and November 2011 (time period IV + V of Embley et al., 2014). Because this area is beyond the obvious morphological extent of the rift zone, it was not mapped during the 2009 AUV bathymetric survey. We attempted to map the site with AUV *Sentry* in 2017, but unfortunately the multibeam sonar failed on this dive (#463) and so no high-resolution bathymetry exists for this site (although a photo survey was collected by *Sentry*). The post-eruption ship bathymetry (**Figure 14a**) and the 2010–2011 depth differences (**Figure 14b**) show that the lava flows that were erupted cover an area of 1300 by 700 m across (0.61×10^6 m^2), are up to 63 m thick along a ridge oriented ENE-WSW in the southern half of the flow field (probably overlying the eruptive fissure), and have a total volume of 16.0×10^6 m^3 (Embley et al., 2014).

The lava flow field is composed entirely of intact lava flows, with no landslide scarps or talus ramps, due to the relatively low slopes that existed in this area before the eruption. The lavas have a fine dusting of light-colored sediment on them. The northern margin of the lava flow field has broad pillow lava lobes (**Figure 15a**), which grade locally into lobate and ropy sheet flow morphology, in some areas with very flat

[3]Walker, S. L., Baker, E. T., Lupton, J. E., and Resing, J. A. (under review). Patterns of fine ash dispersal related to volcanic activity at West Mata volcano, NE Lau Basin. *Front. Mar. Sci.*

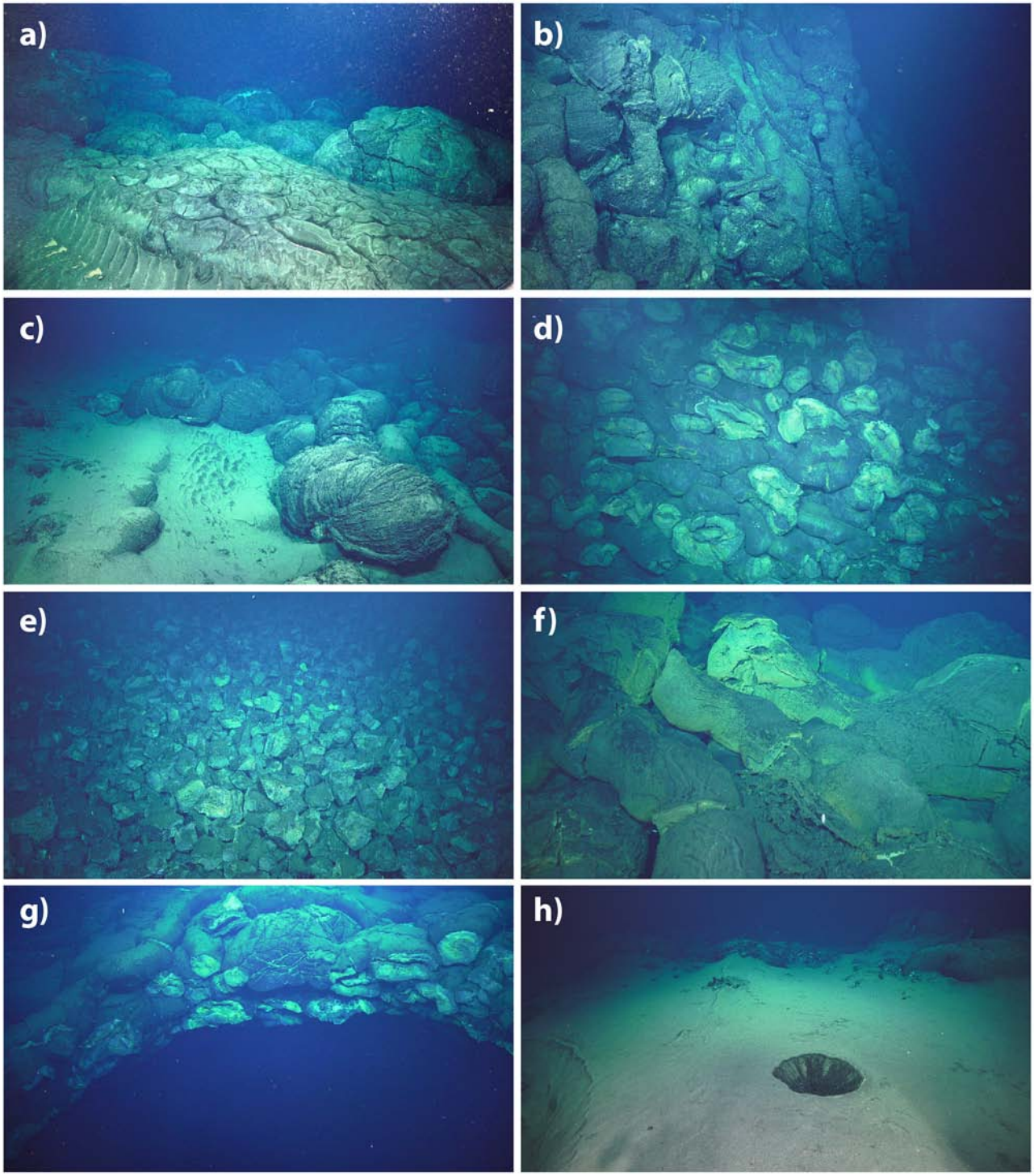

FIGURE 11 | Images of eruption site #3 from ROV *SuBastian* dive S93. All show 2012–2016 eruption products. Numbers in parentheses are time of photo in GMT and horizontal scale. See **Figure 10c** for photo locations. **(a)** Rippled tephra-rich sediment deposited on thin pillow lava flow margin downslope of pillow ridge (21:26:05, 5 m). **(b)** Nearly vertical constructional slope on upslope side of pillow ridge (23:19:35, 5 m). **(c)** Margin of young lavas (at right) on upslope side of pillow ridge (22:48:40, 4 m). **(d)** Truncated pillows in landslide scarp on steeper downslope side of pillow ridge (01:39:25, 8 m). **(e)** Ramp of pillow talus below landslide scarp on downslope side of pillow ridge (01:33:28, 10 m). **(f)** Thin yellow hydrothermal sediment and tephra on lavas at top of pillow ridge (00:32:02, 3 m). **(g)** Overhanging rim of collapse pit at top of pillow mound due to drain-out of molten interior (02:33:15, 4 m). **(h)** Tephra deposit mantling pillow lavas at upslope end of pillow ridge (02:48:08, 5 m).

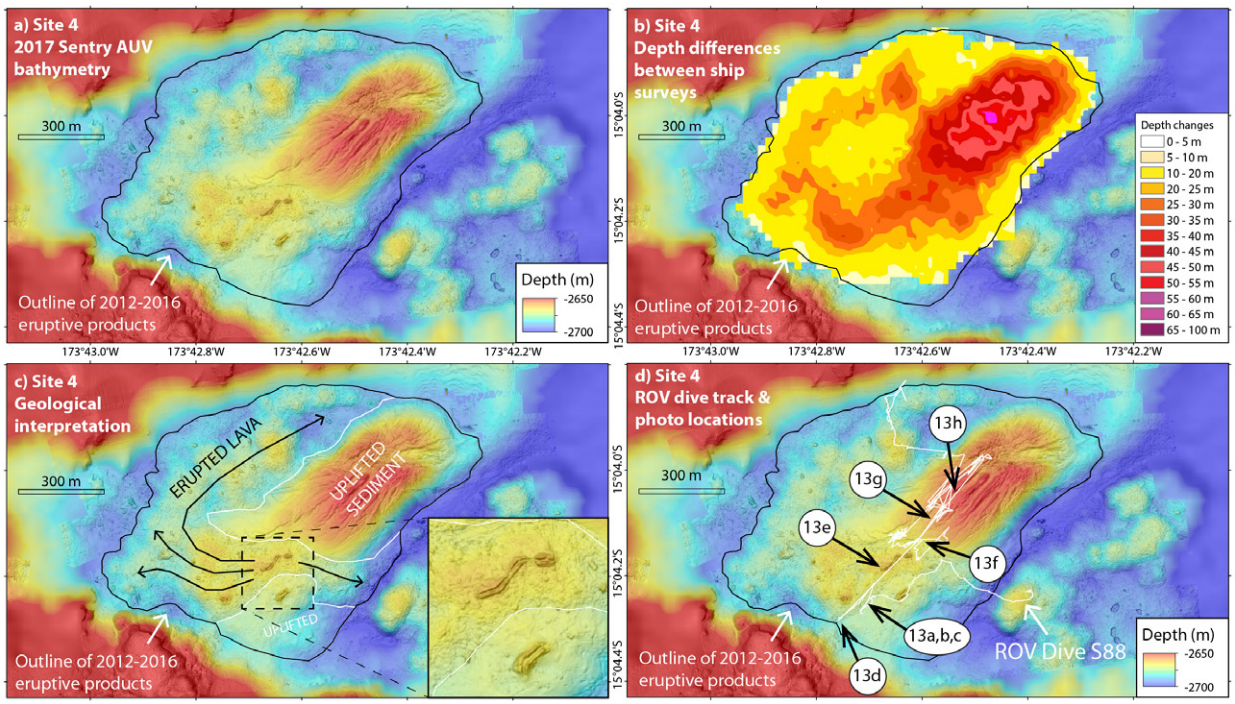

FIGURE 12 | Maps of eruption site #4, at the NE base of West Mata (see **Figure 2**) showing **(a)** post-eruption *Sentry* AUV bathymetry from 2017, **(b)** positive depth differences between ship-based surveys in 2012 and 2016 (**Table 2**), **(c)** geological interpretation on 2017 AUV bathymetry, and **(d)** trackline of *SuBastian* ROV dive S88 (white line) on *Sentry* AUV bathymetry, with locations of images in **Figure 13** (white numbered circles). In **(d)** note that the navigation for this dive was considerably noisier than for others on this expedition due to problems with the acoustic tracking system on *R/V Falkor*. Black outlines enclose the site #4 eruption deposits; white outlines in **(c)** delineate uplifted sediments and inset shows detail of tumuli structures in young lava flows.

upper surfaces that are locally uplifted into tumuli structures (**Figure 15b**), providing evidence for flow inflation. Further south, long tubular pillows mantle the northern slope of the ENE-WSW eruptive ridge (**Figure 15c**). Near the crest of that ridge, the pillows again broadened on the gentler slope, and sheet-like lava morphology with local drainback were observed near an apparent eruptive fissure (**Figure 15d**). On the north side of the flow field where it sloped down and abutted a sedimented ridge, tephra-rich ripple marks in the sediment were oriented perpendicular to the axis of the rift zone with volcaniclastic accumulations on the lee sides (**Figure 15e**), consistent with sediment transport from further upslope by bottom currents. No significant accumulations of tephra were observed on the 2010–2011 lava flows. This is the deepest of the recent eruption sites (2890–2975 mbsl).

Site 6: The 1996–2008 Eruption on the Deep WSW Rift at 2750 mbsl

On the same ROV dive (*SuBastian* S95) we also traversed the eruption site that is just upslope on the WSW rift zone (site #6, **Figure 2**), which was discovered and constrained between the 1996–2008 bathymetric surveys by Embley et al. (2014) (their time period I). In contrast to the previous site, this eruption was on the deepest morphologic expression of the WSW rift zone and so was included in the 2009 AUV bathymetric survey, which is a post-eruption survey in this case (**Figure 14a**). The depth differences between the ship-based surveys in 1996 and 2008 are up to 101 m (**Figure 14b**), with an area of 0.22×10^6 m^2 and a volume of 12.0×10^6 m^3 (Embley et al., 2014).

The morphology of this site is considerably different than the previous one, mostly because the eruption occurred on the much steeper slopes on the rift zone. Consequently, the flow field is composed of repeated sequences of gently sloping intact pillow lavas on the crests of constructional mounds (**Figure 15f**), surrounded by steep slopes of truncated pillows on the margins of the mounds (**Figure 15g**), where the pillows have broken apart and formed talus ramps below (**Figure 15h**), which in turn lap onto the next constructional pillow mound downslope (**Figure 14**). Again, no significant tephra accumulations were observed on these lava flows. Neither site #5 or #6 displayed any evidence of active hydrothermal venting (shimmering water, microbial mats, vent animals, etc.), but local accumulations of yellow hydrothermal sediment showed that it had occurred previously.

DISCUSSION

Comparison of Recent Eruption Sites

The most recent ROV dive observations show that all four of the most recent eruption sites at West Mata (#1–4; 2012–2018)

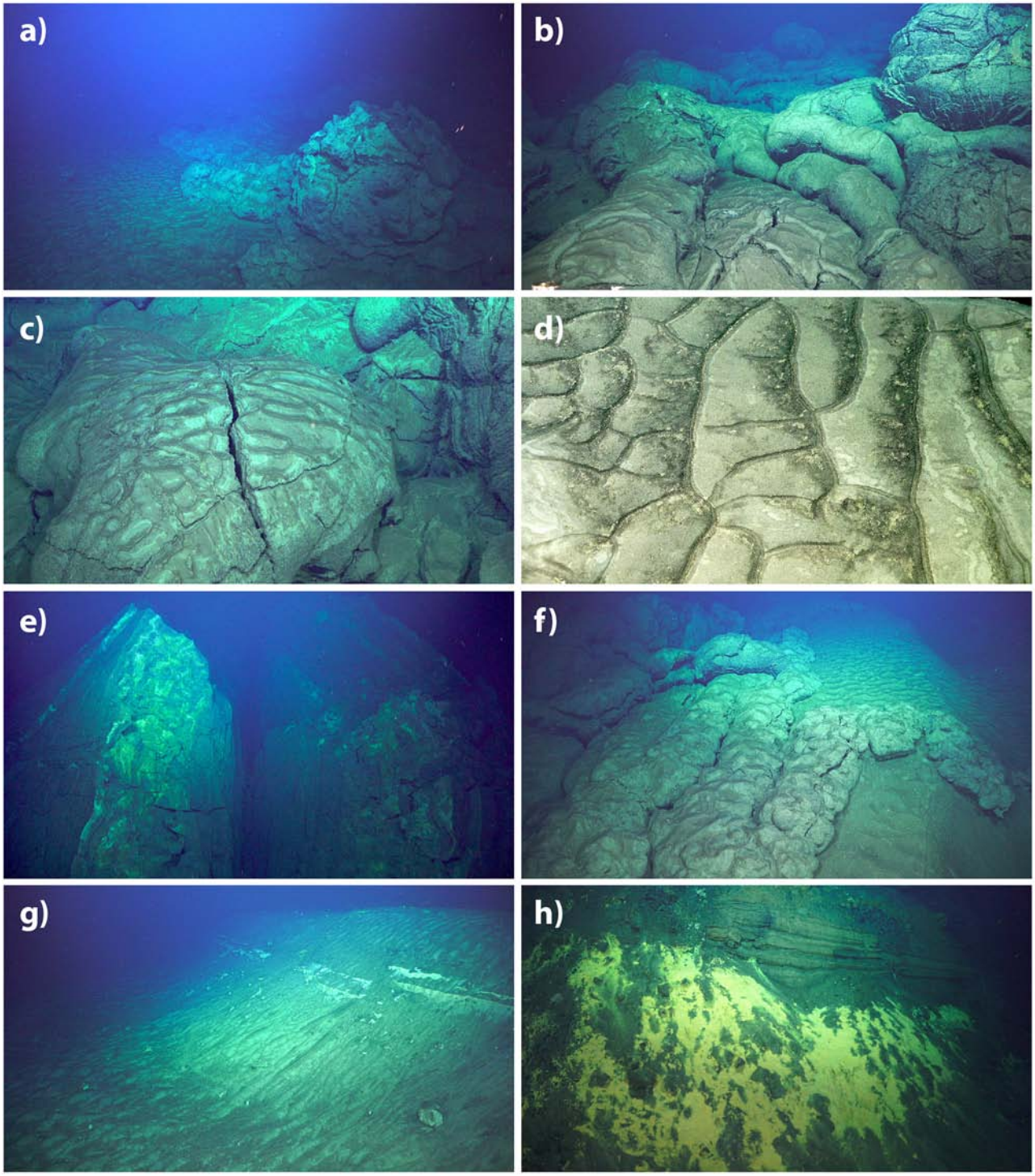

FIGURE 13 | Images of eruption site #4 from ROV *SuBastian* dive S88. Numbers in parentheses are time of photo in GMT and horizontal scale. See **Figure 12d** for photo locations. **(a)** Margin of 2012–2016 pillow lavas at right (21:32:51, 8 m). **(b)** Closer view of 2012–2016 pillow lavas (21:11:48, 3 m). **(c)** Lava lobe with rippled volcaniclastic-rich sediment on surface (21:05:22, 2 m). **(d)** Close up of rippled volcaniclastic-rich sediment (21:47:26, 0.5 m). **(e)** Uplifted lava at tumulus structure (23:18:54, 8 m). **(f)** 2012–2016 pillow lava (left) lapped up on south edge of uplifted sediment dome at right (23:50:51, 3 m). **(g)** Broad swale (left) and edge of extension crack (right) in southern part of uplifted sediment dome (00:32:58, 10 m). **(h)** Yellow microbial mat growing on edge of extensional crack with stratigraphy in central part of uplifted sediment dome (00:35:18, 5 m).

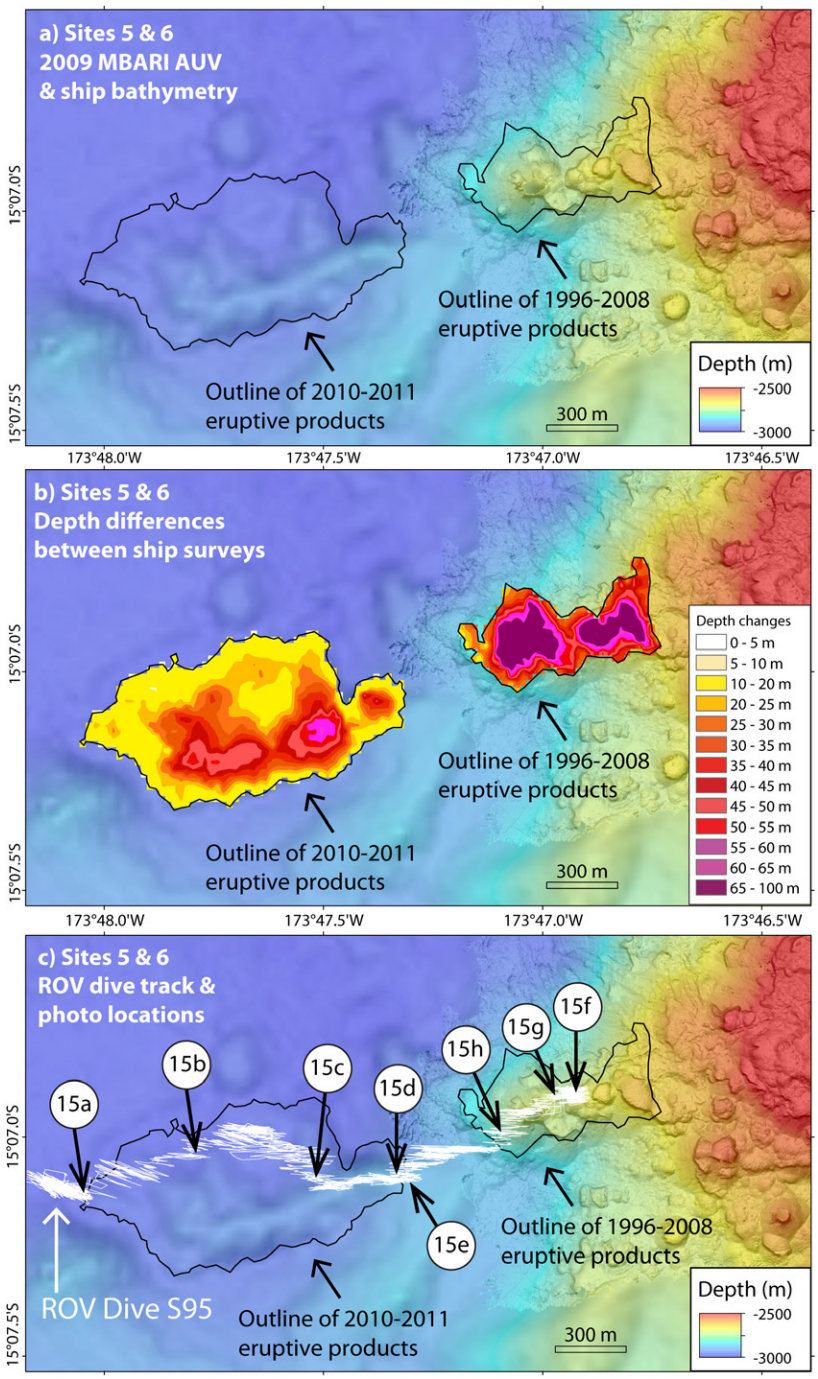

FIGURE 14 | Map of eruption sites #5 (left) and #6 (right), at the SW base of West Mata (see **Figure 2**) showing **(a)** post-site-#5-eruption ship-based bathymetry (left) overlain with post-site-#6-eruption MBARI AUV bathymetry from 2009 (right), **(b)** positive depth differences between ship-based surveys (2010–2011 at left, 1996–2008 at right, see **Table 2**), and **(c)** trackline of *SuBastian* ROV dive S95 (white line) on post-eruption bathymetry, with locations of images in **Figure 15** (white numbered circles). Note that the navigation for this dive was considerably noisier than for others on this expedition due to problems with the acoustic tracking system on *R/V Falkor*. Black outlines enclose the site #5 and #6 eruption deposits.

have deposits that were still warm and cooling in December 2017 (from months to perhaps up to 5 years after they were erupted), exhibiting some combination of diffuse hydrothermal venting colonized by vent animals (particularly shrimp, squat lobsters, and polychetes), microbial mats, and elevated temperatures measured in tephra or sediments just below the surface. In addition, diffuse hydrothermal venting was observed all around the summit, both inside and outside of Hades Crater, despite

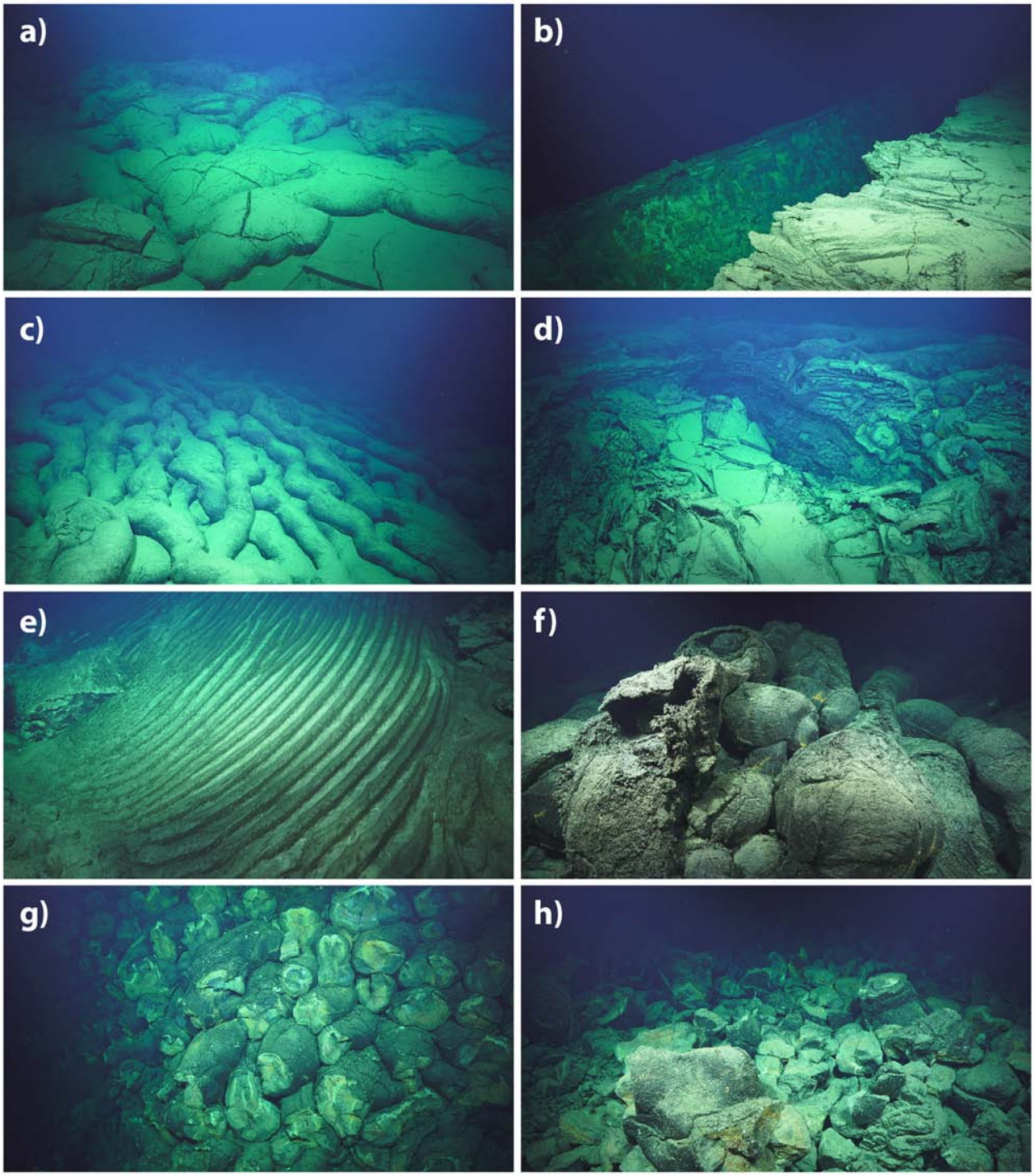

FIGURE 15 | Images of eruption sites #5 (2010–2011) and #6 (1996–2008) from ROV *SuBastian* dive S95. Numbers in parentheses are time of photo in GMT and horizontal scale. See **Figure 14c** for photo locations. **(a)** Broad lobes of 2010–2011 lava near northern flow margin (20:34:50, 5 m). **(b)** Uplifted sheet lava in tumulus structure near northern 2010–2011 flow margin (22:21:14, 5 m). **(c)** elongate pillows on north slope of 2010–2011 pillow ridge (23:14:48, 8 m). **(d)** Eruptive fissure with lava drain-out at crest of 2010–2011 pillow ridge (01:24:04, 8 m). **(e)** Volcaniclastic-rich sediment ripples at southern margin of 2010–2011 pillow ridge, oriented perpendicular to the downslope direction (00:05:08, 5 m). **(f)** Crest of 1996–2008 pillow lava mound with intact lavas (03:35:11, 3 m). **(g)** Landslide scarp of truncated 1996–2008 pillows on downslope edge of pillow mound (03:31:13, 5 m). **(h)** Pillow talus below landslide scarp in 1996–2008 lavas (02:39:27, 5 m).

the end of eruptive activity there by early 2011. This implies that active diffuse hydrothermal activity exists more or less continuously at West Mata due to the heat delivered or mined from recent eruption sites and the relatively short recurrence interval between eruptions. This is important for the continuity of local vent-dependent ecosystems. In contrast, no evidence for continued venting was observed at the two older eruption sites visited by ROV in 2017 (#5–6; 1996–2011), suggesting that venting usually does not persist for longer than 5–10 years at eruption sites on the rift zones.

The ROV dive observations also show that there is a variation in eruptive character with depth at West Mata. The shallower recent eruption sites (sites #1, #2, and to some extent #3) have very significant deposits of tephra near the eruptive vents (up to 1–2 m thick and extending for 100s of m laterally), showing that violent degassing and lava fragmentation are common. We envision this eruptive behavior as similar to the spectacular video observations of explosive activity at the summit vents during ROV *Jason* dives in May 2009 (Resing et al., 2011; Rubin et al., 2012). In addition, there is some evidence that the eruptive style evolves during a single eruption, with a progression from more pyroclastic to more effusive with time. On the other hand, at site #1 a thick tephra deposit overlies pillow lavas, so it appears that pyroclastic activity continued throughout the eruption there. In contrast, the deeper recent eruption sites (sites #4, #5, and #6) do not have locally thick, near-vent deposits of tephra, suggesting that little tephra is produced by eruptions at West Mata below a depth of about 2500 m. Nevertheless, we did observe tephra on the recently erupted lava flows, but these deeper deposits were evenly distributed (on and off the new flows) and heavily rippled, suggesting the tephra was transported from areas further upslope and deposited by episodic turbidite-like bottom currents that move fragmental material downslope, as envisioned by Walker et al., under review[4].

The observations also demonstrate that the map-scale morphology of individual eruption deposits is highly dependent on the underlying slope of each site. For example, the "on-rift" eruption sites that are located on relatively steep slopes (sites #1 & 2, and to some extent site #6) are characterized by pillow lava flows that are locally emplaced as "shingled lava plateaus," which form inflated lava flows with slightly domed upper surfaces that are impounded by levees of nearly vertical elongate pillow lavas at their downslope edges, like perched lava-ponds on land. At sites #1 and #2 there is clear evidence that the recent eruptive vents were localized within the headwall scars of previous landslides on the steep margins of the rift zone. We know the landslide at site #2 occurred between December 2010 and November 2011, whereas at site #1 the slide scar had been there since the first bathymetric survey in 1996. There is also ample evidence for landslides occurring during or soon after eruptions where the recent lava flows are cut by scarps exposing truncated pillows in nearly vertical cliffs with local evidence for lava drain-out, showing that parts of the flow interiors were still molten when the landslides occurred. These processes produce ramps of pillow talus and finer clastic debris downslope. In places, late-stage pillow lava flows were also emplaced within the co-eruption landslide chutes, providing additional evidence for the overlap of volcanic construction and mass-wasting processes at the eruption sites on steep slopes.

In contrast, eruption sites on gentler slopes at "off-rift" sites produced a different set of eruption deposits and morphologies. These sites include #4 and #5, which are both located beyond the morphological expression of West Mata's rift zones on flatter terrain off the main edifice (**Figure 2**). At site #4, based on the distinctive morphologies evident in the AUV bathymetry, we interpret that magma first intruded into the sedimented basin as a sill that thickened and uplifted the overlying sediments. Eventually, continued intrusion allowed the magma to reach the surface, probably along faults on the edge of the uplifted sediment, and lava then erupted onto the seafloor and flowed around the domed uplift. This is similar to the scenario envisioned for intrusions/eruptions into sediment on the Escanaba Trough of the Gorda Ridge (NE Pacific) (Denlinger and Holmes, 1994; Morton and Fox, 1994; Zierenberg et al., 2013) and for several locations on the Pescadero and Tamayo transform faults in the Gulf of California (Clague et al., 2018). At site #5, lava flows erupted onto the gently sloping seafloor adjacent to the rift zone and spread out to form low-relief sheet flows. Both sites produced broad lava flows with evidence of inflation and morphologies ranging from pillows to lobate flows to ropy lava, with local tumulus structures that formed due to internal pressure within the molten interior of the sheet-like flows. Co-eruption landslides or auto-brecciation and talus formation were not components of these eruptions on gentler slopes. These two eruption sites are also the deepest documented at West Mata and show that eruptions can take place beyond the obvious morphological limits of the rift zones at the base of the volcano.

Eruption site #3, the pillow ridge on the NE flank of West Mata, is somewhere in between these end-members, in that it has evidence for both constructional pillow lava mounds and local co-eruption mass-wasting on the steeper downslope side of the pillow ridge. On the other hand, it clearly did not form within a previous landslide scar nor on one of West Mata's rift zones, and indeed its location is hard to explain. One possibility is that if it was the last of the three eruptions that occurred between 2012 and 2016, then because the previous two (sites #2 and #4) would have presumably been fed by dikes that intruded along the ENE rift zone, perhaps the compressional stresses across the rift from those intrusions would not have had enough time to relax so that the next dike intrusion was forced to take a different path to the surface. Instead, a dike intruded outward from beneath the summit in a direction close to radial, but outside of the rift zone. Another possibility is that this eruption site was controlled by deeper crustal structure related to the older ridge NE of the volcano. In any case, this must be a relatively rare event based on West Mata's morphology and the lack of other similar examples. It is clear that most eruptions at West Mata occur either at the summit or along the rift zones.

[4] Walker, S. L., Baker, E. T., Lupton, J. E., and Resing, J. A. (under review). Patterns of fine ash dispersal related to volcanic activity at West Mata volcano, NE Lau Basin. *Front. Mar. Sci.*

Common Patterns in Submarine Effusive Volcanism

Despite the differences in tectonic setting and magma composition, the characteristics of the recent eruption deposits at West Mata volcano are notably similar to the results from studies at many other recent submarine eruption sites. In particular, our observations are quite similar to those at other basaltic submarine volcanoes where high-resolution AUV bathymetry and ROV dives allow direct comparisons of map-scale morphology of lava flows and interpretation of their emplacement. Commonalities include the construction of thick hummocky flows of pillow lava with evidence of molten interiors and steep flanks locally modified by co-eruption landslides forming aprons of talus, as well as evidence for inflation of more fluid lava flows on gentler slopes, and intrusion and eruption processes in sedimented basins. Such comparable AUV/ROV datasets include those from the Juan de Fuca and the Gorda spreading ridges and the Alarcon Rise in the NE Pacific (Caress et al., 2012; Chadwick et al., 2013, 2016; Yeo et al., 2013; Zierenberg et al., 2013; Clague et al., 2014, 2017, 2018), the East Pacific Rise (White et al., 2000, 2002; Fornari et al., 2004; Soule et al., 2007; Fundis et al., 2010; Klein et al., 2013; Deschamps et al., 2014), and the Galapagos spreading ridge (Haymon et al., 2008; White et al., 2008; McClinton et al., 2013). The combined results of these high-resolution geological studies show that the effusive eruptive processes we describe here are not unique to West Mata, but are widespread and common to mafic submarine eruptions in diverse tectonic settings, demonstrating their importance on a global scale and a convergence of scientific understanding about submarine effusive volcanism. On the other hand, the significant deposits of pyroclastic tephra at the shallower eruption sites at West Mata are quite unusual, and probably reflect the high volatile content of its boninite parent magma (Resing et al., 2011; Rubin et al., 2018). These tephra deposits and their implications will be the subject of future studies.

This study shows that the combination of high-resolution bathymetry with visual observations of the seafloor and a time-series of repeat mapping surveys can provide insights into the emplacement processes of effusive submarine eruptions. The documentation of multiple eruptive events over a significant depth range illustrates a variety of eruption styles, products, and environments. Observations over an extended period of time reveal the spatial and temporal evolution of volcanic activity, can constrain rates of magma supply, and show how construction and mass wasting events are closely linked.

Recent Eruption History at West Mata

If we consider the history of known eruptions at West Mata since 1996 (**Figure 3**), the most significant change in the character of that activity was the shift from continuous eruptive activity at the summit to episodic eruptions on the rift zones that occurred around early 2011 (although admittedly we know far less about the activity before 2008 than afterward). This change was accompanied or followed closely in time by the collapse of the summit and the formation of Hades crater. It is possible that the site #5 eruption was directly related to the crater collapse, due to magma withdrawal from shallow levels beneath the summit to the deep WSW rift zone, similar to the recent activity at Kilauea volcano, Hawaii (Neal et al., 2019). However, this connection cannot be demonstrated conclusively because the time constraints on the two events are slightly different. Hades crater formed between December 2010 and November 2011, whereas the site #5 eruption occurred between May 2010 and November 2011, but the difference is only because the site #5 eruption was beyond the coverage of the December 2010 multibeam survey (Embley et al., 2014).

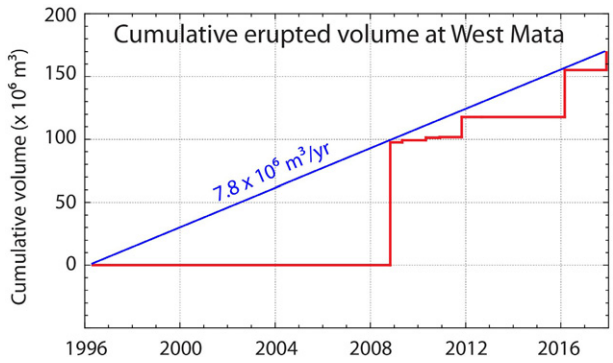

FIGURE 16 | Cumulative erupted volume at West Mata vs. time, based on volumes of depth change between nine repeated ship-based bathymetric surveys listed in **Table 1**. Volumes are from **Table 2** and Embley et al. (2014) and are plotted at the time they were discovered (the second of each pair of surveys). Trend is remarkably linear and implies volume-predictable eruptive behavior in which the volume of the next eruption is predictable from the time since the previous one.

In any case, the transition from continuous to episodic eruptions overlapped in time and it is likely that the onset of activity on the rift zones destabilized the conditions that allowed continuous eruption at the summit. The first three episodic events between 2009 and 2011 were along the WSW rift zone (while activity at the summit was waning), and subsequent events have all been along the ENE rift zone between 2012 and 2018 (after the summit activity had stopped). Over longer periods of time, this distributed volcanism along the rift zones may be the norm at West Mata, intermixed with occasional extended periods of eruptive activity at the summit. Nevertheless, it is remarkable that over the last 22 years the locations of eruptive activity have spanned the entire volcano from the deepest parts of both rift zones, to the summit, to locations in between, and even off the rifts such as on the NE flank. This suggests that when dikes are intruded at West Mata they tend to seek regions within the edifice with relatively low compressive stress, which are likely areas that have not experienced the most recent intrusions and eruptions (Acocella and Neri, 2009). This is similar to the way in which individual dike intrusions were spatially distributed along different parts of the extensional plate boundary during the 1975–1984 Krafla rifting episode in Iceland (Björnsson et al., 1979; Björnsson, 1985; Buck et al., 2006).

The time-series of repeat bathymetry at West Mata allows us to quantify the volume of eruptive products added to the volcano with time. **Figure 16** shows the recent history of cumulative

erupted volume at West Mata, with the volume changes from individual eruptive periods plotted in the year they were discovered (that is, the year of the first subsequent ship-based bathymetric survey), using data from **Table 2** and from Embley et al. (2014). An average linear eruption rate of $\sim 7.8 \times 10^6$ m^3/yr over this time interval fits the cumulative erupted volume time-series remarkably well (**Figure 16**). For comparison, this is about the volume of the 2012–2016 pillow ridge eruption on the NE flank of the volcano (site #3), but most of the other recent eruptions are about twice this volume (**Table 2**), implying an average recurrence interval of about 1–2 years between episodic rift eruptions, which is relatively short. Of course, we have little information about the eruptive activity between 1996 and 2008 – we only know the net volume change between the surveys at the beginning and the end of that period, that most of the volume was added at the summit and on the north flank, and that West Mata was in a state of continuous eruption from the summit near the end of that period. However, it is reasonable to assume that the 1996–2008 erupted volume accumulated over a significant amount of time and that the actual cumulative eruption curve between 1996 and 2008 was probably closer to the longer-term average rate.

If the recent rate of erupted volume at West Mata is approximately linear, it suggests that eruptions are volume-predictable at West Mata, such that the volume of a future eruption can be estimated simply by knowing how much time has elapsed since the previous one. It also suggests that the magma supply is relatively steady over time, which has implications for the underlying magmatic system (Wadge, 1982). The relatively low magma supply rate (for comparison, the magma supply rate to Axial Seamount from 2011 to 2015 was about an order of magnitude higher, Nooner and Chadwick, 2016) and the apparent high frequency of eruptions implies that the magma storage reservoir at West Mata must also be relatively small. In other words, we interpret that a steady rate of magma is being supplied to West Mata's shallow reservoir beneath the summit (at about the long-term eruption rate), but it is only 1–2 years before the pressure within the reservoir exceeds its failure threshold and eruptions occur, which implies the volume of the reservoir is relatively small since it can only accommodate a small increase in volume before failing. Conversely, if the reservoir volume were large, then it would be able to accommodate a small magma supply for longer before eruptions are triggered by high internal pressure. Additional support for this conceptual model comes from the changes in the chemistry of lavas erupted between 2009 and 2011, which are consistent with a small and frequently replenished magma body at West Mata (Rubin et al., 2015, 2018). The apparently low strength of the magma reservoir might be related to the largely clastic character of the volcano. In any case, its recent history implies that West Mata will likely continue to experience frequent eruptions, perhaps every few years, and therefore is an important target for continued re-mapping efforts and perhaps even an ideal candidate for long-term instrumental monitoring. Thus, West Mata continues to be one of the best natural laboratories in the world for the study of active submarine volcanism.

CONCLUSION

The combination of nine repeated ship-based bathymetric surveys, two high-resolution AUV surveys, and the three expeditions that conducted ROV dives provides valuable information about the recent of eruptive history at West Mata submarine volcano since 1996. From this study we make the following conclusions:

(1) The latest two ship-based bathymetric surveys in 2016 and 2017 document four new eruption sites on the ENE rift zone, on the NE flank and at the NE base of the volcano since the previous survey in 2012. AUV and ROV dives in November and December 2017 mapped, sampled, and documented these and other recent eruption sites on the seafloor for the first time.
(2) Early 2011 marked a change in the eruptive behavior of West Mata, from mostly continuous summit activity (1996–2011) to episodic rift eruptions since then (2012–2018).
(3) At the same time, the summit collapsed and the location of subsequent eruptions shifted from the summit and WSW rift zone (1996–2011) to ENE rift zone (2012-present).
(4) Since 2009, there has been an episodic rift eruption every 1–2 years, spanning locations from near the summit to beyond the end of both rift zones at the base of the volcano, a depth range of 1200–3000 mbsl.
(5) These eruptions have had both pyroclastic and effusive components, due to the high volatile content of West Mata's boninite magma. The proportion of tephra decreases with depth, with little or no tephra produced by eruptions below 2500 m. However, downslope tephra transport from shallower parts of the volcano by turbidity currents is common.
(6) The morphology of the recent eruption sites highly depends on the underlying slope, with shingled lava plateaus, landslide scarps, and co-eruption talus more common on steeper slopes, and inflated lava flows with local tumuli but lacking significant fragmental deposits on the gentler slopes at the base of the volcano.
(7) The eruptions at West Mata appear to be volume-predictable with time, suggesting a constant magma supply rate and a relatively small magma storage reservoir that can only accommodate a modest influx of magma between eruptions.
(8) The wide range of recent eruptive sites at West Mata provide well-documented examples of the range of eruption styles and emplacement processes that are common to basaltic submarine volcanoes worldwide.

DATA AVAILABILITY

The data presented in this study are available at the NOAA National Centers for Environmental Information (ship bathymetry), the Rolling Deck to Repository (CTD data

and cruise reports), the IEDA Marine Geoscience Data System (AUV *Sentry* and ROV *SuBastian* data), and ROV video is available on the Schmidt Ocean Institute YouTube channel.

AUTHOR CONTRIBUTIONS

WC wrote the manuscript, made the figures and tables, and was co-chief scientist on the FK171110 expedition. KR was chief scientist on that expedition and co-directed the ROV dives described here. SM processed and analyzed ship-based and AUV-based multibeam sonar bathymetric data. SM and AB assisted with GIS data management, volume calculations, and figure preparation. TK was chief scientist on the FK160320 expedition and collected the 2016 multibeam bathymetric survey. RE helped to interpret the new results in the context of previous observations at West Mata.

FUNDING

We gratefully acknowledge the funding of the NOAA Ocean Exploration and Research (OER) Program and NOAA's Pacific Marine Environmental Laboratory (PMEL) for support of the science at sea and on shore. This research was supported by the PMEL Earth-Ocean Interactions Program and the Cooperative Institute for Marine Resources Studies (CIMRS) under NOAA Cooperative Agreement NA11OAR4320091 and NA15OAR4320063. Ship time on *R/V Falkor* and use of AUV *Sentry* on expedition FK171110 were supported by the Schmidt Ocean Institute.

ACKNOWLEDGMENTS

We thank the Schmidt Ocean Institute for supporting expeditions FK160320 and FK171110 on *R/V Falkor*, as well as the ship's crews and the teams that operated AUV *Sentry* and ROV *SuBastian*, especially expedition leaders Sean Kelley (AUV *Sentry*) and Russell Coffield (ROV *SuBastian*). We also thank the science parties of ROV expeditions TN234, RR1211, and FK171110, who contributed to their success. In addition, we thank Dave Clague, Dave Caress, and Jenny Paduan at MBARI for making the high-resolution data available from the AUV *D. Allan B.* dives at West Mata in 2009 and for helpful comments on an early draft of the manuscript. The text was also improved by the helpful comments from the two reviewers. PMEL contribution number 4927. SOEST contribution number 10724.

REFERENCES

Acocella, V., and Neri, M. (2009). Dike propagation in volcanic edifices: overview and possible developments. *Tectonophysics* 471, 67–77. doi: 10.1016/j.tecto.2008.10.002

Allen, R. W., Berry, C., Henstock, T. J., Collier, J. S., Dondin, F. J.-Y., Rietbrock, A., et al. (2018). 30 years in the life of an active submarine volcano: a time - lapse bathymetry study of the Kick 'em Jenny volcano, Lesser Antilles. *Geochem. Geophys. Geosyst.* 19, 715–731. doi: 10.1002/2017GC007270

Appelgate, B., and Embley, R. W. (1992). Submarine tumuli and inflated tube-fed lava flows on Axial Volcano, Juan de Fuca Ridge. *Bull. Volcanol.* 54, 447–458. doi: 10.1007/bf00301391

Baker, E. T., Walker, S. L., Massoth, G. J., and Resing, J. A. (2019). The NE Lau Basin: widespread and abundant hydrothermal venting in the back-arc region behind a superfast subduction zone. *Front. Mar. Sci.* 6:382. doi: 10.3389/fmars.2019.00382

Baumberger, T., Lilley, M. D., Resing, J. A., Lupton, J. E., Baker, E. T., Butterfield, D. A., et al. (2014). Understanding a submarine eruption through time series hydrothermal plume sampling of dissolved and particulate constituents: West Mata, 2008–2012. *Geochem. Geophys. Geosyst.* 15, 4631–4650. doi: 10.1002/2014GC005460

Bevis, M., Taylor, F. W., Schutz, B. E., Recy, J., Isacks, B. L., Helu, S., et al. (1995). Geodetic observations of very rapid convergence and back-arc extension at the Tonga arc. *Nature* 374, 249–251. doi: 10.1038/374249a0

Björnsson, A. (1985). Dynamics of crustal rifting in NE Iceland. *J. Geophys. Res.* 90, 10151–10162.

Björnsson, A., Johnsen, G., Sigurdsson, S., Thorbergsson, G., and Tryggvason, E. (1979). Rifting of the plate boundary in north Iceland, 1975-1978. *J. Geophys. Res.* 84, 3029–3038.

Bohnenstiehl, D. R., Dziak, R. P., Matsumoto, H., and Conder, J. A. (2014). Acoustic response of submarine volcanoes in the Tofua Arc and northern Lau Basin to two great earthquakes. *Geophys. J. Int.* 196, 1657–1675. doi: 10.1093/gji/ggt472

Buck, W. R., Einarsson, P., and Brandsdottir, B. (2006). Tectonic stress and magma chamber size as controls on dike propagation: constraints from the 1975–1984 Krafla rifting episode. *J. Geophys. Res.* 111:B12404. doi: 10.1029/2005JB003879

Caplan-Auerbach, J., Dziak, R. P., Bohnenstiehl, D. R., Chadwick, W. W. Jr., and Lau, T.-K. A. (2014). Hydroacoustic investigation of submarine landslides at West Mata volcano, Lau Basin. *Geophys. Res. Lett.* 41, 5927–5934. doi: 10.1002/2014GL060964

Caress, D. W., and Chayes, D. N. (2016). *MB-System: Mapping the Seafloor*. Available at: http://www.mbari.org/data/mbsystem/[Online] and software version is v5.5 (accessed September 15, 2016).

Caress, D. W., Clague, D. A., Paduan, J. B., Martin, J., Dreyer, B., Chadwick, W. W. Jr., et al. (2012). Repeat bathymetric surveys at 1-metre resolution of lava flows erupted at Axial Seamount in April 2011. *Nat. Geosci.* 5, 483–488. doi: 10.1038/NGEO1496

Chadwick, W. W. Jr., Cashman, K. V., Embley, R. W., Matsumoto, H., Dziak, R. P., de Ronde, C. E. J., et al. (2008). Direct video and hydrophone observations of submarine explosive eruptions at NW Rota-1 volcano, Mariana arc. *J. Geophys. Res.* 113:B08S10. doi: 10.1029/2007JB005215

Chadwick, W. W. Jr., Clague, D. A., Embley, R. W., Perfit, M. R., Butterfield, D. A., Caress, D. W., et al. (2013). The 1998 eruption of Axial Seamount: new insights on submarine lava flow emplacement from high-resolution mapping. *Geochem. Geophys. Geosyst.* 14, 3939–3968. doi: 10.1002/ggge20202

Chadwick, W. W. Jr., Dziak, R. P., Haxel, J. H., Embley, R. W., and Matsumoto, H. (2012). Submarine landslide triggered by volcanic eruption recorded by in-situ hydrophone. *Geology* 40, 51–54. doi: 10.1130/G32495.1

Chadwick, W. W. Jr., Paduan, B. P., Clague, D. A., Dreyer, B. M., Merle, S. G., Bobbitt, A. M., et al. (2016). Voluminous eruption from a zoned magma body after an increase in supply rate at Axial Seamount. *Geophys. Res. Lett.* 43, 12063–12070. doi: 10.1002/2016GL071327

Clague, D. A. (2015). *Processed Near-Bottom Multibeam Sonar Data (version 2) from the Lau Back-Arc Basin Acquired with AUV D. Allan B. During the Thomas G. Thompson Expedition TN234 (2009)*. Palisades, NY: Interdisciplinary Earth Data Alliance. doi: 10.1594/IEDA/316787

Clague, D. A., Caress, D. W., Dreyer, B. M., Lundsten, L. J., Paduan, J. B., Portner, R. A., et al. (2018). Geology of the Alarcon Rise, southern Gulf of California. *Geochem. Geophys. Geosyst.* 19, 807–837. doi: 10.1002/2017GC007348

Clague, D. A., Dreyer, B. M., Paduan, J. B., Martin, J. F., Caress, D. W., Gill, J. B., et al. (2014). Eruptive and tectonic history of the Endeavour Segment, Juan de

Fuca Ridge, based on AUV mapping data and lava flow ages. *Geochem. Geophys. Geosyst.* 15, 3364–3391. doi: 10.1002/2014GC005415

Clague, D. A., Paduan, J. B., Caress, D. W., Chadwick, W. W. Jr., Saout, M. L., Dreyer, B., et al. (2017). High-resolution AUV mapping and targeted ROV observations of three historical lava flows at Axial Seamount. *Oceanography* 30, 82–99. doi: 10.5670/oceanog.2017.426

Clague, D. A., Paduan, J. B., Caress, D. W., Thomas, H., Chadwick, W. W. Jr., and Merle, S. G. (2011). Volcanic morphology of West Mata Volcano, NE Lau Basin, based on high-resolution bathymetry and depth changes. *Geochem. Geophys. Geosyst.* 12:QOAF03. doi: 10.1029/2011GC003791

Crisp, J. A. (1984). Rates of magma emplacement and volcanic output. *J. Volcanol. Geotherm. Res.* 20, 177–211. doi: 10.1016/0377-0273(84)90039-8

Deardorff, N. D., Cashman, K. V., and Chadwick, W. W. Jr. (2011). Observations of eruptive plumes and pyroclastic deposits from submarine explosive eruptions at NW Rota-1. Mariana Arc. *J. Volcanol. Geothermal Res.* 202, 47–59. doi: 10.1016/j.jvolgeores.2011.01.003

Denlinger, R. P., and Holmes, M. L. (1994). "A thermal and mechanical model for sediment hills and associated sulfide deposits along escanaba trough," in *Geologic, Hydrothermal, and Biologic Studies at Escanaba Trough, Gorda Ridge, Offshore Northern California*, eds J. L. Morton, R. A. Zierenberg, and C. A. Reiss (Virginia, VA: U.S. Geological Survey), 65–75.

Deschamps, A., Grigné, C., Le Saout, M., Soule, S. A., Allemand, P., Van Vliet Lanoe, B., et al. (2014). Morphology and dynamics of inflated subaqueous basaltic lava flows. *Geochem. Geophys. Geosyst.* 15, 2128–2150. doi: 10.1002/2014GC005274

Dziak, R. P., Bohnenstiehl, D. R., Baker, E. T., Matsumoto, H., Caplan-Auerbach, J., Embley, R. W., et al. (2015). Long-term explosive degassing and debris flow activity at West Mata submarine volcano. *Geophys. Res. Lett.* 42, 1480–1487. doi: 10.1002/2014GL062603

Embley, R. W., Chadwick, W. W. Jr., Baker, E. T., Butterfield, D. A., Resing, J. A., De Ronde, C. E. J., et al. (2006). Long-term eruptive activity at a submarine arc volcano. *Nature* 441, 494–497. doi: 10.1038/nature04762

Embley, R. W., Merle, S. G., Baker, E. T., Rubin, K. H., Lupton, J. E., Resing, J. A., et al. (2014). Eruptive modes and hiatus of volcanism at West Mata seamount, NE Lau Basin: 1996-2012. *Geochem. Geophys. Geosyst.* 15, 4093–4115. doi: 10.1002/2014GC005387

Embley, R. W., and Rubin, K. H. (2018). Extensive young silicic volcanism produces large deep submarine lava flows in the NE Lau Basin. *Bull. Volcanol.* 80:36.

Fornari, D. J., Tivey, M. A., Schouten, H., Perfit, M., Yoerger, D., Bradley, A., et al. (2004). "Submarine lava flow emplacement at the East Pacific Rise 9°50'N: Implications for uppermost ocean crust stratigraphy and hydrothermal fluid circulation," in *Mid-Ocean Ridges: Hydrothermal Interactions Between the Lithosphere and Oceans*, eds C. R. German, J. Lin, and L. M. Parson (Washington, DC: American Geophysical Union), 187–217. doi: 10.1029/148gm08

Fundis, A. T., Soule, S. A., Fornari, D. J., and Perfit, M. R. (2010). Paving the seafloor: volcanic emplacement processes during the 2005-2006 eruptions at the fast spreading East Pacific Rise, 9°50'N. *Geochem. Geophys. Geosyst.* 11:Q08024. doi: 10.1029/2010GC003058

Haymon, R. M., White, S. M., Baker, E. T., Anderson, P. G., Macdonald, K. C., and Resing, J. A. (2008). High-resolution surveys along the hot spot – affected Galapagos Spreading Center: 3. Black smoker discoveries and the implications for geological controls on hydrothermal activity. *Geochem. Geophys. Geosyst.* 9:Q12006.

Klein, E. M., White, S. M., Nunnery, J. A., Mason-Stack, J. L., Wanless, V. D., Perfit, M. R., et al. (2013). Seafloor photo-geology and sonar terrain modeling at the 9°N overlapping spreading center, East Pacific Rise. *Geochem. Geophys. Geosyst.* 14, 5146–5170. doi: 10.1002/2013GC004858

McClinton, T., White, S. M., Colman, A., and Sinton, J. M. (2013). Reconstructing lava flow emplacement processes at the hotspot-affected Galapagos Spreading Center, 95°W and 92°W. *Geochem. Geophys. Geosyst.* 14, 2731–2756. doi: 10.1002/ggge.20157

Merle, S., Chadwick, W., and Rubin, K. (2018a). *Processed Gridded Near-Bottom AUV Sentry Bathymetric Sonar Data (NetCDF:GMT format) from the NE Lau Basin Acquired During Falkor Expedition FK171110 (2017).* Palisades, NY: Interdisciplinary Earth Data Alliance. doi: 10.1594/IEDA/324499

Merle, S. M., Chadwick, W. W. Jr., and Rubin, K. H. (2018b). *Processed Gridded Bathymetry Data from the Tonga Volcanic Arc acquired during R/V Falkor Expedition FK171110 (2017).* Palisades, NY: Interdisciplinary Earth Data Alliance. doi: 10.1594/IEDA/324447

Morton, J. L., and Fox, C. G. (1994). "Structural setting and interaction of volcanism and sedimentation at Escanaba Trough: geophysical results," in *Geologic, Hydrothermal, and Biologic Studies at Escanaba Trough, Gorda Ridge, Offshore Northern California*, eds J. L. Morton, R. A. Zierenberg, and C. A. Reiss (Virginia, VA: United States Geological Survey), 21–44.

Neal, C. A., Brantley, S. R., Antolik, L., Babb, J. L., Burgess, M., Calles, K., et al. (2019). The 2018 rift eruption and summit collapse of Kilauea Volcano. *Science* 363, 367–374. doi: 10.1126/science.aav7046

Nooner, S. L., and Chadwick, W. W. Jr. (2016). Inflation-predictable behavior and co-eruption deformation at Axial Seamount. *Science* 354, 1399–1403. doi: 10.1126/science.aah4666

Resing, J. A., Rubin, K. H., Embley, R. W., Lupton, J. E., Baker, E. T., Dziak, R. P., et al. (2011). Active submarine eruption of boninite in the northeastern Lau Basin. *Nat. Geosci.* 4, 799–806. doi: 10.1038/NGEO1275

Rubin, K. H., Chadwick, W. W. Jr., Embley, R. W., Merle, S. G., Shank, T. M., Cho, W., et al. (2018). "Exploration of the Mata Submarine Volcano Group Reveals Volcano-Tectonic-Hydrothermal Links," in *Abstract V14A-08 presented at 2018 Fall Meeting* (Washington, DC: AGU).

Rubin, K. H., Michael, P., Jenner, F., Clague, D., Glancy, S., Hellebrand, E., et al. (2015). "Composition within and between Tonga arc/Lau Basin backarc eruptions reveal wide variety of parent melts linked to eruption styles," in *Proceedings of the Goldschmidt Conference Abstracts*, Prague.

Rubin, K. H., Soule, S. A., Chadwick, W. W. Jr., Fornari, D. J., Clague, D. A., Embley, R. W., et al. (2012). Volcanic eruptions in the deep sea. *Oceanography* 25, 142–157. doi: 10.5670/oceanog.2012.12

Schnur, S. R., Chadwick, W. W. Jr., Embley, R. W., Ferrini, V. L., De Ronde, C. E. J., Cashman, K. V., et al. (2017). A decade of volcanic construction and destruction at the summit of NW Rota-1 seamount: 2004–2014. *J. Geophys. Res.* 122, 1558–1584. doi: 10.1002/2016JB013742

Soule, S. A., Fornari, D. J., Perfit, M. R., and Rubin, K. H. (2007). New insights into mid-ocean ridge volcanic processes from the 2005–2006 eruption of the East Pacific Rise, 9°46'N–9°56'N. *Geology* 35, 1079–1082.

Staudigel, H., Hart, S. R., Pile, A., Bailey, B. E., Baker, E. T., Brooke, S., et al. (2006). Vailulu'u Seamount, Samoa: Life and death on an active submarine volcano. *Proc. Natl. Acad. Sci. U.S.A.* 103, 6448–6453. doi: 10.1073/pnas.0600830103

Wadge, G. (1982). Steady state volcanism: evidence from eruption histories of polygenetic volcanoes. *J. Geophys. Res.* 87, 4035–4049.

Walker, G. P. L. (1991). Structure, and origin by injection of lava under surface crust, of tumuli, "lava rises", "lava-rise pits", and "lava-inflation clefts" in Hawaii. *Bull. Volcanol.* 53, 546–558. doi: 10.1007/bf00298155

Watts, A. B., Peirce, C., Grevemeyer, I., Pauletto, M., Stratford, W. R., Bassett, D., et al. (2012). Rapid rates of growth and collapse of Monowai submarine volcano in the Kermadec Arc. *Nat. Geosci.* 5, 510–515. doi: 10.1038/ngeo1473 doi: 10.1038/ngeo1473

White, S. M., Macdonald, K. C., and Haymon, R. M. (2000). Basaltic lava domes, lava lakes, and volcanic segmentation on the southern East Pacific Rise. *J. Geophys. Res.* 103, 25519–25536.

White, S. M., Macdonald, K. C., and Sinton, J. M. (2002). Volcanic mound fields on the East Pacific Rise, 16°-19°S: low effusion rate eruptions at overlapping spreading centers for the past 1 Myr. *J. Geophys. Res.* 107:2240.

White, S. M., Meyer, J. D., Haymon, R. M., Macdonald, K. C., Baker, E. T., and Resing, J. A. (2008). High-resolution surveys along the hot spot – affected Galapagos Spreading Center: 2. Influence of magma supply on volcanic morphology. *Geochem. Geophys. Geosyst.* 9:Q09004.

Wilcock, W. S. D., Dziak, R. P., Tolstoy, M., Chadwick, W. W. Jr., Nooner, S. L., Bohnenstiehl, D. R., et al. (2018). The recent volcanic history of Axial Seamount: geophysical insights into past eruption dynamics with an eye toward

enhanced observations of future eruptions. *Oceanography* 31, 114–123. doi: 10.5670/oceanog.2018.117

Yeo, I. A., Clague, D. A., Martin, J. F., Paduan, J. B., and Caress, D. W. (2013). Preeruptive flow focussing in dikes feeding historical pillow ridges on the Juan de Fuca and Gorda Ridges. *Geochem. Geophys. Geosyst.* 14, 3586–3599. doi: 10.1002/ggge.20210

Zellmer, K. E., and Taylor, B. (2001). A three-plate kinematic model for Lau Basin opening. *Geochem. Geophys. Geosyst.* 2, 1–26. doi: 10.1029/2000GC000106

Zierenberg, R. A., Clague, D. A., Paduan, J. B., and Caress, D. W. (2013). New maps focus 30-odd years of investigation of the Escanaba Trough spreading center. *Geol. Soc. Am. Abstr. Programs* 47:381.

Conflict of Interest Statement: The authors declare that the research was conducted in the absence of any commercial or financial relationships that could be construed as a potential conflict of interest.

Copyright © 2019 Chadwick, Rubin, Merle, Bobbitt, Kwasnitschka and Embley. This is an open-access article distributed under the terms of the Creative Commons Attribution License (CC BY). The use, distribution or reproduction in other forums is permitted, provided the original author(s) and the copyright owner(s) are credited and that the original publication in this journal is cited, in accordance with accepted academic practice. No use, distribution or reproduction is permitted which does not comply with these terms.

frontiers in Marine Science

ORIGINAL RESEARCH
published: 26 September 2019
doi: 10.3389/fmars.2019.00593

Patterns of Fine Ash Dispersal Related to Volcanic Activity at West Mata Volcano, NE Lau Basin

Sharon L. Walker[1], Edward T. Baker[2], John E. Lupton[3] and Joseph A. Resing[2]*

[1] NOAA/Pacific Marine Environmental Lab, Seattle, WA, United States, [2] University of Washington-JISAO and NOAA/PMEL, Seattle, WA, United States, [3] NOAA/Pacific Marine Environmental Lab, Newport, OR, United States

Extensive deep (>1500 m) non-hydrothermal ash-rich plumes were present in the water column surrounding West Mata submarine volcano (NE Lau basin) during eruptive phases, but were absent when West Mata was quiescent. Deep ash plumes were chemically distinct from hydrothermal plumes originating at West Mata and other hydrothermal sources in the region, and were dominated by very fine shards compositionally similar to the lava erupting at the ∼1200 m summit with morphologies indicative of magma degassing and shattering. Deep ash plume layers occurred at variable water depths (and distances above the seafloor) and were transported by local currents to 10s of km from West Mata. We interpret these deep ash plumes to be syn-eruptively generated ash transported downslope via sediment gravity flows of varying magnitudes, runout distances, and liftoff densities. Final deposition of individual particles will be by settling from suspension (i.e., fallout deposits). The mechanism for initiating gravity flows is uncertain, but their spatial and temporal distribution suggests that eruption column collapse and/or mobilization of unstable volcaniclasts accumulating on steep slopes during the eruption are likely sources. Turbidity within the deep ash plumes decreased by 80% over a 3 week period in 2017, suggesting the eruption that created a new deposit, constrained between March 2016 and November 2017, was likely active as recently as a few weeks to months prior to the FK171110 expedition. Similar deep ash plumes have been observed surrounding other erupting submarine volcanoes. This pattern of syn-eruptive dispersal suggests that fine ash does not have to be lofted high into the water column in event plumes, or enter the ocean from subaerial sources, to be dispersed by local currents and contribute to fallout deposits in regional and distal sediments, which may appear as cryptotephra or thin ash layers if the ash supply exceeds pelagic sedimentation rates; deposits that are often attributed to subaerial eruptions alone. These results also suggest that the presence of deep ash plumes surrounding a submarine volcanic edifice, along with a magmatic-hydrothermal plume above the summit, may be a valuable diagnostic exploration tool for identifying active, or very recently active, submarine eruptions.

Keywords: submarine volcano, explosive eruption, ash plume, hydrothermal plume, cryptotephra, ash dispersal, exploration, fallout deposit

OPEN ACCESS

Edited by:
Diva Amon,
Natural History Museum,
United Kingdom

Reviewed by:
Karoly Nemeth,
Massey University, New Zealand
Sebastian Watt,
University of Birmingham,
United Kingdom

****Correspondence:***
Sharon L. Walker
Sharon.L.Walker@noaa.gov

Specialty section:
This article was submitted to Deep-Sea Environments and Ecology, a section of the journal Frontiers in Marine Science

Received: *01 April 2019*
Accepted: *05 September 2019*
Published: *26 September 2019*

Citation:
Walker SL, Baker ET, Lupton JE and Resing JA (2019) Patterns of Fine Ash Dispersal Related to Volcanic Activity at West Mata Volcano, NE Lau Basin. Front. Mar. Sci. 6:593. doi: 10.3389/fmars.2019.00593

INTRODUCTION

The majority of volcanic activity on Earth occurs on the ocean floor (Crisp, 1984; White et al., 2003), yet the processes that connect deep-sea (>500 m) eruption dynamics to resulting volcaniclastic deposits, especially to the fine fractions of the sedimentary record, are rarely studied in real time due to the considerable challenges of detecting and accessing unpredictable events at remote seafloor locations (Baker et al., 2012; Rubin et al., 2012). As a result, conceptual models infer submarine eruption processes, volcaniclast transport and deposition, and the eruptive histories and evolution of volcanic regions by characterizing deposits on the seafloor (e.g., Head and Wilson, 2003; Clague et al., 2009; Watt et al., 2019), in volcaniclastic layers in marine sediment cores (e.g., Sigurdsson et al., 1980; Hawkins et al., 1994; Schindlbeck et al., 2013; Cassidy et al., 2014), and ancient deposits now accessible on land (e.g., Cashman and Fiske, 1991; White et al., 2003; Németh et al., 2008; Allen and McPhie, 2009; Cas and Giordano, 2014), These methods typically focus on visible deposits that range from millimeters to >100 m in thickness.

Volcaniclastic aprons on the flanks of volcanic islands and submarine volcanoes have morphological textures, bedforms, and internal structures that indicate mobilization and deposition by large-scale sediment gravity flows of either primary or reworked material on proximal-to-regional scales (e.g., Wright, 1996; Chadwick et al., 2005; Embley et al., 2014b; Pope et al., 2018) (see Appendix A of Walker et al., 2008 and **Supplementary Table S1** for review of terminology used here). Sediment gravity flows, however, encompass a wide range of flow types, particle sizes and concentration, and mechanisms for initiating and maintaining the flow. Many factors can be determined from the characteristics of resulting deposits (e.g., Middleton and Hampton, 1976; Fisher, 1983; Mulder and Alexander, 2001; Manville and Wilson, 2004), but care must be taken to avoid misinterpretations (Cassidy et al., 2014).

Fine and very fine volcanic ash fallout deposits occur globally as visible layers in marine sediments and have long been used as chronological markers of significant explosive subaerial eruptions (e.g., Austin et al., 2014, and references therein). Despite recent direct observations of explosive deep sea eruptions (Chadwick et al., 2008; Deardorff et al., 2011; Resing et al., 2011), and known mechanical processes for producing fine ash that are not depth-limited (e.g., Cas and Simmons, 2018, and references therein), potential submarine volcanic sources for distal fallout deposits are often minimized or ignored due to predicted limitations on fine ash production by confining pressures in the deep sea and/or physical properties of seawater that would inhibit long-distance transport of explosively launched volcaniclasts in the submarine environment (e.g., Clift and Lee, 1998; Head and Wilson, 2003; Cas and Simmons, 2018). Instead, fine ash deposits that are located more than a few kilometers from potential submarine volcanic sources are often categorized as reworked turbidites since gravity flows are well-known to transport sediments 10s of km over even relatively gentle slopes (e.g., Middleton and Hampton, 1976; Dade and Huppert, 1995). Yet, it can be difficult to distinguish the distal reaches of volcanic turbidites from fallout deposits, regardless of a subaerial or submarine source (Cassidy et al., 2014; Gill et al., 2018; Watt et al., 2019).

Methods for separating and characterizing cryptotephra (very small "invisible" volcaniclasts in low concentrations that do not form discrete layers) in sediment cores (e.g., Blockley et al., 2005; McCanta et al., 2015) have improved recognition of the contribution of submarine volcanism to fine ash fallout deposits in sediments. Gill et al. (2018), reevaluated very fine sediment units (muds and mudstones) previously considered hemi-pelagic background sediments in Izu rear arc cores (Tamura et al., 2015) and found they were actually >75% very fine ash sourced from regional submarine volcanoes deeper than 1000 m. Still, many studies conclude cryptotephra in marine sediments are the distal and ultra-distal fallout deposits from subaerial eruptions (e.g., Lowe, 2011, 2014), and dismiss the likelihood of submarine volcanic sources, even when some ashes cannot be geochemically correlated with known subaerial events and multiple submarine volcanoes are located in the region (Kohn and Glasby, 1978; Pillans and Wright, 1992; Scudder et al., 2009, 2014). This is likely due to the limited amount of data from potential submarine sources that would be necessary to confirm correlations (Shane et al., 2006).

Fallout deposits from recent, documented submarine eruptions have been sampled at mid-ocean ridges (Clague et al., 2009), including at depths exceeding 4000 m (Sohn et al., 2008; Barreyre et al., 2011), where unconsolidated volcaniclastic ash and sand with morphologies indicating strombolian or hawaiian (lava fountain) eruption styles were found draped atop lava flows or mixed within pelagic sediments. Dispersal distances of 5–10 km from known or presumed vents were much further than predicted by the Head and Wilson (2003) momentum-driven model for these eruptive styles. Clague et al. (2009) and Barreyre et al. (2011) invoke entrainment of volcaniclasts into buoyant event plumes, which rise high into the water column above eruptive vents (Baker, 1995, 1998; Baker et al., 2011), and subsequent settling from suspension as the primary mechanism for transport to the fallout deposits they sampled. However, Barreyre et al. (2011) also found that their model results significantly underestimated the dispersal distances of the ash deposits they mapped, even though they experimentally measured settling velocities of individual particles, applied local water column stratification parameters and current speeds, and assumed entrainment in high-energy event plumes (with rise heights as great as 2500 m above the seafloor).

The serendipitous discovery, in 2008, of an explosive and effusive volcanic eruption at the ∼1200 m deep summit of West Mata, a submarine volcano located in the NE Lau basin, led to a multi-year, multi-parameter time series at a persistently active, deep, rear-arc submarine volcano. This was the second deep-sea eruption to be directly observed, the first being NW Rota-1 in the Mariana arc where an explosive strombolian eruption, at ∼550 m water depth, was also nearly continuous for several years (Embley et al., 2006; Resing et al., 2007; Chadwick et al., 2008, 2012, 2014; Walker et al., 2008; Butterfield et al., 2011; Deardorff et al., 2011; Dziak et al., 2012; Schnur et al., 2017). As with NW Rota-1, the eruption at West Mata has been documented by direct Remotely Operated Vehicle (ROV)

observations and video recordings (Resing et al., 2011), analyses of magmatic-hydrothermal plume chemistry (Baumberger et al., 2014), hydroacoustic monitoring (Bohnenstiehl et al., 2014; Caplan-Auerbach et al., 2014; Dziak et al., 2015), and repeat bathymetric surveys (Clague et al., 2011; Embley et al., 2014a; Chadwick et al., 2019). This paper describes the multi-year record of regional water column surveys that mapped episodic, widely distributed, volcanically sourced, deep (i.e., deeper than the eruptive vents at the summit of West Mata) particle plumes ("deep ash plumes") that were chemically distinct from hydrothermally sourced plumes, and closely associated with periods of eruptive activity at West Mata.

The plumes described here are similar to eruption-fed, laterally dispersing, particle plumes comprising very fine, fresh glass shards and bubble wall fragments, and devoid of magmatic-hydrothermal components that have been found in the water column, at depths deeper than eruptive vents, surrounding other explosively erupting submarine volcanoes [i.e., Kavachi (Solomon Islands, Baker et al., 2002), NW Rota-1 (Mariana arc, Walker et al., 2008), Monowai (Kermadec arc, Walker et al., 2010), and others (**Supplementary Table S2**)]. At NW Rota-1, anhydrite crystals in the deep ash plumes provided evidence that these plumes had originated at the eruptive vents near the summit at ∼550 m and traveled rapidly downslope before dispersing laterally to arrive at the depths (∼600 to >2000 m) and distances where they were found (Walker et al., 2008). Based on the inventory of horizontally dispersing ash suspended in the water column surrounding NW Rota-1, as much as 0.7–3.5 × 10^8 kg of fine ash (equivalent to 0.4–2.0 × 10^5 m^3) could be delivered per year to regional and distal fallout deposits. Individual particles might travel 10s to 100s of kilometers before settling out of the water column depending on particle size, the distance of the laterally dispersing deep ash plume layer above the seafloor, and local current speeds. An eruption column collapse observed near the vent (Figure 3 of Walker et al., 2008; Figure 7 and Movie 7 of Chadwick et al., 2008[1]) and small-scale grain flows easily triggered by ROV movements, showed that (a) mobilization of unstable material accumulating on the steep slopes, and (b) eruption column collapse and base surges were likely mechanisms for initiating sediment gravity flows that delivered fine ash produced by the explosive eruption to the deep ash plumes.

Geologic Setting and Recent Eruptive History at West Mata Volcano

Extensive hydrothermal activity in the NE Lau basin was suspected when Lupton et al. (2004) described a regional ^{3}He plume near Samoa that was distinct from the ^{3}He signal advecting 6000 km across the Pacific from the East Pacific Rise. Since then, several expeditions have explored the area and found a remarkably diverse collection of volcanic and hydrothermal sites in this region (Embley et al., 2009; Kim et al., 2009; Baker et al., 2019). Among the sites discovered was West Mata volcano, the largest and most active edifice in a cluster of nine similarly-shaped boninite volcanoes located in the rear-arc portion of the tectonically complex NE Lau basin (**Figure 1**). West Mata lies ∼20 km west of the active Tofua volcanic arc, 40 km east of the back-arc NE Lau Spreading Center (NELSC), and 30 km south of the east-west portion of the Tonga trench. The Mata volcanoes are surrounded by a depression with deepening bathymetry (by ∼400–700 m) toward the trench to the north. This bathymetric depression is generally defined by the 2500 m contour (**Figures 1**, **2**), and for the purposes of this study we call it the Mata Depression (MD). The bases of the Mata volcanoes are at depths ranging from ∼2600 m at East Mata to >3000 m around the North Matas. The summit of West Mata is ∼1200 m water depth, while the summit of East Mata volcano, 8 km to the east, is ∼1270 m. The North Mata volcanoes, which are more closely spaced than West and East Mata, lie 7–20 km northwest of West Mata and the summits are significantly deeper (1830 to 2680 m below sea level). All but two of the Mata group volcanoes (Taha and Nima) are hydrothermally active.

West Mata was one of two sites discovered to be erupting during a 2008 expedition aimed at systematically surveying the water column throughout the NE Lau basin for evidence of hydrothermal activity (Baker et al., 2011, 2019; Resing et al., 2011). The eruption at West Mata was indicated by: (1) an unusually intense magmatic-hydrothermal plume rising more than 170 m above the summit with significant anomalies of temperature, turbidity, and oxidation–reduction potential (ORP), (2) high concentrations of magmatic gasses (^{3}He, CO_2, and SO_2) and total dissolvable Fe and Mn, (3) extremely high concentrations of dissolved H_2 (>14,000 nM) from the interaction of seawater and/or magmatic water with molten rock (Sansone and Resing, 1995), and (4) numerous sharp-edged mineral/glass shards (Baker et al., 2011; Resing et al., 2011; Baumberger et al., 2014).

Subsequent expeditions to West Mata with ROVs (2009 and 2012) resulted in direct observations of explosive and effusive eruptive activity at summit vents in 2009 (Resing et al., 2011), and that the eruptive phase appeared to have completely subsided by the time of the 2012 expedition (Baumberger et al., 2014; Embley et al., 2014a). Evidence for continued explosive activity through 2010 and 2011 came from repeat bathymetric surveys, hydroacoustic monitoring (see below) and plume sampling (Baumberger et al., 2014; and this work).

Hydroacoustic monitoring between January 2009 and August 2011 provided insight into the long-term intensity and duration of eruptive activity at West Mata volcano. Moored hydrophones recorded sounds from lava bubble bursts, explosive and degassing events, and landslides (Bohnenstiehl et al., 2014; Caplan-Auerbach et al., 2014; Dziak et al., 2015). The activity was nearly continuous through 2009, with a noticeable increase after the September 29, 2009 great Samoan earthquake, then becoming less intense and more sporadic during 2010 until there was a complete absence of explosions by mid-2011. Effusive activity, which may be too quiet for detection by the moored hydrophones, probably continued a while longer (Dziak et al., 2015), but no new eruptive deposits >10 m were detected between the repeat bathymetric surveys of November 2011 and September 2012

[1] http://www.oceanexplorer.noaa.gov/explorations/06fire/logs/april25/media/nwrota_brimstone6.html

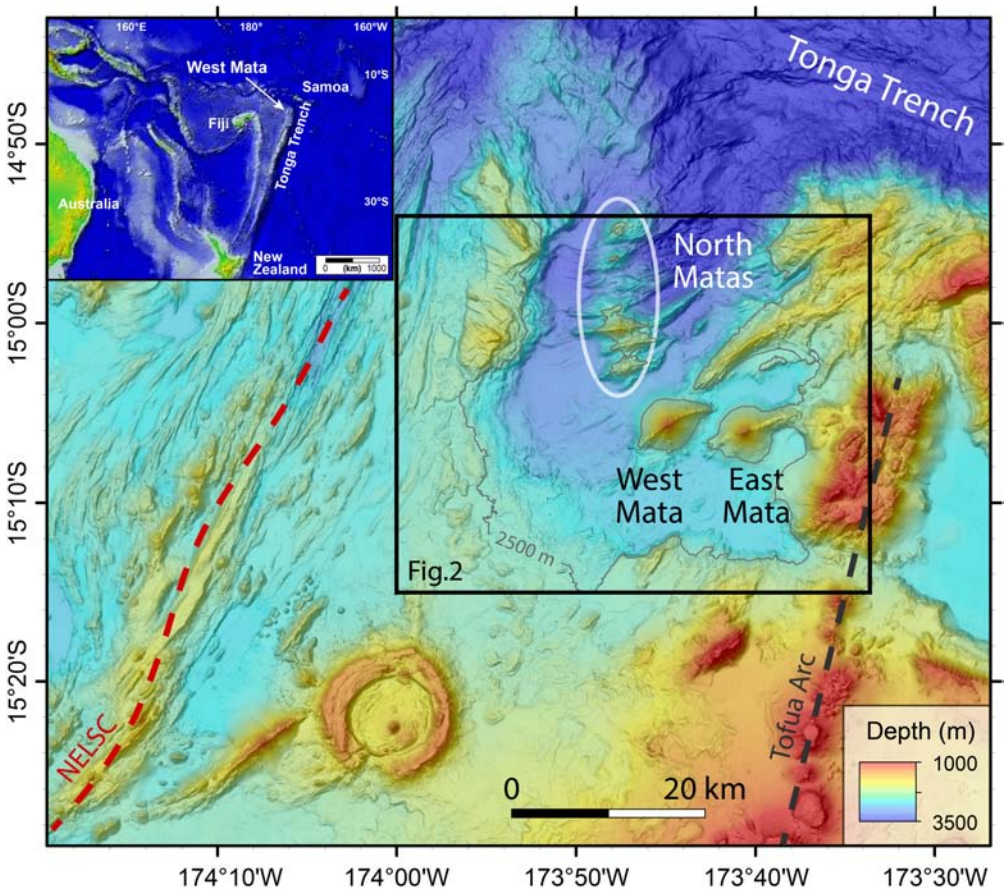

FIGURE 1 | Regional map of the NE Lau basin showing location of West Mata, East Mata and the North Mata volcanoes relative to the Tofua volcanic arc (gray dashed line), NELSC (red dashed line), and Tonga trench (labeled). The black box outlines the area of the map in **Figure 2**. Inset shows location of the region in the Southwest Pacific Ocean. See **Figure 4** for North Mata volcano names. The 2500 m depth contour (solid gray line, shown only within the black box) generally defines the Mata Depression (MD).

(Embley et al., 2014a). Consistent with these data, observations during ROV dives in September 2012 showed the volcano to be quiescent, though hydrothermal venting persisted (Baumberger et al., 2014; Embley et al., 2014a; Baker et al., 2019).

Cycles of constructional deposition and mass wasting at West Mata were demonstrated by Clague et al. (2011) and Embley et al. (2014a) through analyses of repeat bathymetric surveys. The six time periods spanned by seven different multibeam surveys from 1996 to 2012 showed growth, destruction, or both, on the summit, flanks and at the southwest base of West Mata. The volume of new deposits ranged from 3.5×10^5 to 7.6×10^7 m^3, adding a total of 1.5×10^8 m^3 between 1996 and 2012 (Embley et al., 2014a). Pit craters formed at the eruptive vent sites, and a landslide (extending ∼1 km from the summit down to ∼1900 m on the east flank) occurred between December 2010 and November 2011, accounting for most of the measurable losses. This landslide created a gouge as deep as 68 m near the summit. No estimate was made of the total volume removed, but 8.4×10^5 m^3 of this material was re-deposited downslope at depths between ∼1950–2400 m in a layer 10–20 m thick (Embley et al., 2014a).

Additional multibeam bathymetric surveys in March 2016 and November 2017 extend the time series beyond September 2012, and show that West Mata continued to be episodically active (Chadwick et al., 2019). Deposits emplaced during the 2012–2016 interval (total volume = 37.6×10^6 m^3) were located near the summit on the northeast flank, where lava flows partially infilled the previous east landslide area, and at the base of the edifice beyond the northeast rift zone (Chadwick et al., 2019). Of particular relevance to this study is an additional deposit (30–70 m thick) that erupted during the 2016–2017 interval, originating at the south edge of the ENE rift zone at ∼1530 m and extending downslope toward the east to a depth of 2530 m. Chadwick et al. (2019) used high resolution bathymetry and photographs from AUV surveys, and direct observations from ROV dives to describe this new deposit (total volume = 14×10^6 m^3) as a series of overlapping, steep-sided, flat-topped plateaus made up of pillow lavas thickly overlain by coarse tephra near the eruptive vents (∼1530 m water depth), transitioning to a hummocky lobe of pillow lavas thinly dusted with tephra 300–600 m distant from the vents (∼1775–1900 m water depth), below which volcaniclastic deposits having smooth

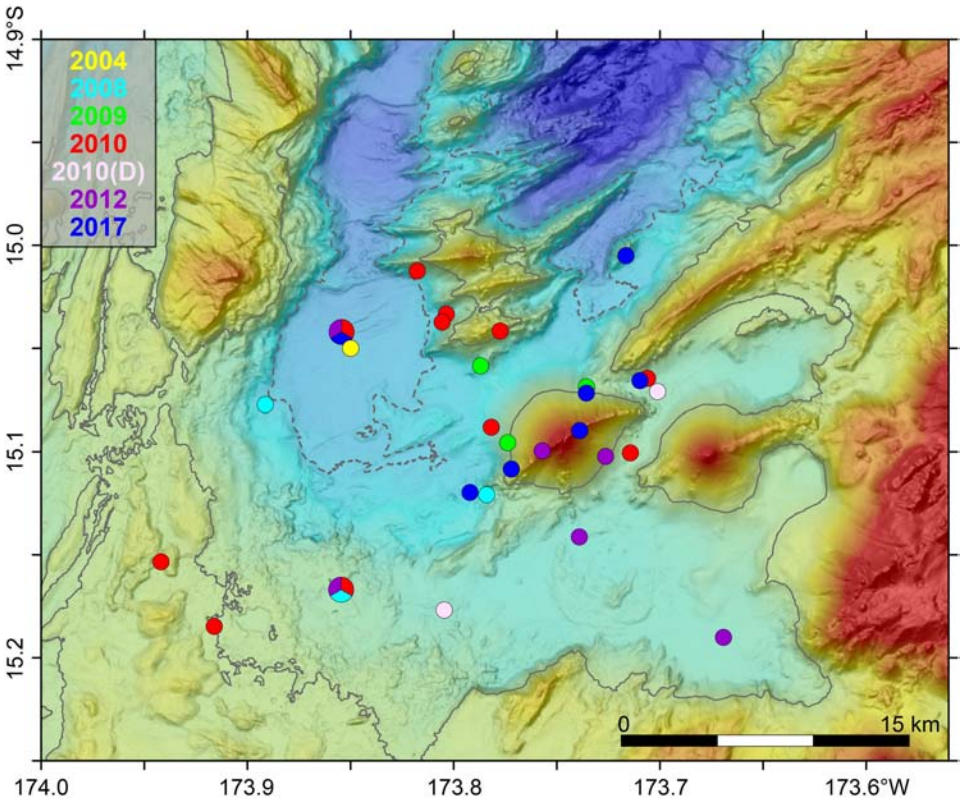

FIGURE 2 | Station locations for all profiles (2004 through 2017) used in this study. Symbol color indicates year. Larger multi-color symbols indicate station locations that were repeated in more than 1 year, with colors indicating which years that location was sampled. Depth contour intervals are: solid gray line = 2500 m, dashed gray line = 3000 m. See **Supplementary Figure S1** for each location labeled with station name, and **Supplementary Table S4** for a list of station locations. For CTD tows, only the initial downcast (↓) or final upcast (↑) was used, as indicated by arrows in labels for **Figure 3** and **Supplementary Figure S1**.

bathymetric texture extend at least 2.2 km downslope (to 2530 m depth). Bacterial mats were present on the tephra overlying the lava flows at shallower depths, and temperatures a few degrees above ambient were measured to ∼10 cm depth within these tephra deposits.

MATERIALS AND METHODS

Plumes surveys were completed using conductivity-temperature-depth (CTD) vertical cast and/or tow-yo operations (Baker et al., 1995; Baker et al., 2016) utilizing a Seabird 9-11*plus* CTD system with integrated sensors for turbidity (measured by optical backscatter) and ORP, along with a rosette of 21 19-L Niskin bottles to collect discrete water samples. Cruises and station locations in 2004, 2008, 2009, 2010, 2012, and 2017 are summarized in **Supplementary Tables S3, S4**, respectively. Miniature Autonomous Plume Recorders (MAPR), which use the same turbidity and ORP sensors as the CTD, were added to the CTD wire to extend the vertical range during tows in 2009, to camera tows and dredges to supplement the CTD data in 2010, and to the AUV *Sentry* and ROV *SuBastian* for high-resolution near-bottom surveys in 2017. **Figure 2** shows the locations of CTD profiles used in this study.

Turbidity anomalies are reported as dimensionless Nephelometric Turbidity Units (American Public Health Association, 1985) above the regional background (ΔNTU). The ORP sensor detects reduced hydrothermal chemical species (e.g., dissolved Fe^{2+}, H_2, sulfides) that oxidize rapidly in dispersing neutrally-buoyant hydrothermal plumes (Walker et al., 2007). ORP signals confirm that a source is (a) hydrothermal, and (b) relatively nearby [i.e., within ∼1–2 km, depending on vent source strength and local current speeds (Baker et al., 2016)]. ORP anomalies are identified by a negative change in potential (E, mV) and are expressed as either the time derivative (dE/dt, mV) that shows a greater change than the ambient drift over time, or as the magnitude of the overall drop in value for any given signal (ΔE, mV). Discrete water samples were selected by monitoring the turbidity and ORP data in real time to obtain plume and non-plume (background) water. Samples were analyzed for helium isotopes (^{3}He and ^{4}He, presented here as δ(^{3}He)%) (see **Supplementary Table S5**) at the NOAA/PMEL Helium Isotope Laboratory (Newport, OR, United States) (Lupton, 1990), bulk particulate elemental composition by x-ray fluorescence spectrometry (XRF) (Feely et al., 1991), and the morphology of individual particles by scanning electron microscopy (SEM) (Resing et al., 2011).

RESULTS

Hydrothermal vs. Non-hydrothermal Plume Sources

The magmatic-hydrothermal plume from the summit of West Mata was widely dispersed throughout the study area, demonstrated here by ΔNTU and δ(^{3}He)% anomalies within the 1000–1270 m depth range (**Figure 3**), to distances of at least 20 km from the summit (**Figure 2** and **Supplementary Figure S1**). Other shallow sites in the region can be eliminated as the source for this widespread plume due to excessive distance (>40 km) from the MD, different source depth than West Mata (i.e., Niua, the northernmost volcano on the Tofua volcanic arc), or having weak anomalies characteristic of low-temperature diffuse venting that would not be expected to extend beyond ∼1–2 km from the source (i.e., East Mata) (Baker et al., 2019). The characteristics of this plume have been described in detail elsewhere (Resing et al., 2011; Baumberger et al., 2014), including observations of how key components changed over time as the eruption evolved.

The distribution of particle plumes in the deep (>1500 m) MD water column were highly variable between 2004 and 2017 (**Figure 3**). The single profile from 2004 indicated that there was at least one unidentified (at that time) deep hydrothermal source in the MD. The North Mata volcanoes were explored systematically in May 2010 by CTD and camera tows (**Figure 4**), which found all but two of the volcanoes in this group were hydrothermally active (Baker et al., 2019). ROV dives in 2012 and 2017 located high temperature vent fields on all of the North Mata volcanoes except Taha (only extinct chimneys found) and Nima (inactive, no ROV explorations) (Embley et al., 2013; Rubin et al., 2018). To date, the North Mata vent sites are the only known hydrothermal sources deeper than 2000 m in the NE Lau basin north of ∼15°30′ S and east of the NELSC (Baker et al., 2019). Due to the close spacing of the edifices, plumes sourced at any one of the North Mata volcanoes may extend to their neighbors, but hydrothermal plumes from the North Mata volcanoes can be distinguished from the widespread turbidity anomalies throughout the surrounding MD because: (1) they cluster into three prominent depth ranges (1740–1910 m for plumes from Tolu; 2045–2350 m for plumes from Ua; and 2350–2620 m for plumes from Fa, Ono, and Fitu); and (2) they have coincident ΔNTU, ORP, and δ(^{3}He)% anomalies that are relatively consistent from year to year (**Figure 4**). Each site is known to have a combination of high-temperature focused venting, diffuse venting, and vent fields at multiple depths (Embley et al., 2013; Rubin et al., 2018), resulting in relatively broad ranges for plume rise heights (20–350 m) (Baker et al., 2019).

The profiles throughout the MD (**Figure 3**) were enriched in δ(^{3}He)% only at the West Mata summit plume depth (1000–1270 m) or within the depth ranges of the North Mata hydrothermal plumes. Turbidity anomalies deeper than 2600 m consistently had background δ(^{3}He)% values in all years despite highly variable ΔNTU, which suggests a non-hydrothermal source of particles creates the deep turbidity layers throughout the MD, overprinting the hydrothermal signal from the North Matas.

The Fe/Si ratio of particles in the deep plumes was distinctly different from that of the hydrothermal particles found in the West Mata summit plume (**Figure 5**). Hydrothermal particles are typically highly enriched in iron. In contrast, the particles from the deep plumes had high amounts of Si with Fe/Si ratios similar to boninite, the primitive andesite lava type that was erupting at West Mata (Resing et al., 2011). SEM analyses of the deep particles showed they were dominated by fine non-vesicular ash shards with sharp-edges and conchoidal fractures (**Figure 6**), establishing a strong similarity to the deep ash plumes found surrounding other actively erupting submarine volcanoes (**Supplementary Table S2**), and thus linking these plumes to the syn-eruptive production of fine ash by the explosive and effusive eruption at West Mata.

Distribution Patterns of Deep Particle Plumes

In addition to their composition, the distribution of the deep (>1500 m) particle plumes described here supports the interpretation that they are clouds of fine ash fed by the explosive eruption and downslope movement of volcaniclastic material accumulating on steep (∼30°) slopes below the summit of West Mata where the observed eruptive vents were located (∼1150–1200 m).

In 2008, the upper limits of the deep turbidity layers (**Figure 3B**) were similar whether located at the base of West Mata (red line) or 15 km distant (blue and green lines) (**Supplementary Figure S1**). Deep ΔNTU increased from background values at 2230 m (∼600 m above the seafloor at the deepest profile) to ΔNTU = 0.040 at 2630 m, and reached a maximum (ΔNTU = 0.050) between 2750 and 2830 m (∼150 m above the seafloor at the deepest profile). The shallower casts (red and green lines) do not show the deepest turbidity maximum because they were limited by the depth of the seafloor. Presumably, if the bathymetry had not been limiting, the plume would have extended to those locations as well. These three casts were located only to the west and southwest of West Mata, so we cannot tell if the plume dispersed equally in all directions, but the near-uniformity of the plume at 5 to 20 km from the slope break at the base of West Mata is consistent with radial dispersal of a sediment gravity flow (Simpson, 1987; Dade and Huppert, 1995; Walker et al., 2008) that originated at West Mata.

In 2010 (**Figure 3D**), the profiles to the northwest (blue lines) and southwest (green lines) again show relatively minor differences in the upper limits of the deep plume, with the downward extent apparently limited by the depth of the seafloor for the shallower casts regardless of distance from West Mata (**Supplementary Figure S1**). However, the profile at the northeast base of West Mata (yellow line) has noticeably lower ΔNTU values compared to the profile at the southwest base (red line; ΔNTU_{max} = 0.007 and 0.020, respectively). This is consistent with the more complex bathymetry to the north and east of West Mata having some directional control on the distribution of an ash cloud

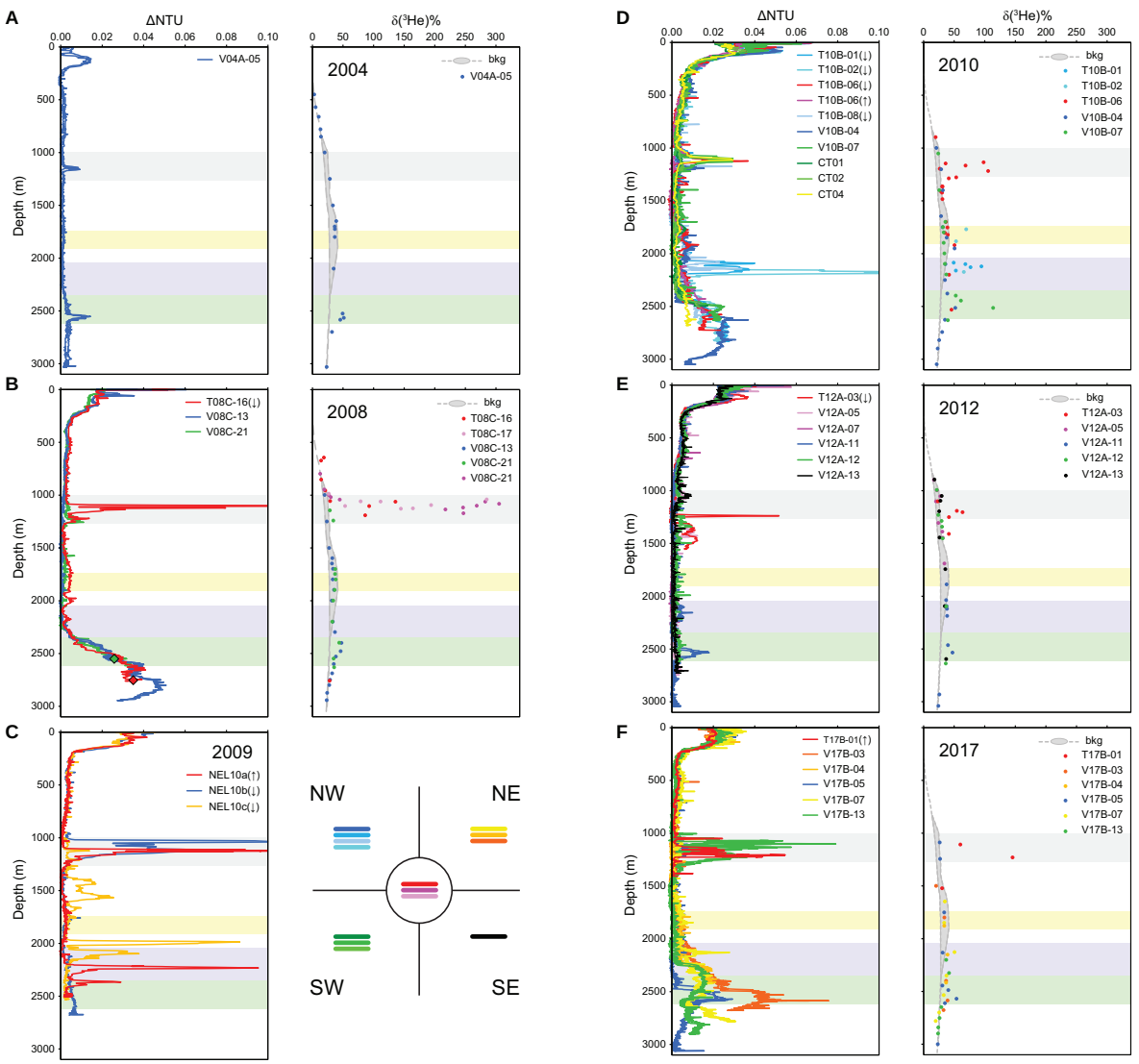

FIGURE 3 | ΔNTU and δ(^{3}He)% profiles for all years. δ(^{3}He)% background (gray) shows the range of values typical of the regional "Samoa plume" of Lupton et al. (2004). Color bands show depth ranges where hydrothermal plumes from the summit of West Mata (gray) and the North Mata volcanoes are found (from **Figure 4**: yellow = Tolu, blue = Ua, and green = Fa/Ono/Fitu). **(A)** ΔNTU and δ(^{3}He)% profiles from 2004; **(B)** ΔNTU and δ(^{3}He)% profiles from 2008, diamond symbols show locations of samples shown in **Figure 6**; **(C)** ΔNTU and δ(^{3}He)% profiles from 2009; **(D)** ΔNTU and δ(^{3}He)% profiles from 2010 (May); **(E)** ΔNTU and δ(^{3}He)% profiles from 2012; **(F)** ΔNTU and δ(^{3}He)% profiles from 2017. No δ(^{3}He)% is available for 2009, so 3c (right side) shows the color scheme used in all years to indicate the relative proximity or direction of each profile from West Mata (red/pinks = closest to West Mata summit, blues = NW quadrant, greens = SW quadrant, black = SE quadrant, yellow/gold/orange = NE quadrant).

from a sediment gravity flow, and is also consistent with ash originating at the north side of the rift zone, west of the summit, where the "PIII Eruptives" deposit was emplaced between May 2009 and May 2010 (see Figure 8 of Embley et al., 2014a).

Profiles from 2009 (**Figure 3C** and **Supplementary Figure S1**) differ from the other years in that two casts (red and gold lines) had multiple, but thinner, turbidity layers between 1400 and 2400 m with highly variable intensity (ranging from ΔNTU_{max} = 0.010 at 1660 m to 0.100 at 2230 m). None of these layers had corresponding ORP signals. We note that these casts were located at the southwest (red) and northeast (gold) base of West Mata, and that the most distant profile (~6 km to the northwest; blue line) showed only a very slight increase in turbidity (ΔNTU_{max} = 0.007) deeper than 2100 m. We know from direct observations during ROV dives (Resing et al., 2011) and moored hydrophones (Resing et al., 2011; Bohnenstiehl et al., 2014) that the eruption at the summit was nearly continuous during this timeframe, so these layers may indicate eruption column collapse, earlier stages of sediment gravity flows or runout and liftoff of multiple events of varying magnitude that had not yet had time to laterally spread very

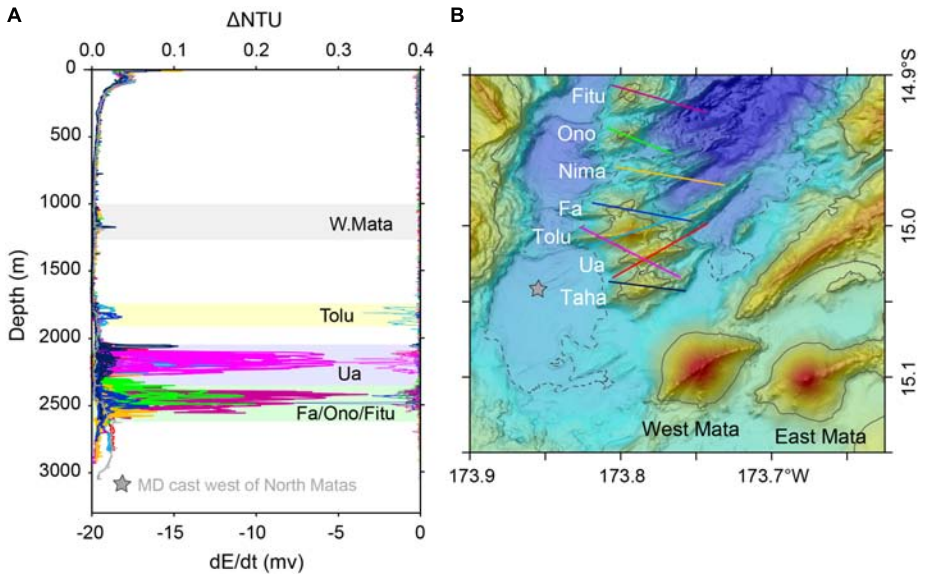

FIGURE 4 | 2010 North Mata hydrothermal plume profiles. **(A)** ΔNTU (left side, top axis) and dE/dt (right side, bottom axis) profiles from CTD tows over the North Mata volcanos; **(B)** map of North Mata CTD tow tracklines. Colors of tracklines in **(B)** correspond to profile line colors in **(A)**.

far beyond the flanks of West Mata. Alternatively, we also know from the repeat bathymetric surveys (Embley et al., 2014a) that ~2 × 10^6 m^3 of new material was added to the southwest rift zone within two depth ranges (1400–1700 and 1900–2100 m) sometime between May 2009 and May 2010 (the "PIII WSWRZ eruptives and downslope deposits" shown in Figure 3C of Embley et al., 2014a). Unfortunately, there were no water samples from these plume layers to evaluate whether any of them had a magmatic-hydrothermal component that might suggest their source was concurrent eruptive activity at those depths. However, the absence of any ORP anomalies strongly suggests these particle plumes were fed by the ongoing eruption at the summit.

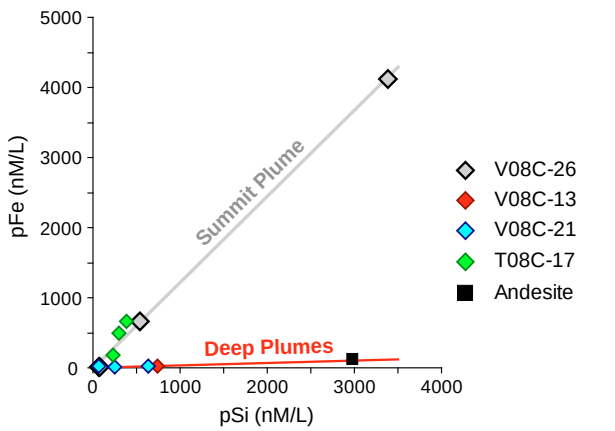

FIGURE 5 | Fe/Si ratio of particulates from deep ash plumes compared to magmatic-hydrothermal plumes from over the summit of West Mata.

Plume mapping in 2017 included CTD vertical casts and tow-yo's, with the addition of a MAPR to AUV *Sentry* missions (November 11-19) and ROV *SuBastian* dives 2–3 weeks later (November 27–December 7). The *Sentry* missions flew 70 m above the seafloor while acquiring high-resolution bathymetry data, and 5 m above the seafloor during more spatially limited photo surveys (**Figure 7**) (Chadwick et al., 2019). Widespread turbidity anomalies surrounded the base of West Mata, primarily to the east and northeast where $\Delta NTU_{max} > 0.050$ (**Figures 3F**, **7** and **Supplementary Movie S1**). Full water depth profiles shared similar characteristics to other years in that (a) ORP anomalies were not coincident with ΔNTU other than for the West Mata summit and North Mata magmatic-hydrothermal plumes, and (b) the upper limit of the deep ΔNTU layer in all profiles increased similarly from 2000 to 2500 m (except for the profile ~14 km to the northwest which showed only slight increases in ΔNTU below the 2550 m North Mata plume). The deep plume surrounding the base of West Mata was asymmetrically distributed to the east and northeast, with limited transport to the northwest, which suggested these plumes were related to the most recent (2016–2017) eruption (Chadwick et al., 2019) that added 1.4 × 10^7 m^3 of effusive lava flows and downslope volcaniclastic deposits on the southeast flank sometime between March 2016 and November 2017, and that the plume distribution was inhibited by the more complex bathymetry to the east of West Mata. Some ORP signals were detected at 70 m above the seafloor directly over the recent (2012–2017) eruption sites but appear to be unrelated to the broader deep ash plume. Hydrothermal staining, warm temperatures within overlying volcaniclastic deposits, and bacterial mats were observed at these locations during ROV SuBastian dives, confirming the lava flows emplaced between 2012 and 2017 were still cooling (Chadwick et al., 2019).

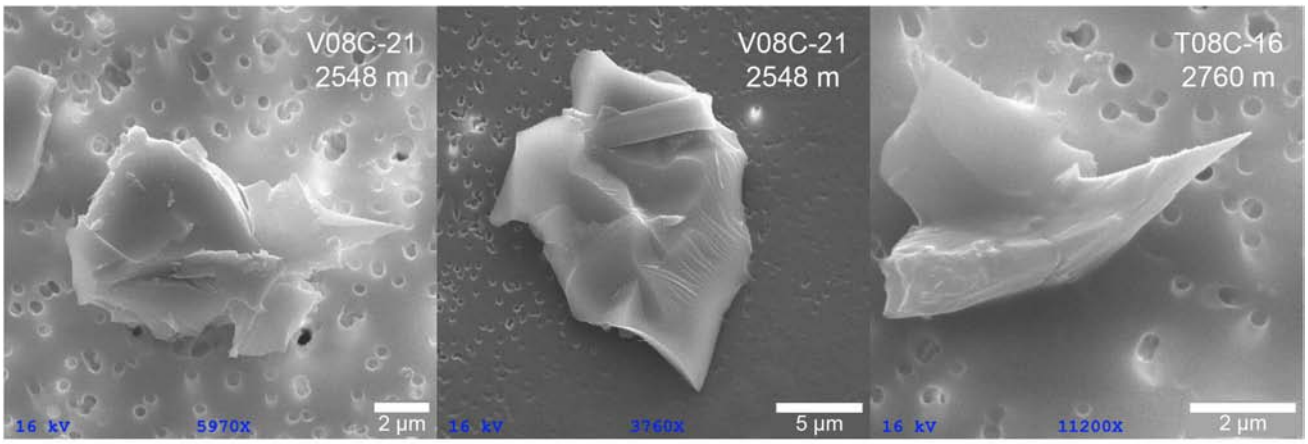

FIGURE 6 | SEM images of shards in deep plumes. Sample depths are shown by diamond symbols in **Figure 3B**.

Short-Term Variability of Deep Plumes

Two of the plume surveys conducted between 2004 and 2012 were separated by as little as 6–7 months and show that the distribution of these deep ash plumes can be significantly different, or completely disappear, over that time interval.

Deep plumes were present in both the November 2008 and May 2009 surveys, but their intensity and depth ranges were dramatically different (**Figure 3**). West Mata was known to be continuously erupting throughout that period (Resing et al., 2011), though no deposits or losses thicker than 10 m were identified by bathymetry differencing.

Two profiles from December 2010 extended deeper than 2500 m for comparison with the May 2010 profiles (**Figure 8A**): V10B-07 (gray) and D11 (red) were both located ∼10–12 km southwest of West Mata (**Supplementary Figure S1**). The December profiles had background turbidity at the West Mata summit plume depth and negligible ΔNTU (<0.004) below 2500 m. Hydroacoustic monitoring showed that explosive activity at West Mata was robust during the May 2010 expedition, but had declined significantly by December 2010 (Dziak et al., 2015).

In 2017, CTD casts, AUV *Sentry* dives, and ROV *SuBastian* dives provided repeat profiles at the northeast base of West Mata separated in time by up to 25 days (**Figure 8B**). The profiles showed turbidity deeper than 2500 m decreased from ΔNTU_{max} >0.050 on November 13 to <0.007 3 weeks later on December 5. Eruptive activity was not directly observed during the ROV dives in 2017 (see Supplementary Figures S1–S5 of Chadwick et al., 2019 for ROV dive tracklines), but the diminishing plume has implications for when the eruption that formed the 2016–2017 deposit occurred, and will be discussed below.

DISCUSSION

The physiochemical characteristics and distribution patterns of the deep ash plumes throughout the MD surrounding West Mata can be compared to similar plumes found surrounding other volcanically active submarine volcanoes (Kavachi, Baker et al., 2002; NW Rota-1, Walker et al., 2008; Monowai, Walker et al., 2010; **Supplementary Table S2**). The MD plumes were also episodic, dominated by fine fresh volcaniclastic ash, devoid of typical hydrothermal tracers, extended laterally to distances of at least 15–20 km, and had particle concentration maximums at multiple depths below the West Mata eruptive vents and above the seafloor. Similar to the other sites, deep ash plumes in the MD were present during known eruptive periods and absent during known quiescent periods, so we interpret them to be volcaniclastic ash produced by the eruption at West Mata with subsequent downslope and lateral transport through the surrounding MD via sediment gravity flows with variable intensity, runout and liftoff dynamics. The variable height of the turbidity maximum above the seafloor can be attributed variable depths where a sediment gravity flow might detach (liftoff) from the slope of West Mata, the variable depth of the seafloor surrounding West Mata (i.e., a neutrally buoyant plume will disperse laterally on an isopycnal surface regardless of seafloor depth), or a dispersal path across bathymetric features that might obstruct the plume at deeper depths. In contrast to NW Rota-1, West Mata is surrounded by more complex bathymetry, especially to the northeast and east, which appears to exert some directional control on the distribution of the deep ash plumes and limits the horizontal distance they can spread in those directions.

The ephemeral nature of these plumes allows us to infer the status of eruptive activity during years when ROV observations or acoustic monitoring were not available. Profiles in years when West Mata was known to be actively erupting (2008, 2009, and 2010) all have significant deep ash plumes, while the profiles in 2012, when West Mata was volcanically quiescent, show only hydrothermal plume layers from chronic venting from the North Matas and the summit of West Mata. The 2004 profile, located 13 km to the northeast of West Mata, is essentially identical to the similarly located 2012 profile (blue lines in **Figures 3A,E**, respectively), and has only small

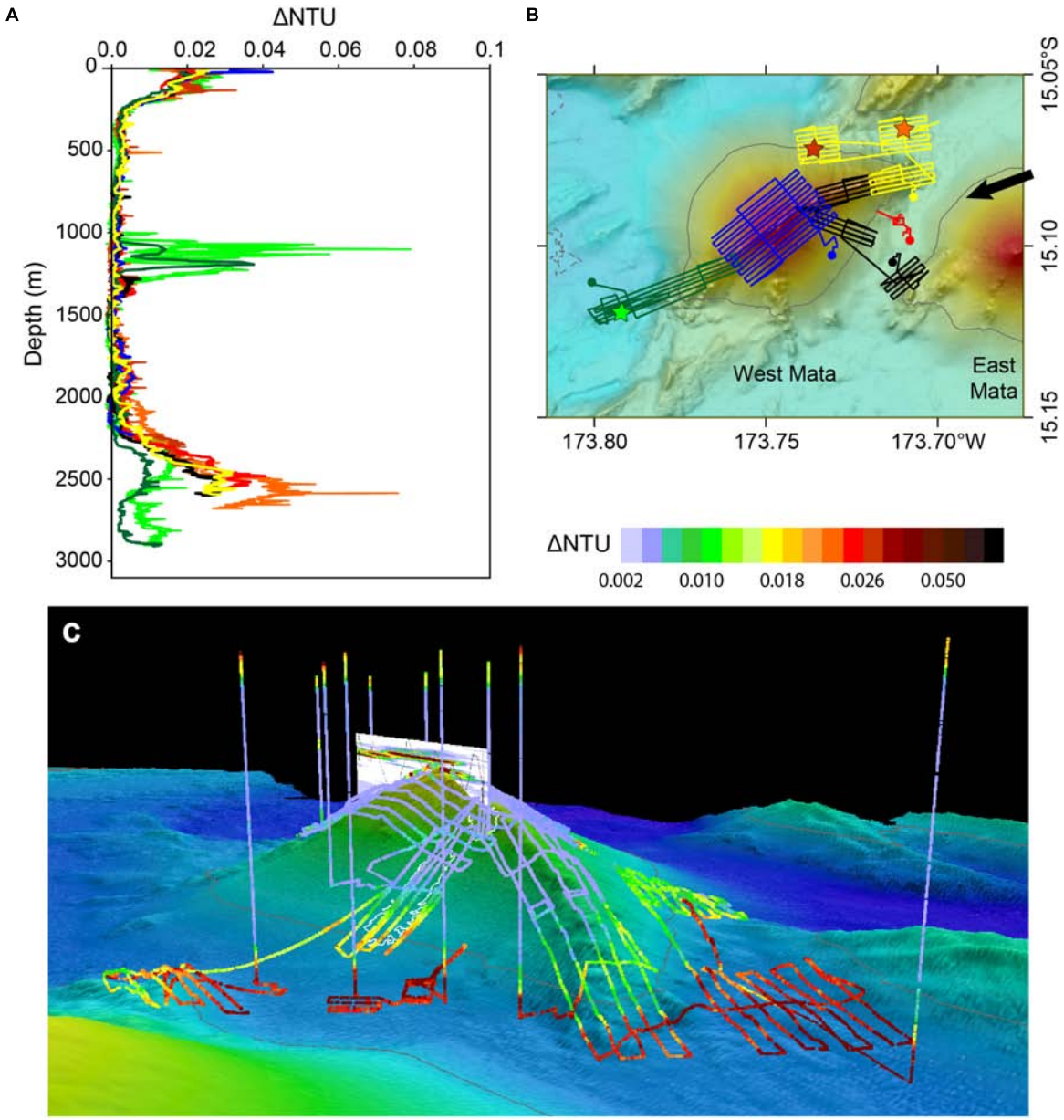

FIGURE 7 | MAPR data from AUV *Sentry* dives. **(A)** MAPR ΔNTU profiles compared to similarly located CTD profiles; **(B)** map with *Sentry* tracklines. Dots show MAPR profile locations (initial descent for each *Sentry* dive), stars show CTD locations. Colors in **(B)** match profile line colors in **(A)**; **(C)** 3-d image of MAPR ΔNTU at 70 m above bottom during *Sentry* dives viewed from the northeast (arrow in **B** shows orientation for this view). The 2016–2017 new deposit is outlined in white on the SE slope of West Mata. Vertical panel above the summit of West Mata shows the plume above the summit (CTD tow T17B-01) dispersing toward the southwest. See also **Supplementary Movie S1** for a virtual tour of the plumes surrounding West Mata.

plume layers at the West Mata summit and North Mata hydrothermal plume depths [elevated $\delta(^3He)\%$ was associated with the North Mata plume; but note the thin West Mata summit plume depth was not sampled in 2004]. The absence of deep ash plume layers suggests that West Mata was hydrothermally active but not erupting within several months prior to February 2004, and the PI eruptives identified by Embley et al. (2014a) were emplaced either sometime after February 2004 or many months before.

The 2017 expedition was interesting in that deep ash plumes were present, but no eruptive activity was observed during ROV dives. We know from bathymetric survey differencing that an eruption occurred sometime between March 2016 and November 2017 that added 14×10^6 m^3 of new material to the southeast side of the ENE rift zone and flank of West Mata (from ∼1530 to 2530 m). During ROV dives, volcaniclastic sand and ash that was generated during the eruption was found draped over the lava flows

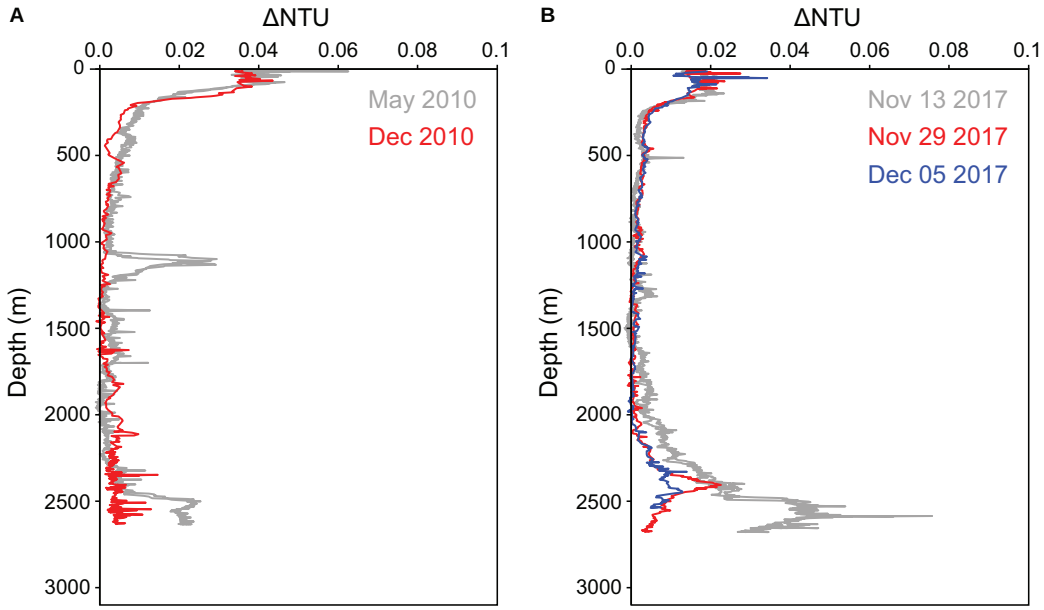

FIGURE 8 | Short-term variability of deep plume turbidity over time: **(A)** May 2010 compared to December 2010; **(B)** repeat profiles over 25 days in November/December 2017.

near the eruptive vents, and the deeper volcaniclastic deposits (up to ∼30 m thick) were consistent with eruptive products moving further down the steep slopes by gravity (Chadwick et al., 2019).

Based on the rate that ΔNTU in the plumes at the northeast base of West Mata decreased over a 25 day period, we can estimate how recently the eruption that formed the 2016–2017 deposit may have occurred. Suspended mass concentration, C_m, is a linear function of ΔNTU ($C_m = a^* \Delta NTU$, where a ranges from 0.3 to 1.2 mg/L, dependent on particle size and composition) (Baker et al., 2001; Dziak et al., 2015). We assume the ash to be very fine aluminosilicates (<5 μm) as was the case for the previous samples from West Mata deep ash plumes, and was not replenished during the sample interval. This results in an estimate of 4.5–18.2 g/m^2 of ash in the water column deeper than 1600 m on November 13, which decreased to 0.9–3.6 g/m^2 on December 05, a total loss of 80%, with an average loss rate of 3% (0.15–0.6 g/m^2) per day to either lateral transport or settling from suspension. This suggests that a plume similar to what was seen on November 13 could last for 8–121 days if not replenished, and implies that the eruption that caused the new lava flow and downslope deposits occurred within weeks to a few months prior to the FK171110 expedition in November 2017. These results also suggest that the presence of deep ash plumes surrounding a submarine volcanic edifice, along with a magmatic-hydrothermal plume above the summit, may be a valuable exploration tool for identifying an active, or very recently active, submarine eruption.

Little is known with certainty about how sediment gravity flows originated at West Mata. Models (e.g., Cashman and Fiske, 1991; Head and Wilson, 2003) acknowledge eruption column collapse or remobilization of accumulated volcaniclasts on unstable slopes as likely mechanisms, and both were observed at NW Rota-1, but it is unclear which may be more important. Both NW Rota-1 and West Mata are mostly conical edifices with steep (>30°) slopes. The hydroacoustic records at each site documented large and small landslides during active periods (Chadwick et al., 2012; Caplan-Auerbach et al., 2014), sometimes occurring as frequently as 35 times per day and lasting from 10s of seconds to minutes (Caplan-Auerbach et al., 2014). A turbidity sensor, moored at 2230 m as part of the December 2009–April 2010 hydrophone deployments ∼5 km south of West Mata, showed spikes in turbidity every week or so that lasted on the order of 1–2 weeks (Caplan-Auerbach et al., 2014; Dziak et al., 2015), consistent with our estimate of the duration of deep plumes. These data show no clear correlation with either explosive activity or landslides, but both were common during the entire period. One particularly intense turbidity maximum appeared ∼2 days after a month-long period of increased explosive activity subsided, leading the authors to favor slope failure of accumulated volcaniclastic debris as the mechanism for mobilizing fine ash into the water column (Dziak et al., 2015). However, shard morphology, including sharp points and non-rounded edges (**Figure 6**), suggests they were generated during explosive eruptions, and were not extensively reworked or subject to substantial particle-particle collisions during transport (Wohletz and Krinsley, 1982; Mattsson, 2010; Jordan et al., 2014). ΔNTU maximums and coherent plume layers at variable distances above the seafloor suggest detachment from deepening slopes (liftoff) and lateral dispersal on isopycnal surfaces rather than elutriation from the dilute outer regions of a ground-hugging density flow.

The profiles from 2008 to 2010 (**Figures 3B,D**) suggest turbidity was relatively uniform throughout the MD at the time of those surveys. We estimate the ash load in the water column

(>2230 m in 2008 and >2450 m in 2010) to be 6–24 g/m^2 on that day in 2008 and 3–13 g/m^2 in 2010, for a total of ∼1–6 × 10^6 kg over an area of ∼250 × 10^6 m^2, or a daily supply of 500–4000 m^3 of ash available for deposition in the MD or transport to more distal locations [based on wet density of ∼1.5 g/cm^3 for vitrious sediments from the NE Lau basin (Lavoie et al., 1994)]. This supply of ash may not be sufficient to form a discrete ash layer in sediments, which are commonly interpreted as tephrochronologic markers of specific eruptions, but these data demonstrate a process whereby ash from low to moderately sized (7.8 × 10^6 m^3/yr; Chadwick et al., 2019) multi-year eruptions at West Mata can be regularly replenished in the water column, and transported by local currents for deposition as thin or possibly invisible fallout deposits in regional and distal sediments. This process is consistent with the interpretation of Scudder et al. (2014) that eruption frequency rather than size is a more important contributor to the cryptotephra record in sediment cores near the Izu arc.

CONCLUSION

Deep ash plume layers in the water column surrounding West Mata demonstrate a mode of syn-eruptive transport for fine ash generated by a submarine explosive eruption that can contribute to fallout deposits at distances greater than have previously been predicted. The temporal and spatial distribution of fine ash in coherent layers along isopycnal surfaces deeper than the eruptive vents suggests emplacement into the water column via sediment gravity flows of varying magnitudes, runout distances, and liftoff densities. After further dispersal by local currents, the ash will contribute to regional and distal sediments via settling of individual particles, which may appear as cryptotephra, or thin ash layers if the ash supply exceeds pelagic sedimentation rates.

To date, only two active eruptions deeper than 500 m water depth have been directly observed in the world's oceans: NW Rota-1 in the Mariana arc (Embley et al., 2006; Chadwick et al., 2008; Deardorff et al., 2011), and West Mata in the NE Lau basin (Resing et al., 2011). Both of these sites erupted explosively with relatively low eruption rates (0.4–8.8 × 10^5 m^3/yr at NW Rota-1 and 7.8 × 10^6 m^3/yr at West Mata) of multi-year duration (Chadwick et al., 2008; Clague et al., 2011; Embley et al., 2014a; Schnur et al., 2017; Chadwick et al., 2019) that transferred a significant amount of ash into suspension in the surrounding water column, often at 100s of meters above the seafloor, where it was transported laterally 10s of km from the volcanic edifices. While these eruptions contributed to the construction of deposits on the steep slopes and occasional slope failure, the presence of deep ash plumes was correlated strongly with the ongoing low to moderately sized eruptions, which suggests that large landslides are not a prerequisite for generating these plume layers.

These observations demonstrate the significance of submarine volcanism to fallout or cryptotephra deposits at regional, and perhaps more distal (where bathymetric barriers are absent) scales, and show that fallout and cryptotephra deposits from submarine eruptions do not require ash to be lofted high into the water column by event plumes rising buoyantly above an eruptive vent, or large-scale landslides and mass wasting, to be transported laterally to more distal sediments. The NE Lau basin has diverse lava types along the volcanic arc, in the back arc, and along the back arc spreading centers (Lupton et al., 2015; Embley and Rubin, 2018). Improved geochemical techniques for separating and characterizing cryptotephra preserved in the sediment record would likely provide valuable insight into the evolution and volcanic history of the region, including the contribution from the large number of submarine volcanoes located here.

Future studies that seek to more thoroughly understand deep submarine eruption processes, the potential hazards they pose, and their impacts to the ocean environment, hydrothermal systems, and chemosynthetic ecosystems, will depend on improved exploration and event detection capabilities. In addition to recognizing the characteristic event plumes rising into the water column above actively erupting sites, widespread ash plumes dispersing at depths deeper than eruptive vents can be diagnostic of ongoing, or very recent, eruptions.

DATA AVAILABILITY STATEMENT

Data is available in the **Supplementary Material** [δ(^{3}He)% (**Supplementary Table S5**)], from the Rolling Deck Repository (R2R), and upon request from the author (see **Supplementary Table S3**).

AUTHOR CONTRIBUTIONS

SW and EB collected the data at sea. SW processed and analyzed the CTD and MAPR data, wrote the manuscript, and made the figures and tables. JL provided the helium data. JR provided the bulk particulate chemistry data and SEM photos.

FUNDING

This work was supported by the NOAA/PMEL Earth-Ocean Interactions Program, the Joint Institute for the Study of the Atmosphere and Ocean (JISAO) under NOAA Cooperative Agreements NA11OAR4320091 and NA10OAR4320148, the NOAA Office of Exploration and Research, the National Science Foundation (OCE0930025, OCE0934660, and OCE15-38121), and the Schmidt Ocean Institute (FK171110).

ACKNOWLEDGMENTS

We thank the numerous colleagues, AUV *Sentry* and ROV teams, and ship mates and crewmembers who worked with us as we explored the NE Lau Basin; the chief scientists (R. Embley, W. Chadwick, J. Lupton, J. Resing, and K. Rubin) all assured the field work was a success. We also thank T. Baumberger and C. Wilkinson for helium sample analyses, S. Merle for providing bathymetry grids

and maps used in the figures, and N. Buck for particulate sample collection and analyses. We also thank Nautilus Minerals, Inc. for providing access to the proprietary data; and the two reviewers who provided valuable comments to improve the manuscript. PMEL contribution number 4950.

SUPPLEMENTARY MATERIAL

The Supplementary Material for this article can be found online at: https://www.frontiersin.org/articles/10.3389/fmars.2019.00593/full#supplementary-material

REFERENCES

Allen, S. R., and McPhie, J. (2009). Products of neptunian eruptions. *Geology* 37, 639–642. doi: 10.1130/g30007a.1

American Public Health Association. (1985). *Standard Methods for the Examination of Water and Wastewater*, 16th Edn (Washington, D.C: American Public Health Association), 1268.

Austin, W., Abbott, P., Davies, S., Pearce, N., and Wastegård, S. (2014). Marine tephrochronology: an introduction to tracing time in the ocean. *Geol. Soc. Lond. Spec. Publ.* 398, 1–5. doi: 10.1144/sp398.12

Baker, E. T. (1995). "Characteristics of hydrothermal discharge following a magmatic intrusion," in *Hydrothermal Vents and Processes*, eds L. M. Parson, C. L. Walker, and D. R. Dixon (Piccadilly: Geological Society London, Special Publication), 65–76. doi: 10.1144/gsl.sp.1995.087.01.06

Baker, E. T. (1998). Patterns of event and chronic hydrothermal venting following a magmatic intrusion: new perspectives from the 1996 gorda ridge eruption. *Deep Sea Res. Pt. II* 45, 2599–2618. doi: 10.1016/s0967-0645(98)00085-x

Baker, E. T., Chadwick, W. W. Jr., Cowen, J. P., Dziak, R. P., Rubin, K. H., and Fornari, D. J. (2012). Hydrothermal discharge during submarine eruptions: the importance of detection, response, and new technology. *Oceanography* 25, 128–141. doi: 10.5670/oceanog.2012.11

Baker, E. T., German, C. R., and Elderfield, H. (1995). "Hydrothermal plumes over spreading-center axes: global distributions and geological inferences," in *Seafloor Hydrothermal Systems: Physical, Chemical, Biological, and Geological Interactions, Geophys. Monogr. Ser*, Vol. 91, eds S. Humphris, R. Zierenberg, L. S. Mullineaux, and R. Thomson (Washington, D. C: American Geophysical Union), 47–71. doi: 10.1029/gm091p0047

Baker, E. T., Lupton, J. E., Resing, J. A., Baumberger, T., Lilley, M. D., Walker, S. L., et al. (2011). Unique event plumes from a 2008 eruption on the northeast lau spreading center. *Geochem. Geophys. Geosyst.* 12, Q0AF02. doi: 10.1029/2011GC003725

Baker, E. T., Massoth, G. J., de Ronde, C. E. J., Lupton, J. E., and McInnes, B. I. A. (2002). Observations and sampling of an ongoing subsurface eruption of Kavachi volcano, Solomon Islands, may 2000. *Geology* 30, 975–978.

Baker, E. T., Resing, J. A., Haymon, R. M., Tunnicliffe, V., Lavelle, J. W., Martinez, F., et al. (2016). How many vent fields? New estimates of vent field populations on ocean ridges from precise mapping of hydrothermal discharge locations. *Earth Planet. Sci. Lett.* 449, 186–196. doi: 10.1016/j.epsl.2016.05.031

Baker, E. T., Tennant, D. A., Feely, R. A., Lebon, G. T., and Walker, S. L. (2001). Field and laboratory studies on the effect of particle size and composition on optical backscattering measurements in hydrothermal plumes. *Deep Sea Res. Pt. I* 48, 593–604. doi: 10.1016/S0967-0637(00)00011-X

Baker, E. T., Walker, S. L., Massoth, G. J., and Resing, J. A. (2019). The NE Lau basin: widespread and abundant hydrothermal venting in the back-arc region behind a superfast subduction zone. *Front. Mar. Sci.* 6:382. doi: 10.3389/fmars.2019.00382

Barreyre, T., Soule, S. A., and Sohn, R. A. (2011). Dispersal of volcaniclasts during deep-sea eruptions: settling velocities and entrainment in buoyant seawater plumes. *J. Volcanol. Geoth. Res.* 205, 84–93. doi: 10.1016/j.jvolgeores.2011.05.006

Baumberger, T., Lilley, M. D., Resing, J. A., Lupton, J. E., Baker, E. T., Butterfield, D. A., et al. (2014). Understanding a submarine eruption through time series hydrothermal plume sampling of dissolved and particulate constituents: west mata, 2008-2012. *Geochem. Geophys. Geosyst.* 15, 4631–4650. doi: 10.1002/2014gc005460

Blockley, S. P. E., Pyne-O'Donnell, S. D. F., Lowe, J. J., Matthews, I. P., Stone, A., Pollard, A. M., et al. (2005). A new and less destructive laboratory procedure for the physical separation of distal glass tephra shards from sediments. *Quat. Sci. Rev.* 24, 1952–1960. doi: 10.1016/j.quascirev.2004.12.008

Bohnenstiehl, D. R., Dziak, R. P., Matsumoto, H., and Conder, J. (2014). Acoustic response of submarine volcanoes in the tofua arc and northern lau basin to two great earthquakes. *Geophys. J. Int.* 196, 1657–1675. doi: 10.1093/gji/ggt472

Butterfield, D. A., Nakamura, K., Takano, B., Lilley, M. D., Lupton, J. E., Resing, J. A., et al. (2011). High SO2 flux, sulfur accumulation, and gas fractionation at an erupting submarine volcano. *Geology* 39, 803–806. doi: 10.1130/g31901.1

Caplan-Auerbach, J., Dziak, R. P., Bohnenstiehl, D. R., Chadwick, W. W., and Lau, T.-K. (2014). Hydroacoustic investigation of submarine landslides at west mata volcano, lau basin. *Geophys. Res. Lett.* 41, 5927–5934. doi: 10.1002/2014gl060964

Cas, R. A. F., and Giordano, G. (2014). Submarine volcanism: a review of the constraints, processes and products, and relevance to the Cabo de Gata volcanic succession. *Ital. J. Geosci.* 133, 362–377. doi: 10.3301/ijg.2014.46

Cas, R. A. F., and Simmons, J. M. (2018). Why deep-water eruptions are So different from subaerial eruptions. *Front. Earth Sci.* 6:198. doi: 10.3389/feart.2018.00198

Cashman, K. V., and Fiske, R. S. (1991). Fallout of pyroclastic debris from submarine volcanic eruptions. *Science* 253, 275–280. doi: 10.1126/science.253.5017.275

Cassidy, M., Watt, S. F. L., Palmer, M. R., Trofimovs, J., Symons, W. O., Maclachlan, S. E., et al. (2014). Construction of volcanic records from marine sediment cores: a review and case study (Monserrat, West Indies). *Earth Sci. Rev.* 138, 137–155. doi: 10.1016/j.earscirev.2014.08.008

Chadwick, W. W. Jr., Cashman, K. V., Embley, R. W., Matsumoto, H., Dziak, R. P., de Ronde, C. E. J., et al. (2008). Direct video and hydrophone observations of submarine explosive eruptions at NW Rota-1 volcano, mariana arc. *J. Geophys. Res.* 113:B08S10. doi: 10.1029/2007JB005215

Chadwick, W. W. Jr., Dziak, R. P., Haxel, J. H., Embley, R. W., and Matsumoto, H. (2012). Submarine landslide triggered by volcanic eruption recorded by in situ hydrophone. *Geology* 40, 51–54. doi: 10.1130/G32495.1

Chadwick, W. W. Jr., Embley, R. W., Johnson, P. D., Merle, S. G., Ristau, S., and Bobbitt, A. (2005). The submarine flanks of anatahan volcano, commonwealth of the northern mariana islands. *J. Volcanol. Geoth. Res.* 146, 8–25. doi: 10.1016/j.jvolgeores.2004.11.032

Chadwick, W. W. Jr., Merle, S. G., Buck, N. J., Lavelle, J. W., Resing, J. A., and Ferrini, V. (2014). Imaging of CO2 bubble plumes above an erupting submarine volcano, NW Rota-1, mariana arc. *Geochem. Geophys. Geosyst.* 15, 4325–4342. doi: 10.1002/2014GC005543

Chadwick, W. W. Jr., Rubin, K. H., Merle, S. G., Bobbitt, A. M., Kwasnitschka, T., and Embley, R. W. (2019). Recent eruptions between 2012 and 2018 discovered at West Mata submarine volcano (NE Lau basin, SW Pacific) and characterized by new ship, AUV, and ROV data. *Front. Mar. Sci.* 6:495. doi: 10.3389/fmars.2019.00495

Clague, D. A., Paduan, J. B., Caress, D. W., Thomas, H., Chadwick, W. W. Jr., and Merle, S. G. (2011). Volcanic morphology of west mata volcano, NE lau basin, based on high-resolution bathymetry and depth changes. *Geochem. Geophys. Geosyst.* 12:QOAF03. doi: 10.1029/2011GC003791

Clague, D. A., Paduan, J. B., and Davis, A. S. (2009). Widespread strombolian eruptions of mid-ocean ridge basalt. *J. Volcanol. Geoth. Res.* 180, 171–188. doi: 10.1016/j.jvolgeores.2008.08.007

Clift, P. D., and Lee, J. (1998). Temporal evolution of the mariana arc during rifting of the mariana trough traced through the volcaniclastic record. *I. Arc* 7, 496–512. doi: 10.1046/j.1440-1738.1998.00206.x

Crisp, J. A. (1984). Rates of magma emplacement and volcanic output. *J. Volcanol. Geoth. Res.* 20, 177–211. doi: 10.1016/0377-0273(84)90039-8

Dade, W. B., and Huppert, H. E. (1995). Runout and fine-sediment deposits of axisymmetric turbidity currents. *J. Geophys. Res.* 100, 18597–18609.

Deardorff, N. D., Cashman, K. V., and Chadwick, W. W. Jr. (2011). Observations of eruptive plume dynamics and pyroclastic deposits from submarine explosive

eruptions at NW Rota-1, mariana arc. *J. Volcanol. Geoth. Res.* 202, 47–59. doi: 10.1016/j.jvolgeores.2011.01.003

Dziak, R. P., Baker, E. T., Shaw, A. M., Bohnenstiehl, D. R., Chadwick, W. W. Jr., Haxel, J. H., et al. (2012). Flux measurements of explosive degassing using a year-long hydroacoustic record at an erupting submarine volcano. *Geochem. Geophys. Geosyst.* 13, Q0AF07. doi: 10.1029/2012GC004211

Dziak, R. P., Bohnenstiehl, D. R., Baker, E. T., Matsumoto, H., Caplan-Auerbach, J., Embley, R. W., et al. (2015). Long-term explosive degassing and debris flow activity at west mata submarine volcano. *Geophys. Res. Lett.* 42, 1480–1487. doi: 10.1002/2014GL062603

Embley, R. W., Chadwick, W. W. Jr., Baker, E. T., Butterfield, D. A., Resing, J. A., de Ronde, C. E. J., et al. (2006). Long-term eruptive activity at a submarine arc volcano. *Nature* 441, 494–497. doi: 10.1038/nature04762

Embley, R. W., Merle, S. G., Baker, E. T., Rubin, K. H., Lupton, J. E., Resing, J. A., et al. (2014a). Eruptive modes and hiatus of volcanism at west mata seamount:, NE lau basin: 1996–2012. *Geochem. Geophys. Geosyst.* 15, 4093–4115. doi: 10.1002/2014GC005387

Embley, R. W., Tamura, Y., Merle, S. G., Sato, T., Oshizuka, O., Chadwick, W. W. Jr., et al. (2014b). Eruption of south sarigan seamount, northern mariana islands: insights into hazards from submarine volcanic eruptions. *Oceanography* 27, 24–31. doi: 10.5670/oceanog.2014.37

Embley, R. W., Merle, S. G., Lupton, J. E., Resing, J. A., Baker, E. T., Lilley, M. D., et al. (2009). "Extensive and diverse submarine volcanism and hydrothermal activity in the NE lau basin," in *Proceedings of the American Geophysical Union, Fall Meeting 2009* (Washington, DC).

Embley, R. W., Resing, J. A., Tebo, B., Baker, E. T., Butterfield, D. A., Chadwick, W., et al. (2013). "Hyperactive hydrothermal activity in the NE Lau basin revealed by ROV dives," in *Proceedings of the Abstract V21C-2738 Presented at 2013 Fall Meeting* (San Francisco: American Geophysical Union).

Embley, R. W., and Rubin, K. (2018). Extensive young silicic volcanism produces large deep submarine lava flows in the NE lau basin. *Bull. Volcanol.* 80:36.

Feely, R. A., Massoth, G. J., and Lebon, G. T. (1991). Sampling of marine particulate matter and analysis by x-ray fluorescence spectrometry. *Mar. Part.* 63, 251–257. doi: 10.1029/gm063p0251

Fisher, R. V. (1983). Flow transformations in sediment gravity flows. *Geology* 11, 273–274.

Gill, J. B., Bongiolo, E. M., Miyazaki, T., Hamelin, C., Jutzeler, M., DeBari, M. S., et al. (2018). Tuffaceous mud is a volumetrically important volcaniclastic facies of submarine arc volcanism and record of climate change. *Geochem. Geophys. Geosyst.* 19, 1217–1243. doi: 10.1002/2017gc007300

Hawkins, J., Parson, L., and Allan, J. (1994). "Introduction to the scientific results of leg 135: lau basin–tonga ridge drilling transect," in *Proceedings of the Ocean Drilling Program, Scientific Results* (College Station, TX: Ocean Drilling Program), 3–5.

Head, J. W. III, and Wilson, L. (2003). Deep submarine pyroclastic eruptions: theory and predicted landforms and deposits. *J. Volcanol. Geoth. Res.* 121, 155–193. doi: 10.1016/s0377-0273(02)00425-0

Jordan, S. C., Dürig, T., Cas, R. A. F., and Zimanowski, B. (2014). Processes controlling the shape of ash particles: results of statistical IPA. *J. Volcanol. Geoth. Res.* 288, 19–27. doi: 10.1016/j.jvolgeores.2014.09.012

Kim, J., Son, S.-K., Son, J.-W., Kim, K.-H., Shim, W. J., Kim, C. H., et al. (2009). Venting sites along the fonualei and northeast lau spreading centers and evidence of hydrothermal activity at an off-axis caldera in the northeastern lau basin. *Geochem. J.* 43, 1–13. doi: 10.2343/geochemj.0.0164

Kohn, B. P., and Glasby, G. P. (1978). Tephra distribution and sedimentation rates in the bay of plenty, New Zealand. *N. Z. J. Geol. Geophys.* 21, 49–70. doi: 10.1080/00288306.1978.10420721

Lavoie, D. L., Bruns, T. R., and Fischer, K. M. (1994). "Geotechnical and logging evidence for underconsolidation of lau basin sediments: rapid sedimentation vs. fluid flow," in *Proceedings of the Ocean Drilling Program, Scientific Results* (College Station, TX: Ocean Drilling Program), 787–795.

Lowe, D. J. (2011). Tephrochronology and its application: a review. *Quat. Geochronol.* 6, 107–153. doi: 10.1016/j.quageo.2010.08.003

Lowe, D. J. (2014). "Marine tephrochronology: a personal perspective," in *Marine Tephrochronology*, eds W. E. N. Austin, P. M. Abbott, S. M. Davies, N. J. G. Pearce, and S. Wastegård (Piccadilly: Geological Society Special Publications), 7–19. doi: 10.1144/sp398.11

Lupton, J., Rubin, K. H., Arculus, R., Lilley, M. D., Butterfield, D. A., Resing, J. A., et al. (2015). Helium isotope, C/3He, and Ba-Nb-Ti signatures in the northern lau basin: distinguishing arc, back-arc, and hotspot affinities. *Geochem. Geophys. Geosyst.* 16, 1133–1155. doi: 10.1002/2014GC005625

Lupton, J. E. (1990). Water column hydrothermal plumes on the Juan de Fuca ridge. *J. Geophys. Res.* 95, 12829–12842. doi: 10.1029/JB095iB08p12829

Lupton, J. E., Pyle, D. G., Jenkins, W. J., Greene, R., and Evans, L. (2004). Evidence for an extensive hydrothermal plume in the Tonga-Fiji region of the south pacific. *Geochem. Geophys. Geosyst.* 5:Q01003.

Manville, V., and Wilson, C. J. N. (2004). Vertical density currents: a review of their potential role in the deposition and interpretation of deep-sea ash layers. *J. Geol. Soc. Lond.* 161, 947–958. doi: 10.1144/0016-764903-067

Mattsson, H. B. (2010). Textural variation in juvenile pyroclasts from an emergent, Surtseyan-type, volcanic eruption: the Capelas tuff cone, São Miguel (Azores). *J. Volcanol. Geoth. Res.* 189, 81–91. doi: 10.1016/j.jvolgeores.2009.10.007

McCanta, M. C., Hatfield, R. G., Thomson, B. J., Hook, S. J., and Fisher, E. (2015). Identifying cryptotephra units using correlated rapid, nondestructive methods: VSWIR spectroscopy, X-ray fluorescence, and magnetic susceptibility. *Geochem. Geophys. Geosyst.* 16, 4029–4056. doi: 10.1002/2015gc005913

Middleton, G. V., and Hampton, M. A. (1976). "Subaqueous sediment transport and deposition by sediment gravity flows," in *Marine Sediment Transport and Environmental Management*, eds D. J. Stanley, and D. J. P. Swift (New York, NY: Wiley), 197–218.

Mulder, T., and Alexander, J. (2001). The physical character of subaqueous sedimentary density flows and their deposits. *Sedimentology* 48, 269–299. doi: 10.1046/j.1365-3091.2001.00360.x

Németh, K., Pécskay, Z., Martin, U., Gméling, K., Molnár, F., and Cronin, S. J. (2008). Hyaloclastites, peperites and soft-sediment deformation textures of a shallow subaqueous miocene rhyolitit dome-cryptodome complex, Pálháza,Hungary. *Geol. Soc. Lond. Spec. Publ.* 302, 63–86. doi: 10.1144/sp302.5

Pillans, B., and Wright, I. (1992). Late quaternary tephrostratigraphy from the southern havre trough - bay of plenty, northeast New Zealand. *N. Z. J. Geol. Geophys.* 35, 129–143. doi: 10.1080/00288306.1992.9514507

Pope, E. L., Jutzeler, M., Cartigny, M. J. B., Shreeve, J., Talling, P. J., Wright, I. C., et al. (2018). Origin of spectacular fields of submarine sediment waves around volcanic islands. *Earth Planet. Sci. Lett.* 493, 12–23.

Resing, J. A., Lebon, G., Baker, E. T., Lupton, J. E., Embley, R. W., Massoth, G. J., et al. (2007). Venting of acid-sulfate fluids in a high-sulfidation setting at NW Rota-1 submarine volcano on the mariana arc. *Econ. Geol.* 102, 1047–1061. doi: 10.2113/gsecongeo.102.6.1047

Resing, J. A., Rubin, K. H., Embley, R. W., Lupton, J. E., Baker, E. T., Dziak, R. P., et al. (2011). Active submarine eruption of boninite in the northeastern lau basin. *Nat. Geosci.* 4, 799–806. doi: 10.1038/ngeo1275

Rubin, K. H., Chadwick, W. W. Jr., Embley, R. W., Merle, S. G., Shank, T. M., Cho, W., et al. (2018). "Exploration of the mata submarine volcano group reveals volcano-tectonic-hydrothermal links," in *Proccedings of the Abstract V14A-08 presented at 2018 Fall Meeting* (Washington, DC: AGU), 10–14.

Rubin, K. H., Soule, S. A., Chadwick, W. W. Jr., Fornari, D. J., Clague, D. A., Embley, R. W., et al. (2012). Volcanic eruptions in the deep sea. *Oceanography* 25, 142–157.

Sansone, F. J., and Resing, J. A. (1995). Hydrography and geochemistry of sea-surface hydrothermal plumes resulting from Hawaiian coastal volcanism. *J. Geophys. Res.* 100, 13555–13569.

Schindlbeck, J. C., Kutterolf, S., Freundt, A., Scudder, R. P., Pickering, K. T., and Murray, R. W. (2013). Emplacement processes of submarine volcaniclastic deposits (IODP Site C0011, Nankai Trough). *Mar. Geol.* 343, 115–124. doi: 10.1016/j.margeo.2013.06.017

Schnur, S. R., Chadwick, W. W. Jr., Embley, R. W., Ferrini, V. L., de Ronde, C. E. J., Cashman, K. V., et al. (2017). A decade of volcanic construction and destruction at the summit of NW Rota-1 seamount: 2004 2014. *J. Geophys. Res.* 122, 1558–1584.

Scudder, R. P., Murray, R. W., and Plank, T. (2009). Dispersed ash in deeply buried sediment from the northwest Pacific Ocean: an example from the Izu–Bonin arc (ODP Site 1149). *Earth Planet. Sci. Lett.* 284, 639–648. doi: 10.1016/j.epsl.2009.05.037

Scudder, R. P., Murray, R. W., Schindlbeck, J. C., Kutterolf, S., Hauff, F., and McKinley, C. C. (2014). Regional-scale input of dispersed and discrete volcanic ash to the Izu-Bonin and mariana subduction zones. *Geochem. Geophys. Geosyst.* 15, 4369–4379. doi: 10.1002/2014gc005561

Shane, P., Sikes, E. L., and Guilderson, T. P. (2006). Tephra beds in deep-sea cores off northern New Zealand: implications for the history of Taupo Volcanic Zone, Mayor Island and White Island volcanoes. *J. Volcanol. Geoth. Res.* 154, 276–290. doi: 10.1016/j.jvolgeores.2006.03.021

Sigurdsson, H., Sparks, R. S. J., Carey, S. N., and Huang, T. C. (1980). Volcanogenic sedimentation in the lesser antilles arc. *J. Geol.* 88, 523–540. doi: 10.1086/628542

Simpson, J. E. (1987). *Gravity Currents in the Environment and the Laboratory*. Chichester: Ellis Horwood.

Sohn, R. A., Willis, C., Humphris, S., Shank, T. M., Singh, H., Edmonds, H. N., et al. (2008). Explosive volcanism on the ultraslow-spreading gakkel ridge, arctic ocean. *Nature* 453, 1236–1238. doi: 10.1038/nature07075

Tamura, Y., Busby, C. J., Blum, P., Guèrin, G., Andrews, G. D. M., Barker, A. K., et al. (2015). "Site U1437," in *Proceedings of the International Ocean Discovery Program, Expedition 350: Izu-Bonin-Mariana Rear Arc* (College Station, TX: International Ocean Discovery Program), doi: 10.14379/iodp.proc.350.104.2015

Walker, S. L., Baker, E. T., Leybourne, M., de Ronde, C. E. R., Greene, R., Faure, K., et al. (2010). "Transport of fine ash through the water column at erupting volcanoes: monowai cone, Kermadec-Tonga arc," in *Proccedings of the Abstract T13B-2193 Presented at 2010 Fall Meeting* (San Francisco, CA: AGU).

Walker, S. L., Baker, E. T., Resing, J. A., Chadwick, W. W. Jr., Lebon, G. T., Lupton, J., et al. (2008). Eruption-fed particle plumes and volcaniclastic deposits at a submarine volcano: NW Rota-1, Mariana arc. *J. Geophys. Res.* 113:B08S11.

Walker, S. L., Baker, E. T., Resing, J. A., Nakamura, K., and McLain, P. D. (2007). "A new tool for detecting hydrothermal plumes: an ORP sensor for the PMEL MAPR,"in *Proceedings of the AGU Fall Meeting Abstracts* (Washington, D.C: American Geophysical Union), 753

Watt, S. F. L., Karstens, J., Micallef, A., Berndt, C., Urlaub, M., Ray, M., et al. (2019). From Catastrophic collapse to multi-phrase deposition: flow transformation, seafloor interaction and triggered eruption following a volcanic-island landslide. *Earth Planet. Sci. Lett.* 517, 135–147. doi: 10.1016/j.epsl.2019.04.024

White, J. D. L., Smellie, J. L., and Clague, D. A. (2003). "Introduction. A deductive outline and typical overview of subaqueous explosive volcanism," in *Submarine Explosive Volcanism*, eds J. D. L. White, J. L. Smellie, and D. A. Clague (Washington, DC: American Geophysical Union, Geophysical Monograph), 1–23. doi: 10.1029/140gm01

Wohletz, K. H., and Krinsley, D. H. (1982). *Scanning electron microscopy of basaltic hydromagmatic ash. Los Alamos National Laboratory Report, LA-UR 82-1433*. Tempe, AZ: Arizona State University.

Wright, I. (1996). Volcanic processes on modern submarine arc stratovolcanoes: sidescan and photographic evidence from the rumble IV and V volcanoes, southern Kermadec arc (SW Pacific). *Mar. Geol.* 136, 21–39. doi: 10.1016/s0025-3227(96)00054-0

Conflict of Interest: The authors declare that the research was conducted in the absence of any commercial or financial relationships that could be construed as a potential conflict of interest.

Copyright © 2019 Walker, Baker, Lupton and Resing. This is an open-access article distributed under the terms of the Creative Commons Attribution License (CC BY). The use, distribution or reproduction in other forums is permitted, provided the original author(s) and the copyright owner(s) are credited and that the original publication in this journal is cited, in accordance with accepted academic practice. No use, distribution or reproduction is permitted which does not comply with these terms.

frontiers in Marine Science

ORIGINAL RESEARCH
published: 30 September 2019
doi: 10.3389/fmars.2019.00605

Preliminary Observations of the Abyssal Megafauna of Kiribati

Erik Simon-Lledó[1], Samuel Thompson[2], Andrew Yool[1], Adrian Flynn[3], Christina Pomee[4], John Parianos[5] and Daniel O. B. Jones[1]*

[1] National Oceanography Centre, Southampton, United Kingdom, [2] National Oceanography Centre, University of Southampton, Southampton, United Kingdom, [3] Fathom Pacific Pty Ltd., Melbourne, VIC, Australia, [4] Nautilus Minerals Tonga Ltd., Nuku'alofa, Tonga, [5] Nautilus Minerals Ltd., Brisbane, QLD, Australia

We report on preliminary observations of the abyssal megafauna communities in the exclusive economic zone of Kiribati, a huge abyssal area with few previous studies. These observations also provide useful context for marine minerals exploration within the exclusive economic zone (EEZ) and for the neighboring Clarion Clipperton Zone (CCZ), where deep-sea mining operations are planned. Seafloor images collected during seabed mining exploration were used to characterize megafaunal communities (fauna > 1 cm) in three abyssal plain areas in the eastern Kiribati EEZ (study area extending from 1 to 5°N and 173 to 156°W). Additionally, hydrographic features in each of the survey locations were inferred by reference to near-seabed current flows modeled using open-sourced oceanographic data. The images showed a dominance of foraminiferal organisms. Metazoan communities were high in morphospecies richness but had low density. These general patterns were comparable to abyssal megabenthic communities in the CCZ. There was evidence of spatial variation between the assemblages in Kiribati, but there was a relatively large pool of shared morphospecies across the entire study area. Low metazoan density limited detailed assessment of spatial variation and diversity at local scales. This finding is instructive of the levels of sampling effort required to determine spatial patterns in low density abyssal communities. The results of this study are preliminary observations that will be useful to guide future biological survey design and marine spatial planning strategies.

Keywords: deep-sea, biodiversity, imagery, conservation, EEZ, Pacific basin

OPEN ACCESS

Edited by:
William W. Chadwick, Pacific Marine Environmental Laboratory (NOAA), United States

Reviewed by:
Chris Mah, National Museum of Natural History (SI), United States
Paulo Yukio Gomes Sumida, University of São Paulo, Brazil
Steven Auscavitch, Temple University, United States

****Correspondence:***
Erik Simon-Lledó
erimon@noc.ac.uk

Specialty section:
This article was submitted to Deep-Sea Environments and Ecology, a section of the journal Frontiers in Marine Science

Received: *21 May 2019*
Accepted: *11 September 2019*
Published: *30 September 2019*

Citation:
Simon-Lledó E, Thompson S, Yool A, Flynn A, Pomee C, Parianos J and Jones DOB (2019) Preliminary Observations of the Abyssal Megafauna of Kiribati. Front. Mar. Sci. 6:605. doi: 10.3389/fmars.2019.00605

INTRODUCTION

The Republic of Kiribati is a Pacific Micronesian small island state comprised of three island groups: the more populous Gilbert Islands in the West, the largely uninhabited Phoenix Islands in the middle and Line Islands to the East. The three groups of islands each occur on major Cretaceous volcanic chains (Epp, 1984) that form approximately NW-SE oriented ridge systems rising from the abyssal seafloor in the central Pacific. Although the total land area of Kiribati is only 811 km^2 (Rotjan et al., 2014), the exclusive economic zone (EEZ) covers around 3.5 million km^2 and >89% of this is abyssal (>4000 m water depth) ocean (Weatherall et al., 2015).

Marine mineral exploration in Kiribati has been intermittent since the early 1980s (e.g., Gauss, 1980) and has revealed extensive deposits of polymetallic nodules and metalliferous sediments on the abyssal seafloor and ferromanganese crust resources on the seamount areas (Okamoto, 2005).

The Line Islands form the westernmost boundary of the Clarion Clipperton Zone (CCZ, at 2–20°N; 115–155°W), which is of significant interest for polymetallic nodules. A Mineral Resource (minerals in sufficient quantities to provide reasonable prospects for eventual economic extraction) has never been declared for the deposits in Kiribati waters. However, baseline knowledge of the environment is important in developing plans for exploitation of mineral resources and management of mining activities particularly in areas of high uncertainty like the deep-sea.

There have been few deep-water seabed biological investigations in Kiribati and almost no assessment of the abyssal plain areas. The only abyssal sample obtained to the authors' knowledge was a single dredge sample that was collected in the Line Islands EEZ at 5029 m depth during the Challenger expedition (station 274) on 11 September 1875, which contained a xenophyophore (*Psammina nummulina*), several sponges (*Euplectella crassistellata* and *Cladorhiza abyssicola*), holothurians (including *Benthodytes selenkiana* and *Psycheotrephes exigua*), an asteroid (*Hyphalaster hyalinus*), an echinoid [*Phormosoma* (now *Tromikosoma*) *tenue*], polymetallic nodules and fossil shark teeth (Théel, 1882; Murray and Renard, 1891; Murray, 1895). On the shallower slopes (1000–1300 m depth) of the Phoenix Islands investigations have been made with baited video (Obura et al., 2011). The limited deeper water work around the Phoenix Islands was stimulated by the creation of the Phoenix Islands Protected area (PIPA) in 2008, which is one of the largest (encompassing 408,250 km^2) marine parks in the world (Rotjan et al., 2014). Deep water assessment of the seamount communities of the Phoenix Islands and primarily the PIPA area have been made recently by ROV in March 2017 (Okeanos Explorer expedition "Discovering the Deep: Exploring Remote Pacific Marine Protected Areas") and October 2017 (RV Falkor expedition "Discovering Deep Sea Corals of the Phoenix Islands"). These assessments primarily focused on the impressive deep-water coral communities associated with seamounts, including those on ferromanganese crusts (Cordes, 2017; Kennedy, 2017).

In this paper we present observations from an opportunistic assessment of some of the first photographs of the abyssal seabed of Kiribati. We aim to describe the variation in epibenthic megafaunal assemblages in the northern Phoenix Islands and Line Islands of Kiribati. We use consistent morphospecies taxonomy with studies carried out in the CCZ, enabling comparison between these areas.

MATERIALS AND METHODS

Study Areas

Data were acquired during the *RV* Yuzhmorgeologiya expedition to the western Kiribati EEZ, between −1 to 5° N and 173 to 156° W, in the mid Pacific Ocean (**Figure 1**). Three abyssal areas of interest were defined from W to E within this region: Area A (east of the Phoenix Group Islands, mean water depth: 5460 m), Area B (west of the Line Island Group, mean water depth: 5020 m), and Area C (east of Line Island Group, mean water depth: 4630 m). Area A and B are ∼1200 km apart, separated by an abyssal basin. Areas B and C are ∼700 km apart and separated by the Line Islands ridge system (**Figure 1**). Areas B and C exhibited a similar seafloor geomorphology with slopes <5° and unconsolidated sediment bed (**Figure 2A**). Area A had similar geomorphology with the exception of one transect (Dive 4, **Figure 2B**) conducted upon on steeper terrain (>5° slope), where hard substratum was present in the form of partially sediment-covered ferromanganese-coated basalt bedrock and polymetallic nodules (see section "Image Data Collection and Processing").

Environmental Assessment

Hydrographic Variations

The potential hydrographic isolation between sites was assessed by reference to near-seabed current flows. Since appropriate measurements were not available, seafloor current velocities for areas greater than 3000 m depth were drawn from a high-resolution ocean general circulation model. The model used was a global 1/12°configuration of the Nucleus for European Modeling of the Ocean model (NEMO; Madec, 2008), simulated for the period 1978 to 2010. The model's temperature and salinity fields were initialized using the World Ocean Atlas (WOA) 2005 climatology, and it was forced at the air-sea boundary using the DFS4.1 reanalysis product, which includes observationally-derived 6-hourly fields of atmospheric properties and winds, daily fields of heat fluxes and monthly precipitation fields (Brodeau et al., 2010). Full details of the simulation can be found in Marzocchi et al. (2015).

Biological Assessment

Image Data Collection and Processing

Seafloor images were collected using a digital camera (Canon D60; 3456 × 2304 pixels) mounted on the towed camera system Neptune, developed by the Russian marine institute Yuzhmorgeologiya (Nautilus Minerals, 2016). The Neptune system was towed at a speed of 0.5–1.0 m s^{-1} and pictures were taken at an altimeter-triggered altitude of 3.5 m above the seafloor, at least every 30 s to avoid overlap between frames. At the target altitude, individual photographs imaged 3.6 m^2 of seabed. A total of six image transects (Dives 1 to 6) were surveyed using the Neptune system, but each of a different length, as these were originally collected for the geological scouting of the area by Nautilus Minerals (Nautilus Minerals, 2016). Four transects were collected in Area A (Dives 1 to 4), one in Area B (Dive 5), and one in Area C (Dive 6) (**Figure 1**, **Table 1**, and **Supplementary Table S1**). The full resultant dataset was composed of data from 4,074 non-overlapping images, representing a total seafloor area of 14,666 m^2 (**Table 1**).

Images were reviewed in random order to minimize time or sequence-related bias (Durden et al., 2016). Megafauna specimens (>1 cm) were identified to the lowest taxonomic hierarchy possible (morphospecies: typically Genus or Family level; see **Supplementary Table S2**), and their physical dimension measured, using BIIGLE 2.0 (Langenkämper et al., 2017).

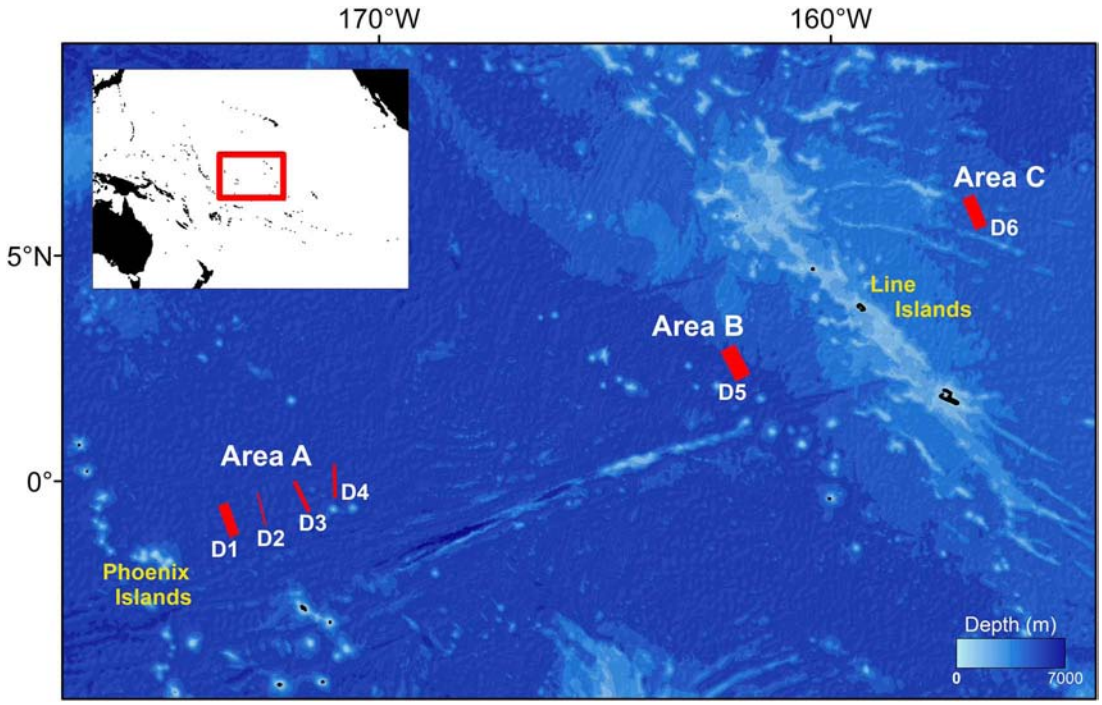

FIGURE 1 | Map of survey locations used for the present study within the eastern Kiribati EEZ. Red lines indicate image transect locations. Line thicknesses represent the relative seabed area coverage (i.e., the length) of each survey dive (D). A map of the mid Pacific Ocean is inset, showing the studied area region (empty red rectangle). Water depth data obtained from Becker et al. (2009). Further survey metadata are provided in **Supplementary Table S1**.

To ensure consistency in specimen identification, an abyssal-Pacific standardized megafauna morphospecies (msp) catalog (e.g., **Figure 3**) was compiled from previous studies in the Pacific basin (Amon et al., 2016; Simon-Lledó et al., 2019a,b,c) and by reference to existing literature (Molodtsova and Opresko, 2017; Kersken et al., 2018; Drazen et al., 2019). The likely feeding behavior of each morphospecies was inferred from similar organisms described in the literature (i.e., Iken et al., 2001). Foraminifera specimens (Protists >1 cm; miliolids and xenophyophores; see e.g., **Figures 3M–O**) were identified in a subset of 2000 images selected at random across the six transects collected (i.e., half of the images of each transect), and these were only classified into four categories (miliolids and plate-, reticular-, and tubular-shaped xenophyophores).

Data Analysis

Observation data (faunal records in images) were pooled for different study areas to investigate variations in megabenthic characteristics between these. A total of four study areas were considered since observation data from Dive 4 were processed separately (Area A_H) from the rest of Area A data, owing to the different seabed morphology and surface composition in this location (i.e., ∼40% of Dive 4 images were collected in areas with >5° slope and hard substratum present). However, the pool of images in Area A_H subsample was about four times smaller than that in each of the other three areas (**Table 1**). Metazoan and foraminiferal data were processed separately and the latter were excluded from diversity assessments because: (i) it is not possible to determine whether foraminifera are alive in images (Hughes and Gooday, 2004); (ii) the taxonomic resolution allowed in image assessments is lower to that achieved in metazoans (see e.g., Gooday et al., 2017b); and (iii) there is a substantial mismatch between the biomass of metazoan and foraminifera specimens, since the protoplasm volume of the latter represents only 1–0.01% of their visible test (Levin and Gooday, 1992; Gooday et al., 2018).

Observation data from each area (Areas: A, A_H, B, and C) were resampled using a modified form of bootstrapping (Davison and Hinkley, 1997). Bootstrapping is a statistical method for estimating the distribution of a given parameter (or a set of these) by sampling with replacement from the original sample. Resampling techniques provide robust estimates of standard errors and confidence intervals of sample parameters (Crowley, 1992; Rodgers, 1999), and are particularly well suited to analyze data derived from survey designs that lack true sample replication (see e.g., Simon-Lledó et al., 2019b). To implement the bootstrap, each study area image data subset was randomly resampled with replacement until a minimum of 500 m^2 of seafloor (139 images) were encompassed, and that process was repeated 1000 times for each area. This resampling process yielded bootstrap-like samples (bootstrap generated sub-samples with fixed size) that ranged in metazoan specimen counts of 17–140. The same process was repeated using only those images where foraminifera were identified, which yielded bootstrap-like samples with foraminiferal specimen counts of 233–2042. We adopted this controlled seabed

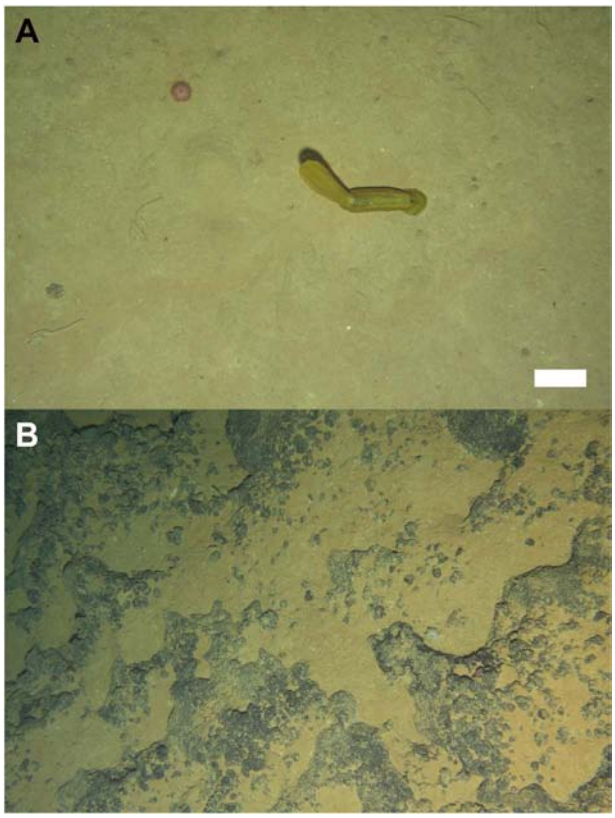

FIGURE 2 | Examples of the seafloor types surveyed in the present study. **(A)** Sediment-only seabed, in Area A, Dive 1 (i.e., idem Dives 1, 2, 3, 5, and 6). Note the presence of the holothurian *Psychropotes longicaudata* -yellow morphotype-, the echinoid *Kamptosoma* sp. msp-2, and several xenophyophore specimens. **(B)** Sediment and hard substratum seabed, in Area A_H, Dive 4. Note the presence of the sponge *Docosaccus nidulus* sp. inc. Scale bar represents 20 cm and applies to both images.

TABLE 1 | Environmental features and sampling details in each of the survey locations investigated in the present study.

	A	A_H	B	C
Survey dive(s)	D1-D3	D4	D5	D6
Center latitude (°)	−0.7404	−0.0001	2.5958	5.9568
Center longitude (°)	−172.9507	−171.0011	−162.1570	−156.8213
Water depth m; min– max)	5536–5224	5575–5250	5116–5020	4667–4631
Images	1400	265	1172	1237
Total area (m^2)	5040	954	4219	4453
POC flux* (g C_{org} m^{-2} y^{-1}; min–max)	1.83–1.96	1.97–1.99	1.75–1.83	1.50–1.56
Bottom current speed (m s^{-1}; min–max)	0.01–0.04	0.01	0.003–0.005	0.008–0.01

**Values interpolated from image locations based on Lutz et al., 2007.*

area approach to control the impact of the physical sample size on the estimation of biological diversity and faunal composition parameters.

A range of ecological parameters was calculated for each of the 4 × 1000 bootstrap-like samples, including metazoan and foraminiferal numerical density (ind m^{-2}) and metazoan taxa density, i.e., morphospecies richness (S) in c. 500 m^2. Variation in metazoan community composition was assessed by 2-d non-metric multidimensional scaling (nMDS) ordination of all 4 × 1000 bootstrap-like samples, based on square-root transformed faunal density and use of the Bray-Curtis dissimilarity measure (Clarke, 1993). Mean values of these parameters were calculated from each bootstrap-like sample set, together with corresponding 95% confidence intervals based on the simple percentile method (Davison and Hinkley, 1997). Data processing and analyses were performed using a custom R (R Core Team, 2017) script incorporating multiple functions from the "vegan" package (Oksanen et al., 2018). We report statistical assessments of variations in ecological parameters between study areas by comparisons of the 95% confidence intervals, i.e., the upper limit of a given estimate must be lower than the lower limits of the estimate that is compared to. Such cases are significant at $p < 0.05$, though the true (undetermined) p-value will, necessarily, be considerably lower.

Additionally, a rarefaction approach was applied to assess the potential impact of sampling unit size on morphospecies density (Chao et al., 2014). Sampling unit size was quantified as both number of individuals and seabed area observed. Metazoan observation data for each separate survey area, and for the whole dataset combined, were randomly resampled 100 times without replacement, to form increasingly larger image sampling units. The mean and 95% confidence intervals of each parameter were calculated at each sampling unit size using Estimate S v.9.1 software (Colwell, 2013).

RESULTS

Hydrographic Variations

Modeled bottom current speeds in seabed areas below 3000 m water depth within the Kiribati EEZ ranged between 0.001 and 0.1 m s^{-1} (**Figure 4A**). Modeled current speeds in the seafloor of Areas A, A_H, and C were similar (∼0.01 m s^{-1}) and substantially stronger than those obtained for Area B (**Table 1**). Model results suggested that the current speed at the seabed area where Dive 01 was collected (in Area A) was ∼4 times stronger than in the rest of Area A survey locations.

Megafauna Assessment

Foraminiferal tests numerically dominated the assemblages recorded during the present study; being overall, almost 15 times more abundant than metazoans (**Figure 5**). A total of 15,196 foraminifera specimens (in 7,200 m^2 of seabed) and 1948 metazoans (in 14,666 m^2 of seabed), all >1 cm, were recorded across all the study areas surveyed within the Kiribati EEZ.

Metazoan Megafauna

A total of 118 metazoan morphospecies, and 5 higher taxonomic categories (i.e., Order, Family), were documented from images (**Table 2** and **Supplementary Table S2**). Rare taxa (≤3 records) represented 46% of the total metazoan morphospecies richness.

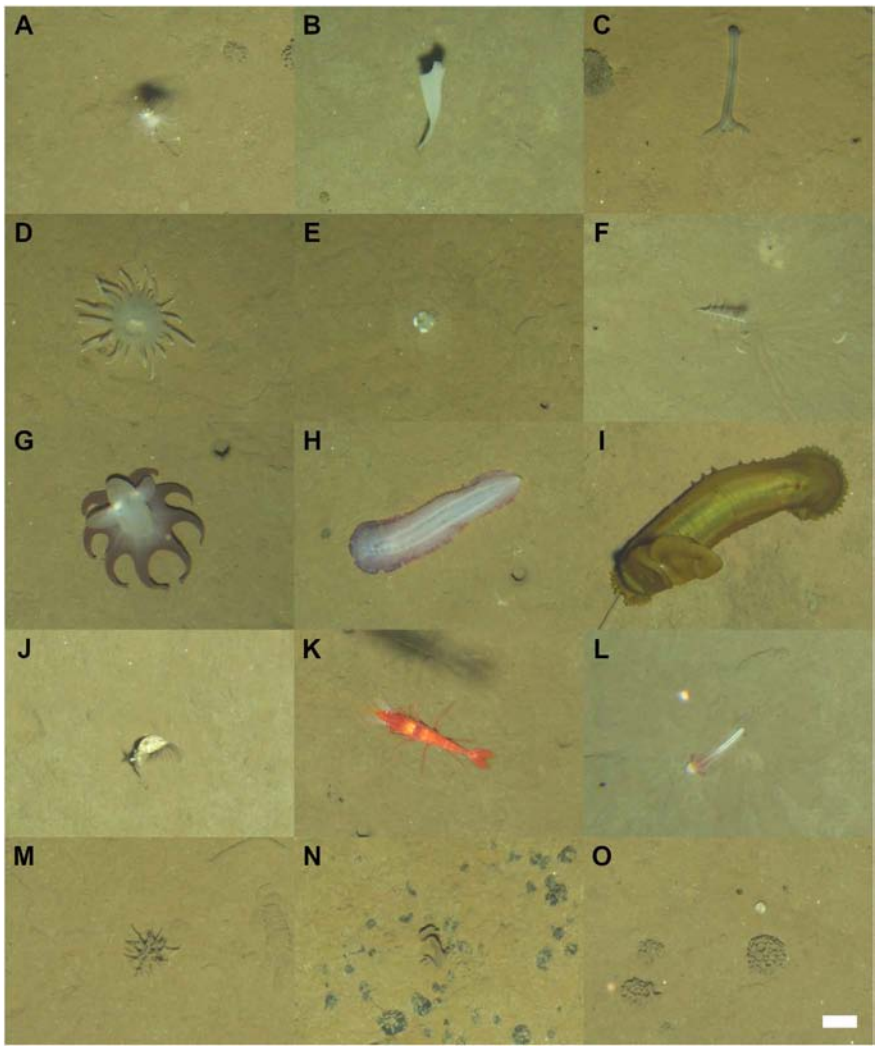

FIGURE 3 | Examples of megafauna photographed at the Kiribati EEZ seafloor during Neptune towed-camera surveys. Scale bar represents 5 cm and applies to all images. **A–L**: Metazoan megafauna. **(A)** *Cladorhiza* sp. msp-4. **(B)** Porifera msp-20. **(C)** Echiura msp-3. **(D)** Actiniaria msp-10. **(E)** Actiniaria msp-36. **(F)** *Bathygorgia* sp. msp-2. **(G)** *Grimpoteuthis* sp. msp-1. **(H)** *Paelopatides* sp. msp-4. **(I)** *Psychropotes longicauda,* yellow-morphotype. **(J)** *Neoscalpellum* msp-1. **(K)** *Cerataspis* sp. msp-3. **(L)** *Torquaratoridae* sp. msp-2. **M–O**: Foraminifera specimens. **(M)** Tubular-shaped xenophyophore. **(N)** Plate-shaped xenophyophore **(O)** Miliolid (white round specimen) and three reticular-shaped xenophyophores.

The metazoan fauna observed were predominantly cnidarians (19 msp; 36% of all metazoan records), arthropods (10 msp; 20% of all metazoan records), sponges (22 msp; 17% of all metazoan records), and echinoderms (37 msp; 15% of all metazoan records). Annelids, chordates, and molluscs (as well as bryozoans, ctenophores, and an enteropneust worm) were also recorded at lower abundances (**Table 2** and **Supplementary Table S2**). Suspension feeding organisms represented >60% of all the metazoan specimens recorded, while deposit feeders and predators and scavengers represented 16 and 23% of all metazoan records, respectively. The three most abundant metazoan morphospecies were: an actiniarian (Actiniaria msp-22; 240 specimens), a barnacle (*Neoscalpellum* sp. msp-1; 150 specimens; **Figure 3J**), and a hexactinellid sponge (*Docosaccus maculatus* sp. inc.; 78 specimens).

Variations in standing stocks

Metazoan numerical density was variable across the different areas surveyed (**Figure 6A**) with mean values ranging between 0.07 and 0.3 ind m^{-2} (in samples c. 500 m^2). Metazoan density was lower in Area B than in Areas A and C, which were similar. In Area A_H, mean metazoan density was around twice that of the rest of Area A and Area C, and was almost five times higher than the density found in Area B (**Figure 6A**). These variations primarily resulted from changes in the suspension feeder standing stock across survey areas (**Figure 6B**). Suspension feeder density was considerably reduced in Area B compared to Areas C and A, and was substantially higher in A_H than in any other study area. Densities of deposit feeder (**Figure 6D**) and predator and scavenger metazoan fauna (**Figure 6F**) were similar across study areas.

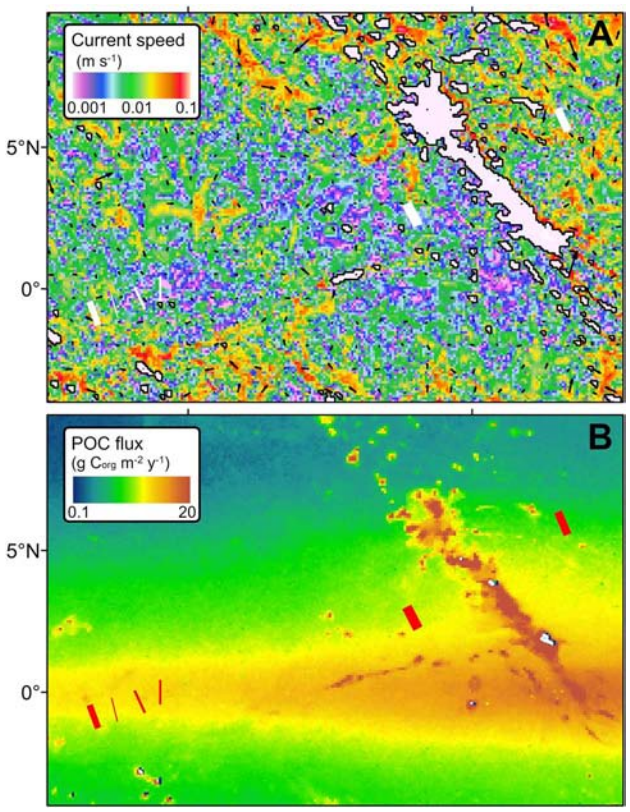

FIGURE 4 | Environmental features of the eastern Kiribati EEZ seabed. **(A)** Modeled bottom water circulation in areas below 3000 m water depth. **(B)** Nutrient flux from surface to the seafloor, as reported by Lutz et al. (2007).

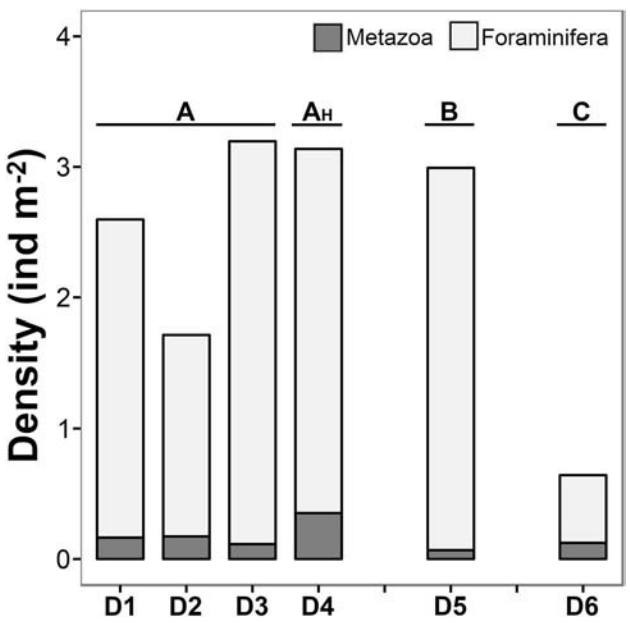

FIGURE 5 | Total density of metazoan and foraminiferal specimens (>1 cm) encountered in each image transect analyzed in the present study.

TABLE 2 | Total abundance and taxon richness of major metazoan taxa encountered during the present study.

Phylum	Class	Order	Morpho species	Area B	Area A_H	Area B	Area C
Porifera	Indet. Class		4	19	22	12	20
	Demospongiae		5	4		7	5
	Hexactinellida		13	45	14	27	157
Ctenophora	Tentaculata		3	4			
Cnidaria	Anthozoa	Actiniaria	8	349	126	23	49
		Alcyonacea	5	13	42	1	11
		Ceriantharia	3	35	2	25	11
		Corallimorpharia	1				2
		Pennatulacea	1	2		2	7
	Hydrozoa	Trachymedusae	1	3		3	
Bryozoa	Gymnolaemata		2	1	12	1	6
Annelida	Polychaeta		9	25	46	32	51
Arthropoda	Hexanauplia		1	52	7	15	76
	Malacostraca	Amphipoda	2		4	2	1
		Decapoda	4	28	8	30	26
		Isopoda	3	52	13	9	24
	Peracarida	Mysida	1	9	11	1	5
Mollusca	Gastropoda		1	3	2	4	2
	Scaphopoda		1				4
	Cephalopoda	Octopoda	1	1		1	
Echinodermata	Asteroidea		5	5	1	2	7
	Crinoidea		4	4	4	1	1
	Echinoidea	Echinothurioida	2	16	2	2	54
	Holothuroidea		23	71	6	21	6
	Ophiuroidea		3	28	4	57	8
Hemichordata	Enteropneusta		1				1
Chordata	Ascidiacea		4	9	1	1	
	Actinopterygii		7	3		8	19

Further taxonomic detail, at the morphospecies level, is provided in ***Supplementary Table S2****. The taxonomic nomenclature used follows Horton (2018).*

Variations in diversity and composition

Mean metazoan morphospecies richness ranged between 19.6 and 29.6 (S, in samples c. 500 m^2) across the different areas surveyed (**Figure 6C**). Area B exhibited the lowest mean taxa richness and Area A_H the highest, but variations between areas were not substantial (i.e., overlapping confidence intervals: **Figure 6C**). Morphospecies richness curves showed no significant variations between different study areas in sample sizes up to 4,000 m^2 (**Figure 7A**). However, individual-based assessments (**Figure 7B**) revealed a different taxa accumulation pattern in Area B, which indicates that the lower taxon richness found in this area resulted from its inherent lower faunal density, as opposed to Area A_H. These patterns were consistent at whole study level (dashed-depicted accumulation curves; **Figure 7**).

In total, 33% of the metazoan morphospecies recorded were present in all three study areas, 18% were noted in only two areas, and 49% were detected in only one area (**Figure 8A**). More than half (53%) of the records exclusively found in a single area were singletons. Areas A and B shared a larger number of metazoan taxa (50%) than Area C with Areas A

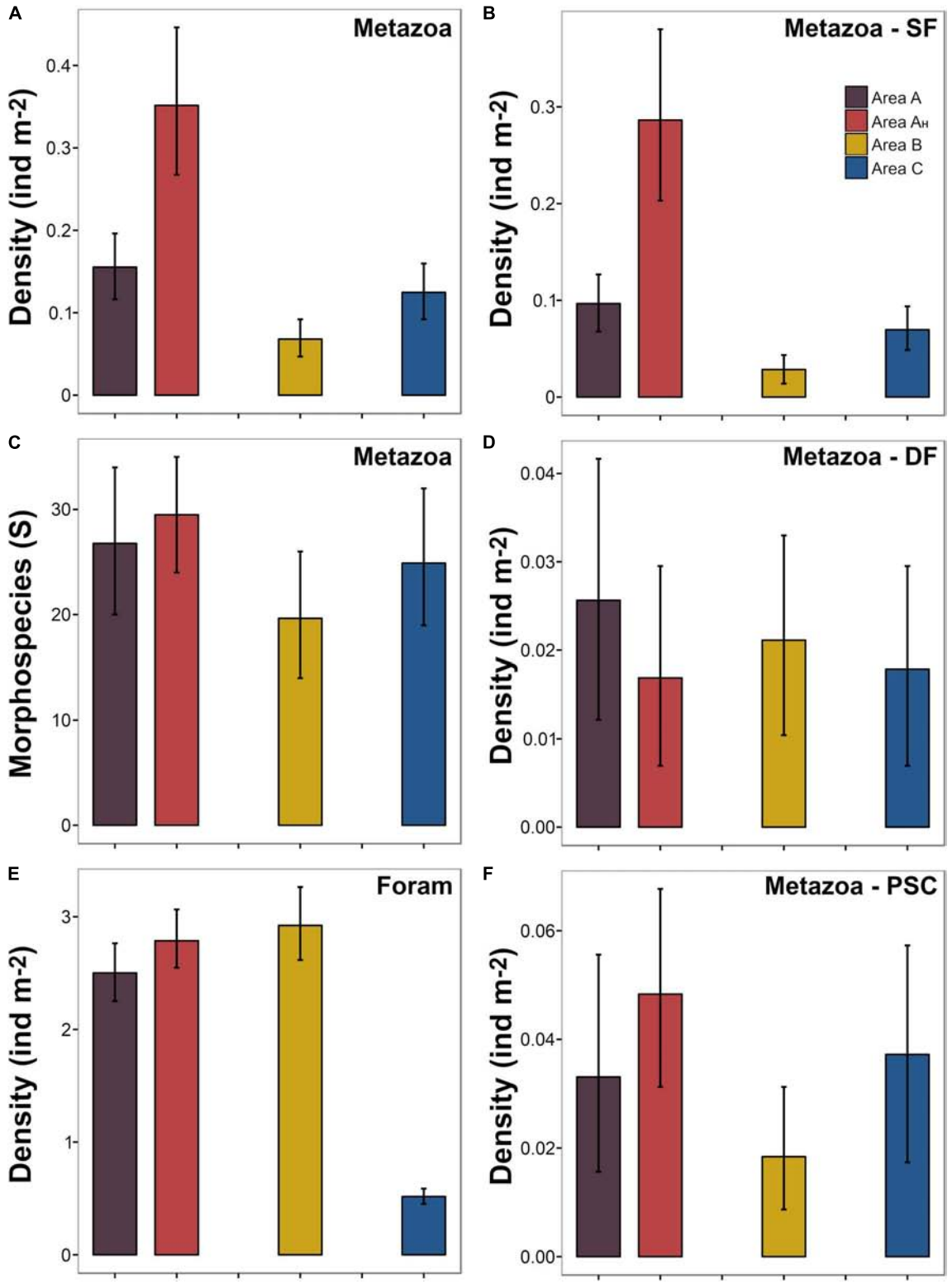

FIGURE 6 | Variation in different biological parameters across the areas surveyed. Bars indicate mean density calculated from the bootstrap-like sample set generated for each area. Error bars represent 95% confidence intervals. **(A)** Density of metazoan fauna (note that B, D, and F are each a subset of A). **(B)** Density of metazoan suspension feeder fauna. **(C)** Metazoan morphospecies richness (in c. 500 m^2 samples). **(D)** Density of metazoan deposit feeders. **(E)** Density of foraminiferal tests. **(F)** Density of metazoan predator and scavenger fauna. Abbreviations: *Foram*: foraminifera; *SF*: suspension feeders; *DF*: deposit feeders; and *PSC*: predators and scavengers.

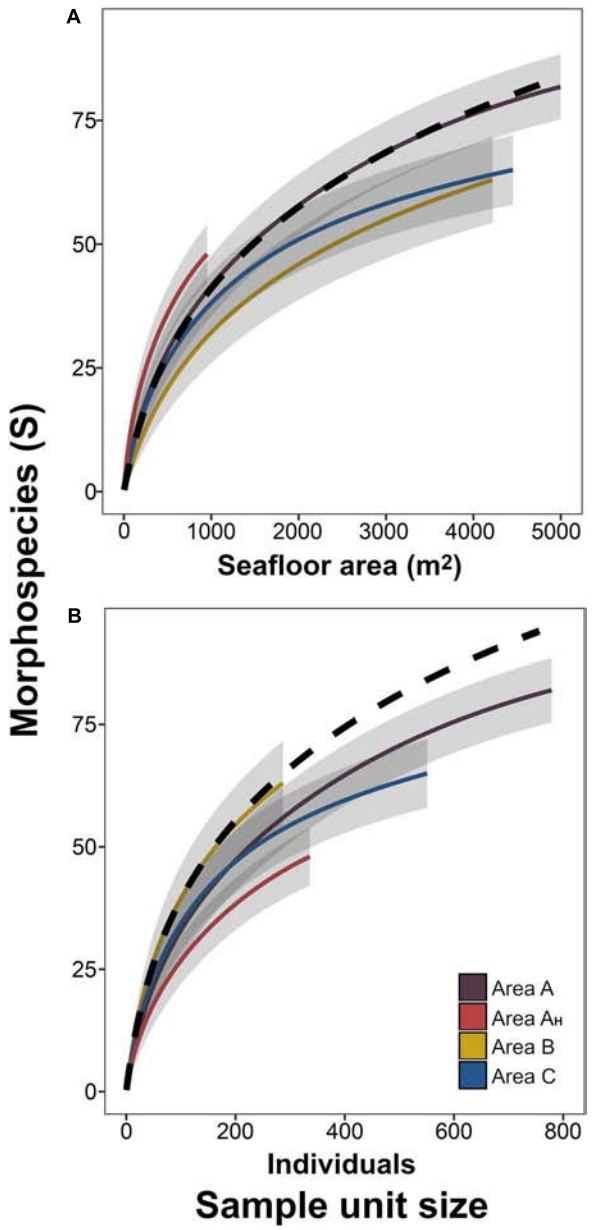

FIGURE 7 | Metazoan morphospecies accumulation curves for each survey area. Curves were calculated as a function of the seabed area **(A)** or the number of individuals encompassed by the sample unit size **(B)**. Lines represent mean values across the 100 randomizations performed at each sample unit size increase, for each study area. Shadowing representing 95% confidence intervals. Dashed line represents mean values of curve calculated using whole-study collated data.

(36%) and B (35%). Two dimensional ordination of faunal composition by density readily distinguished Area A, B, and C samples, and Area A_H samples from the rest of Area A (**Figure 8B**). However, within-site dissimilarity was substantial in Areas A, B, and C, with Area B exhibiting the highest heterogeneity; some bootstrap-like samples generated for Area B showed a higher similarity to those generated for Areas A and C than to other Area B samples. Density distribution of the four most-abundant metazoan phyla across study areas was variable (**Figure 9**). While the mean density (in samples c. 500 m^2) of arthropods and particularly echinoderms was similar across study areas (**Figures 9C,D**), the mean density of cnidarians was substantially higher in Area A, especially in Area A_H, compared to the other two areas (**Figure 9A**). On the other hand, mean sponge density (in samples c. 500 m^2) was substantially higher (and similar) in Areas A_H and C compared to that in Areas A and B (**Figure 9B**). The most remarkable variations in distribution at the morphospecies level between study areas were: (i) 95% of all Actiniaria msp-22 records (n = 228) were found in Areas A and A_H; (ii) 97% of all the records (n = 76) of the sponge *Docosaccus maculatus* sp. inc. were found in Area C, (iii) 97% of all the records (n = 43) of the holothurian *Psychropotes longicaudata* (yellow morphotype; **Figure 3I**) were found in Areas A and B, while only one specimen was recorded in Area C, and (iv) all the records (n = 14) of the fish *Ipnops meadi* were found exclusively in Area C.

Foraminiferal Megafauna

Most foraminiferal specimens observed were xenophyophores exhibiting reticulated (57%), plate-shaped (36%), and tubular (4%) morphologies, while miliolids represented only a small fraction (3%). Mean numerical density of foraminiferal tests was variable across the different areas surveyed (0.5 to 2.9 ind m^{-2}), but exhibited different between-site patterns to those recorded in metazoan fauna (**Figure 6E**). Mean foram density was almost 6 times lower in Area C than in Areas A and B, and test density in Area A_H was similar to that in the rest of Area A (**Figure 6E**). Reticulated xenophyophore morphospecies dominated the foraminiferal assemblages in Areas A (53%) and B (67%), while plate-shaped forms dominated the foraminiferal assemblages in Areas A_H (47%) and C (50%). Total miliolid density in Area A (1230 ind ha^{-1}) was higher than in Areas B (495 ind ha^{-1}) and C (15 ind ha^{-1}).

DISCUSSION

Environmental Setting

Modeled bottom current speeds in the studied areas were relatively modest (~0.01 cm s^{-1}) compared to the ranges estimated below 3000 m water depth in the Kiribati region (~0.001 to ~0.1 m s^{-1}; **Figure 4A**). Bottom current speed ranges obtained in our model were broadly comparable to those reported from *in situ* observations performed in eastern (Aleynik et al., 2017) and western (Hayes, 1979) areas of the CCZ. In turn, presumed ranges of vertical nutrient supply amongst the studied areas (1.50–1.99 g C_{org} m^{-2} y^{-1}) were only comparable to those in more southern areas of the CCZ (Lutz et al., 2007; **Figure 4B**) as spring blooms in surface waters are more pronounced toward the equator (Pennington et al., 2006). As a result, despite that Area C is found ~1000 m shallower than Areas A and B, and food supply usually decreases inversely with water depth (Buesseler et al., 2007), the closer proximity of Areas A and B to the equator

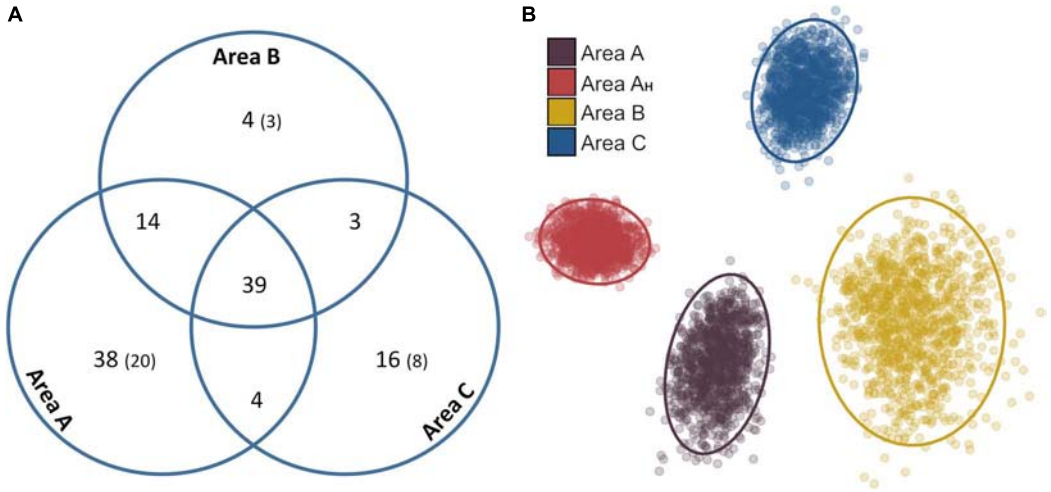

FIGURE 8 | Qualitative and quantitative variations in metazoan community composition between different survey areas. **(A)** Venn diagram showing the total number of metazoan taxa shared between each combination of survey areas. *In brackets*: singleton morphospecies. **(B)** MDS plot describing 2D ordination of abundance-based dissimilarity (distance) between the assemblages of each bootstrap-like sample (stress = 0.08). Ellipses represent 95% confidence intervals for each bootstrap-like sample set.

is presumed to provide these with a comparably higher vertical nutrient input than Area C (Lutz et al., 2007).

Metazoan Megafauna

Standing Stocks

Metazoan standing stocks varied across the abyssal locations explored. Perhaps contrary to expectation, environmental factors differing between study areas (**Table 1**) that typically affect faunal density, such as water depth (Rex et al., 2006) and surface production (Johnson et al., 2007), appeared to have no observable effect on the relative megabenthic standing stock across study areas. The metazoan density surveyed in Area C was similar to that in Area A despite the comparably higher food supply that Area A is presumed to have (Lutz et al., 2007, **Figure 4A**). It is important to consider that differences in metazoan abundance across the areas surveyed were predominantly a result of variations in suspension feeder fauna density (e.g., sessile cnidarians and sponges). These organisms clearly dominated the metazoan megabenthos of the Kiribati abyss, with densities about an order of magnitude higher than those observed in deposit feeding or predator and scavenger fauna, a pattern that has been commonly reported in eastern areas of the CCZ (Amon et al., 2016; Simon-Lledó et al., 2019a). Deep-sea suspension feeder standing stocks are sensitive to variations in bottom water current speeds as these can alter the flux of laterally transported organic particles (Thistle et al., 1985; Angel and Boxshall, 1990). The substantially reduced presence of suspension feeders in Area B may hence be influenced by the comparably weaker bottom water circulation strength expected in this location (**Table 1** and **Figure 4A**). These results suggest that the available environmental information was not sufficient to predict megabenthic standing stocks in this region, which may result from scale mismatches and local effects being more important that broad-scale generalizations. Therefore, further environmental characterization of the Kiribati abyssal seabed will be needed to fully understand the controls on metazoan abundance.

Area A_H, the only survey location where some hard substratum was present in the seabed (i.e., partially sediment-covered exposed bedrock and polymetallic nodules), exhibited a substantially larger metazoan standing stock than the other study areas (**Figure 6A**) as a result of an enhanced abundance of sessile cnidarians (i.e., Actiniaria and alcyonacea; **Table 2** and **Figure 9A**). Simon-Lledó et al. (2019b) recently showed that the availability of hard substratum can be key in the regulation of standing stocks and assemblage composition in abyssal megabenthic communities. For instance, at the CCZ, populations of sessile cnidarians are usually significantly reduced in areas where polymetallic nodules are absent (Vanreusel et al., 2016; Simon-Lledó et al., 2019b), as some of these taxa are typically obligate hard-substratum dwellers (Amon et al., 2016; Lim et al., 2017). In turn, metazoan densities observed in sediment-only areas (Area A, B, and C) were comparable to those reported in nodule-free areas explored in the eastern CCZ (Simon-Lledó et al., 2019b) using a similar image-sampling methodology (i.e., similar altitude of collection above-seabed and resolution). These results support that the availability of hard substratum in abyssal sedimentary habitats may be an important environmental driver in the structuring of local megabenthic communities. However, the total area surveyed in Area A_H (~1000 m^2 of seabed) was substantially lower than those in the other study areas (i.e., 4200–5000 m^2) and hence comparisons between this area and the rest should be drawn with caution, as a larger sampling effort may reveal further/different biological features.

Diversity and Assemblage Compositions

We found similar mean metazoan taxa richness across study areas, but taxa accumulation patterns suggested that the

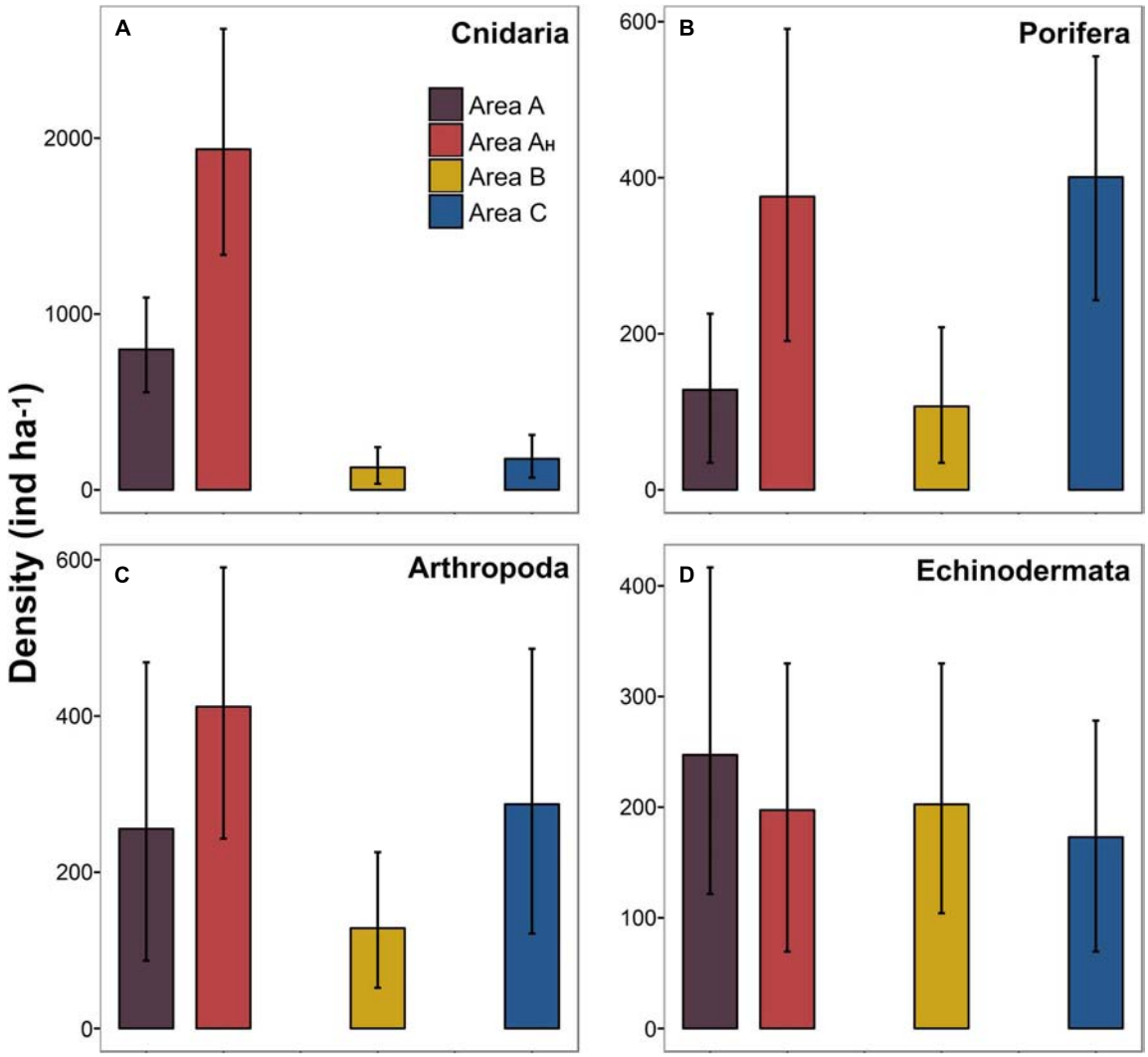

FIGURE 9 | Variation in standing stock of different metazoan taxonomic groups across the study areas surveyed. Bars indicate mean density calculated from the bootstrap-like sample set generated for each area. Error bars represent 95% confidence intervals. **(A)** Cnidarian density. **(B)** Sponge density. **(C)** Arthropod density. **(D)** Echinoderm density.

sampling effort applied was insufficient to fully characterize the richness of each separate study area (**Figure 7**). The low metazoan density characteristic of the North Pacific abyss, especially on sediment beds, can limit the representativeness of image-based megafauna samples (Simon-Lledó et al., 2019a). While the assessment of faunal density in deep-sea benthic environments typically requires relatively small sample sizes (e.g., >30 individuals per sample; Benoist et al., 2019; Simon-Lledó et al., 2019a), precise characterization of taxa richness and composition usually require a larger number of individuals in each sample (e.g., >500 individuals and >140 individuals per sample, respectively; Benoist et al., 2019; Simon-Lledó et al., 2019a) than was possible to obtain here (samples c. 500 m^2, range: 27–151 individuals per sample). Consequently, while discussions of patterns across the areas studied here are presumably robust in terms of standing stocks, our results should be interpreted with caution with respect to community composition and are best limited to whole-of-study-area with respect to taxa richness. The total metazoan richness recorded in the Kiribati abyss (118 morphospecies: **Table 2** and **Supplementary Table S2**) upon collation of all sample data (1948 metazoans) was comparable to that found in eastern CCZ locations, like the APEI6 (7837 metazoans, 133 taxa: Simon-Lledó et al., 2019b) or the UK-1 area (∼3500 metazoans, ∼126 taxa: Amon et al., 2016). Synthesis studies collating taxonomical data across all these studies are critical to determine the variability and biogeographical patterns across the North Pacific abyss.

Qualitative and quantitative analyses enabled a preliminary interpretation of variations in faunal composition across the areas studied. Qualitatively, a larger shared morphospecies pool was found between Areas A and B (42%) than between

each of these and Area C (34–33%) (**Figure 8A**). A possible explanation is that the Line Islands volcanic ridge may isolate Area C populations from those to the west, as shown for other ridge systems on the abyssal plains (Carey, 1981; McClain et al., 2009). However, there was still a relatively large pool of shared taxa (30%) across all the areas, despite the large spatial distances (e.g., Area A to C: ∼2000 km) and the relatively small specimen sample sizes obtained, so dispersal pathways could exist (**Figure 1**). In contrast, quantitatively, faunal compositions varied across the four areas investigated (**Figure 8B**) owing to differences in the relative density of particular suspension feeder taxa between areas, such as sessile cnidarians and sponges (**Figures 9A,B**). Metazoan assemblages in Area A were numerically dominated by actiniarians (e.g., Actiniaria msp-22), whilst hexactinellid sponges (e.g., *Docosaccus maculatus* sp. inc.) dominated the assemblages in Area C. Moreover, the availability of hard substratum in Area A_H appeared to generate a different metazoan aggregation than in the rest of Area A, with an enhanced presence of hard-substratum-dwelling taxa (e.g., alcyonacea soft corals; Cairns, 2016), as typically occurs between nodule-free and nodule-bearing sites at the local scale within the CCZ (Vanreusel et al., 2016; Simon-Lledó et al., 2019b). Results of quantitative analysis of composition were driven by the different faunal abundances encountered across the areas studied. For instance, the mean number of individuals encountered in Area A_H (fixed area) samples was 96 (±11 standard deviation) while this number was 35 (± 6 standard deviation) in Area B samples. Consequently, while Area B exhibited the largest within-site heterogeneity, Area A_H exhibited the most homogeneous assemblage (e.g., **Figure 8B**). These results suggest that further, larger, and comprehensively designed surveys will need to be conducted across the abyssal areas of Kiribati to determine if the preliminary patterns in richness and composition drawn in this study are consistent at larger scales. Future assessments should be sensitive to the environmental stratification (e.g., seabed composition, geomorphological setting, depth, etc.) that can drive biological variations and also to the low density -yet high richness- that is characteristic of metazoan megabenthic communities in the abyssal Pacific (Amon et al., 2016; Simon-Lledó et al., 2019a, this study).

Foraminifera Assemblages

Foraminiferal specimens (forams; xenophyophores and miliolids, **Figures 3M–O**) numerically dominated the megabenthic assemblages in the Kiribati abyss; being overall, an order of magnitude more abundant than metazoans, and reaching a peak density of 16.6 ind m^{-2} in an image from Area B. These results are consistent with previous assessments in abyssal Pacific megabenthic communities, which are typically dominated by giant foraminifera (Kamenskaya et al., 2013; Simon-Lledó et al., 2019a). Standing stocks of the larger sized fauna decrease dramatically with water depth (Rex et al., 2006) as diminishing food supply appears to prevent growth to larger body sizes (McClain et al., 2005). This hypothesis is consistent with the large dominance of foraminifera in the abyssal megabenthos, as their protoplasm volume represents a minor fraction of their visible test (Levin and Gooday, 1992), and because benthic bacteria dominate carbon consumption of these ecosystems (Sweetman et al., 2019).

Mean foram density in Areas A and B was comparable, though slightly lower, to that found in eastern CCZ locations surveyed using a similar sampling methodology (Simon-Lledó et al., 2019a). Forams are a key group in the functioning of abyssal Pacific communities (Kamenskaya et al., 2013), particularly at the CCZ, where these organisms are exceptionally diverse and abundant (Gooday et al., 2017a). The substantially reduced xenophyophore density within Area C is hence remarkable (**Figure 6E**), and somewhat unexpected given the closer proximity of this location to the CCZ compared to Areas A and B. Moreover, previous studies have shown increased abundances of xenophyophores in areas where hard substratum is present (Amon et al., 2016; Simon-Lledó et al., 2019b) as a result of the hard-substratum-attached life-habit of some taxa (Kamenskaya et al., 2013; Gooday et al., 2015). However, we found no substantial differences in the foram density between Area A_H and the rest of Area A, despite the availability of hard substratum in the former, but only a shift in dominance from reticular to plate-shaped morphologies. Further investigation of the factors driving the development of foram taxa in abyssal depths is in urgent need, particularly in the North Pacific, where their extremely large abundance has been suggested to play a crucial role in providing habitat structures and enhancing the organic content of sediments surrounding their tests (Gooday et al., 2017a).

CONCLUSION

This study presents the first quantitative assessment of megafauna in the abyssal benthos of Kiribati, and an example of successful collaboration between industry and academic research. We found clear differences in the density of both the metazoan and the foraminiferal standing stocks across the study areas, but little if any substantive variation in biological diversity, and a potentially sample-size biased variation in community composition. Despite the low metazoan faunal density recorded, this study provides evidence of the high biodiversity of megafauna found in the Kiribati abyss. However, only a minor proportion of Kiribati's deep seabed has been targeted for biological exploration (Rotjan et al., 2014; Cordes, 2017; Kennedy, 2017; this study), and hence further research will be required to characterize the true taxonomic richness of benthic communities in this region. Although no commercial activities have been proposed to date in the Kiribati abyss, future conservation plans and exploration efforts within this area should consider the high biodiversity and low density of megabenthic populations reported in this study if they are to be effective.

DATA AVAILABILITY STATEMENT

All datasets generated for this study are included in the manuscript/**Supplementary Files**.

AUTHOR CONTRIBUTIONS

All authors contributed to the design and implementation of the experimental strategy. JP, AF, and CP supervised the collection and processing of the seafloor imagery data. AY conducted the hydrographic data analysis. ES-L, ST, and CP performed the biological annotation of images. ES-L, AF, and DJ steered the biological survey design. ES-L and ST conducted biological data analysis. ES-L drafted the manuscript, which was critically revised and accepted by all the co-authors.

FUNDING

This work was supported by the United Kingdom Government through the Commonwealth Marine Economies Program, which aims to enable safe and sustainable marine economies across Commonwealth Small Island Developing States. DJ also received support from NERC through National Capability funding to NOC as part of the Climate Linked Atlantic Section Science (CLASS) program, grant number NE/R015953/1. The funders had no role in the study data processing and analysis, decision to publish, or preparation of the manuscript.

ACKNOWLEDGMENTS

We would like to thank Nautilus Minerals Inc., for providing the data for scientific study and the Kiribati Ministry of Fisheries and Marine Resource Development, particularly Tebete England, Kabure Yeeting and Joyce Uan, for their support of the project. The data were obtained under a Marine Scientific Research Permit to Nautilus Minerals Inc., issued by the Environment and Conservation Division of the Kiribati Ministry of Environment, Lands and Agricultural Development. We would also like to thank the scientific party and crew of the Research Vessel "Yuzhmorgeologiya" for their excellent work during marine operations. We would also like to thank Jeffrey Drazen and Astrid Leitner for their help in fish identifications, and Andrew Gooday for his help in the identification of foraminifera specimens.

SUPPLEMENTARY MATERIAL

The Supplementary Material for this article can be found online at: https://www.frontiersin.org/articles/10.3389/fmars.2019.00605/full#supplementary-material

REFERENCES

Aleynik, D., Inall, M. E., Dale, A., and Vink, A. (2017). Impact of remotely generated eddies on plume dispersion at abyssal mining sites in the Pacific. *Sci. Rep.* 7:16959. doi: 10.1038/s41598-017-16912-16912

Amon, D. J., Ziegler, A. F., Dahlgren, T. G., Glover, A. G., Goineau, A., Gooday, A. J., et al. (2016). Insights into the abundance and diversity of abyssal megafauna in a polymetallic-nodule region in the eastern Clarion-Clipperton Zone. *Sci. Rep.* 6:30492. doi: 10.1038/srep30492

Angel, M. V., and Boxshall, G. A. (1990). Life in the benthic boundary layer: connections to the mid-water and sea floor [and Discussion]. *Philos. Trans. R. Soc. Lond. Ser A Math. Phys. Sci.* 331, 15–28. doi: 10.1098/rsta.1990.0053

Becker, J. J., Sandwell, D. T., Smith, W. H. F., Braud, J., Binder, B., Depner, J., et al. (2009). Global bathymetry and elevation data at 30 arc seconds resolution: SRTM30_PLUS. *Marine Geodesy* 32, 355–371. doi: 10.1080/01490410903297766

Benoist, N. M. A., Morris, K. J., Bett, B. J., Durden, J. M., Huvenne, V. A. I., Le Bas, T. P., et al. (2019). Monitoring mosaic biotopes in a marine conservation zone by autonomous underwater vehicle. *Conserv. Biol.* 33, 1174–1186. doi: 10.1111/cobi.13312

Brodeau, L., Barnier, B., Treguier, A. M., Penduff, T., and Gulev, S. (2010). An ERA40-based 461 atmospheric forcing for global ocean circulation models. *Ocean. Model.* 31, 88–104. doi: 10.1016/j.ocemod.2009.10.005

Buesseler, K. O., Lamborg, C. H., Boyd, P. W., Lam, P. J., Trull, T. W., Bidigare, R. R., et al. (2007). Revisiting carbon flux through the ocean's twilight zone. *Science* 316, 567–570. doi: 10.1126/science.1137959

Cairns, S. D. (2016). New abyssal Primnoidae (Anthozoa: Octocorallia) from the clarion-clipperton fracture zone, equatorial northeastern Pacific. *Mar. Biodivers.* 46, 141–150. doi: 10.1007/s12526-015-0340-x

Carey, A. G. (1981). A comparison of benthic infaunal abundance on two abyssal plains in the northeast Pacific Ocean. *Deep Sea Res. Part A Oceanogr. Res. Pap.* 28, 467–479. doi: 10.1016/0198-0149(81)90138-2

Chao, A., Gotelli, N. J., Hsieh, T. C., Sander, E. L., Ma, K. H., Colwell, R. K., et al. (2014). Rarefaction and extrapolation with Hill numbers: a framework for sampling and estimation in species diversity studies. *Ecol. Monogr.* 84, 45–67. doi: 10.1890/13-0133.1

Clarke, K. R. (1993). Non-parametric multivariate analyses of changes in community structure. *Aust. J. Ecol.* 18, 117–143. doi: 10.1111/j.1442-9993.1993.tb00438.x

Colwell, R. (2013). EstimateS: Statistical Estimation of Species Richness and Shared Species From Samples. Version 9. Available at: http://viceroy.eeb.uconn.edu/EstimateS/index.html

Cordes, E. (2017). Discovering deep sea corals of the phoenix islands cruise catalog: FK171005. *Mar. Geosci. Data Syst.* doi: 10.7284/907641

Crowley, P. H. (1992). Resampling methods for computation-intensive data analysis in ecology and evolution. *Annu. Rev. Ecol. Syst.* 23, 405–447. doi: 10.1146/annurev.ecolsys.23.1.405

Davison, A. C., and Hinkley, D. V. (1997). *Bootstrap Methods and Their Application*. Cambridge: Cambridge University Press.

Drazen, J. C., Leitner, A., Morningstar, S., Marcon, Y., Greinert, J., and Purser, A. (2019). Observations of deep-sea fishes and mobile scavengers from the abyssal DISCOL experimental mining area. *Biogeosciences* 16, 3133–3146. doi: 10.5194/bg-16-3133-2019

Durden, J. M., Schoening, T., Althaus, F., Friedman, A., Garcia, R., Glover, A. G., et al. (2016). "Perspectives in visual imaging for marine biology and ecology: from acquisition to understanding," in *Oceanography and Marine Biology: An Annual Review*, Vol. 54, eds R. N. Hughes, D. J. Hughes, I, P. Smith, and A. C. Dale, (Boca Raton, FL: CRC Press), 1–72.

Epp, D. (1984). Possible perturbations to hotspot traces and implications for the origin and structure of the Line Islands. *J. Geophys. Res. Solid Earth* 89, 11273–11286. doi: 10.1029/jb089ib13p11273

Gauss, G. A. (1980). *Kiribati Offshore Survey*. Cruise Report, No. 37 of PE/Kl - l, PE/KI-2; and PE/Kl-3. South Pacific: Joint Offshore Prospecting for Mineral Resources in South Pacific Offshore Areas (CCOP/SOPAC), 14.

Gooday, A. J., Goineau, A., and Voltski, I. (2015). Abyssal foraminifera attached to polymetallic nodules from the eastern Clarion Clipperton Fracture Zone: a preliminary description and comparison with North Atlantic dropstone assemblages. *Mar. Biodivers.* 45, 391–412. doi: 10.1007/s12526-014-0301-9

Gooday, A. J., Holzmann, M., Caulle, C., Goineau, A., Kamenskaya, O., Weber, A. A. T., et al. (2017a). Giant protists (xenophyophores, Foraminifera) are exceptionally diverse in parts of the abyssal eastern Pacific licensed for polymetallic nodule exploration. *Biol. Conserv.* 207, 106–116. doi: 10.1016/j.biocon.2017.01.006

Gooday, A. J., Holzmann, M., Goineau, A., Pearce, R. B., Voltski, I., Weber, A. A. T., et al. (2017b). Five new species and two new genera of xenophyophores (Foraminifera: Rhizaria) from part of the abyssal equatorial Pacific licensed for polymetallic nodule exploration. *Zool. J. Linn. Soc.* 183, 723–748. doi: 10.1093/zoolinnean/zlx093

Gooday, A. J., Sykes, D., Góral, T., Zubkov, M. V., and Glover, A. G. (2018). Micro-CT 3D imaging reveals the internal structure of three abyssal xenophyophore species (Protista, Foraminifera) from the eastern equatorial Pacific Ocean. *Sci. Rep.* 8:12103. doi: 10.1038/s41598-018-30186-30182

Hayes, S. P. (1979). "Benthic current observations at DOMES sites A, B, and C in the tropical north pacific ocean," in *Marine Geology and Oceanography of the Pacific Manganese Nodule Province*, eds J. L. Bischoff, and D. Z. Piper, (Boston, MA: Springer), 83–112. doi: 10.1007/978-1-4684-3518-4_3

Horton, T., et al. (2018). *World Register of Marine Species*. Available at: http://www.marinespecies.org (accessed August 5, 2019).

Hughes, J. A., and Gooday, A. J. (2004). Associations between living benthic foraminifera and dead tests of *Syringammina fragilissima* (Xenophyophorea) in the darwin mounds region (NE Atlantic). *Deep Sea Res. Part I Oceanogr. Res. Pap.* 51, 1741–1758. doi: 10.1016/s0967-0637(04)00112-8

Iken, K., Brey, T., Wand, U., Voigt, J., and Junghans, P. (2001). Food web structure of the benthic community at the porcupine abyssal plain (NE Atlantic): a stable isotope analysis. *Prog. Oceanogr.* 50, 383–405. doi: 10.1016/s0079-6611(01)00062-3

Johnson, N. A., Campbell, J. W., Moore, T. S., Rex, M. A., Etter, R. J., McClain, C. R., et al. (2007). The relationship between the standing stock of deep-sea macrobenthos and surface production in the western North Atlantic. *Deep Sea Res. Part IOceanogr. Res. Pap.* 54, 1350–1360. doi: 10.1016/j.dsr.2007.04.011

Kamenskaya, O. E., Melnik, V. F., and Gooday, A. J. (2013). Giant protists (xenophyophores and komokiaceans) from the Clarion-Clipperton ferromanganese nodule field (eastern Pacific). *Biol. Bull. Rev.* 3, 388–398. doi: 10.1134/s2079086413050046

Kennedy, B. R. C. (2017). *Okeanos Explorer 2017 EX1703 (Collection)*. Silver Spring, MD: National Oceanic and Atmospheric Administration.

Kersken, D., Janussen, D., and Martínez Arbizu, P. (2018). Deep-sea glass sponges (Hexactinellida) from polymetallic nodule fields in the clarion-clipperton fracture Zone (CCFZ), northeastern Pacific: Part I – Amphidiscophora. *Mar. Biodivers.* 48, 545–573. doi: 10.1007/s12526-017-0727-y

Langenkämper, D., Zurowietz, M., Schoening, T., and Nattkemper, T. W. (2017). BIIGLE 2.0 - browsing and annotating large marine image collections. *Front. Mar. Sci.* 4:83. doi: 10.3389/fmars.2017.00083

Levin, L. A., and Gooday, A. J. (1992). "Possible roles for xenophyophores in deep-sea carbon cycling," in *Deep-Sea Food Chains and the Global Carbon Cycle*, eds G. T. Rowe, and V. Pariente, (Dordrecht: Springer), 93–104. doi: 10.1007/978-94-011-2452-2_6

Lim, S.-C., Wiklund, H., Glover, A. G., Dahlgren, T. G., and Tan, K.-S. (2017). A new genus and species of abyssal sponge commonly encrusting polymetallic nodules in the Clarion-Clipperton Zone, East Pacific Ocean. *System. Biodivers.* 15, 507–519. doi: 10.1080/14772000.2017.1358218

Lutz, M. J., Caldeira, K., Dunbar, R. B., and Behrenfeld, M. J. (2007). Seasonal rhythms of net primary production and particulate organic carbon flux to depth describe the efficiency of biological pump in the global ocean. *J. Geophys. Res.* 112:C10011. doi: 10.1029/2006JC003706

Madec, G. (2008). NEMO reference manual, ocean dynamic component: NEMO–OPA. Notes du Pole de modélisation. Institut Pierre-Simon Laplace (IPSL). *Tech. Rep.* 27, 1288–1161.

Marzocchi, A., Hirschi, J. J. M., Holliday, N. P., Cunningham, S. A., Blaker, A. T., and Coward, A. C. (2015). The North Atlantic subpolar circulation in an eddy–resolving global ocean model. *J. Mar. Syst.* 142, 126–143. doi: 10.1016/j.jmarsys.2014.10.007

McClain, C. R., Rex, M. A., and Etter, R. J. (2009). "Deep-sea macroecology," in *Marine Macroecology*, eds J. D. Witman, and K. Roy, (Chicago, IL: University of Chicago Press), 65–100. doi: 10.7208/chicago/9780226904146.003.0003

McClain, C. R., Rex, M. A., and Jabbour, R. (2005). Deconstructing bathymetric body size patterns in deep-sea gastropods. *Mar. Ecol. Prog. Ser.* 297, 181–187. doi: 10.3354/meps297181

Molodtsova, T. N., and Opresko, D. M. (2017). Black corals (Anthozoa: Antipatharia) of the Clarion-Clipperton Fracture Zone. *Mar. Biodivers.* 47, 349–365. doi: 10.1007/s12526-017-0659-6

Murray, J., and Renard, A. F. (1891). *Report on Deep-Sea Deposits Based on the Specimens Collected During the Voyage of H.M.S. Challenger in the years 1872 to 1876. Report on the scientific results of the voyage of HMS Challenger during the years 1873-76*. Edinburgh: H.M. Stationery Office.

Murray, J. W. (1895). *A Summary of the Scientific Results Obtained at the Sounding, Dredging and Trawling Stations of H.M.S. Challenger*. Edinburgh: H.M. Stationery Office.

Nautilus Minerals, (2016). *NI 43-101 Technical Report. TOML Clarion Clipperton Zone Project, Pacific Ocean*. Brisbane, QLD: AMC Consultants, 280.

Obura, D., Stone, G., Mangubhai, S., Bailey, S., Yoshinaga, H., and Barrel, R. (2011). Baseline marine biological surveys of the phoenix islands, July 2000. *Atoll. Res. Bull.* 589, 1–63.

Okamoto, N. (2005). Deep-sea mineral potential in the south pacific region: review of the Japan/SOPAC Deep-sea mineral resources study programme. *Occas. Pap.* 41, 21–30.

Oksanen, J., Guillaume Blanchet, F., Friendly, M., Kindt, R., Legendre, P., McGlinn, D., et al. (2018). *vegan: Community Ecology Package. R package version 2.4-6*. Available at: https://CRAN.R-project.org/package=vegan (accessed April 20, 2019).

Pennington, J. T., Mahoney, K. L., Kuwahara, V. S., Kolber, D. D., Calienes, R., and Chavez, F. P. (2006). Primary production in the eastern tropical Pacific: a review. *Prog. Oceanogr.* 69, 285–317. doi: 10.1016/S0140-6736(14)60844-8

R Core Team, (2017). *R: A Language and Environment for Statistical Computing*. Vienna: R Foundation for Statistical Computing.

Rex, M. A., Etter, R. J., Morris, J. S., Crouse, J., McClain, C. R., Johnson, N. A., et al. (2006). Global bathymetric patterns of standing stock and body size in the deep-sea benthos. *Mar. Ecol. Prog. Ser.* 317, 1–8. doi: 10.3354/meps317001

Rodgers, J. L. (1999). The bootstrap, the jackknife, and the randomization test: a sampling taxonomy. *Multivariate Behav. Res.* 34, 441–456. doi: 10.1207/S15327906MBR3404_2

Rotjan, R., Jamieson, R., Carr, B., Kaufman, L., Mangubhai, S., Obura, D., et al. (2014). "Chapter Eight - establishment, management, and maintenance of the phoenix islands protected area," in *Advance Marine Biology*, eds M. L. Johnson, and J. Sandell, (Cambridge, MA: Academic Press).

Simon-Lledó, E., Bett, B. J., Huvenne, V. A. I., Schoening, T., Benoist, N. M. A., Jeffreys, R. M., et al. (2019a). Megafaunal variation in the abyssal landscape of the clarion clipperton zone. *Prog. Oceanogr.* 170, 119–133. doi: 10.1016/j.pocean.2018.11.003

Simon-Lledó, E., Bett, B. J., Huvenne, V. A. I., Schoening, T., Benoist, N. M. A., and Jones, D. O. B. (2019b). Ecology of a polymetallic nodule occurrence gradient: implications for deep-sea mining. *Limnol. Oceanogr.* 64, 1883–1894. doi: 10.1002/lno.11157

Simon-Lledó, E., Bett, B. J., Huvenne, V. A. I., Köser, K., Schoening, T., Greinert, J., et al. (2019c). Biological effects 26 years after simulated deep-sea mining. *Sci. Rep.* 9:8040. doi: 10.1038/s41598-019-44492-w

Sweetman, A. K., Smith, C. R., Shulse, C. N., Maillot, B., Lindh, M., Church, M. J., et al. (2019). Key role of bacteria in the short-term cycling of carbon at the abyssal seafloor in a low particulate organic carbon flux region of the eastern Pacific Ocean. *Limnol. Oceanogr.* 64, 694–713. doi: 10.1002/lno.11069

Théel, H. (1882). the Holothurioidea, dredged by H.M.S. Challenger during the Years 1873-1876. Part 1. Reports of Science Research Voyage of H.M.S. Challenger. *Zoology* 4, 1–176.

Thistle, D., Yingst, J. Y., and Fauchald, K. (1985). A deep-sea benthic community exposed to strong near-bottom currents on the Scotian Rise (western Atlantic). *Mar. Geol.* 66, 91–112. doi: 10.1016/0025-3227(85)90024-6

Vanreusel, A., Hilario, A., Ribeiro, P. A., Menot, L., and Arbizu, P. M. (2016). Threatened by mining, polymetallic nodules are required to preserve abyssal epifauna. *Sci. Rep.* 6, 26808. doi: 10.1038/srep26808

Weatherall, P., Marks, K. M., Jakobsson, M., Schmitt, T., Tani, S., Arndt, J. E., et al. (2015). A new digital bathymetric model of the World's oceans. *Earth Space Sci.* 2, 331–345. doi: 10.1002/2015ea000107

Conflict of Interest: AF was employed by company Fathom Pacific. JP and CP were employed by company Nautilus Minerals.

The remaining authors declare that the research was conducted in the absence of any commercial or financial relationships that could be construed as a potential conflict of interest.

Copyright © 2019 Simon-Lledó, Thompson, Yool, Flynn, Pomee, Parianos and Jones. This is an open-access article distributed under the terms of the Creative Commons Attribution License (CC BY). The use, distribution or reproduction in other forums is permitted, provided the original author(s) and the copyright owner(s) are credited and that the original publication in this journal is cited, in accordance with accepted academic practice. No use, distribution or reproduction is permitted which does not comply with these terms.

frontiers in Marine Science

ORIGINAL RESEARCH
published: 14 November 2019
doi: 10.3389/fmars.2019.00684

Distributions of the Pelagic Holothurian *Pelagothuria* in the Central Pacific Ocean as Observed by Remotely-Operated Vehicle Surveys

Gina M. Selig[1,2], Amanda N. Netburn[3]* and Mashkoor Malik[3]

[1] Marine Science Department, University of Hawai'i at Hilo, Hilo, HI, United States, [2] National Oceanic and Atmospheric Administration Educational Partnership Program/Minority Serving Institute Scholar, Silver Spring, MD, United States, [3] National Oceanic and Atmospheric Administration Office of Ocean Exploration and Research, Silver Spring, MD, United States

Pelagothuria is the only known genus of holothurian that is considered to be holopelagic. There is thought to be only one species, *Pelagothuria natatrix*, and little is known about its abundance and distribution throughout the global ocean. Most documented observations of *Pelagothuria* are in tropical regions with many in or near water masses with low dissolved oxygen concentrations, suggesting that *Pelagothuria* may be associated with oxygen minimum zone regions. During the spring 2017 NOAA Ship *Okeanos Explorer* Mountains in the Deep Expedition, scientists onboard the ship and participating through telepresence noted seeing an exceptional number of *Pelagothuria* during ROV dives conducted at sites along a transit from Pago Pago, American Samoa to Honolulu, Hawaii. Video from all dives was later reviewed using the video replay and annotation tool SeaTube and *Pelagothuria* were seen at 9 of the 12 ROV dive sites explored. A total of 97 *Pelagothuria* were observed in depths ranging from 196 to 4,440 m, temperatures of 1.3–15.4°C, salinities of 34.5–35.2, and oxygen concentrations of 0.17–3.77 mg L^{-1}. The vertical distribution of *Pelagothuria* averaged 865 m depth, and their observations occurred at means of 5.24°C, 34.56, 1.71 mg L^{-1} for temperature, salinity, and dissolved oxygen, respectively. In 30 percent ($n = 27$) of the occurrences of *Pelagothuria*, the organism was observed at or within site of the seafloor, suggesting that the species may not actually be entirely holopelagic. A literature review was also conducted to look at the biogeography of the taxon. Results suggest that the horizontal distributions of *Pelagothuria* may extend to the Equatorial Pacific region, and the relatively high occurrence of *Pelagothuria* in oxygen minimum zones indicates they may be particularly hypoxia-tolerant. There is some indication that *Pelagothuria* may also be associated with areas of high particle flux. The strong El Niño event that occurred shortly before the expedition and anomalously warm conditions throughout much of the Pacific could have provided conditions favorable to a *Pelagothuria* bloom, however the high abundances of the organism seen on a nearby 2015 expedition and a later 2019 expedition suggest that this may be a persistent feature. The water column in this region has never before been explored with ROVs, and this study demonstrated use of an archived and publicly-accessible exploratory dataset to make novel discoveries.

Keywords: ***Pelagothuria*, oxygen minimum zone, eastern tropical pacific, equatorial pacific, water column exploration, Echinodermata, Holothuroidea**

OPEN ACCESS

Edited by:
Diva Amon, Natural History Museum, United Kingdom

Reviewed by:
George I. Matsumoto, Monterey Bay Aquarium Research Institute (MBARI), United States
Antonina Kremenetskaia, P. P. Shirshov Institute of Oceanology (RAS), Russia

***Correspondence:**
Amanda N. Netburn
amanda.netburn@noaa.gov

Specialty section:
This article was submitted to Deep-Sea Environments and Ecology, a section of the journal Frontiers in Marine Science

Received: *15 June 2019*
Accepted: *22 October 2019*
Published: *14 November 2019*

Citation:
Selig GM, Netburn AN and Malik M (2019) Distributions of the Pelagic Holothurian Pelagothuria in the Central Pacific Ocean as Observed by Remotely-Operated Vehicle Surveys. Front. Mar. Sci. 6:684. doi: 10.3389/fmars.2019.00684

INTRODUCTION

The deep (>200 m) pelagic ocean contains more than 90% of the Earth's habitable volume for multicellular organisms (Robison, 2009; Haddock et al., 2017). Also referred to as the midwater, this environment contains a high abundance and diversity of organisms, yet remains one of the least understood ecosystems on Earth due to the logistical challenges of accessing the deep sea (Robison, 2004; Webb et al., 2010; Netburn et al., 2018). With relatively few direct observations in the pelagic ocean, there is likely a significant amount of undescribed biodiversity of mesopelagic organisms (Webb et al., 2010). It was long thought that the deep pelagic ocean was entirely void of life, but midwater trawling conducted on the HMS Challenger expedition in the 1870s revealed that there is a ubiquitous assemblage of animals inhabiting these depths throughout the global ocean. While trawling continued to reveal the diversity of uniquely-adapted organisms living in the deep pelagic ocean, it was not until William Beebe and Otis Barton began to explore the water column environment with submersibles in the 1930s that the fine-scale spatial distribution and behaviors of midwater organisms could be observed *in situ* (Robison, 2004). While early submersible-based exploration included midwater observations (e.g., Barham, 1966), the focus of deep submergence studies soon largely shifted to seafloor environments. The greatest exception to this was the Johnson Sea-Link program, based at Harbor Branch Oceanographic Institute, which supported significant midwater exploration from the 1970s through the early 2000s (Greene et al., 1988; Widder et al., 1992; Frank and Widder, 1997; Liberatore et al., 1997). In 2016, the human-occupied vehicle (HOV) *Alvin* was used for the first time in decades to survey the pelagic environment in a study of the distribution of water column organisms at Hydrographer Canyon in the northwest Atlantic Ocean (Netburn et al., 2017). The success of this operation in making novel observations and collections demonstrated the value of bringing people directly into the midwater environment. However, HOVs are expensive to operate and their operational endurance is constrained (National Research Council, 1996).

Beginning in the 1980s, remotely operated vehicles (ROVs)—initially developed for industrial uses—were recognized as potential tools for conducting scientific observations in the deep sea. The Monterey Bay Aquarium Research Institute (MBARI), founded in 1987, developed a ROV-based research program to observe and survey midwater environments. Since 1989, MBARI researchers have conducted depth-stratified ROV transects through the upper kilometer of the water column at a reference station in Monterey Canyon (Robison et al., 2017), providing the longest and most comprehensive time series of visual observations in the deep pelagic environment. New taxa are still regularly discovered (e.g., Matsumoto et al., 2003; Dunn et al., 2005; Osborn et al., 2011) and MBARI's annotated and quality-controlled database provides an unprecedented time series (Schlining and Stout, 2006; Schlining et al., 2013) to investigate the relationships between abundance and distributions of organisms in response to environmental variability, as well as a video archive that can be mined for observations such as trophic interactions (Choy et al., 2017) and distributions of bioluminescent organisms (Martini and Haddock, 2017). While limited work has been done in other locations, such as Hawaii, the Gulf of California, and Japan, much of the ocean remains unexplored for water column organisms.

The National Oceanic and Atmospheric Administration's Office of Ocean Exploration and Research (OER) supports ocean exploration to address both current and emerging science and management needs in unexplored areas of the ocean, with a focus on the U.S. Exclusive Economic Zone (EEZ). OER achieves these goals by conducting seafloor mapping, water column acoustic data collection, and ROV surveys with NOAA Ship *Okeanos Explorer* to provide baseline habitat characterizations and sharing the data with the public (Eakins et al., 2019). Standard operations have generally focused on the seafloor, however the *Okeanos Explorer* began conducting water column ROV surveys in 2012 on select dives to collect baseline information on the pelagic environment in response to expressions of interest from the water column scientific community (Ford and Netburn, 2017; Netburn et al., 2018).

During the 2017 Mountains in the Deep Expedition in the Central Pacific ocean, the *Okeanos Explorer* encountered an unexpected abundance of the pelagic holothurian (Class: Holothuroidea), *Pelagothuria*, while conducting both midwater and seafloor ROV surveys (**Figure 1**). There is some disagreement on whether the genus *Pelagothuria* is comprised of multiple species or a single species, *Pelagothuria natatrix* (Ludwig, 1893). Since no specimens were collected during the Mountains in the Deep Expedition for genetic or morphological species confirmation, we refer to these observations by genus only. *Pelagothuria* is the only holothurian that is considered to be holopelagic (Miller and Pawson, 1990) and thus a member of the plankton. Consequently, *Pelagothuria* have an unusual morphology for a holothurian, which Miller and Pawson (1990) described as resembling "an umbrella turned inside out by a gusting wind."

While *Pelagothuria* is anecdotally a cosmopolitan genus, there are only a limited number of confirmed observations in the scientific record and the global abundance and distributions of the taxon remain poorly documented (**Figure 2**). Through a review of published literature and online resources archiving publicly-available data, we identified a total of 428 specimens collected or observed by video (**Figure 2**; **Table S1**; Ludwig, 1893; Chun, 1900; Clark, 1920; Heding, 1940, 1950; Gebruk, 1989; Miller and Pawson, 1990; Jones et al., 2009; Buglass et al., 2019; Morris, 2019; National Museum of Natural History, 2019; Natural History Museum, 2019; OBIS, 2019; Orrell, 2019; Seid, 2019), including 151 specimens collected in the central Pacific in 2015 (Drazen, unpublished data) and 143 *Pelagothuria* seen on a 2019 E/V Nautilus expedition to the same region as our study. *Pelagothuria* are well-documented across tropical regions, however they have been observed in a range of geographies and conditions, such as in the Southern Ocean. The locations of all confirmed *Pelagothuria* observations are available in **Table S1** and **Figure 2**.

Sutton et al. (2017) defined 33 ecoregions—areas with geographically-distinct faunal assemblages (Spalding et al.,

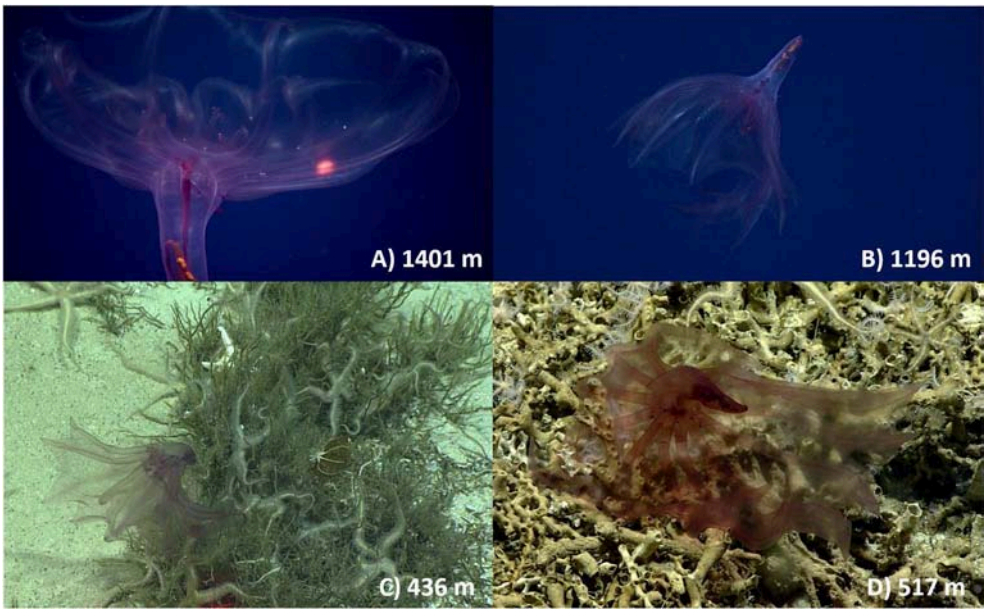

FIGURE 1 | Images of *Pelagothuria* encountered on the NOAA Ship *Okeanos Explorer* Mountains in the Deep Expedition. Depths are indicated in the lower right corner of each image. The images were taken by the ROV *Deep Discoverer* in the water column on: **(A)** Dive 6—Keli'ihananui **(B)** Dive 3—Te Kawhiti a Maui Potiki and at the seafloor: **(C)** Dive 5—Jarvis Island, and **(D)** Dive 5—Jarvis Island. Image credit: NOAA Office of Ocean Exploration and Research, Mountains in the Deep 2017.

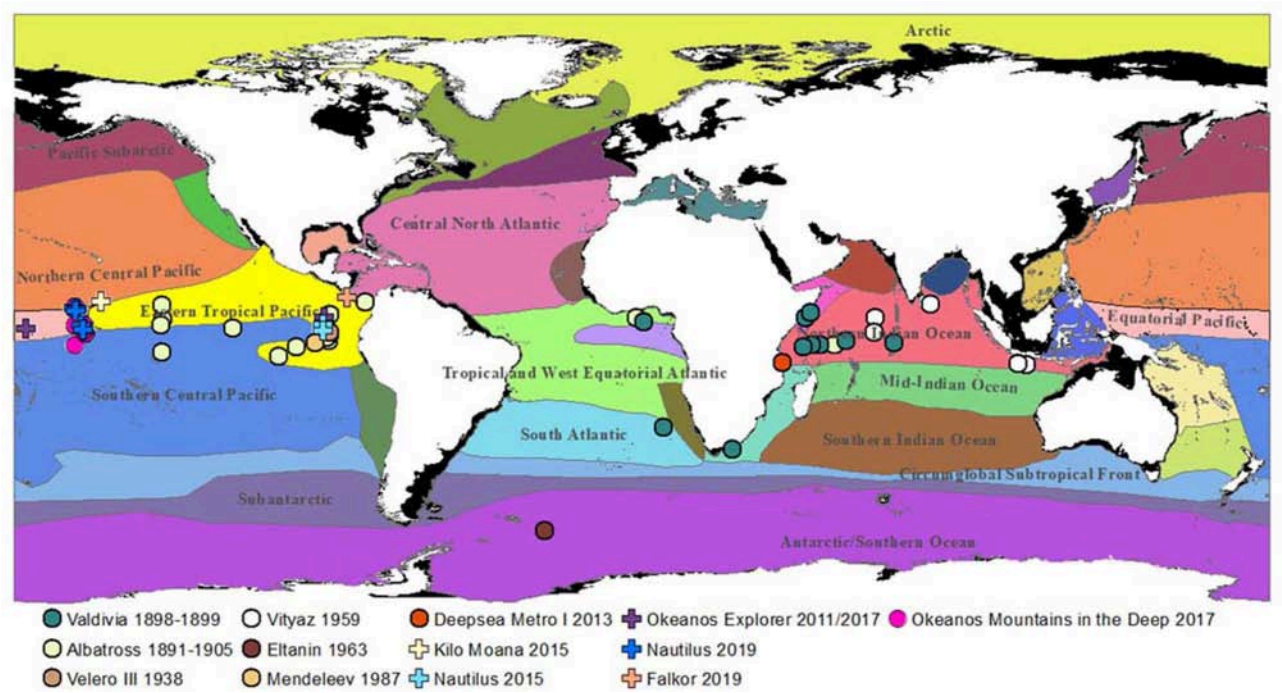

FIGURE 2 | Confirmed observations of *Pelagothuria* overlaid on map of ecoregions as defined by Sutton et al. (2017). Further details on the expeditions are in **Table S1**.

2007)—based on daytime distributions of mesopelagic communities, water masses, presence of an oxygen minimum zone, surface productivity, temperature extremes, and biotic partitioning (**Figure 2**). The limited data available indicate that although *Pelagothuria* likely have a global distribution, they may be especially concentrated at tropical latitudes with

high numbers in the Eastern Tropical Pacific (ETP), Equatorial Pacific, and Northern Indian Ocean ecoregions. Most Pacific observations are associated with the ETP, which is characterized by high primary productivity and strong layering of water masses, indicated by a shallow and abrupt thermocline (Sutton et al., 2017). The circulation of the equatorial Pacific ecoregion is complex, with a westward surface current, an eastward undercurrent within the thermocline, and strong upwelling (Kessler, 2006). This upwelling causes high primary production year round (Sutton et al., 2017). As a result, the assemblage of the mesopelagic fauna of the Equatorial Pacific has been found to differ significantly from those of both the Northern and Southern Central Pacific (Barnett, 1983). The ETP also has an oxygen minimum layer which is notable for both its size and the degree of hypoxia (Fiedler and Talley, 2006). The Northern Indian Ocean has a more broad and homogeneous OMZ than that of the Eastern Pacific margin with localized areas of upwelling (Helly and Levin, 2004; Sutton et al., 2017). Because animals differ greatly in their tolerances to hypoxia (Levin, 2003; Seibel, 2011), the apparent association of *Pelagothuria* with the ETP, Equatorial Pacific, and Northern Indian Ocean ecoregions suggests that the species may be particularly hypoxia-tolerant and thus able to thrive in oxygen minimum zone regions.

While we did not intentionally set out to study *Pelagothuria*, they were observed in high numbers and at multiple sites during ROV-based video surveys conducted on the Mountains in the Deep Expedition (EX1705). The aim of this study was to review video to quantify these observations to describe both geographic and vertical distributions of the poorly understood genus, *Pelagothuria*, examine their distributions in relation to environmental variables to try to identify possible drivers of the high concentrations of *Pelagothuria* observed in the region, and provide a baseline characterization of their habitat. An ancillary goal was to more broadly demonstrate how data collected in an exploratory context can inform understanding of a rare or rarely-observed taxon. Finally, we evaluated the real-time annotation software that was used during this expedition.

METHODS

Shipboard Observations

The Mountains in the Deep Expedition (EX1705) took place on NOAA Ship *Okeanos Explorer* from 27 April to 19 May 2017, as part of NOAA's 2015–2017 Campaign to Address Pacific monument Science, Technology, and Ocean NEeds (CAPSTONE). CAPSTONE was an initiative to collect deepwater baseline information to support science and management decisions in and around the U.S. marine protected areas in the central and western Pacific, areas which include some of the least explored deep waters on Earth (Leonardi et al., 2019). Goals of the Mountains in the Deep Expedition were to collect geological and ecological data in and around two units of the Pacific Remote Islands Marine National Monument—the Jarvis Island Unit and the Kingman Reef and Palmyra Atoll Unit, as well as at Marae Moana in the Cook Islands (Bohnenstiehl et al., 2018). The *Okeanos Explorer* is a 68.3 m vessel equipped with a Kongsberg EM302 30 kHz multibeam sonar for seafloor mapping, Knudsen 3.5 kHz sub-bottom profiler to map geological characteristics below the seafloor, and Simrad 5-frequency EK60 echosounders to detect midwater organisms and features (e.g., gas bubbles). The 6,000 m-rated ROV *Deep Discoverer* (D2) is the primary platform for making *in situ* observations and collections. D2 is tethered to a secondary ROV, *Seirios*, which helps dampen the effects of ship heave, and provides a broad view of operations (Quattrini et al., 2015; Gregory et al., 2016). The forward-facing Insite Pacific Zeus Plus high-definition video Camera on D2 was used as the main scientific camera to direct the mission. Forward-facing illumination was provided by LEDs capable of providing 96,000 lumens of light, some of which were mounted on D2's four adjustable swing arms (D. Rogers, GFOE, pers. comm.). D2 was equipped with two mechanical manipulator arms to sample rocks, corals, and sponges, however at the time of this study, the ROV had no capability to collect pelagic organisms (Gregory et al., 2016). Both D2 and *Seirios* are equipped with SeaBird SBE-911 Plus CTDs with dissolved oxygen, turbidity, and oxygen reduction potential sensors.

All shipboard scientific sonars were typically operating throughout the night and during transits. ROV operations were conducted during the daytime, and the Simrad EK60 echosounders were run during the midwater ROV transects. The ROVs were typically launched at 0830 local time, and recovered after 8 h. Twelve ROV dives were conducted during the expedition between Pago Pago, American Samoa and Honolulu, Hawai'i (**Figure 3**, **Table 1**).

At the beginning of each dive, the ROVs descended to the seafloor, where D2 conducted visual benthic surveys and collected sessile organisms and rocks. At three sites, "Te Kawhiti a Maui Potiki" (Dive 3), "Keliihananui" (Dive 6), and "Kingman Deep" (Dive 12), the total ROV time was extended by 2 h, and exploratory midwater transects were conducted following the seafloor surveys at depths from 300 to 1,800 m during the ascent. While midwater ROV transects should ideally be conducted on descent to minimize known avoidance effects, the dual-body system on the Okeanos Explorer limited operations to ascent only. The *Pelagothuria* did not exhibit notable avoidance behavior, so it is likely that the data were not biased by this limitation. Scientists participating through telepresence selected depths for the midwater transects based on EK60 backscatter (e.g., to target deep scattering layers), ROV CTD profiles (e.g., to target the oxygen minimum), and an interest in surveying across a range of depths. During midwater transects, the ROV proceeded slowly through the water column at 0.1–0.4 kts while maintaining constant depth (within ± 2 m of target depth). Direction of the transects was determined by currents and other conditions to optimize the likelihood of being able to stop the vehicles and take close-up video of target organisms in order to aid species identifications and observe the organisms' behaviors. Exploratory transects were typically conducted for 10 min at each target depth, which included time spent stopped and imaging organisms. Ascent speed between transect depths was on average 30 m min^{-1}. Depths at which the midwater transects were conducted at each site are indicated in **Table 2**.

Seafloor survey locations were selected based on prior knowledge of the region, existing and newly-collected mapping

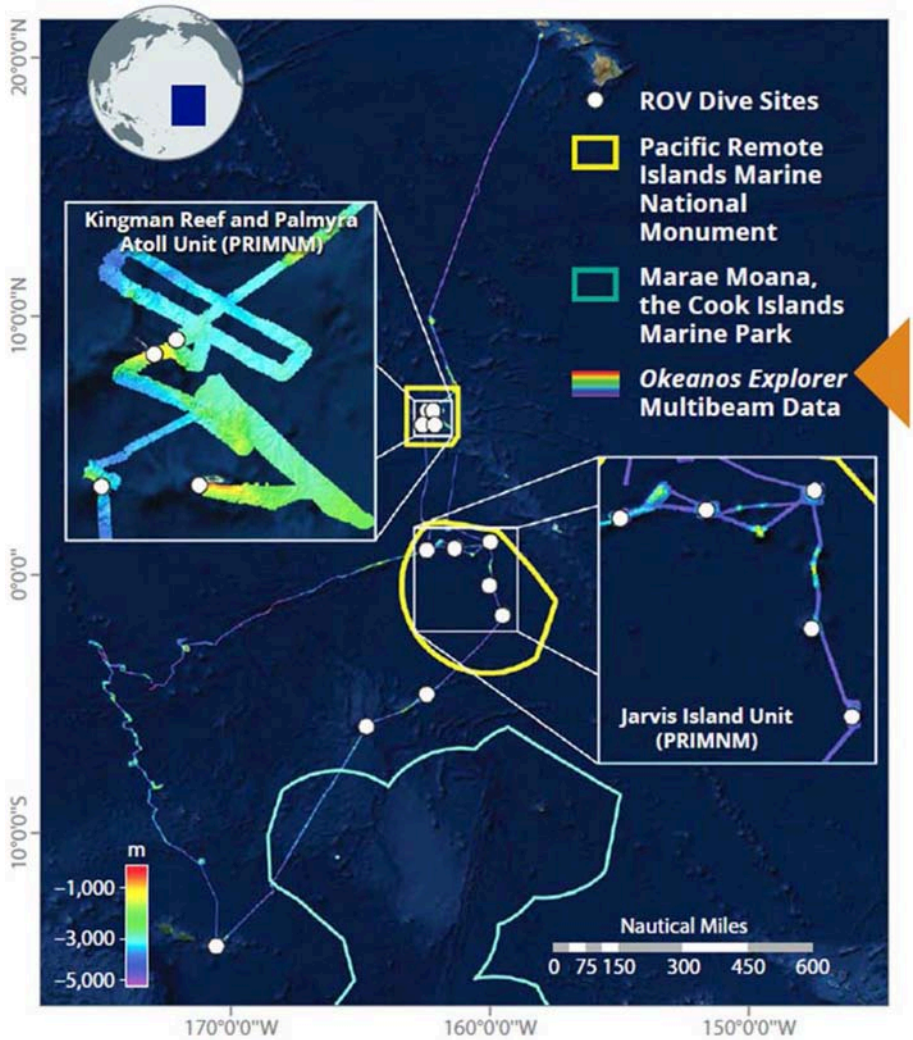

FIGURE 3 | Mountains in the Deep Expedition on NOAA Ship *Okeanos Explorer*, conducted from 27 April to 19 May 2017. The cruise track shows the multibeam bathymetry and the white points are sites where seafloor ROV surveys were conducted. Midwater transects were conducted at three of these sites. *Image courtesy of the NOAA Office of Ocean Exploration and Research*.

data, and science and management interests (e.g., potential for high coral and sponge cover). Seafloor surveys started at the deepest end of the target feature and moved upslope until the dive was complete. D2 transited the seafloor at an average speed of 0.2 kts (∼0.1 m s^{-1}) and intermittently stopped to focus in on or collect samples of characterization targets. The dives had an average ascent and descent rate of 25–30 m min^{-1} (Kennedy et al., 2019).

A unique aspect of *Okeanos Explorer* operations is the use of telepresence technologies to engage a broad range of scientists in expeditions (Peters et al., 2019). Onboard and shore-based scientists collaborated through the use of live-streaming video, a shared conference phone line, a text chatroom, and the SeaScribe annotation system. Live video was broadcast in real time and could be accessed at low-latency through Internet 2 or with a several second delay through standard internet. Scientists from 94 national and international institutions and organizations, as well as 8 divisions within NOAA, participated in the Mountains in the Deep Expedition, providing input on planning, real-time mission guidance, and interpretation of the ROV dives.

Annotations

A new capability introduced to *Okeanos Explorer* in the 2017 field season is the web-based annotation tool, SeaScribe, developed by Ocean Networks Canada (ONC). SeaScribe allows scientists both onshore and onboard the ship to annotate ROV operations (e.g., start and end of midwater transects), organisms observed, and seafloor characteristics (Jenkyns et al., 2013; Gomes-Pereira et al., 2016; Etnoyer et al., 2018). The real-time annotations provide valuable information to researchers and scientists analyzing the video post cruise, however there is currently no standardized process for quality control and assurance, and organism sightings

TABLE 1 | ROV dive locations explored during the Mountains in the Deep expedition.

Dive #	Site #/name	Site description	Date	Latitude	Longitude	Bottom depth (m)	*Total # Pelago.*
1	Aunu'u Unit	NMSAS[a]	4/27/2017	14.28159° S	170.50145° W	239	0
2	Te Tekunga o Fakahotu[†]	Eastern ridge of a mesa in the northern Manikiki Plateau	4/30/2017	5.85984° S	164.69764° W	2,456	0
3*	Te Kawhiti a Maui Potiki[†]	Large ridge structure of Manikiki Plateau	5/2/2017	4.58109° S	162.39475° W	2,179	2
4	Kahalewai[†]	Seamount in Jarvis Island unit of PRIMNM[b]	5/4/2017	1.51171° S	159.45684° W	1,701	20
5	Jarvis Island	Ridge on southeastern slope of Jarvis Island	5/5/2017	0.39815° S	159.96582° W	820	18
6*	Keli'ihananui[†] (proposed name)	Flat topped seamount in Jarvis Island unit of PRIMNM[b]	5/6/2017	1.32337° S	159.93126° W	1,934	14
7	Whaley Seamount[†]	Flat topped seamount in Jarvis Island unit of PRIMNM[b]	5/7/2017	1.08175° N	161.28324° W	1,105	23
8	Fracture Zone	Westernmost edge of Clipperton Fracture Zone	5/8/2017	0.97625° N	162.37959° W	4,572	6
9	West Palmyra Seamount	Unnamed seamount west of Palmyra Atoll	5/10/2017	5.8527° N	162.51034° W	2,172	8
10	South Palmyra Slope	Southwest margin of Palmyra atoll	5/11/2017	5.85802° N	162.13323° W	493	0
11	Kingman Cone	Small cone on flat-topped platform SE of Kingman Reef	5/12/2017	6.36538° N	162.30568° W	1,031	3
12*	Kingman Deep	Small cone NE of Kingman Reef	5/13/2017	6.41887° N	162.22115° W	2,253	3

[*]Sites where midwater transects were conducted.
[†]Proposed name.
[a]National Marine Sanctuary of American Samoa.
[b]Pacific Remote Islands Marine National Monument.

TABLE 2 | For each site, the depths of exploratory water column transects are marked with an X.

Depth (m)	Te Kawhiti a Maui Potiki (Dive 3)	Keli'ihananui (Dive 6)	Kingman deep (Dive 12)
1,800	**X** (13 min)	–	–
1,500	**X** (8)	–	**X** (11 min)
1,400	–	**X** (11 min)	–
1,200	**X** (11)	–	**X** (11)
1,000	–	**X** (11)	–
900	**X** (16)	–	–
750	–	–	–
710	**X** (11)	–	–
600	**X** (11)	–	**X** (12)
475	–	**X** (9)	–
450	**X** (7)	–	–
300	**X** (9)	**X** (9)	**X** (15)

Time (in minutes) spent at each depth is listed in parentheses.

may have been missed or incorrectly annotated during real-time annotations. Detailed review and *post hoc* analysis of the video imagery was therefore required to assure the completeness and accuracy of the real-time annotations.

Within 5–10 min after annotations are made in SeaScribe, they are made publicly available along with streaming video capabilities through a second ONC tool called SeaTube, available at the website: https://data.oceannetworks.ca/SeaTubeV2. OER began beta testing SeaTubeV2 for video playback and annotations in 2017. SeaTube has a function to search the video annotations by text for targets of interest, and has the capability to capture screenshots and video clips, and to bookmark video of interest. An additional capability exists to create and edit new annotations. This function is restricted to registered users in order to track the source of annotations and edit history. We used SeaTube to review and annotate all 12 dives of the *Mountains in the Deep* expedition for *Pelagothuria*, including during midwater transects, seafloor surveys, and the initial descents and final ascents at each site. For each *Pelagothuria* observation entered as an annotation in SeaTube, the position, depth, temperature, salinity, and dissolved oxygen were recorded as measured by sensors on the ROV. The video review and annotations were completed in June–July 2018. A complete list of annotations made during the project is available in **Table S2**.

Analysis/Visualization

We plotted the locations and relative abundances of *Pelagothuria* over the ecoregions defined by Sutton et al. (2017) to qualitatively evaluate whether the taxon is associated with a particular ecoregion within the vicinity of our 2017 study. We also plotted the locations of all known global *Pelagothuria* sightings as identified through literature and database review on a global map of the ecoregions. The depths of the *Pelagothuria*

observations were plotted and overlaid with profiles of salinity, temperature, and dissolved oxygen to inspect for associations with depth, hypoxic waters, and other physical-chemical features throughout the water column. We made frequency histograms of the temperature, salinity, and dissolved oxygen values where *Pelagothuria* were found. The locations of all known *Pelagothuria* observations—including from this study—were plotted over dissolved oxygen at 200 m to qualitatively evaluate for a possible association of *Pelagothuria* with oxygen minimum zone regions (Garcia et al., 2018). We also investigated a possible affinity of *Pelagothuria* for areas with high particle flux by plotting the observations over modeled mean particulate organic carbon flux at 500 m for years 2000–2009 (data provided by A. Yoole; Yoole et al., 2007). Finally, to assess how well the real-time annotations captured occurrences of the taxon, we compared the number of real-time annotations and post-cruise annotations of *Pelagothuria*.

RESULTS

Data from the expedition can be found at the Ocean Exploration Digital Atlas (https://www.ncddc.noaa.gov/website/google_maps/OE/mapsOE.htm; Cantwell et al., 2017). Streaming video can be accessed through SeaTube and higher-resolution clips are available at the OER Video Portal (https://www.nodc.noaa.gov/oer/video/). Video from all 12 ROV dives was reviewed, totaling 96 h of video replay. *Pelagothuria* were observed at 9 of the 12 dive sites, with a total of 97 individuals observed throughout the expedition (**Figure 4**, **Tables 1**, **2**). The last column of **Table 1** lists the total number of *Pelagothuria* observed at each ROV dive site. The ROV dive sites spanned three different ecoregions as defined by Sutton et al. (2017)—Southern Central Pacific, Eastern Tropical Pacific, and the edge of the Northern Central Pacific. Seventy-one percent of the observations of *Pelagothuria* were found in the Equatorial Pacific ecoregion just west of the Eastern Tropical Pacific, 20% were just south of the boundary between the Equatorial Pacific and the Southern Central Pacific ecoregions, and the remainder just north of the boundary between the Equatorial Pacific and the Northern Central Pacific (**Figure 4**).

Pelagothuria were found in depths ranging from 197 to 4,441 m (**Figures 5**, **6**, **Table 3**), temperatures ranging from 1.30 to 15.40°C (**Figures 5–7**, **Table 3**), salinities from 34.6 to 35.2 (**Figures 5**, **6**, **8**, **Table 3**), and dissolved oxygen concentrations from 0.18 to 3.8 mg L^{-1} (**Figures 5**, **6**, **9**, **Table 3**).

DISCUSSION

Biogeography

The data collected from the Mountains in the Deep Expedition, along with the inclusion of other recent unpublished data, significantly increases the number of confirmed direct observations of *Pelagothuria* in the midwater environment, and contributes data points to fill in the global biogeography of the taxon (**Figures 2**, **10**, **11**). While *Pelagothuria* have previously been documented across tropical latitudes, our results add to the known range southerly into the central portion of the Southern Central Pacific and westward into the Equatorial Pacific, which was also corroborated by the observation from the *Okeanos Explorer* Discovering the Deep Expedition (**Figures 2**, **10**, **11**, **Table S1**). However, while the observations made in this study were mostly within the Equatorial Pacific and waters just north and south of this ecoregion, the locations were close to the ETP, where the majority of observations of *Pelagothuria* in the Pacific have previously been made. It is possible that the ETP water mass extended into the Equatorial Pacific ecoregion due to seasonal variation at the time of the Mountains in the Deep Expedition. Sutton et al. (2017) acknowledged that the ecoregion boundaries are not static. We did not see any *Pelagothuria* during dives (sites 1 and 2) in the southernmost portion of the expedition, which are further from the influence of the ETP water mass.

The increased knowledge of the biogeography of a poorly-documented organism demonstrates the value of making exploratory observations in understudied parts of the ocean. Further observations throughout the global ocean are required to fill in the biogeographic gaps in the distribution of *Pelagothuria*. Publicly-available ROV video that was not originally collected for these purposes may be leveraged to observe and document pelagic organisms.

The high numbers of *Pelagothuria* we saw in the Central Pacific begets the question of whether there were environmental parameters that set up conditions favorable to a *Pelagothuria* bloom or whether high abundance of the taxon is a perennial feature of the region. There were some anomalous climatic events in the region in the couple of years before our observations took place that may have put the ocean in an atypical state to support high numbers of these animals (Di Lorenzo et al., 2015). The unusually warm conditions of 2013-15 throughout much of the Pacific (aka "the warm blob"; Bond et al., 2015; Di Lorenzo and Mantua, 2016) and the strong El Niño event of 2015–2016 (Jacox et al., 2016; Chen et al., 2017) had effects on organisms throughout the north Pacific (Cavole et al., 2016; Racault et al., 2017; Brainard et al., 2018), and could have provided conditions favorable for a *Pelagothuria* bloom. The high abundances of the organism seen on a nearby 2015 expedition (J. Drazen, pers. comm.; points labeled "RV Kilo Moana" in **Figures 2**, **10**, **11** and listed in **Table S1**) occurred during the peak of the warming event which supports this hypothesis, but they were also seen in abundance during a 2019 EV Nautilus expedition that occurred after the warm blob/El Niño events. We suggest that dominance of *Pelagothuria* is a persistent, or at least common, feature in the region. Repeat observations in the region across different climatic conditions would continue to provide data to distinguish between these possibilities and understand the factors that are conducive to large populations of this unique organism in this region.

Vertical Distributions

Some notable environmental features were detected in the vertical profiles of temperature, salinity, and dissolved oxygen. The temperature profiles have a stepwise structure at ∼200–300 m at some stations (Dives 4, 5, 6, 7, and 11), indicating there may be submerged mixed layer waters (**Figure 7**). At all but one site (Dive 4), the *Pelagothuria* were found below this

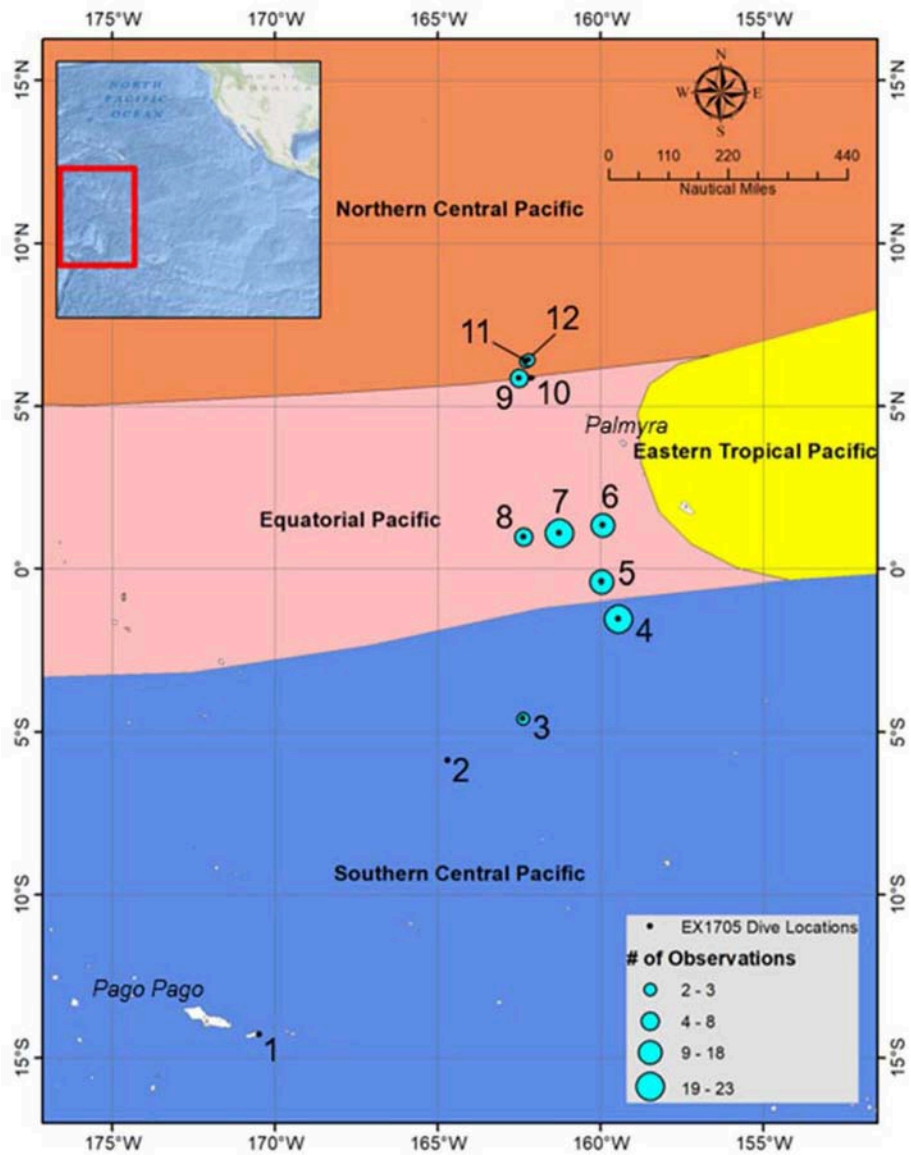

FIGURE 4 | Locations of all dives conducted during the Mountains in the Deep Expedition are marked in black, and labeled by Dive number (refer to **Table 1** for site details). Sites where *Pelagothuria* were observed are indicated by blue circles, sized according to the number of observations. The background is color-coded by ecoregions as defined by Sutton et al. (2017).

layer. At Dive sites 5, 6, 7, 9, 11, and 12 there was a sharp salinity inversion around 200 m (**Figure 8**). The *Pelagothuria* were all observed well below this feature. A pronounced oxygen minimum, with values below (and in some cases, well below) 1.0 mg L^{-1} were observed at stations 4, 5, 9, 11, and 12 (**Figure 9**). At all sites except one (Dive 4), the *Pelagothuria* were found within or below the oxygen minimum, supporting the hypothesis that they are hypoxia tolerant. There was an oxygen inversion between ∼350 and 500 m at Dive sites 3, 4, 5, 7, 9, 11, and 12 that suggest there may be an intrusion at these depths of the more highly-oxygenated Equatorial Pacific water mass into the hypoxic Eastern Tropical Pacific waters. At all but one of these sites, the *Pelagothuria* were encountered either above or below this intrusion, again suggesting that they associate with the ETP. The one site where *Pelagothuria* were found within this layer is at Dive 5, where all individuals encountered were at or very near the seafloor, an anomalous observation we discuss below.

Because all ROV dives were conducted during the daytime, it is not possible to say whether *Pelagothuria* conduct diel vertical migration (DVM), however J. Drazen (pers. comm.) did see distribution patterns suggesting that they *do* based on paired day-night MOCNESS sampling during his nearby expedition off of the R/V *Kilo Moana* in 2015. The depths of peak abundance of *Pelagothuria* as observed by depth-stratified MOCNESS trawls

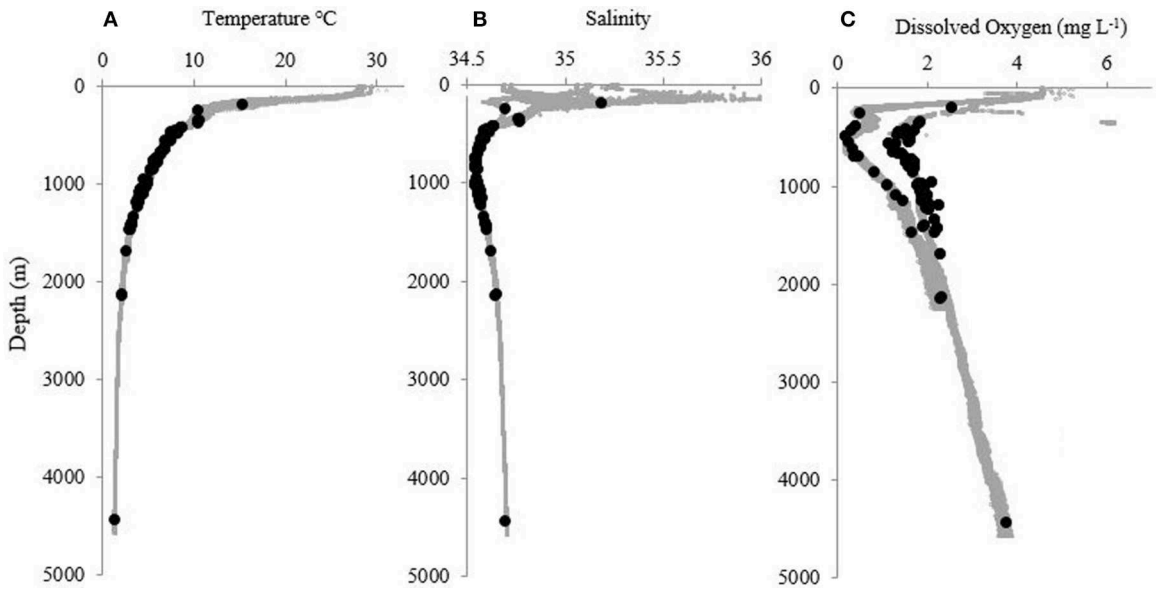

FIGURE 5 | Profiles of **(A)** temperature (°C), **(B)** salinity, and **(C)** dissolved oxygen (mg L^{-1}) at all sites where at least one *Pelagothuria* was observed during the *Mountains in the Deep* expedition. Black points indicate the depth of *Pelagothuria* observations.

were 700–1,500 m during the day with bimodal peaks at night at 100–400 m and 1,000–1,500 m. We suggest that vertically-stratified exploratory transects be conducted throughout the global ocean in order to provide enough data to quantitatively investigate the factors that affect the vertical distributions of *Pelagothuria* and other rarely-observed organisms in the water column. Paired day-night surveys at the same location would not only allow us to look for evidence of DVM, but provide an opportunity to observe the mechanism *Pelagothuria* use to migrate between depths.

Horizontal Distribution

Pelagothuria are broadly distributed across the ocean, and are not limited only to low oxygen regions (**Figure 10**). For example, a documented observation of the animal in the southern ocean suggests they survive in well-oxygenated and cool, high-latitude waters (**Figure 1**, **Table S1**) and they are also seen in relatively well-oxygenated waters off the east coast of Africa. Though observations across the full globe remain limited, we suggest that *Pelagothuria* is cosmopolitan, but may be more common in hypoxic waters because they may be able to outcompete more active animals in these zones.

Another factor that could determine where *Pelagothuria* are found in high abundances is related to their feeding habits. As suspension feeders, they are thought to rely heavily on marine snow and other particulate carbon sources. Numerous benthic deep-sea holothurians are known to be reliant on incoming marine snow (organic particle flux); for example, *Scotoplanes* sp. aggregate toward dead and decaying fish on the seafloor (Miller and Pawson, 1990). A significant correlation between holothurian abundance and organic carbon flux to the seafloor was also found by Sibuet (1985) in the tropical Atlantic. A *Pelagothuria* found in the Indian Ocean had exclusively pelagic components in its gut, such as pelagic diatoms, radiolaria, foraminifera, and copepod feces (Gebruk, 1990). We examined global patterns of organic particle flux from measurements (Mouw et al., 2016) and models (Yoole et al., 2007; Agostini et al., 2009; DeVries and Weber, 2017). There appears to be an association between areas of high carbon flux and *Pelagothuria* sightings, particularly in the Pacific Ocean and in coastal areas, though the association is less clear in the Indian Ocean (**Figure 11**).

Seafloor Observations

Thirty percent ($n = 27$) of the *Pelagothuria* seen on the Mountains in the Deep Expedition were encountered at or within sight of the seafloor. Four individuals were observed directly on the seafloor at Jarvis Island (Dive 5, **Figure 1**), at 517, 473, 436, and 363 m. It was not clear if they were intentionally utilizing the seafloor as habitat or had gotten caught on coral rubble. This benthic survey focused on a small ridge on the southeastern slope of the Jarvis Island Unit of PRIMN which are part of the Line Islands linear volcanic chain (Davis et al., 2002). A high abundance and diversity of marine organisms were observed in this dive compared to others in the expedition which is most likely due to the shallower depth range of 349–820 m. Dead and broken scleractinian coral branches were first encountered at 820 m where the ROV reached bottom. Large carbonate sections of rocks created overhangs that provided a habitat for suspension-feeding fauna. At 415 m bamboo colonies were overgrown by a yellow zoanthid and at 385 m, an area of low relief dense with primnoid fans and urchins was observed (Cantwell et al., 2019).

Pelagothuria are generally described as holopelagic, living and feeding entirely in the water column (Miller and Pawson, 1990). However, there is some evidence that *Pelagothuria* have been

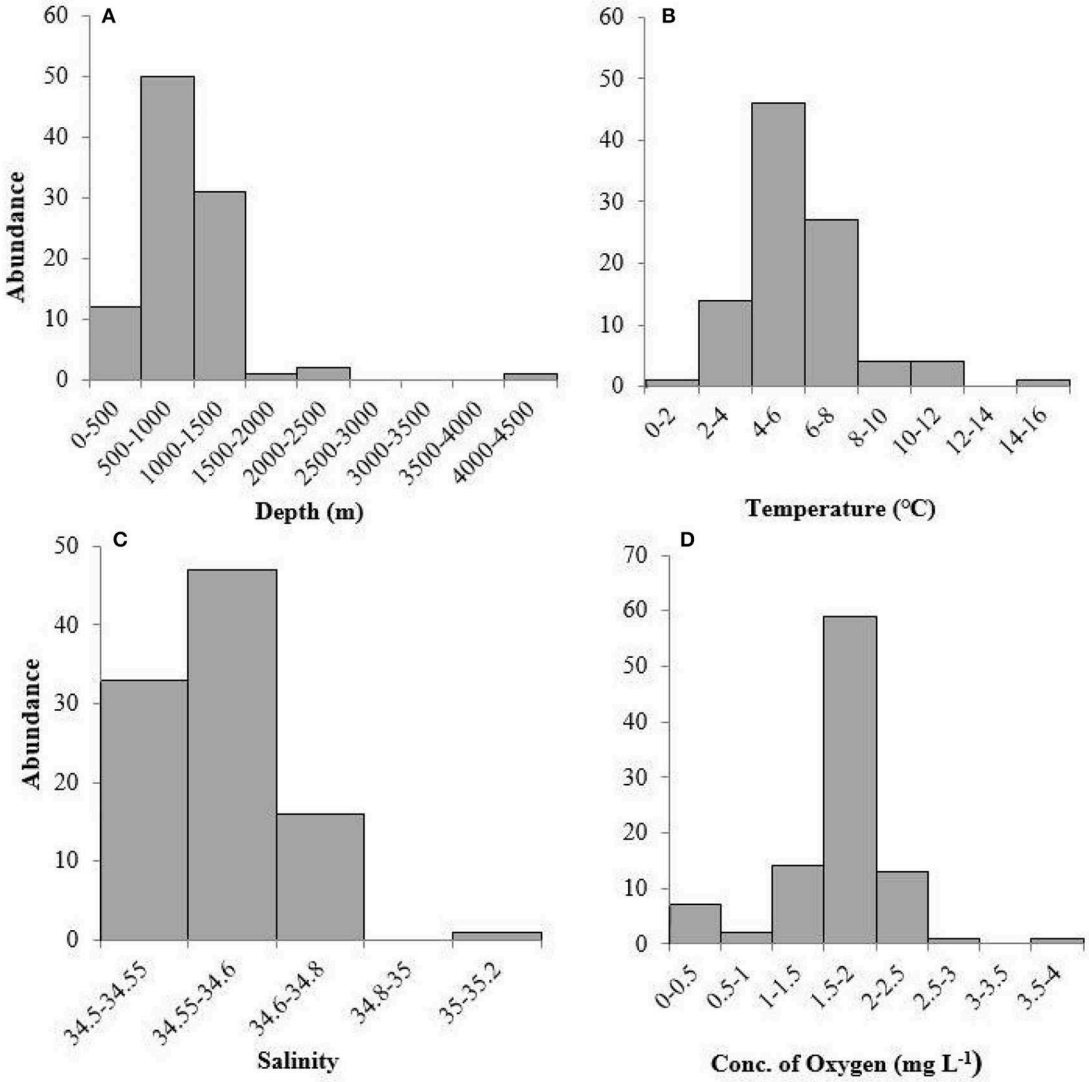

FIGURE 6 | Frequency histograms of **(A)** depth, **(B)** temperature, **(C)** salinity, and **(D)** dissolved oxygen measurements where *Pelagothuria* were observed during the 2017 Mountains in the Deep Expedition.

TABLE 3 | Summary statistics for environmental data where *Pelagothuria* were observed in the 2017 mountains in the Deep Expedition.

	Depth (m)	Temp (°C)	Salinity	Dissolved oxygen (mg L^{-1})
Minimum	197	1.30	34.54	0.17
Maximum	4,441	15.42	35.19	3.77
Mean	929	5.65	34.58	1.65
Standard deviation	503	2.11	0.08	0.53
Median	865	5.24	34.56	1.71

encountered near the seafloor in the past. Lemche et al. (1976) described a *Pelagothuria* from a blurred image that has since been discounted as being a cnidarian (Miller and Pawson, 1990). Miller and Pawson (1990) described the swimming behavior of a *Pelagothuria* that was encountered just meters from the seafloor, but did not consider that the organism may have been associating with the seafloor environment. Though they found only pelagic organisms and unidentifiable organisms in the guts, they only collected a single individual, so there was not a lot of data. It is possible that *Pelagothuria* do settle on the seafloor for periods of time, perhaps related to feeding, reproduction, or shelter. There are thousands of hours of video data available from various deep submergence programs (e.g., Woods Hole Oceanographic Institution's National Deep Submergence Facility, NOAA OER's *Okeanos Explorer* and grant-funded projects, E/V *Nautilus*, etc.) that have been collected over several decades for seafloor investigations. It is likely that numerous individuals of *Pelagothuria* have been imaged but not documented in the literature or available databases. A review of these videos specifically for *Pelagothuria* would help to understand both the prevalence and purpose of their presence on the seafloor. Targeted studies where

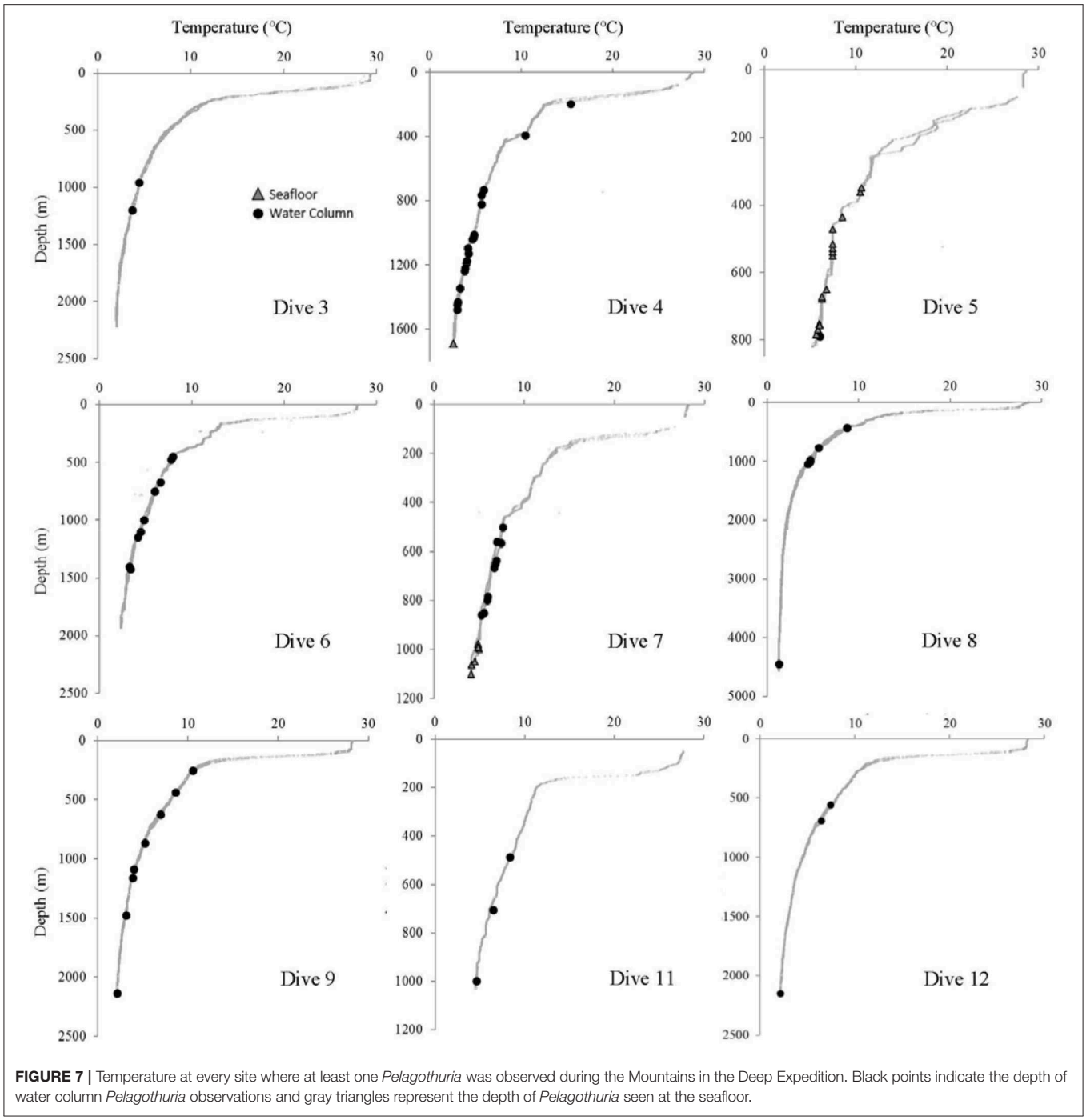

FIGURE 7 | Temperature at every site where at least one *Pelagothuria* was observed during the Mountains in the Deep Expedition. Black points indicate the depth of water column *Pelagothuria* observations and gray triangles represent the depth of *Pelagothuria* seen at the seafloor.

Pelagothuria are known to be abundant, such as in the ETP, could provide an opportunity to make longer observations of the organisms in order to examine their behavior at the seafloor.

Evaluation of Real-Time Annotations

The dataset generated from the real-time annotations and available through SeaTube included 33 annotations of *Pelagothuria*, only about a third of the 97 individuals that were annotated through methodical *post hoc* review of the ROV dives. The accuracy and completeness of the real-time annotations is limited primarily by two factors: (1) available expertise—the researchers annotating the video must have significant expertise to be able to make accurate identifications of a range of different taxa in real time, and (2) limited observation time—organisms in the water column often move past the camera very quickly and multiple organisms may be seen simultaneously, requiring a very fast response time to input all of the annotations. An inherent challenge of the community-based approach to exploration is the

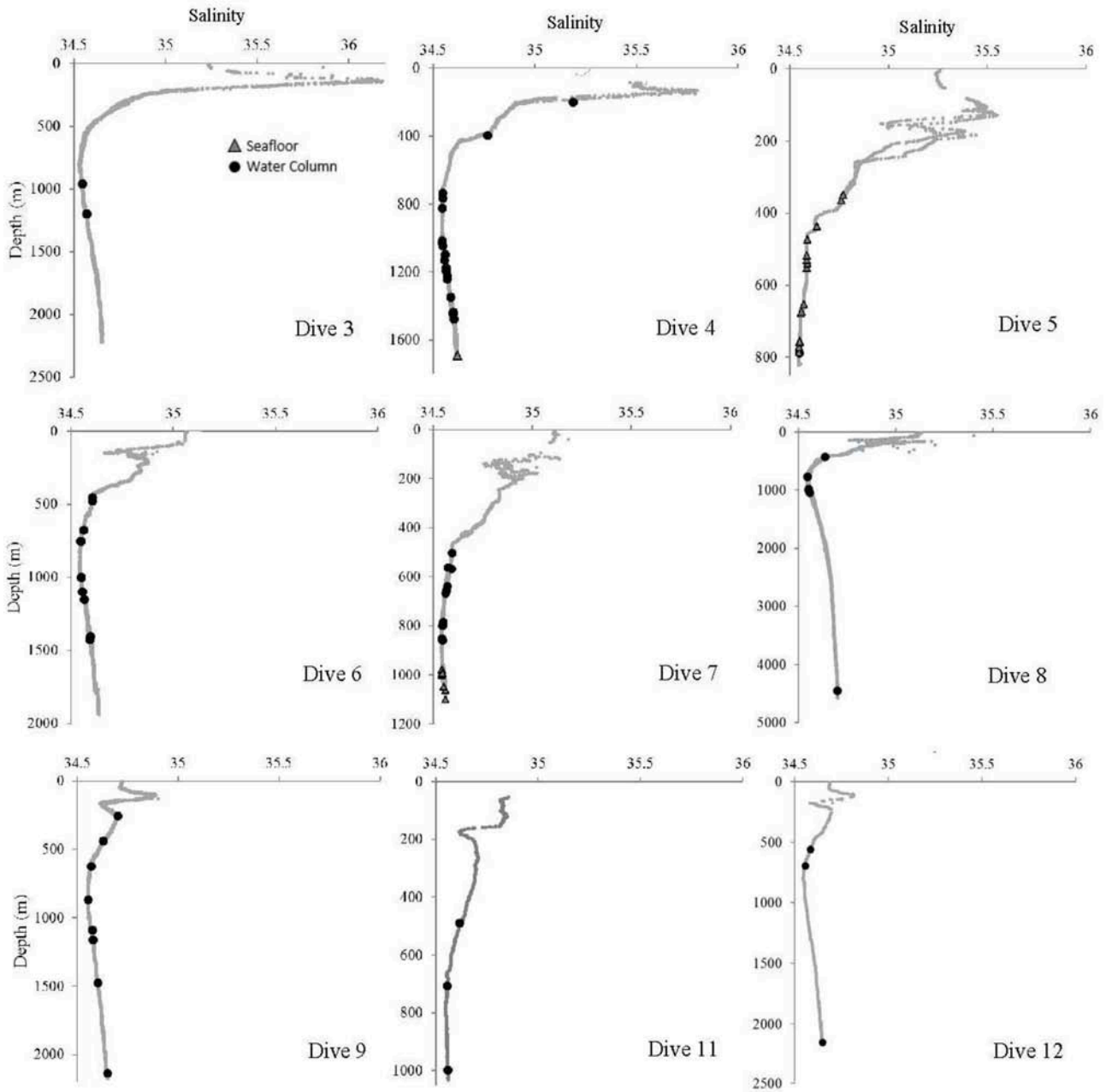

FIGURE 8 | Salinity at each site where at least one *Pelagothuria* was observed during the Mountains in the Deep Expedition. Black points indicate the depth of water column *Pelagothuria* observations and gray triangles represent the depth of *Pelagothuria* seen at the seafloor.

willingness of participating scientists to consistently annotate the video and share these annotations. NOAA Office of Ocean Exploration and Research has started to address this challenge by providing SeaTube as an annotation tool that enables participants to annotate both in real-time and after the dive is complete. However, if the annotations are made only in personal notebooks, in chatrooms, or in individually-managed databases, as often occurs, they will not be available to the broader community.

Creating a quality-controlled database of annotations is a challenge for any operation that utilizes a distributed network of scientists and is committed to providing publicly-available data (e.g., Ocean Exploration Trust's E/V *Nautilus*, Schmidt Ocean Institute's R/V *Falkor*). While some powerful tools exist for making both real-time and *post hoc* annotations, such as Monterey Bay Aquarium Research Institute's Video Annotation and Reference System, such tools are designed for a traditional research expedition, where the onboard team has the needed

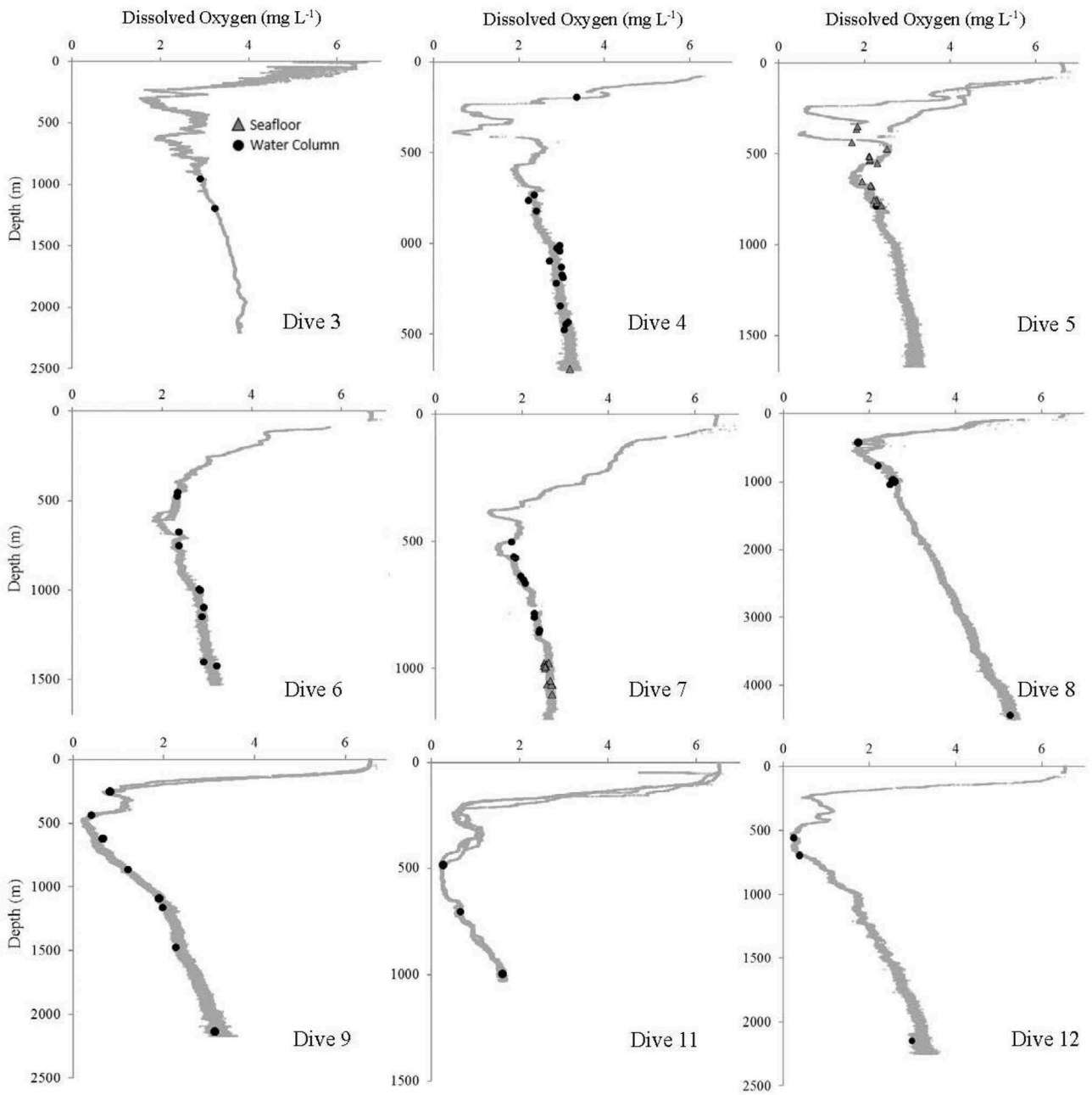

FIGURE 9 | Dissolved oxygen at each site where at least one *Pelagothuria* was observed during the Mountains in the Deep Expedition. Black points indicate the depth of water column *Pelagothuria* observations and gray triangles represent the depth of *Pelagothuria* seen at the seafloor.

expertise. Okeanos Explorer operations sail with a limited science team, and rely on a distributed network of experts for annotations.

Tools like SeaTube make the video and environmental data accessible to interested researchers in an online collaborative environment, which alleviates some issues with accessing and integrating the datasets following an expedition. However, reviewing and annotating video remains extremely labor and time intensive. Reviewing the video to build a complete and accurate dataset of *Pelagothuria* observations for this study required a significant time commitment, around 10 h beyond the 96 h of video reviewed, and this was for a study for just a single target. Though we know of multiple publicly-available video archives, including from other *Okeanos Explorer* expeditions, this study was limited to a single expedition because of this constraint.

Recommendations to improve the completeness and accuracy of real-time annotations include taxonomic training and delegating individuals to make the annotations. These

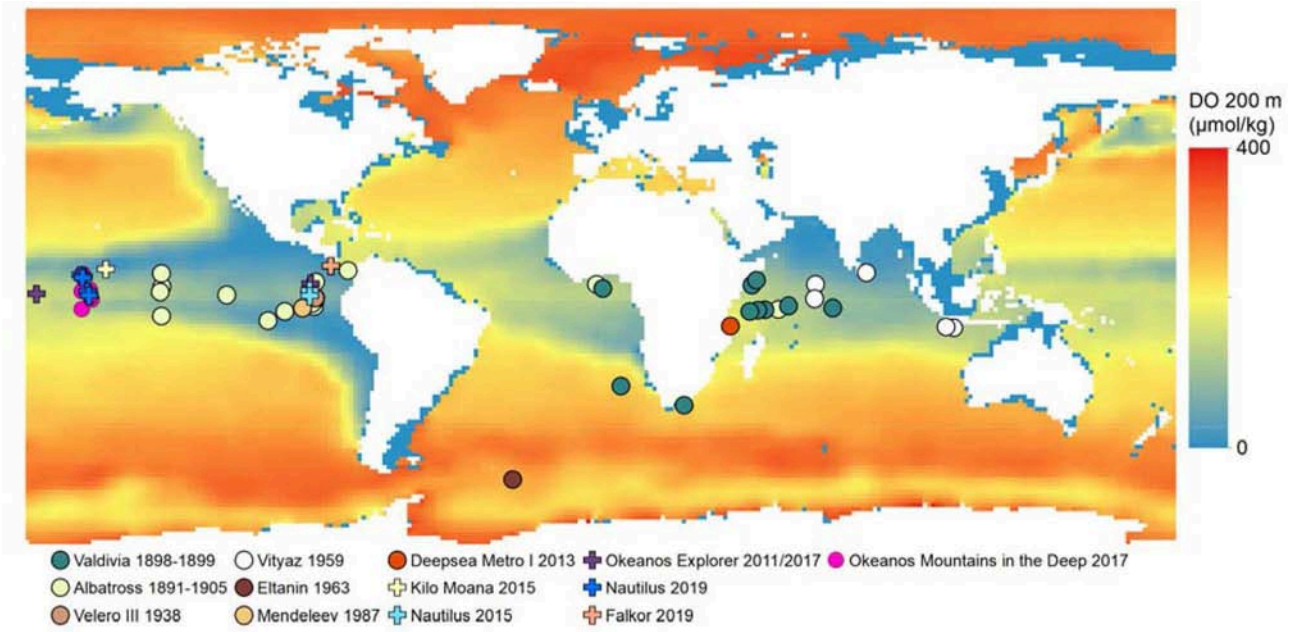

FIGURE 10 | Observations of *Pelagothuria* overlaid on map of dissolved oxygen (µmol kg^{-1}) at 200 m from the NOAA National Center for Environmental Information (NCEI) World Ocean Atlas 2018 (Garcia et al., 2018). Further details on the expeditions are in **Table S1**.

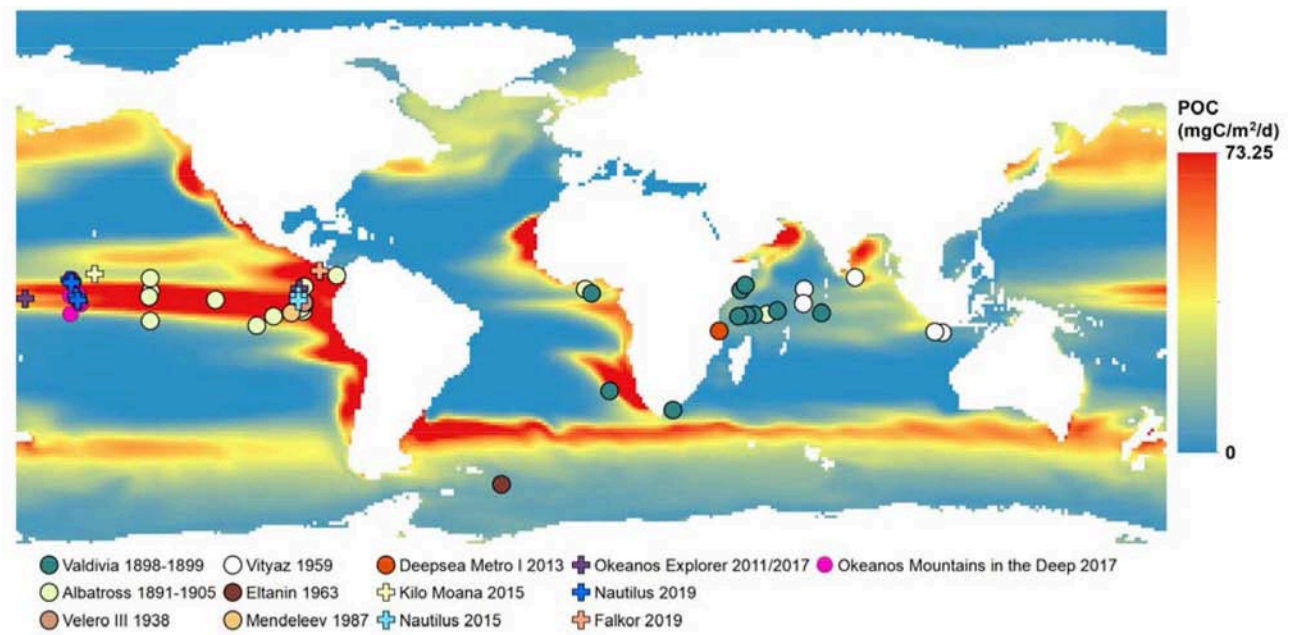

FIGURE 11 | Observations of *Pelagothuria* overlaid on a map of mean particulate organic carbon flux at 500 m as modeled by Yoole et al. (2007, and Yoole, pers. comm.) for years 2000–2009. Further details on the expeditions are in **Table S1**.

recommendations would aid scientists across taxonomic interests and disciplines, and apply to *post hoc* annotations as well. Though there would be costs involved with these approaches (both in money and time), the benefit of having quality-controlled annotations would save scientists significant time in the post-cruise analysis as they would be able to find the video of organisms and features of interest.

A promising opportunity to significantly reduce the time and labor required to make video annotations is to apply machine learning algorithms to image classification. However, many complete and accurate annotations are required in order to train the machine learning algorithms. Other challenges to using machine learning for image classification exist such as the orientation of the marine organism and turbidity of the water (Margolis et al., 2019). Complete and accurate annotations of the whole range of taxa encountered on exploratory expeditions would greatly improve our understanding of biogeography, and provide baseline characterization data at every explored site that can be used to make comparisons between locations and over time.

CONCLUSION

Documented observations of *Pelagothuria* are relatively rare throughout the global ocean, however it is clear from this and several other studies that they are not exactly uncommon. Through this study, we contributed substantially to the number of known encounters with *Pelagothuria*, found evidence that they are able to tolerate highly hypoxic waters, and discovered they associate with the seafloor in fairly significant numbers. Observations throughout the global ocean and over time are required to test whether *Pelagothuria* exist in high abundances in other water masses and conditions and to understand the nature of their association with the seafloor. While this study focused on just a single taxon, we emphasize the value of conducting similar studies on a range of water column organisms in order to provide a comprehensive understanding of abundances and distributions of deep pelagic organisms.

There has been recent interest in increasing understanding of processes and life in the water column (Netburn, 2018). The water column has historically been overlooked by exploration initiatives, despite the outsize role of the deep pelagic environment in supporting marine food webs and fisheries production, and regulating climate through carbon transport to the deep seafloor (Robinson et al., 2010). Data on the diversity and distributions of the organisms living in the water column provide baseline characterizations which may be used to monitor the responses of this community to both natural climate variability and anthropogenic climate change, marine pollution, and overfishing (Ramirez-Llodra et al., 2011). Though *Pelagothuria* are not likely to be the direct targets of fisheries, the high numbers we observed in the Central Pacific Ocean and their circumglobal distributions indicate that they may have a critical role in the marine environment. Thus, understanding their distributions and the factors that support their populations is relevant to understanding the marine environment as a whole. This study demonstrates how dedicating survey time and *post hoc* analysis for water column exploration can fill gaps in our understanding of this underexplored portion of the marine environment. It will take many such studies, as well as a persistent, expansive, and coordinated community effort to achieve the goals of knowing, understanding, and monitoring the distributions and behaviors of the full diversity of fauna in the deep pelagic environment.

DATA AVAILABILITY STATEMENT

All datasets generated for this study are included in the article/**Supplementary Material**.

AUTHOR CONTRIBUTIONS

AN led the conceptualization and design of the work, acquisition of data, interpretation of the data, and the writing and editing the paper. GS led the analysis and initial draft of the manuscript, created figures, and contributed to design, writing, and editing of the manuscript. MM contributed to the conceptualization and design of the work, figure generation, and interpretation of the data, particularly with regards to the evaluation of the real-time annotations. He also contributed to writing and editing of the manuscript. All authors approved the final content for submission.

ACKNOWLEDGMENTS

This study was sponsored by the NOAA Office of Education Educational Partnership Program (EPP) and the NOAA Office of Ocean Exploration and Research and made possible by the efforts of NOAA Ship *Okeanos Explorer* Expedition Coordinator, Kasey Cantwell, Expedition Mapping Lead, Michael White, and the onboard Science Leads Scott France and Del Bohnenstiehl. We thank all the onboard crew, the Global Foundation for Ocean Exploration ROV pilots, and associated personnel involved with the Mountains in the Deep Expedition, as well as the network of scientists participating via telepresence. Data was made available by Jeff Drazen and Yuuki Niimi, from work supported by the National Science Foundation. Data from the Ocean Exploration Trust's E/V Nautilus cruise NA110 was sponsored by the NOAA-OER grant NA17OAR0110336 and permitted by NOAA, the Pacific Remote Islands Marine National Monument, and the U.S. Fish and Wildlife Service (permit 12543-19002). Timothy DeVries and Andrew Yoole provided assistance on POC flux data. We thank Erica Ta for guidance with ArcGIS. English translations of literature were made available by Andrey Gebruk and Antonina Kremenetskaia. Christopher Mah provided previously-translated literature as well.

SUPPLEMENTARY MATERIAL

The Supplementary Material for this article can be found online at: https://www.frontiersin.org/articles/10.3389/fmars.2019.00684/full#supplementary-material

REFERENCES

Agostini, V., Arico, S., Briones, E., Clark, M., Cresswell, I., Gjerde, K., et al. (2009). *Global Open Oceans and Deep Seabed (GOODS) Biogeographic Classification*. UNESCO-IOC Technical Series, 84.

Barham, E. G. (1966). Deep scattering layer migration and composition: observations from a diving saucer. *Science* 151, 1399–1403. doi: 10.1126/science.151.3716.1399

Barnett, M. A. (1983). Species structure and temporal stability of mesopelagic fish assemblages in the Central Gyres of the North and South Pacific Ocean. *Mar. Biol*. 74, 245–256. doi: 10.1007/BF00403448

Bohnenstiehl, D. R., France, S. C., Cantwell, K., and White, M. (2018). "Mountains in the deep: exploration of the seamounts of the Central Pacific Basin," in *New Frontiers in Ocean Exploration: The E/V Nautilus, NOAA Ship Okeanos Explorer, and R/V Falkor 2017 Field Season,* Vol. 31, eds N. A. Raineault, J. Flanders, and A. Bowman (Oceanography), 78–81.

Bond, N. A., Cronin, M. F., Freeland, H., and Mantua, N. (2015). Causes and impacts of the 2014 warm anomaly in the NE Pacific. *Geophys. Res. Lett*. 42, 3414–3420. doi: 10.1002/2015GL063306

Brainard, R. E., Oliver, T., McPhaden, M. J., Cohen, A., Venegas, R., Heenan, A., et al. (2018). Ecological impacts of the 2015/16 El Niño in the central equatorial Pacific. *Bull. Am. Meteorol. Soc*. 99, S21–S26. doi: 10.1175/BAMS-D-17-0128.1

Buglass, S., Arnés-Urgellés, C., Marsh, L., Nagy, S. *Data From: Macroinvertebrate Groups Found on Deep-Sea Volcanic Habitats in the Galapagos Marine Reserve in the Eastern Tropical Pacific Ocean: Echinoderms*. Version 1.9. Charles Darwin Research Station, Occurrence dataset. (2019).

Cantwell, K., France, S., and Bohnenstiehl, D. (2017). *Oceanographic Data and Information Collected During the EX1705 American Samoa, Kingman/Palmyra, Jarvis (ROV and Mapping) Expedition on NOAA Ship Okeanos Explorer in the Pacific Ocean From 2017-04-27 to 2017-05-19 (NCEI Accession 0163984)*. Version 1.1. NOAA National Centers for Environmental Information, Silver Spring, MD.

Cantwell, K., France, S. C., Bohnenstiehl, D. R., White, M. P., Netburn, A. N., and Bowman, A. (2019). *EX1705 Mountains in the Deep: Exploring the Central Pacific Basin Expedition Report*. Office of Ocean Exploration and Research, Office of Oceanic and Atmospheric Research, NOAA, Silver Spring, MD.

Cavole, L. M., Demko, A. M., Diner, R. E., Giddings, A., Koester, I., and Pagniello, C. (2016). Biological impacts of the 2013–2015 warm-water anomaly in the Northeast Pacific: winners, losers, and the future. *Oceanography* 29, 273–285. doi: 10.5670/oceanog.2016.32

Chen, L., Li, T., Wang, B., and Wang, L. (2017). Formation mechanism for 2015/16 super El Niño. *Sci. Rep*. 7:2975. doi: 10.1038/s41598-017-02926-3

Choy, A., Haddock, S., and Robison, B. H. (2017). Deep pelagic food web structure as revealed by *in situ* feeding observations. *Proc. R. Soc. B Biol. Sci*. 284:20172116. doi: 10.1098/rspb.2017.2116

Chun, C. (1900). *Aus den Tiefen des Weltmeeres*. Jena: Gustav Fischer.

Clark, H. L. (1920). Holothuroidea. Report XXXII on the scientific results of the expedition of the "Albatross" to the Tropical Pacific, 1899-1900 and 1904-1905. *Mem. Mus. Comp. Zool. Harv. Coll.* 39, 121–154.

Davis, A. S., Gray, L. B., Clague, D. A., and Hein, J. R. (2002). The Line Islands revisited: new 40Ar/39Ar geochronologic evidence for episodes of volcanism due to lithospheric extension. *Geochem. Geophys. Geosyst*. 3, 1–28. doi: 10.1029/2001GC000190

DeVries, T., and Weber, T. (2017). The export and fate of organic matter in the ocean: new constraints from combining satellite and oceanographic tracer observations. *Global Biogeochem. Cycles* 31, 535–555. doi: 10.1002/2016GB005551

Di Lorenzo, E., Combes, V., Keister, J. E., Strub, P. T., Thomas, A. C., Franks, P. J. S., et al. (2015). Synthesis of Pacific Ocean climate and ecosystem dynamics. *Oceanography* 26, 68–81. doi: 10.5670/oceanog.2013.76

Di Lorenzo, E., and Mantua, N. (2016). Multi-year persistence of the 2014/15 North Pacific marine heatwave. *Nat. Clim. Change* 6, 1042–1047. doi: 10.1038/nclimate3082

Dunn, C. W., Pugh, P. R., and Haddock, S. H. D. (2005). Marrus claudanielis, a new species of deep-sea physonect siphonophore (Siphonophora, Physonectae). *Bull. Mar. Sci*. 76, 699–714.

Eakins, B., Gottfried, S., Murphy, P., Lovalvo, D., and Sowers, D. (2019). "It takes a village! Managing data from Okeanos Explorer," in *New Frontiers in Ocean Exploration: The E/V Nautilus, NOAA Ship Okeanos Explorer, and R/V Falkor 2018 Field Season,* Vol. 150, eds N. A. Raineault and J. Flanders (Oceanography) 106–109.

Etnoyer, P. J., Malik, M., Sowers, D., Ruby, C., Bassett,.R., Dijkstra, J., et al. (2018). "Working with video to improve deep-sea habitat characterization," in *New Frontiers in Ocean Exploration: The E/V Nautilus, NOAA Ship Okeanos Explorer, and R/V Falkor 2017 Field Season*, Vol. 31, eds N. A. Raineault, J. Flanders, and A. Bowman (Oceanography), 64–67. doi: 10.5670/oceanog.2018.supplement.01

Fiedler, P. C., and Talley, L. D. (2006). Hydrography of the Eastern Tropical Pacific: a review. *Prog. Oceanogr*. 69, 143–180. doi: 10.1016/j.pocean.2006.03.008

Ford, M., and Netburn, A. N. (2017). "The 2016 midwater exploration of the Mariana Region," in: *New Frontiers In Ocean Exploration: The E/V Nautilus, NOAA Ship Okeanos Explorer, and R/V Falkor 2016 Field Season*, Vol. 30, eds K. L. C. Bell, J. Flanders, A. Bowman, and N. A.Raineault (Oceanography), 36–37. doi: 10.5670/oceanog.2017.supplement.01

Frank, T. M., and Widder, E. A. (1997). The correlation of downwelling irradiance and staggered vertical migration patterns of zooplankton in Wilkinson Basin, Gulf of Maine. *J. Plankt. Res*. 19, 1975–1991. doi: 10.1093/plankt/19.12.1975

Garcia, H. E. K., Weathers, C. R., Paver, I., Smolyar, T. P., Boyer, R., Locarnini, A., et al. (2018). *Data From: World Ocean Atlas 2018, Volume 3: Dissolved Oxygen, Apparent Oxygen, Utilization, and Oxygen Saturation*. A. Mishonov Technical Ed. NOAA Atlas *NESDIS* 83, 38.

Gebruk, A. V. (1989). Revision of the family Pelagothuriidae (Holothuroidea, Elasipoda) with a review of *Enypniastes eximia* and *Pelagothuria natatrix*. 1. Review of the family Pelagothuriidae (Elasipoda). *Russ. J. Zool*. 68, 57–66.

Gebruk, A. V. (1990). Revision of Pelagothuriidae (Holothurioidea, Elasipoda) with a review of swimming holothurians and their origin. *Russ. J. Zool*. 69, 60–68.

Gomes-Pereira, J. N., Auger, V., Beisiegel, K., Benjamin, R., Bergmann, M., Bowden, D., et al. (2016). Current and future trends in marine image annotation software. *Prog. Oceanogr*. 149, 106–120. doi: 10.1016/j.pocean.2016.07.005

Greene, C. H., Wiebe, P. H., Burczynski, J., and Youngbluth, M. J. (1988). Acoustical detection of high-density krill demersal layers in the submarine canyons off Georges Bank. *Science* 241, 359–361. doi: 10.1126/science.241.4863.359

Gregory, T., Lovalvo, D., Mohr, B., McLetchie, K., and Ryan, M. (2016). "Advancing undersea technology." in: *New Frontiers In Ocean Exploration: The E/V Nautilus and NOAA Ship Okeanos Explorer 2015 Field Season,* Vol. 29, eds K. L. C. Bell, M. L. Brennan, J. Flanders, N. A. Raineault, A. Wagner (Oceanography), 52–55. doi: 10.5670/oceanog.2016.supplement.01

Haddock, S. H. D., Christianson, L. M., Francis, W. R., Martini, S., Dunn, C. W., Pugh, P. R., et al. (2017). Insights into the biodiversity, behavior, and bioluminescence of deep-sea organisms using molecular and maritime technology. *Oceanography* 30, 38–47. doi: 10.5670/oceanog.2017.422

Heding, S. G. (1940). Die Holothurien der Deutschen Tiefsee-Expedition. II. Aspidochirote und Elasipode Formen. *Wiss. Ergebn. Deuts. Tiefsee Exped.* 24, 317–375.

Heding, S. G. (1950). Uber die Planktothuria der deutschen Tiefsee-Expedition, nebsteinigen Bemerkungen uber die Systematik der pelagischen Holothurien. *Zool. Anzeiger*. 145, 111–118.

Helly, J. J., and Levin, L. A. (2004). Global distribution of naturally occurring marine hypoxia on continental margins. *Deep Sea Res. Part I Oceanogr. Res. Pap*. 51, 1159–1168. doi: 10.1016/j.dsr.2004.03.009

Jacox, M. G., Hazen, E. L., Zaba, K. D., Rudnick, D. L., Edwards, C. A., and Moore, A. M. (2016). Impacts of the 2015-2016 El Nino on the California current system: early assessment and comparison to past events. *Geophys. Res. Lett*. 43, 7072–7080. doi: 10.1002/2016GL069716

Jenkyns, R., Gervais, F., and Pirenne, B. (2013). "SeaScribe: an annotation software for remotely operated vehicle dive operations," in *2013 OCEANS-San Diego*, 1–5.

Jones, D. O. B., Gates, A. R., Curry, R. A., Thomson, M., Pile, A., and Benfield, M. (2009). *Data From: SERPENT Project Media Database Archive*. Available online at: http://archive.serpentproject.com/2555/

Kennedy, B. R. C., Cantwell, K., Malik, M., Kelley, C., Potter, J., Elliott, K. P., et al. (2019). The unknown and the unexplored: insights into the Pacific Deep Sea following NOAA CAPSTONE expeditions. *Front. Mar. Sci.* 6:180. doi: 10.3389/fmars.2019.00480

Kessler, W. S. (2006). The circulation of the eastern tropical Pacific: a review. *Prog. Oceanogr*. 69, 181–217. doi: 10.1016/j.pocean.2006.03.009

Lemche, H., Hansen, B., Madsen, F., Tendal, O., and Wolff, T. (1976). Hadal life as analysed from photographs. *Vidensk Medd fra Dansk naturh Foren.* 139, 263–336.

Leonardi, A., Armor, J., Montanio, P., and Cisco, W. (2019). "NOAA's campaign to address pacific monument science, technology, and ocean needs," in *New Frontiers In Ocean Exploration: The E/V Nautilus, NOAA Ship Okeanos Explorer, and R/V Falkor 2018 Field Season*, Vol. 150, eds N. A. Raineault and J. Flanders (Oceanography), 48–53.

Levin, L. A. (2003). Oxygen minimum zone benthos: adaptation and community response to hypoxia. *Oceanogr. Mar. Biol.* 41, 1–45.

Liberatore, D., Askew, T., Tusting, R., and Olson, S. (1997). "The manned submersible as an effective sampling and imaging platform," in *Oceans '97 MTS/IEEE: Conference proceedings: World Trade and Convention Centre, Halifax, Nova Scotia, Canada* (Fort Lauderdale, FL: Oceans '96 MTS/IEEE Conference Committee), 51-58.

Ludwig, H. (1893). Reports of an exploration off the West Coast of Mexico, Central and South America, and off the Galapagos Islands, in charge of Alexander Agassiz, by the U.S. Fish Commission Steamer "Albatross," during 1891, Lieutenant Commander Z.L. Tanner, U.S.N. Commanding, XII: the Holothurioidea. *Mem. Mus. Comp. Zool. Harv. Coll.* 17, 1–183.

Margolis, S., Michaels, W. L., Alger, B., Beaverson, C., Campbell, M. D., Kearns, E. J., et al. (2019). *Accessibility of Big Data Imagery for Next Generation Machine Learning Applications.* NOAA Tech. Memo. NMFS-F/SPO-194.O-164.

Martini, S., and Haddock, S. (2017). Quantification of bioluminescence from the surface to the deep sea demonstrates its predominance as an ecological trait. *Sci. Rep*. 7:45750. doi: 10.1038/srep45750

Matsumoto, G. I., Raskoff, K., and Lindsay, D. (2003). *Tiburonia granrojo* n. sp. a mesopelagic scyphomedusa from the Pacific Ocean representing the type of a new subfamily (class *Scyphozoa*: order Semaeostomeae: family Ulmaridae: subfamily Tiburoniinae subfam. nov.). *Mar. Biol.* 143, 73–77. doi: 10.1007/s00227-003-1047-2

Miller, J. E., and Pawson, D. L. (1990). *Swimming Sea Cucumbers (Echinodermata: Holothuroidea): A Survey, With Analysis of Swimming Behavior in Four Bathyal Species.* Smithsonian Contributions to the Marine Sciences, 35, 1–18. doi: 10.5479/si.01960768.35.1

Morris, P. J. (2019). *Data From: Museum of Comparative, Z.oology, and Harvard University*. Occurrence Dataset. 162, 156.

Mouw, C. B., Barnett, A., McKinley, G. A., Gloege, L., and Pilcher, D. (2016). Data from: global ocean flux rates. PANGAEA. Global ocean particulate organic carbon flux merged with satellite parameters. *Earth Syst. Sci. Data* 8, 531–541. doi: 10.5194/essd-8-531-2016

National Museum of Natural History (NMNH) (2019). *Data From: National Museum of Natural History Collection Records*. Available online at: https://collections.nmnh.si.edu/search/iz/

National Research Council (NRC) (1996). *Undersea Vehicles and National Needs*. Washington, DC: National Academy Press.

Natural History Museum (NHM) (2019). *Data From: Natural History Museum (London) Collection Specimens*. Occurrence dataset.

Netburn, A., Ford, M., and Lindsay, D. (2018). "2017 midwater exploration on Okeanos explorer," in *New Frontiers in Ocean Exploration: The E/V Nautilus, NOAA Ship Okeanos Explorer, and R/V Falkor 2017 Field Season*, Vol. 31, eds N. A. Raineault, J. Flanders, and A. Bowman (Oceanography), 61–63.

Netburn, A., Kinsey, J., Bush, S., Djurhuus, A., Fernandez, J., Hoffman, C., et al. (2017). First HOV Alvin study of the pelagic environment at Hydrographer Canyon (NW Atlantic). *Deep Sea Res. Part II Top. Stud. Oceanogr*. 150, 30–40. doi: 10.1016/j.dsr2.2017.10.001

Netburn, A. N. (ed). (2018). *From Surface to Seafloor: Exploration of the Water Column (Workshop Report), Honolulu, HI, 4-5 March 2017.* NOAA Technical Memorandum OAR OER; 003, NOAA Office of Ocean Exploration and Research, Silver Spring, MD, United States.

OBIS (2019). *Data From:Ocean Biogeographic Information System*. Intergovernmental Oceanographic Commission of UNESCO. Available online at: www.iobis.org

Orrell, T. (2019). *Data From: NMNH Extant Specimen Records.* Version 1.20. National Museum of Natural History and Smithsonian Institution, Occurrence dataset.

Osborn, K. J., Haddock, S. H. D., and Rouse, G. W. (2011). Swima (Annelida, Acrocirridae), holopelagic worms from the deep Pacific. *Zool. J. Linn. Soc*. 163, 663–678. doi: 10.1111/j.1096-3642.2011.00727.x

Peters, C., Coleman, D. F., and Martinez, C. (2019). "Expedition support from the inner space center," in *New Frontiers in Ocean Exploration: The E/V Nautilus, NOAA Ship Okeanos Explorer, and R/V Falkor 2018 Field Season*, Vol. 32, eds N. A. Raineault and J. Flanders (Oceanography), 6–7. doi: 10.5670/oceanog.2019.supplement.01

Quattrini, A. M., Nizinski, M. S., Chaytor, J. D., Demopoulos, A. W. J., Roark, E. B., France, S. C., et al. (2015). Exploration of the canyon-incised continental margin of the Northeastern United States reveals dynamic habitats and diverse communities. *PLoS ONE* 10:e0139904. doi: 10.1371/journal.pone.0139904

Racault, M. F., Sathyendranath, S., Brewin, R. J., Raitsos, D. E., Jackson, T., and Platt, T. (2017). Impact of El Niño variability on oceanic phytoplankton. *Front. Mar. Sci.* 4:133. doi: 10.3389/fmars.2017.00133

Ramirez-Llodra, E., Tyler, P. A., Baker, M. C., Bergstad, O. A., Clark, M. R., Escobar, E., et al. (2011). Man and the last great wilderness: human impact on the deep sea. *PLoS ONE* 6:e22588. doi: 10.1371/journal.pone.0022588

Robinson, C., Steinberg, D. K., Anderson, T. R., Arístegui, J., Carlson, C. A., Frost, J. R., et al. (2010). Mesopelagic zone ecology and biogeochemistry – a synthesis. *Deep Sea Res. Part II Top. Stud. Oceanogr*. 57, 1504–1518. doi: 10.1016/j.dsr2.2010.02.018

Robison, B. H. (2004). Deep pelagic biology. *J. Exp. Mar. Biol. Ecol.* 300, 253–272. doi: 10.1016/j.jembe.2004.01.012

Robison, B. H. (2009). Conservation of deep pelagic biodiversity. *Conserv. Biol.* 23, 847–858. doi: 10.1111/j.1523-1739.2009.01219.x

Robison, B. H., Reisenbichler, K. R., and Sherlock, R. E. (2017). The coevolution of midwater research and ROV technology at MBARI. *Oceanography* 30, 26–37. doi: 10.5670/oceanog.2017.421

Schlining, B. M., and Stout, N. Y. (2006). "MBARI's video annotation and reference system," in *OCEANS 2006*, 1–5. doi: 10.1109/oceans.2006.306879

Schlining, K., von Thun, S., Kuhnz, L., Schlining, B., Lundsten, L., Jacobsen Stout, et al. (2013). Debris in the deep: using a 22-year video annotation database to survey marine litter in Monterey Canyon, central California, USA Deep Sea Res. *Oceanogr. Res. Pap.* 79, 96–105. doi: 10.1016/j.dsr.2013.05.006

Seibel, B. A. (2011). Critical oxygen levels and metabolic suppression in oceanic oxygen minimum zones. *J. Exp. Biol.* 214, 326–336. doi: 10.1242/jeb.049171

Seid, C. (2019). *SIO Benthic Invertebrate Collection*. Scripps Institution of Oceanography. doi: 10.15468/4w9oc7

Sibuet, M. (1985). "Quantitative distribution of echinoderms (Holothuroidea, Asteroidea, Ophiuroidea, Echinoidea) in relation to organic matter in the sediment, in deep-sea basins of the Atlantic Ocean," in *Proceedings of the Fifth International Echinoderm Conference*, eds B. F. Keegan and B. D. S. O'Connor (Rotterdam: Balkema), 99–108.

Spalding, M. D., Fox, H. E., Allen, G. R., Davidson, N., Ferdaña, Z. A., Finlayson, M., et al. (2007). Marine ecoregions of the world: a bioregionalization of coastal and shelf areas. *BioScience* 57, 573–583. doi: 10.1641/B570707

Sutton, T. T., Clark, M. R., Dunn, D. C., Halpin, P. N., Rogers, A. D., Guinotte, J., et al. (2017). A global biogeographic classification of the mesopelagic zone. *Deep Sea Res. Part I Oceanogr. Res. Pap*.126, 85–102. doi: 10.1016/j.dsr.2017.05.006

Webb, T., Berghe, E., and O'Dor, R. (2010). Biodiversity's Big Wet Secret: the global distribution of marine biological records reveals chronic under-exploration of the deep pelagic ocean. *PLoS ONE* 5:e10223. doi: 10.1371/journal.pone.0010223

Widder, E. A., Greene, C. H., and Youngbluth, M. J. (1992). Bioluminescence of sound-scattering layers in the Gulf of Maine. *J. Plankt. Res.* 14, 1607–1624. doi: 10.1093/plankt/14.11.1607

Yoole, A., Martin, A., Fernandez, C., and Clark, D. (2007). The significance of nitrification for ocean production. *Nature* 447, 999–1002. doi: 10.1038/nature05885

Conflict of Interest: The authors declare that the research was conducted in the absence of any commercial or financial relationships that could be construed as a potential conflict of interest.

Copyright © 2019 Selig, Netburn and Malik. This is an open-access article distributed under the terms of the Creative Commons Attribution License (CC BY). The use, distribution or reproduction in other forums is permitted, provided the original author(s) and the copyright owner(s) are credited and that the original publication in this journal is cited, in accordance with accepted academic practice. No use, distribution or reproduction is permitted which does not comply with these terms.

frontiers in Marine Science

ORIGINAL RESEARCH
published: 26 November 2019
doi: 10.3389/fmars.2019.00715

Fine Scale Assemblage Structure of Benthic Invertebrate Megafauna on the North Pacific Seamount Mokumanamana

*Nicole B. Morgan[1], Savannah Goode[1], E. Brendan Roark[2] and Amy R. Baco[1]**

[1] Department of Earth, Ocean and Atmospheric Science, Florida State University, Tallahassee, FL, United States,
[2] Department of Geography, Texas A&M University, College Station, TX, United States

Changes in benthic megafaunal assemblage structure have been found across gradients of environmental variables for many deep-sea habitats, but patterns remain under-investigated on seamounts. To assess the extent of variability in benthic communities at the scale of within a single seamount, and to assess environmental drivers of assemblage changes, Mokumanamana, also known as Necker Island, a seamount in the Papahānaumokuākea Marine National Monument with no known history of human impacts, was surveyed. Replicate 1 km transects were conducted along depth contours at 50 m depth intervals from 200–700 m on three sides of Mokumanamana using the *AUV Sentry*. Megafaunal abundance and substrate parameters were obtained from 26,119 total images. The dominant megafaunal taxa were sponges, corallimorpharians, cup corals, and benthic ctenophores. Sea pens and alcyonacean octocorals were also abundant. Overall, abundance and diversity of megafauna increased with depth. Beta-diversity through species substitution with depth was very high. Beta-diversity was also high between the sides and likewise defined almost exclusively by species substitution. Crossed ANOSIM by depth and side showed community structure differed on Mokumanamana for both factors. NMDS and cluster analyses of Mokumanamana show nine assemblages that were defined by depth and reflect differences between sides of the seamount. Environmental modeling with DISTLM indicates sediment, oxygen, substrate variability and roughness, POC, and surface currents are correlated with these assemblage differences. These results suggest that microhabitats on seamounts can promote unique assemblages along depth gradients as well as on different sides of a feature, and this diversity may be easily overlooked without fine-scale sampling. These findings have implications for management and conservation of seamounts as well as future ecological studies of seamounts, as seamounts are generally sampled on much coarser spatial scales.

Keywords: seamount heterogeneity, deep-sea corals, sponges, diversity, megafauna, assemblage, Pacific

OPEN ACCESS

Edited by:
Randi D. Rotjan,
Boston University, United States

Reviewed by:
Andrea M. Quattrini,
Harvey Mudd College, United States
Tara Harmer Luke,
Stockton University, United States

***Correspondence:**
Amy R. Baco
abacotaylor@fsu.edu

Specialty section:
This article was submitted to Deep-Sea Environments and Ecology, a section of the journal Frontiers in Marine Science

Received: *14 June 2019*
Accepted: *06 November 2019*
Published: *26 November 2019*

Citation:
Morgan NB, Goode S, Roark EB and Baco AR (2019) Fine Scale Assemblage Structure of Benthic Invertebrate Megafauna on the North Pacific Seamount Mokumanamana. Front. Mar. Sci. 6:715. doi: 10.3389/fmars.2019.00715

INTRODUCTION

Seamounts have often been treated as homogenous landscapes in ecological studies and in management efforts, but the potential heterogeneity of seamounts is beginning to emerge in the more recent literature. Rather than consistent slopes of hard substrate, seamounts often have highly irregular geology that ranges from sedimented plateaus to steep rocky cliff faces, with most grain sizes in between, all on the same feature (Levin et al., 2001; Auster et al., 2005). Large bathymetric gradients over short horizontal distances lead to large variations in temperature (Yasuhara and Danovaro, 2016) and oxygen concentrations (Levin, 2002). When those gradients are combined with surface productivity variations in the overlaying water column (Bo et al., 2011; Woolley et al., 2016) the result is a large variety of habitats over a relatively small area. Seamounts can also have higher habitat heterogeneity due to the organisms themselves as the corals and sponges that often dominate in hard substrate areas can create biogenic structures that then provide habitat for other invertebrates and fishes (e.g., Buhl-Mortensen et al., 2009).

In the general deep-sea, variation in many of these same environmental parameters has been found to be correlated with variation in megafaunal assemblage structure, abundance, and diversity. Depth is one of the more prominent parameters influencing assemblage structure (e.g., Howell et al., 2002; Quattrini et al., 2014). Other significant parameters include magnetivity and topography (Boschen et al., 2015), temperature (Mortensen and Buhl-Mortensen, 2004; Wei et al., 2010; Morgan et al., 2015), turbidity (Mamouridis et al., 2011; Brooke et al., 2017), pH (Brooke et al., 2017), oxygen (Wishner et al., 1990; Levin, 2002; De Leo et al., 2017), substrate size and type (Mortensen and Buhl-Mortensen, 2004), and stochastic processes and environmental filtering (Quattrini et al., 2016). Thus, the high habitat heterogeneity that is becoming known on many seamounts, with numerous available habitats, may then contribute to high biodiversity on seamounts. It may also lead to large variations in community structure within a single seamount, as each microhabitat on the seamount has the potential to harbor unique communities of benthic invertebrates. Indeed, several recent seamount studies support variability within and among seamount communities related to environmental variation (Baco, 2007; McClain et al., 2010; Bo et al., 2011; Williams et al., 2011; Baco and Cairns, 2012; Long and Baco, 2014; Schlacher et al., 2014; Thresher et al., 2014; McClain and Lundsten, 2015; Morgan et al., 2015; Victorero et al., 2018a; Mejia-Mercado et al., 2019).

The wide range of environmental factors, the natural variability of those factors within and between seamounts, and the concomitant variability that is likely to occur in seamount fauna, make it challenging to form inferences about the resilience of seamount fauna to anthropogenic effects. Levels of biodiversity and the assemblage structure on seamounts are an ever-growing concern for deep-sea science and ocean conservation due to the numerous anthropogenic disturbances occurring (Ramirez-Llodra et al., 2011; Pusceddu et al., 2014; Levin and Le Bris, 2015). Trawl fisheries on the high seas often target these features as they have aggregating functions for fish, acting either as cover or reproductive hot-spots (Morato and Clark, 2007). However, trawl fishing is also highly destructive to seamount ecosystems and leads to removal of biogenic structures (Althaus et al., 2009; Clark and Rowden, 2009; reviewed in Rossi, 2013; Clark et al., 2016). Clark et al. (2007) reported nearly 2.3 million tons of fish removed by trawling globally with 900,000 tons from seamounts in the North Pacific. More recent data from the Food and Agriculture Organization of the United Nations reports 14.4 million tons of fish caught by trawling globally with 2.07 million tons removed from the North Pacific alone (Victorero et al., 2018b). This translates into large areas of seamounts where any coral and sponge assemblages present, along with their associated communities of invertebrates and fishes, would have been damaged or removed by these fishing activities. Seamounts face even greater impacts from the push for mining of deep-sea substrates for semi-precious and precious metals (Halfar and Fujita, 2007; Mengerink et al., 2014; Cuvelier et al., 2018). Seamount slopes that occur from 800 to 2500 m in depth can accrue cobalt-rich manganese crusts, similar to the nodules that accrue on abyssal plains. Co-precipitates such as molybdenum, manganese, tantalum, bismuth, platinum, zirconium, tungsten, and titanium (Hein et al., 2009) are used in numerous technologies, and because land-based mine sources for these metals are confined to a few areas, terrestrial yields of these economically important resources are dwindling.

To date, most sampling methods for surveying seamounts rely on submersibles, remotely operated vehicles (ROV), towed-camera transects along the flank of the feature, or drop camera images (e.g., Stocks, 2004; Rowden et al., 2010; Vetter et al., 2010; Clark et al., 2012). Operational time constraints at any feature, especially on remote locations, limits the number and length of surveys that can be planned, often resulting in little or no replication across environmental gradients such as depth or substrate. As such, while these surveys are good for providing an ecosystem snapshot and partial species lists for a given seamount, they are not able to provide replicate sampling within features for statistical tests to compare fauna among areas on a given seamount or often even between features (Rowden et al., 2010; Sautya et al., 2011; Higgs and Attrill, 2015).

Automated Underwater Vehicle (AUV) technology, however, has advanced to where these issues of low sample coverage and replication can be rectified. AUVs can cover a greater distance than ROVs and stay on station for long periods of time (Kilgour et al., 2014). AUVs can also provide high definition imagery at a lower altitude than many towed cameras, especially on rougher and steeper topography. With more images there is a greater chance of capturing natural variability in benthic assemblages as well as multiple occurrences of rare species, and of reducing singleton samples, common issues with low replication in many ecological studies (Monk et al., 2018). New challenges arise with large numbers of images to process, but the rise in automated annotation software and machine learning have begun to make large image datasets less onerous (Schoening et al., 2016). Currently human identifications and counts, even by non-specialists, are still the most accurate method of gathering data from imagery (Matabos et al., 2017), but as computer-learning methods advance, the problem is likely to be overcome.

With the encroachment of fishing and mining onto more and more seamounts, it is important to clearly define scales

of variability in faunal communities and in environmental factors on seamounts. Baseline data for variability in seamount assemblage structure are lacking due to the fact that many seamounts close enough to allow for the extended and/or repeated time on station required for thorough ecological surveys, also have a history of human activity [i.e., Northeast Pacific seamounts reviewed in Clark et al. (2007), New Zealand seamounts (Richer de Forges et al., 2000), Tasmania seamounts (Koslow et al., 2001), Mediterranean features (Bo et al., 2014), and Northeast Atlantic seamounts (Hall-Spencer et al., 2002)]. Better data on intra seamount variability are crucial for improving our understanding of seamount ecology as well as for ecological impact studies so that effects from human activity can be clearly identified and separated from natural variations in abundance or diversity. Thus, the goal of this study was to use AUV surveys for a more detailed investigation of variation within a single seamount feature than has been possible in previous seamounts studies. An unimpacted seamount was targeted to fill in gaps in baseline variability data for seamounts, to address changes in diversity and assemblage structure with depth on a single seamount, and also among sides of the same seamount feature. Additionally, environmental data were gathered to assess how observed assemblage variability may be tied to other factors. From these data we make inferences into how current approaches to sampling and managing seamounts may be affected by faunal variability.

MATERIALS AND METHODS

Site Selection

Mokumanamana (Latitude 23.65°N, Longitude 164.80°W), also known as Necker Island, in the Northwest Hawaiian Islands (NWHI) was surveyed as part of a larger project surveying North Pacific seamounts, to understand impacts on deep-sea communities from trawl fisheries and to explore possible recovery times for these habitats (Baco et al., 2019; Baco et al., in review). Oceanic islands with exposed summits are included in the most recent definitions of seamounts as they are geologically identical to unexposed seamounts (Staudigel and Clague, 2010). Though there is some emergent land at Mokumanamana (**Figure 1**), it is a small rocky outcrop of only 0.18 km^2 that does not have the features of a true island that might affect benthic assemblages [i.e., mass or channels to trap phytoplankton, freshwater run-off, increased detritus to the seafloor, or prolonged human habitation (Gilmartin and Revelante, 1974)]. Mokumanamana was selected as a target feature as it has no known history of large-scale bottom contact fishing. The seamount is also 600 km from the main Hawaiian Islands, far enough to limit human influences. Mokumanamana is an important cultural and religious site for native Hawai'ians, and has been protected legally since 1909 when Theodore Roosevelt created the Hawaiian Islands Bird Reservation. In 1988, Mokumanamana was further protected when the island specifically was added to the National Registry of Historic Palaces, and then further protected as part of the Northwestern Hawaiian Islands Coral Ecosystem Reserve in 2000. Mokumanamana continues to be protected with the establishment of the Papahānaumokuākea Marine National Monument in 2008, and further as part of the United Nations Educational, Scientific and Cultural Organization World Heritage site of Papahānaumokuākea established in 2010.

Sampling Strategy and Data Collection

In 2015 the AUV *Sentry* was deployed on the slope of three different sides of Mokumanamana (further referred to as "sides" to avoid confusion with the environmental parameter of slope angle) and conducted 1000 m long triplicate photographic transects at 50 m depth intervals from 200 to 700 m depth, inclusive. Locations for transects were selected based on backscatter that indicated the highest probability of hard substrate across the survey depth range, and were conducted along depth contours with a separation of at least 100 m between transects. A total of 152 km of the feature was surveyed. The specifications of the AUV limited the survey range to areas with a slope less than 50 degrees. Images were taken with a down-looking Allied Vision Technologies Prosilica GE4000C camera every 5 s while the AUV maintained an average altitude off the bottom of 6 m and an average speed of 0.65 m/s. A total of 26,082 images were analyzed for bottom substrate parameters and megafaunal invertebrate abundance.

To describe the substrate and to prevent data duplication, every fourth image was imported into ImageJ (Schneider et al., 2012) and random dots were overlaid to quantify the substrate composition (sand, basalt, carbonate, etc.) and substrate size (based on Wentworth, 1922). Slope and rugosity were quantified from the overall image as a scale from low (value 1) to high (value 4) based on similar methods from Long and Baco (2014) and Morgan et al. (2015). Using the imagery, rather than bathymetric data, allows for finer-scale data collection as the bathymetry has a resolution of 60 m while the images have a scale of 3 m. Rugosity also could not be quantified from bathymetry as missing bathymetric data would have been interpolated by downstream analyses. Standard deviations of slope, rugosity, and substrate size were calculated to describe the variation in the substrate within a transect. *Sentry* collected data on latitude, longitude, depth, and altitude for each photo. Water column data (oxygen, temperature, and conductivity) were also collected by *Sentry* using A Seabird SBE49 Conductivity-Temperature-Depth (CTD) with a Seapoint optical backscatter (OBS) sensor and an Aanderaa optode (model 4330) oxygen concentration sensor and referenced to every image. To compare the direction the transects were facing (i.e., northwest facing or south facing), aspect was calculated in QGIS 2.18 from bathymetry and then converted into the linear form of Mean Direction as formulated by Fisher (1995), due to the circular nature of aspect that makes it unsuitable for direct use in linear modeling. Minimum, maximum, and average values for surface particulate organic carbon (POC), Chlorophyll (chlorophyll-α) and surface currents were collected as 8-year averages from the Environmental Division Data Access Program's Moderate Resolution Imaging Spectroradiometer, the

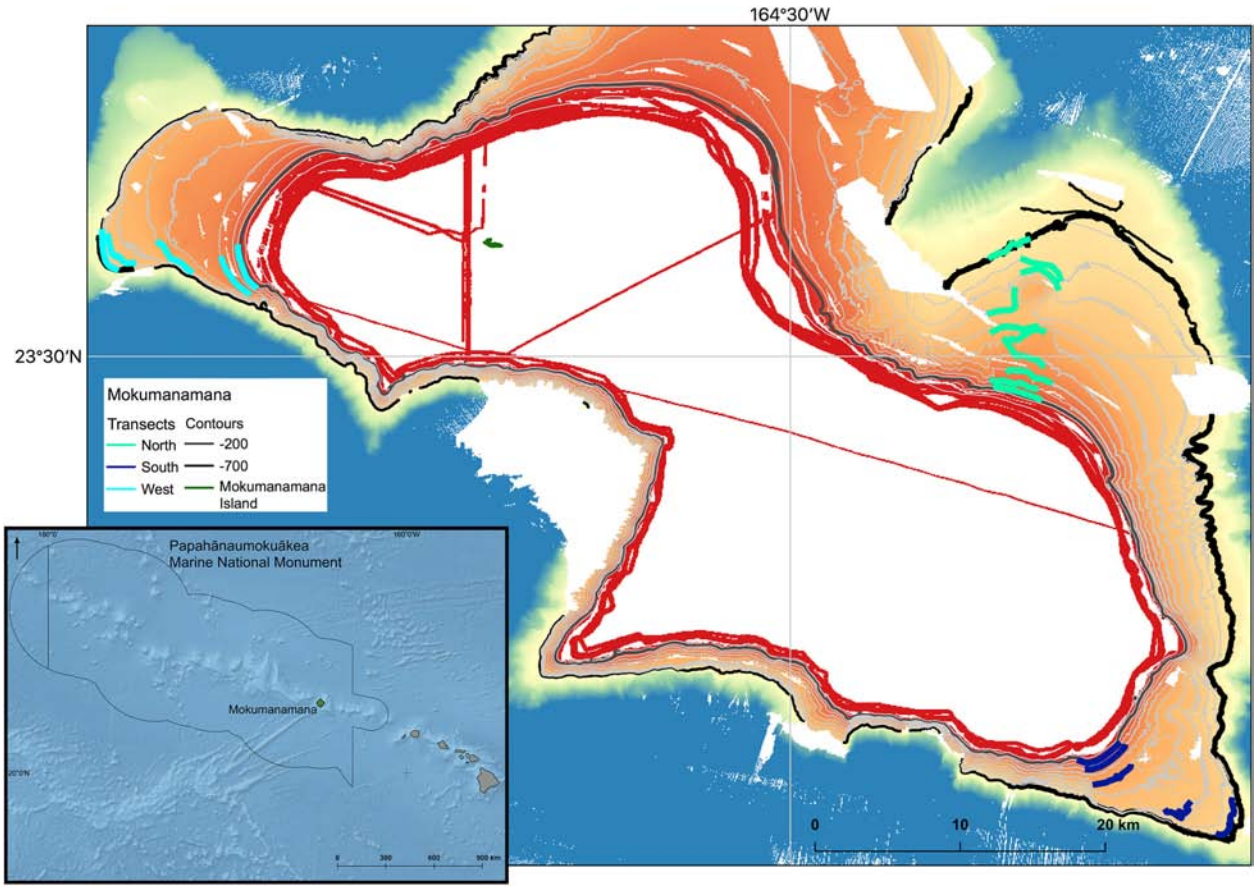

FIGURE 1 | Bathymetry of Mokumanamana with contours from 200–700 m at 50 m intervals shown. 200 and 700 m isobars are thick contours to highlight the depth range of the study. Transects lines on each of the three sides are plotted. Inset: Overview of the location of Mokumanamana (shown in green) within the Northwestern Hawai'ian Islands and Papahânaumokuâkea Marine National Monument.

National Environmental Satellite Data and Information Service, and the Global Hybrid Coordinate Ocean Model as described in Baco et al., in review, providing a total of 31 environmental variables for each transect (**Supplementary Table S1**).

Benthic megafauna were counted by eye in every image, and overlapping areas in images were avoided to prevent duplicate counts. Megafauna were assigned to the lowest possible taxonomic unit, but for many deep-sea species, identifications are difficult from imagery alone, especially down-looking imagery, and many species are still undescribed, thus many animals were given unique operational morphospecies identifications. Confidence levels were assigned for each animal counted from 1 to 4; 1 denotes complete confidence in the morphospecies assignment, 2 denotes confidence at a slightly higher taxonomic level of genus or family, 3 denotes confidence at an even higher taxonomic level, often order level, and 4 denotes the lowest confidence level to where that organism cannot be identified. Invertebrates classified as a "4" confidence level due to image quality were counted to find total abundances of invertebrates but were not included in any assemblage analysis. Algae seen on the bottom was also not included in analyses, as it could not be determined if they were *in situ* or sunken detrital matter. Finally, on the West side a very large aggregation of the urchin *Chaetodiadema pallidum* was found that overwhelmed all other counts; these were included for abundance but also removed from analysis to prevent outlier sample loss. The distribution of these urchins is reported in Morgan and Baco (2019). Initial image analyses began with transects at each 50 m isobath on the North side of Mokumanamana. Preliminary analysis for the North side showed that sampling at 100 m depth intervals would be adequate to capture the variability in assemblage structure, so for more efficient and timely data collection, the 250, 350, 450, 550, and 650 m depth transects were analyzed on the two remaining sides. To keep a balanced design for depth bins when considering all three slopes, the data analyses were split into two phases: a focus on the North side with replicated transects at 50 m depth intervals, followed by a comparison of all three slopes at 100 m depth intervals.

Statistical Analysis

Statistical analyses were run in R version 3.5 (R Core Team, 2018). Environmental data were first normalized, to ensure similar weights between variables with very different ranges, then filtered

for correlating variables using the package "corrplot" (Wei and Simko, 2017) then analyzed with Principle Component Analysis (PCA) using the PCA function from package "FactoMineR" (Le et al., 2008). Abundance values were standardized by the number of photos in a transect to prevent bias in sampling effort. Univariate diversity metrics were calculated with the package "vegan" (Oksanen et al., 2019). ANOSIM was run in PRIMER-E version 7 to test the significance of the *a priori* hypotheses that assemblage structure would be different between depths and sides (Clarke and Gorley, 2015). Beta diversity and partitioning were analyzed with package "betapart" following the methodology proposed by Baselga and Orme (2012); Baselga (2017) using Bray–Curtis dissimilarity values. Multivariate hierarchical cluster analysis was analyzed with "vegan" and "cluster" packages, then Bayesian cluster modeling was done with the package "mclust" (Scrucca et al., 2017) to find the best number of groups. K-cluster analysis from the base R package "stats" was used to assign groups because it follows the hierarchical pattern through centroid sampling of clusters rather than the divisive method of "mclust." NMDS analysis for the assemblage structure was run in "vegan." DISTLM from the PERMANOVA+ statistical software (Anderson et al., 2008) was used to compare models that would describe the relationship between assemblage structure and environmental parameters, then the parameters indicated by DISTLM were included in a final distance-based Redundancy Analysis (dbRDA) in "vegan". Variable inflation factors (VIF) were calculated and variables with VIF greater than 10 were removed. VIF analyzes the multicollinearity of variables, or the level to which any predictor variable is redundant with another within the linear model (Oksanen et al., 2019). Significant variables were analyzed by ANOVA (Oksanen et al., 2019). PRIMER dbRDA plotting only allows for the lowest AIC criterion, but when there is not enough difference between model AIC values the dbRDA method in "vegan" can be used to compare all variables. SIMPER analysis to determine the species that best defined the *a posteriori* k-means assemblage structure was completed in PRIMER.

RESULTS

North Side of Mokumanamana

There was a broad range of variation in the environmental data collected from the North side of Mokumanamana (**Supplementary Table S1**). Oxygen, temperature, and mean POC decreased with increasing depth; these ranged from 49–242 μM, 5–14°C, and 35–48 mg/m^3, respectively. Percent sediment was highest from 250–400 m depth where substrate size variability and rugosity were also the lowest. Rugosity and substrate size variability generally increased with increasing depth. Mean direction ranged from −1.49 to 1.53 and did not follow a depth trend. Average northward and eastward surface components of currents were consistent throughout the slope with ranges of 0.058–0.062 m/s and −0.11 to −0.13 m/s, respectively. Initially 31 environmental variables were collected from Mokumanamana, and for the North side 19 correlated variables were removed. Twelve parameters were then used in a PCA of the environmental data, which showed a gradient of the depth bins from shallow to deep moving from right to left along the PC1 axis (**Figure 2**). PC1 describes 54.61% of the variability in the environmental data, and is most strongly correlated with the standard deviation of substrate size and mean POC, and correlates with a value over 0.75 with oxygen, percent sediment, rugosity, standard deviation of rugosity, and the minimum chlorophyll-α values from MODIS satellite data. PC2 describes 14.29% of the variability and is most strongly correlated with mean direction (**Supplementary Table S2**). In general, the shallower sites on the North side have more consistent substrate type with mostly sediment, an increase in surface POC values, and higher oxygen concentrations.

Overall the North side showed an increase in abundance of Alcyonacea, Antipatharia, Actiniaria, holothurians, urchins, and ophiuroids with increasing depth (**Supplementary Figure S1**). Sea pens, arthropods, and asteroid sea stars were most abundant at shallow depths (250 and 300 m) while sponges and corallimorpharians were highly abundant at 450 and 500 m. Univariate diversity metrics show a general trend of increasing species richness (**Figure 3A**) and Shannon-Weaver index (**Figure 3B**) with increasing depth, though depth bins at 450 and 500 m do not follow the trends as they have much lower Shannon-Weaver indices, likely due to a low evenness component (**Figure 3D**). Simpson's Dominance (**Figure 3C**) was generally low except for the 450 and 500 m transects due to the highly abundant corallimorpharians. Evenness is generally high over the North side except at 250 m and again at 450 and 500 m (**Figure 3D**). The 450 m depth bin was the most variable for all three indices.

ANOSIM analysis for assemblage structure overall showed a significant difference globally for unordered depth bins ($R = 0.78$, $p = 0.001$), but pairwise comparisons between depth bins showed no significant difference between any two pairs (**Supplementary Table S3**). The hierarchical cluster of faunal assemblage data (**Figure 4**) shows three groups defined by depth relationships with shallow (250–350), mid-depth (400–500), and deep (550–700) transects clustering at 85% dissimilarity. The 400 m transects do not neatly fit into this pattern, and instead one replicate falls into each of the three clusters, but otherwise the assemblage grouping shows a strong depth relationship. When the environmental data are correlated to the assemblage structure for the North side of Mokumanamana three factors describe most of the variability: rugosity, oxygen, and mean POC (**Figure 5**). These three factors were highlighted by both the "bioenv" routine in the R vegan package and by the DISTLM routine in PRIMER-E (**Table 1**), however, the AIC value for the best model with three parameters was only 0.26 better than the model with only oxygen and mean POC. Oxygen has the strongest correlation with dbRDA1 (0.97), and this axis explains 48.38% of the variation in the model. dbRDA axis 2 explains 39.70% of the variation and is most strongly correlated to mean POC (0.63). Rugosity does add a small proportion of explained variance compared to a dbRDA model of just oxygen and mean POC, and is the most independent of the three variables (VIF = 1.65)

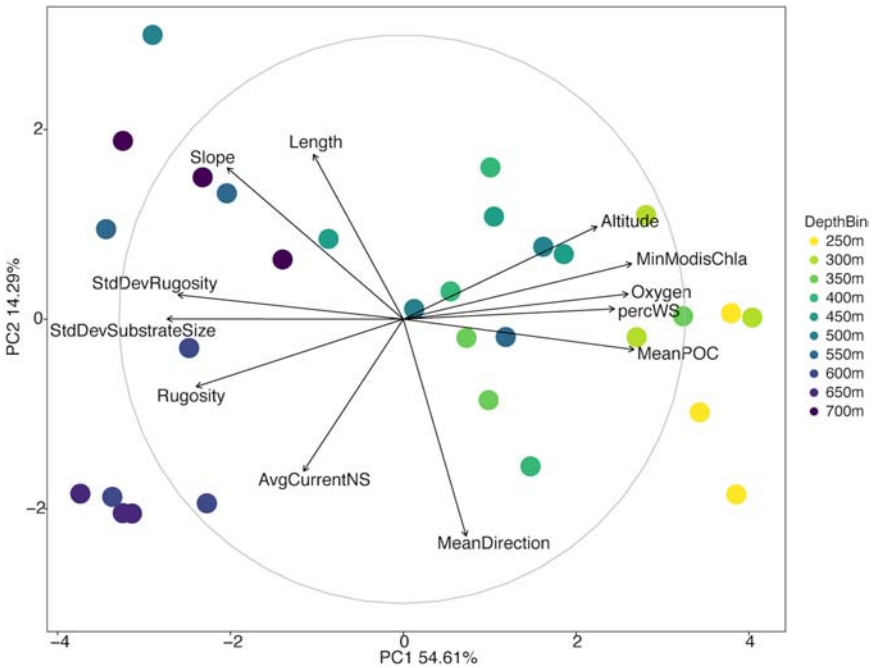

FIGURE 2 | Principal components analysis diagram of environmental variables of the North side of Mokumanamana. Each point represents a single 1 km transect coded by depth.

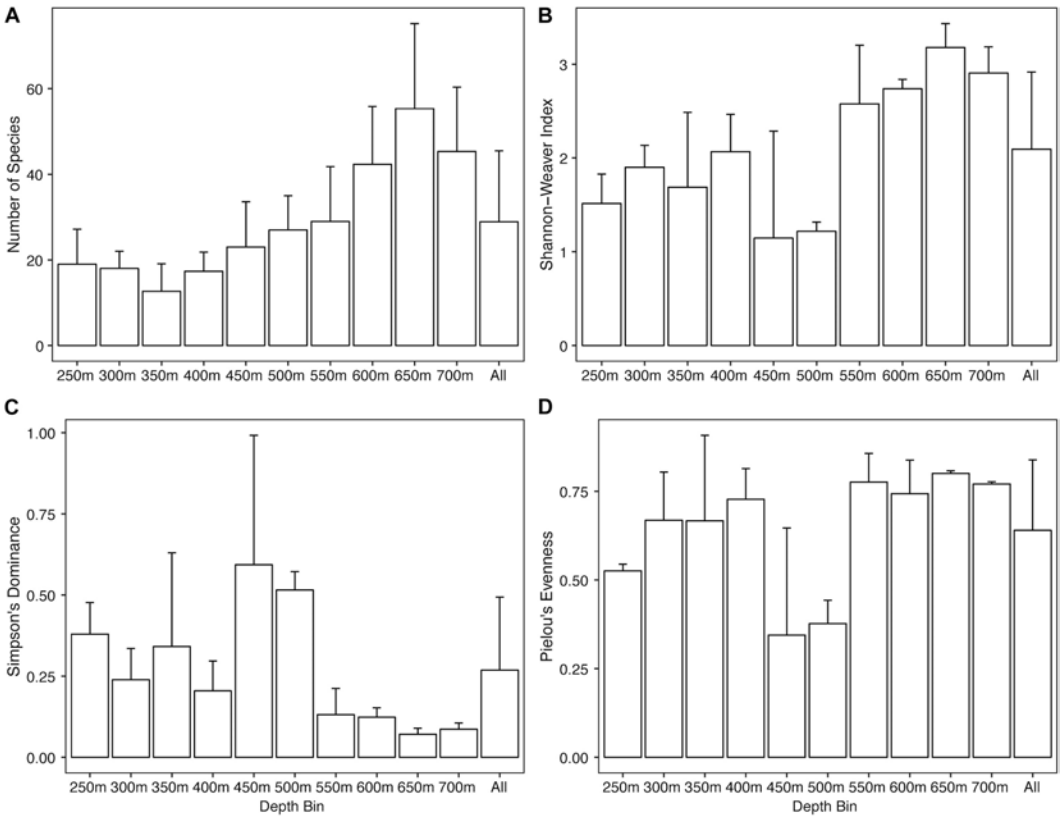

FIGURE 3 | Bar plots of univariate diversity metrics for the North side of Mokumanamana by depth. Panels: **(A)** species richness, **(B)** Shannon-Weaver's Index, **(C)** Simpson's Dominance Index, **(D)** Pielou's Evenness Index.

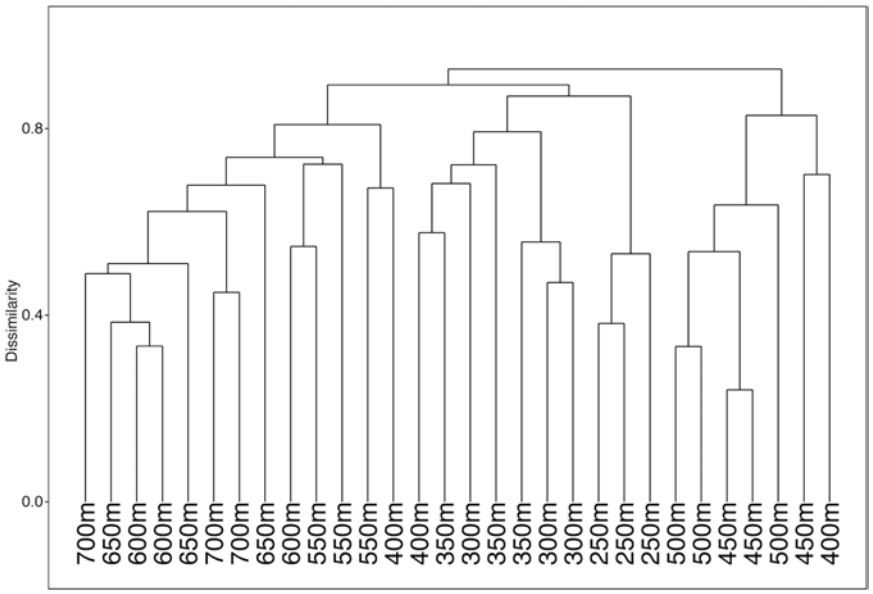

FIGURE 4 | Hierarchical cluster diagram for the North side of Mokumanamana for transects labeled by depth bin.

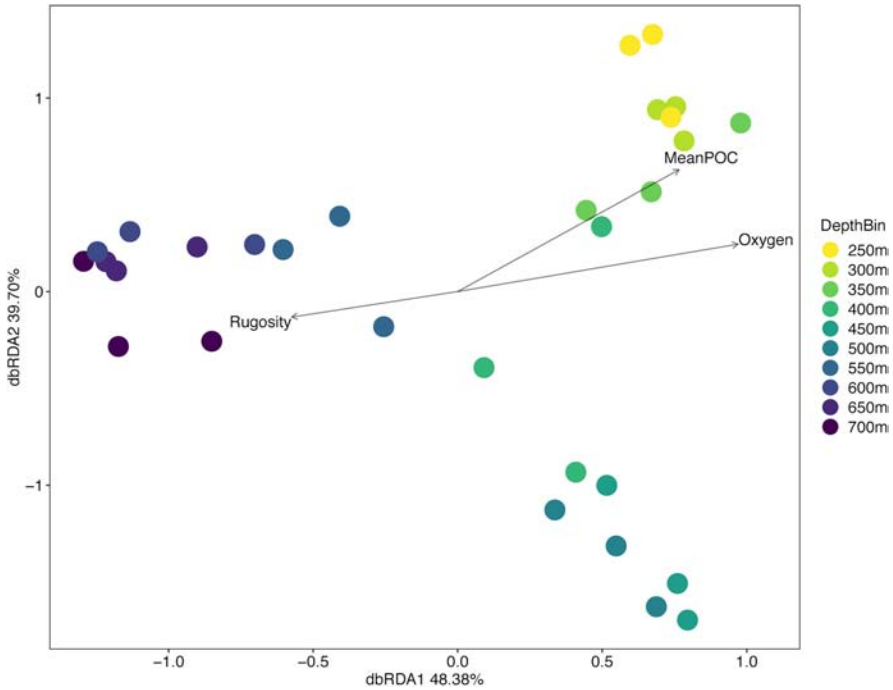

FIGURE 5 | Distance-based redundancy analysis diagram for the North side of Mokumanamana coded by depth.

(**Table 1**). In general, shallow transects had higher POC and oxygen concentrations and lower rugosity than deep transects.

Mokumanamana Overall

Once the scales of the general trend of species turnover with depth were found from the North side, the two remaining sides were analyzed at 100 m depth intervals to allow for more efficient analyses. There was a broad range of variation in the environmental data collected from Mokumanamana as a whole (**Supplementary Table S1**); oxygen and temperature decreased with depth and were very similar for all three sides with ranges of 46–242 μM and 5–16°C, respectively. Mean POC decreased with depth on the North and West sides with ranges of 33–39 mg/m^3 and 36–48 mg/m^3, but was more consistent on the South side

around 31 mg/m^3. Percent sediment also generally decreased with depth, but the North side overall had more sand (35–98%) than the West (22–99%) or South (4–89%) sides. Rugosity increased with depth, and was more consistent across all sides of Mokumanamana. Mean direction was differed between the West (range 0.22–1.32) and South sides (range −1.36–0.12) while the North side encompassed the full range of values (−1.49–1.53); however, mean direction showed no trend with depth at any side. Average surface currents were consistent across depths and instead varied by side with the average north-south surface current faster on the West side (range 0.06 to 0.09 m/s, overall northward direction) and the surface east-west current faster on the North side of the seamount (range −0.11 to −0.13 m/s, overall westward direction).

TABLE 1 | DISTLM and dbRDA scores for the North side of Mokumanamana.

Variable	SS(trace)	Pseudo-F	*P*	Prop.
1.Oxygen	16636.0	5.064	**0.001**	0.1532
2. Altitude	14601.0	4.348	**0.001**	0.1344
3. MeanDirection	5399.9	1.465	0.104	0.0497
4. Length	3874.5	1.036	0.425	0.0357
5. Perc. White Sand	9090.7	2.557	**0.005**	0.0837
6. StdDevSubstrateSize	11556.0	3.333	**0.001**	0.1064
7. Slope	6090.5	1.663	**0.048**	0.0561
8. Rugosity	8665.1	2.427	**0.006**	0.0798
9. StdDevRugosity	11696.0	3.379	**0.001**	0.1077
10. MeanPOC	15280.0	4.584	**0.001**	0.1407
11. Min Chl-a Modis	12791.0	3.737	**0.001**	0.1178
12. AvgCurrentNS	3810.7	1.018	0.411	0.0351
Residual df: 28				

Overall best solutions from DISTLM

Selections	R^2	RSS	No.Vars	AIC
1,8,10	0.33172	72593	3	241.74
1,10,11	0.33015	72764	3	241.81
1,5,10,11	0.37259	68154	4	241.85
1,10	0.27948	78268	2	242.00
1,11,10	0.32521	73300	3	242.03
1,11,8,10	0.36856	68592	4	242.04
1,8,12,10	0.36760	68696	4	242.09
1,8,10,11	0.36578	68893	4	242.17
1,2,10	0.32161	73692	3	242.19
1,2,11,10	0.36536	68939	4	242.19

dbRDA Biplot scores for environmental variables

Variable	dbRDA1	dbRDA2	dbRDA3
Oxygen	**0.970**	0.245	−0.011
MeanPOC	0.766	**0.630**	0.132
Rugosity	−0.574	−0.132	−0.808

ANOVA and multicollinearity results from dbRDA

Variable	SumOfSqs	*F*	*P*	VIF
Oxygen	1.720	6.298	**0.001**	5.034
MeanPOC	1.342	4.914	**0.001**	5.532
Rugosity	0.532	1.948	**0.020**	1.659
Residual Df:26	7.1015			

Numbers in bold denote significant p-values.

Of the initial 31 environmental parameters, 19 were removed due to correlating or missing data (**Supplementary Figure S2**). The PCA for all three sides of Mokumanamana shows gradients in the environment by both depth bin and by the side of the seamount (**Figure 6** and **Supplementary Table S4**), with the South side trending toward the bottom of the ordination and shallower depths to the left. PC1 describes 38.8% of the environmental variability and is most strongly correlated with oxygen, rugosity, the standard deviation of rugosity, and percent sediment. Transects generally cluster along PC1 by depth from left to right. Similar to the North side PCA (**Figure 2**), shallower samples had higher oxygen concentrations, lower rugosity, and more consistent substrate coverage of white sand while deeper samples had more pebbled substrate and rocky outcrops. PC2 describes 14.72% of the variability and is most strongly correlated with mean direction and the average east-west surface current. Along PC2 samples generally cluster by the side of Mokumanamana with the southern transects especially differentiated from the North and West transects due to a much weaker westward current and rocky outcrops at deeper transects that at times reached 25 m high.

The abundances of benthic invertebrates were different among the sides of the seamounts (**Supplementary Table S5**), overall the West side had nearly three times as many animals compared to the North and South sides overall, with the largest differences in arthropods, cnidarians, and echinoderms (**Figure 7**). Arthropods on the West side were mainly comprised of squat lobsters, cnidarians mainly of cup corals, corallimorpharians, and the sea pen *Anthoptilum grandiflorum*. The West side was also characterized by high numbers of benthic ctenophores of the *Lyrocteis* genus. Cnidarians of the North side were mostly comprised of sea pens *Kophobelemnon stelliferum and Virgularia abies*, and the South side mainly *Metallogorgia melanotrichos* and *Anthomastus* sp. Sponges were more abundant on the North and South sides than the West side, and on the North side sponges were dominated by *Sericolophus* sp. while the South side was dominated by *Farrea* sp. Univariate diversity metrics did not vary by side, but did by depth and the interaction of depth and side (**Supplementary Table S5**). Overall the three slopes showed an increase in species richness (**Figure 8A**) with increasing depth, and the West and North sides show an increase in Shannon-Weaver and Pielou's evenness with depth and a decrease in Simpson's Dominance, though the 450 m depth bin for the North side as noted, still does not fit the overall trend (**Figures 8B–D**). While the West side has the highest abundance, the South side generally had a higher diversity as measured by the Shannon-Weaver index and higher evenness as measured by Pielou's Evenness for 250, 350, and 450 m depth bins. The North side has the highest diversity for 550 and 650 m depth bins (**Figures 8B,D**). Diversity metrics are the most consistent across depth bins for the South side.

Crossed ANOSIM of assemblage structure overall by depth bin and side showed significant differences both

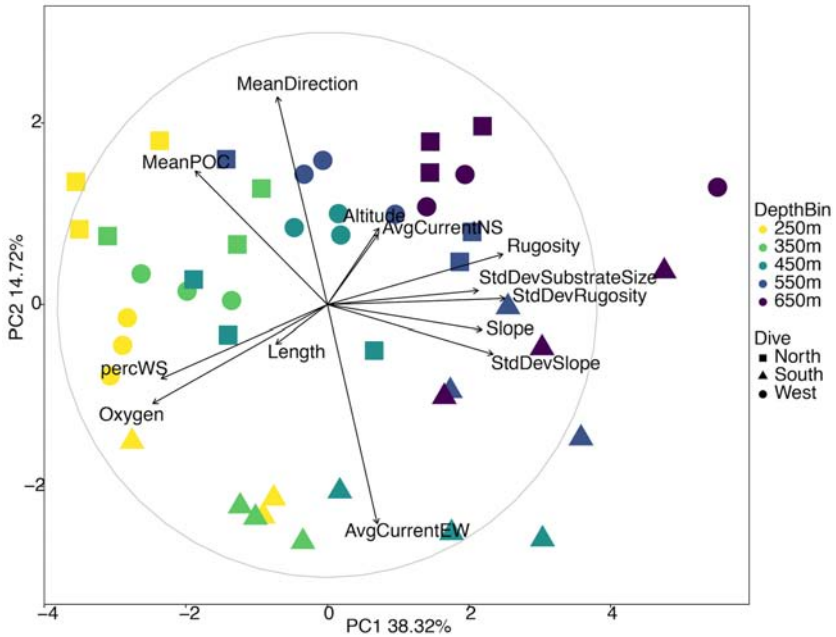

FIGURE 6 | Principal components analysis diagram of environmental variables for three slopes of Mokumanamana. Each point represents a single 1 km transect coded by depth and side.

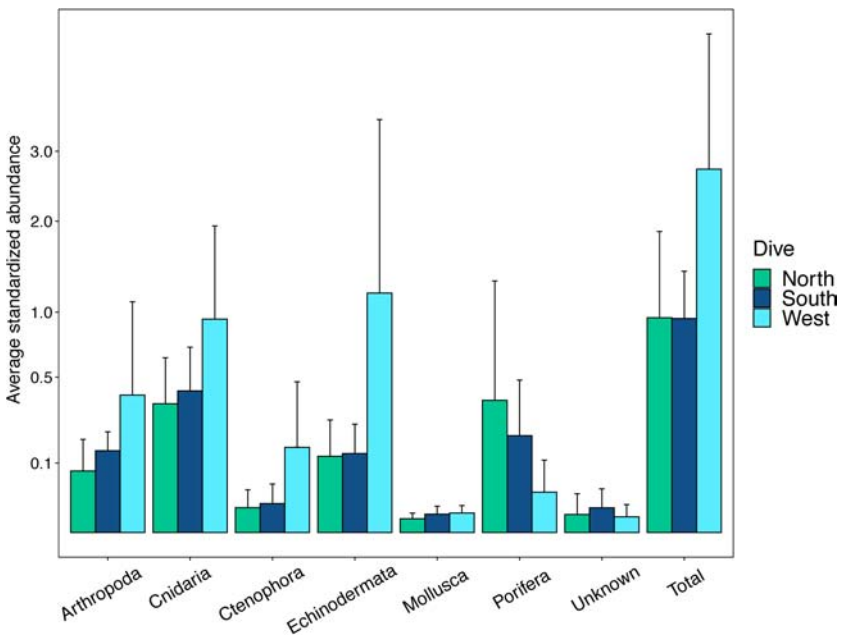

FIGURE 7 | Abundances of major phyla on the three slopes. Abundances are standardized as the number of individuals per number of photos taken in each transect. The *y*-axis values are square root scaled for easier visualization of values.

between depth bins (global $R = 0.80$, $p = 0.001$) and sides of the seamount (global $R = 0.807$, $p = 0.001$). Pairwise comparisons showed significant differences between all pairs of depth bins and between all comparisons of the sides of the seamount (**Supplementary Table S6**). Beta diversity was also high (**Supplementary Figure S3**), and values range from 0.90–0.95 (max. value of 1.00). Beta diversity on all three slopes of Mokumanamana was mostly defined by the substitution of species along the depth gradient rather than the nestedness of species, meaning

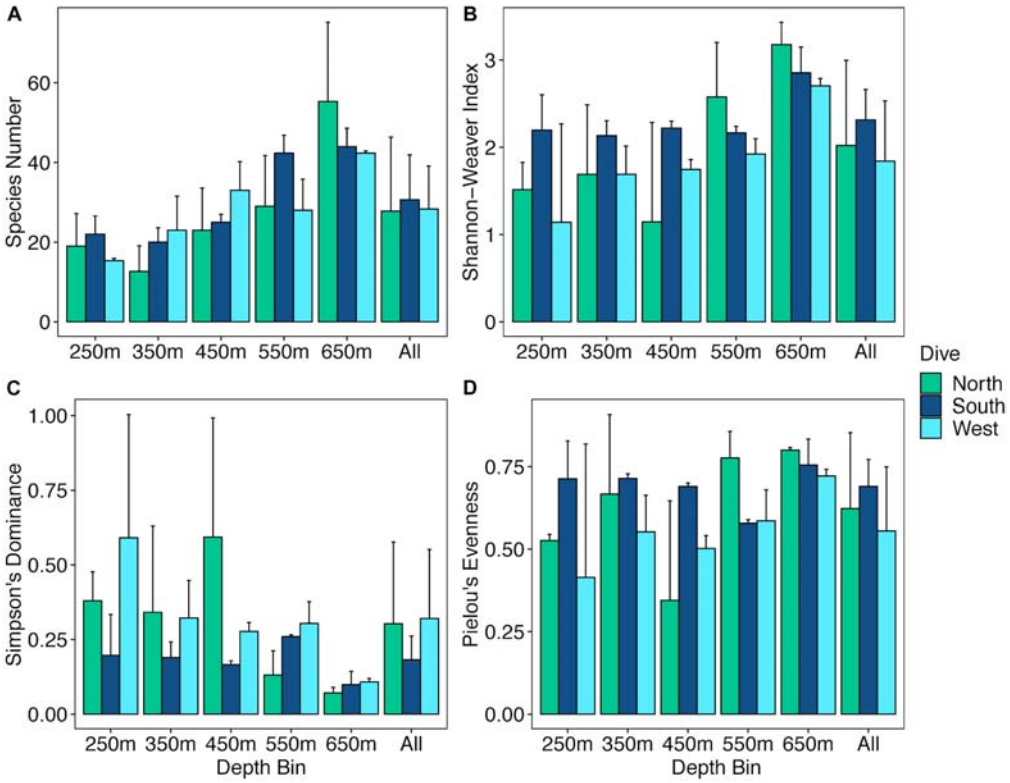

FIGURE 8 | Bar plots of diversity metrics for three slopes of Mokumanamana by depth. Panels: **(A)** species richness, **(B)** Shannon-Weaver's Index, **(C)** Simpson's Dominance Index, **(D)** Pielou's Evenness Index.

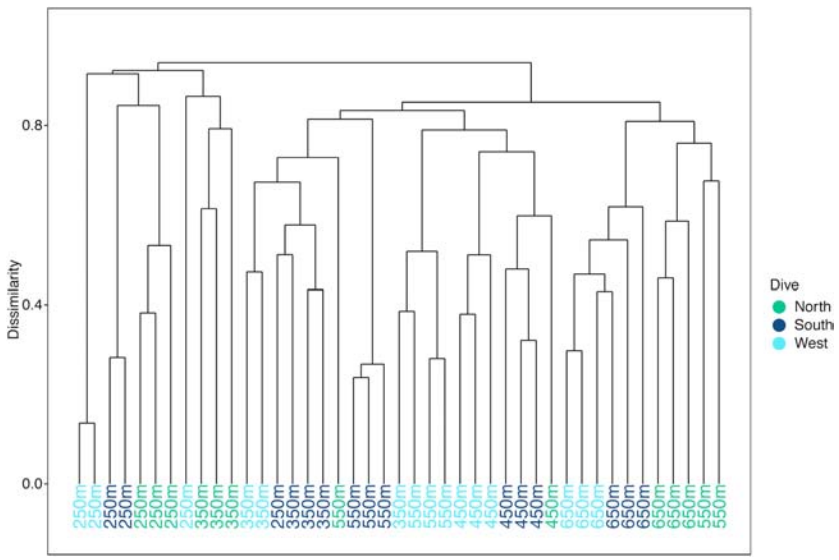

FIGURE 9 | Hierarchical cluster diagram for three slopes of Mokumanamana for transects labeled by depth bin and color coded by side.

that the species turnover was not defined as a loss of species richness but rather a replacement of species with changes in depth. Within a depth bin, beta diversity was also high between the three sides of Mokumanamana (0.81–0.88), and 24.8% of all morphospecies were found on only one side of the seamount, 24.9% were found on only two sides, and 50.3% of all morphospecies were found on all three sides.

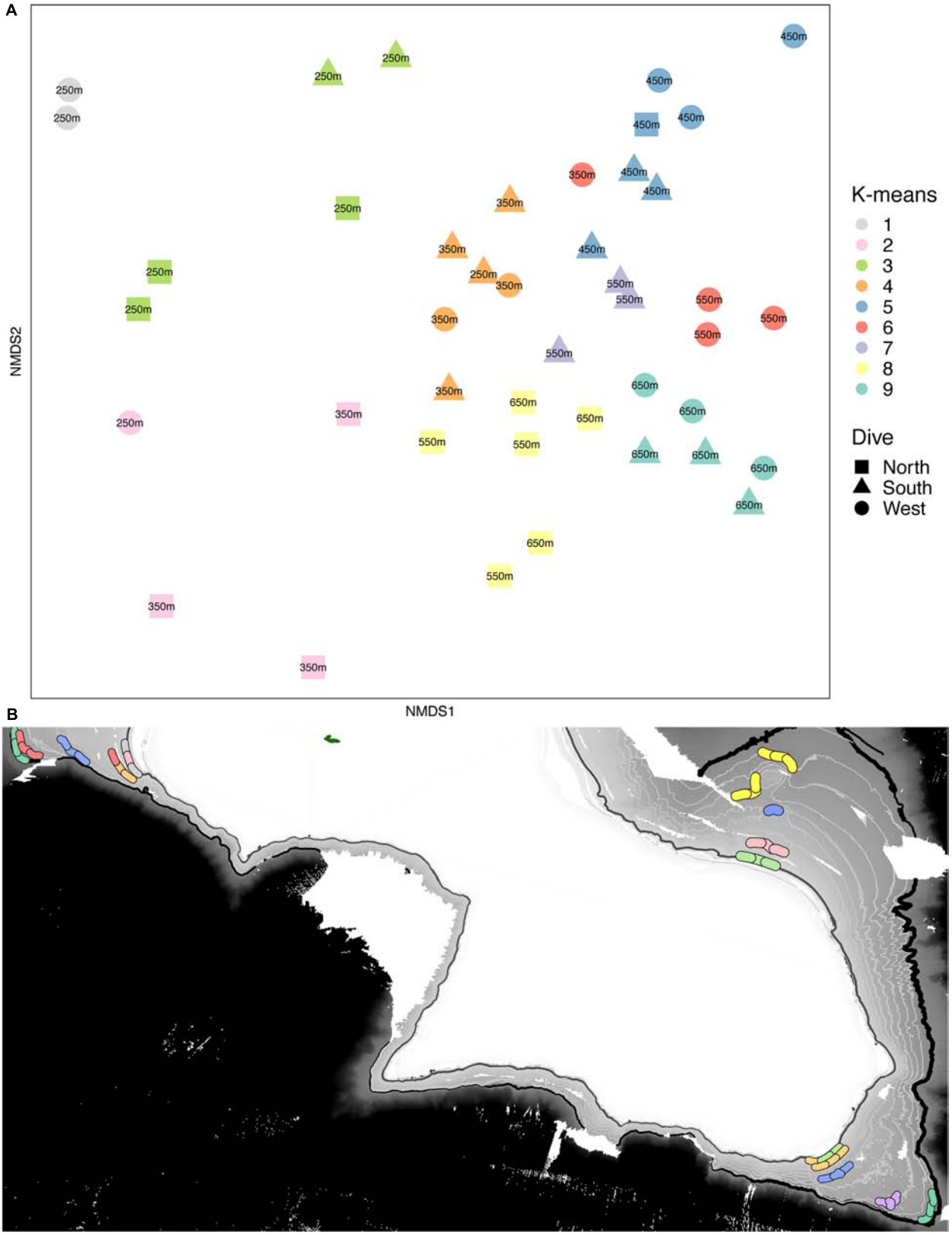

FIGURE 10 | (A) Non-metric multidimensional scaling plot for assemblage structure of Mokumanamana color-coded by k-means clusters labeled by depth bin. **(B)** map with locations of transects denoted by their k-means clusters color code from **(A)**.

TABLE 2 | Results from DISTLM model and dbRDA analysis for Mokumanamana overall.

Marginal tests

Variable	SS(trace)	Pseudo-F	*P*	Prop.
1. Oxygen	18989.0	5.597	**0.001**	0.1201
2. Altitude	4718.2	1.261	0.157	0.0298
3. Mean direction	5705.2	1.535	**0.066**	0.0361
4. Length	4024.8	1.071	0.347	0.0255
5. Perc. White Sand	15202.0	4.362	**0.001**	0.0962
6. StdDevSubstrateSize	11874.0	3.329	**0.001**	0.0751
7. Slope	7024.1	1.906	**0.007**	0.0444
8. StdDevSlope	7982.7	2.180	**0.004**	0.0505
9. Rugosity	12793.0	3.610	**0.001**	0.0809
10. StdDevRugosity	10284.0	2.853	**0.001**	0.0650
11. Mean POC	15753.0	4.537	**0.001**	0.0996
12. AvgCurrentNS	11496.0	3.215	**0.001**	0.0727
13. AvgCurrentEW	10169.0	2.819	**0.001**	0.0643
Residual.df: 41				

Overall best solutions

Selections	R^2	RSS	No. Vars	AIC
1,3–5,7–9,11–13	0.479	82326	10	346.96
1,5,6,9,11–13	0.401	94720	7	346.99
1,3,5–9,11–13	0.479	82411	10	347.01
1,3,5,7–9,11–13	0.453	86415	9	347.05
1,5–9,11–13	0.453	86496	9	347.09
1,3–5,7,8,11–13	0.452	86599	9	347.14
1,5,7–9,11–13	0.426	90820	8	347.18
1,4,5,7–9,11–13	0.452	86697	9	347.19
1,3,5,7,8,11–13	0.425	90836	8	347.19
1,3,5–8,11–13	0.451	86725	9	347.20

Accumulated constrained eigenvalues

	dbRDA1	dbRDA2	dbRDA3	dbRDA4
Eigenvalue	2.0103	1.3562	1.0144	0.9067
Proportion explained	0.2769	0.1868	0.1397	0.1249
Cumulative proportion	0.2769	0.4637	0.6034	0.7283

Biplot scores

Variable	dbRDA1	dbRDA2	dbRDA3	dbRDA4
MeanDirection	−0.0805	0.4054	−0.0889	0.2101
Oxygen	**−0.9367**	−0.2345	−0.0577	−0.2485
Length	−0.1087	0.0316	0.1907	−0.2741
percWS	**−0.8172**	−0.0263	0.2647	−0.1079
MeanPOC	−0.6807	**0.6259**	−0.2875	0.1152
Slope	0.4669	0.0639	0.0962	−0.2811
Rugosity	0.6561	0.3602	0.3118	0.0591
StdDevSubstrateSize	0.6250	−0.2666	−0.2658	0.3580
AvgCurrentEW	0.1686	**−0.5687**	0.4317	−0.5367
AvgCurrentNS	0.5577	−0.1511	−0.4753	−0.3099

ANOVA and Multicollinearity results of dbRDA variables

Variable	Sum of squares	*F*	*P*	VIF
MeanDirection	0.571	2.135	**0.005**	1.910

(Continued)

TABLE 2 | Continued

ANOVA and Multicollinearity results of dbRDA variables

Variable	Sum of squares	*F*	*P*	VIF
Oxygen	1.908	7.141	**0.001**	6.598
Length	0.379	1.419	0.080	1.390
percWS	0.609	2.280	**0.001**	3.249
MeanPOC	1.107	4.142	**0.001**	6.560
Slope	0.351	1.314	0.136	1.862
Rugosity	0.539	2.017	**0.003**	4.478
StdDevSubstrateSize	0.586	2.192	**0.003**	2.438
AvgCurrentEW	0.479	1.794	**0.016**	4.373
AvgCurrentNS	0.733	2.742	**0.001**	2.186
Residual df: 32	8.549			

Notice the close AIC values for all DISTLM solutions. VIF indicates the independence of variables where 1 = independent. Numbers in bold denote significant p-values.

Multivariate analyses also show that both depth and side have strong influences on the faunal assemblage structure of invertebrates on Mokumanamana. Hierarchical cluster analysis first shows two samples from the North side at 450 m are outliers from the rest of the assemblage data (**Supplementary Figure S4**). This is likely due to dense patches of *Sericolophus* sp., and the two outlier transects are subsequently removed from the rest of the analyses. The clustering structure of the remaining samples does not change once the outliers are removed and a trend of samples from the same depth bin and slope being more similar can be seen (**Figure 9**), though three transects do instead cluster with other depths (a South 250 m) and other slopes (a West 250 m and a North 550 m). The K-means clustering algorithm defined nine clusters by Bayesian modeling that can be seen in the NMDS plot and map in **Figure 10**. Eight of the clusters each contain 1–2 depth groups and 1–2 sides of the seamount. Only cluster 5, which was comprised of 450 m depth transects, had at least 1 transect from each of the 3 sides. Notably, the South 550 m transects form group 7, North 550 and 650 m transects form group 8, and West and South 650 m transects form group 9. The only deviation from shallow, mid-depth, and deep groupings that originally came out in the North-side-only analyses within the k-means groups is in group 6 where a 350 m transect clusters with its fellow West-side 550 m transects.

When the assemblage structure is modeled with the environmental data there was still a strong effect by depth and side. Of the top 10 DISTLM models, the best one included 10 variables (**Table 2**); however, no model AIC was significantly higher than any other so all eleven variables indicated by DISTLM were analyzed together. VIF shows mean direction is the most independent variable in the model (v = 1.95) while oxygen is the least independent (v = 6.59). Standard deviation of slope was removed due to a VIF > 10. Ten environmental variables were included in the final model, and eight are significantly correlated to the assemblage data (*p*-value range: 0.004–0.001); the non-significant variables are transect-length and slope (**Table 2**). In **Figure 11**, dbRDA1 was most strongly correlated to oxygen and percent sediment and described 27.69% of the constrained (modeled) variation, while dbRDA2 was most strongly correlated

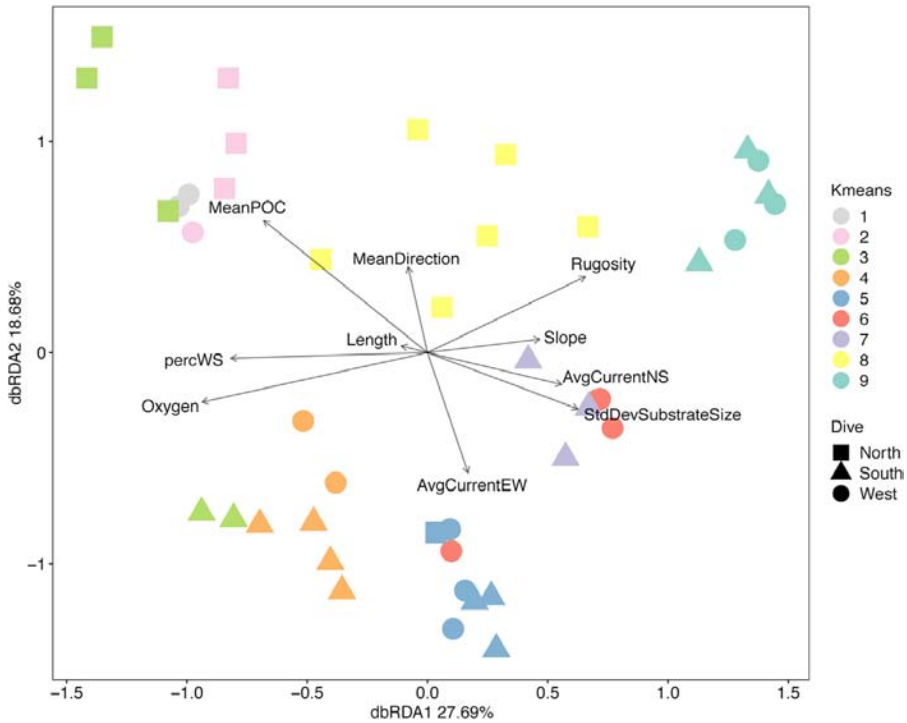

FIGURE 11 | Distance-based redundancy analysis diagram for three slopes of Mokumanamana.

to mean POC and average eastward current and explained 18.68% of the variation in the model. Ten axes were needed overall to explain all variation in the model, but only the first four axes were significant ($p \leq 0.0002$).

When the environmental values were overlaid on the assemblage structure NMDS, the variables that were correlated with the differences between depth bins and sides become more apparent. One-way ANOVAs were run for each variable by depth and side to compare whether the variable changed more vertically or horizontally (**Supplementary Table S7**). **Figures 12A–D**, shows those variables found significant in the dbRDA that changed most with depth. Shallower samples have a higher percent sediment (**Figure 12A**), which also decreases the rugosity (**Figure 12C**) and variability in the slope (**Figure 12D**) in these areas. Deeper samples may have up to 50% soft sediment, but the high rugosity and variability in the slopes of these transects is due to more exposed hard substrate. Oxygen decreased quickly with depth (**Figure 12B**). **Figures 12E–H**, shows those variables that changed most with the side of the seamount. Mean surface POC (**Figure 12E**) was highest on the North side and lowest on the South side. Mean direction (**Figure 12F**) was more consistent on the West side while transects on the South side were the most variable. The 8-year average surface currents do not change direction over Mokumanamana, with the predominantly northward current weakest on the North side (**Figure 12G**) and strongest on the West side. The east-west component of surface current was predominantly westward flowing and was strongest on the northern slope, but weakest on the South facing slope (**Figure 12H**; more negative values are stronger westward currents).

The number of species that best define each k-means group from SIMPER analysis is generally small, especially for shallower groups (**Supplementary Table S8**). **Figure 13** uses the abundance data of the species designated by SIMPER and shows the square root transformed relative abundances of those throughout the dataset. Groups 1–3 are shallow transects at 250 m, and they are generally comprised of few species. Group 1 was strongly defined by the numerous squat lobsters though *V. abies* sea pens were also common. Group 2 was defined by the sea pen *K. stelliferum* and an asteroid *Calliderma* sp. along with squat lobsters. Cup corals were present, but not highlighted as significant by SIMPER. Group 3 was defined by the highly abundant *V. abies* as well as Brisingid sp.3 and the cidaroid urchin *Stylocidaris calacantha*. Groups 4–6 were more mid-depth transects (350–450 m) though one 250 m transect and three 550 m transects from the West side fell into this group. All three groups were defined by an abundance of shrimp. Group 4 was also defined by the presence of spatangoid heart urchins and *K. stelliferum*. Group 5 was comprised of all the transects from 450 m and was defined by cup corals *Caryophyllid* sp., benthic ctenophores *Lyrocteis* sp., and corallimorpharian *Corallimorphus pilatus*. Group 6 was defined by shrimp and *C. pilatus*. Groups 7–9 were comprised of 550 and 650 m transects, and Group 7 was defined only by shrimp and *Farrea* sp. sponges. Groups 8 and 9 showed a greater number of species contributing to the within group similarity, consistent with the higher diversity found on the deeper transects and were defined

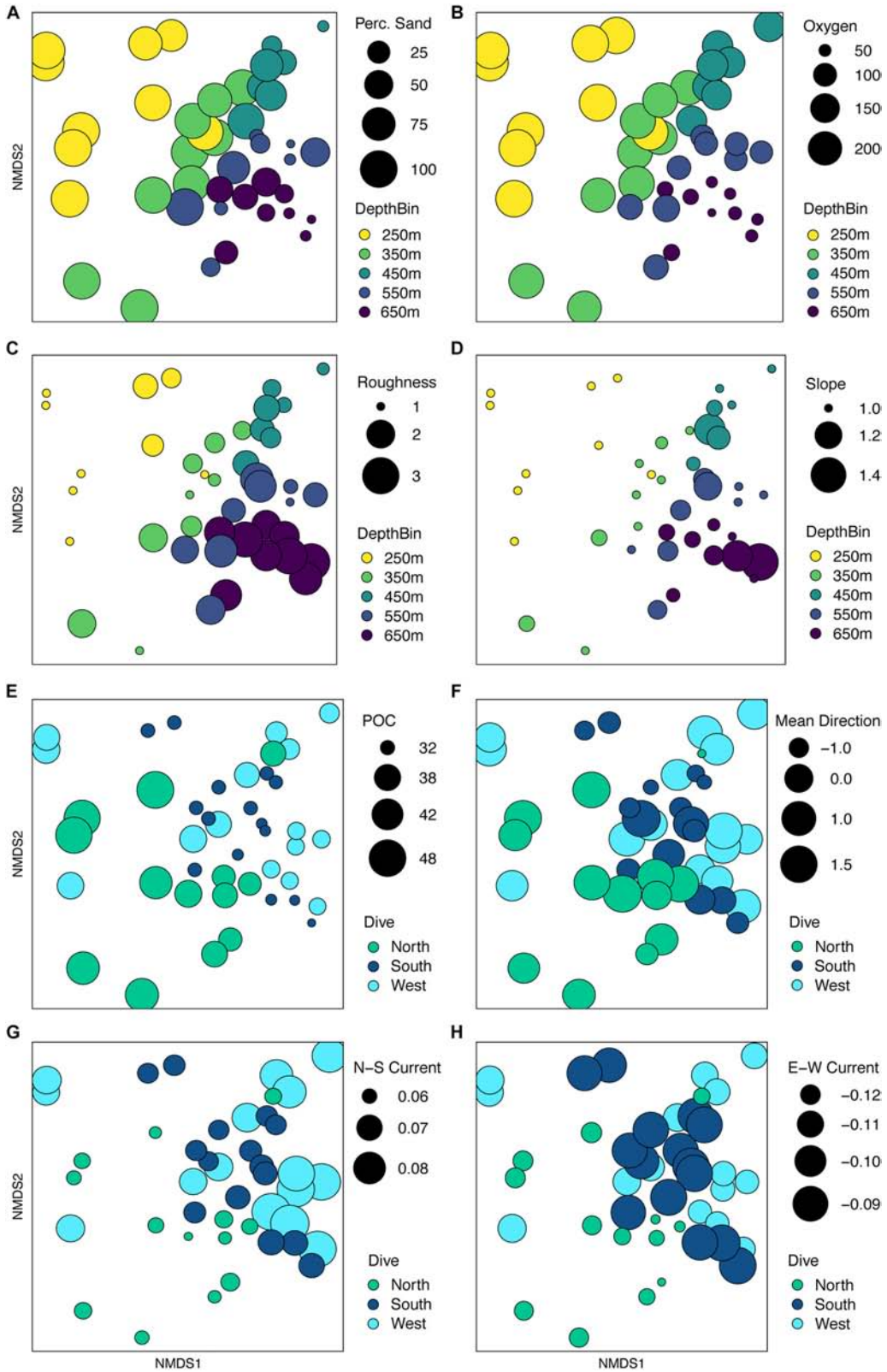

FIGURE 12 | Non-metric multidimensional scaling plot for assemblage structure of Mokumanamana from **Figure 10** with overlay of environmental gradients. Circle size is relative to values of variables that change with depth or dive. Panels: **(A)** percent sediment, **(B)** oxygen (μM), **(C)** roughness, **(D)** standard deviation of slope, **(E)** mean particulate organic matter (mg/m^3), **(F)** mean direction, **(G)** northward current (m/s), **(H)** westward current (m/s).

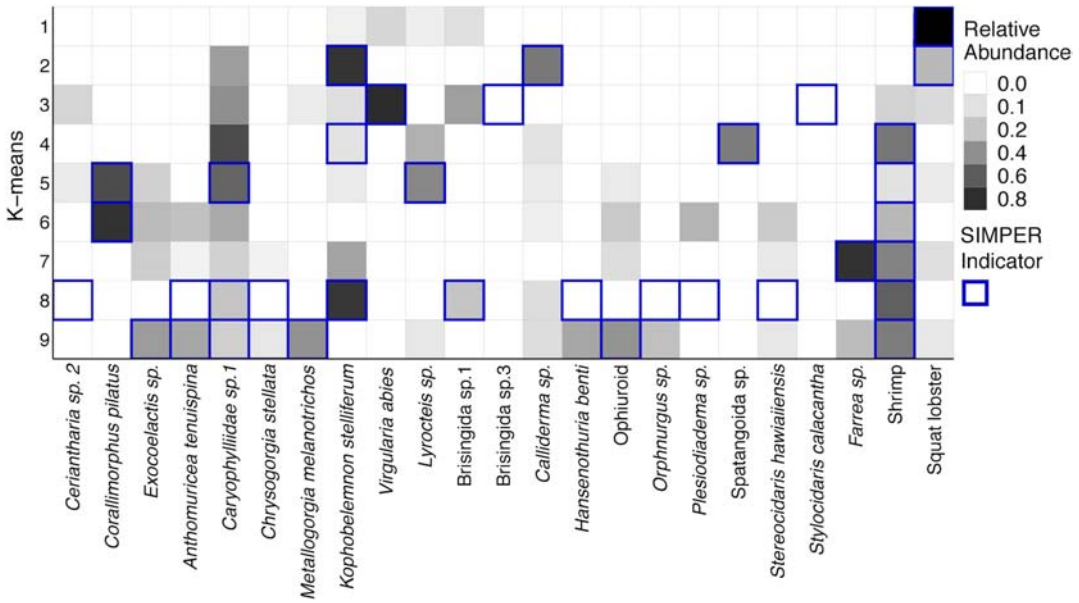

FIGURE 13 | Heatmap of the square root transformed relative abundances of species that define k-means clusters from SIMPER analysis. Along the row for each k-means group, the species indicated by SIMPER analysis as drivers of within-group similarity are outlined in dark blue.

by numerous species of corals and echinoderms, including the corals *Anthomuricea tenuspina*, *Metallogorgia melanotrichos, Chrysogorgia stellata*, and holothurians *Hansenothuria benti* and *Orphnurgus* sp.

DISCUSSION

Environmental Gradients at Fine Scales

Opportunities for intensive investigations of variability in faunal communities and environmental parameters on the scale of a single seamount feature have been rare, but have suggested that there may be significant habitat heterogeneity on individual seamounts, which can be expected to translate into significant variation in community structure and species composition within a single feature (Baco, 2007; McClain et al., 2010; Bo et al., 2011; Long and Baco, 2014; Thresher et al., 2014; Morgan et al., 2015; Victorero et al., 2018a; Mejia-Mercado et al., 2019). The data presented here represent one of the most extensive investigations of a single seamount, with over 150 km of the untrawled seamount Mokumanamana surveyed using an AUV. Despite the relatively narrow depth range surveyed (200–700 m), enough variability was observed in habitat parameters among transects that depth and the different sides of Mokumanamana were apparent in the ordination plots of environmental data, confirming the presence of high habitat heterogeneity on this seamount. In particular, substrate size, mean POC, oxygen, percent sediment, rugosity, chlorophyll-α values and mean direction were strongly correlated with variation among transects in the PCA on the North side (**Figure 2**); while in the PCA for all three sides, oxygen, rugosity, percent sediment, mean direction and the average east-west surface current were the significant factors (**Figure 6**).

Even though depth was not included in the data used for the PCA, there was a clear depth gradient along the PC1 axis, correlated to several substrate parameters. The slope became steeper with increasing depth, percent sand decreased, and roughness increased (**Figure 12**). Larger outcrops and boulders became the dominant substrate forms at deeper depths, though patches of high sediment cover were still present. Though some deep transects had sediment as the dominant substrate type, there were still secondary substrate types (Mortensen and Buhl-Mortensen, 2004; Neves et al., 2014) of boulders, cobble, or hardpan, which can provide hard substrate habitat. All of this contributed to a general increase in substrate complexity (variability in substrate size and type, rugosity, and slope) with depth, which increases the types of habitats available, likely contributing to the higher diversity observed on deeper transects (**Figures 3**, **8**).

In contrast to these substrate parameters, oxygen decreased with depth (**Figure 12B**). Decreases in oxygen would usually suggest decreased species richness and diversity (e.g., Wishner et al., 1990; Gooday et al., 2009), instead of the increases seen on Mokumanamana (**Figures 3**, **8**), but while oxygen levels do decrease with depth from around 250 μM at 250 m to 50 μM at 650 m (8 mg/L to 1.6 mg/L), they do not approach lethal or sublethal values for the dominant benthic invertebrates on this feature (Vaquer-Sunyer and Duarte, 2008), with one exception being crustaceans. Vaquer-Sunyer and Duarte (2008) found crustaceans to be affected by oxygen levels less than 63 uM (2 mg/L) and to have the highest sensitivity to low oxygen values. Crustaceans overall are still present at deeper transects, but in much lower abundances than at 250 m, which

could suggest more sensitive species are restricted to shallower depths. However, increased rugosity at deeper transects could also make counting smaller crustaceans from imagery more difficult. Shrimp and palinurid lobsters are the only crustaceans to increase with depth, suggesting these organisms are less sensitive to low oxygen concentrations.

Oxygen was strongly correlated with temperature and conductivity, which predicated the removal of these two parameters prior to multivariate analyses; however, these variables could still have an influence on assemblage structure. The observed temperature range on Mokumanamana (5–16°C) is very similar to other features studied in the NWHI in the same depth range (Parrish, 2007). Temperature is known to influence physiology and metabolism, which in turn can influence biodiversity and assemblage structure in an ecosystem. Diversity in the deep-sea has a unimodal relationship with temperature, with the peak expected around 6°C (Yasuhara and Danovaro, 2016). Diversity on Mokumanamana follows the expected trend with the highest values of species richness and diversity occurring around 5°C. Conductivity ranged from 3.2 to 4.2 S/m and is also within the expected range for this area (Tyler et al., 2017). Conductivity/salinity is not expected to be influential in many deep-sea assemblages as it is considered mostly constant (Roberts et al., 2009).

The three sides of Mokumanamana were also apparent in the environmental PCA plot with the South side being more distinct from the North and West than either of those were from each other (**Figure 6**). Even though the North and West sides were more similar to each other based on the available environmental data, this did not translate into comparable diversity and abundance metrics. The West side had much higher abundances especially among the echinoderms, arthropods and cnidarians, while the North had the highest abundance of sponges. The West side was the least diverse and the South side had the lowest evenness of the three sides (**Figures 7**, **8**).

Factors that varied most strongly among the sides were surface POC, mean direction, and direction of the surface currents (**Figure 12**). POC was highest on the North side and lowest on the South. Higher POC values would typically be related to increased abundance and biomass (e.g., De Rijk et al., 2000), yet the highest abundances of animals, except sponges, occurred on the West side (**Figure 7**). The range of POC is relatively narrow (31–48 mg/m^3), and the values are still oligotrophic for the feature as a whole. The data are also surface POC values, and the interaction of surface and deeper currents may affect the distribution of available POC by the time it reaches the slopes of the seamount. Seamount flanks have been shown to accelerate currents, generate internal tides, and trap mesoscale eddies along their flanks, especially on the west side of the seamount in the Northern Hemisphere (Genin et al., 1986, 1989; Eriksen, 1991, reviewed in White and Mohn, 2004). With the horizontal current component dominantly westward over Mokumanamana (**Supplementary Figure S5**), mesoscale eddies could be trapping sinking POC along the western flank, allowing for the nearly three-fold increase in abundance of invertebrates on that side. A parallel study of fishes on Mokumanamana found they were most abundant on the South and West sides, likely due to a higher prevalence of rocky substrate providing more protected areas for organic matter to accumulate (Mejia-Mercado et al., 2019). On seamounts in Tasmania, Thresher et al. (2011) found an extremely dense community, with much more biomass than was expected to be possible based on surface primary productivity above the features. Instead, they hypothesize that the biomass is supported by pulses of food advected from more productive waters further offshore. Other labile organic matter not measured from satellite data can also be more concentrated on seamount flanks; Kiriakoulakis et al. (2009) found increased concentrations of both suspended POC and polyunsaturated fatty-acids near the summit of Seine Seamount in the North Atlantic compared to open water at similar depths. Gori et al. (2014) found four species of cold-water corals were able to use free amino acids as a food source. Thus, in the oligotrophic waters above Mokumanamana, other organic compounds such as fatty acids, amino acids, and sugars could also be important food sources.

Species richness in the deep-sea generally increases with depth and peaks around 2000 m (Rex and Etter, 2010). The increase in species richness with depth on Mokumanamana (**Figure 8A**) follows this general trend. Overall, Mokumanamana had high alpha diversity and overall diversity, as described by Shannon-Weaver index, compared to other features within the NWHI at similar depths (Vetter et al., 2010), and were on average similar to the diversity of the Necker Ridge at depths of 1400–1800 m (Morgan et al., 2015). Surface primary productivity is similar on Necker Ridge to Mokumanamana, which may explain their similar levels of diversity despite the depth differences. Long and Baco (2014) surveyed comparable depths to the current study in a precious coral bed on the Island of Oahu in the Main Hawaiian Islands, but focused only on sponges and corals. That study had lower species richness, but higher abundances than Mokumanamana. Primary productivity is higher around Oahu and the Main Hawaiian Islands, which may explain the higher abundances found there (NOAA STAR Ocean Color, Wang and Jiang, 2018).

Assemblage Structure

On Mokumanamana, the environmental gradients that occur both vertically and horizontally have a strong effect on assemblage structure, augmented by biogenic structures of octocorals and sponges, which provide numerous landscapes for diverse assemblages to exist. Hierarchical clustering demonstrated a pattern of transects clustering mostly by depth, but also by side within depth clusters, resulting in 9 assemblage groups (**Figure 9**). The NMDS representation of assemblage structure shows that the 250–350 m depth transects have higher dissimilarity among them as compared to deeper transects (**Figure 10**). Within this depth range, all three sides had similar sandy habitats, instead current strength and mean POC vary among the sides and may be contributing to variation in assemblage structure. Within the faunal data, low evenness and low species richness at these depths (**Figures 8A,D**) may further contribute to their dissimilarity. The only k-means group with transects from all 3 sides, Group 5 at 450 m depth (**Figure 10**) stands out because many transects in this cluster have low evenness and the habitats were quite different between the three

sides; the West side was mostly hardpan with low sediment, the South side was more pebble and sand with some larger boulders, and the North side at 450 m was mostly sand with some pebble. However, at all three sides 450 m was a transition zone from a dominantly sandy substrate to more hard-bottom habitat. That shared transitional nature could influence the shared assemblage structure between the three sides of the seamount.

Modeling assemblage structure with the environmental variables highlights the patchiness and high variability possible on a single seamount. The North and South side transects show very little similarity between assemblages, and instead occupy different regions of the overall assemblage representation (**Figure 11**). The West side has the most within-side dissimilarity and shows larger changes along the depth gradient. Insights into the environmental parameters that might influence this variation in assemblage structure from the DISTLM analyses are limited because the first two axes of dbRDA describe relatively little of the variation in assemblage structure (less than 50%). Analyses of each phylum separately did not improve the explanatory power of the model (Quattrini et al., 2015), likely due to the high variability within corals and echinoderms throughout Mokumanamana, and the patchy distribution of sponges (**Supplementary Table S9**). The high variability in the environment combined with high variability in the species distributions along both the depth gradient and between sides, is likely a large influence in the uncertainty in the model. The increase in rugosity and substrate variability with depth appears to be most important for the overall increased species richness and diversity with depth, as previously discussed decreases in oxygen and POC should have an opposite effect. Slope is less informative than expected (*sensu* Yesson et al., 2012), but this is likely due to the constraints of the AUV narrowing the slope range sampled, thus most transects have a similar slope value. The differences in abundances and assemblage structure between sides of the seamount is likely instead influenced by POC and the westward current (**Table 2**). Increases in rugosity, substrate variability, and slope variability increase habitat complexity, which has been shown to support higher levels of diversity, which in turn affects assemblage structure (Lacharité and Metaxas, 2017).

Increased habitat complexity with depth translated into more diverse assemblages defined by SIMPER, where most of the 550 and 600 m k-means groups had both more species and a wider number of taxonomic groups driving the overall structure. The relationship between increased habitat complexity, combined with increased biogenic complexity from increased tree-like octocoral and antipatharian abundance, likely has an additive effect on the diversity. Comparatively, sand-dominated shallow transects were defined by fewer species, many of which do not provide biogenic habitat, like echinoderms *Calliderma* sp., *Stylocidaris calancantha*, and Brisingida. Sea pens were also abundant at these depths, and while some species do have known associates (Baillon et al., 2014), the smaller sizes of *V. abies* and *K. stelliferum* likely means these species make less than optimal habitat for associates (although our ability to observe associates on these may have been affected by timing of sampling and the coarse image resolution).

The changes in assemblages between depths and sides led to high beta-diversity overall on Mokumanamana. Only 100 m of depth change, or 30–80 km in horizontal distance around the seamount, translated into large differences in the types and abundances of species present. Mokumanamana has high species replacement with changes in depth, similar to Long and Baco (2014); Schlacher et al. (2014); and Victorero et al. (2018a). While deeper samples did have higher species richness, the species not seen in shallower samples have been replaced, rather than lost from an overarching species list. Nestedness is often seen in abyssal and hadal sink communities being supplied by shallower communities (McClain and Rex, 2015). Species replacement instead suggests the species turnover is due to preferential recruitment within depth zones. Within the relatively shallow depths studied here, there are greater environmental changes than normally seen for deeper ecosystems, which could bolster preferential recruitment.

We also found high levels of beta-diversity and species replacement along horizontal changes within a given depth. Horizontal species turnover is not often strong in deep-sea habitats (reviewed in McClain and Rex, 2015), but seamount flanks appear to defy that generality as seen in this research and on other features (Bo et al., 2011; Long and Baco, 2014; Schlacher et al., 2014; Morgan et al., 2015; Mejia-Mercado et al., 2019). The large size of Mokumanamana perhaps allows for greater differences between habitats within the same depth bin. The differences in surface current strengths between the three sides could also have a sorting effect on recruitment around the seamount.

Conclusions and Management Implications

Overall, Mokumanamana, which has been largely unimpacted by human activity, shows high levels of alpha and beta-diversity. Although the environmental data support high habitat heterogeneity, and the faunal data support significant assemblage structure among sides and depths of the seamount (**Figures 10**, **11**), the patterns for the environmental data do not predict the patterns in abundance, diversity, or assemblage structure. In the environmental data, the South side stands out as the most distinct habitat (**Figure 6**) while the North and West strongly overlap, yet in the abundance data, the west side had the highest abundances, and in the NMDS plot (**Figure 10**), the North side transects were the most distinct while the South side transects fall almost entirely within the ordination range of the West side.

This suggests that although changes in topography are important to assemblage structure, substrate is not enough to adequately model distributions and assemblage structure (*sensu* Bennecke and Metaxas, 2017b). Even with the addition of hydrographic/productivity/water column data, the DISTLM model does not describe a large part of the variation in assemblage structure (less than 50%). Frequently DISTLM modeling from environmental variables does not provide strong explanations for deep-sea assemblages of invertebrates (O'Hara et al., 2010; Morgan et al., 2015), algae

(O'Hara et al., 2010), and fishes (Clark et al., 2010), which suggests other factors such as community interactions, reproductive and recruitment methods, and near-bottom hydrodynamics likely have significant impacts on assemblage structure. These types of data are difficult, time consuming, and costly to collect, yet their necessity is highlighted by the limited ability of environmental proxies to define fine-scale assemblage variation.

These biological variables plus niche sorting within microhabitats that could accumulate over time (Diamond, 1988; Auster et al., 2005), as well as important stochastic effects (Quattrini et al., 2016), are likely to lead to highly dynamic and heterogeneous assemblages that have high diversity over fine spatial scales. Future human impacts need to be paired with mitigation techniques (e.g., Cuvelier et al., 2018) that preserve an offset of biodiversity that will be disturbed. This is an especially important step as ecosystem recovery is slow enough in the deep sea (Williams et al., 2010; Bennecke and Metaxas, 2017a; Baco et al., 2019) that most human impacts will be very long lasting.

Taken together, these results suggest that surveys of seamounts that include only a single transect, focus on only a single side, or focus a narrow depth range of a seamount will not yield adequate information on species abundances, diversity or composition. The high habitat heterogeneity of seamounts precludes the extrapolation of diversity data from geographically or bathymetrically narrow surveys. At even the relatively coarse taxonomic level of morphospecies, this study found that 25% of the morphospecies occurred on only one side of the seamount, which highlights the levels of biodiversity that may be missed in surveys that do not cover a broader area of a feature. Temporal changes in assemblage structure and community dynamics should also be considered during impact assessments and mitigation planning. Many metanalyses of seamounts have only a handful of records, and many rely on broad-scale survey data. Impact assessments will extremely underestimate losses in biodiversity and biomass if seamounts are continually managed as homogenous units. Instead quantifying the biodiversity of seamounts to comprehensively represent them in reserves (e.g., Althaus et al., 2017) will require more fine-scale environmental impact assessments than typically employed.

DATA AVAILABILITY STATEMENT

All of the environmental data are available in **Supplementary Table 1** and all of the faunal data have been uploaded to Mendeley: Morgan (2019).

AUTHOR CONTRIBUTIONS

AB and NM: conceptualization and formal analysis. NM, AB, SG, and ER: data curation. AB and ER: funding acquisition. NM, AB, and SG: methodology. AB: supervision. NM: visualization and writing – original draft. NM, AB, SG, and ER: writing – review and editing.

FUNDING

This work was supported by NSF grant #OCE-1334652 to AB and #OCE-1334675 to ER. Work in the Papahānaumokuākea Marine National Monument was permitted under permits #PMNM-2014-028 and #PMNM-2016-021.

ACKNOWLEDGMENTS

We would like to thank the captains and crew of the *RV Kilo Moana*, and the crew of the *AUV Sentry*, as well as the assistance of volunteers at sea Kelci Miller, Mackenzie Schoemann, Arvind Shantharam, and John Schiff. We would also like to thank Travis Ferguson and Alexis Rentz for their aid in data collection. This paper benefited methodologically and statistically from discussions with Arvind Shantharam and Beatriz Mejia. NMDS and Heatmap base R scripts were from the online tutorial of Umer Zeeshan Ija (http://userweb.eng.gla.ac.uk/umer.ijaz).

SUPPLEMENTARY MATERIAL

The Supplementary Material for this article can be found online at: https://www.frontiersin.org/articles/10.3389/fmars.2019.00715/full#supplementary-material

REFERENCES

Althaus, F., Williams, A., Alderslade, P., and Schlacher, T. A. (2017). Conservation of marine biodiversity on a very large deep continental margin: how representative is a very large offshore reserve network for deep-water octocorals? *Divers. Distrib.* 23, 90–103. doi: 10.1111/ddi.12501

Althaus, F., Williams, A., Schlacher, T., Kloser, R., Green, M., Barker, B., et al. (2009). Impacts of bottom trawling on deep-coral ecosystems of seamounts are long-lasting. *Mar. Ecol. Prog. Ser.* 397, 279–294. doi: 10.3354/meps08248

Anderson, M., Gorley, R. N., and Clarke, R. K. (2008). *PERMANOVA+ for PRIMER: Guide to Software and Statistical Methods*. Plymouth: PRIMER-E.

Auster, P. J., Moore, J., Heinonen, K. B., and Watling, L. (2005). "A habitat classification scheme for seamount landscapes: assessing the functional role of deep-water corals as fish habitat," in *Cold-Water Corals and Ecosystems*, eds A. Friewald, and J. M. Roberts, (New York, NY: Springer-Verlag), 761–769. doi: 10.1007/3-540-27673-4_40

Baco, A. R. (2007). Exploration for deep-sea corals. *Oceanography* 20, 108–117. doi: 10.5670/oceanog.2007.11

Baco, A. R., and Cairns, S. D. (2012). Comparing molecular variation to morphological species designations in the deep-sea coral Narella reveals new insights into seamount coral ranges. *PLoS One* 7:e45555. doi: 10.1371/journal.pone.0045555

Baco, A. R., Morgan, N. B., Roark, E. B., Silva, M., Shamberger, K. E. F., and Miller, K. (2017). Defying dissolution: discovery of deep-sea scleractinian coral reefs in the North Pacific. *Sci. Rep.* 7:5436. doi: 10.1038/s41598-017-05492-w

Baco, A. R., Roark, E. B., and Morgan, N. B. (2019). Amid fields of rubble, scars, and lost gear, signs of recovery observed on seamounts on 30-40 year time scales. *Sci. Adv.* 5:eaaw4513. doi: 10.1126/sciadv.aaw4513

Baillon, S., Hamel, J., and Mercier, A. (2014). Diversity, distribution and nature of faunal associations with deep-sea pennatulacean corals in the Northwest Atlantic. *Plos One* 9:e111519. doi: 10.1371/journal.pone.0111519

Baselga, A. (2017). Partitioning abundance-based multiple-site dissimilarity into components: balanced variation in abundance and abundance gradients. *Methods Ecol. Evol.* 8, 799–808. doi: 10.1111/2041-210X.12693

Baselga, A., and Orme, C. D. L. (2012). betapart: an R package for the study of beta diversity. *Methods Ecol. Evol.* 3, 808–812. doi: 10.1111/j.2041-210x.2012.00224.x

Bennecke, S., and Metaxas, A. (2017b). Is substrate composition a suitable predictor for deep-water coral occurrence on fine scales? *Deep Sea Res. I.* 124, 55–65. doi: 10.1016/j.dsr.2017.04.011

Bennecke, S., and Metaxas, A. (2017a). Effectiveness of a deep-water coral conservation area: evaluation of its boundaries and changes in octocoral communities over 13 years. *Deep Sea Research Part II* 137, 420–435. doi: 10.1016/j.dsr2.2016.06.005

Bo, M., Bava, S., Canese, S., Angiolillo, M., Cattaneo-Vietti, R., and Bavestrello, G. (2014). Fishing impact on deep mediterranean rocky habitats as revealed by ROV investigation. *Biol. Conserv.* 171, 167–176. doi: 10.1016/j.biocon.2014.01.011

Bo, M., Pusceddu, A., Schroeder, K., Bavestrello, G., Bertolino, M., Borghini, M., et al. (2011). Characteristics of the mesophotic megabenthic assemblages of the vercelli seamount (North Tyrrhenian Sea). *PLoS One* 6:e16357. doi: 10.1371/journal.pone.0016357

Boschen, R. E., Rowden, A. A., Clark, M. R., Barton, S. J., Pallentin, A., and Gardner, J. P. A. (2015). Megabenthic assemblage structure on three New Zealand seamounts: implications for seafloor massive sulfide mining. *Mar. Ecol. Prog. Ser.* 523, 1–14. doi: 10.3354/meps11239

Brooke, S. D., Watts, M. W., Heil, A. D., Rhode, M., Mienis, F., Duineveld, G. C. A., et al. (2017). Distributions and habitat associations of deep-water corals in norfolk and baltimore canyons, mid-atlantic bight, USA. *Deep Sea Res. Part II* 137, 131–147. doi: 10.1016/j.dsr2.2016.05.008

Buhl-Mortensen, L., Vanreusel, A., Gooday, A. J., Levin, L. A., Priede, I. G., Buhl-Mortensen, P., et al. (2009). Biological structures as a source of habitat heterogeneity and biodiversity on the deep ocean margins. *Mar. Ecol.* 31, 21–50. doi: 10.1111/j.1439-0485.2010.00359.x

Clark, M. R., Althaus, F., Schlacher, T. A., Williams, A., Bowden, D. A., and Rowden, A. A. (2016). The impacts of deep-sea fisheries on benthic communities: a review. *ICES J. Mar. Sci.* 73(Suppl._1), i51–i69. doi: 10.1093/icesjms/fsv123

Clark, M. R., Althaus, F., Williams, A., Niklitschek, E., Menezes, G. M., Hareide, N., et al. (2010). Are deep-sea demersal fish assemblages globally homogenous? *Insights from seamounts. Mar. Ecol.* 31, 39–51. doi: 10.1111/j.1439-0485.2010.00384.x

Clark, M. R., and Rowden, A. A. (2009). Effect of deepwater trawling on the macro-invertebrate assemblages of seamounts on the Chatham Rise, New Zealand. *Deep Sea Res. I.* 56, 1540–1554. doi: 10.1016/j.dsr.2009.04.015

Clark, M. R., Schlacher, T. A., Rowden, A. A., Stocks, K. I., and Consalvey, M. (2012). Science priorities for seamounts: research links to conservation and management. *PLoS One* 7:e29232. doi: 10.1371/journal.pone.0029232

Clark, M. R., Vinnichenko, V. I., Gordon, J. D., Beck-Bulat, G. Z., Kukharev, N. N., and Kakora, A. F. (2007). "Large-scale distant-water trawl fisheries on seamounts," in *Seamounts: Ecology, Fisheries & Conservation*, eds T. J. Pitcher, T. Morato, P. J. B. Hart, M. R. Clark, N. Haggan, and R. S. Santos, (Hoboken, NJ: Wiley-Blackwell), 361–399. doi: 10.1002/9780470691953.ch17

Clarke, K. R., and Gorley, R. N. (2015). *Getting Started with PRIMER V7: Plymouth, Plymouth Marine Laboratory*. Plymouth: PRIMER-E Ltd.

Core Team, R. (2018). *R: A Language and Environment for Statistical Computing*. Vienna: R Foundation for Statistical Computing.

Cuvelier, D., Gollner, S., Jones, D. O., Kaiser, S., Arbizu, P. M., Menzel, L., et al. (2018). Potential mitigation and restoration actions in ecosystems impacted by seabed mining. *Front. Mar. Sci.* 5:467. doi: 10.3389/fmars.2018.00467

De Leo, F. C., Gauthier, M., Nephin, J., Mihály, S., and Juniper, S. K. (2017). Bottom trawling and oxygen minimum zone influences on continental slope benthic community structure off Vancouver Island (NE Pacific). *Deep Sea Res. Part II* 137, 404–419. doi: 10.1016/j.dsr2.2016.11.014

De Rijk, S., Jorissen, F. J., Rohling, E. J., and Troelstra, S. R. (2000). Organic flux control on bathymetric zonation of mediterranean benthic foraminifera. *Mar. Micropaleontol.* 40, 151–166. doi: 10.1016/S0377-8398(00)00037-2

Diamond, J. (1988). Factors controlling species diversity: overview and synthesis. *Ann. Mo. Bot. Gard* 75, 117–129. doi: 10.1016/j.tibs.2018.04.002

Eriksen, C. C. (1991). Observations of amplified flows atop a large seamount. *J. Geophys. Res. Oceans.* 96, 15227–15236.

Fisher, N. I. (1995). *Statistical Analysis of Circular Data*. Cambridge: Cambridge University Press.

Genin, A., Dayton, P. K., Lonsdale, P. F., and Spiess, F. N. (1986). Corals on seamount peaks provide evidence of current acceleration over deep-sea topography. *Nature* 322, 59–61. doi: 10.1038/322059a0

Genin, A., Noble, M., and Lonsdale, P. F. (1989). Tidal currents and anticyclonic motions on two North Pacific seamounts. *Deep Sea Res. A.* 36, 1803–1815. doi: 10.1016/0198-0149(89)90113-1

Gilmartin, M., and Revelante, N. (1974). The 'island mass' effect on the phytoplankton and primary production of the Hawaiian Islands. *J. Exp. Mar. Biol. Ecol.* 16, 181–204. doi: 10.1016/0022-0981(74)90019-7

Gooday, A. J., Levin, L. A., Aranda da Silva, A., Bett, B. J., Cowie, G. L., Dissard, D., et al. (2009). Faunal responses to oxygen gradients on the Pakistan margin: a comparison of foraminiferans, macrofauna and megafauna. *Deep Sea Res. Part II* 56, 488–502. doi: 10.1016/j.dsr2.2008.10.003

Gori, A., Grover, R., Orejas, C., Sikorski, S., and Ferrier-Pagès, C. (2014). Uptake of dissolved free amino acids by four cold-water coral species from the mediterranean Sea. *Deep Sea Res. II.* 99, 42–50. doi: 10.1016/j.dsr2.2013.06.007

Halfar, J., and Fujita, R. M. (2007). Danger of deep-sea mining. *Science* 316:987. doi: 10.1126/science.1138289

Hall-Spencer, J., Allain, V., and Fosså, J. H. (2002). Trawling damage to Northeast Atlantic ancient coral reefs. *Proc. R. Soc. B.* 269, 507–511. doi: 10.1098/rspb.2001.1910

Hein, J. R., Conrad, T. A., and Dunham, R. E. (2009). Seamount characteristics and mine-site model applied to exploration-and mining-lease-block selection for cobalt-rich ferromanganese crusts. *Mar. Georesour. Geotech.* 27, 160–176. doi: 10.1080/10641190902852485

Higgs, N. D., and Attrill, M. (2015). Biases in biodiversity: wide-ranging species are discovered first in the deep sea. *Front. Mar. Sci.* 2:61. doi: 10.3389/fmars.2015.00061

Howell, K. L., Billett, D. S., and Tyler, P. A. (2002). Depth-related distribution and abundance of seastars (*Echinodermata*: *Asteroidea*) in the porcupine seabight and porcupine abyssal plain, N.E. Atlantic. *Deep Sea Res. I.* 49, 1901–1920. doi: 10.1016/S0967-0637(02)00090-0

Kilgour, M. J., Auster, P. J., Packer, D., Purcell, M., Packard, G., Dessner, M., et al. (2014). Use of AUVs to inform management of deep-sea corals. *Mar. Technol. Soc. J.* 48, 21–27. doi: 10.4031/MTSJ.48.1.2

Kiriakoulakis, K., Vilas, J., Blackbird, S., Aristegui, J., and Wolff, G. (2009). Seamounts and organic matter—is there an effect? the case of sedlo and seine seamounts, Part 2. *Comp. Suspend. Particulate Organ. Matter. Deep Sea Res. II* 56, 2631–2645. doi: 10.1016/j.dsr2.2008.12.024

Koslow, J., Gowlett-Holmes, K., Lowry, J., O'Hara, T., Poore, G., and Williams, A. (2001). Seamount benthic macrofauna off southern Tasmania: community structure and impacts of trawling. *Mar. Ecol. Prog. Ser.* 213, 111–125. doi: 10.3354/meps213111

Lacharité, M., and Metaxas, A. (2017). Hard substrate in the deep ocean: how sediment features influence epibenthic megafauna on the eastern Canadian margin. *Deep Sea Res. I.* 126, 50–61. doi: 10.1016/j.dsr.2017.05.013

Le, S., Josse, J., and Husson, F. (2008). FactoMineR: an R package for multivariate analysis. *J. Stat. Softw.* 25, 1–18. doi: 10.18637/jss.v025.i01

Levin, L. A. (2002). Deep-ocean life where oxygen is scarce: oxygen-deprived zones are common and might become more so with climate change. here life hangs on, with some unusual adaptations. *Am. Sci.* 90, 436–444.

Levin, L. A., Etter, R. J., Rex, M. A., Gooday, A. J., Smith, C. R., Pineda, J., et al. (2001). Environmental influences on regional deep-sea species diversity. *Annu. Rev. Ecol. Syst.* 32, 51–93. doi: 10.1146/annurev.ecolsys.32.081501.114002

Levin, L. A., and Le Bris, N. (2015). The deep ocean under climate change. *Science* 350, 766–768. doi: 10.1126/science.aad0126

Long, D. J., and Baco, A. R. (2014). Rapid change with depth in megabenthic structure-forming communities of the Makapu'u deep-sea coral bed. *Deep Sea Res. II.* 99, 158–168. doi: 10.1016/j.dsr2.2013.05.032

Mamouridis, V., Cartes, J. E., Parra, S., Fanelli, E., and Salinas, J. S. (2011). A temporal analysis on the dynamics of deep-sea macrofauna: influence of environmental variability off Catalonia coasts (western Mediterranean). *Deep Sea Res. I.* 58, 323–337. doi: 10.1016/j.dsr.2011.01.005

Matabos, M., Hoeberechts, M., Doya, C., Aguzzi, J., Nephin, J., Reimchen, T. E., et al. (2017). Expert, crowd, students or algorithm: who holds the key to deep-sea imagery 'big data'processing? *Methods Ecol. Evol.* 8, 996–1004. doi: 10.1111/2041-210X.12746

McClain, C. R., and Lundsten, L. (2015). Assemblage structure is related to slope and depth on a deep offshore Pacific seamount chain. *Mar. Ecol.* 36, 210–220. doi: 10.1111/maec.12136

McClain, C. R., Lundsten, L., Barry, J., and DeVogelaere, A. (2010). Assemblage structure, but not diversity or density, change with depth on a northeast Pacific seamount. *Mar. Ecol.* 31, 14–25. doi: 10.1111/j.1439-0485.2010.00367.x

McClain, C. R., and Rex, M. A. (2015). Toward a conceptual understanding of β-diversity in the deep-sea benthos. *Ann. Rev. Ecol. Evol. Systemat.* 46, 623–642. doi: 10.1146/annurev-ecolsys-120213-091640

Mejia-Mercado, B. E., Mundy, B., and Baco, A. R. (2019). Variation in the structure of the deep-sea fish assemblages on necker island, Northwestern Hawaiian Islands. *Deep Sea Res. I.* 152:103086. doi: 10.1016/j.dsr.2019.103086

Mengerink, K. J., Van Dover, C. L., Ardron, J. A., Baker, M. C., Escobar-Briones, E., Gjerde, K., et al. (2014). A call for deep-ocean stewardship. *Science* 344, 696–698. doi: 10.1126/science.1251458

Monk, J., Barrett, N. S., Peel, D., Lawrence, E., Hill, N. A., Lucieer, V., et al. (2018). An evaluation of the error and uncertainty in epibenthos cover estimates from AUV images collected with an efficient, spatially-balanced design. *PLoS One* 13:e0203827. doi: 10.1371/journal.pone.0203827

Morato, T., and Clark, M. R. (2007). "Seamount fishes: ecology and life histories," in *Seamounts: Ecology, Fisheries, and Conservation, Fisheries and Aquatic Resources Series 12*, eds T. J. Pitcher, T. Morato, P. J. B. Hart, M. R. Clark, N. Haggan and R. S. Santos (Oxford: Blackwell Publishing), 170–188.

Morgan, N. (2019). Fine scale assemblage structure of benthic invertebrate megafauna on the North Pacific seamount Mokumanamana. *Mendeley Data* 1. doi: 10.17632/kddjgvbrhj.1

Morgan, N. B., and Baco, A. R. (2019). Observation of a high abundance aggregation of the deep-sea urchin chaetodiadema pallidum (Agassiz and Clark 1907) on the Northwestern Hawaiian Island Mokumanamana. *Deep Sea Res. I.* 150:103067. doi: 10.1016/j.dsr.2019.06.013

Morgan, N. B., Cairns, S., Reiswig, H., and Baco, A. R. (2015). Benthic megafaunal community structure of cobalt-rich manganese crusts on Necker Ridge. *Deep Sea Res. I.* 104, 92–105. doi: 10.1016/j.dsr.2015.07.003

Mortensen, P. B., and Buhl-Mortensen, L. (2004). Distribution of deep-water gorgonian corals in relation to benthic habitat features in the northeast channel (Atlantic Canada). *Mar. Biol.* 144, 1223–1238. doi: 10.1007/s00227-003-1280-8

Neves, B. M., Du Preez, C., and Edinger, E. (2014). Mapping coral and sponge habitats on a shelf-depth environment using multibeam sonar and ROV video observations: learmonth bank, northern British Columbia. Canada. *Deep Sea Res. II.* 99, 169–183. doi: 10.1016/j.dsr2.2013.05.026

O'Hara, T. D., Consalvey, M., Lavrado, H. P., and Stocks, K. I. (2010). Environmental predictors and turnover of biota along a seamount chain. *Mar. Ecol.* 31, 84–94. doi: 10.1111/j.1439-0485.2010.00379.x

Oksanen, J., Blanchet, F. G., Friendly, M., Kindt, R., Legendre, P., McGlinn, D., et al. (2019). *Vegan: Community Ecology Package. R Package Version 2.5-4.* Available at: https://cran.r-project.org/web/packages/vegan/index.html (accessed September 8, 2016).

Parrish F. A. (2007). Density and habitat of three deep-sea corals in the lower Hawaiian chain. *Bull. Mar. Sci.* 81(Suppl. 1), 185–194.

Pusceddu, A., Bianchelli, S., Martin, J., Puig, P., Palanques, A., Masque, P., et al. (2014). Chronic and intensive bottom trawling impairs deep-sea biodiversity and ecosystem functioning. *Proc. Natl. Acad. Sci. U.S.A.* 111, 8861–8866. doi: 10.1073/pnas.1405454111

Quattrini, A. M., Etnoyer, P. J., Doughty, C., English, L., Falco, R., Remon, N., et al. (2014). A phylogenetic approach to octocoral community structure in the deep Gulf of Mexico. *Deep Sea Res. II.* 99, 92–102. doi: 10.1016/j.dsr2.2013.05.027

Quattrini, A. M., Gómez, C. E., and Cordes, E. E. (2016). Environmental filtering and neutral processes shape octocoral community assembly in the deep sea. *Oecologia* 183, 221–236. doi: 10.1007/s00442-016-3765-3764

Quattrini, A. M., Nizinski, M. S., Chaytor, J. D., Demopoulos, A. W., Roark, E. B., France, S. C., et al. (2015). Exploration of the canyon-incised continental margin of the northeastern United States reveals dynamic habitats and diverse communities. *PLoS One* 10:e0139904. doi: 10.1371/journal.pone.0139904

Ramirez-Llodra, E., Tyler, P. A., Baker, M. C., Bergstad, O. A., Clark, M. R., Escobar, E., et al. (2011). Man and the last great wilderness: human impact on the deep sea. *PLoS One* 6:e22588. doi: 10.1371/journal.pone.0022588

Rex, M. A., and Etter, R. J. (2010). *Deep-Sea Biodiversity: Pattern and Scale*. Cambridge: Harvard University Press.

Richer de Forges, B., Koslow, J. A., and Poore, G. (2000). Diversity and endemism of the benthic seamount fauna in the southwest Pacific. *Nature* 405, 944–947. doi: 10.1038/35016066

Roberts, J. M., Wheeler, A., Freiwald, A., and Cairns, S. (2009). *Cold-Water Corals: the Biology and Geology of Deep-Sea Coral Habitats*. Cambridge: Cambridge University Press.

Rossi, S. (2013). The destruction of the 'animal forests' in the oceans: towards an over-simplification of the benthic ecosystems. *Ocean Coast. Manage.* 84, 77–85. doi: 10.1016/j.ocecoaman.2013.07.004

Rowden, A. A., Dower, J. F., Schlacher, T. A., Consalvey, M., and Clark, M. R. (2010). Paradigms in seamount ecology: fact, fiction and future. *Mar. Ecol.* 31, 226–241. doi: 10.1111/j.1439-0485.2010.00400.x

Sautya, S., Ingole, B., Ray, D., Stöhr, S., Samudrala, K., Raju, K. K., et al. (2011). Megafaunal community structure of andaman seamounts including the back-arc basin–a quantitative exploration from the Indian Ocean. *PLoS One* 6:e16162. doi: 10.1371/journal.pone.0016162

Schlacher, T. A., Baco, A. R., Rowden, A. A., O'Hara, T. D., Clark, M. R., Kelley, C., et al. (2014). Seamount benthos in a cobalt-rich crust region of the central Pacific: conservation challenges for future seabed mining. *Diver. Distrib.* 20, 491–502. doi: 10.1111/ddi.12142

Schneider, C. A., Rasband, W. S., and Eliceiri, K. W. (2012). NIH Image to ImageJ: 25 years of image analysis. *Nat. Methods* 9:671. doi: 10.1038/nmeth.2089

Schoening, T., Osterloff, J., and Nattkemper, T. W. (2016). RecoMIA: recommendations for marine image annotation: lessons learned and future directions. *Front. Mar. Sci.* 3:59. doi: 10.3389/fmars.2016.00059

Scrucca, L., Fop, M., Murphy, T. B., and Raftery, A. E. (2017). mclust 5: clustering, classification and density estimation using gaussian finite mixture models. *R J.* 8, 205–233.

Staudigel, H., and Clague, D. A. (2010). The geological history of deep-sea volcanoes: biosphere, hydrosphere, and lithosphere interactions. *Oceanography* 23, 58–71. doi: 10.5670/oceanog.2010.62

Stocks, K. (2004). "Seamount invertebrates: composition and vulnerability to fishing," in *in Fisheries Centre Research Reports*, eds T. Morato, and D. Pauly, (Vancouver, CO: University in Vancouver), 17–24.

Thresher, R., Adkins, J., Fallon, S., Gowlett-Holmes, K., Althaus, F., and Williams, A. (2011). Extraordinarily high biomass benthic community on Southern Ocean seamounts. *Sci. Rep.* 1, 119. doi: 10.1038/srep00119

Thresher, R., Althaus, F., Adkins, J., Gowlett-Holmes, K., Alderslade, P., Dowdney, J., et al. (2014). Strong depth-related zonation of megabenthos on a rocky continental margin (~700-4000 m) off Southern Tasmania, Australia. *PLoS One* 9:e85872. doi: 10.1371/journal.pone.0085872

Tyler, R. H., Boyer, T. P., Minami, T., Zweng, M. M., and Reagan, J. R. (2017). Electrical conductivity of the global ocean. *Earth Planets Space* 69:156. doi: 10.1186/s40623-017-0739-7

Vaquer-Sunyer, R., and Duarte, C. M. (2008). Thresholds of hypoxia for marine biodiversity. *Proc. Natl. Acad. Sci. U.S.A.* 105, 15452–15457. doi: 10.1073/pnas.0803833105

Vetter, E. W., Smith, C. R., and De Leo, F. C. (2010). Hawaiian hotspots: enhanced megafaunal abundance and diversity in submarine canyons on the oceanic islands of Hawaii. *Mar. Ecol.* 31, 183–199. doi: 10.1111/j.1439-0485.2009.00351.x

Victorero, L., Robert, K., Robinson, L. F., Taylor, M. L., and Huvenne, V. A. I. (2018a). Species replacement dominates megabenthos beta diversity

in a remote seamount setting. *Sci. Rep.* 8:4152. doi: 10.1038/s41598-018-22296-8

Victorero, L., Watling, L., Deng Palomares, M. L., and Nouvian, C. (2018b). Out of sight, but within reach: a global history of bottom-trawled deep-sea fisheries from> 400 m depth. *Front. Mar. Sci.* 5:98. doi: 10.3389/fmars.2018.00098

Wang, M., and Jiang, L. (2018). VIIRS-derived ocean color product using the imaging bands. *Remote Sens. Environ.* 206, 275–286. doi: 10.1016/j.rse.2017.12.042

Wei, C. L., Rowe, G. T., Hubbard, G. F., Scheltema, A. H., Wilson, G. D., Petrescu, I., et al. (2010). Bathymetric zonation of deep-sea macrofauna in relation to export of surface phytoplankton production. *Mar. Ecol. Prog. Ser.* 399, 1–14. doi: 10.3354/meps08388

Wei, T., and Simko, V. (2017). *R Package "corrplot": Visualization of a Correlation Matrix (Version 0.84)*. Available at: https://github.com/taiyun/corrplot (accessed September 3, 2017).

Wentworth, C. K. (1922). A scale of grade and class terms for clastic sediments. *J. Geol.* 30, 377–392. doi: 10.1086/622910

White, M., and Mohn, C. (2004). Seamounts: a review of physical processes and their influence on the seamount ecosystem. *OASIS Rep.* 1–38.

Williams, A., Althaus, F., Clark, M. R., and Gowlett-Holmes, K. (2011). Composition and distribution of deep-sea benthic invertebrate megafauna on the lord howe rise and norfolk ridge, southwest Pacific Ocean. *Deep Sea Res. II.* 58, 948–958. doi: 10.1016/j.dsr2.2010.10.050

Williams, A., Schlacher, T. A., Rowden, A. A., Althaus, F., Clark, M. R., Bowden, D. A., et al. (2010). Seamount megabenthic assemblages fail to recover from trawling impacts. *Mar. Ecol.* 31, 183–199. doi: 10.1111/j.1439-0485.2010.00385.x

Wishner, K., Levin, L., Gowing, M., and Mullineaux, L. (1990). Involvement of the oxygen minimum in benthic zonation on a deep seamount. *Nature* 346, 57–59. doi: 10.1038/346057a0

Woolley, S. N. C., Tittensor, D. P., Dunstan, P. K., Guillera-Arroita, G., Lahoz-Monfort, J., Wintle, B. A., et al. (2016). Deep-sea diversity patterns are shaped by energy availability. *Nature* 533:393. doi: 10.1038/nature17937

Yasuhara, M., and Danovaro, R. (2016). Temperature impacts on deep-sea biodiversity. *Biol. Rev.* 91, 275–287. doi: 10.1111/brv.12169

Yesson, C., Taylor, M. L., Tittensor, D. P., Davies, A. J., Guinotte, J., Baco, A., et al. (2012). Global habitat suitability of cold-water octocorals. *J. Biogeogr.* 39, 1278–1292. doi: 10.1111/j.1365-2699.2011.02681.x

Conflict of Interest: The authors declare that the research was conducted in the absence of any commercial or financial relationships that could be construed as a potential conflict of interest.

Copyright © 2019 Morgan, Goode, Roark and Baco. This is an open-access article distributed under the terms of the Creative Commons Attribution License (CC BY). The use, distribution or reproduction in other forums is permitted, provided the original author(s) and the copyright owner(s) are credited and that the original publication in this journal is cited, in accordance with accepted academic practice. No use, distribution or reproduction is permitted which does not comply with these terms.

frontiers in Marine Science

ORIGINAL RESEARCH
published: 14 January 2020
doi: 10.3389/fmars.2019.00798

"Little Red Jellies" in Monterey Bay, California (Cnidaria: Hydrozoa: Trachymedusae: Rhopalonematidae)

George I. Matsumoto[1], Bastian Bentlage[2], Rob Sherlock[1], Kristine Walz[1] and Bruce H. Robison[1]*

[1] Monterey Bay Aquarium Research Institute, Moss Landing, CA, United States, [2] Marine Laboratory, University of Guam, Mangilao, GU, United States

Several species of small, red, deep-sea Trachymedusae have been described and then re-described over the past 20 years, leading to some confusion in the scientific literature. This paper provides an overview of three genera (*Benthocodon*, *Crossota*, and *Pectis*) in the family Rhopalonematidae (Cnidaria: Hydrozoa) that have been observed and examined both in the field and in the laboratory. Twenty years of *in situ* observations in Monterey Bay indicate that two of the genera, *Benthocodon* and *Pectis*, are often associated with the benthic boundary layer and can occur in dense patches. They have been observed resting on soft sediments with their subumbrellar surface down but are also found swimming up to several 100 m above the bottom. Individuals in the genus *Crossota* tend to be solitary and more pelagic in nature. Although *Crossota* may be found near the bottom as well, down to depths of 4,000 m, they have not been observed resting on the bottom. The three genera are morphologically similar and difficult to distinguish from each other. As a group, they are small (<5 cm) and sometimes darkly pigmented, making *in situ* identifications challenging. We show that these three genera can be differentiated morphologically and we provide a key to the genera and species common in Monterey Bay. Further, the genera differ in their depth distribution and behavior. Molecular genetics suggest that the genera and species are distinct from each other but that their taxonomy needs revision. This paper reviews the generic characteristics along with species identifications and provides images and video (Supplementary Material) that may be helpful in identification.

Keywords: Trachymedusae, *Crossota*, *Pectis*, *Benthocodon*, Monterey Submarine Canyon, ROV, phylogenetics

OPEN ACCESS

Edited by:
Diva Amon,
Natural History Museum,
United Kingdom

Reviewed by:
Tina Molodtsova,
P.P. Shirshov Institute of Oceanology (RAS), Russia
Dale R. Calder,
Royal Ontario Museum, Canada

****Correspondence:***
George I. Matsumoto
mage@mbari.org

Specialty section:
This article was submitted to Deep-Sea Environments and Ecology, a section of the journal Frontiers in Marine Science

Received: *26 March 2019*
Accepted: *11 December 2019*
Published: *14 January 2020*

Citation:
Matsumoto GI, Bentlage B, Sherlock R, Walz K and Robison BH (2020) "Little Red Jellies" in Monterey Bay, California (Cnidaria: Hydrozoa: Trachymedusae: Rhopalonematidae). Front. Mar. Sci. 6:798. doi: 10.3389/fmars.2019.00798

INTRODUCTION

The Trachymedusae are a diverse group of jellyfish, most of which live below the euphotic zone (Mayer, 1910). In Monterey Bay, California, they can be found in the water column all the way to the ocean floor at 4,000 m. This marks both the deepest extent of the Monterey Submarine Canyon as well as the depth limitation for the remotely operated vehicles (ROVs) used in this study. Three genera (*Pectis* Haeckel, 1879; *Benthocodon* Larson and Harbison, 1990; and *Crossota* Vanhöffen, 1902) in the family Rhopalonematidae are commonly reddish in hue, similar in size, and have been difficult to distinguish from one another. The most common species: *Benthocodon pedunculata* (Bigelow, 1913) and *Pectis profundicola* (Naumov, 1971) are benthopelagic and, although

patchy, have been recorded in numbers up to 80/m^2 (Larson et al., 1992). They often swim in short bursts, usually followed by bouts of sinking (Larson and Harbison, 1990; Larson et al., 1992; Matsumoto et al., 1997). *Crossota* species are typically found singly in the water column (Thuesen, 2003). Previous observations from human occupied vehicles and remotely operated vehicles consisted mostly of comments about "little red jellies" and the occasional specimen collection. Based on their abundance and mobility, these genera likely represent an ecologically important group (Alldredge, 1984). A similar conclusion was reached by Thuesen and Childress (1994) based on their physiological research which indicated that the metabolism of some deep-sea medusae is close to that of deep-sea fishes and crustaceans.

Representatives of *Benthocodon*, *Crossota*, and *Pectis* are abundant in the deep waters off Monterey and we present a morphological key and a molecular phylogenetic analysis that facilitates identification of each genus and species common to Monterey Bay. Lastly, we summarize field and laboratory observations that provide a better understanding of the natural history of these deep-sea jellies.

MATERIALS AND METHODS

Field Observations and Collection

Observations and collections were made using remotely operated vehicles from the Monterey Bay Aquarium Research Institute (MBARI) (Robison et al., 2017). The ROV *Ventana* is depth rated to 1,850 m. ROV *Tiburon* was, and ROV *Doc Ricketts* is, depth rated to 4,000 m (http://www.mbari.org/at-sea/vehicles/). High definition video cameras are mounted on these vehicles and the video signal is conveyed to the surface support vessel (ROV *Ventana*—R/V *Point Lobos* and R/V *Rachel Carson*; ROV *Tiburon* and ROV *Doc Ricketts*—R/V *Western Flier*) through optical fibers at the core of the ROV's tether. At the surface, the video signal is viewed on a high-resolution monitor and was recorded initially on digital BetaCam tape, then MBARI switched to a High Definition camera system and recorded on High Definition tape, and we are now recording the video digitally. The observer's comments and descriptions are recorded on the audio track of the recording. Environmental data (depth, location, temperature, dissolved oxygen, and salinity) for each dive are collected and, after each dive, this information is integrated into a database. These data and all frame grabs from video images collected by our ROVs, are annotated into a comprehensive relational database (http://www.mbari.org/vars) that is available to the public.

Specimens were collected in 6.5 l "detritus" samplers, designed for the gentle capture of delicate material in midwater (Youngbluth, 1984), or in a "suction" sampler consisting of a transparent funnel and 2 m of flexible tubing leading back to 12 separate 6-l collection cylinders within the ROV toolsled. For the detritus samplers, the ROV pilot positions the vehicle so that the open cylinder of the sampler encloses the medusa, then the doors at either end are gently closed by hydraulic rams. For the suction sampler, the funnel, attached to a clear plexiglass tube and flexible tubing, can be extended in front of the ROV (https://www.mbari.org/high-frequency-suction-samplers/). When a medusa is near the wide opening of the funnel, the suction pump is turned on and the animal is gently collected and deposited into a sample container.

Molecular Genetic Data

Tissue samples for molecular analysis were collected with the ROVs and either frozen at −80°C or pressed onto Whatman FTA cards (Sigma-Aldrich, St. Louis, MO). Genomic DNA was extracted from frozen tissue samples using a modified CTAB-DTAB protocol (Gustinich et al., 1991). Approximately 300 μl of tissue was placed into a 2 ml Eppendorf tube and 600 μl of "blood lysis buffer" (8% DTAB, 1.5 M NaCl, 100 mM Tris-Cl, pH 8.6, 50 mM EDTA) was added. The tissue was incubated at 68°C for 5 min and then 900 μl of chloroform were added to deproteinize the tissue. The tube was inverted 2–3 times and then spun at 10,000 rpm for 2 min. The supernatant was removed (discarding the lower portion and being careful to avoid the tissue detritus at the interface of phases) and DNA was precipitated from the supernatant by adding 900 μl of ultrapure water and 100 μl of a 5% CTAB solution that contained 0.4 M NaCl. This was followed by gentle inversion of the tube and centrifugation at 10,000 rpm for 2 min. The resulting pellet was resuspended in 300 μl 1.2 M NaCl and 750 μl EtOH were added, the sample was gently mixed and spun at 10,000 rpm for 10 min to precipitate the DNA again, followed by a rinse with 300 μl 70% EtOH. Additional extractions were performed using the Qiagen DNeasy Blood and Tissue Kit following the manufacturer's protocol for animal tissue extractions with some modifications: after the addition of Buffer AL, 200 μl of cold isopropanol was added to each sample. In addition, two elutions were done on each sample for a total of 70 μl genomic DNA. Genomic DNA was also obtained from FTA paper following the manufacturer's protocol. The resulting pellets were resuspended in 50 μl of ultrapure water; 1–2 μl of genomic DNA were used for either 30 or 10 μl PCR reactions.

The nuclear large subunit ribosomal RNA (LSU or 28S) gene was amplified (initial denaturation at 94°C for 2 min; 30 cycles at 94°C for 30 s, 55°C for 30 s, and 72°C for 70 s; final elongation at 72°C for 7 min) using slightly modified (LSUD1F ACCCGCTGAATTTAAGCATA; D3Ca ACGAA CGATTTGCACGTCAG or LSUD4Ra AACCAGCTACTA GRYGGTTCGAT) universal primers (Scholin and Anderson, 1994). The PCR product was either sequenced directly from a gel cut or cloned into TOPO TA vector. In both cases, the results from multiple PCR reactions or plasmid DNAs from 2 to 5 individual clones were sequenced individually and as a pool with the SequiTherm EXCEL II Long-Read DNA sequencing kit (Epicenter Technologies) and analyzed on a LI-COR 4200 IR2 instrument. Some of the clones were also sequenced with the BigDye Terminator v.2 sequencing kit and analyzed on an ABI 3100 instrument.

The nuclear small subunit ribosomal RNA (SSU or 18S) gene was amplified using the modified universal primers *mitchA* and *mitchB* from (4 cycles of 94°C for 60 s, 58°C for 60 s, 72°C for 2 min, followed by 29 cycles of 94°C for 60 s, 64°C for 60 s, 72°C for 90 s; Medlin et al., 1988). All products were bi-directionally sequenced using BigDye® Terminator v3.1 Cycle Sequencing Kit

on an ABI 3100 or ABI 3500 sequencer (Applied Biosystems, Foster City, CA, USA).

Two mitochondrial genes were amplified and sequenced, the mitochondrial cytochrome oxidase one (COI) gene and the gene encoding the large RNA subunit of the mitochondrial ribosome (16S). COI were amplified using the forward primer of Leray et al. (2013) and the Folmer et al. (1994) reverse primer (16 cycles at 94°C for 10 s, starting annealing temperature of 62°C for 30 s that was lowered by 1°C during each subsequent cycle, and 68°C for 60 s, followed by 25 cycles of 94°C for 10 s, 46°C for 30 s, and 68°C for 60 s with a final elongation of 72°C for 10 min). 16S sequences were generated following the protocols described in Bentlage et al. (2018).

Phylogenetic Analyses

All sequences were assembled in Geneious (various versions; Biomatters Limited, NZ, RRID:SCR_010519) and a dataset was compiled that comprised newly generated and previously published sequences of Trachymedusae and Narcomedusae (**Table 1** and **Figure 1**). Individual loci were aligned using MAFTT (v7.205; Katoh and Standley, 2013). Unreliably aligned positions were identified and excluded using Gblocks (Talavera and Castresana, 2007, RRID:SCR_015945), as implemented in the alignment viewer Seaview (version 4; Gouy et al., 2010, RRID:SCR_015059), allowing for smaller blocks, gap positions, and less strict flanking positions. The four resulting alignments were concatenated using the catfasta2phyml script available from https://github.com/nylander/catfasta2phyml.

Partitionfinder (version 1.1.0; Lanfear et al., 2012) was used to identify the appropriate substitution models and best partitioning scheme for inferring phylogenetic relationships from the concatenated alignment; partitioning schemes were evaluated and ranked using the Bayesian information criterion (Bic). Partitioning schemes tested were the following: (1) all loci evolve under the same model (no partitioning), (2) all loci evolve under a different model of evolution (separate 16S, COI, 18S, and 28S partitions), (3) mitochondrial (16S and COI) and nuclear (18S and 28S) loci evolve under a different model, (4) nuclear loci (18S and 28S) evolve under one model while the mitochondrial loci (16S and COI) can be best modeled by separate models, and (5) mitochondrial loci (16S and COI) evolve under one model while the nuclear loci (18S and 28S) can be best modeled separately. The best partitioning scheme was then encoded in RAxML (version 8.2.7; Stamatakis, 2014, RRID:SCR_006086) to infer the maximum likelihood phylogeny. Robustness of the phylogeny was evaluated using 1,000 non-parametric bootstrap replicates using RAxML's rapid bootstrapping algorithm (-fa-m GTRGAMMAI-p $RANDOM-x $RANDOM-# 1000). Following the phylogenetic framework presented in Bentlage et al. (2018), the resulting phylogeny was rooted on the trachymedusan family Halicreatidae.

RESULTS

Phylogeny and Taxonomy

We have observed, collected, and sequenced several specimens of *Pectis profundicola* previously identified incorrectly as *Benthocodon pedunculata* (Larson et al., 1992; Matsumoto et al., 1997) and as *Voragonema pedunculata* (Bouillon et al., 2001; Lindsay and Pagès, 2010), several species of *Crossota*, and *Benthocodon pedunculatus* (see discussion for the change in the species name from *B. pedunculata* to *B. pedunculatus*).

We increased taxon sampling compared to the recent phylogeny of Bentlage et al. (2018) with respect to *Crossota*, *Benthocodon*, and *Pectis*, and provide information to help discriminate between the three genera while expanding on the taxa and sampling in recent work (Bentlage et al., 2018). We support the earlier finding (Bentlage et al., 2018) that *Crossota* is not a monophyletic clade (**Figure 1**) with *Crossota millsae* (Thuesen, 2003) being most closely related to *Tetrorchis erythrogaster* (Bigelow, 1909). Note that *C. millsae* is paraphyletic with respect to *Tetrorchis*, albeit at low bootstrap support. Overall, the remainder of the genus *Crossota,* other than *C. millsae,* were paraphyletic with respect to *Benthocodon*, *Pectis*, and *Vampyrocrossota*. *Crossota* is separated according to nominal species, supporting their distinction based on morphology (**Figures 2**, **3**). A putatively undescribed species (*Crossota* n. sp.—**Figure 3**) photographed and collected in the Gulf of California appears to be the closest relative of *Vampyrocrossota* and a specimen from Bentlage et al. (2018) that appears to have been misidentified (*Crossota alba* auct). *Benthocodon* and *Pectis*, the other two genera of interest in this contribution are nested firmly within a clade of *Crossota* species but some nodes remain poorly supported. Monophyly of *Benthocodon* and *Pectis* cannot be confirmed or rejected until additional species in these genera have been sampled.

Vertical Distribution and Behavior

Over 20 years of *in situ* observations in Monterey Bay have revealed that *Crossota*, *Benthocodon*, and *Pectis* exhibit distinct depth distributions.

All species of *Crossota* that we observed found in the water column at depths from 500 to 4,000 m and were never observed on the bottom, although they have been seen swimming in the benthic boundary layer. *Crossota* swims with a series of strong pulsing contractions, usually followed by a period of quiescence.

Benthocodon species are generally found in deeper waters (>2,500 m) although the type specimen (*Crossota pedunculata*) was collected in <100 m of water. While *Benthocodon hyalinus* is found in the water column or near the bottom, *Benthocodon pedunculatus* is typically found drifting above the sediment (up to 100 m from the bottom) or either on or just above the bottom (see **Supplemental Video**). Those *Benthocodon pedunculatus* specimens that are not on the sediment, generally pulse consistently but weakly every few seconds (see **Supplemental Video**). They are negatively buoyant and sink between pulses, thus maintaining a somewhat constant position on or just above the bottom. They are capable of stronger bouts of swimming, but these tend to be followed by longer sinking/rest periods. Abundance of these medusae was as high as 11 per square meter (based on video transects—**Figure 4**).

In Monterey Bay, *Pectis* specimens can be found throughout the water column with *P. tatsunoko* in the water column and *P. profundicola* associated with the benthic boundary layer

TABLE 1 | Genbank accession numbers for sequence data used in phylogenetic reconstruction.

	Species	18S	28S	16S	COI	Lab ID	Collection code	Collection date	Latitude	Longitude	Locality	Voucher
Narcomedusae	*Aeginona brunnea*	KY007602				DLSI443	20100627-1-ORI-4-Ab	27-Jun-2010	34° 29.39′ N	140° 1.63′ E	South-east of Sagami Bay, Japan	
	Aeginopsis laurentii	MG979347	MG979317	MG979377		GR10.122		***	***	***	Russ Hopcroft	
	Aeginura grimaldii	KY007605	MG979307	KY007590		DLSI451	KT10-24_St3	24-Oct-2010	27° 14.54′ N	127° 5.40′ E	Izena Hole, Japan	
	Bathykorus bouilloni	MG979341	MG979308	MG979371		PS11406.4		***	***	***	Russ Hopcroft	
	Cunina frugifera	AF358059	KY077276	MG979372		AGC1026		Nov-1998	33° 10′ N	118° 30′ W	Catalina Channel, CA, USA	
	Cunina octonaria	KY007606	MG979310	KY007592		DLSI188	KT07-18_ORI-2-E	31-Jul-2007	35° 0′ N	139° 20′ E	Sagami Bay, Japan	
	Pegantha martagon	MG979344	MG979314	MG979375	**MN068291**	DLSI040	stUM15, RMT-D-8-2	28-Jan-2004			Dhugal Lindsay	
	Pegantha cf. *martagon*	MG979343	MG979313	MG979374		ss4ed.1		***	***	***	Karen Osborn	
	Pegantha rubiginosa	MG979345	MG979315	MG979376	**MN068292**	DLSI250	MOC1-12-7	***	***	***		
	Pseudaegina rhodina	EU247813			**MN068275**	RBMOC1001N7		13-Apr-2006	33° 31.47′ N	69° 53.46′ W	WNW of Bermuda	
	Solmaris sp.	MG979346	MG979316		**MN068298**	DLSI359	St. P-MTD-6 Cruise-KT09-4	24-Apr-2009	35° 0′ N	139° 20′ E	Sagami Bay, Japan	
	Sigiweddellia sp.	KY007607	MG979309	KY007593	**MN068296**	DLSI022	IO60320C, net 1	***	***	***	Dhugal Lindsay	
	Solmundaegina nematophora	AF358058	AY920789	EU293997		AGC1045		Sep-1997	33° 37′ N	118° 21′ W	off San Pedro CA, USA	
	Solmundella bitentaculata	EU247812	EU247795	EU293998	**MN068300**	Sch085	2001.05.03.1	3-May-01	43° 41.16′ N	7° 19.02′ E	Villefranche-sur-Mer, Ligurian Sea, Mediterranean	
	Solmissus albescens	MG979342	MG979311	MG979373		AGC506		27-Oct-2009	43° 36′ N	7° 10.56′ E	Bay of Angels, Cote d'Azur, France	
	Solmissus incisa	KY007609	MG979312	KY007596		DLSI361	HD519SS4	01-Mar-2006	35° 0.26′ N	139° 21.40′ E	Sagami Bay, Japan	
	Solmissus marshalli	AF358060	AY920790	EU294001	**MN068299**	AGC1025		Nov-1998	33° 10′ N	118° 30′ W	Catalina Channel, CA, USA	
	Tetraplatia chuni	MG979348	MG979318	KY007599	**MN068301**	DLSI261	I060322b-3	22-Mar-2006	34° 57.40′ N	140° 13.50′ E	Off Kamogawa, Japan	
	Tetraplatia volitans	DQ002501	DQ002502	EU293999		AGC139	V2508	2-Apr-2004	36° 31.89′ N	122° 30.46′ W	Monterey Bay Canyon, CA, USA	KUMIP 314322
Trachymedusae	*Arctapodema* sp.	MG979356	MG979327	MG979383	**MN068279**	DLSI358	St. P-MTD-3 Cruise-KT09-4	23-Apr-2009	35° 0′ N	139° 20′ E	Sagami Bay, Japan	

(Continued)

TABLE 1 | Continued

Species	18S	28S	16S	COI	Lab ID	Collection code	Collection date	Latitude	Longitude	Locality	Voucher
Aglantha digitale	MG979354	MG979324	EU293985		AGC208		Jun-2004	48° 32.82′ N	123° 0.78′ W	Friday Harbor, WA, USA	USNM 1073329
Aglaura hemistoma	EU247820	MG979325	EU293984	**MN068277**	06Jap2301		7-Aug-2006	33° 41.63′ N	135° 20.275′ E	Seto Lab beach, Shirahama, Wayakama, Japan	
Amphogona apicata	MG979355	MG979326	MG979382	**MN068278**	DLSI282	I060326a-0	***	***	***	Off Oshima, Japan	
Benthocodon pedunculatus (1)			**MN065485**		T894SS1	3,500 m	20-sept-2005	36° 19.48′ N	122° 54.1′ W	Monterey Canyon, CA, USA	
Benthocodon pedunculatus (2)	MG979357	MG979328	MG979384		BB015	T1106SS12, 3,582 m	28-Jul-2007	36° 7′ N	123° 33′ W	Monterey Canyon, CA, USA	USNM 1452215
Benthocodon pedunculatus (3)	**MK547161**		**MN065486**		T894SS4	3,500 m	20-sept-2005	36° 19.47′ N	122° 54.1′ W	Monterey Canyon, CA, USA	
Botrynema brucei	EU247822	EU247798	EU293982			I060319bN4	19-Mar-2006	35° 0.6′ N	139° 19.8′ E	Sagami Bay, Japan	
Botrynema ellinorae	MG979349	MG979319	MG979378		PS11109.4		***	***	***	Russ Hopcroft	
Colobonema sericeum	MG979358	MG979329	MG979385		BB012	Tucker Trawl	28-Jul-2007	36° 09.40′ N	123° 33.7′ W	Monterey Canyon, CA, USA	
Crossota alba (1)	**MK547162**		**MN065487**	**MN094795**	DR716SS1	2,955 m	28-Feb-2015	25° 26.27′ N	109° 50.43′ W	Carmen Basin, Gulf of California, Mexico	
Crossota alba (2)				**MN068303**	DR90SS3	1,535 m	23-Oct-2009	36° 38.31′ N	122° 07.27′ W	Monterey Canyon, CA, USA	
Crossota alba auct.	MG979359	MG979330	MG979386		BB014	T1105SS4, 1,363 m	27-Jul-2007	36° 41.48′ N	122° 34.99′ W	Monterey Canyon, CA, USA	
Crossota brunnea (1)	MG979360	MG979331	MG979387	**MN068280**	DLSI093	stUM9, 1YGPT1000	***	***	***	Dhugal Lindsay	
Crossota millsae (1)	MG979361	MG979332	MG979388		BB009	T1106SS8, 2,281 m	28-Jul-2007	36° 07′ N	123° 33′ W	Monterey Canyon, CA, USA	
Crossota millsae (2)	**MK547164**		**MN065488**	**MN068307**	DR216SS5	2,837 m	18-Nov-2010	36° 33.2′ N	122° 30.8′ W	Monterey Canyon, CA, USA	
Crossota millsae (3)			**MN065489**	**MN068306**	DR88D2	2,115 m	21-Oct-2009	36° 20.3′ N	122° 55.0′ W	Monterey Canyon, CA, USA	

(Continued)

TABLE 1 | Continued

Species	18S	28S	16S	COI	Lab ID	Collection code	Collection date	Latitude	Longitude	Locality	Voucher
Crossota millsae (4)	**MK547165**			**MN068308**	DR437ss12	2,555 m	25-Oct-2012	36° 32.10′ N	122° 30.30′ W	Monterey Canyon, CA, USA	
Crossota norvegica	MG979362	MG979333	MG979389	**MN068281**	PS11-217		***	***	***	Russ Hopcroft	
Crossota n. sp.	**MK547166**		**MN065490**		DR726D4	2,992 m	12-Mar-2015	22° 54.59′ N	108° 6.55′ W	Mazatlan Basin, Gulf of California, Mexico	
Crossota rufobrunnea (1)	EU247823	EU247799	EU293987		AGC1061		***	***	***	Allen Collins	
Crossota rufobrunnea (2)	EU247824	EU247800	EU293986	**MN068282**		I060319bN4	19-Mar-2006	35° 0.6′ N	139° 19.8′ E	Sagami Bay, Japan	
Crossota rufobrunnea (3)			**MN065492**		DR90SS3	1,516 m	23-Oct-2009	36° 38.31′ N	122° 7.27′ W	Monterey Canyon, CA, USA	
Crossota rufobrunnea (4)	**MK547167**		**MN065493**	**MN068305**	DR716SS3	2,955 m	28-Feb-2015	25° 26.27′ N	109° 50.43′ W	Carmen Basin, Gulf of California, Mexico	
Crossota rufobrunnea (5)			**MN065494**		D794T	Tucker Trawl	12-Aug-2015	36° 44.99′ N	122° 6.2′ W	Monterey Canyon, CA, USA	USNM 1284404
Halicreas minimum	MG979350	MG979320	EU293983		I060320A-N1		19-Mar-2006	35° 0.6′ N	139° 19.8′ E	Sagami Bay, Japan	
Haliscera conica	EU247825	EU247797	EU293981		AGC1057		Sep-1997	33° 37′ N	118° 21′ W	off San Pedro, CA, USA	
Haliscera bigelowi	MG979351	MG979321	MG979379		BB013	T1105SS8, 1,106 m	27-Jul-2007	36° 41.48′ N	122° 34.99′ W	Monterey Canyon, CA, USA	
Halitrephes maasi	MG979352	MG979322	MG979380		BB004	T1105DS4, 9,878 m	27-Jul-2007	36° 41.48′ W	122° 34.99′ W	Monterey Canyon, CA, USA	
Pantachogon haeckeli (1)			**MN065495**		DR787SS5	950 m	8-Aug-2015	36° 41.23′ W	122° 2.26′ W	Monterey Canyon, CA, USA	
Pantachogon haeckeli (2)	AF358062	AY920792	KY077291		AGC1049		***	***	***	Allen Collins	
Pantachogon haeckeli (3)	**MK547168**	**MK537356**			BB010	Tucker Trawl	28-Jul-2007	36° 9.4′ N	123° 33.7′ W	Monterey Canyon, CA, USA	
Pectis profundicola (1)	MG979363	MG979334	MG979390		DR793SS7	607 m	12-Aug-2015	36° 44.39′ N	122° 6.12′ W	Monterey Canyon, CA, USA	

(Continued)

TABLE 1 | Continued

Species	18S	28S	16S	COI	Lab ID	Collection code	Collection date	Latitude	Longitude	Locality	Voucher
Pectis profundicola (2)	**MK547171**				DR719SS12	945 m	12-Aug-2015	36° 44.99′ N	122° 6.19′ W	Monterey Canyon, CA, USA	USNM 1284394
Ptychogastria polaris	MG979353	MG979323	MG979381	**MN068293**	DLSI257	2K1285SS3e	***	***	***	Dhugal Lindsay	
Rhopalonema velatum	EU247819	EU247804	EU293992	**MN068294**	Sch355	Vfr05.6	4-Apr-2005	43° 41.16′ N	7° 19.02′ E	Villefranche-sur-Mer, Ligurian Sea, Mediterranean	
Sminthea arctica	MG979364	MG979335	MG979391	**MN068297**	PS11334.4		***	***	***	Russ Hopcroft	
Sminthea eurygaster	KY077284		KY077293		DLSI090	stUM6, WP2	***	***	***	Dhugal Lindsay	
Tetrorchis erythrogaster	KY077285	KY077274	EU293995		T981SS5	492 m	12-May-2006	36° 36.9′ N	122° 22.35′ W	Monterey Canyon, CA, USA	
Vampyrocrossota sp.	**MK547172**			**MN068302**	T842SS2	1,192 m	7-Apr-2005	35° 29.60′ N	123° 52.0′ W	Monterey Canyon, CA, USA	

***Location not provided.

Accession numbers in bold were generated as part of this study. Collection IDs provide information regarding source of specimen (some information is still pending). DR refers to the ROV Doc Ricketts; T refers to the ROV Tiburon, and V refers to the ROV Ventana with the numbers following representing the dive number and then the collection method (DS, Detritus Sampler; SS Suction Sampler; T, Tucker Trawl) followed by the number of the collection container.

(Matsumoto et al., 1997) similar to *Benthocodon pedunculatus* but are usually observed shallower than the latter near the bottom in depths <3,000 m. *Pectis profundicola* specimens have longer escape bouts of pulsing and shorter rest periods between pulsing bouts than *Benthocodon pedunculatus* (see **Supplemental Video**).

DISCUSSION

As more research vehicles spend time in the deeper waters of the ocean collecting specimens and video footage, it is likely that more species within the three genera of *Crossota*, *Benthocodon*, and *Pectis* will be observed and described. This paper is not intended to be a full taxonomic species review of the three genera but is an attempt to provide guidelines for placing initial observations into the appropriate genus as well as provide some preliminary information for those who want to delve deeper into the species within each genus. Full species descriptions will require additional specimen collections and close examination of taxonomic and molecular characters. Nonetheless, phylogeny and imagery provided here demonstrate that the diversity of these taxa is larger than currently described, even in such a well-studied location as the Monterey Submarine Canyon. An issue that remains to be resolved is that the classification of rhopalonematids does not align with its phylogenetic history, as shown by the analyses presented here (**Figure 1**) and previously (Bentlage et al., 2018).

Naumov (1971) described a new genus and the type species (*Voragonema profundicola*), based upon a single specimen. He used the presence of prominent centripetal canals as a defining feature rather than the presence of a peduncle. Bouillon et al. (2001) noted that (Naumov, 1971) original description of *Voragonema* was incomplete, with some of the characters based solely on the holotype illustration that lacked detail. To address this issue, Bouillon et al. (2001) redescribed the genus *Voragonema* and described a new species, *V. laciniata*. Galea et al. (2016) proposed that *Pectis antarctica* (Haeckel, 1879) possesses all of the published characteristics of *Voragonema* and appears identical to *Voragonema laciniata* (Bouillon et al., 2001). The genus name *Pectis* has precedence over *Voragonema* and, following Galea et al. (2016), *Pectis* is used in this paper when referring to specimens previously identified as *Voragonema*. While *Pectis pedunculata* is in the literature, the type specimen is the same for both this species and *Benthocodon pedunculatus* and upon examination (by the primary author GIM), the type specimen is lacking centripetal canals and belongs in the genus *Benthocodon* and not *Pectis*, therefore *Pectis pedunculata* cannot be considered as valid.

The genus *Crossota* was erected in 1902 by Vanhöffen as a trachymedusa with a distinctive dark red coloration, several rows of tentacles, and 8 pendant gonads hanging adjacent to the stomach. Vanhöffen (1902) described two species (*C. norvegica* and *C. brunnea*) differentiating *C. brunnea* (the type species) from *C. norvegica* by the latter's brighter red coloration. Both Vanhöffen (1902) and Maas (1906) originally grouped *Crossota* with *Ptychogastria* (Allman, 1878) due to the arrangement of the tentacles (despite the fact that *Crossota* lacks

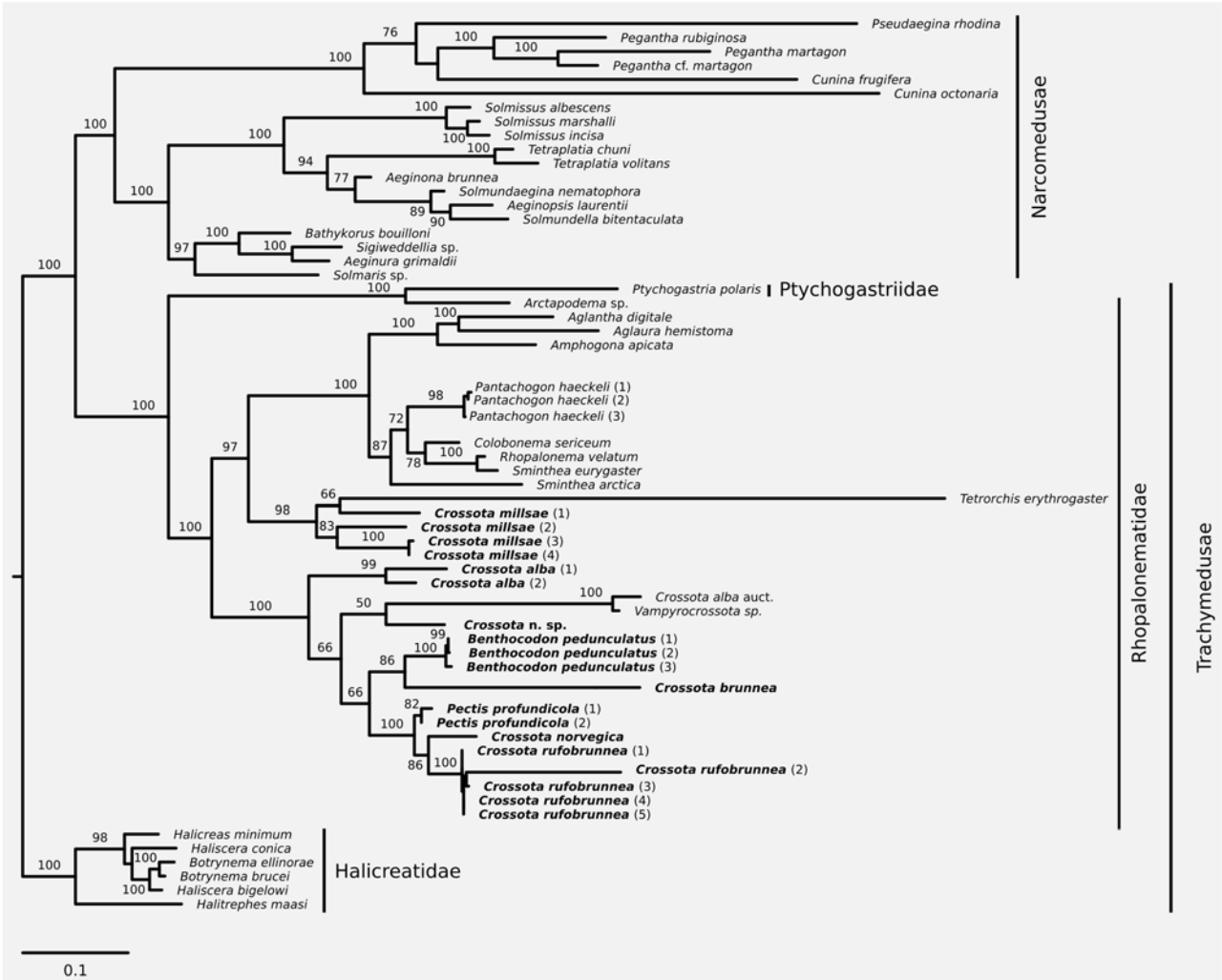

FIGURE 1 | Maximum likelihood phylogeny based on a combined dataset of nuclear 18S and 28S plus mitochondrial 16S and COI. Taxa discussed in this contribution in bold font. Node support was inferred using 1,000 non-parametric bootstrap replicates. Substitution model for phylogenetic reconstruction and bootstrapping was GTR+I+G; scale bar represents substitutions per site.

the clusters of tentacles and adhesive pads that are characteristic of *Ptychogastria*). Bigelow (1913) described two new species (*C. alba* and *C. pedunculata*) and noted that the presence of a peduncle in these two new species might be sufficient basis to erect a new genus. *Ptychogastria* has since been placed into the Ptychogastriidae, separate from *Crossota* (Rhopalonematidae) and the two genera were shown not to be monophyletic (Grange et al., 2017; Bentlage et al., 2018). *Ptychogastria* can be found in Monterey Bay on both hard and soft sediment with a transparent exumbrella and different colored tentacles making them relatively easy to distinguish from *Benthocodon*, *Pectis*, or *Crossota*.

The third genus of "little red jellies" encountered in the Monterey Submarine Canyon is *Benthocodon*, a genus described by Larson and Harbison (1990) based upon: (1) the presence of a peduncle, and (2) gonads that are continuous along the upper part of the radial canals with the proximal part of the gonad somewhat detached. Larson and Harbison (1990) erected *Benthocodon* to accommodate a new species, *B. hyalinus* described from a single specimen (the type species, Holotype USNM 87603) and a photograph published by Curtsinger (1986) and incorrectly identified as *Arctapodema* (taken near McMurdo Station Antarctica). Larson and Harbison (1990) also moved *Crossota pedunculata* (Bigelow, 1913) into the genus *Benthocodon* along with their newly described species *B. hyalinus*. Unfortunately, Larson and Harbison (1990) did not match the gender of *Benthocodon* with the species name upon moving *Crossota pedunculata*. To match gender (male), the correct spelling is *Benthocodon pedunculatus* which is how it is referred to in this paper.

At this time, we recognize two species of *Pectis* (*P. profundicola* and *P. tatsunoko*), five species of *Crossota* (*C.*

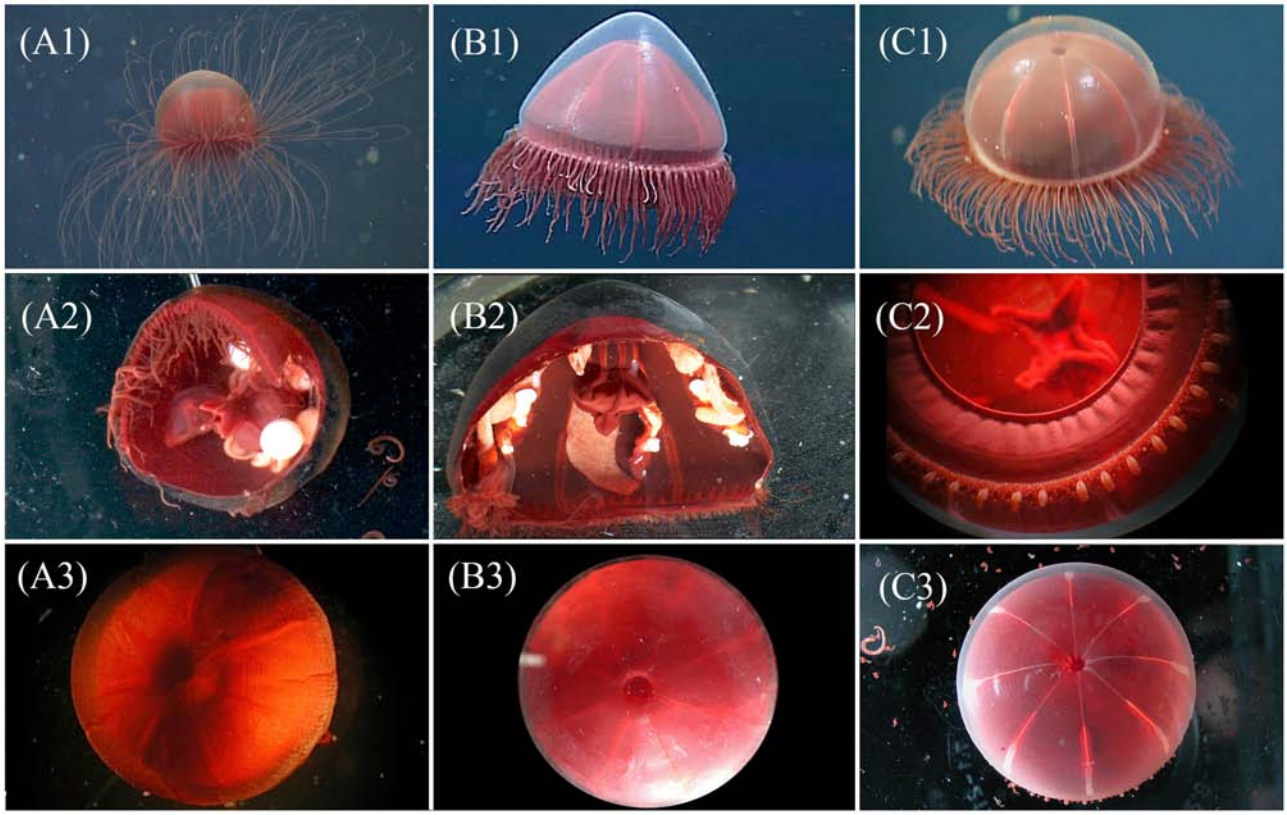

FIGURE 2 | Visual comparison for three genera of "little red jellies" provided for assistance with identification of genera, each image is a unique specimen: *Crossota* **(A1-3)**, *Pectis* **(B1-3)**, and *Benthocodon* **(C1-3)**. Top row, left to right: *in situ* images for *C. rufobrunnea* (**A1**—DR457 @ 968 m in Monterey Bay), *P. profundicola* (**B1**—T622 @ 777 m in Monterey Bay), and *B. pedunculatus* (**C1**—T1113 @ 3,483 m in Monterey Bay, California) taken by MBARI ROVs. Of the three genera, only *Pectis* **(B1)** has centripetal canals and this individual has 8 in each quadrant, irregular in size and just above the canal ring. Row 2 **(A2,B2,C2)** provides closeup and partial dissections taken in lab for different individuals of *C. rufobrunnea* (**A2**—T1023SS1 @ 955 m in Astoria Canyon, Oregon), *P. profundicola* (**B2**—T1023SS2 @ 1,117 m in Astoria Canyon, Oregon), and *B. pedunculatus* (**C2**—T623b @ 3,607 m in Monterey Bay, California). Note the pendant gonads and absent peduncle of *Crossota* **(A2)**, and the semi-pendant gonads and short peduncle for *Pectis* **(B2)**. *Benthocodon* **(C2)** shows the folded, per-radial lips, tentacular arrangement, and well-developed velum. See **Figure 4** for a better view of the peduncle for which *Benthocodon pedunculatus* is named. Row 3 **(A3,B3,C3)** provides a dorsal view of the subumbrella region. The subumbrella for *C. rufobrunnea* (**A3**—T766 @ 1,375 m in Monterey Bay, California), unlike both *P. profundicola* (**B3**—T834SS9 @ 1,384 m in Monterey Bay, California), and *B. pedunculatus* (**C3**—T835SS5 @ 3,285 m in Monterey Bay, California), appears closed and does not allow a view through clear mesoglea into the peduncle.

alba, *C. norvegica*, *C. millsae*, *C. brunnea*, and *C. rufobrunnea*), and two *Benthocodon* species (*B. pedunculatus* and *B. hyalinus*) from the west coast of North America and in the Monterey Submarine Canyon in particular. We did not collect enough specimens of either *P. tatsunoko* or *B. hyalinus* to include them in the molecular analysis. Two specimens not found in Monterey—*Crossota norvegica* and a potential new *Crossota* species collected in the Gulf of California—are included in the phylogeny but *Pectis antarctica* is not included as we have not had access to specimens. All of the species in this paper can be identified using morphological characters taken from personal observations and existing descriptions. It is possible that further taxonomic work may result in either splitting up the different species of *Crossota* or combining genera (*Pectis*, *Crossota*, *Benthocodon*, and a fourth genus of a small black jelly-*Vampyrocrossota*) into a single genus. At this point, we do not have enough information to justify either approach. Consistent identifications will be necessary to interpret the ecological data collected alongside deep-sea jellyfish specimens (cf. Lindsay et al., 2017).

At the generic level, the medusae discussed herein occupy different depth layers of the water column, providing insight into deep-living jelly community structure. Ultimately, accurate taxonomy will give a clearer picture of deep-sea community composition and assembly. For example, gelatinous zooplankton have been shown to be an important component of deep-water food webs as predators and prey (Choy et al., 2017), and clarifying species identities holds potential for further resolving the roles different genera and species play in these food webs (Grange et al., 2017).

The phylogeny presented herein provides further evidence that *Crossota* is a polyphyletic group. The taxonomic key presented reflects our understanding of the current classification status of "little red jellies" and some of their relatives. It

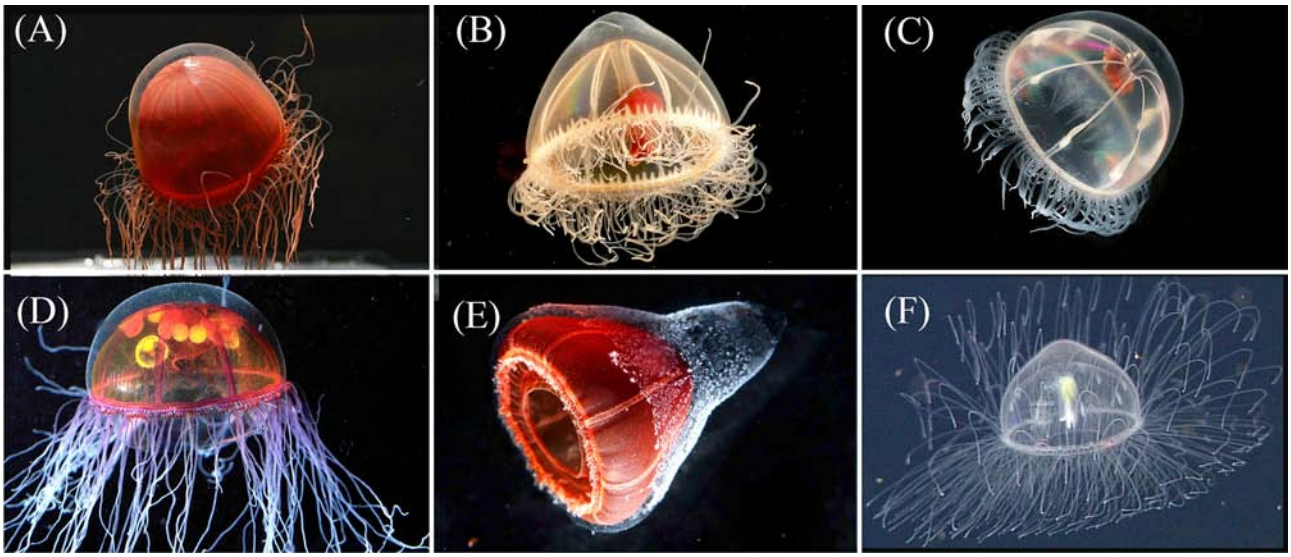

FIGURE 3 | Row 1: The exumbrella of *Crossota norvegica* [**(A)**—photo by K. Raskoff from 1,595 m in the Chukchi Basin, Arctic] appears more transparent than its congeners. *Pectis tatsunoko* [**(B)**—T1024SS11 from 1,028 m in Astoria Canyon, Oregon] has eight centripetal canals, often irregular in height along each quadrant and are more hemispherical in shape than *Benthocodon hyalinus* [**(C)**—photo by K. Raskoff, from 635 m along the Northwind Ridge, Arctic]. Note the presence of a mostly clear peduncle and red lips in both *P. tatsunoko* and *B. hyalinus*. Row 2 provides images of two additional species of *Crossota* that we have observed and were included in the molecular analysis: *Crossota millsae* [**(D)**—DR88 @ 2,115 m in Monterey Bay], *Crossota* n. sp. [**(E)**—DR726 @ 2,292 m in Mazatlan Basin, Gulf of California], and one that was not included in the molecular analysis *Crossota alba* [**(F)**—DR723 @ 2,600 m in Farallon Basin, Gulf of California]. Specimens **(A)** and **(C)** were collected in the Arctic *(Raskoff et al., 2010).

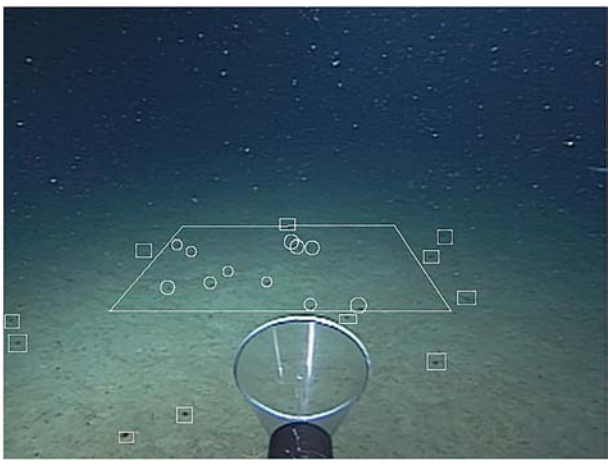

FIGURE 4 | A one square meter quadrat superimposed on video from the ROV Tiburon (04/15/2000, dive #132) to illustrate the abundance of *Benthocodon pedunculatus.* Medusae within the quadrat ($n = 11$) are encircled and medusa outside the quadrat have squares drawn around them. Depth is 3,009 m in the Monterey Submarine Canyon.

provides an operational framework for identifying these taxa until further taxonomic revisions may provide additional characters and/or a reinterpretation of known characters that align taxonomy with phylogeny in Trachymedusae. Coloration and exumbrellar furrows have previously been used as diagnostic characteristics for species identification of *Crossota*, *Benthocodon*, and *Pectis* but those features need to be validated in the field and post-collection via photographs as both are frequently lost upon collection (Bigelow, 1913; Galea et al., 2016) and coloration is often lost or reduced upon collection (**Figure 4**) and/or preservation. *Crossota* specimens sometimes retain the deep red color of their subumbrella upon fixation while both *Pectis* and *Benthocodon* specimens often become more faintly colored, the latter to the point of transparency. Consequently, we omitted these coloration and exumbrellar furrows from our key to facilitate the identification of fixed specimens. Both *Pectis* and *Benthocodon* have abcission points at the base of the tentacles, *Crossota* does not.

Key* to the Three Genera (Figure 2)

1a. With distinct centripetal canals (**Figures 2B1,B2**).... *Pectis*
1b. Without distinct centripetal canals (**Figures 2A1,C1**)..... 2
2a. With subumbrella appearing to have a distinct 'hole' that leads down to peduncle (**Figure 2C3**).....*Benthocodon*
2b. With subumbrella lacking a 'hole-like' invagination at the apex (**Figures 2A3,B3**).....*Crossota*

Generic Diagnosis

Genus *Pectis* (Haeckel, 1879)

Pectis (Haeckel, 1879): 266.

Voragonema (Naumov, 1971): 13

Rhopalonematidae with a thick, hemispherical bell. Eight pendant gonads, medusa buds may be present, centripetal canals, and a gastric peduncle. Tentacles in multiple rows

and while capable of autotomization, many tentacles remain after collection.

Valid Species

- *Pectis antarctica* (Haeckel, 1879) [Galea et al. (2016) considers *Voragonema laciniata* (Bouillon et al., 2001) as a junior synonym]—type species, 11–13 triangular centripetal canals but usually 12; 1,000–1,200 tentacles arranged in 5–6 rows; gonads wide, folded, thick-walled and slightly pendant distally (Haeckel, 1881, p. 5; **Figure 2**); does have a peduncle—Not included in this study as we have no specimens and have not observed this species in Monterey Bay.
- *Pectis profundicola* (Naumov, 1971). Original description based on trawled specimen from 6,800 to 8,700 m); Eight conical centripetal canals; ∼500 tentacles; gonads unknown; does have a short peduncle; brown manubrium; and clear umbrella. Our specimens differ from the original described species by the latter having a clear subumbrella. We believe that the transparent exumbrella from the original description is likely a collection artifact as some of the preserved specimens that we have collected have lost their pigmentation and *in situ* images reveal that they did have pigmentation prior to collection (**Figures 3**, **5**). Otherwise, our specimens match the incomplete description provided by Naumov (1971) although we have found specimens with more tentacles (1000–2000) and with irregular centripetal canals as well as specimens with seven, eight, and nine centripetal canals.
- *Pectis tatsunoko* (Lindsay and Pagès, 2010). Nine triangular centripetal canals originating from the ring canal; ∼1,050 tentacles; 6–7 rows of tentacles, rose-orange-colored subumbrella. The coloration of the umbrella and tentacles is not maintained upon preservation. This species was not included in our molecular analysis as we did not have access to enough specimens.

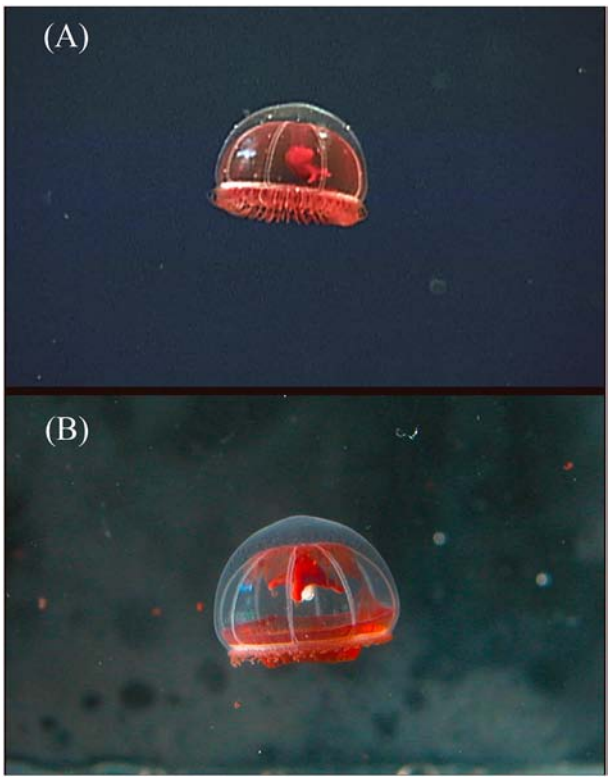

FIGURE 5 | *Benthocodon pedunculatus* collected on ROV *Tiburon* dive #836 at a depth of 3,419 m in Monterey Bay, California in 2005. The two photos are of the same specimen, **(A)** is *in situ* and **(B)** is in the laboratory taken just after return to the surface. The red subumbrella had completely disappeared by the time the animal was preserved. This animal survived collection but has autotomized its outer ring of tentacles. The normally long manubrium has also retracted by at least 50% in length between the top and bottom image and the peduncle is harder to observe as well.

Species Key for *Pectis*

1a. Eight centripetal canals present ..... *P. profundicola*
1b. More than eight centripetal canals present..... 2
2a. More than ten rounded centripetal canals..... ..... *P. antarctica*
2b. Less than 10 pointed centripetal canals..... ..... *P. tatsunoko*

Genus Crossota (Vanhöffen, 1902)

Crossota (Vanhöffen, 1902): 72.

Rhopalonematidae with a hemispherical bell. Eight tubular or pendant gonads, medusa buds may be present. No centripetal canals. Tentacles in single or multiple rows and while capable of autonomization, many tentacles remain after collection.

Valid Species

- *Crossota brunnea* (Vanhöffen, 1902) Type species, multiple rows of tentacles (up to 84 tentacles/octant observed); gonads hanging from radial canals next to manubrium, still immature in specimens 17 mm in diameter.
- *Crossota norvegica* (Vanhöffen, 1902) synonymized with *C. brunnea* by Bigelow (1913)—*C. brunnea* var. *norvegica*. Fewer than 600 tentacles (up to 43/octant observed); eight pendant gonads from near the manubrium and as long as the manubrium in specimens 15–20 mm in diameter; umbrella deep reddish-brown.
- *Crossota rufobrunnea* (Kramp, 1913)—medusa buds (Theusen, personal communication); 250+ tentacles in one row; eight pendant gonads hanging from radial canals next to short peduncle; umbrella reddish brown.
- *Crossota alba* (Bigelow, 1913)—∼179 tentacles in three rows; eight sausage shaped hanging gonads midway between apex and ring canal; medusa buds not yet observed; long unpigmented peduncle; manubrium darkly pigmented (chocolate-brown to black); subumbrella unpigmented.
- *Crossota millsae* (Thuesen, 1993)—up to 220 tentacles in one row with clear abscission zones; eight sausage shaped pendant gonads hang from ∼1/3 of the way down radial canal from apex; medusa buds sometimes present; no peduncle; bright pink to lavender color to manubrium and gonads; mesoglea clear; umbrella may have burnt-tangerine pigmentation.

Species Key for *Crossota*

1a. Gonads midway along radial canal; umbrella colorless. . . . . .*C. alba*
1b. Gonads located nearer manubrium than ring canal, umbrella pigmented. 2
2a. Gonads located approximately halfway between base of manubrium and mid-point of radial canal, umbrella with burnt-tangerine pigment. . . . . .*C. millsae*
2b. Gonads near base of manubrium, coloration not burnt-tangerine. 3
3a. With one row of 200–250 tentacles . . . . . .*C. rufobrunnea* (umbrella deep reddish brown)
3b. With multiple rows of tentacles. 4
4a. With 600 or more tentacles in several rows; umbrella pale brown, immature at 17 mm diameter. . . . . .*C. brunnea*
4b. Less than 600 tentacles, umbrella bright red/brown, mature at 18 mm in diameter. . . . . .*C. norvegica*

Genus *Benthocodon* (Larson and Harbison, 1990)

Benthocodon (Larson and Harbison, 1990): 22.

Rhopalonematidae with a thick, hemispherical bell. Eight linear to sinuous, flattened, partially pendant gonads occur on the eight radial canals; not known to have medusa buds; centripetal canals absent; manubrium with a well-developed gastric peduncle; tentacles numerous (about 800). Tentacles in multiple rows that tend to autotomize upon collection.

Valid Species

- *Benthocodon pedunculatus* Type species was first described as *Crossota pedunculata* (Bigelow, 1913) (Holotype USNM 31057). It was then reclassified as *B. pedunculata* (Larson and Harbison, 1990). *Benthocodon pedunculatus* lacks centripetal canals; short peduncle; 8 sausage shaped gonads only attached to radial canals for a short distance and mostly hanging distally; 3–4 rows of tentacles ∼350 tentacles; reddish brown pigmentation on subumbrella. Has a deeper depth distribution than *Pectis profundicola* (down to at least 4,000 m in Monterey Bay). Dense aggregations often observed.
- *Benthocodon hyalinus* (Larson and Harbison, 1990). Peduncle ¼ or more the length of the manubrium; eight linear to sinuous gonads attached along most of the radial canals becoming pendant distally; lacks pigmentation on the subumbrella, and the gonads extend along most of the length of the radial canals, only at their distal ends are the 8 linear gonads pendant; more than 800 tentacles of different sizes but one type. Reaches up to 4 cm in diameter and has been observed in moderately dense aggregations just above the bottom. This species was not included in the molecular analysis due to lack of sufficient specimens for DNA extraction.

DATA AVAILABILITY STATEMENT

Accession numbers (in bold) in **Table 1** represent sequences generated as part of this study. Specific sequence data can be found in GenBank using the provided accession number.

ETHICS STATEMENT

All specimens were collected under valid US Scientific Collecting Permit guidelines and restrictions.

AUTHOR CONTRIBUTIONS

GM, RS, and BR contributed to the conception and design of the study as well as the collection and identification of specimens. GM, KW, and BB performed the DNA extractions. BB performed the phylogenetic analysis. All authors contributed to the manuscript revision, read, and approved the submitted version.

ACKNOWLEDGMENTS

The authors are grateful for the work of many others who have contributed to this paper (Francesc Pages, Kim Reisenbichler, Chuck Baxter, Esther Chen, Joanna Tenant, Lou Zeidberg, Steve Haddock, and Lynne Christiansen) as well as the crews and pilots of MBARI's research vessels (R/V *Point Lobos*, R/V *Rachel Carson*, R/V *Western Flier*, and the remotely operated vehicles *Ventana*, *Tiburon*, and *Doc Ricketts*). Additionally, BB was supported by the Smithsonian Institution and Guam EPSCoR (National Science Foundation grant number OIA-1457769) and the MBARI staff were supported by the generous support of the David and Lucile Packard Foundation to the Monterey Bay Aquarium Research Institute. Comments and suggestions by three reviewers have greatly enhanced the clarity and content of this manuscript.

SUPPLEMENTARY MATERIAL

The Supplementary Material for this article can be found online at: https://www.frontiersin.org/articles/10.3389/fmars.2019.00798/full#supplementary-material

Supplemental Video | Four supplemental videos are provided. *Benthocodon pendunculatus* filmed in the water column on ROV *Tiburon* dive #837; *Benthocodon pedunculatus* filmed just above the seafloor during ROV *Tiburon* dive #894; *Pectis profundicola* filmed in the water column from ROV *Ventana* dive #4176; and *Crossota millsae* filmed in the water column during ROV *Doc Ricketts* dive #1049. Depths and identifications are on each video clip. All clips were filmed in Monterey Bay, California.

REFERENCES

Alldredge, A. L. (1984). "The quantitative significance of gelatinous zooplankton as pelagic consumers," in *Flows of Energy and Materials in Marine Ecosystems*, ed M. J. R. Fasham (Boston, MA: Plenum Publishing Corporation), 407–433.

Allman, G. J. (1878). "Hydrozoa," in *G. S. Nares, Narrative of a Voyage to the Polar Sea During 1875–76, in H.M.S. Ships Alert and Discovery.*

With Notes on the Natural History, Vol. 2, ed H. W. Feilden, (London: Sampson Low, Marston, Searle, and Rivington), 290–292.

Bentlage, B., Osborn, K. J., Lindsay, D. J., Hopcroft, R. R., and Collins, A. G. (2018). Loss of metagenesis and evolution of a parasitic life style in a group of open-ocean jellyfish. *Mol. Phylogenet. Evol.* 124, 50–59. doi: 10.1016/j.ympev.2018.02.030

Bigelow, H. B. (1909). "The Medusae," in *Reports on the Scientific Results of the Expedition to the Eastern Tropical pacific, in charge of Alexander Agassiz, by the U. S. Fish Commission steamer "Albatross" from October, 1904, to March, 1905. XVI.* The Medusae. Mem. Mus. Comp. Zoology Harv. Coll. 37, 1–243, plates 1–48. Available online at: http://www.biodiversitylibrary.org/item/30084.

Bigelow, H. B. (1913). "Medusae and Siphonophorae collected by the U.S. Fisheries steamer "Albatross" in the Northwestern Pacific, 1906," in *Proceedings of the United States National Museum*, Vol. 44, 1–119. Available online at: https://repository.si.edu/handle/10088/14430

Bouillon, J., Pages, F., and Gili, J. M. (2001). New species of benthopelagic hydromedusae from the Weddell Sea. *Polar Biol.* 24, 839–845. doi: 10.1007/s003000100289

Choy, C. A., Haddock, S. H. D., and Robison, B. H. (2017). Deep pelagic food web structure as revealed by *in situ* feeding observations. *Proc. Biol. Sci.* 284, 20172116. doi: 10.1098/rspb.2017.2116

Curtsinger, W. (1986). Under Antarctic ice. *Natl. Geogr.* 169, 497–511.

Folmer, O., Black, M., Hoeh, W., Lutz, R., and Vrijenhoek, R. (1994). DNA primers for amplification of mitochondrial cytochrome c oxidase subunit I from diverse metazoan invertebrate. *Mol. Mar. Biol. Biotechnol.* 3, 294–299.

Galea, H. R., Roder, C., Walcher, C., Wamuth, M., Kohlberg, E., and Fischer, P. F. (2016). *Glaciambulata neumayeri* gen. et sp. nov., a new Antarctic trachymedusa (Cnidaria: Hydrozoa), with a revision of the family Ptychogastridae. *Eur. J. Taxon.* 252, 1–30. doi: 10.5852/ejt.2016.252

Gouy, M., Guindon, S., and Gascuel, O. (2010). SeaView version 4: a multiplatform graphical user interface for sequence alignment and phylogenetic tree building. *Mol. Biol. Evol.* 27, 221–224. doi: 10.1093/molbev/msp259

Grange, L. J., Smith, C. R., Lindsay, D. J., Bentlage, B., and Youngbluth, M. J. (2017). High abundance of the epibenthic Trachymedusa *Ptychogastria polaris* Allman, 1878 (Hydrozoa, Trachylina) in Subpolar Fjords along the West Antarctic Peninsula. *PLoS ONE.* 12:e0168648. doi: 10.1371/journal.pone.0168648

Gustinich, S., Manfioletti, G., Del Sal, G., Schneider, C., and Carninci, P. (1991). A fast method for high-quality genomic DNA extraction from whole human blood. *BioTech.* 11, 298–301.

Haeckel, E. (1879). Das System der Medusen. Erster Teil einer Monographie der Medusen. *Denkschriften der Medicinisch-Naturwissenschaftlichen Gesellschaft zu Jena.* 1, XX+1–360, 320 plates. Available online at: http://www.biodiversitylibrary.org/item/101461.

Haeckel, E. (1881). Monographie der Medusen. Zweiter Theil. Erste Hälfte: Die Tiefsee-Medusen der Challenger-Reise. Zweite Hälfte: Der Organismus der Medusen. Jena: Gustav Fischer. Available online at: https://www.biodiversitylibrary.org/item/101236#page/36/mode/1up

Katoh, K., and Standley, D. M. (2013). MAFFT multiple sequence alignment software version 7: improvements in performance and usability. *Mol. Biol. Evol.* 30, 772–780. doi: 10.1093/molbev/mst010

Kramp, P. L. (1913). Medusae collected by the "Tjalfe" Expedition (in Greenland waters). *Videnskabelige Meddelelser fra Dansk naturhistorisk Forening i Kjøbenhavn.* 65, 257–286. Available online at: https://biodiversitylibrary.org/page/36397336

Lanfear, R., Calcott, B., Ho, S. Y. W., and Guindon, S. (2012). PartitionFinder: combined selection of partitioning schemes and substitution models for phylogenetic analyses. *Mol. Biol. Evol.* 29, 1695–1701. doi: 10.1093/molbev/mss020

Larson, R. J., and Harbison, G. R. (1990). Medusae from McMurdo Sound, Ross Sea including the descriptions of two new species, *Leuckartiara brownie* and *Benthocodon hyalinus*. *Polar Biol.* 11, 19–25. doi: 10.1007/BF00236517

Larson, R. J., Matsumoto, G. I., Madin, L. P., and Lewis, L. M. (1992). Deep-sea benthic and benthopelagic medusae, recent observations from submersibles and a remotely operated vehicle. *Bull. Mar. Sci.* 51, 277–286.

Leray, M., Yang, J. Y., Meyer, C. P., Mills, S. C., Agudelo, N., Ranwez, V., et al. (2013). A new versatile primer set targeting a short fragment of the mitochondrial COI region for metabarcoding metazoan diversity: application for characterizing coral reef fish gut contents. *Front. Zool.* 10, 34. doi: 10.1186/1742-9994-10-34

Lindsay, D., and Pagès, F. (2010). *Voragonema tatsunoko* (Trachymedusae: Rhopalonematidae), a new species of benthopelagic medusa, host to the hyperiid amphipod *Mimonectes spandli* (Physosomata: Mimonectidae). *Zootaxa.* 2671, 31–39. doi: 10.5281/zenodo.199149

Lindsay, D. J., Grossman, M. M., Bentlage, B., Collins, A. G., Minemizu, R., Hopcroft, R. R., et al.. (2017). The perils of online biogeographic databases: a case study with the 'monospecific' genus *Aegina* (Cnidaria, Hydrozoa, Narcomedusae). *Mar. Biol. Res.* 13, 494–512. doi: 10.1080/17451000.2016.1268261

Maas, O. (1906). Médusen. Rapports Scientifiques. Résultats du voyage du S.Y. Belgica en 1897–1898–1899. *Zoologie.* R51, 3–32, pls 1–3. Available online at: http://www.biodiversitylibrary.org/item/18741#page/7/mode/1up.

Matsumoto, G. I., Baxter, C., and Chen, E. H. (1997). Observations of the deep-sea trachymedusa *Benthocodon pedunculata*. *Invert. Biol.* 116, 17–25. doi: 10.2307/3226920

Mayer, A. G. (1910). Medusae of the world. Hydromedusae, Vols. I & II. Scyphomedusae, Vol. III. Carnegie Institution, Washington. 735, plates 1–76. Available online at: http://www.biodiversitylibrary.org/item/16794#page/7/mode/1up

Medlin, L., Elwood, H. J., Stickel, S., and Sogin, M. L. (1988). The characterization of enzymatically amplified eukaryotic 16S-like rRNA-coding regions. *Gene* 71, 491–499. doi: 10.1016/0378-1119(88)90066-2

Naumov, D. V. (1971). Gydroidnye i stsifoidnye medusy iz Kurilo-Kamchatskogo zhelova (Hydromedusae and Scyphomedusae from the Kurile-Kamchatka trench). *Trudy Inst. Okeanol.* 92, 9–17.

Raskoff, K. A., Hopcroft, R. R., Kosobokova, K. N., Purcell, J. E., and Youngbluth, M. (2010). Jellies under ice: ROV observations from the Arctic 2005 hidden ocean expedition. *Deep Sea Res. II.* 57, 111–126. doi: 10.1016/j.dsr2.2009.08.010

Robison, B. H., Reisenbichler, K. R., and Sherlock, R. E. (2017). The coevolution of midwater research and ROV technology at MBARI. *Oceanogr.* 30, 26–37. doi: 10.5670/oceanog.2017.421

Scholin, C. A., and Anderson, D. M. (1994). Identification of species and strain-specific genetic markers for globally distributed *Alexandrium* (Dinophyceae). 1. RFLP analysis of SSU rRNA genes. *J. Phycol.* 30, 744–754. doi: 10.1111/j.0022-3646.1994.00744.x

Stamatakis, A. (2014). RAxML version 8: a tool for phylogenetic analysis and post-analysis of large phylogenies. *Bioinformatics.* 30, 1312–1313. doi: 10.1093/bioinformatics/btu033

Talavera, G., and Castresana, J. (2007). Improvement of phylogenies after removing divergent and ambiguously aligned blocks from protein sequence alignments. *Syst. Biol.* 56, 564–577. doi: 10.1080/10635150701472164

Thuesen, E. V. (1993). *Vampyrocrossota childressi*, a new genus and species of black medusa from the bathypelagic zone off California (Cnidaria: Trachymedusae: Rhopalonematidae). *Proc. Biol. Soc. Wash.* 106, 190–194.

Thuesen, E. V. (2003). *Crossota millsae* (Cnidaria: Trachymedusae: Rhopalonematidae), a new species of viviparous hydromedusa from the deep sea off California and Hawaii. *Zootaxa.* 309, 1–12. doi: 10.11646/zootaxa.309.1.1

Thuesen, E. V., and Childress, J. J. (1994). Oxygen consumption rates and metabolic enzyme activities of oceanic California medusae in relation to body size and habitat depth. *Biol. Bull*. 187, 84–98. doi: 10.2307/1542168

Vanhöffen, E. (1902). Die acraspeden Medusen der Deutschen Tiefsee-Expedition 1898–1899. I. Trachymedusen. *Wissenschaftliche Ergebnisse der Deutschen Tiefsee Expedition "Valdivia"*. 3, 55–86. Available online at: https://www.biodiversitylibrary.org/item/16279#page/7/mode/1up

Youngbluth, M. J. (1984). "Manned submersibles and sophisticated instrumentation: tools for oceanographic research," in *Proceedings of SUBTECH'83 Symposium, Society for Underwater Technology* (London), 235–244.

Conflict of Interest: The authors declare that the research was conducted in the absence of any commercial or financial relationships that could be construed as a potential conflict of interest.

Copyright © 2020 Matsumoto, Bentlage, Sherlock, Walz and Robison. This is an open-access article distributed under the terms of the Creative Commons Attribution License (CC BY). The use, distribution or reproduction in other forums is permitted, provided the original author(s) and the copyright owner(s) are credited and that the original publication in this journal is cited, in accordance with accepted academic practice. No use, distribution or reproduction is permitted which does not comply with these terms.

frontiers in Marine Science

ORIGINAL RESEARCH
published: 24 January 2020
doi: 10.3389/fmars.2019.00832

Animal Community Dynamics at Senescent and Active Vents at the 9°N East Pacific Rise After a Volcanic Eruption

Sabine Gollner[1], Breea Govenar[2], Pedro Martinez Arbizu[3], Lauren S. Mullineaux[4], Susan Mills[4], Nadine Le Bris[5], Markus Weinbauer[6], Timothy M. Shank[4] and Monika Bright[7]*

[1] Ocean Systems, Royal Netherlands Institute for Sea Research and Utrecht University, Den Burg, Netherlands, [2] Biology Department, Rhode Island College, Providence, RI, United States, [3] German Center for Marine Biodiversity Research, Senckenberg am Meer, Wilhelmshaven, Germany, [4] Biology Department, Woods Hole Oceanographic Institution, Woods Hole, MA, United States, [5] Laboratoire d'Ecogéochimie des Environnements Benthiques, CNRS, Sorbonne Université, Banyuls-sur-Mer, France, [6] Laboratoire d'Océanographie de Villefranche, CNRS, Sorbonne Université, Villefranche-sur-Mer, France, [7] Department of Functional and Evolutionary Ecology, University of Vienna, Vienna, Austria

OPEN ACCESS

Edited by:
Stephen Hammond,
Office of Oceanic and Atmospheric Research (NOAA), United States

Reviewed by:
Christoph Plum,
University of Oldenburg, Germany
Amanda N. Netburn,
NOAA's Office of Ocean Exploration and Research, United States

***Correspondence:**
Sabine Gollner
sabine.gollner@nioz.nl

Specialty section:
This article was submitted to Deep-Sea Environments and Ecology, a section of the journal Frontiers in Marine Science

Received: 30 May 2019
Accepted: 27 December 2019
Published: 24 January 2020

Citation:
Gollner S, Govenar B, Martinez Arbizu P, Mullineaux LS, Mills S, Le Bris N, Weinbauer M, Shank TM and Bright M (2020) Animal Community Dynamics at Senescent and Active Vents at the 9°N East Pacific Rise After a Volcanic Eruption. Front. Mar. Sci. 6:832. doi: 10.3389/fmars.2019.00832

In 2005/2006, a major volcanic eruption buried faunal communities over a large area of the 9°N East Pacific Rise (EPR) vent field. In late 2006, we initiated colonization studies at several types of post eruption vent communities including those that either survived the eruption, re-established after the eruption, or arisen at new sites. Some of these vents were active whereas others appeared senescent. Although the spatial scale of non-paved (surviving) vent communities was small (several m^2 compared to several km^2 of total paved area), the remnant individuals at surviving active and senescent vent sites may be important for recolonization. A total of 46 meio- and macrofauna species were encountered at non-paved areas with 33 of those species detected were also present at new sites in 2006. The animals living at non-paved areas represent refuge populations that could act as source populations for new vent sites directly after disturbance. Remnants may be especially important for the meiofauna, where many taxa have limited or no larval dispersal. Meiofauna may reach new vent sites predominantly via migration from local refuge areas, where a reproductive and abundant meiofauna is thriving. These findings are important to consider in any potential future deep-sea mining scenario at deep-sea hydrothermal vents. Within our 4-year study period, we regularly observed vent habitats with tubeworm assemblages that became senescent and died, as vent fluid emissions locally stopped at patches within active vent sites. Senescent vents harbored a species rich mix of typical vent species as well as rare yet undescribed species. The senescent vents contributed significantly to diversity at the 9°N EPR with 55 macrofaunal species (11 singletons) and 74 meiofaunal species (19 singletons). Of these 129 species associated with senescent vents, 60 have not been reported from active vents. Tubeworms and other vent megafauna not only act as foundation species when alive but provide habitat also when dead, sustaining abundant and diverse small sized fauna.

Keywords: senescent vent, biodiversity, volcanic eruption, recovery, meiofauna, macrofaunal, deep-sea mining

INTRODUCTION

Animals at deep-sea hydrothermal vents can be exposed to a very dynamic environment of changing vent fluid conditions and associated productivity regimes. On a second to minute timeframe, they can be exposed to highly variable hydrothermal fluids emissions, with temperatures ranging from 2 to about 40°C, and high sulfide and mineral concentrations at diffuse flow active vent sites (Fisher et al., 2007). On fast spreading centers, on yearly to decadal timescales, local venting features within active sites can become inactive, resulting in the death of large symbiotic fauna. After a vent became inactive, animals are exposed to stable ambient deep-sea temperatures, lack of vent fluid emissions, and loss of primary production through chemosynthesis (Tsurumi and Tunnicliffe, 2003). In addition, communities at hydrothermal vents that are associated with magmatic activity can be exposed to large-scale disturbances by volcanic eruptions that can kill animals by burying them with lava (Tolstoy et al., 2006). At the studied 9°N East Pacific Rise (EPR), animal communities are exposed to all of the above-mentioned stressors and disturbances. The large majority of vent research has focused on fauna at active hydrothermal vents. Megafauna associated with chemoautotrophic symbionts such as tubeworms or mussels depend on active venting, as their symbionts require reduced sulfur species to provide organic carbon to their hosts (Childress and Fisher, 1992). The megafauna act as foundation species and host a high biomass and high abundance, but relatively low diversity macrofaunal community that is adapted to the extreme active vent environment and that is largely restricted to the active hydrothermal vent environment (Van Dover, 2000; Fisher et al., 2007). The meiofaunal communities are overall much less studied than the mega- and macrofaunal, but many species that occur at active vents are also present in the vent periphery (Gollner et al., 2015a; Plum et al., 2017).

Senescent or waning vents are poorly studied. They are characterized by: (1) absence of vent fluid emissions, i.e., no visible shimmering water and a temperature anomaly lower than 0.1°C above the ambient (Van Dover, 2002) and (2) presence of (mostly) dead large symbiotic fauna, i.e., vestimentiferan tubes with no visible branchial plumes (Tsurumi and Tunnicliffe, 2003). Senescent vents are ecotones, i.e., areas of environmental transition, where ecological communities coincide. In the case of senescent vents, a former active hydrothermal vent site or patch loses the energy provided by vent fluid emissions, causing the death of symbiotic megafaunal species such as tubeworms that depend on chemolithoautotrophic bacteria (Van Dover, 2000). The patch/site exposed to stable ambient deep-sea temperatures of ∼2°C transits into a biomass rich area without *in situ* primary production and without hydrothermal vent fluid emissions with very low/no temperature anomaly and reduced toxicity, as the H_2S flow decreases but can persist at low levels as a degradation product of organic matter or sulfide minerals. The biomass degrades until the patch/site finally becomes similar to typical biomass poor hard substrate deep-sea areas that are sustained by lateral fluxes of particle from distant active vent patches and downward flux of organic matter from the ocean's surface waters (Smith et al., 2008). The very few studies from senescent vents show that communities are characterized by a subset of fauna found at active fields as well as several non-vent deep-sea taxa (Van Dover, 2002; Tsurumi and Tunnicliffe, 2003; Gollner et al., 2013). In contrast to the senescent/waning vents that can be viewed as the latest stage of succession at active vents, at old inactive chimneys no vent symbiotic megafauna remainings are visible. Such old inactive vents typically host sessile taxa such as sponges, corals, hydroids, crabs, and echinoderms (Tunnicliffe et al., 1986; Galkin, 1997; Erickson et al., 2009). Boschen et al. (2015) found that megafaunal assemblages on inactive sulfide-rich chimneys may be distinct from both active vents communities and those on seamounts (Boschen et al., 2015).

Succession of active vents after violent volcanic eruptions was studied at the fast spreading Juan de Fuca Ridge and at the 9°N EPR, and showed recovery of benthic communities at active sites in less than a decade (Shank et al., 1998; Marcus et al., 2009; Gollner et al., 2015b, 2017). After such a major disturbance event at the EPR, colonization of new vent sites by macrofaunal larvae from distant areas was found to be one of the major drivers during recovery (Mullineaux et al., 2010, 2012). Simulations on recoverability of vent fields in the western Pacific Ocean suggested substantial variation in recovery time due to variation in regional connectivity, ranging from ∼6 to 140 years (Suzuki et al., 2018), but comparison to the EPR and Juan de Fuca Ridge is not really possible due to the limited knowledge of the temporal dynamics of habitats and lack of knowledge on adaptation of species to environmental instabilities in this area. Time-series studies showed that vent communities along the slow-spreading Mid-Atlantic and recent revisited vent fields along Back-Arc Basins are very stable on decadal time-scale (Cuvelier et al., 2011; Gollner et al., 2017; Du Preez and Fisher, 2018).

Natural disturbances [*sensu* destruction or removal of biomass (Grime, 1977; Sousa, 2001)], only rarely completely eliminate existing communities (Sousa, 2001). Instead, post-disturbance landscapes are usually mosaics of patches having different species composition. Individuals that survive disturbance may influence colonization and succession after disturbance. Depending on their life-history traits, these remnant individuals, so called legacies (Franklin et al., 1988), can accelerate or impede recovery to its pre-disturbance state (Platt and Connell, 2003). Mullineaux et al. (2009) experimentally tested the imprint of past environmental regime on the vent community succession at the 9°N EPR (Mullineaux et al., 2009). By using transplant experiments, placing communities from warm to cool environments (simulating waning of vent fluids) and from cool to warm (simulating new vent sites), they found that productivity enhancement may outweigh potential physiological stress in setting limits to distributions of vent macrofauna. Most macrofauna species of established "warm" communities were unable to survive in the cold environment with less productivity. Species limited by primary productivity may survive an increase but not a decrease in vent fluid emission (Mullineaux et al., 2009). The legacies of meiofauna are to date not studied, although the different life-history traits of meio- and macrofauna may influence recovery after disturbance.

The size and associated life-history traits of meio- and macrofauna are fundamentally different. Permanent meiofauna,

such as nematodes or copepods, remain small as adults (< 1 mm). Macrofauna, such as gastropods, bivalves, and polychaetes, are > 1 mm when adult. During their larvae and juvenile stages, macrofauna are in the same size class as the permanent meiofauna (< 1 mm) (Warwick, 1984; Giere, 2009). Meio- and macrofauna highly influence each other's community structure (Ólafsson, 2003). The discrimination of meio- and macrofauna is based on life-history traits that are optimized at certain body size (∼1 mm) and weight (45 μg dry weight). They comprise two separate evolutionary units each with an internally coherent set of biological characteristics, such as development (direct benthic versus planktonic), dispersal (as adults versus planktonic larvae), generation time (less than 1 year versus more than 1 year), growth (reach asymptotic adult size versus continue growth throughout life), or mobility (motile versus sedentary or motile) (Warwick, 1984). At hydrothermal vents, patterns of habitat fidelity differ for the meio- and macrofauna: macrofaunal species are primarily limited to direct contact with venting fluids, while meiofaunal species are distributed across proximate and distant habitats to vent openings and are thus not restricted to vent habitats. The presence of vent meiofauna on basalt may suggest that meiofauna is in contrast to macrofauna rather limited by physico-chemical stress than by productivity (Gollner et al., 2015a). One thus may expect that vent meiofauna is present at senescent vents as well.

Once seen as oases within a barren deep ocean, it is now recognized that vent communities interact with surrounding ecosystems on the sea floor and in the water column. Yet, especially the role of waning vents that provide organic remains of dead symbiotic vent megafauna is to date not quantified (Levin et al., 2016). Here, we take the unique opportunity to: (1) investigate the meio- and macrofauna abundance and diversity patterns at senescent vents and to (2) explore the role of fauna present at non-paved senescent and active vents for recovery processes of new vent sites after volcanic eruptions. We monitored site activity from 2006 to 2009 and present meio- and macrofaunal data on one active site where diffuse venting remained after the volcanic eruption (Bio9 Vent) as well as from two sites where the activity had totally ceased after the eruption probably due to clogging or reconstruction of the main high-temperature subseafloor vent fluid channels during the eruption (Q Vent and East Wall). In addition, we show data from two sites which were covered by lava and were active after the eruption, visible by the presence of new *Tevnia* tubeworm in 2006, but where patches of tubeworms within vent sites locally ceased due to the progressing clogging of the low-temperature emission network on new basalt in the first years after the eruption (Sketchy and P Vent). We hypothesize that (1) senescent vents at the 9°N EPR support a rich meio- and macrofaunal community. We further hypothesize that (2) active and senescent vents that were not paved by lava may play pivotal roles for recovery after disturbance: they provide remnants, i.e., legacies which may act as source populations for the close by new active vents. In addition, we (3) bring the data into a temporal context by comparing our new results to our previous studies on faunal diversity from active vents before and after the eruption (Gollner et al., 2010, 2015a,b). In the final section of the manuscript, we consider our results in the context of deep-sea mining disturbance.

MATERIALS AND METHODS

Numerous dives were made with the DSV *Alvin* in order to explore the 9°N EPR vent field after it was covered by lava due to an eruption in late 2005/early 2006 (Tolstoy et al., 2006; Soule et al., 2007). During a first cruise in October 2006, we deployed settlement substrates at six vent sites: Bio9 Vent (not paved by lava, old active black smoker with Pompeii worms); East Wall and Q Vent (not paved by lava but vent fluid stopped after eruption; senescent vent with dead tubeworms/mussels and dead *Alvinella* polychaetes); Tica Vent, P Vent, Sketchy (paved with lava by the eruption, new venting activity and *Tevnia* tubeworms in late 2006) (**Figure 1**). In addition, we deployed settlement substrates also in the vent periphery of each site. In this manuscript, we use the term "new basalt" for peripheral areas that were covered with lava in 2006, and "old basalt" for areas that were not covered with lava in 2006. All sites were located at ∼2500 m depth in the 9°N region of the EPR. We recovered settlement substrates in December 2006, November 2007, and December 2009 (**Table 1** and **Figures 1**, **2**). Each settlement substrate used at new active vent patches consisted of two plastic kitchen sponges with a circular surface area of ∼64 cm^2 (Gollner et al., 2015b). Each settlement substrate used on basalt or at senescent vents consisted of four plastic kitchen sponges in order to enhance sample size. The suitability of sponges as settlement substrates for fauna was carefully tested. Throughout the entire sampling period (2006–2009), animals from natural community samples were taken

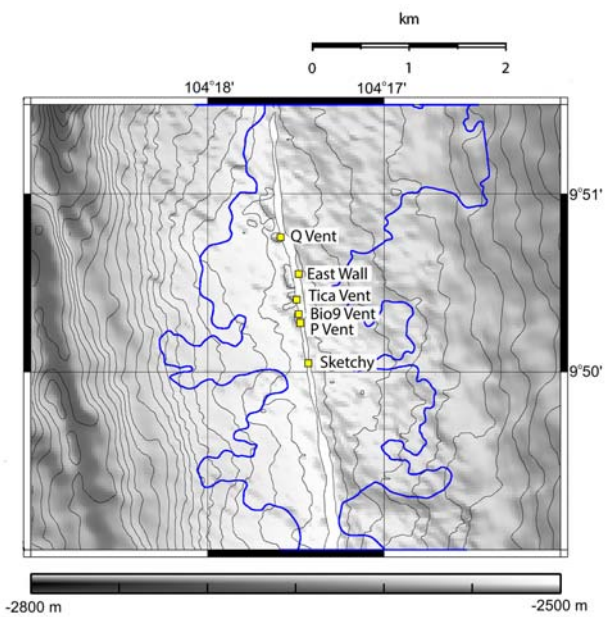

FIGURE 1 | Map showing the studied sites East Wall, Q Vent, Bio9 Vent, Tica Vent, Sketchy patch in the Ty-Io site, and P Vent in the 9°N East Pacific Rise area. Several km^2 (blue outline) of the area were flooded with lava during an eruption in 2005/2006. We observed that Bio9 Vent, East Wall and Q Vent were not covered by lava. Tica Vent, Ty-Io/Sketchy, and P Vent were covered by lava. Depth gray scale is given in meters. Map courtesy of Soule et al. (2007).

TABLE 1 | Habitat and animal community characteristics of sites that were not covered with lava by the volcanic eruption in 2005/06 (for habitat and animal community characteristics from lava paved sites, including new vent sites and new basalt see Gollner et al., 2015b).

Site(name)_age(years)	Bio9 Vent_ 12 + 1	Q Vent_ 12 + 1	East Wall_ 15 + 1	East Wall_ 15 + 2	East Wall_ 15 + 4	Basalt_ 15 + 1	Basalt_ 15 + 2	Basalt_ 15 + 4	Sketchy_ 0 + 2	Sketchy_ 0 + 4	P Vent_ 0 + 4
Site	Bio9 Vent	Q Vent	East Wall	East Wall	East Wall	Basalt	Basalt	Basalt	Ty-Io/Sketchy	Ty-Io/Sketchy	P Vent
Habitat	old active vent	senescent vent	senescent vent	senescent vent	senescent vent	old basalt	old basalt	old basalt	senescent vent	senescent vent	senescent vent
Paved by lava in 2006	No	No	No	No	No	No	No	No	Yes	Yes	Yes
Age of site at sampling	> 12 + 1	>12 + 1	15 + 1	15 + 2	15 + 4	15 + 1	15 + 2	15 + 4	0 + 2	0 + 4	0 + 4
Year of sampling	2006	2006	2006	2007	2009	2006	2007	2009	2007	2009	2009
Number of samples	1	1	2	2	2	3	1	1	3	3	3
Max. T (°C)	59	2	2	2	2	2	2	2	2	2	2
Mean H_2S	> 2000	0	0	n.a.	n.a.	0	n.a.	n.a.	n.a.	n.a.	n.a.
Mean pH	4.4	7.9	7.6–7.9	n.a.	n.a.	7.9	n.a.	n.a.	n.a.	n.a.	n.a.
MEMA ab.	304	224	193 ± 174	1451 ± 549	6399 ± 2293	67 ± 59	322	976	207 ± 51	50 ± 11	412 ± 61
ME ab.	258	214	165 ± 162	934 ± 213	6133 ± 2221	30 ± 10	254	894	114 ± 36	47 ± 12	108 ± 85
MA ab.	46	10	28 ± 12	517 ± 336	266 ± 72	37 ± 49	68	82	92 ± 20	3 ± 1	304 ± 139
ME% juvenile ab.	2	66	47 ± 14	53 ± 32	61 ± 2	33 ± 8	69	57	40 ± 2	25 ± 19	31 ± 12
MA% < 1 mm ab.	11	73	70 ± 5	94 ± 1	76 ± 5	85 ± 13	91	94	93 ± 5	78 ± 38	59 ± 12
MEMA S	7	17	26 ± 1	30 ± 6	40 ± 7	18 ± 5	28	37	20 ± 3	14 ± 2	20 ± 4
ME S	2	11	17 ± 2	15 ± 2	23 ± 4	10 ± 2	18	32	12 ± 1	12 ± 1	11 ± 5
MA S	5	6	9 ± 3	15 ± 4	17 ± 3	7 ± 3	10	5	9 ± 2	2 ± 1	9 ± 1
MEMA ES(300)	7	17	25 ± 0	23 ± 2	29 ± 3	18 ± 5	24	26	20 ± 2	14 ± 2	16 ± 3
ME ES(300)	2	11	17 ± 2	14 ± 2	19 ± 3	10 ± 2	18	24	12 ± 1	12 ± 1	11 ± 4
MA ES(300)	5	6	9 ± 3	13 ± 1	17 ± 3	7 ± 3	10	5	9 ± 2	2 ± 1	8 ± 1
MEMA H'(loge)	0.7	0.9	2.2 ± 0.4	2.0 ± 0.0	2.2 ± 0.0	2.1 ± 0.6	2.1	2.4	1.9 ± 0	1.8 ± 0.2	1.8 ± 0.4
ME H'(loge)	0.2	0.8	1.8 ± 0.4	2.1 ± 0.2	2.0 ± 0.0	1.5 ± 0.4	1.8	2.2	1.4 ± 0	1.7 ± 0.1	1.6 ± 0.2
MA H'(loge)	0.7	1.6	1.8 ± 0.2	0.4 ± 0.0	1.9 ± 0.0	1.7 ± 0.4	0.4	0.6	0.9 ± 0	0.5 ± 0.4	1.1 ± 0.0
MEMA J'	0.4	0.3	0.7 ± 0.1	0.6 ± 0.0	0.6 ± 0.0	0.7 ± 0.1	0.6	0.7	0.6 ± 0	0.7 ± 0.0	0.6 ± 0.0
ME J'	0.3	0.3	0.7 ± 0.1	0.8 ± 0.0	0.6 ± 0.0	0.6 ± 0.1	0.6	0.6	0.6 ± 0	0.7 ± 0.0	0.7 ± 0.0
MA J'	0.4	0.9	0.8 ± 0.0	0.1 ± 0.0	0.7 ± 0.0	0.9 ± 0.0	0.2	0.4	0.4 ± 0	0.8 ± 0.0	0.5 ± 0.0

Bio9 Vent remained an active vent with alive Pompeii worms; Q Vent and East Wall vent sites turned entirely inactive and became senescent with dead symbiotic megafaua; the old basalt in the close surrounding of these sites was not covered with lava. In addition, data from senescent vent patches from Sketchy and P Vent are presented. Sketchy and P Vent were new and active in 2006. At Sketchy and P Vent, the studied patches where we had placed colonization substrates were found to be hydrothermally inactive in 2007 and 2009, while many other patches within these sites remained hydrothermal active at the same time. Age of site at sampling is indicated. For example, for 2006: Sketchy_0 + 2: "0" indicates no animal community from prior eruption because Sketchy was covered by lava; " + 2" indicates that the sampling occurred 2 years after the eruption and that the community was ~2 years old; East Wall_15 + 1: "15" indicates a 15 year old community from prior eruption that was not covered by lava; " + 1" indicates that the sampling occurred 1 year after the eruption. Age the East Wall community was 15 + 1 = 16 years at the time of sampling in late 2006. Age of communities, time of sampling, abiotic characteristics, and habitat (active vent, senescent vent, basalt) are given. Biotic characteristics such as mean total abundance (ab.) of meio- and macrofauna (MEMA) per settlement substrate (64 cm^2), meio- (ME), and macrofauna (MA) abundance, relative abundance of meiofauna juveniles and macrofauna individuals < 1 mm, and diversity indices [S: species richness, ES(300): expected number of species after identifying 300 individuals, H'_{loge}: Shannon diversity, J': Pielou's evenness] are given.

and compared to animals from settlement devices. Statistical tests revealed that the plastic kitchen sponges can be considered efficient to quantitatively sample the mobile meiofauna, as well as mobile and sessile macrofauna (for details on statistical test, please see Chapter 2.1. benthic collections and Supplementary Material in Gollner et al., 2015b).

All settlement substrates and natural samples were deployed and/or recovered into isolated boxes with the hydraulic arm of the submersible *Alvin*. Temperature was measured with the temperature probe of the submersible during deployment and recoveries. *In situ* sulfide and pH measurements were conducted with combined potentiometric pH and sulfide sensors, as described in Mullineaux et al. (2012). To remove animals from settlement substrates, each sponge (consisting of a 55 m long and 1 mm thin plastic thread woven to a loose net, which was furled and fixed with a rubber band) was uncoiled and placed into 37‰ MgCl in water for 10 min to relax the animals (Higgins and Thiel, 1988). Animals were then sieved through a 32 μm and 1 mm net with 32 μm filtered, cold seawater to separate the meio- from the macrofauna. Animals were preserved in 4% buffered formaldehyde (for details see Gollner et al., 2015b). All animals were sorted and counted using a dissecting microscope.

In total ∼96,100 meiofaunal and ∼20,400 macrofaunal individuals were analyzed from senescent vents, from active old Bio9 Vent, and from old basalt for this study (**Table 1**). In addition, we compare these data to our published datasets of 40,050 meio- and 60,175 macrofauna individuals from new active vent sites and new basalt sites after the eruption from the years 2006–2009 (Gollner et al., 2015b) and to 69,000 meio- and 105,000 macrofauna individuals that had been collected before the eruption in the years 2001–2004 (Gollner et al., 2015a). All three studies exclude abundances of megafauna (Pompeii worms, tubeworms, mussels). All macrofauna > 1 mm were identified to species level. Macrofauna < 1 mm were also identified to species level whenever this was morphologically possible. If this was not possible, they were recorded as juveniles—for example "juvenile gastropods" or "juvenile polychaetes." For the meiofauna, at least 200 individuals per higher taxon (e.g., copepods, nematodes) were identified per settlement substrate/*in situ* natural collection to species level unless fewer were found in the sample. All meiofauna specimens were morphologically identified to species level which the exception of juveniles that were grouped into for example "juvenile copepods" or "juvenile nematodes." Data from meio- and macrofaunal juveniles that could not be identified to species level were included in abundance calculations but excluded from diversity calculations, which are all based on species level identification. All species abundance data are shown in **Supplementary Datasheet S1**. A detailed faunistic description as well as prokaryote abundances are given in **Supplementary Material S1**.

Species richness (S obs.), Shannon diversity (H'_{loge}), Pielou's evenness (J'), and expected number of species after identifying 300 individuals [ES(300)] were calculated from quantitative species abundance data by DIVERSE subroutines in PRIMER Version 6 package (Clarke and Gorley, 2001). ES(300) was chosen because > 300 individuals were identified in samples and in order to compare values to data published by Gollner et al. (2015a,b). For statistical analyses of univariate measurements from prokaryotes and fauna at different sites and years, non-parametric Kruskal–Wallis tests were conducted, followed by multiple pairwise comparisons between groups using the Wilcox test, using the standard package S in the program R studio (Ihaka and Gentleman, 1996). The SIMPROF (similarity profile) test was performed to look for statistically significant differences of clusters of sites without making any *a priori* hypothesis. This shows in addition to the multi-dimensional-scaling (MDS), the determination of groupings, especially when stress of the MDS is high (Clarke and Warwick, 2001). One-way and two-way crossed analysis of similarity (ANOSIM) and SIMPER (similarity percentage) were used in order to determine (dis)similarity between samples from distinct years (2006, 2007, 2009, pre-eruption) and distinct habitats (active vent, senescent vent, basalt). Two-way analysis was used when testing multiple sites per year. SIMPROF ($p < 0.05$), SIMPER, ANOSIM, and MDS plots were performed for settlement substrates with PRIMERv6. To demonstrate communities' time trajectory from distinct sites within the study period, we used overlays in the MDS plots. Bubble plots were used to visualize occurrence of selected species in different habitats and years. To create Bray–Curtis similarity matrices for these analyses, abundances of species were standardized to compensate for varying abundances, and square-root transformed to down-weight the importance of very abundant species without losing the influence of rarer species (Clarke and Gorley, 2001).

RESULTS

Post-disturbance Landscape at the 9°N EPR After the Volcanic Eruption in 2006

In 2006, the 9°N EPR area comprised a very complex environment with three major different habitats (active vent, senescent vent, basalt) and two major different aged communities (old communities that survived the volcanic eruption and new communities that had newly formed after the volcanic eruption). Several sites in the 9°N EPR were visually observed and photographs were taken during a series of *Alvin* dives in ∼2500 m water depth at the 9°N EPR in October 2006, December 2006, November 2007, and October 2009 (**Figures 1**, **2** and **Table 1**).

We observed that the site Bio9 Vent was not covered with lava and the Bio9 black smoker hosted live Pompeii worms (*Alvinella pompeiana*) and was hydrothermally active in 2006. Bio9 Vent had very hot hydrothermal fluid emissions—the settlement substrates (plastic kitchen sponges) deployed in October 2006 were found to be partly melted after recovery in December 2006, indicating temperature peaks of > 100°C during October and December 2006. Settlement substrates that were intended for recovery from Bio9 Vent in December 2007 were never found back: the smoker had collapsed and eventually buried the settlement substrates and fauna.

The sites Q Vent and East Wall were also not covered with lava but were hydrothermally inactive with no temperature anomalies in 2006 (**Table 1** and **Figure 2**). At Q Vent empty tubes from Pompeii worms were observed. At East Wall empty tubes from *Riftia pachyptila* and shells from *Bathymodiolus thermophilus* were found. Q Vent and East Wall are therefore so called

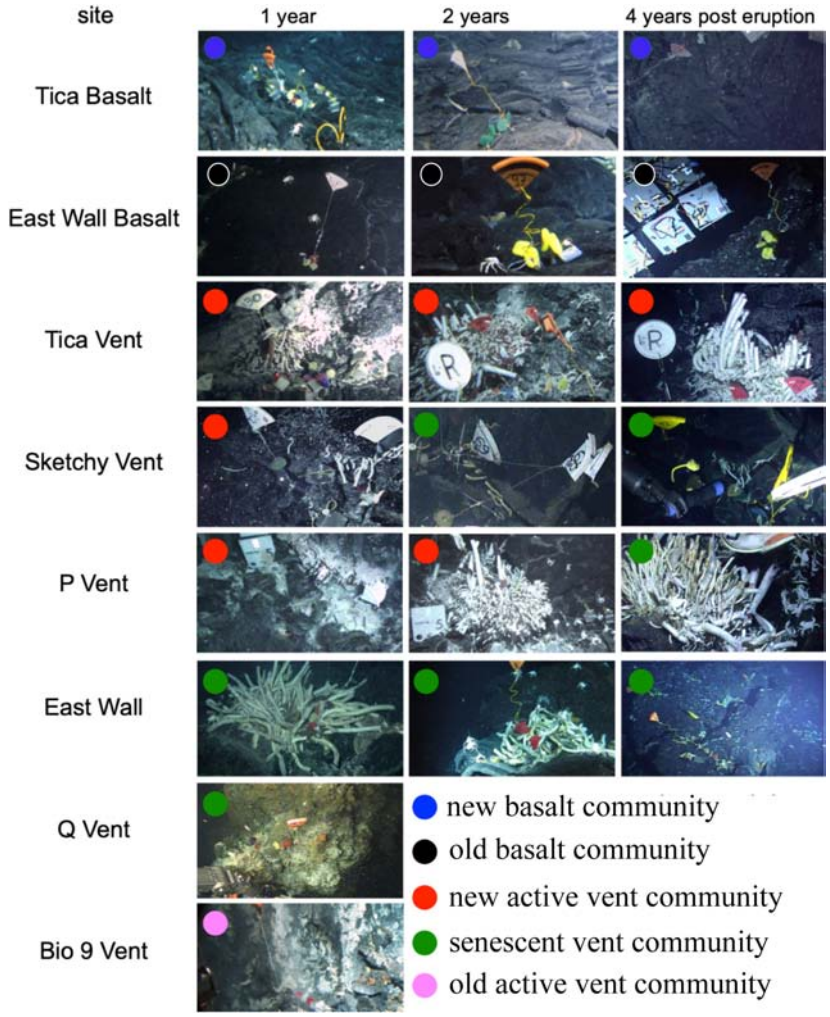

FIGURE 2 | Photographs of studied patches at sites at the 9°N East Pacific Rise from 1 year, 2 years, and 4 years post eruption taken in 2006, 2007, and 2009. Blue dots: new basalt in the periphery of new active vents (new basalt areas covered with lava in 2005/06). Black dots: old basalt not covered with lava. Red dots: new active vents that became active in 2006. Green dots: senescent vents (vent site East Wall and Q Vent were not covered with lava, but no vent fluids in 2006; patches at new Sketchy vent became inactive in the second year post eruption, patches at new P Vent became inactive in the fourth year post eruption). Pink dot: old active vent (active vent site not covered by lava).

senescent vents. Due to dive-plan constraints, Q Vent could only be visited in 2006. At East Wall, we collected samples in 2006, 2007, and 2009. Beside the dead megafauna, also very few individuals ($\sim < 10$) of alive *Bathymodiolus* were present at East Wall in 2006 and 2007. At the East Wall site, tubes and shells further degraded in 2007 and were not visually recognizable as tubes and shells anymore in 2009. Only a fluffy organic layer was left on the basalt 4 years after venting had ceased at East Wall (see **Figure 2**).

Tica Vent, Ty-Io/Sketchy, and P Vent were covered by lava in 2005/2006 and vent fauna that were present pre-eruption such as large *Riftia* and the associated meio- and macrofauna was disturbed: biomass was removed as it was covered with lava. In late 2006 predominantly new *Tevnia* tubeworms were established at these sites. Tubeworm communities were visually dominated by *Tevnia* tubeworms, but *Riftia* and *Oasisia* were also present in small numbers (Schimak et al., 2012). Data on active vent communities are published elsewhere (Gollner et al., 2015b). We observed high temporal variation in vent fluid emissions within these active sites during the studied period. Settlement substrates that had been deployed at Sketchy within the Ty-Io area were exposed to no vent activity in 2007 and 2009. The Sketchy patch became a small senescent vent (with dead *Tevnia* tubes and no temperature anomalies) although the Ty-Io area overall remained active. Similarly, our studied tubeworm patch at P Vent was found to be senescent in 2009, although the site in general remained hydrothermally active. Data on senescent vent patches from Sketchy and P Vent are shown in this manuscript. We also observed similar patch dynamics—tubeworm patches locally become senescent within an active vent site—at the Tica Vent site (Klose et al., 2015).

Faunal Communities at Senescent Vents

At senescent vents, we encountered on average 1145 animals per settlement device (64 cm^{-2}), with 968 meiofauna and 178 macrofauna individuals. Abundances were variable and ranged from 38 to 8020 individuals. The highest animal abundances were observed at the 4 yearlong hydrothermal inactive East Wall site, the lowest abundances at 2 yearlong hydrothermal inactive Sketchy site (**Table 1**). The mean abundances per settlement device at senescent communities at East Wall and Q Vent, which were active for > 12 years before venting waned, were 2330 ± 2995. Mean abundances at senescent Sketchy and P Vent, which had been active for < 3 years, were 223 ± 162. All encountered abundances at senescent vents were similar to active vents (all p = ns). Active vents had a mean abundance of 869 animals per settlement device (64 cm^{-2}), with 258 meiofauna and 610 macrofauna individuals (data from Gollner et al., 2015b). The mean relative abundance of meiofauna juveniles was high at senescent vents (42%) and was higher, but not significantly compared to active vents (23%) (p = ns). The mean relative abundance of macrofauna individuals < 1 mm was very high with mean 78% at senescent vents, and was lower, although also not significantly (p = ns) at active vent sites (mean 30%).

In our entire sample collections within the Axial Summit Trough (AST) (including vent and basalt samples with ∼175,000 individuals from pre-eruption and ∼217,000 individuals from post eruption; this study and data from Gollner et al., 2010, 2015a), we detected a total of 189 species, including 76 macrofaunal species (13 singletons) and 113 meiofaunal species (42 singletons). Senescent vents contributed significantly to these numbers with ∼100,000 counted individuals, containing 55 macrofaunal species (11 singletons) and 74 meiofaunal species (19 singletons). Of these 129 species, 60 are not reported from active vents.

The macrofaunal singletons, species that were only encountered with one specimen in our sample collections, at senescent vents were mostly unidentified polychaetes, amphipods, hydrozoans, isopods, gastropods, ophiorids and include potentially new species such as for example *Archinome* sp. nov. 1. Dominant macrofaunal species at senescent vents were *Ophyrotrocha akessoni*, *Lepetodrilus elevatus*, *Ventiella sulfuris*, *Prionospio sandersi*, *Lepetodrilus tevnianus*, *Amphisamytha galapagensis*, *Hesospina vestimentifera*, and *Archinome rosacea*. All these species occur also in high abundances at active vents.

The meiofaunal singletons at senescent vents were mostly unidentified nematodes, copepods, and foraminifera species. From the 19 singletons, 16 were distinguished within our own sample collections as distinct species but were not further studied, and three could be classified as known or new species: the copepod *Mesocletodes elmari*, the copepod *Ferregastes* sp. nov.1, and the nematode *Halomonhystera* sp. nov. 2. The species *Thalassomonhystera* sp. nov. 11 occurred four times and was only detected at the senescent East Wall site. The kinorhynch *Desmodasys abyssalis* was known from the active Tica Vent pre-eruption and occurred in high abundances (total > 100 individuals) at the senescent East Wall site. Most dominant meiofauna at senescent vents were the foraminifera *Abyssotherma pacifica*, the harpacticoid copepods *Amphiascus* aff. *varians*, *Ameira* sp. nov. 1, and *Tisbe* sp. nov.1, the nematodes *Neochromadora* aff. *poecilosoma* and *Thalassomonhystera fisheri* and the ostracod *Xylocythere vanharteni*. All the dominant species from senescent vents also occur at active vents (in varying abundances). The active vent dominating dirivultid copepods (e.g., *Aphotopontius acanthinus*) occurred only in low abundances at senescent vents.

All ANOSIM results from senescent vent samples (considering distinct time and sites) were not significant due to low number of permutations and due to high sample variability. ANOSIM results based on groupings per year while neglecting a possible effect of different sites showed a significant change in meiofaunal community at senescent vents in all years (2006–2007: R = 0.549 with p = 0.036; 2007–2009: R = 0.353 with p = 0.026) and a significant change in the marcofauna community only from 2006 to 2007 (2006–2007: R = 0.959 with p = 0.018; 2007–2009: R = 0.137 with p = ns). SIMPER revealed that similarity at senescent vents was ranging from 63 to 75% in distinct years (**Table 2**). Species contributing most to similarity in 2006 and 2007 were the copepod *Amphiascus* aff. *varians* and the polychaete *O. akessoni* and in 2009, the copepod *Ameira* sp. 1. and the foraminifera *A. pacifica*.

Faunal Communities Not Covered by Lava After the Eruption in 2006

The sites that were not covered by lava in early 2006 (old active Bio9 Vent, senescent Q Vent, senescent East Wall, and the neighboring old basalt) harbored between 26 and 315 individuals per 64 cm^2 in late 2006. In total 46 species were found in these samples; 13 of these 46 species were not detected at new vent sites or new basalt (**Table 3**, species in bold); 33 of the 46 species occurred at old and newly formed vent sites and basalt, and most of them were detected in typically high abundances in late 2006 (**Table 3**, active vent data from Gollner et al., 2015a,b). Several species that were detected in these 2006 samples were not detected in samples from pre-eruption. These included rare species like the copepod *M. elmari*, but also abundant species like the limpet *L. tevnianus* or the copepod *Tisbe* sp. nov.1.

Bubble plots in the nMDS visualize that animals occur in different abundances at distinct sites in 2006 (**Figure 3**). The vent endemic dirivultid copepod *A. acanthinus* was highly abundant at old active Bio9 Vent. The meiofauna species *X. vanharteni* (ostracod) and *T. fisheri* (nematode) occurred predominantly at senescent vent sites and old basalt. The harpacticoid copepod *Amphiascus* aff. *varians* was present at old and new sites. Vent endemic macrofauna species like the limpet *L. tevnianus* and the amphipod *V. sulfuris* occurred in high abundance at new vent sites.

In 2006, similarity at the senescent vents and on old and new basalt was low and ranged from 36 to 63% with the meiofaunal species *Tisbe* sp. nov. 1 contributing most to similarity. Similarity within new active vents ranged from 54 to 70% with macrofaunal species *V. sulfuris* and *L. tevnianus* contributing most to similarity (**Table 2**) (Gollner et al., 2015b). ANOSIM results were not significant (p > 0.1) allowing no interpretation of R values which ranged from 1 (highly different) to 0 (similar). The nMDS

plot (**Figure 3**) shows loose grouping of senescent East Wall, senescent Q Vent, and old basalt, as well as grouping of the new active vents Tica Vent, Sketchy, and new basalt in 2006. Communities from P Vent, and Bio9 Vent which both were exposed to the most extreme temperature and chemical regime of vent fluid emissions also formed own groups.

Meio- and Macrofaunal Trends in Community Succession

Considering all 67 samples from senescent vents, active vents, and basalt from pre-eruption (2001–2004) and from post eruption (2006, 2007, 2009) two large-scale trends emerge when looking at meio- and macrofaunal community patterns related to time and productivity regimes (**Figure 4**). The overlays shown in the nMDS plot point to a change in meiofaunal communities over time (**Figure 4C**) and ANOSIM proofed that meiofaunal communities were typically significantly dissimilar in different years (R = 0.42–0.631; **Table 4**). In contrast, there was no grouping according to habitat for the meiofauna (active vent, senescent vent, basalt; **Figure 4A**) and ANOSIM revealed that meiofaunal communities from active and senescent vents and basalt are all similar to each other although this was not significant (R = 0.019–0.142; p = 0.083–0.39; **Table 4**). The macrofaunal communities are grouped according to productivity (active vent versus basalt and senescent vent; **Figure 4B**) and ANOSIM for macrofaunal communities showed slightly higher R values (more dissimilar) for the factor of habitat (active vent, senescent vent, basalt) and little lower R values (more similar) for the factor time (**Table 4**). The time overlay in the nMDS plots for macrofauna (**Figure 4D**) does not show a clear trend of change of macrofaunal communities over years. ANOSIM R values were always higher (thus more dissimilar) for the meiofauna than for the macrofauna when considering the influence of years, while R values were always higher for the macrofauna than for the meiofauna when considering habitat.

DISCUSSION

Senescent Vents — A Species Rich Ecotone

Senescent vents at the 9°N EPR harbor at least 55 macrofaunal species and 74 meiofaunal species, supporting the idea that ecotones act as taxonomic diversity

TABLE 2 | SIMPER similarity and dissimilarity including three species that contributed most to (dis)similarity from Q Vent, East Wall, Bio9 Vent, and surrounding old basalt, as well as from senescent patches at Sketchy and P Vent.

2006	**Similarity**			
East Wall_15 + 1 (senescent)	63%	*Amphiascus* aff. *varians* (19%)	*Tisbe* sp. nov. 1 (16%)	*Thalassomonhystera fisheri* (7%)
Basalt_15 + 1 (old basalt)	52%	*Tisbe* sp. nov. 1 (26%)	*Ophryotrocha akessoni* (9%)	*Thalassomonhystera fisheri* (7%)
Basalt_0 + 1 (new basalt)	36%	*Ophryotrocha akessoni* (20%)	*Lepetodrilus elevatus* (14%)	*Tisbe* sp. nov. 1 (12%)
Sketchy_0 + 1 (active)	70%	*Ventiella sulfuris* (31%)	*Lepetodrilus tevnianus* (25%)	*Lepetodrilus elevatus* (20%)
P Vent_0 + 1 (active)	54%	*Paralvinella pandorae* (22%)	*Aphotopontius acanthinus* (22%)	*Benthoxynus tumidiseta* (20%)
Tica Vent_0 + 1 (active)	66%	*Ventiella sulfuris* (52%)	*Lepetodrilus tevnianus* (19%)	
2007	**Similarity**			
Sketchy_0 + 2 (senescent)	76%	*Amphiascus* aff. varians (24%)	*Ophryotrocha akessoni* (19%)	*Thomontocypris brightae* (10%)
East Wall_15 + 2 (senescent)	72%	*Ophryotrocha akessoni* (21%)	*Amphiascus* aff. *varians* (11%)	Neochromadora aff. poecilosoma (9%)
2009	**Similarity**			
East Wall_15 + 4 (senescent)	66%	*Ameira* sp. nov. 1 (16%)	*Neochromadora* aff. *poecilosoma* (13%)	*Abyssotherma pacifica* (12%)
Sketchy_0 + 4 (senescent)	68%	*Abyssotherma pacifica* (30%)	Foraminifera sp. 4 (18%)	*Ameira* sp. nov. 1 (12%)
P Vent_0 + 4 (senescent)	62%	*Ventiella sulfuris* (25%)	*Ophryotrocha akessoni* (15%)	*Lepetodrilus elevatus* (15%)
Senescent vents	**Dissimilarity**			
Q Vent_12 + 1 and East Wall_15 + 1	48%	*Tisbe* sp. nov. 1 (12%)	*Stygiopontius hispidulus* (8%)	*Amphiascus* aff. *varians* (7%)
Sketchy_0 + 2 and East Wall_15 + 2	53%	*Neochromadora* aff. *poecilosoma* (10%)	Amphiascus sp. 1 (aff. varians) (9%)	*Thomontocypris brightae* (7%)
Sketchy_0 + 4 and East Wall_15 + 4	68%	Foraminifera sp. 4 (9%)	Neochromadora aff. poecilosoma (8%)	*Linhomeus caudipapillosus* (7%)
P Vent_0 + 4 and East Wall_15 + 4	72%	*Ventiella sulfuris* (11%)	*Lepetodrilus elevatus* (7%)	*Abyssotherma pacifica* (7%)
Sketchy_0 + 4 and P Vent_0 + 4	80%	*Abyssotherma pacifica* (12%)	*Ventiella sulfuris* (12%)	Foraminifera sp. 4 (9%)
Sketchy_0 + 2 and Sketchy_0 + 4	79%	*Abyssotherma pacifica* (13%)	*Ophyrotrocha akessoni* (11%)	*Amphiascus* aff. *varians* (10%)
East Wall_15 + 1 and East Wall_15 + 2	62%	*Tisbe* sp. nov. 1 (7%)	*Ophyrotrocha akessoni* (6%)	*Bathylaophonte pacifica* (4%)
East Wall_15 + 2 and East Wall_15 + 4	54%	*Ohpyrotrocha akessoni* (7%)	*Abyssothera pacifica* (5%)	*Linhomeus caudipapillosus* (4%)
East Wall_15 + 1 and East Wall_15 + 4	78%	*Tisbe* sp. nov.1 (7%)	*Amphiascus* aff. *varians* (6%)	*Ameira* sp. nov. 1 (5%)

hotspots (Kark and van Rensburg, 2006). At the senescent vents, we find a biodiversity rich community of typical active vent fauna, and of species that are known from the background. This is in accordance to earlier observations by Tsurumi and Tunnicliffe (2003) who studied fauna from five senescent vent samples at Juan de Fuca Ridge. They detected 49 species of which 20 were

TABLE 3 | Species presence at sites that were not paved by lava during the eruption in 2005/06.

Species	Size class	Taxon	Bio 9 Vent	Q Vent	East Wall	Old basalt	New sites	Pre-eruption
Stygiopontius hispidulus	Meio	Copepoda	x		x	x	x	x
Aphotopontius acanthinus	Meio	Copepoda	x		x	x	x	x
Thomontocypris gollnerae	Meio	Ostracoda		x	x	x	x	x
Xylocythere vanharteni	Meio	Ostracoda		x		x	x	x
Halomonhystera hickeyi	Meio	Nematoda		x	x	x	x	x
Thalassomonhystera fisheri	Meio	Nematoda		x	x	x	x	x
Amphiascus aff. *varians*	Meio	Copepoda		x	x	x	x	x
Ecbathyrion prolixicauda	Meio	Copepoda		x	x	x		x
Ameira sp. nov. 1	Meio	Copepoda		x	x		x	x
Thomontocypris brightae	Meio	Ostracoda			x	x	x	x
Neochromadora aff.poecilosoma	Meio	Nematoda			x		x	x
***Linhomeus* sp. 1**	Meio	Nematoda			x			x
Aphotopontius mammilatus	Meio	Copepoda			x		x	x
Benthoxynus tumidiseta	Meio	Copepoda			x		x	x
Halectinisoma sp. 1	Meio	Copepoda			x		x	x
Scotoecetes introrsus	Meio	Copepoda			x		x	x
Xylora bathyalis	Meio	Copepoda			x			x
Aphotopontius limatulus	Meio	Copepoda				x	x	x
Ventiella sulfuris	Macro	Amphipoda	x		x	x	x	x
Lepetodrilus elevatus	Macro	Gastropoda	x	x		x	x	x
Hesiospina vestimentifera	Macro	Polychaeta	x	x	x	x	x	x
Paralvinella grasslei	Macro	Polychaeta	x					x
Paralvinella pandorae	Macro	Polychaeta	x				x	x
Ophryotrocha akessoni	Macro	Polychaeta		x	x	x	x	x
Clypeosectus delectus	Macro	Gastropoda			x	x	x	x
Gorgoleptis spiralis	Macro	Gastropoda			x		x	x
Lepidonotopodium williamsae	Macro	Polychaeta			x		x	x
Halice hesmonectes juv	Macro	Polychaeta			x			x
Phymorrhyncus major juv	Macro	Gastropoda			x			x
Lepetodrilus pustolosus	Macro	Gastropoda				x	x	x
Amphisamyta galapagenis	Macro	Polychaeta				x	x	x
Lepidonotpodium fimbriatum	Macro	Polychaeta				x		x
Prionospio sandersi	Macro	Polychaeta				x	x	x
Cheramyzon abyssale	Meio	Copepoda		x	x	x	x	
Barathricola rimensis	Meio	Copepoda		x	x	x		
Tisbe sp. 1	Meio	Copepoda		x	x	x	x	
Tisbe sp. 2	Meio	Copepoda		x			x	
***Copidognathus* sp. 1**	Meio	Acari			x			
Mesocletodes elmari	Meio	Copepoda			x			
Mesochra sp. nov. 1	Meio	Copepoda				x	x	
Lepetodrilus tevnianus	Macro	Gastropoda		x	x		x	
Aplacophora sp. 1	Macro	Gastropoda		x		x	x	
Platyhelminthes sp. 1	Macro	Platyhelminthes		x	x			
Orbinid sp. nov. juv	Macro	Polychaeta			x		x	
Tanaidacea	Macro	Tanaidacea				x		
Sipunculid?	Macro	Sipunculdia				x		
Total			7	17	32	26	33	33

Samples are from Bio9 Vent, Q Vent, East Wall, and old basalt next to these sites from 2006. On top, presence of these species at new active vent sites and new basalt after eruption in 2006 (new sites) is indicated, as well as occurrence of these species in our pre-eruption samples (Gollner et al., 2015a). Species in bold were present at Bio9 Vent, Q Vent, and East Wall in 2006 but not at newly formed vent or basalt in 2006. Meio = meiofauna. Macro = macrofauna. Juv = juvenile.

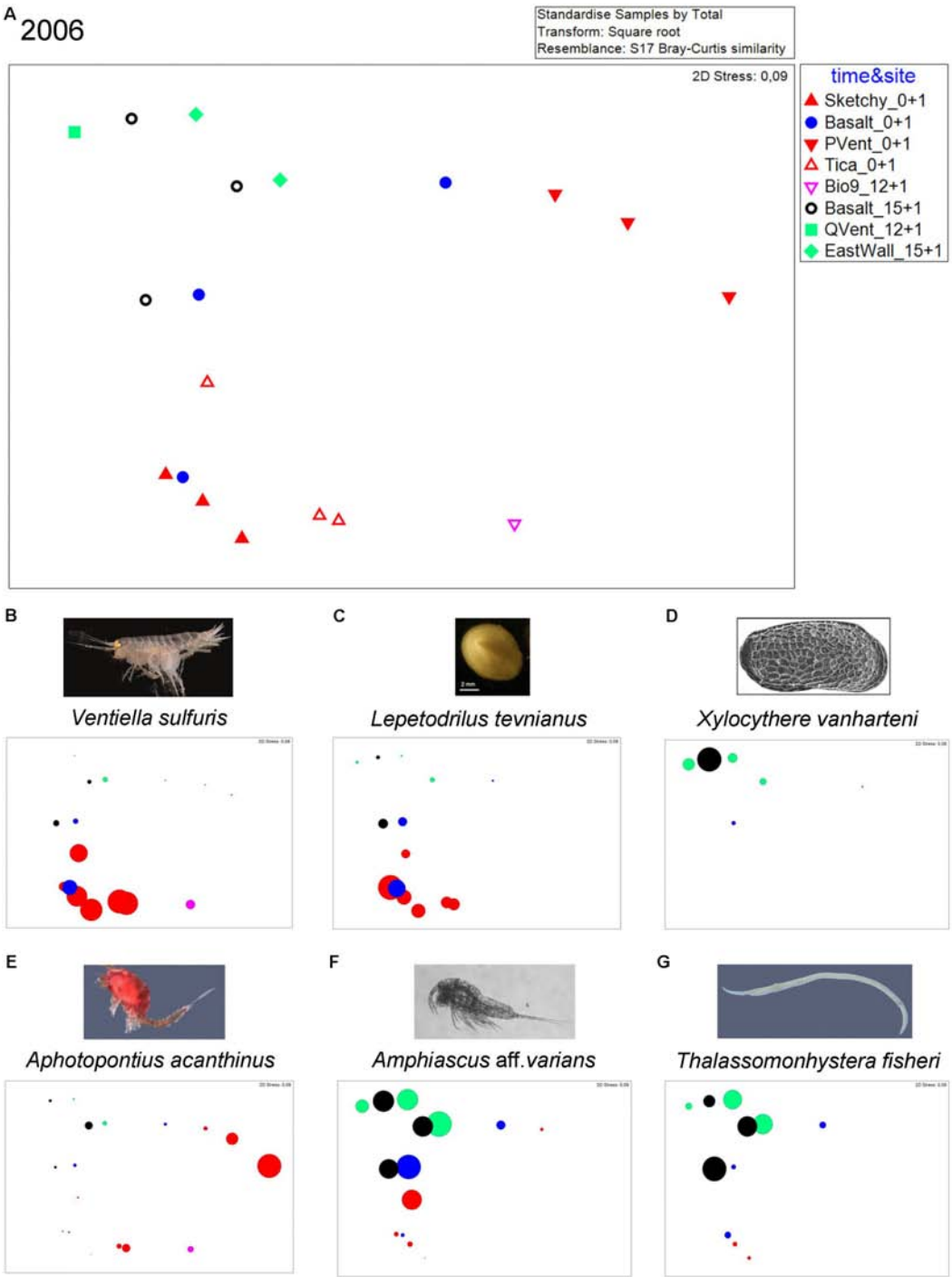

FIGURE 3 | (A) nMDS plot for samples from sites collected in the year 2006: old active Bio9 Vent (pink) that was not directly affected by the volcanic eruption, senescent East Wall and Q Vent (green), old basalt that was not covered by lava (black), new basalt (blue), newly active vent sites Tica Vent, Sketchy and P Vent (red). **(B–G)** Bubble plots showing relative abundance of species at the different sites. **(B)** Amphipod *Ventiella sulfuris* (photograph © Bright), **(C)** limpet *Lepetodrilus tevnianus* [image of limpet *L. tevnianus* reprinted by permission from Springer Nature, Marine Biology, Bayer et al. (2011)], **(D)** ostracod *Xylocythere vanharteni* [image provided by Rosalie F. Maddocks (Maddocks, 2005], **(E)** dirivultid copepod *Aphotopontius acanthinus* (image *Aphotopontius* sp. © Bright), **(F)** harpacticoid copepod *Amphiascus* aff. *varians* (image *Amphiascus* sp. © Gollner), and **(G)** nematode *Thalassomonhystera fisheri* (image *Thalassomonhystera* sp. © Bright). Numbers after site names indicate age of communities: Sketchy 0+1: "0" indicates no animal community from prior eruption because Sketchy was covered by lava; "+ 1" indicates that the sampling occurred 1 year after the eruption and that the community was ∼1 year old; East Wall 15+ 1: "15" indicates that the community from prior eruption that was not paved by lava and was ∼15 years old in 2005; "+ 1" indicates that the sampling occurred 1 year after the eruption. Total age the East Wall community was ∼16 years at the time of sampling in 2006.

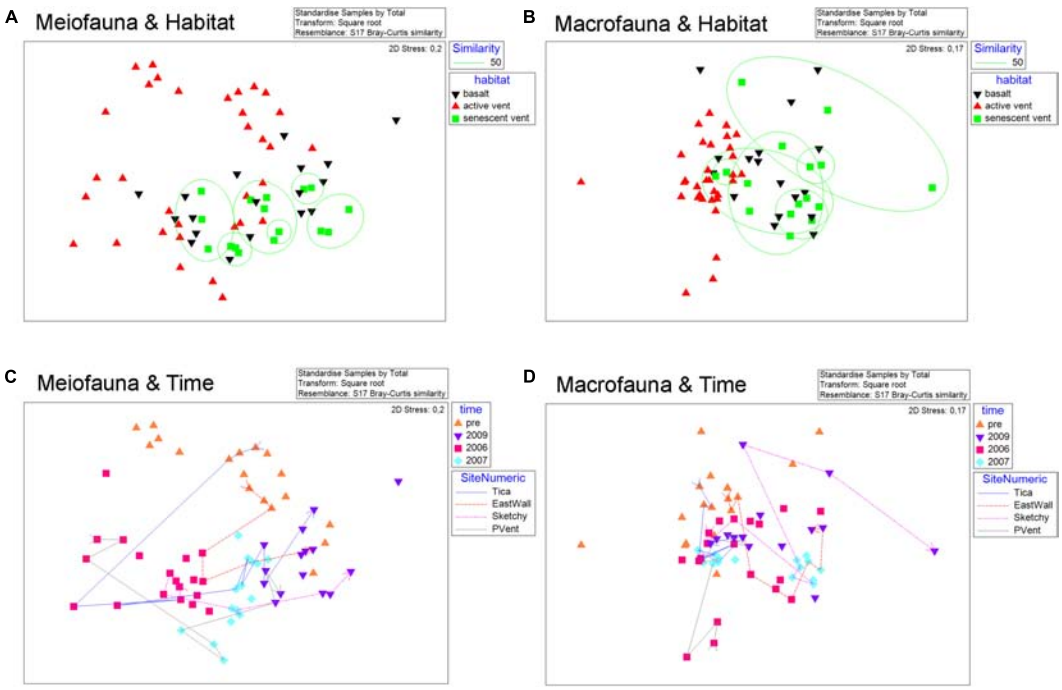

FIGURE 4 | nMDS plots for meiofauna (left) and macrofauna (right) of all active vent, senescent vent, and basalt samples pre- and post eruption analyzed in this study and by Gollner et al. (2015a; 2015b). **(A,B)** Meiofauna and macrofauna nMDS with color codes according to habitat (active vent, senescent vent, basalt). Overlay for similarity percent (50%) shows no grouping of sites according to habitat for the meiofauna **(A)** but for the macrofauna **(B)**. **(C,D)** Meiofauna and macrofauna nMDS with color codes according to years (pre-eruption, 2006, 2007, 2009). Overlay for numeric sites indicates position change (and thus similarity) of distinct sites over years for East Wall, Tica Vent, Sketchy, and P Vent. The meiofauna communities change their position on the MDS rather uniformly from top/left against to clock to the right side of the nMDS, according to year of collection **(C)**. For the macrofauna communities, no such uniform change of similarities over time can be seen **(D)**.

non-vent species (Tsurumi and Tunnicliffe, 2003), while at the 9°N EPR, we report 129 species of which 60 were non-vent. From these two studies, one may conclude that about half of species at senescent vents are associated with vent environments and the other half from non-vent environments. Similar, Van Dover (2002) observed a mix of vent and non-vent fauna at a senescent mussel bed. These authors attributed this observation to the decrease in the levels of toxic sulfide that may allow non-vent taxa to invade the senescent vent (Van Dover, 2002). Whether these non-vent fauna are background fauna or fauna restricted to senescent vents cannot be judged currently due to paucity of data from both environments. For example, one non-vent species that was detected in our study at senescent East Wall but never at active vents is the copepod *M. elmari*, a species with broad abyssal distribution (Menzel, 2011). However, most non-vent species at mid-ocean ridges are new to science and are not yet described.

At our current stage of knowledge, it remains difficult to compare senescent vents, where communities can rely on megafauna biomass previously produced by *in situ* chemosynthetic primary production, to old inactive vents. Old inactive vents, or hydrothermal sulfide deposits, can be tens of thousands years old and could also produce bacterial biomass by local chemosynthetic activity (Le Bris et al., 2019). To our knowledge, studies at older inactive vents considered only visually observed megafauna. Old inactive chimneys typically host sessile taxa such as sponges, cnidarians including corals, and echinoderms (Tunnicliffe et al., 1986; Galkin, 1997). At Manus Basin, inactive chimneys were characterized by *Vulcanolepas cf. parensis*, *Munidopsis* spp., hydroids, *Abyssocladia dominalba*, and *Keratoisis* sp. (Erickson et al., 2009). Boschen et al. (2015) found that megafaunal assemblages on inactive, sulfide-rich chimneys may be distinctive to those found on chimneys of active vents and to hard substrates on seamounts with no current or past hydrothermal activity. To our knowledge, meio- and macrofauna associated with these old inactive vent megafauna has to date not been investigated and thus we cannot compare data to senescent vents.

Senescent Vents May Provide Food for an Abundant Small Sized Fauna

Dead megafauna at senescent vents at the 9°N EPR likely provide nutrition for an abundant meio- and macrofauna consumer community. Even in the small (less than a few square meter sized) patches of decaying tubeworm tubes at East Wall, up to more than 6000 mostly meiofaunal individuals could be found on an area of 64 cm^2 (size of colonization substrates that have been investigated in this study). In theory, up to one million small sized animals could thus live in 1 square meter of decaying vent megafauna. Interestingly, the highest meiofauna abundances were encountered in the oldest, namely, 4 yearlong hydrothermally inactive, senescent vent, where visually no remaining tubeworm tube could be observed, but instead fluffy

TABLE 4 | ANOSIM *R* and *p* values in% for meio- and macrofauna communities.

	Meiofauna		Macrofauna	
	R	***p* [%]**	***R***	***p* [%]**
Factor of time				
Pre, 2006	0.631	0.1	0.369	0.1
Pre, 2007	0.53	0.1	0.343	0.2
Pre, 2009	0.199	6.3	0.037	29.9
2006, 2007	0.413	0.1	0.275	1
2006, 2009	0.8	0.1	0.007	36.6
2007, 2009	0.42	0.1	0.297	1.5
Factor of habitat				
Active, basalt	0.107	8.3	0.414	0.3
Active, senescent	0.142	8.4	0.321	1.4
Basalt, senescent	0.019	39	−0.097	80.1

Data include all samples analyzed by Gollner et al. (2015a; vent and basalt samples from pre-eruption) and Gollner et al. (2015b; new vent and new basalt samples after the eruption in 2006) as well as samples from sites that where not paved by the eruption (this study: senescent Q Vent, senescent East Wall, active Bio9 Vent, old basalt) and from newly senescent vent patches after the eruption (this study: Sketchy 2007, Sketchy 2009, P Vent 2009). To view large-scale trends of faunal community similarities, samples were grouped according to year of sampling (pre-eruption, 2006, 2007, 2009; regardless of productivity regime) and according to habitat (active vent, senescent vent, basalt; regardless of time). Fauna is separated into meio- and macrofauna.

organic matter was present (see **Figure 2**, East Wall site in 2009). Potentially this old more highly degraded material may be used more efficiently by the meiofauna than the younger less degraded tubes. In coastal areas, meiofauna abundance and diversity is known to be influenced by food quality and quantity (van der Heijden et al., 2018). We have not quantified or qualified the nutritional link from the old dead megafauna to the living animals by isotopes but the observed high meiofaunal abundances point out that such a link may be likely.

Other potential pathways of energy transfer include horizontal advection of particulate organic material derived from vents to peripheral areas (Levin et al., 2016) and may have also contributed to the high meiofauna abundances found at senescent vents at the 9°N EPR. Erickson et al. (2009) showed that for example, bamboo corals and other non-vent organisms from old inactive vents at Manus Basin had sulfur isotopic compositions that are consistent with a diet of particulate organic material derived from microbial chemoautotrophy (Erickson et al., 2009). Also anemones and serpulid worms in close vicinity to vents feed on chemoautotrophically derived particulate organic matter (Hessler et al., 1988; Levin et al., 2016). The distance of the nearest active vent site to senescent East Wall was 250 m. We cannot tell with our analyses if horizontal advection plays an important role but it is likely to be significant within the axial valley were bottom currents can be strong and particle export known to be significant (Adams et al., 2011; Thurnherr et al., 2011).

Release of gametes and larvae is a yet unquantified source of export of particulate carbon from chemosynthetic ecosystems, given the high fecundity of many vent taxa with dispersive larval stages (Tyler and Young, 1999; Adams et al., 2011; Levin et al., 2016). Continuous and high presence of vent macrofauna < 1 mm in body size at the studied senescent vents shows that larvae of vent macrofauna can settle and/or grow at senescent vents in high numbers. The low proportion of macrofauna > 1 mm is extraordinary and shows that it is currently not clear if and to what extant/how long typical vent macrofauna can reproduce at senescent vents. There are three potential scenarios: (1) The macrofauna at senescent vents can reproduce and offspring may settle at the same site. (2) There is continuous and abundant transfer of gametes and larvae originating from active vents toward the senescent vents. These larvae can settle and grow only to a limited size/biomass before they die. (3) The senescent vents may act as a nursery area and larger mobile individuals eventually migrate to food-richer areas (active vents) at a late juvenile/young adult age.

Body size related food demands could cause demographic pattern biased toward small sized vent macrofauna at senescent vents, similar to what was suggested for basalt in the periphery of active vents (Gollner et al., 2015a). The specialized vent macrofauna could be food limited at senescent vents and on basalt and must migrate into the active vent environment to develop into adults and reproduce. Meiofaunal species at senescent vents do not have such a strong bias toward juveniles. All live stages including juveniles, and adult females carrying eggs and males carrying spermatophores have been detected. Where the particulate carbon of juvenile macrofauna from senescent vents is used/ending up is currently unclear. Macrofauna may leave senescent vents in the search for more food at active vent sites or may die and become food for meiofauna.

While small macrofauna individuals (< 1 mm) were common at senescent vents, hardly any small juvenile symbiotic megafauna recruits have been detected at senescent vents. Symbiotic megafauna may have very different settlement cues compared to non-symbiotic macro- and meiofauna. Instead of food they mostly rely on hydrothermal fluid emissions for their symbionts (Van Dover, 2000). In total we detected only 10 individuals of *Bathymodiolus* mussels and tubeworms < 1 mm in all of our senescent samples. This in stark contrast to the thousands of small vent macrofauna individuals (for example, limpets *Lepetodrilus*). The almost absence of symbiotic megafauna larvae recruits is in accordance with the finding of Van Dover (2002) who observed lack of post-juvenile mussels at the senescent Animal Farm site at the EPR. These findings may point to different settlement cues of symbiotic and non-symbiotic fauna. We speculate that symbiotic fauna may use, for example, chemical cues, while macro- and meiofauna may settle more randomly or use other/additional cues.

Recovery After Disturbance: Local Remnants and Regional Dispersal Networks

Natural disturbances are rarely absolute and not all individuals die. More often, some individuals survive within or near a disturbed area and influence recolonization (Platt and Connell, 2003). This type of historical influence occurs in a variety of terrestrial and marine habitats. Our study has shown that

even though the spatial scale of areas not covered by lava was small (several m^2 compared to several km^2 lava paved area), the importance of remnant fauna in these areas for community recovery cannot be underestimated. The active vent Bio9 Vent and the two senescent vents East Wall and Q Vent were not paved by lava at the 9°N EPR and harbored at least 33 species in 2006 that potentially may have directly colonized the close by emerging vent sites, where the same species were detected. Larval supply and migrants after the volcanic eruption thus very likely came from local as well as regional sources (**Figure 5**).

The distinct relative abundances of species in our 2006 samples at active and senescent vents (**Figure 3**) let us speculate that animals may have very different strategies to recover from disturbance. Animals living at hydrothermal vents are characterized by very different life traits such as mode of dispersal or nutritional needs (Gollner et al., 2015a). The absence of the limpet *L. tevnianus* and *C. porifera* before the eruption at 9°N EPR and their high abundance at the new vent sites showed that larvae from afar can colonize vents after a volcanic eruption (Mullineaux et al., 2010). Adult limpets have limited mobility and are known to produce high numbers of lecithotrophic larvae that are abundant in the water column above vents (Mullineaux et al., 2005, 2010). The finding of these species at senescent vents in 2006 shows that vent macrofaunal species can settle in any habitat, although in different abundances and/or with different survival rates. Another successful early colonizer was the amphipod *V. sulfuris*. In contrast to the semi-sessile limpets, this species can swim at a speed of ∼5–10 cm^{-1} and is a brooder with lecithotrophic larvae and has moderate gene flow (France et al., 1992; Kaartvedt et al., 1994; Vrijenhoek, 2010). *Ventiella* may have swum from Bio9 Vent toward the new vent sites. Dirivultid copepods, like *A. acanthinus* or *Stygiopontius hispidulus* were abundant at new vents. Dirivultids are crawlers and have rather limited swimming capabilities (Heptner and Ivanenko, 2002). Dirivultid adults occur rarely in the water column, but their juvenile copepodite stages are the most abundant specimens among all vent animals encountered in pelagic pump samples with ∼50 ind. per 1000 L at 3 m above vents (Gollner et al., 2015b). Their presence at the sites not covered by lava and their high dispersal abilities may have allowed them to very quickly invade the new vent sites. In contrast to the dirivultid copepods, harpacticoid copepods have more eggs but their copepodites are much less abundant (< 1% relative abundance) in the waters above vents (Gollner et al., 2015b). However, their high abundance at senescent East Wall and Q Vent as well as on old basalt may have helped the harpacticoids to colonize the new vent sites relatively quickly. On top, the leg morphology trait of the most successful harpacticoids, having a prehensile P1 endopod and seven to eight setae on terminal segments of podia (Bell et al., 1987; Thistle and Sedlacek, 2004), show enhanced migration potential for these species. Nematode abundance and richness were extremely low at all studied active sites in late 2006 and increased only slightly by 2009, although nematodes were present at senescent East Wall, Q Vent, and old basalt (Gollner et al., 2013). The limited dispersal abilities of nematodes, including lack of larvae, extremely rare occurrence of adults in the water column above vents, and limited adult mobility might have delayed their establishment at new active vents and new basalt.

To conclude, species at vents may have developed different strategies to cope with extreme disturbance events and patchy distribution of productivity rich but environmentally challenging vent environments (**Figure 5**). Strategies may include: (1) new vent colonizers arrive as larvae from a regional pool. Such species may be characterized by long-distance dispersal capabilities, as seen for typical vent mega- and macrofauna species as well as dirivultid copepods; (2) remnant vent fauna arrive via migration or larval dispersal from local vents not paved by lava; and (3) remnant fauna with or without larvae migrate from local senescent vents toward new active vents. Many generalist meiofauna species including harpacticoid copepods or nematodes may use this strategy as they have limited larval dispersal.

Meio- and Macrofaunal Trends in Community Succession at the 9°N EPR

Primary succession—the non-seasonal, directional continuous pattern of colonization and extinction (Begon et al., 1990)—is typically initiated by formation of new habitat, such as from lava flow caused by a volcanic eruption. The post-disturbance landscape at the 9°N EPR consists of mosaics of patches, including old and new active vents, senescent vents, and old and new basalt. Metapopulations at vents are shaped by different processes and different scales, including disturbance, local controls (influence of habitat and biological interactions), and regional controls (larval exchange, connectivity) (Mullineaux et al., 2018).

Regional controls, i.e., larval dispersal and supply, have strong influence on the primary succession, because they determine which species are able to arrive first and eventually become established. The arrival of the gastropod pioneer colonists *Ctenopelta porifera*, an immigrant from possibly more than 300 km away, and *L. tevnianus*, a species that occurred in low abundance prior eruption, demonstrated that larval supply can change markedly after removal of local source populations at the 9°N EPR (Mullineaux et al., 2009). However, we did not detect a clear directional continuous pattern of colonization for the macrofauna during our study period (see **Figure 4D**), which may be linked to the fact that larval supply of some species may be continuous while others arrive only episodically (Adams and Mullineaux, 2008; Mullineaux et al., 2012; Mills et al., 2013). In contrast, meiofaunal succession was very likely shaped by dispersal potential of species, with rapid recovery of dispersive copepods and slow recovery of nematodes which lack pelagic dispersal stages (Gollner et al., 2013, 2015b). In this study, we could further show that larval supply after a volcanic eruption is not restricted to regional controls, but local remnant fauna may be crucial for colonization (see section "Recovery After Disturbance: Local Remnants and Regional Dispersal Networks").

Local environmental conditions at active vents can be extreme, and distribution and zonation of mega-, macro-, and meiofauna are shaped by vent fluid conditions. At the 9°N

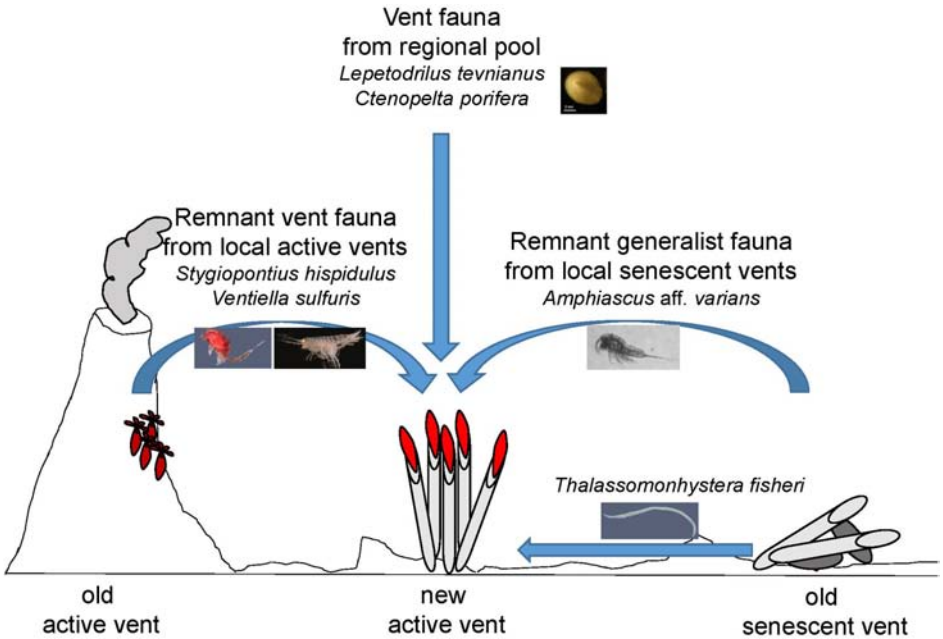

FIGURE 5 | Concept of meio- and macrofauna colonization at new active vent sites after the volcanic eruption from local as well as from regional pool at the 9°N EPR. Vent megafauna like sessile *Tevnia* and semi-sessile macrofauna like the limpets *Lepetodrilus tevnianus* and *Ctenopelta porifera* must have arrived as larvae from a regional pool since these species were not present in the area pre-eruption. Mobile macrofauna like the vent amphipod *Ventiella sulfuris* and vent specialized dirivultid copepods like *Stygiopontius hispidulus* were present at the local active Bio9 Vent smoker that was not covered by lava during the eruption. These remnants may have migrated either as larvae and/or free-swimming as adults from this old local active vent source to the new active vent sites. Generalist fauna like harpacticoid copepods such as *Amphiascus aff. varians* (having nauplii) and like nematodes such as *Thalassomonhystera fisheri* (lacking larval dispersal stages) were abundant at the senescent vents not covered by lava. The remnant meiofauna may have populated the new vents sites via crawling or swimming/drifting from the local senescent vents and old basalt areas. Many meiofauna species are generalists and can live on basalt, at senescent vents and at active vents. Typical vent macrofauna species are also found on basalt and at senescent vents, but often remain small (and unfertile?) in body size.

EPR, with increasing temperature and toxic hydrogen sulfide concentrations and increasing amplitude of variation of these factors, fewer species are able to cope with these extreme conditions, resulting in typically less diverse communities in more extreme habitats (Galkin and Goroslavskaya, 2008; Gollner et al., 2010, 2015a). Changes in community composition after major disturbance coincide with changes in vent flow conditions, as at the 9°N EPR hydrothermal fluid emissions typically wane within a few years after an eruption (Shank et al., 1998; Le Bris et al., 2006) and species diversity tends to increase (Mullineaux et al., 2012; Gollner et al., 2015b). Manipulative colonization experiments at the 9°N EPR showed that successional mechanism of macrofauna varies along a gradient in hydrothermal fluid flux. Inhibition of later colonists by early mobile colonizers was found to be predominant in tubeworms areas with relatively higher vent fluid flux. Facilitation of later colonists by early sessile colonists played an important role in the suspension feeder zone with relatively lower vent fluid flux (Mullineaux et al., 2003). Biological controls are yet unknown from senescent vents and basalt. Facilitation and inhibition for the meiofauna remains to be determined at active and senescent vents as well as on basalt, but in general, it can be expected that mega- and macrofauna do structure meiofaunal communities (and the other way round) (Ólafsson, 2003).

Local environmental conditions at senescent vents may be experienced very differently by meio- and macrofaunal metapopulations as faunae differ in energy requirements. Stopping of vent fluids causes death of symbiont-bearing vent megafauna, as the direct source of energy for the symbionts is cut off. One to 4 years after vent fluids had stopped, we encountered a predominantly juvenile marcofaunal community and a highly abundant and reproductive meiofaunal community at the studied senescent vents (see sections "Senescent Vents—A Species Rich Ecotone" and "Senescent Vents May Provide Food for an Abundant Small Sized Fauna"). Our MDS plot shows that macrofaunal communities are mainly grouped according to distinct productivity regimes (active vent, senescent vent, basalt) and not according to year within our study period (**Figures 4B,D**). This may be related to macrofaunal habitat fidelity patterns. Macrofaunal species occur primarily at active vents and are typically restricted (endemic) to this habitat (Van Dover, 2000; Gollner et al., 2015a). In contrast, meiofaunal species are not restricted to active and senescent vents but also occur on basalt (Gollner et al., 2015a; Plum et al., 2017). This is shown by our MDS (**Figure 4A**), where meiofaunal communities at active vents, senescent vents, and basalt are rather similar. The contrasting habitat fidelity patterns of a vent endemic macrofauna and a generalist meiofauna, which may be evolutionary driven by distinct food demands and reproduction

strategies inherent to fauna of different sizes (Gollner et al., 2015a), may shape succession of AST communities.

Overall, our study suggests that size class specific traits may influence AST communities' succession after major disturbance. Meiofaunal communities were predominantly structured over years by the apparent distinct dispersal abilities of meiofauna taxa, with good copepod dispersers and poor nematode dispersers (Gollner et al., 2015b). This was found independent of habitat type in the AST, including basalt, senescent vent, and active vents. Productivity regimes appeared highly distinct in these habitats (see prokaryote abundances in **Supplementary Material S1**), but we did not detect significant meiofaunal community dissimilarities. In contrast, macrofaunal communities' dissimilarities were higher between habitats of different productivity regimes than between different years. Productivity may set the limits for vent macrofauna distribution (Mullineaux et al., 2009).

Relevance for Deep-Sea Mining

There is an increasing interest in mining minerals at deep-sea hydrothermal vents. First, mining tests have been carried out in the national waters of Papua New Guinea and Japan and seven contractors have signed contracts for mineral exploration of seafloor massive sulfides in international waters with the International Seabed authority (ISA) (Gollner et al., 2017). The ISA is currently drafting a Mining Code, including environmental regulations, for the exploitation of minerals in international waters. In just a few years' time, mining in the deep-sea might become a legal reality. Potential long-lasting impacts of seabed mining emphasize the need for effective environmental management plans (Cuvelier et al., 2018; Tunnicliffe et al., 2018). Such plans should include efforts to mitigate deep-sea mining impact such as avoidance and the designation of undisturbed areas (refuges). A recent publication argued that active hydrothermal vent ecosystems shall be excluded from deep-sea mining at all (Van Dover et al., 2018).

Deep-sea mining will cause large-scale disturbances and will kill animals. Our study shows that many species at vents may not be adapted to complete destruction of their populations. Even the large-scale volcanic eruption at the 9°N EPR in 2005/2006 did not pave all areas with lava. The elevated areas—like smoker structures at Bio9 Vent and Q Vent or the elevated East Wall site harbored many remnants that may have played crucial roles for recovery of communities on lava paved areas. Recovery of several (many?) species at new vents and new basalt may depend on survival at local non-disturbed areas and local migration. These findings should be integrated into future models of dispersal networks. Suzuki et al. (2018) demonstrated a population dynamic model estimating resilience of vent communities by selecting for one species with larval dispersal in the West Pacific. Ideally, in the future, such models should also integrate species with non-larval dispersal. To summarize, mining of entire vent sites could have even more dramatic impact than volcanic eruptions. Hydrothermal vent communities may not be adapted to complete disturbance and local remnants may play pivotal roles for recovery after disturbance.

CONCLUSION

Entirely senescent vent sites like Q Vent and East Wall as well as senescent vent patches within active vent sites like Sketchy and P Vent occur regularly at the 9°N EPR and harbor a species rich mix of species from active vents as well as rare and mostly yet undescribed species. Our findings are in accordance with Mullineaux et al. (2009) whose experimental results indicated that abrupt environmental change at deep-sea vents does not necessarily result in elimination of existing macrofauna and rapid replacement but instead an imprint may persist for many months after the disturbance. Also, Van Dover (2002) and Tsurumi and Tunnicliffe (2003) found vent macrofauna and background fauna at senescent vents. We detected an abundant and reproductive meiofaunal community including adults and juveniles at senescent vents that have not been exposed to hydrothermal venting for up to 4 years. It is not clear yet if and to what extant/how long typical vent macrofauna can reproduce at senescent vents, and if the presence of a predominantly juvenile macrofauna results from continuous settlement from active vents or from *in situ* reproduction.

After the volcanic eruption in 2005/2006, remnants from small areas that were not paved by lava, including two senescent vent sites and one active vent site, may have provided source populations for the close by new emerging vent sites. In addition, vent animals known as early colonizers originating from remote areas after the volcanic eruptions, such as the limpet *L. tevnianus*, could settle at senescent vents and new active vents, pointing to settlement processes that do not solely rely on the presence of hydrothermal fluid flux. Meiofaunal community dynamics during early succession at the 9°N EPR seem to be driven by distinct dispersal capabilities of different higher taxa such as copepods and nematodes, while macrofaunal community dynamics may be more linked to productivity/vent fluid regimes. Vent meio- and macrofauna have fundamentally different life traits that may determine their success (in terms of abundance, diversity, and reproduction) to live at senescent vents and on basalt with no direct *in situ* primary production. Their intrinsic reproduction and dispersal strategies further influence mode of recovery after major disturbance. Remnant individuals after disturbance may be especially important for meiofauna recovery since they have rather limited dispersal abilities but may profit from higher habitat flexibility related to lower food demands, enabling them to live and reproduce at senescent vents and on basalt. Different modes of animal dispersal and habitat flexibility need to be integrated into future spatial management strategies on environmental protection with regard to future deep-sea mining at vents. Also, it has to be considered that hydrothermal vent communities may not be adapted to complete disturbance and mining of entire sites could have even more dramatic impact than volcanic eruptions.

DATA AVAILABILITY STATEMENT

Data are presented in the article and in the **Supplementary Material**.

AUTHOR CONTRIBUTIONS

SG designed the project, identified animals, analyzed the data, and wrote the manuscript. MB designed the project and edited the manuscript. BG and PM identified animals. LM provided samples, advised on experimental design, and edited the manuscript. SM and TS provided samples and edited the manuscript. NL measured chemistry and edited the manuscript. MW measured prokaryote abundances.

FUNDING

We received funding from the Austrian FWF (GrantP20190-B17; MB), the U.S. National Science Foundation (OCE-0424953; to LM, D. McGillicuddy, A. Thurnherr, J. Ledwell, and W. Lavelle; and OCE-1356738 to LM), and the European Union Seventh Framework Programme (FP7/2007-2013) under the MIDAS project, Grant Agreement No. 603418. Ifremer and CNRS (France) supported NL cruise participation and sensor developments. BG was supported by a postdoctoral fellowship from the Deep Ocean Exploration Institute at WHOI (United States). TS was supported by the U.S. National Science Foundation (OCE-0327261 to TS and OCE-0937395 to TS and BG).

ACKNOWLEDGMENTS

The authors thank the crew of R/V *Atlantis* and DSV *Alvin*, and scientists on board for their tremendous support during cruises. Special thanks to Ingrid Kolar and Salvador Espada Hinojosa (technicians involved in numerous parts of this project), Sigrid Katz and Bettina Pflugfelder (help during cruises), and Maria Miljutina (help in nematode identification).

SUPPLEMENTARY MATERIAL

The Supplementary Material for this article can be found online at: https://www.frontiersin.org/articles/10.3389/fmars.2019.00832/full#supplementary-material

DATASHEET S1 | Meio- and macrofauna species abundance per 64 cm^2 from all samples.

MATERIAL S1 | Details on prokaryote abundances and animal communities.

REFERENCES

Adams, D., McGillicuddy, D., Zamudio, L., Thurnherr, A., Liang, X., Rouxel, O., et al. (2011). Surface-generated mesoscale eddies transport deep-sea products from hydrothermal vents. *Science* 332, 580–583. doi: 10.1126/science.1201066

Adams, D. K., and Mullineaux, L. S. (2008). Supply of gastropod larvae to hydrothermal vents reflects transport from local larval sources. *Limnol. Oceanogr.* 53, 1945–1955. doi: 10.4319/lo.2008.53.5.1945

Bayer, S. R., Mullineaux, L. S., Waller, R. G., and Solow, A. R. (2011). Reproductive traits of pioneer gastropod species colonizing deep-sea hydrothermal vents after an eruption. *Mar. Biol.* 158, 181–192. doi: 10.1007/s00227-010-1550-1

Begon, M., Harper, J. L., and Townsend, C. R. (1990). *Ecology: Individuals Populations and Communities*. Oxford: Blackwell.

Bell, S. S., Walters, K., and Hall, M. O. (1987). Habitat utilization by harpacticoid copepods: a morphometric approach. *Mar. Ecol. Prog. Ser.* 35, 59–64. doi: 10.3354/meps035059

Boschen, R. E., Rowden, A. A., Clark, M. R., Barton, J. S., Pallentin, A., Gardner, J. P. A., et al. (2015). Megabenthic assemblage structure on three New Zealand seamounts: implications for seafloor massive sulfide mining. *Mar. Ecol. Prog. Ser.* 523, 1–14. doi: 10.3354/meps11239

Childress, J. J., and Fisher, C. R. (1992). The biology of hydrothermal vent animals: physiology, biochemistry and autotrophic symbiosis. *Oceanogr. Mar. Biol. Annu. Rev.* 30, 337–441.

Clarke, K. R., and Gorley, R. N. (2001). *PRIMER v5: User Manual / Tutorial*. Plymouth: PRIMER-E Ltd.

Clarke, K. R., and Warwick, R. M. (2001). *Change in Marine Communities: An Approach to Statistical Analysis and Interpretation*. Primer-E Ltd: Plymouth.

Cuvelier, D., Gollner, S., Jones, D. O. B., Kaiser, S., Arbizu, P. M., Menzel, L., et al. (2018). Potential mitigation and restoration actions in ecosystems impacted by seabed mining. *Front. Mar. Sci.* 5:467. doi: 10.3389/fmars.2018.00467

Cuvelier, D., Sarrazin, J., Colaço, A., Copley, J., Glover, A., Tyler, P., et al. (2011). Community dynamics over 14 years at the eiffel tower hydrothermal edifice on the mid-atlantic ridge. *Limnol. Oceanogr.* 56, 1624–1640. doi: 10.4319/lo.2011.56.5.1624

Du Preez, C., and Fisher, C. R. (2018). Long-term stability of back-arc basin hydrothermal vents. *Front. Mar. Sci.* 5:54. doi: 10.3389/fmars.2018.00054

Erickson, K. L., Macko, S. A., and Van Dover, C. L. (2009). Evidence for a chemoautotrophically based food web at inactive hydrothermal vents (Manus Basin). *Deep-Sea Res. II* 56, 1577–1585. doi: 10.1016/j.dsr2.2009.05.002

Fisher, C. R., Takai, K., and Le Bris, N. (2007). Hydrothermal vent ecosystems. *Oceanography* 20, 14–23. doi: 10.5670/oceanog.2007.75

France, S. C., Hessler, R. R., and Vrijenhoek, R. C. (1992). Genetic differentiation between spatially-disjunct populations of the deep-sea hydrothermal vent endemic amphipod ventiella sulfuris. *Mar. Biol.* 114, 551–559. doi: 10.1007/bf00357252

Franklin, J. F., Frenzen, P., and Swanson, F. J. (1988). "Re-creation of ecosystems at Mt. St. Helens: contrasts in artificial and natural approaches," in *Rehabilitating Damaged Ecosystems, vol II*, ed. J. Cairns (Boca Raton: CRC Press), 1–37.

Galkin, S. V. (1997). Megafauna associated with hydrothermal vents in the manus back-arc basin (Bismarck Sea). *Mar. Geol.* 142, 197–206. doi: 10.1016/s0025-3227(97)00051-0

Galkin, S. V., and Goroslavskaya, E. I. (2008). Bottom fauna associated with mussel beds and alvinellid communities in the hydrothermal field at 9°n of the east pacific rise. *Oceanology* 48, 509–516. doi: 10.1134/s0001437008040061

Giere, O. (2009). *Meiobenthology, the Microscopic Mobile Fauna of Aquatic Sediments*, 2nd Edn. Berlin: Springer Verlag.

Gollner, S., Govenar, B., Fisher, C. R., and Bright, M. (2015a). Size matters at deep-sea hydrothermal vents: different diversity and habitat fidelity patterns of meio- and macrofauna. *Mar. Ecol. Prog. Ser.* 520, 57–66. doi: 10.3354/meps11078

Gollner, S., Govenar, B., Martinez Arbizu, P., Mills, S., Le Bris, N., Weinbauer, M., et al. (2015b). Differences in recovery between deep-sea hydrothermal vent and vent-proximate communities after a volcanic eruption. *Deep-Sea Res. I* 106, 167–182. doi: 10.1016/j.dsr.2015.10.008

Gollner, S., Kaiser, S., Menzel, L., Jones, D. O. B., van Oevelen, D., Menot, L., et al. (2017). Resilience of benthic deep-sea fauna to mineral mining activities. *Mar. Environ. Res.* 129, 76–101. doi: 10.1016/j.marenvres.2017.04.010

Gollner, S., Miljutina, M., and Bright, M. (2013). Nematode succession at deep-sea hydrothermal vents after a recent volcanic eruption with the desciption of two dominant species. *Organ. Divers. Evol.* 13, 349–371. doi: 10.1007/s13127-012-0122-2

Gollner, S., Riemer, B., Martinez Arbizu, P., Le Bris, N., and Bright, M. (2010). Diversity of meiofauna from the 9°50′N east pacific rise across a gradient of

hydrothermal fluid emissions. *PLoS One* 5:e12321. doi: 10.1371/journal.pone.0012321

Grime, J. P. (1977). Evidence for the existence of three primary strategies in the plants and its relevance to ecological and evolutionary theory. *Amer. Nat.* 111, 1169–1194. doi: 10.1086/283244

Heptner, M. V., and Ivanenko, V. N. (2002). Copepoda (Crustacea) of hydrothmerl ecosystems of the world ocean. *Arthropoda Sel.* 11, 117–134.

Hessler, R. R., Smithey, W. M., Boudrias, M. A., Keller, C. H., Lutz, R. A., and Childress, J. J. (1988). Temporal change in megafauna at the rose garden hydrothermal vent (Galapagos Rift; eastern tropical Pacific). *Deep Sea Res. Part A. Oceanogr. Res. Pap.* 35, 1681–1709. doi: 10.1016/0198-0149(88)90044-1

Higgins, P. R., and Thiel, H. (1988). *Introduction to the Study of Meiofauna*. Washington DC: Smithsonian Insitution Press.

Ihaka, R., and Gentleman, R. (1996). R: a language for data analysis and graphics. *J. Comput. Graph. Stat.* 5, 299–314.

Kaartvedt, S., Van Dover, C. L., Mullineaux, L. S., Wiebe, P. H., and Bollens, S. M. (1994). Amphipods on a deep-sea hydrothermal treadmill. *Deep Sea Res. Part I: Oceanogr. Res. Pap.* 41, 179–195. doi: 10.1016/0967-0637(94)90032-9

Kark, S., and van Rensburg, B. J. (2006). Ecotones: marginal or central areas of transition? *Isr. J. Ecol. Evol.* 52, 29–53. doi: 10.1560/ijee.52.1.29

Klose, J., Polz, M. F., Wagner, M., Schimak, M. P., Gollner, S., and Bright, M. (2015). Endosymbionts escape dead hydrothermal vent tubeworms to enrich the free-living population. *Proc. Natl. Acad. Sci. U.S.A.* 112, 11300–11305. doi: 10.1073/pnas.1501160112

Le Bris, N., Govenar, B., Le Gall, C., and Fisher, C. R. (2006). Variability of physico-chemical conditions in 9°50′N EPR diffuse flow vent habitats. *Mar. Chem.* 98, 167–182. doi: 10.1016/j.marchem.2005.08.008

Le Bris, N., Yücel, M., Das, A., Sievert, S., Ponnapakkam, L., and Girguis, P. (2019). Hydrothermal energy transfer and organic carbon production at the deep seafloor. *Front. Mar. Sci.* 5:531. doi: 10.3389/fmars.2018.00531

Levin, L. A., Baco, A. R., Bowden, D. A., Colaco, A., Cordes, E. E., Cunha, M. R., et al. (2016). Hydrothermal vents and methane seeps: rethinking the sphere of influence. *Front. Mar. Sci.* 3:72. doi: 10.3389/fmars.2016.00072

Maddocks, R. F. (2005). Three new species of podocopid ostracoda from hydrothermal vent fields at 9°50′n on the east pacific rise. *Micropaleontology* 51, 345–372. doi: 10.2113/gsmicropal.51.5.345

Marcus, J., Tunnicliffe, V., and Butterfield, D. A. (2009). Post-eruption succession of macrofaunal communities at diffuse flow hydrothermal vents on axial volcano. Juan de Fuca Ridge, Northeast Pacific. *Deep-Sea Res. II Top. Stud. Oceanogr.* 56, 1586–1598. doi: 10.1016/j.dsr2.2009.05.004

Menzel, L. (2011). First descriptions of copepodid stages, sexual dimorphism and intraspecific variability of mesocletodes sars, 1909 (Copepoda, Harpacticoida, Argestidae), including the description of a new species with broad abyssal distribution. *ZooKeys* 96, 39–80. doi: 10.3897/zookeys.96.1496

Mills, S. W., Mullineaux, L. S., Beaulieu, S. E., and Adams, D. K. (2013). Persistent effects of disturbance on larval patterns in the plankton after an eruption on the East Pacific Rise. *Mar. Ecol. Prog. Ser.* 491, 67–76. doi: 10.3354/meps10463

Mullineaux, L. S., Adams, D. K., Mills, S. W., and Beaulieu, S. E. (2010). Larvae from afar colonize deep-sea hydrothermal vents after a ctastrophic eruption. *Proc. Natl. Acad. Sci. U.S.A.* 107, 7829–7834. doi: 10.1073/pnas.0913187107

Mullineaux, L. S., Le Bris, N., Mills, S. W., Henri, P., Bayer, S. R., Secrist, R. G., et al. (2012). Detecting the influence of initial pioneers on succession at deep-sea vents. *PLoS One* 7:e50015. doi: 10.1371/journal.pone.0050015

Mullineaux, L. S., Metaxas, A., Beaulieu, S. E., Bright, M., Gollner, S., Grupe, B. M., et al. (2018). Exploring the ecology of deep-sea hydrothermal vents in a metacommunity framework. *Front. Mar. Sci.* 5:49. doi: 10.3389/fmars.2018.00049

Mullineaux, L. S., Micheli, F., Peterson, C. H., Lenihan, H. S., and Markus, L. (2009). Imprint of past environmental regimes on structure and succession of a deep-sea hydrothermal vent community. *Oecologia* 161, 387–440. doi: 10.1007/s00442-009-1390-1

Mullineaux, L. S., Mills, S. W., Sweetman, A. K., Beaudreau, A. H., Metaxas, A., and Hunt, H. L. (2005). Vertical, lateral and temporal structure in larval distributions at hydrothermal vents. *Mar. Ecol. Prog. Ser.* 293, 1–16. doi: 10.3354/meps293001

Mullineaux, L. S., Peterson, C. H., Micheli, F., and Mills, S. W. (2003). Successional mechanism varies along a gradient in hydrothermal fluid flux at deep-sea vents. *Ecol. Monogr.* 73, 523–542. doi: 10.1890/02-0674

Ólafsson, E. (2003). Do macrofauna structure meiofauna assemblages in marine soft-bottoms? *Vie Milieu* 53, 249–265.

Platt, W., and Connell, J. H. (2003). Natural disturbances and directional replacement of species. *Ecol. Monogr.* 73, 507–522. doi: 10.1890/01-0552

Plum, C., Pradillon, F., Fujiwara, Y., and Sarrazin, J. (2017). Copepod colonization of organic and inorganic substrata at a deep-sea hydrothermal vent site on the Mid-Atlantic Ridge. *Deep Sea Res. II* 137, 335–348. doi: 10.1016/j.dsr2.2016.06.008

Schimak, M. P., Toenshoff, E. R., and Bright, M. (2012). Simultaneous 16S and 18S rRNA fluorescence in situ hybridization (FISH) on LR White sections demonstrated in vestimentifera (Siboglinidae) tubeworms. *Acta Histochem.* 144, 122–130. doi: 10.1016/j.acthis.2011.03.008

Shank, T. M., Fornari, D. J., Von Damm, K. L., Haymon, R. M., and Lutz, R. A. (1998). Temporal and spatial patterns of biological community development at nascent deep-sea hydrothermal vents (9°50′N, East Pacific Rise). *Deep-Sea Res. Part II* 45, 465–515. doi: 10.1016/s0967-0645(97)00089-1

Smith, C. R., De Leo, F. C., Bernardino, A. F., Sweetman, A. K., and Martinez Arbizu, P. (2008). Abyssal food limitation, ecosystem structure and climate change. *Tree* 23, 518–528. doi: 10.1016/j.tree.2008.05.002

Soule, S. A., Fornari, D. J., Perfit, M. R., and Rubin, K. H. (2007). New insights into mid-ocean ridge volcanic processes from the 2005–2006 eruption of the East Pacific Rise, 9°46′N–9°56′N. *Geology* 35, 1079–1082.

Sousa, W. P. (2001). "Natural disturbance and the dynamcis of marine benthic communities," in *Marine Community Ecology*, eds M. D. Bertness, S. D. Gaines, and M. E. Hay, (Sunderland, MA: Sinauer Associates, Inc), 85–130.

Suzuki, K., Yoshida, K., Watanabe, H., and Yamamoto, H. (2018). Mapping the resilience of chemosynthetic communities in hydrothermal vent fields. *Sci. Rep.* 8:9364. doi: 10.1038/s41598-018-27596-7

Thistle, D., and Sedlacek, L. (2004). Emergent and non-emergent species of harpacticoid copepods can be recognized morphologically. *Mar. Ecol. Prog. Ser.* 266, 195–200. doi: 10.3354/meps266195

Thurnherr, A. M., Ledwell, J. R., Lavelle, W., and Mullineaux, L. S. (2011). Hydrography and circulation near the crest of the East Pacific Rise between 9° and 10°N. *Deep Sea Res. I* 58, 365–376. doi: 10.1016/j.dsr.2011.01.009

Tolstoy, M., Cowen, J. P., Baker, E. T., Fornari, D. J., Rubin, K. H., Shank, T. M., et al. (2006). A sea-floor spreading event captured by seismometers. *Science* 314, 1920–1922. doi: 10.1126/science.1133950

Tsurumi, M., and Tunnicliffe, V. (2003). Tubeworm-associated communities at hydrothermal vents on the juan de fuca ridge, northeast Pacific. *Deep-Sea Res. Part I* 50, 611–629. doi: 10.1016/s0967-0637(03)00039-6

Tunnicliffe, V., Botros, M., De Burgh, M. E., Dinet, A., Johnson, H. P., and Juniper, S. K. (1986). Hydrothermal vents of explorer ridge, northeast Pacific. *Deep Sea Res. Part A. Oceanogr. Res. Pap.* 33, 401–412. doi: 10.1016/0198-0149(86)90100-7

Tunnicliffe, V., Metaxas, A., Le, J., Ramirez-Llodra, E., and Levin, L. A. (2018). Strategic environmental goals and objectives: setting the basis for environmental regulation of deep seabed mining. *Mar. Policy* 95, 388–393.

Tyler, P. A., and Young, C. M. (1999). Reproduction and dispersal at vents and cold seeps. *J. Mar. Biol. Associat.* 79, 193–208. doi: 10.1017/s0025315499000235

van der Heijden, L. H., Rzeznik-Orignac, J., Asmus, R. M., Fichet, D., Bréret, M., Kadel, P., et al. (2018). How do food sources drive meiofauna community structure in soft-bottom coastal food webs? *Mar. Biol.* 165:166.

Van Dover, C. L. (2000). *The ecology of Hydrothermal Vents*. Princeton NJ: Princeton University Press.

Van Dover, C. L. (2002). Community structure of mussel beds at deep-sea hydrothermal vents. *Mar. Ecol. Prog. Ser.* 230, 137–158. doi: 10.3354/meps230137

Van Dover, C. L., Arnaud-Haond, S., Gianni, M., Helmreich, S., Huber, J. A., Jaeckel, A. L., et al. (2018). Scientific rationale and international obligations for protection of active hydrothermal vent ecosystems from deep-sea mining. *Mar. Policy* 90, 20–28. doi: 10.1016/j.marpol.2018.01.020

Vrijenhoek, R. C. (2010). Genetic diversity and connectivity of deep-sea hydrothermal vent metapopulations. *Mol. Ecol.* 19, 4391–4411. doi: 10.1111/j.1365-294X.2010.04789.x

Warwick, R. M. (1984). Species size distributions in marine benthic communities. *Oecologia* 61, 32–41. doi: 10.1007/BF00379085

Conflict of Interest: The authors declare that the research was conducted in the absence of any commercial or financial relationships that could be construed as a potential conflict of interest.

Copyright © 2020 Gollner, Govenar, Martinez Arbizu, Mullineaux, Mills, Le Bris, Weinbauer, Shank and Bright. This is an open-access article distributed under the terms of the Creative Commons Attribution License (CC BY). The use, distribution or reproduction in other forums is permitted, provided the original author(s) and the copyright owner(s) are credited and that the original publication in this journal is cited, in accordance with accepted academic practice. No use, distribution or reproduction is permitted which does not comply with these terms.

frontiers in Marine Science

ORIGINAL RESEARCH
published: 13 February 2020
doi: 10.3389/fmars.2020.00042

Oceanographic Drivers of Deep-Sea Coral Species Distribution and Community Assembly on Seamounts, Islands, Atolls, and Reefs Within the Phoenix Islands Protected Area

Steven R. Auscavitch[1], Mary C. Deere[1], Abigail G. Keller[1], Randi D. Rotjan[2], Timothy M. Shank[3] and Erik E. Cordes[1]*

[1] Department of Biology, Temple University, Philadelphia, PA, United States, [2] Department of Biology, Boston University, Boston, MA, United States, [3] Woods Hole Oceanographic Institution, Woods Hole, MA, United States

OPEN ACCESS

Edited by:
Ricardo Serrão Santos,
University of the Azores, Portugal

Reviewed by:
Amy Baco-Taylor,
Florida State University, United States
Frank Alan Parrish,
Pacific Islands Fisheries Science Center (NOAA), United States
Marco Taviani,
Italian National Research Council, Italy

***Correspondence:**
Steven R. Auscavitch
steven.auscavitch@temple.edu

Specialty section:
This article was submitted to Deep-Sea Environments and Ecology, a section of the journal Frontiers in Marine Science

Received: 14 April 2019
Accepted: 22 January 2020
Published: 13 February 2020

Citation:
Auscavitch SR, Deere MC, Keller AG, Rotjan RD, Shank TM and Cordes EE (2020) Oceanographic Drivers of Deep-Sea Coral Species Distribution and Community Assembly on Seamounts, Islands, Atolls, and Reefs Within the Phoenix Islands Protected Area. Front. Mar. Sci. 7:42. doi: 10.3389/fmars.2020.00042

The Phoenix Islands Protected Area, in the central Pacific waters of the Republic of Kiribati, is a model for large marine protected area (MPA) development and maintenance, but baseline records of the protected biodiversity in its largest environment, the deep sea (>200 m), have not yet been determined. In general, the equatorial central Pacific lacks biogeographic perspective on deep-sea benthic communities compared to more well-studied regions of the North and South Pacific Ocean. In 2017, explorations by the NOAA ship *Okeanos Explorer* and R/V *Falkor* were among the first to document the diversity and distribution of deep-water benthic megafauna on numerous seamounts, islands, shallow coral reef banks, and atolls in the region. Here, we present baseline deep-sea coral species distribution and community assembly patterns within the Scleractinia, Octocorallia, Antipatharia, and Zoantharia with respect to different seafloor features and abiotic environmental variables across bathyal depths (200–2500 m). Remotely operated vehicle (ROV) transects were performed on 17 features throughout the Phoenix Islands and Tokelau Ridge Seamounts resulting in the observation of 12,828 deep-water corals and 167 identifiable morphospecies. Anthozoan assemblages were largely octocoral-dominated consisting of 78% of all observations with seamounts having a greater number of observed morphospecies compared to other feature types. Overlying water masses were observed to have significant effects on community assembly across bathyal depths. Revised species inventories further suggest that the protected area it is an area of biogeographic overlap for Pacific deep-water corals, containing species observed across bathyal provinces in the North Pacific, Southwest Pacific, and Western Pacific. These results underscore significant geographic and environmental complexity associated with deep-sea coral communities that remain in under-characterized in the equatorial central Pacific, but also highlight the additional efforts that need to be brought forth to effectively establish baseline ecological metrics in data deficient bathyal provinces.

Keywords: deep sea coral, seamounts, marine protected area, marine biogeography, community structure, equatorial central Pacific, water masses

INTRODUCTION

Established in 2008, and later closed to commercial fishing in 2015, the Phoenix Islands Protected Area (PIPA) is among the largest (408,250 km^2) closed marine protected areas (MPA) and the deepest UNESCO world heritage site on Earth (Claudino-Sales, 2019). Despite these designations, the deep-sea benthos below 200 m in this MPA remained vastly unexplored hindering the full understanding of what habitats the protected area encompasses. In 2017, several deep-sea exploration expeditions passed through PIPA on the NOAA ship Okeanos *Explorer*, as a part of the CAPSTONE (Campaign to Address Pacific monument Science, Technology, and Ocean Needs) program (Demopoulos et al., 2018), and on the R/V *Falkor* with the goal of enhancing understanding of deep-sea ecosystems in the MPA via international partnerships (McKinnie et al., 2018; Mangubhai et al., 2019).

Deep-sea exploration has been an on-going priority for PIPA, starting with the first formal research plan (Rotjan and Obura, 2010), and continuing in the first and second PIPA management plans. The earliest deep-sea surveys consisted of baited drop cameras deployed to observed fish communities below 1000 m depth (Obura et al., 2011). Recent expeditions contributed high-definition multibeam mapping and seafloor exploration (Kennedy et al., 2019), which also helps to better define and manage the features that lie within protected boundaries. A United Nations voluntary commitment stemming from the Oceans Sustainable Development Goals (SDG14) was recently written by the PIPA Scientific Advisory Committee, with the specific goal to increase scientific knowledge and research capacity to improve ocean health in Kiribati. Deep-sea exploration in PIPA directly helps to fulfill these goals of increased knowledge and research capacity, as well as advancing the biodiversity inventory within PIPA boundaries.

The deep slopes of islands, atolls, reef-capped shallow banks (herein referred to as reefs), and seamounts comprise the majority of high-profile seafloor relief in PIPA with at least two major geographic seamount or island clusters, the Tokelau Seamount Chain and Phoenix Island cluster, occurring entirely within or passing through its boundaries (**Figure 1**). Globally, seamounts are among the most extensive biomes in the Pacific Ocean with only a small percentage having been explored worldwide (Etnoyer et al., 2010). While seamounts are abundant deep-sea features, particularly in the western and central Pacific Ocean, exploration of these features and characterization of seafloor communities at bathyal depths are lacking in the region (Watling et al., 2013; Bohnenstiehl et al., 2018; Cantwell et al., 2018; Demopoulos et al., 2018; Herrera et al., 2018; Kelley et al., 2018). Deep-sea corals, primarily from the Octocorallia (soft corals), Scleractinia (stony corals), and Antipatharia (black corals), represent some of the most common groups observed on seamounts studied worldwide (Rogers et al., 2007), making them a useful group of taxa for understanding how the oceanographic and physical environment influences benthic communities across a range of spatial scales. Structures produced by deep-water corals provide important vertical relief for associated species in deep-sea ecosystems (Buhl-Mortensen et al., 2010), in addition to supporting unique symbioses with invertebrate fauna (Mosher and Watling, 2009). Benthic invertebrate and demersal fish communities on seamounts have been reported to be strongly influenced by variables including local water column productivity, overlying water masses, depth, substrate type, and topographic variability (Genin et al., 1986; Auster et al., 2005; Clark et al., 2010; Shank, 2010; Quattrini et al., 2017; Rogers, 2018).

The exploration and exploitation of mineral resources from seafloor crusts and the impact to benthic fauna have become an increasing regional concern given the poor state of knowledge of deep-sea biodiversity (Miller et al., 2018). World-wide, seamounts have been found to harbor benthic communities that are vulnerable to a range of disturbances and are often slow to recover to their pre-disturbed state (Watling and Norse, 1998; Williams et al., 2010; Watling and Auster, 2017). In the central Pacific, cobalt-rich mineral crusts occur on seamounts at depths that coincide with those of deep-water coral and sponge communities (Morgan et al., 2015). Such species, which are characteristically slow-growing and long-lived, stand to be disrupted should such activities occur and result in physical disturbance and increased sedimentation rates within and around affected areas (Gollner et al., 2017). Identifying and quantifying species diversity within deep-water coral communities on features throughout the Pacific that exhibit a range of geomorphological characteristics (e.g., guyots, sharp-peaked seamounts, as well as on the flanks of atolls and islands) is essential to properly manage these species and communities.

This study provides insight into the composition, diversity, and patterns among coral communities at bathyal depths in the Phoenix Islands Protected Area. Using ROV-collected high-resolution video and collections-based approaches, we provide the first deep-sea coral species inventory within PIPA boundaries. Additionally, we test two exploratory hypotheses designed to identify broader differences in community similarity between geographic features and across depth. The first being, do different feature types like islands, atolls, reefs, or seamounts harbor distinct deep-water assemblages within the protected area? Second, does vertical structure of the water column (i.e., water masses) result in differences in assemblages across depth? If so, which species might contribute most to the observed differences? And finally, which oceanographic environmental variables most strongly influence the observed variation in community structure at bathyal depths?

Due to the geographic remoteness of these features and the protected status of the area, we suggest that deep-water communities within PIPA are likely to rank among the least human-impacted environments in the deep Pacific Ocean and act as a foundation for comparison to other unprotected deep-sea features in the greater Central Pacific. The results of this work will help to set a much-needed baseline understanding of large remote marine reserves, specifically with respect to identifying abundant and diverse deep-sea communities and ensuring their future conservation.

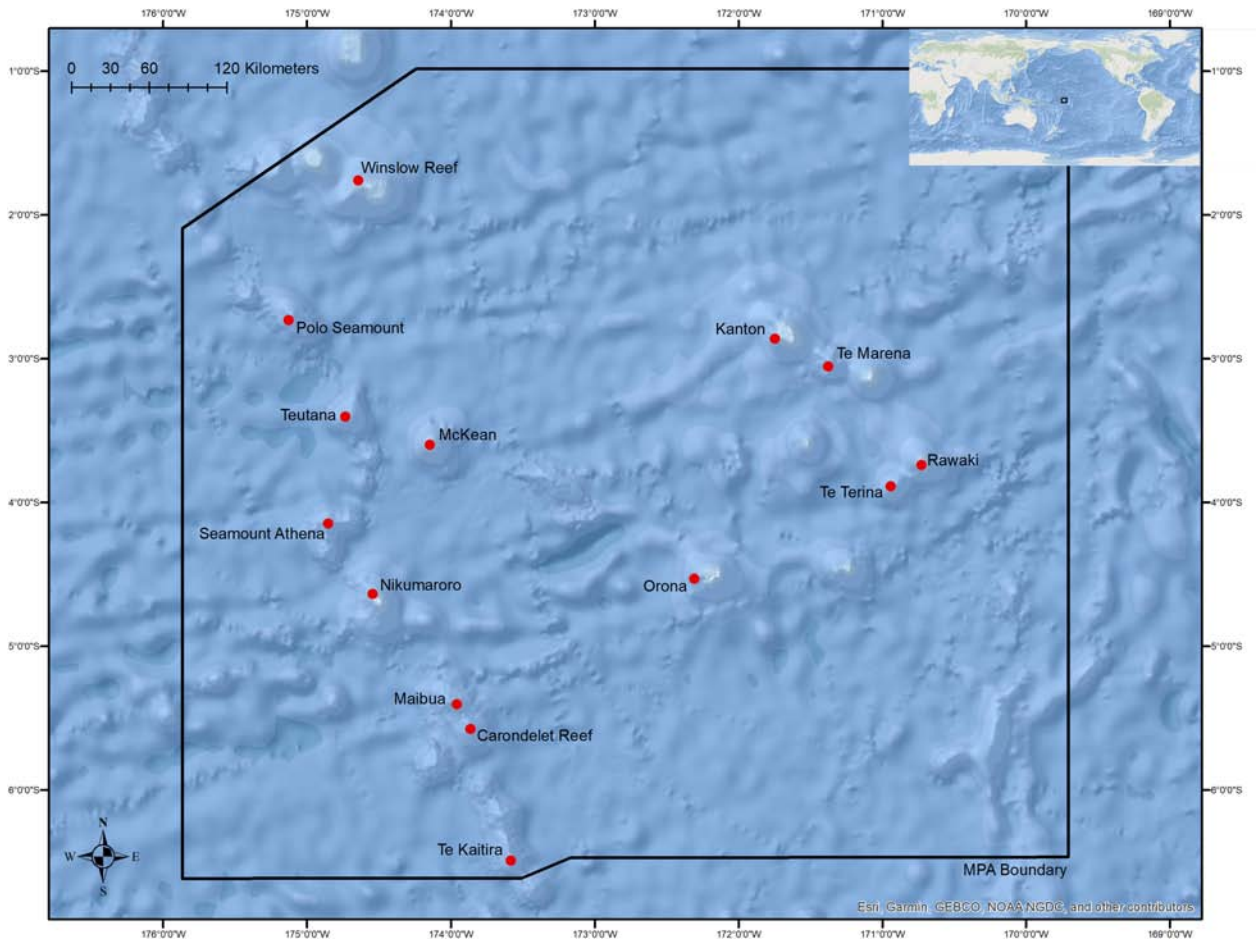

FIGURE 1 | Overview of the boundaries of the Phoenix Islands Protected Area with locations of sites where dives were conducted in this study. **Table 1** and **Supplementary Figure S1** provide detailed dive site names, coordinates, and depth ranges.

MATERIALS AND METHODS

Data for this study were collected from two expeditions to the Phoenix Islands Protected Area in March and October 2017 (**Table 1**). In March, the NOAA Ship *Okeanos Explorer* (ROV *Deep Discoverer*) surveyed and explored the western portion of PIPA along the Tokelau Ridge seamounts; in October, the R/V *Falkor* (ROV *Subastian*) focused on islands, atolls, and seamounts in the eastern Phoenix Islands, as well as additional dives along the Tokelau seamount chain. Both expeditions utilized remotely operated vehicle (ROV) systems to survey and characterize deep-water coral communities in the area. ROV *Deep Discoverer* completed 7 transects along 7 features on the Tokelau Seamount Chain and the ROV *Subastian* completed 17 transects across 10 features throughout the Phoenix Islands, Phoenix Seamounts, and Tokelau Seamounts (**Supplementary Figure S1**).

Seafloor transects were conducted upslope from deeper to shallower depths across each feature. In each case, vehicles moved upslope, perpendicular to the contours of the slope, with only occasional short zooms to confirm identifications. Motion across the seafloor occurred at an average of 0.25 kt. Video segments on the seafloor spent sampling, during long duration zooming, not in forward motion, or otherwise not in visual contact with the seabed was not included in analyses. Collection opportunities were utilized to obtain voucher specimens for further identification of coral morphospecies (**Supplementary Table S1**).

ROV Video Analysis

Video segments where collections were made, where the vehicle was more than 3 m off bottom, moving backwards, during sampling events, or of generally poor quality, were not assessed. Individuals or colonies were identifiable above a 5 cm height threshold, with measurements based on 10 cm wide parallel lasers in the ROV field of view. If colonies or individuals were below this size threshold, they could not be consistently identified and were omitted from analysis. Each occurrence was associated with a UTC time-stamp, and this was used to associate each observation with *in situ* environmental data including latitude-longitude coordinates, temperature, depth, dissolved oxygen concentration, and salinity.

TABLE 1 | Summary of dives conducted at seamounts, islands, atolls, and reefs during EX1703 and FK171005.

Cruise	Dive	Location	Feature type	On bottom (Lat, Long Dec. Degrees)	Off bottom (Lat, Lon Dec. Degrees)	Depth range (m)	Bottom duration (hh:mm)	Seafloor distance covered (m)
EX1703	Dive03	Carondelet Reef	Reef	−5.62715, −173.835083	−5.6280833, −173.8394167	1603–1844	6:01	490
EX1703	Dive04	Seamount Athena	Seamount	−4.1469167, −174.8521	−4.150267, −174.854333	1030–1223	6:43	447
EX1703	Dive05	Polo Seamount	Seamount	−2.7300667, −175.12615	−2.72805, −175.1310667	1834–2134	5:44	590
EX1703	Dive14	Winslow Reef	Seamount	−1.70345, −175.2022667	−1.70431667, −175.205667	1303–1527	6:03	390
EX1703	DIve15	Teutana	Seamount	−3.40145, −174.73211667	−3.399516, −174.735766	976–1325	4:57	453
EX1703	Dive17	Maibua	Seamount	−5.403283, −173.958233	−5.40135, −173.9615	463–746	7:10	420
EX1703	Dive18	Te Kaitira	Seamount	−6.490766, −173.58045	−6.4918833, −173.58345	1778–2105	5:43	354
FK171005	SB0067	Kanton	Atoll	−2.859174, −171.744569	−2.826730, −171.714738	247–2135	19:06	4895
FK171005	SB0068	Te Marena	Seamount	−3.0539191, −171.374616	−3.036057, −171.357612	804–1856	9:50	2739
FK171005	SB0069	Rawaki	Island	−3.7819294, −170.731466	−3.759379, −170.718154	1550–2313	9:04	2908
FK171005	SB0070	Rawaki	Island	−3.738242, −170.725524	−3.732776, −170.716769	367–1198	7:40	1145
FK171005	SB0071	Te Terina	Seamount	−3.887563, −170.939562	−3.890913, −170.935158	1489–1724	3:44	614
FK171005	SB0072	Te Terina	Seamount	−3.891529, −170.933927	−3.891579, −170.930155	1127–1426	1:47	418
FK171005	SB0073	Orona	Atoll	−4.528743, −172.306548	−4.5205168, −172.307271	2050–2439	11:02	918
FK171005	SB0074	Orona	Atoll	−4.5121363, −172.272042	−4.51443033, −172.261741	600–1361	6:25	1169
FK171005	SB0075	Orona	Atoll	−4.498947, −172.25421	−4.5102886, −172.2421938	484–613	22:41	1833
FK171005	SB0076	Winslow Reef	Reef	−1.655299, −174.980157	−1.6391061, −174.973467	229–1502	9:19	1947
FK171005	SB0077	Winslow Reef	Reef	−1.660755, −174.952322	−1.6530499, −174.943519	561–1424	9:14	1300
FK171005	SB0078	Winslow Reef	Reef	−1.759119, −174.641697	−1.7685911, −174.64309	723–1365	9:52	1064
FK171005	SB0079	Winslow Reef	Seamount	−1.929302, −174.736812	−1.9221619, −174.732316	1375–1957	9:15	937
FK171005	SB0080	McKean	Island	−3.597142, −174.145254	−3.5947105, −174.136795	363–1206	9:37	976
FK171005	SB0081	Nikumaroro	Atoll	−4.634481, −174.543162	−4.6574490, −174.556903	829–1028	10:37	2972
FK171005	SB0082	Carondelet Reef	Reef	−5.5760301, −173.862591	−5.575719, −173.8616971	152–275	1:59	105
FK171005	SB0083	Carondelet Reef	Reef	−5.604389, −173.844220	−5.595109, −173.856552	429–1342	19:09	1710

Location identifiers are based on both official geographic names and unofficial identifiers, as in the case of unnamed seamounts.

Video was analyzed for coral occurrences from four major anthozoan taxonomic groups: the Scleractinia, Octocorallia, Zoantharia, and Antipatharia. Individuals or colonies were identified to the lowest taxonomic level possible or assigned morphospecies (msp.) identifiers. Only visibly live colonies were counted. If particular colonies could not be identified reliably to such a level, they were placed in family or genus-level groupings (i.e., family spp. or genus spp.). Observations with any uncertainty were flagged and underwent quality control by examining and omitting the potentially erroneous identifications. Final identification of coral species, using both photographic and voucher specimens, were

made using published taxonomic keys, and assistance from taxonomic specialists.

Community Analyses

Deep-water coral patterns were assessed by dividing each of the 24 dive transects into 100 m depth bins. Each bin provided a sampling that consisted of all coral morphospecies observations occurring within that 100 m depth interval. Community-level analyses were conducted using standardized and 4th root transformed species abundance data in a resemblance matrix in PRIMER v7 with PERMANOVA add-on (Clarke and Gorley, 2006; Anderson et al., 2008). In all, 153 samples were identified across 24 dives (**Supplementary Table S2**). Samples were compiled into a Bray-Curtis similarity resemblance matrix for further analyses. Cluster analysis and non-metric multidimensional scaling ordinations (nMDS) were initially conducted to identify associations between groups of samples. For these analyses only, in order to reduce the effect of noise in the dataset, species abundances were averaged across samples in 100 m depth bins resulting in one data point for each depth stratum. The significance of associations between sample clusters were evaluated using the similarity profile (SIMPROF) routine (Clarke et al., 2008).

Before conducting assessments of similarity in communities, adequacy of sampling effort and species richness comparisons were evaluated using permuted sample-based species accumulation and individual-based rarefaction for feature types and water masses in Vegan 2.5-3 in R (Oksanen et al., 2015). In order to test for similarities among coral assemblages between factors, analysis of similarity (ANOSIM) tests were employed. The first comparison tested differences between feature types while controlling for the effect of depth differences using a two-way nested ANOSIM. A one-way ANOSIM test was also used to determine if differences could be identified between assemblages bathed by different water masses. All ANOSIM tests were conducted using 999 random permutations.

In order to incorporate environmental data for each sample, an average of depth, temperature, salinity, dissolved oxygen was calculated in each 100 m sample. The mean was then normalized within each variable to reduce the effects of differences in unit scales. The BEST routine (BIO-ENV) was employed to explore correlations between biological observations and environmental predictors. A distance-based linear model (distLM) was applied using the PERMANOVA package and utilized the Akaike Information Criterion (AIC) to identify environmental variables with strong explanatory power for observed variation within samples (Anderson et al., 2008). Visualizations of the resemblance matrix with predictor variables were paired with a dbRDA (distance-based redundancy analysis) ordination with distLM overlay.

RESULTS

ROV Video Analysis Summary

Across both cruises, 212 h and 42 min of video were assessed from 24 dives, 7 dives from EX1703 and 17 dives from FK171005 (**Table 1**). A preliminary comparison revealed no significant difference between cruises due to methodology and thus both datasets were treated as one (two-way ANOSIM between cruises (depth within cruise), Global $R = 0.018$, $p = 0.292$). Dives spanned the depths of 152–2439 m with deep-water corals being recorded across the depths of 192–2438 m (**Figure 2**). In total, 12,828 observations of deep-water corals were identified with 10,995 of those being assigned a morphospecies (msp.) or species-level identifier (**Supplementary Table S1**). The remaining 1833 records fell into coarser identification groupings at the genus or family level. All corals were identified and categorized using consistent morphospecies identifications from the Octocorallia, Antipatharia, Scleractinia, and Zoantharia. From these groups, 167 unique morphospecies identifiers were assigned based on visual identification, morphological identification from voucher collections, or a combination of those methods (**Table 2**).

Oceanographic Summary

In order to determine water mass structure in the area, downcast shipboard CTD profiles of the upper 3000 m of the water column were examined for temperature and salinity changes across depth (**Figure 3**). Using these characteristics, major deep-ocean water masses present in this area were generally defined as Pacific Equatorial Water (PEW) between 200 and 500 m, Equatorial Pacific Intermediate Water (EqPIW) between 500 and 1500 m, and Pacific Deep Water (PDW) below 1500 m (**Table 2**). Temperature, salinity, and dissolved oxygen ranges for each water mass were consistent with accepted ranges from published records in the equatorial Pacific (Bostock et al., 2010).

Environmental variables from ROV-mounted CTD units were in agreement with downcast CTD profiles and provided *in situ* records at each coral observation (**Figure 4**). Bottom temperatures overlying coral observations ranged from 1.91 to 21.34°C. Salinity and dissolved oxygen across those same intervals ranged from 34.52 to 35.92 psu and 79.85 to 201.70 μmol/kg, respectively. Below the thermocline at 200–300 m depth, temperature decreased to a minimum of 1.91°C at 2438 m (**Figure 4A**). Salinity decreased rapidly with depth to a minimum of 34.52 at 800 m, gradually increasing at deeper depths (**Figure 4B**). A persistent mid-water oxygen minimum of 110–120 μmol/kg was observed between 1000 and 1100 m, but oxygen values in the viscinity of Winslow Reef were reported substantially lower at shallower depths (**Figure 4C**). The lowest values concurrent with coral observations occurred at Winslow Reef where dissolved oxygen was measured at 79 μmol/kg at 608 m. Low oxygen values (91 μmol/kg) were also identified at Rawaki Island at between 483 and 540 m.

Coral Distribution Patterns

The dominant taxonomic group across all depths were the octocorals, followed by antipatharians, scleractinians, and finally zoantharians (**Table 3**). Pennatulaceans were only observed deeper than 1191 m and thus one of the only groups restricted to lower-bathyal depths (**Figure 2**). Rapid coral morphospecies turnover was observed in the upper 600 m of the water column with most morphospecies in this range occurring across a relatively narrow ranges of depth. The single most abundant

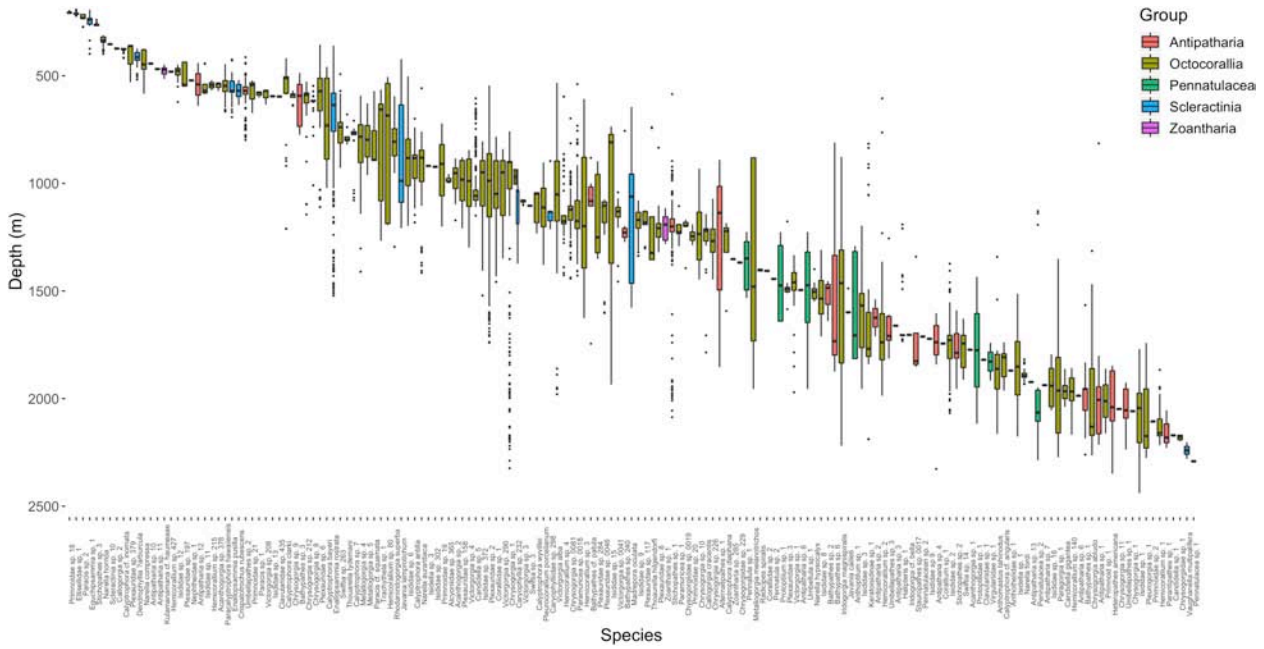

FIGURE 2 | Depth distribution of 167 morphospecies observed from video analyses within PIPA. Boxes are colored according to taxonomic groupings and are arranged by increasing median depth of occurrence.

TABLE 2 | Water masses and environmental characteristics observed in the Phoenix Islands Protected Area during cruises FK171005 and EX1703.

Water mass	Temperature (°C)	Salinity (psu)	*Dissolved oxygen (μmol/kg)*	Characteristics	Observed depth range (m)
Pacific Equatorial Water (PEW)	7.80–21.30	34.6–35.9	89–201	Decreasing oxygen concentration, decreasing temperature with increasing depth	197–500
Equatorial Pacific Intermediate Water (EqPIW)	3.08–7.80	34.5–34.6	79–150	Oxygen and salinity minima	500–1500
Pacific Deep Water (PDW)	1.90–3.05	>34.6	132–163	Increasing oxygen concentration, decreasing temperature with increasing depth	1500–2197

coral morphospecies was *Pleurogorgia* sp. 1, with 1046 colonies observed between 1741 and 2276 m, primarily encountered at high densities on vertical walls or steep inclines.

Octocorals, inclusive of the Pennatulacea, accounted for 78% of all deep-water coral observations. Primnoids were the most speciose as well as the most abundant family in the Octocorallia. With 672 records *Candidella* sp. 5 (605–1150 m), and *Narella aurantiaca* with 738 records (558–1416 m) were the dominant primnoid taxa. Chrysogorgiids followed with the two most abundant taxa being *Pleurogorgia* sp. 1 and *Chrysogorgia* sp. 1. Plexaurids were widespread, both geographically and across depth (213–2055 m) but 38% of observations fell into coarser identifications as *Plexauridae* spp. due to difficulty in identifying distinguishing characters between morphospecies. *Plexauridae* sp. 2, *Plexauridae* sp. 6, and *Paramuricea* sp. 0018 were the most abundant taxa in this family (**Supplementary Table S1**). Among the 605 bamboo coral colonies observed, *Isididae* sp. 9 (n = 271), a branched colony, was locally abundant at Te Marena and Orona between the depths of 1079–1336 m. The broadly distributed unbranched *Isididae* sp. 2 (n = 91) was observed at 7 sites throughout PIPA but only deeper than 1373 m. Precious corals representation was dominated by *Pleurocorallium porcellanum* Pasternak, 1981, by abundance (n = 179), and *Hemicorallium* spp. by morphospecies richness, with 8 morphospecies present (**Supplementary Table S1**). Victorgorgiids were also bathymetrically widespread with 202 observations among 8 morphospecies between the depths of 532 and 1979 m.

Black corals were the second most abundant taxon by number of observed colonies with 1645 records, or 12% of all records. The most abundant morphotype was *Stichopathes* sp. 1 with 981 records between 585 and 2086 m followed by *Umbellapathes* sp. 2 with 413 colonies between 414 and 799 m. *Bathypathes* was the most speciose genus but individual taxa were not very abundant with most morphospecies having 30 or fewer observations (**Supplementary Table S1**). At least 88 black coral

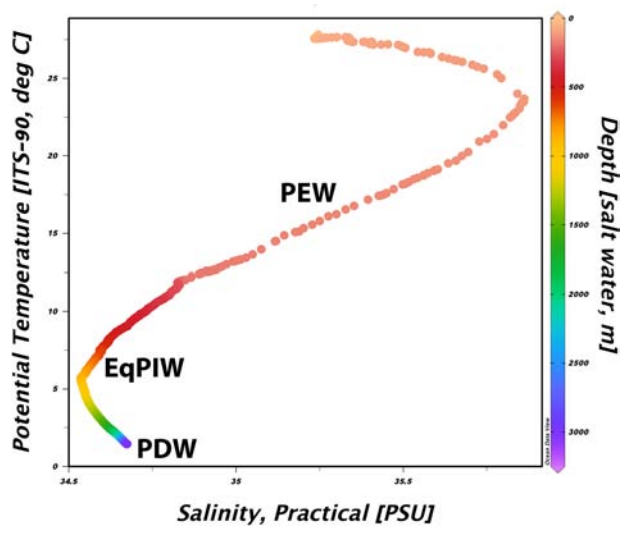

FIGURE 3 | Temperature-salinity diagram from the sea surface to 3000 m collected via CTD rosette downcast North of Kanton Atoll. The approximate depth of each water mass identified below 200 m is overlaid in bold. Plot was constructed using Ocean Data View v5.1 (Schlitzer, 2019).

colonies could not be identified to the family level due to low resolution singleton observations, or lack of voucher specimens for reference (**Supplementary Table S1**).

Scleractinians were most commonly distributed between 600 and 1500 m depth, with only one solitary coral species (*Vaughanella multipalifera*) present below 2000 m depth (**Figure 2**). The deepest occurrences of framework-forming colonial scleractinians were *Madrepora oculata* (n = 45) colonies found between the depths of 644 and 1577 m. The most abundant colonial scleractinian species, *Enallopsammia rostrata* (n = 462) was found to have a slightly shallower distribution between 359 and 1521 m. A second species in the genus, *Enallopsammia pusilla*, was found to have a distribution that partially overlapped the shallower range of its congener, between 425 and 692 m. Solitary coral species were the deepest scleractinians observed but most individuals occurred shallower than 650 m. The single most abundant species, *Crispatotrochus rubesecens*, occurred across a depth range of 519–635 m with other solitary species, *Javania cailleti* and *Javania lamprotichum* occurring deeper up to 1599 and 1208 m, respectively (**Figure 2**).

Patterns in Coral Community Structure

In order to evaluate sampling effort, sample-based species accumulation analyses were conducted by feature type and water mass to evaluate the completeness of species inventories. Among feature types species accumulated at similar rates on seamounts, atolls, reefs, and islands. Overall, seamounts had the largest morphospecies inventory compared to reefs which exhibited the lowest despite similar sample sizes (**Figure 5A**). Among all feature types, morphospecies accumulation approached asymptotic values signifying a potential to accumulate additional species with increased effort (**Figure 5A**). Between water masses, morphospecies accumulation rates and numbers of morphospecies observed were highest across the depths bathed by EqPIW (**Figure 5B**). Lower rates of accumulation and numbers of morphospecies were observed in PDW (76 mspp.) and PEW (30 mspp.). As sample sizes were smaller in PEW and PDW compared to EqPIW, accumulation curves did not approach asymptomatic values and suggest increased morphospecies richness with additional sampling effort in those water masses (**Figure 5B**).

Individual-based rarefaction analyses indicated that the total number of species observed was higher at seamounts (86 mspp.) and atolls (82 mspp.) compared to reefs (77 mspp.) and islands (67 mspp). Greater morphospecies evenness, demonstrated by a rapid increase in morphospecies with increasing number of individuals was also higher on seamounts and atolls compared to reefs and islands (**Figure 5C**). Overall, shallow-water reef banks accounted for the greatest number of coral observations (**Figure 5C**). Between water masses, EqPIW was found to have

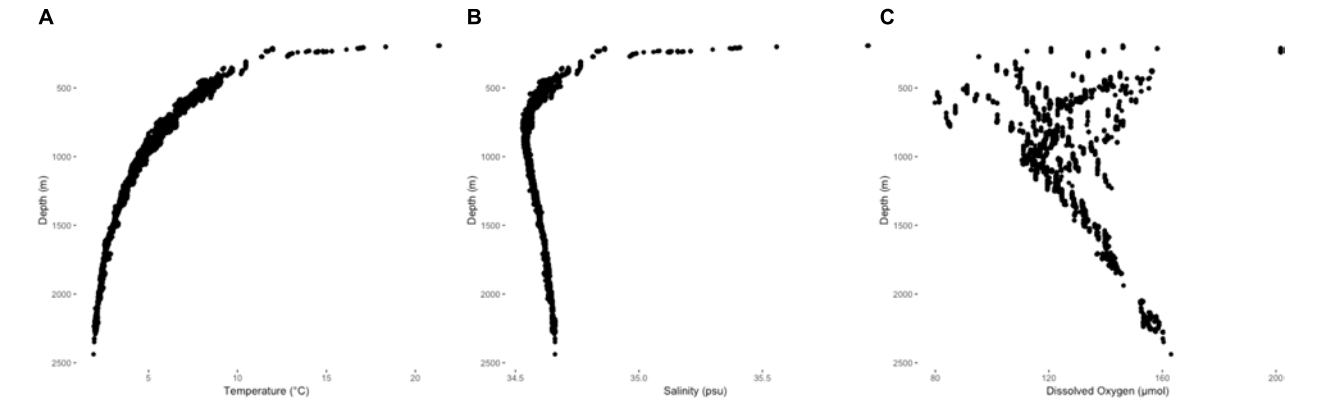

FIGURE 4 | Temperature **(A)**, salinity **(B)**, and dissolved oxygen **(C)** profiles from ROV CTD unit records co-occurring with deep-water coral observations between 193 and 2439 m.

TABLE 3 | Summary of deep-water coral observations from ROV video by taxonomic groupings.

	Octocorallia		Hexacorallia		
	Alcyonacea	**Pennatulacea**	**Scleractinia**	**Antipatharia**	**Zoantharia**
Number of observations	9910	145	1095	1645	33
Number of families	13	6	4	3	1
Number of morphospecies	113	10	12	29	3
Observed depth range (m)	193–2439	1129–2291	Colonial: 193–1578 All: 193–2280	241–2349	448–1352

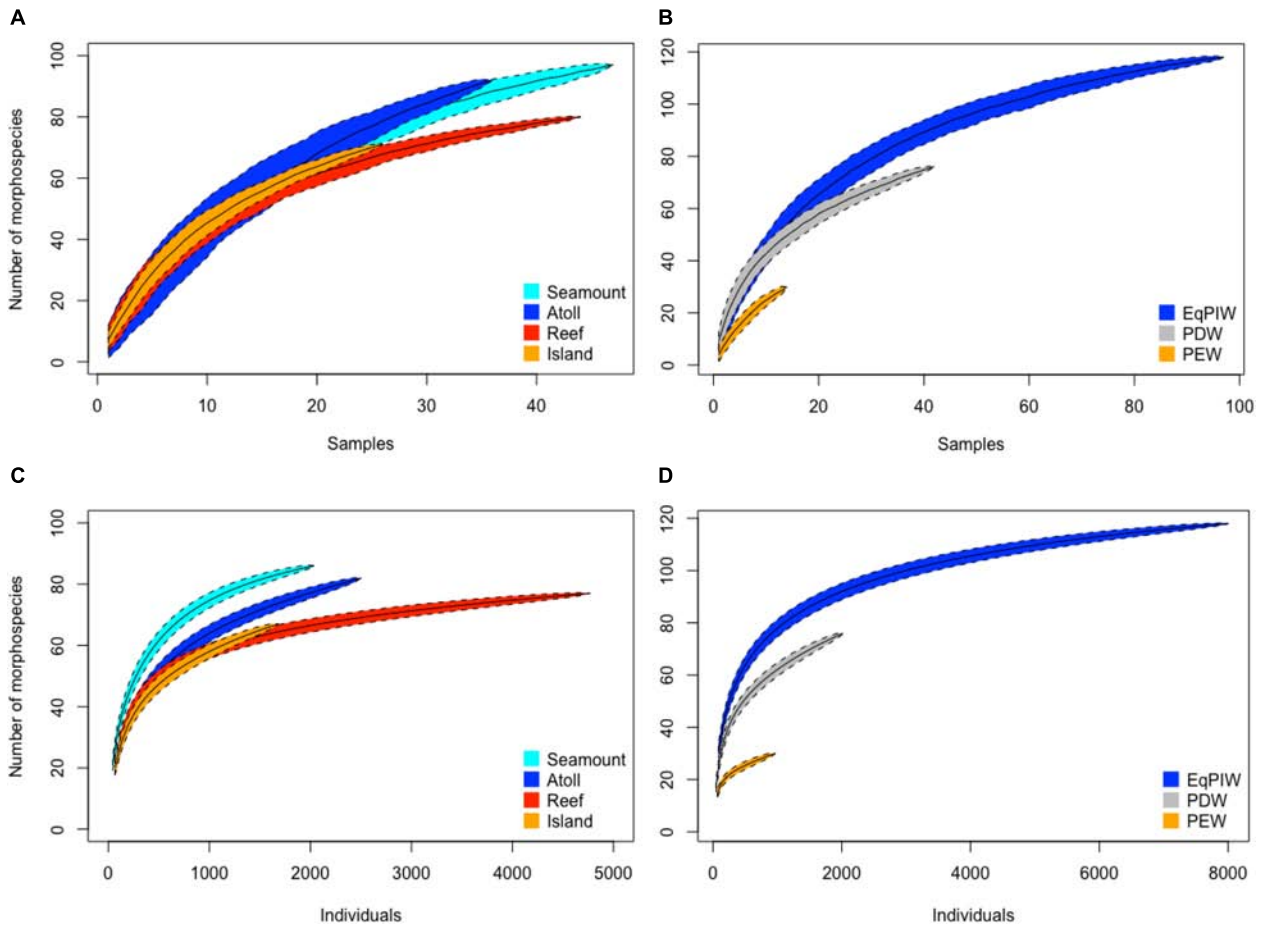

FIGURE 5 | Species accumulation and individual-based rarefaction analyses by feature type and water mass. Sample-based species accumulation curves are presented for feature types **(A)** and water mass **(B).** All depths were included for each feature type with $N = 26$ samples for islands, $N = 36$ for atolls, $N = 47$ for seamounts, $N = 44$ for reefs. For water masses, $N = 14$ samples were used for the PEW (197–500 m), $N = 97$ for EqPIW (500–1500 m), and $N = 42$ for PDW (1500–2197 m). Rarefaction curves are indicated for feature types **(C)** and water masses **(D)**. Curves are plotted with 95% confidence interval indicated by the colored polygons.

both greater morphospecies richness (118 mspp.) and greater evenness than both PDW and PEW at comparable numbers of individuals (**Figure 5D**).

Cluster analysis and non-metric multidimensional scaling analyses identified patterns in assemblage structure with depth. Similarities were highest in EqPIW samples and lowest among those in PEW (**Figure 6**). SIMPROF analysis indicated that the significance of the 8 identified clusters were driven by a close proximity in depth between samples (**Figure 6**). More SIMPROF groupings were identified encompassing samples covering the depths of EqPIW versus the above or underlying water masses (**Figure 7**). The most dissimilar samples occurred on both the extreme upper and lower ends of the survey range. Similarities between samples were also found to occur along a clear gradient with increasing sampling depth, except those between 2300 and 2500 m (**Figure 7**). These two samples were the two deepest

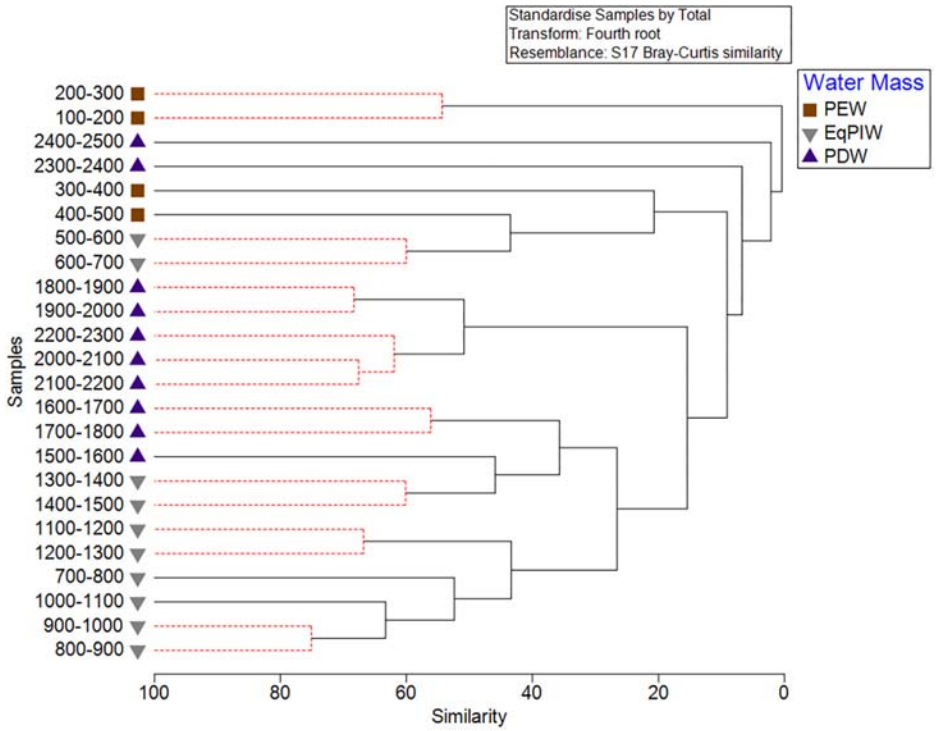

FIGURE 6 | Cluster analysis of 100 m depth-averaged samples. Significant clusters are identified using SIMPROF analysis and are indicated by solid black lines. Symbols indicate the water masses in which those samples occurred.

depth bins and contained only four combined coral observations (**Supplementary Table S2**).

A two-way nested ANOSIM between feature types (depth within feature type) failed to identify differences in assemblages between most comparisons with the exception of reef-type features (Global R = 0.036, p = 0.096). For reefs, significant differences in assemblages were observed between each other feature, but R-statistic values remained very low indicating a high degree of similarity between samples in those comparisons (**Supplementary Table S3**). A one-way ANOSIM between water mass factors identified significant and highly dissimilar coral assemblages (Global R = 0.302, p = 0.001) between all 3 bathyal water masses (**Supplementary Table S4**). The highest dissimilarity was observed between PEW and PDW (R-statistic = 0.619, p = 0.001) and the lowest between EqPIW and PEW (R-statistic = 0.177, p = 0.006).

The similarity percentage (SIMPER) routine identified particular species that contributed a disproportionate influence among significantly different water mass assemblages (**Figure 8**). Average community similarity increased with increasing water mass depth from PEW (9.68%), to EqPIW (9.8%), to PDW (14.7%). Similarities between samples within the PEW assemblage (200–500 m) were driven by 3 species, *Enallopsammia rostrata*, Plexauridae sp. 6, and *Paracalyptrophora hawaiiensis* contributed 58% of the within-group similarity (**Figure 8**). In EqPIW (500–1500 m), *Enallopsammia rostrata*, *Plexauridae* sp. 2, and *Iridogorgia magnispiralis* contributed to 45% of the similarity in the group (**Figure 8**). Within PDW (1000–2500 m), the top 3 species *Iridogorgia magnispiralis*, *Chrysogorgia* sp. 1, *and Pleurocorallium porcellanum* contributed to 40% of the observed similarity (**Figure 8**). Between water masses, the greatest dissimilarity was found between the shallowest and deepest water masses PDW and PEW (99.4% dissimilar). Present in each water mass, differences in the abundance of *Enallopsammia rostrata* alone was the dominant, single-species contributor (between 4.5 and 7%) of the dissimilarity observed between water masses.

Results from the BEST (BIO-ENV, Spearman Rank correlation) routine examined which environmental variable or combination of variables provided the best match for the observed variation in community among all samples. Depth and salinity together were found to be the best combination of variables describing resemblances between samples (Global test, 999 permutations, Rho = 0.445, p = 0.001). Yet, together, depth, temperature, salinity, and dissolved oxygen resulted in only a slightly lower correlation (Rho = 0.415). In the distLM and dbRDA analyses, depth, temperature, salinity, and dissolved oxygen were found to explain 7.2% (dbRDA axis 1) and 3.6% (dbRDA axis 2) of the community variation for a total of 10.8% (**Figure 9**). From the fitted model, 49.2% of the biological variation was correlated with dbRDA axis 1 and 24.9% with axis 2. DbRDA Axis 1 was most strongly correlated with depth (r = -0.773) and dbRDA axis 2 with temperature (r = 0.800) (**Supplementary Table S5**).

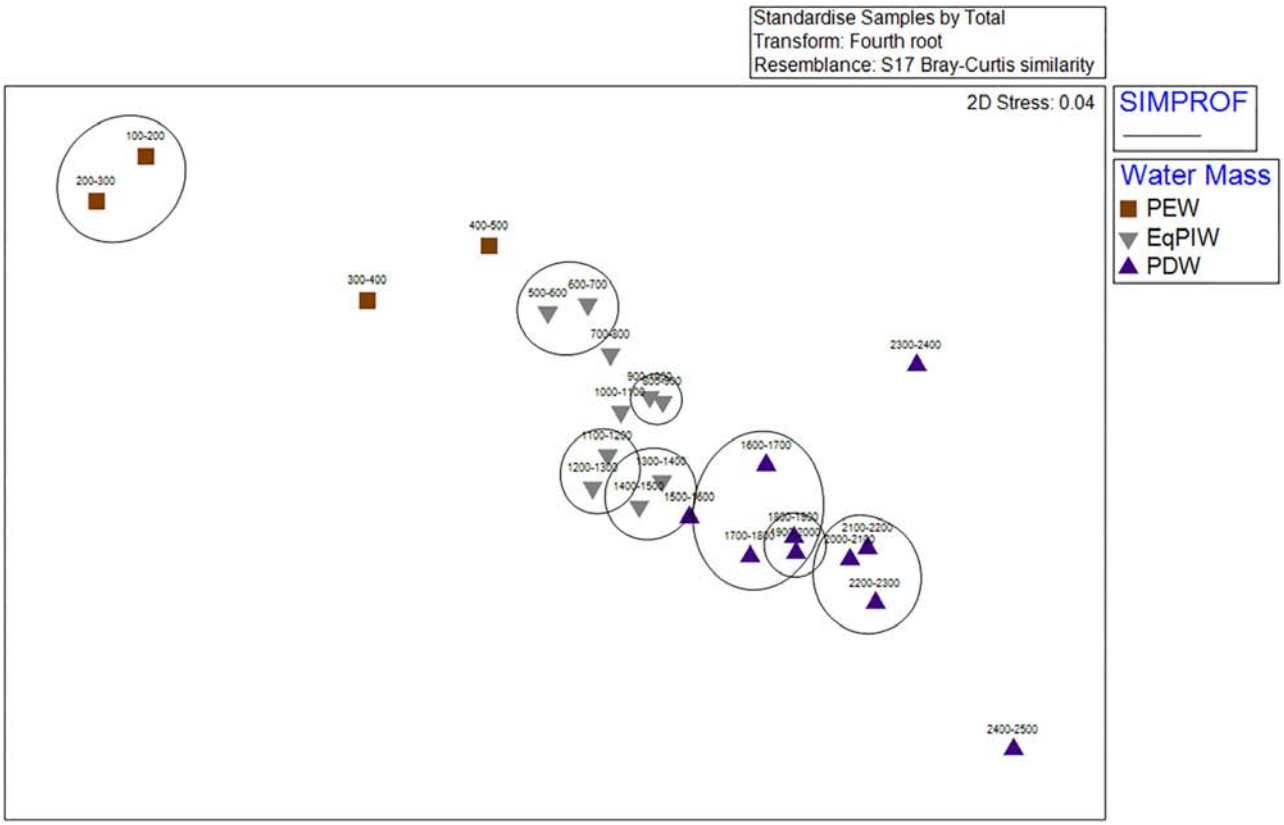

FIGURE 7 | Non-metric multidimensional scaling ordination (nMDS) of 100 m depth-averaged samples. Abundances within samples were 4th root transformed, standardized, and analyses were conducted using a Bray-Curtis Similarity matrix. Symbols indicate the water masses in which those samples occurred. Significant SIMPROF groupings from cluster analysis are overlaid in black.

DISCUSSION

This study provides a significant number of new deep-sea coral species records for a largely unexplored area of the equatorial central Pacific as well as within the boundaries of one of the largest MPAs in the world. Prior to these expeditions in 2017, no published records of any deep-water coral species were available from the Phoenix Islands below 200 m (OBIS, 2019). Over 2 cruises, this study has identified 12,828 deep-sea coral observations and 167 morphospecies at bathyal depths within the boundaries of PIPA from ROV video. From these observations we sought to test two exploratory hypotheses of community assembly in the protected area based on differences in feature type and overlying water masses.

There was no clear evidence of different assemblages across most feature types. While reefs did have some statistically significance differences among assemblages compared to each other feature type, the assemblages themselves were still identified as having high degree of similarity based on low R-statistic (R = 0.01–0.12) values (**Supplementary Table S3**). In comparison, the three bathyal water masses in the area, Pacific Equatorial Water, Equatorial Pacific Intermediate Water, and Pacific Deep Water were identified as having distinctly different deep-water coral assemblages (**Supplementary Table S4**), largely dominated by widely distributed cosmopolitan deep-water coral species (**Figure 8**). Furthermore, intermediate waters were found to have a greater number of morphospecies and greater evenness than shallower and deeper water masses suggesting that they are important pools of biodiversity at bathyal depths (**Figure 5D**).

Finally, we sought to identify which environmental variables were most important for explaining variation in coral assemblages. Community models and redundancy analyses indicated that depth and temperature were the most important oceanographic variables for explaining biological variation (**Figure 9**). However, dissolved oxygen and salinity also contributed significantly to the explanation of biological variation in the model (**Supplementary Table S5**). As a relatively low percentage (10.8%) of the total community variation was explained by oceanographic variables, it is likely that other environmental factors such as seafloor substrate and terrain variables would be useful to include in subsequent models (**Supplementary Table S5**). From a methodological perspective, both temperature and depth exhibited the greatest correlation between any two input variables ($|r| = 0.84$). However, it was not deemed necessary to remove either of these two variables due to concerns of collinearity prior to the analysis as they contained sufficiently different predictive information that would permit their inclusion to the model (Anderson et al.,

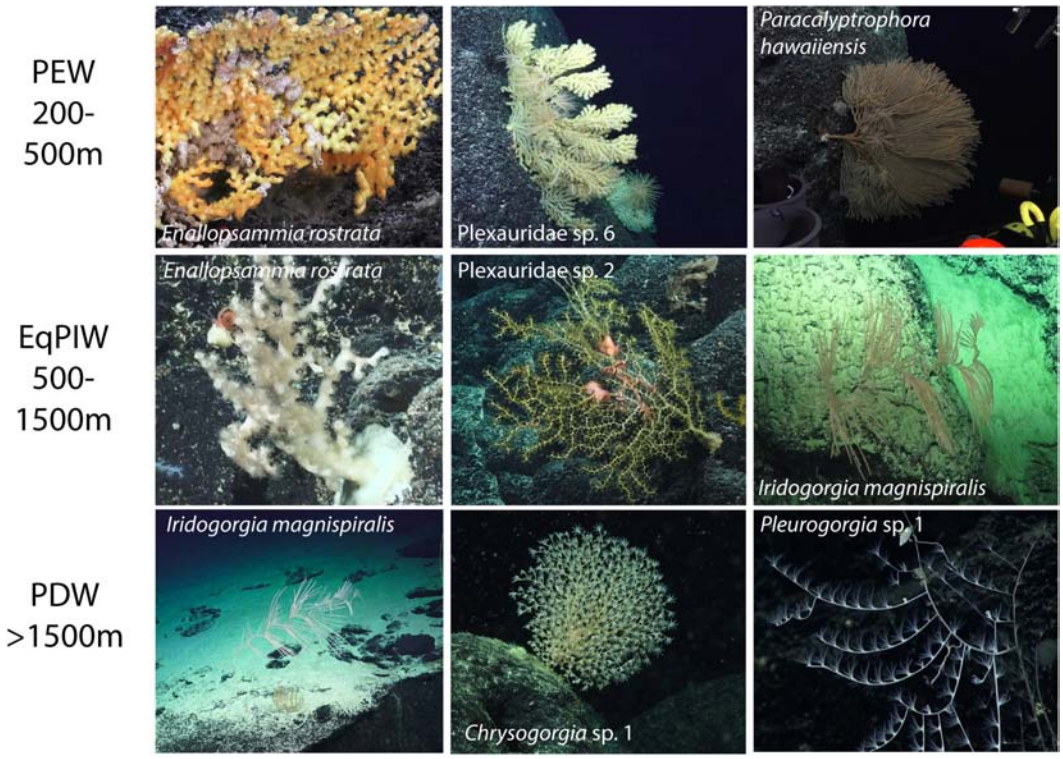

FIGURE 8 | Top 3 morphospecies with disproportionate influence on coral assemblage similarity within each water mass as a result of the SIMPER analysis. Morphospecies on the far left are the largest contributors to within-water mass similarity with influence rank decreasing toward the right.

2008). As temperature, salinity, and oxygen are the primary defining characteristics of major water masses (**Figure 3**), water masses themselves can be useful units for predicting deep-water species occurrences and community structure.

The role that water masses play in structuring biological communities in the deep-sea have been suggested as a major factor influencing species biogeography (Carney, 2005). In this study, differences were found to occur between coral assemblages bathed by PEW, EqPIW, and PDW indicating that oceanographic structure has a significant role in structuring communities. The pattern of within water mass similarities in species occurrence and community composition has been observed across multiple taxa including deep-water corals (Arantes et al., 2009; Miller et al., 2011; Radice et al., 2016), ostrocods (Ayress et al., 2004), and fishes (Quattrini et al., 2017). Furthermore, the boundaries of such water mass boundaries have been identified as important contributors to regional biodiversity in the deep ocean (Victorero et al., 2018). However, the mechanisms of why communities bear strong similarities within water masses are less clear but may include physical retention of planktotrophic larvae within water mass strata or relatively narrow physiological tolerances of species co-occurring within a water mass (Carney, 2005). The relationship between community similarities and water column structure requires further investigation to identify potential mechanisms driving such patterns.

Seamounts comprised the majority of features explored in this study and contained the greatest diversity of coral morphospecies of all feature types examined. Despite accounting for only 24% of all coral observations, seamounts hosted more than half of all morphospecies observed in this study. Diversity patterns on remote seamounts have been found to be strongly driven by species replacement along depth and temperature gradients, as well as topographic variability and along water mass interfaces (Victorero et al., 2018). From a population biogeographic perspective, seamounts may act as critical stepping stones for species distribution and population connectivity in the Pacific Ocean (Miller et al., 2011; Bors et al., 2012; Miller and Gunasekera, 2017). These baseline records of deep-sea coral abundance and diversity on seamounts in PIPA, as well as environmental factors driving community variation, will help generate new hypotheses for understanding benthic biodiversity on remote Pacific seamounts.

Insights to Bathyal Pacific Biogeography

The Phoenix Islands Protected Area lies in an area of the equatorial central Pacific that has been identified as a biodiversity and abundance hotspot for shallow-water marine organisms (Rotjan et al., 2014). At bathyal depths, benthic biodiversity is largely unknown and species inventories of deep-sea corals and sponges are lacking. One recently proposed biogeography of the bathyal regions of the Pacific suggests that the majority of seafloor features in PIPA lay in the BY14 (North Pacific Bathyal) biogeographic province (Watling et al., 2013). The PIPA boundaries also border the BY5 (Southeast Pacific Ridges),

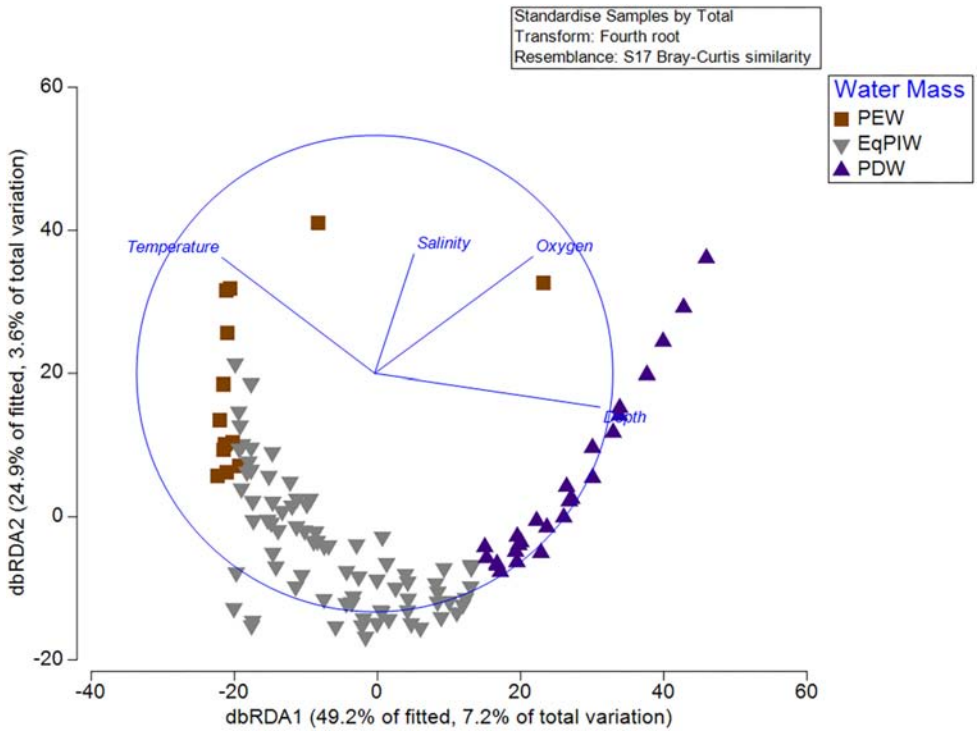

FIGURE 9 | Distance-based redundancy analysis (dbRDA) from standardized and 4th root-transformed species abundances and normalized depth, temperature, salinity, and dissolved oxygen variables. DistLM circle is superimposed in blue with depth, temperature, salinity, and dissolved oxygen vectors. Symbol color and shape denote overlying water mass for each sample.

BY6 (New Zealand – Kermadec), and BY12 (West Pacific Bathyal) provinces suggesting that this area represents an area of biogeographic overlap, transition, or convergence. Still, further specimen collections and seafloor observations are necessary in refining proposed province boundaries and expanding species inventories within those provinces at bathyal depths.

Several deep-water coral species were found to have widespread geographic distributions in Pacific Ocean, but mechanisms for those observed distribution patterns remain poorly understood. Cosmopolitan deep-water coral taxa including *Enallopsammia rostrata*, *Metallogorgia melanotrichos*, *Paragorgia* spp., *Hemicorallium* spp., *Pleurocorallium* sp., and *Iridogorgia* spp., and several members of the Primnoidae were present throughout multiple sites in the Phoenix Islands at depths below 1000 m providing a biogeographic continuity for species widely reported on seamounts in both the north and south Pacific Ocean (**Supplementary Table S1**). Some of these same species, like *Enallopsammia rostrata* and *Iridogorgia magnispiralis*, and were also found to exhibit a disproportionate effect on assemblage differences between water masses (**Figure 8**). As a major source of hard substrate, seamounts and seamount chains likely provide pathways for species distribution across equatorial latitudes.

The large geographic extent of Pacific bathyal water masses may also help explain the prevalence of cosmopolitan species in PIPA. In the central and north Pacific below 1500 m, PDW dominates much of the bathyal depth range but across tropical latitudes PDW contributes to the composition of EqPIW south of 20° N (Bostock et al., 2010). Environmental homogeneity and large geographic extent of PDW may provide a mechanism for species to become widely distributed within that water mass throughout the north Pacific Ocean while also extending their range southward via EqPIW. At the same time, mid-bathyal species in the southern hemisphere occurring in Antarctic Intermediate Water (AAIW) may be encountered in equatorial intermediate waters as this water mass contributes to EqPIW north of 20°S (Bostock et al., 2010). At upper bathyal depths, PEW (200–500 m) has been identified as having a well-developed circulation along the equator (Emery, 2001) which could provide a potential distribution mechanism for species among low-latitude seafloor features.

Noteworthy Observations

During both EX1703 and FK171005 expeditions, several collected specimens have been identified as new species and many others represent significant range extensions. Voucher samples were examined alongside records of visual observations to better understand the distribution of these species in their known localities (**Supplementary Table S1**). Recently, octocorals in the family Primnoidae have been relatively well-studied in the Pacific compared to other octocoral taxa, thus the majority of the new species encountered occur in that group (Cairns, 2018). In the genus *Narella*, two new species were described with material from sites within the Phoenix Islands. The type specimen

of *Narella fordi* Cairns (2018) was identified from Te Kaitira Seamount at 1899 m. This species was only been observed at Te Kaitira Seamount between the depths of 1817 and 1932 m. *Narella aurantiaca* Cairns (2018) was identified off Nikumaroro at 1112 m but also observed at McKean Island and Winslow Reef between 558 and 1105 m. This species was also encountered in the Musicians Seamounts and off Wake Island at similar depths (Cairns, 2018). *Narella compressa* Kinoshita, 1908, was identified off Carondelet Reef at 497 m and is likely the first record since its encounter in 1906 off Japan (Cairns, pers. comm.). *N. compressa* was observed and collected within PIPA at Carondelet Reef and Maibua Seamount between 373 and 583 m. One colony of *Thouarella tydemani* Versluys, 1906, a relatively rare species in that genus originally reported from Indonesia at 520 m, was only observed 33 times and sampled at Winslow Reef at 801 m. The sea fan, *Paracalyptrophora hawaiiensis* Cairns, 2009, was reported from the Phoenix Islands Protected Area between 445 and 666 m. Along with new records from Tokelau (Pao Pao Seamount), American Samoa, and Rawaki Island, this suggests *P. hawaiiensis* has a wider distribution throughout the southwest Pacific and north to Hawaii at upper bathyal depths (Cairns, 2018). *Calyptrophora clarki* Bayer, 1951 was observed 48 times and sampled 3 times between 418 and 1211 m in PIPA. Originally described from Hawaii, it has since been found in the Northern Mariana Islands and Phoenix Islands, representing a significant southward range extension. In the same genus, *Calyptrophora diaphana* Cairns, 2012 initially described off the North Island of New Zealand in 2012 was collected at a recorded depth of 1225 m at Orona Atoll but also was recently found around Wake Island in the western Pacific (Cairns, 2018). Only 4 colonies of *C. diaphana* were observed in total, all occurring at Orona Atoll.

Despite efforts to identify many deep-water coral species from physical specimens in PIPA, a significant number morphospecies as well as voucher collections from the 2017 expeditions remain unidentified to the species level. From the 167 morphospecies identified, only 39 species were identifiable to the species level from voucher collections. Nevertheless, some similarities were seen among morphotypes observed in imagery to those encountered elsewhere in the region as a part of the CAPSTONE expeditions (Kennedy et al., 2019). In this study, the abundant *Pleurogorgia* sp. 1 strongly resembles *Pleurogorgia militaris*, a widely distributed Pacific deep-water coral, but cannot yet be confirmed because specimens were not taken of this morphotype within PIPA. In addition, 8 morphospecies were identified as distinct in both the precious coral genus *Hemicorallium* as well as the genus *Victorgorgia* with none being identified to species yet. A significant number of collections were also made in the enigmatic octocoral families Plexauridae and Isididae but detailed morphological taxonomic keys for these families in the central and south Pacific are incomplete and require further attention. Recent efforts to revise the taxonomy of families and genera within the Octocorallia have provided significant contributions to our knowledge of deep-water coral diversity in the Pacific Ocean (Tu et al., 2016; Moore et al., 2017; Cairns, 2018). It is likely that as these specimens are more widely scrutinized using both molecular and morphological taxonomic tools, more species identifications can be determined.

Conservation Considerations

The Phoenix Islands Protected Area was designated as an ecologically and biologically significant area (EBSA) by the Convention on Biological Diversity[1] and, upon further examination, it is becoming increasingly clear that its biological significance extends well into the deep-sea. Still, deep-sea biodiversity on remote features is still threatened by several factors including the effects of climate-driven ocean change (Tittensor et al., 2010; Sweetman et al., 2017) as well as physical disturbance from fishing gear (Clark and Koslow, 2007; Clark et al., 2016), and marine debris. Since PIPA has been closed to most fishing since 2015, with the exception of a small subsistence fishery around Kanton, it has been largely isolated from these negative impacts (Rotjan et al., 2014). Still, seamounts in the western and central Pacific have been found to be aggregators for commercially-important large pelagic fishes (Morato et al., 2011). Debris from derelict longline fishing gear, which remain prevalent in the region (McDermott et al., 2018), have the potential to have far-reaching effects deep-water benthic communities.

Other more significant risks to deep-sea coral conservation in the region include direct disturbance to the seafloor in the form of deep-sea mineral crust mining. Recently, commercial mining of ferromanganese crusts accumulating on seamounts have been proposed as a way to extract mineral resources (Hein et al., 2013; Miller et al., 2018). Detailed biological characterizations and species inventories for much of the adjacent Pacific Prime Crust Zone and south Pacific seamounts with cobalt-rich mineral crusts are critically lacking (Schlacher et al., 2014). As crust attributes are difficult to estimate from ROV video transects, it remains a question where deep-water coral communities lie with respect to areas that harbor economically viable mineral crusts in the Phoenix Islands, but crust habitats in the South Pacific have been found to be important indicators of sensitive deep-sea communities (Delavenne et al., 2019). The precautionary approach should be applied to these resources to conserve seamount benthic communities for their biodiversity, unique evolutionary histories, and ecosystem services.

DATA AVAILABILITY STATEMENT

The datasets generated for this study are available on request to the corresponding author.

AUTHOR CONTRIBUTIONS

The research was conceived and designed by EC, RR, TS, and SA. Fieldwork was conducted by SA, RR, EC, TS, and AK. SA, MD, and AK performed the video review and annotations. SA performed data quality control and statistical analyses. Figures and tables were created by SA with support from MD and AK. All authors contributed to the writing and editing of the final manuscript.

[1] https://www.cbd.int/ebsa/

FUNDING

Funding for this work was provided by NOAA Office of Ocean Exploration and Research (Grant No. NA17OAR0110083) to RR, EC, TS, and David Gruber.

ACKNOWLEDGMENTS

We would like to thank the Schmidt Ocean Institute for ship time on the R/V *Falkor* during FK171005, *Discovering Deep-Sea Corals of the Phoenix Islands*, and to the science party and crew of this expedition for their efforts. We would also thank the expedition coordinator B. Kennedy, science co-lead A. Demopoulos, science party, as well as the crew of the NOAA ship *Okeanos Explorer* during the EX-17-03 *Discovering the Deep: Exploring Remote Pacific Marine Protected Areas* expedition. Taxonomic assistance was provided by S. Cairns. We would like to extend our deepest gratitude to the Republic of Kiribati for the opportunity to work in the Phoenix Islands under permits PFA3 No. 1/17 and 4/17 issued by the PIPA Implementation Office. We also thank Mr. Betarim Rimon and Mr. Arenteiti Tekiau, who were the official Kiribati Observers on the EX-1703 and FK171005 cruises, respectively. Finally, we would like to thank three manuscript reviewers for their input in greatly improving the quality of this manuscript.

SUPPLEMENTARY MATERIAL

The Supplementary Material for this article can be found online at: https://www.frontiersin.org/articles/10.3389/fmars.2020.00042/full#supplementary-material

REFERENCES

Anderson, M., Gorley, R. N., and Clarke, R. K. (2008). *Permanova+ for Primer: Guide to Software and Statisticl Methods*. Plymouth: Primer-E Limited.

Arantes, R. C. M., Castro, C. B., Pires, D. O., and Seoane, J. C. S. (2009). Depth and water mass zonation and species associations of cold-water octocoral and stony coral communities in the southwestern Atlantic. *Mar. Ecol. Prog. Ser.* 397, 71–79. doi: 10.3354/meps08230

Auster, P. J., Moore, J., Heinonen, K. B., and Watling, L. (2005). "A habitat classification scheme for seamount landscapes: assessing the functional role of deep-water corals as fish habitat," in *Cold-Water Corals and Ecosystems*, eds A. Freiwald, and J. M. Roberts, (Cham: Springer), 761–769. doi: 10.1007/3-540-27673-4_40

Ayress, M. A., De Deckker, P., and Coles, G. P. (2004). A taxonomic and distributional survey of marine benthonic Ostracoda off Kerguelen and Heard Islands, South Indian Ocean. *J. Micropalaeontol.* 23, 15–38. doi: 10.1144/jm.23.1.15

Bohnenstiehl, D. R., France, S. C., Cantwell, K., and White, M. (2018). Mountains in the deep: exploration of the seamounts of the Central Pacific Basin. *Oceanography* 31, 78–79.

Bors, E. K., Rowden, A. A., Maas, E. W., Clark, M. R., and Shank, T. M. (2012). Patterns of deep-sea genetic connectivity in the New Zealand region: implications for management of benthic ecosystems. *PLoS One* 7:e49474. doi: 10.1371/journal.pone.0049474

Bostock, H. C., Opdyke, B. N., and Williams, M. J. M. (2010). Characterising the intermediate depth waters of the Pacific Ocean using d 13 C and other geochemical tracers. *Deep Res. Part I* 57, 847–859. doi: 10.1016/j.dsr.2010.04.005

Buhl-Mortensen, L., Vanreusel, A., Gooday, A. J., Levin, L. A., Priede, I. G., Buhl-Mortensen, P., et al. (2010). Biological structures as a source of habitat heterogeneity and biodiversity on the deep ocean margins. *Mar. Ecol.* 31, 21–50. doi: 10.1111/j.1439-0485.2010.00359.x

Cairns, S. D. (2018). Primnoidae (Cnidaria: Octocorallia: Calcaxonia) of the okeanos explorer expeditions (CAPSTONE) to the central Pacific. *Zootaxa* 4532, 1–43. doi: 10.11646/zootaxa.4532.1.1

Cantwell, K., Elliott, K., and Kennedy, B. R. C. (2018). Deepwater exploration of the pacific remote islands marine national monument and Central Pacific Basin. *Oceanography* 31, 74–75.

Carney, R. S. (2005). Zonation of deep biota on continental margins. *Oceanogr. Mar. Biol.* 43, 211–278. doi: 10.1201/9781420037449.ch6

Clark, M. R., Althaus, F., Schlacher, T. A., Williams, A., Bowden, D. A., and Rowden, A. A. (2016). The impacts of deep-sea fisheries on benthic communities: a review. *ICES J. Mar. Sci.* 73, i51–i69. doi: 10.1093/icesjms/fsv123

Clark, M. R., and Koslow, J. A. (2007). Impacts of fisheries on seamounts. *Seamounts Ecol. Fish. Conserv.* 12, 413–441. doi: 10.1002/9780470691953.ch19

Clark, M. R., Rowden, A. A., Schlacher, T., Williams, A., Consalvey, M., Stocks, K. I., et al. (2010). The ecology of seamounts: structure, function, and human impacts. *Ann. Rev. Mar. Sci.* 2, 253–278. doi: 10.1146/annurev-marine-120308-081109

Clarke, K. R., and Gorley, R. N. (2006). *User Manual/Tutorial*. Plymouth: Primer-E Limited.

Clarke, K. R., Somerfield, P. J., and Gorley, R. N. (2008). Testing of null hypotheses in exploratory community analyses: similarity profiles and biota-environment linkage. *J. Exp. Mar. Bio. Ecol.* 366, 56–69. doi: 10.1016/j.jembe.2008.07.009

Claudino-Sales, V. (2019). *Coastal World Heritage Sites*. Cham: Springer, 355–360.

Delavenne, J., Keszler, L., Castelin, M., Lozouet, P., Maestrati, P., and Samadi, S. (2019). Deep-sea benthic communities in the largest oceanic desert are structured by the presence of polymetallic crust. *Sci. Rep.* 9, 1–11. doi: 10.1038/s41598-019-43325-0

Demopoulos, A. W. J., Auscavitch, S., Sowers, D., Pawlenko, N., and Kennedy, B. R. C. (2018). Discovering the deep: exploring remote Pacific marine protected areas. *Oceanography* 31, 76–77.

Emery, W. J. (2001). Water types and water masses. *Encycl. Ocean Sci.* 6, 3179–3187. doi: 10.1006/rwos.2001.0108

Etnoyer, P. J., Wood, J., and Shirley, T. C. (2010). BOX 12| how large is the seamount biome? *Oceanography* 23, 206–209. doi: 10.5670/oceanog.2010.96

Genin, A., Dayton, P. K., Lonsdale, P. F., and Spiess, F. N. (1986). Corals on seamount peaks provide evidence of current acceleration over deep-sea topography. *Nature* 322, 59–61. doi: 10.1038/322059a0

Gollner, S., Kaiser, S., Menzel, L., Jones, D. O. B., Brown, A., Mestre, N. C., et al. (2017). Resilience of benthic deep-sea fauna to mining activities. *Mar. Environ. Res.* 129, 76–101. doi: 10.1016/j.marenvres.2017.04.010

Hein, J. R., Mizell, K., Koschinsky, A., and Conrad, T. A. (2013). Deep-ocean mineral deposits as a source of critical metals for high- and green-technology applications: comparison with land-based resources. *Ore Geol. Rev.* 51, 1–14. doi: 10.1016/j.oregeorev.2012.12.001

Herrera, S., Jackson, M., Konter, J., Lobecker, E., and Elliott, K. (2018). 2017 American samoa expedition: suesuega o le moana Amerika Samoa. *Oceanography* 31, 72–73.

Kelley, C., Mah, C., Malik, M., and Elliott, K. (2018). Laulima O Ka moana: exploring deep monument waters around johnston atoll. *Oceanography* 31, 80–81.

Kennedy, B. R. C., Cantwell, K., Malik, M., Kelley, C., Potter, J., Elliott, K., et al. (2019). The unknown and the unexplored: insights into the pacific deep-sea following NOAA CAPSTONE expeditions. *Front. Mar. Sci.* 6:480. doi: 10.3389/fmars.2019.00480

Mangubhai, S., Lovell, E., Abeta, R., Donner, S., Redfern, F. M., O'Brien, M., et al. (2019). "Kiribati: atolls and marine ecosystems," in *World Seas: An Environmental Evaluation*, ed. C. Sheppard, (Amsterdam: Elsevier), 807–826. doi: 10.1016/b978-0-08-100853-9.00054-3

McDermott, G. R., Meng, K. C., Mcdonald, G. G., and Costello, C. J. (2018). The blue paradox: preemptive overfishing in marine reserves. *Proc. Natl. Acad. Sci. U.S.A.* 116, 5319–5325. doi: 10.1073/pnas.1802862115

McKinnie, D., Rotjan, R., and Peau, A. L. (2018). Exploring the Pacific through international partnerships. *Oceanography* 31, 86–87.

Miller, K. A., Thompson, K. F., Johnston, P., and Santillo, D. (2018). An overview of seabed mining including the current state of development, environmental impacts, and knowledge gaps. *Front. Mar. Sci.* 4:418. doi: 10.3389/fmars.2017.00418

Miller, K. J., and Gunasekera, R. M. (2017). A comparison of genetic connectivity in two deep sea corals to examine whether seamounts are isolated islands or stepping stones for dispersal. *Sci. Rep.* 7, 1–14. doi: 10.1038/srep46103

Miller, K. J., Rowden, A. A., Williams, A., and Haussermann, V. (2011). Out of their depth? Isolated deep populations of the cosmopolitan coral Desmophyllum dianthus may be highly vulnerable to environmental change. *PLoS One* 6:e19004. doi: 10.1371/journal.pone.0019004

Moore, K. M., Alderslade, P., and Miller, K. J. (2017). A taxonomic revision of *Anthothela* (Octocorallia: Scleraxonia: Anthothelidae) and related genera, with the addition of new taxa, using morphological and molecular data. *Zootaxa* 4304, 1–212.

Morato, T., Hoyle, S. D., Allain, V., and Nicol, S. J. (2011). Tuna longline fishing around west and central Pacific seamounts. *PLoS One* 5:e14453. doi: 10.1371/journal.pone.0014453

Morgan, N. B., Cairns, S., Reiswig, H., and Baco, A. R. (2015). Benthic megafaunal community structure of cobalt-rich manganese crusts on Necker Ridge. *Deep Sea Res. Part I Oceanogr. Res. Pap.* 104, 92–105. doi: 10.1016/j.dsr.2015.07.003

Mosher, C. V., and Watling, L. (2009). Partners for life: a brittle star and its octocoral host. *Mar. Ecol. Prog. Ser.* 397, 81–88. doi: 10.3354/meps08113

OBIS (2019). *Ocean Biogeographic Information System*. Paris: UNESCO.

Obura, D., Stone, G., Mangubhai, S., Bailey, S., Yoshinaga, H., and Barrel, R. (2011). Baseline marine biological surveys of the Phoenix Islands, July 2000. *Atoll Res. Bull.* 589, 1–61. doi: 10.5479/si.00775630.589.1

Oksanen, J., Blanchet, F. G., Kindt, R., Legendre, P., Minchin, P. R., O'hara, R. B., et al. (2015). *Package 'Vegan.' Community Ecol. Packag. Version 2*.

Quattrini, A. M., Demopoulos, A. W. J., Singer, R., Roa-Varon, A., and Chaytor, J. D. (2017). Demersal fish assemblages on seamounts and other rugged features in the northeastern Caribbean. *Deep Sea Res. Part I Oceanogr. Res. Pap.* 123, 90–104. doi: 10.1016/j.dsr.2017.03.009

Radice, V. Z., Quattrini, A. M., Wareham, V. E., Edinger, E. N., and Cordes, E. E. (2016). Vertical water mass structure in the North Atlantic influences the bathymetric distribution of species in the deep-sea coral genus *Paramuricea*. *Deep Sea Res. Part I Oceanogr. Res. Pap.* 116, 253–263. doi: 10.1016/j.dsr.2016.08.014

Rogers, A. D. (2018). The biology of seamounts: 25 Years on. *Adv. Mar. Biol.* 79, 137–224. doi: 10.1016/BS.AMB.2018.06.001

Rogers, A. D., Baco, A., Griffiths, H., and Hall-Spencer, J. M. (2007). "Corals on seamounts," in *Seamounts: Ecology Fisheries and Conservation, Blackwell Fisheries and Aquatic Resources Series*, eds T. J. Pitcher, T. Morato, P. J. B. Hart, M. R. Clark, N. Haggan, and R. S. Santos, (Oxford: Blackwell Scientific), 3343–3352.

Rotjan, R., Jamieson, R., Carr, B., Kaufman, L., Mangubhai, S., Obura, D., et al. (2014). Establishment, management, and maintenance of the phoenix islands protected area. *Adv. Mar. Biol.* 69, 289–324. doi: 10.1016/B978-0-12-800214-8.00008-6

Rotjan, R., and Obura, D. (2010). *Phoenix Islands Protected Area 10-Year Research Vision*. Boston, MA: New England Aquarium.

Schlacher, T. A., Baco, A. R., Rowden, A. A., O'Hara, T. D., Clark, M. R., Kelley, C., et al. (2014). Seamount benthos in a cobalt-rich crust region of the central P acific: conservation challenges for future seabed mining. *Divers. Distrib.* 20, 491–502. doi: 10.1111/ddi.12142

Schlitzer, R. (2019). *Ocean Data View*. Available at: https://odv.awi.de/ (accessed May 29, 2019).

Shank, T. M. (2010). Seamounts: deep-ocean laboratories of faunal connectivity, evolution, and endemism. *Oceanography* 23, 108–122. doi: 10.5670/oceanog.2010.65

Sweetman, A. K., Thurber, A. R., Smith, C. R., Levin, L. A., Mora, C., Wei, C.-L., et al. (2017). Major impacts of climate change on deep-sea benthic ecosystems. *Elem. Sci. Anth.* 5:4. doi: 10.1525/elementa.203

Tittensor, D. P., Baco, A. R., Hall-Spencer, J. M., Orr, J. C., and Rogers, A. D. (2010). Seamounts as refugia from ocean acidification for cold-water stony corals. *Mar. Ecol.* 31, 212–225. doi: 10.1111/j.1439-0485.2010.00393.x

Tu, T.-H., Dai, C.-F., and Jeng, M.-S. (2016). Taxonomic revision of Coralliidae with descriptions of new species from New Caledonia and the Hawaiian Archipelago. *Mar. Biol. Res.* 12, 1003–1038. doi: 10.1080/17451000.2016.1241411

Victorero, L., Robert, K., Robinson, L. F., Taylor, M. L., and Huvenne, V. A. I. (2018). Species replacement dominates megabenthos beta diversity in a remote seamount setting. *Sci. Rep.* 8:4152. doi: 10.1038/s41598-018-22296-8

Watling, L., and Auster, P. J. (2017). Seamounts on the high seas should be managed as vulnerable marine ecosystems. *Front. Mar. Sci.* 4:14. doi: 10.3389/fmars.2017.00014

Watling, L., Guinotte, J., Clark, M. R., and Smith, C. R. (2013). A proposed biogeography of the deep ocean floor. *Prog. Oceanogr.* 111, 91–112. doi: 10.1016/j.pocean.2012.11.003

Watling, L., and Norse, E. A. (1998). Disturbance of the seabed by mobile fishing gear: a comparison to forest clearcutting. *Conserv. Biol.* 12, 1180–1197. doi: 10.1046/j.1523-1739.1998.0120061180.x

Williams, A., Schlacher, T. A., Rowden, A. A., Althaus, F., Clark, M. R., Bowden, D. A., et al. (2010). Seamount megabenthic assemblages fail to recover from trawling impacts. *Mar. Ecol.* 31, 183–199. doi: 10.1111/j.1439-0485.2010.00385.x

Conflict of Interest: The authors declare that the research was conducted in the absence of any commercial or financial relationships that could be construed as a potential conflict of interest.

Copyright © 2020 Auscavitch, Deere, Keller, Rotjan, Shank and Cordes. This is an open-access article distributed under the terms of the Creative Commons Attribution License (CC BY). The use, distribution or reproduction in other forums is permitted, provided the original author(s) and the copyright owner(s) are credited and that the original publication in this journal is cited, in accordance with accepted academic practice. No use, distribution or reproduction is permitted which does not comply with these terms.

frontiers in Marine Science

ORIGINAL RESEARCH
published: 21 February 2020
doi: 10.3389/fmars.2020.00108

Discovery and Mapping of the *Triton* Seep Site, *Redondo Knoll*: Fluid Flow and Microbial Colonization Within an Oxygen Minimum Zone

*Jamie K. S. Wagner[1], Clara Smart[2] and Christopher R. German[3]**

[1] Department of Biology, Duke University, Durham, NC, United States, [2] Applied Physics Laboratory, Johns Hopkins University, Laurel, MD, United States, [3] Woods Hole Oceanographic Institution, Woods Hole, MA, United States

This paper examines a deep-water (∼900 m) cold-seep discovered in a low oxygen environment ∼30 km off the California coast in 2015 during an E/V *Nautilus* telepresence-enabled cruise. This *Triton* site was initially detected from bubble flares identified via shipboard multibeam sonar and was then confirmed visually using the remotely operated vehicle (ROV) *Hercules*. High resolution mapping (to 1 cm resolution) and co-registered imaging has provided us with a comprehensive site overview – both of the geologic setting and the extent of the associated microbial colonization. The *Triton* site represents an active cold-seep where microorganisms can act as primary producers at the base of a chemosynthesis-driven food chain. But it is also located near the core of a local oxygen minimum zone (OMZ), averaging <0.75 μM oxygen, which is significantly below average ocean levels (180–270 μM) and, indeed, extreme even among OMZs as a whole which are defined to occur at all oxygen concentrations <22 μM. Extensive microbial mats, extending for >100 m across the seafloor, dominate the site, while typical seep-endemic macro-fauna were noticeably absent from our co-registered photographic and high-resolution mapping surveys – especially when compared to all adjacent seep sites within the same California Borderlands region. While such absences of abundant macro-fauna could be attributable to variations in the availability of dissolved oxygen in the overlying water column this need not necessarily be the case. An alternate possibility is that the zonation in microbial activity that is readily observable at the seafloor at *Triton* reflects, instead, a concentric pattern of radially diminishing fluxes of reductants from the underlying seafloor. This unusual but readily accessible discovery, in close proximity to Los Angeles harbor, provides an intriguing new natural laboratory at which to examine biogeochemical and microbiological interactions associated with the functioning of cold seep ecosystems within an OMZ.

Keywords: cold seep, oxygen minimum zone, California Borderlands, microbial mats, continental margin

OPEN ACCESS

Edited by:
Randi D. Rotjan,
Boston University, United States

Reviewed by:
Florence Schubotz,
University of Bremen, Germany
Haley M. Sapers,
California Institute of Technology,
United States

***Correspondence:**
Christopher R. German
cgerman@whoi.edu

Specialty section:
This article was submitted to Deep-Sea Environments and Ecology, a section of the journal Frontiers in Marine Science

Received: *02 April 2019*
Accepted: *10 February 2020*
Published: *21 February 2020*

Citation:
Wagner JKS, Smart C and German CR (2020) Discovery and Mapping of the Triton Seep Site, Redondo Knoll: Fluid Flow and Microbial Colonization Within an Oxygen Minimum Zone. Front. Mar. Sci. 7:108. doi: 10.3389/fmars.2020.00108

INTRODUCTION

Historically, our understanding of cold seep distributions and their attendant chemosynthetic fauna (e.g. Sibuet and Olu, 1998) was limited due to the cost, time, and technology required for systematic search patterns. However, more accessible and higher resolution modern multibeam bathymetric approaches allow detection of gas-rich bubble flares in the water column rising above cold-seep

sites that can be traced very efficiently back to their seafloor source (Merewether et al., 1985; Weber et al., 2012; Skarke et al., 2014; Levin et al., 2016). In this study, we utilized these techniques to locate a unique environment off the Los Angeles coast, which, despite its proximity to a major U.S. city, had yet to be visually explored. In this paper, we report the discovery of this ∼30 m × 40 m *Triton* site, which exhibits the dual redox-active characteristics of being a gas-rich seep site that is located within the core of an oxygen minimum zone (OMZ).

Along the Pacific coast of North and South America the majority of cold seeps located, to-date, have been characterized by various combinations of soft sediments, exposed authigenic carbonates, methane-rich fluid flow, microbial mats, and endemic megafauna. In the case of cold seeps located along the U.S. West Coast, the predominant megafauna reported from such sites are vesicomyid clams, although vestimentiferan tubeworms and diverse less abundant megafauna (including solemyid clams, galatheid crabs, limpets, and snails) have also been described, as well as a diversity of macrofaunal and meiofaunal species (e.g. Barry et al., 1996; Levin et al., 2003, 2010; Grupe et al., 2015).

Oxygen minimum zones are widespread along the eastern Pacific Ocean, where the dissolved oxygen concentration falls <22 μM, equivalent to 0.5 mg/L (Helly and Levin, 2004; Karstensen et al., 2008), in comparison to 180–270 μM (4–6 mg/L) typically found in the ocean. Strong upwelling of nutrients along the continental slope results in rapid growth of phytoplankton and zooplankton biomass, which then sinks and decomposes, overwhelming the rate of dissolved oxygen resupply during the degradation process (Wyrtki, 1962; Karstensen et al., 2008). In combination with reduced circulation and mixing, stratification can create a persistent zone of low oxygen levels within the water column, typically within the 200–1000 m depth range (Levin, 2003). Along the Eastern Pacific boundary, such OMZs repeatedly intersect the continental slope, affecting benthic ecosystems by limiting fauna and decreasing diversity within the zones. Helly and Levin (2004) estimated that there are >1 million km^2 of shelf and seafloor along the margins of the eastern Pacific, western Atlantic, and Indian Ocean basins under permanent OMZ conditions.

In this study, we report the discovery of a particularly interesting site of seafloor fluid flow that appears unique, at least among the California Borderlands seep-sites: a chemosynthetic ecosystem located at the base of *Redondo Knoll*, ∼30 km from Los Angeles, that is situated at the same depth as the core of the local OMZ. Using state of the art mapping techniques we have achieved high resolution imaging and mapping (at better than 1 cm resolution), which is rare for such environments and has allowed us to complete a detailed examination of the site's surface morphology and its associated microbial colonization without perturbing the pristine ecosystem.

GEOLOGICAL SETTING

The California Borderlands extend up to 200 km offshore from the densely populated California coastline and display an unusually rugged topography for a continental margin. They are made up of a series of deep (500–2,000 m) basins separated by shallow ridges – some of which outcrop above sea level as islands, such as Catalina Island. Surprisingly, this area of seafloor has only been sparsely investigated, and while there has been extensive mapping undertaken by ships passing through the region along transits of opportunity (the area underlies a major shipping route between Los Angeles harbor and the port of San Francisco) what has remained lacking, to date, is a comprehensive and systematic campaign to map this complex region of seafloor, despite its proximity to metropolitan Los Angeles. Geologically, the California Borderlands are a component of the same Pacific/North American tectonic plate boundary as the San Andreas Fault (SAF). But while the latter, which lies above sea-level, is now increasingly well characterized, about 20% of all plate motion associated with the SAF system takes place offshore within the relatively poorly studied California Borderlands. This includes multiple sub-orthogonal faults that extend from onshore through the Los Angeles metropolitan area to offshore across the shelf and margin, representing a major potential earthquake and coastal tsunami hazard. While much of the seafloor of the California Borderlands remains unmapped, our work illustrates that the tectonic faults crossing this highly tectonized region of seafloor also have the potential to host a diversity of styles of seafloor fluid flow, sustaining associated chemosynthetic biological communities.

The *Redondo Knoll* (**Figure 1**) represents just one of numerous uplifted blocks of seafloor within the larger California Borderlands area. It is centered at ∼33°45′N, 118°40′W, ∼30 km

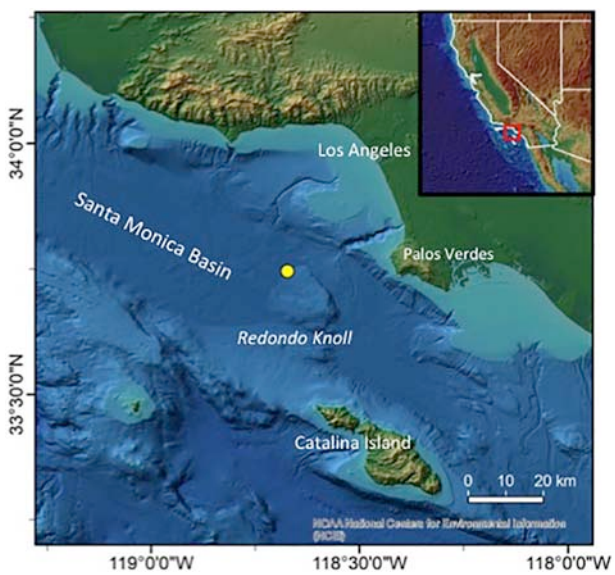

FIGURE 1 | Study location. Inset overview map **(upper right)** shows the location of our study area within the California Borderlands region, SW United States. The larger map (seafloor topography derived primarily from satellite altimetry) shows the *Redondo Knoll*, ∼30 km offshore from Palos Verdes (CA), north of Catalina Island, and at the south east limit of the Santa Monica Basin. *Triton*, the cold-seep site discussed in this paper, is located at the base of *Redondo Knoll*, on its NW side, at ∼900 m depth (yellow circle).

North of Catalina Island's most northwestern limit and <30 km west of Palos Verdes, CA, United States. As such, it defines the southeastern limit of the deep Santa Monica Basin, which extends NW for ≥70 km. A flare appearing within the multibeam water column data, diagnostic of active gas bubble release, was identified toward the base of the Knoll on its NW side (i.e. at the south-east limit of the Santa Barbara basin) during multibeam mapping within the California Borderlands region in 2015. Tracing the acoustic signals to the seafloor indicated a location immediately adjacent to the primary shipping lanes between Los Angeles and San Francisco. The source of the active fluid flow, together with associated microbial colonization, was confirmed at ∼900 m depth during a subsequent dive with the ROV *Hercules*.

MATERIALS AND METHODS

E/V *Nautilus*

The tandem ROVs *Hercules* (**Figure 2A**) and *Argus*, deployed from E/V *Nautilus* (Ocean Exploration Trust), were used for exploring, imaging, and surveying the *Triton* site. Data for this study were collected during E/V *Nautilus* Cruise NA067 in August 2015, on ROV *Hercules* dive H1461 (Levin et al., 2016). The *Triton* seep site, hosting active fluid flow and associated microbial colonization, was centered at 33°45′N, 118°40′W.

Seafloor mapping was initially conducted from the E/V *Nautilus* using a hull mounted Kongsberg EM 302 multibeam sonar system. Operating at 30 Hz, this system is capable of gathering bathymetric data at depths of up to 7000 m, resulting in grid resolutions of up to 1% of water depth. Resulting seafloor data products include bathymetry maps and acoustic backscatter, which can be useful for investigating geologic processes at the seafloor including changes in sediment cover (thickness and composition). Additionally, data collected within the water column can indicate differentials in acoustic impedance, thus allowing for the detection of rising "bubble-flares" indicative of gas-rich seafloor seep activity (e.g., Merewether et al., 1985). Bubbles rising from a vigorous seep are typically apparent within two to five sequential multibeam water column fan images and can be identified at rise-heights of tens to hundreds of meters above the seafloor. Correlation between acoustic water column images and the ships differential GPS allows for the positions of the seeps that produce these detected gas bubble "flares" to be located precisely at the underlying seafloor. In this study, sonar data from the EM302 multibeam system revealed bubbles rising through the water column over the NW corner of *Redondo Knoll*. Once it had been confirmed to be a previously unknown seep site, the target was located and selected for detailed seafloor exploration using the ROV *Hercules*.

ROV *Hercules* Systems

A forward mounted high definition video camera (Deep Sea Power and Light) was used for site reconnaissance and for recording video footage. Additional sensors included a Sea-Bird FastCAT 49 conductivity, temperature, and depth sensor (CTD), an Aanderaa 3830 Oxygen sensor, and a temperature probe (0–450°C).

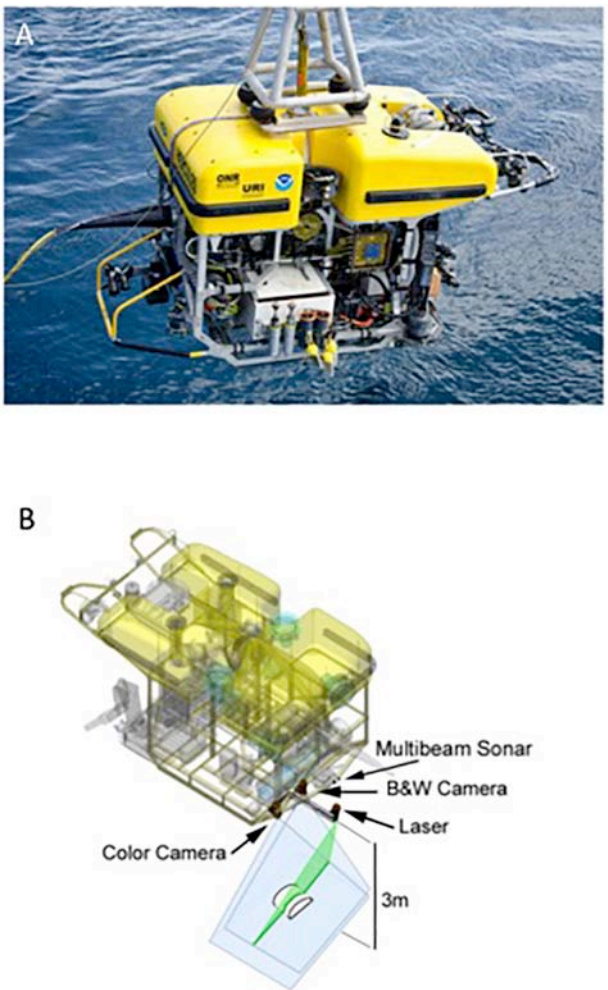

FIGURE 2 | ROV Hercules **(A)** during deployment. The imaging suite is mounted on the aft of the vehicle. **(B)** CAD drawing showing the high resolution imaging system and sensor footprints.

Mapping and imaging surveys at the *Triton* site were conducted using a state-of-the-art high resolution imaging suite (Inglis et al., 2012; Roman et al., 2012) mounted on the ROV *Hercules* (**Figure 2**). Optical and acoustic data for centimeter resolution bathymetric and photographic maps were collected to gain a spatial understanding of the site both visually and bathymetrically. Color and monochromatic stereo images were collected with two 12-bit Prosilica GC1380 computer vision cameras. The structured light laser sensor, for high resolution bathymetric data collection, consists of a 12-bit mono Prosilica GC1380 camera and verged 100 mW 532 nm Coherent PowerLine sheet laser mounted on a rigid frame with known relative geometry. The stereo camera frame rate was 0.33 Hz, interlacing images with the structured light laser system, collecting images at 20 Hz. Acoustic bathymetric data were collected by a 1350 kHz BlueView multibeam sonar system. Placing the imaging suite at the back of the vehicle separated it from the forward mounted operational HD video camera

and lights to minimize lighting artifacts. All imaging data were collected simultaneously and, hence, were both navigationally and temporally co-registered.

During high resolution imaging surveys, a closed loop control system on the ROV was used to complete organized track-line surveys at prescribed velocities and altitudes. High-resolution mapping data that could be gridded at a sub-centimeter scale were collected from 3 m above the seafloor along track-lines completed at a velocity of 0.15–0.20 m/s. The navigation sensor suite included a 600 kHz Teledyne RDI Doppler velocity log (DVL), a Paroscientific pressure depth sensor, and an IXSEA Octans fiber optic gyro system for heading and attitude information.

Note that all capabilities of the investigations described here were non-invasive, by design, and involved no physical interactions with the seafloor. Because the site discovery was unexpected and because we did not have the equipment and expertise aboard ship to fully process any samples for fluid geochemistry or microbiology it was decided to preserve the site in pristine and unperturbed condition to await dedicated future process-oriented studies.

RESULTS

Overview of the *Triton* Seep Site

The *Triton* site located just off the California coast exhibits features characteristic of a cold seep fluid flow site hosting associated microbial colonization but it is simultaneously located at the core of an OMZ. An initial exploration transect of the area with the ROV, oriented approximately from East to West, progressed from flat tan sediment onto a region of rougher, and rising/shallowing seafloor covered in extensive white microbial mats (**Figure 3A**). Continuing west toward a bubble target detected by *Hercules*' forward-looking sonar, the ROV next encountered a sharp drop in terrain that was coincident with a marked change in the color of the microbial mats draped over the seafloor from white to a bright yellow–orange color (**Figure 3B**). Toward the center of this low-lying area covered with thick yellow–orange mats (subsequently revealed to be the floor of a quasi-circular "crater") were a series of deeper ∼1–2 m diameter pits exposing dark gray sediment that were devoid of any visible evidence for microbial life. Vigorous plumes of bubbles were observed rising from at least one of these pits (**Figure 3C**), coincident with where the original shipboard multibeam survey had predicted that the source of the water column "flare" should occur. Subsequently, an imaging survey of the entire site (see next section) revealed that this same observational sequence was repeated in all directions away from the center of the site with quasi-radial symmetry (**Figures 4**, **5**). The microbial mats extended for ∼135 m in the longest dimension. Located at close to 900 m water depth, close to the base of the East Pacific OMZ (Helly and Levin, 2004), what was perhaps just as notable as the presence of abundant microbial mats across this seep site was the corresponding absence of abundant endemic seep megafauna. This represented a striking contrast to adjacent seep sites at other depths studied within the California Borderlands region as part of the same expedition (Levin et al., 2016). The only evidence for multi-cellular organisms observed at the *Triton* site were dark red cnidarians (jellies) swimming in the overlying water column and small kelp falls, covered in microbial mat, at the seafloor.

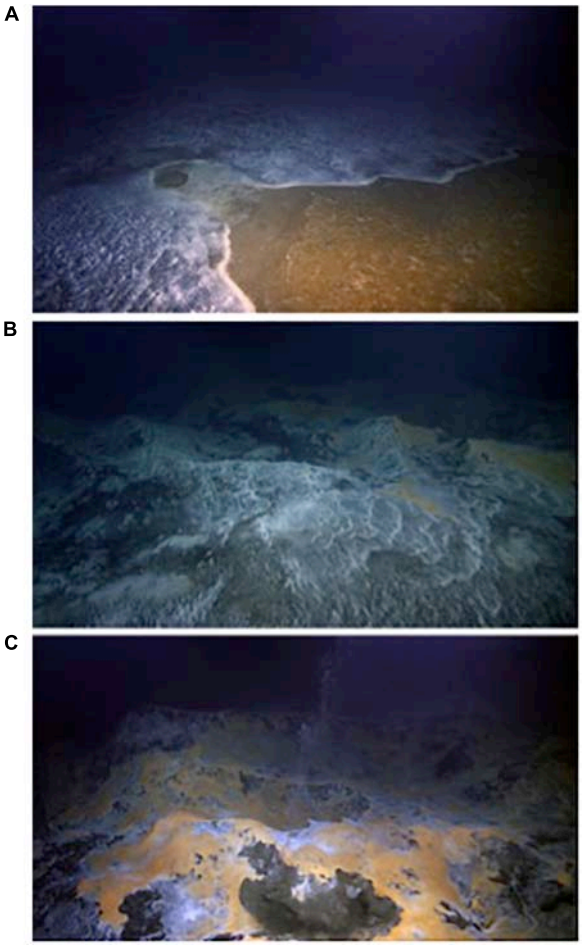

FIGURE 3 | *Triton* seep overview. Still images captured from the forward looking HD Video Camera mounted on ROV Hercules during a preliminary ∼E-W reconnaissance transect across the *Triton* mud volcano seep site at the base of *Redondo Knoll*. **(A)** At the periphery of the site, monotonous brown sediment transitions into rising terrain covered in extensive white microbial mats; **(B)** closer to the center of the site, there is a sharp transition across the rim of a pronounced depression (∼10 m in diameter, 0.5 m deep) from white to brightly colored yellow–orange microbial mat covering the inner walls and floor of the mud volcano; and **(C)** at the center of the site, a vigorous bubble plume was observed rising from a pit of dark gray sediment that was devoid of any visible microbial life. Copyright Ocean Exploration Trust, Inc.

High-Resolution Spatial Surveys of the *Triton* Seep Site

Following our initial ROV reconnaissance transect, a 30 m × 40 m area that included the actively bubbling seep was mapped using the high-resolution imaging suite outlined in the Materials and Methods section. A north-south "raster" survey pattern was established, which was completed at a vehicle altitude of 3 m above the seafloor and at a programed velocity

FIGURE 4 | Photomosaic of the *Triton* cold seep site. An ∼30 × 40 m area centered on the site of active fluid flow was selected for co-registered imaging and high resolution mapping surveys. This photomosaic is comprised of approximately 1500 color images. Within this image white microbial mats cover the gently upward sloping seafloor while within the center of the image, the steep-walled depression around the active seep exhibits higher rugosity and the microbial mats coating the walls and floor of that depression are a bright yellow–orange in color. Images were taken at an elevation of 3 m above the seafloor. Co-registered bathymetry is shown in **Figure 5**.

of 0.18 m/s. The resulting photomosaic (**Figure 4**) comprises approximately 1500 separate color still images. To create a bathymetric map from the same survey, the structured light laser data were gridded to centimeter level resolution and co-registered with ROV vehicle navigation. Track lines were spaced to ensure 30–40% overlap between adjacent survey lines to ensure complete coverage of the site (**Figure 5**). *In situ* sensor data (including CTD and oxygen) were collected from the ROV along the same track lines to provide co-registered information about overlying water column properties (**Figure 6**). Consideration of the imagery and bathymetric data, together, reveals a near concentric pattern in which an extensive area covered in white microbial mat surrounds a 1–2 m lower lying central region, ∼10 m in diameter, that is covered in bright yellow–orange microbial mat. It is within this central region that discrete sub-circular pits are observed lined with dark gray sediments and lacking any evidence of microbial colonization. These barren pits display the most vigorous bubble plume activity (**Figure 3C**). Across the entire survey, dissolved oxygen concentrations were close to the limits of detection at <1.0 μM, representing <0.2% of saturation levels at the ocean surface. Beyond the limits of the imaged area, the surrounding habitat consisted of soft tan sediment, which was much flatter than the rugose (1–2 m topography) region associated with active fluid flow (**Figures 4**, **5**). No evidence for authigenic carbonate was observed throughout the dive.

Time-Variable Fluid Flow at the *Triton* Seep Site

Active gas bubbles at the NW limit of *Redondo Knoll* were originally detected, as discussed in Section 2.2, from the ship-mounted multibeam system. Imaging of the cold seep site included an initial reconnaissance of the site, which revealed a steady stream of rising bubbles early in the dive both in our forward-looking sonar and as imaged directly from our forward-looking camera at 03:24:09 GMT (**Figure 3C**). During the subsequent high-resolution mapping and imaging survey centered on the same site, bubble-flow remained visible but, on a like-for-like basis, appeared much less vigorous based on the forward-looking HD video monitored by the watch leaders when passing over the same site (04:35:43 GMT). Upon completion of the survey, the ROV returned to these same central pits to conduct temperature probe measurements only to find that, by 05:26 GMT, active fluid flow and gas bubbling at this location had (at least temporarily) ceased (**Figure 7**).

DISCUSSION

Temporal Variability in Seafloor Fluid Flow at the *Triton* Seep Site

The time-variant nature of flow that we observed at the *Triton* seep site aligns directly with the local diurnal tidal cycle. In our study of how fluid flow at *Triton* varied while we were on-site on 16 August 2015 (vigorous at 03:24 GMT; diminished at 04:35 GMT; absent at 05:26GMT), the highest flux-rates that we observed, at the very start of our ROV dive, occurred at ∼4 h after local low-tide along the adjacent Los Angeles shoreline (23:20 GMT, 15 August; 49 cm height). Our subsequent observation that all flow had ceased coincided almost perfectly with local peak high tide (05:21 GMT, 16 August, 171 cm height). Tidal-related changes in seafloor fluid-flow have been well documented for decades at submarine hydrothermal vent-sites (e.g., Johnson et al., 1988; Little et al., 1988) and a similar correlation between methane flux and tidal height at cold seeps has subsequently been hypothesized to arise from a causative mechanism in which fluxes vary according to a reduction in hydrostatic pressure at low tide (e.g., Boles et al., 2001; Torres et al., 2002; Krabbenhöft et al., 2010). It is entirely consistent with such a hypothesis that the flow of bubbles from the seafloor at *Triton* only ceased completely as peak high tide was approached. Had this ROV dive (H1461) been extended beyond an operationally imposed vehicle recovery time, we can hypothesize that the flow of bubbles from this site

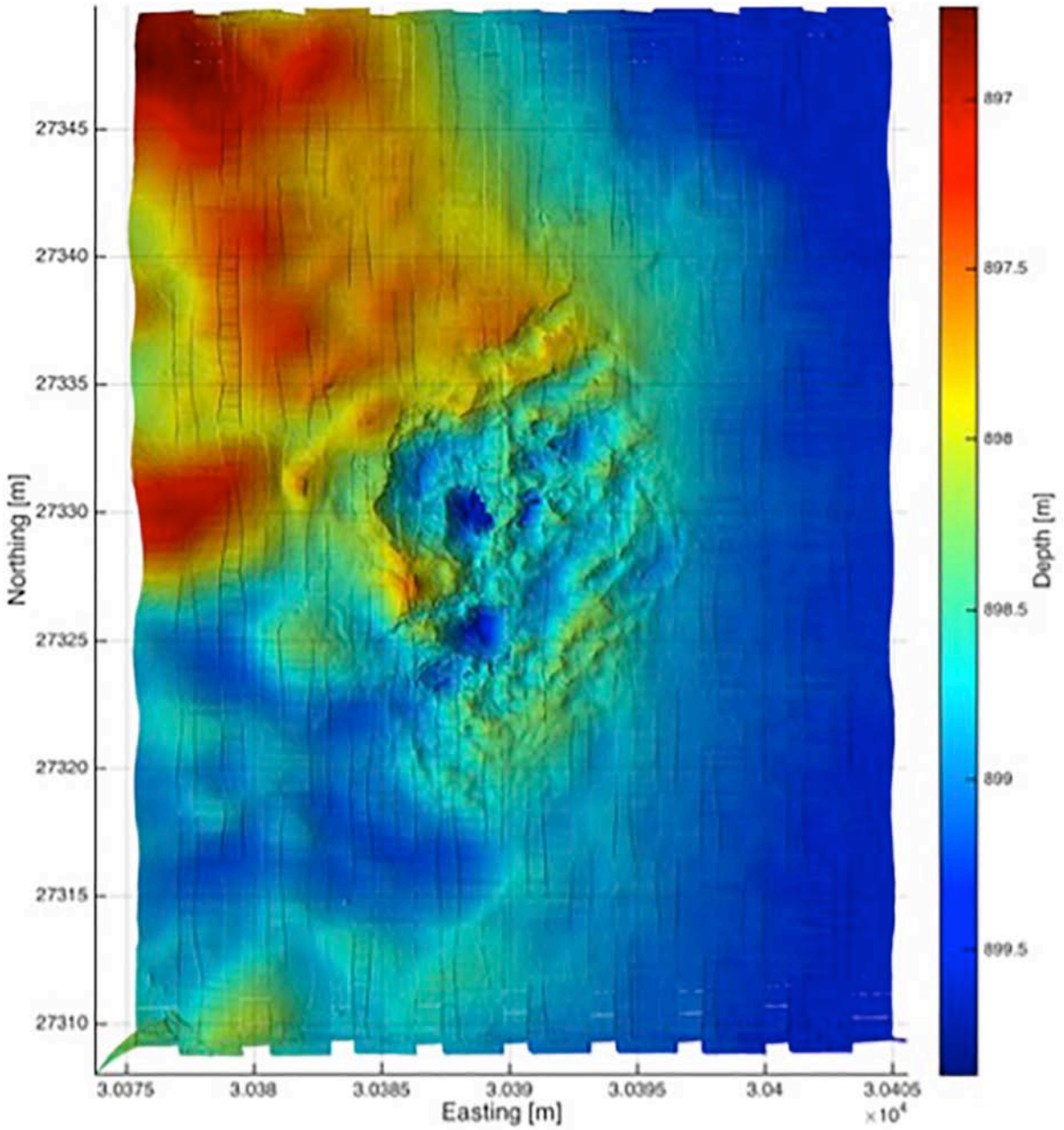

FIGURE 5 | High resolution bathymetric map of the *Triton* cold seep site. This map was created using structured light laser data, and gridded to 1-cm level resolution. Bathymetry was obtained while the ROV surveyed at 3 m above the seafloor. The bathymetric data shown here are co-registered with the photomosaic shown in **Figure 4**.

would have been seen to resume within as little as 1 h of further on-bottom time beyond peak local high-tide.

Microbiological Distributions Across the *Triton* Seep Site

Because *Triton* appeared to represent such an unusual setting among the California Borderlands sites investigated during our cruise (Levin et al., 2016), a conscious decision was made during our sole exploratory dive not to conduct any seafloor sampling that might perturb this otherwise pristine site. While that absence of sampling precludes definitive determination of what the dominant microbial species responsible for the extensive colonization of the seafloor at *Triton* might be, we do note the following: (a) chemoautotrophic bacteria that thrive on hydrogen sulfide commonly form mats at all sites of active seepage along ocean margins (Levin et al., 2003); (b) *Beggiatoa* spp. bacteria are one of the most common types of sulfide-oxidizing and

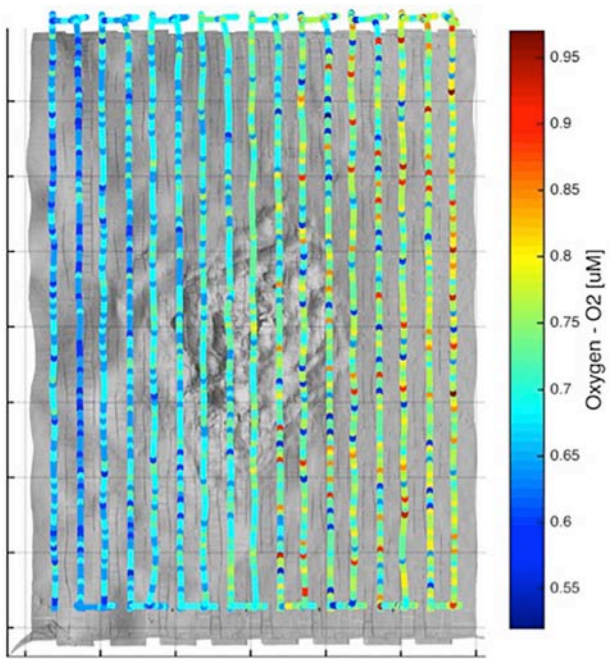

FIGURE 6 | Tracklines with dissolved oxygen concentrations overlying the *Triton* cold seep site. Very low oxygen levels were observed at all locations overlying the *Triton* cold seep site, as measured from 3 m above the seafloor during surveying. All data projected here are co-registered with the photographic and multibeam surveys shown in **Figures 4**, **5**.

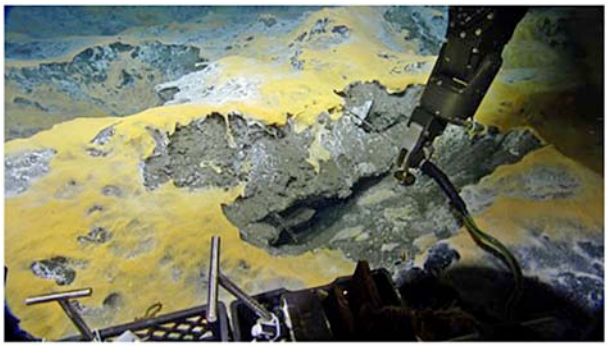

FIGURE 7 | Temporal variability in seafloor fluid flow at the *Triton* seep site. Temperature probe deployment at the same deep pit site as imaged in **Figure 3C**, but bubbling had ceased by 05:26 GMT. Copyright Ocean Exploration Trust, Inc.

mat-forming microbial species found at seeps worldwide (Larkin and Henk, 1996; Gilhooly et al., 2007; Fischer et al., 2012); (c) *Beggiatoa* spp. bacteria are also known to thrive in OMZs (Jørgensen and Gallardo, 1999; Schulz et al., 1999); (d) the morphology of the mats observed at the *Triton* site match closely to the characteristics identified as diagnostic of *Beggiatoa* spp. bacteria: a large (20–200 μm diameter, up to 2 cm in length) filamentous sulfur-oxidizing organism (Larkin and Henk, 1996). Pursuing this line of reasoning further, mats of *Beggiatoa* spp. have also been found, previously, to exhibit "color-coded" bi-modal distributions similar to those shown here, with orange coloration at areas of greater sulfide flux, and white coloration at areas of lower sulfide flux at seep-sites in the Gulf of Mexico and at the Pakistan margin (Gilhooly et al., 2007; Fischer et al., 2012). It will be interesting to investigate, in future dives, whether the microbial mats distributed extensively across the *Triton* cold seep site are dominated by *Beggiatoa* spp. sulfide-oxidizing bacteria.

Absence of Seep-Endemic Macrofauna at the *Triton* Seep Site

While *Triton* lacked any endemic seep-related megafauna and macrofauna, the adjacent *Point Dume* seep site, located ∼40 km to the NW, was found to host dense populations of vesicomyid and lucinid clams, aggregations of polychaetes, foraminifera, galatheid crabs, anemones, soles, rockfish, and catsharks (Levin et al., 2016). Importantly, however, the *Point Dume* site was 150–200 m shallower than *Redondo Knoll*, at 700–750 m water depth rather than 900 m. This meant that it was poised at a shallower depth within the East Pacific OMZ, such that the benthos at that location were exposed to significantly higher dissolved oxygen concentrations of 1–5 μM when compared to the ∼0.75 μM that is more typical of seafloor conditions at the ∼900 m *Triton* site. One possibility, therefore, is that the notably lower levels of dissolved oxygen found at the *Redondo Knoll* seafloor could be responsible for the notable absence of seep-endemic macro-fauna at this specific California Borderlands seep site. Certainly, prior work in OMZ regions off Chile, Pakistan, and the United States (Oregon) has indicated that community structure at seep sites can vary depending on their location within an OMZ: near the fringes (where oxygen levels are higher) or closer to the core (where oxygen levels approach zero). For example, some seep sites with nothing but microbial mats have been observed at OMZ settings off Chile and Pakistan, while others have also hosted vesicomyid clams, and polychaete worms (Sellanes et al., 2010; Fischer et al., 2012; Himmler et al., 2015). Two lines of reasoning suggest that we should exhibit caution before attributing an absence of visually observed seep-endemic macro-fauna at *Triton* to its positioning within the OMZ, however. First, in the absence of any direct sampling, it is possible that small fauna were present on the seafloor at *Triton* but fell below the spatial resolution of the imaging undertaken using our high definition cameras (we calculate ∼3 mm/pixel resolution for our 3 m altitude survey, thus any organism <1 cm across may not have been well resolved). Alternately, there might also have been fauna present at the *Triton* site but living beneath the seafloor within the underlying sediments. At *Hydrate Ridge*, on the Oregon Margin, Guilini et al. (2012) have studied the abundance and species richness of OMZ-tolerant nematodes found in sediment cores collected at and away from cold seep fluid flow settings indicating that the absence of observed multi-cellular organisms at the seafloor at the *Triton* site does not preclude the presence of abundant sediment in-fauna. Importantly, however, in that same study cold seep sites were identified along *Hydrate Ridge* that were at depths directly

comparable to that of the *Triton* site (700–900 m) which meant that they were comparably close to the core of the local OMZ (∼800 m) but they were characterized, variably, by the presence of microbial mats alone – as seen at the *Triton* site – or by clam beds replete with the vesicomyids *Calyptogenica pacifica* and *Calyptogenica klimeri* (Sahling et al., 2002; Levin et al., 2003). Thus, while our observations of the seafloor at the *Redondo Knoll* and adjacent *Point Dume* seep sites, on consecutive days during our 2015 cruise, revealed clear and distinct differences in the abundances of seep-endemic macrofauna present, it may be an over-simplification to attribute those variations exclusively to differences in the depths of their seafloor settings and associated ambient deep ocean oxygen levels, above or at the core of the local OMZ. What else, then, could account for the absence of abundant seep-endemic macro-fauna at the *Triton* seep site?

The Importance of Fluid Flow Rates at the *Triton* Seep Site?

The presence of an area of seafloor thickly carpeted with microbial mats but with a region at its center that is devoid of microbial life, at the *Triton* seep site, is somewhat reminiscent of what has previously been reported, extensively, from another active and vigorous cold seep site at an ocean margin setting: the Haakon Mosby mud volcano (de Beer et al., 2006; Jørgensen and Boetius, 2007; Feseker et al., 2014). There, albeit over a larger (∼1 km) diameter, a central region that is devoid of microbial colonization hosts active bubble-fluxing from the seafloor while a surrounding zone with less active fluid flow is colonized extensively by thick microbial mats. In that system, it has been concluded that the flow rate of methane from the seabed toward the center of the mud volcano is so fast that it precludes any anaerobic oxidation of methane within the sediment pore-fluids prior to release from the seafloor. Consequently, insufficient sulfide is generated in the pore fluids to sustain sulfur oxidizing *Beggiatoa* spp. bacteria and, hence, bacterial mats are absent from the center of the site. Instead, it is only toward the outer reaches of the mud volcano at *Haakon Mosby* that flux rates of dissolved methane are sufficiently slow (and concomitant pore-water sulfide concentrations are correspondingly high) that extensive microbial mats are observed (de Beer et al., 2006). Could concentric zonation of flow rate at the *Triton* seep site explain both the absence and distributions of microbial mats reported here? Two further lines of reasoning suggest that this might be the case.

First, while the core of the *Triton* cold seep site appears completely devoid of microbial life, when compared to our observations of the surrounding seafloor, there is also a further distinction that is immediately apparent in **Figure 4** between the yellow–orange coloration of the microbial mats draping the inner walls and floor of the *Triton* cold seep system and the white coloration of the microbial mats draping the outer flanks of the site, onlapping the surrounding tan sediments. In the Gulf of Mexico, exactly the same bi-modal distribution of coloring has been reported for *Beggiatoa* spp. bacterial mats surrounding a seafloor cold-seep site and, at that location, the readily visible color change was shown to coincide with a marked decrease in sulfide concentrations from >6 nM in the sediments underlying yellow–orange mats to concentrations that were a factor of 5 lower beneath white-colored mats of the same species (Gilhooly et al., 2007). The same bi-modal color distribution has also been reported for microbial mats along the Pakistan margin (Fischer et al., 2012) where pore fluid sulfide concentrations were ∼6 mM beneath orange mats but significantly lower (∼0.75 mM) beneath white mats. At *Hydrate Ridge*, an even more marked variation in seafloor colonization of cold seeps in an OMZ setting is apparent as a function of net fluid flux rates and H_2S concentrations. There, sulfide concentrations in excess of 28 mM have been reported from the uppermost sediments directly underlying sites characterized by microbial mats only, whereas clam bed sites at the same depths within the OMZ are characterized by much lower flux rates and much lower H_2S concentrations at the same depths into the underlying sediments (Sahling et al., 2002; Valentine et al., 2005; Sommer et al., 2007).

Combining the above arguments with our direct observations of concentric microbial color-zonation and gas bubbles streaming from the seafloor it seems evident that the maximum flux of methane from the *Triton* seep site must occur at the center of our survey area. We can then hypothesize that the surrounding yellow–orange mats correspond to regions of sufficiently less vigorous flow that anaerobic methane oxidation can occur within the underlying sediment pore-spaces, together with concomitant hydrogen sulfide generation. Extending the analogy to what has been observed at other cold seeps, we would then infer that the outer concentric region that is dominated by *white* microbial mats at the *Triton* seep site (**Figure 4**) represents a zone of still lower net fluid flux rates and hydrogen sulfide generation – but that even here the conditions remain too hostile for colonization by seep-endemic macro-fauna. In this scenario, it would be the rates of methane flux and sulfide generation associated with the *Triton* seep that preclude colonization of the site by endemic macro-fauna rather than just the low oxygen concentrations found here, at the core of the OMZ. Continuing the analogy further, the central dark gray sediment pits that are devoid of microbial life at *Triton*, coincident with where vigorous bubble activity was observed, would correspond to environments reported elsewhere (e.g. at the center of the *Haakon Mosby Mud Volcano*) where the physical flux of reductants exiting the underlying sediments is so high that it overwhelms the ability of any chemosynthetic microorganisms to exploit redox couples at the seafloor leading to a central "dead zone" (de Beer et al., 2006). The occurrence of such extremes at *Triton* both for macro-faunal and microbial colonization is, of course, all the more plausible precisely because of the extremely low dissolved oxygen concentrations observed across the entire survey area (**Figure 6**).

CONCLUSION

We report the discovery of a new cold seep site, *Triton*, that is located at ∼900 m water depth and within <30 km from

Los Angeles in the California Borderlands region. The site is distinct from adjacent cold seep sites that were already known in this area in two regards. First, *Triton* is deeper than other previously studied seep sites in the California Borderlands region and, hence, lies closer toward the core of the OMZ with lower concentrations of dissolved oxygen in the overlying water column (<0.75 μM) placing this site toward the lower bounds of known OMZ settings worldwide. Second, the site is notably devoid of the same seep-endemic macro-fauna that are observed in abundance at other seep-hosted chemosynthetic ecosystems in the California Borderlands region. At *Triton*, what is observed is a concentric distribution of features: a rugose and concentric morphologic feature, ∼30–40 m in radial extent, slopes upward toward the center and is covered in white microbial mats. At the rim of a central "crater" the color of this microbial mat switches to a bright yellow–orange color that drapes the inward facing walls and floor of the central depression which measures ∼10 m across. Within that central depression lie a series of deeper pits of the order 1–2 m in diameter and up to 1 m deep that are devoid of microbial life and from which active (but time-varying) gas bubbling is observed. From a comparison with other cold seep systems associated with OMZs, both in the California Borderlands and along other ocean margin settings, we hypothesize that both the absence of abundant macrofauna at the seafloor at *Triton*, and the concentric nature of the distributions of microorganisms may be attributable to variations in the flux of reductants from the underlying seafloor (with highest fluxes at the center) rather than the low oxygen concentrations in the overlying water column. The discovery of this new and intriguing study site, in such a readily accessible location close to Los Angeles harbor, provides a novel natural laboratory at which to test this and other hypotheses concerning the functioning of, and biogeochemical–microbiological interactions at, cold seep ecosystems associated with OMZs.

DATA AVAILABILITY STATEMENT

The datasets generated for this study are available on request to the corresponding author.

AUTHOR CONTRIBUTIONS

JW conducted the analysis of the biological and fluid flow data. CS conducted the mapping surveys and performed the analysis of the bathymetric, photo, ROV sensor, and navigation data. CG led the ROV dive to the study site and provided geological insights. All authors contributed to the writing of the manuscript.

FUNDING

Ship time was funded by NOAA – Office of Exploration and Research and the Ocean Exploration Trust. This material is based upon work supported by a National Science Foundation Graduate Research Fellowship (to JW), the Office of Naval Research (to CS), and NASA's Astrobiology program (to CG).

ACKNOWLEDGMENTS

We would like to acknowledge the scientists, shore scientists, and crew of the E/V *Nautilus*. This research used data provided by the Ocean Exploration Trust's *Nautilus* Exploration Program, Cruise NA067. We thank Dr. Lisa Levin and Dr. Mark Rausher's Lab for helpful feedback and Dr. Chris Roman's Lab at URI for high resolution imaging capability. We particularly thank Guest Associate Editor Randi Rotjan and two reviewers who helped us streamline and greatly improve the focus of this manuscript.

REFERENCES

Barry, J. P., Greene, H. G., Orange, D. L., Baxter, C. H., Robison, B. H., Kochevar, R. E., et al. (1996). Biologic and geologic characteristics of cold seeps in Monterey Bay, California. *Deep Sea Res. I Oceanogr. Res. Pap.* 43, 1739–1762. doi: 10.1016/s0967-0637(96)00075-1

Boles, J. R., Clark, J. F., Leifer, I., and Washburn, L. (2001). Temporal variation in natural methane seep rate due to tides, coal oil point area, California. *J. Geophys. Res. Oceans* 106, 27077–27086. doi: 10.1029/2000jc000774

de Beer, D., Sauter, E., Niemann, H., Karl, N., Foucher, J.-P., Witte, U., et al. (2006). In situ fluxes and zonation of microbial activity in surface sediments of the Haakon Mosby Mud Volcano. *Limnol. Oceanogr.* 51, 1315–1331. doi: 10.4319/lo.2006.51.3.1315

Feseker, T., Boetius, A., Wenzhöfer, F., Blandin, J., Olu, K., Yoerger, D. R., et al. (2014). Eruption of a deep-sea mud volcano triggers rapid sediment movement. *Nat. Commun.* 5:5385. doi: 10.1038/ncomms6385

Fischer, D., Sahling, H., Nöthen, K., Bohrmann, G., Zabel, M., and Kasten, S. (2012). Interaction between hydrocarbon seepage, chemosynthetic communities, and bottom water redox at cold seeps of the Makran accretionary prism: insights from habitat-specific pore water sampling and modeling. *Biogeosciences* 9, 2013–2031. doi: 10.5194/bg-9-2013-2012

Gilhooly, W. P., Carney, R. S., and Macko, S. A. (2007). Relationships between sulfide-oxidizing bacterial mats and their carbon sources in northern Gulf of Mexico cold seeps. *Organ. Geochem.* 38, 380–393. doi: 10.1016/j.orggeochem.2006.06.005

Grupe, B. M., Krach, M. L., Pasulka, A. L., Maloney, J. M., Levin, L. A., and Frieder, C. A. (2015). Methane seep ecosystem functions and services from a recently discovered southern California seep. *Mar. Ecol.* 36, 91–108. doi: 10.1111/maec.12243

Guilini, K., Levin, L. A., and Vanreusel, A. (2012). Cold seep and oxygen minimum zone associated sources of margin heterogeneity affect benthic assemblages, diversity and nutrition at the cascadian margin (NE Pacific Ocean). *Prog. Oceanogr.* 96, 77–92. doi: 10.1016/j.pocean.2011.10.003

Helly, J. J., and Levin, L. A. (2004). Global distribution of naturally occurring marine hypoxia on continental margins. *Deep Sea Res. I Oceanogr. Res. Pap.* 51, 1159–1168. doi: 10.1016/j.dsr.2004.03.009

Himmler, T., Birgel, D., Bayon, G., Pape, T., Ge, L., Bohrmann, G., et al. (2015). Formation of seep carbonates along the Makran convergent margin, northern Arabian Sea and a molecular and isotopic approach to constrain the carbon isotopic composition of parent methane. *Chem. Geol.* 415, 102–117. doi: 10.1016/j.chemgeo.2015.09.016

Inglis, G., Smart, C., Vaughn, J., and Roman, C. (2012). "A pipeline for structured light bathymetric mapping," in *Proceedings of the IEEE/RSJ International Conference Intelligent Robots and Systems*, Portugal.

Johnson, K. S., Childress, J. J., and Beehler, C. L. (1988). Short-term temperature variability in the rose garden hydrothermal vent field: an unstable deep-sea

environment. *Deep Sea Res. A Oceanogr. Res. Pap.* 35, 1711–1721. doi: 10.1016/0198-0149(88)90045-3

Jørgensen, B. B., and Boetius, A. (2007). Feast and famine–microbial life in the deep-sea bed. *Nat. Rev. Microbiol.* 5:770. doi: 10.1038/nrmicro1745

Jørgensen, B. B., and Gallardo, V. A. (1999). Thioploca spp: filamentous sulfur bacteria with nitrate vacuoles. *FEMS Microbiol. Ecol.* 28, 301–313. doi: 10.1111/j.1574-6941.1999.tb00585.x

Karstensen, J., Stramma, L., and Visbeck, M. (2008). Oxygen minimum zones in the eastern tropical Atlantic and Pacific oceans. *Prog. Oceanogr.* 77, 331–350. doi: 10.1016/j.pocean.2007.05.009

Krabbenhöft, A., Netzeband, G. L., Bialas, J., and Papenberg, C. (2010). Episodic methane concentrations at seep sites on the upper slope Opouawe Bank, southern Hikurangi Margin, New Zealand. *Mar. Geol.* 272, 71–78. doi: 10.1016/j.margeo.2009.08.001

Larkin, J. M., and Henk, M. C. (1996). Filamentous sulfide-oxidizing bacteria at hydrocarbon seeps of the Gulf of Mexico. *Microsc. Res. Tech.* 33, 23–31. doi: 10.1002/(sici)1097-0029(199601)33:1<23::aid-jemt4>3.0.co;2-1

Levin, L., Girguis, P. R., German, C. R., Brennan, M. L., Tuzun, S., Wagner, J., et al. (2016). Exploration and discovery of methane seeps and associated communities in the California Borderland. *Oceanography* 28, 40–43.

Levin, L. A. (2003). Oxygen minimum zone benthos: adaptation and community response to hypoxia. *Oceanogr. Mar. Biol. Annu. Rev.* 41, 1–45.

Levin, L. A., Mendoza, G. F., Gonzalez, J. P., Thurber, A. R., and Cordes, E. E. (2010). Diversity of bathyal macrofauna on the northeastern Pacific margin: the influence of methane seeps and oxygen minimum zones. *Mar. Ecol.* 31, 94–110. doi: 10.1111/j.1439-0485.2009.00335.x

Levin, L. A., Ziebis, W., Mendoza, G. F., Growney, V. A., Tryon, M. D., Brown, K. M., et al. (2003). Spatial heterogeneity of macrofauna at northern California methane seeps: influence of sulfide concentration and fluid flow. *Mar. Ecol. Prog. Ser.* 265, 123–139. doi: 10.3354/meps265123

Little, S. A., Stolzenbach, K. D., and Grassle, F. J. (1988). Tidal current effects on temperature in diffuse hydrothermal flow: Guaymas Basin. *Geophys. Res. Lett.* 15, 1491–1494. doi: 10.1029/gl015i013p01491

Merewether, R., Olsson, M. S., and Lonsdale, P. (1985). Acoustically detected hydrocarbon plumes rising from 2-km depths in Guaymas Basin, Gulf of California. *J. Geophys. Res. Solid Earth* 90, 3075–3085.

Roman, C., Inglis, G., Vaughn, J. I., Smart, C., Douillard, B., and Williams, S. (2012). The development of high-resolution seafloor mapping techniques. *Oceanography* 25, 42–45.

Sahling, H., Rickert, D., Lee, R. W., Linke, P., and Suess, E. (2002). Macrofaunal community structure and sulfide flux at gas hydrate deposits from the Cascadia convergent margin, NE Pacific. *Mar. Ecol. Prog. Ser.* 231, 121–138. doi: 10.3354/meps231121

Schulz, H. N., Brinkhoff, T., Ferdelman, T. G., Hernandez, M., Teske, A., and Jørgensen, B. B. (1999). Dense populations of a giant sulfur bacterium in Namibian shelf sediments. *Science* 284, 493–495. doi: 10.1126/science.284.5413.493

Sellanes, J., Neira, C., Quiroga, E., and Teixido, N. (2010). Diversity patterns along and across the Chilean margin: a continental slope encompassing oxygen gradients and methane seep benthic habitats. *Mar. Ecol.* 31, 111–124. doi: 10.1111/j.1439-0485.2009.00332.x

Sibuet, M., and Olu, K. (1998). Biogeography, biodiversity and fluid dependence of deep-sea cold-seep communities at active and passive margins. *Deep Sea Res. II Top. Stud. Oceanogr.* 45, 517–567. doi: 10.1016/s0967-0645(97)00074-x

Skarke, A., Ruppel, C., Kodis, M., Brothers, D., and Lobecker, E. (2014). Widespread methane leakage from the seafloor on the northern US Atlantic margin. *Nat. Geosci.* 7, 657–661. doi: 10.1038/ngeo2232

Sommer, S., Gutzmann, E., and Pfannkuche, O. (2007). Sediments hosting gas hydrates: oases of metazoan meiofauna. *Mar. Ecol. Prog. Ser.* 337, 27–37. doi: 10.3354/meps337027

Torres, M. E., McManus, J., Hammond, D. E., De Angelis, M. A., Heeschen, K. U., Colbert, S. L., et al. (2002). Fluid and chemical fluxes in and out of sediments hosting methane hydrate deposits on hydrate ridge, or, I: hydrological provinces. *Earth Planet. Sci. Lett.* 201, 525–540. doi: 10.1016/s0012-821x(02)00733-1

Valentine, D. L., Jastner, M., Wardlaw, G. D., Wang, X., Purdy, A., and Bartlett, D. H. (2005). Biogeochemical investigations of marine methane seeps, Hydrate Ridge, Oregon. *J. Geophys. Res.* 110:G02005. doi: 10.1029/2005JG000025

Weber, T. C., Mayer, L. A., Beaudoin, J., Jerram, K., Shedd, W., and Rice, G. (2012). Mapping gas seeps with the deepwater multibeamechosounder on okeanos explorer. *Oceanography* 25(Suppl. 1), 54–55.

Wyrtki, K. (1962). The oxygen minima in relation to ocean circulation. *Deep Sea Res.* 9, 11–23. doi: 10.1242/jeb.060236 doi: 10.1016/0011-7471(62)90243-7

Conflict of Interest: The authors declare that the research was conducted in the absence of any commercial or financial relationships that could be construed as a potential conflict of interest.

Copyright © 2020 Wagner, Smart and German. This is an open-access article distributed under the terms of the Creative Commons Attribution License (CC BY). The use, distribution or reproduction in other forums is permitted, provided the original author(s) and the copyright owner(s) are credited and that the original publication in this journal is cited, in accordance with accepted academic practice. No use, distribution or reproduction is permitted which does not comply with these terms.

frontiers in Marine Science

ORIGINAL RESEARCH
published: 21 February 2020
doi: 10.3389/fmars.2020.00073

Hydrothermal Activity and Seismicity at Teahitia Seamount: Reactivation of the Society Islands Hotspot?

Christopher R. German[1], Joseph A. Resing[2,3], Guangyu Xu[1†], Isobel A. Yeo[4†], Sharon L. Walker[3], Colin W. Devey[4], James W. Moffett[5], Gregory A. Cutter[6], Olivier Hyvernaud[7] and Dominique Reymond[7]*

[1] Geology & Geophysics, Woods Hole Oceanographic Institution, Woods Hole, MA, United States, [2] Joint Institute for the Study of the Atmosphere and Ocean, University of Washington, Seattle, WA, United States, [3] NOAA Pacific Marine Environmental Laboratory, Seattle, WA, United States, [4] GEOMAR - Helmholtz Centre for Ocean Research Kiel, Kiel, Germany, [5] Biological Sciences & Earth Sciences, University of Southern California, Los Angeles, CA, United States, [6] Ocean, Earth & Atmospheric Sciences, Old Dominion University, Norfolk, VA, United States, [7] CEA/DIF/DASE, Laboratoire de Géophysique, Papeete, Tahiti, French Polynesia

OPEN ACCESS

Edited by:
Diva Amon,
Natural History Museum,
United Kingdom

Reviewed by:
Mustafa Yucel,
Middle East Technical University,
Turkey
Benjamin Tutolo,
University of Calgary, Canada

***Correspondence:**
Christopher R. German
cgerman@whoi.edu

†Present address:
Guangyu Xu,
Applied Physics Laboratory, University of Washington, Seattle, WA,
United States
Isobel A. Yeo,
National Oceanography Centre Southampton, Southampton,
United Kingdom

Specialty section:
This article was submitted to Deep-Sea Environments and Ecology, a section of the journal Frontiers in Marine Science

Received: 01 April 2019
Accepted: 30 January 2020
Published: 21 February 2020

Citation:
German CR, Resing JA, Xu G, Yeo IA, Walker SL, Devey CW, Moffett JW, Cutter GA, Hyvernaud O and Reymond D (2020) Hydrothermal Activity and Seismicity at Teahitia Seamount: Reactivation of the Society Islands Hotspot? Front. Mar. Sci. 7:73. doi: 10.3389/fmars.2020.00073

Along mid-ocean ridges, submarine venting has been found at all spreading rates and in every ocean basin. By contrast, intraplate hydrothermal activity has only been reported from five locations, worldwide. Here we extend the time series at one of those sites, Teahitia Seamount, which was first shown to be hydrothermally active in 1983 but had not been revisited since 1999. Previously, submersible investigations had led to the discovery of low-temperature (≤30°C) venting associated with the summit of Teahitia Seamount at ≤1500 m. In December 2013 we returned to the same site at the culmination of the US GEOTRACES Eastern South Tropical Pacific (GP16) transect and found evidence for ongoing venting in the form of a non-buoyant hydrothermal plume at a depth of 1400 m. Multi-beam mapping revealed the same composite volcano morphology described previously for Teahitia including four prominent cones. The plume overlying the summit showed distinct *in situ* optical backscatter and redox anomalies, coupled with high concentrations of total dissolvable Fe (≤186 nmol/L) and Mn (≤33 nmol/L) that are all diagnostic of venting at the underlying seafloor. Continuous seismic records from 1986-present reveal a ∼15 year period of quiescence at Teahitia, following the seismic crisis that first stimulated its submersible-led investigation. Since 2007, however, the frequency of seismicity at Teahitia, coupled with the low magnitude of those events, are suggestive of magmatic reactivation. Separately, distinct seismicity at the adjacent Rocard seamount has also been attributed to submarine extrusive volcanism in 2011 and in 2013. Theoretical modeling of the hydrothermal plume signals detected suggest a minimum heat flux of 10 MW at the summit of Teahitia. Those model simulations can only be sourced from an area of low-temperature venting such as that originally reported from Teahitia if the temperature of the fluids exiting the seabed has increased significantly, from ≤30°C to ∼70°C. These model seafloor temperatures and our direct plume observations are both consistent with reports from Loihi Seamount, Hawaii, ∼10 year following an episode of seafloor volcanism. We hypothesize that the Society Islands hotspot may be undergoing a similar episode of both magmatic and hydrothermal reactivation.

Keywords: hydrothermal, seamount, hotspot, Teahitia, Tahiti, Pacific

INTRODUCTION

More than 40 years after the first discovery of seafloor hydrothermal activity, systematic exploration along the global mid-ocean ridge crest has established that submarine venting can occur in every ocean basin and along ridges of every spreading rate (Beaulieu et al., 2013). While the rate of discovery of submarine hydrothermal systems along tectonic plate boundaries has accelerated over the past 25 years, however (Baker et al., 1995; Baker and German, 2004; Beaulieu et al., 2015), exploration for intraplate hydrothermal activity across the vast interior of Earth's ocean basins has stagnated. Only five such submarine vent systems have ever been reported to the InterRidge vents data base, four of which are located in the central Pacific Ocean (**Figure 1**). Further, only one of these vent-sites represents a new discovery since the start of the current millenium – the Vailulu'u Seamount, Samoa, where venting was only discovered in 2005 (Staudigel et al., 2006). With the recent recognition that even deep-sea hydrothermal sources of Fe can provide a significant impact on global-scale ocean biogeochemical cycles, however (Resing et al., 2015) there is now a renewed interest in investigating the role that shallower-sourced (including intra-plate) volcanism and associated hydrothermal activity could also play in stimulating upper ocean productivity.

The Society Islands hotspot (**Figure 2**) extends for approximately 100 km, east, from the (now inactive) island of Tahiti to the volcanically active island of Mehetia which rises to ∼450 m above sealevel (Cheminée et al., 1989). Teahitia ("Standing Fire" in Polynesian) represents the most westerly active seamount within this chain, and rises from ∼3300 m at its base to ≤1500 m at its summit. Together Mehetia and Teahitia share a history of intense recorded seismicity. In March 1981, a seismic episode centered to the SE of Mehetia was followed by a series of further swarms of activity, starting in 1982, that were centered at and around Teahitia (Talandier and Okal, 1984). Over a 4 year period (1981–1985), approximately 32,000 separate earthquakes ($M_L > 1.0$) were detected with the vast majority occurring at Teahitia, including a ∼2 week swarm located at its summit in July 1983. Analysis of that seismicity suggested the presence of initially deep magmatic activity at both locales that culminated in seafloor eruptive volcanism at Teahitia (Talandier and Okal, 1984, 1987).

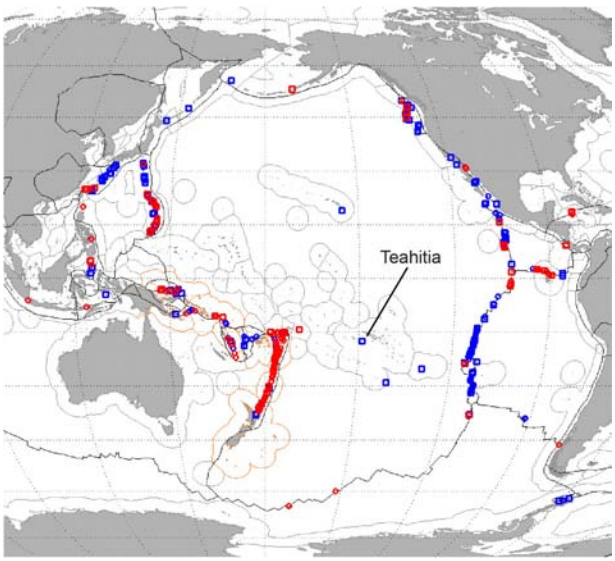

FIGURE 1 | Plot of all known locations of submarine hydrothermal venting in the Circum-Pacific as reported to the InterRidge Vents Data Base (Beaulieu et al., 2013). Red symbols denote sites located since 2000, while blue symbols denote sites already known at the turn of the millennium. The location of the Teahitia site is indicated, close to 17°30′S, 148°50′W.

FIGURE 2 | Bathymetric map showing the position of Teahitia Seamount in the context of the currently active portion of the Society Islands hotspot trace which extends for ∼100 km from Tahiti to Mehitia (Cheminée et al., 1989).

Following detection of the seismicity and inferred volcanism at Teahitia, a single Cyana submersible dive in 1983 confirmed the presence of low-temperature (∼30°C) hydrothermal venting close to the summit of the seamount (Cheminée et al., 1989). SeaBeam mapping subsequently revealed Teahitia to be a composite volcano comprising four distinct cones and this informed a more extensive series of *Cyana* dives in Austral Summer 1988–1989 (Binard et al., 1992). Those dives revealed shimmering fluids exiting from small Fe oxyhydroxide chimneys and from orifices in the seafloor close to the summits of two of Teahitia's four cones (TH1, TH2) while no activity was observed at the adjacent summits (TH3, TH4). Vent-fluids from TH1 sampled during that expedition exhibited fluid temperatures of ∼30°C, pH values that fell in the range 5.3–5.6, high concentrations of Si (0.8–0.9 mmol/kg), Fe (170–190 μmol/kg) and Mn (6–13 μmol/kg) but no detectable dissolved H_2S (Michard et al., 1993). Repeat submersible dives with the Nautile a decade later (Hékinian, 1999) confirmed that venting was on-going at TH1 (T_{max} ∼30°C) but that activity had waned ($T_{max} \leq 16$°C) at the adjacent TH2 summit. No subsequent studies of hydrothermal activity at this site were conducted in the ensuing ∼15 years.

MATERIALS AND METHODS

Fieldwork for this project was conducted aboard RV Thomas G Thompson cruise TN303 at the culmination of the US GEOTRACES East Pacific Zonal Transect (Moffett and German, 2018). Multibeam mapping of the summit of Teahitia Seamount

was conducted using the EM302 multibeam sonar mounted aboard the RV Thompson. Survey lines were occupied in a NW/SE orientation to accommodate prevailing wind directions and the entire seamount was mapped in a series of overlapping ∼9 km surveys, offset from one another by 2 km and surveyed at 7.5 kts.

Seismic data for the study area are collected continuously by the Polynesian Seismic Network/Réseau Sismique, Polynésie (RSP). Data are monitored continuously at the Laboratoire de Géophysique in Papeete, Tahiti, where the seismic energy of each event is calculated using the standard methods described by Gutenberg and Richter (1954). Earthquake magnitude (M_L) coefficients are assigned according to the approach established by J. Talandier and colleagues, as described in Talandier and Kuster (1976), Okal et al. (1980) and Talandier and Okal (1984).

Water column studies at Teahitia were conducted using a CTD-rosette system furnished by the Scripps Institution of Oceanography's Ocean Data Facility. The system comprised a Sea-Bird SBE9 + conductivity temperature depth (CTD) instrument mounted on a rosette frame equipped with a 12-position carousel holding 30L General Oceanics Niskin sampling bottles. In addition to conventional *in situ* sensors (dissolved oxygen, fluorometer, transmissometer), two additional sensors were employed, specifically, for the hydrothermal plume studies conducted on this cruise: a Seapoint STM11 turbidity meter and a NOAA-PMEL Oxidation-Reduction Potential (ORP) sensor.

Upon arrival at Teahitia, the CTD rosette was lowered directly over the summit of the TH1 cone as the ship's position was maintained in dynamic positioning mode (**Figure 3**). *In situ* sensor data, monitored on board ship throughout the cast, were used to inform the twelve discrete depths at which water column samples were collected during the upcast. Upon recovery aboard ship, samples were drawn, *unfiltered* into acid-washed 100 mL low density polyethylene (LDPE) bottles and acidified to pH ∼1.7 with 12N ultra-pure hydrochloric acid. Total dissolvable Fe and Mn concentrations (TDFe and TDMn, respectively, hereafter) were determined in the laboratory in Seattle, post cruise, using Flow-Injection Analysis. A detailed description of the methods used across the entire US GEOTRACES EPZT cruise is provided in Resing et al. (2015).

RESULTS

The multibeam bathymetry for Teahitia Seamount (**Figure 3**) reveals near identical morphology (within the resolution of the earlier data set) as that from the only prior multibeam survey of the seamount (Cheminée et al., 1989). Profiles of temperature, salinity, dissolved oxygen concentrations and light transmission throughout the entire water column are shown in **Figure 4**. All four traces reveal monotonous trends throughout the lower half of the water column, below 800 m water depth, with the notable exception of the transmissometer data which show a distinct particle-rich (low light transmission) anomaly at ∼1400 m depth, i.e., ∼100 m shallower than the summit of Teahitia seamount. When examined in closer detail this deep portion of the water column also shows clear evidence of hydrothermal plume activity in the profiles for the two dedicated hydrothermal *in situ* sensors as well as in the profiles for TDFe and TDMn concentrations (**Figure 5**). The SeaPoint Turbidity (STM) sensor, like the transmissometer, shows clear evidence for a lens of particle-rich water centered at ∼1400 m (**Figure 5A**) together with a secondary plume maximum at ∼1450 m that is also apparent in the transmissometer profile (**Figure 4B**). Optically clear water is observed both immediately above (≤1350 m) and immediately below (≥1475 m) these plume depths. The profile for the NOAA-PMEL oxidation-reduction probe (ORP) also shows a distinct response across the top of the hydrothermal plume layer with a steep drop in voltage across the same depth range as the uppermost horizon of the STM-defined plume (**Figure 5A**). Despite the non-instantaneous nature of this sensor's response, there are clear changes in gradient in the ORP profile below 1400 m, as well, and the sign of the gradient reverses below ∼1450 m, roughly coincident with the depth of the lower STM particle maximum. Profiles of TDFe and TDMn concentrations in water samples collected during the upcast of the same CTD-rosette deployment are shown in **Figure 5B**; the corresponding analytical data are listed in **Table 1**. Maximum TDFe and TDMn concentrations occur at 1400 m, coincident with the maximum *in situ* STM anomaly and the depth at which the ORP sensor profile shows the steepest negative gradient. The sharp increases and decreases in TDMn concentrations, immediately above and below 1400 m, are particularly reminiscent of the STM profile, as is the presence of lower (but still anomalously high) TDMn concentrations beneath the plume maximum, extending down to 1460 m water depth. Background TDMn concentrations were observed at all depths shallower than 1375 m and deeper than 1475 m, coincident with the narrow (∼100 m thick) STM-defined non-buoyant hydrothermal plume. Similar trends are observed in the TDFe profile with the exception that the maximum plume concentrations are observed across a broader depth range of 1390–1425 m and deep concentrations below 1475 m remained significantly higher (6–15 nM) than above-plume background concentrations (≤1 nM), perhaps due to settling of particulate Fe oxyhydroxide material from the overlying non-buoyant plume.

DISCUSSION

Hydrothermal Plume Signals Over Teahitia Seamount

Historically, InterRidge led exploration along the global mid-ocean ridge crest has assumed that particle-rich lenses of water detected from CTD profiling activities were indicative of a source of high temperature "black smoker" hydrothermal venting on the adjacent and underlying seafloor (see, e.g., Baker et al., 1995; Baker and German, 2004; Beaulieu et al., 2013). Traditionally, this interpretation has been further reinforced whenever suspended particulate anomalies of the kind detected here, using *in situ* optical sensors (**Figures 4B**, **5A**), have been found to be coincident with both *in situ* redox anomalies (**Figure 5A**) and measurable concentrations of geochemical tracers (e.g., Fe, Mn, CH_4, ∂^3He_{xs}) that are known to be present in extremely high concentrations in seafloor hydrothermal vent fluids but

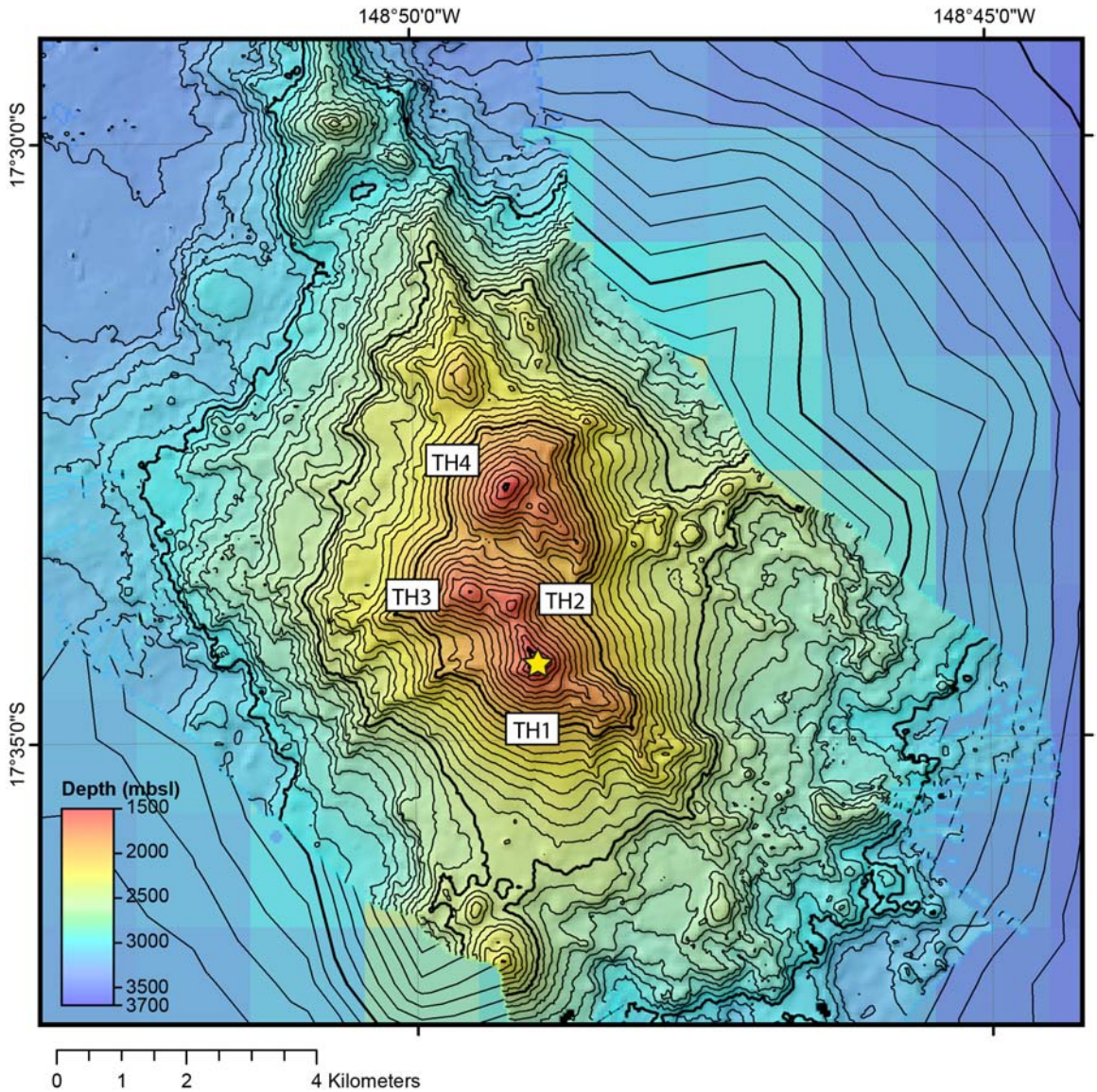

FIGURE 3 | Multibeam bathymetric plot of Teahitia Seamount as mapped during RV Thomas G. Thompson cruise TGT303 in December 2013. TH1-TH4 represent the four principle cones of this composite volcano. Yellow star shows the location of US GEOTRACES CTD Station GP16- 37 occupied directly above the TH1 cone at 17°34.4′S, 148°49.0′W using the ship's dynamic positioning system.

otherwise present in only minute concentrations in background seawater elsewhere in the ocean (German and Seyfried, 2014). From that perspective, a simple explanation of the plume data presented here, in isolation, might appear to be that a "black smoker" source of high temperature hydrothermal venting was active at the underlying seafloor. Recognizing that Teahitia is part of a rare family of isolated hot-spot hosted intraplate volcanic systems, however, such an interpretation is problematic. First, the depth of venting at this location should be too shallow to preclude phase separation occurring at temperatures significantly lower than the ∼350°C temperatures typical of "black smoker" hydrothermal vents: eruption of such high-temperature fluids should be physically impossible (German and Seyfried, 2014). Second, the only forms of submarine venting reported previously from the summit of Teahitia, in the 1980s and again in 1999, were relatively low temperature (15–30°C) venting from small Fe-oxide rich chimneys, similar to those reported contemporaneously during first discoveries of venting at Loihi Seamount, off Hawaii (≤30°C (Karl et al., 1988). At Loihi seamount, the highest vent temperatures ever recorded were ≤200°C, immediately following an episode of volcanism that led to the formation of the present-day summit collapse pits (Davis and Clague, 1998) but vent temperatures at those sites have subsequently relaxed back to near pre-eruption temperatures (60–30°C) over the ensuing decades (Glazer and Rouxel, 2009; German et al., 2018).

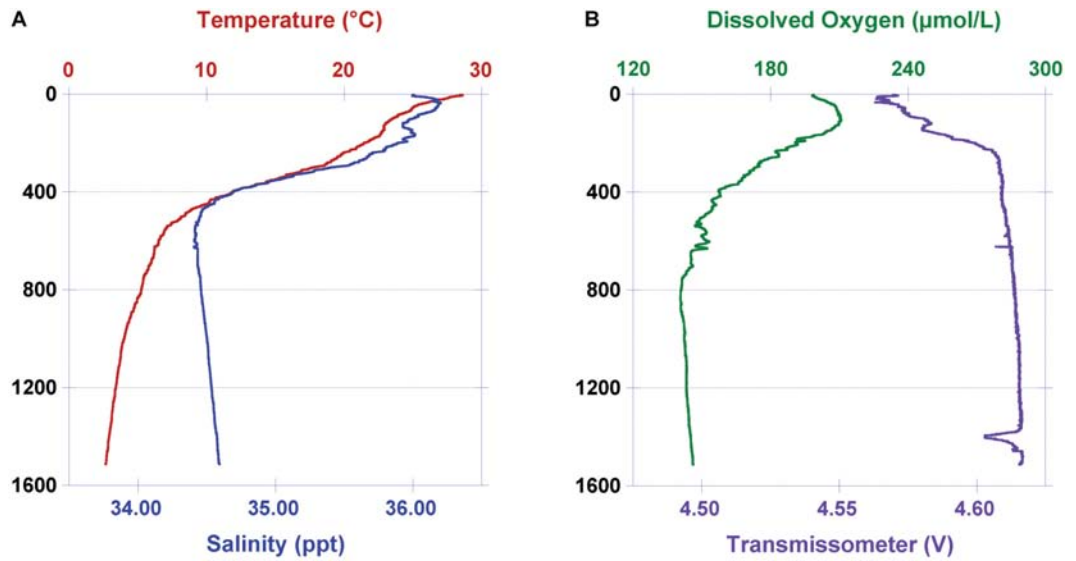

FIGURE 4 | Vertical profiles for **(A)** Temperature and Salinity and **(B)** Dissolved Oxygen and Light Transmission above the TH1 summit of Teahitia Seamount from US GEOTRACES CTD Station GP16-37.

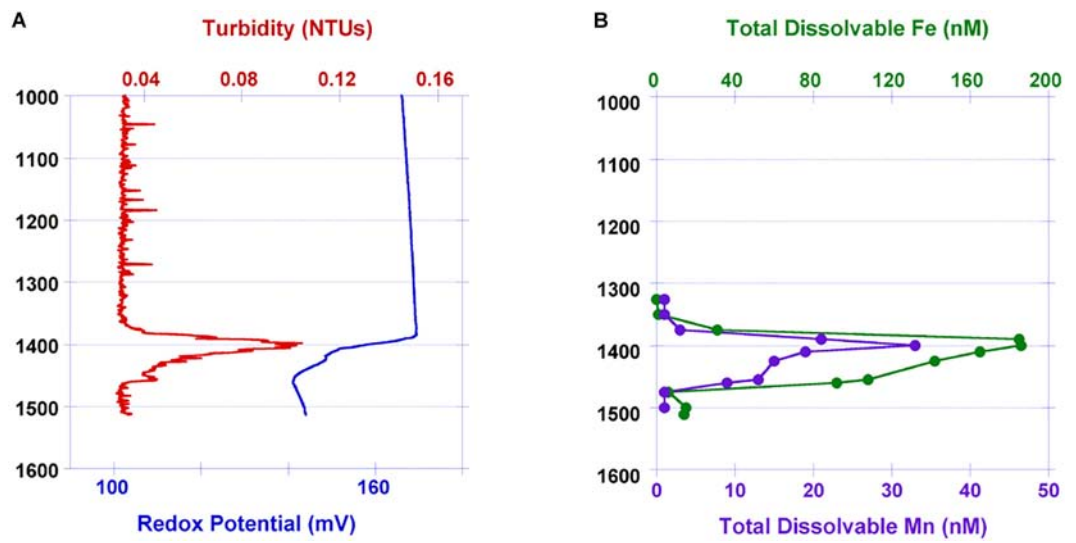

FIGURE 5 | Vertical profiles for **(A)** Turbidity (NTUs; Seapoint Turbidity Meter) and Redox Potential (mV; NOAA-PMEL Oxidation Reduction Probe) and **(B)** Total Dissolvable Fe and Total Dissolvable Mn concentrations from the deep portion (>1000 m) of US GEOTRACES CTD Station GP16-37.

The most complete published CTD data from directly above the currently active vent-fields at Loihi Seamount (Bennett et al., 2011) show similar features to those reported here (**Figure 5**): *in situ* optical and redox sensor anomalies are accompanied by increases in metal concentrations in a sub-horizontal plume, ∼100 m above the seafloor, that reach maximum concentrations of 465 nM TDFe and 23 nM TDMn. Those results were collected approximately 10 years after the formation of the Pele's Pit in which modern venting is hosted, at a time when the source vent-sites at the seafloor exhibited maximum vent-fluid temperatures of 50–60°C (Glazer and Rouxel, 2009). In earlier work at Loihi, Sakai et al. (1987) had analyzed unfiltered water samples from a profile above Loihi Seamount and reported maximum plume concentrations of 200–250 nM Fe and 15–20 nM Mn at ∼1100 m depth. We note that those analyses date from 1985, prior to the formation of the collapse pits that host current hydrothermal venting. Concentrations of Fe and Mn from near-contemporaneous vent fluids, collected from the (since destroyed) Pele's Vents (30°C, 975 m depth) contained 1010 µM Fe and 21 µM Mn (Karl et al., 1988). Those values are approximately 5 times higher in Fe, and double the concentration in Mn than the similar-temperature fluids sampled at Teahitia in

1989 (Michard et al., 1993). A contemporaneous hydrothermal plume study at Teahtia reported maximum TDFe and TDMn concentrations of 68 nM and 19 nM, respectively, at the TH1 summit (Stüben et al., 1992) both of which are significantly lower (particularly for Fe) than the concentrations that we report here (**Table 1** and **Figure 5B**). Higher concentrations were reported from a station closer to TH4 (125 nM TDFe, 7 nM TDMn) but in both cases, what is important to note is that those signals were reported from plume depths of 1580 m (TH1) and 1540 m (TH4). Significantly, these depths are not only 140–180 m deeper than the plume data reported here (**Figure 5**) but also ∼100 m deeper than the source vent-fluids that were sampled on the same cruise (Michard et al., 1993). Thus, those data cannot readily be considered as a part of a time-series relevant to the plume data reported here, nor, indeed, as a product of the TH1 vent fluids. The origins of those early plume data remain enigmatic. Perhaps the most simple interpretation is that they represented output rising up from sources on the flanks of Teahitia, located deeper than the summit, at the time of that study. Because our sole CTD cast in 2013 targeted the TH1 site, our package could only descend as far as the seabed at that site and, hence, we do not have any additional information regarding what else might still be present in the water column below ∼1510 m depth.

Geophysical Evidence for Volcano-Tectonic Perturbations at Teahitia Seamount

At the time of their discovery, it was immediately noted that the venting discovered at the summit of Teahitia Seamount was very similar to that which had just been discovered at Loihi (Karl et al., 1988; Michard et al., 1993). Approximately a decade later, however, Loihi seamount experienced an episode of seafloor activity that led to volcanic pit collapse and a complete reconfiguration of the seafloor hydrothermal system. Fluid temperatures at the newly established vents inside Pele's Pit initially reached as high as 200°C (Davis and Clague, 1998) but intermittent studies of those same vent-sites over the following decades, have revealed that fluid temperatures had subsequently relaxed back to 50–60°C (∼10 years post-eruption (Glazer and Rouxel, 2009) and now fall in the range 30–40°C (German et al., 2018) – i.e., comparable to fluid temperatures at the pre-eruption vent-sites. From this perspective, it is interesting to ask whether any similar geological/hydrothermal perturbation event could have occurred at Teahitia between the last reported *Nautile* dives and our fieldwork in 2013. While the Society Islands hot-spot lacks the same opportunities for repeat submersible investigations as Lo'ihi, we can use geophysical approaches to address this issue.

First, we note that the morphology of the seafloor at Teahitia as surveyed in 2013 (**Figure 3**) is remarkably similar to that observed in the original 1986 SeaBeam survey (Cheminée et al., 1989) with the same 4 peaks of the composite volcano prominent (TH1-TH4). Certainly, there is no evidence for the drastic changes in surface morphology (including pit collapse) observed at Loihi over the same time frame (Clague et al., 2019). More specifically, we also note that the shallowest summit of the TH1 cone in our 2013 survey is 1460 m (**Figure 3**) which coincides exactly with the depth at which submarine venting was located at the summit of this same cone in both 1989 (Michard et al., 1993) and 1999 (Hékinian, 1999). There is no bathymetric evidence for seamount inflation or deflation. Perhaps uniquely for this deep ocean study site, however, the Polynesian seismic array (Réseau Sismique Polynésian; RSP) provides a continuous record of seafloor activity across the Society Islands hotspot area, with a sensitivity that extends down to $\leq M_L$ 1.0 magnitude events. This record dates from 1985 and, hence, spans the entirety of the time period under consideration here (**Figure 6**). Following the periods of intense seismicity that coincided with the first multibeam survey and submersible-based investigations of Teahitia seamount (1986–1992), a period of quiescence ensued (≤5 events per year, ∼1993–2009) that continued beyond the repeat seafloor observations conducted using *Nautile* in 1999 (Hékinian, 1999). Since 2010, however, the frequency of occurrence of seismic events at Teahitia has shown an increase back to sustained rates not observed since the end of the 1980s. Interestingly the majority of events over this recent cycle have all been relatively weak ($M_L < 1.0$), indicative of magmatic rather than tectonic sub-seafloor activity (Talandier and Okal, 1987). The one exception to that rule, at Teahitia, was a single M_L 4.9 earthquake in August 2012. Similarly large ($M_L > 4.0$) earthquakes detected at Mehetia and Teahitia at the time of the 1981–1985 seismicity crisis were attributed to tectonic events, perhaps linked to seafloor volcanic pit collapse (Talandier and Okal, 1984). As such, that work accurately presaged exactly the processes that arose in association with seafloor volcanic activity at Loihi Seamount, more than a decade later (Davis and Clague, 1998; Clague et al., 2019). In their original Teahitia study, Talandier and Okal (1984) also noted that a comparable abundance of seismic tremors, similar to that witnessed during the 1980s, had only previously been detected on Tahiti in 1918 (Lespinasse, 1919). This led the same authors to infer that episodes of renewed activity at the Society Islands hotspot might recur periodically, every 20–60 years. From this perspective, and at a 35 year remove from the last major

TABLE 1 | Total Dissolvable Fe and Mn concentrations at Teahitia Seamount.

Depth (m)	TDFe (nmol/L)	TDMn (nmol/L)	GEOTRACES I.D.
1326	0	1	10469
1350	1	1	10468
1375	31	3	10467
1390	185	21	10466
1400	186	33	10465
1410	165	19	10464
1425	142	15	10463
1455	108	13	10462
1460	92	9	10461
1475	6	1	10460
1500	15	1	10459
1511	14	n.d.	10458

US GEOTRACES CTD Station GP16-37 (17°34.4′S, 148°49.0′W).

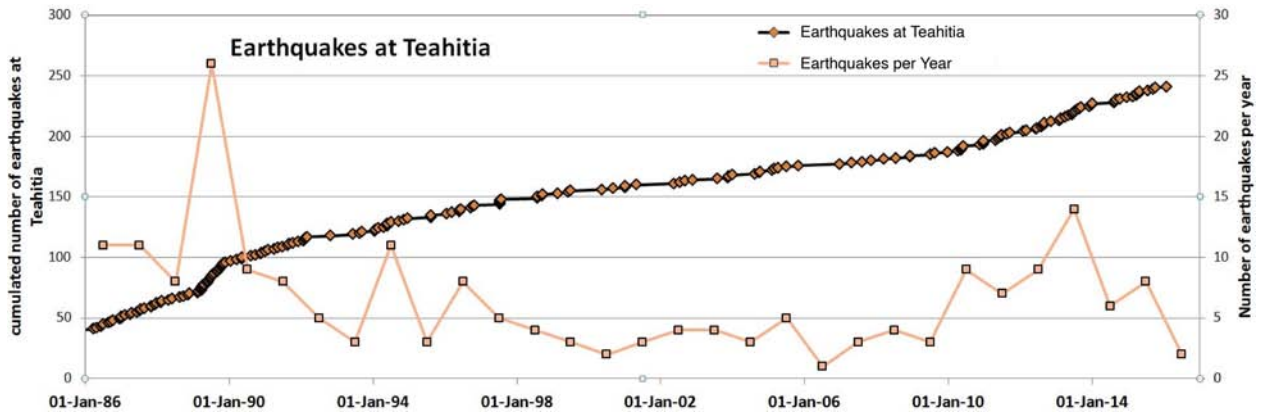

FIGURE 6 | Time series plot for cumulative number of seismic earthquake events detected at Teahitia Seamount via the Réseau Sismique Polynésie (Polynesian Seismic Network), 1986–2019, and the frequency (events per year) of those earthquakes over the same period.

seismicity crisis, it is interesting to note that the large (M_L 4.9) seismic event at Teahitia in August 2012 was bracketed by two additional, distinctive, seismic events in March 2011 and April 2013, at the Rocard seamount, just 20 km to the East (**Figure 2**). Those records were sufficiently distinctive that they could be interpreted to represent transient periods of strong hydrostatic pressure acting on the rift zones of the Rocard submarine shield volcano (Talandier et al., 2016). In that work, it was inferred that these seismic signatures were each diagnostic of an episode in which lava flowed through a shallow open conduit in the subseafloor, for example in a meter-wide dike or vertical upflow pipe, prior to eruptive outpouring at the seafloor. Could all of these data be consistent with a reactivation of the Society Islands hot-spot?

Oceanographic Evidence for Hydrothermal Perturbations at Teahitia Seamount

In the preceding section, we presented geophysical evidence that document temporal variability in the volcano-tectonic cycle at Teahitia, and beyond, that could be consistent with a re-activation of that seamount specifically, and/or across the Society Islands hotspot in general. But a question that we can address using our CTD plume data from directly above Teahitia is: do the heat-flux values that can be derived from our water column investigations *require* any departure from what was observed at the seafloor previously?

To address this question, a first calculation that we can pursue is to determine the heat flux implicit in our observed plume data. The optical and redox sensor data from our CTD cast provide clear evidence for a neutrally buoyant hydrothermal plume at ∼1400 m (**Figure 5**), i.e., at a height of ∼100 m above the seafloor source, assuming hydrothermal activity continues to be focused at the TH1 Summit (Michard et al., 1993; Hékinian, 1999). This terminal height for a hydrothermal plume depends mainly on its source buoyancy flux, together with the ambient stratification of the water column that it is injected into (Lupton, 1995). The scaling analysis of Turner (1986) suggests:

$$Z_{max} = 3.8B^{1/4}N^{-3/4} \quad (1)$$

where Z_{max} (m) is the terminal height of a plume, B (m^4s^{-3}) is the source buoyancy flux, and N (rad/s) is the buoyancy frequency of the ambient stratification. Using the temperature and salinity profiles from the nearest available "background" station (WOCE Station P16-220: 17°31′S, 150°30′W), over the depth range from 1200–1600 m that spans from below the TH1 summit to above the non-buoyant plume, we arrive at a value for $N = 0.0018$ rad/s. Substituting this value, and $Z_{max} = 100$ m into equation (1) allows us to calculate a value of $B = 0.0028\ m^4s^{-3}$ for the source of venting at Teahitia seamount. Assuming this buoyancy flux results primarily from the temperature anomaly of the source hydrothermal fluid (hydrothermal fluids are typically within a factor of two of seawater salinities and mix rapidly post-eruption (German and Seyfried, 2014), we calculate a corresponding heat flux, H, using the equation:

$$H = \frac{C_{p0}\rho_0}{g\alpha}B \quad (2)$$

in which C_{p0} = 3947 J/kg/°C and ρ_0 = 1027 kg/m^3 are the specific heat capacity and density of the ambient seawater at the depth of the vent source, respectively, $\alpha = 1.23 \times 10^{-4}$°C^{-1} is the corresponding thermal expansion coefficient, and $g = 9.8$ m/s^2 is the gravitational acceleration. For a value of $B = 0.0028\ m^4s^{-3}$, the corresponding heat flux that we calculate for hydrothermal activity at the TH1 summit of Teahitia seamount is ∼9.5 MW.

A potential weakness to this traditional approach to hydrothermal heat-flux determinations from static CTD profile data, however, is that the derivation of equation (1) assumes an idealized plume that originates from an idealized point source and rises in a calm (i.e., zero ambient flow) and linearly stratified environment. In reality, the plume overlying any hydrothermal field, world-wide, must rise above a source that is distributed over a finite area (even if only the size of a single vent-chimney

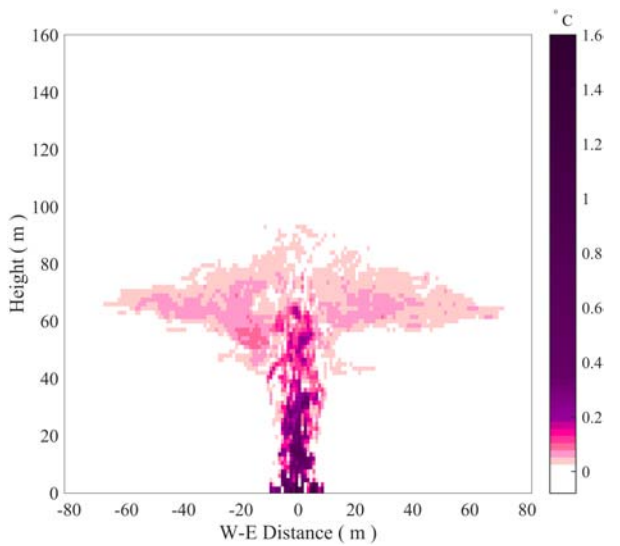

FIGURE 7 | Temperature anomalies for a simulated plume rising from a flat bottom into a stratified environment with zero ambient flow. The source heat flux for the plume is 10 MW and the area over which that source is distributed is 20 × 20 m. Background hydrography for the model is derived from CTD data taken from WOCE Station P16-220. The maximum height reached by the simulated plume is ∼90 m above the seafloor and the lateral dispersion height for the non-buoyant plume is centered at ∼65 m above bottom (equivalent to 1395–1400 m depth for a plume source situated on the shallowest 5 m of the TH1 cone at Teahitia (1460–1465 m).

orifice). Further, in a deep ocean seamount setting there are almost certainly lateral currents present that can also affect plume rise. To obtain a more sophisticated/less idealized estimate of the source heat flux at Teahitia, therefore, we have also conducted a 3-D numerical simulation using the plume model described in Lavelle et al. (2013). The model is a 3-D non-hydrostatic, time-dependent, turbulent convection construct for a domain that is open to flow on all four sides. Injection of heat flux over a 20 by 20 m area through the bottom boundary drives the buoyant rise of a plume into a calm, stratified, rotating (f-plane) water column. The spatial resolution of the model simulation run for Teahitia was 1.5 m in all three dimensions. The background temperature and salinity used in the model were imported from the same WOCE Station P16-220 data set used to calculate the buoyancy frequency, previously (see above). An example of our model output is shown in **Figure 7**: calculated temperature anomalies for a hydrothermal plume driven by a 10 MW heat flux, 4 h after initiation of the simulation. In this example, the plume rises to a maximum height of ∼90 m above the seafloor before relaxing back to disperse, laterally, at a height of 60–70 m above the seafloor. Assuming a constant depth of seafloor venting at the TH1 summit of Teahitia (1460 m) this would be consistent with the formation of a non-buoyant plume dispersing at 1390–1400 m providing a reassuringly close fit to what we have observed from our geochemical data (**Figure 5**).

The results from our scaling analysis and our 3-D simulation approaches, above, both suggest that a hydrothermal heat flux of ∼ 10 MW could be responsible for the dispersing non-buoyant hydrothermal plume signals observed in 2013 at Teahitia. However, neither case takes into account ambient flows and previous studies suggest that a hydrothermal plume injected into a cross-flow will rise to a lower level than a plume injected into a calm environment (Middleton and Thomson, 1986). Consequently, this estimate of 10 MW should be considered to be a highly conservative value, considering the likelihood of the presence of seamount related currents present at and above Teahitia. Accordingly, in the following discussion, we use 10 MW as the *minimum* source heat flux for the current state of venting at Teahitia.

Previously, seafloor surveys had revealed no evidence for high temperature venting at Teahitia. Instead, all that had been reported were a cluster of low-temperature chimneys, venting fluids at just 30°C at this intra-plate hot spot hydrothermal field. A question, arises, therefore, whether such a form of seafloor fluid flow could give rise to a coherent upflow of ≥10 MW that, in turn, could give rise to the non-buoyant hydrothermal plume signals that we have observed (**Figure 5**). If the answer is negative, then it implies that the hydrothermal venting at Teahitia, in 2013, could not be sustained by the venting observed previously and would, instead, be more consistent with a system that has been re-invigorated. To complete this next set of calculations, we first had to estimate an area over which low temperature venting might be taking place at Teahitia seamount in such a way that the cumulative flux may coalesce into a single coherent buoyant plume. The lateral extent of the venting area observed during past submersible dives at Teahitia is not well documented but detailed reading of the two Polynaut dive reports reveals a consistent pattern for the summit of the TH1 cone: while inactive Fe-rich chimneys became apparent at all depths shallower than 1470 m, it was only in the shallowest 4–5 m of each dive that active chimneys were observed. This potentially provides us with an important constraint because a detailed examination of the bathymetry close to the TH1 summit from 2013 (**Figure 3**) reveals that the shallowest 1470 m contour describes a roughly rectangular area of ∼50 × 100 m (**Figure 8**). Assuming regular geometry from there to the 1460 m summit, this would suggest that the uppermost 5 m (by depth) of the TH1 peak should represent an area of ∼20 m x 40 m yielding an area of venting, assuming 50% coverage of that uppermost region (Hékinian, 1999) of ∼400 m^2. For the calculations that follow, therefore, this is the idealized surface area that we have assumed for the source of input to our non-buoyant plume. For comparison, the largest contiguous area of low temperature flow documented anywhere at Loihi, the Spillway site, has recently been measured to cover an area of ≤450 m^2 (German et al., 2018). To estimate the heat flux that could be carried by ≤30°C fluids from the summit of Teahitia, we next need to obtain an estimate of the venting flow rate averaged over the source area. In the absence of direct flow rate measurements, we assume that the subsurface hydrothermal circulation at Teahitia follows *Darcy's Law* (Darcy, 1856; Whitaker, 1986) as viscous fluid flows through

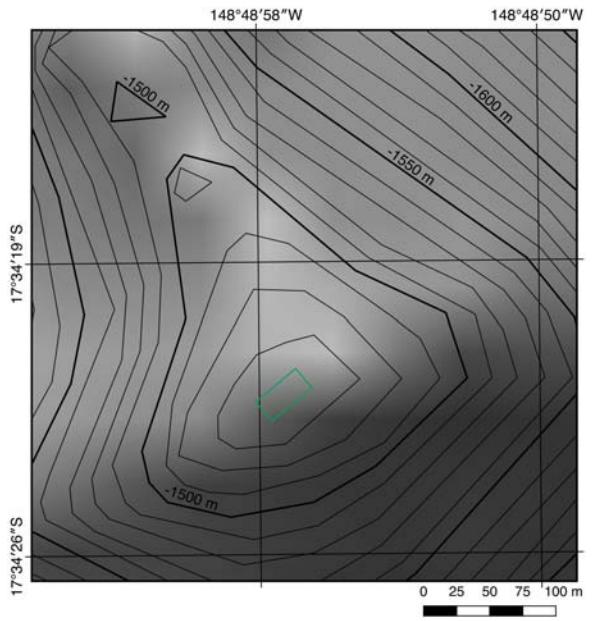

FIGURE 8 | Detailed bathymetric map (10 m contours) for the summit of the TH1 cone at Teahitia seamount (see **Figure 3**). Green rectangle illustrates a projected area of ∼40 × 20 m for the upper 4–5 m of the cone where low-temperature venting had previously been noted to be concentrated (Hékinian, 1999).

a porous medium, and calculate the venting flow rate, following Germanovich and Lowell (2004), as:

$$w = \frac{k}{\mu_h} g \rho_h \alpha_h (T_h - T_b), \tag{3}$$

in which k is the crustal permeability, μ_h, ρ_h, α_h, T_h are the dynamic viscosity, density, thermal expansion coefficient, and temperature of hydrothermal fluids, respectively, and T_b is the temperature of background pore fluids, which are assumed to be the same as local bottom water (2.6°C). According to Germanovich et al. (2000), the dynamic viscosity can be estimated as $\mu_h(T_h) = C_1/(T_h + C_2)$ where $C_1 = 0.032$ Pa s °C and $C_2 = 15.4$°C. We calculate ρ_h and α_h using the equation of state developed by Driesner (2007) as functions of T_h at a reference salinity of 34.76 ppt and a pressure of 149.4 bar. These values correspond to the salinity and pressure of background seawater at Teahitia at a depth of 1480 m. Subsequently, we calculate the source heat flux as:

$$H = C_{ph} \rho_h (T_h - T_b) wA, \tag{4}$$

where C_{ph} is the specific heat capacity of the vent fluids calculated using the Driesner (2007) equation of state as a function of T_h at the same reference salinity and pressure mentioned above, and A = 400 m^2 is the source area. To the best of our knowledge, there have been no previous estimates of crustal permeability at Teahitia. In the absence of relevant data from that site (or, indeed, any of the other four known intra-plate hotspot hydrothermal fields) we rely, instead, upon the known crustal permeability values from the Endeavor Segment, Juan de Fuca Ridge, as a surrogate (Endeavor is known for its vigorous hydrothermal activity, which consists of five major vent fields with a combined heat flux >1000 MW (Kellogg, 2011). In the following calculation, we use the upper limit for estimated crustal permeability at Endeavor, $k \sim 10^{-10}$ m^2 (Hearn et al., 2013), to establish a *maximum* crustal permeability at Teahitia. Substituting $k = 10^{-10}$m^2 along with $T_h = 30°C$ and $T_b = 2.6°C$ into equations (3) and (4) gives $w = 1.34 \times 10^{-5}$ m/s and, consequently, an estimate of heat-flux, $H = 0.6$ MW.

This is much lower than the *minimum* value of 10 MW that we had previously established would be required to sustain the non-buoyant hydrothermal plume signals that we have observed (**Figure 5**). Apparently, then, the plume signals that we have observed could not be sustained by an area of low-temperature flow restricted to the uppermost portion of TH1 with venting at ≤30°C as reported from Teahitia in 1989 and again in 1999 (Michard et al., 1993; Hékinian, 1999). Nevertheless, we do know that very similar hydrothermal plume signals have subsequently been reported from above Loihi seamount (Bennett et al., 2011) at a time when the underlying vent-fluids, also exiting from Fe-rich hydrothermal chimneys, were significantly hotter, at 50–60°C (Glazer and Rouxel, 2009). Could the hydrothermal heat output at Teahitia have increased by more than an order of magnitude between the time of the last Nautile submersible dives in 1999, therefore, and our return study in 2013? To investigate this, we allowed T_h to vary from 30 up to 100°C while recalculating predicted heat-flux values, H, using equations (3) and (4). Our results (**Figure 9**) indicate that an area of low-temperature flow exiting the seafloor at the summit of Teahitia *could* sustain a source heat flux of ≥10 MW over the prescribed 400 m^2 area (and, hence, generate the non-buoyant plume observed in our CTD data) if the effective vent-temperatures for that low temperature flow were ≥70°C, rather than ≤30°C. We consider this entirely plausible, given that the model temperatures required match so closely to those

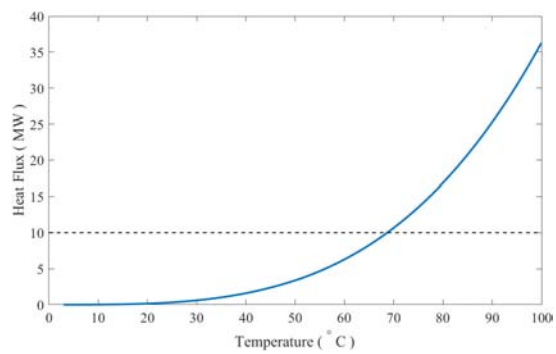

FIGURE 9 | Plot of calculated heat flux responsible for the oceanographic plume observations reported at Teahitia, assuming venting occurs as low-temperature flow distributed across the summit of Teahita (see section "Discussion"). To reach the heat flux values calculated in this study (≥10 MW) requires seafloor fluid temperatures of ≥70°C which are significantly higher than what was observed 25 years earlier but fits closely to the range of post-eruption vent-fluid temperatures at Loihi seamount (German et al., 2018).

recorded from Loihi across the decade immediately following the most recent volcanic activity at that site in 1996, with temperatures up to 200°C soon after the event (Davis and Clague, 1998) relaxing back to 50–60°C a decade later in 2005–2007 (Glazer and Rouxel, 2009). In summary, the oceanographic data for Teahitia do appear to be consistent with a field of low temperature hydrothermal venting clustered at the summit of the TH1 cone, similar to what had been described previously, but only if the temperature of that venting, at the time of our field program in 2013, was ≥70°C, i.e., significantly hotter than the maximum temperatures reported when the site was last visited by submersible 15–25 years earlier. Given the close similarity between this work (both in terms of model-required source temperatures *and* water column plume observations) with their conjugate data sets for Loihi, approximately 10 years after the most recent seafloor volcanic event, we tentatively conclude that our oceanographic data, coupled with those from our geophysical observations, do indeed, provide evidence that the Society Islands hot spot may be in the process of renewing activity. We strongly recommend detailed follow-up investigations of this possibility in the nearest possible future.

SUMMARY

The Teahitia Seamount, at the western limit of the currently active Society Islands hotspot, hosts one of just five intraplate hydrothermal fields ever to have been discovered, worldwide. More than 30 years after low temperature (≤30°C) submarine venting was first discovered at Teahitia, the presence of a non-buoyant plume overlying its summit confirms that hydrothermal activity continues at this site. While there has only been one direct observation of seafloor venting in the intervening 25 years, continuous seismic monitoring of the region suggests that a ∼15 year period of quiescence followed the seismicity crisis that first led to submersible-led exploration of this area, from 1992–2007. Since then, the Polynesian Seismic Network has revealed a return to the same level of frequency of occurrence of seismic events at Teahitia reported in the late 1980s that could be consistent with a reactiviation of the Society Islands hotspot. Specifically, the preponderance of events detected at Teahitia are $M_L < 1.0$, consistent with magmatic rather than tectonic activity, while distinct seismic signatures of events at the adjacent Rocard seamount (25 km to the East) have also been interpreted to be indicative of submarine extrusive events, in 2011 and 2013. Theoretical modeling of output for the hydrothermal plume reported here requires an input of hot, chemically enriched fluids with a net heat output of ∼10 MW. From comparison with the similar hydrothermal plume signals overlying the Loihi seamount, we recognize that such signatures do not necessarily imply a focused high-temperature hydrothermal vent source at the seafloor. However, our model simulations do suggest that if low-temperature hydrothermal activity of the kind identified previously at the summit of Teahitia is responsible, the plume signatures we observe can only be sustained if the erupting vent fluids have increased in temperature from ≤30°C to closer to 70°C. Again, such changes could be entirely consistent with renewed volcanic and hydrothermal activity at the Society Islands hotspot. Return submersible-led visits to the area are clearly merited – if not long overdue!

DATA AVAILABILITY STATEMENT

The datasets generated for this study are available on request to the corresponding author.

AUTHOR CONTRIBUTIONS

CG, JM, and GC were PIs for the cruise in 2013. CG directed shipboard operations. JR was responsible for sampling and post-cruise Fe and Mn analyses discussed in section "Hydrothermal Plume Signals Over Teahitia Seamount." CG, JR, and CD were PIs for a planned follow-on cruise with IY, GX, and OH instead of which, IY, OH, and DR processed the geophysical data discussed in section "Geophysical Evidence for Volcano-Tectonic Perturbations at Teahitia Seamount." GX processed the data discussed, together with complementary model simulations, in section "Oceanographic Evidence for Hydrothermal Perturbations at Teahitia Seamount." SW prepared the NOAA-PMEL ORP probe for deployment and contributed to the processing of those data post cruise. All authors participated in the interpretation of the data and writing of the manuscript.

FUNDING

Field work for this project was funded through NSF Awards to CG (OCE-1130870), JR (OCE-1237011), GC (OCE-1130245), and JM (OCE-1131731). Post-cruise, additional support was provided through NOAA Cooperative Agreement NA15OAR432006 and funding from WHOI and GEOMAR Helmholtz Centre for Ocean Research Kiel. The Réseau Sismique Polynésie was supported at LDG by the Commissariat à l'Energie Atomique et aux Energies Renouvelables. Open Access publication charges for this paper were provided by the Schmidt Ocean Institute.

ACKNOWLEDGMENTS

We thank the Captain and crew of the RV Thomas G. Thompson cruise TN303 and, especially, Rob Palomares (SIO) for his support of our CTD operations and Patrick A'Hearn and Steve Jalickee (UW) for their support in conducting the EM302 multibeam survey. GX thanks J. W. Lavelle for support in conducting the 3D numerical simulations of the Teahitia plume. We also thank the Schmidt Ocean Institute for bringing this team of collaborators together and, in particular, Captain Bernd Buchner and the crew of the RV Falkor for their hospitality aboard ship in Papeete, where the first draft of this manuscript was generated. Finally, we thank Guest Editor DA and two reviewers for their contributions in improving the original version of this manuscript.

REFERENCES

Baker, E. T., and German, C. R. (2004). On the global distribution of mid-ocean ridge hydrothermal vent-fields. *Geophys. Monogr.* 148, 245–266. doi: 10.1029/148gm10

Baker, E. T., German, C. R., and Elderfield, H. (1995). Hydrothermal plumes: global distributions and geological inferences. *Geophys. Monogr.* 91, 47–71. doi: 10.1029/gm091p0047

Beaulieu, S. E., Baker, E. T., and German, C. R. (2015). Where are the undiscovered hydrothermal vents on oceanic spreading ridges? *Deep Sea Res. II* 121, 202–212. doi: 10.1016/j.dsr2.2015.05.001

Beaulieu, S. E., Baker, E. T., German, C. R., and Maffei, A. (2013). An authoritative global database for active submarine hydrothermal vent fields. *Geochem. Geophys. Geosystems* 14, 4892–4905. doi: 10.1002/2013gc004998

Bennett, S. A., Hansman, R. L., Sessions, A. L., Nakamura, K., and Edwards, K. J. (2011). Tracing iron-fueled microbial carbon production within the hydrothermal plume at the Loihi seamount. *Geochim. Cosmochim. Acta* 75, 5526–5539. doi: 10.1016/j.gca.2011.06.039

Binard, N., Hékinian, R., Cheminée, J.-L., and Stoffers, P. (1992). Styles of eruptive activity on interaplate volcanoes in the Society and Austral hot spot regions: bathymetry, petrology and submersible operations. *J. Geophys. Res.* 97, 13999–14015.

Cheminée, J. L., Hékinian, R., Talandier, J., Albarède, F., Devey, C. W., Francheteau, J., et al. (1989). Geology of an active hot spot: Teahitia-Mehetia region in the South Central Pacific. *Mar. Geophys. Res.* 11, 27–50. doi: 10.1007/bf00286246

Clague, D. A., Paduan, J. B., Caress, D. W., Moyer, C. L., Glazer, B. T., and Yoerger, D. R. (2019). Structure of Loihi Seamount, Hawaii and lava flow morphology from high-resolution mapping. *Front. Earth. Sci.* 7:58. doi: 10.3389/feart.2019.00058

Darcy, H. (1856). *Les Fontaines Publiques De La Ville De dijon*. Paris: Dalmont.

Davis, A. S., and Clague, D. A. (1998). Changes in the hydrothermal system at Loihi Seamount after the formation of Pele's pit in 1996. *Geology* 26, 399–402.

Driesner, T. (2007). The system H2O—NaCl. Part II: Correlations for molar volume, enthalpy, and isobaric heat capacity from 0 to 1000 8C, 1 to 5000 bar, and 0 to 1 XNaCl. *Geochim. Cosmochim. Acta* 71, 4902–4919. doi: 10.1016/j.gca.2007.05.026

German, C. R., Lim, D. S. S., Breier, J. A., Huber, J. A., Nawotniak, S. K., Shock, E., et al. (2018). "Time series study of hydrothermal venting at Lo'ihi Seamount following the 2018 Kilauea eruption," *Proceedings of the Fall Meeting 2018* (Washington, DC: AGU V14A-07).

German, C. R., and Seyfried, W. E. (2014). Hydrothermal Processes. *Treatise Geochem.* 8, 191–233.

Germanovich, L. N., and Lowell, R. P. (2004). Hydrothermal processes at Mid-Ocean Ridges: results from scale analysis and single pass models. *Geophys. Monogr.* 148, 219–244. doi: 10.1029/148gm09

Germanovich, L. N., Lowell, R. P., and Astakhov, D. K. (2000). Stress-dependent permeability and the formation of seafloor event plumes. *J. Geophys. Res.* 105, 8341–8354. doi: 10.1029/1999jb900431

Glazer, B. T., and Rouxel, O. J. (2009). Redox speciation and distribution within diverse iron-dominated microbial habitats at Loihi Seamount. *Geomicrobiol. J.* 26, 606–622. doi: 10.1080/01490450903263392

Gutenberg, B., and Richter, C. F. (1954). *Seismicity of the Earth and Associated Phenomena*. Princeton, NJ: Princeton University Press, 310.

Hearn, C. K., Homola, K. L., and Johnson, H. P. (2013). Surficial permeability of the axial valley seafloor: Endeavour segment, Juan de Fuca ridge. *Geochem. Geophys. Geosyst.* 14, 3409–3424. doi: 10.1002/ggge.20209

Hékinian, R. (1999). *Polynaut Tahiti-Pitcairn-Tahiti. RV L'Atalante Cruise Report*. France: IFREMER.

Karl, D. M., McMurtry, G. M., Malahoff, A., and Garcia, M. O. (1988). Loihi Seamount, Hawaii: a mid-plate volcano with a distinctive hydrothermal system. *Nature* 335, 532–535. doi: 10.1038/335532a0

Kellogg, J. P. (2011). *Temporal and Spatial Variability of Hydrothermal Fluxes Within a Mid-Ocean Ridge Segment*. Washington: University of Washington, 141. Ph.D. Thesis.

Lavelle, J. W., Di Iorio, D., and Rona, P. (2013). A turbulent convection model with an observational context for a deep-sea hydrothermal plume in a time-variable cross flow. *J. Geophys. Res.* 118, 6145–6160. doi: 10.1002/2013JC009165

Lespinasse, A. (1919). Observations météorologiques faites à l'Observatoire de l'hôpital de Papeete. *Bull. Soc. Étud. Océanienne Polynésie Fr.* 5, 62–63.

Lupton, J. E. (1995). Hydrothermal plumes: near and far-field. *Geophys. Monogr.* 91, 317–346. doi: 10.1029/gm091p0317

Michard, A., Michard, G., Stüben, D., Stoffers, P., Cheminée, J.-L., and Binard, N. (1993). Submarine thermal springs associated with young volcanoes: The Teahitia vents, Society Islands, Pacific Ocean. *Geochim. Cosmochim. Acta* 57, 4977–4986. doi: 10.1016/s0016-7037(05)80003-1

Middleton, J. M., and Thomson, R. E. (1986). Modeling the rise of hydrothermal plumes, Can. *Tech. Rep. Hydrogr. Ocean Sci* 69, 18.

Moffett, J. W., and German, C. R. (2018). The US GEOTRACES Eastern Tropical Pacific Transect (GP16). *Mar. Chem.* 201, 1–262. doi: 10.1016/j.marchem.2017.12.001

Okal, E. A., Talandier, J., Sverdrup, K. A., and Jordan, T. H. (1980). Seismicity and tectonic stress in the Southcentral Pacific. *J. Geophys. Res.* 85, 6479–6495. doi: 10.1029/jb085ib11p06479

Resing, J. A., Sedwick, P. N., German, C. R., Jenkins, W. J., Moffett, J. W., Sohst, B. M., et al. (2015). Basin-scale transport of hydrothermal dissolved metals across the South Pacific Ocean. *Nature* 523, 200–203. doi: 10.1038/nature14577

Sakai, H., Tsubota, H., Nakai, T., Ishibashi, J., Akagi, T., Gamo, T., et al. (1987). Hydrothermal activity on the summit of Loihi Seamount. *Hawaii. Geochem. J.* 21, 11–21. doi: 10.2343/geochemj.21.11

Staudigel, H., Hart, S. R., Pile, A., Bailey, B. E., Baker, E. T., Brooke, S., et al. (2006). Vailulu'u Seamount, Samoa: life and death on an active submarine volcano. *Proc. Natl. Acad. Sci.U.S.A.* 103, 6448–6453. doi: 10.1073/pnas.0600830103

Stüben, D., Stoffers, P., Cheminée, J.-L., Hartmann, M., McMurtry, G. M., Richnow, H.-H., et al. (1992). Manganese, methane, iron, zinc and nickel anomalies in hydrothermal plumes from Teahitia and Macdonald volcanoes. *Geochim. Cosmochim. Acta* 56, 3693–3704. doi: 10.1016/0016-7037(92)90162-c

Talandier, J., Hyvernaud, O., and Maury, R. C. (2016). Unusual seismic activity in 2011 and 2013 at the submarine volcano Rocard, Society hot spot (French Polynesia). *Geophys. Res. Lett.* 43, 4247–4254. doi: 10.1002/2016gl068342

Talandier, J., and Kuster, G. T. (1976). Seismicity and submarine volcanic activity in French Polynesia. *J. Geophys. Res.* 81, 936–948. doi: 10.1029/jb081i005p00936

Talandier, J., and Okal, E. A. (1984). The volcanoseismic swarm of 1981-1983 in the Tahiti-Mehetia area, French Polynesia. *J. Geophys. Res.* 89, 11216–11234. doi: 10.1029/jb089ib13p11216

Talandier, J., and Okal, E. A. (1987). Seismic detection of underwater volcanism: the example of French Polynesia. *Pure Appl. Geophys.* 125, 919–950. doi: 10.1007/bf00879361

Turner, J. S. (1986). Turbulent entrainment: The development of the entrainment assumption, and its application to geophysical flows. *J. Fluid Mech.* 173, 431–471. doi: 10.1017/s0022112086001222

Whitaker, S. (1986). Flow in porous media I: a theoretical derivation of Darcy's Law. *Transp. Porous Med.* 1, 3–25. doi: 10.1007/bf01036523

Conflict of Interest: The authors declare that the research was conducted in the absence of any commercial or financial relationships that could be construed as a potential conflict of interest.

The handling Editor declared a past collaboration with one of the authors CG.

Copyright © 2020 German, Resing, Xu, Yeo, Walker, Devey, Moffett, Cutter, Hyvernaud and Reymond. This is an open-access article distributed under the terms of the Creative Commons Attribution License (CC BY). The use, distribution or reproduction in other forums is permitted, provided the original author(s) and the copyright owner(s) are credited and that the original publication in this journal is cited, in accordance with accepted academic practice. No use, distribution or reproduction is permitted which does not comply with these terms.

frontiers in Marine Science

ORIGINAL RESEARCH
published: 03 March 2020
doi: 10.3389/fmars.2020.00027

Lava Flows Erupted in 1996 on North Gorda Ridge Segment and the Geology of the Nearby Sea Cliff Hydrothermal Vent Field From 1-M Resolution AUV Mapping

David A. Clague[1], Jennifer B. Paduan[1], David W. Caress[1], James McClain[2] and Robert A. Zierenberg[2]*

[1] Monterey Bay Aquarium Research Institute, Moss Landing, CA, United States, [2] Department of Geology, University of California, Davis, Davis, CA, United States

The northernmost segment of the Gorda mid-ocean ridge is the site of a small-volume eruption in 1996 and the persistent off-axis Sea Cliff hydrothermal vent field. To better understand the geologic setting and formation of these features, 1-m resolution bathymetric mapping using autonomous underwater vehicles was completed in 2016. The mapped region covers 35 km^2 and 15.6 km of the volcanic axis from south of the 1996 lava flows, and a cross section for ∼4.5 km perpendicular to the axis, that extends beyond the Sea Cliff hydrothermal vent field. A proposed 1996 flow ∼7 km south of previously mapped flows is an artifact from a poor pre-eruption survey. The 1996 flows consist of three discrete steep hummocky mounds of pillows and syneruptive talus. The Sea Cliff hydrothermal field is located a few km north of the narrowest, shallowest section of the ridge segment, 2.6 km east of the center of the neovolcanic zone, and ∼370 m above the average depth of the axial graben on the largest offset ridge-parallel fault. No evidence supports the prior hypothesis that the site is located where two fault systems intersect. The axial graben is asymmetrical with larger fault offsets on the east side. The ridge axis below the hydrothermal field and to the south toward the 1996 flows is constructed dominantly of hummocky flows of pillow basalt, many unusually steep-sided, with syneruptive talus at the base of their steep slopes. Three channelized flows ponded between steep hummocky flows, and then partially drained. Some low-eruption-rate hummocky flows and high-eruption-rate channelized flows have nearly identical compositions, supporting the idea that eruption rates on mid-ocean ridges vary because of different dike widths. Four volcanic structures with volumes between 0.18 and 0.25 km^3 occur in the axial graben south of the 1996 flows. Two are flat-topped cones, another is a 1.5-km diameter inflated hummocky flow with 7 pit craters that demonstrate that the flow had a molten interior during growth. The fourth voluminous structure is a steep ridge with abundant syneruptive talus on its lower slopes. The North Gorda segment is an end-member, structurally and volcanically, compared with other Pacific intermediate-rate spreading ridges.

Keywords: mapping AUV, hydrothermal vent field, mid-ocean ridge volcanism, Gorda Ridge, MORB

OPEN ACCESS

Edited by:
Stephen Hammond, Office of Oceanic and Atmospheric Research (NOAA), United States

Reviewed by:
Colin Devey, GEOMAR Helmholtz Centre for Ocean Research Kiel, Germany
Roger Searle, Durham University, United Kingdom

****Correspondence:***
David A. Clague
clague@mbari.org

Specialty section:
This article was submitted to Deep-Sea Environments and Ecology, a section of the journal Frontiers in Marine Science

Received: *30 May 2019*
Accepted: *16 January 2020*
Published: *03 March 2020*

Citation:
Clague DA, Paduan JB, Caress DW, McClain J and Zierenberg RA (2020) Lava Flows Erupted in 1996 on North Gorda Ridge Segment and the Geology of the Nearby Sea Cliff Hydrothermal Vent Field From 1-M Resolution AUV Mapping. Front. Mar. Sci. 7:27. doi: 10.3389/fmars.2020.00027

INTRODUCTION

Construction of the oceanic crust requires frequent eruptions along the 65,000 km-long mid-ocean ridge system. Yet, such eruptions are infrequently documented or studied in detail (Rubin et al., 2012) to decipher how the crust is constructed and then modified as it migrates away from the neovolcanic axis of the ridge. What are the volumes, rates, styles, and frequency of eruptions at mid-ocean ridges with different spreading rates? What percent of eruptions produce hummocky flows of pillow lavas and what percent channelized flows of sheet lava? Is talus formed along younger axis-parallel normal faults or is some syneruptive? These are volcanological questions that have been addressed for decades (e.g., Perfit and Chadwick, 1998). Subsequent modification of the crust introduces more questions. What controls the location of on-and off-axis hydrothermal venting? Sediment accumulates on new lava flows, but how quickly does it subdue the surface morphology of the flows and bury them? As crustal accretion continues, how and where is the newly formed crust faulted?

Answers to these and other questions about crustal formation and modification require detailed observations and sampling at a range of ridge segments spreading at different rates and with different axial morphologies. Most such studies have been done at faster spreading segments of the East Pacific Rise (e.g., White et al., 2000, 2002; Fornari et al., 2004; Soule et al., 2005, 2007, 2009; Fundis et al., 2010; Waters et al., 2013; Le Saout et al., 2014) or the slow spreading Mid-Atlantic Ridge (MAR) (e.g., Ballard and van Andel, 1977; Smith and Cann, 1992, 1993; Bideau et al., 1998; Yeo et al., 2012; Yeo and Searle, 2013). Similar high-resolution studies are published for some intermediate-spreading ridges in the Pacific that range from full-spreading rates of 4.9 to 6.0 cm/yr, including the southern Juan de Fuca Ridge (Stakes et al., 2006), the Galapagos Spreading Center (Colman et al., 2012), the Endeavor Segment of the Juan de Fuca Ridge (Clague et al., 2014), and the northernmost segment of the East Pacific Rise named Alarcon Rise (Clague et al., 2018a).

Observations and sampling are expensive and time-consuming to acquire, and much of what has been collected on the Gorda Ridge, the intermediate-spreading-rate mid-ocean ridge offshore southern Oregon and northern California (**Figure 1**), was acquired prior to availability of reliable GPS ship navigation or with bathymetric control too poor to define their geological setting. These older data can be repurposed to constrain modern studies if they can be placed into a spatial and temporal framework, such as provided by 1–1.5 m resolution bathymetry collected by autonomous underwater vehicles (AUVs). Here, we combine newly acquired AUV maps with mostly published dive observations and hydrothermal deposit and lava flow samples collected between 1983 and 2005 on the North Gorda segment of the Gorda Ridge. These data provide new insights into an eruption that occurred in 1996, crustal accretion processes, petrology and ridge structure along and across the segment, variables that control eruption rates and therefore lava flow morphology, and the geology and setting of the off-axis Sea Cliff hydrothermal site.

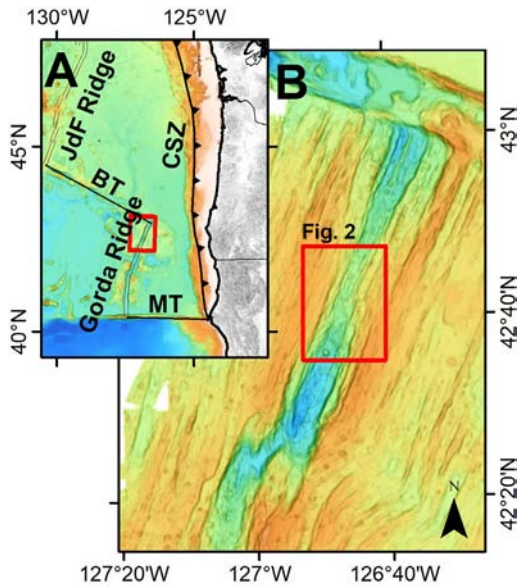

FIGURE 1 | (A) Regional map showing the location of North Gorda Segment of the Gorda mid-ocean ridge spreading center. BT is Blanco Transform, MT is Mendocino Transform, and CSZ is Cascade Subduction Zone. Depth ranges from –5000 (deep blue) to 0 m (white) and red box shows extent of part B. **(B)** Ship bathymetry of North Gorda segment. Red box encompasses central part of segment where high-resolution AUV bathymetric surveys shown in **Figure 2** were collected. Depth range is from –4500 m (blue) to –1500 m (orange).

GEOLOGIC SETTING

The Gorda Ridge is an intermediate-rate ridge with a full-spreading rate of 55 mm/yr, roughly the middle of the 49–60 mm/yr range of spreading rates of Pacific intermediate-rate ridges (DeMets et al., 2010). Despite its average intermediate spreading rate, the Gorda Ridge is a structural end-member because its unusually deep, wide axial graben resembles those on slower-spreading ridges such as the MAR (e.g., Murton and Rona, 2015), as noted by Clague and Holmes (1987) and Chadwick et al. (1998). The Gorda Ridge graben, at up to 700 m deeper than the surrounding seafloor and 20 km wide, is neither as deep nor as wide as the MAR axial graben, but is still wider and deeper than axial graben at other intermediate-rate ridges such as the Endeavor segment of the Juan de Fuca Ridge (Clague et al., 2014). The Gorda Ridge is divided into five offset segments named North Gorda, Jackson, Central, Phoenix and Escanaba from north to south (Chadwick et al., 1998). An eruption occurred in 1996 less than 10 km south of the narrowest, shallowest part of the North Gorda segment, but still where the spreading rate is fastest and the magma supply is most robust on Gorda Ridge (Chadwick et al., 1998). The North Gorda segment is 65 km long and has a narrow (2 km wide), 3000 m below sea level deep axial valley in the central part, widening to 5–10 km wide and 3500–4000 m deep to the north and south.

Most work on Gorda Ridge has been conducted on the North Gorda (**Figure 1**) and Escanaba segments where active

hydrothermal vent fields named, respectively, Sea Cliff or alternately, GR 14 (Rona et al., 1990; Von Damm et al., 2006) and NESCA (Zierenberg et al., 1994; Von Damm et al., 2005) are located. An additional hydrothermal discharge site near the Blanco Transform existed in 1985 and is termed the GR 15 site (Rona et al., 1992), but the vents have never been pin-pointed nor sampled. The Sea Cliff vent field is located ∼3 km north of the narrowest, shallowest portion of the North Gorda axis, but is unusual in being located 2.2 km east of and ∼350 m above the axial valley at −2720 m depth (distances and depths modified from Rona et al., 1990; Von Damm et al., 2006).

PRIOR WORK

Most geological studies on the North Gorda segment of the Gorda mid-ocean ridge were completed prior to introduction of GPS navigation, in contrast to many other parts of the global ridge system. The first such study focused on dredging of lava samples along the entire Gorda Ridge in 1983 (Davis and Clague, 1987). This was closely followed by hydrocast surveys to assess the potential for hydrothermal discharge (Baker et al., 1987). Camera tows, coring, and dredging surveys (Howard and Fisk, 1988; Rona and Clague, 1989; Clague and Rona, 1990; Davis and Clague, 1990) pinpointed a likely hydrothermal source high on the east wall of the axial graben after a water column anomaly was discovered. Active high-temperature venting was discovered during a series of five dives using the U.S. Navy's *Sea Cliff* manned submersible in 1988 and named the Sea Cliff hydrothermal field (Rona et al., 1990). Recovered samples consisted of silicified volcaniclastic rocks (Zierenberg et al., 1995). Hydrothermal fluids were not collected during the *Sea Cliff* dives, but the clear ∼305°C hydrothermal fluids collected during ROV *Tiburon* dives from 2000 to 2004 had lower Cl contents than seawater and contained extremely low transition metal concentrations (Von Damm et al., 2006). The inference was that the metals had precipitated out below the seafloor due to the slightly elevated pH of the fluids. The elevated pH was attributed to dissolution of calcite in the ocean crust during the roughly 100,000 years since the host lavas erupted on the ridge axis. The hydrothermal fluids at the Sea Cliff site were analyzed by *in situ* Raman spectroscopy during four ROV *Tiburon* dives in 2004 (White et al., 2006), and showed removal of seawater sulfate in the subsurface, leading to formation of anhydrite that hydrates to gypsum in the chimney samples. Fluid samples from one of these dives are the most recently collected vent fluids (Von Damm et al., 2006). The vent-specific biological community contains many of the same animals as seen at the NESCA site on the Escanaba Trough segment of the ridge (Van Dover et al., 1990; Clague et al., 2001). A new vent field 775 m north of Sea Cliff field was discovered in 2019 during Ocean Exploration Trust's R/V *Nautilus* cruise NA108 and named Apollo (C. German, personal communication). It is at 2727 m depth along the same fault bench and has similar characteristics to the Sea Cliff site (**Figure 2**).

In February 1996, seismic activity (Fox and Dziak, 1998) ∼11 km south of the Sea Cliff hydrothermal site was detected with the Navy's SOSUS hydrophone array. Several rapid response cruises using hull-mounted multibeam sonar, towed camera, and the remotely operated vehicles (ROV) *ATV* and *Jason* discovered, mapped, and sampled a new lava flow (Chadwick et al., 1998; Cowen and Baker, 1998; Rubin et al., 1998). MBARI began exploration and sampling of the lava flows along the entire Gorda Ridge using ROV *Tiburon* in 2000 (Clague et al., 2003, 2009; Davis et al., 2008; Yeo et al., 2013), including the 1996 pillow mounds in 2005. Davis et al. (2008) reported on the major and trace element and radiogenic isotopic compositions of axial basalt samples from the length of the North Gorda segment and evaluated their petrogenesis, but did not focus on their spatial or temporal variability, nor identify which of their samples were from the 1996 flows.

METHODS

The 1-m resolution bathymetric data were collected by MBARI using Dorado class AUVs equipped for seafloor mapping with multibeam sonar, chirp sidescan sonar, and chirp sub-bottom profiler (Caress et al., 2008). A single survey in 2009 was centered over the 1996 flows (Yeo et al., 2013). Two additional surveys in 2016 expanded the coverage to include the Sea Cliff hydrothermal site and the ridge axis between the 1996 flows and Sea Cliff site (**Figure 2**). The three surveys mapped 35 km^2, of which 26.2 km^2 is of the graben floor along the axis, and the remainder is of a series of fault blocks to the east of the axis. Prior lava sample locations (Davis and Clague, 1987, 1990: Rubin et al., 1998; Davis et al., 2008) are also shown on **Figure 2**, subdivided by the MgO content of the recovered glasses.

The 2009 survey was conducted using the AUV *D. Allan B.* operated from R/V *Zephyr*; at that time the AUV fielded a 200 kHz Reson 7125 multibeam, dual frequency 110 kHz/410 kHz Edgetech chirp sidescan sonar, and a 2–16 kHz sweep Edgetech sub-bottom profiler. The 2016 surveys were collected using two mapping AUVs operated simultaneously from R/V *Rachel Carson*; these vehicles each fielded a 400 kHz Reson 7125 multibeam, a 110 kHz Edgetech chirp sidescan, and a 1–6 kHz swap Edgetech sub-bottom profiler. All three AUV survey missions were conducted using a 50 m altitude and a 1.5 m/s (5.4 km/hr) speed for a 16–17 h duration. The AUVs also carry SeaBird SBE-49 fastCat CTD and Paroscientific pressure sensors; during the 2009 survey the AUV also carried Eh, optical backscatter, and magnetometer sensors.

The 200 kHz multibeam used in 2009 produced 256 1° × 1° beams across a 135° swath, and the 400 kHz sonars used in 2016 produced 512 1° × 0.5° beams across a 165° swath (though generally about a 140° swath is achieved in volcanic terrain). A 1° × 1° beam at nadir corresponds to a 0.7 m diameter footprint from a 50 m altitude, and the footprints spread out larger toward the outer swath, yielding an average resolution scale of about 1 m. Following tidal correction, the repeatable bathymetric vertical precision is 0.1 m.

MBARI mapping AUV realtime navigation derives from a Kearfott SeaDevil inertial navigation system (INS) which integrates a 24 cm ring laser gyro, accelerometers, and a 300 kHz

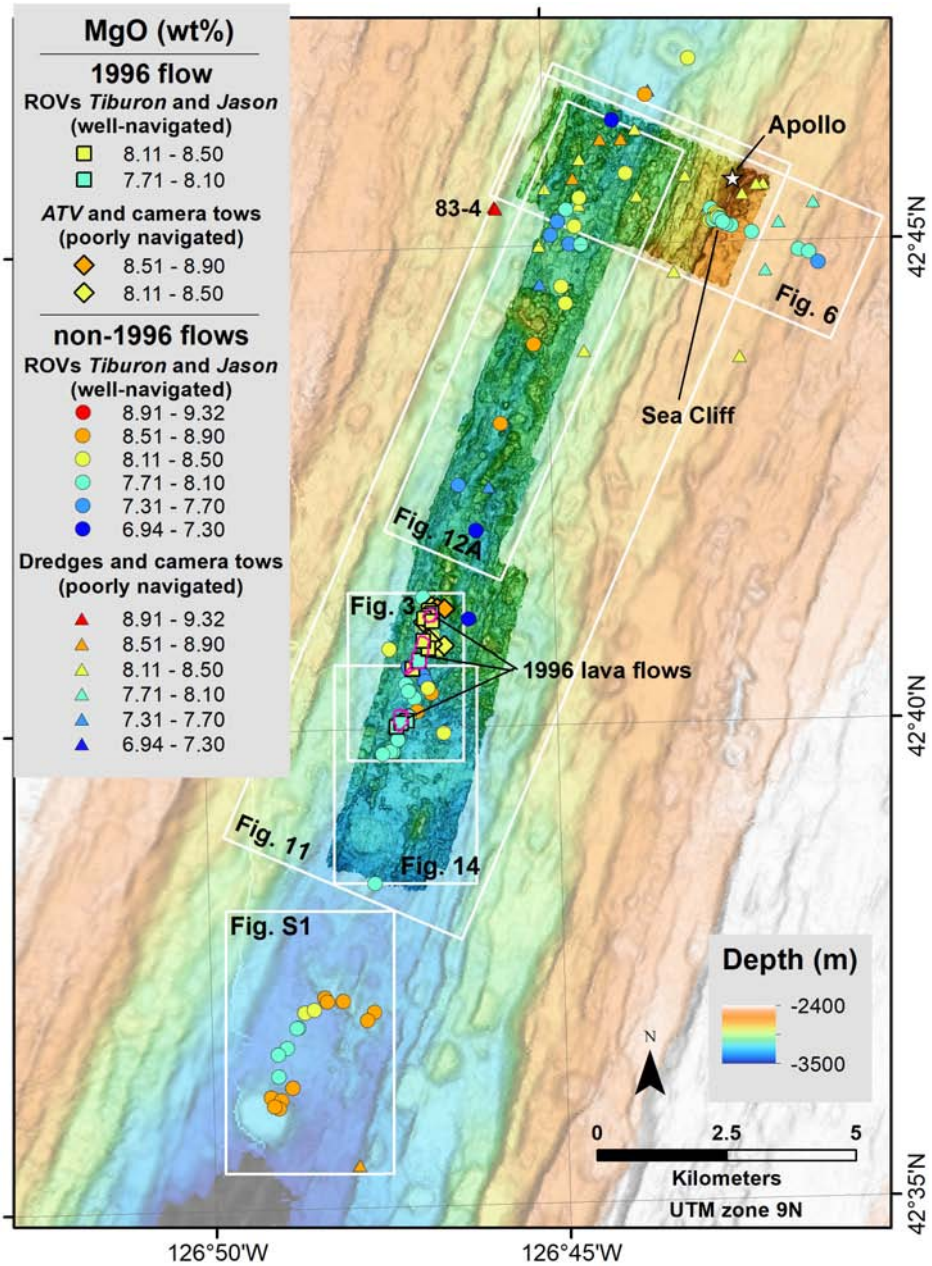

FIGURE 2 | Map of AUV 1-m resolution coverage on top of faded Simrad EM300 and EM302 bathymetry on top of regional multibeam survey data. Lava samples are color-coded by MgO content (using values from **Supplementary Table S1**) with different symbols for 1996 and older samples depending on the reliability of the navigation during collection (Rubin et al., 1998; Davis et al., 2008). Dredged sample 83-4 (Davis and Clague, 1987) has sheet-flow morphology and is the most-MgO-rich lava recovered from the Gorda Ridge. The 1983–1986 dredged samples are plotted at the center of the dredge tracks, and samples recovered on camera sleds that collided with the bottom are located where the camera was inferred to be when it crashed (Davis and Clague, 1987, 1990; Rubin et al., 1998). White boxes indicate the extents of **Figures 3**, **6**, **11**, **12A**, **14**, and **Supplementary Figure S1**. The locations of the Sea Cliff hydrothermal field, newly discovered Apollo vent field (white star) and the 1996 lava flows (with red outline) are labeled.

Doppler Velocity Log (DVL) through an embedded Kalman filter. The INS is initialized by GPS at the surface and aided during descent by a Sonardyne ultra short baseline (USBL) acoustic tracking system with position fixes transmitted to the vehicles by acoustic telemetry. The INS achieves a position accuracy of 0.05% of distance traveled as long as DVL bottom lock is maintained. In cases where the AUV altitude becomes too small (typically in rugged terrain), the propeller shuts off and the AUV floats up to a safe altitude before resuming the mission. Often DVL lock is lost during these altitude abort events, resulting in discrete jumps in INS positioning that can be in excess of 100 m, resulting in degradation of the mission navigation.

The AUV survey on the eastern slope of the axial graben was designed to cover the Sea Cliff site with a diagonal crossing line and to survey parallel to the slope, starting at the top of the slope (**Figure 2**). This design was to minimize altitude aborts by having all slope-parallel lines end with a turn away from the slope. The steep terrain nevertheless resulted in multiple altitude aborts and loss of DVL bottom lock despite this planning. The combination of steep terrain and altitude aborts led to multiple gaps in coverage and to areas, including the Sea Cliff hydrothermal site, with degraded coverage.

Multibeam Data Processing

The mapping data were processed using the open source MB-System software package (http://www.mbari.org/data/mbsystem/; Caress and Chayes, 1996). After editing of outliers, navigation adjustment was performed to match features in overlapping and crossing swaths and to set the starting points of each of the three AUV surveys to be global fixed points in the navigation inversion.

The multibeam bathymetry were gridded at 1-m resolution using an algorithm that incorporates the variable beam footprints. Multibeam backscatter maps were constructed by correcting the snippet backscatter samples for grazing angle using the three-dimensional topographic model and the average variation of amplitude with grazing angle for the entire survey.

The outlines of the 1996 lava flows were drawn in GIS to surround flow morphologies in the AUV maps while incorporating dive observation and sample locations from the one ROV *Jason* dive in 1996 and from MBARI ROV *Tiburon* dives T885 and T886 in 2005 (Yeo et al., 2013). The 1996 ROV *ATV* sample locations were poorly constrained and were not utilized. The location of the Sea Cliff hydrothermal vent site was re-determined based on navigation of ROV *Tiburon* T695–698 in 2004 and T884 in 2005, which had the best navigation of the MBARI dives.

Geochemical Data

Compositions of glasses collected during cruises in 1983, 1985, 1986, 2000, 2002, 2004, and 2005 (Davis and Clague, 1987, 1990; Rubin et al., 1998; Clague et al., 2003, 2009; Davis et al., 2008) are mostly published. These papers discuss the petrogenesis of the lavas in detail, whereas here we focus on combining the compositional data with mapped flow morphology to evaluate emplacement processes. Glass sampling during the three MBARI ROV dives in 2005 included collection of rock samples using the manipulator arm (Davis et al., 2008), and previously unpublished glass samples collected using a 29-jar carousel suction sampler (Clague et al., 2009), and glass recovered in ten 30-cm long push cores collected in small sediment ponds between pillow lobes on older (non-1996) flows (Clague et al., 2003, 2009; **Supplementary Table S1**). Clague et al. (2013) describe the equipment and sampling methodologies employed. Six of 28 samples collected with the suction sampler, wax-tip rock core GR00RC7, and all push cores contained glass shards have more than one composition. Normal and transitional mid-ocean ridge basalt (N-MORB and T-MORB) are subdivided by K_2O/TiO_2 with N-MORB < 0.10 and T-MORB > 0.10, as proposed by Dreyer et al. (2013) for Juan de Fuca MORBs.

Davis and Clague (1987, 1990) used a value of 6.96 wt% for MgO in Smithsonian glass standard VG2 determined against other standards in the 1980s and 1990s, but the data in Davis et al. (2008) and Clague et al. (2003, 2009) used the reported standard value of 6.72 wt%. The analyses in all these papers and new data in **Supplementary Table S1** have been adjusted based on reassessment of the MgO content of glass standard VG2 to 7.07 wt% (Clague et al., 2018b) and their MgO values are now internally consistent and consistent with secondary standard ALVIN 2392-9 from the East Pacific Rise. The electron microprobe equipment and settings, methods, and standards are described in Davis and Clague (1987) and Davis et al. (2008).

Three samples of deposits from the Sea Cliff hydrothermal site were analyzed at ActLabs using a variety of techniques that are outlined in Paduan et al. (2019), which also includes analyses of standards and analytical precision and accuracy. The analytical data (**Table 1**) are for a fragment from an inactive chimney, a silica-rich crust, and a barite-rich crust.

RESULTS

The 1996 Eruption Site

The 1996 flow boundaries were mapped by Chadwick et al. (1998) based on comparison of pre-eruption and post-eruption ship-based multibeam surveys, camera tows, and visual observations and lava flow sampling during two ROV dives done soon after the eruption took place. They identified a single elongate lava flow a little less than 3 km long. At the same time, Chadwick et al. (1998) suggested another possible 1.5-km long flow located nearly 7 km south of the southernmost end of the established 1996 flows. Yeo et al. (2013) used the AUV data presented here, and observations and samples from ROV dives T885 and T886 done in 2005, to redefine the flow margins and to show that the 1996 flows comprised three discrete steep-sided mounds (**Figure 3**). The contacts are clearly identifiable with black lava flows (**Figure 4A**) draped on older flows covered with sediment and hosting extensive animal communities. These mounds occupy the sites of the thickest depth anomalies mapped by Chadwick et al. (1998) in their Figure 6B. The pillow mounds were still covered in part by tan deposits of hydrothermal sediment/bacterial mats 9 years after the eruption (**Figure 4B**). The regions with smaller depth anomalies that were thought to connect the thicker mounds turn out to be older, pre-1996 lava flows. Yeo et al. (2013) compared the new flow outline (also used here in **Figure 3**) with that of Chadwick et al. (1998). The three 1996 hummocky flows cover just 0.31 km^2 and the three mounds have a combined volume of 0.007 km^3 (Yeo et al., 2013), both just 39% of the area and volume estimated soon after the eruption (Chadwick et al., 1998). The thickest of the pillow mounds is ∼114 m tall, although the pre-eruption surface depth is uncertain due to lack of high-resolution pre-eruption bathymetric data.

The hummocky flows erupted in 1996 form composite pillow mounds with near-vertical outer upper margins (**Figure 4C**) and extensive talus deposits at the base of the steep to vertical

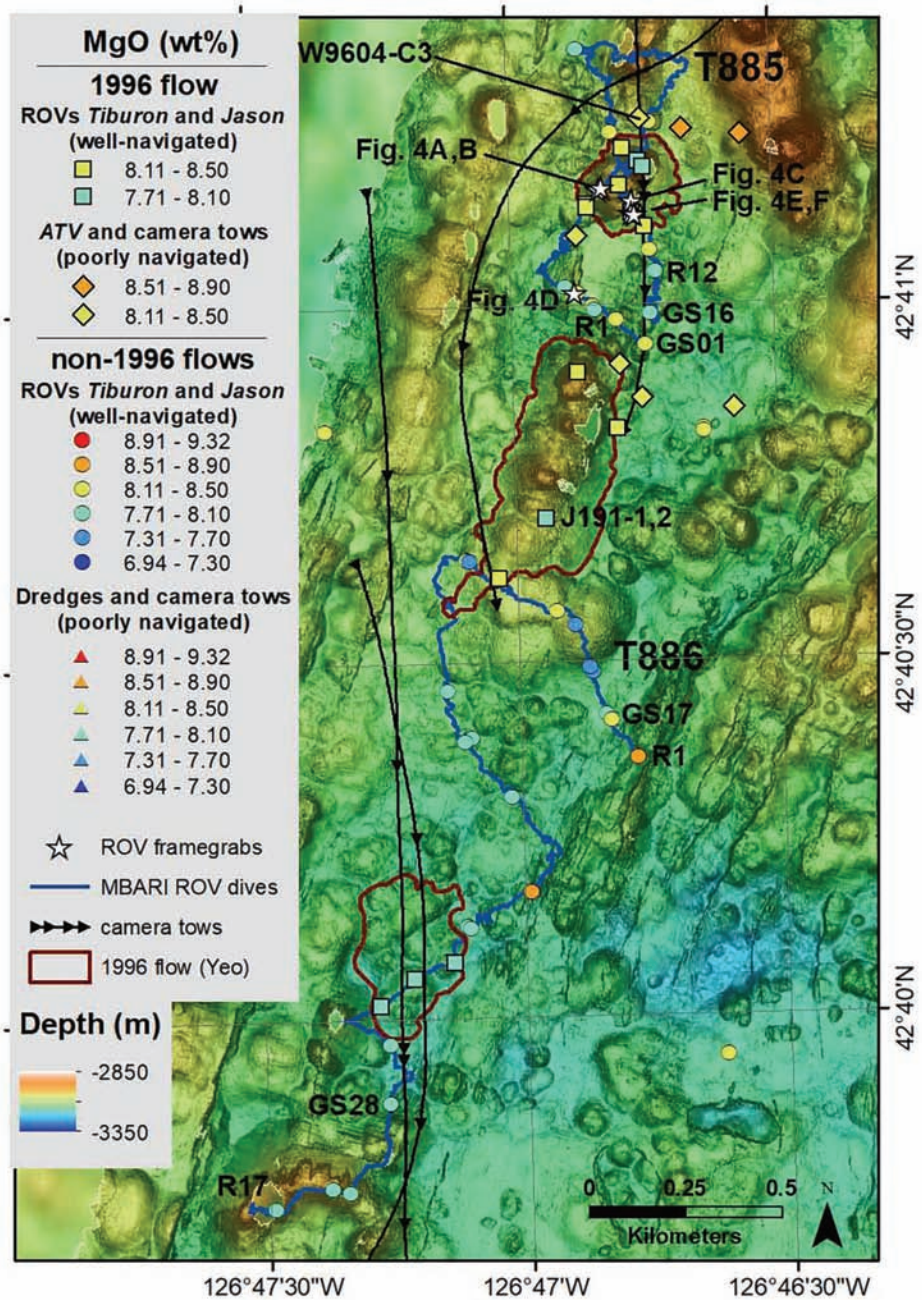

FIGURE 3 | Map of 1996 lava flows with flow extent from Yeo et al. (2013) as red outline. Blue lines are tracks of ROV *Tiburon* dives T885 and T886 (Davis et al., 2008; **Supplementary Table S1**) with some rock (R) and glass suction (GS) samples labeled. Fifteen 1996 flow samples from Rubin et al. (1998) include seven well-located ROV *Jason* samples, seven poorly located ROV *ATV* samples, and one sample recovered on a camera sled (black curved lines show camera tow tracks from Chadwick et al., 1998, note that the camera tow sample – yellow diamond near N end of map – does not plot within the AUV mapped 1996 flow). Locations of video framegrabs from dive T885 in **Figure 4** are labeled.

slopes. Talus deposits have a distinctive smooth texture on sloping topography in the AUV data (Clague et al., 2011, 2014, 2018b). Within a few m of the margin of the talus, pillow fragments have loose shards of glass (**Figure 4D**) on their surfaces. Some of the talus fragments are elongate "lavacicles" ∼10-cm in diameter and as long as several meters (**Figure 4E**), and some are tear-drop shaped at one end (**Figure 4F**). Clague et al. (2018b) describe lava forms similar to the lavacicles from the base of the steep pillow ridge that formed on the distal southern rift zone of Axial Seamount in 2011.

Twelve lava samples identified by Rubin et al. (1998) as 1996 flow samples were collected during the three 1996 event

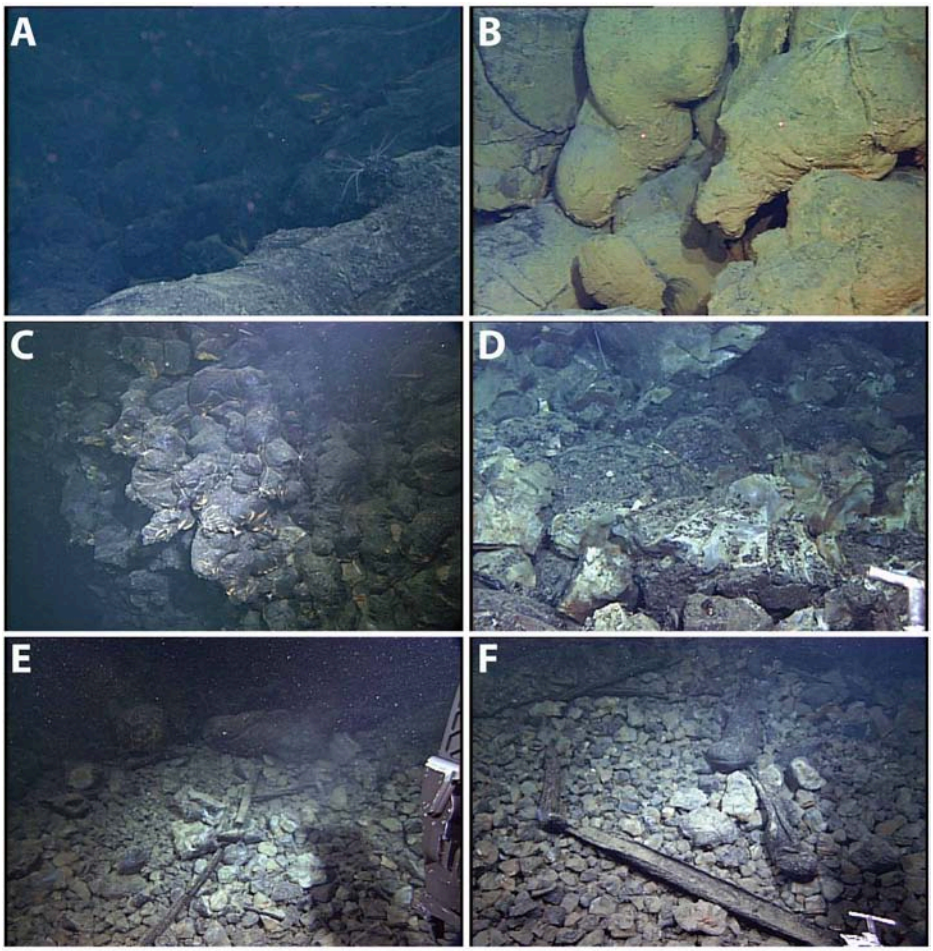

FIGURE 4 | Video framegrabs from dive T885; images **B**, **D**, and **F** are 2–3 m across and **A**, **C**, and **E** are 4–5 m across. **(A)** Contact showing black 1996 lava pillows (upper left) on top of slightly altered and sediment-covered older flow (lower right). Image taken at 3058 m depth at 42.686030°, –126.780538°. **(B)** Elongate 1996 pillow lavas with thin yellow-brown hydrothermal deposits. Photo taken 9 years after the eruption. Image taken at 3052 m depth at 42.686072°, –126.7804625°. **(C)** Upper surface of northern pillow mound with vertical to overhanging scarp to left. Image taken at 3053 m depth at 42.685767°, –126.7795013°. **(D)** Pillow talus at base of scarp with scattering of glass shards produced when pillow fragments fall down scarp and glass rinds spall off. Image taken at 3115 m depth at 42.683628°, –126.781378°. **(E)** Lavacicles found on top of talus at base of vertical scarp. These form as molten lava cascades over the scarp and drip as vertical cylinders of lava. Image taken at 3101 m depth at 42.685471°, –126.779523°. **(F)** Lavacicles showing teardrop shapes formed at bottom of lavacicles. Some lavacicles have slightly bent ends showing that they were still plastic when they fell to the talus slope. Image taken at 3101 m depth at 42.685447°, –126.779418°.

response cruises. Fifteen additional samples (8 Rocks and 7 Glass Suction samples identified as 1996 flow samples (**Supplementary Table S1**) were collected during two 2005 MBARI ROV dives and are plotted on **Figure 3**. Many of the ROV *ATV* samples identified by Rubin et al. (1998) as 1996 flow samples are located significantly outside the mapped flow margins. Of the seven ATV178 samples only ATV178-7R and ATV178-1R1 are unequivocally established as 1996 flow samples by ^{210}Po-^{210}Pb dating (Rubin et al., 1998) and mis-identification of samples as 1996 lavas is possible, but poor navigation of the ATV dive is a more likely explanation for the plotted positions. The 1996 lavas are normal-MORB (N-MORB with average K_2O/TiO_2 = 0.079, MgO in glass between 7.87 and 8.65% (average of 8.27%), and with relatively high Na_2O content, averaging ∼2.8%. The variability is significantly greater than precision of the analyses; the analyses from Rubin et al. (1998) average 0.18% higher MgO than those from Davis et al. (2008) and **Supplementary Table S1**. The compositions are not randomly distributed as those with the lowest MgO contents are from the tops of several mounds, and presumably extruded near the end of the eruption.

Pre-1996 lava flow compositions (MgO, K_2O/TiO_2, and Na_2O) of samples collected within the axial valley and lavas with 1996 flow compositions are plotted as function of latitude (**Figure 5**). Along the ridge, MgO content (**Figure 5A**), an indicator of degree of fractionation, varies from∼7% to 8.8%, although almost half that range is displayed by the 1996 flow samples. At the southern end of the study area, all samples have > 7.9% MgO. The K_2O/TiO_2, an indicator of enrichment, varies from 0.06 to 0.16, so includes N-MORBs with ratios < 0.10 and T-MORBS with ratios > 0.10 (**Figure 5B**). The 1996 lava

flows are N-MORB with similar K_2O/TiO_2 to surrounding older lava flows. The 1996 samples have a narrow range of Na_2O values (**Figure 5C**) that is roughly the analytical uncertainty. The 1996 flows and the older flows surrounding them have a similar range of values. Most of the southernmost samples (dive T187) have low Na_2O (< ∼2.4%) whereas the samples from the rest of the study area have higher Na_2O (generally >2.5%).

The site of a proposed more southerly 1996 flow (Chadwick et al., 1998, their Figure 7) was explored and sampled during ROV *Tiburon* dive T187 in 2000 (**Supplementary Figure S1**), but all flows observed and sampled had moderate to thick sediment cover and sessile animal communities and were therefore much older than 4 years. This proposed flow is probably an artifact of the poorly located swath bathymetry that predated the eruption, as noted by Chadwick et al. (1998). Sample W9604-C2 (Rubin et al., 1998) was recovered on a towed camera sled about 8 km south of the southern end of the 1996 flows; its location is replotted on the eastern axial valley wall (**Figure 2** and **Supplementary Figure S1**). It contains Na_2O of 2.39%, similar to most samples from T187 (**Supplementary Table S1**) and distinctly lower than samples from further north along the camera tow (**Figure 3**).

A 4.5-km Transect Across and East of the Axis

Sampling and observations were made on a cross section of the ridge near 42°45′N, extending ∼4.5 km from the center of the axial graben up the eastern flank of the ridge centered on the Sea Cliff hydrothermal site (Rona et al., 1990; Von Damm et al., 2006). One AUV survey mapped this area, establishing high-resolution bathymetry of the axial graben and major fault blocks to the east (**Figure 6A**). A profile of the ridge was constructed (Line X-X′ in **Figures 6B,C**) from the AUV 1-m bathymetry and, farther to the east, from a hull-mounted multibeam EM300 (MBARI Mapping Team, 2001) and EM302 collected in 2019 during Ocean Exploration Trust's R/V Nautilus cruise NA108.

The bathymetric data show numerous faults, which we have subdivided into major faults based on their having 30–70 m of throw, to minor faults with smaller vertical offsets. Both types are mapped in **Figure 6B**, which shows the complexity of the faulting. The faults are mostly normal faults with the downthrown side toward the axis, as expected. However, a few small-offset normal faults have the opposite throw. Such faults especially occur in a zone southeast of the axis and northwest of the cross-section (Line X-X′ in **Figure 6B**). Major faults with larger throw or clusters of faults with larger combined vertical offsets are identified in the cross section of **Figure 6C**.

The major faults nearest the axis are asymmetrical. The first major fault east of the axis (between fault blocks *A* and *Be* in **Figure 6C**) has no single counterpart west of the axis with a similar throw. On closer inspection, the axial graben includes the unfaulted neovolcanic zone (through which the blue line is drawn in **Figure 6B**), symmetrically increasingly faulted flows away from that zone (which are included in the block labeled *A* in **Figure 6C**), and an inferred block, *Bw* to the west. The similar appearance of block *Be* to *Bw,* supported by the

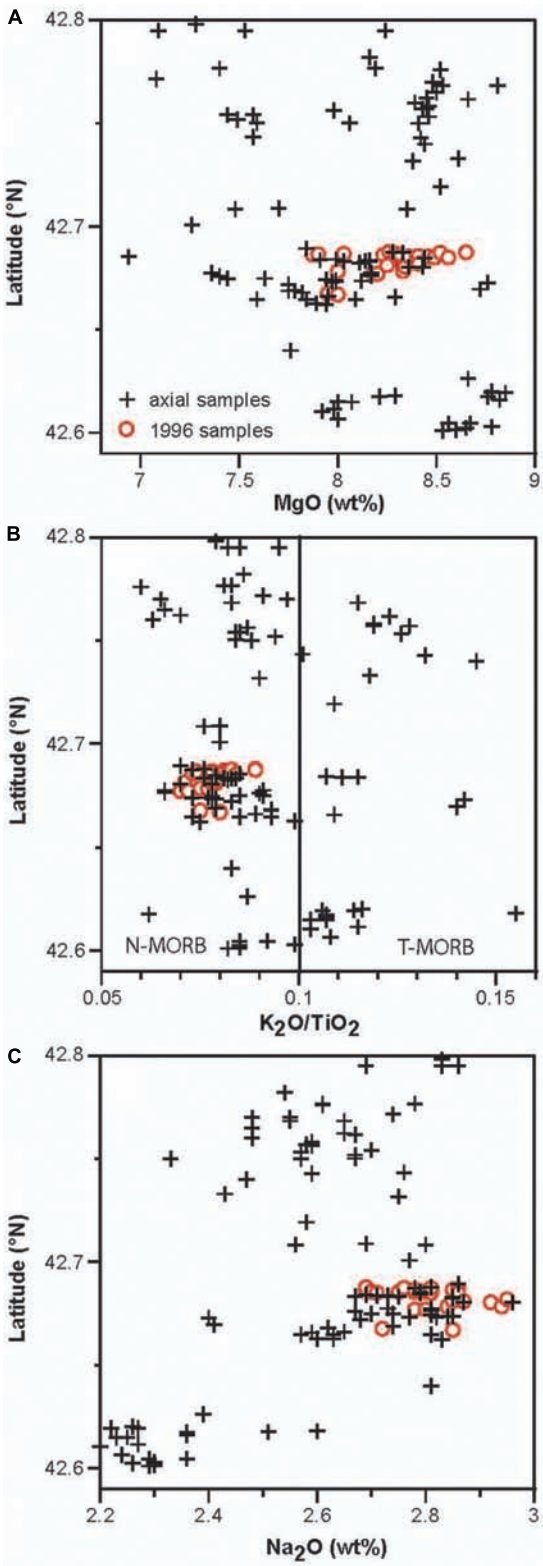

FIGURE 5 | Lava geochemistry as a function of latitude for samples collected from the axial valley and divided into 1996 flow samples and older flow samples. **(A)** MgO, **(B)** K_2O/TiO_2 with values < 0.10 classified as N-MORB and values > 0.10 classified as T-MORB, **(C)** Na_2O.

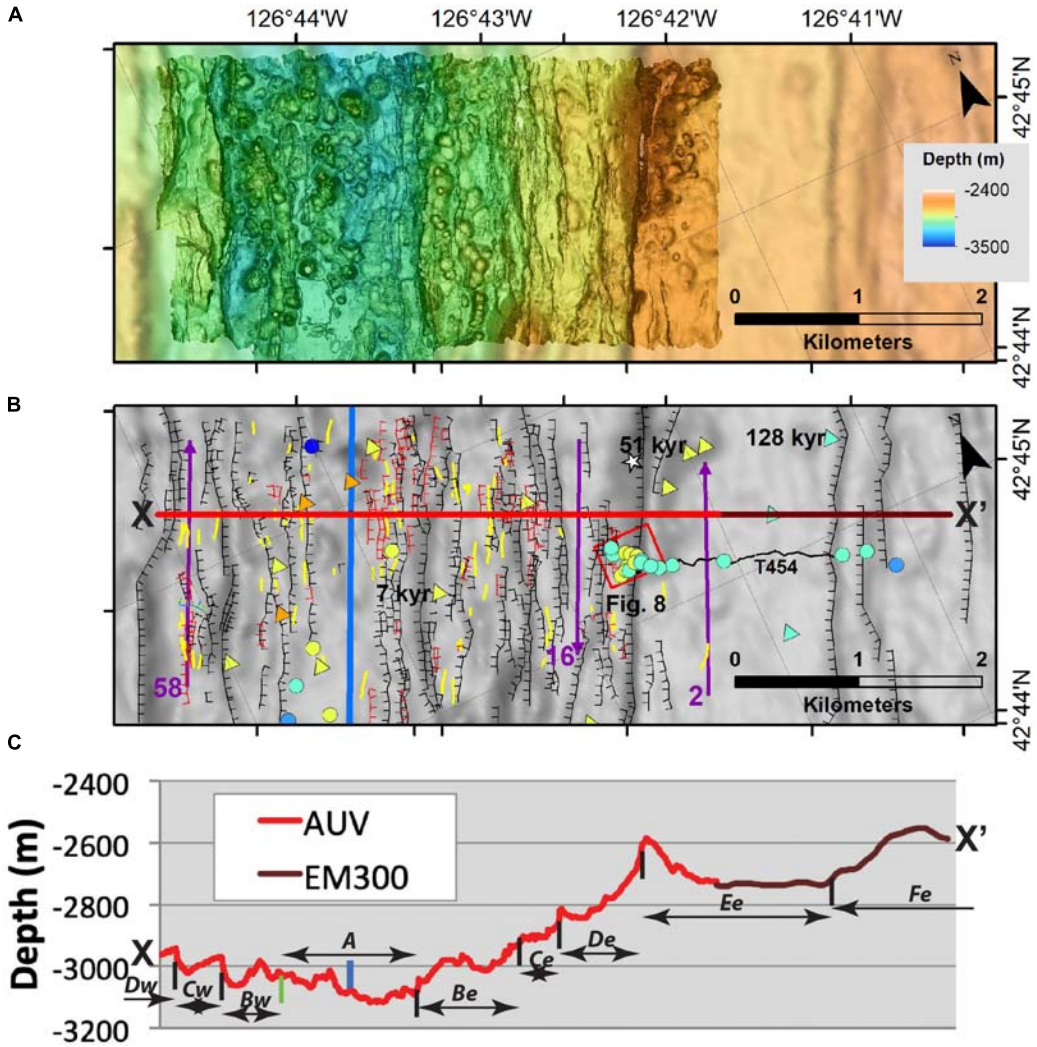

FIGURE 6 | (A) Maps and interpretations of a transect across the narrowest, shallowest part of the North Gorda segment east beyond the Sea Cliff hydrothermal vent field. All maps are rotated 23°clockwise and at the same scale. AUV bathymetry is shown on top of Simrad EM300 and EM302 bathymetry. **(B)** Locations of lava samples are indicated on faded bathymetry from map A, with symbols as in **Figure 2**. Sea Cliff hydrothermal field is within the box outlining the location of **Figure 8** and the newly discovered Apollo field is the white star. Line labeled X-X′ is the location of the cross section in panel **C**. Three NNE-SSW purple lines labeled 2, 16, and 58 are the locations of sub-bottom seismic profiles in **Supplementary Figure S2**. Blue line is the estimated center of the axial graben (labeled *A* in panel **C**), and used to measure distance that samples are located off-axis in **Figure 7**. Linework shows inward-facing fault scarps in black, outward-facing fault scarps in red, fissures in yellow, and a pair of north- and south-facing scarps in green and blue. The numbers 7, 51, and 128 show the ages (in kyr) and locations of three lava samples dated by $^{238}U/^{230}Th$ disequilibria (Goldstein et al., 1991). Track of ROV *Tiburon* dive T454 is labeled. **(C)** Profile across the North Gorda segment, constructed from AUV survey data (red line) and Simrad EM300 ship data (brown line) to the east of the AUV survey, along the cross-section X to X′ in panel **B**. The profile has 2.5X vertical exaggeration and extends from ∼ 1 km west of the axis to 3 km east of the Sea Cliff hydrothermal site. Normal faults with 30–70 m vertical offsets are indicated by vertical black lines. Boundary between *A* and *Bw* (green vertical line) is where a major-offset fault should occur (to mirror the eastern blocks) but only a cluster of small offset faults are observed. The fault blocks labeled *Dw, Cw, Bw, A, Be, Ce, De, Ee, and Fe* from west *(w)* to east *(e)* are labeled.

matching morphology of the eastern and western blocks of *C* and *D,* suggests the counterpart to *Bw* is the uplifted fault block *Be,* despite its being at a similar depth to the axial zone *A*. The overall faulting balances out over longer time periods, however, as there are blocks with similar structures and depths as *Ee* and *Fe* beyond the AUV coverage west of the axis (**Figure 2**) and the total accumulated rift valley depth is equal on both sides (**Figure 2**). This suggests the asymmetry may shift over time. Furthermore, the axis has a slight shift to the west in the shallow area (**Figures 1**, **6A**). This shift is accommodated by the major faults that define a series of ridge-parallel blocks that step up from the axis and are between 350 m to 1750 m wide (blocks *Ce* and *Ee*, respectively, **Figure 6C**). Block *Be* and its inferred western counterpart *Bw* differ in width by about a factor of two, whereas blocks *Ce* and *Cw* are similar in width. Without high-resolution data farther to the NW, comparisons of blocks NW and SE of the axis are less reliable as the smaller faults are not detected in the lower-resolution ship data.

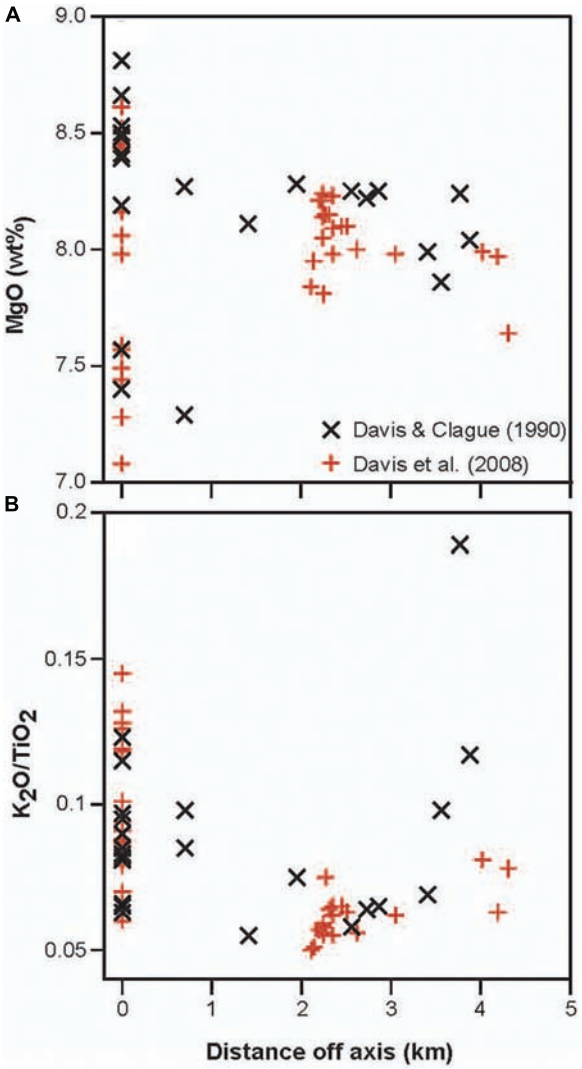

FIGURE 7 | Geochemistry of samples from east side of axial valley projected onto cross section in **Figure 6C**. Distance is from the center of the axial graben. Dredge samples from Davis and Clague (1990) are plotted in the middle of the dredge track. **(A)** MgO vs. distance from center of axis. **(B)** K_2O/TiO_2 vs. distance from center of axis.

The bathymetric data (**Figure 6A**) also show a marked smoothing of the bathymetry on the fault blocks more distal from the axis. AUV sub-bottom profile data (**Supplementary Figure S2**) show that the easternmost block *Ee* (line 2 on **Figure 6B** and **Supplementary Figure S2A**) above the Sea Cliff hydrothermal site is buried by up to 0.005 s two-way travel time (TWTT) of sediment, or ∼5 m, which is consistent with ROV *Tiburon* dive T454 observations (**Figure 6B**) of complete burial of the lava flows. Continuing west toward the axis, block *De* (line 16 on **Figure 6B** and **Supplementary Figure S2B**) just below the Sea Cliff site is buried by up to 0.002–0.003 s TWTT of sediment, or ∼2–3 m. Block *Be* has no detected sediment in the sub-bottom records (*A* on **Figure 6C**). Continuing west, away from the axis, fault block *Cw* (**Figure 6C**) has up to 0.003 s TWTT of sediment (line 58 on **Figure 6B** and **Supplementary Figure S2C**) or 3 m, similar to that on block *De* just below Sea Cliff.

There are also differences in the flow morphology of the fault blocks progressing away from the axis (**Figure 6A**). *A*, *Bw* and *Be* have abundant small, hummocky flows. Ponded channelized flows are found only on block A. Fault blocks *Cw* and *Ce* are more fractured than *A*, *Bw* and *Be*, and consist of low-relief hummocky flows dissected by faults. Block *Ee*, east of the steep flows truncated by the fault that Sea Cliff lies on, is even smoother due to the thick sediment cover, although several small steep hummocky flows constructed of pillow lava with summit collapse craters can still be identified.

Three samples from this transect were dated using $^{238}U/^{230}Th$ disequilibrium (Goldstein et al., 1991) and are plotted on **Figure 6B**. A MORB sample from block *Be*, dredged 0.7 ± 0.3 km from the axis center (dredge L585NC-13), yielded an age of 7 ± 10 ka. A second MORB sample from near the western margin of block *Ee*, dredged 2.7 ± 0.1 km from the axis center [L585NC-7; labeled 85-7 in **Supplementary Table S1**)] yielded an age of 51 ± 12 ka. This age is significantly younger than the 98 ± 4 ka age predicted based on half-spreading rate and the sample is from a shallower portion of block *Ee* with thinner sediment cover (NE end of line 2 in **Supplementary Figure S2**). A third MORB sample from the distal part of block *Ee* was dredged 3.9 ± 0.4 km from the axis center (L585NC-4) and yielded an age of 128 ± 13 ka, within error of the predicted age of 142 ± 16 ka based on the half-spreading rate. Combining this age and the roughly 5 m of sediment on block *Ee* observed on dive T454 to the south (**Figure 6B**) suggests a sediment accumulation rate of ∼3.9 cm/kyr, less than the 5–14 cm/kyr estimated for the Holocene in Escanaba Trough (Karlin and Zierenberg, 1994).

Lava samples were collected along this transect as a combination of dredged rocks from 21 sites (Davis and Clague, 1987, 1990), two *Sea Cliff* submersible samples, 20 ROV *Tiburon* samples, and, in the axial graben only, 13 wax-tipped rock core samples (Davis et al., 2008). The MgO content and K_2O/TiO_2 are plotted in **Figure 7** as a function of distance from the center of the axial graben (blue line in **Figure 6B**) projected onto the cross section (red X-X′ line in **Figure 6B**). The axial graben samples have MgO between 7.1 and 8.8% (∼40% crystallization) and range from N-MORB with K_2O/TiO_2 of 0.06 to T-MORB with K_2O/TiO_2 up to 0.15. The observed variations in lava compositions along the axis (**Figure 5**, left edge of **Figure 7**) are not observed back in time in the cross section east of the axis (**Figure 7**) where increasing distance from the axis is taken to mean increasing age of the lavas. Instead, the off-axis lavas < 3.5 km from the axis are mostly uniform N-MORB with MgO contents mostly in a narrow range from 7.8 to 8.25% (< ∼15% crystallization) and in K_2O/TiO_2 from 0.05 to 0.09, with two T-MORB with K_2O/TiO_2 of 0.12 and 0.19 collected about 4 km east of the axis. Primitive melts (with MgO > 8.3%) and samples that have undergone more extensive crystal fractionation (with MgO < 7.6%) are not represented among the off-axis samples. Lavas from farther away include one T-MORB with K_2O/TiO_2 as high as 0.19 (**Figure 7B**), although all but one (the most distant sample in the study) of these more distal lavas have similar MgO contents as those closer to the axis.

The sampling off-axis is not as dense as along-axis, but dredged (Davis and Clague, 1990) and ROV-collected (Davis et al., 2008) samples have similar patterns, with more T-MORBs among the dredged samples. The least fractionated (MgO = 9.3%) and most depleted (K_2O/TiO_2 = 0.042) lava from the Gorda Ridge (Davis and Clague, 1987) is a poorly located dredge sample from west of the AUV mapped region.

In summary, the youngest axial lavas include more fractionated and more primitive samples than the flank, and many of them also are T-MORBs not seen on the flank closer than ∼4 km from the axis. The most distal, presumably oldest samples include more enriched T-MORB compositions, but have a narrow range of fractionation with neither strongly fractionated nor primitive compositions. In addition, the most depleted and the most enriched MORBs (highest and lowest K_2O/TiO_2) from the Gorda Ridge north of Escanaba Trough are from opposite sides of the axis (Davis and Clague, 1987, 1990; Davis et al., 2008).

Sea Cliff Hydrothermal Site

An AUV mapping survey in 2016 added 1-m bathymetry over the Sea Cliff hydrothermal vent field. Here we present new details about the geologic setting of the Sea Cliff vents based on the AUV mapping, an improved map of the vent field and high- and low-temperature deposits (**Figure 8**), new observations from the ROV *Tiburon* dives (**Figure 9**), and three new bulk analyses of the deposits (**Supplementary Table S2**).

Of the 11 ROV *Tiburon* dives at the Sea Cliff site, six in 2000 and 2002 suffered from poor navigation and four in 2004 did limited exploration beyond the immediate area of active venting. Observations from dive T884 in 2005 were therefore used to construct the new map of the vent field. Vent animal communities and vent locations observed during dives T685-T688 in 2004 are consistent with locations based on T884 observations, adding confidence to the location and extent of the vent field and its surrounding biologic footprint. The early dives collected fluids (Von Damm et al., 2006) from active vents located adjacent to markers deployed in the 2000 and 2002 dives. The vent field is centered at 2720 ± 10 m and the axial depth directly dowslope from the vent field ranges from 2983 to 3108 m, so Sea Cliff is ∼330 ± 60 m above the average depth of the axis. The location of the vent field is roughly 120 m south and 45 m east of the locations shown in Rona et al. (1990), which is remarkable considering that the three Sea Cliff submersible dives that discovered and explored the vent field in 1988 lacked GPS navigation and lost the transponder signals when it was near the bottom.

The volcanic axis, as defined in the previous section, is the eastern 2/3 of the axial graben (blue line on **Figure 6B**), and the vent field is ∼2.6 km east of the center of the volcanic axis. At a 5.5 cm/yr full spreading rate, the ocean crust under the vent field should be slightly less than 100 kyr old, as noted in Von Damm et al. (2006). The ridge-parallel fault immediately above Sea Cliff vent field has the largest throw of the many ridge-parallel faults on the east side of the volcanic axis (**Figures 6B,C**). Outcrops above the Sea Cliff site are volcanic breccia (Rona et al., 1990) and most of the vent field is among talus blocks and fragments of pillow lavas. It appears that the breccia is impermeable, except where isolated fractures occur. Small amounts of warm hydrothermal fluids seep through, as evidenced by the presence of abundant mollusks along the fractures. It is possible that the breccia prevents most of the fluids from migrating upslope in the subsurface. They then may rise to the surface in the Sea Cliff field.

The vent field (**Figure 8**) includes several rows of active anhydrite/amorphous silica/Mg-rich clay chimneys (Von Damm et al., 2006) oriented up-down slope (**Figures 9A,B**). These chimneys are perched atop low ridges (**Figure 9C**) of collapsed chimney debris, as the chimneys are fragile and collapse before they grow taller than a few m. The ridges and chimneys are noticeably devoid of vent fauna, but large areas more distant from the active high-temperature chimneys have broad, dense clumps of *Ridgeia piscesae* tube worms (**Figure 9D**). Even more distant from the active chimneys, *Ridgeia piscesae* become scattered clumps in fields of talus blocks (**Figure 9E**). The extent of the tube worm clumps is ∼140 m by ∼90 m, elongate parallel to the axis. The nearest vent fauna to the active chimneys are mats (**Figure 9F**) of blue ciliate *Eufolliculina caerulea* (Pasulka et al., 2017), and white limpets *Lepidodrilus fucensis* on hydrothermal crusts consisting mainly of amorphous silica and clays or of barite.

Nineteen samples of the hydrothermal chimneys and crusts were collected during the 11 ROV *Tiburon* dives in 2000, 2002, and 2005. Many of these samples are remarkably similar so only three representative samples were analyzed. These analyses of an inactive chimney, a silica-rich crust and a massive barite crust (**Table 1**) reflect the paucity of sulfides of Fe (0.58–1.48 wt%), Cu (0.15–0.26 wt%), Zn (0.19–2.58 wt%), and Pb (0.01–0.76 wt%). The samples contain 9.8–135 ppm Ag and 561–1310 ppb Au, with the barite crust having the highest Au and Ag. Anhydrite, which forms a major component of the active chimneys, has dissolved from the inactive chimney, leaving behind mainly amorphous silica as seen in the 81.3–84.7% SiO_2 of the silica-rich crust and inactive chimney fragment as described by Zierenberg et al. (1995) and Von Damm et al. (2006). The chimney fragment with 2.94% MgO has more abundant Mg-rich clay than the silica crust with only 0.88% MgO.

Chondrite normalized REE (McDonough and Sun, 1995) from the collapsed chimney and silica crust (**Figure 10** and **Table 1**) match the pattern of hydrothermal fluids, whereas REE concentrations of northern Gorda Ridge basalts (Davis et al., 2008), inferred source rocks for the Sea Cliff hydrothermal system, show relatively smooth REE patterns (**Figure 10**). REE are relatively immobile during hydrothermal alteration, so REE patterns are often used to infer protoliths for hydrothermally altered rocks, although extensively altered basalt hyaloclastites sometimes show light REE depletion and negative Eu anomaly due to selective loss of some of the REE to the altering hydrothermal fluid (Fowler and Zierenberg, 2015). Chondrite normalized REE concentrations from basalt-hosted seawater recharged hydrothermal fluids show enrichment of the light REE and a strong positive Eu anomaly (e.g., Klinkhammer et al., 1994; Mitra et al., 1994; Fowler et al., 2019). Hydrothermal precipitates in vein minerals inherit this pattern (Fowler and Zierenberg, 2015), as do the Sea Cliff deposits.

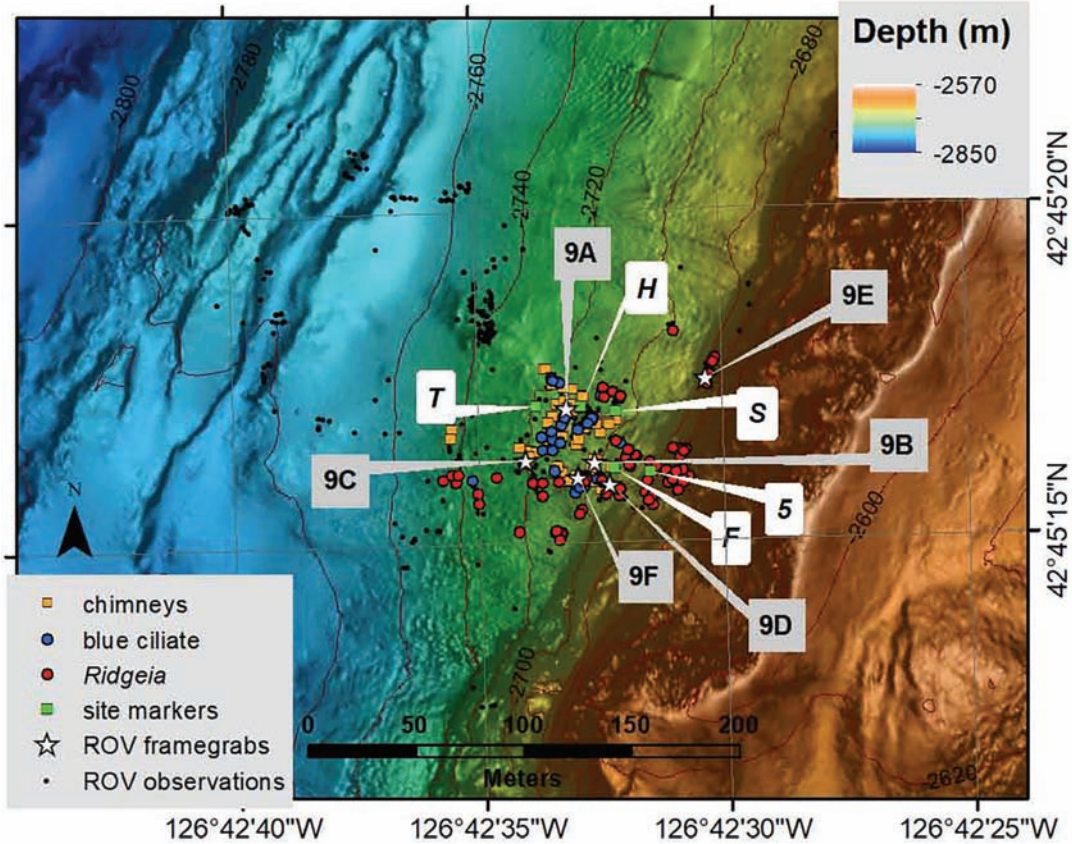

FIGURE 8 | Map of the Sea Cliff hydrothermal site based on dive observations from dive T884 in 2005. All video annotations are shown as small black dots, and observations of *Ridgeia piscesae* tube worms (red dots), blue ciliate mat (blue dots), hydrothermal chimneys (gold squares), and markers deployed on 2000 and 2002 dives (green squares) shown. The symbols are the location of the ROV when a specific feature was observed in the video, so a single feature can result in multiple observations. Locations of video framegrabs in **Figure 9** are labeled, as are site markers. The S "marker" is two *Sea Cliff* submersible steel plate dive weights located about 2 m apart. The cluster of video annotations on the –2740 m contour are an area with abundant brooding octopuses.

Hummocky Flows of Pillow Lava

The most abundant flow morphology on the northern Gorda Segment are hummocky flows of pillows that form mounds smaller than ∼200 m in diameter and usually < 100 m tall. The tallest are almost 150 m tall and the smallest are < 25 m across. Such hummocky flows are abundant within the axial graben and on the fault blocks mapped east and west of the axis, and the 1996 lava flows consist of three such mounds. Within the mapped 35 km^2 area, there are hundreds of hummocky flows forming isolated mounds or chains of mounds. Many have faults and fissures cutting them, especially away from the axis. Some hummocky flows have some special attributes, described below.

Steep-Sided Hummocky Flows Surrounded by Talus

Talus like that observed at the base of steep-sided pillow mounds that comprise the 1996 flows is a common landform around most steep-sided mounds along the ridge axis. Talus covers 1.57 km^2 of the 26.2 km^2 of axial graben mapped by AUVs, or 6% by area. The extent of such deposits is illustrated in **Figure 11** and contrasted with talus deposits along steep fault scarps. Calculations done in ArcGIS on the shapefiles of talus deposits indicate talus at the base of steep-sided cones and volcanic ridges comprises ∼4.6% of the axial graben floor and is far more common than talus along fault scarps, which covers just ∼0.8% of the axial valley (the remaining 0.6% could be either along faults or at the base of steep cones). Additional talus is produced along ridge-parallel faults off-axis, and small, rare, talus slopes may form due to faulting that cuts hummocky flows soon after their formation. As blocks are faulted during uplift outside the axial graben, fault-related talus increases. Lavacicles were not observed in any of these other talus deposits.

Hummocky Flows With Summit Collapses

In the entire AUV-mapped region there are just four hummocky flows (three 150–200 m across and one 100 m across) that have summit collapse pits. These are in a north-south row east of the southern part of the extensive ponded channelized flow described

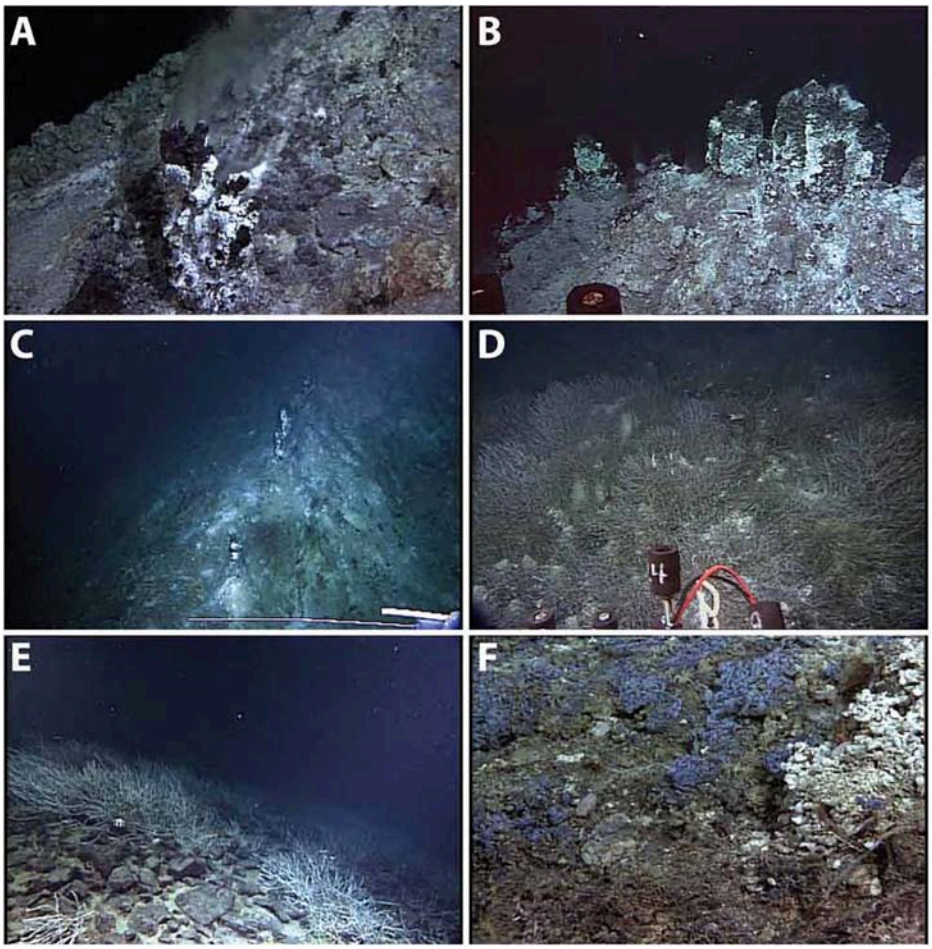

FIGURE 9 | Video framegrabs of features at the Sea Cliff hydrothermal vent field. Images **A**, **B**, **D,** and **F** are ∼2–3 m across and images **C** and **E** are ∼5–10 m across. Locations are indicated on **Figure 8**. **(A)** Active anhydrite/saponite/amorphous silica chimney. Clear venting fluid is ∼305°C. Image taken at 2721 m depth at 42.754725°, –126.709302°. **(B)** Chimneys are aligned in an upslope-downslope array along crests of low ridges of collapsed chimney fragments. Image taken at –2718 m at 42.754501°, –126.709152°. **(C)** View looking upslope along the low-relief ridge of chimney debris with small chimneys along crest. Image taken at 2728 m depth at 42.754513°, –126.709544°. **(D)** Area with abundant *Ridgeia piscesae* tube worm clumps on hydrothermal crust over talus blocks. Image taken at 2700 m depth at 42.754406°, –126.709066°. **(E)** Scattered clumps of *Ridgeia piscesae* tube worms among talus blocks. Sediment partly buries the talus blocks. Image taken at 2694 m depth at 42.754844°, –126.708510°. **(F)** Mats of blue ciliate *Eufolliculina caerulea* (Pasulka et al., 2017) and white limpets *Lepidodrilus fucensis* on low-temperature hydrothermal crusts composed dominantly of amorphous silica, although barite-rich crusts are also present. Image taken at 2716 m depth at 42.754437°, –126.709246°.

below (**cc** on **Figure 12B**). Hummocky flows with summit craters are common on Axial Seamount, including some that formed in 2015 (Clague et al., 2018b).

Ponded Channelized Flows

The AUV maps reveal channelized flows (**Figures 12A,B**) with ponded and drained sheet flow morphology as described based on AUV data in Clague et al. (2011, 2013, 2018a,b) and Chadwick et al. (2013, 2016). Such flows appear to be rare on the Gorda Ridge, with the only other known occurrences being the extensive flows at NESCA and SESCA in the Escanaba Trough (Ross and Zierenberg, 1994) that erupted through ring faults surrounding sills that uplifted sediment hills.

The ponded channelized flows on North Gorda cover 0.79 km^2 of 26.2 km^2 of the axis mapped by the AUVs or 3.0% of the axial graben. The four northern channelized flows on North Gorda may have formed during a single eruption, as their lake levels are similar (**Figure 12B**). They are relatively undisrupted by faults and fissures, although one fault, downthrown to the east by 2.7–9 m (greater offset to the north), cuts the eastern edge of the flows (**f** on **Figure 12B**). In addition, rare linear fissures cut through the ponded flows. The drained ponds are 3–11 m deep (**dp** on **Figures 13C,D**), and the shallowest one has numerous lava pillars near its margin (**p** on **Figure 13D**). The combined volume is < 0.06 km^3, and much of that volume eventually drained out and the ponds collapsed, leaving the original lava lake surface as bath-tub rings against adjacent flows (**ll** in **Figures 13C,D**). The shapes of the bath-tub rings mirror the shapes of the mounds they ponded against, so relative ages can be established. The ponded flows are younger than almost all

TABLE 1 | Composition of hydrothermal samples from sea cliff vent field.

Oxide/Element	Unit	T186-R2 Silica Crust	T186-R3 Inactive Chimney	T186-R6 Massive Barite
SiO_2	%	84.73	81.29	7.75
Al_2O_3	%	0.64	0.83	0.11
MnO	%	0.011	0.023	0
MgO	%	0.88	2.94	0.04
CaO	%	0.06	0.09	0.21
Na_2O	%	0.38	0.61	0.56
K_2O	%	0.04	0.09	0.04
TiO_2	%	0.01	0.003	0.002
P_2O_5	%	0.02	0.03	0
Fe	%	1.27	1.48	0.058
Cu	%	0.16	0.15	0.26
Pb	%	0.02	0.01	0.76
Zn	%	0.19	0.34	2.58
Ba	%	3.2	3	48.1
Sulfide	%	1.91	1.76	1.87
Sulfate	%	3.74	3.88	35.52
LOI – Sulfide	%	4.55	5.55	2.09
C	%	0.12	0.12	0.01
Cl	%	0.34	0.34	0.34
Total	%	101.39	99.14	99.91
Br	ppm	8.1	16.8	5.2
Ag	ppm	16.7	9.8	137
As	ppm	217	271	135
Au	ppb	561	922	1310
Bi	ppm	0	0	0
Cd	ppm	15.7	19.9	122
Co	ppm	14.5	10.6	4.9
Cr	ppm	10.8	5.3	0
Ge	ppm	1.3	1.4	7.2
Hg	ppm	8	20	12
Mo	ppm	19	12	110
Ni	ppm	9	9	1
Sb	ppm	3.3	2.9	61.9
Se	ppm	18	15.3	87.7
Tl	ppm	74.4	192	6.39
Ga	ppm	6	5	55
Hf	ppm	0.8	0.4	1.7
Nb	ppm	0.6	0.3	0.9
Sc	ppm	0.38	0.21	0.03
Sr	ppm	1014	1190	4802
Zr	ppm	3	2	2
U	ppm	9.56	10.54	0.32
La	ppm	0.84	0.65	2.76
Ce	ppm	0.38	0.23	0.9
Pr	ppm	0.05	0.03	0.9
Nd	ppm	0.17	0.14	0.28
Sm	ppm	0.05	0.05	0.05
Eu	ppm	0.1	0.1	0
Gd	ppm	0.07	0.06	0.51
Dy	ppm	0.05	0.04	0
Ho	ppm	0.01	0	0
Er	ppm	0.04	0.03	0
Tm	ppm	0.007	0.005	0.025
Yb	ppm	0.05	0.04	0.04
Lu	ppm	0.008	0.006	0.004

LOI, loss on ignition.

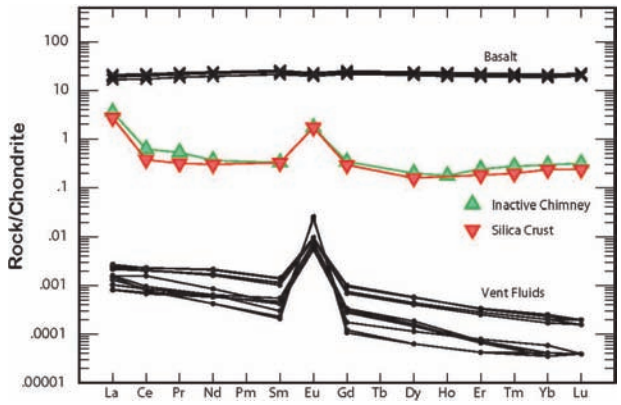

FIGURE 10 | Chondrite-normalized rare earth patterns for Sea Cliff hydrothermal deposits (green and red symbols, from **Table 1**), hydrothermal fluids (black dots, from Fowler et al., 2019) and a range of patterns for North Gorda basalt samples (Xs, from Davis et al., 2008). The deposit samples mirror the fluid compositions in having positive Eu anomalies.

surrounding flows, except the southern-most flow (**Figure 13C**) where hummocky flows (hf_y) over-rode the surface of the lava lake. Talus has predated and postdated the lakes (t_o and t_y, respectively, on **Figure 13D**). Despite their relative youth, they are still older than several hundreds of years as deduced from observations of sediment cover and sessile animal abundance during *Sea Cliff* dive 771 in 1988 (Rona et al., 1990) and USGS camera tows collected in 1985–1986 (Figure 3.13 in Clague and Rona, 1990). In addition, a fault with vertical offset as great as 9 m cuts the largest flow (**f** on **Figure 12B**) and attests to its relative old age. The surface of this flow deepens by ∼7 m from north to south.

This largest flow (**Figure 12B**) was sampled as R1 and R3 during *Sea Cliff* dive 771 and by three wax-tip rock cores in 2000 (GR00-RC11, RC17, and RC18) using ship-based bathymetry to guide the core deployment. These five samples have statistically identical T-MORB compositions (Davis et al., 2008; **Supplementary Table S1**) with 8.42–8.46 wt% MgO and K_2O/TiO_2 of 0.12 to 0.13. The flow is sparsely plagioclase microphyric. The northern RC11 sample contains common, mostly round, vesicles compared to the other two samples which have only rare vesicles in the glass rinds. Dredge 86-11 (Davis and Clague, 1990) is located on the northernmost part of the flow,

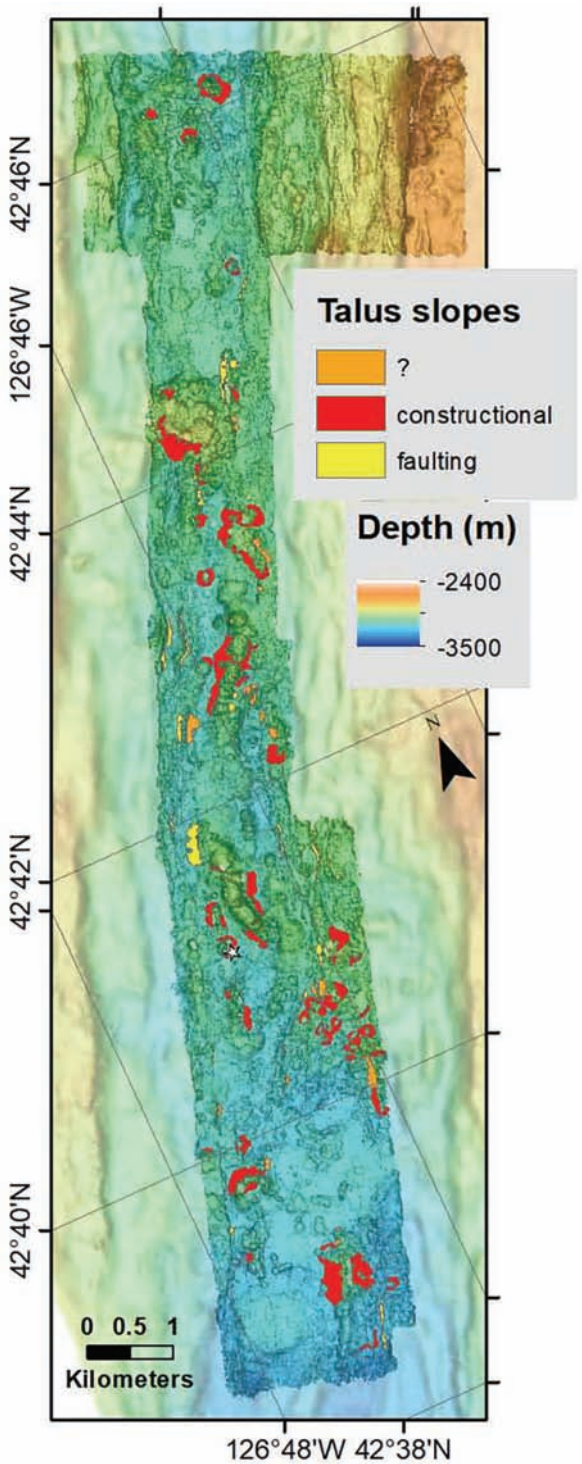

FIGURE 11 | Map showing the distributions of syn-eruptive talus and talus along fault scarps in the axial graben. Talus around the 1996 flow contains lavacicle fragments formed during the eruption as lava cascaded over near-vertical scarps (location marked with white star). This constructional talus forms a sloping surface around the base of steep-sided hummocky flows and constitutes the majority of talus in the mapped area. Talus accumulated at the base of fault scarps is also shown, as are some talus deposits that could be either constructional or fault-related. Map is rotated 23°counterclockwise.

but the recovered fragments are pillow basalt and the chemistry does not match the southern samples of what are most likely flows from the same eruption.

Sample GR00-RC14 (Davis et al., 2008) is from the southern of two separate ponded channelized flows (**Figure 13A**). It is an aphyric T-MORB with common vesicles and has similar composition to the northern flow with 8.52% MgO and K_2O/TiO_2 of 0.11. RC14 is from a distinct flow that is slightly more primitive (Mg# = 100Mg/(Mg + 0.85Fe) = 67.7) compared to Mg#s = 66.6–67.4 for the more northern ponded channelized flow. The glass contains more abundant plagioclase compared to the 5 samples from the extensive ponded channelized flows to the north. The two remaining small areas of ponded channelized flows (**Figure 13B**) remain unsampled. The temporal relationships of flows are clear at this site with the ponded channelized flow occurring both before and after emplacement of hummocky flows of pillow lava. The ponded flow abuts older hummocky flows and left a bathtub ring along the contact (**Figure 13D**) and then younger hummocky flows filled most of the drained pond. All sampled ponded channelized flows and the one dredged flow (83-4 on **Figure 2**) that recovered lava fragments with sheet-flow morphology have MgO contents > 8.4%.

ROV video during dive T885 imaged a lobate flow with a collapsed channel just NW of the northernmost 1996 hummocky flow. The drained channel displayed a series of lava shelves formed as the channel drained. This drained lobate flow and the channel collapse are too small to identify in the AUV maps. However, it demonstrates that fluid channelized flows erupted over a larger region than identified from the AUV maps.

High-Volume Volcanic Structures

Almost all channelized and hummocky flows have volumes that are estimated at < 0.05 km^3, like the 1996 flows. Several volcanic structures, however, are estimated to have volumes 3–5 times larger. These high-volume structures formed during long-duration moderate effusion-rate eruptions, not high enough rates to form channelized flows, but higher than eruptions forming steep hummocky flows. The high-volume constructs are located near the southern end of the mapped area, south of the 1996 lava flows (**Figure 14A**), within the axial graben. The southwestern one (**Figure 14C**) is similar to, but not as flat-topped nor as steep sided as, flat-topped volcanic cones (Clague et al., 2000) that are common on mid-ocean ridges and on the submarine flanks of Hawaiian volcanoes. This low flat-topped cone is ∼1.4 × 1.6 km in diameter at the base and the flat top is ∼800 by 950 m across. The cone is ∼ 90 m tall with a volume estimated at ∼0.24 km^3, with large uncertainty because there was no pre-eruptive survey so the basal horizon is simply an average of the depths around the base. The summit contains a 5-m deep depression (**Figure 14C**). The cone is unsampled.

A second high-volume structure is an inflated hummocky flow (nomenclature from Clague et al., 2017; **Figure 14D**) ∼1500 m across and ∼100 m tall. It has a rough volume estimate of 0.18 km^3. This structure is an amalgamation of numerous hummocky pillow flows. It is unusual in that the central part has seven

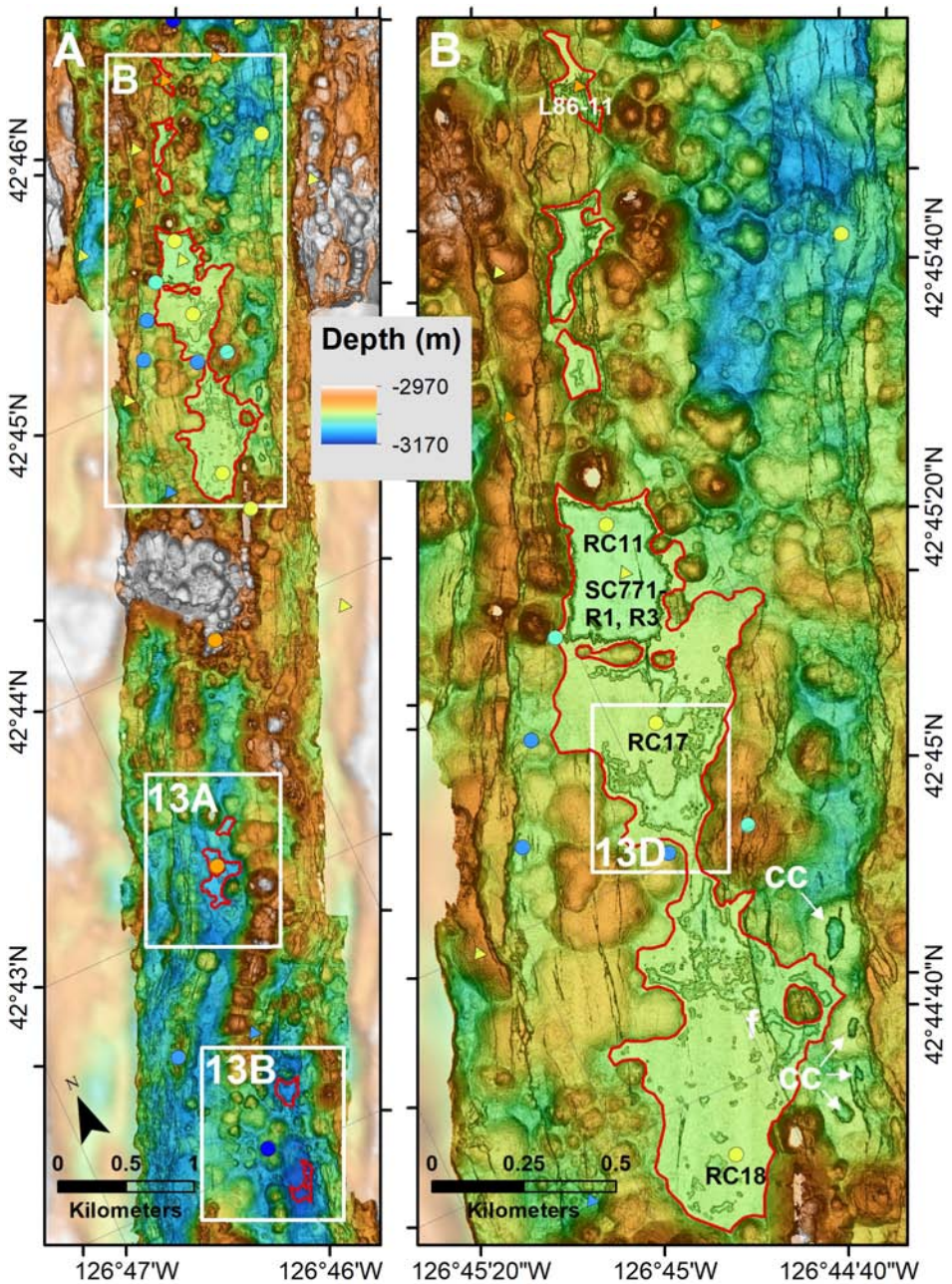

FIGURE 12 | (A) Map showing the distribution of ponded channelized flows. At least three eruptions produced ponded channelized flows in the axis (outlined by red lines), each with two or more separate flows. The locations of **Figures 12B**, **13A,B** are shown as white boxes. **(B)** The four northern flows were sampled twice during Sea Cliff dive 771 (Rona et al., 1990) and by three rock cores (Davis et al., 2008). The flows are younger than the older surrounding hummocky flows they ponded against, but are cut by a fault (f) and have thin sediment cover as observed during the *Sea Cliff* dive (Rona et al., 1990) and in several camera tows (Clague and Rona, 1990). Four inflated hummocky flows with summit craters (cc) are labeled. The location of **Figure 13D** is shown by the white box. Maps A and B are rotated counterclockwise 23°.

irregular pit crater-like collapses (with the two largest shown in **Figure 14D**). The pits range from 15 m across and 7 m deep to 270 × 150 m across with near-vertical walls up to 54 m tall. The wall of one crater is partly buried by a subsequent small pillow mound (labeled **c** on **Figure 14D**) that is similar in size to numerous other mounds that decorate the surface of the inflated hummocky flow that is also cut by numerous narrow and discontinuous fissures. A single wax-tipped rock core sample (GR00-RC08) of T-MORB collected near its center contains 7.82% MgO and has $K_2O/TiO_2 = 0.109$.

A third voluminous structure is an elongate volcanic ridge (green outline in **Figure 14B**) that is oriented parallel to the

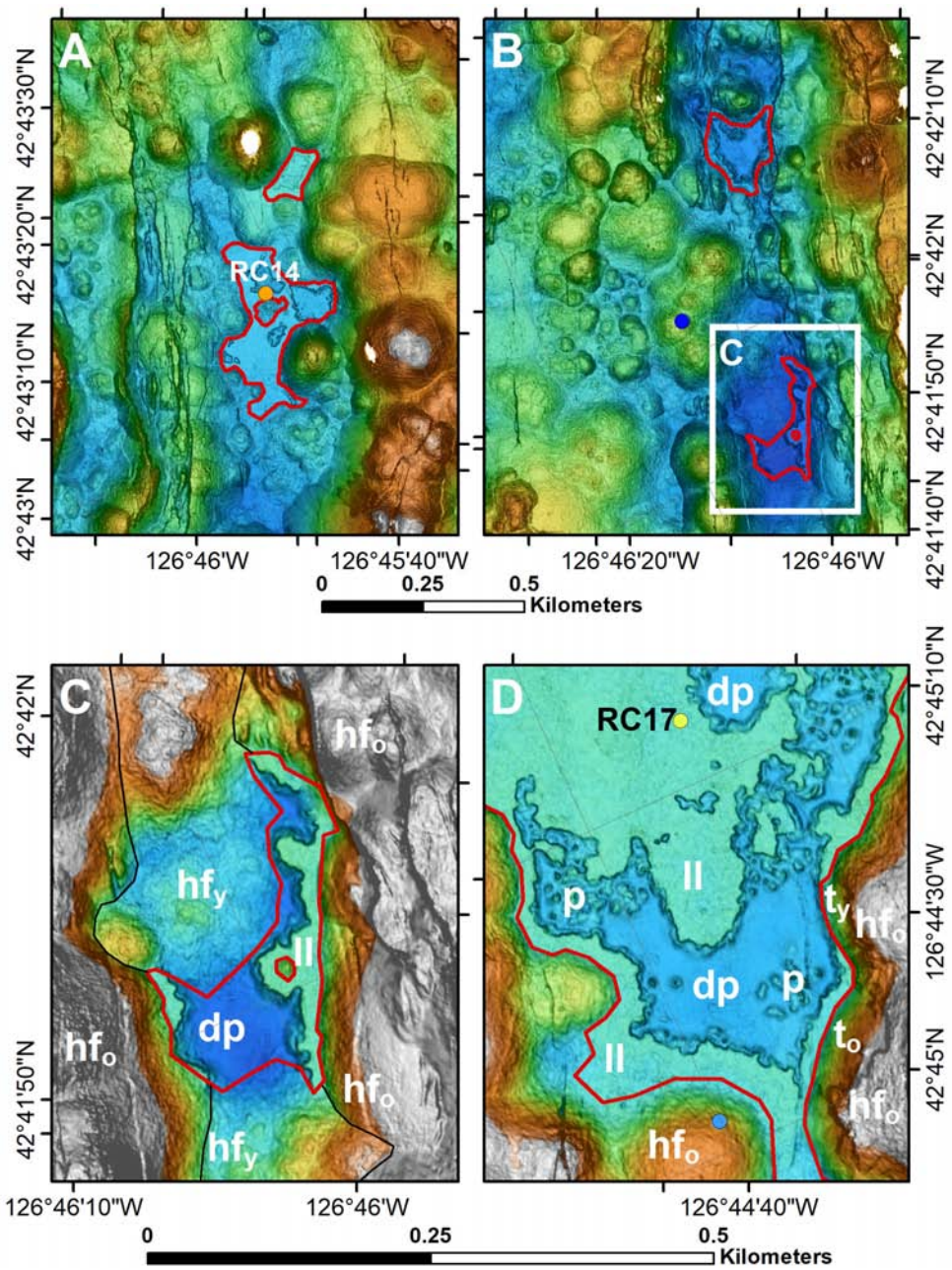

FIGURE 13 | (A) The central two small flows ponded between older hummocky flows and are of unknown age. The sampled (RC14) southern one is chemically and mineralogically distinct from the northern flows in **Figure 12B**. **(B)** The southern flows also ponded between older hummocky flows. The location of the close-up view of this flow remnant shown in **Figure 13C** is indicated by the white box. Color ramp for A and B is blue = −3170 m and orange = −2970 m. **(C)** Small remnants of a ponded channelized flow that filled in between older hummocky flows (**hf**$_o$) to east and west. The drained pond (**dp**) is partially filled in by younger hummocky flows (**hf**$_y$) from both the north and south. The margins of the pond record the original lake level (**ll**). Color ramp is blue = –3165 m to orange = –3130 m, white is shallower than –3130 m. **(D)** Close-up view of the largest ponded channelized flow, showing the drained pond (**dp**) with lava pillars (**p**) near the margins, and the original lake level (**ll**) that formed as a levee adjacent to older hummocky flows (**hf**$_o$). Talus emplaced prior to the pond on the flank of a hummocky flow (**hf**$_o$) to the east is labeled **t**$_o$, whereas talus that fell later and covers a portion of the lava pond levee is labeled **t**$_y$. Color ramp of blue = –3080 m to orange = –3040m. Maps A to D are all rotated counterclockwise 23°.

axis and is surrounded by abundant talus (see **Figure 11**). It is located south of the inflated hummocky flow and east of the flat-topped cone. This ridge has a similar estimated volume of 0.25 km^3 but formed during a different style of long-duration low-effusion rate eruption, similar to the 1996 hummocky flows. It was sampled by a wax-tip rock core GR00RC7 that recovered glass chips with three distinct compositions, making it uncertain which, if any, represents the underlying ridge and

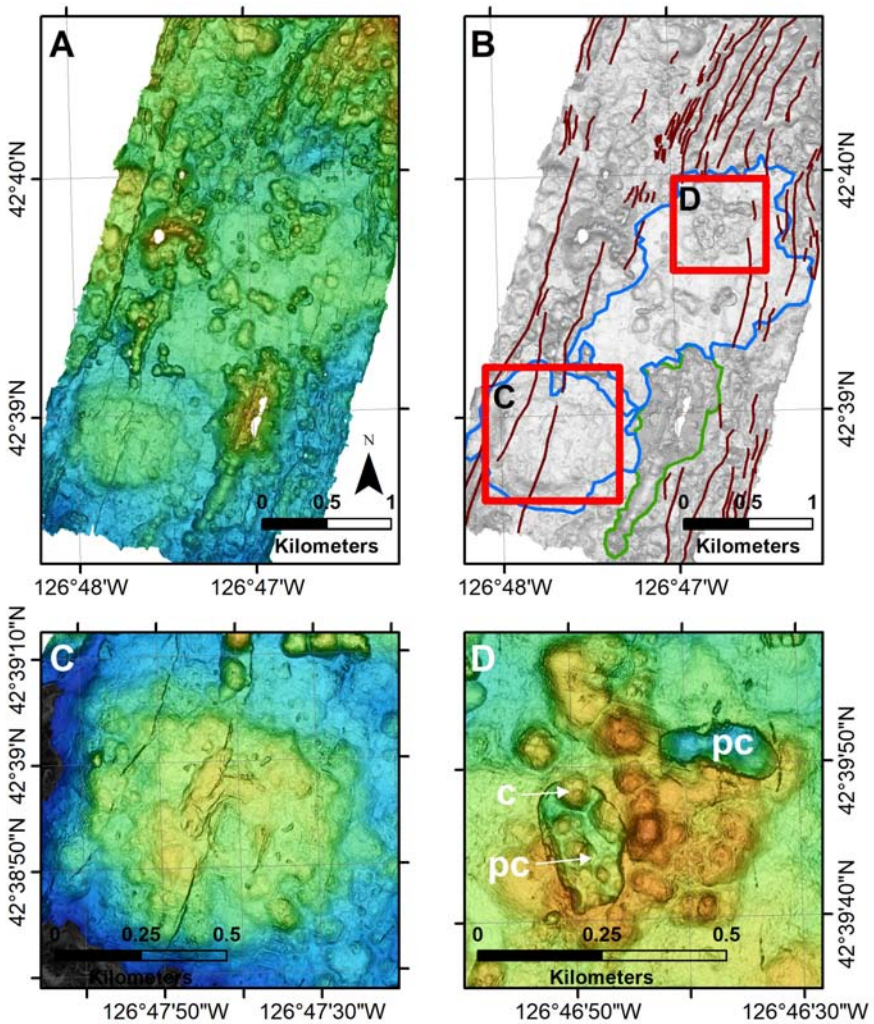

FIGURE 14 | (A) Regional view of inflated hummocky flow, flat-topped cone, and large-volume elongate ridge at southern end of the surveyed area. Color ramp of blue = –3400 m to orange = –2800 m. **(B)** Same area with blue outlines of flat-topped cone **(C)** and inflated hummocky flow **(D)**, and green outline of elongate ridge. Linework of faults showing that they bend eastward around northern inflated hummocky flow. The elongate ridge has abundant syneruptive talus on its lower slopes. Red boxes show the extents of maps in C and D. **(C)** Summit of flat-topped cone showing cross-cutting fissures, tumuli, channels and small drained lava ponds around a shallow central depression. **(D)** Close-up of two of seven pit craters on the complex inflated hummocky flow. The pit craters cross-cut some hummocky flow mounds, and younger hummocky flow mounds (north end of southwest crater) bury the ring fault bounding the crater. Both C and D have color ramp of blue = –3225 m to orange = –3075 m.

which are pyroclastic glass shards deposited on top of the cone (Clague et al., 2003, 2009). Four chips of each of the two more MgO-rich composition were analyzed, and two of the lowest MgO composition (**Supplementary Table S1**). Neither of the more-MgO rich compositions (GR00-RC7a and 7c) match analyses of other samples recovered from the area, whereas GR00-RC7b is similar to a number of analyses of sediment and glass suction samples from dives T885 and T886 on and around the 1996 flows. It is likely that the ridge is built of MORB on the boundary between N- and T-MORB with 8.38% MgO or T-MORB with 8.78% MgO.

A fourth voluminous structure, mapped using a ship-based EM300 (MBARI Mapping Team, 2001) and EM302 (Ocean Exploration Trust cruise NA108) multibeams, is a flat-topped cone at the southern end of dive T187 (**Supplementary Figure S1**). It is ∼1.4 × 1.2 km in diameter at the base and the flat top is ∼700 by 900 m across. The cone is ∼180 m tall (250 m maximum), covers 1.89 km^2, and has a rough volume of 0.23 km^3. Dive T187 recovered six N-MORB samples from the north side of the cone with MgO = 8.5–8.78% and K_2O/TiO_2 = 0.082 to 0.092.

DISCUSSION

The 1996 Eruption and Lava Flows

The 1996 eruption produced three hummocky flows with a volume of just 0.007 km^3 spread along eruption fissures that extended 1.3 km with gaps of 0.3 and 0.8 km between the three

hummocks (Yeo et al., 2013). The hypothesized southern flow located five km south of the southern of the three confirmed 1996 hummocks (**Supplementary Figure S1**; Chadwick et al., 1998) was not a young flow. The seismic activity associated with the eruption lasted for 523 h starting on February 28, 1996 (Fox and Dziak, 1998), so the eruption rate, assuming the seismic activity marks the start and end of activity, is ∼13,000 m^3/hr (Yeo et al., 2013) distributed along ∼1.3 km of eruptive fissure (**Figure 3**). The eruption rate is therefore just 10 $m^3hr^{-1}m^{-1}$ of active fissure, so at the low end of the range explored by Gregg and Fink (1995), and consistent with the morphology of the flows. If the eruption either started after the seismic swarm or ended before the swarm ended, then the rate would increase.

One result of such a slow eruption rate is that the hummocky flows are extremely steep-sided pillow mounds, shaped like haystacks. The mounds were so steep that advancing pillow flows broke off to form talus blocks of pillow fragments. As the top of the mound grew upwards, lava poured over the margin of the mound and cascaded vertically down to the talus slope below forming lavacicles, first observed here. They form in a manner analogous to lava stream "firehose" flow from truncated tubes at ocean-entries observed on Kilauea Volcano during the Pu'u O'o eruption (Hawaiian Volcano Observatory, 2017). The lava was rapidly quenched in the cold bottom seawater, but many lavacicles were still plastic when they landed as one end is commonly bent (**Figure 4F**). The lavacicles are an extreme form of "elephant trunk" lava morphology and more elongate than those reported from the 2011 Axial south rift pillow ridge (Clague et al., 2018b). Their significance is that they demonstrate that the talus at the base of the steep scarps around hummocky flows formed during the eruption that formed the hummocky flows.

The 1996 flows are geochemically heterogeneous N-MORB (**Figure 5**) with MgO content from ∼7.8 to 8.6%, Na_2O content from ∼2.7 to 2.95%, and K_2O/TiO_2 from ∼0.07 to 0.09, but overlap in composition with other prior lava flows erupted in the same portion of the North Gorda segment (Davis et al., 2008), although they are at the high end of the range for Na_2O. Rubin et al. (1998, 2001) calculated that the 12 samples had a Homogeneity Index (HI) of 2.06, roughly twice the variability expected from analytical uncertainty alone and on trend for the spreading rate at North Gorda. A HI for the combined 27 samples cannot be readily calculated since the analyses were done in different laboratories that have different analytical uncertainties, but the similar standard deviations of the different data sets (**Supplementary Table S1**) suggest that the 1996 flows are moderately heterogeneous. The significant new finding is that lavas with nearly identical compositions erupted previously in the same areas as the 1996 flows. Eruption of such similar lavas in the same location makes it even more important to sample new lava flows within a matter of years, as composition alone, even distinctive compositions like that of the 1996 flows, will not distinguish them from earlier flows.

Variations Along Axis in the Axial Graben

The petrogenesis of the lavas along the North Gorda Segment was described in Davis et al. (2008). MORB recovered from the neovolcanic zone are variable compared to other NE Pacific ridge segments ranging from near-primary melts with Mg# (100Mg/(0.85Fe + Mg) of 68 (8.8% MgO) to melts that have Mg# as low as 57 (MgO as low as 6.9%). Endeavor Segment lavas are even more variable in degree of fractionation and enrichment (Gill et al., 2016), The North Gorda magmas underwent between ∼4% and ∼40–45% crystal fractionation, based on simple enrichment factors of incompatible elements. Likewise, the lavas range in K_2O/TiO_2 from 0.06 to 0.15 and so from N-MORB to T-MORB. There are no obvious trends in either MgO content or K_2O/TiO_2 along the axis away from the shallowest point along the segment at about 42.75°N. The only trend in MgO is that the lavas from the southern part of the segment (near 42.6°N) are lacking samples that are more fractionated (none with < 7.9% MgO). On the other hand, Na_2O contents vary with the southernmost lavas having lower Na_2O than those closer to the shallowest part of the segment at 42.75°N. The higher, but variable, Na_2O contents of the lavas from the shallowest point along the axis indicate that these magmas are derived from a deeper depth range (Klein and Langmuir, 1987). The high variability in compositions on small spatial scales is consistent with, but does not require, a lack of mixing between small chemically distinct magma batches (e.g., Bohrson et al., 2014). The heterogeneity of magmas along the axis is in turn consistent with absence of a crustal axial magma lens and the magma-starved deep-axial-valley morphology of the Gorda Ridge (e.g., Buck et al., 2005) discussed in a later section.

The Cross-Section to the East of the Axis

As expected, but rarely demonstrated, the fault blocks have thicker sediment cover away from the axis. Sediment thickness (as indicated by bottom smoothness in the multibeam bathymetry, sub-bottom seismic lines, and direct observations) appears to increase in steps defined by wide fault blocks (*Be, Ce, De, Ee, and Fe* on **Figure 6**). The $^{230}Th/^{238}U$ disequilibrium ages (Goldstein et al., 1991) increase in age with increasing distance from the center of the axis, although sample 85-7 at 51 kyr (from the inner part of block *Ee*) is half that expected from the spreading rate and distance to the axis. Even if the flows erupted along the eastern margin of an axial block the same width as block A (**Figure 6C**), this flow is still too young by ∼35 ka. The area has not been directly observed, but the steep hummocky flows also have less sediment than the southwestern part of the same fault block (**Supplementary Figure S2A**). This may be a site of off-axis volcanism, as documented elsewhere along the MOR (e.g., Reynolds and Langmuir, 2000). However, the volcanic activity, if it occurred off-axis, still took place 51 ± 12 ka ago (Goldstein et al., 1991) and is therefore not the current source of heat driving the off-axis hydrothermal activity at the Sea Cliff site.

The Sea Cliff hydrothermal site is located on the off-axis fault with the largest throw. The site is not located at the intersection of two cross-cutting fault systems as originally proposed by Rona and Clague (1989) and Rona et al. (1990). The same geological setting was also proposed for the TAG hydrothermal field on the MAR (Rona, 1988; Karson and Rona, 1990), but the concept of cross-cutting faults localizing fluid flow has also been supplanted there (Canales et al., 2007) who proposed the heat is derived

from hot mantle rocks that underlie a low-angle fault (Canales et al., 2007). Such a mechanism does not seem feasible for the Sea Cliff site where such low-angle faults are not evident. At Sea Cliff, the hydrothermal fluids are apparently heated beneath the ridge axis and flow upward along the off-axis normal fault with the largest throw, which may also have the deepest crustal penetration. This large-offset normal fault also produced volcanic breccia (Rona et al., 1990).

The increasing thickness of sediment cover off-axis that we have documented at North Gorda segment may also seal the crust on these older off-axis fault blocks, forcing fluid flow along the faults. The sediment also buries and subdues the fine-scale topography of volcanic features in this high-sediment-rate region (∼5–6 cm/kyr) and crust as young as perhaps 50 kyr has 2–3 m of sediment, which may be enough to seal the crust.

Abundances of Different Lava Morphologies on the Intermediate-Rate North Gorda Segment

The North Gorda Segment is characterized by abundant small-volume hummocky flows. Many hummocky flow mounds can be produced during single eruptions, as occurred during the 1996 North Gorda eruption, which produced 29 pillow mounds that coalesced into just three larger composite mounds (Yeo et al., 2013). A more extreme example is the 1986 eruption on the North Cleft Segment of the Juan de Fuca Ridge which produced 130 mounds, coalesced into 17 ridges and composite mounds (Yeo et al., 2013). To determine which mounds are part of each eruption most likely requires sampling each mound and hoping that each eruption has a distinct composition or compositional range. Mapping historical flows soon after they erupt is the only feasible way to determine which mounds formed during single eruptions, and therefore the volume of lava erupted and the eruptive fissure length, so that eruption rates can be estimated.

The axial graben of the North Gorda Segment consists of 91% hummocky flows including a high-volume inflated hummocky flow, large elongate ridge and a flat-topped cone; 3% channelized flows that are ponded between hummocky flows; and 6% talus, with most talus formed during eruptions that formed the hummocky flows. Of the roughly 96% of the surface produced during low-rate eruptions that produce these hummocky flows, all but three eruptions were brief and produced small-volume hummocky flows comprised of pillow lava. The three largest-volume eruptions (**Figure 14**) each produced hummocky flows that had volumes estimated at 0.18 to 0.25 km^3, but make up only 1% of the area mapped. These larger-volume eruptions occurred distal from the shallowest point on the axis. The highest eruption rate flows, the channelized flows, occurred within 5 km of the shallowest point along the segment. The largest of the channelized flows (**Figure 12B**) erupted < 0.06 km^3, but a large portion drained back down either the eruptive fissures or older open fissures when the eruption ended, leaving areas of drained ponds (**dp** on **Figures 12E,F**) that are surrounded by hummocky flow mounds. There are also rare hummocky flows that erupted more rapidly than most hummocky flows and therefore maintained molten cores, as described for flows from the 2015 eruption at Axial Seamount (Clague et al., 2017). Such flows are rare on North Gorda, with just four small hummocks with summit craters, the flat-topped cone with channels on the summit (**Figure 14C**), and the low inflated hummocky flow with seven pit craters (**Figures 13B,D**). The vast majority of North Gorda hummocky flows show no evidence of having had molten cores and are inferred to have erupted at low rates or, for the steeper mounds, at very low rates.

The large-volume volcanic edifices exert structural control on the locations of faults and fissures in the axial graben. These faults and fissures bend around the eastern inflated hummocky flow with the 7 pit craters (**Figure 14B**) suggesting that such volcanic units form thick, coherent material that is not easily fractured during extension events, such that the faults bend to capitalize on less rigid adjacent crust.

Channelized flows, inferred from their morphology to have erupted at high rates (Griffiths and Fink, 1992; Gregg et al., 1996), are rare and geochemically within the range of melt MgO contents and crystal contents of that of the hummocky flows, including those erupted in 1996. Since viscosity in low-volatile MORBs is largely determined from melt temperature and crystal content (Shaw, 1972), their rapid eruption rates are not caused by their having lower viscosities than the hummocky flows. Their high eruption rates are therefore caused by either wider dikes or more buoyant magma (Head et al., 1996), presumably caused by higher bubble abundances. Higher bubble contents are associated with the sections of fissure that had the highest eruption rates during the 2011 eruption of channelized flows on Axial Seamount (Jones et al., 2018) and one of the samples of the ponded channelized flows on North Gorda also has abundant vesicles. This difference may have contributed to more rapid eruption of the channelized flows, but we suspect that the width of the feeder dike is the primary control on eruption rate since that rate per m of eruptive fissure increases by a factor of 1000 as a dike widens from 0.2 to 2.2 m (Table 1 in Head et al., 1996). A wider dike with higher eruption rate could occur when eruptions are less frequent, whereas a narrower dike with lower eruption rate would be consistent with more frequent eruptions. The change in frequency of eruptions does not need to vary by large amounts to result in large differences in dike width and eruption rates since eruption rate per m of fissure varies as the cube of dike width but linearly with changes in viscosity (equation 2 in Head et al., 1996).

Changes in the Sea Cliff Hydrothermal Field

Data on the vent fluid chlorinity collected in 2000, 2002, and 2004 showed a slight increase with time, but the magnitude of the increase was small enough to be within the error of individual measurements, and Von Damm et al. (2006) concluded that the fluid composition was stable over the 4-year period. A linear regression of the Von Damm et al. (2006) data indicates, however, increasing salinity with time with an r^2 value of 0.71. Extrapolating this fit to the data predicts that the chlorinity of the vent fluid will have increased from an average 454 ± 2 mmol/kg Cl in 2000 to slightly > 500 mmol/kg Cl by mid-2019 and to

seawater values by ∼2040. Resampling of the vents to determine fluid composition changes can test this extrapolation.

Seafloor markers were deployed where hydrothermal fluids were sampled (Von Damm et al., 2006). Comparison of photos that include the markers show that some chimneys became inactive and collapsed during the 5 years of observation and that the most active venting shifted with time.

Samples of hydrothermal crusts from the vent field collected in 1988 consisted mostly of highly altered and silicified hyaloclastite breccia (Zierenberg et al., 1995). Samples of active chimneys collected on later expeditions showed that the chimneys are dominantly composed of anhydrite with less abundant Mg-saponite, amorphous silica and minor pyrite, chalcopyrite and sphalerite (Von Damm et al., 2006). As the chimneys collapse, anhydrite is selectively dissolved, but evidence of its former presence is often preserved due to overgrowth and/or pseudomorphic replacement of the anhydrite by amorphous silica and saponite, as observed in sample T186-R3. This process of repeated chimney growth, collapse, and dissolution forms the low ridges that host the active vents (**Figure 9C**). Continued diffuse flow of hydrothermal fluid through the collapsed chimney rubble, coupled with conductive cooling, leads to further precipitation of amorphous silica forming hydrothermal silica crusts with a clastic texture that appear similar to the highly altered hyaloclastite crusts (i.e., T186-R2).

Zierenberg et al. (1995), used relatively immobile trace elements to establish the basaltic parentage of the silicified hyaloclastites. The relatively immobile rare earth elements (REE) demonstrate that much of the material in the vent field is a residual product of hydrothermal chimney collapse (**Figure 10**), i.e., the material formed mostly by hydrothermal precipitation, not leaching and silicification of volcaniclastites.

The North Gorda Segment Compared With Other Pacific Intermediate-Rate Ridges

The volcanic terrain along the axial zone consists mainly of hummocky flows with only rare channelized flows. Axial volcanic ridges characteristic of the slow-spreading MAR (e.g., Yeo and Searle, 2013) are absent in the axial graben, although one similar ridge occurs off-axis immediately upslope from the Sea Cliff hydrothermal site. Parameters such as axial graben width and depth at the segment center, eruption rates that produce different volcanic landforms, volumes of eruptions, and homogeneity or heterogeneity of lava compositions (as measured by Mg#, K_2O/TiO_2, or trace element ratios such as La/Sm) in the axis vary among the limited number of mapped and sampled Pacific intermediate-rate spreading centers (**Table 2**). In almost all of these parameters, the North Gorda segment is an end-member among intermediate-rate ridges in the Pacific. For example, the North Gorda axial graben at the shallowest point near the center of the segment is ∼18 km wide and ∼700 m deep, compared to 3.2 km wide and 100 m deep on the Cleft segment (Stakes et al., 2006), > 2 km wide and ∼200 m deep at the low-magma supply portion of the Galapagos Spreading Center at −94°50′ longitude (Colman et al., 2012), and ∼1 km wide and 200 m deep on the Endeavor segment (Clague et al., 2014). Axial highs are found on the Alarcon Rise (Clague et al., 2018a), the high-magma-supply portion of the Galapagos Spreading Center at −91°55′ to −92° longitude (Colman et al., 2012), and the older flanks of the Endeavor (Clague et al., 2014) and North Gorda (**Figure 1**) segments. The intermediate-rate ridges with a high-magma supply portion are cut by a narrow axial cleft, that at Galapagos is 10–40 m deep, on the Cleft segment is 30–90 m wide and 10–15 m deep (Stakes et al., 2006), and at Alarcon Rise is an en echelon fissure system ∼9 km long (Clague et al., 2018a). For comparison, the slow-spreading MAR commonly has an axial graben > 20 km wide, although at the TAG site it is only 8–10 km wide (Karson and Rona, 1990), and the axial graben structure is complicated by the abundance of detachment faults that commonly occur on one side of the axis or the other, but rarely on opposing sides (Cann et al., 2015). None of the intermediate-rate ridges in the Pacific share a history of detachment faulting with the slower-spreading ridges of the Atlantic, Indian, and Arctic Oceans.

At Pacific intermediate-rate ridges, many of the morphologic and geologic features depend largely on magma supply rates (**Table 2**). As magma supply can vary at similar spreading rates, eruptions also vary in magma flux, volume, and uniformity

TABLE 2 | Intermediate-rate pacific ridge comparison.

Segment: time period or magma flux	Reference	Graben width (km)	Graben depth (m)	Channelized vs. hummocky flows	Volumes of larger hummocky flows	Chemical variability
Lower magma supply						
N. Gorda: recent	This paper	15	700	97% hummocky flows	0.1–0.3 km3	High
South Cleft	Stakes et al., 2006	3.2	100	100% channelized flows	ND	Low
Galapagos: low flux	Colman et al., 2012	>2	200	85% hummocky flows	0.09–1.31 km3	High
Endeavor: 0–4.3 ka	Clague et al., 2014	1	200	Mostly hummocky flows	ND	High
Higher magma supply						
N Gorda: 15–125 ka	This paper	NA	NA	All hummocky flows	ND	Low
Endeavor: > 4.3 ka	Clague et al., 2014	NA	NA	> 50% channelized flows	ND	Low
Alarcon Rise	Clague et al., 2018a	NA	NA	> 50% channelized flows	ND	Low
Galapagos: high-flux	Colman et al., 2012	NA	NA	53% channelized and lobate flows	0.002–0.13 km3	Low

NA, not applicable; ND, not determined.

in lava composition (e.g., Colman et al., 2012). The present day North Gorda segment is constructed by mostly small-volume, low-flux eruptions having a range of melt compositions, both in terms of enrichment (e.g., K_2O/TiO_2) and residence times in the crust (MgO contents). The limited sampling of off-axis, older, lavas at North Gorda have a much narrower compositional range. Endeavor segment also has a wide range of lava compositions (Gill et al., 2016) and few channelized flows within the axial graben, erupted while the magma supply was low. Flank lavas, erupted when the segment was in a high-volume magmatic phase, are more compositionally homogeneous (Clague et al., 2014). The North Gorda segment may be entering a period of increasing magma supply, marked by eruption of a few brief, higher-effusion rate channelized flows near the shallowest portion of the neovolcanic zone, and a few larger-volume volcanic structures (inflated hummocky flow, flat-topped cones, and more voluminous ridges) that indicate equally rare longer-lived eruptions. Off-axis, lavas are hummocky flows formed during low-flux eruptions that apparently were also mostly short-lived as few large-volume edifices were constructed. The lavas have more homogeneous evolved compositions, so may have been more thoroughly mixed in sub-axial magma reservoirs and cooled longer or more efficiently (perhaps at shallower depths). Even further off-axis, when the segment may have been characterized by an axial high (**Figure 1**), mapping and sampling are inadequate to determine the eruption rates, eruption durations, or variability of the flow compositions.

It is tempting to try to arrange all these different intermediate-rate ridges into the Kappel and Ryan (1986) model of alternating tectonic and magmatic cycles. Furthermore, the three-phase cycle of magmatism, tectonism, and hydrothermalism proposed for the Endeavor segment (Clague et al., 2014) may only apply to that segment as none of the other intermediate-rate segments have a phase dominated by hydrothermal discharge when magma supply begins to increase at the beginning of the next magmatic phase. The segments listed in **Table 2** are roughly organized in terms of width and depth of the axial graben, percent high- and low flux lava flows, volumes of larger flows, and chemical variability (**Table 2**). These variations in parameters indicate that, at nearly constant spreading rates, magma supply rate provides the primary control on ridge structure, but other unidentified factors must also exert secondary control.

Faulting on North Gorda consists of sub-parallel normal faults with larger-throw faults spaced about 1 km apart, but with additional small-throw normal faults in between (**Figure 6B**). This axial structure is distinct from that at some slow spreading ridges (e.g., Smith et al., 2012; Cann et al., 2015) that develop detachment faults that expose lower crust or mantle rocks. North Gorda faulting is also distinct from the broad axial bulge, commonly with a small summit graben, that characterized fast-spreading ridges (e.g., Buck et al., 2005). Numerical modeling (Lavier and Buck, 2002) suggests extension of brittle thick lithosphere, or lithosphere with efficient hydrothermal cooling, can produce a rift with multiple graben structures, such as observed at North Gorda.

CONCLUSION

The 1996 eruption on the North Gorda segment produced three small hummocky lava flows that erupted at extremely low rates, thereby producing hummocks with near-vertical margins. Flows cascading over the edge of these steep-sided hummocks produced abundant syneruptive talus and rare lavacicles when molten lava fell vertically.

Individual lava flows that construct the North Gorda crust have small volumes from 0.007 km^3 for the 1996 flows to 0.25 km^3 for the largest flat-topped cones and inflated hummocky flows. Lava flows with similar chemical compositions erupted at a range of rates to produce highly varied volcanic landforms. These landforms range from rapidly erupted channelized flows that ponded in the axial graben to very slowly erupted steep-sided hummocky flows like the 1996 hummocky flows. These observations indicate that dike width rather than physical lava properties or magmatic gas content is the primary control on eruption rate.

The Sea Cliff hydrothermal site is located 2.6 km east of the center of the axial graben, and 370 m above the floor of the axial graben where the graben-bounding fault with the largest throw is located. The hydrothermal system emits 305°C colorless fluids that mainly precipitate anhydrite and Mg-rich smectite, with only traces of sulfide phases. Observations in 2019 (C. German, personal communication) suggest minimal changes in the system since last observed and sampled in 2005, or since discovery in 1988. The active vent site is not located where two fault systems intersect, as proposed previously.

Sub-bottom seismic profiles and multibeam bathymetric data collected from the AUV show that sediment thickness increases with distance to the axial graben, as expected but rarely shown on such a small scale. Sediment cover close to the axis that is too thin to detect seismically smooths the bathymetry. The normal faults bounding the axial graben are asymmetrical with limited uplift on the west side of the graben compared with the east side.

Comparison with other Pacific intermediate-spreading rate ridges indicates that North Gorda, following a period of tectonic extension, may be re-entering a more magmatically robust phase with eruption of some larger-volume flows and volcanic constructs, as well as more rapidly erupted channelized flows in the axial graben.

Addition of 1-m resolution mapping data collected by AUVs enhances the value of legacy data sets and enables reinterpretation of the history of spreading and volcanism on mid-ocean ridges. A large amount of such legacy data exists along the global mid-ocean ridge system that will yield new insights if it can be placed in a high-resolution spatial framework. The only requirement is that the legacy data must be well-navigated, have features that allow co-registration with the new high-resolution mapping data, or have sampled large features.

DATA AVAILABILITY STATEMENT

The AUV multibeam and sub-bottom seismic data can be found in the IEDA seafloor bathymetry archives.

AUTHOR CONTRIBUTIONS

DAC was chief scientist on the cruises in 2000, 2002, and 2005, managed the sample analysis and processing of the multibeam data, and wrote most of the manuscript. JP participated on the ROV dive cruises in 2002 and 2005, processed the multibeam data, prepared most of the figures, and edited the manuscript. DWC collected the AUV multibeam data and did the initial data processing. JM obtained funding for the dives at the Sea Cliff hydrothermal site, participated on the cruises in 2000 and 2002, and discussed the setting and character of the site with coauthors. RZ participated on the cruises in 2000 and 2002 and interpreted the analytical data on the hydrothermal samples.

FUNDING

The ROV dives at Sea Cliff site in 2000 and 2002 were supported by a grant from the West Coast NURP office of NOAA. The remaining ROV dives and collection of the AUV data were funded by a grant to the Monterey Bay Aquarium Research Institute from the David and Lucile Packard Foundation, which also supported the salaries of DAC, JP, and DWC.

ACKNOWLEDGMENTS

Samples and observations were collected in 2000, 2002, and 2005 during ROV *Tiburon* dives done from the R/V *Western Flyer*. The mapping AUV surveys were completed in 2009 from the R/V *Zephyr* and in 2016 from the R/V *Rachel Carson*. The dedication and skill of the captains, ships crews, ROV pilots, and AUV team at MBARI are reflected in the high-quality data available for this study. We thank Chris German and Ocean Exploration Trust for sharing regional EM302 bathymetric data collected by the R/V *Nautilus* during cruise NA108 in 2019. Observations from their NASA- and NOAA-funded ROV program confirm that the Sea Cliff vent field remains active in 2019 and expands the area of active vent along strike 775 m to the north with discovery of the Apollo vent field.

SUPPLEMENTARY MATERIAL

The Supplementary Material for this article can be found online at: https://www.frontiersin.org/articles/10.3389/fmars.2020.00027/full#supplementary-material

FIGURE S1 | Map of proposed southern 1996 flow (Chadwick et al., 1998) and track of ROV *Tiburon* dive T187 with samples coded by MgO content as in **Figure 2** and the first and last rock samples labeled. The orange triangle in the SE corner is the inferred location of W9604-C2 (Rubin et al., 1998) plotted on the track of the towed camera survey. The hypothesized flow (Chadwick et al., 1998) is defined by depth anomalies (shown with maximum difference of 60 m and contour interval of 5 m) determined by difference from pre- and post-1996 bathymetric maps. It is an artifact as no young flows were encountered on T187. Color ramp is −3550 m (dark blue) to −3000 m (orange).

FIGURE S2 | Three ridge-parallel seismic profiles collected by the AUV mounted Edgetech FS-AU sonar 2–16 kHz chirp sub-bottom profilers showing thicker sediment on distal line 2 than more proximal line 16, which has similar sediment cover to that on line 58 on the opposite side of the axis. The locations of the lines are shown in **Figure 6B** with line 2 from fault block *Ee*, line 16 from block *De*, and line 58 from block *Cw*. The maximum sediment thickness decreases from 5 to 7 m on block *Ee* to 2–3 m on blocks *De* and *Cw* to undetected sediment on blocks *A, Bw,* and *Be*.

TABLE S1 | Microprobe glass compositions.

REFERENCES

Baker, E. T., Massoth, G. J., Collier, R. W., Trefry, J. H., Kadko, D., Nelson, T. A., et al. (1987). Evidence for high-temperature hydrothermal venting on the Gorda Ridge, northeast Pacific Ocean. *Deep Sea Res.* 34, 1461–1476. doi: 10.1016/0198-0149(87)90137-3

Ballard, R. D., and van Andel, T. H. (1977). Morphology and tectonics of inner rift valley at lat 36°50'N on Mid-Atlantic Ridge. *Geol. Soc. Am. Bull.* 88, 507–530.

Bideau, D., Hekinian, R., Sichler, B., Gracia, E., Bollinger, C., Constantin, M., et al. (1998). Contrasting volcanictectonic processes during the past 2Ma on the Mid-Atlantic Ridge: submersible mapping, petrological and magnetic results at lat. 34°52' N and 33°55' N. *Mar. Geophys. Res.* 20, 425–458.

Bohrson, W. A., Spera, F. J., Ghiorso, M. S., Brown, G. A., Creamer, J., and Mayfield, A. (2014). Thermodynamic model for energy-constrained open system evolution of crustal magma bodies undergoing simultaneous assimilation, recharge, and crystallization: the magma chamber simulator. *J. Petrol.* 55, 1685–1717. doi: 10.1093/petrology/egu036

Buck, W. R., Lavier, L. L., and Poliakov, A. N. B. (2005). Modes of faulting at mid-ocean ridges. *Nature* 434, 719–723.

Canales, J. P., Sohn, R. A., and deMartin, B. J. (2007). Crustal structure of the Trans-Atlantic Geotraverse (TAG) segment (Mid-Atlantic Ridge, 26°10′N): Implications for the nature of hydrothermal circulation and detachment faulting at slow spreading ridges. *Geochem. Geophys. Geosyst.* 8, 1–18. doi: 10.1029/2007GC001629

Cann, J. R., Smith, D. K., Escartin, J., and Shouten, H. (2015). Tectonic evolution of 200 km of Mi-Atlantic ridge over 10 million years: interplay of volcanism and faulting. *Geochem. Geophys. Geosyst.* 16, 2303–2331. doi: 10.1002/2015GC005797

Caress, D. W., and Chayes, D. N. (1996). Improved processing of hydrosweep DS multibeam data on the R/V Maurice Ewing. *Mar. Geophys. Res.* 18, 631–650. doi: 10.1007/BF00313878

Caress, D. W., Thomas, H., Kirkwood, W. J., McEwen, R., Henthorn, R., Clague, D. A., et al. (2008). "High-resolution multibeam, sidescan, and subbottom surveys using the MBARI AUV D. Allan B," in *Marine Habitat Mapping Technology for Alaska*, eds J. R. Reynolds, and H. G. Greene, (Fairbanks: University of Alaska), 47–69. doi: 10.4027/mhmta.2008.04

Chadwick, W. W. Jr., Clague, D. A., Embley, R. W., Perfit, M. R., Butterfield, D. A., Caress, D. W., et al. (2013). The 1998 eruption of Axial Seamount: new insights on submarine lava flow emplacement from high-resolution mapping. *Geochem. Geophys. Geosyst.* 14, 3939–3968. doi: 10.1002/ggge.20202

Chadwick, W. W. Jr., Embley, R. W., and Shanks, T. M. (1998). The 1996 Gorda Ridge eruption: geologic mapping, sidescan sonar, and SeaBeam comparison results. *Deep Sea Res. II* 45, 2547–2569. doi: 10.1016/s0967-0645(98)00083-6

Chadwick, W. W. Jr., Paduan, J. B., Clague, D. A., Dreyer, B. M., Merle, S. G., Bobbitt, A. M., et al. (2016). Voluminous eruption from a zoned magma body after and increases in supply rate at Axial Seamount. *Geophys. Res. Lett.*, 43 12:70. doi: 10.1002/2016GL071327

Clague, D. A., Paduan, J. B., Dreyer, B. M., Chadwick, W. W. Jr., Rubin, K. R., Perfit, M. R., et al. (2018b). Chemical variations in the 1998, 2011, and 2015 lava flows from Axial Seamount, Juan de Fuca Ridge: cooling during ascent, lateral transport, and flow. *Geochem. Geophys. Geosyst.* 19, 2915–2933. doi: 10.1029/2018GC007708

Clague, D. A., Davis, A. S., and Dixon, J. E. (2003). "Submarine strombolian eruptions along the Gorda mid-ocean ridge," in *Explosive Subaequeous Volcanism, American Geophysical Union Monograph*, eds J. D. L. White, J. L. Smellie, and D. A. Clague, (Hoboken, NJ: Wiley), 11–12.

Clague, D. A., Dreyer, B. M., Paduan, J. B., Martin, J. F., Caress, D. W., Gill, J. B., et al. (2014). Eruptive and tectonic history of the Endeavour Segment of the Juan de Fuca Ridge based on AUV mapping and lava flow ages. *Geochem. Geophys. Geosyst.* 15, 1–28. doi: 10.1002/2014GC005415

Clague, D. A., Dreyer, B. M., Paduan, J. B., Martin, J. F., Chadwick, W. W. Jr., Caress, D. W., et al. (2013). Geologic history of the summit of Axial Seamount, Juan de Fuca Ridge. *Geochem. Geophys. Geosyst.* 14, 4403–4443. doi: 10.1002/ggge.20240

Clague, D. A., and Holmes, M. L. (1987). "Geology, petrology, and mineral potential of the Gorda Ridge," in *Geology and Resource Potential of the Continental Margin of Western North America and Adjacent Ocean Basins—Beaufort Sea to Baja California: Circum-Pacific Council for Energy and Mineral Resources, Circum-Pacific Earth Science Series*, eds D. W. Scholl, A. Grantz, and J. G. Vedder, (Berelin: Springer), 563–580.

Clague, D. A., Moore, J. G., and Reynolds, J. R. (2000). Formation of submarine flat-topped volcanic cones in Hawaii. *Bull. Volcanol.* 62, 214–233. doi: 10.1007/s004450000088

Clague, D. A., Paduan, J. B., Caress, D. W., Chadwick, W. W. Jr., Le Saout, M., Dreyer, B., et al. (2017). High-resolution AUV mapping and targeted ROV observations of three historical lava flows at Axial Seamount. *Oceanography* 30, 82–99. doi: 10.5670/oceanog.2017.426

Clague, D. A., Paduan, J. B., Caress, D. W., Thomas, H., Chadwick, W. W. Jr., and Merle, S. G. (2011). Volcanic morphology of West Mata Volcano, NE Lau basin, based on high-resolution bathymetry and depth changes. *Geochem. Geophys. Geosyst.* 12:QOAF03. doi: 10.1029/2011GC003791

Clague, D. A., Paduan, J. B., and Davis, A. S. (2009). Widespread strombolian eruptions of mid-ocean ridge basalt. *J. Volcanol. Geother. Res.* 180, 171–188. doi: 10.1016/j.jvolgeores.2008.08.007

Clague, D. A., Caress, D. W., Dreyer, B. M., Lundsten, L., Paduan, J. B., Portner, R. A., et al. (2018a). Geology of the Alarcon Rise, Southern Gulf of California. *Geochem. Geophys. Geosyst.* 19, 807–837. doi: 10.1002/2017GC007348

Clague, D. A., and Rona, P. (1990). "Geology of the GR-14 site on the northern Gorda Ridge," in *Gorda Ridge: A frontier area in the United States Exclusive Economic Zone*, ed. G. R. McMurray, (New York: Springer-Verlag), 31–50. doi: 10.1007/978-1-4612-3258-2_3

Clague, D. A., Zierenberg, R. A., Davis, A., Goffredi, S., McClain, J., Maher, N., et al. (2001). MBARI's 2000 expedition to the Gorda Ridge. *Newslett. U.S. Ridge Initiat.* 11, 5–12.

Colman, A., Sinton, J., White, S. M., McClinton, J. T., Bowles, J. A., Rubin, K. H., et al. (2012). Effects of variable magma supply on mid-ocean ridge eruptions: constraints from mapped lava flow fields along the Galápagos Spreading Center. *Geochem. Geophys. Geosyst.* 13:Q08014. doi: 10.1029/2012GC004163

Cowen, J. P., and Baker, E. T. (1998). The 1996 Gorda Ridge event detection and response activities: historical perspective and future implications. *Deep Sea Res. II* 45, 2503–2511.

Davis, A. S., and Clague, D. A. (1987). Geochemistry, mineralogy, and petrogenesis of lava from the Gorda Ridge between latitude 43°N and 41.4°N. *J. Geophys. Res.* 92, 467–410.

Davis, A. S., and Clague, D. A. (1990). Gabbroic xenoliths from the Northern Gorda Ridge: implications for magma chamber processes under slow-spreading centers. *J. Geophys. Res.* 95, 885–810.

Davis, A. S., Clague, D. A., Cousens, B. L., Keaten, R., and Paduan, J. B. (2008). Geochemistry of basalt from the North Gorda segment of the Gorda Ridge: evolution toward ultra-slow spreading ridge lavas due to decreasing magma supply. *Geochem. Geophys. Geosyst.* 9:Q04004. doi: 10.1029/2007GC001775

DeMets, C., Gordon, R. G., and Argus, D. F. (2010). Geologically current plate motions. *Geophys. J. Int.* 181, 1–80. doi: 10.1111/j.1365-246x.2009.04491.x

Dreyer, B. M., Clague, D. A., and Gill, J. (2013). Petrological variability of recent magmatism at Axial Seamount summit, Juan de Fuca ridge. *Geochem. Geophys. Geosyst.* 14, 4306–4333. doi: 10.1002/ggge.20239

Fornari, D. J., Tivey, M. A., Schouten, H., Perfit, M. R., Yoerger, D., Bradley, A., et al. (2004). "Submarine lava flow emplacement at the East Pacific Rise 9°50'N: implications for uppermost ocean crust stratigraphy and hydrothermal fluid circulation," in *Mid-Ocean Ridges: Hydrothermal Interactions between the Lithosphere and Oceans, Geophysical Monograph Series*, eds C. R. German, J. Lin, and L. M. Parson, (Washington, DC: American Geophysical Union), 187–218.

Fowler, A. P. G., and Zierenberg, R. A. (2015). "Rare earth element concentrations in geothermal fluids and epidote from the Reykjanes geothermal system, Iceland," in *Proceedings World Geothermal Congress 2015*, Melbourn.

Fowler, A. P. G., Zierenberg, R. A., Reed, M., Palandri, J., Óskarsson, F., and Gunnarson, I. (2019). Rare earth element systematics in boiled fluids from basalt-hosted geothermal systems. *Geochim. Cosmochim. Acta* 244, 129–154. doi: 10.1016/j.gca.2018.10.001

Fox, C. G., and Dziak, R. P. (1998). Hydroacoustic detection of volcanic activity on the Gorda Ridge, February-March 1996. *Deep Sea Res. II* 45, 2513–2530. doi: 10.1016/s0967-0645(98)00081-2

Fundis, A. T., Soule, S., Fornari, D. J., and Perfit, M. R. (2010). Paving the seafloor: Volcanic emplacement processes during the 2005–2006 eruptions at the fast spreading East Pacific Rise, 9°N. *Geochem. Geophys. Geosyst.* 11:Q08024. doi: 10.1029/2010GC003058

Gill, J. B., Michaels, P., Woodcock, J., Ramos, F., Dreyer, B. M., Clague, D. A., et al. (2016). Origins of enriched MORB at the Endeavour Segment, Juan de Fuca Ridge. *J. Petrol.* 57, 863–896. doi: 10.1093/petrology/egw024

Goldstein, S. J., Murrel, M. T., Janceky, D. R., Delaney, J. R., and Clague, D. A. (1991). Geochronology and petrogenesis of young MORB from the Juan de Fuca and Gorda Ridges by 238U - 230Th disequilibrium. *Earth Planet. Sci. Lett.* 107, 25–41. doi: 10.1016/0012-821x(91)90041-f

Gregg, T. K. P., and Fink, J. H. (1995). Quantification of submarine lava-flow morphology through analog experiments. *Geology* 23, 73–76.

Gregg, T. K. P., Fornari, D. J., Perct, M. R., Haymon, R. M., and Fink, J. H. (1996). Rapid emplacement of a mid-ocean ridge lava flow on the East Pacific Rise at 9° 46°51'N. *Earth Planet. Sci. Lett.* 144, E1–E7.

Griffiths, R. W., and Fink, J. H. (1992). Solidification and morphology of submarine lavas: a dependence on extrusion rate. *J. Geophys. Res.* 97, 19729–19737.

Hawaiian Volcano Observatory (2017). *Kīlauea Volcano's Kamokuna Ocean Entry Reaches its One-Year Anniversary*. Hawaii: Hawaiian Volcano Observatory.

Head, J. W. Jr., Wilson, L., and Smith, D. K. (1996). Mid-ocean ridge eruptive vent morphology and substructure: evidence for dike widths, eruptive rates, and evolution of eruptions and axial volcanic ridges. *J. Geophys. Res.* 101, 28265–28280. doi: 10.1029/96jb02275

Howard, K. J., and Fisk, M. R. (1988). Hydrothermal alumina-rich clays and boehmite on Gorda Ridge. *Geochem. Cosmochem. Acta* 52, 2269–2279. doi: 10.1016/0016-7037(88)90129-9

Jones, M. R., Soule, S. A., Gonnermann, H., LeRoux, V., and Clague, D. A. (2018).). Ascent and emplacement rates during the 2011 Axial Seamount eruption based on CO_2 degassing. *Earth Planet. Sci.* 494, 32–41. doi: 10.1016/j.epsl.2018.04.044

Kappel, E. S., and Ryan, W. B. F. (1986). Volcanic episodicity and a non-steady state rift valley along northeast Pacific spreading centers: evidence from Sea MARC I. *J. Geophys. Res.* 91, 13925–13940. doi: 10.1029/JB091iB14p13925

Karlin, R. E., and Zierenberg, R. A. (1994). "Sedimentation and neotectonism in the SESCA area, Escanaba Trough, southern gorda ridge," in *Geologic, Hydrothermal, and biologic studies at Escanaba Trough, Gorda Ridge, Offshore Northern California, U.S. Geological Survey Bulletin 2022*, eds J. L. Morton, R. A. Zierenberg, and C. A. Reiss, (Reston, VA: USGS), 131–141.

Karson, J. A., and Rona, P. A. (1990). Block-tilting, transfer faults, and structural control of magmatic and hydrothermal processes in the TAG area, Mid-Atlantic Ridge 26°N. *Geol. Soc. Am. Bull.* 102, 1635–1645. doi: 10.1130/0016-7606(1990)102<1635:bttfas>2.3.co;2

Klein, E. M., and Langmuir, C. H. (1987). Global correlations of mid-ocean ridge basalt chemistry with axial depth and crustal thickness. *J. Geophys. Res.* 92, 8089–8115. doi: 10.1038/s41598-019-57344-4

Klinkhammer, G. P., German, C. R., Elderfield, H., Greaves, M. J., and Mitra, A. (1994). Rare earth elements in hydrothermal fluids and plume particulates by inductively coupled plasma mass spectrometry. *Mar. Chem.* 45, 179–186. doi: 10.1016/0304-4203(94)90001-9

Lavier, L. L., and Buck, W. R. (2002). Half-graben versus large-offset low-angle normal fault: importance of keeping cool during normal faulting. *J. Geophys. Res.* 107, ETG8–1–ETG8–13.

Le Saout, M., Deschamps, A., Soule, S. A., and Gente, P. (2014). Segmentation and eruptive activity along the East Pacific Rise at 16°N, in relation with the nearby Mathematician hotspot. *Geochem. Geophys. Geosyst.* 15, 4380–4399. doi: 10.1002/2014GC005560

MBARI Mapping Team (2001). *MBARI West Coast Seamounts and Ridges Multibeam Survey*. Moss Landing, CA: MBARI.

McDonough, W. F., and Sun, S. S. (1995). The composition of the Earth. *Chem. Geol.* 120, 223–253.

Mitra, A., Elderfield, H., and Greaves, M. J. (1994). Rare earth elements in submarine hydrothermal fluids and plumes from the Mid-Atlantic Ridge. *Mar. Chem.* 45, 217–235. doi: 10.1016/0304-4203(94)90079-5

Murton, B. L., and Rona, P. A. (2015). Carlsberg Ridge and Mid-Atlantic Ridge: comparison of slow spreading centre analogues. *Deep Sea Res. II* 121, 71–84. doi: 10.1016/j.dsr2.2015.04.021

Paduan, J. B., Zierenberg, R. A., Clague, D. A., Caress, D. W., Thomas, H., Troni, G., et al. (2019). Hydrothermal vent fields on Alarcon Rise and in the southern Pescadero Basin, southern Gulf of California. *Geochem. Geophys. Geosyst.* 19, 4788–4819. doi: 10.1029/2018GC007771

Pasulka, A. L., Goffredi, S. K., Tavormina, P. L., Dawson, K. S., Levin, L. A., Rouse, G. W., et al. (2017). Colonial tube-dwelling ciliates influence methane cycling and microbial diversity within methane seep ecosystems. *Front. Mar. Sci.* 3:276. doi: 10.3389/fmars.2016.00276

Perfit, M. R., and Chadwick, W. W. Jr. (1998). "Magmatism at mid-ocean ridges: Constraints from volcanological and geochemical investigations," in *Faulting and magmatism at Mid-Ocean Ridges, Geophysical Monograph Series*, ed. W. R. Buck, (Washington DC: American Geophysical Union), 59–115. doi: 10.1029/gm106p0059

Reynolds, J. R., and Langmuir, C. H. (2000). Identification and implications of off-axis lava flows around the East Pacific Rise. *Geochem. Geophys. Geosyst.* 1:1019. doi: 10.1029/1999GC000033

Rona, P. A. (1988). Hydrothermal mineralization at ocean ridges. *Can. Mineral.* 26, 431–465.

Rona, P. A., and Clague, D. A. (1989). Geologic controls of hydrothermal discharge on the northern Gorda Ridge. *Geology* 17, 1097–1101.

Rona, P. A., Denlinger, R. P., Fisk, M. R., Howad, K. J., Taghon, G. L., Klitgord, K. D., et al. (1990). Major off-axis hydrothermal activity on the northern Gorda Ridge. *Geology* 18, 493–496.

Rona, P. A., Meis, P. J., Beaverson, C. A., Embley, R. W., and Fox, C. G. (1992). Geological setting of hydrothermal activity at the northern Gorda Ridge. *Mar. Geol.* 106, 189–201. doi: 10.1016/0025-3227(92)90129-6

Ross, S. L., and Zierenberg, R. A. (1994). "Volcanic geomorphology of the SESCA and NESCA sites, Escanaba Trough," in *Geologic, Hydrothermal, and Biologic Studies at Escanaba Trough, Gorda Ridge, Offshore Northern California, U.S. Geological Survey Bulletin 2022*, eds J. L. Morton, R. A. Zierenberg, and C. A. Reiss, (Los Angeles, CA: UGSC), 143–151.

Rubin, K. H., Smith, M. C., Bergmanis, E. C., Perfit, M. R., Sinton, J. M., and Batiza, R. (2001). Geochemical heterogeneity within mid-ocean ridge lava flows: insights into eruption, emplacement and global variations in magma generation. *Earth Planet. Sci. Lett.* 188, 349–367. doi: 10.1016/s0012-821x(01)00339-9

Rubin, K. H., Smith, M. C., Perfit, M. R., Christie, D. M., and Sacks, L. F. (1998). Geochronology and geochemistry of lavas from the 1996 north Gorda Ridge eruption. *Deep Sea Res. II* 45, 2571–2597. doi: 10.1016/s0967-0645(98)00084-8

Rubin, K. H., Soule, S. A., Chadwick, W. W. Jr., Fornari, D. J., Clague, D. A., Embley, R. W., et al. (2012). Volcanic eruptions in the deep sea. *Oceanogr. Magaz.* 25, 142–157.

Shaw, H. R. (1972). Viscosities of magmatic silicate liquids: an empirical method of prediction. *Am. J. Sci.* 272, 870–893. doi: 10.2475/ajs.272.9.870

Smith, D. K., and Cann, J. R. (1992). The role of seamount volcanism in crustal construction at the Mid-Atlantic Ridge (24°-30°N). *J. Geophys. Res.* 97, 1645–1658. doi: 10.1029/91jb02507

Smith, D. K., and Cann, J. R. (1993). Building the crust at the Mid-Atlantic Ridge. *Nature* 365, 707–715. doi: 10.1038/365707a0

Smith, D. K., Escartín, J., Schouten, H., and Cann, J. R. (2012). Active long-lived faults emerging along slow-spreading mid-ocean ridges. *Oceanography* 25, 94–99. doi: 10.5670/oceanog.2012.07

Soule, S. A., Escartın, J., and Fornari, D. J. (2009). A record of eruption and intrusion at a fast spreading ridge axis: axial summit trough of the East Pacific Rise at 9–10°N. *Geochem. Geophys. Geosyst.* 10:Q10T07. doi: 10.1029/2008GC002354

Soule, S. A., Fornari, D. J., Perfit, M. R., and Rubin, K. H. (2007). New insights into mid-ocean ridge volcanic processes from the 2005–2006 eruption of the East Pacific Rise, 9°46'N–9°56'N. *Geology* 35, 1079–1082. doi: 10.1130/G23924A.1

Soule, S. A., Fornari, D. J., Perfit, M. R., Tivey, M. A., Ridley, W. I., and Schouten, H. (2005). Channelized lava flows at the East Pacific Rise crest 9°–10°N: the importance of off-axis lava transport in developing the architecture of young oceanic crust. *Geochem. Geophys. Geosyst.* 6:Q08005. doi: 10.1029/2005GC000912

Stakes, D. S., Perfit, M. R., Tivey, M. A., Caress, D. W., Ramirez, T. M., and Maher, N. (2006). The Cleft revealed: geologic, magnetic, and morphologic evidence for construction of the upper oceanic crust along the southern Juan de Fuca Ridge. *Geochem. Geophys. Geosyst.* 7:Q04003. doi: 10.1029/2005GC001038

Van Dover, C. L., Grassle, J. F., and Boudrias, M. (1990). "Hydrothermal vent fauna of Escanaba Trough," in *Gorda Ridge: A Frontier Area in the United States Exclusive Economic Zone*, ed. G. R. McMurray, (New York, NY: Springer-Verlag), 285–287. doi: 10.1007/978-1-4612-3258-2_21

Von Damm, K. L., Parker, C. M., Lilley, M. D., Clague, D. A., Zierenberg, R. A., Olson, E. J., et al. (2006). Chemistry of vent fluids and its implications for subsurface conditions at Sea Cliff hydrothermal field, Gorda Ridge. *Geochem. Geophys. Geosyst.* 7:Q05005. doi: 10.1029/2005GC001034

Von Damm, K. L., Parker, C. M., Zierenberg, R. A., Lilley, M. D., Olsen, E. J., Clague, D. A., et al. (2005). The Escanaba Trough, Gorda Ridge hydrothermal system: temporal stability and subseafloor complexity. *Geochim. Cosmochim. Acta* 69, 4971–4984. doi: 10.1016/j.gca.2005.04.018

Waters, C. L., Sims, K. W. W., Soule, S., Blichert-Toft, J., Dunbar, N. W., Plank, T., et al. (2013). Recent volcanic accretion at 98N–108N East Pacific Rise as resolved by combined geochemical and geological observations. *Geochem. Geophys. Geosyst.* 14, 2547–2574. doi: 10.1002/ggge.20134

White, S. M., Haymon, R. M., Fornari, D. J., Perfit, M. R., and Macdonald, K. C. (2002). Correlation between volcanic and tectonic segmentation of fast-spreading ridges: evidence from volcanic structures and lava morphology on the East Pacific Rise, 9°–10°N. *J. Geophys. Res.* 107:2173. doi: 10.1029/2001JB000571

White, S. M., Macdonald, K. C., and Haymon, R. M. (2000). Basaltic lava domes, lava lakes, and volcanic segmentation on the southern East Pacific Rise. *J. Geophys. Res.* 105, 23519–23536. doi: 10.1029/2000JB900248

White, S. N., Dunk, R. M., Peltzer, E. T., Freeman, J. J., and Brewer, P. G. (2006). In situ Raman analysis of deep-sea hydrothermal and cold seep systems (Gorda Ridge and hydrate ridge. *Geochem. Geophys. Geosyst.* 7:1204. doi: 10.1029/2005GC001204

Yeo, I., and Searle, R. C. (2013). High-resolution remotely operated vehicle (ROV) mapping of the slow-spreading ridge: mid-Atlantic ridge 45°N. *Geochem. Geophys. Geosyst.* 14, 1693–1702. doi: 10.1002/ggge.20082

Yeo, I., Searle, R. C., Achenbach, K. L., Le Bas, T. P., and Murton, B. J. (2012). Eruptive hummocks, building blocks of the upper crust. *Geology* 40, 91–94. doi: 10.1130/G31892.1

Yeo, I. A., Clague, D. A., Martin, J. F., Paduan, J. B., and Caress, D. W. (2013). Pre-eruptive flow focusing in dikes feeding historic pillow ridges on and Juan de Fuca and Gorda Ridges. *Geochem. Geophys. Geosyst.* 14, 3586–3599. doi: 10.1002/ggge.20210

Zierenberg, R. A., Morton, J. L., Koski, R. A., and Ross, S. L. (1994). "Geologic setting of massive sulfide mineralization in Escanaba Trough," in *Geologic, Hydrothermal, and Biologic Studies at Escanaba Trough, Gorda Ridge, Offshore Northern California, U.S. Geological Survey Bulletin 2022*, eds J. L. Morton, and CA Reiss, (Los Angeles, CA: UGSC), 171–197.

Zierenberg, R. A., Schiffman, P., Jonasson, I. R., Tosdal, R., Pickthorn, W., and McClain, J. (1995). Alteration of basalt hyaloclastite at the off-axis Sea Cliff hydrothermal field, Gorda Ridge. *Chem. Geol.* 126, 77–99. doi: 10.1016/0009-2541(95)00111-2

Conflict of Interest: The authors declare that the research was conducted in the absence of any commercial or financial relationships that could be construed as a potential conflict of interest.

Copyright © 2020 Clague, Paduan, Caress, McClain and Zierenberg. This is an open-access article distributed under the terms of the Creative Commons Attribution License (CC BY). The use, distribution or reproduction in other forums is permitted, provided the original author(s) and the copyright owner(s) are credited and that the original publication in this journal is cited, in accordance with accepted academic practice. No use, distribution or reproduction is permitted which does not comply with these terms.

frontiers in Marine Science

ORIGINAL RESEARCH
published: 24 March 2020
doi: 10.3389/fmars.2020.00171

Dissolved Gas and Metal Composition of Hydrothermal Plumes From a 2008 Submarine Eruption on the Northeast Lau Spreading Center

Tamara Baumberger[1], Marvin D. Lilley[2], John E. Lupton[3], Edward T. Baker[4], Joseph A. Resing[4], Nathaniel J. Buck[4], Sharon L. Walker[5] and Gretchen L. Früh-Green[6]*

[1] Cooperative Institute for Marine Resources Studies, Oregon State University, Newport, OR, United States, [2] School of Oceanography, University of Washington, Seattle, WA, United States, [3] Pacific Marine Environmental Laboratory, National Oceanic and Atmospheric Administration, Newport, OR, United States, [4] Joint Institute for the Study of the Atmosphere and Ocean, University of Washington, Seattle, WA, United States, [5] Pacific Marine Environmental Laboratory, National Oceanic and Atmospheric Administration, Seattle, WA, United States, [6] Department of Earth Sciences, ETH Zurich, Zurich, Switzerland

OPEN ACCESS

Edited by:
Peter R. Girguis,
Harvard University, United States

Reviewed by:
Mustafa Yucel,
Middle East Technical University, Turkey
Shinsuke Kawagucci,
Japan Agency for Marine-Earth Science and Technology (JAMSTEC), Japan

***Correspondence:**
Tamara Baumberger
tamara.baumberger@noaa.gov

Specialty section:
This article was submitted to Deep-Sea Environments and Ecology, a section of the journal Frontiers in Marine Science

Received: 24 May 2019
Accepted: 04 March 2020
Published: 24 March 2020

Citation:
Baumberger T, Lilley MD, Lupton JE, Baker ET, Resing JA, Buck NJ, Walker SL and Früh-Green GL (2020) Dissolved Gas and Metal Composition of Hydrothermal Plumes From a 2008 Submarine Eruption on the Northeast Lau Spreading Center. Front. Mar. Sci. 7:171. doi: 10.3389/fmars.2020.00171

Extrusion of lava onto the seafloor transports heat and mass from the lithosphere to the hydrosphere and the biosphere. During this process, large amounts of dissolved gases can be released into the ocean as hydrothermal plumes and serve as nutrients for microbial activity. Here, we report the dissolved gas and metal composition of hydrothermal plumes associated with a submarine eruption at the Northeast Lau Spreading Center (NELSC) in the SW Pacific Ocean in November 2008. During this eruption, two different types of plumes were observed in the water column: a shallow event plume rich in H_2 and poor in ^3He and CH_4, and a deep near-seafloor plume with high CH_4, metals and ^3He and intermediate H_2 concentrations. Both were generated at the same time and at the same location. While the high abundance of H_2 in the event plume points to ongoing reactions between hot rock and seawater, the distinct chemical characteristics of the near-seafloor plume likely result from the release of a mature fluid stored in the crust. The plume chemistry of the event plume favors a seawater-lava interaction event plume generation model. However, the heat budget asks for an additional process releasing enough heat to lift the plume within the time frame of this short event. The extremely high H_2 concentrations suggest that the eruption was locally more explosive than assumed. A more explosive eruption style might enhance the heat flux from lava cooling.

Keywords: NE Lau Spreading Center, submarine volcanic eruption, hydrothermal plume, dissolved gas, hydrogen, methane, helium, event plume

INTRODUCTION

Observations of volcanic eruptions in the deep-sea are rare (Rubin et al., 2012). To date, only two submarine volcanoes have been visually observed during an eruption: NW Rota-1 in the Mariana arc (Chadwick et al., 2008) and West Mata in the NE Lau Basin (Resing et al., 2011). Data on real-time characterization of volatiles and metals in hydrothermal plumes associated with seafloor

eruptions is more frequent but still sparse, due both to the rapid consumption of reduced chemical species and short-lived nature of event plumes as well as the limited resources to rapidly respond to eruptions (Baker et al., 1987, 1995a,b; de Angelis et al., 1993; Lilley et al., 1995, 2003; McLaughlin et al., 1996; Kelley et al., 1998; Resing et al., 2007; Baumberger et al., 2014; Chadwick et al., 2018). In particular, H_2 and CH_4 concentration data from young hydrothermal plumes associated with eruptions are very limited (Kelley et al., 1998; McLaughlin, 1998; McLaughlin-West et al., 1999; Resing et al., 2007; Baumberger et al., 2014). In addition, the volatiles released during eruption events drive chemosynthetic ecosystems, and knowledge of the chemical plume composition is relevant for the biosphere. Diverse and abundant microbial populations in event plumes as well as in steady hydrothermal plumes were observed in numerous studies (e.g., Huber et al., 2003; Dick et al., 2013). Processes forming the unique hydrothermal plumes generated by magmatic events are not yet fully understood and different formation hypotheses such as the release of a stored, mature fluid, rapid cooling of a dike intrusion or rapid cooling of a lava flow, have been proposed (Baker et al., 1989, 2011; Baker and Lupton, 1990; Lowell and Germanovich, 1995; Lupton, 1995; Butterfield et al., 1997; Palmer and Ernst, 1998; Lupton et al., 1999, 2000).

The NE Lau region in the South Pacific is a complex tectonic location that combines an arc, backarc and a trench/backarc intersection. This region had been investigated for volcanic and hydrothermal activity prior to 2008 (e.g., German et al., 2006; Kim et al., 2009), but never as systematically as during the NE Lau expedition series starting in 2008 (Baker et al., 2011; Embley et al., 2014). In 2008, extensive hydrothermal event plumes were observed above the neovolcanic zone of the southernmost segment of the Northeast Lau Spreading Center, with the plumes being associated with the "Puipui" eruption (Rubin et al., 2009; Baker et al., 2011). The Puipui flow at the NELSC was visited by the remotely operated vehicle (ROV) *Jason* in 2009 and was described as consisting of highly vesicular basalts in the form of sheet and lobate flows (Clague et al., 2010). Simultaneously, vigorous eruptions were ongoing at the submarine rear-arc volcano West Mata, about 60 km NE of the NELSC (Resing et al., 2011; Baumberger et al., 2014; Embley et al., 2014; Chadwick et al., 2019). The West Mata hydrothermal plume was characterized by exceptionally high dissolved H_2 concentrations and glass shards in the water column indicating reactions between hot rock and seawater (Sansone et al., 1991; Resing et al., 2011; Baumberger et al., 2014).

In this study, we present H_2, CH_4, He, Mn, and Fe concentrations and He isotope ratios collected in deep-sea hydrothermal plumes generated during the Puipui eruption at the NELSC (approximately 174.25°W and 15.39°S) in November 2008. The generated plumes were sampled during or within a short time after the eruption of lava on the seafloor. We then compare and contrast our findings with the findings from the simultaneously erupting submarine volcano West Mata (Resing et al., 2011; Baumberger et al., 2014; Embley et al., 2014). These data provide more insights into the properties of young hydrothermal plumes from submarine volcanic eruptions and event plume formation.

Geological Setting

The Northeast Lau back-arc basin is located in the Pacific Ocean SW of the Samoan Islands (**Figure 1**). It is part of the Tonga subduction system, where the Pacific Plate is being subducted westwards beneath the Indo-Australian Plate. The Tonga Trench on the north, the Tofua arc front on the east, and a complex back-arc spreading center system on the west define the Northeast Lau Basin (Hawkins, 1995).

In this paper, we focus on the hydrothermal plumes released during the Puipui eruption located at the NE end of an approximately 15 km long section of the southernmost segment of the NELSC. This section is part of a very complex fast-spreading back-arc spreading center. The spreading rate is believed to be similar to the rate of 85 to 94 mm/yr determined at the NE branch of the nearby Mangatolu Triple Junction (Zellmer and Taylor, 2001; German et al., 2006). This section of the NELSC hosts two known volcanic edifices named Maka and Tafu. Maka is a ridge volcano situated at the southern end of the segment. Several small black-smoker chimneys were observed on the sulfide mound at Maka summit at about 1525 m below sea level during seafloor video surveys in May 2009. Tafu is a ridge volcano northeast of Maka with a summit depth of 1369 m below sea level. Hydrothermal plumes along the southern segment of the NELSC at water depths between 1300 and 1500 m were detected in 2004 (German et al., 2006) and in 2006 (Kim et al., 2009), possibly resulting from Maka or Tafu. Another well-known feature in the NE Lau Basin is the submarine rear-arc volcano West Mata. It is situated about 60 km northeast of the fast-spreading back-arc NELSC, with the Tofua arc front to its east and the westward bending Tonga Trench to its north (**Figure 1**) and a summit depth of 1165 m in 2009. Along the NELSC erupted lavas range from back arc basin basalt (BABB) to basaltic andesite, while West Mata has boninitic magma composition. Multiple other lava flows in the Lau Basin are composed of dacite (Resing et al., 2011; Embley and Rubin, 2018).

MATERIALS AND METHODS

Most of the data presented here were collected during the *Northeast Lau Basin* cruise on the R/V *Thomas G. Thompson* during expedition TN227 from November 13–28, 2008. Some additional data was collected during the *Northeast Lau Basin Response Cruise* on the R/V *Thomas G. Thompson* (TN234) in May 2009 and during the *2010 NE Lau Basin* expedition on the R/V *Kilo Moana* (KM1008) in April/May 2010.

Plume samples were collected using an instrument package consisting of a Sea-Bird 911 *plus* CTD with an adjunct light scattering sensor (LSS) and an oxidation–reduction potential (ORP) sensor. Water samples were collected using 18.5 L Niskin bottles equipped with Derlin spigots for gas collection and Teflon stopcocks for trace metal sampling. A total of five vertical hydrocasts and seven tow-yos (a sampling technique where the CTD-rosette package is raised and lowered in a saw-tooth like pattern as the ship proceeds on a transect) were conducted to sample and analyze the NELSC plumes and background seawater for ^3He, ^4He, H_2, CH_4, TDFe, TDMn, DFe, and DMn.

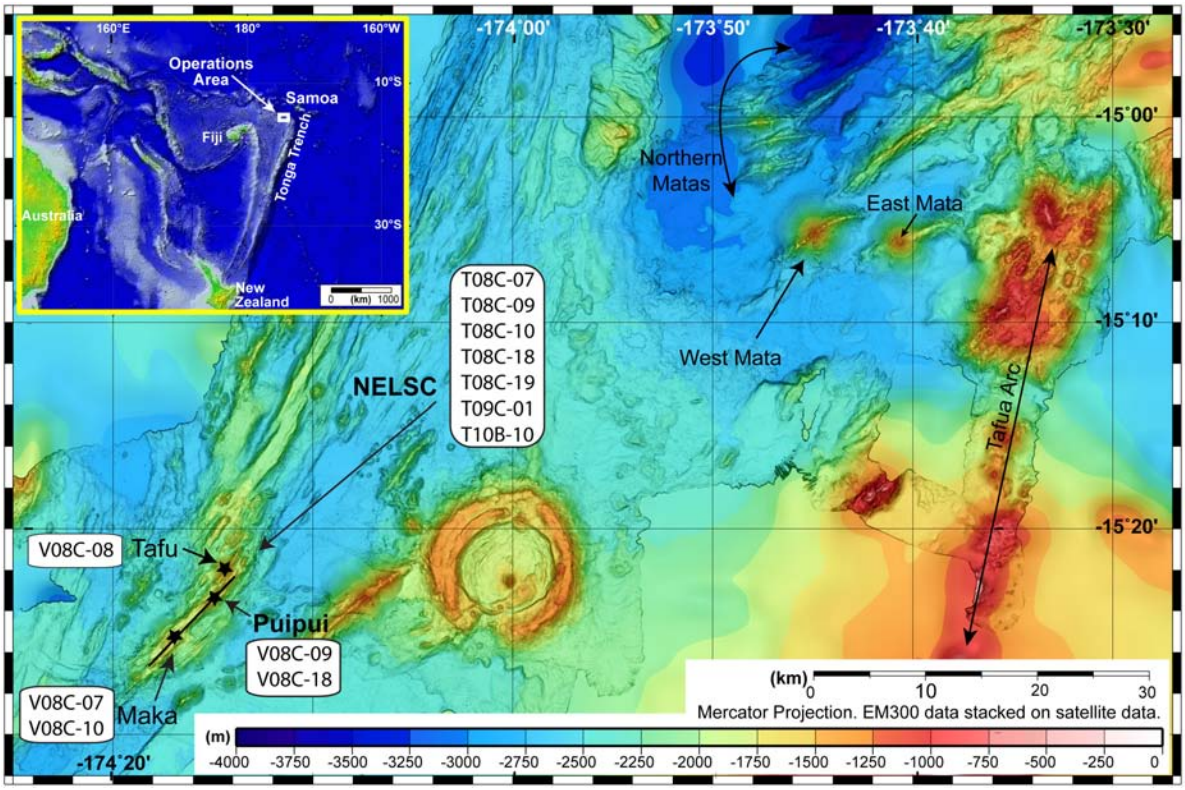

FIGURE 1 | Bathymetric map and location of the Northeast Lau Basin in the Pacific Ocean. Several CTD tow-yos and vertical casts were conducted along the Northeast Lau Spreading Center (NELSC). Vertical casts (V) are indicated with a black star. The tow lines of the conducted tow-yos (T) followed the NELSC axis (black line). Figure after Baumberger et al. (2014).

To determine the dissolved H_2 and CH_4 gas concentrations at sea, 100 ml of bubble-free fluid (any air bubbles were removed immediately after drawing the fluid in the syringe) was drawn directly from the Niskin bottle sampling port into 140 ml syringes followed by the addition of 40 ml headspace gas of ultra-pure helium (Kelley et al., 1998). Each sample was vigorously shaken and allowed to warm to room temperature for about 30 min to reach equilibrium for H_2 and CH_4 between the water and gas phase. After equilibration, about 20 ml of the headspace gas was injected into a SRI 8610C gas chromatograph through an ascarite/drierite tube trap. Separation of CH_4 and H_2 was attained by using a 15 m long Molecular Sieve 5A column. Hydrogen concentrations were determined with a highly sensitive helium-pulsed discharge detector, while CH_4 concentrations were measured with a flame ionization detector. Both detectors were mounted in series and it was thus possible to measure both, CH_4 and H_2 during the same run. Standards were diluted from 100 ppm CH_4 in He and 100 ppm H_2 in He from Scotty gas calibration standards. Where sample concentrations exceeded the standard concentrations, samples were diluted to fit the range of the standard curve. The measured background seawater H_2 and CH_4 concentrations were ~0.2 and ~0.4 nM, respectively. The sampling and analytical precision, determined through replicate draws, was about 2.5% of the measured concentrations or ± 0.1 nM, whichever is greater.

Immediately upon recovery of the underwater sampling package, air-free water samples were flushed through 24-inch-long sections of refrigeration grade Cu tubing with duplicate half-sections cold-weld sealed for later laboratory determinations of He concentration and isotope ratios (Young and Lupton, 1983). Isotope ratios and concentrations of helium were then determined at the NOAA/PMEL Helium Isotope Laboratory in Newport, OR, United States using a dual collector, 21-cm-radius mass spectrometer with 1σ precision of 0.2% in δ^3He, where δ^3He is the percentage deviation of ^{3}He/^{4}He from the atmospheric ratio, and a concentration accuracy of 1% relative to a laboratory air standard. Because helium is a conservative tracer, excess ^{3}He is only lost from the ocean by ventilation into the atmosphere at the ocean surface. Consequently, there is a considerable oceanic background level of ^{3}He, which has accumulated due to hydrothermal venting. In order to compare ^{3}He concentrations against other tracers, we have calculated $[^3\mathrm{He}]^{\Delta}$, which is the ^{3}He concentration measured in the hydrothermal plume with the regional background ^{3}He concentration subtracted.

Water column samples for total dissolvable Mn and Fe (TDMn and TDFe) were collected directly into 125 ml I-Chem™ polyethylene bottles. Dissolved Mn and Fe (DMn and DFe) samples were collected as the filtrate from 0.4 μm acid-washed polycarbonate filters into 125 ml I-Chem™ polyethylene bottles after the passage of 2 L of water through the filters. Trace metal

samples were then acidified with 0.5 ml 6N HCl, purified by sub-boiling distillation using a quartz still. Mn was determined with a precision of ± 1 nM or 4%, whichever is greater, by modifying the direct injection method of Resing and Mottl (1992) by adding 4 g of nitrilo-triacetic acid to each liter of buffer. Fe was determined with a precision of ± 2 nM by modifying the method of Measures et al. (1995) for direct injection analysis. Background seawater concentrations of Mn and Fe were below detection.

RESULTS

Event Plume Chemistry

A table with all measured data can be found in the **Supplementary Material**. The first indication of an on-going eruption at the NELSC was observed on 20 November 2008 in tow-yo T08C-07 at 174.25°W and 15.40°S and at a water depth of 1170 m (**Figure 2** and **Table 1**). An extremely high dissolved H_2 concentration of 6424 nM was measured, which is > 30000 times the concentration seen in local background seawater, while CH_4 showed no enrichment above background and $[^3He]^{\Delta}$ was not higher than 0.76 fM, indicating only a small magmatic component. Also on 20 November 2008 we conducted a vertical cast over Maka (V08C-07) and a vertical cast over Tafu (V08C-08) to locate the possible eruption center at the seafloor (**Figures 1**, **2**). Both of these stations were over known volcanic cones at the southern segment of the NELSC and both casts showed enhanced H_2 concentrations (Maka: 1962 nM and Tafu: 3040 nM) at water depths between 1010 and 1300 m, but showed no indication for ongoing volcanic eruptions in water samples collected close to the seafloor.

By 21 November 2008, two distinguishable shallow event plume layers were present above the NELSC between 900 and 1500 m water depth (T08C-09, V08C-09, V08C-10) (**Figure 2**; Baker et al., 2011). The upper event plume layer (between 900 and 1300 m water depth) was characterized by very high dissolved H_2 concentrations (**Figure 2** and **Table 1**) up to 9123 nM (T08C-09), comparable to H_2 values of 14840 nM sampled at West Mata volcano during the same cruise (Baumberger et al., 2014) and much higher than measured in other known event plumes (Kelley et al., 1998; McLaughlin-West et al., 1999). Methane concentrations did not exceed 4.6 nM and were only slightly enriched above background seawater values (0.4 nM) measured in the NELSC area. Helium-3 values in the upper layer reached 3.0 fM, about 1.58 fM higher than local background seawater values and low compared to peak concentrations of 5.4 fM measured at the Gorda Ridge in 1996 (Kelley et al., 1998) or 47 fM observed at West Mata (Baumberger et al., 2014). Thus, only small enrichments in ^3He and CH_4 were detected, whereas H_2 concentrations were strongly elevated. TDMn and TDFe concentrations in the upper layer reached 73 and 403 nM, respectively, but were much lower than the highest values (2738 nM TDMn and 5686 nM TDFe) measured in the near seafloor plume at the NELSC (**Table 1**). Over 87% of the TDMn and over 15% of the TDFe were present in the dissolved form.

The lower layer of the event plumes (see **Figure 2**), located between 1300 and 1500 m water depths, exhibited H_2 concentrations similar to the upper layer (up to 9250 nM in V08C-10), whereas methane concentrations were slightly higher (up to 12 nM). The $[^3He]^{\Delta}$ concentration was 1.2 fM, again only slightly above background. TDMn values were elevated up to 150 nM and TDFe values up to 465 nM and thus both higher

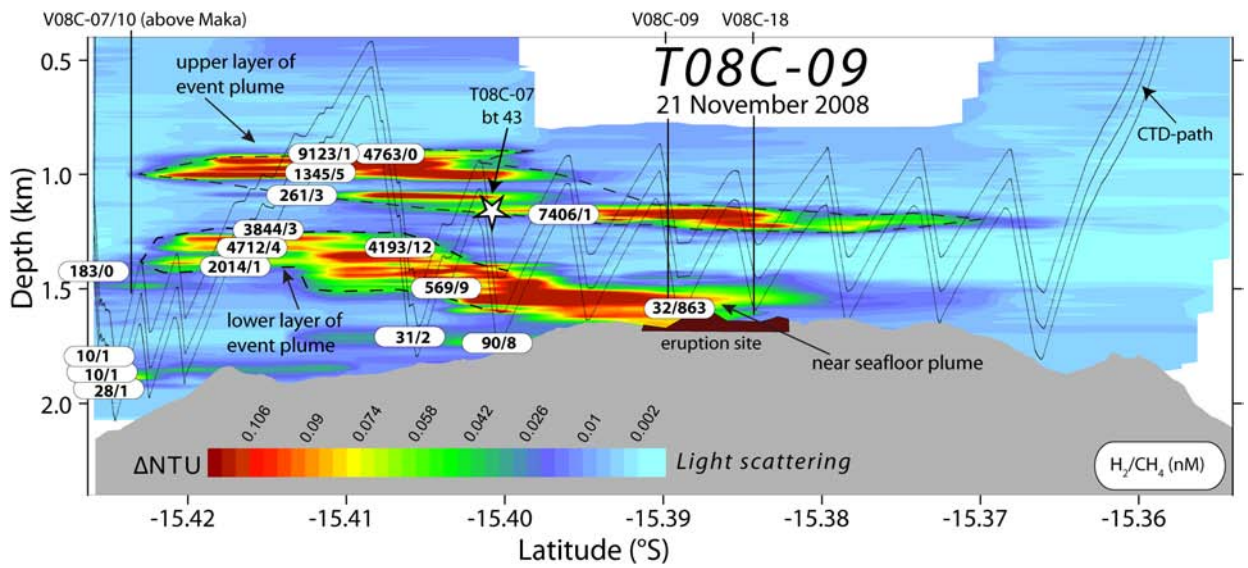

FIGURE 2 | Water column profile on November 21, 2008 showing particle anomalies of the upper and the lower layer of the event plume and the near seafloor plume. The eruption site is highlighted at the seafloor. The white star indicates position and depth where the first indication of a hydrothermal plume was found on November 20, 2008 in T08C-07 bottle (bt) 43. The black wriggly line shows the CTD-path of T08C-09. Where water samples were taken during this tow, the measured H_2 and CH_4 concentrations are noted in nM at the corresponding location. The locations of the vertical casts are indicated with a black line and cast number. Figure after Baker et al. (2011).

TABLE 1 | Temporal evolution of the maximum concentrations of H_2, CH_4, $[^3He]^\Delta$, TDMn and TDFe in the event, near seafloor and deep plumes above the Puipui eruption site.

Plume	H_2 (nM)	CH_4 (nM)	$[^3He]^\Delta$ (fM)	TDMn (nM)	TDFe (nM)
Event plume – upper layer					
20 November 2008	6424	0.4	0.76	68	403
21 November 2008	9123	4.6	1.58	73	379
22 November 2008	674	0.4	0.67	39	222
27 November 2008	6.3	0	na	nd	34
08 May 2009	7.7	0.8	na	0	6
Event plume – lower layer					
20 November 2008	Not distinguished from upper layer.				
21 November 2008	9250	12	1.2	150	465
22 November 2008	5082	5.4	0.99	113	361
27 November 2008	2.0	0	na	nd	34
Near seafloor plume					
20 November 2008	No data collected.				
21 November 2008	101	1092	8.50	2738	5686
22 November 2008	74.6	301	2.32	403	1092
27 November 2008	5.5	651	2.23	166	203
06 May 2010	1.7	2.9	na	39	57
Deep plume					
20 November 2008	No data collected.				
21 November 2008	90	8	10.3	199	260
22 November 2008	9.8	0.5	1.64	36	73
27 November 2008	9.3	6.8	7.48	260	298
Background seawater	0.2	0.4	0	0	0

nd, not detected; na, not analyzed.

than in the upper layer (**Table 1**). Dissolved Mn in the lower layer of the shallow plume reached a percentage of 88 to 100 of the TDMn. Dissolved Fe in the lower layer ranged from 10.7 to 27.2% of the TDFe.

On 22 November 2008, 18 h after T08C-09, T08C-10 was conducted in the same area. Two bottles were triggered in the event plumes, one at 900 m and one at 1350 m (**Table 1**). Both samples had similar plume chemistry to what was observed 18 h earlier: highly enriched H_2, enhanced TDMn and TDFe and near background seawater CH_4 and ^3He concentrations, but with lower maximum concentrations.

On 27 November 2008, 7 days after the first surveys, only small H_2 enrichments of 6.3 nM were observed in the area where the event plume had been detected (T08C-18 and T08C-19; **Table 1**). Thus, the extensive formation of H_2 had ceased and most of the H_2 had been either consumed or advected from the local water column during these 7 days (^3He data at these depths are not available). The TDFe concentrations were still slightly elevated above background (34 nM), and CH_4 and TDMn concentrations were not distinguishable from background seawater values.

Near-Seafloor Plume Chemistry

On 21 November 2008, T08C-09 mapped a near-seafloor plume between 1500 and 1620 m centered at 15.389°S (**Figure 2** and **Table 1**). Maximum volatile and metal concentrations were found in vertical cast V08C-09 (about 6 h after T08C-09), approximately 30 m above the seafloor. In this sample we measured 1092 nM CH_4 and 101 nM H_2. The ^3He concentrations were elevated to 8.5 fM above local background [δ^3He (%) = 222] at the same depth. TDMn values were the highest of those sampled at the NELSC (2738 nM) with > 97% of the TDMn present in the dissolved form. TDFe (5686 nM) were also the highest measured along the NELSC with up to 70% in its dissolved form.

Tows conducted over the eruption site over the next 7 days (T08C-10 and T08C-18) and sampling within ∼60 m of the seafloor found high CH_4 (up to 651 nM), moderate H_2 (up to 74.6 nM), ^3He (up to 2.23 fM above background) and TDMn (up to 403 nM) and TDFe (up to 1092 nM) values still enriched above background seawater concentrations (**Table 1**).

Deep Plume Chemistry

During casts T08C-09, T08C-10 and T08C-18, a plume deeper than the depth of the Puipui lava flow was observed (**Table 1**). Maximum measured H_2 concentrations in this plume were 90 nM and maximum CH_4 concentrations were 8 nM. This deep plume was characterized by high ^3He concentrations with a δ^3He (%) value of up to 255 and $[^3He]^\Delta$ concentrations of 10.3. Over 97% of the TDMn (74 nM) and up to 75.9% of the TDFe (298 nM) were present in the dissolved form.

NELSC Plume Chemistry in 2009 and 2010

During the Northeast Lau Basin response cruise 6 months later in May 2009, visual observations by the ROV *Jason* along with water column surveys showed that the eruption at the NELSC had ceased prior to the response cruise. Dissolved H_2, CH_4, ^3He, TDFe, and TDMn concentrations measured in the water column above the Puipui lava flow had returned to or near to background values, except for one sample at 1000 m water depth that showed a H_2 value of 7.7 nM (**Table 1**). By May 2010, when the Puipui lava flow was revisited, only weak H_2, CH_4, TDMn, and TDFe enrichments close to the seafloor were found above the zone that was intensively erupting in 2008 (**Table 1**). Sensors mounted on the CTD did not pick up any anomalies higher up in the water column and consequently no water samples were collected at water depths corresponding to the 2008 event plume layers.

DISCUSSION

During the 2008 NELSC Puipui eruption, an event plume 200 to 1000 m above the seafloor, a plume near the seafloor eruption and a plume from a source deeper than the Puipui lava flow were observed. The chemistry of these plumes differ from each other as discussed in the following section. We will also compare the plumes associated with the NELSC eruption with those associated with the eruption of the submarine volcanoes West Mata, located 60 km NE of the NELSC, and NW Rota-1 located on the Mariana Arc. We use the data from the NELSC Puipui eruption along with those from other past event plumes, to chemically constrain mechanisms of event plume formation.

Plume Chemistry and Eruption Modes

Baker et al. (2011) identified the shallow plumes as event plumes. The lowermost layer of the event plumes in T08C-09 intersected with the seafloor, indicating a likely seafloor eruption zone at approximately 15.39°S (Baker et al., 2011). Even though the NELSC eruptions were never visually observed, ROV *Jason* located fresh pillow lava, sheet, and lobate flows as well as vesicular glass fragments and highly degassed pyroclasts during dives at the eruption site in 2009 (Clague et al., 2010). The observed lava flow was named Puipui and had an along-axis extent of about 1.7 km (Clague et al., 2010). The ^{210}Po activity of three lava samples suggested an eruption in November 2008 (Rubin et al., 2009) that clearly corresponds with our water column observations. To fully exclude Maka as the source of the event plume, we compared the highest $H_2/[^3He]^{\Delta}$ ratio of the event plumes (9152×10^6) with the ratio measured in the Maka end member fluid (2.2×10^6). The fact that the $H_2/[^3He]^{\Delta}$ ratio in the plume is about 4000 times higher excludes the hydrothermal vent field at Maka as a source fluid for the event plume.

The extremely high H_2 concentrations were a striking feature of the high-rising event plumes at the NELSC and provided strong evidence for on-going or very recent reactions between seawater and molten or extremely hot rock at the seafloor (**Figure 2**). Extremely high water column H_2 concentrations were also observed at West Mata during the same cruise (Baumberger et al., 2014) and in May 2009, when concurrent visual observations of ongoing eruptions and H_2 measurements in the water column and of the fluids close to erupting lava at the seafloor confirmed the relationship between eruption and the production of H_2 (Resing et al., 2011; Baumberger et al., 2014). By comparison, H_2 concentrations obtained from event plume EP96A at the Gorda Ridge in 1996, reached a maximum of 47 nM (Kelley et al., 1998). The differences in H_2 concentrations are at least partially due to the time elapsed after eruption, as chemical aging of EP96A had already begun when the plume was sampled (Kelley et al., 1998). At the NELSC, between 11 and 29% of the total Fe ($TDFe_{max}$ = 465 nM) in the event plumes was present in its dissolved form on November 21, 2008 indicating that these plumes were less than 1 day old when sampled, assuming a Fe oxidation half-time in the Pacific between 2 and 6 h (Field and Sherrell, 2000). In the same H_2-rich event plumes, CH_4 values did not exceed 12 nM. This suggests that during the H_2-producing processes, the production of CH_4 is almost negligible and therefore CH_4 is not generated in significant quantities during reactions between hot rock and seawater, at either quiescent lava flows or from explosive volcanic eruptions. This trend has also been observed at other volcanoes that were sampled while erupting or while in early stage of post-eruption evolution, such as West Mata (Baumberger et al., 2014), NW Rota-1 (Resing et al., 2007; Butterfield et al., 2011), Gorda Ridge in 1996 (Kelley et al., 1998), along the coastline of Kilauea Volcano when lava enters the ocean (Sansone et al., 1991; Sansone and Resing, 1995) and more recently at Ahyi seamount (Buck et al., 2018). Significantly higher CH_4 concentrations of 522 nM were measured in a possible, but not confirmed event plume at Axial Volcano 18 days after an eruption in 1998 (McLaughlin-West et al., 1999; Baker et al., 2011). The CH_4 values in the shallow NELSC event plume layers were poorly correlated with H_2 and ^{3}He. Juvenile carbon and inorganic CH_4 synthesis as a source for the slight CH_4 enrichment in the shallow event plume layers is unlikely because a good correlation with ^{3}He would be expected, at least close to the eruption site (Welhan, 1988; Mottl et al., 1995). Methane can originate from microbial production in a more evolved system, where hydrothermal fluid stored at depth can be released during magmatic eruptions as some models for event plume formation suggest (Baker and Lupton, 1990; Lupton et al., 1995; Butterfield et al., 2004; Von Damm and Lilley, 2004). In this scenario, higher CH_4 concentrations and a higher degree of correlation with ^{3}He would be expected in the plume. The most likely source for CH_4 in the event plume layers is thermogenically degraded organic matter caused by hot lava enveloping biological communities (Welhan, 1988). Although the presence of a lava flow was confirmed in 2009 by video images, there is no information regarding preexisting biological communities at this site.

In contrast to the low CH_4 concentrations in the event plume, high CH_4 concentrations were detected in the near seafloor plume close to the Puipui eruption zone (**Figure 2** and **Tables 1**, **2**). Methane and ^{3}He were well-correlated with $CH_4/[^3He]^{\Delta} = 122 \times 10^6$ (r^2 = 0.87). This ratio is 6 to 1200 times higher than in the event plume. In addition, CH_4 is well-correlated with TDMn (r^2 = 0.91) and TDFe (r^2 = 0.91). The excellent correlations between CH_4, $[^3He]^{\Delta}$, TDFe, and TDMn suggest that we sampled a young plume that had experienced limited oxidation. Dissolved Fe in hydrothermal vents is typically in its reduced form. It has been thought from earlier studies that iron dissolved in a hydrothermal plume oxidizes within hours, rapidly forming particulates (Field and Sherrell, 2000). More recent studies suggest that stabilization of dissolved iron in the hydrothermal plume results in transportation of dissolved iron over long distances at near conservative behavior (Bennett et al., 2008; Sander and Koschinsky, 2011; Yücel et al., 2011; Resing et al., 2015). However, rapid oxidation and loss of hydrothermal Fe from the dissolved phase close to the eruption center is still valid (Resing et al., 2015). Thus, dissolved Fe reaching up to 70% of the TDFe in the near seafloor plume confirms a young age of the plume. Furthermore, ratios of CH_4 relative to $[^3He]^{\Delta}$, H_2 and TDMn clearly distinguish the event plume layers from the near seafloor plume (**Table 2**). Hydrogen/CH_4 ratios are up to 1200 times smaller than in the event plume and require a CH_4-rich source. The elevated H_2 in the event plume layers and the high CH_4 in the near-seafloor plume likely have distinct fluid sources and reflect different fluid evolution processes. A likely source for the near seafloor plume is the release of a stored, mature hydrothermal fluid containing microbial CH_4 and likely triggered by the eruption. Methane/TDMn ratios in the near seafloor plume were between 0.4 and 0.8 and fall in the range typical for magmatic degassing, bacterial production or the reaction between seawater and basalt as CH_4 sources (Mottl et al., 1995). Bacterial production is in agreement with the release of a pre-stored fluid as a likely CH_4 source. Manganese concentrations in hydrothermal fluids are reflective of two main factors: the ratio of water to rock and the length the of

TABLE 2 | Summary of temporal evolution of geochemical ratios in the Puipui event and near seafloor plumes compared to geochemical ratios observed in other event and volcanic eruption plumes.

	$H_2/[^3He]^\Delta$ $\times 10^6$	$CH_4/[^3He]^\Delta$ $\times 10^6$	H_2/CH_4	H_2/TDMn	CH_4/TDMn	TDMn/$[^3He]^\Delta$ $\times 10^6$	TDFe/TDMn	References
NELSC 2008								
November 20								
Event plume	8453[b]	0.5[b]	16060[b]	94.5[b]	0.006[b]	90[b]	5[b]	This study
November 21								
Upper plume layer	6500 (0.92)[a]	0.1 to 16[c]	79 to 47631[c]	86 (0.32)[a]	0.01 to 0.32[c]	21 (0.23)[a]	5 (0.73)[a]	This study
Lower plume layer	9152 (0.79)[a]	0.5 to 19[c]	63 to 9026[c]	66 (0.90)[a]	0.03 to 0.17[c]	134 (0.82)[a]	3 (0.92)[a]	This study
Near seafloor plume	8 (0.56)[a]	122 (0.87)[a]	0.05 (0.31)[a]	0.02 (0.56)[a]	0.4 (0.91)[a]	336 (0.99)[a]	2 (1.00)[a]	This study
November 22								
Upper plume layer	1002[b]	0.6[b]	1685[b]	17[b]	0.01[b]	58[b]	6[b]	This study
Lower plume layer	5150[b]	5.5[b]	941[b]	45[b]	0.05[b]	115[b]	3[b]	This study
Near seafloor plume	10 to 43[c]	44 to 227[c]	0.2 to 0.7[c]	0.1 to 0.2[c]	0.3 to 0.9[c]	203 (0.94)[a]	3 (0.88)[a]	This study
November 27								
Upper plume layer	nd	nd	nd	nd	nd	nd	nd	This study
Lower plume layer	nd	nd	nd	nd	nd	nd	nd	This study
Near seafloor plume	4[b]	130[b]	0[b]	0.03[b]	0.5[b]	271[b]	1[b]	This study
Other plumes								
West Mata November 2008	425	0.2 to 3.5	35 to 3452	26	0.02	22	8	Baumberger et al., 2014
NW Rota-1	nd	0.1 to 0.4	nd	nd	0.014	9.8	14	Resing et al., 2007, 2009
Plume Axial Volcano	nd	17 to 37	nd	nd	2.2	8.5 to 15	nd	McLaughlin-West et al., 1999
Gorda plume EP96A	20.9	3.2	nd	0.8	0.11	29	nd	Kelley et al., 1998
Gorda plume EP96B	4.9	2.3	nd	0.2	0.10	23	nd	Kelley et al., 1998
Cleft Event Plume 1986	nd	nd	nd	nd	0.3	nd	nd	Kelley et al., 1998

nd = not determined. [a]Ratios derived from regressions of all samples collected in the corresponding plume layer at the reported time. R-squared values given in brackets. [b]Calculated ratio from one available sample in the corresponding plume layer at the reported time. [c]Calculated ratios from a range of samples in the corresponding plume layer at the reported time with an R-squared of linear regression line < 0.20.

the water-rock reaction pathway within the magma chamber (Bowers et al., 1988). An Fe/Mn ratio of 2 in the near seafloor plume is at the low end of the typical range (Fe/Mn = 1 to 5) for mid-ocean ridge hydrothermal fluids (e.g., Von Damm, 1990), possibly due to the longer reaction time between host rock and fluid in a mature system. A hydrothermal plume close the seafloor was observed at Axial Seamount in the Northeast Pacific after the 2015 eruption (Xu et al., 2018). Numerical modeling supports the hypothesis that the 2015 Axial eruption triggered the release of warm brines and that these formed the observed plume near the seafloor. In contrast, density, temperature, and salinity data collected in the NELSC near-seafloor plume point to a buoyant plume and the release of a fluid with different chemistry.

The δ^3He values measured in the H_2-rich and CH_4-poor event plume were lower than the δ^3He values in the more mature near seafloor plume. Primordial ^3He is released from the Earth's interior through volcanic processes. Because of its conservative behavior in marine geochemical and biological processes, ^3He in a hydrothermal plume is only reduced by dilution. Ratios of $H_2/[^3He]^\Delta$ in hydrothermal plumes are thus a function of source composition and plume age. At the NELSC, $H_2/[^3He]^\Delta$ ratios of both layers of the event plume on 21 November, 2008 were in the same range and H_2 and $[^3He]^\Delta$ were well-correlated with each other (**Figures 3**, **4** and **Table 2**). The stronger correlation of the upper layer might be caused by spatial and temporal differences in H_2 production during the reaction of molten rock with seawater (Baker et al., 2011). The $H_2/[^3He]^\Delta$ ratios in the event plume were substantially higher (up to 9152×10^6) than in the near seafloor plume and in the axial plumes originated deeper than the eruption site. In addition, $H_2/[^3He]^\Delta$ ratios in the event plume at the NELSC were 100 times higher than ratios detected in hydrothermal event plumes after eruptions studied previously at other sites (Kelley et al., 1998; McLaughlin-West et al., 1999). The high $H_2/[^3He]^\Delta$ ratios are not only a result of age difference compared to previously studied plumes, but also due to the extraordinary high levels of H_2 and weak ^3He signals observed in the event plume at the NELSC. In fact, based on ^3He/heat ratios, the ^3He load in the NELSC event plume was only 20 to 25% of the load observed at other event plume sites (Baker et al., 2011). Elevated H_2 is the result of extensive production during hot rock – seawater interaction, while the comparatively low ^3He concentrations indicate a small magmatic contribution to the event plume (Baker et al., 2011). On 22 November, $H_2/[^3He]^\Delta$ ratios were 1002×10^6 (900 m) and 5150×10^6 (1350 m), respectively (**Table 2**). Both ratios decreased significantly within 18 h, which suggests that H_2 oxidation started to affect the concentration measurements of the first plumes and dilution cannot be the only reason for the lower H_2 concentrations (McLaughlin et al., 1996). Abiotic oxidation and biological uptake are possible pathways for H_2 removal (e.g., McCollom and Shock, 1997; McCollom, 2000; Dick, 2019). Due

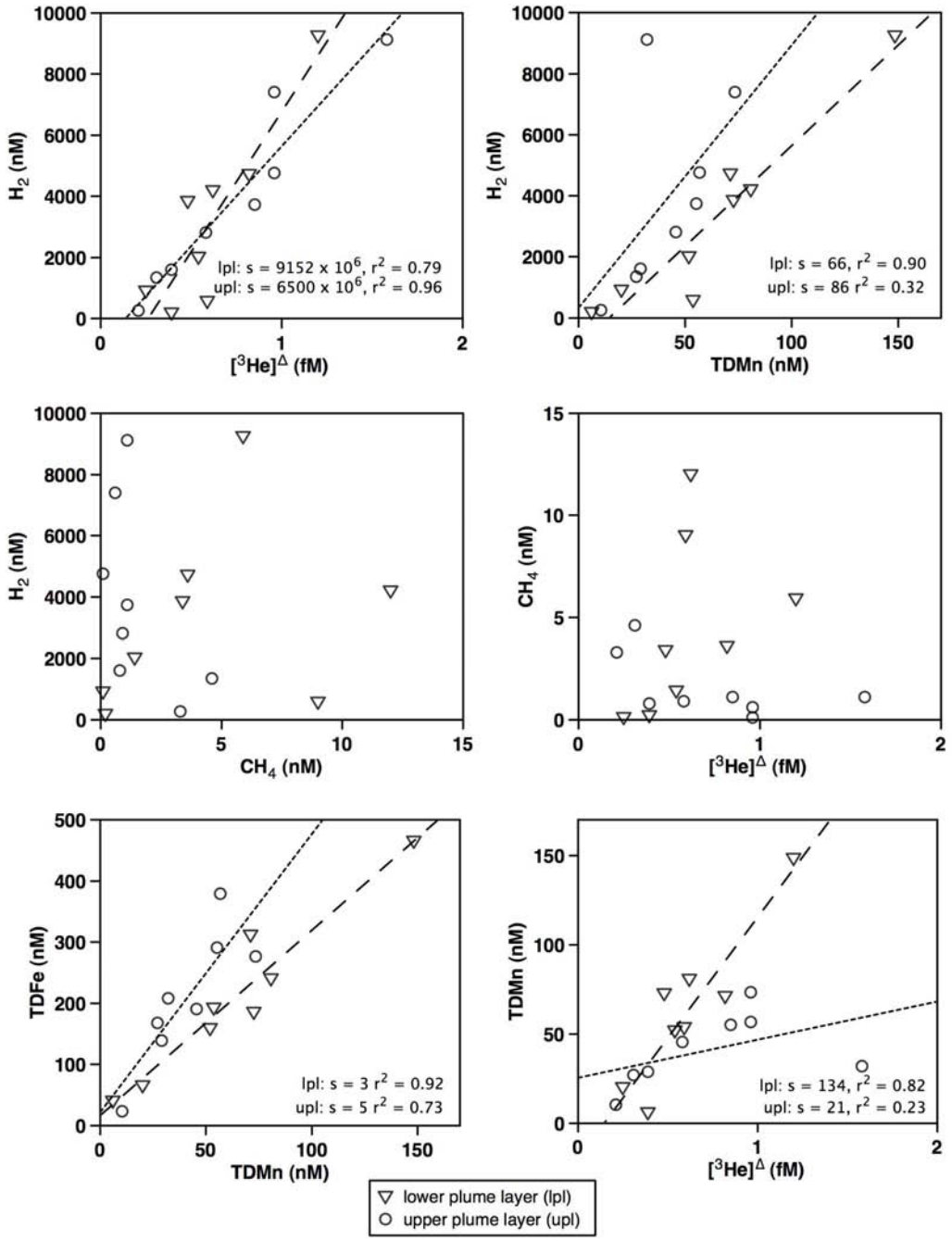

FIGURE 3 | Hydrogen concentrations in the event plume above the NELSC on November 21st plotted against $[^3He]^{\Delta}$, TDMn, heat and CH_4 contents as well as CH_4 plotted against $[^3He]^{\Delta}$ contents. S = slope.

to the high H_2 availability in the event plume, H_2-oxidizers could grow rapidly and consume the abundant H_2 quickly, in addition to ongoing chemical oxidation. This is consistent with the dramatic decrease of H_2 concentrations and $H_2/^3He$ ratios within 18 h observed here at the NELSC. Such volcanic events can thus significantly enhance the locally available catabolic energy in the water column and potentially cause a post-eruption microbial bloom of H_2 oxidizers (Amend et al., 2011). Anantharaman et al. (2013) suggest that microbial H_2 oxidation can be a key energy source in the deep ocean. Seven days after the first H_2 measurements in the event plume, concentrations were decreased by a factor of 1000 to about 10 to 15 times above background concentrations. A microbial bloom of H_2 oxidizers generated by an event plume would thus last for only a short time.

Figure 5 shows distinct $H_2/[^3He]^{\Delta}$ relationships in the NELSC event plumes, the NELSC near seafloor plume, and

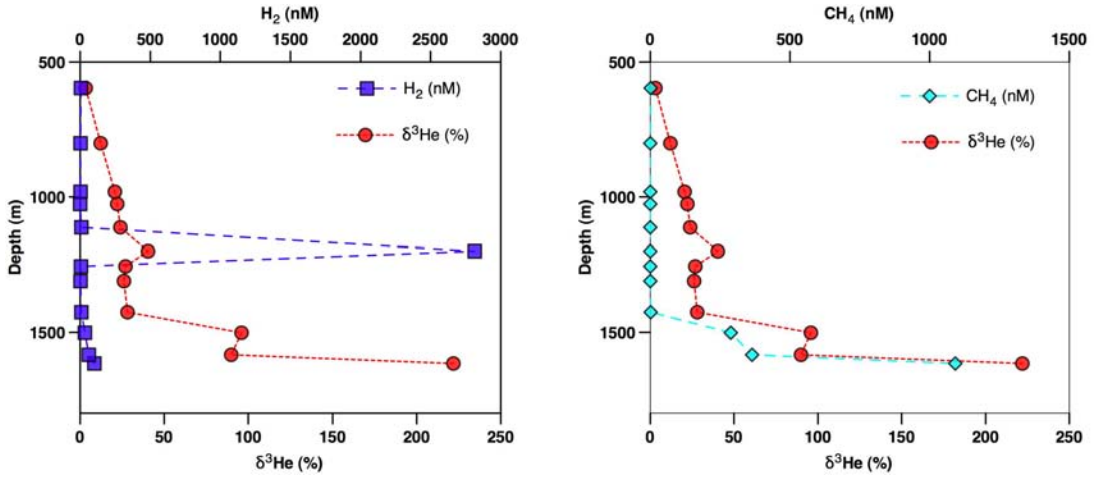

FIGURE 4 | Concentrations of H_2 and CH_4, and δ^3He plotted against depth in the water column above the Puipui eruption site during cast V08C-09.

the hydrothermal plume above the erupting submarine volcano West Mata (Baumberger et al., 2014). The ratios of the three plumes are clearly distinguishable. The slope representing the high $H_2/[^3He]^{\Delta}$ ratio in the event plume is very steep. The comparatively low H_2 and high ^{3}He concentrations found in the near seafloor plume result in a flat slope. At West Mata, $H_2/[^3He]^{\Delta}$ ratios were characterized by high H_2 and high ^{3}He concentrations at the time of sampling and were thus intermediate between the two types observed at the NELSC. These ratios represent the prevailing processes at the different sites. At West Mata, small, almost continuous submarine volcanic eruptions with hot rock-fluid interactions and concurrent release of magmatic volatiles are prominent. At the NELSC, two different processes may be responsible for the striking $H_2/[^3He]^{\Delta}$ pattern. High ratios in the event plume derive from H_2 generation during hot rock and seawater interactions induced by a relatively large lava flow accompanied by a decoupled release of ^{3}He. Hydrogen was produced at the eruptive fissure and along the whole lava flow as long as seawater was in contact with hot lava, while some low-level degassing of ^{3}He likely caused the small ^{3}He elevations in the event plume. It is thought that ^{3}He and other primordial gases separate from the magma in the magma chamber and that these gases are released in excess upon eruption (Graham et al., 2018). Most of the ^{3}He may have degassed during the initial rise of the magma and/or when the magma exited from the seafloor leading to a spatial and temporal separation of ^{3}He degassing and H_2 production.

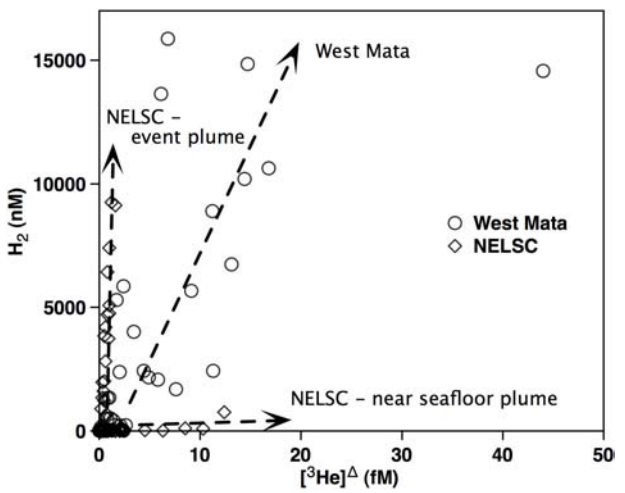

FIGURE 5 | Hydrogen and ^{3}He concentrations of the event and the near seafloor plumes at the NELSC and of West Mata (Baumberger et al., 2014).

The deep plume observed in the same time frame as the event plume layers and the near seafloor plume have a typical high temperature hydrothermal vent composition and indicate venting of a fluid from an edifice located deeper than the ongoing lava eruption. No such hydrothermal vent system was located during the 2009 ROV dives. However, the dives were mainly focused on the Puipui flows and on Maka and may have missed the remains of such a system.

Comparison of the NELSC With the West Mata and NW Rota-1 Eruptions

Table 3 is a summary of the main characteristics of the NELSC Puipui, West Mata and NW Rota-1 eruptions. The West Mata and NW Rota-1 eruptions were both observed visually, are located close to a volcanic arc and have an explosive/strombolian eruption type. In contrast, the Puipui lava flow erupted on a back-arc spreading center. The Puipui NELSC lava eruption and the eruption of West Mata were both ongoing during the same time in November 2008. Both were initially identified by very high H_2 concentrations measured in the water column above the eruption sites. At West Mata, the enormous H_2 enrichments resulted from water/rock interactions during gas-rich eruptions accompanied by quiet, degassed outflow of magma forming pillow lava as observed by ROV *Jason* in May 2009 (Resing et al., 2011;

TABLE 3 | Comparison of geochemical data and other characteristics of the NELSC plumes, the West Mata plume and the NW Rota-1 plume.

Site	**NE Lau Spreading Center**			**West Mata**	**NW Rota-1**
References	This study; Baker et al., 2011; Embley and Rubin, 2018			Resing et al., 2011; Baumberger et al., 2014; Embley et al., 2014	Resing et al., 2007, 2009; Chadwick et al., 2008; Stern et al., 2008
Plume type	**Event plume**	**Near-seafloor plume**	**Deep plume**	**Focused plume**	**Focused plume**
Geological setting	Back-arc	Back-arc	Back-arc	Rear-arc	Arc
Eruption type	Short-lived, explosive?	Effusive?	Effusive	Explosive/strombolian	Explosive/strombolian
Time-frame eruption	Event	Event?	Event?	Continuous	Continuous
Chemical character plume	Rich in H_2, poor in ^3He	Rich in CH_4 and ^3He	Rich in ^3He	Rich in ^3He, H_2, S, CO_2	Rich in Al, S, Si, CO_2, Fe, Mn, ^3He, acid
Max H_2 measured (nM)	9250	101	90	14843	Not measured
Max CH_4 measured (nM)	12	1092	8	10	5
Max TDMn measured (nM)	150	2738	74	359	150
Max % DMn	100	100	99.9	>95	>95
Max TDFe measured (nM)	465	5686	298	3275	2300
Max % DFe	72.2	69.7	39.7	11	<10
Max δ^3He (%)	67.5	222	255	442	314
Max $[^3He]^\Delta$ measured (fM)	1.6	8.5	10.4	47	15.3
$H_2/[^3He]^\Delta$ (x 10^6)	9152	43	13.2	2839	No H_2 measured
$CH_4/[^3He]^\Delta$ (x 10^6)	19	227	1	0.3	0.3
H_2/CH_4	47631	0.7	13.7	2370	No H_2 measured
Estimated R/Ra	7.9 to 8.6	8	Not Determined	7.2	8.4
Plume rise height (m)	200 to 1000	<30 to 130	Unknown	130	100
Glass shards in plume	Yes	No	No	Yes	Yes
Bubble plume	No	No	No	No	Yes
Lava type	Basalt, basaltic andesite	Basalt, basaltic andesite	Basalt, basaltic andesite	Boninite	Basalt, basaltic andesite, andesite

Baumberger et al., 2014). In contrast to the size of the volcanic eruption at West Mata where explosive deposits and pillow flows formed in a restricted area, the high H_2 concentrations at the NELSC eruption resulted from water/rock interactions of a lava flow extending about 1.7 km along the ridge axis (Rubin et al., 2009; Resing et al., 2011). Despite this difference in size, the maximum measured H_2 concentrations in both plumes are in a comparable range and probably result from explosive eruption activity. Hydrogen concentrations were not analyzed in the NW Rota-1 plume and we thus have no information as to whether the NW Rota-1 plumes were rich in H_2. Maximum measured CH_4 concentrations are low in the NELSC event plume as well as in the two plumes generated from the continuous explosive eruptions at West Mata and NW Rota-1. This confirms that CH_4 plays only a minor role in the formation of high rising plumes from submarine volcanic eruptions and lava outflows. The ^3He patterns are less uniform over the three eruption sites. Whereas low ^3He input in event plumes has been observed during several historical events (with the NELSC event plume having the lowest input), both volcanic eruptions, West Mata and NW-Rota-1, are rich in mantle helium and have a continuous supply of magmatic gas input (Resing et al., 2007; Baker et al., 2011; Butterfield et al., 2011; Baumberger et al., 2014). The NELSC event plume as well as the focused plumes from the two volcanic eruptions have variable TDMn/DMn ratios, likely resulting from the different plume ages sampled. In contrast, the near seafloor plume at the NELSC has highly elevated CH_4, TDMn, and TDFe contents with the high percentage of dissolved Fe pointing to a very young plume. Despite similarities in volcanic activities, TDFe/TDMn ratios in the NW Rota plume (TDFe/TDMn = 14) were considerably higher than at West Mata (TDFe/TDMn = 8) and in the NELSC event plumes (TDFe/TDMn = 3–6). At NW Rota, venting of highly acidic fluids likely causes dissolution of the host rock resulting in fluids with higher TDFe/TDMn ratios closer to the host rock (Resing et al., 2007). Acidic fluids were also reported at West Mata (Resing et al., 2011). However, the short reaction time with the host rock during the ongoing eruptions as well as the boninite magma composition likely lead to lower ratios than observed at NW Rota. In contrast, the NELSC plumes are more similar to the low Fe/Mn hydrothermal systems found on mid-ocean ridges.

To determine the role of the geological setting for the magmatic gas source during these three eruptions, we use helium isotope ratios. The $^3He/^4He$ helium isotope ratio R/R_a, where $R = {}^3He/^4He$ and $R_a = R_{air} = 1.39 \times 10^{-6}$ (Graham, 2002), can be used to obtain information about the source of the helium. This is especially useful in complex tectonic settings, such as arc-backarc settings or where hot spots are nearby. The R/R_a

of the upper mantle is 8.0 ± 1 based on values observed in MOR basalts and hydrothermal fluids (Poreda and Craig, 1989; Graham, 2002). R/R_a ratios at volcanic arcs are about 5 to 7, generated by a mixture of mantle helium and slab material that is relatively enriched in ^4He (Hilton et al., 2002). The $^3He/^4He$ ratios are usually determined from direct measurements in end member fluids collected at the seafloor. Where direct sampling of seafloor vent or eruption fluids is not possible, dilute water column samples can be used to estimate $^3He/^4He$ ratios in the end member fluid erupted at the seafloor (Lupton et al., 2015). We used the vertical cast V08C-09, collected over the Puipui eruption site, to estimate the end member R/R_a value of the near seafloor plume by plotting ^3He vs. ^4He concentrations of both, the plume and the background concentrations. The resulting slope corresponds to the $^3He/^4He$ ratio = R. We estimated an R value of 8.0 R_a for the near seafloor plume, which falls in the MORB field (**Figure 6**). We did the same exercise with the event plume and estimated an R/Ra = 8.6 for the upper layer and R/Ra = 7.9 for the lower layer. These ratios correspond well with the measured $^3He/^4He$ ratios in the high temperature end member vent fluids at Maka located on the NELSC (8.7 R_a), and the ratio measured in fluids from a diffuse vent site (8.0 R_a) located on the SW-NELSC (Lupton et al., 2015). As expected from the geological setting of the back-arc spreading center, the established NELSC hydrothermal vent fields as well as the recent Puipui eruption have the upper mantle as their main helium source, similar to mid-ocean ridges, and are apparently not impacted by the Samoan hot spot, nor by the volcanic arc, which is in good agreement with Lupton et al. (2015). In contrast, $^3He/^4He$ ratios of the rear-arc volcano West Mata, erupting at the same time 60 km NE of the NELSC, had an estimated ratio of 7.2 R_a and arc-like $^3He/^4He$-C/^3He attributes (Lupton et al., 2015). At NW Rota-1, despite being an arc volcano, the upper mantle was the main source for its helium (R = 8.4 Ra; Resing et al., 2009), possibly reflecting source heterogeneity within small distances as observed in the Manus Basin (Fourre et al., 2006).

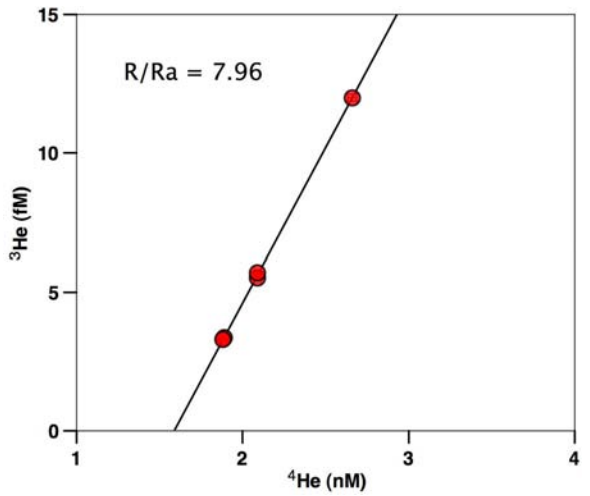

FIGURE 6 | Example of the estimation of an R/R_a value from water column ^3He and ^4He concentrations. The slope of ^3He vs. ^4He in V08C-09 yields 7.96 R/R_a for the near seafloor plume.

Chemical Constraints on Event Plume Formation

Baker et al. (1987) described the first discovery of an event plume, or megaplume, on the Cleft segment of the southern Juan de Fuca Ridge in 1986. They reported the formation of an extensive plume of a thickness of 700 m and a diameter of 20 km created by a brief and massive release of high-temperature hydrothermal fluid (Lupton et al., 1989; Baker and Lupton, 1990). Another event plume with heat and chemical anomalies was discovered above the North Fiji Basin in 1987, a very different tectonic environment compared to the Juan de Fuca Ridge (Nojiri et al., 1989). In 1993, a series of event plumes, with plume volumes from 1.3 to 4 × 10^{10} m^3 was observed above the CoAxial segment of the Juan de Fuca Ridge (Baker et al., 1995b; Embley et al., 1995; Lupton et al., 1995). After the remote detection of seismic swarms, event plumes above the northern Gorda Ridge were also observed during quick response cruises in 1996. There, a major event plume was detected rising nearly 1500 m with a thickness of approximately 1 km and an extension of 15 km along and at least 8 km across axis (Baker, 1998). However, dissolved H_2 and CH_4 have not often been measured in event plumes. The most comprehensive data set with respect to H_2 and CH_4 was collected from EP96A and EP96B at the Gorda Ridge in 1996 when H_2 and CH_4 concentrations reached maximum values of 47 and 7 nM, respectively (Kelley et al., 1998).

The generation of these voluminous plumes associated with magmatic events at the seafloor is not yet fully understood. To date, three different generation models have been proposed. The first model suggested that event plumes at the Cleft Segment, Juan de Fuca Ridge were generated through the sudden release of a crustal hydrothermal fluid reservoir by crustal rupture (Baker et al., 1989; Baker and Lupton, 1990; Lupton et al., 1999, 2000). A second model proposed event plume generation through the release of heat and chemical fluxes during a dike intrusion (Lowell and Germanovich, 1995). A third model postulates that event plumes form during interactions of seawater with emplaced lava flows or pillow lavas (Butterfield et al., 1997; Palmer and Ernst, 1998).

Based on physical and chemical data collected during the 2008 NELSC event plume, Baker et al. (2011) provided the first new clues on event plume formation in more than a decade. The study found that event plume volumes span over several orders of magnitude, the source fluid interacts with molten lava, and that the heat content in event plumes is roughly equivalent to that in the erupted lava. However, they also found that lava cooling is not fast enough to generate enough heat over short time to lift the plume up to 1000 m. Here we present further constraints on the NELSC event plume formation based on a more comprehensive chemical data set of the same event plume.

In the event plume over the NELSC eruption site, extraordinarily high H_2 concentrations corresponded with nearly background ^3He values. Thus, significant amounts of magmatic gases do not appear to be involved in the

formation of this event plume, consistent with previous event plume observations. As observed, Mn and Fe ascended together with H_2 in the plume released by this volcanic event. This is consistent with the results at Kilauea where both Mn and H_2 were abundant in the sea-surface eruptive plume (Sansone and Resing, 1995). Methane is present in low concentrations, is poorly correlated, and apparently decoupled from the other constituents in the shallow NELSC event plume.

Both the first and the second model suggest the release of a pre-existing hydrothermal fluid as a source fluid for the event plume. Our data is difficult to match to these models because of the very low and unsystematic CH_4 concentrations as well as the high H_2 values measured in the event plume. In contrast, the fluid chemistry data supports the third model, which suggests event plume generation during interaction of seawater with lava. This model is also consistent with the positive relationship between plume and lava heat (Baker et al., 2011). However, because the cooling rate of emplaced lava is argued to be too slow to generate enough buoyancy to lift the plume and much too slow to match the short release time of event plumes (Lavelle, 1995; Baker et al., 2011), other processes must occur during event plume formation. In the case at the NELSC, a process that releases enough heat in a short time is required to provide the required buoyancy flux for hydrothermal plume rise. Baker et al. (2011) argue that the amount of lava needed to interact with seawater to produce the high H_2 concentrations is relatively low and does not release enough heat to allow for the level of plume rise. Even if some of the lava exited as lava fountains, quenching of the pyroclastic material would not generate enough heat, if the mass fraction of pyroclasts is as low as, e.g., $< 0.02\%$ at Gorda Ridge, Escanaba Trough (Clague et al., 2009; Baker et al., 2011). However, glass shards that were commonly found in association with volcanic eruptions were discovered in the hydrothermal plumes at the NELSC. The shards together with the high H_2 concentrations could support the hypothesis that part of the lava emplacement was much more violent, probably similar to the West Mata eruptions, rather than just quiescent lava outflow. The larger surface area of lava available for interaction with seawater could have led to extensive H_2 production, possibly elevated cooling rates and only a minimum release of magmatic gas. Even though no evidence was found for a massive amount of pyroclastic debris, pyroclastic deposits were observed on the Puipui flow and on older proximate lava flows during ROV surveys in 2009 and their amounts could be underestimated. However, we still lack knowledge on event plume formation and the full extent of their generation processes remains unclear.

CONCLUSION

1. The extremely high H_2 concentrations measured in the 2008 NELSC event plume confirm interaction of hot rock and seawater at the seafloor and point to an ongoing eruption. Methane input is insignificant during event plume formation and rules out a mature, pre-stored fluid as fluid source. As observed in historical event plumes, significant amounts of magmatic gases do not appear to be involved in the formation of event plumes. The event plume chemistry favors a seawater-lava interaction formation model. However, the heat budget requires an additional process releasing enough heat to lift the plume within the short-lived event.
2. The extremely high H_2 concentrations in the event plume point to a large surface-area of hot-rock interacting with seawater and suggest that the Puipui eruption was locally more explosive than assumed, comparable to West Mata. This process might enhance the heat flux from lava cooling.
3. The near seafloor plume has a different source fluid than the event plume and likely results from the release of a more mature, pre-stored fluid rich in CH_4 and ^3He, either during event plume formation or shortly after.
4. The upper mantle is the main helium source of the NELSC eruption, similar to mid-ocean ridges.

DATA AVAILABILITY STATEMENT

All chemical datasets generated for this study are included in the article and the **Supplementary Material**. Expedition reports for Lau Basin cruises in 2008, 2009, and 2010 can be downloaded at http://www.pmel.noaa.gov/eoi/laubasin.html. The CTD data is available at the Rolling Deck to Repository.

AUTHOR CONTRIBUTIONS

TB wrote the manuscript made most of the figures, and analyzed CTD water samples for methane and hydrogen. ML was the lead PI for dissolved gases during the NE Lau 2008 expedition, analyzed CTD water samples for methane and hydrogen, and helped drafting this manuscript. JL was chief scientist on the NE Lau 2008 expedition and analyzed seawater samples for helium on shore. EB and SW collected and processed the CTD sensor data. JR and NB collected and analyzed seawater samples for manganese and iron. GF-G helped drafting the manuscript. All co-authors contributed to the interpretation of the results and to the editing of the manuscript.

FUNDING

Support for this study was supplied by the NOAA Vents (now Earth-Ocean Interactions) Program, the Cooperative Institute for Marine Resources Studies (CIMRS) under NOAA Cooperative Agreement No. NA11OAR4320091, and the Joint

Institute for the Study of the Atmosphere and Ocean (JISAO) under NOAA Cooperative Agreement No. NA10OAR4320148. Financial support by the Swiss National Science Foundation grant #20MA21-115916 to GF-G was gratefully acknowledged. Funding for research cruises was provided by the U.S. National Science Foundation (NSF) and NOAA Office of Ocean Exploration and Research. This is PMEL contribution 4943.

ACKNOWLEDGMENTS

We thank the crew and technical staff of the research vessel *T.G. Thompson* and the ROV *Jason* team for excellent support during our expeditions. We thank Ron Greene, Leigh Evans, and Hoang-My Christensen for assistance with sampling and analyses and Susan Merle for creating the bathymetric map in **Figure 1**. The manuscript was improved by the helpful comments from the two reviewers and the Topic Editors.

SUPPLEMENTARY MATERIAL

The Supplementary Material for this article can be found online at: https://www.frontiersin.org/articles/10.3389/fmars.2020.00171/full#supplementary-material

TABLE S1 | Summary of concentrations of H_2, CH_4, $[^3He]^{\Delta}$, TDMn, and TDFe and ratios thereof in the event, near seafloor and deep plumes above the Puipui eruption site in 2008, 2009, and 2010 and it the background waters of the eruption site.

REFERENCES

Amend, J. P., McCollom, T. M., Hentscher, M., and Bach, W. (2011). Catabolic and anabolic energy for chemolithoautotrophs in deep-sea hydrothermal systems hosted in different rock types. *Geochim. Cosmochim. Acta* 75, 5736–5748. doi: 10.1016/j.gca.2011.07.041

Anantharaman, K., Breier, J. A., Sheik, C. S., and Dick, G. J. (2013). Evidence for hydrogen oxidation and metabolic plasticity in widespread deep-sea sulfur-oxidizing bacteria. *Proc. Natl. Acad. Sci. U.S.A.* 110, 330–335. doi: 10.1073/pnas.1215340110

Baker, E. T. (1998). Patterns of event and chronic hydrothermal venting following a magmatic intrusion: new perspectives from the 1996 Gorda Ridge eruption. *Deep Sea Res. Pt. II* 45, 2599–2618. doi: 10.1016/S0967-0645(98)00085-X

Baker, E. T., German, C. R., and Elderfield, H. (1995a). "Hydrothermal plumes over spreading-center axes: global distributions and geological inferences," in *Seafloor Hydrothermal Systems: Physical, Chemical, Biological, and Geological Interactions*, eds S. E. Humphris, et al. (Washington, DC: American Geophysical Union), 47–71. doi: 10.1029/gm091p0047

Baker, E. T., Lavelle, J. W., Feely, R. A., Massoth, G. J., Walker, S. L., and Lupton, J. E. (1989). Episodic venting of hydrothermal fluids from the juan de fuca ridge. *J. Geophys. Res.* 94, 9237–9250. doi: 10.1029/JB094iB7p09237

Baker, E. T., and Lupton, J. E. (1990). Changes in submarine hydrothermal He-3/heat ratios as an indicator of magmatic tectonic activity. *Nature* 346, 556–558. doi: 10.1038/346556a0

Baker, E. T., Lupton, J. E., Resing, J. A., Baumberger, T., Lilley, M. D., Walker, S. L., et al. (2011). Unique event plumes from a 2008 eruption on the Northeast Lau Spreading center. *Geochem. Geophys. Geosyst.* 12:Q0AF02. doi: 10.1029/2011GC003725

Baker, E. T., Massoth, G. J., and Feely, R. A. (1987). Cataclysmic hydrothermal venting on the juan-de-fuca ridge. *Nature* 329, 149–151. doi: 10.1038/329149a0

Baker, E. T., Massoth, G. J., Feely, R. A., Embley, R. W., Thomson, R. E., and Burd, B. J. (1995b). Hydrothermal event plumes from the CoAxial seafloor Eruption Site, Juan de Fuca Ridge. *Geophys. Res. Lett.* 22, 147–150. doi: 10.1029/94GL02403

Baumberger, T., Lilley, M. D., Resing, J. A., Lupton, J. E., Baker, E. T., Butterfield, D. A., et al. (2014). Understanding a submarine eruption through time series hydrothermal plume sampling of dissolved and particulate constituents: West Mata, 2008-2012. *Geochem. Geophys. Geosyst.* 15, 4631–4650. doi: 10.1002/2014GC005460

Bennett, S. A., Achterberg, E. P., Connelly, D. P., Statham, P. J., Fones, G. R., and German, C. R. (2008). The distribution and stabilization of dissolved Fe in deep-sea hydrothermal plumes. *Earth Planet. Sci. Lett.* 270, 157–167. doi: 10.1016/j.epsl.2008.01.048

Bowers, T. S., Campbell, A. C., Measures, C. I., Spivack, A. J., Khadem, M., and Edmond, J. E. (1988). Chemical controls on the composition of vent fluids at 13° - 11°N, and 21°N, East Pacific Rise. *J. Geophys. Res.* 93, 4522–4536. doi: 10.1029/JB093iB05p04522

Buck, N. J., Resing, J. A., Baker, E. T., and Lupton, J. E. (2018). Chemical fluxes from a recently erupted shallow submarine volcano on the Mariana Arc. *Geochem. Geophys. Geosyst* 19, 1660–1673. doi: 10.1029/2018GC007470

Butterfield, D. A., Jonasson, I. R., Massoth, G. J., Feely, R. A., Roe, K. K., Embley, R. E., et al. (1997). Seafloor eruptions and evolution of hydrothermal fluid chemistry. *Philos. Trans. R. Soc. Lond.* 355, 369–386. doi: 10.1098/rsta.1997.0013

Butterfield, D. A., Nakamura, K., Takano, B., Lilley, M. D., Lupton, J. E., Resing, J. A., et al. (2011). High SO2 flux, sulfur accumulation and gas fractionation at an erupting submarine volcano. *Geology* 39, 803–806. doi: 10.1130/G31901.1

Butterfield, D. A., Roe, K. K., Lilley, M. D., Huber, J. A., Baross, J. A., Embley, R. W., et al. (2004). "Mixing, Reaction and Microbial activity in the sub-seafloor revealed by temporal and spatial variation in diffuse flow vents at axial volcano," in *The Subseafloor Biosphere at Mid-Ocean Ridges*, eds W. S. D. Wilcock, et al. (Washington, DC: American Geophysical Union), 269–289. doi: 10.1029/144gm17

Chadwick, W. W. Jr., Cashman, K. V., Embley, R. W., Matsumoto, H., and Dziak, R. P. (2008). Direct video and hydrophone observations of submarine explosive eruptions at NW Rota-1 Volcano, Mariana Arc. *J. Geophys. Res.* 113:B08S10. doi: 10.1029/2007JB005215

Chadwick, W. W. Jr., Merle, S. G., Baker, E. T., Walker, S. L., Resing, J. A., Butterfield, D. A., et al. (2018). A recent volcanic eruption discovered on the central Mariana back-arc spreading center. *Front. Earth Sci.* 6:172. doi: 10.3389/feart.2018.00172

Chadwick, W. W. Jr., Rubin, K. H., Merle, S. G., Bobbitt, A. M., Kwasnitschka, T., and Embley, R. W. (2019). Recent eruptions between 2012-2018 discovered at West Mata submarine volcano (NE Lau Basin, SW Pacific) and characterized by new ship, AUV, and ROV data. *Front. Mar. Sci* 6:495. doi: 10.3389/fmars.2019.00495

Clague, D. A., Caress, D. W., Rubin, K. H., and Paduan, J. B. (2010). The 2008 puipui eruption and morphology of the northeast lau spreading center between maka and tafu. *Paper Presented at the 2010 AGU Fall Meeting*, San Francisco, CA.

Clague, D. A., Paduan, J. B., and Davis, A. S. (2009). Widespread strombolian eruptions of mid-ocean ridge basalt. *J. Volcanol. Geotherm. Res.* 180, 171–188. doi: 10.1016/j.jvolgeores.2008.08.007

de Angelis, M. A., Lilley, M. D., and Baross, J. (1993). Methane oxidation in deep-sea hydrothermal plumes of the Endeavour segment of the Juan de Fuca Ridge. *Deep Sea Res. Pt. I* 40, 1169–1186. doi: 10.1016/0967-0637(93)90132-M

Dick, G. J. (2019). The microbiomes of deep-sea hydrothermal vents: distributed globally, shaped locally. *Nat. Rev. Microbiol.* 17, 271–283. doi: 10.1038/s41579-019-0160-2

Dick, G. J., Anantharaman, K., Baker, B. J., Li, M., Reed, D. C., and Sheik, C. S. (2013). The microbiology of deep-sea hydrothermal vent plumes: ecological and biogeographic linkages to seafloor and water column habitats. *Front. Microbiol.* 4:124. doi: 10.3389/fmicb.2013.00124

Embley, R. W., Chadwick, W. W. Jr., Jonasson, I. R., Butterfield, D. A., and Baker, E. T. (1995). Initial results of the rapid response to the 1993 CoAxial event: relationships between hydrothermal and volcanic processes. *Geophys. Res. Lett.* 22, 143–146. doi: 10.1029/94GL02281

Embley, R. W., Merle, S. G., Baker, E. T., Rubin, K. H., Lupton, J. E., Resing, J. A., et al. (2014). Eruptive modes and hiatus of volcanism at West Mata seamount, NE Lau basin: 1996-2012. *Geochem. Geophys. Geosyst.* 15, 4093–4115. doi: 10.1002/2014GC005387

Embley, R. W., and Rubin, K. H. (2018). Extensive young silicic volcanism produces large deep submarine lava flow in the NE Lau Basin. *Bull. Volcanol* 80:36.

Field, M. P., and Sherrell, R. M. (2000). Dissolved and particulate Fe in a hydrothermal plume at 9° 45'N, East Pacific Rise: slow Fe (II) oxidation kinetics in Pacific plumes. *Geochim. Cosmochim. Acta.* 64, 619–628. doi: 10.1016/S0016-7037(99)00333-6

Fourre, E., Jean-Baptiste, P., Charlou, J.-L., Donval, J. P., and Ishibashi, J. I. (2006). Helium Isotope composition of hydrothermal fluids from the Manus back-arc Basin, Papua New Guinea. *Geochem. J.* 40, 245–252. doi: 10.2343/geochemj.40.245

German, C. R., Baker, E. T., Connelly, D. P., Lupton, J. E., Resing, J. A., Prien, R. D., et al. (2006). Hydrothermal exploration of the fonualei rift and spreading center and the northeast lau spreading center. *Geochem. Geophys. Geosyst.* 7:Q11022. doi: 10.1029/2006GC001324

Graham, D. W. (2002). "Noble gas isotope geochemistry of mid-ocean ridge and ocean island basalts; characterization of mantle sources reservoirs," in *Noble Gases in Geochemistry and Cosmochemistry*, eds D. Porcelli, R. Wieler, and C. Ballantine, (Washington, DC: Mineralogical Society of America), 247–318. doi: 10.1515/9781501509056-010

Graham, D. W., Michael, P. J., and Rubin, K. H. (2018). An investigation of mid-ocean ridge degassing using He, CO2, and δ13C variations during the 2005-06 eruption at 9°50′N on the East Pacific Rise. *Earth Planet. Sci. Lett.* 504, 84–93. doi: 10.1016/j.epsl.2018.09.040

Hawkins, J. W. (1995). "Evolution of the lau basin - insights from ODP leg 135," in *Active Margins and Marginal Basins of the Western Pacific*, eds B. Taylor, and J. Natland, (Washington, DC: American Geophysical Society), 125–173. doi: 10.1029/gm088p0125

Hilton, D. R., Fisher, T. P., and Marty, B. (2002). Noble gases and volatile recycling at subduction zones. *Rev. Mineral. Geochem.* 47, 319–370. doi: 10.1515/9781501509056-011

Huber, J. A., Butterfield, D. A., and Baross, J. A. (2003). Bacterial diversity in a subseafloor habitat following a deep-sea volcanic eruption. *FEMS Microbiol. Ecol.* 43, 393–409. doi: 10.1111/j.1574-6941.2003.tb01080.x

Kelley, D. S., Lilley, M. D., Lupton, J. E., and Olsen, E. J. (1998). Enriched H2, CH4 and 3He concentrations in hydrothermal plumes associated with the 1996 Gorda Ridge eruptive event. *Deep Sea Res. Pt. II* 45, 2665–2682. doi: 10.1016/S0967-0645(98)00088-5

Kim, J., Son, S. K., Son, J. W., Kim, K. H., Shim, W. J., Kim, C. H., et al. (2009). Venting sites along the fonualei and Northeast lau spreading centers and evidence of hydrothermal activity at an off-axis caldera in the northeastern lau basin. *Geochem. J.* 43, 1–13. doi: 10.2343/geochemj.0.0164

Lavelle, J. W. (1995). The initial rise of a hydrothermal plume from a line segment source - results from a three-dimensional numerical model. *Geophys. Res. Lett.* 22, 159–162. doi: 10.1029/94GL01463

Lilley, M. D., Butterfield, D. A., Lupton, J. E., and Olsen, E. J. (2003). Magmatic events can produce rapid changes in hydrothermal vent chemistry. *Nature* 422, 878–881. doi: 10.1038/nature01569

Lilley, M. D., Feely, R. A., and Trefry, J. H. (1995). "Chemical and biological transformations in hydrothermal plumes," in *Seafloor Hydrothermal Systems: Physical, Biological, and Geological Interactions*, eds S. E. Humphris, et al. (Washington, D.C: American Geophysical Union), 369–391. doi: 10.1029/gm091p0369

Lowell, R. P., and Germanovich, L. N. (1995). Dike injection and the formation of megaplumes at ocean ridges. *Science* 267, 1804–1807. doi: 10.1126/science.267.5205.1804

Lupton, J. E. (1995). "Hydrothermal plumes: near and far field," in *Seafloor Hydrothermal Systems: Physical, Chemical, Biological, and Geological Interactions*, eds S. E. Humphris, et al. (Washington, DC: American Geophysical Union), 317–346. doi: 10.1029/gm091p0317

Lupton, J. E., Baker, E. T., and Massoth, G. J. (1989). Variable 3He/heat ratios in submarine hydrothermal systems: evidence from two plumes over the juan de fuca ridge. *Nature* 337, 161–164. doi: 10.1038/337161a0

Lupton, J. E., Baker, E. T., and Massoth, G. J. (1999). Helium, heat, and the generation of hydrothermal event plumes at mid-ocean ridges. *Earth Planet. Sci. Lett.* 171, 343–350. doi: 10.1016/S0012-821X(99)00149-1

Lupton, J. E., Baker, E. T., and Massoth, G. J. (2000). Reply to Comment on "Helium, heat and the generation of hydrothermal event plumes at mid-ocean ridges", by J.E. Lupton, E.T. Baker and G.J. Massoth. *Earth Planet. Sci. Lett.* 180, 219–222. doi: 10.1016/S0012-821X(00)00151-5

Lupton, J. E., Baker, E. T., Massoth, G. J., Thomson, R. E., Burd, B. J., Butterfield, D. A., et al. (1995). Variations in water-column 3He/heat ratios associated with the 1993 CoAxial event, Juan de Fuca ridge. *Geophys. Res. Lett.* 22, 155–158. doi: 10.1029/94GL02797

Lupton, J. E., Rubin, K. H., Arculus, R., Lilley, M. D., Butterfield, D. A., Resing, J. A., et al. (2015). Helium isotope, C/3He, and Ba-Nb-Ti signatures in the northern Lau Basin: distinguishing arc, back-arc, and hotspot affinities. *Geochem. Geophys. Geosyst* 16, 1133–1155. doi: 10.1002/2014GC005625

McCollom, T. M. (2000). Geochemical constraints on primary productivity in submarine hydrothermal vent plumes. *Deep Sea Res. Pt. I* 47, 85–101. doi: 10.1016/S0967-0637(99)00048-5

McCollom, T. M., and Shock, E. L. (1997). Geochemical constraints on chemolithoautotrophic metabolism by microorganisms in seafloor hydrothermal systems. *Geochim. Cosmochim. Acta* 61, 4375–4391. doi: 10.1016/S0016-7037(97)00241-X

McLaughlin, E. A. (1998). *Microbial Hydrogen Oxidation Associated With Deep-sea Hydrothermal Vent Environments*. Ph.D. dissertation, University of Washington, Seattle,WA.

McLaughlin, E. A., Lilley, M. D., Olsen, E. J., and Rust, T. (1996). Microbial hydrogen oxidation in the Loihi event plumes: microbial rapid response. *Eos Trans. Am. Geophys. Union* 46:398.

McLaughlin-West, E. A., Olson, E. J., Lilley, M. D., Resing, J. A., Lupton, J. E., Baker, E. T., et al. (1999). Variations in hydrothermal methane and hydrogen concentrations following the 1998 eruption at Axial Volcano. *Geophys. Res. Lett.* 26, 3453–3456. doi: 10.1029/1999GL002336

Measures, C. I., Yuan, J., and Resing, J. A. (1995). Determination of iron in seawater by flow injection analysis using in-line preconcentration and spectrophotometric detection. *Mar. Chem.* 50, 3–12. doi: 10.1016/0304-4203(95)00022-J

Mottl, M. J., Sansone, F. J., Wheat, C. G., Resing, J. A., Baker, E. T., and Lupton, J. E. (1995). Manganese and methane in hydrothermal plumes along the east pacific rise, 8°40′ to 11°50′N. *Geochim. Cosmochim. Acta* 59, 4147–4165. doi: 10.1016/0016-7037(95)00245-U

Nojiri, Y., Ishibashi, J., Kawai, T., and Sakai, H. (1989). Hydrothermal plumes along the north fiji basin spreading axis. *Nature* 342, 667–670. doi: 10.1038/342667a0

Palmer, M. R., and Ernst, G. G. J. (1998). Generation of hydrothermal megaplumes by cooling of pillow basalts at mid-ocean ridges. *Nature* 393, 643–647. doi: 10.1038/31397

Poreda, R., and Craig, H. (1989). Helium isotope ratios in Circum Pacific volcanic arcs. *Nature* 473–478. doi: 10.1038/338473a0

Resing, J. A., Baker, E. T., Lupton, J. E., Walker, S. L., Butterfield, D. A., Massoth, G. J., et al. (2009). Chemistry of the hydrothermal plumes above submarine volcanoes of the Mariana Arc. *Geochem. Geophys. Geosyst.* 10:Q02009. doi: 10.1029/2008GC002141

Resing, J. A., Lebon, G., Baker, E. T., Lupton, J. E., Embley, R. W., Massoth, G. J., et al. (2007). Venting of acid-sulfate fluids in a high-sulfidation setting at NW Rota-1 submarine Volcano on the Mariana Arc. *Econ. Geol.* 102, 1047–1061. doi: 10.2113/gsecongeo.102.6.1047

Resing, J. A., and Mottl, M. J. (1992). Determination of manganese in seawater using flow injection analysis with on-line preconcentration and spectrophotometric detection. *Anal. Chem.* 64, 2682–2687. doi: 10.1021/ac00046a006

Resing, J. A., Rubin, K. H., Embley, R. W., Lupton, J. E., Baker, E. T., Dziak, R. P., et al. (2011). Active submarine eruption of boninite in the northeast Lau Basin. *Nat. Geosci.* 4, 799–806. doi: 10.1038/NGEO1275

Resing, J. A., Sedwick, P. N., German, C. R., Jenkins, W. J., Moffett, J. W., Sohst, B. M., et al. (2015). Basin-scale transport of hydrothermal dissolved metals across the South Pacific Ocean. *Nature* 523, 200–203. doi: 10.1038/nature14577

Rubin, K. H., Embley, R. W., Clague, D. A., Resing, J. A., Michael, P. J., Keller, N. S., et al. (2009). Lavas from active boninite and very recent basalt eruptions at two submarine NE Lau basin sites. *Paper Presented at the 2009 AGU Fall Meeting*, San Francisco, CA.

Rubin, K. H., Soule, S. A., Chadwick, W. W. Jr., Fornari, D. J., and Clague, D. A. (2012). Volcanic eruptions in the deep sea. *Oceanography* 25, 142–157. doi: 10.5670/oceanog.2012.12

Sander, S. G., and Koschinsky, A. (2011). Metal flux from hydrothermal vents increased by organic complexation. *Nat. Geosci.* 4, 145–150. doi: 10.1038/NGEO1088

Sansone, F. J., and Resing, J. A. (1995). Hydrography and geochemistry of sea-surface hydrothermal plumes resulting from Hawaiian coastal volcanism. *J. Geophys. Res.* 100, 13555–13569.

Sansone, F. J., Resing, J. A., Tribble, G. W., Sedwick, P. N., Kelley, K. M., and Hon, K. (1991). Lava-seawater interactions at shallow-water submarine lava flows. *Geophys. Res. Lett.* 18, 1731–1734. doi: 10.1029/91GL01279

Stern, R. J., Tamura, Y., Embley, R. W., Ishizuka, O., Merle, S., Basu, N. K., et al. (2008). Evolution of West Rota Volcano, an extinct submarine volcano in Southern Mariana Arc: evidence from sea floor morphology, remotely operated vehicle observations, and 40Ar-39Ar geochronological studies. *Isl. Arc.* 17, 70–89. doi: 10.1111/j.1440-1738.2007.00600.x

Von Damm, K. L. (1990). Seafloor hydrothermal activity: black smoker chemistry and chimneys. *Annu. Rev. Earth Planet. Sci.* 18, 173–204. doi: 10.1146/annurev.ea.18.050190.001133

Von Damm, K. L., and Lilley, M. D. (2004). "Diffuse flow hydrothermal fluids from 9° 50′ N East Pacific Rise: origin, evolution and biogeochemical controls," in *The Subseafloor Biosphere at Mid-Ocean Ridges*, eds W. S. D. Wilcock, et al. (Washington, DC: American Geophysical Union), 245–268. doi: 10.1029/144gm16

Welhan, J. A. (1988). Origins of methane in hydrothermal systems. *Chem. Geol.* 71, 183–198. doi: 10.1016/0009-2541(88)90114-3

Xu, G., Chadwick, W. W. Jr., Wilcock, W. S. D., Bemis, K. G., and Delaney, J. (2018). Observation and modeling of hydrothermal response to the 2015 Eruption at Axial Seamount, Northeast Pacific. *Geochem. Geophys. Geosyst.* 19, 2780–2797. doi: 10.1029/2018GC007607

Young, C., and Lupton, J. E. (1983). An ultra-tight fluid sampling system using cold-welded copper tubing. *Eos Trans. Am. Geophys. Union* 64:735.

Yücel, M., Gartman, A., Chan, C. S., and Luther, G. W. III (2011). Hydrothermal vents as a kinetically stable source of iron-sulphide-bearing nanoparticles to the ocean. *Nat. Geosci.* 4, 367–371. doi: 10.1038/NGEO1148

Zellmer, K. E., and Taylor, B. (2001). A three-plate kinematic model for Lau Basin opening. *Geochem. Geophys. Geosyst.* 2:1020. doi: 10.1029/2000GC000106

Conflict of Interest: The authors declare that the research was conducted in the absence of any commercial or financial relationships that could be construed as a potential conflict of interest.

Copyright © 2020 Baumberger, Lilley, Lupton, Baker, Resing, Buck, Walker and Früh-Green. This is an open-access article distributed under the terms of the Creative Commons Attribution License (CC BY). The use, distribution or reproduction in other forums is permitted, provided the original author(s) and the copyright owner(s) are credited and that the original publication in this journal is cited, in accordance with accepted academic practice. No use, distribution or reproduction is permitted which does not comply with these terms.

frontiers in Marine Science

ORIGINAL RESEARCH
published: 31 March 2020
doi: 10.3389/fmars.2020.00154

ROV's Video Recordings as a Tool to Estimate Variation in Megabenthic Epifauna Diversity and Community Composition in the Guaymas Basin

Pedro H. López-Garrido[1,2], James P. Barry[3], Juan Ignacio González-Gordillo[4] and Elva Escobar-Briones[5]**

[1] Posgrado en Ciencias del Mar y Limnología, Universidad Nacional Autónoma de México, Mexico City, Mexico, [2] Programa de Doctorado en Ciencias y Tecnologías Marinas, Universidad de Cádiz, Cádiz, Spain, [3] Monterey Bay Aquarium Research Institute, Moss Landing, CA, United States, [4] Instituto Universitario de Investigación Marina, Universidad de Cádiz, Cádiz, Spain, [5] Instituto de Ciencias del Mar y Limnología, Universidad Nacional Autónoma de México, Mexico City, Mexico

OPEN ACCESS

Edited by:
Diva Amon,
Natural History Museum,
United Kingdom

Reviewed by:
Lenaick Menot,
Institut Français de Recherche pour l'Exploitation de la Mer (IFREMER),
France
Georgios Kazanidis,
The University of Edinburgh,
United Kingdom

***Correspondence:**
Pedro H. Lopez-Garrido
pedro_lopez@comunidad.unam.mx
Elva Escobar-Briones
escobri@cmarl.unam.mx

Specialty section:
This article was submitted to Deep-Sea Environments and Ecology, a section of the journal Frontiers in Marine Science

Received: 14 June 2019
Accepted: 28 February 2020
Published: 31 March 2020

Citation:
Lopez-Garrido PH, Barry JP, González-Gordillo JI and Escobar-Briones E (2020) ROV's Video Recordings as a Tool to Estimate Variation in Megabenthic Epifauna Diversity and Community Composition in the Guaymas Basin. Front. Mar. Sci. 7:154. doi: 10.3389/fmars.2020.00154

Patterns in benthic megafauna diversity in littoral and intertidal zones in the Gulf of California have been associated with both habitat heterogeneity and substrate type. Current knowledge of invertebrate communities in hard bottom habitats at depths > 200 m in the Gulf is poor due to the methodological limitations inherent in sampling deep habitats. Using video imagery of benthic habitats coupled with environmental data from the Remotely Operated Vehicle *Doc Ricketts*, we documented variation in the diversity and community composition of the benthos from 849 to 990 m depth in the NW limit of the Guaymas Basin, in relation to dissolved oxygen and substrate characteristics. This depth range overlaps an oxygen minimum zone where oxygen drops to levels < 0.5 ml L^{-1} and strong gradients in a narrow depth range occur. Dissolved oxygen varied along our benthic survey from 0.200 to 0.135 ml L^{-1}. We observed high taxonomic richness across an area of rocky outcrops through the lower transition zone. This megafaunal pattern differs from reports from other oxygen minimum zones characterized by a great abundance of a few species. Taxonomic richness diminished at depths with reduced dissolved oxygen in the lower boundary of the oxygen minimum zone with increasing soft sediment cover. We found that rocky outcrops and structure-forming organisms such as corals, sponges, and oyster aggregations supported a higher diversity (H' = 0.8) than soft sediment (H' = 0.7) as have been observed in other habitats such as seamounts. Environmental variables that explained most of the megafaunal variation were substrate type (18.4%), depth (1.14%) and temperature (0.9%). Salinity (0.45%) and dissolved oxygen (0.3%) were less important factors to explain the megafaunal composition variance. Substrate type played a key role in the diversity and composition of benthic megafauna. These results broaden our understanding concerning the potential roles of substrate characteristics in the community composition of the deep-sea benthic megafaunal assemblages in the Gulf of California and oxygen minimum zones in general.

Keywords: Sonoran Margin, megafauna, bathyal, substrate, structural complexity, continental slope, Guaymas Basin, Gulf of California

INTRODUCTION

Habitat is defined by the space and abiotic factors in which an organism, population or species assemblage lives (Norse, 1993; Davies et al., 2004; Tapia de la Yossellin, 2018). The Gulf of California (GoC), hosts a wide variety of shallow-water habitats (e.g., coral reefs at the southern end in both margins, rocky habitats in the peninsular shore and sandy beaches in continental shore) (Lluch-Cota et al., 2007) in which biological diversity is thought to vary with substrate heterogeneity (Brusca and Hendrickx, 2010). However, biological patterns of invertebrate communities and processes are perhaps known better in littoral and intertidal zones than in hard bottom habitats at depths greater than 200 m in the GoC (Brusca and Hendrickx, 2010) due to the methodological limitations inherent in sampling deep habitats, such as the time and cost required to deploy equipment at great depths or the effectiveness of the samplers.

In the last three decades, the development of imaging methods coupled with the use of submersibles and remotely operated vehicles (ROV's) to obtain high resolution video images of the deep seabed, has allowed a more extended overview of the habitats and faunal communities, as well as the possibility of doing long-term studies (Pilgrim et al., 2000; Méndez, 2007; Cuvelier et al., 2012; Ayma et al., 2016). ROV video surveys have been used more commonly for hard, steep, and rugged substrate and in areas of cold-water corals (CWC's) (Du Preez and Tunnicliffe, 2012; Ayma et al., 2016). Traditional methods of sampling, such as dredge and sledges are difficult to use in hard and rugged substrate and cannot be used in areas inhabited by delicate and vulnerable structure forming-organisms (Tyler et al., 2016). Therefore, the analysis of images recorded by ROVs has become a non-invasive and complementary method (to conventional methodologies) for sampling deep water fauna in all habitats and substrate types (Cuvelier et al., 2012; Ayma et al., 2016; Tyler et al., 2016).

Preliminary data collected mainly by sledges, dredges and box cores indicate that the southeast GoC has an abundant and diverse deep-sea benthic fauna dominated by polychaetes, decapod crustaceans, echinoderms, and mollusks (Hendrickx, 2006; Lluch-Cota et al., 2007; Méndez, 2007; Zamorano et al., 2007; Zamorano and Hendrickx, 2012; Hendrickx and Serrano, 2014; Hendrickx et al., 2014; Hernández-Alcántara et al., 2014; Mejía-Mercado et al., 2014; Papiol and Hendrickx, 2016).

Many physical variables are known to be important factors associated with patterns of community composition and diversity (McArthur et al., 2010; Anderson et al., 2011). For example, substrate characteristics, structural complexity, sediment composition, organic matter, oxygen, among others, have been identified sources of heterogeneity and important descriptors of biological patterns (Gooday et al., 2010; Ramirez-Llodra et al., 2010; Anderson et al., 2011). Several studies conducted in submarine canyons, such as Schlacher et al. (2010), revealed that structural complexity enhances benthic diversity and biomass. Structural complexity refers to the physical heterogeneity of the habitat related to the rugosity of the seabed substrate and the complex architecture of biogenic aggregations (Laguionie-Marchais et al., 2015; Bartholomew et al., 2016; Ferrari et al., 2016). Increased habitat heterogeneity provides refugia, sites for settlement, feeding, predation, and parasitism of organisms (Buhl-Mortensen et al., 2010; Storlazzi et al., 2016). Consequently, substrate type and structural complexity have been identified as important descriptors of biological patterns (Anderson et al., 2011; Du Preez and Tunnicliffe, 2012). High structural complexity likely contributes to the high taxonomic wealth observed in the GoC funds is precisely a reflection of their structural complexity.

On the other hand, previous studies have documented changes in the abundance, density, and diversity of bathyal macrofauna and megafauna in habitats worldwide where the Oxygen Minimum Zone (OMZ) impinges the seafloor (Levin and Gage, 1998; Rogers, 2000; Levin et al., 2001; Levin, 2003). Macrofaunal and megafaunal densities decreased dramatically in the cores of most OMZ′s where bottom-water dissolved oxygen (DO) is < 0.15 ml l^{-1} (Levin, 2003). In the GoC several oceanographic processes, including wind-induced upwelling, tidal mixing, regional circulation and global thermohaline circulation (Roden, 1958; Santamaría-del-Angel et al., 1994; Álvarez-Borrego, 2010), contribute to the development of an OMZ in the southern GoC, where DO concentrations are < 0.5 ml l^{-1} (Levin, 2003). In the southern Gulf the OMZ has been reported from 82 to 1300 m depth and in the central Gulf from 232 to 1705 m depth, decreasing in thickness and eventually disappearing to the northern region (Hendrickx and Serrano, 2014).

In the GoC, low bottom water DO is strongly associated with the density or diversity of a range of taxa, such as Polychaeta (Méndez, 2007), Bivalvia (Zamorano et al., 2007; Zamorano and Hendrickx, 2012) and Decapoda (Hendrickx and Serrano, 2014; Papiol and Hendrickx, 2016). Nevertheless, these studies also document that other factors (e.g., temperature, depth and sediment composition) also influence deep-sea macrofaunal assemblages. The distribution and diversity of deep water polychaetes from the GoC are correlated with depth and temperature; diversity of polychaetes increased with depth and reached a maximum value at 1270 m depth, while higher density and diversity are found between 2.5 and 4.0°C (Méndez, 2007). Species richness of mollusks from the southern GoC decreases with depth, but reaches a maximum value between 1000 and 1300 m depth (Zamorano et al., 2007). Studies of decapod crustaceans in the southeastern GoC also indicate highest species richness between 1000 and 1380 m depth, suggesting that the availability of food, nature of substrate, currents, or other factors could affect their distribution (Hendrickx, 2006). While these water quality factors show strong relationships with bathyal faunal patterns, the influence of substrate type and structural complexity in a fine scale on deep-sea benthos in the GoC has received little study.

In this study, we aim to document the variation in the diversity, composition and coverage of epibenthic megafauna in relation to DO and habitat quality at bathyal depths from 849 to 990 m in the Guaymas Basin by using benthic imagery recorded on video coupled with environmental data from the ROV *Doc Ricketts*. These two factors in particular – substrate heterogeneity and DO concentration - are expected to play a large role in

deep-sea benthic communities. Thus, we hypothesize that the taxonomic richness of megabenthos would be highest in rocky benthic habitats with the greatest structural complexity, and that soft sediment habitats will be the least diverse.

MATERIALS AND METHODS

Study Area

The GoC is divided into semi-isolated basins (separated from each other by transverse ridges) which become deeper to the south (Lonsdale, 1989). The Guaymas Basin (**Figure 1**) in the central Gulf province is the largest depression within the Gulf (Rusnak et al., 1964; Bischoff and Henyey, 1974), with a maximum depth of 2100 m (Brusca et al., 2005; Mejía-Mercado et al., 2014). This basin is characterized by its rapid deposition of organic-matter rich sediments, particularly where the OMZ impinges on the seafloor (Bischoff and Henyey, 1974; Lonsdale, 1989; Kluesner, 2011; Kurnosov and Blinova, 2015; Teske et al., 2016). The seafloor in Guaymas Basin is mainly composed of fine-grained mud turbidites (Bischoff and Henyey, 1974), though basaltic rocks have been dredged from widespread outcrops on the southern wall of the basin (Lonsdale, 1989).

The Sonoran Margin, the northernmost physiographic province in the basin, extends from the distal portion of the continental shelf adjacent to the state of Sonora to ca. 1300 m depth, has a gentle slope (1.7°) and is characterized by a flat and regular bathymetric relief (Figueroa Albornoz, 2013). The transitional zone from the Sonoran Margin to the floor of Guaymas Basin is affected by different tectonic processes, as well as erosion and gravitational instability (Lonsdale, 1989; Figueroa Albornoz, 2013).

The thermohaline structure of the water column in this region comprises several water masses, principally the Pacific Intermediate Water (PIW) (1200–500 m depth with salinities of 34.50 to 34.80 psu and temperature from 4 to $< 9°C$) and OMZ waters protruding into the southern and central regions (Álvarez-Borrego and Schwartzlose, 1979; Páez-Osuna et al., 2016).

Visual Survey of Benthic Megafauna and Data Collection

Benthic video transects were performed using the ROV *Doc Ricketts* operated from the R/V *Western Flyer* by the Monterey Bay Aquarium Research Institute. The ROV survey sites were determined during the "2012 Gulf of California Expedition" on the basis of maps created with the sonar data gathered previously by the *D. Allan B.* autonomous underwater vehicle (AUV) on board of the R/V *Zephyr*. Transects were located (dive D347, March 2012) in an unexplored area in NW limit of Guaymas Basin and the Sonoran Margin (27.91° N, 111.982° W) (**Figure 1**). Overall, a total of four seabed video transects (**Table 1**) corresponding to 51 min and 0.436 km of seabed length were performed. ROV *Doc Ricketts* has a maximum operation depth of 4000 m and was equipped with a high definition camera (1080 × 1920 resolution) with 10× zoom, an illumination system of six 17700 Lumen LED lights and four 250 W incandescent lights and navigation instrumentation allowing determination of ROV location to ca. 1 m of dive depth, science tools (e.g., suction sampler, swing arm and manipulators) and a CTD equipped with a transmissometer and oxygen sensor. During video transects, the ROV *Doc Ricketts* moved at an altitude of ∼2 m above the seafloor and a constant speed 0.14 m s^{-1} and the focal axis of the camera was kept tilted downward and zoomed to view a ca. 1 m wide portion of the seabed near the ROV. Visibility in seawater was appropriate enough for image analysis. Thus two-parallel lasers mounted 29 cm apart projected red dots on the seafloor to serve as a spatial scale. ROV position was determined by an ultrashort baseline acoustic tracking systems, coupled to the ship's GPS system. Navigation information for the ROV were logged along with near-bottom environmental parameters (depth, temperature, salinity and bottom-water DO) throughout the survey.

Video and Image Analysis

Benthic images extracted from video recorded along transects during ROV dive D347 were edited using Corel Video Studio Pro X5©. Transect images of the seafloor were selected manually at 15 s intervals, equivalent to 1 image per 1.4 m along the video transect, based on the average ROV speed over the bottom and the mobility, size and behavior of the organisms related to the field of view of the camera (Bakus, 2007; Clark et al., 2012). Furthermore, this distance avoids any overlap between successive images.

For each of the images, all epibenthic megafauna > 3 cm were counted and identified to the lowest possible taxon. In cases where organisms could not be assigned to a determinate taxon, they were defined as distinct morphospecies in relation to the available taxonomic information. The identity of organisms was determined using general and specialized literature (Gage and Tyler, 1992; Ruppert and Barnes, 1996; Marshal and Richer de Forges, 2004; Solís-Marín et al., 2005, 2014; Hendrickx et al., 2007, 2014, 2016; Roberts et al., 2009; Álvarez et al., 2014; Hendrickx and Serrano, 2014; Mejía-Mercado et al., 2014; Villalobos Vazquez de la Parra, 2014), as well as specialized databases to validate the taxonomic identification (Brusca and Hendrickx, 2008; Jacobsen Stout et al., 2015; NOAA Office of Ocean Exploration and Research, 2018; WoRMS Editorial Board, 2018; OBIS, 2019). To aid the identification we supplemented these sources with a previous study that identified specimens of taxa collected during dive D347 (Villalobos Vazquez de la Parra, 2014). Additionally, to maximizes the comparability of our results with other studies, we grouped specimens and coverage data of sponges recorded in each benthic images into one of the following morphotypes categories based on the criteria proposed by Boury-Esnault and Rützler (1997) and Kazanidis et al. (2019): amorphous, tubular and clavate ("club-shaped") (see the sponge morphotype examples provide as **Supplementary Material**). Taxonomic richness described the total number of morphospecies per image. Occurrences of morphospecies on each substrate type was recorded in each transect image. The cover of epibenthic megafauna (m^2) was measured on-screen with Image J© software, by tracing the surfaces covered by the sessile and motile fauna visible in each transect image. We

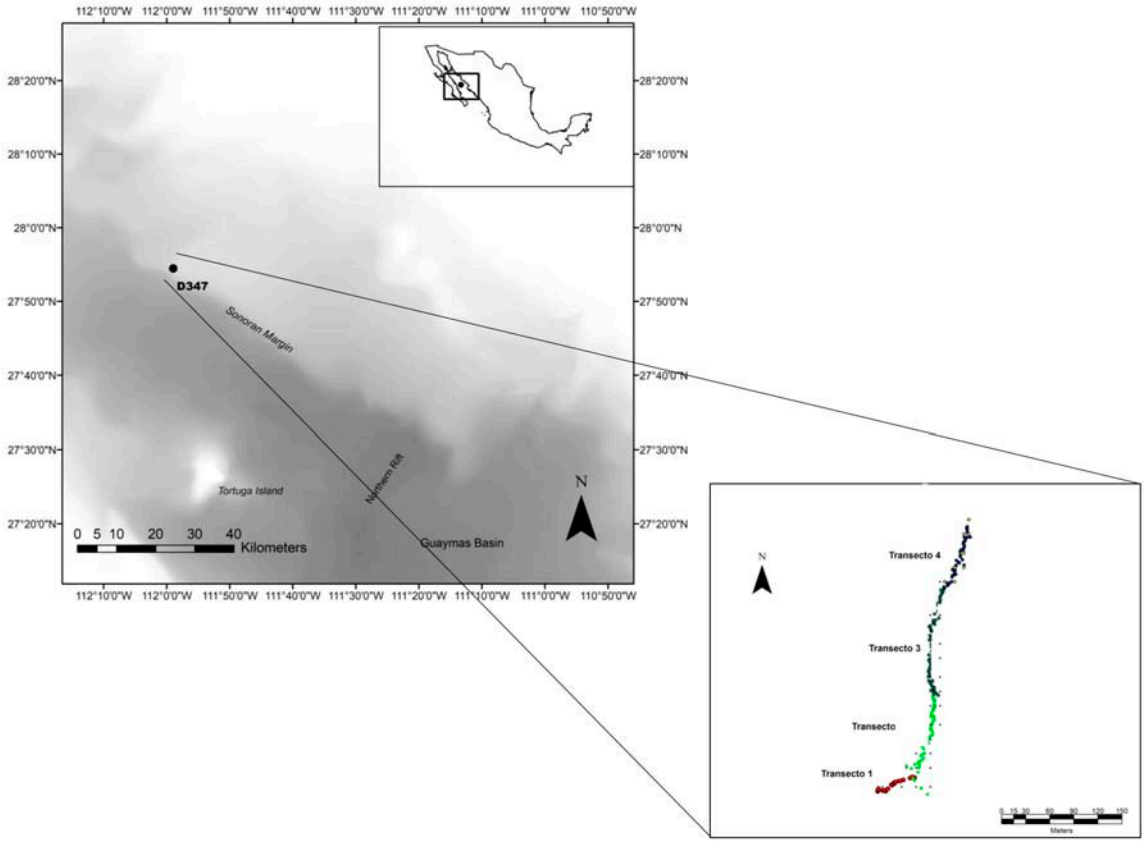

FIGURE 1 | Location of dive D347 in the NW limit of Guaymas Basin and Sonoran Margin in the Gulf of California where four video sections for megabenthic epifauna prospection were performed at a depth range of 849–990 m.

included fauna with low motility (demersal fishes, decapods, holothurians), completely passive taxa, those swimming slowly over the bottom, as well as fauna exhibiting no raction to ROV motion or lights (Lorance and Trenkel, 2006). Several studies that compared ROV observations with sampling methods, have revealed that estimations of the presence and/or abundance of motile megafauna, particularly fishes, decapod crustaceans and mollusks, are more accurate based on imagery than sampling, since the mobile fauna tend to escape during sampling (Spanier et al., 1994; Lorance and Trenkel, 2006; Cuvelier et al., 2012; Gates et al., 2012; Porteiro et al., 2013; Ayma et al., 2016). Moreover, imagery analysis has a high acccuracy in assessing surface areas, epibenthic faunal coverage and the presence of associated fauna in different habitats, such as cold-water corals (Guinan et al., 2009; Cuvelier et al., 2012; Du Preez and Tunnicliffe, 2012). Therefore, coverage (m^2) of substrata also was estimated for each transect image using Image J© software.

Habitat was visually classified on the basis of substrate type (soft and hard) (Greene et al., 1999; van den Beld et al., 2017) and its structural complexity followed the rugosity criteria (Ferrari et al., 2016; Storlazzi et al., 2016; De la Torriente et al., 2018). For fine-scale habitat characteristics, we assigned seabed sub-habitats based on their composition (e.g., soft sediments and rocky outcrops), structure-forming organisms (e.g., corals, sponges and oyster aggregations that are used by other species as substrate for attachment or feeding) (Buhl-Mortensen et al., 2010) and associated biological assemblages (Greene et al., 1999). Environmental variables (depth, temperature, salinity and DO) and ROV location data (geographic coordinates) registered during dive D347 were coupled to each video transect image.

Statistical Analyses

To assess the adequacy of megabenthos sampling, we plotted species-area curves following criteria from several studies (Estacio, 1996; Krebs, 1999; Bianchi et al., 2004; Underwood,

TABLE 1 | Transects performed with the ROV *Doc Ricketts* during 2012 Gulf of California Expedition.

Transect No.	Depth (m)	Number of images sampled	Distance covered (m)	Total area (m^2)
1	990.0–984.5	24	50.0	15.9
2	984.3–940.8	62	128.8	41.4
3	940.2–890.7	79	164.5	50.9
4	889.9–848.6	35	76	20.19
Total		200	419.3	128.39

TABLE 2 | Taxonomic list in the NW limit of Guaymas Basin and the Sonoran Margin (849–990 m) inhabiting soft and hard substrate.

Phylum	Class	Order	Family	Genus/Morphospecies
Porifera				sp1(Porifera)
				sp2(Porifera)
				sp3(Porifera)
				sp4(Porifera)
				sp5(Porifera)
				sp6(Porifera)
				sp7(Porifera)
				sp8(Porifera)
				sp9(Porifera)
				sp10(Porifera)
				sp11(Porifera)
				sp34(Porifera)
Echinodermata	Asteroidea			sp1(Asteroidea)
				sp2(Asteroidea)
				sp3(Asteroidea)
				sp4(Asteroidea)
	Ophiuroidea			sp1(Ophiuroidea)
				sp10(Ophiuroidea)
	Holothuroidea	Elasipodida	Laetmogonidae	*Pannychia* Théel, 1882
Cnidaria				sp1 (Cnidaria)
	Anthozoa	Actiniaria		sp1(Actiniaria)
				sp2(Actiniaria)
				sp3(Actiniaria)
				sp4(Actiniaria)
				sp7(Actiniaria)
			Actinoscyphiidae	*Actinoscyphia* Stephenson, 1920
		Ceriantharia		sp1(Ceriantharia)
				sp2(Ceriantharia)
		Pennatulacea		sp1(Pennatulacea)
		Antipatharia		sp1(Antipatharia)
				sp2(Antipatharia)
				sp3(Antipatharia)
				sp4(Antipatharia)
				sp5(Antipatharia)
				sp6(Antipatharia)
			Antipathidae	*Stichopathes* Brook, 1889
		Alcyonacea		sp1(Alcyonacea)
				sp2(Alcyonacea)
				sp3(Alcyonacea)
			Primnoidae	*Narella* Gray, 1870
		Hexacorrallia	Corallimorphidae	sp1(Corallimorphidae)
Mollusca	Bivalvia	Ostreida	Pectinidae	sp1(Pectinidae)
				sp2(Pectinidae)
Arthropoda				sp1(Arthropoda)
	Malacostraca	Decapoda		sp1(Decapoda)
				sp2(Decapoda)
			Galatheidae	sp1(Galatheidae)
				sp3(Galatheidae)
			Chirostylidae	*Gastroptychus* Caullery, 1896
			Lithodidae	*Paralomis* White, 1856
Chordata	Actinopterygii	Gadiformes	Macrouridae	sp1(Macrouridae)
				sp2(Macrouridae)
		Lophiiformes	Ogcocephalidae	*Dibranchus* Peters, 1876

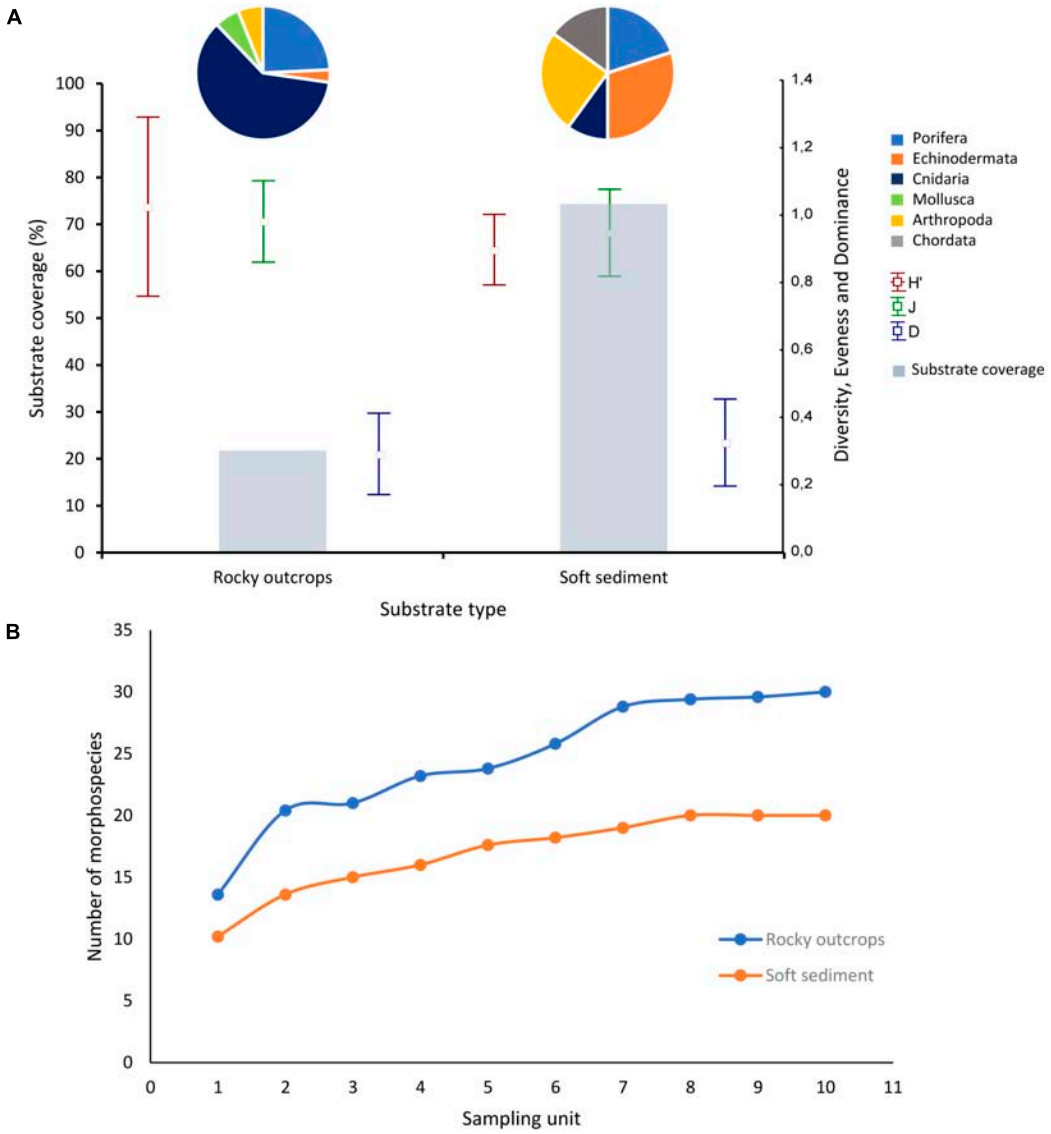

FIGURE 2 | (A) Composition, proportional taxonomic richness and mean diversity indices by substrate type percent coverage. Pie graphs represent percent taxonomic richness contribution by phylum in each substrate type. Dots denote means of descriptors H′ = Shannon-Wiener diversity index; J = evenness index; D = dominance index. Vertical bars denote ± standard deviation. Bar graph represent substrate type percent coverage. **(B)** Rarefaction plots corresponding to the megafaunal assemblages on soft sediment and rocky outcrops.

2006; Bakus, 2007; Clark et al., 2012). Species accumulation curves included data from all extracted images from transects T1 and T2, removing all species that appeared only once among all images. We repeated species accumulation curves for an area of soft sediment (where no rocks were present) between a field of rocky outcrops on soft sediment. A minimum sampling area (with a mean of 0.7 m^2/image) was defined as the number of images (selected randomly) analyzed before no new taxa were added with an additional image sampled. The minimum sampling area determined for the area of rocky outcrops was 14 m^2, corresponding to 20 video images. For sediment dominated habitat, the minimum sampling area was 7 m^2 or 10 benthic images. Sample size for comparisons between rocky outcrops and soft sediment were then standardized to 20 benthic images (with a mean of 0.7 m^2/image) and n = 10. Images for integrate samples were selected randomly. Sample size for comparisons between OMZ zones were standardized to 20 benthic images (selected randomly and with a mean of 0.7 m^2/image) and n = 3 for each OMZ zone.

Morphospecies rarefaction curves (Sanders, 1968) were obtained using the Biodiversity Professional© V.2 program and plotted per rocky outcrops and soft sediment. The cover data for each morphospecies at the two substrata (soft sediment and rocky outcrops) in each sample was used to calculate diversity indices. Diversity and related indices were estimated with the Biodiversity Professional© V.2 program. Shannon-Wiener diversity index is

TABLE 3 | Environmental variables recorded near the seafloor during the ROV dive D347 in the NW limit of Guaymas Basin and the Sonoran Margin.

Dive	Depth (m)	Temperature (°C)	Salinity(psu)	Bottom-water DO (mL L^{-1})
D347	849–990	4.920–4.480	34.536–34.547	0.135–0.200

herein expressed as:

$$H' = -\sum_{i=1}^{s}(Pi)(\log(10)\ Pi)$$

The evenness index is expressed as:

$$J = \frac{H'}{H'\ max}$$

The dominance index was calculated as the complement of evenness:

$$D = 1 - J$$

A Shannon-Wiener diversity index was calculated for each sample and the results pooled by soft sediment and rocky outcrops. Means and standard deviations were plotted. To test for differences in Shannon-Wiener diversity index between soft sediment and rocky outcrops, we used a Kruskal–Wallis non-parametric analysis of variance. Kruskal–Wallis test was performed with software Statistica© V.8.

Redundancy analysis (RDA) was used to assessed environmental factors that were most correlated with changes in the composition of benthic assemblages. This analysis was performed in R studio software. A Hellinger transformation was applied to morphospecies cover data for images (Borcard et al., 2011; Legendre and Legendre, 2012). Environmental variables (substrate, depth temperature salinity and bottom-water dissolved oxygen) were log-transformed and then standardized to a zero mean to obtain a *z*-scores data matrix (Borcard et al., 2011). Water mass was interpreted on the basis of depth, temperature and salinity gathered during the survey and those from the published hydrology of the region (Álvarez-Borrego and Schwartzlose, 1979; Lavín and Marinone, 2003; Álvarez-Borrego, 2010).

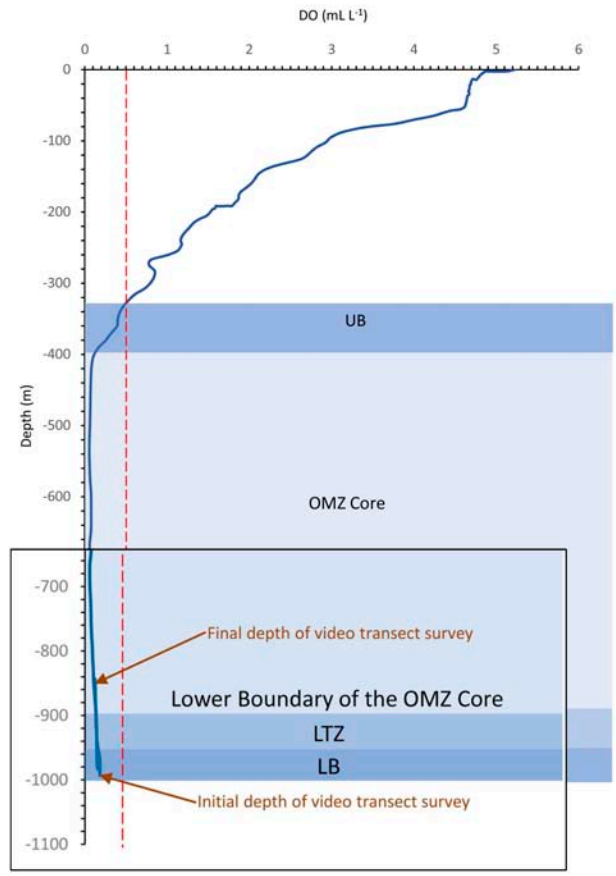

FIGURE 3 | Dissolved oxygen profile during dive D347 in the NW limit of Guaymas Basin and the Sonoran Margin. Oxygen minimum zone (OMZ) where dissolved oxygen (DO) is < 0.5 mL L^{-1}; red dotted line represents the limit where DO = 0.5 mL L^{-1}; LB = lower OMZ boundary; LTZ = lower OMZ transitional zone; UB = upper boundary of the OMZ. Note the magnifying over OMZ survey zones.

RESULTS

Benthic Megafaunal Composition

A total of 200 transect images were selected from the video transect recordings to be used for benthic megafauna and substrate analyses. The video sequences covered a depth range from 849 to 990 m and a linear distance of 0.419 km that include soft sediments with no visible rocks and a field of rocky outcrops on soft sediment. A total of 53 benthic taxa (or morphospecies) belonging to 6 phyla (Porifera, Echinodermata, Cnidaria, Mollusca, Arthropoda and Chordata) were identified in the analysis (**Table 2**). 12 sponges morphospecies, 7 echinoderm morphospecies, 22 cnidarian morphospecies, 2 bivalve morphospecies, 7 crustaceans morphospecies and 3 Actinopterygii morphospecies. Cnidaria was the most diverse phylum with 22 morphospecies including structure-forming cold-water corals (CWC's) (e.g., antipatharians, zoanthids and alcyonarians) (**Table 2**).

Physical Environment

The substrate along the survey was dominated by soft sediment that constituted 74.4% of the total area analyzed in all benthic images (**Figure 2A**). Rocky outcrops covered 25.6% of the total sampled area (**Figure 2A**).

Environmental sensors documented variation in near-bottom temperature (T = 4.920–4.480°C) and salinity (S = 34.536–34.547) during ROV dive D347 (**Table 3**). These data indicates the influence of the Pacific Intermediate Water between 1200 and 500 m depth (Álvarez-Borrego and Schwartzlose, 1979; Álvarez-Borrego, 2010; Páez-Osuna et al., 2016) in the study area. DO levels were very low (DO < 0.5 ml L^{-1}) in the OMZ at these depths (**Table 3**). Changes in DO levels across this depth range allowed us to identify zonation in the OMZ, including the

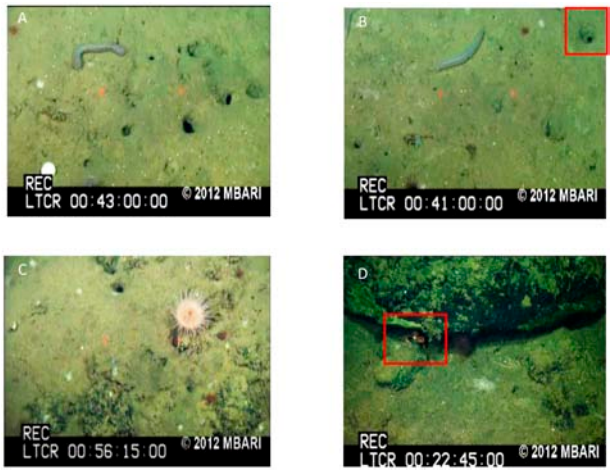

FIGURE 4 | Seafloor images showing sub-habitats identified during the transects performed between 849 and 990 m depth in Dive D347 in the NW limit of Guaymas Basin and the Sonoran Margin within the oxygen minimum zone (OMZ). **(A)** Soft sediments in the lower OMZ boundary dominated by the elasipodid holothurian of the genus *Pannychia*, some benthopelagic fish and burrows. **(B)** Tubular sponges in unconsolidated sediments in the lower OMZ boundary. **(C)** Small rocky outcrops colonized by anemones and sponges in the lower OMZ transitional zone to the lower OMZ boundary. **(D)** Large rocky outcrops (> 30 cm) in the lower OMZ transitional zone to the lower OMZ boundary that provide refuge for small decapod crustacean. Images courtesy of MBARI.

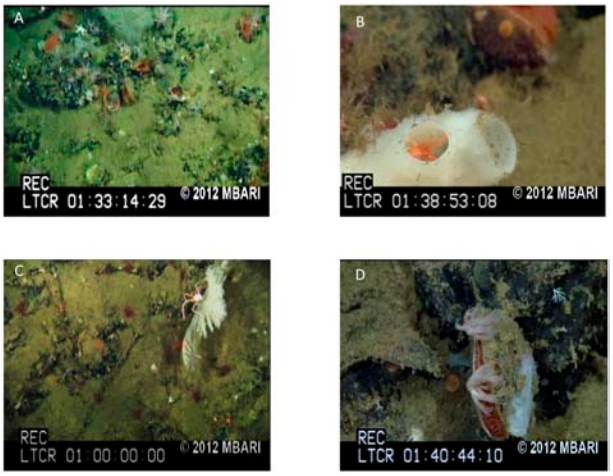

FIGURE 5 | Seafloor images showing sub-habitats identified during the transects performed between 849 and 990 m depth in Dive D347 in the NW limit of Guaymas Basin and the Sonoran Margin within the oxygen minimum zone (OMZ). **(A)** Structure-forming cold-water corals (CWC′s) (antipatharians and alcyonarians) on rocky outcrops in the lower OMZ transitional zone. **(B)** Structure-forming sponges in the lower OMZ transitional zone that provide a refuge from predators and an enhanced food supply for diverse species. Note a decapod crustacean living in the atrium of sponge. **(C)** CWC′s on rocky outcrops that provided an elevated position for spider crabs (*Gastroptychus*) in the lower OMZ transitional zone and in the lower boundary of the OMZ core. **(D)** Oyster (Pectinidae) aggregations that provide with their shell a hard substrate for the attachment of solitary corals and alcyonarians. This type of habitat was observed all along the lower boundary of the OMZ core. Note that these aggregations also allow the association of solitary corals in their surroundings. Images courtesy of MBARI.

lower boundary of the OMZ core (849–901 m), the lower OMZ transitional zone (LTZ) (901–954 m), and the lower boundary (LB) of OMZ (955–990 m) (**Figure 3**).

Fine-Scale Habitat Characterization

Images analysis showed in the fine scale the presence of ten distinct sub-habitats associated to rocky outcrops and soft sediments (**Figures 4**, **5** and **Table 4**). Rocky outcrops typically had more structure-forming taxa such as CWC′s and sponges which provide a variety of habitats for decapod crustaceans (*Gastroptychus*) and other alcyonarians (Primnoidae). In comparison, the diversity of sub-habitats decreased considerably in soft sediment habitats (**Figures 4**, **5** and **Table 4**).

Megafaunal Patterns Among Major Habitat

Taxonomic richness was greater in rocky outcrops (33 taxa, including structure-forming organisms), than on soft sediment (20) (**Table 5**). The morphospecies list in table showing the occurrence of each morphospecies in each substrate is shown in **Table 5**. Structure-forming organisms (corals, sponges and oyster aggregations) were common on rocky outcrops and providing additional substrata for a variety of taxa such as sponges, ophiuroids, decapod crustaceans, alcyonarians, and corallimorpharians (**Table 5**). The variety of sponge morphotypes that occurred on rocky outcrops including amorphous, tubular and clavate, whereas sponges morphotypes occurring on soft sediments were tubular and clavate.

The composition of megafaunal assemblages differed among rocky outcrops and soft sediment (**Figure 2A** and **Table 6**). Cnidaria (particularly diverse habitat-forming CWC′s species) and Porifera were far more diverse on rocky outcrops, whereas Echinodermata and Arthropoda had peak taxonomic richness on soft sediment (**Figure 2A** and **Table 5**).

Relative coverage of epibenthic megafauna taxa was greater on rocky outcrops (68.8%) where Cnidaria, Mollusca and Porifera dominated, compared to soft sediment (31.2%) where Echinodermata and Arthropoda were most dominant (**Figure 6A**). Taxa that contributed to differences among the total coverage on rocky outcrops were structure-forming organisms such as CWC′s, oyster aggregations and sponges, whereas a sea cucumber (*Pannychia* sp.) and galatheids dominated soft sediment (**Figure 6A**). The dominant sponge morphotypes on rocky outcrops and soft sediments were clavate (**Table 7**).

Morphospecies rarefaction curves for rocky outcrops showed a general tendency to increase above the soft substrate curve (**Figure 2B**). These graphic results are in agreement with the significant differences (Kruskal–Wallis, $H_{(1;19)} = 6.4123$; $p = 0.0113$) of mean Shannon-Wiener diversity index (H′) observed between rocky outcrops and soft sediment (**Table 6**). The mean Shannon-Wiener diversity index for rocky outcrops (H′ = 0.8) was higher than measured for the megafaunal assemblages on soft sediment ($H' = 0.7$) (**Figure 2A** and **Table 6**).

TABLE 4 | Fine-scale epibenthic habitat characterization.

Habitat	Sub-habitat	Depth range (m)	DO zone	Associated biological assemblages
Soft sediment	Soft sediment	967–990	LB	elasipodid holothurian of the genera *Pannychia*, ceriantharians, tubular sponges, some benthopelagic fish and characterized by burrow areas of a possible arthropod
	Tubular sponges in soft sediment	967–990	LB	
Rocky outcrops	Small rocky outcrops	849–968	LB/LTZ	anemones and sponges attached to the surface
	Large rocky outcrops (> 30 cm)	849–968	LB/LTZ	small decapod crustaceans that live under these rocks
	Antipatharians and alcyonarians on rocky outcrops	849–968	LTZ	fauna in their surroundings like sponges, galatheids, sea stars, among others.
	Oyster aggregations on rocky outcrops	849–968	Lower Boundary of the OMZ core/LTZ	solitary corals and sponges in their surroundings
	Sponges on rocky outcrops	849–968	Lower Boundary of the OMZ core/LTZ	galatheids in their surroundings
	Antipatharians and alcyonarians that provide a hard substrate for an elevated position of other species	849 to 901	Lower Boundary of the OMZ core/LTZ	specimens of *Gastroptychus* sp., *Narella* sp. and ophiuroids on the surface of habitat-forming species
	Sponges that provide a refuge for predation and an enhanced food supply for other fauna	849 to 901	LB	decapod crustaceans living in the atrium of sponges
	Shells of oyster aggregations that provide hard substrate for the attachment of other fauna	849 to 901	Lower Boundary of the OMZ core/LTZ	anemones, solitary corals and alcyonarians attached to the shell of oyster (Pectinidae) aggregations.

There were no significative differences in the mean evenness index (Kruskal–Wallis, $H_{(1;19)} = 0.1667$; $p = 0.6831$) or mean dominance index (Kruskal–Wallis, $H_{(1;19)} = 0.1667$; $p = 0.6831$) of megafaunal assemblages among substrata (**Figure 2A**).

Megafaunal Patterns and DO

Taxonomic richness in the LTZ and in the lower boundary of the OMZ core was greater than in the LB (**Table 8**). Taxonomic richness within the LB decreased with decreasing DO conditions and where soft sediments dominated. Although the taxonomic richness of OMZ assemblages varied with DO, their taxonomic composition showed little variation among OMZ zones (**Figure 7**). Cnidaria, Porifera, Echinodermata and Arthropoda were the most diverse taxa through all three OMZ zones (**Figure 7**).

Megafaunal Composition and Environmental Variables

The RDA analysis indicated that 21.15% of the variation in megafaunal abundance was explained by environmental variables (substrata type, depth, temperature, salinity and DO). A permutation test (with 999 permutations) indicated that global model ($p = 0.001$) was significant. Environmental variables that explained the most megafaunal variation were substrate type (18.4%), depth (1.14%) and temperature (0.9%). Salinity (0.45%) and DO (0.3%) were less important factors to explain the megafaunal composition variance. The triplot (**Figure 6B**) showed that substrate type, temperature and depth were correlated with megafaunal morphospecies. As illustrated by the triplot in **Figure 6B**, most morphospecies are bunched together with short projections at the centroid oriented toward rocky outcrops, temperature and soft sediment, but away from most of the environmental variables. We interpret this to indicate that megafaunal patterns are related to muliple explanatory variables.

DISCUSSION

The principal aim of our study was to document variation in the diversity and composition of epibenthic megafauna in relation to DO and habitat characteristics at bathyal depths from 849 to 990 m in the Guaymas Basin in the GoC. Our data indicates a diverse fauna of Cnidaria, Porifera, Arthropoda and Echinodermata common on rocky outcrops and soft sediments in the NW limit of Guaymas Basin and the Sonoran Margin. Similarly, in the southern to central region of the Gulf (between 438 and 3747 m depth) Hinojosa-Corona (2014) found a diverse fauna of antipatharians, gorgonians and sponges on scarps and other deep-sea hard bottoms habitats. Patterns of benthic megafaunal diversity in littoral and intertidal zones in the GoC have been widely reported in relation to habitat and substrate type (Brusca and Hendrickx, 2010). These patterns are little known in the GoC at > 200 m depth, particularly for hard bottom habitats that are not easily sampled using traditional methods.

This study spans a narrow bathymetric range (849–990 m) where a strong gradient in DO levels occurred and crosses distinct OMZ zones defined on the basis of DO criteria (Hendrickx, 2006; Hendrickx and Serrano, 2014; Papiol and Hendrickx, 2016) for the southern and central regions in the GoC. We observed a great

TABLE 5 | Rocky outcrops and soft sediment morphospecies in the NW limit of Guaymas Basin and the Sonoran Margin (849–990 m).

Phylum	Morphospecies	Rocky outcrops	Soft sediment
Porifera	sp1(Porifera)	0	1
	sp2(Porifera)	0	1
	sp3(Porifera)	0	1
	sp4(Porifera)	1	0
	sp5(Porifera)	0	1
	sp6(Porifera)*	1	0
	sp7(Porifera)*	1	0
	sp8(Porifera)*	1	0
	sp9(Porifera)	1	0
	sp10(Porifera)	1	0
	sp11(Porifera)	1	0
	sp34(Porifera)	1	0
Echinodermata	sp1(Asteroidea)	0	1
	sp2(Asteroidea)	0	1
	sp3(Asteroidea)	0	1
	sp4(Asteroidea)	0	1
	sp1(Ophiuroidea)	0	1
	sp10(Ophiuroidea)*	1	0
	Pannychia Théel, 1882	0	1
Cnidaria	sp1 (Cnidaria)	1	0
	sp1(Actiniaria)	1	0
	sp2(Actiniaria)	1	0
	sp3(Actiniaria)	1	0
	sp4(Actiniaria)	1	0
	Actinia Linnaeus, 1767	1	0
	Actinoscyphia Stephenson, 1920	1	0
	sp1(Ceriantharia)	0	1
	sp2(Ceriantharia)	0	1
	sp1(Pennatulacea)	1	0
	sp1(Antipatharia)	1	0
	sp2(Antipatharia)	1	0
	sp3(Antipatharia)	1	0
	sp4(Antipatharia)	1	0
	sp5(Antipatharia)	1	0
	sp6(Antipatharia)	1	0
	Stichopathes Brook, 1889	1	0
	sp1(Alcyonacea)	1	0
	sp2(Alcyonacea)	1	0
	sp3(Alcyonacea)*	1	0
	Narella Gray, 1870*	1	0
	sp1(Corallimorphidae)*	1	0
Mollusca	sp1(Pectinidae)	1	0
	sp2(Pectinidae)	1	0
Arthropoda	sp1(Arthropoda)	0	1
	sp1(Decapoda)	0	1
	sp2(Decapoda)*	1	0
	sp1(Galatheidae)	0	1
	sp3(Galatheidae)	0	1
	Gastroptychus Caullery, 1896*	1	0
	Paralomis White, 1856	0	1
Chordata	sp1(Macrouridae)	0	1
	sp2(Macrouridae)	0	1
	Dibranchus Peters, 1876	0	1
	Total	**33**	**20**

*0 = Absence; 1 = Presence. *Morphospecies observed also using structure-forming organisms as substrate.*

taxonomic richness through the LTZ across an area with rocky outcrops. This megafaunal pattern observed is different to that reported in other OMZs where they are characterized by a great abundance of a few species (Levin et al., 2000; Gooday et al., 2010; Papiol and Hendrickx, 2016). For instance, previous studies conducted in the southeast GoC, showed that soft sediments between 800 and 1000 m depth in the LTZ were dominated by a galatheid (*Munidopsis depressa*) (Papiol and Hendrickx, 2016). In Volcano 7 in the eastern tropical Pacific, the Oman margin in the Arabian Sea, and off central California, was observed high densities of crustaceans and echinoderms near the LB of the OMZ (Levin, 2003). DO appears to be an important factor that controls the diversity in the core regions of OMZs (Levin and Gage, 1998; Gooday et al., 2010). However, as DO starts to rise below the OMZ core and the potential stress related to hypoxia diminishes, other environmental factors could influence on diversity patterns (Levin and Gage, 1998; Levin, 2003; Gooday et al., 2010; Papiol and Hendrickx, 2016). Among these factors, hard substrate in the LTZ where food is not a limiting factor could allow the colonization of species (e.g., filter and suspension feeders) that already tolerate hypoxic conditions, resulting in an increase of taxonomic richness.

On the other hand, low taxonomic richness of megabenthic fauna was observed at depths with reduced DO and greater cover of soft sediment in the LB of the OMZ. Several studies in this region (Méndez, 2007; Zamorano et al., 2007; Zamorano and Hendrickx, 2012; Hendrickx and Serrano, 2014; Hinojosa-Corona, 2014; Hendrickx et al., 2016; Papiol and Hendrickx, 2016) have reported that the OMZ is coupled closely to the diversity, composition, abundance and distribution of megafauna inhabiting the water column and the benthos. Differences in the tolerances of megafauna to OMZ conditions very likely influence the shift in the species composition of communities in the LTZ (Levin, 2003; Gooday et al., 2010). However, it should be noted that in our study the distribution of a field of soft sediments with no visible rocks overlaps almost totally with the LB of the OMZ. Under these conditions, the influence of the OMZ on the composition of the megafauna is hard to interpret and our results are limited by the collinearity of substrate and DO.

We found that environmental variables under study are responsible for some of the megafaunal variation. Although, the global model explain only 21.15% of the faunal variation, this result is consistent with variation explained by environmental variables in a study realized in Seco de los Olivos seamount (De la Torriente et al., 2018). However, our model results are probably related somewhat to the spatial scale of the sampling and collection of environmental variables. We speculate that on a larger environmental scale (e.g., if the transects crossed all zones of the OMZ and more), the role of environmental factors may have been larger.

Our results indicate that variation in megafaunal composition was mostly explained by substrate type. Thus, substrate characteristics very likely play a key role in regulating community patterns. The composition of megafaunal assemblages on rocky outcrops differed from those on soft sediments. We found an abundant and diverse fauna of CWC′s (antipatharians, alcyonarians) and sponges, attached to volcanic rocky outcrops

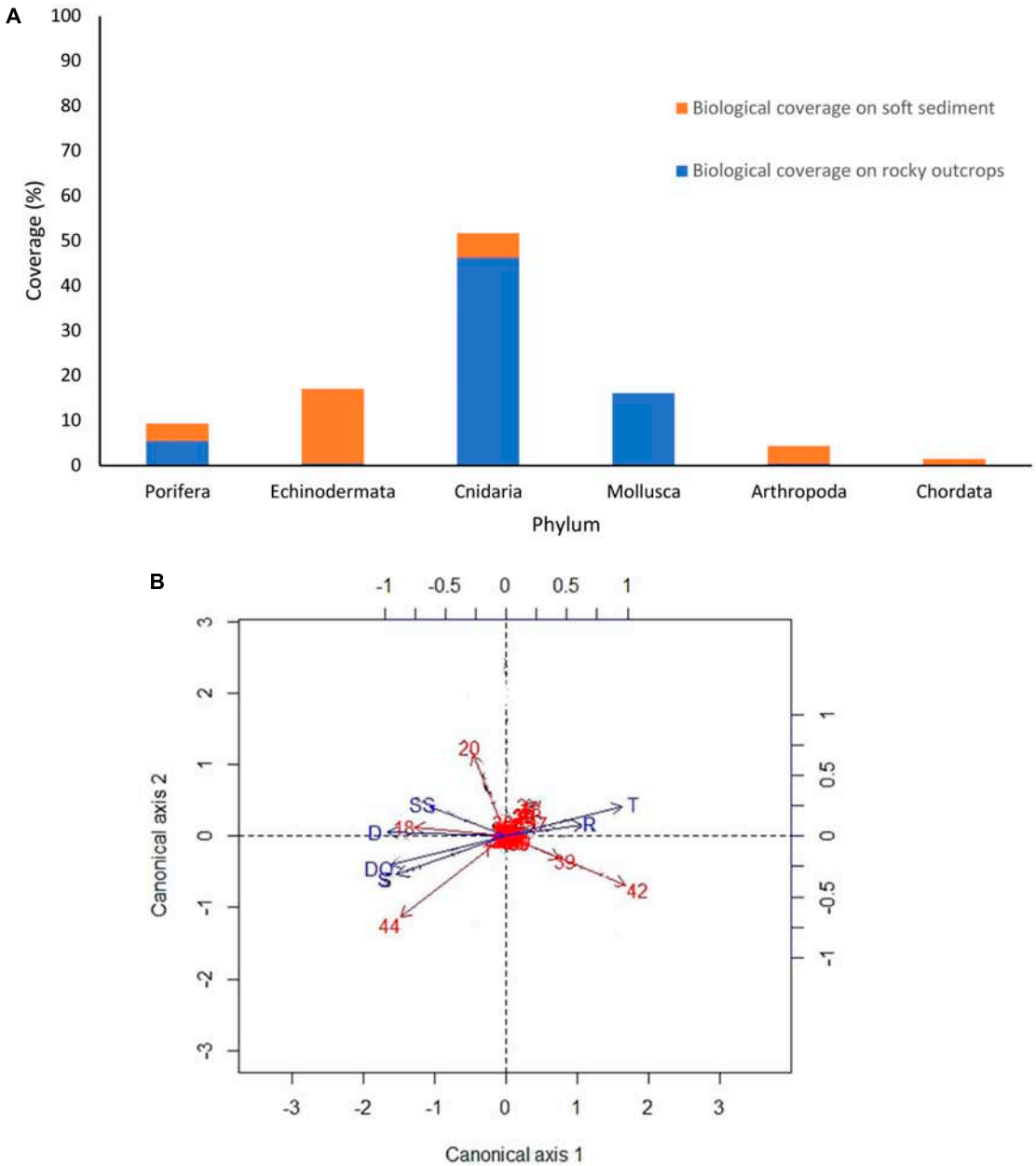

FIGURE 6 | (A) Biological coverage of epibenthic megafauna by phylum on soft sediment and rocky outcrops at dive D347 in the NW limit of Guaymas Basin and Sonoran Margin. **(B)** RDA triplot of the Hellinger-transformed cover data constrained by all environmental variables. Numbers = morphospecies code; SS = soft sediment; R = rocky outcrops; T = temperature; D = depth; S = salinity; DO = dissolved oxygen.

through the LTZ and LB of OMZ. Hard substrate within an OMZ are often formed by materials such as phosphorite, carbonate and volcanic materials (Levin et al., 2010). In comparison, studies realized in the seamount Volcano-7 in the eastern Pacific that protrude into the OMZ have shown a dense aggregation of sponges and serpulid polychaetes attached to basalt substrate and manganese crust (Gooday et al., 2010). Several studies of benthic megafauna have also reported higher species richness on hard substrata than on soft sediments. Canyons in the Gulf of Gioia (Pierdomenico et al., 2016; van den Beld et al., 2017; De la Torriente et al., 2018), the Bay of Biscay (800–1200 m) as well as in the seamount Seco de los Olivos (< 700 m) are sites where hard substrata (including structure-forming organisms) were shown to have higher species richness and diversity than soft sediments. Here, the higher diversity, taxonomic richness and cover of megafauna that we observed on rocky outcrops was because the species associated with hard substrate occur attached to the surface of rocky outcrops and structure-forming organisms, within or around the three-dimensional complex structures constituted by rocky outcrops

TABLE 6 | Shannon-Wiener diversity index (H′), evenness (J) and dominance calculated for each sample and per substrate.

Sample ID	Rocky outcrops			Soft sediment		
	H'	*J*	*D*	*H'*	*J*	*D*
1	0.282	0.937	0.063	0.660	0.66	0.34
2	–	–	–	0.554	0.656	0.344
3	0.817	0.856	0.144	0.664	0.596	0.404
4	0.817	0.785	0.215	0.689	0.689	0.311
5	0.916	0.761	0.239	0.704	0.676	0.324
6	0.907	0.723	0.277	0.751	0.787	0.213
7	0.94	0.82	0.18	0.878	0.878	0.122
8	0.779	0.68	0.32	0.746	0.826	0.174
9	0.988	0.759	0.241	0.687	0.882	0.118
10	0.803	0.617	0.383	0.718	0.795	0.205
ẋ	0.805	0.771	0.229	0.705	0.745	0.256
σ	0.209	0.095	0.095	0.082	0.101	0.101

TABLE 7 | Composition of sponge morphotypes found at the NW limit of Guaymas Basin and the Sonoran Margin (849–990 m).

Substrate type	Amorphous (mean coverage ± SD) (m^2) *n* = 10	Clavate (mean coverage ± SD) (m^2) *n* = 10	Tubular (mean coverage ± SD) (m^2) *n* = 10
Rocky outcrops	0.018 ± 0.040	0.044 ± 0.072	0.011 ± 0.017
Soft sediment	0	0.022 ± 0.018	0.016 ± 0.036

TABLE 8 | Taxonomic richness by OMZ strata and its dissolved oxygen concentration range.

Phylum	Lower boundary of the OMZ core (DO < 0.15 ml L^{-1}; Depth = 849–901 m); *n* = 3	LTZ (DO = 0.15 - 0.18 ml L^{-1}; Depth = 901–954 m); *n* = 3	LB (DO > 0.18–0,5 mL/L^{-1}; Depth = 955–990 m); *n* = 3
Porifera	8	8	4
Echinodermata	4	6	4
Cnidaria	15	18	10
Mollusca	2	1	0
Arthropoda	5	5	5
Chordata	2	2	3
Total	36	40	26

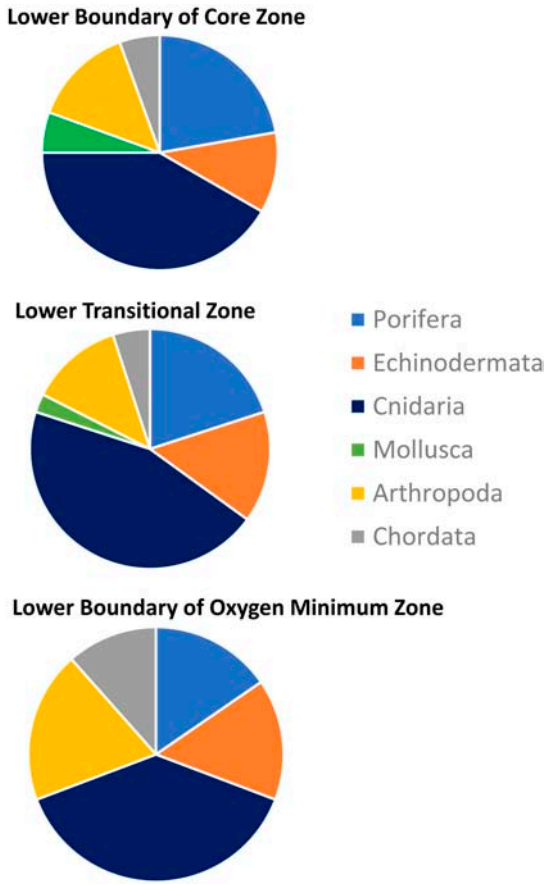

FIGURE 7 | Composition and proportional taxonomic richness by phylum through the oxygen minimum zones during dive D347 in the NW limit of Guaymas Basin and Sonoran Margin.

and habitat-forming organisms and in crevices. More species were also recorded on soft sediment between rocks. Habitats with hard substrate and three-dimensional complex structures, generally supported a higher epibenthic megafauna diversity in comparison with more uniform substrate habitats, such as soft bottom plains (Schlacher et al., 2007; Buhl-Mortensen et al., 2012; Rowden et al., 2016; Åström et al., 2018). Structural habitat complexity was positively related to the local species diversity of sessile and mobile species (Buhl-Mortensen et al., 2010; Matias et al., 2010; Bartholomew et al., 2016; Ferrari et al., 2016; Storlazzi et al., 2016). The underlying substratum and habitat-forming organisms provide a significant proportion of three-dimensional habitat in marine communities (Ferrari et al., 2016). Numerous studies have documented that structure-forming organisms such as sponges and CWC′s play a key structural and functional role in the marine benthos, because they can modified physical properties of the sea floor and influence composition, abundance and distribution of epibenthic megafauna (Schlacher et al., 2007; Beazley et al., 2013; Howell et al., 2016; Huvenne et al., 2016; van den Beld et al., 2017; Kazanidis et al., 2019).

Taxa identified in the NW limit of Guaymas basin and Sonoran Margin span several trophic levels including filter and suspension feeders, deposit feeders and carnivorous benthophages (Sokolova, 2000). Among filter-feeding fauna we found that clavate sponge morphotypes were dominant on rocky outcrops and soft sediment habitats. These results are different to the results found by Kazanidis et al. (2019) in the northeast Atlantic (∼500 m depth), where sponges aggregations on rock and sand substrate were mainly composed of massive and flabellate sponges. Several studies have shown that environmental and anthropogenic factors, such as hydrography or trawling respectively, have an influence in the sponge morphotypes inhabiting in an specific area (Cryer et al., 2008;

Kazanidis et al., 2019). For example, a study realized by Bell and Barnes (2000) showed that encrusting forms were more abundant on high flow areas. At a local scale the morphology of structure-forming organisms can also vary with local hydrodynamic patterns and create microhabitats differing in flow and the transport or settlement of particles (Buhl-Mortensen et al., 2010). Furthermore, the evolutionary origin of the fauna may account for the differences observed. Most invertebrate fauna of the Gulf of California were derived from the Caribbean Sea, the temperate shores of California and from the tropical Indo-west Pacific (Brusca and Hendrickx, 2010).

The findings of this study support the hypothesis that taxonomic richness in the NW limit of Guaymas Basin are highest in rocky benthic habitats with the greatest structural complexity in comparison with soft sediment habitats, but also, we found that diversity, composition and cover of benthic megafauna vary among soft sediment and rocky outcrops.

In our study we found that depth and temperature were also important environmental factors related to variation in the composition of benthic megafauna as reported in other studies of the southern and central regions in the GoC (Hendrickx, 1996, 2006; Méndez, 2007; Zamorano et al., 2007; Zamorano and Hendrickx, 2012). However, multiple interacting factors ranging from hydrographic (DO, water masses) to food supply and interactions act in synergy with DO and substratum type to influence the structure of these communities.

CONCLUSION

The present study documented that diversity, taxonomic richness, composition and cover of benthic megafauna within the OMZs from 849 to 990 m depth in the NW limit of the Guaymas Basin varied among rocky outcrops and soft sediments. Variation in megafaunal composition was highly correlated with substrate type (rocky outcrops and soft sediments) depth and temperature. Salinity and DO had a minor role in explaining variation in the composition of megafaunal assemblages. We found high taxonomic richness through the LTZ across an area with rocky outcrops, in contrast with some previous reports from other OMZ habitats where a high abundance of few species has been observed. We documented that taxonomic richness diminished at depths with reduced DO in the LB of OMZ with increasing soft sediment cover, however, the relative influence on the observed pattern is limited by the collinearity of DO and substrate. Taxonomic richness and diversity of megabenthos in the NW limit of Guaymas Basin and Sonoran Margin were positively correlated with the increase in structural habitat complexity and heterogeneity of rocky outcrops and structure-forming organisms in the lower boundary of OMZ core and LTZ of the OMZ. These results broaden our understanding concerning the potential roles of substrate characteristics in the community composition of the deep-sea benthic megafaunal assemblages in the GOC and OMZs in general. Our results also contribute to the information required by decision-makers for Marine Protected Areas and design of habitats conservation.

DATA AVAILABILITY STATEMENT

The dataset analyzed for this study can be found in the UNINMAR repository at: http://metadata.icmyl.unam.mx/handle/20.500.12201/10238, http://metadata.icmyl.unam.mx/handle/20.500.12201/10239, http://metadata.icmyl.unam.mx/handle/20.500.12201/10240, http://metadata.icmyl.unam.mx/handle/20.500.12201/10241, http://metadata.icmyl.unam.mx/handle/20.500.12201/10242.

AUTHOR CONTRIBUTIONS

PL-G coordinated the study, elaborated the manuscript, responsible for the integration of datasets, and carried out the analysis and results presented in this article. JB chief scientist of leg 3 of MBARI's 2012 Gulf of California Expedition, and responsible for data collection and editing of the manuscript. JG-G collaborated with the design of the method for video and images analysis, as well as the results analysis, and reviewed the manuscript. EE-B collaborated with the theoretical framework of the study, contributed as the international counterpart during the 2012 MBARI Gulf of California Expedition, assisted in the results analysis, and reviewed the manuscript.

FUNDING

This work was possible thanks to the financial support (Beca Nacional 345620/630445) of National Council for Science and Technology (CONACYT) of Mexico, Santander Universidades through the program "Jovenes Profesores e Investigadores 2018-1" and the David and Lucile Packard Foundation.

ACKNOWLEDGMENTS

This work was possible thanks to the shared metadata produced during the 2012 Gulf of California Expedition performed by Monterey Bay Aquarium Research Institute, and generous support from the David and Lucile Packard Foundation. We are also grateful to CONACyT and Santander Universidades for the doctoral grant to PL-G, for technical support to the UNINMAR at Instituto de Ciencias del Mar y Limnología UNAM and the Unidad de Informática Marina and the Instituto de Investigaciones Marinas de la Universidad de Cádiz. J. Yager, Research Associate, Department of Invertebrate Zoology, Smithsonian Institution edited English language.

SUPPLEMENTARY MATERIAL

The Supplementary Material for this article can be found online at: https://www.frontiersin.org/articles/10.3389/fmars.2020.00154/full#supplementary-material

REFERENCES

Álvarez, F., Villalobos, J. L., Hendrickx, M. E., Escobar-Briones, E., Rodríguez-Almaraz, G., and Campos, E. (2014). Biodiversidad de crustáceos decápodos (Crustacea: Decapoda) en México. *Rev. Mex. Biodivers.* 85, 208–219. doi: 10.7550/rmb.38758

Álvarez-Borrego, S. (2010). Physical, chemical and biological oceanography of the Gulf of California. *Gulf Calif. Biodivers. Conserv.* 400. 24–48.

Álvarez-Borrego, S., and Schwartzlose, R. A. (1979). Water masses of the gulf of california. *Ciencias Mar.* 6, 43–63. doi: 10.7773/cm.v6i1.350

Anderson, T. J., Nichol, S. L., Syms, C., Przeslawski, R., and Harris, P. T. (2011). Deep-sea bio-physical variables as surrogates for biological assemblages, an example from the Lord Howe Rise. *Deep. Res. Part II Top. Stud. Oceanogr.* 58, 979–991. doi: 10.1016/j.dsr2.2010.10.053

Åström, E. K. L., Carroll, M. L., Ambrose, W. G., Sen, A., Silyakova, A., and Carroll, J. L. (2018). Methane cold seeps as biological oases in the high-Arctic deep sea. *Limnol. Oceanogr.* 63, S209–S231. doi: 10.1002/lno.10732

Ayma, A., Aguzzi, J., Canals, M., Lastras, G., Bahamon, N., Mecho, A., et al. (2016). Comparison between ROV video and Agassiz trawl methods for sampling deep water fauna of submarine canyons in the Northwestern Mediterranean Sea with observations on behavioural reactions of target species. *Deep. Res. Part I Oceanogr. Res. Pap.* 114, 149–159. doi: 10.1016/j.dsr.2016.05.013

Bakus, J. G. (2007). *Quantitative Analysys of Marine Biological Communities. Field Biology and Environment*. Hoboken, NJ: Jhon Wiley & Sons.

Bartholomew, A., Hafezi, S. A., and Karimi, S. (2016). Effects of habitat complexity on the abundance, species richness and size of darkling beetles (Tenebrionidae) in artificial vegetation. *J. Arid Environ.* 129, 35–41. doi: 10.1016/j.jaridenv.2016.02.004

Beazley, L. I., Kenchington, E. L., Murillo, F. J., and Sacau, M. (2013). of epibenthic megafauna in the Northwest Atlantic. *ICES J. Mar. Sci.* 70, 1471–1490. doi: 10.1093/icesjms/fst124

Bell, J. J., and Barnes, D. K. A. (2000). The influences of bathymetry and flow regime upon the morphology of sublittoral sponge communities. *J. Mar. Biol. Assoc.* 80, 707–718. doi: 10.1017/S0025315400002538

Bianchi, C. N., Pronzato, R., Cattaneo-Vietti, R., Benedetti Cecchi, L., Morri, C., Pansini, M., et al. (2004). "Hard Bottoms," in *Mediterranean Marine Benthos: A Manual of Methods for its Sampling and Study*, eds C. M. Gambi, and M. Dappiano, (Cham: Springer), 185–215.

Bischoff, J. L., and Henyey, T. L. (1974). Tectonic elements of the central part of the Gulf of California. *Geol. Soc. Am. Bull.* 85, 1893–1904.

Borcard, D., Gillet, F., Legendre, L., and Legendre, P. (2011). *Numerical Ecology with R*. Berlin: Springer, doi: 10.1017/CBO9781107415324.004

Boury-Esnault, N., and Rützler, K. (1997). Thesaurus of sponge morphology. *Smithson. Librar.* 596, 1–55. doi: 10.5479/si.00810282.596

Brusca, R. C., Findley, L. T., Hastings, P. A., Hendrickx, M. E., Torre-Cosío, J., and Van Der Heiden, A. M. (2005). *Macrofaunal Diversity in the Gulf of California. In Biodiversity, Ecosystems, and Conservation in Northern Mexico*. Oxford: Oxford University Press, 179–203.

Brusca, R. C., and Hendrickx, M. E. (2008). *The Gulf of California Invertebrate Database: The Invertebrate Portion of the Macrofauna Golfo Database*. Available at: http://www.desertmuseum.org/center/seaofcortez/database.php (accessed September 14, 2018).

Brusca, R. C., and Hendrickx, M. E. (2010). "Invertebrate biodiversity and conservation in the Gulf of California," in *The Gulf of California Biodiversity and Conservation*, ed. R. C. Brusca, (Oxford: Oxford University Press), 72–95.

Buhl-Mortensen, L., Buhl-Mortensen, P., Dolan, M. F. J., Dannheim, J., Bellec, V., and Holte, B. (2012). Habitat complexity and bottom fauna composition at different scales on the continental shelf and slope of northern Norway. *Hydrobiologia* 685, 191–219. doi: 10.1007/s10750-011-0988-6

Buhl-Mortensen, L., Vanreusel, A., Gooday, A. J., Levin, L. A., Priede, I. G., Buhl-Mortensen, P., et al. (2010). Biological structures as a source of habitat heterogeneity and biodiversity on the deep ocean margins. *Mar. Ecol.* 31, 21–50. doi: 10.1111/j.1439-0485.2010.00359.x

Clark, M. R., Consalvey, M., and Rowden, A. A. (2012). *Biological Sampling in the Deep Sea*. Hoboken, NJ: Wiley-Blackwell, doi: 10.1002/ejoc.201200111

Cryer, M., Hartill, B., and Shea, S. O. (2008). Modification of marine benthos by trawling?: toward a generalization for the deep ocean?? *Ecol. Soc.* 12, 1824–1839.

Cuvelier, D., de Busserolles, F., Lavaud, R., Floc'h, E., Fabri, M. C., Sarradin, P. M., et al. (2012). Biological data extraction from imagery - How far can we go? A case study from the Mid-Atlantic Ridge. *Mar. Environ. Res.* 82, 15–27. doi: 10.1016/j.marenvres.2012.09.001

Davies, C. E., Moss, D., and Hill, M. O. (2004). *EuNIS Habitat Classification Revised 2004. Report to the European Topic Centre on Nature Protection and Biodiversity*. Denmark: European Environmental Agency.

De la Torriente, A., Serrano, A., Fernández-Salas, L. M., García, M., and Aguilar, R. (2018). Identifying epibenthic habitats on the seco de los olivos seamount: species assemblages and environmental characteristics. *Deep. Res. Part I Oceanogr. Res. Pap.* 135, 9–22. doi: 10.1016/j.dsr.2018.03.015

Du Preez, C., and Tunnicliffe, V. (2012). A new video survey method of microtopographic laser scanning (MiLS) to measure small-scale seafloor bottom roughness. *Limnol. Oceanogr. Methods* 10, 899–909. doi: 10.4319/lom.2012.10.899

Estacio, G. F. J. (1996). *Distribución Espacio-Temporal de las Comunidades Macrobentónicas del Sedimento en la Bahía de Algeciras. Implicaciones en la Evolución de la Calidad Ambiental del Medio Marino*. Dissertation's thesis, University of Sevilla, Sevilla, Spain.

Ferrari, R., Bryson, M., Bridge, T., Hustache, J., Williams, S. B., Byrne, M., et al. (2016). Quantifying the response of structural complexity and community composition to environmental change in marine communities. *Glob. Chang. Biol.* 22, 1965–1975. doi: 10.1111/gcb.13197

Figueroa Albornoz, J. L. (2013). *Estudio tectono-estratigráfico de la cuenca transtensional en el Margen de Sonora frente al rift de Guaymas, Golfo de California*. 171. M.S. thesis, Universidad Nacional Autónoma de México, México.

Gage, J. D., and Tyler, P. A. (1992). *Deep-Sea Biology: A Natural History of Organism at the Deep-Sea Floor*. Cambridge: Cambridge University Press.

Gates, A. R., Jones, D. O. B., and Cartes, J. E. (2012). In situ video observations of benthic megafauna and fishes from the deep eastern Mediterranean Sea off Egypt. *Afric. J. Mar. Sci.* 34, 215–222. doi: 10.2989/1814232X.2012.675121

Gooday, A. J., Bett, B. J., Escobar, E., Ingole, B., Levin, L. A., Neira, C., et al. (2010). Habitat heterogeneity and its influence on benthic biodiversity in oxygen minimum zones. *Mar. Ecol.* 31, 125–147. doi: 10.1111/j.1439-0485.2009.00348.x

Greene, H. G., Yoklavich, M. M., Starr, R. M., O'Connell, V. M., Wakefield, W. W., Sullivan, D. E., et al. (1999). A classification scheme for deep seafloor habitats. *Oceanol. Acta* 22, 663–678. doi: 10.1016/S0399-1784(00)88957-4

Guinan, J., Grehan, A. J., Dolan, M. F. J., and Brown, C. (2009). Quantifying relationships between video observations of cold-water coral cover and seafloor features in rockall trough, west of Ireland. *Mar. Ecol. Prog. Ser.* 375, 125–138. doi: 10.3354/meps07739

Hendrickx, M., Brusca, R., Cordero, M., and Ramírez, R. G. (2007). Marine and brackish-water molluscan biodiversity in the Gulf of California, Mexico. *Sci. Mar.* 71, 637–647. doi: 10.3989/scimar.2007.71n4637

Hendrickx, M., Valentich-Scott, P., and Suárez-Mozo, N. (2016). Deep-water bivalve mollusks collected during the TALUD XV cruise off the west coast of the southern Baja California Peninsula, Mexico. *Biodivers. Data J.* 4, e8661. doi: 10.3897/BDJ.4.e8661

Hendrickx, M. E. (1996). Habitats and biodiversity of decapod crustaceans in the SE Gulf of California, México. *Rev. Biol. Trop.* 44, 603–617.

Hendrickx, M. E. (2006). Occurrence of a continental slope decapod crustacean community along the edge of the minimum oxygen zone in the south eastern Gulf of California. *Mexico. Belg. J. Zool.* 131, 95–110.

Hendrickx, M. E., Salgado-Barragán, J., Toledano-Granados, A., and Cordero-Ruiz, M. (2014). Los moluscos (Pelecypoda, Gastropoda, Cephalopoda, Polyplacophora y Scaphopoda) recolectados en el SE del golfo de California durante las campañas SIPCO a bordo del B/O "El Puma". Elenco faunístico. *Rev. Mex. Biodivers.* 85, 682–722. doi: 10.7550/rmb.43077

Hendrickx, M. E., and Serrano, D. (2014). Effects of the oxygen minimum zone on squat lobster distributions in the Gulf of California, Mexico. *Cent. Eur. J. Biol.* 9, 92–103. doi: 10.2478/s11535-013-0165-6

Hernández-Alcántara, P., Salas-de León, D. A., Solís-Weiss, V., and Monreal-Gómez, M. A. (2014). Bathymetric patterns of polychaete (Annelida) species

richness in the continental shelf of the Gulf of California, Eastern Pacific. *J. Sea Res.* 91, 79–87. doi: 10.1016/j.seares.2014.04.012

Hinojosa-Corona, A. (2014). "Explorando el mar de Cortés profundo," in *Explorando el Mar Profundo del Golfo de California 2008-2014*, eds B. E. Mejía-Mercado, A. Hinojosa-Corona, and M. E. Hendrickx, (Ensenada: CICESE), 1–24.

Howell, K. L., Piechaud, N., Downie, A. L., and Kenny, A. (2016). The distribution of deep-sea sponge aggregations in the North Atlantic and implications for their effective spatial management. *Deep. Res. Part I Oceanogr. Res. Pap.* 115, 203–220. doi: 10.1016/j.dsr.2016.07.005

Huvenne, V. A. I., Bett, B. J., Masson, D. G., Le Bas, T. P., and Wheeler, A. J. (2016). Effectiveness of a deep-sea cold-water coral Marine protected area, following eight years of fisheries closure. *Biol. Conserv.* 200, 60–69. doi: 10.1016/J.BIOCON.2016.05.030

Jacobsen Stout, N., Kuhnz, L., Lundsten, L., Schlining, B., Schlining, K., and Von Thun, S. (2015). *The Deep-Sea Guide (DSG). Monterey Bay Aquarium Research Institute (MBARI)*. Available at: http://dsg.mbari.org/dsg/home (accessed September 14, 2018).

Kazanidis, G., Vad, J., Henry, L. A., Neat, F., Berx, B., Georgoulas, K., et al. (2019). Distribution of deep-sea sponge aggregations in an area of multisectoral activities and changing oceanic conditions. *Front. Mar. Sci.* 6:163. doi: 10.3389/fmars.2019.00163

Kluesner, J. (2011). *Marine Geophysical Study of Cyclic Sedimentation and Shallow Sill Intrusion in the Floor of the Central Gulf of California*. San Diego, CA: University of California.

Krebs, C. (1999). *Ecological Methodology*, 2nd Edn, Amsterdam: Benjamin.

Kurnosov, V., and Blinova, E. (2015). Hydrothermal alteration of sediments and compositional evolution of solutions in the Guaymas basin of the Gulf of California. *Dokl. Earth Sci.* 461, 217–220. doi: 10.1134/S1028334X15030149

Laguionie-Marchais, C., Kuhnz, L. A., Huffard, C. L., Ruhl, H. A., and Smith, K. L. (2015). Spatial and temporal variation in sponge spicule patches at Station M, northeast Pacific. *Mar. Biol.* 162, 617–624. doi: 10.1007/s00227-014-2609-1

Lavín, M. F., and Marinone, S. G. (2003). "An overview of the physical oceanography of the gulf of california," in *Nonlinear Processes in Geophysical Fluid Dynamics*, eds O. U. Velasco-Fuentes, J. Sheinbaum, and J. L. Ochoa de la Torre, (Berlin: Kluwer Academic Publishers), 173–204. doi: 10.1007/978-94-010-0074-1_11

Legendre, P., and Legendre, L. (2012). *Numerical Ecology. Developments in Environmental Modeling*, 3rd Edn. Amsterdem: Elsevier.

Levin, L. (2003). Oxygen minimum zone benthos: adaptation and community response to hypoxia. *Oceanogr. Mar. Biol. Annu. Rev.* 41, 1–45.

Levin, L. A., Etter, R. J., Rex, M. A., Gooday, A. J., Smith, C. R., Pineda, J., et al. (2001). Environmental influences on regional deep-sea species diversity. *Annu. Rev. Ecol. Syst.* 32, 51–93. doi: 10.1146/annurev.ecolsys.32.081501.114002

Levin, L. A., and Gage, J. D. (1998). Relationships between oxygen, organic matter and the diversity of bathyal macrofauna. *Deep Sea Res. Part II Top. Stud. Oceanogr.* 45, 129–163. doi: 10.1016/s0967-0645(97)00085-4

Levin, L. A., Gage, J. D., Martin, C., Lamont, P. A., Levin, J. D., Gage, L. A., et al. (2000). Macrobenthic community structure within and beneath the oxygen minimum zone, NW Arabian Sea. *Deep Res. II* 47, 189–226. doi: 10.1016/S0967-0645(99)00103-4

Levin, L. A., Sibuet, M., Gooday, A. J., Smith, C. R., and Vanreusel, A. (2010). The roles of habitat heterogeneity in generating and maintaining biodiversity on continental margins: An introduction. *Mar. Ecol.* 31, 1–5. doi: 10.1111/j.1439-0485.2009.00358.x

Lluch-Cota, S. E., Aragón-Noriega, E. A., Arreguín-Sánchez, F., Aurioles-Gamboa, D., Jesús Bautista-Romero, J., Brusca, R. C., et al. (2007). The Gulf of California: review of ecosystem status and sustainability challenges. *Prog. Oceanogr.* 73, 1–26. doi: 10.1016/j.pocean.2007.01.013

Lonsdale, P. (1989). "Geology and tectonic history of the Gulf of California," in *The Eastern Pacific Ocean and Hawaii. The Geology of North America*, eds E. L. Winterer, D. M. Hussong, and R. W. Decker, (Boulder, CO: Geological Society of America), 499–521. doi: 10.1130/dnag-gna-n.499

Lorance, P., and Trenkel, V. M. (2006). Variability in natural behaviour, and observed reactions to an ROV, by mid-slope fish species. *J. Exp. Mar. Bio. Ecol.* 332, 106–119. doi: 10.1016/j.jembe.2005.11.007

Marshal, B., and Richer de Forges, B. (eds) (2004). *Tropical Deep-Sea Benthos*. Paris: Muséum national d'Histoire naturelle.

Matias, M. G., Underwood, A. J., Hochuli, D. F., and Coleman, R. A. (2010). Independent effects of patch size and structural complexity on diversity of benthic macroinvertebrates. *Ecology* 91, 1908–1915. doi: 10.1890/09-1083.1

McArthur, M. A., Brooke, B. P., Przeslawski, R., Ryan, D. A., Lucieer, V. L., Nichol, S., et al. (2010). On the use of abiotic surrogates to describe marine benthic biodiversity. *Estuar. Coast. Shelf Sci.* 88, 21–32. doi: 10.1016/j.ecss.2010.03.003

Mejía-Mercado, B. E., Hinojosa-Corona, A., and Hendrickx, M. E. (eds) (2014). *Explorando el Mar Profundo del Golfo de California 2008-2014*. Mexico: CICESE, 245.

Méndez, N. (2007). Relationships between deep-water polychaete fauna and environmental factors in the southeastern Gulf of California, Mexico. *Sci. Mar.* 71, 605–622. doi: 10.3989/scimar.2010.74n1025

NOAA Office of Ocean Exploration and Research (2018). *Benthic Deepwater Animal Identification Guide*. Available online at: https://oceanexplorer.noaa.gov/okeanos/animal_guide/animal_guide.html (accessed September 14, 2018).

Norse, E. A. (1993). *Global Marine Biological Diversity*. Switzerland: IUCN.

OBIS (2019). *Ocean Biogeographic Information System*. Available online at: https://obis.org/ (accessed June 2, 2019).

Páez-Osuna, F., Sanchez-Cabeza, J. A., Ruiz-Fernández, A. C., Alonso-Rodríguez, R., Piñón-Gimate, A., Cardoso-Mohedano, J. G., et al. (2016). Environmental status of the Gulf of California: a review of responses to climate change and climate variability. *Earth Sci. Rev.* 162, 253–268. doi: 10.1016/j.earscirev.2016.09.015

Papiol, V., and Hendrickx, M. E. (2016). Community structure of deep-water decapod crustaceans below the oxygen minimum zone in the south-east Gulf of California and analysis of environmental drivers. *Mar. Freshw. Res.* 67, 1862–1879. doi: 10.1071/MF15040

Pierdomenico, M., Martorelli, E., Dominguez-Carrió, C., Gili, J. M., and Chiocci, F. L. (2016). Seafloor characterization and benthic megafaunal distribution of an active submarine canyon and surrounding sectors: the case of Gioia Canyon (Southern Tyrrhenian Sea). *J. Mar. Syst.* 157, 101–117. doi: 10.1016/j.jmarsys.2016.01.005

Pilgrim, D. A., Parry, D. M., Jones, M. B., and Kendall, M. A. (2000). ROV image scaling with laser spot patterns. *Underw. Technol.* 24, 93–103. doi: 10.3723/175605400783259684

Porteiro, F. M., Gomes-Pereira, J. N., Pham, C. K., Tempera, F., and Santos, R. S. (2013). Distribution and habitat association of benthic fish on the Condor seamount (NE Atlantic, Azores) from in situ observations. *Deep Res. Part II Top. Stud. Oceanogr.* 98, 114–128. doi: 10.1016/j.dsr2.2013.09.015

Ramirez-Llodra, E., Company, J. B., Sardà, F., and Rotllant, G. (2010). Megabenthic diversity patterns and community structure of the Blanes submarine canyon and adjacent slope in the Northwestern Mediterranean: a human overprint? *Mar. Ecol.* 31, 167–182. doi: 10.1111/j.1439-0485.2009.00336.x

Roberts, J. M., Wheeler, A. J., Freiwald, A., and Cairns, S. (2009). *Cold-Water Corals*. Cambridge: Cambridge University Press.

Roden, G. I. (1958). Oceanographic and meteorological aspects of the Gulf of California. *Pac. Sci.* 12, 21–45.

Rogers, A. D. (2000). The role of the oceanic oxygen minima in generating biodiversity in the deep sea. *Deep Res. Part II Top. Stud. Oceanogr.* 47, 119–148. doi: 10.1016/S0967-0645(99)00107-1

Rowden, A. A., Leduc, D., Clark, M. R., and Bowden, D. A. (2016). Habitat differences in deep-sea megafaunal communities off New Zealand: implications for vulnerability to anthropogenic disturbance and management. *Front. Mar. Sci.* 3:241. doi: 10.3389/fmars.2016.00241

Ruppert, E. E., and Barnes, R. D. (1996). *Zoología de los Invertebrados*. New York, NY: McGraw-Hill Interam.

Rusnak, G. A., Fisher, R. L., and Shepard, F. P. (1964). "Bathymetry and faults of Gulf of California," in *Marine Geology of the Gulf of California*, eds T. van Andel, and G. G. Shor, (Wisconsin: The American Association of Petroleum Geologists), 50–75.

Sanders, H. L. (1968). Marine benthic diversity: a comparative study. *Science* 102, 243–282. doi: 10.1086/282541

Santamaría-del-Angel, E., Alvarez-Borrego, S., and Müller-Karger, F. E. (1994). Gulf of California biogeographic regions based on coastal zone color scanner imagery. *J. Geophys. Res.* 99:7411. doi: 10.1029/93JC02154

Schlacher, T., Schlacher-Hoenlinger, M., Williams, A., Althaus, F., Hooper, J., and Kloser, R. (2007). Richness and distribution of sponge megabenthos in continental margin canyons off southeastern Australia. *Mar. Ecol. Prog. Ser.* 340, 73–88. doi: 10.3354/meps340073

Schlacher, T. A., Williams, A., Althaus, F., and Schlacher-Hoenlinger, M. A. (2010). High-resolution seabed imagery as a tool for biodiversity conservation planning on continental margins. *Mar. Ecol.* 31, 200–221. doi: 10.1111/j.1439-0485.2009.00286.x

Sokolova, M. (2000). *Feeding and Trophic Structure of the Deep-Sea Macrobenthos*. Cambridge: Science Publishers, Inc.

Solís-Marín, F. A., Laguarda-Figueras, A., Durán-González, A., Ahearn, C. G., and Torres Vega, J. (2005). Echinoderms (Echinodermata) from the Gulf of California, Mexico. *Rev. Biol. Trop.* 53(Suppl. 3), 123–137.

Solís-Marín, F. A., Laguarda-Figueras, A., and Honey-Escandón, M. (2014). Biodiversidad de equinodermos (Echinodermata) en Mexico. *Rev. Mex. Biodivers.* 85, 441–449. doi: 10.7550/rmb.31805

Spanier, E., Cobb, J. S., and Clancy, M. (1994). Impacts of remotely operated vehicles (ROVs) on the behavior of marine animals: an example using American lobsters. *Mar. Ecol. Prog. Ser.* 104, 257–266. doi: 10.3354/meps104257

Storlazzi, C. D., Dartnell, P., Hatcher, G. A., and Gibbs, A. E. (2016). End of the chain? Rugosity and fine-scale bathymetry from existing underwater digital imagery using structure-from-motion (SfM) technology. *Coral Reefs* 35, 889–894. doi: 10.1007/s00338-016-1462-8

Tapia de la Yossellin, O. (2018). *Ofiuroideos (Echinodermata) de hábitats con características para la conservación de Cuencas hipóxicas del Golfo de California*. 222. M.S. thesis, Universidad Nacional Autónoma de México, Mexico.

Teske, A., De Beer, D., McKay, L. J., Tivey, M. K., Biddle, J. F., Hoer, D., et al. (2016). The Guaymas Basin hiking guide to hydrothermal mounds, chimneys, and microbial mats: complex seafloor expressions of subsurface hydrothermal circulation. *Front. Microbiol.* 7:75. doi: 10.3389/fmicb.2016.00075

Tyler, P. A., Baker, M., and Ramirez-Llodra, E. (2016). "Deep-Sea benthic habitats," in *Biological Sampling in the Deep Sea*, eds M. R. Clark, C. Mireille, and A. A. Rowden, (Hoboken: John Wiley & Sons, Ltd.), 1–15. doi: 10.1002/9781118332535.ch1

Underwood, A. J. (2006). *Experiments in Ecology*, 9th Edn, Cambridge: Cambridge University Press.

van den Beld, I. M. J., Bourillet, J.-F., Arnaud-Haond, S., de Chambure, L., Davies, J. S., Guillaumont, B., et al. (2017). Cold-water coral habitats in submarine canyons of the bay of biscay. *Front. Mar. Sci.* 4:118. doi: 10.3389/fmars.2017.00118

Villalobos Vazquez de la Parra, R. (2014). *Diversidad y Distribución de la Megafauna Bentónica en el norte del Golfo de California (Isla Tortuga, Cuenca de Guaymas, Salsipuedes y Delfín)*. 100. M.S. thesis, Universidad Nacional Autónoma de México, Mexico.

WoRMS Editorial Board, (2018). *World Register of Marine Species*. Belgium: WoRMS Editorial Board.

Zamorano, P., and Hendrickx, M. E. (2012). Distribution of *Lucinoma heroica* (Mollusca: Bivalvia: Lucinidae) in the minimum oxygen zone in the Gulf of California, Mexico. *Mar. Biodivers. Rec.* 5, 1–8. doi: 10.1017/S1755267212000644

Zamorano, P., Hendrickx, M. E., and Toledano-Granados, A. (2007). Distribution and ecology of deep-water mollusks from the continental slope, southeastern Gulf of California, Mexico. *Mar. Biol.* 150, 883–892. doi: 10.1007/s00227-006-0390-5

Conflict of Interest: The authors declare that the research was conducted in the absence of any commercial or financial relationships that could be construed as a potential conflict of interest.

Copyright © 2020 Lopez-Garrido, Barry, González-Gordillo and Escobar-Briones. This is an open-access article distributed under the terms of the Creative Commons Attribution License (CC BY). The use, distribution or reproduction in other forums is permitted, provided the original author(s) and the copyright owner(s) are credited and that the original publication in this journal is cited, in accordance with accepted academic practice. No use, distribution or reproduction is permitted which does not comply with these terms.

frontiers in Marine Science

BRIEF RESEARCH REPORT
published: 05 May 2020
doi: 10.3389/fmars.2020.00288

Control of Deep Currents on Sediment and Cold-Water Coral Distribution on the Northern Manihiki Plateau

Sara Bashah[1], Kimberly C. Galvez[1], Gregor P. Eberli[1] and Kasey Cantwell[2,3]*

[1] Comparative Sedimentology Laboratory – Center for Carbonate Research, Rosenstiel School for Marine and Atmospheric Science, University of Miami, Miami, FL, United States, [2] Office of Ocean Exploration and Research, National Oceanic and Atmospheric Administration, U.S. Department of Commerce, Silver Spring, MD, United States, [3] Cherokee Nation Strategic Programs, Arlington, VA, United States

High-definition video surveys of remotely-operated vehicle (ROV) dives from the NOAA's Mountains in the Deep 2017 expedition (EX1705) along volcanic ridges and seamounts of the Manihiki Plateau coupled with multibeam bathymetry data and water column profiles, reveal no or minimal sediment cover on the basaltic edifice, but variable amounts of cold-water corals on ferromanganese-encrusted basaltic rocks. Coarse sediment, however, accumulates in crevasses and sedimentary ripples testify the existence of currents in the area. Collectively, these observations illustrate the strong influence of deep currents on the surficial geology and cold-water coral distribution at ∼2,000 m water depths. Dive transects along two basaltic seamounts show stark differences of sedimentary features and cold-water coral distribution. On the ridges of "Te Kawhiti" (water depth: 2,089–2,220 m), basaltic slabs, and cold-water corals are far more abundant in comparison to the slope of a mesa in "Te Tuku" (water depth: 2,440–2,495 m). The increased abundance on "Te Kawhiti" is due to the exposure of "Te Kawhiti" to Lower Circumpolar Deep Water that sweeps the summit of the ridges as indicated by frequent ripples observed in between the basaltic rocks. The currents are strong enough to sweep fine-grained sediments away, leaving coarse-grained sediments behind, inducing the formation of ferromanganese crust on the basaltic rocks. Both dive sites are below the high-Mg calcite saturation horizon, and as a result, the cold-water coral community is dominated by Isididae, which can build a high-Mg calcite skeleton in water undersaturated in regards to high-Mg calcite.

Keywords: seamounts, current deposits, cold-water corals, high-Mg calcite saturation horizon, Lower Circumpolar Deep Water

OPEN ACCESS

Edited by:
Jose Angel Alvarez Perez, Universidade do Vale do Itajaí, Brazil

Reviewed by:
Tina Molodtsova, P.P. Shirshov Institute of Oceanology (RAS), Russia
Ian David Tuck, National Institute of Water and Atmospheric Research (NIWA), New Zealand

****Correspondence:***
Sara Bashah
nbashah@rsmas.miami.edu

Specialty section:
This article was submitted to Deep-Sea Environments and Ecology, a section of the journal Frontiers in Marine Science

Received: *15 June 2019*
Accepted: *08 April 2020*
Published: *05 May 2020*

Citation:
Bashah S, Galvez KC, Eberli GP and Cantwell K (2020) Control of Deep Currents on Sediment and Cold-Water Coral Distribution on the Northern Manihiki Plateau. Front. Mar. Sci. 7:288. doi: 10.3389/fmars.2020.00288

INTRODUCTION

Seamounts are isolated topographic elevations with summit depths at least 1,000 m above the seafloor, which includes large plateaus and platforms. Seamounts have a significant effect on circulation patterns and currents locally and regionally, influencing the morphology and sedimentology of the surrounding seafloor (Batiza, 2001; Rogers, 2013). On seamounts, sediments accumulate from settling particles through the water column, forming a drape of pelagic ooze. The Manihiki Plateau formed by volcanic activity approximately 125 million years ago as part of the

giant Ontong Java-Manihiki-Hikurangi plateau in the Pacific Ocean (Pietsch and Uenzelmann-Neben, 2015; Timm et al., 2011). The sediment accumulation rate at the Manihiki Plateau is 10 m/million year and, in some areas in the deep troughs, up to 1 km of sediments were accumulated due to redeposition of plateau sediments by slumps and turbidity currents (Winterer et al., 1974). In other areas, however, the seamounts consist of bare basaltic rocks with little to no sediment cover, indicating that sediment falling through the water column is swept off the basaltic edifice by deep ocean currents.

This study focuses on two such areas along the Northern Manihiki Plateau surveyed during the Mountains in the Deep 2017 expedition (EX1705) – the slope of the "Te Tuku" mesa and the summit of "Te Kawhiti" ridges. These sites were selected from the National Oceanic and Atmospheric Administration's Campaign to Address Pacific monument Science, Technology, and Ocean NEeds (CAPSTONE; Kennedy et al., 2019). We rely on multibeam bathymetry, conductivity, temperature, and depth (CTD) data, and remotely-operated vehicle (ROV) video footage to show the influence of currents conditions on the sediment accumulation and Isididae occurrences in water depths below the high-Mg calcite saturation horizon (HMCSH). Isididae or "bamboo-corals" are octocorals characterized by their calcite internodes alternating with organic nodes skeletal arrangements, resembling bamboo plants (Grant, 1976; France, 2007). The calcitic part of the skeleton are made of high-Mg calcite fibers and granular crystals which are precipitated from the surrounding seawater dissolved inorganic carbon (Roark et al., 2005; Noé and Dullo, 2006).

We map the seafloor facies and fauna along two dive transects with the goal of investigating the relationship between the sediments and Isididae distribution with the current conditions in the Northern Manihiki Plateau. Observations from the ROV also document a viable community of Isididae found below 2,000 m on a seamount-ridge. We further outline possible processes of how the isidids can precipitate their skeleton in the high-Mg calcite undersaturated seawater.

STUDY AREA

The Manihiki Plateau is a ∼600,000 km^2 section of elevated ocean floor in the western equatorial Pacific Ocean (**Figure 1A**), surrounded by approximately 6-km-deep basins, which include the Penrhyn Basin to the east, Samoan Basin to the southwest, Tokelau Basin to the northwest, and the Central Basin of the Pacific to the north (Heezen et al., 1966; Winterer et al., 1974). The Lower Circumpolar Deep Water (LCDW), which enters the Pacific basin southeast of New Zealand as a deep western boundary current and flows northward, touches the Manihiki Plateau and the two dive sites (**Figure 1B**; Kawabe and Fujio, 2010). "Te Tuku" is located at the leeward of the LCDW, while "Te Kawhiti" is located facing the LCDW flow direction. Within the water masses of the southwest Pacific are levels of chemical concentrations in seawater that directly affect the surrounding environment. The aragonite saturation horizon (ASH) and the calcite saturation horizon (CSH) fall under this category. Below the ASH is the depth at which the seawater becomes undersaturated with respect to aragonite. The CSH is similar to the ASH, except it is for all calcite concentrations; usually, the CSH is at a greater depth than that of the ASH due to the increased solubility of aragonite. The ASH in the Southwest Pacific is ∼200 to 1,320 m (Feely et al., 2002), while the CSH is at ∼2,800 m water depth (Feely et al., 2002; Bostock et al., 2011). The solubility of high-Mg calcite is similar to or slightly higher than aragonite, which is between 1 and 1.5 km (Morse et al., 2006). Calcifying organisms that use carbonate concentrations in seawater to produce their skeletons are limited to depths that are above the ASH or CSH, respectively (Feely et al., 2002).

MATERIALS AND METHODS

Bathymetric data, ROV videos and images, and CTD data were used from two dives in the Northern Manihiki Plateau at sites named in consultation with the Office of the Prime Minister in the Cook Islands and Ui Ariki Ngateteitei o Te Kuki Airani (The Paramount Kings and Queens of the Cook Islands) "Te Tukunga o Fakahotu" ("Te Tuku") and "Te Kawhiti a Maui Potiki" ("Te Kawhiti"). The two dives were conducted using the ROV *Deep Discoverer* and a camera and lighting platform, ROV *Seirios*. The ROVs captured high-definition videos, collected both biological and geological samples, and measured parameters such as salinity, water temperature, depth, and dissolved oxygen using on-board sensors. The "Te Tuku" dive (Dive 02) was conducted from 2,440 to 2,495 m, and the "Te Kawhiti" dive (Dive 03) from 2,089 to 2,220 m. The seafloor bathymetry was mapped using a Kongsberg EM302 multibeam system and analyzed using Fledermaus software (**Figures 1C,D**). Conductivity, temperature, and depth measurements from the ROV determined general water mass characteristics and the influence of physical parameters of water masses (**Figures 1E,F**). Current measurements were conducted with an acoustic doppler current profiler (ADCP) mounted to the ship measuring currents in the top 600 m of the water column and, thus, did not provide information at study sites more than 2 km deep. However, the direction of the ripples observed at the dive sites are in concert with the direction of current measured from ADCP. Cold-water corals and associated surficial sedimentary facies distribution were analyzed from the ROV videos and images (Cantwell et al., 2017). The mapping of the cold-water corals focuses on the distribution of the Isididae as their skeleton is made up of high-Mg calcite.

RESULTS

Bathymetric Settings of the Dives Location

The elongated mesa of "Te Tuku" is 82 km-long, 15 km-wide, and 2,300 m-tall. The mesa shows a tapered shape with the northwest end being the widest section and narrowing to the southeast. The dive on the eastern slope of the mesa moved up the slope from 2,495 to 2,440 m water depth, covering roughly 60 m of water

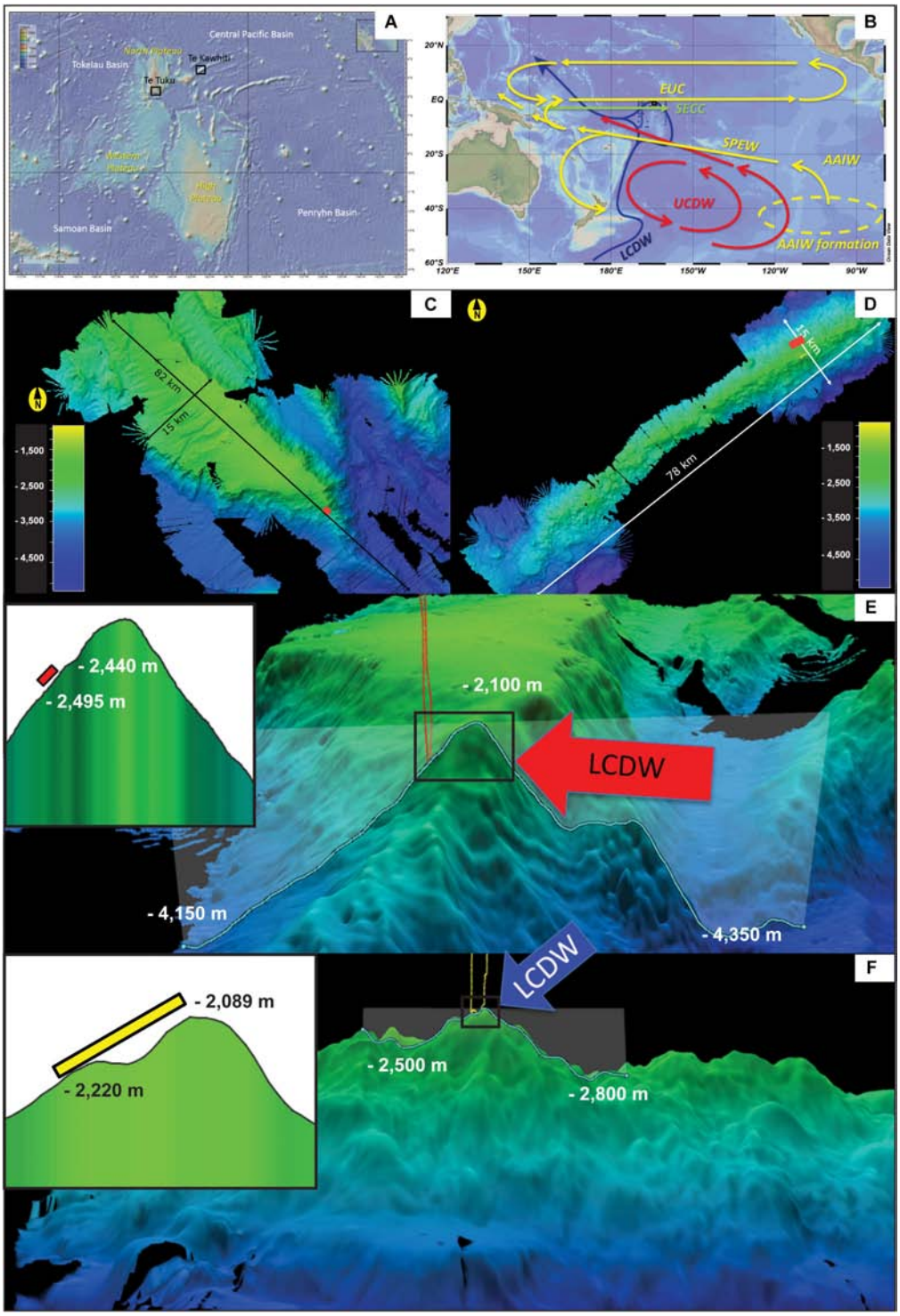

FIGURE 1 | (A) Map of the Northern Manihiki Plateau displaying ROV dives location in black boxes. Plateau regions are labeled in yellow and basins are in white. **(B)** Map from Ocean Data View showing main circulation patterns and directions (according to Kawabe and Fujio, 2010 and Werner et al., 2013) are displayed with green arrows (<1,000 m water depth) yellow arrows (1,000–1,500 m water depth), red arrows (1,500–3,000 m water depth), and blue arrows (bottom water, >3,000 m water depth). Yellow oval indicates the AAIW formation region. Water masses in the area are AAIW, Antarctic Intermediate Water; UCDW, Upper Circumpolar Deep Water; LCDW, Lower Circumpolar Deep Water; SPEW, South Pacific Equatorial Water; EUC, Equatorial Undercurrent and SECC: south Equatorial Counter Current (modified from Molina-Kescher et al., 2018). Blue dots represent CTD data available from the World Ocean Database (Boyer et al., 2018). **(C)** Bathymetry of the "Te Tuku" mesa. **(D)** Bathymetry of the "Te Kawhiti" ridges. **(E)** Cross-section of the mesa at "Te Tuku" with dive transect (black box) and LCDW direction (red arrow). **(F)** Cross-section of seamounts summit at Te Kahwiti with dive transect marked in black box LCDW direction (blue arrow).

depth. The slope angles of the dive transect range from 12° to 22° (**Figures 1C,E**).

The Te Kawhiti ridge is 78 km-long, 17 km-wide, and 2,300 m-tall with a series of peaks. The dive began on the southwest side of the ridge, following the slope upward, then along the crest of the ridge for 160 m reaching the summit of a local high point on the ridge crest. The slope angles at the dive sites ranged from −3° to 23° (**Figures 1D,F**).

Physical Water Mass Properties

Different water masses exist in the Manihiki Plateau area based on the temperature–salinity (T-S) plot from the ROV CTD and CTD data from Boyer et al. (2018). From the surface down, the water masses are the South Equatorial Counter Current (SECC), the Equatorial Undercurrent (EUC), Antarctic Intermediate Water (AAIW), South Pacific Equatorial Water (SPEW), Upper Circumpolar Deep Water (UCDW), and LCDW. Both dive locations are located in the range of the LCDW (Tomczak and Godfrey, 2003; Kawabe and Fujio, 2010; Hartin et al., 2011; **Figures 2A1,2**).

The vertical profiles of the ROV CTD show that throughout the dives, the LCDW temperature varied between 1.5 and 2.5°C, with average temperatures at "Te Kawhiti" warmer by 1°C than at "Te Tuku." The salinity recorded throughout both dives were quite uniform at 34.5 PSU. Oxygen saturation at "Te Tuku" ranged from 125 to 130 μmol/kg but was uniform at 116 μmol/kg at "Te Kawhiti" (**Figures 2B1,2**). Both dives are located below the HMCSH (**Figure 2B**). Assuming that the current at 2,000–2,500 m is in the same direction as measured with ADCP at 600 m, the "Te Tuku" dive is located on the "leeward" side of the northeast bottom current flow. At "Te Kawhiti," where the dive path is perpendicular to the south-flowing LCDW (**Figure 2A3**).

Video Footage-Based Mapping

The video footage from ROV *Deep Discoverer* reveals the basaltic basement, some sediment coverage, and a variable amount of cold-water corals. The facies of the seascape is divided into eight groups: basaltic cobbles, boulders and slabs, coarse sands, coral debris, ripples, living single Isididae, and living Isididae thickets (**Figure 3**).

"Te Tuku"

Figure 4A displays the distribution of the basaltic basement, sediments, and Isididae along the dive path at "Te Tuku." The substrate along this dive consists only of cobbles and boulders. Coarse sediments fill the depressions in between these substrates, but the sediments do not cover the cobbles and boulders. Asymmetric ripples in coarse sand layers were observed only once at 2,455 m water depth. Living single Isididae are found at 2,440, 2,460, and 2,490 m water depths.

"Te Kawhiti"

Figure 4B displays the distribution of the basaltic basement, sediments, and Isididae along the dive path at "Te Kawhiti." The substrate observed along this dive consists of cobbles, boulders, and basaltic slabs. Coarse sediments fill the depressions in between the substrates and covers them. Ripple structures are present frequently along the dive path, except on the steeper slope toward the summit of the ridge. Isididae thrive as thickets along the dive except at 2,220 m water depth. Here, the Isididae live as singles between coarse sands and coral debris. Coral debris is sparse but is observed at 2,160 and 2,135 m water depths.

Difference Between the Two Sites

Although the morphology of the "Te Tuku" mesa and the "Te Kawhiti" ridges are different, the bedrock at both locations is composed of ferromanganese-encrusted basaltic rocks. The slope of the "Te Tuku" mesa consists of scattered basaltic cobbles and boulders lying exposed on soft sediments with depressions infilled with trapped sediment (**Figures 3A,B**). In contrast, the ridges of "Te Kawhiti" are dominated by large basaltic slabs that exhibit a smooth surface with small crevices infilled with sediment (**Figure 3C**).

Three main sediment features are observed: coarse sands, ripples, and rare coral debris. Coarse sands, likely consisting of foraminifera and ossicles of carbonate-secreting organisms, are deposited between the basaltic boulders and cobbles (**Figure 3D**). Little to no sediment accumulates on top of the boulders. The carbonate sands sometimes form small, symmetric current ripples between the boulders (**Figure 3H**). In one area at "Te Kawhiti," the ripples are arranged in a fan-like pattern, indicating that a strong current that is deflected by the topography of the seamounts. There is a stark contrast of sediment distribution in both dives; the "Te Tuku" site has a large abundance of coarse sands with no ripples and no occurrence of coral debris. At "Te Kawhiti," sediments show an abundance of ripples, some coral debris, but lack the coarse sand (**Figures 3**, **4**).

Among various types of biota observed, cold-water corals were abundant. The identification of coral species based solely on video footage is difficult, but based on the combined observations of onboard and shore-based EX1705 deep-sea biologists, cold-water corals along the dives include Isididae, *Paragorgia*, Zoantharia, and Antipatharia. As with the sediments and substrates, we observed a significant contrast in Isididae occurrences. At the slope of the "Te Tuku" mesa, solitary Isididae corals live on the basaltic cobbles and boulders. No coral thickets were observed. In contrast, Isididae thickets thrive and are well-distributed along the summit of the ridge at "Te Kawhiti" from 2,089 to 2,220 m depth (**Figures 3F**, **4B**). Many of these thickets are taller than the ROV *Deep Discoverer* (2.6 m tall). In areas with coarse mobile sands, generally no corals were observed, but few living single Isididae and coral debris were found at depths greater than 2,200 m (**Figure 4**).

DISCUSSION

Sedimentological Features as Indicators of Current Strength and Direction

At the two sites, there is a stark contrast in the distribution of coarse carbonate sand. The coarse sand layers at "Te Tuku" have asymmetric ripples that indicate a southward direction of the current. Ripples in such coarse-grained sediments are formed by currents, with a strength that likely reaches up to 0.5 m/s

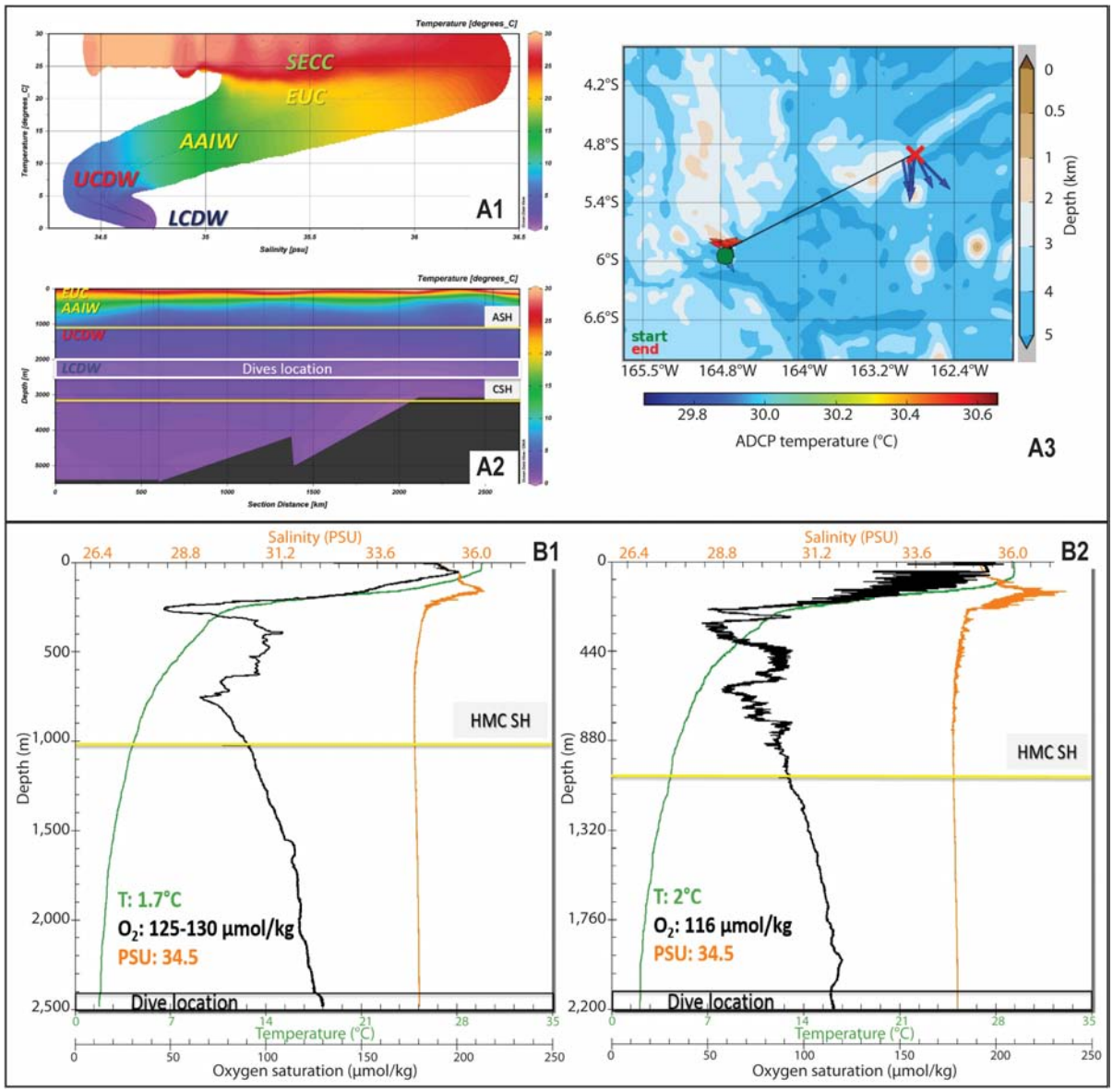

FIGURE 2 | Current data at the dives transect **(A1)** Temperature-salinity diagram with water masses identified. AAIW, Antarctic Intermediate Water; UCDW, Upper Circumpolar Deep Water; LCDW, Lower Circumpolar Deep Water; SPEW, South Pacific Equatorial Water; EUC, Equatorial Undercurrent, and SECC, South Equatorial Counter Current. **(A2)** Water masses across the water depths. The dives depths are within the LCDW (white box). Yellow lines indicate the approximate depths of the aragonite saturation horizon (ASH) and calcite saturation horizon (CSH). **(A3)** Current direction of the top 600 m, collected from ADCP during EX1705. The red arrows give the temperature and shallow water current direction in "Te Tuku." The blue arrows give the temperature and shallow water current direction in "Te Kawhiti." **(B1)** and **(B2)** are ROV CTD temperature (green lines), oxygen saturation (black lines), and salinity (orange lines) profiles of "Te Tuku" dive **(B1)** and "Te Kawhiti" dive **(B2)**. High-Mg calcite saturation horizon (HMCSH) is indicated with yellow lines. Rectangular boxes at the bottom of the graphs show the dive locations.

(Stow et al., 2009; **Figures 3H**, **4B**). The limited occurrence of sand and ripples at "Te Kawhiti" implies even stronger currents on the summit of the ridges, which inhibit the deposition of sediments, causing the formation of ferromanganese crust on the basaltic rocks. The fact that the 125 million years old basaltic seamounts are not covered by sediment or diagenetically altered limestone implies that currents were sweeping the study site since their formation. The acting currents must have changed through time as the Manihiki Plateau moved with the plates in the Pacific (Winterer et al., 1974). Currents in the Pacific also change through time due to the combined result of the closure of the Tethys seaway 80 million years ago and the concomitant mixing of Atlantic and Pacific waters (Stille, 1992) and the onset of Antarctic Circumpolar Current in the Oligocene (Lyle et al., 2007). Despite these changes and the resulting changes in the strength of the current, no relict sediment beds or limestone caps were observed during the dives, indicating a permanent, strong current system at 2,000 m water depth in the Pacific

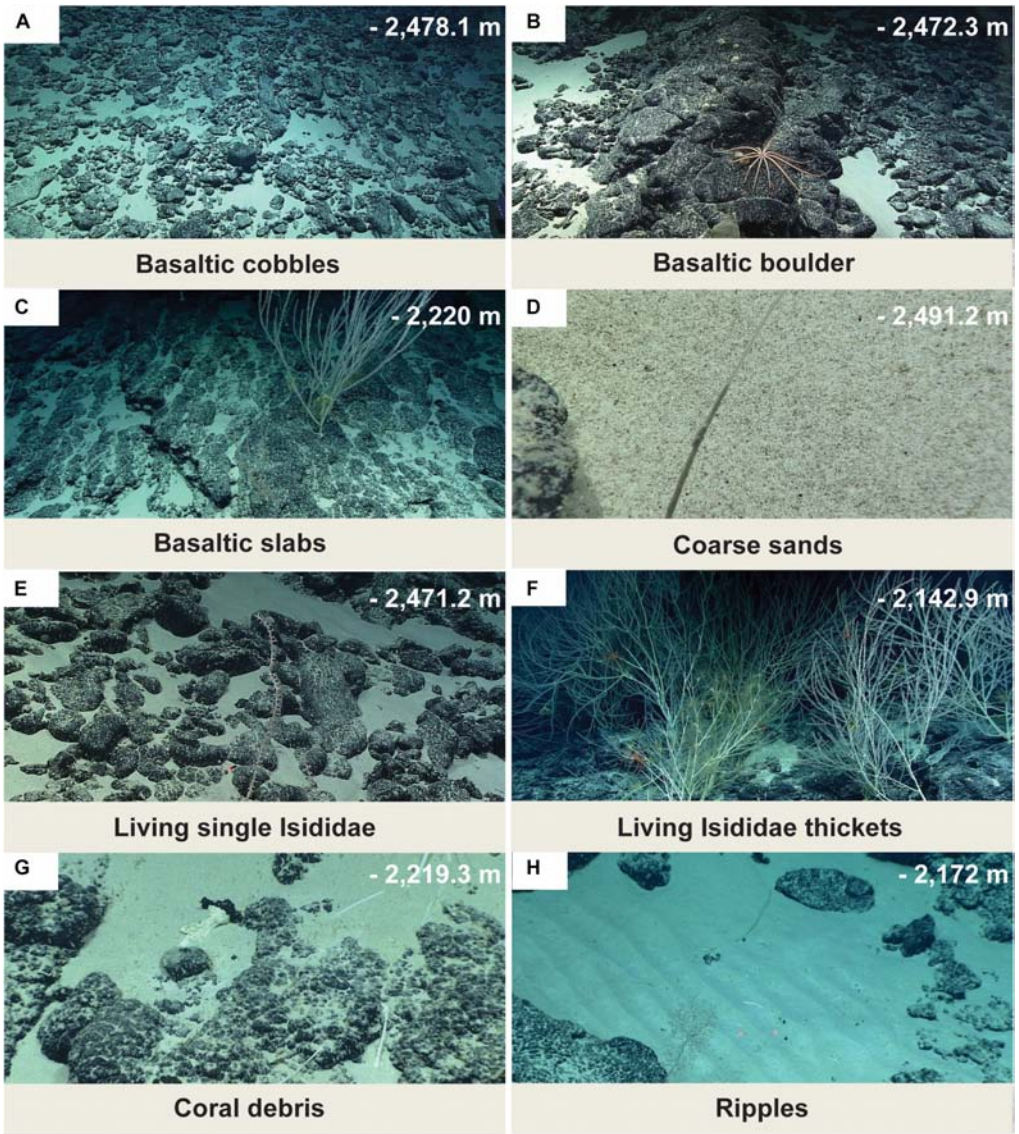

FIGURE 3 | Eight facies observed on the seafloor of the dive sites. **(A)** Ferromanganese-encrusted basaltic cobbles, **(B)** Ferromanganese-encrusted basaltic boulder, **(C)** Ferromanganese-encrusted basaltic slabs, **(D)** Coarse sands, **(E)** Living single Isididae, **(F)** Living Isididae thickets, **(G)** Coral debris, and **(H)** Ripples of coarse sediments between the basaltic boulders. Image courtesy of the NOAA's Office of Ocean Exploration and Research, Mountains in the Deep: Exploring the Central Pacific Basin.

since the Mid-Cretaceous. The current-removed sediment likely accumulates in drifts surrounding the Manihiki Plateau.

Deep Ocean Currents Control on Isididae Distribution

At both dive locations, Isididae colonize the ferromanganese-encrusted basaltic boulders and cobbles. The abundance of large slabs available in "Te Kawhiti" likely created favorable conditions for cold-water coral larvae to settle and colonize (Edinger et al., 2011; Thresher et al., 2014), although deep-water bamboo forests have been reported from muddy environments (de Moura Neves et al., 2015). The abundance of isidids coverage is markedly different at the two dive sites, likely the result of the different flow direction of the LCDW at each dive site. Isidids are suspension feeders and depend on current flow to deliver organic material to their polyps (Roark et al., 2005; Tracey et al., 2007; Hill et al., 2014). Current-facing ridge flanks are optimal for the interception of food particles, and coral colonies in this position experience higher survivorship (Dorschel et al., 2007; Correa et al., 2012). The "Te Tuku" site is on the leeward side of the current flow, while the site "Te Kawhiti" is exposed to the southward flowing current regime. As a result, isidid colonies flourish at "Te Kawhiti," reaching great heights forming thickets, while at site "Te Tuku," only individual isidids were observed. In areas of mobile sediments, no corals are present likely due to the

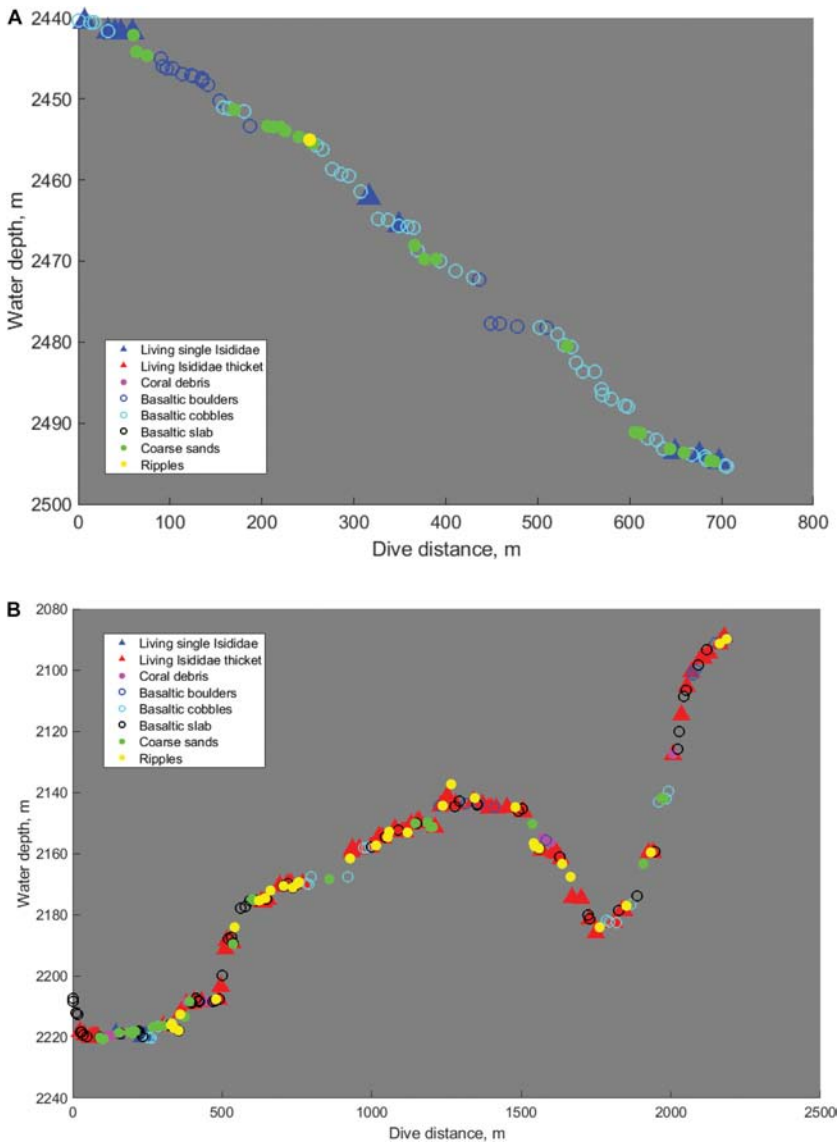

FIGURE 4 | Facies distribution along "Te Tuku" mesa **(A)** and "Te Kawhiti" ridges summit **(B)**. Red and blue filled triangles represent the occurrence of single Isididae and Isididae thickets. No Isididae thickets and basaltic slabs were observed along "Te Tuku" dive. Fewer Isididae were observed at depths where coarse sands are dominant. The substrates for the Isididae are ferromanganese-encrusted basaltic boulders, cobbles, and slabs represented in circles. Green, yellow, and magenta dots represent coarse sands, ripples, and coral debris.

combined result of (1) a lack of a stable surface for coral larvae to settle and (2) exposure to stronger currents that inhibit the settling of the coral larvae.

Isididae Growth Below the High-Mg Calcite Saturation Horizon

The solubility of high-Mg calcite is similar to or slightly higher than that of aragonite (Morse et al., 2006); hence, these dive sites are 1–1.5 km below the probable HMCSH. Despite being located below the HMCSH, cold-water corals and other carbonate secreting organisms are abundant on the seamounts and ridges visited during the Central Pacific Basin expedition (EX1705). This is possible because isidids have an absolute low tolerance limit of about 40% undersaturation as suggested by Thresher et al. (2011). The outer layer of organic tissue protecting the skeleton of live corals, and food availability facilitates the growth of isidids in the low-carbonate conditions (Cohen and Holcomb, 2009; Sherwood et al., 2009; Thresher et al., 2011).

CONCLUSION

Two dives on volcanic mesa and ridges at ∼2,000–2,500 m water depth of the Northern Manihiki Plateau give insight into the influence of deep ocean currents on sediments and Isididae

distribution. Direct evidence of persistent sweeping by the currents is given by the fact that the basaltic edifices do not exhibit pelagic drapes or remnants of old sediment cover, although they formed 125 million years ago and are subjected to pelagic sedimentation and carbonate sediment production by benthic organisms. As a result of non-deposition, ferromanganese crusts cover the basaltic cobbles, boulders, and slabs. Coarse sediments, however, accumulate in crevasses and depressions and record current activity and direction with asymmetric ripples.

The hard substrates and the currents enable cold-water corals to grow. Isidids abundance is related to the current strength with single isidids in the lee side of currents (as seen at "Te Tuku"), and thickets of isidids in the more current-exposed "Te Kawhiti" ridge summit. Here, the isidids flourish, although the sites are located below ∼2,000 m water depth and thus, below the HMCSH, where the water masses are undersaturated in regards to high-Mg calcite. The growth of isidids on these dive sites indicates that water depths is not the factor of growth for this species. A reason for the abundant growth is the food availability through the bottom currents flow at the dive sites.

DATA AVAILABILITY STATEMENT

The datasets generated for this study are available on request to the corresponding author.

AUTHOR CONTRIBUTIONS

SB contributed to the conception and design of the study. KG contributed to the oceanography and cold-water corals' section. GE contributed to concepts and all sections of the manuscript. KC contributed to the dataset and methods of the study.

FUNDING

EX1705 expedition was funded by the NOAA's Office of Ocean Exploration and Research. This organization also funded Kasey Cantwell via contract. Sara Bashah acknowledges financial support from the Schlumberger Foundation. Gregor Eberli was supported by contributions from industrial associates to the CSL – Center for Carbonate Research at the University of Miami. Kimberly Galvez received funds from a grant to Gregor Eberli.

ACKNOWLEDGMENTS

The authors thank the EX1705 *Okeanos Explorer* Program Manager, Craig Russell, and mapping lead, Michael White, from NOAA's Office of Ocean Exploration and Research for the help with the bathymetric data. The authors would also like to thank the science leads, Scott C. France from the University of Louisiana at Lafayette and Del Bohnenstiehl from the North Carolina State University, all EX1705 expedition members as well as the officers and crew of NOAA Ship *Okeanos Explorer* for the data used in the study. GE and SB thank Shirley Pomponi for inviting them to the Exploration Command Center and for the costs during their stay at the Harbor Branch Oceanographic Institute. The scientific input and stimulating discussions with her and Diva Amon helped clarify the scientific ideas.

REFERENCES

Batiza, R. (2001). Seamounts and off-ridge volcanism. *Encycl. Ocean Sci.* 5, 292–304. doi: 10.1016/B978-012374473-9.00097-7

Bostock, H. C., Hayward, B. W., Neil, H. L., Currie, K. I., and Dunbar, G. B. (2011). Deep-water carbonate concentrations in the southwest Pacific. *Deep. Res. I* 58, 72–85. doi: 10.1016/j.dsr.2010.11.010

Boyer, T. P., Baranova, O. K., Coleman, C., Garcia, H. E., Grodsky, A., Locarnini, R. A., et al. (2018). *World Ocean Database 2018*. Asheville, NC: NOAA.

Cantwell, K., France, S., and Bohnenstiehl, D. (2017). *Oceanographic data and information collected during the EX1705 American Samoa, Kingman/Palmyra, Jarvis (ROV & Mapping) expedition on NOAA Ship OKEANOS EXPLORER in the Pacific Ocean from 2017-04-27 to 2017-05-19 (NCEI Accession 0163984). [ROV DIVE02 AND DIVE 03]*. Asheville, NC: NOAA National Centers for Environmental Information.

Cohen, A. L., and Holcomb, M. (2009). Why corals care about acidification. *Oceanography* 22, 118–127.

Correa, T. B. S., Grasmueck, M., Eberli, G. P., Reed, J. K., Verwer, K., and Purkis, S. (2012). Variability of cold-water coral mounds in a high sediment input and tidal current regime. Straits of Florida. *Sedimentology* 59, 1278–1304. doi: 10.1111/j.1365-3091.2011.01306.x

de Moura Neves, B., Edinger, E. N., Hillaire-Marcel, C., Saucier, E. H., France, S. C., Treble, M. A., et al. (2015). Deep-water bamboo coral forests in a muddy Arctic environment. *Mar. Biodivers.* 45, 867–871. doi: 10.1007/s12526-014-0291-7

Dorschel, B., Hebbeln, D., Foubert, A., White, M., and Wheeler, A. J. (2007). Hydrodynamics and cold-water coral facies distribution related to recent sedimentary processes at Galway Mound west of Ireland. *Mar. Geol.* 244, 184–195. doi: 10.1016/j.margeo.2007.06.010

Edinger, E. N., Sherwood, O. A., Piper, D. J. W., Wareham, V. E., Baker, K. D., Gilkinson, K. D., et al. (2011). Geological features supporting deep-sea coral habitat in Atlantic Canada. *Cont Shelf Res.* 31, S69–S84. doi: 10.1016/j.csr.2010.07.004

Feely, R. A., Sabine, C. L., Lee, K., Millero, F. J., Lamb, M. F., Greeley, D., et al. (2002). In situ calcium carbonate dissolution in the Pacific Ocean. *Glob. Biogeochem. Cycles* 16:91. doi: 10.1029/2002GB001866

France, S. C. (2007). Genetic analysis of bamboo corals (Cnidaria: Octocorallia: Isididae): does lack of colony branching distinguish Lepidisis from Keratoisis? *Bull. Mar. Sci.* 81, 323–333.

Grant, R. (1976). *The marine fauna of New Zealand: Isididae (Octocorallia: Gorgonacea) from New Zealand and the Antarctic*. Wellington: New Zealand Oceanographic Institute Memoir.

Hartin, C. A., Fine, R. A., Sloyan, B. M., Talley, L. D., Chereskin, T. K., and Happell, J. (2011). Formation rates of Subantarctic mode water and Antarctic intermediate water within the South Pacific. *Deep Sea Res. I* 58, 524–534. doi: 10.1016/j.dsr.2011.02.010

Heezen, B. C., Glass, B., and Menard, H. W. (1966). The manihiki plateau. *Deep. Res.* 13, 445–458.

Hill, T. M., Myrvold, C. R., Spero, H. J., and Guilderson, T. P. (2014). Evidence for benthic-pelagic food web coupling and carbon export from California margin bamboo coral archives. *Biogeosciences* 11, 3845–3854. doi: 10.5194/bg-11-3845-2014

Kawabe, M., and Fujio, S. (2010). Pacific ocean circulation based on observation. *J. Oceanogr.* 66, 389–403. doi: 10.1007/s10872-010-0034-8

Kennedy, B. R. C., Cantwell, K., Malik, M., Kelley, C., Potter, J., Elliott, K. P., et al. (2019). The unknown and the unexplored: insights into the Pacific Deep Sea following NOAA CAPSTONE expeditions. *Front. Mar. Sci.* 6:180. doi: 10.3389/fmars.2019.00480

Lyle, M., Gibbs, S., Moore, T. C., and Rea, D. K. (2007). Late Oligocene initiation of the Antarctic circumpolar current: evidence from the South Pacific. *Geology* 35, 691–694. doi: 10.1130/G23806A.1

Molina-Kescher, M., Hathorne, E. C., Osborne, A. H., Behrens, M. K., Pahnke, K., Kölling, M. et al. (2018). The influence of basaltic islands on the oceanic REE distribution: a case study from the tropical south pacific. *Front. Mar. Sci.* 5:50. doi: 10.3389/fmars.2018.00050

Morse, J. W., Andersson, A. J., and Mackenzie, F. T. (2006). Initial responses of carbonate-rich shelf sediments to rising atmospheric pCO2 and "ocean acidification": role of high Mg-calcites. *Geochim. Cosmochim. Acta* 70, 5814–5830. doi: 10.1016/j.gca.2006.08.017

Noé, S. U., and Dullo, W.-C. (2006). Skeletal morphogenesis and growth mode of modern and fossil deep-water isidid gorgonians (Octocorallia) in the west Pacific (New Zealand and Sea of Okhotsk). *Coral Reefs* 25, 303–320.

Pietsch, R., and Uenzelmann-Neben, G. (2015). The Manihiki Plateau—A multistage volcanic emplacement history. *Geochem. Geophys. Geosyst.* 16, 2480–2498. doi: 10.1002/2015GC005852

Roark, E. B., Guilderson, T. P., Flood-Page, S., Dunbar, R. B., Ingram, B. L., Fallon, S. J., et al. (2005). Radiocarbon-based ages and growth rates of bamboo corals from the Gulf of Alaska. *Geophys. Res. Lett.* 32, 1–5. doi: 10.1029/2004GL021919

Rogers, A. D. (2013). *Seamounts Project: An Ecosystem Approach to Management of Seamounts in the Southern Indian Ocean*. Gland: IUCN, 60.

Sherwood, O. A., Thresher, R. E., Fallon, S. J., Davies, D. M., and Trull, T. W. (2009). Multi-century time-series of 15N and 14C in bamboo corals from deep Tasmanian seamounts: evidence for stable oceanographic conditions. *Mar. Ecol. Prog. Ser.* 397, 209–218.

Stille, P. (1992). Nd-Sr isotope evidence for dramatic changes of paleocurrents in the Atlantic Ocean during the past 80 m.y. *Geology* 20, 387–390.

Stow, D. A. V., Hernández-Molina, F. J., Llave, E., Sayago-Gil, M., Díaz-del Río, V., and Branson, A. (2009). Bedform-velocity matrix: the estimation of bottom current velocity from bedform observations. *Geology* 37, 327–330. doi: 10.1130/G25259A.1

Thresher, R., Althaus, F., Adkins, J., Gowlett-Holmes, K., Alderslade, P., Dowdney, J., et al. (2014). Strong depth-related zonation of megabenthos on a rocky continental margin (700-4000 m) off Southern Tasmania. Australia. *PLoS One* 9:e85872. doi: 10.1371/journal.pone.0085872

Thresher, R. E., Tilbrook, B., Fallon, S., Wilson, N. C., and Adkins, J. (2011). Effects of chronic low carbonate saturation levels on the distribution, growth and skeletal chemistry of deep-sea corals and other seamount megabenthos. *Mar. Ecol. Prog. Ser.* 442, 87–96. doi: 10.3354/meps09400

Timm, C., Hoernle, K., Werner, R., Hauff, F., den Bogaard, P., van Michael, P., et al. (2011). Age and geochemistry of the oceanic Manihiki Plateau. SW Pacific: new evidence for a plume origin. *Earth Planet. Sci. Lett.* 304, 135–146. doi: 10.1016/j.epsl.2011.01.025

Tomczak, M., and Godfrey, J. S. (2003). *Regional Oceanography: An Introduction*. Delhi: Daya Publishing House.

Tracey, D. M., Neil, H., Marriott, P., Andrews, A. H., Cailliet, G. M., and Sanchez, J. A. (2007). Age and growth of two genera of deep-sea bamboo corals (Family Isididae) in New Zealand waters. *Bull. Mar. Sci.* 81, 393–408.

Werner, R., Nürnberg, D., Hauff, F., and Shipboard scientific Party (2013). *RV Sonne Fahrtbericht / Cruise Report SO225 Manihiki II Leg 2 The Manihiki Plateau - Origin, Structure and Effects of Oceanic Plateaus and Pleistocene Dynamic of the West Pacific Warm Water Pool*. Germany: Kiel, doi: 10.3289/GEOMAR_REP_NS_7_2013

Winterer, E. L., Lonsdale, P. F., Matthews, J. L., and Rosendahl, B. R. (1974). Structure and acoustic stratigraphy of the Manihiki Plateau. *Deep. Res.* 21, 793–814. doi: 10.1016/0011-7471(74)90001-1

Conflict of Interest: The authors declare that the research was conducted in the absence of any commercial or financial relationships that could be construed as a potential conflict of interest.

Copyright © 2020 Bashah, Galvez, Eberli and Cantwell. This is an open-access article distributed under the terms of the Creative Commons Attribution License (CC BY). The use, distribution or reproduction in other forums is permitted, provided the original author(s) and the copyright owner(s) are credited and that the original publication in this journal is cited, in accordance with accepted academic practice. No use, distribution or reproduction is permitted which does not comply with these terms.

frontiers in Marine Science

ORIGINAL RESEARCH
published: 27 May 2020
doi: 10.3389/fmars.2020.00369

Deep-Sea Debris in the Central and Western Pacific Ocean

Diva J. Amon[1], Brian R. C. Kennedy[2], Kasey Cantwell[3], Kelley Suhre[3], Deborah Glickson[4], Timothy M. Shank[5] and Randi D. Rotjan[2]*

[1] Department of Life Sciences, Natural History Museum, London, United Kingdom, [2] Department of Biology, Boston University, Boston, MA, United States, [3] NOAA Office of Ocean Exploration and Research, Silver Spring, MD, United States, [4] National Academy of Sciences, Engineering, and Medicine, Washington, DC, United States, [5] Department of Biology, Woods Hole Oceanographic Institution, Woods Hole, MA, United States

Marine debris is a growing problem in the world's deep ocean. The naturally slow biological and chemical processes operating at depth, coupled with the types of materials that are used commercially, suggest that debris is likely to persist in the deep ocean for long periods of time, ranging from hundreds to thousands of years. However, the realized scale of marine debris accumulation in the deep ocean is unknown due to the logistical, technological, and financial constraints related to deep-ocean exploration. Coordinated deep-water exploration from 2015 to 2017 enabled new insights into the status of deep-sea marine debris throughout the central and western Pacific Basin via ROV expeditions conducted onboard NOAA Ship *Okeanos Explorer* and RV *Falkor*. These expeditions included sites in United States protected areas and monuments, other Exclusive Economic Zones, international protected areas, and areas beyond national jurisdiction. Metal, glass, plastic, rubber, cloth, fishing gear, and other marine debris were encountered during 17.5% of the 188 dives from 150 to 6,000 m depth. Correlations were observed between deep-sea debris densities and depth, geological features, and distance from human-settled land. The highest densities occurred off American Samoa and the main Hawaiian Islands. Debris, mostly consisting of fishing gear and plastic, were also observed in most of the large-scale marine protected areas, adding to the growing body of evidence that even deep, remote areas of the ocean are not immune from human impacts. Interactions with and impacts on biological communities were noted, though further study is required to understand the full extent of these impacts. We also discuss potential sources and long-term implications of this debris.

Keywords: remotely operated vehicle, CAPSTONE, litter, anthropogenic, plastics, fishing gear, marine protected area, national marine monument

OPEN ACCESS

Edited by:
Cristina Gambi,
Marche Polytechnic University, Italy

Reviewed by:
Kristina M. Gjerde,
International Union for Conservation of Nature, Switzerland
Kyle S. Van Houtan,
Monterey Bay Aquarium, United States

****Correspondence:***
Diva J. Amon
divaamon@gmail.com

Specialty section:
This article was submitted to Deep-Sea Environments and Ecology, a section of the journal Frontiers in Marine Science

Received: *23 October 2019*
Accepted: *30 April 2020*
Published: *27 May 2020*

Citation:
Amon DJ, Kennedy BRC, Cantwell K, Suhre K, Glickson D, Shank TM and Rotjan RD (2020) Deep-Sea Debris in the Central and Western Pacific Ocean. Front. Mar. Sci. 7:369. doi: 10.3389/fmars.2020.00369

INTRODUCTION

The deep ocean is often perceived as a remote wilderness, however, it has been a repository for debris for hundreds of years (Ramirez-Llodra et al., 2011). The intentional disposal of solid non-natural material began in earnest toward the end of the 18th century, progressing to pharmaceuticals, radioactive waste, munitions, and even larger structures including deliberate sinking of wrecks, which ceased in the late 20th century when the London Convention was enacted to control

pollution of the ocean caused by dumping (Ramirez-Llodra et al., 2011). Since 2012, the International Convention for the Prevention of Pollution from Ships (MARPOL) Annex 5 has prohibited the discharge of all garbage into the sea from ships (excluding food wastes, identified cargo residues, animal carcasses, and identified non-harmful cleaning agents, additives and cargo residues entrained in washwater). However, debris has continued to accrue in the deep ocean via both illegal intentional means and the accidental influx from rivers, coasts, and vessels (Schmidt et al., 2017).

Despite the remoteness and harsh conditions of the deep ocean, there is a growing literature on the reach and impact of deep macro debris across all ocean basins. For example, in the Atlantic and western Indian Oceans, debris was observed in all deep locations surveyed, even those far from the coast. Indian-Ocean sites were dominated by fishing gear whereas the North Atlantic Ocean hosted a greater variety of marine debris (Pham et al., 2014; Woodall et al., 2015). Similarly, many studies in the Mediterranean deep sea have also documented a diversity of debris, showing that plastic (e.g., bags and bottles), glass, and metal (e.g., tins and cans) were the most prevalent forms (Galil et al., 1995; Galgani et al., 2000; Ramirez-Llodra et al., 2011; Pham et al., 2014; Quattrini et al., 2015; Cau et al., 2018). Even in the Arctic, 86% of bottom trawls contained plastic macros debris (Grøsvik et al., 2018).

An extensive global study, with emphasis on the northwestern Pacific Ocean, found that 33% of macros debris below 2,000 m were plastic, of which 89% were single-use items, and below 6,000 m, this increased to 52% plastic and 92% single-use plastic (Chiba et al., 2018). This study also recorded the deepest observation of marine debris known (10,898 m in the Mariana Trench) (Chiba et al., 2018). Other studies in the Pacific Ocean revealed metal items (including shipping containers), plastics, and miscellaneous items occurring at depth (Keller et al., 2010; Watters et al., 2010; Miyake et al., 2011; Schlining et al., 2013). Additionally, this substantial increase in observations has revealed that debris accumulates on geological seafloor features such as seamounts, submarine canyons, trenches, and depressions (Miyake et al., 2011; Schlining et al., 2013; Pham et al., 2014; Woodall et al., 2015).

While this topic has become more mainstream and the scale of the problem shown to be global, there is still little known about deep-sea macro debris in many ocean areas, including the central and western Pacific Ocean. This includes over 1.9 million km^2 of land, coral reef, ocean, and maritime heritage resources that have some degree of protection, such as United States Marine National Monuments and Sanctuaries, and the Phoenix Islands Protected Area (PIPA). There has been little to no deep-sea exploration and research in these areas due to the vastness, remoteness, and lack of financial, technical, and technological capacity. In an effort to remedy this issue, the NOAA Office of Ocean Exploration and Research (NOAA OER) and partners launched the Campaign to Address the Pacific monument Science, Technology, and Ocean Needs (CAPSTONE) in 2015 (Leonardi et al., 2018; Kennedy et al., 2019). This multi-year scientific effort explored the deep-water areas of the central and western Pacific Ocean in and around United States marine protected areas (MPAs) that were of high interest for research and management (Cantwell et al., 2018), and included international partnerships to explore areas near US waters (McKinnie et al., 2018). CAPSTONE provided a foundation of publicly accessible baseline data from the central and western Pacific, including information on anthropogenic impacts encountered in the deep ocean.

In this study, we explored the density and type of benthic macro debris in the deep central and western Pacific Ocean, including in large-scale protected areas. We also tested whether debris density and type were correlated with depth, geological features and distance from settled land. Potential impacts of debris on deep-sea communities were also noted. From the diversity and density of debris encountered, we also hypothesized potential sources of debris. Finally, we discuss long-term implications of deep-sea debris with a view to the effective management and monitoring of these expansive and near-pristine habitats.

MATERIALS AND METHODS

Remotely Operated Vehicle Surveys From the NOAA Ship Okeanos Explorer

From 2015 to 2017, mission teams onboard the NOAA Ship *Okeanos Explorer* conducted 12 remotely operated vehicle (ROV) expeditions in the central and western Pacific as part of CAPSTONE (**Figure 1** and **Supplementary Tables 1–3**). During these expeditions, 187 ROV dives conducting exploratory benthic and midwater surveys were conducted (Kennedy et al., 2019). A subsample of 171 ROV surveys, excluding special purpose dives such as exclusively water-column surveys or dives that were aborted before the ROV reached the seafloor, was used for this analysis. These 171 dives were analyzed to assess benthic macro debris over 29.3 km^2 of seafloor from 233 to 6,000 m, using the 6,000 m-rated dual-body system, ROV *Deep Discoverer* (*D2*), and camera sled, *Seirios* (**Supplementary Table 1**). *Seirios* was tethered to the ship with a standard oceanographic armored, fiber-optic cable (1.73 cm diameter) (Gregory et al., 2016). The ROV *D2* was linked to *Seirios* with a neutrally buoyant tether, isolating the ROV from surface ship's motion and allowing precise maneuvering in precipitous topography. The ROV *D2* used two high-definition (HD) video cameras (Insite Zeus Plus and Mini Zeus) for scientific observations, but there were several additional cameras used for piloting that were not normally recorded. Paired lasers (10 cm apart), mounted on the fixed HD video camera, were used for scaling objects, although these mostly remained switched off. *Seirios* carried an additional Insite Zeus Plus camera for a wide area view of the seafloor. Both vehicles were equipped with high powered LED lighting systems that provided more than 272,000 lumens of light combined (Gregory et al., 2016). During ROV exploration, the cameras were generally set on wide-angle view, but zooms were frequently conducted to obtain detailed imagery (stills and video) to facilitate taxonomic identification.

Throughout the benthic portion of all ROV dives, real-time annotations were made of taxonomic identifications, geological observations, and other objects of interest. For cruises before

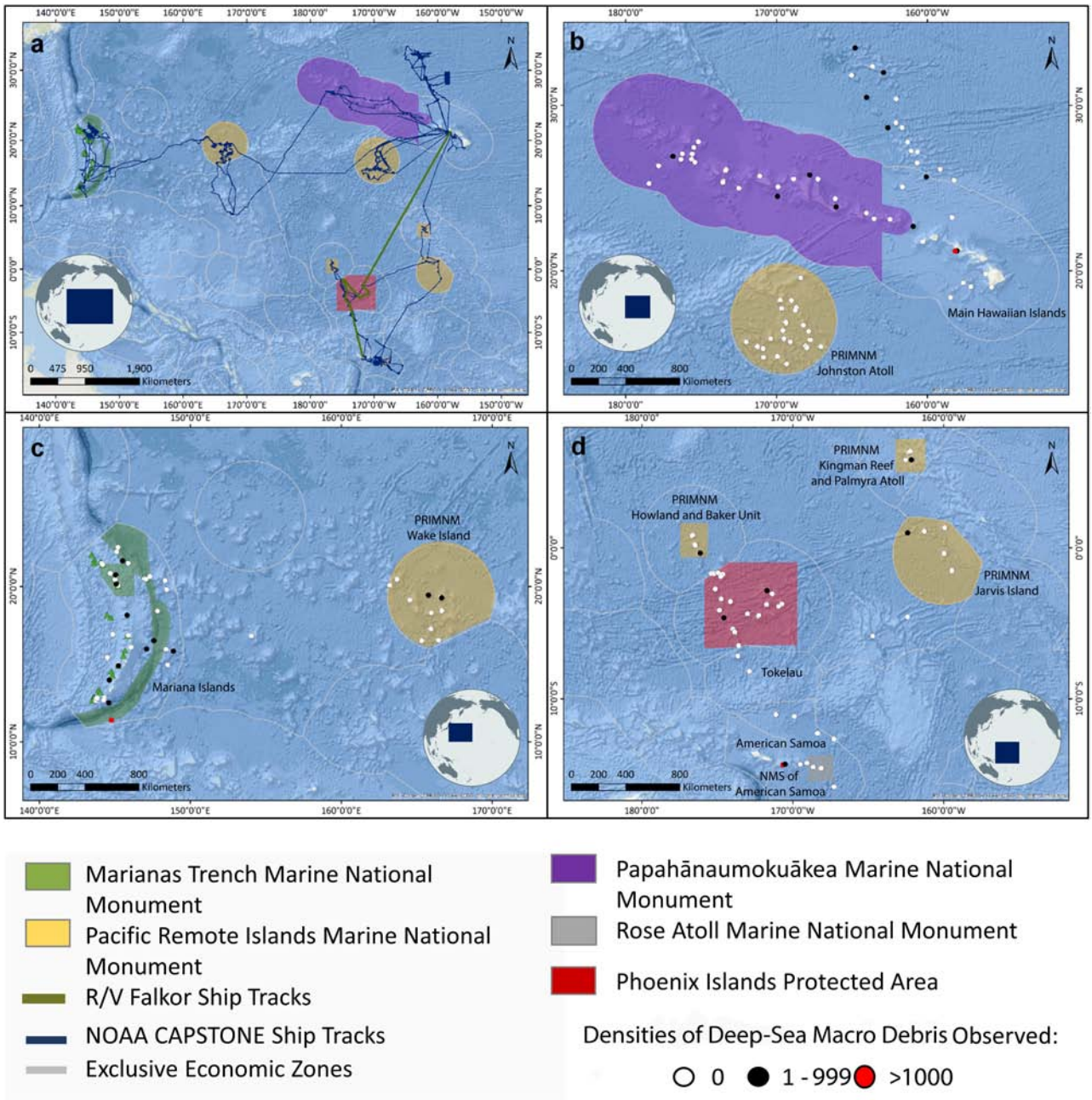

FIGURE 1 | Estimated deep-sea debris densities (items km^{-2}) from observations by ROVs in the central and western Pacific Ocean. **(a)** General footprint of NOAA Ship *Okeanos Explorer* cruises, adapted from Kennedy et al., 2019. **(b)** Estimated deep-sea debris densities in Papahānaumokuākea Marine National Monument, the main Hawaiian Islands, ABNJ, and the Johnston Atoll Unit of PRIMNM; **(c)** the Mariana Islands, Marianas Trench Marine National Monument, and the Wake Island Unit of PRIMNM; **(d)** American Samoa, NMS of American Samoa, Phoenix Islands Protected Area, Tokelau, ABNJ, and the Howland and Baker Islands, Kingman Reef and Palmyra Atoll, and Jarvis Island Units of PRIMNM. Green triangles in **(c)** are the volcanic unit of the Marianas Trench Marine National Monument. PRIMNM, Pacific Remote Islands Marine National Monument; NMS, National Marine Sanctuary.

2017, annotations were made in a system called the "eventlog." This telepresence-enabled system consisted of an online chat room that time stamped entry and was available to both shore-based and ship-based science participants through a high bandwidth satellite connection (Kennedy et al., 2016). With the start of the 2017 field season, NOAA transitioned to a more sophisticated real-time annotation system provided by Ocean Networks Canada called SeaScribe (Jenkyns et al., 2013; Malik et al., 2020). Both systems served the same basic function of providing a first level of annotations for the ROV video and a searchable record of what was seen throughout the dive. Internal NOAA quality-control tests did not show a significant

difference in the number of annotations made between the two systems. During dive operations, the ROV *D2* was operated in "exploration" mode, where the vehicles do not follow a prescribed transect or path but instead the vehicle investigates any seafloor anomalies (observed visually or in the forward-looking sonar) that Science Leads deemed of potential interest. Given that marine debris is relatively rare of the seafloor, anthropogenic items often stood out from the biology and geology, so these items were nearly always focused and zoomed on with the camera. The ROV pilots were also continually scanning for marine debris may posed an entanglement hazard, e.g., fishing gear, to the ROVs. As a result, there was a high degree of confidence that the majority of marine debris in the area that ROV *D2* operated in was seen and noted.

Most ROV dives were conducted at sites that had never been explored and each varied in exploration length and depth (**Supplementary Table 1**). Detailed description of the ROV dive site selection process is available in Kennedy et al. (2019). The ROV *D2* traversed the seafloor at a speed of approximately ∼0.1–0.3 knots. *Seirios* surveyed approximately 10 m above and behind *D2*, providing background lighting to visualize features, as well as situational awareness for the pilots and scientists. NOAA Ship *Okeanos Explorer* maintained position with the vehicles using dynamic positioning and tracked vehicle position relative to the ship with an ultra-short baseline tracking (USBL) system. The accuracy of the system was heavily dependent on water depth and, to a lesser degree, sea state and local bathymetry, and ranged from ∼5 to 50 m depending on conditions. Additionally, the vehicles' motions and directions varied greatly as novel organisms or geological features were investigated, making differentiating between errors in the USBL navigation and rapid changes in vehicle position difficult.

While the ROV seafloor track did not follow a predefined transect for the purpose of this analysis, we treated the seafloor track that was visually covered by the ROV as a non-linear transect. This treatment helps to correct for some of the challenges associated with USBL navigation within the operational paradigm adopted by NOAA, which also make determining the exact area of seafloor imaged difficult. As a result, the minimum and maximum area of seafloor documented during a dive were quantified to provide a range of possible areas visualized (Kennedy et al., 2019). To accomplish this, the linear distance traveled by ROV *D2* was measured by manually tracing a line of best fit based on the 1 Hz USBL navigation file provided by NOAA as part of the ROV data collection available via the OER Digital Atlas. When ROV *D2* was at an altitude of 1 m, and the angle of the primary HD camera was at a 45° angle, the field of view yielded 2.7 m of seafloor horizontally across the video frame (assuming a consistent ROV heading). The field of view for the cameras on both *D2* and *Seirios* is 65° laterally in water. Because the pilots were nearly continuously changing the heading of the vehicle while scanning the seafloor, as well as flying the vehicle at variable altitudes as the bathymetry dictated, a visual swath width of a minimum of 5 m (2.5 m on either side of the vehicle path over the bottom) and a maximum of 50 m (calculated as twice the effective length of the tether connecting ROV *D2* and *Seirios*) was estimated. The minimum range value of 5 m corrected for the changes of altitude and heading changes. The maximum range value of 50 m estimated the effective length of the neutrally buoyant tether between ROV *D2* and *Seirios* and assumed that *D2* never moved more than 50 m quickly without having to move the ship, which controls the movement and placement of *Seirios*. Any move of more than 50 m was slower and would be obvious in the USBL navigation. Based on these assumptions and estimates, the area surveyed during CAPSTONE dives included the seafloor between 2.5 and 25 m on both sides of the averaged dive track. For the purposes of this study, we used the average between these two edges, hence all area estimates were based on a 25 m transect width. Additional information on CAPSTONE methods is provided in Kennedy et al. (2019).

Remotely Operated Vehicle Surveys From the RV Falkor

In October 2017, the RV *Falkor*, operated by the Schmidt Ocean Institute, conducted 17 ROV surveys in PIPA (FK171005) (**Figure 1** and **Supplementary Tables 1, 2**). ROV dives were undertaken from 150 to 2,400 m (0.22–2.21 km^2 seafloor surveyed) using the 4,500-m rated ROV *SuBastian*. ROV *SuBastian* was equipped with an Insite Pacific Mini Zeus HD 1080i CMOS camera for situational awareness and an Insite Zeus Plus or SULIS 4K 12× Zoom camera for science surveys (5.1–51 mm wide angle zoom lens). In addition, the vehicle hosted a Seabird FastCAT CTD Sensor (SBE49), and a Paroscientific 8000 Series Submersible Depth Sensor for measuring depth of observations (Auscavitch et al., 2019).

Similar to operations onboard the NOAA Ship *Okeanos Explorer*, ROV dives from the RV *Falkor* followed an exploratory operational paradigm without pre-defined transects resulting in similar issues estimating the range of possible seafloor area visualized, with the minimum and maximum area of seafloor documented as a result. A similar methodology to above was used when measuring the linear distance traveled by ROV *SuBastian*. When ROV *SuBastian* was at an altitude of 1 m, and the primary HD camera was at a 45° angle, the field of view yielded 2.47 m of seafloor horizontally across the video frame with an estimated visual swath width of a minimum of ∼5 m (2.5 m on either side of the vehicle path over the bottom) and a maximum of 20 m (10 m on either side of the vehicle path over the bottom). Based on these assumptions and estimates, we assumed that the area surveyed during RV *Falkor* dives included the seafloor between 2.5 and 10 m on both sides of the averaged dive track.

Analysis of Remotely Operated Vehicle Imagery

Macro-debris annotations, which included metadata (time, location, and depth), from 171 NOAA Ship *Okeanos Explorer* dives were isolated and enumerated. Marine debris records from NOAA Ship *Okeanos Explorer* real-time annotations systems were extracted by reviewing the records for each dive. This data was then used to locate the video segments containing debris, which were reviewed to find the debris record. During dives conducted from the RV *Falkor*, marine debris was not recorded

in real time. Instead, all ROV imagery was reviewed post-cruise, explicitly for marine debris. The criteria used for identifying macro debris in ROV video was any items of anthropogenic origin and of a size greater than 2 cm in maximum dimension.

Imagery was then viewed for each debris annotation to (a) confirm the observation and (b) capture a frame (**Supplementary Table 3** and **Supplementary Debris Occurrences**). From this imagery, information on each observation was recorded including the type of material comprising the debris: plastic, glass, metal, rubber, cloth, fishing gear and other, and interactions between debris and surrounding biology: shelter, encrustation, entanglement, and multiple interactions. Plastic debris was further categorized into single-use products and other plastics, following the methodology of Chiba et al. (2018). Observed debris was categorized as either light or heavy based on their relative tendency to float or be transported horizontally before reaching the seafloor. Metal and glass were labeled as heavy items while plastic, fishing gear, cloth, rubber and other types of debris were coded as light. The distance of the debris from human settlement was also noted in order to assess the impact on the density of seafloor marine debris. We defined a settlement as any piece of land with more than 1,000 people in residence at any point since the 1920s. Population numbers were sourced from various publicly available records.

The analysis of NOAA Ship *Okeanos Explorer* imagery was based solely on real-time annotations that were made during the dives, so it remains possible that some instances of debris were not noted by the real-time annotators, but likely only presents a small under-sampling error. Additionally, we recognize the inherent differences in the limitation of detecting specific types of trash. For example, the ability to see metal (which could be more reflective or less reflective, depending on the extent of rust) is different from plastic (which is inherently also more likely to move in the current than metal). These differences in detection could present sampling biases toward objects that were more brightly colored or reflective making them easier to spot using the ROV cameras, however this would, again, only present a small bias given the attention paid to expressly looking for debris, novel shapes and colors, as well as high-resolution camera zooms on these shapes during exploration-style ROV operations. No marine debris was collected by either ROV, therefore it was not possible to undertake further analyses such as aging or Laser Raman techniques to better characterize the plastics observed.

Statistical Analyses

Analyses of debris by the categorical geological features: islands and atolls, abyssal features (below 4,000 m), hydrothermal areas, seamounts, and banks, were undertaken. Debris occurrences relative to (1) large MPAs – Pacific Remote Islands Marine National Monument (PRIMNM) Johnston Atoll, PRIMNM Howland and Baker Unit, PRIMNM Wake Island, PRIMNM Kingman Reef and Palmyra Atoll, PRIMNM Jarvis Island, as well as Rose Atoll Marine National Monument, Mariana Trench Marine National Monument (MTMNM), Papahānaumokuākea Marine National Monument (PMNM), the National Marine Sanctuary of American Samoa (NMS of American Samoa), and PIPA; (2) Exclusive Economic Zones (EEZs) of Tokelau (New Zealand), as well as the Mariana Islands, the main Hawaiian Islands and American Samoa (United States); and (3) Areas Beyond National Jurisdiction (ABNJ), were analyzed. Non-parametric Kruskal–Wallis comparisons were used to test for significant differences between deep-sea debris densities and depth and geological features. A Mann–Whitney test was used to measure whether there was a significant difference between debris density within and outside of MPAs. We used a Pearson's Chi-Squared test to determine whether debris observations across distances from human settlements were consistent for both heavy debris (metal and glass) and light debris (plastic, cloth, paper, lumber, and other). A p-value of 0.05 was used throughout as the criterion for statistical significance. These analyses were conducted in SYSTAT version 13.1 (Systat Software, Inc.).

RESULTS

Deep-Sea Debris Locations

During 188 ROV dives across the central and western Pacific, there were 115 observations of marine macro debris (**Table 1**, **Figure 1**, and **Supplementary Table 3** and Debris Occurrences). Deep-sea debris was encountered on 17.5% of the dives. There were no debris items recorded during dives in the Tokelau EEZ, Rose Atoll Marine National Monument, and PRIMNM Johnston Atoll (**Figures 1**, **3** and **Table 1**). The highest estimates of marine debris were observed within the United States EEZ (not within protected areas) around American Samoa and the main Hawaiian Islands (196–1,961 items km^{-2} and 97–965 items km^{-2}, respectively) (**Table 1**). Two sites harbored the majority of debris off the main Hawaiian Islands and American Samoa and the highest abundances surveyed: CAIMAN/I-203 (44 items) and Tutaila (20 items), respectively (**Supplementary Table 3** and **Supplementary Debris Occurrences**).

Of the total debris found, 28.5% items were observed within the United States Protected Areas (127–1,267 items km^{-2}), whereas the PIPA had only 0.37% of the total debris densities observed (2–17 items km^{-2}), leading to a total of 28.9% of debris observed within protected areas (**Table 1**). Debris densities in ABNJ were sparse (3.2% or 14–143 items km^{-2}), while areas surveyed within the United States EEZ, not including protected areas, had the highest densities of debris at 302–3,020 items km^{-2} (67.9%) (**Table 1**). There was no significant difference between the number of items km^{-2} found within protected areas and outside (Mann–Whitney: U = 16, η1 = 71 η2 = 49, p = 0.307 two-tailed).

By depth, 71.3% of debris were recorded between 150 and 1,000 m, with decreases in density as depth increased (9.6% at 1,000–2,000 m, 7.0% at 3,000–4,000 m, 6.1% at 2,000–3,000 m, 5.3% at 4,000–5,000 m, and 0.9% at 5,000–6,000 m) (**Figures 2**, **3**). The two sites with the highest debris contributed to this observation with both falling between 150 and 1,000 m depth (CAIMAN anomaly in the "Hawaii" data grouping and Tutaila in the "Central" data grouping (**Figure 2** and **Supplementary Table 3**). The shallowest and deepest records of debris observed within this study were 158 and 5,899 m, respectively (**Supplementary Table 3**). The highest densities of

TABLE 1 | Deep-sea debris observed in the central and western Pacific.

Location	No. of usable dives	Approximate total seafloor surveyed (km^2)	No. of debris observations	Total debris observed per km^2
Tokelau, New Zealand	2	0.01–0.071	0	0
United States – PRIMNM Johnston Atoll	25	0.08–0.80	0	0
United States – Rose Atoll Marine National Monument	4	0.01–0.11	0	0
Kiribati – Phoenix Islands Protected Area	25	0.24–2.42	4	2–17
United States – Papahānaumokuākea Marine National Monument	26	0.09–0.94	4	4–43
United States – PRIMNM Howland and Baker Unit	8	0.02–0.19	1	5–52
United States EEZ, not in Monument – Mariana Islands	22	0.09–0.85	8	9–94
United States – PRIMNM Wake Island	11	0.03–0.34	4	12–119
United States – PRIMNM Kingman Reef and Palmyra Atoll	4	0.01–0.08	1	12–121
United States – PRIMNM Jarvis Island	5	0.02–0.15	2	13–131
ABNJ – Musician Seamounts and others	18	0.04–0.42	6	14–143
United States – Mariana Trench Marine National Monument	18	0.05–0.55	11	20–202
United States – National Marine Sanctuary of American Samoa	3	0.01–0.07	4	60–602
United States EEZ, not in Monument – Main Hawaiian Islands	11	0.05–0.52	50	97–965
United States EEZ, not in Monument – American Samoa	6	0.01–0.10	20	196–1961
Total	188	0.76–7.60	115	445–4448

All surveyed areas within monuments and other protected areas are highlighted in blue. PRIMNM, Pacific Remote Islands Marine National Monument; NMS, National Marine Sanctuary.

debris outside of MPAs occurred between 500 and 1,000 m (212 items km^{-2}) and 4,500–5,000 m (254 items km^{-2}) but within MPAs, the highest density was observed between 3,500 and 4,000 m (155 items km^{-2}) (**Figure 2**). There was a significant difference between the number of items km^{-2} found within different depth categories across different regions (Kruskal–Wallis = 9.829, $p = 0.04$, $df = 5$).

Over 50% of deep-sea debris was observed near islands and atolls (37–368 items km^{-2}), with the second highest density found on abyssal features (17–173 items km^{-2} or 24.84%). Less than 11% of debris was observed on dives exploring hydrothermal areas (10.04%), seamounts (8.50%), and banks (3.89%). Debris observations differed significantly between geological features (Kruskal–Wallis = 11.479, $p = 0.022$, df = 4). However, no pairwise comparisons were found to be different among features (Dwass Steel Chritchlow Fligner Test for all pairwise comparisons; for all, $p < 0.05$).

Types of Deep-Sea Debris

Over 80% of the debris consisted of metal (46.96%), derelict fishing gear (18.26%) and plastic debris (18.26%) (**Figures 3**, **4** and **Supplementary Table 3** and **Supplementary Debris Occurrences**). Cloth, glass, rubber, and other debris made up the remaining 16.52% (**Figure 3**). Metal debris included cans, tins, cables, and ammunition, while 42.86% of plastic debris was single-use bags or cups. 5.2% of the debris observed was likely related to World War II, including a dock, bombs, and bullets. Fishing debris consisted of line, net, and cable. Cloth consisted mostly of pieces of canvas but also some clothing. The only glass debris encountered were bottles. The only rubber debris observed was a gasket, and other debris types included concrete and ceramic items.

Fishing debris was not found deeper than 2,006 m (**Figure 3**). Most fishing (76.19%), metal (81.48%), cloth (88.88%), and glass (71.42%) debris were observed off the shores of islands and atolls. Islands and atolls, as well as seamounts, had the highest plastic debris (38.10% each) of any geological feature. Within protected areas, fishing gear and plastic were the most abundant types of debris (32.26% and 29.03%, respectively), with metal debris at 25.81% (**Figure 3**).

Analysis of deep-sea debris observations by distance from settlement on land showed that debris was not evenly distributed across distance (**Figure 5**, Pearson's $X_2 = 26.491$, $df = 8$, $p = 0.0009$). In addition, the majority of debris (both heavy and light) was found very near to settlements (within the first 60 km). Although heavy and light debris both show uneven distribution from shore ($X_2 = 427.69$, $p < 0.00001$; $X_2 = 199.06$, $p < 0.00001$, respectively), beyond 60 km, the heavy debris was relatively evenly distributed ($X_2 = 11.497$, $df = 7$, $p = 0.1184$). The distribution for light debris past 60 km was still uneven ($X_2 = 47.245$, $df = 7$, $p < 0.00001$). Within this study, glass debris observed at Shostakovich Seamount was the furthest recorded from settlement on land (1,324 km from Kauai in the main Hawaiian Islands) (**Figure 5**). A total of 55.6% of sites where debris was found over 500 km from settled land were on seamounts.

Interactions of Deep-Sea Biological Communities With Debris

Of the debris observed, fauna interacted directly with 39.13% (**Table 2**, **Figure 6**, and **Supplementary Table 3** and **Supplementary Debris Occurrences**). Of those, 37.78% were pieces of debris that had been encrusted by fauna, whereas faunal interactions of multiple types were observed on 28.89% of debris. Specifically, 17.78% of debris provided shelter to animals and 15.56% of debris were entangled in coral colonies. Deep-sea organisms noted on or near debris included corals, bryozoans,

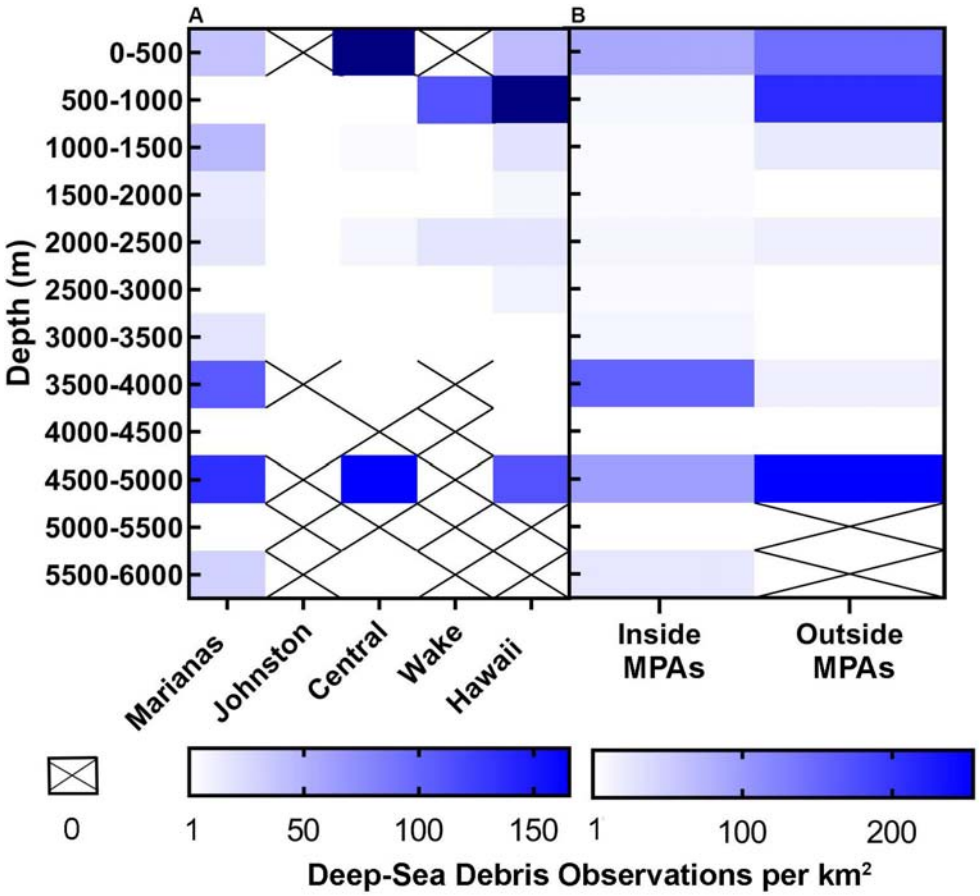

FIGURE 2 | Densities of deep-sea debris by depth observed in the central and western Pacific Ocean. **(A)** All sites were collapsed into five regions to allow for sufficient data density – "Marianas" (MTMNM and Mariana Islands), "Johnston" (PRIMNM Johnston Atoll only), "Central" (Rose Atoll Marine National Monument, NMS of American Samoa, American Samoa, PIPA, PRIMNM Howland and Baker Unit, PRIMNM Jarvis Island, PRIMNM Kingman Reef, and Palmyra Atoll), "Wake" (PRIMNM Wake Island only), and "Hawaii" (Papahānaumokuākea MNM and main Hawaiian Islands). It should be noted that the densities observed at 0–500 m in "Central" and 500–1,000 m in "Hawaii" exceeded the scale (both were >735 items of debris km^{-2}). **(B)** Debris observations by depth within and outside of marine protected areas.

hydroids, anemones, sponges, serpulids, crinoids, ophiuroids, echinoids, gastropods, cirripeds, squat lobsters, crabs, shrimp, and fish. Of the debris entangled in coral colonies, 42.9% were fishing gear and 57.1% were plastic bags or rope. The corals entangled with fishing gear or plastic included several primnoids, a paragorgiid, a field of large antipatharians and an isidid skeleton (**Figure 6**). Other notable interactions included an actiniarian attached to a bucket with a crinoid sheltering, a crab sheltering within fishing line encrusted with cirripeds and a plastic bag, and a World War II dock observed in the Main Hawaiian Islands that provided substrate for a range of cnidarians (**Figure 6**).

DISCUSSION

Patterns and Sources of Debris in the Pacific Deep Ocean

This study was the first to explore marine debris on such a wide scale across the central Pacific, finding that it is present in many deep-sea locations, including within MPAs that are largely devoid of human activity. Marine debris was encountered on 17.5% of the dives undertaken at depths from 158 to 6,000 m and ranged from 0 to 9,524 items km^{-2}. This is in line with other deep-sea debris studies: 200 to 13,000 items km^{-2} on the Northeast United States continental margin (Quattrini et al., 2015), 4 to >1,300 items km^{-2} off Sardinia (Cau et al., 2018), and 59 to 1,739 items km^{-2} on seamounts in the Indian and Atlantic Oceans (Woodall et al., 2015), however, Galgani et al. (2000) recorded much higher densities of 101,000 items km^{-2} in the Mediterranean Sea. In our study, the highest densities were observed within the United States EEZ around American Samoa and the main Hawaiian Islands, likely due to an anomalous site in each location with notably high densities – a site close to Tutuila, the largest and main island in the American Samoa archipelago, and a site close to Oahu, the most densely populated of the main Hawaiian Islands, showing the patchy nature of deep-sea debris and potential implications of nearby dense human populations. Chiba

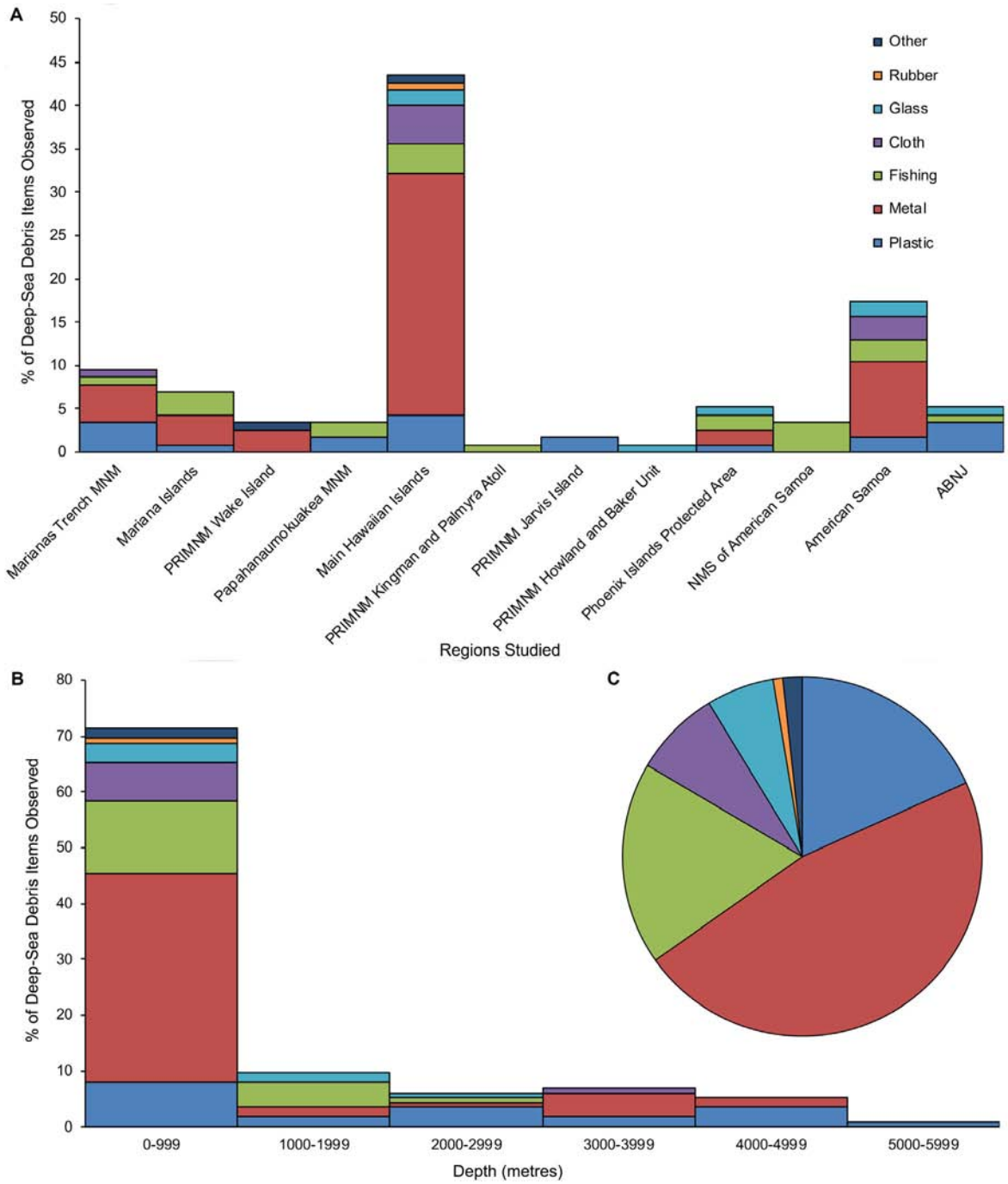

FIGURE 3 | Percentage types of deep-sea debris items observed **(A)** by region; **(B)** by depth; and **(C)** overall. No debris observations were made in PRIMNM Johnston Atoll, Rose Atoll Marine National Monument, and Tokelau. MNM, Marine National Monument; PRIMNM, Pacific Remote Islands Marine National Monument; NMS, National Marine Sanctuary.

et al. (2018) found most debris between 1,000 and 2,000 m, but reported that this might have been due to sampling bias. Contrastingly, Schlining et al. (2013) found most debris below 2,000 m, with the highest densities of plastic and metal debris between 2,000 and 4,000 m. Chiba et al. (2018) reported that the relative dominance of plastic debris was larger at depths greater than 6,000 m. In our study, the majority of the debris was observed between 150 and 999 m depth, with decreases in density as depth increased, however, this could have been as a result of sampling bias as survey distance would have been the greatest at shallower depths given the minimal ROV ascent and descent time.

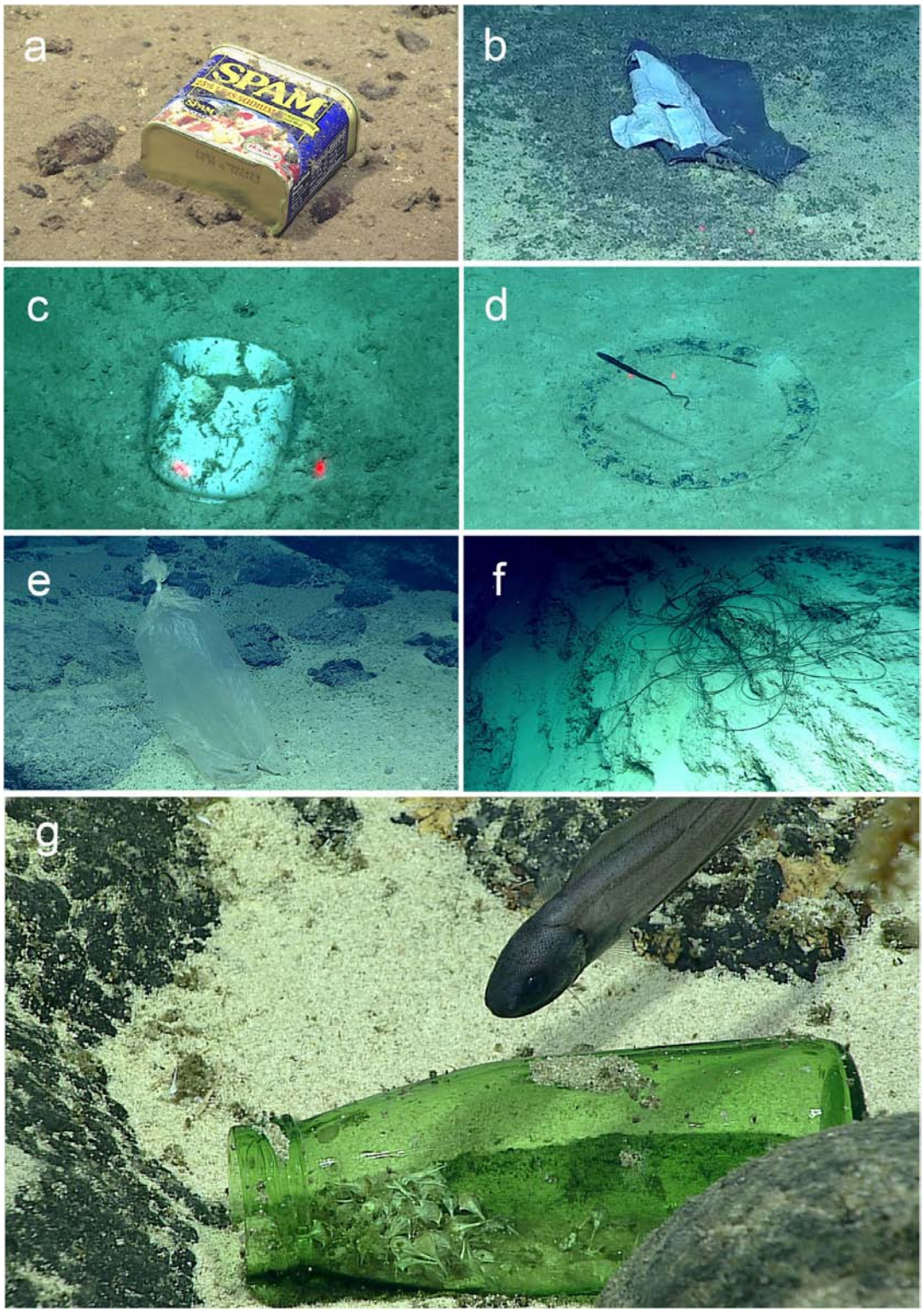

FIGURE 4 | Types of deep-sea debris observed. **(a)** Metal debris – a food tin at 4,947 m in Sirena Canyon off the Mariana Islands. **(b)** Cloth debris – a piece of canvas at 3,780 m on Enigma Seamount off the Mariana Islands. **(c)** Other debris – a ceramic cup at 838 m at CAIMAN/I-203 off the main Hawaiian Islands. **(d)** Rubber debris – a gasket at 839 m at CAIMAN/I-203 off the main Hawaiian Islands. **(e)** Plastic debris – a plastic bag at 3,767 m on Enigma Seamount off the Mariana Islands. **(f)** Fishing debris – fishing line at 453 m on South Palmyra Slope in PRIMNM Kingman Reef and Palmyra Atoll. **(g)** Glass debris – a glass bottle at 1,152 m at Titov 2 in PRIMNM Howland and Baker Unit. The central red lasers points indicate 10 cm scale in 4b, 4c, 4d, and 4e.

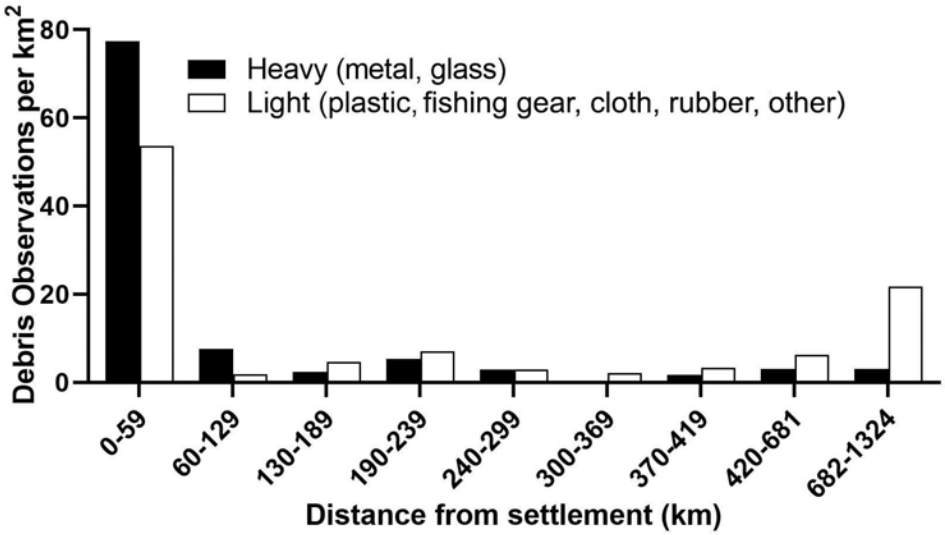

FIGURE 5 | Deep-sea debris density by distance from human settlement (km). In an attempt to standardize sampling effort, each distance category contained 21 deep-sea ROV dives except for the last category, which had 20 dives.

TABLE 2 | Interactions of fauna with deep-sea debris in the central and western Pacific.

Location	Types of interactions between fauna and debris				
	Shelter	Encrustation	Entanglement	Multiple	None
Tokelau, New Zealand	–	–	–	–	–
United States – PRIMNM Johnston Atoll	–	–	–	–	–
United States – Rose Atoll Marine National Monument	–	–	–	–	–
Kiribati – Phoenix Islands Protected Area	–	1	–	–	3
United States – Papahānaumokuākea Marine National Monument	–	–	–	1	3
United States – PRIMNM Howland and Baker Unit	1	–	–	–	–
United States EEZ, not in Monument – Mariana Islands	–	–	2	1	5
United States – PRIMNM Wake Island	–	1	–	1	2
United States – PRIMNM Kingman Reef and Palmyra Atoll	1	–	–	–	–
United States – PRIMNM Jarvis Island	–	–	–	–	2
ABNJ – Musician Seamounts and Others	–	–	5	–	1
United States – Mariana Trench Marine National Monument	2	–	–	1	8
United States – National Marine Sanctuary of American Samoa	–	–	–	–	4
United States EEZ, not in Monument – Main Hawaiian Islands	4	15	–	9	22
United States EEZ, not in Monument – American Samoa	–	–	–	–	20
Total	8	17	7	13	70

All surveyed areas within monuments and other protected areas are highlighted in blue. Interactions were listed as "Multiple" if there were more than two types of interaction per piece of debris. PRIMNM, Pacific Remote Islands Marine National Monument; NMS, National Marine Sanctuary.

As highlighted by Ramirez-Llodra et al. (2013); Schlining et al. (2013), and Woodall et al. (2015), hydrography, geology, and anthropogenic activity determine the amount, type, and location of debris reaching the deep seafloor. The central and western Pacific supports shipping and other forms of boat traffic. This study shows that debris was not evenly distributed across distance, and that the majority of debris (both heavy and light) was found very near to settlements (within the first 60 km). Heavier debris (metal and glass – 53.04%) rapidly sink close to the site of discard, indicating many of the offshore items observed during this study were likely discarded intentionally or accidentally from marine vessels and that despite strict ocean-wide regulations, enforcement can be problematic. A total of 5.2% of all debris observed were likely related to World War II, serving as a reminder of the history of this region of the Pacific Ocean. Lighter debris may have floated from the sources for some time or been blown out to sea (Pham et al., 2014; Chiba et al., 2018), then eventually sunk, gaining more distance from shore and leaving greater room for speculation on their place of origin, as was seen during this study. However, although we observed light debris in the farthest distances from settlement, the origin of discard is not known: light debris could have been discarded terrestrially,

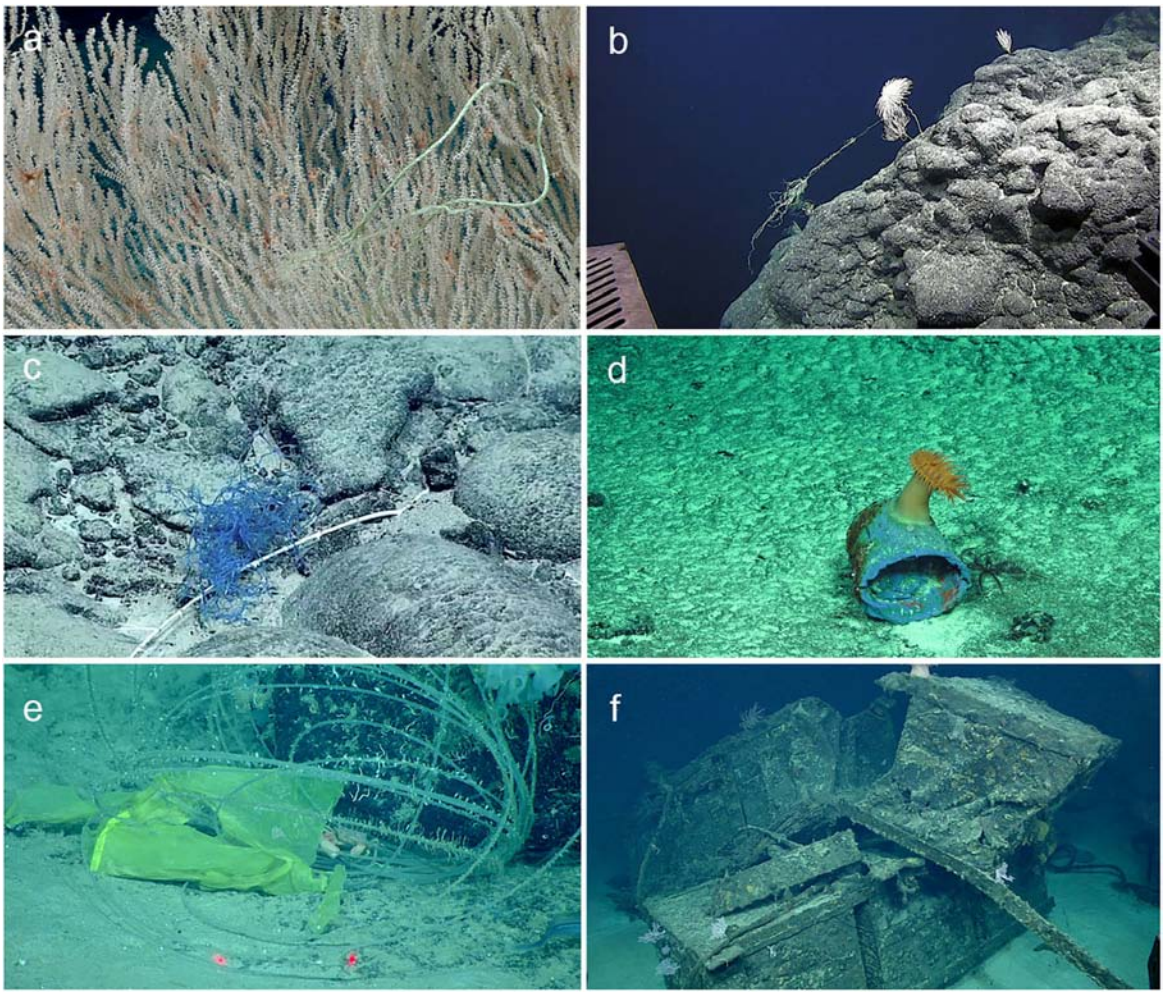

FIGURE 6 | Biological interactions with deep-sea debris. **(a)** Fishing line entangled in a large primnoid coral at 1,772 m in the Musician Seamounts in ABNJ. **(b)** Fishing line entangled in a primnoid coral at 1,167 m in the northwestern Hawaiian Islands. **(c)** The skeleton of an isidid coral entangled in fishing line at 2,005 m on Pigafetta Guyot off the Mariana Islands. This may have contributed to its death. **(d)** A plastic bucket providing substrate for an actiniarian at 1,025 m in the PIPA. **(e)** A plastic bag and fishing line providing shelter for a crab and substrate for cirripeds at 791 m at CAIMAN/I-203 off the main Hawaiian Islands. **(f)** A metal dock from World War II intentionally sunk at 784 m off the main Hawaiian Islands and now providing shelter and substrate for a variety of species including multiple octocorals, crabs, squat lobsters, sponges, barnacles, and anemones. The central red lasers points indicate 10 cm scale in 6e.

or from an at-sea vessel. Although the furthest occurrence of debris from settled coast during our study was 1,324 km, Pham et al. (2014) observed debris over 2,000 km from land. While the decline of debris density from shore has been previously observed by Schlining et al. (2013) and Pham et al. (2014), this does not appear to be universal. For example, Woodall et al. (2015) did not find that the distance from shore was a good predictor of debris density. Even in our study, we found that light debris increased away from settlements (**Figure 5**), making it difficult to predict light debris density from shore distance alone.

As with previous studies, debris varied from fishing gear to metal items such as cans, to glass bottles, cloth, plastic bags and more, although proportions varied (Quattrini et al., 2015; Cau et al., 2018). During this study, metal was the most abundant, followed by derelict fishing gear and plastic debris, whereas off Sardinia, plastic accounted for 56% of the total items, followed by glass and metal (Cau et al., 2018). Schlining et al. (2013); Pham et al. (2014), and Galgani et al. (2000) also found plastic to be the most abundant type of debris.

Geologically, most debris (fishing, metal, cloth, and glass) was found off islands and atolls, with the second highest abundance on abyssal features, followed by hydrothermal areas, seamounts, and banks. Additionally, islands, atolls, and seamounts had the highest plastic debris of any geological feature. This is likely due to the inhabitation of islands and atolls as well as proximity to fishing grounds near-shore or on seamounts. Over half of the sites where debris was found over 500 km from settled land were seamounts; this could be related to use for fishing, as these areas are known to have increased productivity (Clark and Koslow, 2007). Pham et al. (2014) and Woodall et al. (2015) commonly observed fishing debris on seamounts, banks, mounds, and ocean ridges around Europe and in the Indian Ocean, respectively.

For the majority of debris, it is not possible to estimate when deposition on the deep seafloor occurred, especially as degradation rates in the deep ocean are slow due to low oxygen levels and a lack of sunlight (Barnes et al., 2009). Apart from ammunition and other items likely from World War II and therefore nearly a century old, the ages of approximately 95% of observed debris are unknown but could be weeks to nearly a century. Unfortunately, the extremely slow rates of degradation in the deep sea combined with increasing use of the deep oceans and quantities of trash entering the ocean, deep-sea debris will likely increase in the future.

Effectiveness of Protected Areas With Regards to Deep-Sea Debris

Marine protected areas are often established as a potentially effective measure to protect ecosystems against the threats of direct resource exploitation and industrialization in order to better conserve areas of importance. These areas can have a significant cultural value, e.g., Papahānaumokuākea Marine National Monument, or contain organisms, communities and habitats of ecological or functional importance, such as vulnerable marine ecosystems (VMEs). This study shows that no region of the world's ocean is immune from deep-sea debris, including areas conferred with some degree of protection. There were occurrences of debris both within the majority of MPAs surveyed, as well as at VMEs, such as deep-sea coral beds and hydrothermal vents, in both MPAs and unprotected areas. Debris in MPAs likely pre-dates protection, has accumulated pre- or post-protection arriving via currents, and/or was illegally deposited post-protection.

During this study, only 27% of deep-sea debris was observed in MPAs, with 23.5% in United States protected areas. Similar observations were made within MPAs in the Indian Ocean; the Coral Seamount and Atlantis Bank, both Voluntary Benthic Protected Areas, were the two sites with the lowest debris densities (Woodall et al., 2015). Most large MPAs have only been in place for a decade or less and have focused on relatively remote ocean areas (Campbell and Gray, 2019). As such, the relatively low proportion of debris found in these large MPAs may be an artifact of their remoteness rather than their protected status. While this data may not be robust enough to draw conclusions about MPA effectiveness, in part because it was not possible to age the deep-sea debris observed, the slow degradation rates in the deep ocean have ensured that the debris present in many Pacific MPAs showed little sign of breakdown, and as a result, will be present for much longer periods of time. As MPA coverage expands to ABNJ, future research should estimate the likely debris densities in these remote regions.

Of the debris found within MPAs, fishing debris was responsible for 32.26%. PIPA had the second lowest abundance of deep-sea debris of all protected areas surveyed (1.8%), with PRIMNM Johnston Atoll recording no debris. Half of the debris in PIPA (two items at two sites) was attributed to fishing, which may have been deposited prior to the banning of commercial extractive activities in 2015. Three of the four total debris observations were made off Kanton Island, which currently has a small sustainable-use zone for limited activities to support the resident population, but historically has had a significant but ephemeral population, at one time supporting almost a thousand people. Likewise in Papahānaumokuākea Marine National Monument, PRIMNM Kingman Reef and Palmyra Atoll, NMS of American Samoa, and MTMNM, fishing debris may have either been deposited prior to the banning of all commercial fishing, have floated in on currents, or be of an artisanal nature, but again, it is currently impossible to be certain.

Interactions of Deep-Sea Biota With Debris

Interactions of deep-sea life with debris have not been well documented, especially in the central and western Pacific Ocean, but are fast becoming a topic of increased study. This study showed that deep-sea fauna directly interacted with over a third of the debris observed (**Table 2** and **Supplementary Table 3** and Debris Occurrences). This is in line with other deep-sea debris studies, e.g., 37% off the coast of California (Schlining et al., 2013). However, our observations likely underestimate the instances as, for example, some of the fauna may be too small to be visualized or there may be sub-lethal interactions.

The only readily observable negative interaction was entanglement by plastic or fishing gear occurring in 6.1% of debris observations. During this study, entanglement was observed only on deep-sea corals and resulted in physical damage (**Figure 6**), however, in other studies, deep-sea fauna have been observed entangled, including chemosynthetic methane-seep communities, fish, sponges and crustacea (Schlining et al., 2013; Quattrini et al., 2015; Woodall et al., 2015; Chiba et al., 2018). Woodall et al. (2015) observed three forms of entanglement: simple, benthic scraping, and ghost fishing. During this study, only simple entanglement was observed (**Figure 5**). However, this is still of concern as deep-sea corals are slow growing and slow to recover from disturbance (Williams et al., 2010).

This study focused on benthic or bentho-pelagic fauna and macro debris items visible in ROV imagery, but as has been exposed in the last six years, there are unseen threats from microplastics (Van Cauwenberghe et al., 2013; Woodall et al., 2014; Taylor et al., 2016; Courtene-Jones et al., 2017; Wieczorek et al., 2018; Courtene-Jones et al., 2019; Jamieson et al., 2019) and chemical pollution (Jamieson et al., 2017), which are ubiquitous in the deep ocean. Some cold-water corals, such as *Lophelia pertusa*, are particularly vulnerable to microplastics acting as physical barriers for food supply decreasing prey capture rates (Chapron et al., 2018). While the true knowledge of occurrences in the deep ocean and impacts to deep-sea fauna are only now being unearthed, studies in shallow waters can provide insight (Hall et al., 2015; Barboza et al., 2019a,b; Rotjan et al., 2019).

Additionally, during the degradation of marine macro debris, chemicals can leach into the water and either into animals in direct contact with the debris (e.g., via ingestion or attachment) or indirectly into animals further afield via water currents thereby widening the impact footprint. Multiple types of plastic debris are known to leach endocrine disruptors (e.g., phthalates and benzophenones) resulting in sub-lethal impacts including to

reproductive viability, as well as morbidity in shallow-water fauna (Hermabessiere et al., 2017; Windsor et al., 2018). Metals, either dissolved or as particulates, can also disrupt organism physiology and performance leading to severe impacts (Hauton et al., 2017). Toxicants from plastics, metals, and other forms of debris, could lead to reproductive failure in marine organisms at all community levels, and thereby raise the levels of population mortality in the deep ocean, however, this is further complicated by a lack of data on the toxicity of metals and other chemicals under deep-ocean conditions (low temperature, high hydrostatic pressure, and potentially altered pH). Therefore, impacts on shallow-water organisms may not be representative of the toxicity in deep-sea organisms (Hauton et al., 2017). Furthermore, it is challenging to understand not only the specific impacts of marine debris but also cumulative or synergistic impacts arising from increasing exploitation, pollution, and climate change in the global oceans (Laffoley et al., 2019). The true impact of the observed debris, as well as deep-ocean debris globally, is certainly underestimated.

Despite the many known negative impacts of marine debris, there is some potential utility of debris items by deep-sea fauna through the provision of shelter and attachment surfaces, a conclusion shared by Watters et al. (2010); Miyake et al. (2011), and Schlining et al. (2013). Woodall et al. (2015) also observed similar levels of fauna encrusting or sheltering in debris including corals and hydroids, crinoids, anemones, echinoids, and ophiuroids, as well as fauna using deep-sea debris to lay eggs, however, this was not observed during this study. The presence of debris may enable settlement of benthic taxa in novel habitats (e.g., hard-substrate settlers living on debris in otherwise sandy sediments); the resulting ecological impact of these anthropogenically facilitated interactions remains a topic for future investigation.

Slowing the Flow of Marine Debris

This study has provided added evidence that deep-sea debris are present in the central and western Pacific, even within protected areas far removed from settled land. The prevalence of marine debris, including in MPAs, will likely increase given that human use of the ocean, including the deep ocean, is expanding rapidly (Ramirez-Llodra et al., 2011). As indicated by multiple studies, as well as the United Nations' Sustainable Development Goal 14.1, every opportunity to stem the flow of debris into the ocean, and ultimately into the deep ocean, should be taken as many studies have shown negative impacts to marine life (e.g., Gall and Thompson, 2015; Lamb et al., 2018).

Reducing the production of debris, as well as preventing existing debris from entering the oceans is key and requires a global-level response (Vince and Hardesty, 2016; Laffoley et al., 2019). There is a need to implement and enforce stringent and novel policy actions at multiple levels of social and economic hierarchies, with an emphasis on managing and monitoring explicit pollution sources as point sources of origin, rather than ambiguous non-point sources of pollution (Laffoley et al., 2019). The International Maritime Organisation's Action Plan To Address Marine Plastics From Ships, adopted in late 2018, is a step in the right direction, however, is limited to one type of debris, which accounted for less than 20% of the deep-sea debris observed during this study. Innovating to replace single-use materials with biodegradable alternatives is also of importance but requires investment and political backing (Laffoley et al., 2019). Education and awareness will also play a role in mitigation. Finally, this study has reaffirmed that there is indeed a paucity of data on the extent of this issue as well as the impact on deep-sea fauna, and thus future studies should be directed to this important and timely cause.

DATA AVAILABILITY STATEMENT

All datasets generated for this study are included in the article/**Supplementary Material**. Raw data used in this study from CAPSTONE expeditions are publicity available through the NOAA archives. Citations and data access are included in **Supplementary Table 2**.

AUTHOR CONTRIBUTIONS

All authors were involved in the fieldwork in the Pacific Ocean and processed the ROV imagery. DA, RR, BK, TS, and KC constructed the figures. DA, RR, TS, and BK analyzed the data. DA wrote the bulk of the manuscript with assistance from all co-authors.

ACKNOWLEDGMENTS

We wish to thank the Officers and crew of the NOAA Ship *Okeanos Explorer* for shipboard support, NOAA OER, and the Global Foundation for Ocean Exploration team for their tremendous support during the fieldwork in the Pacific Ocean. We appreciate NOAA's support for CAPSTONE which was a collaboration between OER, Office of Marine and Aviation Operations, Pacific Island Fisheries Science Center, Pacific Islands Regional Office, Deep Sea Coral Research and Technology Program, Office of National Marine Sanctuaries, National Center for Environmental Information, National Ocean Service, National Environmental Satellite, Data, and Information Service, Oceanic and Atmospheric Research, and National Marine Fisheries Service. We also thank the Schmidt Ocean Institute, the Master and crew, the Master and crew of the RV *Falkor*, Kiribati Observer Arenteiti Tekiau, and Expedition Chief Scientist Erik Cordes, while working in the Phoenix Islands Protected Area under PIPA Research Permit #4/17, funded by NOAA OER (#NA17OAR0110083 awarded to RR, TS, and Erik Cordes). Further thanks to the scientists on board and on shore during all voyages. DA has received funding from the European Union's Horizon 2020 Research and Innovation Program under the Marie Skłodowska-Curie grant agreement number 747946. DA would also like to acknowledge TBA21-Academy for providing a space for peaceful writing. CAPSTONE was completed in accordance with all regulations regarding environmental compliance and local permitting including the following permits: Kiribati Phoenix Islands Protected Area permit #1/17, Commonwealth of the Northern

Mariana Islands Department of Lands and Natural Resources permit #03345; Hawai'i Department of Land and Natural Resources permit #SAP-2016-64; Cook Islands Marae Moana Permit #05/17, National Marine Sanctuary of American Samoa permit #NMAS-2017-001; American Samoa Department of Marine and Wildlife Resources permit #2017/001; U.S. Fish and Wildlife Convention on International Trade in Endangered Species (CITES) import permit #17US36207C/9; Papahānaumokuākea Marine National Monument permit #PMN-2015-018; and Marshall Islands Ministry of Foreign Affairs #US/98-15. Any use of trade, product, or firm names is for descriptive purposes only and does not imply endorsement by the United States Government.

SUPPLEMENTARY MATERIAL

The Supplementary Material for this article can be found online at: https://www.frontiersin.org/articles/10.3389/fmars.2020.00369/full#supplementary-material

REFERENCES

Auscavitch, S. R., Deere, M. C., Keller, A. G., Rotjan, R. D., Shank, T. M., and Cordes, E. E. (2019). Oceanographic drivers of deep-sea coral species distribution and community assembly on seamounts, islands, atolls, and reefs within the Phoenix Islands protected area. *Front. Mar. Sci.* 7:42. doi: 10.3389/fmars.2020.00042

Barboza, L. G. A., Cózar, A., Gimenez, B. C. G., Barros, T. L., Kershaw, P. J., and Guilhermino, L. (2019a). "Chapter 17 – Macroplastics pollution in the marine environment," in *World Seas Volume III: Ecological Issues and Environmental Impacts*, ed. C. Sheppard (London: Elsevier), 305–328. doi: 10.1016/b978-0-12-805052-1.00019-x

Barboza, L. G. A., Frias, J. P. G. L., Booth, A. M., Vieira, L. R. J., Baker, J., Foster, G., et al. (2019b). "Chapter 18 – Microplastics pollution in the marine environment," in *World Seas Volume III: Ecological Issues and Environmental Impacts*, ed. C. Sheppard (London: Elsevier).

Barnes, D. K. A., Galgani, F., Thompson, R. C., and Morton, B. (2009). Accumulation and fragmentation of plastic debris in global environments. *Philos. Trans. R. Soc. B Biol. Sci.* 364, 1985–1998. doi: 10.1098/rstb.2008.0205

Campbell, L. M., and Gray, N. J. (2019). Area expansion versus effective and equitable management in international marine protected areas goals and targets. *Mar. Policy* 100, 192–199. doi: 10.1016/j.marpol.2018.11.030

Cantwell, K., Elliott, K. P., and Kennedy, B. R. C. (2018). Deepwater exploration of the pacific remote islands marine national monument. *Oceanography* 31:126.

Cau, A., Bellodi, A., Moccia, D., Mulas, A., Pesci, P., Cannas, R., et al. (2018). Dumping to the abyss: single-use marine litter invading bathyal plains of the Sardinian margin (Tyrrhenian Sea). *Mar. Pollut. Bull.* 135, 845–851. doi: 10.1016/j.marpolbul.2018.08.007

Chapron, L., Peru, E., Engler, A., Ghiglione, J. F., Meistertzheim, A. L., Pruski, A. M., et al. (2018). Macro- and microplastics affect cold-water corals growth, feeding and behaviour. *Sci. Rep.* 8:15299. doi: 10.1038/s41598-018-33683-6

Chiba, S., Saito, H., Fletcher, R., Yogi, T., Kayo, M., Miyagi, S., et al. (2018). Human footprint in the abyss: 30 year records of deep-sea plastic debris. *Mar. Policy* 96, 204–212. doi: 10.1016/j.marpol.2018.03.022

Clark, M. R., and Koslow, J. A. (2007). "Impacts of fisheries on seamounts," in *Seamounts: Ecology, Fisheries, and Conservation*, eds T. J. Pitcher, T. Morato, P. J. B. Hart, M. R. Clark, N. Haggan, and R. S. Santos (Hoboken, NJ: John Wiley & Sons, Inc), 413–441. doi: 10.1002/9780470691953.ch19

Courtene-Jones, W., Quinn, B., Ewins, C., Gary, S. F., and Narayanaswamy, B. E. (2019). Consistent microplastic ingestion by deep-sea invertebrates over the last four decades (1976–2015), a study from the North East Atlantic. *Environ. Pollut.* 244, 503–512. doi: 10.1016/j.envpol.2018.10.090

Courtene-Jones, W., Quinn, B., Gary, S. F., Mogg, A. O. M., and Narayanaswamy, B. E. (2017). Microplastic pollution identified in deep-sea water and ingested by benthic invertebrates in the Rockall Trough, North Atlantic Ocean. *Environ. Pollut.* 231, 271–280. doi: 10.1016/j.envpol.2017.08.026

Galgani, F., Leaute, J. P., Moguedet, P., Souplet, A., Verin, Y., Carpentier, A., et al. (2000). Litter on the Sea Floor Along European Coasts. *Mar. Pollut. Bull.* 40, 516–527. doi: 10.1016/s0025-326x(99)00234-9

Galil, B., Golik, A., and Turkay, M. (1995). Litter at the bottom of the sea: a sea bed survey in the Eastern Mediterranean. *Mar. Pollut. Bull.* 30, 22–24. doi: 10.1016/0025-326x(94)00103-g

Gall, S. C., and Thompson, R. C. (2015). The impact of debris on marine life. *Mar. Pollut. Bull.* 92, 170–179. doi: 10.1016/j.marpolbul.2014.12.041

Gregory, T., Lovalvo, D., Mohr, B., McLetchie, K., and Ryan, M. (2016). Advancing undersea technology. *Oceanography* 29, 52–55. doi: 10.5670/oceanog.2016.supplement.01

Grøsvik, B. E., Prokhorova, T., Eriksen, E., Krivosheya, P., Horneland, P. A., and Prozorkevich, D. (2018). Assessment of marine litter in the Barents sea, a part of the joint Norwegian–Russian ecosystem survey. *Front. Mar. Sci.* 5:72. doi: 10.3389/fmars.2018.00072

Hall, N. M., Berry, K. L. E., Rintoul, L., and Hoogenboom, M. O. (2015). Microplastic ingestion by scleractinian corals. *Mar. Biol.* 162, 725–732. doi: 10.1007/s00227-015-2619-7

Hauton, C., Brown, A., Thatje, S., Mestre, N. C., Bebianno, M. J., Martins, I., et al. (2017). Identifying toxic impacts of metals potentially released during deep-sea mining—a synthesis of the challenges to quantifying risk. *Front. Mar. Sci.* 4:368. doi: 10.3389/fmars.2017.00368

Hermabessiere, L., Dehaut, A., Paul-Pont, I., Lacrois, C., Jezequel, R., Soudant, P., et al. (2017). Occurrence and effects of plastic additives on marine environments and organisms: a review. *Chemosphere* 182, 781–793. doi: 10.1016/j.chemosphere.2017.05.096

Jamieson, A. J., Brooks, L. S. R., Reid, W. D. K., Piertney, S. B., Narayanaswamy, B. E., and Linley, T. D. (2019). Microplastics and synthetic particles ingested by deep-sea amphipods in six of the deepest marine ecosystems on Earth. *R. Soc. Open Sci.* 6:180667. doi: 10.1098/rsos.180667

Jamieson, A. J., Malkocs, T., Piertney, S. B., Fujii, T., and Zhang, Z. (2017). Bioaccumulation of persistent organic pollutants in the deepest ocean fauna. *Nat. Ecol. Evol.* 1:0051. doi: 10.1038/s41559-016-0051

Jenkyns, R., Gervais, F., and Pirenne, B. (2013). "SeaScribe: an annotation software for Remotely Operated Vehicle dive operations," in *Proceedings of the 2013 OCEANS – San Diego* (San Diego, CA: IEEE), doi: 10.23919/OCEANS.2013.6741250

Keller, A., Fruh, E., Johnson, M., Simon, V., and Mcgourty, C. (2010). Distribution and abundance of anthropogenic marine debris along the shelf and slope of the US West Coast. *Mar. Pollut. Bull.* 60, 692–700. doi: 10.1016/j.marpolbul.2009.12.006

Kennedy, B. R., Cantwell, K., Malik, M., Kelley, C., Potter, J., Elliott, K., et al. (2019). The unknown and the unexplored: insights into the Pacific deep-sea following NOAA CAPSTONE expeditions. *Front. Mar. Sci.* 6:480. doi: 10.3389/fmars.2019.00480

Kennedy, B. R. C., Elliott, K. P., Cantwell, K., and Mesick, S. (2016). Telepresence-enabled exploration with NOAA ship okeanos explorer. *Oceanography* 29, 50–51. doi: 10.5670/oceanog.2016.supplement.01

Laffoley, D., Baxter, J. M., Amon, D. J., Currie, D. E., Downs, C. A., Hall-Spencer, J. M., et al. (2019). Eight urgent, fundamental and simultaneous steps needed to restore ocean health, and the consequences for humanity and the planet of inaction or delay. *Aquat. Conserv.* 30, 194–208. doi: 10.1002/aqc.3182

Lamb, J. B., Willis, B. L., Fiorenza, E. A., Couch, C. S., Howard, R., Rader, D. N., et al. (2018). Plastic waste associated with disease on coral reefs. *Science* 359, 460–462. doi: 10.1126/science.aar3320

Leonardi, A., Armor, J., Montanio, P., and Werner, C. (2018). CAPSTONE: NOAA's campaign to address Pacific monument science, technology, and ocean needs. *Oceanography* 29, 48–52.

Malik, M., Rees, G., Cromwell, M., Robinson, J., and France, S. C. (2020). OER-ONC collaboration to improve video annotations. *Oceanography* 33:120. doi: 10.5670/oceanog.2020.supplement.01

McKinnie, D., Rotjan, R. D., and Lelei Peau A. (2018). "Exploring the pacific through international partnerships," in *New frontiers in ocean exploration: The E/V Nautilus, NOAA Ship Okeanos Explorer, and R/V Falkor 2017 Field Season*. eds N. A. Raineault, J. Flanders, and A. Bowman. Oceanography, 31:126.

Miyake, H., Shibata, H., and Furushima, Y. (2011). "Deep-sea litter study using deep-sea observation tools," in *Interdisciplinary Studies on Environmental Chemistry-Marine Environmental Modeling and Analysis*, eds K. Omori, X. Guo, N. Yoshie, N. Fujii, I. C. Handoh, A. Isobe, et al. (Setagaya-ku: Terrapub), 261–269.

Pham, C. K., Ramirez-Llodra, E., Alt, C. H. S., Amaro, T., Bergmann, M., Canals, M., et al. (2014). Marine litter distribution and density in European seas, from the shelves to deep basins. *PLoS One* 9:e95839. doi: 10.1371/journal.pone.0095839

Quattrini, A. M., Nizinski, M. S., Chaytor, J. D., Demopoulos, A. W. J., Roark, E. B., France, S. C., et al. (2015). Exploration of the canyon-incised continental margin of the northeastern United States reveals dynamic habitats and diverse communities. *PLoS One* 10:e0139904. doi: 10.1371/journal.pone.0139904

Ramirez-Llodra, E., Demol, B., Company, J. B., Coll, M., and Sardà, F. (2013). Effects of natural and anthropogenic processes in the distribution of marine litter in the deep Mediterranean Sea. *Prog. Oceanogr.* 118, 273–287. doi: 10.1016/j.pocean.2013.07.027

Ramirez-Llodra, E., Tyler, P. A., Baker, M. C., Askel Bergstad, O., Clark, M. R., Escobar Briones, E., et al. (2011). Man and the last great wilderness: human impact on the deep sea. *PLoS One* 6:e22588. doi: 10.1371/journal.pone.0022588

Rotjan, R. D., Sharp, K. H., Gauthier, A. E., Yelton, R., Lopez, E. M. B., Carilli, J., et al. (2019). Patterns, dynamics and consequences of microplastic ingestion by the temperate coral, *Astrangia poculata*. *Proc. R. Soc. B* 286:20190726. doi: 10.1098/rspb.2019.0726

Schlining, K., Von Thun, S., Kuhnz, L., Schlining, B., Lundsten, L., Jacobsen Stout, N., et al. (2013). Debris in the deep: using a 22-year video annotation database to survey marine litter in Monterey Canyon, central California, USA. *Deep Sea Res. Part I Oceanogr. Res. Pap.* 79, 96–105. doi: 10.1016/j.dsr.2013.05.006

Schmidt, C., Krauth, T., and Wagner, S. (2017). Export of plastic debris by rivers into the sea. *Environ. Sci. Technol.* 51, 12246–12253. doi: 10.1021/acs.est.7b02368

Taylor, M. L., Gwinnett, C., Robinson, L. F., and Woodall, L. C. (2016). Plastic microfibre ingestion by deep-sea organisms. *Sci. Rep.* 6:33997. doi: 10.1038/srep33997

Van Cauwenberghe, L., Vanreusel, A., Mees, J., and Janssen, C. R. (2013). Microplastic pollution in deep-sea sediments. *Environ. Pollut.* 182, 495–499. doi: 10.1016/j.envpol.2013.08.013

Vince, J., and Hardesty, B. D. (2016). Plastic pollution challenges in marine and coastal environments: from local to global governance. *Restor. Ecol.* 25, 123–128. doi: 10.1111/rec.12388

Watters, D., Yoklavich, M., Love, M., and Schroeder, D. (2010). Assessing marine debris in deep seafloor habitats off California. *Mar. Pollut. Bull.* 60, 131–138. doi: 10.1016/j.marpolbul.2009.08.019

Wieczorek, A. M., Morrison, L., Croot, P. L., Allcock, A. L., Macloughlin, E., Savard, O., et al. (2018). Frequency of microplastics in mesopelagic fishes from the Northwest Atlantic. *Front. Mar. Sci.* 5:39. doi: 10.3389/fmars.2018.00039

Williams, A., Schlacher, T. A., Rowden, A. A., Althaus, F., Clark, M. R., Bowden, D. A., et al. (2010). Seamount megabenthic assemblages fail to recover from trawling impacts. *Mar. Ecol.* 31, 183–199. doi: 10.1111/j.1439-0485.2010.00385.x

Windsor, F. M., Ormerod, S. J., and Tyler, C. R. (2018). Endocrine disruption in aquatic systems: up-scaling research to address ecological consequences. *Biol. Rev.* 93, 626–641. doi: 10.1111/brv.12360

Woodall, L. C., Robinson, L. F., Rogers, A. D., Narayanaswamy, B. E., and Paterson, G. L. J. (2015). Deep sea litter: a comparison of seamounts, banks and a ridge in the Atlantic and Indian Oceans reveals both environmental and anthropogenic factors impact accumulation and composition. *Front. Mar. Sci.* 2:3. doi: 10.3389/fmars.2015.00003

Woodall, L. C., Sanchez-Vidal, A., Canals, M., Paterson, G. L., Coppock, R., Sleight, V., et al. (2014). The deep sea is a major sink for microplastic debris. *R. Soc. Open Sci.* 1:140317. doi: 10.1098/rsos.140317

Conflict of Interest: The authors declare that the research was conducted in the absence of any commercial or financial relationships that could be construed as a potential conflict of interest.

Copyright © 2020 Amon, Kennedy, Cantwell, Suhre, Glickson, Shank and Rotjan. This is an open-access article distributed under the terms of the Creative Commons Attribution License (CC BY). The use, distribution or reproduction in other forums is permitted, provided the original author(s) and the copyright owner(s) are credited and that the original publication in this journal is cited, in accordance with accepted academic practice. No use, distribution or reproduction is permitted which does not comply with these terms.

Advantages of publishing in Frontiers

OPEN ACCESS
Articles are free to read for greatest visibility and readership

FAST PUBLICATION
Around 90 days from submission to decision

HIGH QUALITY PEER-REVIEW
Rigorous, collaborative, and constructive peer-review

TRANSPARENT PEER-REVIEW
Editors and reviewers acknowledged by name on published articles

Frontiers
Avenue du Tribunal-Fédéral 34
1005 Lausanne | Switzerland

Visit us: www.frontiersin.org
Contact us: frontiersin.org/about/contact

REPRODUCIBILITY OF RESEARCH
Support open data and methods to enhance research reproducibility

DIGITAL PUBLISHING
Articles designed for optimal readership across devices

FOLLOW US
@frontiersin

IMPACT METRICS
Advanced article metrics track visibility across digital media

EXTENSIVE PROMOTION
Marketing and promotion of impactful research

LOOP RESEARCH NETWORK
Our network increases your article's readership